Principles of Helicopter Aerodynamics

Second Edition

The helicopter is truly a unique form of aircraft and a mastery of modern aeronautical engineering that fulfills a variety of civilian and military roles. The usefulness of the helicopter lies in its unique ability to take off and land vertically on almost any terrain, to hover stationary relative to the ground, and to fly forward, backward, or sideways. These unique flying characteristics, however, come at a price, including complex aerodynamic problems, significant vibrations, high levels of noise, and relatively large power requirements compared to a fixed-wing aircraft of the same weight.

This book, written by an internationally recognized teacher and researcher in the field, provides a thorough, modern treatment of the aerodynamic principles of helicopters and other rotating-wing vertical lift aircraft such as tilt-rotors and autogiros. The first part of the text begins with a unique technical history of helicopter flight and then covers basic methods of rotor aerodynamic analysis and related issues associated with the performance of the helicopter and its aerodynamic design. The second part is devoted to more advanced topics in helicopter aerodynamics, including airfoil flows, unsteady aerodynamics, dynamic stall, rotor wakes and rotor–airframe aerodynamic interactions. The third part of the book contains chapters on autogiros and advanced methods of helicopter aerodynamic analysis. A companion chapter on the aerodynamics of wind turbines recognizes both the commonalities and differences with the aerodynamic problems found on helicopters. Every chapter is extensively illustrated and concludes with a comprehensive bibliography and a set of homework problems.

Advanced undergraduate and graduate students, as well as practicing engineers and researchers, will welcome this thorough and up-to-date text on the principles of helicopter and rotating-wing aerodynamics.

Dr. J. Gordon Leishman is the Minta Martin Chair of Engineering and Professor of Aerospace Engineering at the University of Maryland. He is a former aerodynamicist at Westland Helicopters and has written extensively on topics in helicopter aerodynamics. Dr. Leishman is a Fellow of the Royal Aeronautical Society and an Associate Fellow of the American Institute of Aeronautics & Astronautics. He is also the Editor-in-Chief for the *Journal of the American Helicopter Society*.

Cambridge Aerospace Series

Editors
Wei Shyy
and
Michael J. Rycroft

1. J.M. Rolfe and K.J. Staples (eds.): *Flight Simulation*
2. P. Berlin: *The Geostationary Applications Satellite*
3. M.J.T. Smith: *Aircraft Noise*
4. N.X. Vinh: *Flight Mechanics of High-Performance Aircraft*
5. W.A. Mair and D.L. Birdsall: *Aircraft Performance*
6. M.J. Abzug and E.E. Larrabee: *Airplane Stability and Control*
7. M.J. Sidi: *Spacecraft Dynamics and Control*
8. J.D. Anderson: *A History of Aerodynamics*
9. A.M. Cruise, J.A. Bowles, C.V. Goodall, and T.J. Patrick: *Principles of Space Instrument Design*
10. G.A. Khoury and J.D. Gillett (eds.): *Airship Technology*
11. J. Fielding: *Introduction to Aircraft Design*
12. J.G. Leishman: *Principles of Helicopter Aerodynamics*
13. J. Katz and A. Plotkin: *Low Speed Aerodynamics*, 2nd Edition
14. M.J. Abzug and E.E. Larrabee: *Airplane Stability and Control: A History of the Technologies that Made Aviation Possible*, 2nd Edition
15. D.H. Hodges and G.A. Pierce: *Introduction to Structural Dynamics and Aeroelasticity*
16. W. Fehse: *Automatic Rendezvous and Docking of Spacecraft*
17. R.D. Flack: *Fundamentals of Jet Propulsion with Applications*
18. J.G. Leishman: *Principles of Helicopter Aerodynamics*, 2nd Edition
19. E.A. Baskharone: *Principles of Turbomachinery in Air-Breathing Engines*

Principles of Helicopter Aerodynamics

Second Edition

J. GORDON LEISHMAN, D.Sc.(Eng.), Ph.D., F.R.Ae.S.
University of Maryland

CAMBRIDGE
UNIVERSITY PRESS

CAMBRIDGE UNIVERSITY PRESS
Cambridge, New York, Melbourne, Madrid, Cape Town, Singapore, São Paulo, Delhi

Cambridge University Press
32 Avenue of the Americas, New York, NY 10013-2473, USA

www.cambridge.org
Information on this title: www.cambridge.org/9780521858601

© Cambridge University Press 2006

This publication is in copyright. Subject to statutory exception
and to the provisions of relevant collective licensing agreements,
no reproduction of any part may take place without
the written permission of Cambridge University Press.

First published 2000
Reprinted with corrections 2001, 2002, 2003
Second edition 2006
Reprinted 2007, 2008

Printed in the United States of America

A catalog record for this publication is available from the British Library.

Library of Congress Cataloging in Publication Data

Leishman, J. Gordon.
Principles of helicopter aerodynamics / J. Gordon Leishman. – 2nd ed.
p. cm. – (Cambridge aerospace series)
Includes bibliographical references and index.
ISBN 0-521-85860-7 (hardback)
1. Helicopters – Aerodynamics. I. Title. II. Series.
TL716.L43 2005
629.133'352 – dc22 2005025467

ISBN 978-0-521-85860-1 hardback

Cambridge University Press has no responsibility for
the persistence or accuracy of URLs for external or
third-party Internet Web sites referred to in this publication
and does not guarantee that any content on such
Web sites is, or will remain, accurate or appropriate.

TO MY STUDENTS

in appreciation of all they have taught me

Contents

Preface to the Second Edition *page* xix
Preface to the First Edition xxiii
Acknowledgments xxvii
List of Main Symbols xxxi

1 Introduction: A History of Helicopter Flight 1

1.1 Rising Vertically 1
1.2 Producing Thrust 4
1.3 Key Technical Problems in Attaining Vertical Flight 5
1.4 Early Thinking 6
1.5 The Hoppers 11
1.6 The First Hoverers 17
1.7 Not Quite a Helicopter 20
1.8 Engines: A Key Enabling Technology 23
1.9 On the Verge of Success 25
1.10 The First Successes 28
1.11 Toward Mass Production 33
1.12 Maturing Technology 40
1.13 Compounds, Tilt-Wings, and Tilt-Rotors 47
1.14 Chapter Review 49
1.15 Questions 50
Bibliography 51

2 Fundamentals of Rotor Aerodynamics 55

2.1 Introduction 55
2.2 Momentum Theory Analysis in Hovering Flight 58
2.2.1 Flow Near a Hovering Rotor 59
2.2.2 Conservation Laws of Aerodynamics 60
2.2.3 Application to a Hovering Rotor 61
2.3 Disk Loading and Power Loading 65
2.4 Induced Inflow Ratio 66
2.5 Thrust and Power Coefficients 66
2.6 Comparison of Theory with Measured Rotor Performance 68
2.7 Nonideal Effects on Rotor Performance 68
2.8 Figure of Merit 70
2.9 Estimating Nonideal Effects from Rotor Measurements 74
2.10 Induced Tip Loss 74
2.11 Rotor Solidity and Blade Loading Coefficient 77
2.12 Power Loading 80

2.13 Momentum Analysis in Axial Climb and Descent 81
2.13.1 Axial Climb 81
2.13.2 Axial Descent 83
2.13.3 Region between Hover and Windmill State 86
2.13.4 Power Required in Axial Climbing and Descending Flight 87
2.13.5 Four Working States of the Rotor in Axial Flight 88
2.13.6 Vortex Ring State 90
2.13.7 Autorotation 91
2.14 Momentum Analysis in Forward Flight 93
2.14.1 Induced Velocity in Forward Flight 95
2.14.2 Special Case, $\alpha = 0$ 96
2.14.3 Numerical Solution to Inflow Equation 97
2.14.4 General Form of the Inflow Equation 99
2.14.5 Validity of the Inflow Equation 99
2.14.6 Rotor Power Requirements in Forward Flight 99
2.15 Other Applications of the Momentum Theory 101
2.15.1 Coaxial Rotor Systems 101
2.15.2 Tandem Rotor Systems 106
2.16 Chapter Review 110
2.17 Questions 110
Bibliography 113

3 Blade Element Analysis 115

3.1 Introduction 115
3.2 Blade Element Analysis in Hover and Axial Flight 117
3.2.1 Integrated Rotor Thrust and Power 119
3.2.2 Thrust Approximations 119
3.2.3 Torque–Power Approximations 122
3.2.4 Tip-Loss Factor 122
3.3 Blade Element Momentum Theory (BEMT) 125
3.3.1 Assumed Radial Distributions of Inflow on the Blades 126
3.3.2 Radial Inflow Equation 127
3.3.3 Ideal Twist 128
3.3.4 BEMT: Numerical Solution 130
3.3.5 Distributions of Inflow and Airloads 131
3.3.6 Effects of Swirl Velocity 134
3.3.7 The Optimum Hovering Rotor 135
3.3.8 Circulation Theory of Lift 138
3.3.9 Power Estimates for the Rotor 139
3.3.10 Prandtl's Tip-Loss Function 141
3.3.11 Blade Design and Figure of Merit 145
3.3.12 BEMT in Climbing Flight 146
3.3.13 Further Comparisons of BEMT with Experiment 148
3.3.14 Compressibility Corrections to Rotor Performance 150
3.4 Equivalent Blade Chords and Weighted Solidity 152
3.4.1 Mean Wing Chords 152
3.4.2 Thrust Weighted Solidity 153
3.4.3 Power–Torque Weighted Solidity 153
3.4.4 Weighted Solidity of the Optimum Rotor 154

3.4.5 Weighted Solidities of Tapered Blades 154
3.4.6 Mean Lift Coefficient 155
3.5 Blade Element Analysis in Forward Flight 156
3.5.1 Determining Blade Forces 156
3.5.2 Definition of the Approximate Induced Velocity Field 158
3.6 Chapter Review 166
3.7 Questions 167
Bibliography 169

4 Rotating Blade Motion 171

4.1 Introduction 171
4.2 Types of Rotors 172
4.3 Equilibrium about the Flapping Hinge 174
4.4 Equilibrium about the Lead–Lag Hinge 176
4.5 Equation of Motion for a Flapping Blade 178
4.6 Physical Description of Blade Flapping 183
4.6.1 Coning Angle 183
4.6.2 Longitudinal Flapping Angle 183
4.6.3 Lateral Flapping Angle 185
4.6.4 Higher Harmonics of Blade Flapping 185
4.7 Dynamics of Blade Flapping with a Hinge Offset 186
4.8 Blade Feathering and the Swashplate 188
4.9 Review of Rotor Reference Axes 190
4.10 Dynamics of a Lagging Blade with a Hinge Offset 194
4.11 Coupled Flap–Lag Motion 196
4.12 Coupled Pitch–Flap Motion 198
4.13 Other Types of Rotors 199
4.13.1 Teetering Rotor 199
4.13.2 Semi-Rigid or Hingeless Rotors 200
4.14 Introduction to Rotor Trim 202
4.14.1 Equations for Free-Flight Trim 204
4.14.2 Typical Trim Solution Procedure for Level Flight 207
4.15 Chapter Review 209
4.16 Questions 209
Bibliography 211

5 Helicopter Performance 212

5.1 Introduction 212
5.2 The International Standard Atmosphere 212
5.3 Hovering and Axial Climb Performance 215
5.4 Forward Flight Performance 217
5.4.1 Induced Power 218
5.4.2 Blade Profile Power 219
5.4.3 Compressibility Losses and Tip Relief 220
5.4.4 Reverse Flow 223
5.4.5 Parasitic Power 225
5.4.6 Climb Power 226
5.4.7 Tail Rotor Power 226
5.4.8 Total Power 227

5.5 Performance Analysis 228
5.5.1 Effect of Gross Weight 228
5.5.2 Effect of Density Altitude 229
5.5.3 Lift-to-Drag Ratios 229
5.5.4 Climb Performance 230
5.5.5 Engine Fuel Consumption 231
5.5.6 Speed for Minimum Power 233
5.5.7 Speed for Maximum Range 235
5.5.8 Range–Payload and Endurance–Payload Relations 237
5.5.9 Maximum Altitude or Ceiling 238
5.5.10 Factors Affecting Maximum Attainable Forward Speed 239
5.5.11 Performance of Coaxial and Tandem Dual Rotor Systems 240
5.6 Autorotational Performance 242
5.6.1 Autorotation in Forward Flight 246
5.6.2 Height–Velocity (H–V) Curve 249
5.6.3 Autorotation Index 251
5.7 Vortex Ring State (VRS) 252
5.7.1 Quantification of VRS Effects 252
5.7.2 Implications of VRS on Flight Boundary 256
5.8 Ground Effect 257
5.8.1 Hovering Flight Near the Ground 258
5.8.2 Forward Flight Near the Ground 260
5.9 Performance in Maneuvering Flight 263
5.9.1 Steady Maneuvers 264
5.9.2 Transient Maneuvers 265
5.10 Factors Influencing Performance Degradation 269
5.11 Chapter Review 271
5.12 Questions 272
Bibliography 273

6 Aerodynamic Design of Helicopters 277

6.1 Introduction 277
6.2 Overall Design Requirements 277
6.3 Conceptual and Preliminary Design Processes 279
6.4 Design of the Main Rotor 280
6.4.1 Rotor Diameter 281
6.4.2 Tip Speed 283
6.4.3 Rotor Solidity 285
6.4.4 Number of Blades 288
6.4.5 Blade Twist 290
6.4.6 Blade Planform and Tip Shape 292
6.4.7 Airfoil Sections 295
6.5 Case Study: The BERP Rotor 301
6.6 Fuselage Aerodynamic Design Issues 304
6.6.1 Fuselage Drag 304
6.6.2 Vertical Drag and Download Penalty 307
6.6.3 Vertical Drag Recovery 309
6.6.4 Fuselage Side-Force 310

6.7 Empennage Design 311
6.7.1 Horizontal Stabilizer 311
6.7.2 Vertical Stabilizer 312
6.8 Role of Wind Tunnels in Aerodynamic Design 313
6.9 Design of Tail Rotors 314
6.9.1 Physical Size 315
6.9.2 Thrust Requirements 315
6.9.3 Precessional Stall Issues 317
6.9.4 "Pushers" versus "Tractors" 318
6.9.5 Design Requirements 319
6.9.6 Representative Tail Rotor Designs 320
6.10 Other Anti-Torque Devices 321
6.10.1 Fan-in-Fin 321
6.10.2 NOTAR Design 324
6.11 High-Speed Rotorcraft 325
6.11.1 Compound Helicopters 325
6.11.2 Tilt-Rotors 327
6.11.3 Other High-Speed Concepts 328
6.12 Smart Rotor Systems 330
6.13 Human-Powered Helicopter 331
6.14 Hovering Micro Air Vehicles 334
6.15 Chapter Review 338
6.16 Questions 338
Bibliography 340

7 Aerodynamics of Rotor Airfoils 347

7.1 Introduction 347
7.2 Helicopter Rotor Airfoil Requirements 348
7.3 Reynolds Number and Mach Number Effects 350
7.3.1 Reynolds Number 350
7.3.2 Concept of the Boundary Layer 352
7.3.3 Mach Number 357
7.3.4 Model Rotor Similarity Parameters 359
7.4 Airfoil Shape Definition 360
7.5 Airfoil Pressure Distributions 363
7.5.1 Pressure Coefficient 363
7.5.2 Critical Pressure Coefficient 364
7.5.3 Synthesis of Chordwise Pressure 365
7.5.4 Measurements of Chordwise Pressure 366
7.6 Aerodynamics of a Representative Airfoil Section 368
7.6.1 Integration of Distributed Forces 368
7.6.2 Pressure Integration 370
7.6.3 Representative Force and Moment Results 371
7.7 Pitching Moment and Related Issues 374
7.7.1 Aerodynamic Center 375
7.7.2 Center of Pressure 377
7.7.3 Effect of Airfoil Shape on Pitching Moment 378
7.7.4 Use of Trailing Edge Tabs 381
7.7.5 Reflexed Airfoils 383

7.8 Drag 383
7.9 Maximum Lift and Stall Characteristics 385
7.9.1 Effects of Reynolds Number 389
7.9.2 Effects of Mach Number 392
7.10 Advanced Rotor Airfoil Design 398
7.11 Representing Static Airfoil Characteristics 401
7.11.1 Linear Aerodynamic Models 401
7.11.2 Nonlinear Aerodynamic Models 403
7.11.3 Table Look-Up 403
7.11.4 Direct Curve Fitting 403
7.11.5 Beddoes Method 404
7.11.6 High Angle of Attack Range 407
7.12 Circulation Controlled Airfoils 409
7.13 Very Low Reynolds Number Airfoil Characteristics 411
7.14 Effects of Damage on Airfoil Performance 412
7.15 Chapter Review 415
7.16 Questions 416
Bibliography 418

8 Unsteady Airfoil Behavior 423

8.1 Introduction 423
8.2 Sources of Unsteady Aerodynamic Loading 424
8.3 Concepts of the Blade Wake 424
8.4 Reduced Frequency and Reduced Time 427
8.5 Unsteady Attached Flow 428
8.6 Principles of Quasi-Steady Thin-Airfoil Theory 429
8.7 Theodorsen's Theory 431
8.7.1 Pure Angle of Attack Oscillations 434
8.7.2 Pure Plunging Oscillations 436
8.7.3 Pitching Oscillations 438
8.8 The Returning Wake: Loewy's Problem 441
8.9 Sinusoidal Gust: Sears's Problem 442
8.10 Indicial Response: Wagner's Problem 446
8.11 Sharp-Edged Gust: Küssner's Problem 448
8.12 Traveling Sharp-Edged Gust: Miles's Problem 450
8.13 Time-Varying Incident Velocity 453
8.14 General Application of the Indicial Response Method 457
8.14.1 Recurrence Solution to the Duhamel Integral 459
8.14.2 State-Space Solution for Arbitrary Motion 463
8.15 Indicial Method for Subsonic Compressible Flow 465
8.15.1 Approximations to the Indicial Response 467
8.15.2 Indicial Lift from Angle of Attack 469
8.15.3 Indicial Lift from Pitch Rate 470
8.15.4 Determination of Indicial Function Coefficients 471
8.15.5 Indicial Pitching Moment from Angle of Attack 474
8.15.6 Indicial Pitching Moment from Pitch Rate 474
8.15.7 Unsteady Axial Force and Airfoil Drag 476
8.15.8 State-Space Aerodynamic Model for Compressible Flow 478
8.15.9 Comparison with Experiment 480

8.16 Nonuniform Vertical Velocity Fields 483
8.16.1 Exact Subsonic Linear Theory 483
8.16.2 Approximations to the Sharp-Edged Gust Functions 484
8.16.3 Response to an Arbitrary Vertical Gust 487
8.16.4 Blade–Vortex Interaction (BVI) Problem 488
8.16.5 Convecting Vertical Gusts in Subsonic Flow 490
8.17 Time-Varying Incident Mach Number 492
8.18 Unsteady Aerodynamics of Flaps 492
8.18.1 Incompressible Flow Theory 493
8.18.2 Subsonic Flow Theory 497
8.18.3 Comparison with Measurements 500
8.19 Principles of Noise Produced by Unsteady Forces 502
8.19.1 Retarded Time and Source Time 504
8.19.2 Wave Tracing 505
8.19.3 Compactness 506
8.19.4 Trace or Phase Mach Number 507
8.19.5 Ffowcs-Williams–Hawkins Equation 508
8.19.6 BVI Acoustic Model Problem 510
8.19.7 Comparison of Aeroacoustic Methods 513
8.19.8 Methods of Rotor Noise Reduction 515
8.20 Chapter Review 516
8.21 Questions 517
Bibliography 519

9 Dynamic Stall 525

9.1 Introduction 525
9.2 Flow Morphology of Dynamic Stall 527
9.3 Dynamic Stall in the Rotor Environment 529
9.4 Effects of Forcing Conditions on Dynamic Stall 531
9.5 Modeling of Dynamic Stall 535
9.5.1 Semi-Empirical Models of Dynamic Stall 536
9.5.2 Capabilities of Dynamic Stall Modeling 541
9.5.3 Future Modeling Goals with Semi-Empirical Models 543
9.6 Torsional Damping 545
9.7 Effects of Sweep Angle on Dynamic Stall 547
9.8 Effect of Airfoil Shape on Dynamic Stall 551
9.9 Three-Dimensional Effects on Dynamic Stall 553
9.10 Time-Varying Velocity Effects on Dynamic Stall 556
9.11 Prediction of In-Flight Airloads 557
9.12 Stall Control 559
9.13 Chapter Review 560
9.14 Questions 561
Bibliography 562

10 Rotor Wakes and Blade Tip Vortices 567

10.1 Introduction 567
10.2 Flow Visualization Techniques 568
10.2.1 Natural Condensation Effects 568
10.2.2 Smoke Flow Visualization 569
10.2.3 Density Gradient Methods 570

10.3 Characteristics of the Rotor Wake in Hover 572
10.3.1 General Features 572
10.3.2 Wake Geometry in Hover 573
10.4 Characteristics of the Rotor Wake in Forward Flight 575
10.4.1 Wake Boundaries 577
10.4.2 Blade–Vortex Interactions (BVIs) 578
10.5 Other Characteristics of Rotor Wakes 582
10.5.1 Periodicity versus Aperiodicity 582
10.5.2 Vortex Perturbations and Instabilities 582
10.6 Detailed Structure of the Tip Vortices 584
10.6.1 Velocity Field 585
10.6.2 Models for the Tip Vortex 586
10.6.3 Vorticity Diffusion Effects and Vortex Core Growth 592
10.6.4 Correlation of Rotor Tip Vortex Data 594
10.6.5 Flow Rotation Effects on Turbulence Inside Vortices 595
10.7 Vortex Models of the Rotor Wake 598
10.7.1 Biot–Savart Law 599
10.7.2 Vortex Segmentation 601
10.7.3 Governing Equations for the Convecting Vortex Wake 602
10.7.4 Prescribed Wake Models for Hovering Flight 604
10.7.5 Prescribed Vortex Wake Models for Forward Flight 607
10.7.6 Free-Vortex Wake Analyses 614
10.8 Aperiodic Wake Developments 627
10.8.1 Wake Stability Analysis 627
10.8.2 Flow Visualization of Transient Wake Problems 630
10.8.3 Dynamic Inflow 631
10.8.4 Time-Marching Free-Vortex Wakes 633
10.8.5 Simulation of Carpenter & Friedovich Problem 633
10.9 General Dynamic Inflow Models 635
10.10 Descending Flight and the Vortex Ring State 638
10.11 Wake Developments in Maneuvering Flight 640
10.12 Chapter Review 645
10.13 Questions 646
Bibliography 647

11 Rotor–Airframe Interactional Aerodynamics 655

11.1 Introduction 655
11.2 Rotor–Fuselage Interactions 657
11.2.1 Effects of the Fuselage on Rotor Performance 658
11.2.2 Time-Averaged Effects on the Airframe 662
11.2.3 Unsteady Rotor–Fuselage Interactions 666
11.2.4 Fuselage Side-Forces 673
11.2.5 Modeling of Rotor–Fuselage Interactions 674
11.3 Rotor–Empennage Interactions 676
11.3.1 Airloads on the Horizontal Tail 679
11.3.2 Modeling of Rotor–Empennage Interactions 680
11.4 Rotor–Tail Rotor Interactions 682
11.5 Chapter Review 685
11.6 Questions 686
Bibliography 687

12 Autogiros and Gyroplanes 692

12.1 Introduction 692
12.2 The Curious Phenomenon of Autorotation 693
12.3 Review of Autorotational Physics 694
12.4 Rolling Rotors: The Dilemma of Asymmetric Lift 699
12.5 Innovation of the Flapping and Lagging Hinges 700
12.6 Prerotating the Rotor 701
12.7 Autogiro Theory Meets Practice 702
12.8 Vertical Flight Performance of the Autogiro 704
12.9 Forward Flight Performance of the Autogiro 705
12.10 Comparison of Autogiro Performance with the Helicopter 708
12.11 Airfoils for Autogiros 709
12.12 NACA Research on Autogiros 710
12.13 Giving Better Control: Orientable Rotors 712
12.14 Improving Performance: Jump and Towering Takeoffs 713
12.15 Ground and Air Resonance 715
12.16 Helicopters Eclipse Autogiros 716
12.17 Renaissance of the Autogiro? 717
12.18 Chapter Review 719
12.19 Questions 720
Bibliography 720

13 Aerodynamics of Wind Turbines 723

13.1 Introduction 723
13.2 History of Wind Turbine Development 724
13.3 Power in the Wind 726
13.4 Momentum Theory Analysis for a Wind Turbine 727
13.4.1 Power and Thrust Coefficients for a Wind Turbine 729
13.4.2 Theoretical Maximum Efficiency 730
13.5 Representative Power Curve for a Wind Turbine 731
13.6 Elementary Wind Models 733
13.7 Blade Element Model for the Wind Turbine 735
13.8 Blade Element Momentum Theory for a Wind Turbine 738
13.8.1 Effect of Number of Blades 742
13.8.2 Effect of Viscous Drag 742
13.8.3 Tip-Loss Effects 743
13.8.4 Tip Losses and Other Viscous Losses 745
13.8.5 Effects of Stall 747
13.9 Airfoils for Wind Turbines 747
13.10 Yawed Flow Operation 750
13.11 Vortex Wake Considerations 751
13.12 Unsteady Aerodynamic Effects on Wind Turbines 757
13.12.1 Tower Shadow 760
13.12.2 Dynamic Stall and Stall Delay 761
13.13 Advanced Aerodynamic Modeling Requirements 763
13.14 Chapter Review 764
13.15 Questions 765
Bibliography 767

14 Computational Methods for Helicopter Aerodynamics 771

14.1 Introduction 771
14.2 Fundamental Governing Equations of Aerodynamics 772
14.2.1 Navier–Stokes Equations 773
14.2.2 Euler Equations 776
14.3 Vorticity Transport Equations 777
14.4 Vortex Methods 779
14.5 Boundary Layer Equations 780
14.6 Potential Equations 783
14.7 Surface Singularity Methods 783
14.8 Thin Airfoil Theory 786
14.9 Lifting-Line Blade Model 787
14.10 Applications of Advanced Computational Methods 790
14.10.1 Unsteady Airfoil Performance 790
14.10.2 Tip Vortex Formation 794
14.10.3 CFD Modeling of the Rotor Wake 797
14.10.4 Airframe Flows 798
14.10.5 Vibrations and Acoustics 801
14.10.6 Ground Effect 803
14.10.7 Vortex Ring State 803
14.11 Comprehensive Rotor Analyses 805
14.12 Chapter Review 808
14.13 Questions 809
Bibliography 810

Appendix 815
Index 817

Preface to the Second Edition

The reader will see many changes to this second and much enlarged edition of *Principles of Helicopter Aerodynamics*. However, the goal in writing the book remains the same, to give a reasonably adequate description of background theory and present an up-to-date treatment of the subject of helicopter aerodynamics, or at least as up to date as it can be. With the life span of a modern engineering textbook being measured in a few years, it seemed appropriate to regularly update the book with both revised and new material that, in part, reflect both current areas of topical interest as well as areas of ongoing fundamental research. The revised text will continue to appeal both to those learning the field anew and to those who are practicing engineers. The text requires some familiarity with basic aerodynamics and mathematical concepts, although no prior background in rotating-wing aerodynamics is assumed. Both new and updated questions at the end of each chapter will satisfy instructors who have used the first edition of the book in the classroom and have found the solutions manual useful in their teaching.

Work on revising the first edition and compiling the second edition started early in 2003, although planning, gathering materials, and writing started well before then. The new material was finally defined late in 2003 and some of it was taught in my "Helicopter Aerodynamics II" class during the spring of 2004. In this second edition I have taken the opportunity to thoroughly revise the original text for content and clarity, as well as to finally weed out the remaining evasive typographical errors that made it into the third printing of the first edition. Any errors that do remain are entirely of my own doing. Many revisions to the text have been made based on my own rereading during the last five years, as well as on the feedback and suggestions received from many readers, a lot of them students. In the first instance, I have put back some important parts of the original manuscript that were edited out of the first published edition. This by itself has provided much better detail and continuity between sections and chapters, as well as giving a fresh new look to the book. A few original sections have been deemed duplicative or redundant with the addition of the new chapters and so have been edited out completely. Other parts of the text have been moved to the new chapters. Most of the original figures have been revised or updated, or have been reordered in a more logical sequence.

The introductory chapter on the development of the helicopter has been completely revised. I have taken the opportunity to thoroughly check historical events, dates, and other details, which are often conflicting between different publications. Tracing original documents back over ninety years in some cases has proved challenging, but I have been helped in this task by many willing individuals. I am particularly grateful to Roger Connor of the National Air and Space Museum for sharing his extensive knowledge of helicopters and VTOL aircraft. I have also added new material to this chapter that has strengthened the description of the technological advances needed for vertical flight. The addition of new material on engines has helped put the development of the helicopter into a better perspective when compared to the development of other aircraft. Chapters 2 and 3 describe the fundamental aerodynamic characteristics of helicopter rotors, and these two chapters have seen the fewest changes in the second edition. Even here, however, several additions

have been made to better introduce the fundamentals of helicopter flight and to provide an essential primer for the more advanced materials contained in the subsequent chapters of the book. Chapter 4 on rotating blade motion has seen the addition of sections on teetering and semi-rigid rotors to complement the discussion on the articulated form of rotor. A discussion of pitch–flap coupling and an introductory section on ground resonance helps round out the revised chapter. Finally, the discussion on the methods of solving for rotor trim has expanded to complete this chapter. Chapter 5 is on helicopter performance. Initially I focused on a better description of the international standard atmosphere and why it is used in performance work. The addition of a section on compressibility losses on the rotor operating at higher forward speeds helps better explain the impact of this deleterious effect on helicopter performance. A new section on engines and the issues of specific fuel consumption connect better to a revised section on flight range and endurance. There is also a new section on maximum altitude (ceiling) performance. Performance issues in rapidly descending flight have received some recent attention and this seems to be a topic that is very poorly understood from a fundamental standpoint. To this end, revised and expanded sections on autorotational flight and the vortex ring state should help cover the field. Finally, a section on maneuvering flight performance helps round out Chapter 5.

The first part of the book concludes with Chapter 6, which addresses helicopter aerodynamic design issues. This chapter has seen an expanded consideration of airframe download and other performance penalties. A new section on the use of wind tunnel testing in the evaluation of rotor air loads and helicopter performance helps put the difficulties of accurate flight performance estimation into proper perspective. The issues of maneuvering flight are considered again through a discussion of precessional stall effects, both on the main rotor and the tail rotor. Four new sections have been added to Chapter 6. The first is on "smart" rotor systems, which may be one approach whereby the performance of the helicopter could be significantly improved. It remains to be seen, however, if the practical issues in building and certifying a cost-competitive smart rotor system can be overcome. Second, the ideas of a human-powered helicopter are introduced. This is a problem that continues to interest generation after generation of students, although, as the discussion shows, the physiological limits of humans severely limit the possibilities of ever achieving successful human-powered vertical flight. Nevertheless, it remains a problem that will continue to hold great fascination and it is worthy of consideration from both an aerodynamics and a vehicle design perspective. Third, there is a new section on micro air vehicles (MAVs). The flight of MAVs involves low Reynolds number issues for which there is little existing knowledge of their aerodynamics, and so they require special considerations in their performance estimation. Fourth, a brief section on performance degradation issues associated with rotor and airframe icing completes this chapter.

The second part of the book starts in Chapter 7 with a revised discussion on airfoil sections used for helicopter applications. The chapter is enhanced by a more thorough and up-to-date discussion on advanced airfoil design. The addition of a section on circulation controlled airfoils reflects renewed interest in this concept for alternative rotorcraft concepts. A short section on very low Reynolds number airfoil characteristics complements the discussion on MAVs found in Chapter 6. Finally, a section on the aerodynamic degradation of helicopter rotor airfoils from ballistic damage completes this chapter. Chapter 8 is a fairly large chapter on unsteady aerodynamics, and the existing material has seen several changes. A new section on the unsteady aerodynamics of airfoils with trailing edge flaps recognizes their use on modern rotors for vibration and noise reduction and perhaps as a primary means of rotor control by replacing the swashplate. The addition of a new section on rotor aeroacoustics in this chapter helps make the connection between unsteady aerodynamic forces and the

often obtrusive noise that seems to plague the modern helicopter. This section also provides a primer for students and aerodynamicists learning the field of acoustics anew, as well as lending a bridge to practicing acousticians who need greater than superficial knowledge about helicopter related acoustic problems. Chapter 10 on rotor wakes has seen the addition of new material throughout. This includes a fresh discussion on tip vortex modeling, including the effects of turbulence within the vortex core. The understanding of helicopters in maneuvering flight has received much recent attention by the technical community, so a section on time-accurate wake modeling seemed a natural addition to the book.

Chapters 11 through 14 are all new chapters. Chapter 11 is on rotor–airframe interactional aerodynamics that contains material left over from the draft of the first edition. Because the helicopter as a system must function properly and predictably throughout its operational flight envelope, an understanding of component-interaction aerodynamics is essential to the successful design of the modern helicopter. Several sections on this topic from the original text have now been parsed out and integrated with the new material that forms this chapter. Chapter 12 describes the technological development of autogiros and gyroplanes, and recognizes the fundamental role that the autogiro played in the development of the helicopter. This chapter also contains the essential aerodynamic theory of the autogiro. The need for this chapter also reflects a renaissance of interest in the commercialization of a modern gyroplane, for which new engineers must be suitably knowledgeable.

Chapter 13 is on the aerodynamics of wind turbines. It may seem surprising to some to find a chapter on wind turbines in a book on helicopters, but the aerodynamics of wind turbines have many similarities to the aerodynamics of helicopters, yet also with important differences. There are so relatively few books on wind turbines and those describing the aerodynamics are frequently out of print. Environmental concerns about global warming and the storage of waste from nuclear power plants has seen an increased emphasis on the use of wind energy, which is likely to see much more rapid and expansive use in years to come. The performance of wind turbines can be analyzed by many of the same methods used for helicopters, and the cross fertilization of expertise in the two areas will hopefully help foster a new understanding of both fields.

Finally, Chapter 14 explains the basis of modern computational methods for rotor and helicopter analysis, and these are put into context with the capabilities classical methods and modern engineering approaches. Dr. Richard Brown of Imperial College at the University of London contributed heavily the writing of this chapter. To some, the development of the field of computational fluid dynamics (CFD) by itself is held out to be the "Holy Grail" for the helicopter aerodynamicist. But this is a very misleading perspective because CFD does not, by itself, hold the answer to all of the various problems found on helicopters. The answer lies more in the successful integration of advanced forms of aerodynamic analysis into other disciplines of analysis. It is also unwise for other approaches to be abandoned in the shorter term while CFD matures to an accepted level of capability, given that this could still be decades off, despite more optimistic claims. These CFD models require continuous and careful validation, both against more complete solutions and/or analytical results and against detailed experimental measurements. This is one reason why wind tunnel testing of helicopters and subsystems will continue to be essential to better understand and predict the capabilities of the helicopter in response to specific aerodynamic phenomena. The future offers many opportunities for new research focused toward the development of more innovative computational models with greater predictive capabilities for helicopter applications. Only then can the problems that limit the performance and capabilities of the helicopter be understood and mitigated.

Preface to the First Edition

This book is a college-level analytical and applied level exposition of the aerodynamic principles of helicopters and other rotating-wing vertical lift aircraft. It is written for students who have no background in rotating-wing aerodynamics but have had at least two semesters of basic aerodynamics at the undergraduate level and possibly one course at graduate level. The material covered has grown mainly out of two graduate-level courses in "Helicopter Aerodynamics" that I have taught at the University of Maryland since 1988. I have also taught a somewhat more general senior-level undergraduate course in "Helicopter Theory" about every other year, which is centered around the first half of this book. These courses have been offered as part of the formal curriculum in the Center for Rotorcraft Education and Research, which was originally founded in 1982, partly through the efforts of Professor Alfred Gessow. It is now nearly fifty years since Alfred Gessow and Gary Myers' well-known book *The Aerodynamics of the Helicopter* was first published. I am pleased to record in the preface to this book that in his status as Professor Emeritus, Alfred Gessow continues to be active in activities at the University of Maryland and also within government and professional organizations. As a testimony to his life-long dedication to education and research in helicopter technology, the Rotorcraft Center at the University of Maryland has been recently named in his honor.

In the institutions where formal courses in helicopter technology have been taught, either at the undergraduate or graduate level, my experience is that they have been well received and very popular with the students. What is often most attractive to students is the highly multidisciplinary nature of helicopter engineering problems. Therefore, an introductory course in helicopters provides a good capstone to the aerospace engineering curriculum. Another factor for most students who have taken a helicopter course is the realization that so much more remains to be learned about fundamental aerodynamics, especially as it applies to rotating-wing aircraft. This is reflected in the experience levels in predicting the aerodynamics and overall behavior of helicopters before their first flight, which are less than desirable. Consequently, it is fair to say that the various aerodynamic problems associated with helicopters and other new forms of rotary-wing aircraft probably provide the scientists and engineers of the future with some of the most outstanding research challenges to be found in the field of theoretical and applied aerodynamics.

Serious work on this book project started about three years ago and was motivated primarily by my students. It has grown out of a relatively informal collection of classroom notes and research papers and an overwhelming need to synthesize both older and newer information on the subject of helicopter aerodynamics into one coherent volume. With the ever increasing content of new research material on helicopters and the increasing proportion of recent research material being included in the course, especially in the second semester, the development of a formal textbook was really a logical step. Even since 1980, when Wayne Johnson's excellent book *Helicopter Theory* was published, progress in understanding helicopter aerodynamics and other related fields has been remarkable. A glance at the content of recent proceedings of the Annual Forum of the American Helicopter Society or the European Rotorcraft Forum shows the scope and depth of new work being

conducted today, which continues despite tightly controlled budgets. This has been fueled, in part, by the great advances in computer technology, which has fostered ambitious new analytical and numerical approaches to solving helicopter technology problems. Some of these approaches now come under the banner of computational fluid dynamics (CFD) using numerical solutions to the Euler and Navier–Stokes equations. While these techniques are not yet mature, CFD methods have begun to provide new insight into the complicated aerodynamic problems associated with helicopters that were previously intractable with existing mathematical methods or were limited by available experimental techniques. As these new numerical methods continue to mature and become better validated, the first decade of the twenty-first century will see an increasing use of CFD tools in the design of new and improved helicopters. The past twenty years has also marked a revolution in the experimental studies of helicopter aerodynamics, where advances in flow diagnostic and other instrumentation has allowed measurements on rotors to be made with a fidelity that was considered impossible just a few years ago. The complex nature of the problems found on helicopters means that both experiment and theory must continue to go hand in hand to forge a better understanding of the whole. This will result in the development of new rotating-wing aircraft with better performance, lower vibration, better reliability and maintainability, and with lower direct and operational costs. The modern spirit of international cooperation in research and development makes the years ahead in the twenty-first century very exciting.

As I have already mentioned, a significant part of the content of this book has been focused toward students at the graduate level who are learning the principles of helicopter aerodynamics and are exploring the tools available to approach the vigorous, multidisciplinary research and development of the modern helicopter. In planning the content of this book, I have organized the material in two main parts. The first part will be appropriate for a one-semester course in helicopter aerodynamics for senior undergraduate and first-year graduate students. This material essentially represents a thorough introduction to fundamental helicopter problems, basic methods of rotor analysis, issues associated with helicopter performance, and conceptual design issues. I have attempted to follow the spirit of Gessow & Myers's book, where theory is supported throughout by liberal references to experimental observations and measurements. In this regard, rediscovering the less well-known early NACA and RAE technical literature on the subject of helicopter aerodynamics proved to be one of the most satisfying aspects of writing this book. The rapid progress made in understanding the problems of the helicopter during the period between 1930 and 1950, and the ingenuity shown in both the experimental and analytical work, are quite remarkable.

The second part of the book gives a more advanced treatment of more detailed aspects of helicopter aerodynamics, again with emphasis on physical concepts and basic methods of analysis. This part will appeal more to those students who plan to conduct research in helicopter aerodynamics and related fields or who are already practicing engineers in industry and government laboratories. However, I do hope that practicing engineers will relish in the opportunity to revisit the first part of the book to review the basics and also to review the inherent assumptions and limitations of the fundamental concepts and methods. These are so often taken for granted, but they form the backbone of many modern forms of helicopter analysis. Because I have always found a need to bring "industrial practice" into the classroom, I have tried to incorporate engineering practice as well as some of my own industrial experience into the second part of the book. For this, I thank my former colleagues at Westland Helicopters for sharing their knowledge with me.

Like most textbooks, the final product has turned out to be not exactly what was originally planned. Along the way, topics have been added, parts of the text rearranged, and some other

topics deleted. Also, in light of the reviews of the preliminary manuscript, new figures have been added, many were modified, and others deleted. While more than 400 figures were originally prepared, less than 275 finally made it to the finished book. In the interests of space and publication costs, two chapters have been left out completely. These were "Interactional Aerodynamics" and "Advanced Computational Aerodynamic Techniques." Both topics are referred to, albeit briefly, throughout the book, but to include them would have made the final size of the book prohibitively long. There have also been such rapid recent advances in these areas in the past few years that they are best left for a second edition. The list of key references for each chapter is extensive but by no means complete, and the reader is encouraged to follow through with the references contained in each publication, as required. Problems are provided at the end of each chapter and have been drawn on time-proven homework and examination questions. Solutions have been provided in a companion instructors' solution manual.

Chapter 1 introduces the helicopter through its technical history. This chapter grew out of my personal research into the Berliner helicopter experiments that were conducted during the early 1920s at the College Park Airport, which is close to the University of Maryland. Whereas in the technical development of fixed-wing aircraft it is possible to point to several key historical events, it becomes quickly apparent that things are much less clear in the development of the helicopter. There are already many authoritative publications that detail the historical development of the helicopter, so I have tried to approach the discussion on more of a technical theme and to put the background and difficulties in understanding the aerodynamics of vertical flight into broader perspective. This introduction is followed in Chapter 2 by an analysis of hovering and axial flight using the Rankine–Froude momentum theory. The basic momentum theory concept was extended to forward flight by Glauert and others from the RAE at Farnborough, inspired not by the helicopter, but by the success of Cierva's Autogiro. It is shown that many of the important performance and operational characteristics of the helicopter can be deduced from Glauert's extension of the basic momentum theory. The blade element and combined blade-element momentum theory is discussed in Chapter 3. These ideas were developed in the 1940s and provide the foundation for a more modern treatment of the aerodynamics of rotors. On the basis of certain assumptions, important information on blade design, such as optimum or ideal shapes for the blade planform and blade twist, can be deduced from the combined blade element momentum theory. Because helicopter blades have articulation, in that they can flap and lag about hinges located near the root of each blade, it is not possible to understand the behavior of the helicopter solely from an aerodynamics perspective. Therefore, in Chapter 4 a discussion of rigid blade motion leads naturally into an understanding of the issues associated with rotor response to the changing aerodynamic loads and also to rotor control. Also introduced here are the ideas of rotor trim; that is, the pilot's control inputs required to enable equilibrium flight of the helicopter. Chapter 5 gives an introduction to helicopter performance and operational issues such as climbing and descending flight, including the autorotative state and flight near the ground. The first part of the book concludes in Chapter 6, which reviews issues associated with the conceptual aerodynamic design of helicopters, including the main rotor, the fuselage and empennage, and the tail rotor. Although it might have been more appropriate to place this chapter at the end of the book, it provides a good bridge between the fundamentals and results to many problems that are still more of a research nature for which experimental research is incomplete and predictive capabilities are not yet mature.

Chapter 7 starts the second part of the book with an important practical review of basic airfoil aerodynamics, including boundary layer and viscous aerodynamics, and the role of compressibility. This is followed by applications of these concepts to understanding some

of the special requirements and characteristics of rotor airfoils. Again, liberal reference to experimental measurements makes the present treatment relatively unique amongst textbooks on helicopters. Chapters 8 and 9 comprise a comprehensive discussion on unsteady aerodynamics, with emphasis on the relevance to helicopter problems. Classical techniques of unsteady aerodynamics, including Theodorsen's theory and Loewy's theory, the indicial response method, and dynamic inflow, are reviewed in Chapter 8. Extensions of some of these methods to the compressible flow problems found on helicopters are described, with validation with experimental measurements where possible. Indicial methods are treated in some detail because they form the foundation for many modern methods of helicopter analysis and are not covered in any previous helicopter text. Chapter 9 discusses the problem of dynamic stall, which is known to be a barrier to attaining high speed forward flight with a conventional helicopter. Engineering methods of dynamic stall prediction are also reviewed, along with some examples of the general predictive capability to be found with these models. The physical nature of helicopter rotor wakes, both in hovering and forward flight, are discussed in Chapter 10. Nearly all of what we know about rotor wakes comes from empirical observations, and this has led to the development of well-validated mathematical models of the rotor wake using vortex techniques. Chapter 10 concludes with a brief discussion on interactional aerodynamics. Although many the problems of rotor aerodynamics can be studied by considering the rotor in isolation to the fuselage, tail rotor and empennage, aerodynamic interactions between the components lead to many problems that are not yet fully understood.

A word about systems of units is in order. In the preparation of this book, I have found it necessary to use both the British (Imperial) and metric (SI) systems. Any preference for one over the other is done simply for the sake of convenience, and I think there is really little reason to change units for the sake of standardization in the text. As aerospace engineers, and particularly helicopter engineers, we are used to working with both systems and even with mixed units in the same breath, and so most readers will have no problems with this approach. For the foreseeable future, students will have to learn to become fully conversant in both systems. Where I have felt it would be helpful, units in both systems are stated. For convenience, a table of conversion factors is also included in the appendix.

Having said all this and made my excuses, I hope this edition of the book will be judged, especially by the practicing engineer, on what it contains and not on what else could potentially have been included. Like everything in aviation, the final product is always a compromise and is always under a continuous state of revision, development, and improvement. As a final comment, it seems appropriate to quote Igor Sikorsky who has said: "At that time [1908] aeronautics was neither an industry nor even a science ... it was an art, I might say, a passion. Indeed at that time it was a miracle." As we stand now at the turn of the new millennium, I'm sure that if he was alive Igor Sikorsky would have agreed that the past century has indeed seen many miracles, both in aeronautics and in helicopter technology. The new century will almost certainly see more.

Acknowledgments

This book is the product of an opportunity afforded to me by the University of Maryland. The research and writing of the first edition of this book was unique experience and has led to many lessons. It was gratifying to see how well the first edition was received, with feedback being received from the four corners of the world. The first edition took the best part of 2,500 desk hours, mainly during evenings and weekends and spread over three years. In this regard, I am forever grateful to my wife, Alice Marie Leishman, for her love and understanding, and for providing me continuous support where writing, proofreading, drawing figures, and plotting graphs meant many long nights and all too short weekends. Preparing this second edition required about 1,300 desk hours, spread over about eighteen months, but ultimately even with the benefit of experience and hindsight, it proved to be no lesser a task than the first edition.

Special acknowledgment is due to a great many people, both on and off the University of Maryland campus. I am most grateful for the council of my colleagues at the University of Maryland, Professors Alfred Gessow (now deceased), Inderjit Chopra, Roberto Celi, James Baeder, Christopher Cadou, and Dr. Vengalattore Nagaraj. Professor Gessow had read substantial parts of the first edition and offered many useful suggestions for improvement. Before he passed away in May of 2002, Alfred Gessow and I had many significant discussions about the autogiro and the role it played in the fundamental development of the helicopter, from the point of view of both engineering theory and practice. Chapter 12 in this second edition reflects the spirit of our discussions, and I dedicate this chapter to his memory. Al Gessow's knowledge and first-hand experience working at NACA Langley during the 1940s and 1950s in the technical development of early helicopters was also invaluable to me. Professors Inderjit Chopra and Roberto Celi provided good suggestions for Chapter 4 and kindly allowed me to use some of their own course material on blade motion and rotor trim. Professor James Baeder read Chapter 8 on unsteady aerodynamics and Chapter 14 on computational methods for helicopter applications, and I am grateful to him and his students for their willingness to help me with figure preparation. Dr. Chris Cadou read the revised parts of Chapter 1, and I enjoyed our engaging conversations on early engine development and the history of aircraft technology in general. Dr. Nagaraj read the revised Chapters 5 and 6 and offered more good suggestions on helicopter design issues.

I am particularly grateful to Dr. Richard Brown of Imperial College at the University of London who is responsible for a substantial part of the writing in Chapter 14 of the second edition. This chapter on computational methods proved to be one of the most satisfying to write, although it took the longest amount of time out of the four new chapters with numerous iterations required to finally define the appropriate content. Dr. Brown also provided useful feedback for improvement on the other three new chapters.

I am indebted to my graduate students at the University of Maryland, both past and current, who have both directly and indirectly contributed to the content of both the first and second editions of this book. The current members of my research group, namely Shreyas Ananthan, Sandeep Gupta, Arun Jose, Robin Preator, and Manikandan Ramasamy,

enthusiastically read many parts of the second edition and offered useful advice and constructive criticism from a student's perspective. Many of the students in my classes proofread drafts of revised chapters, and I am particularly grateful to the group of Moble Benedict, Brandon Bush, Mamta Jangid, Nitin Gupta, Vinit Gupta, Vinod Lakshminarayan, and Eric Schroeder for their careful reading and checking of equations. Sandeep Gupta did much to help me refine the material in Chapter 13 on wind turbines. Yik-Loon Lee and Karthikeyan Duraisamy spent time with me explaining the intricacies of advanced computational methods and grid generation techniques, and I appreciate them lending me some of the results from their own research for Chapter 14 in the second edition of this book. I am grateful to Dr. Mahendra Bhagwat (now at US Army/NASA Ames) for running the prescribed- and free-vortex wake solutions and for allowing me to adapt his analysis of the tip vortex aging problem in Chapter 10. Dr. Preston Martin (also now at US Army/NASA Ames) took several of the rotor wake visualization images for Chapter 10 and did much to help me find references and other material on airfoils and airfoil design for Chapter 7. Jacob Park (now at Bell Helicopter Textron) ran several of the rotor wake calculations, sifted through lots of experimental results on rotor wakes, and organized the data for a good number of the figures in Chapter 10. Gregory Pugliese read many of the draft chapters for the first edition, made endless trips to the library to hunt down reports, cross checked more than several hundred references, and helped me turn more than a few of my many crude sketches into professional looking figures. Other former students who have directly or indirectly contributed material used in this book include Dr. Ashish Bagai (Sikorsky), Dr. Peter Bi (US Navy NSWC), Dr. Gilbert Crouse (Da Vinci Technologies), Dr. Berend van der Wall (DLR), Mark Daghir (Boeing), Erwin Moederesheim, Joe Tyler, Alan Coyne (Sikorsky), Col. Keith Robinson (US Army), Greg Pugliese, and Dan Griffiths (Sikorsky). A special thanks to Dr. Ashish Bagai and Dr. Mahendra Bhagwat for their generosity in allowing me to adapt some of their results and graphics for Chapter 10. Dr. Peter Bi provided me with good feedback on the new content included in Chapter 11.

Off the university campus there are a great many people and colleagues who provided advice during the writing of both the first and second editions. I remain indebted to the reviewers of my original book proposal, who were able to make good suggestions on what should be included and what should be left out, particularly Prof. Edward Smith and Dr. Andrew Lemnios. The draft second edition saw many more critical eyes, and I was humbled by the care and thoroughness that each reviewer took over their respective chapters. All of their comments were duly taken into account and they led to a better book as a result. Many other people made suggestions on the originally published text or recommended topics for the second edition. Some colleagues read draft copies of the new chapters, while still others sent me hard-to-find reports, computer files of experimental data, figures, photographs, or other information that was used or adapted for the book. In particular, I appreciate the contributions of Douglas Baldwin, Tom Beddoes, Dr. John Berry, Dr. Bill Bousman, Dr. Richard Brown, Marshall Buhl, Tim Candsdale, Dr. Mark Chaffin, Prof. Muguru Chandrasekhara, Dr. Bruce Charnov, Dr. Colin Coleman, Roger Connor, Shawn Coyle, Prof. George Done, Lee-Jay Fingersh, Prof. Peretz Friedmann, Susan Gorton, Dr. Richard Green, David Groen, Jay Groen, Robert Hansford, Franklin Harris, Jennifer Henderson, Michael Hirschberg, Dr. Stuart Houston, Dr. Wayne Johnson, Markus Krekel, Andrew Line, James Mayfield, Dr. Kenneth McAlister, Dr. Patrick Moriarty, Dr. Khanh Nguyen, James Mayfield, Dr. Reinert Müller, Prof. Gareth Padfield, John Perry, Prof. Ganesh Rajagopalan, Dr. Rex Rivolo, Dr. Scott Schreck, Prof. Michael Sellig, Sergei Sikorsky, Dr. Roger Strawn, Prof. Edward Smith, Dr. James Tangler, Dr. Chee Tung, Dr. Hal Youngren, Dr. Daniel Wachspress, and Dr. David Wood. A great number of people, too

numerous to mention, sent me letters or e-mail about the first edition giving me comments for improvement, pointing out remaining typographical errors, or suggesting areas for further clarification. Instructors who have used the book and the solutions manual for their classes gave me excellent feedback, which was duly taken into consideration. As they will see in this second edition of the book, most of their suggestions were enthusiastically incorporated and their critiques are most gratefully acknowledged.

Thanks are due to the helicopter companies, who were kind enough to send me photographs of their various helicopters or give me permission to publish those that I found in publicity materials and on their web sites. In particular, I acknowledge Madelyn Bush and Jack Satterfield of Boeing Helicopters, Kevin Hale of Bell Helicopter Textron, David Long of Kaman Aircraft Corporation, Eurocopter, and the Public Affairs Department at GKN Westland (now Agusta-Westland). Other photographs were obtained from NASA, the National Renewable Energy Laboratory, Sandia National Laboratories, and the photo archive at Patuxent Naval Air Station. I am also grateful to the staff of the National Air and Space Museum for giving permission to publish some of the historical photographs included in Chapter 1 and to Brian Riddle of the Royal Aeronautical Society in London for finding some early published papers and reports on autogiros and helicopters.

I want to express my sincere gratitude to the staff at Cambridge University Press for their help and support during the writing and publication process of both the first and second editions of this book. Florence Padgett was the editor for the first edition, and my thanks extend also to Ellen Carlin for her help with the various editing and production issues. Peter Gordon was the editor for the second edition, and I am grateful for his enthusiastic support and encouragement throughout. Finally, my thanks again to the staff at TechBooks for their help in the production of the second edition of this book.

List of Main Symbols

Listed below alphabetically are the main symbols used in this book. Note that more than one meaning may be assigned to a symbol. Other symbols are defined internally within each chapter.

a	sonic velocity
a	wake induction factor (for a wind turbine)
A	rotor disk area, πR^2
A	axial (chord) force
A_b	blade area, σA
A_{ov}	rotor overlap area
B	tip-loss factor
B	temperature lapse rate
c	blade chord
C	Theodorsen's function
C'	Loewy's function
C_d	section drag coefficient
C_{d_0}	section zero-lift drag coefficient
C_{D_f}	fuselage drag coefficient
C_{D_v}	fuselage vertical drag coefficient
c_f	local skin friction coefficient, $\tau_w/\frac{1}{2}\rho V_\infty^2$
C_H	H-force coefficient, $H/\rho A(\Omega R)^2$
C_l	section lift coefficient, $L/\frac{1}{2}\rho U^2 c$
$C_{l_{max}}$	maximum lift coefficient
C_{l_α}	section lift-curve slope
$\bar{C}_L$	rotor mean lift coefficient, $6(C_T/\sigma)$
C_m	airfoil pitching moment coefficient, $M/\frac{1}{2}\rho U^2 c^2$
$C_{m_{1/4}}$	airfoil pitching moment coefficient about 1/4 chord, $M_{1/4}/\frac{1}{2}\rho U^2 c^2$
$C_{m_{0.25}}$	airfoil pitching moment coefficient about 1/4 chord, $M_{0.25}/\frac{1}{2}\rho U^2 c^2$
$C_{m_{ac}}$	airfoil pitching moment coefficient about aerodynamic center, $M_{ac}/\frac{1}{2}\rho U^2 c^2$
C_{M_x}	rolling moment coefficient, $M_x/\rho AR(\Omega R)^2$
C_{M_y}	pitching moment coefficient, $M_y/\rho AR(\Omega R)^2$
C_n	normal force coefficient, $N/\frac{1}{2}\rho U^2 c$
C_{n_α}	slope of normal force coefficient versus α curve
C_p	specific heat at a constant pressure
C_p	pressure coefficient, $(p - p_\infty)/0.5\rho V_\infty^2$
C'_p	pressure coefficient, $100(p - p_\infty)/0.5\rho\Omega^2 R^2$
C_P	rotor power coefficient, $P/\rho A(\Omega R)^3$
C_{P_c}	climb power coefficient, $P_c/\rho A(\Omega R)^3$
C_{P_i}	induced power coefficient, $P_i/\rho A(\Omega R)^3$

C_{P_0}	profile power coefficient, $P_0/\rho A(\Omega R)^3$
C_{P_p}	parasitic power coefficient, $P_p/\rho A(\Omega R)^3$
C_R	resultant force coefficient, $R/\frac{1}{2}\rho V_\infty^2 c$
C_Q	rotor torque coefficient, $Q/\rho A(\Omega R)^2 R$
C_T	rotor thrust coefficient, $T/\rho A(\Omega R)^2$
C_T/σ	blade loading coefficient
C_W	weight coefficient, $W/\rho A(\Omega R)^2$
C_W	work coefficient or torsional damping factor, $\oint C_m d\alpha$
C_X	X-force (longitudinal-force) coefficient, $X/\rho A(\Omega R)^2$
C_Y	Y-force (side-force) coefficient, $Y/\rho A(\Omega R)^2$
C_μ	jet momentum coefficient, $\dot{m}V_j/\frac{1}{2}\rho V_\infty^2 c$
D	drag force
DL	rotor disk loading, T/A
$D.F.$	torsional damping factor, $\oint C_m d\alpha$
e	flapping hinge offset as a fraction of rotor radius
f	equivalent flat plate area of fuselage, etc., $D/\frac{1}{2}\rho V_\infty^2$
f	effective flow separation point as a fraction of chord
F	Prandtl's tip-loss function
FM	figure of merit, $C_T^{3/2}/(\sqrt{2}C_P)$
F_x	aerodynamic force parallel to disk plane
F_z	aerodynamic force normal to disk plane
h	altitude or elevation (height)
h	plunge displacement
h	perpendicular distance from vortex to evaluation point
h_p	pressure altitude
h_ρ	density altitude
H	rotor drag force
H	Hankel function
i	blade control point index
$I_{b_{i,j}}$	influence coefficient
I_b	blade mass moment of inertia
I_β	blade mass moment of inertia about the flapping hinge
I_ζ	blade mass moment of inertia about the lagging hinge
$\Im$	imaginary or out-of-phase part
J	Bessel function of the first kind
k	reduced frequency, $\omega c/2V_\infty$
k_g	gust reduced frequency, $\omega_g c/2V_\infty$
k_x, k_y	longitudinal and lateral inflow gradients, respectively
KE	kinetic energy
l	length of influencing vortex filament
L	section lift force per unit span
m	mass per unit length of rotor blade
m	maximum camber
m	tandem rotor overlap fraction
$\dot{m}$	mass flow rate
M	Mach number or local free-stream Mach number, U/a
M^*	critical Mach number
M	mass

M	moment per unit span
M_∞	free-stream Mach number, V_∞/a
M_{dd}	drag divergence Mach number
M_{tip}	rotor hover tip Mach number, $\Omega R/a$
M_x	rotor rolling moment, positive to right (starboard)
M_y	rotor pitching moment, positive nose-up
M_β	aerodynamic flapping moment
N	normal force
N_b	number of rotor blades
p	pressure
p	roll rate about the x axis
p	point of maximum camber
$\bar{p}$	nondimensional roll rate, p/Ω
p	Laplace variable
P	rotor power
PL	rotor power loading, T/P
q	airfoil nondimensional pitch rate, $\dot{\alpha}c/V$
q	dynamic pressure
q	roll rate about the y axis
q_∞	free-stream dynamic pressure, $\frac{1}{2}\rho V_\infty$
$\bar{q}$	nondimensional pitch rate, q/Ω
Q	rotor torque
r	nondimensional radial distance
r_0	blade root cut out
r_c	vortex core radius
r_v	vortex release point along blade span
$\vec{r}$	position vector of a point in space
$\bar{r}$	nondimensional radial coordinate, r/r_c
R	blade radius
R	gas constant
Re	Reynolds number based on chord, $\rho Vc/\mu$
Re_x	Reynolds number based on distance x, $\rho Vx/\mu$
$\Re$	real part
Ri	Richardson's number
s	relative distance traveled by airfoil in semi chords, $2Vt/c$
S	Sears's function, referenced with respect to airfoil midchord
S	reference area or surface area
S_{ref}	reference area
S'	Sears's function, referenced with respect to airfoil leading edge
SFC	specific fuel consumption
t	time
t	maximum airfoil thickness
T	temperature
T	rotor thrust
T/A	rotor disk loading
U	resultant velocity at blade element, $\sqrt{U_P^2 + U_T^2}$
U_P	out-of-plane velocity normal to rotor disk plane
U_R	radial velocity along blade at disk plane

U_T	in-plane velocity parallel to rotor disk plane
v_h	hover induced velocity, $\sqrt{T/2\rho A}$
V_r, V_θ, V_z	radial, tangential, axial velocity components, respectively
V	velocity
$V_{\Omega R}$	hover tip speed
$\vec{V}$	velocity vector
V_∞	magnitude of free-stream velocity
$\vec{V}_\infty$	free-stream velocity vector
V_c	climb velocity
V_g	gust convection velocity
V_j	jet velocity
V_{mp}	speed to fly for minimum power
V_{mr}	speed to fly for maximum range
w	slipstream velocity
w	velocity normal to chord
w_g	upwash or gust velocity normal to chord
W	weight
W	work done on fluid
W_f	weight of fuel
x, y, z	Cartesian coordinate system
$\bar{x}$	nondimensional distance along airfoil chord, x/c
X	rotor longitudinal force, positive aft
X_n, Y_n	recurrence functions
X_{TSR}	wind turbine tip speed ratio, $\Omega R/V_\infty$
Y	rotor side force, positive right (starboard)
Y	Bessel function of the second kind
α	blade section angle of attack
α	rotor disk angle of attack
α_0	zero-lift angle of attack
α_e	effective angle of attack
α_{ind}	induced angle of attack
α_{TPP}	rotor tip-path-plane angle of attack, positive tilted forward
β	Glauert's compressibility factor, $\sqrt{1-M^2}$
β	blade flapping angle, positive up
β_0	blade coning angle, positive up
β_{1c}	longitudinal flapping angle
β_{1s}	lateral flapping angle
γ	ratio of specific heats
γ	blade Lock number, $\rho C_{l_\alpha} c R^4/I_b$
γ_b	bound vortex sheet strength
γ_w	vortex sheet strength in wake
Γ_b	bound vortex strength
Γ_v	vortex circulation strength
$\hat{\Gamma}$	nondimensional circulation strength, $\Gamma/(\Omega RC)$
δ	boundary layer thickness
δ	effective viscosity coefficient multiplier
ζ	blade lag angle, positive aft
η	efficiency factor

η	flap deflection angle
θ	blade pitch angle
θ_0	blade collective pitch
θ_{1c}	lateral cyclic pitch
θ_{1s}	longitudinal cyclic pitch
θ_{tip}	geometric pitch at blade tip
θ_{tw}	linear blade twist rate
$\theta_{0.75}$, θ_{75}	pitch angle at 75% radius
κ	induced power factor
κ_{int}	induced power factor from rotor-on-rotor interference
λ	rotor inflow ratio, positive downward through disk
λ	gust speed ratio, $V/(V + V_g)$
λ_c	climb inflow ratio
λ_g	wavelength of sinusoidal gust
λ_i	rotor induced inflow ratio, $v_i/\Omega R$
Λ	local sweep or yaw angle, $\tan^{-1}(U_R/U_T)$
μ	rotor advance ratio, $V_\infty \cos\alpha/\Omega R$
μ	dynamic viscosity
μ_x	rotor advance ratio parallel to disk, $V_\infty \cos\alpha/\Omega R$
μ_z	rotor advance ratio perpendicular to disk, $V_\infty \sin\alpha/\Omega R$
ν	kinematic viscosity coefficient
ν_β	blade rotating flap frequency (nondimensional)
ν_ζ	blade rotating lag frequency (nondimensional)
ρ	density of air
σ	rotor solidity, $N_b c/\pi R$
σ_e	equivalent rotor solidity
τ	time constant
τ_w	wall shear stress
ϕ	inflow angle of attack, $\tan^{-1}(U_P/U_T)$
ϕ	general indicial response function
ϕ_W	Wagner indicial response function
ψ	azimuth angle
ψ	Küssner sharp-edged gust function
ψ_b	blade azimuth angle
ψ_w	wake age
ω	angular velocity (circular frequency)
ω_g	gust frequency
Ω	rotational frequency of rotor
χ	wake skew angle

Subscripts and Superscripts

∞	free-stream conditions
0	profile part
$1c$	first harmonic cosine component
$1s$	first harmonic sine component
1/4	quarter chord
3/4	three-quarter chord
ac	aerodynamic center

b	associated with bound vortex
c	climb
c	associated with camber
c	circulatory part
cg	with respect to the center of gravity
CP	control plane
FP	flight path
h	hover
HT	horizontal tail
i	induced
l	lower surface
LE	leading edge
max	maximum
MR	main rotor
n	normal to leading edge
nc	noncirculatory part
NFP	no feathering plane
p	parasitic part
p	roll rate
q	airfoil nondimensional pitch rate
qs	quasi-steady part
req	required
t	associated with thickness
tip	blade tip component
TPP	tip path plane
TR	tail rotor
u	upper surface
VT	vertical tail
α	component resulting from angle of attack

Other Symbols

$\rightarrow$	vector quantity
[ ]	matrix
{ }	column vector

Abbreviations

AGARD	Advisory Group for Aerospace Research and Development
AHS	American Helicopter Society
AIAA	American Institute of Aeronautics and Astronautics (formally IAS)
AoA	angle of attack
ARL	Army Research Laboratories
ARC	Aeronautical Research Committee
BEMT	blade element momentum theory
BET	blade element theory
BVI	blade vortex interaction
CF	centrifugal force
CFD	computational fluid dynamics
DARPA	Defense Advanced Research Projects Agency
DERA	Defence Evaluation Research Agency

FAI	Fédération Aeronautique Internationale
FAR/FARs	Federal Aviation Regulations
FBW	fly by wire (flight controls)
FVM	free-vortex method
GTOW	gross takeoff weight
HWA	hot wire anemometry
HMSO	Her Majesty's Stationary Office
HOT	higher-order term
HPH	human powered helicopter
IAS	Institute of Aeronautical Sciences (now AIAA)
ICAN	International Commission for Air Navigation
ICAO	International Civil Aviation Organization
ISA	International Standard Atmosphere
LDV	laser Doppler velocimetry
LE	leading edge
MAV	micro air vehicle
MSL	mean sea level
NACA	National Advisory Committee for Aeronautics (now NASA)
NASA	National Aeronautics and Space Administration (formally NACA)
NASM	National Air and Space Museum
NLF	natural laminar flow
NREL	National Renewable Energy Laboratory
NTIS	National Technical Information Service
NPL	National Physical Laboratory
ONERA	Office National d'Etude et de Reserches Aerospatiales
RAE	Royal Aircraft Establishment (became DERA)
RAeS	Royal Aeronautical Society
PDE	partial differential equation
PIV	partial image velocimetry
rpm	revolutions per minute
RFP	request for proposal
R & M	Reports & Memoranda (British ARC)
SAE	Society of Automotive Engineers
TE	trailing edge
TPP	tip path plane
TsAGAI	Russian Central AeroHydrodynamic Institute
TSR	tip speed ratio (for wind turbines)
USAAVLABS	US Army Aviation Laboratories
USAAMRDL	US Army Aviation Air Mobility Research & Development Laboratories
USARTL	US Army Research and Technology Laboratories
VRS	vortex ring state
VTM	vorticity transport method
VTOL	vertical takeoff and landing
WW1	World War 1
WW2	World War 2
1-D	one-dimensional
2-D	two-dimensional
3-D	three-dimensional

CHAPTER 1

Introduction: A History of Helicopter Flight

The idea of a vehicle that could lift itself vertically from the ground and hover motionless in the air was probably born at the same time that man first dreamed of flying.

Igor Ivanovitch Sikorsky (1955)

1.1 Rising Vertically

Aerodynamics is the science of all flight. The role of aerodynamics in the engineering analysis and design of rotating-wing vertical lift aircraft, such as the helicopter, is the primary subject of this book. A helicopter can be defined as any flying machine using rotating wings (i.e., rotors) to provide lift, propulsion, and control forces. The rotor produces a lift force equal to the weight of the helicopter and because the generation of this lift force does not require any forward flight speed, the helicopter can rise vertically from the ground and hover. A simpler definition, therefore, is that a helicopter is an aircraft using a rotor (or rotors) that can hover – see Hafner (1954). Tilting the orientation of the rotor disk(s) provides the forces and moments to control the helicopter in flight. Tilting the rotor disk fore and aft provides pitch control, and tilting it left and right gives roll control. If a single main lifting rotor is used, then a sideward thrusting tail rotor provides anti-torque and directional (yaw) control. If the rotor disk is tilted progressively forward, the rotor provides a propulsive force, accelerating the helicopter into forward flight.

Although the helicopter has been described as an "ungainly, aerodynamic maverick" [Carlson (2002)], the modern helicopter is indeed a machine of considerable engineering sophistication and refinement (Fig. 1.1) and plays a unique role in modern aviation provided by no other aircraft. It is truly a unique form of aircraft and a mastery of modern aeronautical engineering. The helicopter can take off, fly forward or backward, climb and descend, and move in almost any direction at the whim of the pilot. This is the form of true flight that inspired humankind literally hundreds of years before the helicopter became a reality. Igor Sikorsky's vision of a rotating-wing aircraft that could "lift itself vertically" and safely perform all these desirable flight maneuvers under full control of a pilot was ultimately only to be achieved in the mid-1930s, some thirty years after fixed-wing aircraft (airplanes) were flying successfully. In the last seventy years, the helicopter has matured from a cumbersome, vibrating contraption that could barely lift its own weight, into a modern and efficient aircraft that has become an indispensable part of modern life. Its modern civilian roles are almost limitless and encompass sea and land rescue, police surveillance, oil rig servicing, homeland defense, and other important missions. Without question, helicopters are an essential part of any modern military.

Rotating-wing aircraft are far more complicated than they might first appear. Aerodynamically, the airflow through the helicopter rotor is extremely difficult to define and even after many years of intense study it still defies a fully adequate description. The ability to define and predict the rotor aerodynamics, however, is key to the prediction of the performance of the helicopter as a whole. Mechanically, the helicopter is complicated as well. The long slender rotor blades twist and bend, flap up and down, and lead and lag about

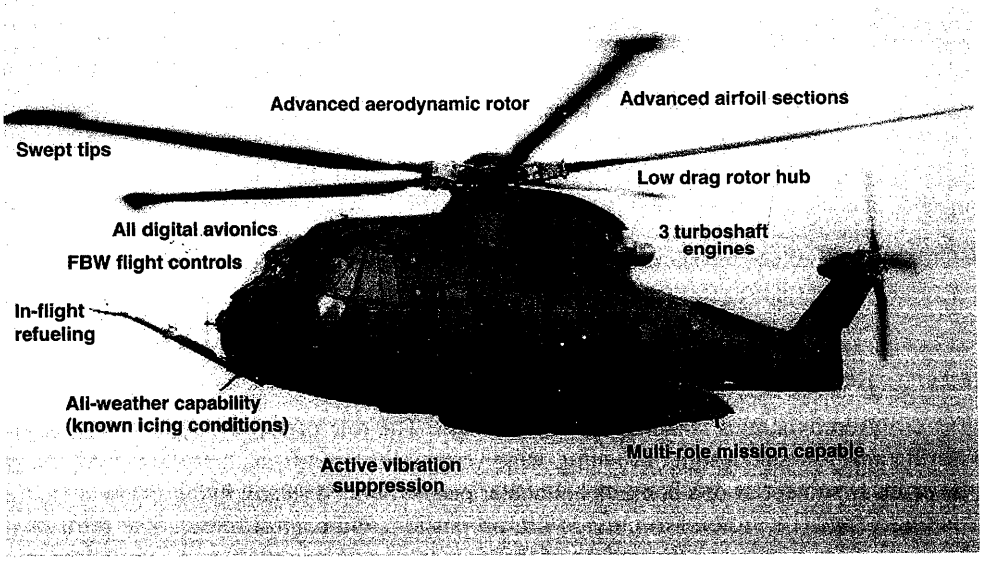

Figure 1.1 Modern helicopters have matured into sophisticated machines with extraordinary capability, which fulfill many civilian and military aviation roles. Agusta–Westland EH–Industries EH-101. (Photo by permission of Agusta–Westland.)

hinges that attach them to the rotor shaft. The need to control the aerodynamic forces on the rotor requires that the pitch of each blade be changed individually as the blades rotate about the shaft. Despite the relatively high aerodynamic and mechanical complexity of the rotor system and the helicopter as a whole, there are still many parallels in their development when compared to fixed-wing aircraft. However, the longer and more tumultuous

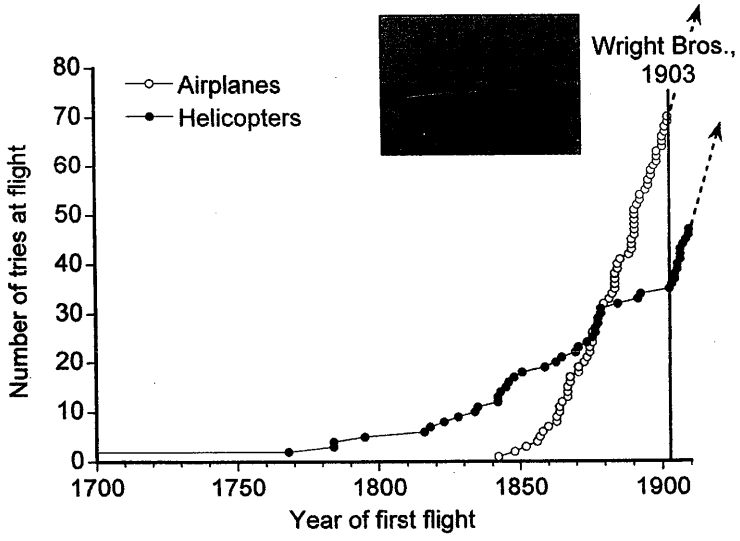

Figure 1.2 Until the middle of the nineteenth century, more attempts had been made to build rotating-wing aircraft than airplanes. Data source: Hafner (1954) and adapted from Harris (1994).

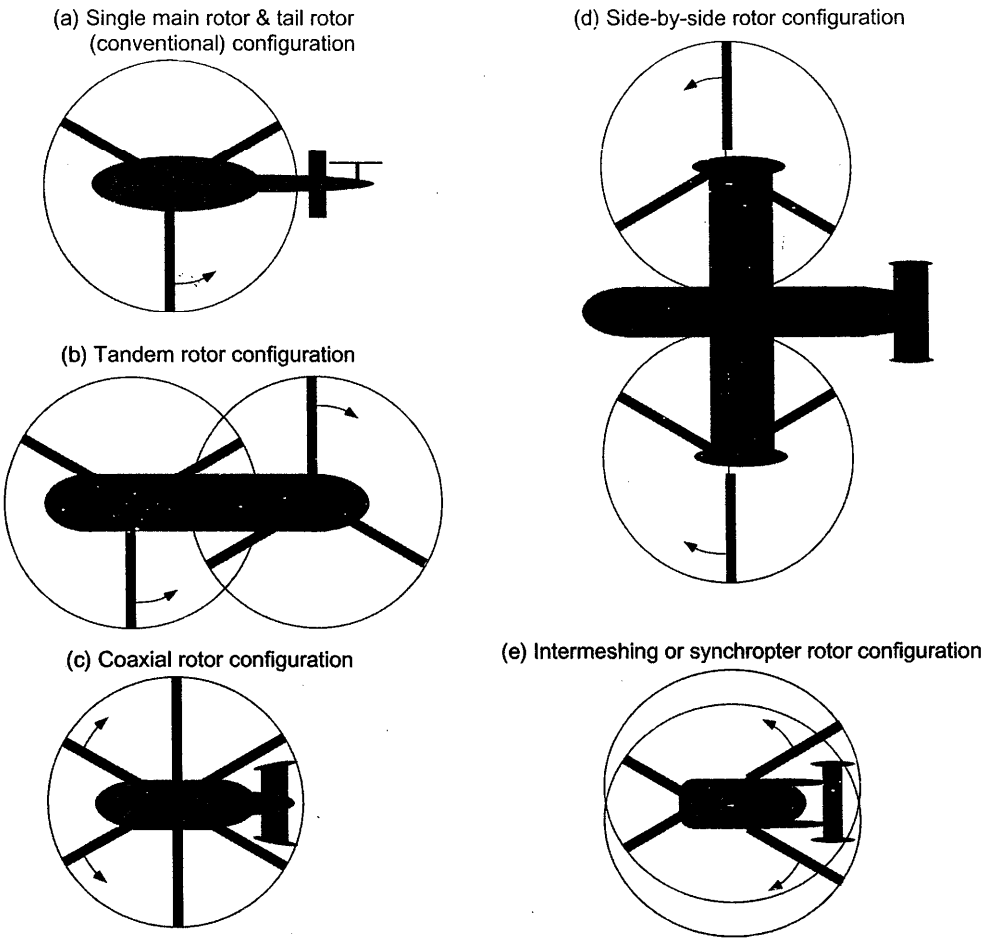

Figure 1.3 Types of helicopter. (a) Single main rotor/tail rotor (conventional) configuration. (b) Tandem rotors. (c) Coaxial rotors. (d) Side-by-side rotors. (e) Intermeshing rotors.

gestation period of the helicopter is clearly attributable to the greater depth of scientific and aeronautical knowledge that was required before all the various technical problems could be understood and overcome. Along with the need to understand the basic aerodynamics of vertical flight and improve upon the aerodynamic efficiency of the helicopter, technical barriers included the need to develop suitable high power-to-weight ratio engines and high strength-to-weight ratio materials for the rotor blades, hub, fuselage, and transmission.

Compared to airplanes – the development of which can be clearly traced to Lilienthal in Germany, Pilcher in Britain, Langley in the United States, and the first controlled flight of a piloted powered aircraft by the Wright Brothers in 1903 – the origins of successful helicopter flight are less clear. It may seem surprising that until the middle of the nineteenth century there had been more attempts to build helicopters than fixed-wing aircraft (see Fig. 1.2). Yet the early preference of helicopters over airplanes is perhaps not so surprising given the rapid adoption of the marine propeller during the same time period. Therefore it would seem that the preferred means of vertical-rising locomotion through a fluid would be a propeller of some type. Yet, other than making short hops off the ground, none of these early machines were successful in demonstrating sustained, fully controlled vertical and hovering flight.

Many problems plagued the early attempts at powered vertical flight with rotating wings. This included the relatively poor understanding of rotating-wing aeromechanics[1] to allow for efficient rotors, the lack of suitable engines, counteracting torque reaction from the shaft driven rotor(s), and providing the machine with enough stability and control. Many of the early machines were of the coaxial or side-by-side (lateral) rotor configuration – see Fig. 1.3. Contrarotating rotors – one rotor above the other on a concentric shaft – automatically balance torque reaction on the airframe, despite the greater mechanical complexity involved in gearing and controlling the two rotors. Side-by-side rotors, especially if the shafts were inclined inwards, gave the early machines somewhat better lateral stability, but again there was a greater level of mechanical complexity associated with this type of design. The intermeshing rotor design has outward tilted contrarotating shafts. The simplest idea of using a single rotor with a sideward thrusting tail rotor to compensate for torque reaction was not used until much later in the initial development of the helicopter.

1.2 Producing Thrust

In its simplest terms, the thrust on the helicopter rotor is generated by the aerodynamic lift forces created on the spinning blades. To turn the rotor, power from an engine must be transmitted to the rotor shaft. It is the relatively low amount of power required to lift the machine compared to other vertical take off and landing (VTOL) aircraft that makes the helicopter unique. Efficient hovering flight with low power requirements comes about by accelerating a large mass of air at a relatively low velocity; hence we have the large diameter rotors that are one obvious characteristic of helicopters. In addition, the helicopter must be able to fly forward, climb, cruise at speed, and then descend and come back into a hover for landing. This demanding flight capability comes at a price, including mechanical and aerodynamic complexity and higher power requirements than for a fixed-wing aircraft of the same gross weight. All of these factors influence the design, acquisition, and operational costs of the helicopter. It is clear that much has been accomplished over the last sixty years in improving the capabilities and efficiency of the helicopter, but one must wonder what would really be possible with future helicopters if these complex aerodynamics could be fully understood and controlled to harness its maximum efficiency!

Besides generating all of the vertical lift, the rotor is also the primary source of control and propulsion for the helicopter, whereas these functions are separated on a fixed-wing aircraft. For forward flight, the rotor-disk plane must be tilted so that the rotor-thrust vector is inclined forward to provide a propulsive component to overcome both rotor and airframe drag. The orientation of the rotor disk to the airflow also provides the forces and moments to control the attitude and position of the helicopter. The pilot controls the magnitude and direction of the rotor thrust vector by changing the blade pitch angles (using collective and cyclic pitch inputs through the controls), which changes the blade lift and the distribution of lift forces over the rotor disk. By incorporating articulation into the rotor design through the use of mechanical flapping and lead–lag hinges that are situated near the root of each blade, the rotor disk can be tilted in any direction in response to these blade pitch inputs. However, the mechanical complexity of the rotor hub required to allow for articulation and pitch control leads to high design and maintenance costs. As the helicopter begins to move into forward flight, the blades on the side of the rotor disk that advance into the relative wind will experience a higher dynamic pressure and lift than the blades on the retreating side of the disk, and as a result asymmetric aerodynamic forces and moments will be

[1] A branch of mechanics that deals with the motion of air and the effects on bodies.

produced on the rotor. Articulation helps allow the blades to naturally flap and lag so as to help balance out these asymmetric aerodynamic effects. With the inherently asymmetric airflow environment and the flapping and pitching blades, the aerodynamics of the rotor become relatively complicated and lead to unsteady forces. These forces are transmitted from the rotor to the airframe and are a source of vibrations, resulting in not only crew and passenger discomfort, but also considerably reduced airframe component lives and higher maintenance costs. However, with a thorough knowledge of the aerodynamics and careful design, all these adverse factors can be minimized or overcome to produce a highly reliable and versatile aircraft.

1.3 Key Technical Problems in Attaining Vertical Flight

There are many authoritative sources that record the development of helicopters and other rotating-wing aircraft such as autogiros. These include Gregory (1944), Lambermont (1958), Gablehouse (1967), Gunston (1983), Apostolo (1984), Boulet (1984), Lopez & Boyne (1984), Taylor (1984), Everett-Heath (1986), Fay (1987), and Spenser (1999), among others. Boulet (1984) takes a unique approach in that he gives a first-hand account of the early helicopter developments though interviews with the pioneers, constructors, and pilots of the machines. A remarkably detailed history of early helicopter developments is given by Liberatore (1950, 1988, 1998). For original publications documenting early technical developments of the autogiro and helicopter, see Warner (1920), von Kármán (1921), Balaban (1923), Moreno-Caracciolo (1923), Klemin (1925), Wimperis (1926), and Seiferth (1927).

As Liberatore (1998) described, the early work on the development of the helicopter can be placed into two distinct categories: inventive and scientific. The former is one where intuition is used in lieu of formal technical training, and the latter is one where a trained, systematic approach is used. Prior to the nineteenth century there were few scientific investigations of flight or the science of aerodynamics. The inherent mechanical and aerodynamic complexities in building a practical helicopter that had adequate power and control and did not vibrate itself to pieces, resisted many ambitious efforts. The history of flight documents literally hundreds of failed helicopter projects, which at most made only brief uncontrolled hops into the air. Clearly, some designs provided a contribution to new knowledge that ultimately led to the successful development of the modern helicopter. Yet, it was not until the more scientific contributions of engineers such as Juan de la Cierva, Henrich Focke, Raoul Hafner, Harold Pitcairn, Igor Sikorsky, Arthur Young, and others did the design of a truly safe and practical helicopter become a reality.

Seven fundamental technical problems can be identified that limited early experiments with helicopters. These problems are described by Sikorsky (1938 and various editions) and in many other sources. In summary, these problems were:

1. Understanding the basic aerodynamics of vertical flight. The theoretical power required to produce a fixed amount of lift was an unknown quantity to the earliest experimenters, who were guided more by intuition than by science. The first significant application of aerodynamic theory to helicopter rotors came about in the early 1920s. [See also Liberatore (1998) for a historical discussion of this point.]
2. The lack of a suitable engine. This was a problem that was not to be overcome until the beginning of the twentieth century through the development of practical internal combustion (gasoline-powered) engines. The steam engine was never a viable concept for any type of aircraft. However, the development of internal

combustion engines with sufficient power-to-weight ratios suitable for use on a helicopter did not occur until the 1920s.

3. Keeping structural weight and engine weight down so the machine could lift a pilot and a payload. Early power plants were made of cast iron and were heavy. Aluminum was not available commercially until about 1890 and was inordinately expensive, it not being used as a construction material for airframes and aircraft engines until about 1915.
4. Counteracting rotor–torque reaction. The relatively simple idea of a tail rotor to counter torque reaction was not used on most early helicopter designs, these machines were either coaxial or side-by-side rotor configurations. Yet, building and controlling two or more primary lifting rotors was even more difficult than controlling one rotor, a fact that seemed to evade many inventors and constructors.
5. Providing stability and properly controlling the machine, including a means of defeating the unequal lift produced on the blades advancing into and retreating from the relative wind when in forward flight. These were problems that were only to be fully overcome with the use of blade articulation, ideas that were pioneered by Cierva, Breguet, and others, and with the development of practical forms of cyclic blade pitch control by Hafner and others.
6. Conquering the problem of vibrations. This was a source of many mechanical failures of the rotor and airframe because of an insufficient understanding of the dynamic and aerodynamic behavior of rotating wings. It was to be many years before such problems could be reduced to the thresholds where the helicopter was to become as reliable as a fixed-wing aircraft.
7. The capability to recover safely to the ground in the event of engine failure (i.e., a "gliding" or autorotational requirement – see page 28). It is fair to say that this capability is critical to the success of any practical helicopter or other type of rotorcraft because it would simply not be accepted otherwise.

The relatively high weight of the structure, engine, and transmission was mainly responsible for the painfully slow initial development of the helicopter. In particular, the success of the helicopter had to wait until aircraft engine technology could be refined to the point that lightweight engines with considerable power could be built. By 1920, gasoline-powered reciprocating engines with higher power-to-weight ratios were more widely available and the anti-torque and control problems of achieving successful vertical flight were at the forefront. This resulted in the development of a vast number of prototype helicopters. Many of the early designs were built in Britain, France, Germany, and Italy, which led the field in several technical areas. However, with all the various incremental improvements that had been made to the basic helicopter concept during the pre–WW2 years, it was not until the late interwar period that significant technical advances were made and more practical helicopter designs began to appear. One of the most important advances of all was in engine technology, with powerful reciprocating and gas turbine (turboshaft) engines, the latter of which revolutionized both fixed-wing and rotating-wing borne flight.

1.4 Early Thinking

A timeline documenting the evolution of some key rotating-wing aircraft through 1950 is shown in Fig. 1.4, the year 1950 being the onset of large-scale commercial success for the helicopter. The ideas of vertical flight can be traced back to early Chinese tops, a toy first used about 400 BC. Everett-Heath (1986) and Liberatore (1998) give a detailed

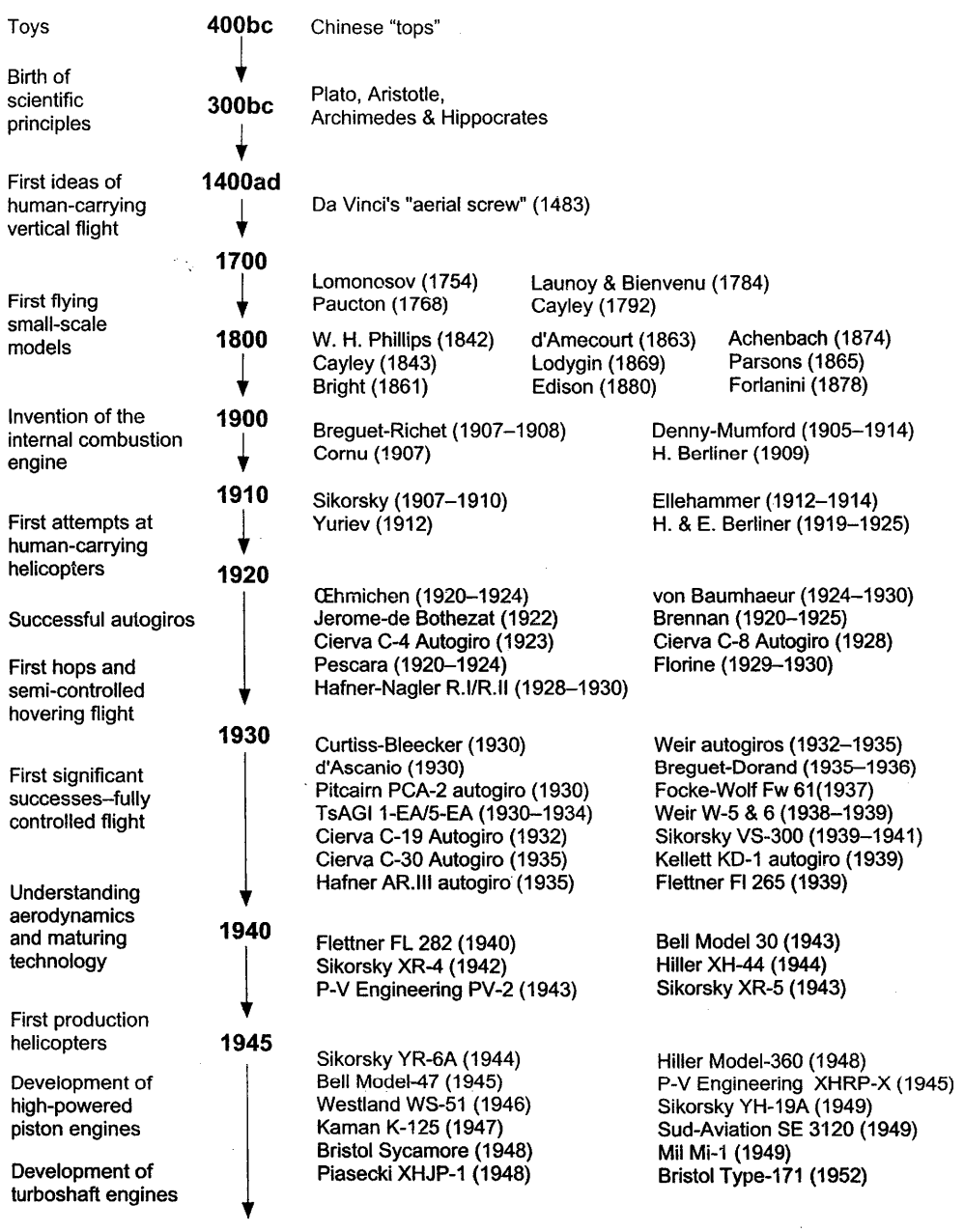

Figure 1.4 Timeline showing the development of helicopters and autogiros up to 1950.

history of such devices. The earliest versions of the Chinese top consisted of feathers at the end of a stick, which was rapidly spun between the hands to generate lift and then released into free flight. These toys were probably inspired by observations of the seeds of trees such as the maple and sycamore, whose whirling, autorotating seeds carry far on the breeze. While the Chinese top was no more than a toy, it is perhaps the first tangible device of what we may understand as a helicopter. The Chinese top is still a popular toy today.

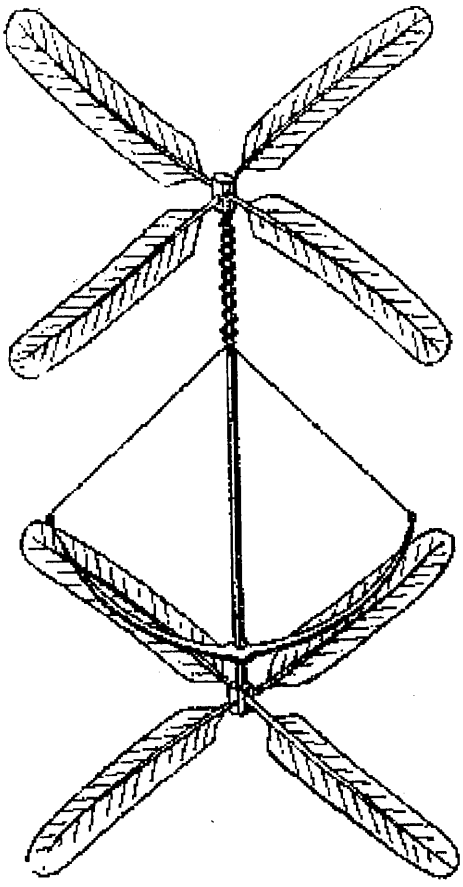

Figure 1.5 A facsimile of the "Chinese Top" built by Launoy & Bienvenu in 1783.

More than two millennia later, about 1754, Mikhail Lomonosov of Russia had developed a small coaxial rotor modeled after the Chinese top but powered by a wound-up spring device. In 1783, the French naturalist Launoy, with the assistance of a mechanic named Bienvenu, used a coaxial version of the Chinese top in a model consisting of a contrarotating set of turkey feathers. Their device was powered by a string wound around the rotor shaft that was tensioned by a crossbow (Fig. 1.5). When the tension was released, the rotor spun and the device climbed high into the air. Launoy & Bienvenu's invention flew well and its success even created quite a stir in scientific circles. Inspired by the early success with these whirling tops, in 1786 the French mathematician A. J. P. Paucton (1768) published a scientific paper titled "Théorie de la vis D'Archimède," where he proposed one of the first concepts of a human-carrying helicopter.

Among his many hundreds of intricate drawings, the Renaissance visionary Leonardo da Vinci shows what is a basic human-carrying helicopter-like machine, which was an obvious elaboration of an Archemedes water-screw. His sketch of the "aerial-screw" or "air gyroscope" device (Fig. 1.6) is dated to 1483, but it was not published until the end of the eighteenth century. The device comprises a helical surface formed out of iron wire, with linen surfaces made "airtight with starch." Da Vinci describes that the machine should be "rotated with speed that said screw bores through the air and climbs high." He realized that the density of air was much less than that of water and so da Vinci describes how the device

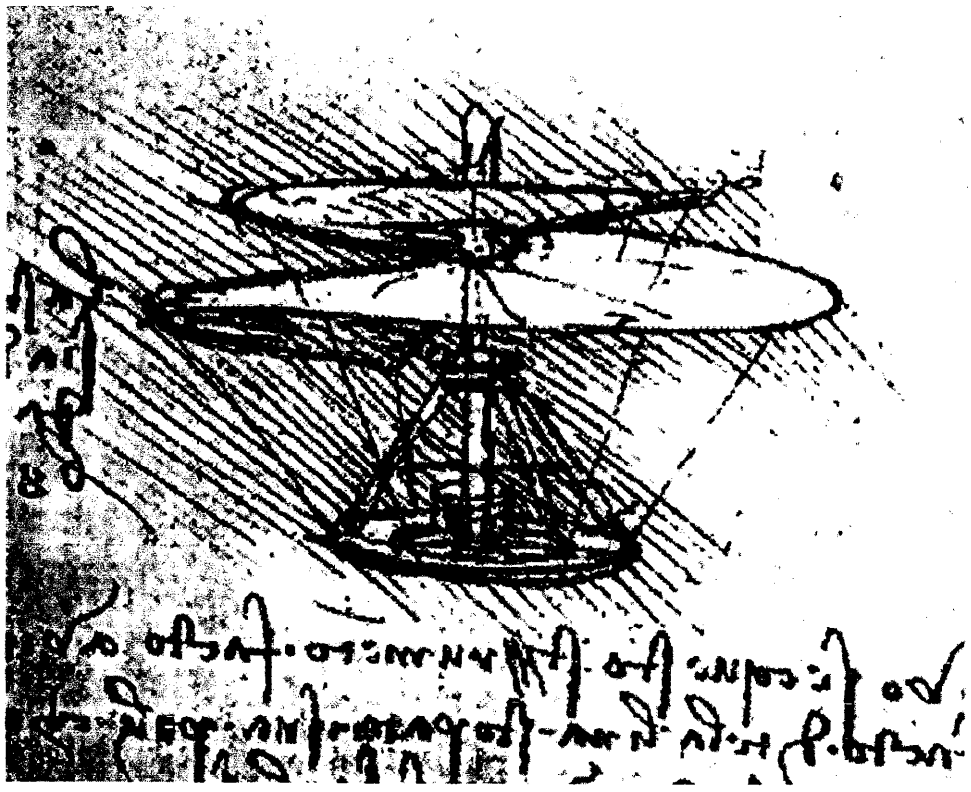

Figure 1.6 Leonardo da Vinci's aerial screw machine, dated to 1483. Original drawing is MS 2173 of Manuscript (codex) B, folio 83 verso, in the collection of the Biblothèque L'Institute de France (Paris).

needed to be relatively large to produce enough lift to accomplish this feat – the number '8' in his backward mirror image script and to the left of the sketch (Fig. 1.6) indicates that the size of the rotor is 8 *braccia*,[2] which translates into a rotor of up to 26 ft (7.9 m) in diameter. Da Vinci clearly did not build his proposed machine except perhaps for some small models, but his idea was far ahead of its time. Although da Vinci worked on various concepts for engines, turbines, and gears, he did not seem to unite the ideas of his aerial-screw machine with an engine, nor did he seem to appreciate the concept of *torque-reaction*.[3] Therefore, a torque applied to the rotor shaft will result in a reaction torque tending to rotate the platform from which the torque is applied. See Hart (1961) or Giacomelli (1930) for further details of da Vinci's aeronautical inventions.

The great polymath, Sir George Cayley, is famous for his work on the basic principles of flight, which dates from the 1790s – see Pritchard (1961). As a young boy, Cayley had been fascinated by the Chinese top and by the end of the eighteenth century he had constructed several successful vertical-flight models with rotors made of sheets of tin and driven by wound-up clock springs. His fascination with flight led him to design and construct a whirling-arm device in 1804, which was probably one of the first scientific attempts to study the aerodynamic forces produced by lifting wings. Cayley (1809–1910) published

[2] A *braccia* is an old Florentine unit of measure, approximately equal to one arm's length, although it has been defined variously between 15 and 39 in (0.28 to 1 m).

[3] Newton's third law states that for every action (force) there is an equal and opposite reaction (force).

a three-part paper that was to lay down the scientific principles of aerodynamics – see Anderson (1997). In a later paper, published in 1843, Cayley gives details of a relatively large vertical flight aircraft design that he called an "Aerial Carriage." The machine had two pairs of rotors, arranged side by side, to provide lift. However, the device remained an idea because the only powerplants available at the time were steam engines and these were much too heavy to allow for successful powered flight. Cayley's convertiplane is, nevertheless, an interesting concept. The issue of torque reaction was solved by using contrarotating rotors and two propellers provided horizontal thrust to push the aircraft through the air. The design of the rotors was such that they flattened down to become solid disks and act as wings in forward flight, an idea possibly gleaned from the American Robert Taylor – see Liberatore (1998). Cayley suggested that an engine with considerable power would be needed to accomplish this feat and he even mentioned in his paper that "very great power, in proportion to the weight of the engine, is necessary." While Cayley worked on engine concepts, it is not clear, however, if he ever actually attempted to establish the power requirements for vertical flight by means of theoretical calculations.

The lack of a suitable powerplant continued to stifle aeronautical progress, but the use of miniature, lightweight steam engines met with some success in powering smaller free-flying model helicopters. In the 1840s, another Englishman, W. H. Phillips, constructed a steam-driven vertical flight machine, where steam generated by boiling water in a miniature boiler was ejected out of the blade tips. Although impractical on a larger scale, Phillips's machine was significant in that it marked the first time that a model helicopter had flown under the power of an engine rather than stored energy devices such as bowstrings or other types of wound-up springs. In the early 1860s, Ponton d'Amécourt of France attempted to fly a number of small steam-powered helicopter models. He called his machines *hélicoptères*, which is a word derived from the Greek adjective *elikoeioas*, meaning spiral or winding, and the noun *pteron*, meaning feather or wing – see Wolf (1974) and Liberatore (1998). The novelist Jules Verne was impressed with d'Amécourt's attempts at vertical flight and in 1886 he wrote "Robur le Conquerant" (later published in English as "The Clipper of the Clouds") where the hero cruised around the skies in a giant helicopter-like machine that was lifted by thirty-seven small coaxial rotors and pulled through the air by two propellers. It was probably Jules Verne rather than d'Amécourt who is responsible for the word *helicopter* entering the standard lexicon.

Other notable vertical flight models that were constructed at about this time include Bright's coaxial design in 1861 and Dieuaide's twin-rotor steam-driven model in 1877. In 1865 Sir Charles Parsons of England built another type of helicopter model driven by a steam engine. Wilheim von Achenbach of Germany built a single rotor model in 1874, and he was probably the first to use the idea of a tail rotor to counteract the torque reaction from the main rotor. About 1869, a Russian helicopter concept was developed by Lodygin using a rotor for lift and a propeller for propulsion and control. Around 1878, Enrico Forlanini of Italy also built a flying steam-driven helicopter model. This model had dual contrarotating rotors, and it flew freely at heights of over 40 ft (12.2 m) for as much as twenty seconds.

In the 1880s, Thomas Alva Edison experimented with small helicopter models in the United States. He tested several rotor configurations driven by a guncotton engine, which was an early form of internal combustion engine. Later, Edison used an electric motor for power and he was one of the first to realize from his experiments the need for a large diameter rotor with low blade area to give good hovering efficiency [see Liberatore (1998)]. Edison was to say: "I got the motor and put it on the scales and tried a number of different things and contrivances [rotors] connected to the motor to see how it would lighten itself on the scale. I got some data and made up my mind that what was needed was a very powerful

engine for its weight." Unlike other experimenters of the times, Edison's more scientific approach to the problem proved that both high aerodynamic efficiency of the rotor and high power from an engine were required if successful vertical flight was ever to be achieved. In 1910, Edison patented a rather cumbersome looking full-scale helicopter concept with very nonaerodynamic looking boxkite blades, but there is no record that it was ever constructed – see Liberatore (1998) for further details.

1.5 The Hoppers

In 1907, about four years after the Wright Brothers' first successful powered flights in fixed-wing airplanes at Kitty Hawk in the United States, Paul Cornu of France constructed a helicopter that is reported to have carried a human off the ground for the first time. Boulet (1984) gives a good account of the work. Although Cornu had conducted experiments with small rotor models, he lacked the necessary theoretical understanding of rotor aerodynamics and performance to enable these results to be properly scaled to a full-size helicopter. Such theoretical analyses were not to be widely understood and used until the 1920s. Cornu's machine (Fig. 1.7) used a skeletal airframe of very simple construction and relatively light weight, being constructed of a 20 ft (6.1 m) length of steel beam bent into a wide U-shape, with six "star" frames all tied together with cables. A rotor was mounted at each end of the main structural beam. The rotors rotated in opposite directions, a necessary requirement to cancel torque reaction. The inner hub part of each rotor looked like large bicycle wheels. At the periphery of each rotor, there were two light, wide-chord and fabric-covered blades. Power was supplied to the rotors by a 24 hp (17.9 kW) Antoinette gasoline motor through a driving belt and pulley transmission, a mechanism that it seems caused Cornu many problems and much frustration. The whole machine sat on four bicycle wheels. A primitive means of control was achieved by placing a "plane" or a wing in the slipstream below each of the rotors; the inclination and force on the these wings was controlled by the pilot with two hand operated levers. On November 13, 1907, at Normandy in France, Cornu's "flying bicycle" was reported to have made several tethered flights of a few minutes at low altitude. In Cornu's own words, "... the aircraft left the ground with four wheels all together...."

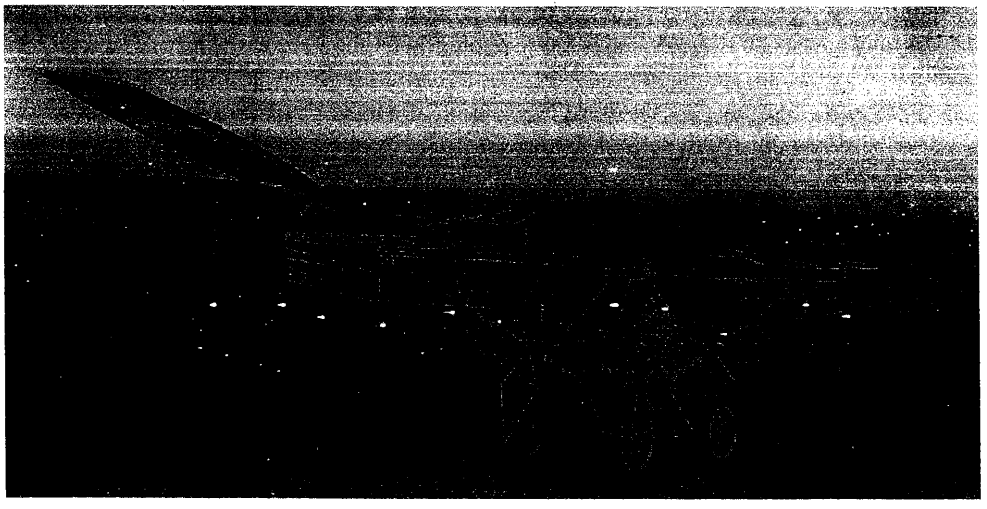

Figure 1.7 The Cornu helicopter, circa 1907. (Courtesy NASM, Smithsonian Institution, SI Neg. No. 74-8533).

Figure 1.8 The Breguet *Gyroplane No. 1*, looking somewhat like an assemblage of ladders, made some uncontrolled hops off the ground in 1907.

However, no supporting photographs or eyewitness accounts of his flights have ever been produced. See Boulet (1984) and Leishman (2001a) for further details.

In 1904, the French scientist Charles Richet built a small unpiloted helicopter. Even then, Richet was well-known for work in aerodynamics and had given many lectures on the subject at the French Académie des Sciences. One of Richet's students, Louis Breguet, was soon to become a famous aviation pioneer. During the latter part of 1906, the Breguet Brothers had begun to conduct helicopter experiments under the guidance of Richet. In 1907 the Breguet Brothers made experiments with a rotary-winged test rig with a force-balance [see Breguet (1936)] and shortly thereafter they built their first helicopter. Their ungainly quadrotor *Gyroplane No. 1* consisted of four long girders made of steel tubes and arranged in the form of a horizontal cross (Fig. 1.8). A rotor consisting of four biplane blades was placed at each of the four corners of the cross, giving a total of 32 separate lifting surfaces. The pilot sat in the center of the cross next to the 40 hp (29.8 kW) engine. The machine is reported to have carried a pilot off of the ground into free flight, albeit briefly. These claims may have been exaggerated because photographs show the assistance of several men stabilizing and lifting the machine. Clearly, the machine could never have flown completely freely because, like the Cornu machine, it lacked flight stability and a proper means of control. However, the Breguet machine was probably closer to achieving vertical flight than the one made by Paul Cornu – see Boulet (1984) and Leishman (2001b).

Aldridge (1954) describes a helicopter that was built by the designer Edwin Mumford at the William Denny & Brothers' shipyard in Scotland during 1905. This helicopter consisted of six two-bladed rotors, which were mounted on each side of a skeletal frame. The rotors looked much like ship propellers and could not have been efficient for use in air. Control was provided for by tilting the rotor shafts, with a rudder at the tail for directional control. It is claimed that tethered and free flights of the helicopter were made during 1909, where the craft apparently reached altitudes of 10 ft (3.05 m) and forward speeds of 20 mph (32.2 km/h). Tests apparently continued through to 1914, when the machine was destroyed in a storm. Further work on the project was abandoned because of the start of WW1. See Rees (1990) for further details.

In the early 1900s, Igor Sikorsky and Boris Yuriev independently began to design and build vertical-lift machines in Czarist Russia. By 1909, inspired by the work of Cornu,

Breguet, and other French aviators, Sikorsky had built an unpiloted coaxial helicopter prototype. This machine did not fly because of vibration problems and the lack of a powerful enough engine. Sikorsky (1938) stated that he had to await "better engines, lighter materials, and experienced mechanics." His first design was unable to lift its own weight and the second in 1910, even with a more powerful engine, only made short (nonpiloted) hops. Discouraged, Sikorsky abandoned the helicopter idea and devoted his skills to fixed-wing (conventional airplane) designs at which he was very successful. Although Sikorsky never gave up his vision of the helicopter, it was not until the 1930s after he had emigrated to the United States that he pursued his ideas again (see later). Good accounts of the life and work of Igor Sikorsky are documented by Bartlett (1947), Delear (1969), Sikorsky (1964, 1971), Sikorsky & Andrews (1984), Finne (1987), and Cochrane et al. (1989).

The famous Russian aeronautical engineer Konstantine Antonov had also built a prototype coaxial rotor helicopter about 1910. A propeller was used for forward propulsion. The rotors were about 20 ft (6.1 m) in diameter and consisted of many triangular shaped blades. A collective pitch mechanism was used to change the pitch of the blades, which could be set into flat pitch forming a flat disk. The machine did not fly. Unbeknown to Sikorsky, Boris Yuriev had also tried to build a helicopter in Russia around 1912, but with a somewhat modern looking single rotor and tail rotor configuration (Fig. 1.9). This was a revolutionary concept for the time compared to all of the multirotor machines being built, and the concept was patented in 1911. Like Sikorsky's machine, however, Yuriev's helicopter lacked a powerful enough engine. Good accounts of Yuriev's machine are given by Gablehouse (1967), Everett-Heath (1988), and Liberatore (1998). Yuriev was to guide Soviet helicopter development and trained a number of leading Soviet designers, including Mikhail Mil. He was also to author a book, *The Aerodynamic Design of Helicopters*, which was published in Russian in the early 1950s.

Besides being one of the first to use a tail rotor design, Yuriev was another one of several firsts to propose the concept of cyclic pitch for rotor control using a form of swashplate. However, he did not actually use the cyclic mechanism on his 1912 machine. Another early cyclic pitch concept was patented by Gaetano A. Crocco of Italy in 1906. Crocco, who was an engineer and prolific inventor, recognized that if a helicopter was to work properly, a means of changing the pitch on the blades would be needed to account for the

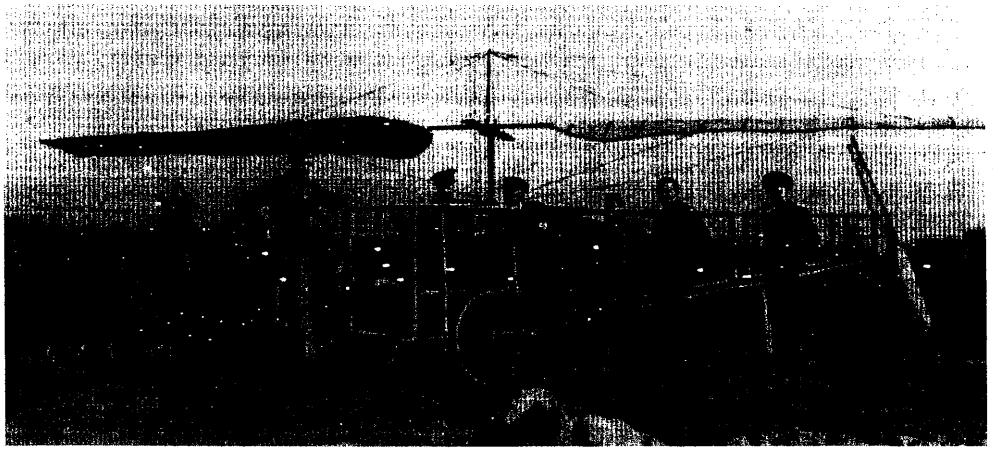

Figure 1.9 In 1912 Boris Yuriev of Russia built helicopter using a single rotor and tail rotor for anti-torque, but it did not fly for want of a suitable engine.

dissymmetry in the airflow between the side of the rotor advancing into the relative wind and the side retreating away from the wind when in forward flight. The concept of cyclic pitch was one key to attaining full control of the helicopter, although the successful mechanical implementation of this concept was not to occur for many more years until it was properly married with the flapping hinge.

Professor Zhukovskii (Joukowski) and his students constructed a primitive coaxial helicopter at Moscow University in 1910 – see Gablehouse (1967) and Everett-Heath (1988). Joukowski is well known for his theoretical contributions to aerodynamics and he published several papers on the subject of rotating wings and helicopters – see also Margoulis (1922) and Tokaty (1971). While Rankine and Froude had already established the general theory of propellers and rotors using momentum theory prior to 1890 (see Chapter 2), there were a number of other notable developments in the basic aerodynamic theory. The Frenchman Drzewiecky had developed a hybrid momentum–blade element concept as early as 1900 and in 1909 he published a book on rotors titled "Des Hélices Aériennes Théorie Générale des Propulseurs." In 1904, Joukowski published a paper titled "On the Useful Load Lifted by a Helicopter." In 1906, Joukowski's better known work "About Connected Vortices" was published. A year later a paper titled "A Multi-Bladed Propeller-Screw" appeared. In 1909 Joukowski investigated the theory of the effects of forward flight speed on a rotor. This paper was titled "Experiments on the Theoretical Determination of the Effect of the Airflow on the Surface of a Propeller." Here Joukowski proved that because of the nonaxisymmetric distribution of velocity and airloads, asymmetric forces and moments act on a propeller in edgewise flight. Of course, this implied that to control a helicopter such that it could fly forward would be a difficult task indeed. Although this problem was later solved with the invention of cyclic blade pitch control and the incorporation of blade flapping hinges, Joukowski offered no method of solution in his paper.

About 1912, the Danish aviation pioneer Jacob C. Ellehammer designed a coaxial rotor helicopter. Boulet (1984) gives a good description of the machine, which is shown in Fig. 1.10. The rotor blades themselves were very short; six of these were attached to the periphery of each of two large circular rings of about 20 ft (6.1 m) in diameter, with the blades extending out about another 5 ft (1.52 m). The lower disk was covered with fabric and was actually intended to serve as a parachute in the event the blades or the engine failed. A cyclic pitch mechanism was used to change the pitch of the rotating blades and provide control, this being another one of many early applications of the cyclic pitch concept. The pilot was supported in a seat that could be moved forward and sideways below the rotor, allowing for additional kinesthetic control. This helicopter made many short hops into the air but it never made a properly controlled free flight. It was finally destroyed in a crash, although it carries the distinction of being one of the first early helicopters to be photographed in free-flight.

An Austrian, Stephan Petroczy, with the assistance of the well-known aerodynamicist Theodore von Kármán, built and flew a coaxial rotor helicopter (Fig. 1.11) during the period 1917–1920. Interesting design features of this machine included a pilot/observer position above the rotors, inflated bags for landing gear and a quick-opening parachute. The machine was powered by three rotary engines, a good example of redundancy in the event of an engine failure. Although the machine never flew freely, it accomplished numerous tethered vertical flights restrained by cables. It was actually used for military observation, and was a more economical and easily recovered alternative to observation balloons. The work is summarized in a report by von Kármán (1921) and published by NACA. It is significant that von Kármán also gives results of laboratory tests on the rotors, which were really oversize propellers. The results (see Fig. 1.11) agree with elementary rotor theory

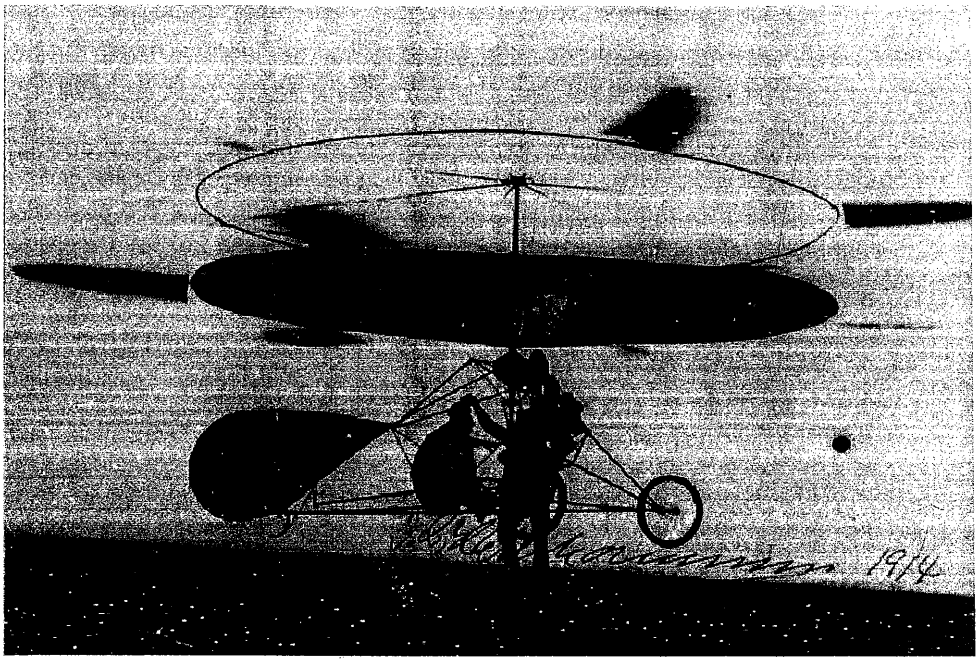

Figure 1.10 Danish aviation pioneer Jacob Ellehammer flew a coaxial rotor helicopter design in 1912.

in that the thrust and power should increase with the square and cube of rotor rpm, respectively (see page 54), and had a decent hovering efficiency of 60% (i.e., a figure of merit of 0.6 – see discussion in Section 28).

By the end of the nineteenth century there is more evidence that scientific means were being used to understand the lifting capability of rotors and the power required for vertical flight, especially in Britain and France. In the 1860s, F. H. Wenham had made experiments with a two-bladed airscrew in an attempt to measure the forces produced. He was able to conclude that the laws governing the behavior of a propeller in air were the same as for water.

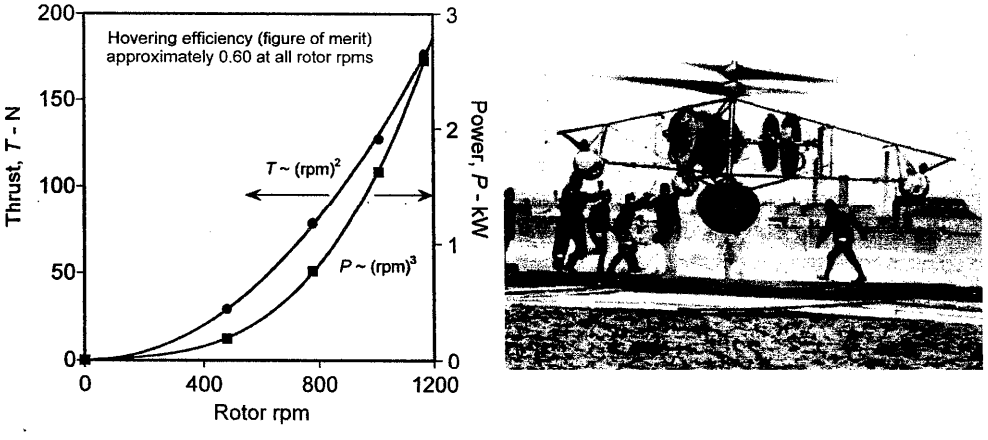

Figure 1.11 The rotor performance of the Petroczy helicopter was measured by Theodore von Kármán, which was one of the first scientific studies of rotor performance.

During the period 1900–1905, W. G. Walker [see Walker (1900, 1905)] was to conduct some of the first scientific studies of the lifting capability of multi-bladed rotors. The experiments were made on rotors with blades constructed of tubular steel frames covered with stretched canvas. The rotor was powered by a steam engine and connected to a spring balance. In the period 1908–1911, H. Chatley developed one of the first mathematical analyses for a lifting rotor [Chatley (1908)]. However, these theories were woefully inadequate to explain the principles of vertical flight and development of the helicopter still proceeded mostly along inventive rather than scientific lines. In 1906, Louis and Jacques Breguet of France built a whirling-arm device called a "Balance Aérodynamétrique," which allowed a means of measuring the performance of rotating-wings – see Breguet (1936). They made meticulous tests of airfoil shapes and rotors, and had begun to understand the essential aerodynamic theory of the helicopter. The works of von Kármán (1921) and William F. Durand [see Warner (1920) and the analysis by Munk (1923)] were also some of the first attempts to scientifically study rotor performance and the power required for vertical flight. Oscar de Asboth conducted similar experiments with propellers, the results of which were published by NACA – see Asboth (1923). In the period 1928–1930, Asboth was also to build four helicopter prototypes, one of which flew in 1930 although it was not a successful design.

In the United States, Émile and Henry Berliner (a father and son) were interested in vertical flight aircraft. As early as 1909, they had designed and built a helicopter based on pioneering forward-flight experiments with a wheeled test rig called an *Aeromobile*. The machine used a 55 hp (41 kW) gasoline engine of Émile Berliner's own design and it was to be one of the first rotary piston engines used for aeronautical purposes. The Berliners were also among the first to notice that the power required for flight with a helicopter is initially lower as it moves from hover into forward flight. Berliner (1908) stated: "It is an accepted theory, which has been proven by practical tests, that a propeller moving forward is more efficient than moored fast in one position. Hence, the lifting power of the *Aeromobile* would increase in free-flight." This novel experiment confirmed the earlier observations of Maxim (1897) and Riabouchinsky (1906).

In 1918 the Berliners patented a single rotor helicopter design, but there is no record that this machine was actually built. Instead, by about 1919, Henry Berliner had built a contrarotating coaxial rotor machine, which made brief uncontrolled hops into the air and reached a height of about 4 ft (1.22 m). By the early 1920s at the College Park Airport in Maryland, the Berliners were flying a helicopter with side-by-side rotors (Fig. 1.12). The rotors were oversized wooden propellers, but made with special airfoil profiles and blade twist distributions. Differential longitudinal tilt of the rotor shafts provided yaw control. Lateral control was aided by cascades of wings located in the slipstream of the rotors. All variants used a conventional elevator and rudder assembly at the tail. A small, variable-pitch vertically thrusting auxiliary rotor on the rear of the fuselage was used as the primary means of pitch control.

Because the performance of their helicopter was very limited, and they were concerned about engine failure, the Berliners soon abandoned the pure helicopter in favor of another hybrid machine. This machine still used the rotors for vertical lift but incorporated a set of triplane wings and a larger oversized rudder. This variant was more successful but it was not a helicopter. The Berliner's final hybrid machine of 1924 was a biplane wing configuration with side-by-side rotors called a "Helicoplane," but it did not fly out of ground effect. However, the Berliner's early flights with the coaxial rotor and side-by-side rotor machines are credited as some of the first rudimentary piloted helicopter developments in the United States. See also Berliner (1908, 1915) and Leishman (2002a) for further details.

Figure 1.12 This Berliner helicopter with side-by-side rotors made short flights at College Park Airport in Maryland in 1922. (Courtesy of College Park Airport Museum.)

The Berliners subsequently went on to form the Erco Company in Riverdale, Maryland, which became a manufacturer of light airplanes and propellers.

1.6 The First Hoverers

During 1919–1926 Louis Brennan worked on a helicopter concept with a large single two-bladed rotor of 60 ft (18.3 m) in diameter. Graham (1973), Everett-Heath (1986), and Fay (1987) give good accounts of Brennan's work. Brennan, an affluent scientist who had previously invented the modern torpedo and a monorail system, had a different approach to solving the problem of torque reaction by powering the rotor with propellers mounted on the blades (Fig. 1.13). These were driven by drive shafts running along the blades to gearboxes. Control was achieved by the use of "ailerons" inboard of the propellers, which were actuated by means of compressed air. The machine was powered by a 230-hp Bentley rotary. While Brennan's work was initially carried out with considerable secrecy, in 1921 the machine was officially being tested at the Royal Aircraft Establishment at Farnborough. In 1922, the machine flew successfully inside a hangar, apparently at one point carrying four "passengers." Further flights outdoors were undertaken through 1926, where the machine made flights at low altitude and was able to fly about 600 ft (182 m) forward. Lack of stability and control caused the machine to crash on its seventh flight, even with the addition of stability enhancing devices. By 1928 the Air Ministry ordered a concept called a "Hélicogyre" designed by the Italian Vittorio Isacco to be built in Britain. The machine made only a few tethered flights. British interest in helicopters quickly faded because of concurrent interest in the autogiro (see Section 1.7).

During the early 1920s, Raul Pescara, an Argentinean living and working in Spain and France, was building and attempting to fly a coaxial helicopter with biplane-type rotor blades (Fig. 1.14). On his first machine, each rotor had six sets of blades that were mounted rigidly to the rotor shaft and this was later decreased to four sets per rotor. As described by Boulet (1984), Pescara's work focused on the need for proper control of the machine, which

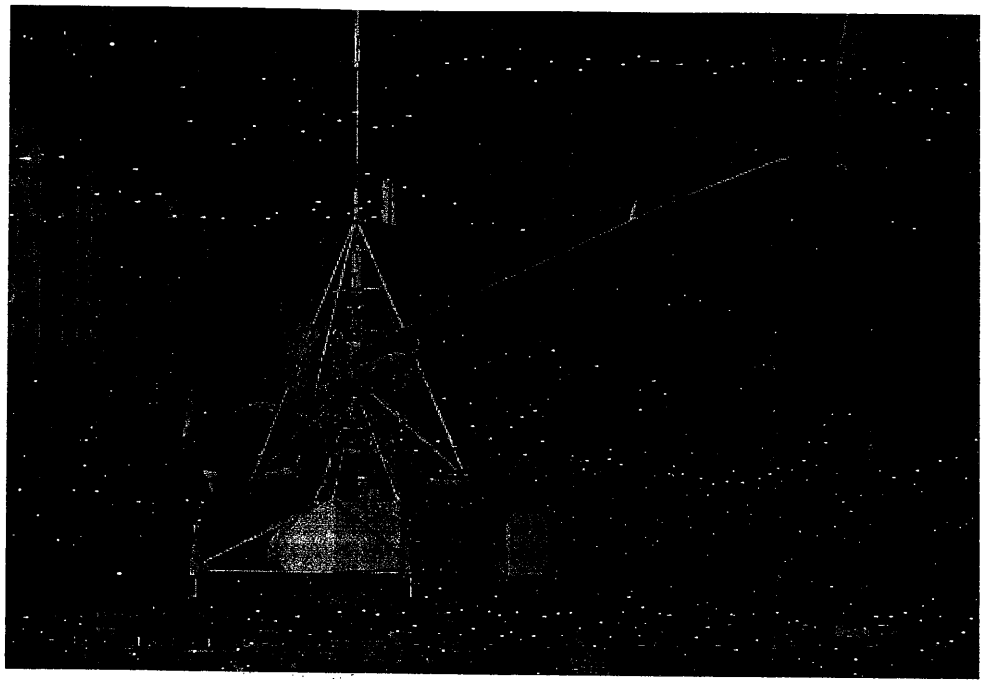

Figure 1.13 The Brennan helicopter inside a hangar at RAE Farnborough, circa 1922.

was achieved through cyclic pitch changes that could be obtained by warping (twisting) the blades periodically as they rotated. This was one of the first successful applications of a cyclic pitch concept to a helicopter. Yaw was controlled by differential collective pitch between the two rotors. Early versions of Pescara's machine were underpowered, which

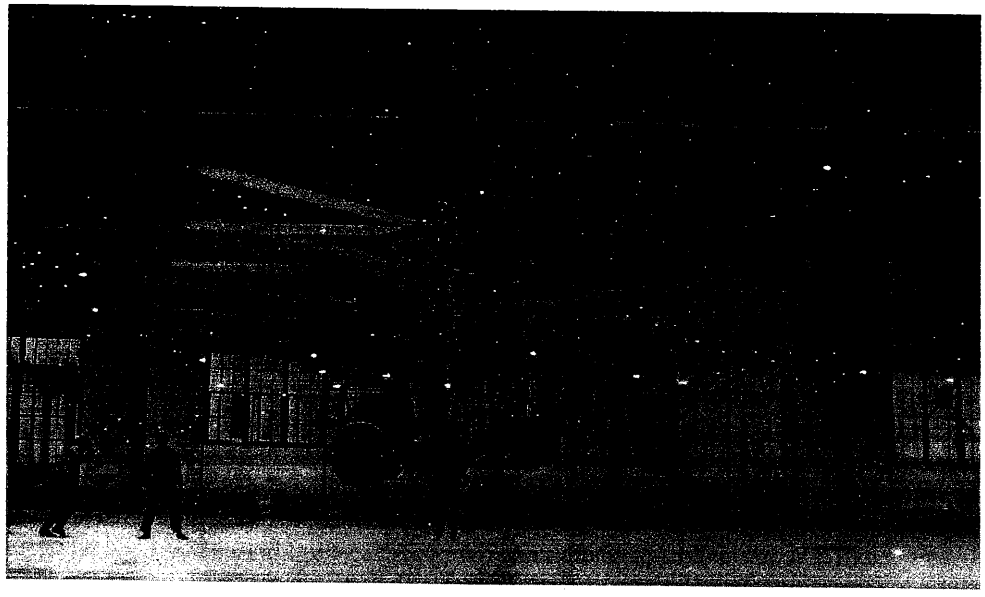

Figure 1.14 Pescara's helicopter hovering in a hanger circa 1922. (Courtesy NASM, Smithsonian Institution, SI Neg. No. 83-16343.)

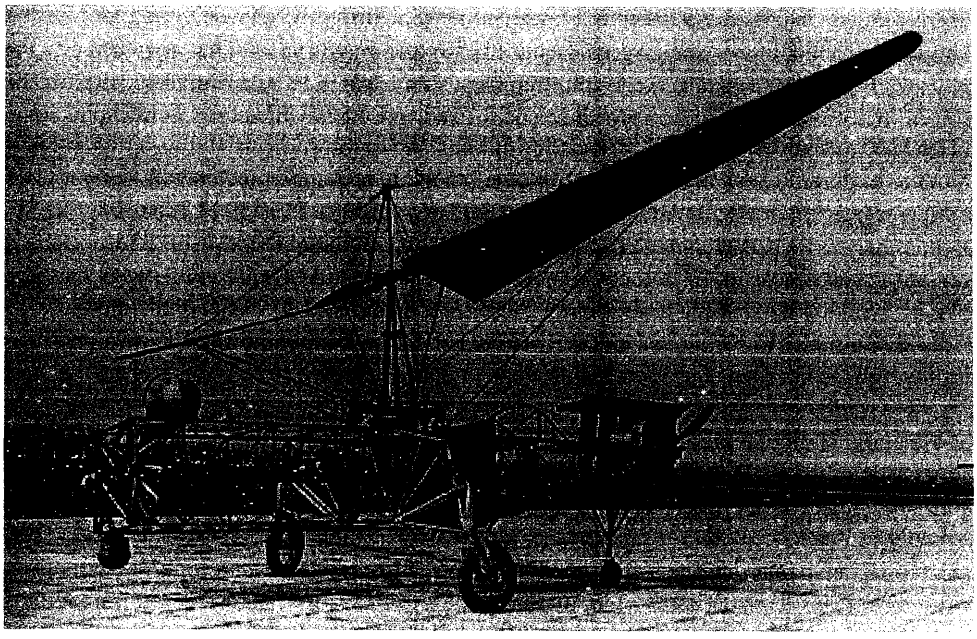

Figure 1.15 Between 1924 and 1930, A. G. von Baumhaeur made attempts to fly a single main rotor helicopter with a separately powered tail rotor. (Courtesy NASM, Smithsonian Institution, SI Neg. No. 77-721.)

may not be surprising considering the large number of blades and high profile drag of the bracing wires of his rotor, and the aircraft did not fly. With a later version of his helicopter using a more powerful engine, some successful flights were accomplished. This attempt reflects much early thinking on helicopters, where more powerful (and heavier) engines were often used rather than trying to make the rotors more efficient. However, as might be expected, these flights were not very successful and with the limited control available they resulted in damage or serious crashes followed by long periods of rebuilding. By 1925 Pescara had finally abandoned his helicopter projects.

Between 1924 and 1930, a Dutchman named A. G. von Baumhaeur designed and built one of the first single rotor helicopters with a tail rotor to counteract torque reaction. Boulet (1984) gives a good description of the machine. Figure 1.15 shows that the fuselage of the von Baumhaeur machine consisted essentially of a tubular truss, with an engine mounted on one end. The other end carried a smaller engine, which turned a conventional propeller to provide a side force and so countering the main rotor torque reaction. The main rotor had two blades, which were restrained by cables so that the blades flapped about a hinge like a seesaw or teeter board. Control was achieved by a swashplate mechanism, which was another early application of this device that was later to provide one standard means of providing blade feathering for collective and cyclic pitch control on the modern helicopter.[4] Unfortunately, von Baumhaeur did not interconnect the main and tail rotors with a transmission, so this caused considerable difficulties in balancing torque and giving proper directional control. Nevertheless, the machine was reported to have made numerous short, hovering flights. It was, however, considerably less capable than the Pescara machine.

[4] In 1897, a British patent was to be granted to White (1898) for a vertically lifting machine with variable pitch (feathering) blades, but it was a windmill concept by Lewis & Lewis (1838) that probably saw the first use of a swashplate for blade pitch control on a rotating-wing.

In the late 1920s, the Austrians Raoul Hafner and Bruno Nagler designed and built a single-seat helicopter – see Everett-Heath (1986) and Fay (1987). The two variants, the R.I and R.II, used a single rotor configuration with a pair of fixed wings located in the rotor downwash to provide anti-torque. The flights were mostly unsuccessful despite some brief tethered hovering flights of up to a minute. For rotor control, Hafner's machine in notable in that it used a continuously variable blade pitch change mechanism using a large diameter bearing or swashplate – see Nagler & Hafner (1932). In 1932 Hafner emigrated to Britain, where he and Juan de la Cierva independently continued work on blade articulation for autogiros and later for helicopters. A later variant of the Hafner R.II used flapping blades, which gave the machine improved control capability. In 1938 Nagler joined Franz Rolz in Germany to form the Nagler Rolz Flugzeugbau, who continued to develop small lightweight helicopter concepts. Hafner was to stay in Britain and became a prolific and forward-thinking rotorcraft designer for Bristol Helicopters [see Hafner (1954)] and later at Westland Helicopters.

1.7 Not Quite a Helicopter

The Spanish engineer Juan de la Cierva had built and flown another type of rotating-wing aircraft as early as 1923 – see Juan de la Cierva (1926, 1930). This aircraft looked like a hybrid between a fixed-wing airplane and a helicopter, with a set of conventional wings and a tail, but with a rotor mounted on a vertical shaft above the fuselage. However, unlike a helicopter, this rotor was not powered directly and was completely free to turn on its shaft. Cierva found that when the rotor disk was inclined backward at a small angle of attack and as the machine was pulled forward by a propeller, the rotor was turned by the action of the airflow on the blades. This aerodynamic self-rotation of the rotor is called "autorotation," and had been understood by Crocco and Yuriev before 1910. Yet the idea of pulling the rotor horizontally through the air to generate lift was clearly that of Cierva. He called his rotating-wing aircraft an "Autogiro." The name "Autogiro" (with an "A" and an "i") was later to be coined by Cierva as a proprietary trademarked name for his machines, but when spelled starting with a small "a" and using a "y" it is normally used as a generic name for this class of aircraft. Today, "gyroplane" is the official term used to describe such an aircraft, although the names "autogiro," "autogyro," and "gyroplane" are often used synonymously.

Cierva's first Autogiro was a coaxial design, the airframe being from a converted WW1 fixed-wing aircraft. The problem of asymmetric lift was well known to Cierva and his first idea of using a contrarotating coaxial design was that the lower rotor would counteract the asymmetry of lift produced on the upper rotor, thereby balancing the net rolling moment on the autogiro. It is the subject of Spanish patent No. 74,322 "Nuevo Aparato de Aviacion" of June 1920. However, the aerodynamic interference produced between the rotors resulted in different rotor speeds, spoiling the required aerodynamic roll balance and the aircraft crashed. Undeterred, Cierva conducted basic wind tunnel experiments on model rotors, and he was one of the first to establish a scientific understanding of their aerodynamic behavior, especially in autorotation. He built two more full-scale machines with single rotors before he achieved final success in January 1923 with the C-4. Based on his tests with small models, this fourth machine incorporated blades with mechanical "flapping" hinges at the root, which Cierva used as a means of equalizing the lift on the two sides of the rotor in forward flight – see Cierva & Rose (1931). This novel solution allowed the blades to flap up or down about these hinges, responding to the changing airloads during each revolution of the blades and providing a means of equalizing the lift between the advancing and retreating

sides of the rotor disk. The development of the flapping hinge was to be one key to the future success of the helicopter.

The principle of flapping blades had actually first been suggested for the application to propellers [see Rosen (1984)] apparently by Charles Renard, but the idea of hinged blades was formally patented by Louis Breguet in 1908 and then by Max Bartha & Josef Madzer in 1913 – see Liberatore (1998) for details. Juan de la Cierva, however, must be credited with the first successful practical application of the flapping hinge to a rotor. Cierva noticed that the incorporation of the flapping hinge eliminated any adverse gyroscopic effects and also allowed the lift forces on the two sides of the rotor to become more equalized in forward flight. Metal ties with turnbuckles located near the mid-span linked each of the blades together in an attempt to reduce the in-plane or lead–lag motion of the blades (see Chapters 4 and 12 for details). Cierva's initial avoidance of using a lead–lag hinge to alleviate the in-plane blade drag and Coriolis forces (resulting from the flapping motion) was an oversight that was rectified on later models of his Autogiro.

In all of Cierva's Autogiros, the engine drove only the propeller. Clearly this makes the autogiro mechanically simpler than a shaft driven helicopter because the engine gearbox and rotor transmission can be dispensed with. Furthermore, it is not necessary to develop a separate means of countering torque reaction, as on the helicopter. This all significantly reduces weight and also reduces design, production, and capital costs. Starting the rotor, however, required a team of helpers to pull a rope wound around the rotor shaft, or taxiing around on the ground could also get the rotor spinning. Later models used a mechanical prerotator – see Section 12.6. Thereafter, the pilot opened the throttle and the thrusting propeller pulled the machine forward until it quickly lifted off into flight. The freely spinning rotor turned relatively slowly in flight compared to a helicopter, about 100–150 rpm.

With the success of his Autogiros, in 1925 Cierva was invited to Britain by the Weir Company. His C-6 Autogiro was demonstrated at the Royal Aircraft Establishment (RAE) and these flights stimulated early theoretical work on rotating-wing aerodynamics by H. Glauert and C. Lock in Britain, and M. Munk in the United States. Cierva was to write two books for the fledgling rotorcraft industry, albeit formally unpublished – see page 701. In later models of his Autogiro, the first of which was the C-8 (Fig. 1.16), Cierva added a lag hinge to each of the blades, which alleviated stresses caused by in-plane drag and Coriolis forces and completed the development of the articulated rotor hub. In later models, a control stick was connected to the rotor hub, which allowed the rotor disk to be tilted for control purposes (orientable direct rotor control). While this allowed the ailerons to be dispensed with, the rudder and elevator on the machine were retained. The Cierva Autogiro Company and its licensees went on to build many more versions of the Autogiro through 1938.

Although the autogiro was still not a direct-lift machine and could not hover, it required only minimal forward airspeed to maintain flight. Cierva proved that his autogiros were very safe and because of their low-speed handling capability, they could be landed in confined areas. Takeoffs required a short runway, but this problem was solved with the advent of the "jump" and "towering" takeoff techniques, although this required a lot of piloting skill – see Section 12.14. For a jump takeoff the blades are set to flat pitch and the rotor rpm is increased above the normal flight rpm using the engine. This is followed by the rapid application of collective blade pitch, while simultaneously declutching the rotor and thereby avoiding any torque reaction on the fuselage. This technique lifts the aircraft rapidly off the ground, powered only by the stored kinetic energy in the rotor system. As forward speed builds, the rotor settles into its normal autorotative state – see Prewitt (1938) for a technical description. To achieve jump takeoffs, in 1935 Cierva introduced a pitch change mechanism into the rotor design, which was installed in later production versions of the

Figure 1.16 A version of Cierva's C-8 Autogiro, circa 1928. The Autogiro was the first successful rotating-wing aircraft and the first type of aircraft to fly successfully after the conventional airplane.

C-30. These machines saw some service with the British Royal Air Force during WW2 for radar calibration missions.

About the same time, Raul Hafner introduced the "spider" cyclic pitch control system to his design of autogiro – see Fay (1987) and Hobbs (1984). This provided a means of increasing collective pitch and also tilting the rotor disk without tilting the rotor shaft with a control stick as in Cierva's direct control system, giving the pilot better control with lower control forces. Hafner used this design in his AR.III autogiro, which flew in 1935. About the same time, another autogiro using lateral cyclic control was built by W. R. Kay in Scotland. With its nearly vertical towering takeoff capability, low handling speeds and short landing run, this form of the autogiro was to closely rival the soon to be successful helicopter in terms of its performance capability.

Several other British companies, including Weir, A.V. Roe (Avro), Parnall, de Havilland and Westland went on to build variants of the Cierva Autogiro designs. The first Weir designs were developments of Cierva's models and used the orientable direct rotor control system. The Weir W-1 through W-4 models were all autogiros and were some of the first machines to use a prerotator to help bring up the rotor rpm prior to takeoff (see Section 12.6). The de Havilland and Westland company built a few larger prototype autogiros. The Westland C-29 was a five-seat cabin autogiro built in 1934. The aircraft was never flown because it exhibited serious ground resonance problems and the project was canceled with the untimely death of Juan de la Cierva in 1936. However, Cierva's work was carried on by designers from Weir and another Westland designed autogiro called the CL-20 was flown just before WW2 although it did not show sufficient performance – see Mondey (1982).

The Kellett and Pitcairn companies entered into licensing agreements with Cierva, resulting in the first flight of an autogiro in the United States in 1928. Harold Pitcairn went on

to design and patent many improvements into the Cierva rotor system [see Smith (1985)], but it became clear that it was a true helicopter with power delivered to the rotor shaft that was required. The autogiro was extensively tested in the United States by the NACA. Gustafson (1971) gives an authoritative account of the early NACA technical work on autogiros and helicopters.[5] In Russia, the TsAGI built autogiros derived from the Cierva designs. Kuznetsov and Mil built the 2-EA, which was derived from the Cierva C-19 – see Everett-Heath (1986). Later developments of this design led to the first Russian helicopters built with the assistance of Vittorio Isacco, who had earlier led basic helicopter developments in Italy, Spain, and France during the 1920s. The Japanese even made copies of the Cierva and Kellett autogiro designs, combining some of their best attributes and used them as submarine spotters during WW2 – see Gablehouse (1967).

During WW2 the Focke Achelis company built the Fa 330 Kite. This aircraft was a pure autogiro with a relatively simple lightweight construction and was designed as observation platform for one man while being towed behind a surfaced submarine. It was attached to the submarine by a steel cable wound out from a winch on the deck. When returning to the submarine, the winch wound in the cable and pulled the Fa 330 onto the deck. The Hafner Rotachute [see Everett-Heath (1986)] was a skeletal autogiro designed to replace a conventional parachute, but it never saw operational use. The simplicity of both these platforms later formed the inspiration for inexpensive amateur homebuilt autogiros, many of which are still popular today.

While the autogiro did see some commercial success, mainly in the United States, it was never on a large scale. During the 1930s and 1940s it was used by the US Post Office for regular mail service between Washington DC and Philadelphia, as well as in other cities, including Chicago and New Orleans. The 1920s and 1930s were an exciting and adventurous time for aviation despite the Great Depression and the autogiro was widely popularized as a super-safe, easy-to-fly aircraft, which it was for the most part. The autogiro subsequently found its way into the private market, where it gained good popularity with pilots and some level of public acceptance for a somewhat unusual aircraft. It was also used for aerial photography and advertising, the latter role giving it good public exposure. The Buhl Aircraft Corporation of Detroit, Michigan, was another company involved in autogiros. They designed and built a small two-seater autogiro with a pusher propeller, the first of its kind, which had no fixed aerodynamic surfaces other than a tail.

Despite the ultimate demise of the autogiro in the post-WW2 era, it got the public, government and the aircraft industry used to seeing a practical rotorcraft. When serious helicopter proposals started to appear in the early 1940s, they were not rejected out of hand but instead received more respect and consideration than most nascent aircraft technologies receive at that early stage of development. See also Chapter 12 for further details on the technical development of autogiros and modern gyroplanes.

1.8 Engines: A Key Enabling Technology

The development of the engine (powerplant) is fundamental to any form of flight. While airplanes could fly with engines of relatively lower power, the success of the helicopter had to wait until aircraft engine technology could be refined to the point that much more powerful and lightweight engines could be built. A look at the historical record

[5] In addition, the content of the entire first issue of the *Journal of the American Helicopter Soc.*, 1 (1), Jan. 1956, was devoted to the early autogiro and helicopter developments in the United States.

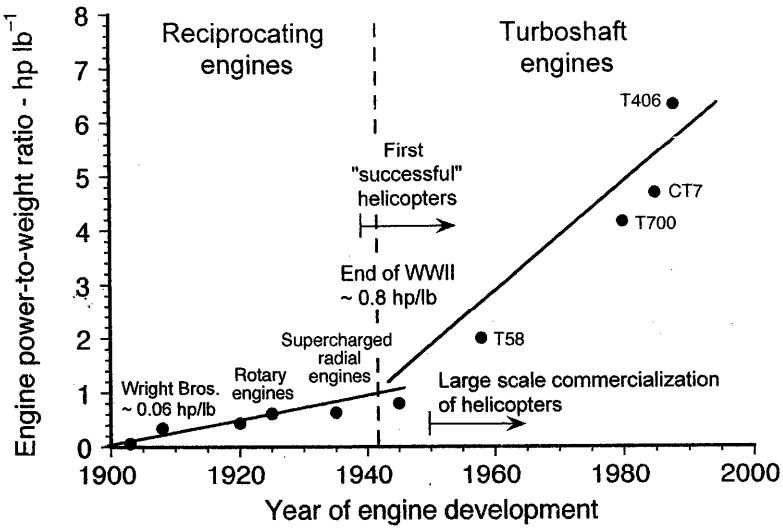

Figure 1.17 Even after airplanes were flying, engines were to need another twenty years of development before helicopters were to be successful. The advent of the turboshaft engine led to dramatic increases in overall power-to-weight ratio such that it was finally to give the helicopter the performance and payload that made it a commercial success.

(Fig. 1.17) shows that the need for engines of sufficient power-to-weight ratio was really a key enabling technology for the success of the helicopter.

To the early pioneers, the power required for successful vertical flight was an unknown quantity and an understanding of the problem proceeded mostly on a trial and error basis. The early rotor systems had extremely poor aerodynamic performance, with efficiencies (figures of merit) of no more than 50%. This is reflected in the engines used in some of the helicopter concepts designed in the early 1900s, which were significantly overpowered and very overweight. Prior to 1870, the steam engine was the only powerplant available for use in most mechanical devices. The steam engine is an *external* combustion engine and, relatively speaking, it is quite a primitive form of powerplant. It requires a separate boiler, combustor, recirculating pump, condenser, power producing piston and cylinder, as well as fuel and an ample supply of water. All of these components would make it very difficult to raise the power-to-weight ratio of a steam engine to a level suitable for aeronautical use. Nonetheless, until the internal combustion engine was developed, the performance of steam engines was to be steadily improved upon, being brought to a high level of practicality by the innovations of James Watt.

The state of the art of aeronautical steam engine technology in the mid-nineteenth century is reflected in the works of British engineers Stringfellow and Hensen and also the American, Charles Manly. The Hensen steam engine weighed about 16 lb (7.26 kg) and produced about 1 hp (0.746 kW), giving a power-to-weight ratio of about 0.06, which as about three times that of a traditional steam plant of the era. Fueled by methyl alcohol, this was also a more practical fuel for use in aeronautical applications. However, to save weight the engine lacked a condenser and so ran on a fixed supply of water. With a representative steam consumption of 30 lb/hp/hr (18.25 kg/kW/hr) this was too high for aircraft use. A steam engine of this type was also used by Enrico Forlanini of Italy in about 1878 for his experiments with coaxial helicopter rotor models.

In the United States, Charles Manly built a relatively sophisticated five cylinder steam engine for use on Langley's *Aerodrome*. The cylinders were arranged radially around the crankcase, a form of construction that was later to become a basis for the popular air-cooled radial reciprocating internal combustion aircraft engine. Manly's engine produced about 52 hp (36.76 kW) and weighed about 151 lb (68.5 kg), giving a power-to-weight ratio of 0.34 hp/lb (0.56 kW/kg). The Australian, Lawrence Hargreve, worked on many different engine concepts, including those powered by steam and gasoline. Hargreve, along with the Berliners, was one of the first to devise the concept of a rotary engine, where the cylinders rotated about a fixed crankshaft, another popular design that was later to be used on many different types of aircraft, including helicopters.

The *internal* combustion engine came about toward the end of the nineteenth century and was a result of the scientific contributions from many individuals. Realizing the limitations of the steam engine, there was gradual accumulation of knowledge in thermodynamics, mechanics, materials, and liquid fuels science. One of the earliest studies of the thermodynamic principles was by Sadi Carnot in 1824 in his famous paper "Reflections on the Motive Power of Heat." In 1862, Alphose Beau de Rochas published the first theory describing the four-stroke combustion cycle. In 1876, Nikolaus Otto was to use Rochas's theory to design an engine that was to form the basis for the modern gasoline-powered reciprocating engine. The development of the internal combustion engine eliminated many parts, simplified the overall powerplant system and for the first time enabled the construction of a compact powerplant of relatively high power-to-weight ratio suitable for an aircraft.

The earliest successful gasoline-powered aircraft engines were of the air-cooled rotary type. The popular French "Gnôme" and "Le Rhône" rotary engines had power-to-weight ratios of 0.35 hp/lb (0.58 kW/kg) and were probably the most advanced lightweight engines of their time.[6] This type of engine was used by many helicopter pioneers of the era, including Igor Sikorsky in his test rig of 1910. The rotary engine suffered from inherent disadvantages, but compared to other types of engines that were available at the time, they were smooth running and sufficiently lightweight to be suitable for aircraft use. One major technology to enable vertical flight, the powerplant, was now finally at hand.

1.9 On the Verge of Success

In 1922, under contract to the US Army, a Russian émigré to the United States by the name of Georges de Bothezat built one of the largest helicopters of the time. De Bothezat had been a student of Professor Joukowski) in Russia (see previously) and had written one of the first technical manuscripts on rotating-wing aerodynamics – see de Bothezat (1919). De Bothezat's machine was a quadrotor with a rotor located at each end of a truss structure of intersecting beams, placed in the shape of a cross (see Fig. 1.18). Ivan Jerome was the codesigner. Each rotor had six wide chord blades. Control of the machine was achieved by collective, differential collective, and cyclic blade pitch variations. The blade control design likely derived directly from those of Yuriev. A set of four smaller rotors served to help control the machine. In 1922, the ungainly Jerome–de Bothezat quadrotor or "Flying Octopus" flew many times, albeit at low altitudes and slow forward speeds. It was not very controllable and its "forward motion" was really a result of wind drift. Because of insufficient performance and the increasing military interest in autogiros at the time, the

[6] Of interest is the rotary engine built by Berliner in 1905, which predates the Le Rhône engine, and this was built also with the specific purpose of installing it in a helicopter.

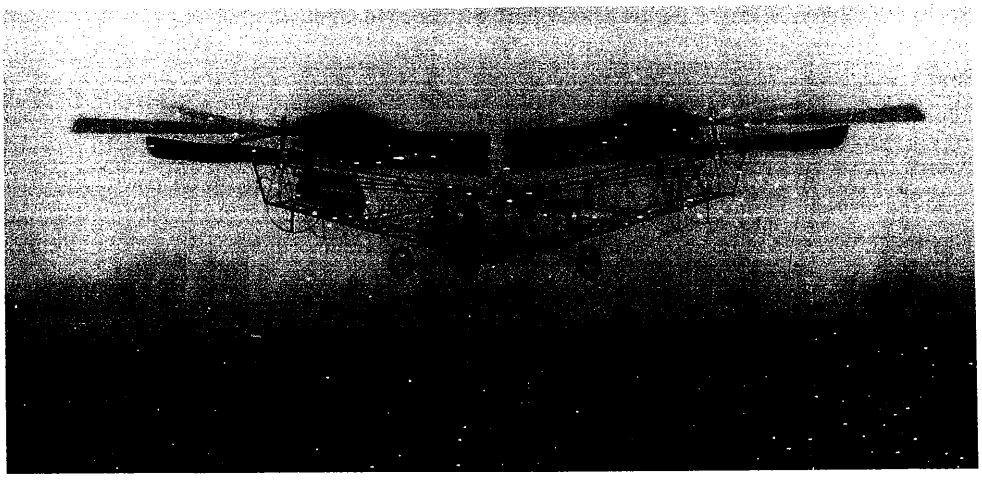

Figure 1.18 The Jerome–de Bothezat helicopter, which made limited controlled flights in 1922. (Courtesy NASM, Smithsonian Institution, SI Neg. No. 87-6022.)

project was soon to be canceled. But it was to be twenty or more years before a helicopter was again to fly again in the United States and better de Bothezat's accomplishments.

In 1921, Étienne Œhmichen of France built a quadrotor machine in a similar style to that of de Bothezat, but with eight additional smaller rotors for control and propulsion. Œhmichen conducted many rotor experiments, including tests made in a wind tunnel of his own design. His quadrotor machine (Fig. 1.19), however, typified the cumbrous mechanical complexity of several other helicopters of this era. His initial design was underpowered and it was fitted with a hydrogen balloon to provide additional lift and stability during the initial period of development. Œhmichen's No. 2 machine was flown between 1923 and 1924. By 1924, Œhmichen was making reasonable flights and his machine proved

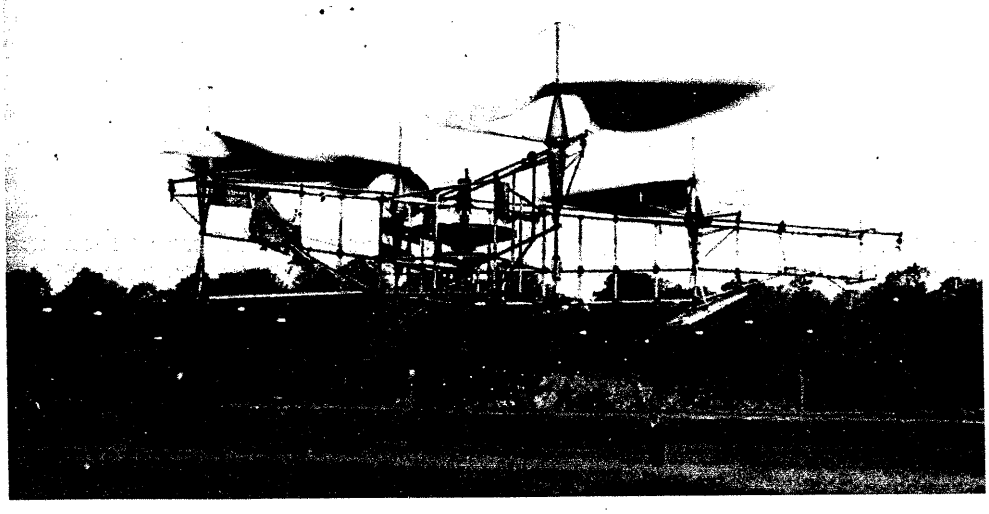

Figure 1.19 The Œhmichen quadrotor machine typified the mechanical complexity and impracticality of most early helicopters.

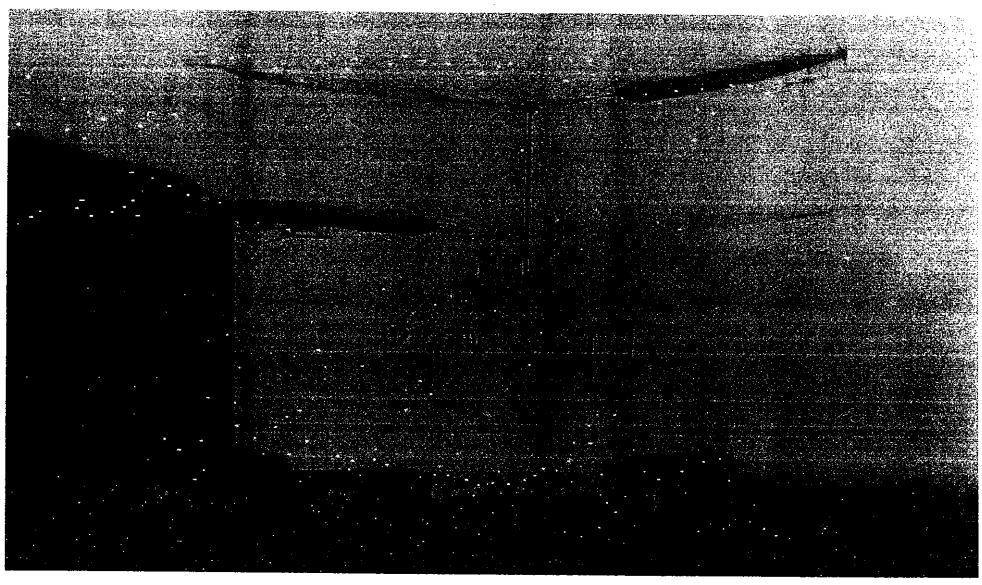

Figure 1.20 Corradino d'Ascanio's coaxial machine, circa 1930, which used servo-tabs to twist the blades and cyclically change their lift. (Courtesy of John Schnieder.)

"perfectly maneuverable and stable." In May 1924 he was awarded a prize by the FAI for demonstrating the first helicopter to fly a standard closed 1 km circuit with a 410 lb (200 kg) payload, which took 7 minutes 40 seconds. The machine, however, was largely impractical. Œhmichen was to build other forms of rotorcraft, including a hélicostat, which was developed and flown through 1935. See also NACA (1921) and Œhmichen (1923).

In 1930, Corradino d'Ascanio of Italy built a coaxial helicopter. Figure 1.20 shows that this relatively large machine had two, two-bladed, contrarotating rotors. Following the work of Cierva, the blades had mechanical hinges that allowed for flapping but a feathering capability was added to change blade pitch. Control was achieved by auxiliary wings or servo-tabs on the trailing edges of the blades, a concept that was later adopted by others, including Bleecker and Kaman in the United States. D'Ascanio designed these servo-tabs so that they could be deflected periodically by a system of cables and pulleys, thereby cyclically twisting the blades and changing their lift. For vertical flight, the tabs on all the blades moved collectively to increase the rotor thrust. Three small propellers mounted to the airframe were used for additional pitch, roll and yaw control. This machine held modest speed and altitude records for the time, including altitude (57 ft, 17.4 m), duration (8 minutes 45 seconds) and distance flown (3,589 ft, 1,078 m). D'Ascanio later developed a single rotor helicopter in Italy during WW2, but it was destroyed during a bombing raid.

In 1930, Maitland Bleecker of the United States followed Brennan's approach to the torque reaction problem by delivering power to propellers that were mounted on each rotor blade. The machine was made by the Curtiss Company. Power was supplied through a system of chains and gears from an engine mounted at the center of the machine. Like d'Ascanio's machine, Bleecker's helicopter was controlled by auxiliary aerodynamic surfaces he called "stabovators," which were fastened to the trailing edges of each blade (see Fig. 1.21). Both collective and cyclic blade pitch were incorporated into the design. Bleecker's machine accomplished numerous short hops and hovers, but high vibrations and various control problems caused the project to be abandoned in 1933. Liberatore (1998) gives one of the best accounts of the project.

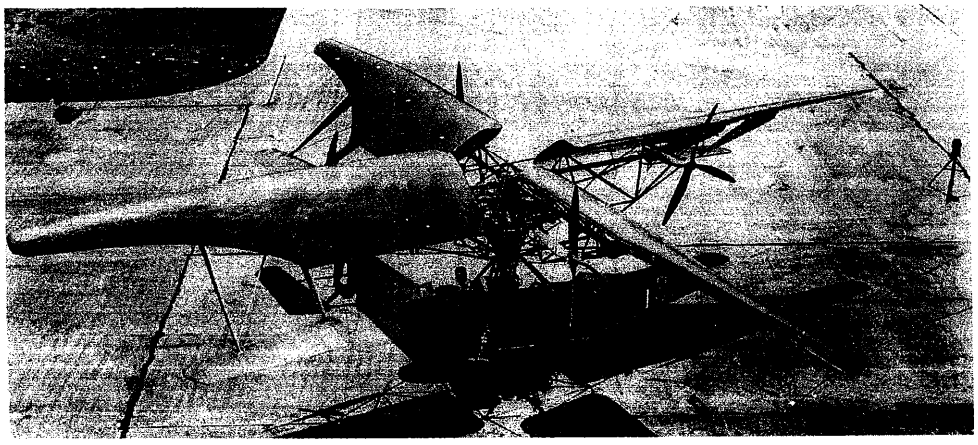

Figure 1.21 The Curtiss–Bleecker helicopter photographed at NACA Langley Research Center in 1930. (NASA photo.)

During 1929–1930, the Russian born engineer Nicolas Florine built a tandem rotor helicopter in Belgium. The rotors turned in the same direction but were tilted in opposite directions to cancel torque reaction. This idea was later used on the Cierva–Weir W-11 tri-rotor helicopter. Boulet (1984) describes the mechanical aspects of the machine. Florine's first aircraft was destroyed in 1930, but he had a second design flying successfully by 1933, which made a flight of over 9 minutes to an altitude of 15 ft (4.57 m), exceeding d'Ascanio's flight duration record of the time. Yet, Florine's designs suffered many setbacks and work was discontinued in the mid-1930s.

1.10 The First Successes

During the period 1930–1936, the famous French aviation pioneers Louis Breguet and René Dorand made notable advances in helicopter development. Figure 1.22 shows their machine of 1935, which was relatively large with coaxial rotors. Boulet (1984) and Kretz (1987) give an excellent account of the work. Each rotor had two tapered blades that were mounted with flap and lag hinges and were controlled in cyclic pitch using a swashplate design. Yaw control was achieved by differential torque on one rotor with respect to the other. Horizontal and vertical tails were used for increased stability. For its time, the aircraft held several flight records, including a duration of 62 minutes and distance flown (27 mi, 44 km). This was arguably the first successful helicopter because, not only did it demonstrate a remarkable new level of performance, but it had a good level of flight safety in that it could autorotate to the ground – see page 6. Clearly, all aircraft must possess safe flight characteristics after a loss of power. While a fixed-wing aircraft can glide, the helicopter can take advantage of *autorotation* with the rotor unpowered as a means of maintaining rotor rpm, lift, and control in the event of engine failure. In this mode, the helicopter behaves very much like an autogiro so that the relative wind comes upward through the rotor disk. The pilot, in effect, gives up altitude (potential energy) at a controlled rate for kinetic energy to drive the rotor and, with skill, can autorotate the aircraft safely onto the ground.[7] However, with the higher disk loadings found on helicopters compared to autogiros, to get the rotor to autorotate the helicopter must descend at a relatively high rate. While autorotations were

[7] The ability to autorotate is really a distinguishing feature of a successful and practical helicopter.

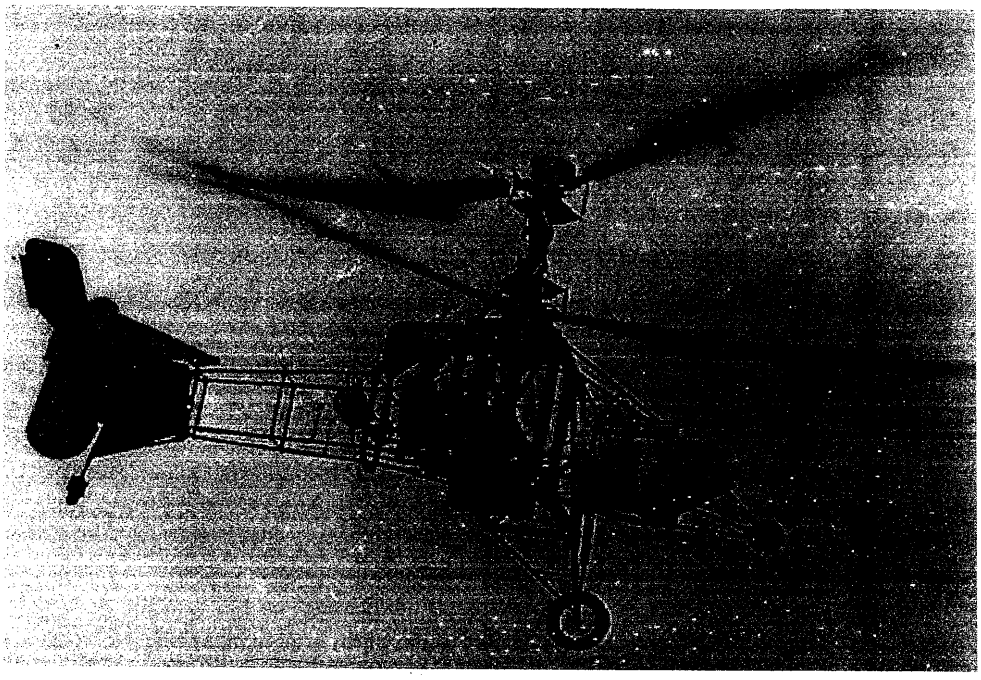

Figure 1.22 The technically successful Breguet-Dorand coaxial helicopter, circa 1936. (Courtesy NASM, Smithsonian Institution, SI Neg. No. A-42078-C.)

attempted with the Breguet–Dorand machine, some moderately successful, the aircraft crashed, and further work stopped prior to the outbreak of WW2.

Henrich Focke of the Focke Wulf Company began his work on rotating-wing aircraft as early as 1923. He acquired a license to build Cierva's autogiros and successfully manufactured the C-19 and the C-30 models. From the experience he gained and after many wind tunnel tests, Focke began developing the Fw 61 helicopter as a private venture in 1934. Focke was later to state in a RAeS lecture [see Focke (1965)] that "I was brought to the task of making the first practical helicopter because Cierva did not do it himself." In 1937, Henrich Focke finally built and demonstrated a successful side-by-side, two-rotor machine, called the Fw 61. The details of the machine are described by Focke (1938, 1947, 1965), Boulet (1984), and Coates (2002). Figure 1.23 shows that the rotors were mounted on outriggers and were inclined slightly inward to provide lateral stability. The blades were tapered in planform and were attached to the rotor hub by both flapping and lagging hinges. Longitudinal control was achieved by tilting the rotors forward and aft by means of a swashplate mechanism, whereas yaw control was gained by tilting the rotors differentially. The rotors had no variable collective pitch, instead using a slow and clumsy system of changing rotor speed to change the rotor thrust. A vertical rudder and horizontal tail provided additional directional stability.

Focke's Fw 61 machine is significant in that besides demonstrating fully controlled flight, it was the first helicopter to repeatedly demonstrate successful autorotations to the ground. Provision was made in the design for a fixed low collective pitch setting to keep the rotor from stalling during the descent. It also set records at the time for duration, climb to altitude (11,427 ft, 3,427 m), forward speed (76 mph, 122 km/h), and distance flown in a straight line (143 miles, 230 km). The machine gained considerable publicity prior to the outbreak of WW2 when the famous test-pilot Hanna Reitsch flew it inside a Berlin sports

Figure 1.23 The Focke Fw 61 flew successfully in 1936 and was arguably the world's first practical helicopter. (Courtesy NASM, Smithsonian Institution, SI Neg. No. A-2316.)

arena. While apparently portrayed as a well-mannered helicopter, Reitsch reported that it was not an easy machine to fly and it had some concerning handling defects. The Fw 61 was developed further in collaboration with Gerd Achgelis (which was known in some circles as the Fa 61) and was used as a basis to develop the Fa 266 (Fa 233E), which first flew in 1940. This was a fairly large helicopter, with two three-bladed rotors and could carry up to four crew. It went into limited production during WW2. Boulet (1984) and Coates (2002) give good accounts of the later helicopter work of Focke.

A few examples of the Fa 233 survived WW2 and were taken to Britain, France, and Russia for further evaluation. The French developed the SE 3000 from the Fa 233, which flew in 1948 but it did not go into service. Some the German machines were used as a basis to develop helicopters in Russia, a good account being given by Everett-Heath (1988). The Platt–Le Page XR-1 (see page 32), which was built in the United States after WW2 was based on the Fa 233 design. Yet, despite the apparent success of the side-by-side rotor design, it suffered from a serious lateral instability while hovering in ground effect.

With the assistance of Cierva, the Weir Company had formed an aircraft department in Scotland in 1932. The W-5 was their first true helicopter design, the W-1 through W-4 having all been autogiros. Initially, the W-5 was a coaxial design, however, because of various technical concerns, Weir instead capitalized on the success and apparent flight stability of the German Fw 61 and adopted the side-by-side rotor configuration with the rotors on outriggers. The resulting W-5 incorporated the engine and rotors from the W-4 autogiro and was a rather diminutive machine overall. The two rotors used two untwisted blades with full articulation using flapping and lead–lag hinges, and were given cyclic pitch capability by using a swashplate mechanism. Pitch and yaw control was obtained by tilting the rotor disks, with roll control being obtained by a differential pitch input to the rotors. There was no direct collective pitch, with rotor thrust changes being effected by changes in rotor rpm, a rather slow and unresponsive procedure that was to remain a feature of the

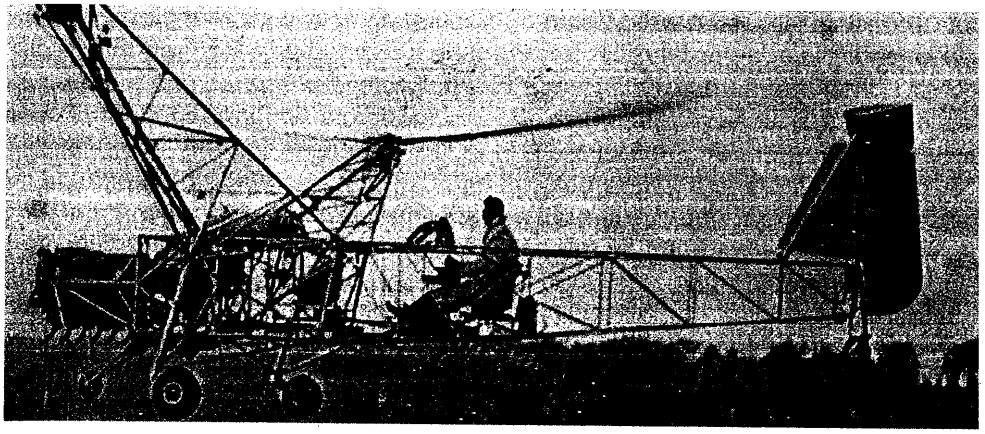

Figure 1.24 The Weir W-6 was Britain's third helicopter and in 1939 was the first helicopter to carry a pilot and a passenger.

later Weir–Cierva helicopter designs. The first free hovering flights of the W-5 were made in June of 1938.

The Weir W-6 retained the side-by-side rotor concept of the successful W-5, but used two, three-bladed rotors, each of 26 ft (7.93 m) in diameter. The blades were fully articulated with flapping and lead–lag hinges, with a feathering capability. As shown in Fig. 1.24, a skeletal airframe (of welded steel and light alloy tubing) formed the primary structure. Rotor control was achieved using cyclic and differential collective pitch, with the same method of changing rotor rpm used on the W-5 to effect changes in rotor thrust. The first flights of the W-6 were conducted during October of 1939 and the machine demonstrated good control and performance with speeds in forward flight of over 80 mph and rates of climb in excess of 600 ft/min (3.05 m/s) being attained. See Everett-Heath (1986) and Leishman (2002b, 2004) for further information on the Weir machines.

The imminent outbreak of WW2 ended all research and development on British rotorcraft. The Government's effective moratorium on British rotorcraft developments in favor of the American Sikorsky designs, albeit only for a few years, was to be a serious blow to the Cierva, Weir, and Hafner companies. It was not to be until 1943, in response to the first official British government design specification for a helicopter, that British rotorcraft development was to start again. By that time, the US had accelerated into the technical lead. With the rapid advances by Igor Sikorsky in 1939 and early 1940s, engineers in the US were to shelve any further technical development of the autogiro and were to focus all new work on helicopters. Much of the future technical work on rotorcraft, both experimental and theoretical, took up where the autogiro had left off. In Britain, this saw the revival of the Cierva Company in 1944 and the development of the Cierva W-9, which was a single rotor helicopter.

During the period 1938–1943, Anton Flettner of Germany developed several helicopter designs. His Fl 184 was an autogiro but like the Hafner AR.III it used cyclic pitch control, allowing the pilot to tilt the rotor. This machine was modified to a single rotor shaft driven helicopter (the Fl 185), with the addition of collective pitch control and two smaller differentially thrusting propellers on outriggers for anti-torque. While the Fl 185 flew, Flettner's big success came with using a side-by-side intermeshing rotor configuration, which became known as a *synchropter* – see Braun (2003). This intermeshing design was first patented by Bourcart in 1903 and by Mees in 1910. In the synchropter design, the rotor shafts are close

together but arranged so that they are at a significant outward angle with the overlapping rotors turning in opposite directions [see Fig. 1.3(e)]. A gearing system ensured the exact phasing of the rotors. In 1939, Flettner's Fl 265 synchropter was the first helicopter to demonstrate transition into autorotation and then back again into powered flight. Flettner built several other machines, including the Fl 282 Hummingbird. The Fl 282 was probably one of the first helicopters to be produced in quantity and saw some limited use (but no operational service) during WW2 – see Coates (2002). In the United States, the Kellett Aircraft Company (which also built autogiros as a licensee to Pitcairn) also developed a synchropter configuration and built the XR-8 in 1944 using three-bladed intermeshing rotors. The aircraft flew successfully, but it never went into production. The synchropter concept was also adopted by Charles Kaman, but this time the Kaman Aircraft Corp. was to put the type into quantity production for the US military.

In the early 1940s Friedrich von Doblhoff of Germany began investigating the application of the tip-jet principle to a helicopter and by 1942 had built the first helicopter to take off using tip jets. A conventional piston engine drove a compressor, and the compressed air was mixed with fuel before passing through hollow rotor blades to combustion chambers situated at the blade tips. Because of their high specific fuel consumption, tip jets can be used economically only for takeoff, hovering and landing. For forward flight, the tip jets were shut off and the rotor operated in autorotation like an autogiro. After WW2, von Doblhoff was involved in the development of the McDonnell XV-1 compound helicopter – see Section 12.17.

The Americans too were working on helicopter designs. As described earlier, Igor Sikorsky had experimented in Czarist Russia with primitive vertical lift aircraft as early as 1907 – see Sikorsky (1938) and Finne (1987). After Sikorsky had emigrated to the United States, he went on to design and build flying boats. A 1935 Sikorsky patent (No. 1,994,488) shows a relatively modern-looking single rotor/tail rotor helicopter design with flapping hinges and a form of cyclic pitch control. Although Sikorsky encountered many technical challenges, he tackled them systematically and carefully. To some the machine was known as "Igor's folly," an unjustified designation by those who did not believe in the future of rotating-wing aircraft, but it also reflected the relative mechanical complexity and difficult flying characteristics of the early helicopter prototypes. Sikorsky's first helicopter, the VS-300, was flying in free, untethered flight by May 1940. A good summary of the technical design is given by Sikorsky (1941, 1942, 1943).

Sikorsky's first machine (Fig. 1.25) had one main rotor and three auxiliary tail rotors, with longitudinal and lateral control being obtained by means of pitch variations on the two vertically thrusting horizontal tail rotors. The machine could hover, fly sidewards and backwards, yet it could not fly forward very well, exhibiting a sudden nose-up pitching characteristic at a low forward airspeeds. This was because of the downwash of the main rotor wake, which as airspeed built, blew back onto the two vertically thrusting tail rotors and destroyed their lift. The main lifting rotor of the VS-300 was used in the later VS-300A, but now only the vertical (sideward thrusting) tail rotor was retained out of the original three auxiliary rotors. In this configuration, longitudinal and lateral control was achieved by tilting the main rotor by means of cyclic pitch inputs; the single tail rotor was used for anti-torque and directional (yaw) control purposes. This configuration was to become the standard for most later helicopters.

In June of 1941, the Platt–LePage XR-1 helicopter was to make its first free flights. Developed by two American engineers, W. Laurence LePage and Havilland H. Platt, the XR-1 was funded by a government contract under the Dorsey–Logan Act (see page 713). W. Laurence LePage had previously worked the Pitcairn and Kellett companies. The XR-1 followed the lead of the Focke Fw 61 by using a side-by-side rotor configuration. The

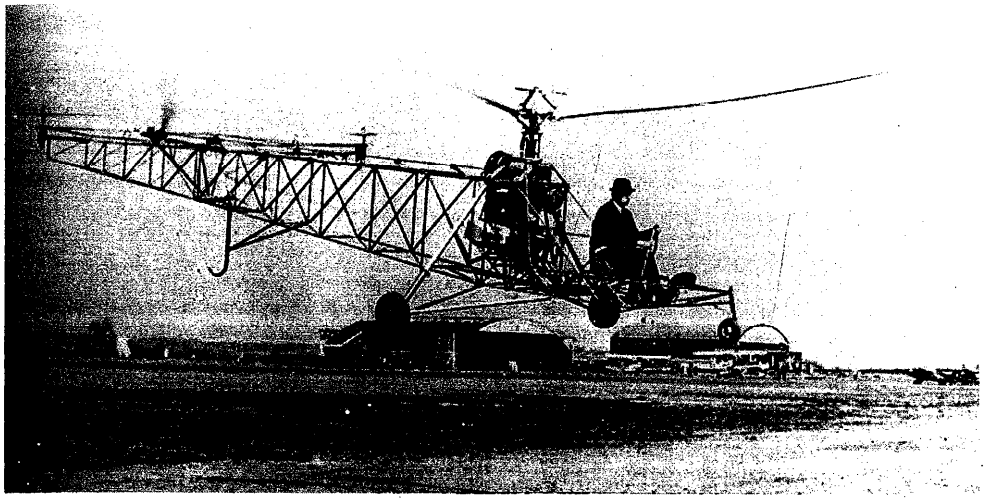

Figure 1.25 Sikorsky's VS-300 helicopter flew in 1940 and pioneered the single rotor configuration, but it followed several European helicopter designs. (Photo courtesy of Sikorsky Aircraft.)

XR-1 was found to be difficult to fly, with high vibrations and control problems. Several years of development followed, although its capabilities were soon eclipsed by the Sikorsky machines and the XR-1 was never to go into production. After WWII, McDonnell continued to develop the side-by-side rotor concept under contract to the US Navy. The McDonnell XHJD-1 Whirlaway was a similar but larger and heavier helicopter than the XR-1, using a separate engine to drive each rotor. Like the XR-1, the XHJD-1 was to suffer from a host of technical problems and McDonnell quickly fell behind the Sikorsky and Piasecki Companies in helicopter development. While the side-by-side rotor configuration proved to be a bad design choice for helicopters, it is perhaps significant to note that the configuration was later adopted for use in tilt-rotors – see Section 1.13.

1.11 Toward Mass Production

The immediate post–WW2 era is marked by a significant increase in the number of prototype helicopters, many of which went into scale production. It has already been mentioned how the development of the engine was an enabling technology for the helicopter, with rapid advancements in power output and reductions in engine weight taking place during the war. This was accompanied by simultaneous reductions in the empty airframe weight of the helicopter through the use of high-strength, lightweight construction materials such as aluminum and lighter alloys of steel, as well as developments in aerodynamics, flight control effectiveness and improved flight stability. This period represents a concrescence of various technologies and the onset of commercial success for the helicopter. This time period also coincides with the postwar economic recovery, which led to the maturation of helicopter technology and mass production, with increasing use of the helicopter in both military and civilian roles.

Before long, Sikorsky had refined his VS-300 machine and by 1941 he had started production of the R-4 (Fig. 1.26). In 1943 Sikorsky developed the R-6, which, although still only a two-seater helicopter, was larger and had notably better performance than the R-4. The R-6 was produced in substantial numbers and some of them saw action in the Pacific

Figure 1.26 The Sikorsky R-4B (Navy/Coast Guard HNS-1) being flown by famed helicopter pilot Frank Erickson, circa 1945.

during WW2. In 1946 Westland Helicopters in Britain obtained a license to build variants of the Sikorsky machines, the first being designated as the WS-51A after the S-51, which was a civilian development of the R-5D. This period was the start of a long relationship between the two companies, which continued for decades. Westland already had a history as a successful fixed-wing manufacturer and, as previously mentioned, they had briefly flirted with autogiros in the 1930s, but the company decided to specialize in helicopters in 1946 [see Mondey (1982)]. After significantly reengineering the Sikorsky machine, Westland called the aircraft the Dragonfly. The Widgeon later followed and this was a very modern looking and powerful version of the Dragonfly with a larger passenger cabin. However, it was the Bristol Aircraft Company that was to build the first fully British designed helicopter, with the Bristol-171 Sycamore (Fig. 1.27) taking to first flight in 1947.

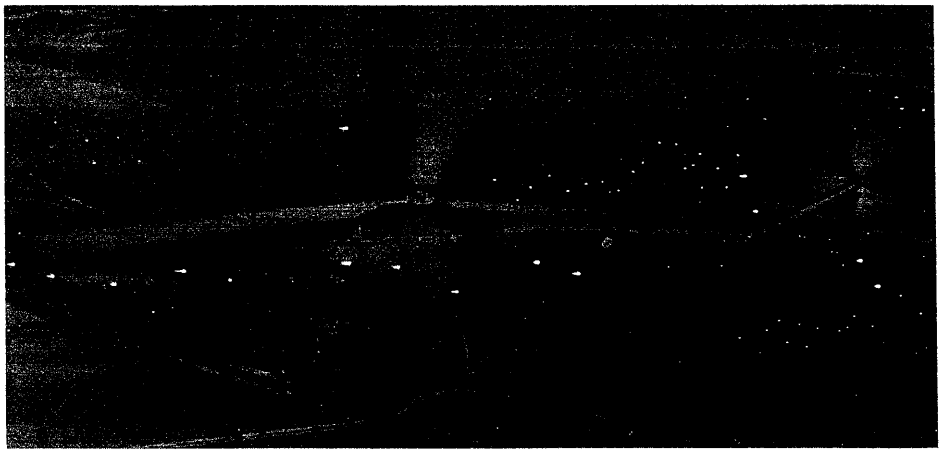

Figure 1.27 In 1947, the Bristol 171 Sycamore was Britain's first certified helicopter. (Westland Helicopters photo.)

Design refinements and material advancements led to lighter weight water-cooled engines, with cylinders arranged in two banks in the form of a "V." These engines saw considerable development up to and through WW2, with power-to-weight ratios of about 0.75 hp/lb (1.23 kW/kg) in normally aspirated form and up to ratios of unity in supercharged form (see Fig. 1.17, shown previously). Air-cooled radial engines too underwent significant developments during this period. In 1925, the radial engine had a power-to-weight ratio of about 0.5 hp/lb (0.82 kW/kg), but ratios of 0.9 hp/lb (1.48 kW/kg) were more commonplace by the mid-1930s. It was engines in this class that were to give the helicopter the performance that led to its first success as a practical and useful flight vehicle, although still not without problems. Early helicopters tended to utilize standard airplane powerplants turned vertically, which caused problems with oil fouling of the spark plugs. Also, because the engines had to operate at near to maximum rated power for nearly all of a flight, they had a far lower lifespan than was typical when the engine was used in airplanes. Cooling was also a serious concern, especially in hovering flight. WWII did see the development of purpose-built helicopter engines (derated, repositioned accessories, improved cooling and oil sumps, etc.) to overcome these challenges, but development delays prevented them from seeing much service until after the war. Simultaneous reductions in airframe weight that were brought about by advances in lighter materials saw very rapid improvements in overall performance and payload capability of the helicopter by the mid-1940s.

During 1942, the Cierva–Weir Company, prompted by the success of Sikorsky's XR-4, proposed a relatively large single rotor machine called the W-9, which was unique in its use of jet thrust to counteract rotor torque reaction – see Everett-Heath (1986). The rotor lacked any collective pitch control and rotor thrust was controlled through changing rotor speed as in the pre–WW2 Weir W-5 and W-6 models. The machine demonstrated several technical innovations for the era, including hydraulically boosted flight controls. However, the W-9 crashed during a test flight in 1946 and the project was subsequently abandoned. The Weir and Cierva companies later went on to design the W-11 Air-Horse, which was a unorthodox three-rotor helicopter with considerable lifting capability – see Everett-Heath (1986) and Leishman (2003). While successful, this machine also crashed during a test flight and further work was terminated. The final helicopter of the Cierva–Weir line was the W-14 Skeeter, which was a small two-seater training helicopter designed in 1948. This machine saw a production run through 1960, and was used by the British and German armed forces.

One measure of the lifting efficiency of a helicopter is its power loading, which is defined as the ratio of the weight of the machine to the power required for hovering flight (see Chapter 2). This can be further qualified by defining the power as that delivered to the rotor shaft and not the installed engine power. The higher the power loading, therefore, the more efficient the machine as a vertical lifter and hoverer. Figure 1.28 shows power loading as a function of year of helicopter development. Several points are worthy of note here. First, notice that early helicopters had a relatively high power loading, a result contrary to initial expectations, yet these machines were not successful other than making brief hops or hovers. This is because they were overweight (high empty weight fraction) and underpowered, and also because the rotors had poor aerodynamic efficiency. The point of initial "success" for the helicopter, which is about 1938–1940, represents the concrescence of engine, materials, and airframe construction technology, along with advances in the aerodynamic performance of the rotor. At this point, the values of power loading to enable basic hovering and forward flight with significant useful payload were first realized. This coincides with a significant increase in the number of prototype helicopters. Second, notice that there is a distinct "knee" in the curve in Fig. 1.28 in the late 1940s and early 1950s. This

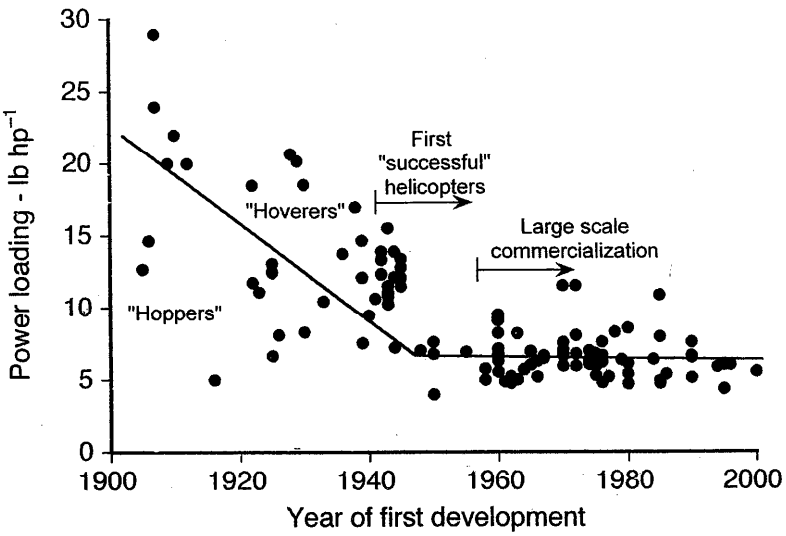

Figure 1.28 Power loading (rotor thrust per unit power required) versus year of helicopter development. Data source, in part, from Carlson (2002).

coincides with the postwar economic recovery, which led to the maturation of helicopter technology and mass production, with increasing use of the helicopter in both military and civilian roles. Finally, notice from Fig. 1.28 that after this period the values of power loading for later helicopters stay relatively constant at between 5 and 7 lb/hp (1.7 to 2.35 kg/kW), whereas one might have expected to see increases in power loading as a result of further technological advances and lightweight engines. While these advances have indeed taken place [e.g., Carlson (2002)], parallel increases in main rotor disk loading to reduce the size and cost of the helicopter have caused power loading values to stay relatively constant.

It is significant to note that while helicopters were becoming more and more successful, the development of the autogiro continued in Europe and the United States well into the 1950s. Considerable development work was undertaken by the Pitcairn [see Pitcairn (1930) and Smith (1985)] and Kellett aircraft companies in the United States. Harold Pitcairn patented many concepts in rotor blade design and rotor control, many of which were licensed and used by various helicopter manufacturers. The unfortunate timing of autogiro development, however, led to its limited success with the military. The US Navy considered the autogiro for shipborne use in submarine detection and convoy defense. Initial trials of the Pitcairn XOP-1 autogiro, however, were less than impressive, with the Navy citing poor range, insufficient payload capability and limited center of gravity travel. While later models of the autogiro had much improved capabilities, the Navy remained unconvinced. The US Army later tested both the Kellett and Pitcairn machines in a variety of roles, including reconnaissance and battlefield observation. The low-speed loiter capability of the autogiro seemed particularly promising for artillery spotting roles, and the Army saw the autogiro as a promising start to a new class of aircraft. The Navy would continue to reject any rotating-wing aircraft concept out-of-hand (until ordered by Congress to desist in 1943) and did buy some autogiros built by Kellett. Other rotor design patents from the Weir and Cierva companies in Britain were transferred to the Pitcairn–Larsen Company (as it was later known) and then to the G&A (Gliders & Aircraft) Division of the Firestone Tire & Rubber Company. They subsequently built a small prototype helicopter, first flown in 1946, called the G&A XR-9, which was designed by Harold Pitcairn.

In Britain during the 1940s and 1950s, the autorotating rotor concept was pursued to some significant end by the Fairey Aviation Company. The Fairey Girodyne compound aircraft (or convertiplane) used a propeller set on the end of a stub wing to provide both propulsion and anti-torque – see Everett-Heath (1986). The Fairey Company went on to develop the Jet Girodyne in which the rotor system was driven by tip jets based on the von Doblhoff principle. This ultimately led to the Rotodyne, which was the world's biggest gyroplane with a cabin big enough for forty passengers – see Hislop (1958) and the more detailed description Section 12.17. The aircraft set a world speed record for a convertiplane in 1959 before the project was canceled. Smaller single- and two-seat autogiros were later developed by various individuals and small companies for the private market.

Besides Igor Sikorsky, there were several other designers in the United States who were pioneering the helicopter during the 1940s. These included Arthur Young, Frank Piasecki, Stanley Hiller, and Charles Kaman. In the late 1930s, Arthur Young began a series of experiments with model helicopters that were ultimately to lead to the design of the renowned Bell Model 47 helicopter. After much research, Young invented the teetering rotor with a stabilizer bar; see Young (1948, 1979). This bar had bob weights attached to each end and was directly linked to the rotor blades through the pitch control linkages. The idea was that if the rotor was disturbed in pitch or roll, the gyroscopic inertia of the bar could be used to introduce a compensating cyclic pitch into the main rotor system, increasing the effective damping to disturbances and giving stability to the rotor system – see also Kelly (1954).

The prototype Bell Model 30 was built in 1942 and had a single main teetering rotor with Young's stabilizer bar. The first untethered flights took place in 1943 and the machine was soon flying at speeds in excess of 70 mph (112 kph). The Bell Model 30 design led to the famous Bell Model 47 (Fig. 1.29), which was the world's first commercially certified helicopter. During its nearly thirty-year manufacturing period over 5,000 were produced in the United States alone and many were also license built in more than twenty other countries. Tipton (1989), Brown (1995), and Spenser (1999) give a good historical overview of the

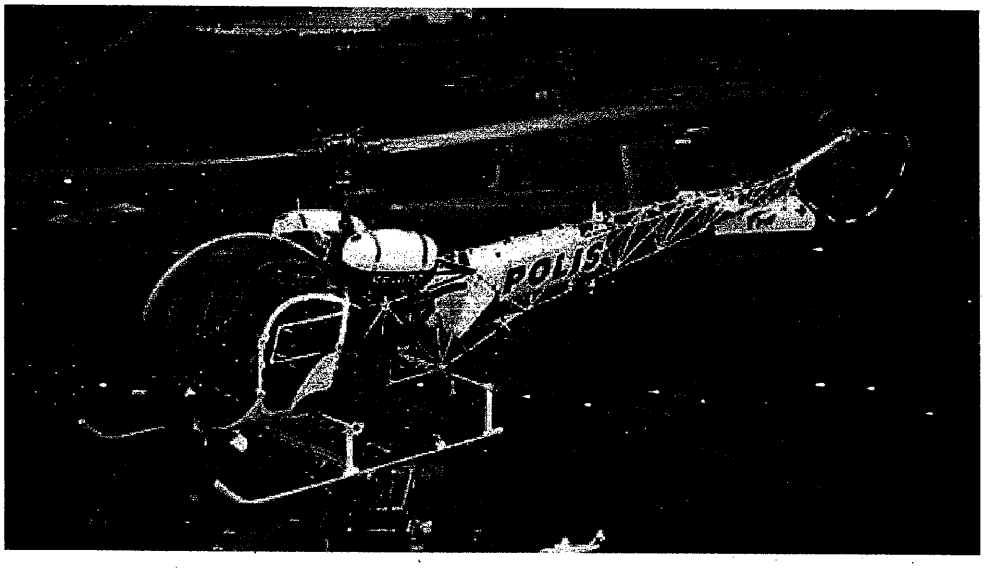

Figure 1.29 A version of the Bell Model 47, which was the world's first commercially certified helicopter. (By permission of Bell Helicopter Textron.)

Figure 1.30 The Boeing-Vertol HC.1 (CH-47), which is one of the largest and most widely used military transport helicopters. (By permission of the Boeing Company.)

Bell machines. Schneider (1995) gives a short biography of Arthur Young and his novel teetering rotor design.

In 1943, Frank Piasecki designed and flew a small helicopter that was called the PV-2. Piasecki, who had previously worked for Platt–LePage, developed the fourth helicopter to fly in free-flight in the United States after the Platt–LePage XR-1 and Sikorsky's VS-300, and the successful XR-4. Piasecki's company was to develop the overlapping tandem rotor configuration, a concept patented by Gish Jovanovich and demonstrated as early as 1944. Piasecki immediately turned to larger helicopters and in 1945 his company, the P-V Engineering Forum, built a tandem rotor helicopter called the PV-3 Dogship. Details are given by The Piasecki Corporation (1967) and Spenser (1999). This aircraft was popularly called the "Flying Banana" because of its distinctive curved fuselage shape. Despite its unfortunate nickname, however, the aircraft was very successful and larger and more powerful versions quickly followed, including the H-16 and H-21 "Workhorse" models of 1952, which were built by the Piasecki Corporation. The Piasecki Corporation became the Vertol Company who developed the Model 107 (CH-46) in 1956 and a larger military tandem rotor model, the CH-47 (Fig. 1.30), was to be the mainstay product for the company. The Vertol Company finally became Boeing Helicopters. An overview of the Boeing-Vertol machines produced up to the mid-1970s is given by Grina (1975). In the late 1980s, the company produced a demonstrator of an advanced technology tandem rotor helicopter called the Model 360. The only other company in the United States to build a tandem helicopter design was Bell, who manufactured the unsuccessful HSL-1 during the 1950s.[8] In 1998, Boeing announced the launch of the CH-47F and the CH-47SD "Super-D" Chinook, with the latest model being the MH-47G. See The Boeing Company (2005).

The British company, Bristol Helicopters, had designed and built a single rotor helicopter and later tandem helicopter during the late 1940s under the leadership of the helicopter

[8] The failure of the HSL-1 was partly responsible for the amazing success of Sikorsky's S-58.

pioneer Raoul Hafner – see Hobbs (1984) and Everett-Heath (1986). The Type-171 Sycamore (Fig. 1.27) was the first British helicopter to be certified for civil use – see Hafner (1949) and Dowling (1992) for details. The Bristol Type-173 had a long, slim fuselage with two three-bladed rotors at each end, similar to the Piasecki machines. The Bristol Type-192 Belvedere was an improved tandem rotor design, which followed in 1958 with more powerful turboshaft engines. However, the Bristol company found it difficult to compete with helicopters being produced by Sikorsky and Westland, and more limited numbers of their helicopters were produced.

In the United States, Charles Kaman adopted Anton Flettner's synchropter rotor design. One of Kaman's innovations was the use of torsionally compliant solid spar spruce rotor blades with servo-flaps. The servo-flaps were mounted at the three-quarter rotor radius, some distance behind the elastic axis of the blade. When these flaps were deflected cyclically, the aerodynamic moments caused the blades to twist, changing their angle of attack and thus introducing a cyclic pitch rotor control capability – a system first used by d'Ascanio (Fig. 1.20). The first Kaman helicopter, the K-125A, flew in 1947. By the 1950s the turboshaft engine had almost entirely replaced the reciprocating engine in most aircraft, including the helicopter. The Kaman K-225, became the first helicopter to fly powered by a turboshaft engine. A family of larger machines, known as the H-43 Huskie and its derivatives, were produced through 1964. While Kaman reverted to conventional single rotor helicopter designs in the later 1950s, the servo-flap concept continued to be a trademark of all of the Kaman helicopters. The H-2 Seasprite first flew in 1959 and has been produced in considerable numbers. Kaman has recently returned to the synchropter concept with the design of the K-Max (Fig. 1.31), which first flew in 1991. See Kaman Aircraft Corporation (2005) for further details of their helicopter lineage.

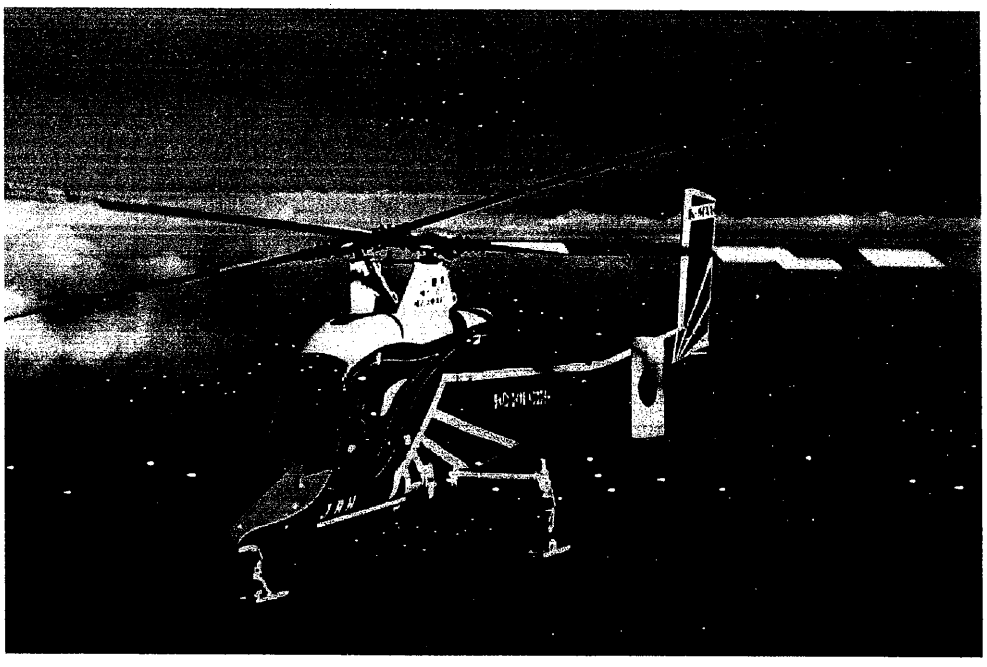

Figure 1.31 A modern synchropter design, the Kaman K-Max. (By permission of Kaman Aircraft Corporation.)

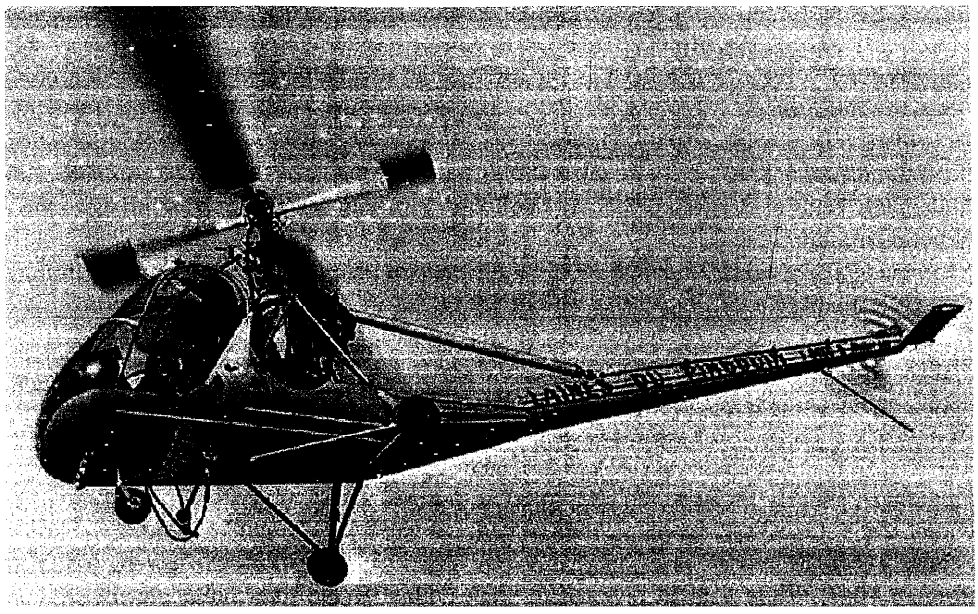

Figure 1.32 A Hiller 360, showing the distinctive Rotor-Matic "paddles" to enhance flight stability.

Stanley Hiller is another American pioneer in the development of the modern helicopter – see Straubel (1964) and Spenser (1992, 1999). Hiller built several helicopter prototypes, including the coaxial XH-44, which flew successfully in 1944. Although Hiller pursued other coaxial and tip-jet driven rotor machines, his later helicopters used a conventional main rotor and tail rotor configuration. His main breakthrough was the development of the "Rotor-Matic" main rotor design, where the cyclic pitch controls were connected to a set of small auxiliary blades set at 90° to the main rotor blades. These auxiliary blades or "paddles" worked in a similar manner to the Bell stabilizer bar, providing compensating cyclic pitch inputs and effecting damping in pitch and roll helping to augment the hovering stability of the machine. The basic theory of both stabilizing concepts are nicely explained by Sissingh (1948). It is significant to note that both Hiller and Young designed stability-producing mechanisms for their helicopters, whereas the Sikorsky machines had none and so they had a reputation for being harder to fly. While the Hiller machines are probably less well known than those of Sikorsky or Bell, the Hiller Company went on to build thousands of helicopters, including the 360 model (Fig. 1.32) and its further evolutions – the UH-12A and H-23.

1.12 Maturing Technology

The early 1950s saw helicopters quickly maturing into safe, successful, and viable aircraft that were easier to fly and more comfortable for crew and passengers alike. This era is marked by significant mass production of helicopters by various manufacturers in the United States, Britain, France, and elsewhere. There were rapid strides in the development of turboshaft engines (Fig. 1.17), with continuous improvements in power output and specific fuel consumption, low weight and high mechanical reliability. This was also accompanied by reductions in the net cost of an engine per unit of power output. Thereafter, the helicopter was to become a wide-scale commercial success.

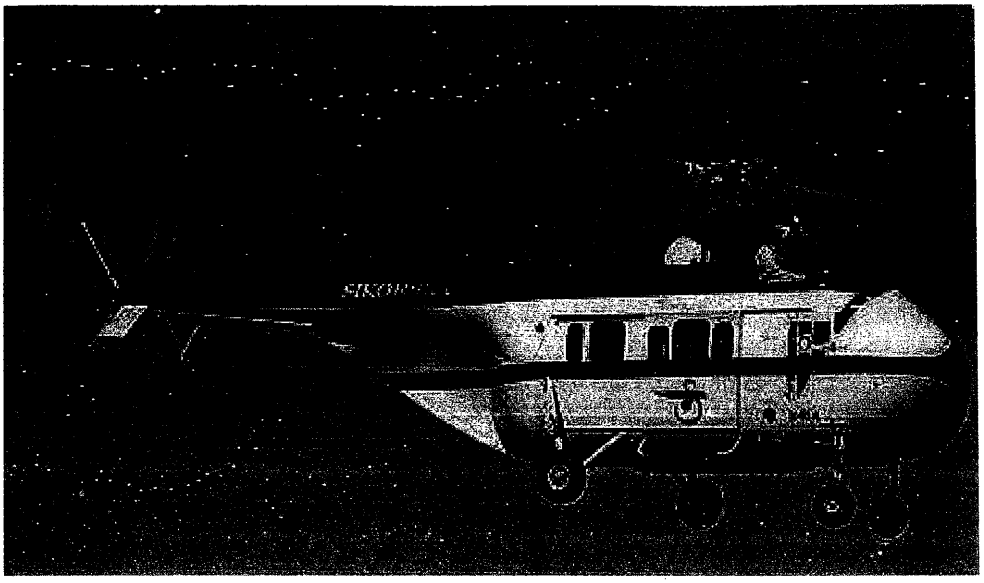

Figure 1.33 The Sikorsky S-55 was quantum-leap in terms of flight performance and payload capability for a single rotor helicopter. (Photo courtesy of Sikorsky Aircraft.)

The Sikorsky S-55 (see Fig. 1.33) and the S-58 models made great advances in helicopter design. These aircraft sported a large cabin under the rotor and to give a wide allowable center of gravity position, the engine was placed in the nose. Westland also maintained their relationship with Sikorsky and built versions called the S-55 Whirlwind and S-58 Wessex. The 1960s saw the development of the Sikorsky S-61 Sea King, the HH-52 (S-62), the heavy-lift S-64 Sky Crane and the larger five- and seven-bladed CH-53 models. The HH-52 (S-62) is arguably one of the greatest lifesaving aircraft ever created – see Beard (1996). Later, the S-70 (UH-60) Blackhawk was to become the mainstay of the Sikorsky company and the machine is expected to remain in production well into the twenty-first century. The civilian S-76 has been successful in its role as an executive transport and air ambulance, amongst other roles. In the 1970s, Sikorsky and Boeing teamed to build the military RAH-66 Comanche (Fig. 1.34). While producing one of the most advanced combat helicopters ever built, this program was cancelled by the Pentagon in 2004. The latest Sikorsky machine, the civilian medium lift S-92 flew for the first time in 1998 and was certified in 2002. In 2005, Sikorsky proposed a series of coaxial rotor helicopters, ranging from small unmanned velicles to heavy-lifters. For more information, see Sikorsky Aircraft (2005).

The success with the Model-47 led Bell Helicopter to develop the UH-1 Huey, which was delivered starting in 1959. The Bell 212 was a two-engine development of the UH-1D and proved to be a successful military and civilian machine. The Huey-Cobra also grew out of the UH-1 series, retaining the same rotor components but having a more streamlined fuselage with the crew seated in tandem. First flown in 1966, the type was in production in 1999 as the AH-1W Super-Cobra, which uses an advanced composite four-bladed rotor. The "Z" model is the current state of the art. The Bell 412 is basically a 212 model, but with a four-bladed composite rotor replacing the two-bladed teetering rotor. Bell led the civilian market with its Model 206 Jet-Ranger and variants, which first flew in 1966 and has become one of the most widely used helicopters. The OH-58 military version was sold in considerable numbers and with sustained performance improvements over the years,

Figure 1.34 The Boeing-Sikorsky RAH-66 Comanche, which first flew in 1996. (By permission of the Boeing Company.)

with the OH-58D having an advanced four-bladed rotor with a mast-mounted sight. One of most recent civil variants is the Bell 427, which is an eight-place light twin. See also Bell Helicopter Textron (2005).

Hughes Aircraft built the military TH-55 and later the Hughes 500 series, which has seen extensive civilian use in various models. However, the AH-64 Apache, which was designed in 1976, proved to be the biggest success story for the Hughes company, which became part of McDonnell–Douglas in 1984 and finally part of Boeing in the late 1990s. The AH-64D Longbow model (Fig. 1.35) is still in production. It was also produced under license in Britain by Agusta–Westland, with sixty-seven helicopters being delivered to the British Army by 2004. McDonnell–Douglas have produced a line of light commercial helicopters including the MD 500 and 600 series, and most recently have marketed the MD 900 Explorer. This aircraft uses a new bearingless rotor design and the "No Tail Rotor" (NOTAR) circulation control anti-torque concept (see Section 6.10.2). In 1999 Boeing sold the commercial helicopter line to MD Helicopters, a subsidiary of a European company.

Although most medium- and heavy-lift helicopters are produced for the military, the civil market still has a substantial market share. Several manufacturers produce training and light-utility helicopters or helicopters aimed at the general aviation market, including Robinson, Schweizer, Rotorway, Brantley, and Enstrom. Robinson produces the highly successful R-22 two-seat and R-44 four-seat helicopters. Both models are powered by piston engines and their success has done much to turn the civil helicopter industry away from the trend toward turbine engines. In 2004, nearly 80% of all helicopters built in North America were made by Robinson, who has substantially lowered the economic barriers for entry into the light-utility market. Schweizer, which as of 2004 became part of Sikorsky, produces an updated version of the two-seat Hughes 300 for the training market and a larger derivative designated as the Model-330, has a turboshaft engine.

European manufactures such as Aerospatiale and Messerschmitt-Bölkow-Blohm (MBB) (together they are now Eurocopter), Agusta, and Westland have produced many successful helicopter designs since the 1960s. Agusta and Westland have also license-produced

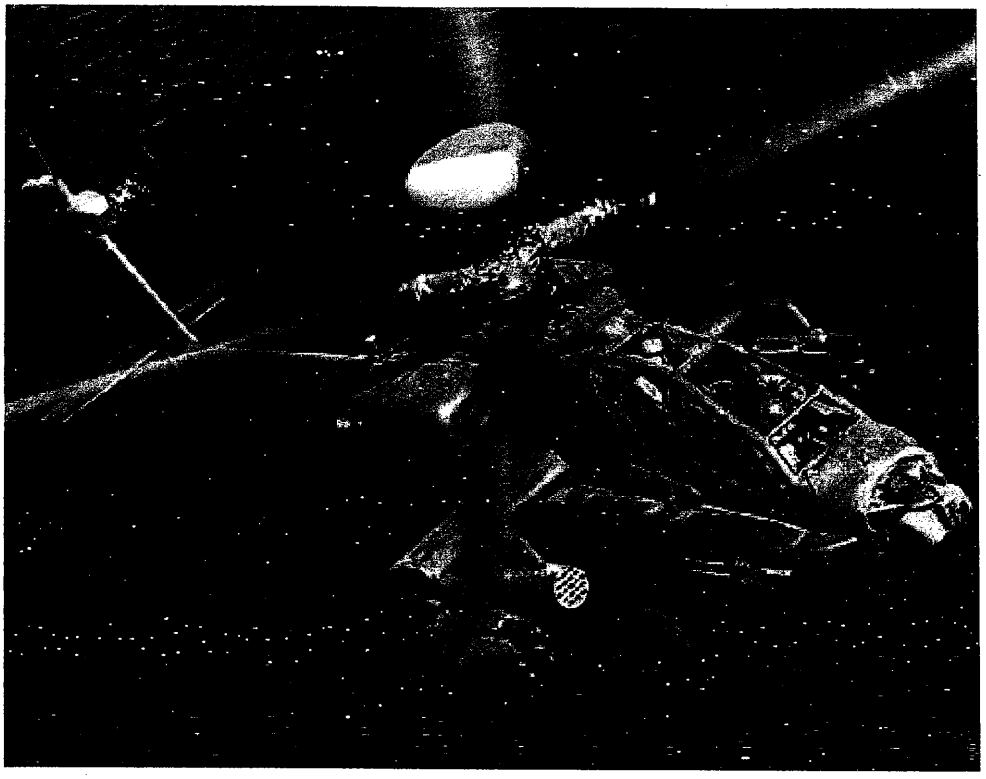

Figure 1.35 A version of the McDonnell–Douglas (now Boeing) AH-64 Apache. (By permission of the Boeing Company.)

helicopters designed in the United States, such as those of Sikorsky and Bell. The Aerospatiale (Sud-Aviation) Alouette II/III was one of the most successful European helicopters and in 1955 it was one of the first machines to be powered by a turboshaft engine. The Djinn (Genie) was the only mass-produced helicopter using a tip-jet design. The Aerospatiale Super Frelon was a large transport helicopter, first flown in 1962. In the early 1970s the Aerospatiale/Westland SA330 Puma became Europe's best selling transport helicopter. The Aerospatiale/Westland Gazelle was a successful successor to the Alouette, first flown in 1967 and it introduced the fenestron tail rotor. The fenestron is a ducted tail rotor design, fully integrated into the fuselage and vertical fin and, like the NOTAR, essentially eliminates the all-too-common problem of tail rotor strikes. The Dauphin, first flown in 1972, used an improved fenestron tail rotor and a composite main rotor hub. MBB introduced the BO 105 in 1967 with a hingeless rotor, with the larger and more capable BK 117 machine first flying in 1979. In the 1990s, Aerospatiale and MBB joined resources to form Eurocopter, which produces a large range of civil and military helicopter models – see Eurocopter (2005). A Eurocopter derivative of the BK 117, the EC 145, is a medium-weight, twin-engined multi-mission helicopter (Fig. 1.36).

In 1952, Agusta of Italy began to license build the Bell Model-47 and through 1965 it built several variants of the Bell machine to their own specifications. Agusta also began to design their own helicopters, with the large three-engined A-101 flying in 1964, but it never went into production. The Agusta A-109 was one of the most aerodynamically attractive

Figure 1.36 A version of the Eurocopter EC 145. (Photo by Wolfgang Obrusnik, with permission of Eurocopter.)

helicopters. First flown in 1971, this high-speed transport and multi-role helicopter has been very successful in both civilian and military roles. The A-129 Mangusta, first flown in 1983, is a military version of the A109 with a gunship fuselage.

Westland Helicopters (now Agusta–Westland) has been a key player in British aviation since the 1930s – see Mondey (1982). The earliest helicopters built by Westland were under license from Sikorsky, but these were significantly modified to meet British airworthiness standards. During 1959–1960, Westland took over the operation of the Bristol, Saunders-Roe, and Fairey companies. Saunders-Roe (SARO) had previously taken over the Cierva Company in 1951. The Westland/SARO/Cierva Skeeter was a small two-seat training helicopter, which led to the bigger and relatively successful Wasp in 1962. The Westland Wessex was a development of the Sikorsky S-58, which was built in many specialized configurations through 1970. The Sea King and Commando were both derived from the S-61, which were steadily improved upon since the first models flew in the late 1960s. The latest versions of the Sea King have used composite rotor blades and various airframe improvements. Westland designed its own line of helicopters, starting with the military Lynx, which first flew in 1971. The Westland WG-30 was a larger multirole transport version of the Lynx using a five-bladed hingeless rotor. Although this aircraft saw some civilian use, production was limited. New versions of the Lynx (Super Lynx) are fitted with the Westland/RAE British Experimental Rotor Program (BERP) blade, which has improved airfoil sections and special tip shapes (see Section 65). A Lynx with the BERP rotor currently holds the absolute straight line speed record for a single rotor helicopter at some 216 kts (240 mi/h; 400 km/hr). The BERP blade design is also used on the Agusta–Westland built EH Industries EH-101 (Fig. 1.1), which is a medium-lift helicopter that entered production in 1996 in both civilian and military variants. See also Agusta–Westland (2005) for more information on the current lineage.

Significant numbers of helicopters have also been built in the former Soviet Union, which deserves credit for being the nation that has most profited economically by the development of the modern helicopter. In the 1930s, the TsAGI Technical Institute in Moscow built a series of autogiros based on the Cierva designs. Everett-Heath (1988) gives a good account of early Russian work on both autogiros and helicopters. The TsAGI 1-EA was the most successful pre–Sikorsky single rotor helicopter. Later, work with the Focke Achgelis Flugzeugbau GmbH of Germany resulted in a number of prototype helicopter designs with a side-by-side rotor configuration. The Mil, Kamov, and Yak companies all went on to build successful helicopter lines. An overview of the early Soviet machines is given by Free (1970).

Mikhail Mil adopted the single main rotor and tail rotor helicopter configuration, with the Mi-1 flying in 1950. The Mi-2 was a turbine-powered version. The more efficient Mi-3 (a Mi-1 variant) and larger Mi-4 machines quickly followed. The Mi-4 looked very much like the Sikorsky S-55, but it was actually much bigger and had a greater payload and better performance. The Mi-2 was also built in significant numbers in Poland, with the Mi-4 being produced in China. The Mi-6 of 1957 was one of the largest helicopters ever built, with a rotor diameter of 115 ft (35 m) and a gross weight of over 93,700 lb (42,500 kg). This was followed by the smaller Mi-8 (similar to the Mi-4), which went into civilian service. The Mi-10 of 1961 was a flying crane development of the Mi-6, with a tall, wide, quadricycle landing gear. However, the credit for the world's largest helicopter goes to the Mi-12, which was designed to carry nuclear missiles. This aircraft had a side-by-side rotor configuration, with the span of the aircraft from rotor tip to rotor tip, exceeding the wing span of the Boeing 747. Power was provided by four turboshaft engines, installed as pairs at the end of each wing pylon. The Mi-24 was designed in 1972 as an evolution of the Huey gunships, and it has been produced in large numbers. The Mi-26 entered service in 1982 and is the largest and heaviest helicopter currently flying (Fig 1.37). It has a rotor diameter of 105 feet

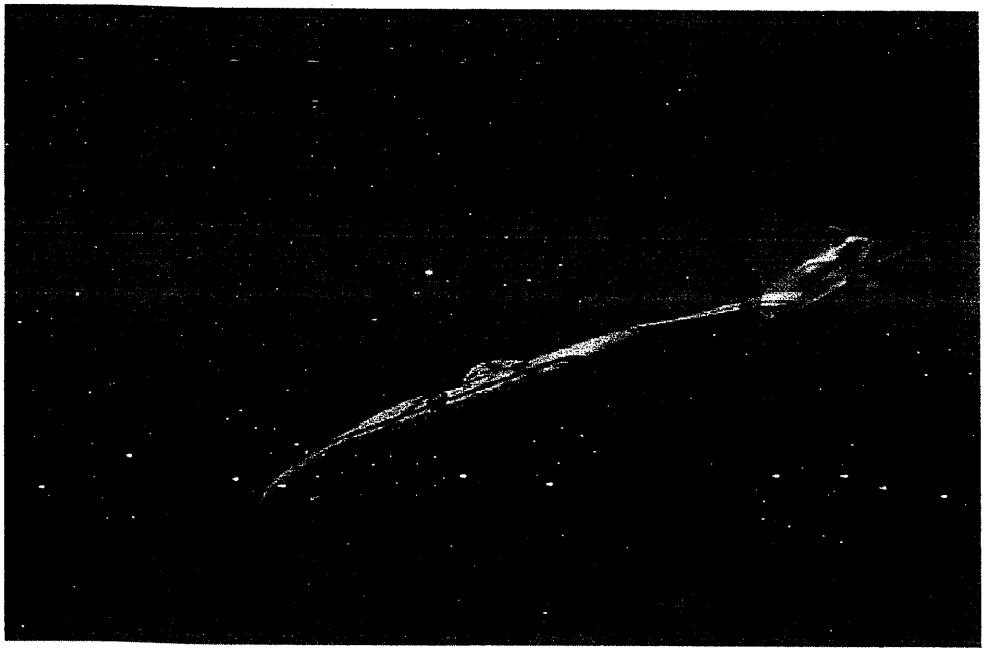

Figure 1.37 An unusual view of the eight-bladed rotor of the Mil Mi-26, the world's largest and heaviest helicopter. (Photo by Stephen Koch and courtesy of Helispot.)

(32 m), with a useful payload of up to 44,092 lb (20,000 kg) and a maximum gross weight of 123,459 lb (56,000 kg). The Mi-28 is an attack helicopter, similar in configuration to the AH-64 Apache. The latest Mil design, the Mi-38, is planned as a successor to the Mi-8/17, which is similar in size and weight to the Agusta–Westland EH-101.

The Kamov company has built a series of very successful light- and medium-weight coaxial rotor helicopter designs, including the Ka-15 and Ka-18 in 1956 and the Ka-20 in 1961. Kamov has been the only company to ever put the coaxial helicopter design into mass production, although there have been many proposed and prototype coaxial rotor helicopter designs. Nikolai Kamov had built an autogiro as early as 1929, inspired by the success of Juan de la Cierva. Kamov built several other models of autogiros through 1943. The Kamov helicopter company was formed in 1945 and was at first a naval design bureau; the relatively compact coaxial rotor was the only configuration that allowed a helicopter to operate from the small deck of a ship. The Ka-8 and Ka-10 were small lightweight coaxial rotor designs, but they were underpowered. The first real success came with the Ka-15 and Ka-18 in the late 1950s. The Ka-26 used radial engines, but the Ka-126 and later models were all turboshaft powered. The Ka-27 and the civilian model Ka-32 (see Fig 1.38) have been in production since 1972. One of the most recent Kamov designs is the Ka-50, which is a lightweight attack helicopter of considerable performance. One exception to the Kamov coaxial line was the Ka-22 convertiplane of 1961. Another new design is the Kamov Ka-62, which is a conventional light-utility helicopter design incorporating a fenestron that in 2004 was in the prototype stage. See the Kamov Company (2004) for more information.

Another famous Russian designer, Alexander Yakolev, built many successful fixed-wing designs, but with the assistance of Mil designed the large tandem Yak-24 "Flying Boxcar" helicopter in the early 1950s. This helicopter was produced from about 1952 to 1959, but

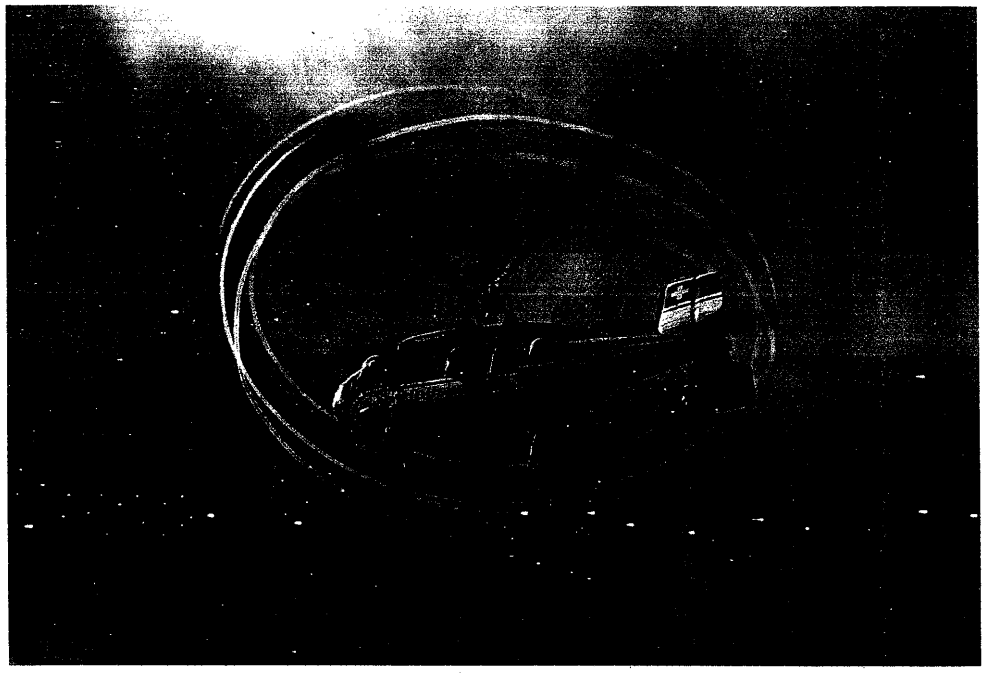

Figure 1.38 A Kamov Ka-32 coaxial rotor helicopter revealing its dual rotor wake structure through natural condensation effects. (Photo courtesy of Dany Gaulé and http://www.Airliners.net.)

it was not very successful with persistent vibration problems and relatively few of the type saw actual service. Further information on Russian helicopter developments is given by Anoschenko (1968) and Everett-Heath (1988).

1.13 Compounds, Tilt-Wings, and Tilt-Rotors

The conventional helicopter is limited in forward flight performance by the aerodynamic lift and propulsion limitations of the main rotor. These rotor limits arise because of compressibility effects on the advancing blade, as well as stall on the retreating blade (see page 57). In addition, the relatively high parasitic drag of the rotor hub and other airframe components leads to a relatively poor overall lift-to-drag ratio of the helicopter (less than 6). This generally limits performance of conventional helicopters to level-flight cruise speeds in the range of 150 kts (278 km/h; 172 mi/h), with dash speeds up to 200 kts (370 km/h; 230 mi/h) and unrefueled ranges of less than 500 miles. Although somewhat higher flight speeds are possible with compound designs, which use auxiliary propulsion devices and wings to offload the rotor, this is always at the expense of much higher power required and fuel burn than would be necessary with a fixed-wing aircraft of the same gross-weight and cruise speed. One example of a revolutionary compound helicopter was the Lockheed AH-56 Cheyenne, which was built in 1969 – see Fig. 1.39. This machine used both lift compounding with a wing and propulsion compounding using a pusher propeller. It flew at over 220 kts (407.77 km/h; 253.4 mi/h). It did not, however, go into production – see Forman (1996).

The need for an aircraft that could combine the benefits of a vertical takeoff and landing (VTOL) capability with the high speed cruise of a fixed-wing aircraft has led to the evolution of *tilt-wing* and *tilt-rotor* concepts. A good history of the many VTOL designs, including tilt-wings and tilt-rotors, is given by Hirschberg (1997). However, this potential capability

Figure 1.39 The Lockheed AH-56 Cheyenne was a revolutionary compound helicopter. (Photo courtesy of AHS.)

comes at an even greater price than for either a conventional or compound helicopter, including increased mechanical complexity, increased weight and the susceptibility for the rotors and wing to exhibit various aeroelastic problems.

The tilt-wing is basically a convertiplane concept, but it never became a viable rotating-wing concept to replace or surpass the capabilities of the helicopter. The idea is that the wing can be tilted from its normal flying position with the propellers providing forward thrust, to a vertical position with the propellers providing vertical lift. Several companies seriously considered the tilt-wing concept in the 1950s, with Boeing, Hiller, Vought–Hiller–Ryan (later Ling–Temco–Vought) and Canadair all producing flying prototype aircraft. The Vertol VZ-2 first flew in 1957 and went on to make many successful conversions from hover into forward flight. However, the unsteady airloads produced by airflow separation on the wing as it stalled during conversion flight resulted in some difficult piloting and these issues were never satisfactorily resolved. The Hiller X-18 was a large tilt-wing aircraft compared to the VZ-2. The aircraft used two large diameter counterrotating propellers (used from the earlier Ryan Pogo concept) – see Straubel (1964). The aircraft underwent flight testing in 1960, but never did make a full conversion. The program was canceled in 1961 after the aircraft suffered a loss of control. In the 1980s, the Ishida Company developed the TW-68 tilt-wing aircraft as a private venture, but the company went into bankruptcy before the aircraft could be built.

The tilt-rotor aircraft takes off and lands vertically with the rotors oriented like a helicopter. For forward flight, the wing tip-mounted rotors are progressively tilted to convert the aircraft into something that looks like a fixed-wing turboprop airplane. In this mode, the tilt-rotor is able to achieve considerably higher flight speeds (about 300 kts; 555 km/h; 344 mi/h) than would be possible with a helicopter. Therefore, the tilt-rotor combines some attributes of the conventional helicopter with those of a fixed-wing aircraft. During WW2, the Focke Achgelis Fa 269 was proposed as a tilt-rotor. The side-by-side rotors pointed downward for takeoff and then rotated aft to provide propulsion in normal flight with conventional wings providing lift. However, the aircraft remained a paper project. A practical tilt-rotor concept was first demonstrated in a joint project between the Transcendental Aircraft Corporation and Bell in 1954. Various technical problems were encountered with the first aircraft, the Model 1-G, especially in the conversion from helicopter mode to fixed-wing flight. Bell later led the development of the XV-3 in 1951, which had two fully articulated three-bladed rotors. The XV-3 was damaged in an accident in 1956 after an aeroelastic problem with the rotor. The second XV-3 used a two-bladed teetering rotor system and the aircraft was successfully flown in 1958. However, several aeromechanical problems were again encountered, including pylon whirl flutter.

By the late 1960s, Bell had developed the Model 266 tilt-rotor and later the Model 300. Various wind-tunnel tests of scaled models led to an improved understanding of the rotor and wing aeroelastic issues involved with tilt-rotors, especially during the conversion mode and Bell continued to develop the Model 301. This aircraft later became the XV-15, which demonstrated the viability of the tilt-rotor concept. The XV-15 was purely experimental and never designed for production, and flew experimentally through 2003. However, in 1983 the much larger V-22 Osprey tilt-rotor program was begun (see Fig. 1.40). This joint Bell–Boeing project has resulted in several test and preproduction aircraft and in 1997 the decision was made to put the aircraft into production for the US Marines, Navy, and Air Force. As of 2005, however, it was still in the developmental stage with low rate production. Because the rotors of a tilt-rotor cannot be as large as those of a helicopter, the hovering efficiency of the tilt-rotor is not as good as that of a helicopter. In the design of the Bell–Boeing V-22 Osprey, the rotor diameter was also limited by the need to operate and hangar

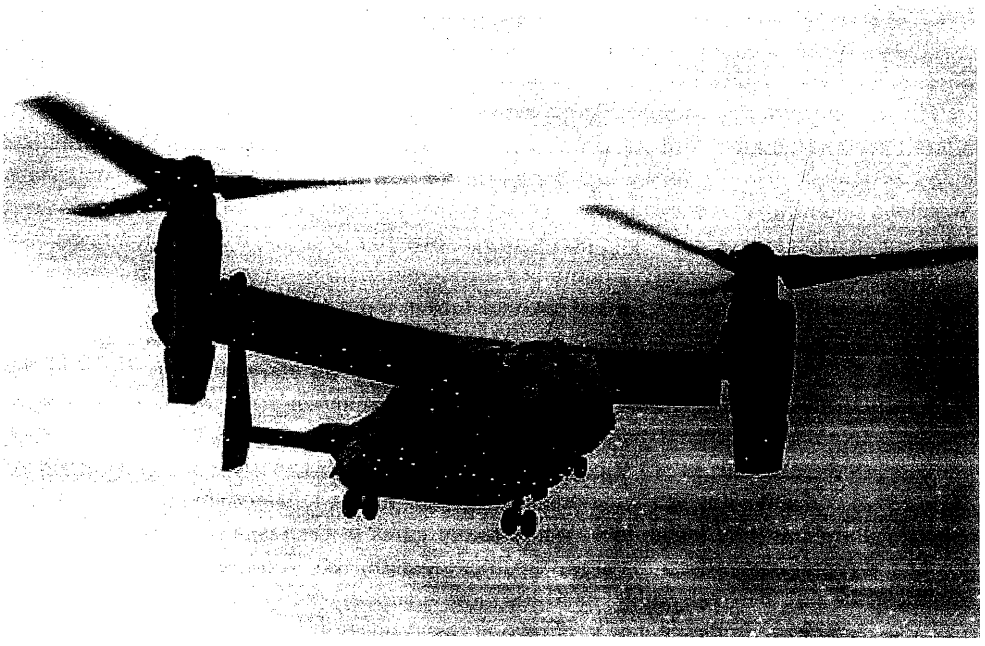

Figure 1.40 The Bell–Boeing V-22 Osprey tilt-rotor. (By permission of the Boeing Company.)

the aircraft on board an aircraft carrier. The tilt-rotor, however, has the ability to fly much faster than a conventional helicopter.

The Agusta–Bell Model 609 civilian tilt-rotor first flew in 2003 and will be capable of transporting 9 passengers at 275 kts (509 km/h; 315 mi/h) over 750 nm (1,390 km; 860 mi) sectors. It is expected to be certified in 2007. See Bell Helicopter Textron (2005) for further information. The Europeans too have embarked on fundamental research toward a civil tilt-rotor program suited to scheduled passenger transport. The project is being undertaken by a consortium of twelve partners representing five European nations. The ultimate aim is to develop a 19-seat, twin-engine tilt-rotor aircraft that can be flown by a single pilot to be sold to airlines and corporations. While the work is expected to culminate in the first flight of the new tilt-rotor aircraft in 2008, the lengthy half-decade-long development of the American tilt-rotor program suggests that realistically the flights of a European tilt-rotor may be further away than this. The success of any civil tilt-rotor program, European or American, may be tied to the ultimate success or otherwise of the V-22 Osprey.

1.14 Chapter Review

During the past sixty years since the first successful flights, helicopters have matured from noisy, unstable, rickety vibrating contraptions that could barely lift the pilot and a small payload into sophisticated machines of quite extraordinary capability. Igor Sikorsky's dream has certainly been fulfilled, perhaps in many ways that he could not have possibly imagined. At the beginning of the twenty-first century, there were about 40,000 helicopters flying worldwide. Its roles encompass air ambulance, sea and mountain rescue, police surveillance, corporate services and oil rig servicing in the civilian world and troop transport and antitank gunships in military use. In rescue operations alone, the helicopter

has saved the lives of well over a million people. The helicopter today is a safe, versatile, and reliable aircraft and it will continue to be an indispensable part of modern life well into the twenty-first century.

The improved design of the helicopter and the increasing viability of other vertical lift aircraft such as the tilt-rotor continue to advance as a result of the revolution in computer-aided design and manufacturing and the advent of new lightweight composite materials. Sustained scientific research and development in many aeronautical disciplines has allowed for dramatic increases in helicopter performance, overall lifting and cruise efficiencies, and excellent mechanical reliability. Continuous aerodynamic improvements to rotor efficiency have allowed the helicopter to lift a payload that is more than its empty weight and to fly in level flight at speeds in excess of 200 kts (370 km/h; 229 mi/h). Since the 1980s, there has been an accelerating scientific effort to understand and overcome some of the most difficult technical problems associated with helicopter flight, particularly in regard to aerodynamic limitations associated with the main rotor. In more recent years, however, increases in the capabilities of helicopters has been much more incremental, despite major advances in understanding using various types of computational aerodynamic methods and experimental measuring techniques. While future gains in performance will certainly be attained, the immediate need for more capable, efficient, safer, and economic helicopters centers on the ability to really understand and more accurately predict its aerodynamics. This may also require the implementation of revolutionary developments to control its complex aerodynamics. Only then will the helicopter fulfill a wider variety of civilian and military roles.

1.15 Questions

1.1. Give an overview of the main technological problems that were encountered when trying to design and fly a successful helicopter prior to 1900. In your discussion, consider issues such as overall levels of aeronautical knowledge, stability, and control requirements, the availability of suitable power plants, and construction materials.

1.2. Engines are often viewed as the one of the enabling technologies for powered flight. However, it could be argued that it was the development of a ready supply of inexpensive fuel for the engine (i.e., gasoline) that was really the enabling technology. Discuss this viewpoint.

1.3. Most modern helicopters are of the single main rotor and tail rotor (conventional) configuration. For the same overall aircraft gross weight, what might be the relative advantages of a tandem rotor helicopter over a conventional helicopter? Also, compare the potential relative merits of a coaxial rotor over a tandem design.

1.4. Explain the physical design features that distinguish a helicopter from an autogiro. Discuss the reasons as to why the autogiro was quickly eclipsed by the success of the helicopter when it appeared in the early 1940s.

1.5. Although tilt-wing and tilt-rotor concepts date back more than forty years, it is only in the past few years that civilian tilt-rotor aircraft have been proposed. Discuss the technical, economic, and any other reasons for this long gestation period.

1.6. For a truly heavy lift helicopter, say in excess of 100,000 kg (220,000 lb) gross takeoff weight, a single rotor design would be considered impractical. Discuss the reasons why this might be so.

1.7. So-called "compound" helicopter designs have enjoyed periodic popularity over the past fifty years, but none have entered production. What is meant by a compound helicopter? Briefly, suggest some of the advantages and disadvantages of a compound helicopter design. In particular, explain the difference between "lift" compounding and "thrust" compounding.

1.8. Think about some of the issues in the design of a tilt-rotor type of rotorcraft. While the tilt-rotor has the advantages of flight speed compared to a helicopter, compare and contrast their capabilities in other flight regimes including sustained hovering flight. Why do you think it has taken many decades to get a practical tilt-rotor concept to fruition?

Bibliography

Agusta–Westland. 2005. http://www.whl.co.uk/.

Aldridge, P. J. 1954. "The Development of an Early Helicopter," *J. of the Royal Aeronautical Society*, 58, Aug., pp. 556–559.

Anderson, J. D., Jr. 1997. *A History of Aerodynamics and Its Impact on Flying Machines*, Cambridge University Press, New York, NY.

Anoschenko, N. D. (ed.). 1968. "History of Aviation and Cosmonautics," Vol. 5, NASA TT F-11851.

Apostolo, G. 1984. *The Illustrated Encyclopedia of Helicopters*, Bonanza, New York, NY.

Asboth, O. de. 1923. "Variation in the Number of Revolutions of Air Propellers," NACA Technical Note 131.

Balaban, K. 1923. "Evolution of the Helicopter," NACA TN 196.

Bartlett, R. M. 1947. *Sky Pioneer: The Story of Igor I. Sikorsky*, Charles Scribner's & Sons, New York, NY.

Beard, T. B. 1996. *Wonderful Flying Machines*, Naval Institute Press, Annapolis, MD.

Bell Helicopter Textron. 2005. http://www.bellhelicopter.textron.com/.

Berliner, E. 1908. "The Berliner Helicopter," *Aeronautics*, Vol. 3.

Berliner, E. 1915. "Elements of a Girocopter," *Aeronautics*, Vol. 10. See also *Scientific American*, May 27, 1921.

Boeing Company. 2005. Helicopter Division. http://www.boeing.com/.

Boulet, J. 1984. *The History of the Helicopter as Told by its Pioneers 1907–1956*, Editions France-Empire, Paris.

Braun, K. 2003. "Anton Flettner: His Life for the Rotor," *Vertiflite*, 39 (2), pp. 36–44.

Breguet, M. L. 1936. "Les Gyroplanes Leurs Possibiliteés de Vitesse et de Rayon d'Action," Confeérence faite le 16 Juin 1936 à L'amphithéâtre de Physique de la Sorbonne, Paris.

Brown, D. A. 1995. *The Bell Helicopter Textron Story*, Aerofax, Arlington, TX.

Carlson, R. M. 2002. "Helicopter Performance–Transportation's Latest Chromosome: The 21st Annual Alexander A. Nikolsky Lecture," *J. of the American Helicopter Soc.*, 47 (1), pp. 3–17.

Cayley, G. 1809–10. "On Aerial Navigation," *Nicholson's J. of Natural Philosophy, Chemistry, and the Arts*, Nov. 1809, Feb. 1810, and Mar. 1810.

Chatley, H. 1908. "Helicoptere v. Aeroplane," *Aeronautical J.*, Oct., pp. 102–107.

Cierva, J. 1926. "The Development of the Autogiro," *J. of the Royal Aeronautical Soc.*, 30 (181), pp. 8–29.

Cierva, J. 1930. "The Autogiro," *J. of the Royal Aeronautical Soc.*, 39 (239), pp. 902–921.

Cierva, J. 1935. "New Developments of the Autogiro," *J. of the Royal Aeronautical Soc.*, 39, Dec., pp. 1125–1143.

Cierva, J. and Rose, D. 1931. *Wings of Tomorrow: The Story of the Autogiro*, Brewer, Warren & Putnam, New York, NY.

Coates, S. 2002. *Helicopters of the Third Reich*, Classic Publications, Hersham.

Cochrane, D., Von Hardesty, and Lee, R. 1989. *The Aviation Careers of Igor Sikorsky*, University of Washington Press, Seattle & London.

de Bothezat, G. 1919. "The General Theory of Blade Screws," NACA TR 29.

Delear, F. J. 1969. *Igor Sikorsky: His Three Careers in Aviation*, Dodd, Mead & Co., New York, NY.

Dowling, J. 1992. *RAF Helicopters; The First Twenty Years*, HMSO, London.

Eurocopter Company. 2005. http://www.eurocopter.com/.

Everett-Heath, J. 1986. *British Military Helicopters*, Arms and Armour Press, London.

Everett-Heath, J. 1988. *Soviet Helicopters–Design, Development and Tactics*, Jane's, London.

Fay, J. 1987. *The Helicopter: History, Piloting and How It Flies*, Hippocrene, New York, NY.

Finne, K. N. 1987. *Igor Sikorsky: The Russian Years*, edited by C. J. Brobrow and Von Hardesty, Smithsonian Institution Press, Washington DC.

Focke, E. H. H. 1938. "The Focke Helicopter," NACA TM 858.

Focke, E. H. H. 1947. "The Focke Helicopters," *American Helicopter*, 5 (2), 1947, pp. 14–16, 37–40.

Focke, E. H. H. 1965. "German Thinking on Rotary Wing Development," *J. of the Royal Aeronautical Soc.*, 69 (653), pp. 293–305.

Forman, B. 1996. "What Killed the Cheyenne?" *Vertiflite*, 42 (3), pp. 22–27.

Free, F. W. 1970. "Russian Helicopters," *Aeronautical J.*, 74 (717), pp. 767–785.

Gablehouse, C. 1967. *Helicopters and Autogiros: A Chronicle of Rotating Wing Aircraft*, Lippincott, Philadelphia & New York.

Giacomelli, R. 1930. "The Aerodynamics of Leonardo da Vinci," *J. of the Royal Aeronautical Soc.*, 34 (240), pp. 1016–1038.

Graham, R. 1973. "Brennan–His Helicopter and Other Inventions," *Aeronautical J.*, 77, Feb., pp. 74–82.

Gregory, H. F. 1944. *Anything a Horse Can Do: The Story of the Helicopter*, Introduction by Igor Sikorsky, Reynal & Hitchcock, New York, NY.

Grina, K. I. 1975. "Helicopter Development at Boeing-Vertol Company," *The Aeronautical J.*, 79 (777), pp. 401–416.

Gunston, B. 1983. *Helicopters of the World*, Crescent Publishers, New York, NY.

Gustafson, F. B. 1971. "A History of NACA/NASA Rotating-Wing Aircraft Research, 1915–1970," Limited-Edition Reprint (VF-70) from *Vertiflite*, American Helicopter Soc., Alexandria, VA.

Hafner, R. 1949. "The Bristol 171 Helicopter," *J. of the Royal Aeronautical Soc.*, 53, April, pp. 324–333.

Hafner, R. 1954. "The Domain of the Helicopter," *J. of the Royal Aeronautical Soc.*, 58 (536), pp. 663–702.

Harris, F. D. 1994. "Practical Powered Lift Arrives," In: From da Vinci to Today: The Top Technology Achievements in Vertical Flight History," Published by the American Helicopter Soc., Alexandria, VA.

Hart, I. B. 1961. *The World of Leonardo da Vinci*, MacDonald, London.

Hirschberg, M. J. 1997. "V/STOL: The First Half-Century," *Vertiflite*, 43 (2), pp. 34–54.

Hislop, G. S. 1958. "The Fairey Rotodyne," Meetings of The Helicopter Association of Great Britain & The Royal Aeronautical Soc., London, Nov. 7.

Hobbs, J. 1984. *Bristol Helicopters: A Tribute to Raoul Hafner*, Frenchay Publications, Bristol, UK.

Kaman Aircraft Corporation. 2005. http://www.kaman.com/.

Kamov Company. 2004. http://www.kamov.ru/.

Kelly, B. 1954. "Helicopter Stability and Young's Lifting Rotor," *SAE J.*, 53 (12), pp. 685–690.

Klemin, A. 1925. "An Introduction to the Helicopter," NACA TM 340.

Kretz, M. 1987. "René Dorand: The Life of a Pioneer," 13th European Rotorcraft Forum, Arles, France, Sept. 8–11.

Lambermont, P. (with Price, A.) 1958. *Helicopters and Autogiros of the World*, Cassell & Co., London.

Leishman, J. G. 2001a. "The Cornu Helicopter–First in Flight?" *Vertiflite*, 47 (4), pp. 54–55.

Leishman, J. G. 2001b. "The Breguet–Richet Quadrotor Helicopter of 1907," *Vertiflite*, 47 (3), pp. 30–32.

Leishman, J. G. 2002a. "The Berliner Vertical Lift Aircraft 1909–1924," *Vertiflite*, 48 (2), pp. 58–60.

Leishman, J. G. 2002b. "The Weir W-5 and W-6 Helicopters," *Vertiflite*, 48 (4), pp. 66–69.

Leishman, J. G. 2003. "The Cierva W-11 Air Horse," *Vertiflite*, 49 (1), pp. 52–55.

Leishman, J. G. 2004. "A Chronology of Early British Rotorcraft," American Helicopter Soc. 60th Annual Forum, Baltimore, MD, June 7–10.

Lewis, W. and Lewis, T. J. 1938. "Improvement in Horizontal Windmills," US Patent 583, Jan. 27, 1838.

Liberatore, E. K. (ed.) 1950. Rotary Wing Handbooks and History, US Air Force Air Materiel Command. 18 volumes. (Available through the American Helicopter Soc. International or the NASM.)

Liberatore, E. K. 1988. "An Eclectic Bibliography of Rotorcraft," *Vertiflite*, 34 (1), pp. 50–59.

Liberatore, E. K. 1998. *Helicopters Before Helicopters*, Krieger Publishing, Malabar, FL.

Lopez, D. S. and Boyne, W. J. (eds.) 1984. *Vertical Flight: The Age of the Helicopter*, Smithsonian Institution Press, Washington DC.

Margoulis, W. 1922. "Propeller Theory of Professor Joukowski and His Pupils," NACA TM 79.

Maxim, H. S. 1897. "Screw Propellers Working in Air," *Aeronautical Annual*, Royal Aeronatical Soc., London.

Mondey, D. 1982. *Planemakers 2: Westland*, Janes Publishing, London.

Moreno-Caracciolo, M. 1923. "The Autogiro," NACA TM 218.

Munk, M. M. 1923. "Analysis of Dr. Schaffran's Propeller Model Tests," NACA TN 153.

NACA. 1921. "The Œhmichen–Peugeot Helicopter," NACA TM 13.

Negler, B. and Hafner, R. 1932. "Improvements in or Relating to Helicopter Aircraft," British Patent 385,101, Dec. 22.

Œhmichen, E. 1923. "My Experiments with Helicopters," NACA TM 199.

Paucton, A. J. P. 1768. "Théorie de las vis d'Archimède," Paris, 1768.

Piasecki Aircraft Corp. 1967. *The Piasecki Story of Vertical Lift: Pioneers in Progress for Over Forty Years*, Lakehurst, NJ.

Pitcairn, H. F. 1930. *The Autogiro: Its Characteristics and Accomplishments*, Annual Report of the Board of Regents to the Smithsonian Institution, US Government Printing Office, pp. 265–272.

Prewitt, R. H. 1938. "Possibilities of the Jump-Off Autogiro," *J. of Aeronautical Sciences*, 6 (1), pp. 10–14.

Pritchard, J. L. 1961. *Sir George Cayley: The Inventor of the Airplane*, Max Parrish & Co., London.

Rees, Elfan ap 1990. "Glasgow–Helicopter Birthplace," 16th European Rotorcraft Forum, Glasgow, Sept. 18–20.

Riabouchinsky, D. 1906. "Recherches sur l'hélice aérienne se Mouvant Dans un Courant Aérien Dirigé Perpendiculairement à l'axe de l'hélice," Bulletin de l'Institut Aérodynamique de Koutchinio I, 13.

Rosen, G. 1984. *Thrusting Forward–A History of the Propeller*, Hamilton Standard, East Hartford, CT, p. 25.

Schneider, J. 1995. "Arthur Young–Inventor, Developer and Metaphysicist, the Developer of the Bell Teetering Rotor," *Vertiflite*, 41 (2), pp. 36–39.

Seiferth, R. 1927. "Testing a Windmill Airplane (Autogiro)," NACA TM 394.

Sikorsky, I. I. 1938 (Rev. 1958, 1967). *The Story of the Winged-S: An Autobiography*, Dodd, Mead & Co., New York, NY.

Sikorsky, I. I. 1941. "Development of the VS-300 Helicopter," Paper presented at the Rotating Wing Aircraft Meeting of the Institute of the Aeronautical Sciences, The Franklin Institute, Philadelphia, Jan. 29.

Sikorsky, I. I. 1942. "Technical Development of the VS-300 Helicopter During 1941," *J. of the Aeronautical Sciences*, 9 (8), pp. 309–311.

Sikorsky, I. I. 1943. "Progress of the Vought–Sikorsky Helicopter Program in 1942," *Aeronaut. Eng. Rev.*, 2 (4), pp. 41–43.

Sikorsky, I. I. 1955. Quote from comments made by Igor Sikorsky to new engineers of the Sikorsky Aircraft Corporation, about 1955.

Sikorsky, I. I. 1964. "Recollections and Thoughts of a Pioneer," Lecture Presented to the Wings Club, New York, NY, Nov. 16.

Sikorsky, I. I. 1971. "Sixty Years of Flying." *Aeronautical J.*, (731), Nov., pp. 761–768.

Sikorsky, S. and Andrews, A. 1984. *Straight Up*, Sikorsky Aircraft, United Technologies Corp.

Sikorsky Aircraft Corp. 2005. http://www.sikorsky.com/.

Sissingh, G. J. 1948. "Automatic Stabilization of Helicopters," *J. of the Helicopter Association of Great Britain*, Vol. 2 (3), pp. 4–25 (including discussion).

Smith, F. K. 1985. *Legacy of Wings: The Story of Harold Pitcairn*, Jason Aronson, New York, NY.

Spenser, J. P. 1992. *Vertical Challenge: The Hiller Aircraft Story*, University of Washington Press, Seattle & London.

Spenser, J. P. 1999. *Whirlybirds: A History of the US Helicopter Pioneers*, University of Washington Press, Seattle & London.

Straubel, J. F. 1964. *One Way Up*, Hiller Aircraft Co., Palo Alto, CA.

Taylor, M. J. 1984. *History of the Helicopter*, Hamlyn Publishing, London.

Tipton, R. S. 1989. *They Filled the Skies*, Bell Helicopter Textron, Fort Worth, TX.

Tokaty, G. A. 1971. *A History and Philosophy of Fluid Mechanics*, Foulis & Co., Henley-on-Thames, England.

von Kármán, Th. 1921. "Tests Made With Captive Helicopters." In the report: "Recent European Developments in Helicopters," NACA TN 47.

Walker, W. G. 1900. "Lifting Power of Air Propellers, Being Experiments with Propellers 30 ft in Diameter," *Aeronautical J.*, Oct., pp. 156–161.

Walker, W. G. 1905. "The Vertical Screw Aerial Machine, with Special Notes on the Lifting Propellers," *Aeronautical J.*, Oct., pp. 57–64.

Warner, E. P. 1920. "The Problem of the Helicopter," NACA TN 4.

White, J. D. 1898. "Patent for a Flying Machine," *Aeronautical J.*, July, pp. 71–72.

Wimperis, H. E. 1926. "The Rotating Wing in Aircraft," ARC R & M 1108.

Wolf, A. L. 1974. "The Vision of d'Amécourt," *Vertiflite*, 20 (5), pp. 2–6.

Young, A. M. 1948. "The Helicopter and Stability," *American Helicopter Magazine*, March, pp. 6–25.

Young, A. M. 1979. *The Bell Notes: A Journey from Metaphysics to Physics*, Delacorte Press/Seymour Lawrence, New York, NY.

CHAPTER 2

Fundamentals of Rotor Aerodynamics

The essential theory of flight can be reduced to a comparatively simple statement, though it becomes a highly complicated affair as it is presented in figures and formulae.

Juan de la Cierva (1931)

2.1 Introduction

Advances in the understanding of helicopter aerodynamics has led to many gains in helicopter performance compared to even just two decades ago. In most cases, the understanding of the various aerodynamic problems have been approached using analytic theories, numerical modeling, and experimentation, which have worked in conjunction with developments in other disciplines to advance the better understanding of the helicopter as a whole. The rotor of a helicopter provides three functions: 1. The generation of a vertical lifting force (thrust) in opposition to the helicopter's weight; 2. The generation of a horizontal propulsive force for forward flight; and 3. A means of generating forces and moments to control the attitude and position of the helicopter in three-dimensional space. All three of these functions must be under the full control of the pilot. Unlike a fixed-wing aircraft where these functions are separated, the helicopter rotor alone must provide all three functions. To meet these demanding roles, the rotor designer requires considerable knowledge of both the aerodynamic environment in which the rotor operates, as well as how the aerodynamic loads affect the dynamic response of the flapping blades and the overall rotor behavior.

The lifting capability of any part of a rotating blade is related to its local angle of attack (AoA) and local dynamic pressure. The blade position can be defined in terms of an azimuth angle, ψ, which is defined as zero when the blade is pointing downstream, as shown in Fig. 2.1. In hovering flight, Fig. 2.1(a) shows that the velocity variation along the blade is azimuthally axisymmetric and radially linear, with zero flow velocity at the rotational axis and the velocity reaching a maximum, V_{tip}, at the blade tip. The local dynamic pressure at any blade element is proportional to the square of the distance from the rotational axis. Based on elementary considerations, for a constant blade AoA, the average rotor thrust will depend on the square of the rotor tip speed, $V_{\text{tip}} = \Omega R$, that is $T \propto V_{\text{tip}}^2$. Also, the rotor power, P, will depend on the cube of the tip speed, that is $P \propto V_{\text{tip}}^3$ (see Question 2.1).

In forward flight, a component of the free stream, V_∞, adds to or subtracts from the rotational velocity at each part of the blade, that is, V_{tip} now becomes $\Omega R + V_\infty \sin\psi$. As shown by Fig. 2.1(b), while the distribution of velocity along the blade remains linear, it is no longer axisymmetric and varies in magnitude with respect to blade azimuth angle. It will also be evident that forward flight speed, blade pitch angle and any blade flapping, as well as the distribution of induced inflow through the rotor, will all affect the blade section AoA and, therefore, the blade lift distribution, rotor thrust, and rotor power consumption. This nonuniformity of the AoA over the rotor disk is the complication with the helicopter rotor that makes its aerodynamic analysis difficult.

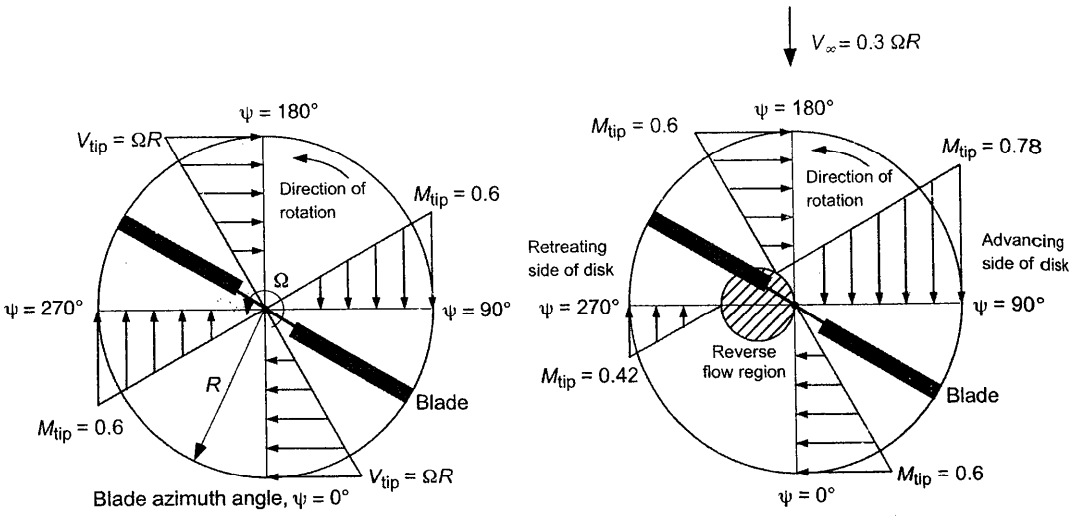

Figure 2.1 Distribution of incident velocity normal to the leading edge of the rotor blade. (a) Hovering flight. (b) Forward flight at $\mu = 0.3$.

Unlike on a fixed-wing, which has a relatively uniform lift loading over its span, the high dynamic pressure found at the tips of a helicopter blade produces a concentration of aerodynamic forces there. As a consequence, strong vortices form and trail from each blade tip. Figure 2.2 shows an example of the physical nature of the vortical wake generated by a helicopter rotor in hovering flight (see also Figs. 1.38, 10.1, and 10.2). Here, the blade tip vortices are rendered visible by natural condensation of water vapor in the

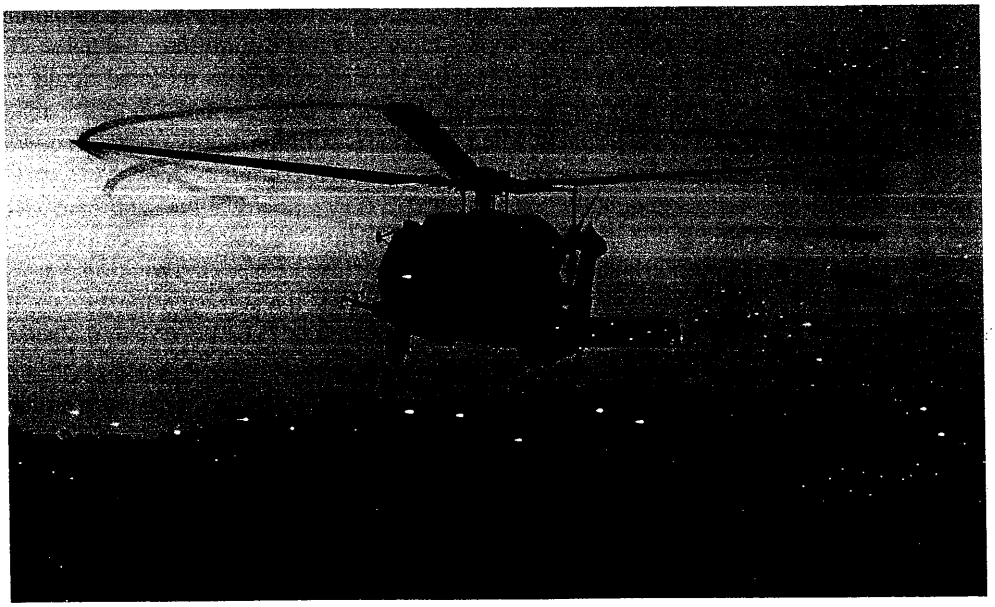

Figure 2.2 Hovering helicopter showing the vortical rotor wake through natural condensation of water vapor inside the tip vortex cores. (Courtesy of the US Navy, Patuxent River Navel Air Station.)

air. These vapor trails are only obtained under conditions when the air temperature is close to the dew point; it is produced by the small amount of cooling that takes place inside the low pressure vortex cores. It will be seen that the vortices are convected downward below the rotor and form a series of interlocking, almost helical trajectories. For the most part, the net flow velocity at the plane of the rotor and in the rotor wake itself is comprised of the velocities induced by these tip vortices. For this reason, predicting the strengths and locations of the tip vortices (see Chapter 10) plays an important role in determining blade airloads and rotor performance, as well as in designing the blades and rotor as a system.

All helicopters spend considerable time in hover, which is a flight condition where they are specifically designed to be operationally efficient. In hover, the main purposes of the rotor are to provide a vertical lifting force in opposition to the weight of the helicopter and flight control. However, in forward flight the rotor must also provide a propulsive and force to overcome the drag of the helicopter. This is obtained by tilting the plane of the rotor forward, while increasing the overall rotor thrust so that that the vertical component of thrust (lift) remains equal to the aircraft weight. In forward flight the rotor blades encounter an asymmetric velocity field, which is a maximum on the blade that advances into the relative wind and a minimum on the blade that retreats away from the relative wind [see Fig. 2.1(b)]. The local dynamic pressure and the blade airloads, therefore, become periodic primarily at the rotational speed of the rotor (i.e., once per revolution or 1/rev). Because of the articulation built into helicopter blade designs, the rotor blades will begin to flap about their hinges causing the rotor disk to tilt. This inherent tendency can be compensated for by the pilot by using appropriate cyclic pitch inputs to the blades. This changes the magnitude and phasing of the 1/rev aerodynamic lift forces over the disk, and so it can be used to maintain a desirable orientation of the rotor disk to meet propulsion and flight control requirements. The inherent coupling among blade pitch inputs, the aerodynamic forces and the blade flapping response is discussed in detail in Chapter 4.

The overall aerodynamic complexity of the helicopter in forward flight can be appreciated from Fig. 2.3. The flow field in which the rotor operates is considerably more complex

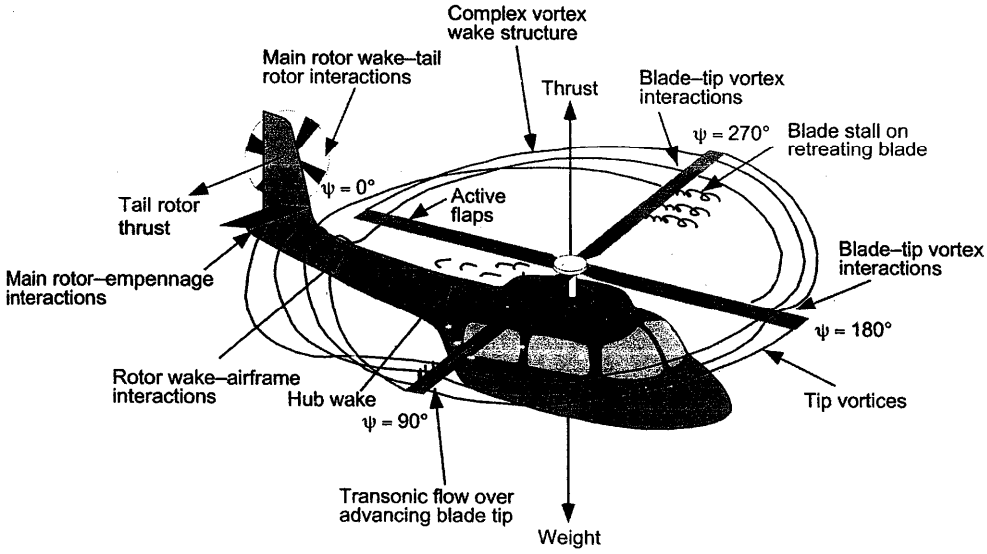

Figure 2.3 Schematic showing the flow structure and some aerodynamic problem areas on a helicopter in forward flight.

than that of a fixed-wing aircraft, mainly because of the individual wakes trailed from each blade. For a fixed-wing aircraft, the wing wake and tip vortices trail downstream of the aircraft. However, for a helicopter in forward flight, the blade tip vortices can remain close to the rotor and to following blades for several rotor revolutions. As a result of the low disk loading (thrust carried per unit area of the rotor disk) and generally low average flow velocity through the rotor disk, these vortices remain close enough to produce a strongly three-dimensional induced velocity field. As following blades encounter this induced velocity field, fluctuating airloads are produced on the blades.[1] Besides affecting the rotor performance, these time-varying airloads can be a source of high rotor vibrations and strongly focused obtrusive noise.

At higher forward flight speeds, the inherently asymmetric nature of the flow over the rotor disk gives rise to a number of aerodynamic problems that ultimately limit the rotor performance. The most obvious is that the blade tips on the advancing side of the rotor disk can start to penetrate into supercritical and transonic flow regimes, with the associated formation of compressibility zones and, ultimately, strong shock waves. In addition to the occurrence of wave drag and the possibilities of shock induced flow separation, both phenomena require much more power to drive the rotor, the periodic formation of shock waves is another source of obtrusive noise. The increased power demands placed on the rotor system, when compressibility effects manifest, will eventually limit forward flight speeds. Although compressibility effects on contemporary rotors can be relieved to some extent by the use of swept tip blades and thin "transonic" airfoils, the problems of increased power requirements and noise are only delayed to moderately higher forward flight speeds and are not eliminated.

On the retreating side of the disk, that is, where the blades are retreating away from the relative wind because of the forward flight velocity of the helicopter, the local velocity and dynamic pressure at the blade are relatively low and the blades are required to operate at higher AoA to maintain lift. If these values of AoA become too large, then the retreating blade will stall. This results in a loss of overall lifting and propulsive capability from the rotor and sets an intrinsic barrier to further increases in forward flight speed. It is interesting to note that while stall on a fixed-wing aircraft occurs at low flight speeds, a helicopter encounters the problem of stall at relatively high flight speeds. Because of the inherent time-dependent nature of the flow environment on the rotor blades in forward flight, retreating blade stall is highly unsteady in nature and is referred to as dynamic stall (see Chapter 9). The unsteady airloads produced during dynamic stall are an additional source of vibration on the helicopter, which can significantly limit its forward flight and maneuvering capability. The various aerodynamic interactions that can exist between the rotor wake and the airframe, including the tail rotor and empennage, are also worthy of note (see Fig. 2.3). Although fundamentally complicated, these interactions can lead to various significant aerodynamic interference effects that cannot be ignored in the design of the helicopter. These issues are discussed in Chapter 11.

2.2 Momentum Theory Analysis in Hovering Flight

The helicopter, or any other rotating-wing vehicle, must operate in a variety of flight regimes. These include hover, climb, descent, or forward flight. In addition, the helicopter may undergo maneuvers, which may comprise a combination of these basic flight regimes. In hover or axial flight, the flow is axisymmetric and the flow through the rotor

[1] This phenomenon is called blade vortex interaction or BVI – see Chapters 8, 10, and 14.

is either upward or downward. This is the easiest flow regime to analyze and, at least in principle, it should be the easiest to predict by means of mathematical models. It has been found, however, that even with modern mathematical models of the rotor flow, accurate prediction of hovering performance is by no means straightforward. Although it must be remembered that the actual physical flow about the rotor will comprise a complicated vortical wake structure, as previously shown in Fig. 2.2, the basic performance of the rotor can be analyzed by a simpler approach that has become known as the Rankine–Froude *momentum theory*. The momentum theory approach allows the derivation of a first-order prediction of the rotor thrust and power, and the principles also form a foundation for more elaborate treatments of the rotor aerodynamics problem.

2.2.1 *Flow Near a Hovering Rotor*

Hover is a very unique flight condition. Here, the rotor has zero forward speed and zero vertical speed (no climb or descent). The rotor flow field is, therefore, azimuthially axisymmetric. A set of velocity measurements near a subscale hovering rotor and in its wake is shown in Fig. 2.4. Notice that the fluid velocity is increased smoothly as it is entrained into and through the rotor disk plane. There is no jump in velocity across the disk, although because a thrust is produced on the rotor, there must be a jump in pressure over the rotor disk. The existence of a wake boundary or slipstream is apparent, with the flow velocity outside this boundary being relatively quiescent. The blade tip vortices trail behind and below each blade and are convected along this wake boundary. Inside the wake boundary, the flow velocities are substantial and may be distributed nonuniformly across the slipstream. Note also the contraction in the diameter of the wake below the rotor corresponding to an increase in the slipstream velocity.

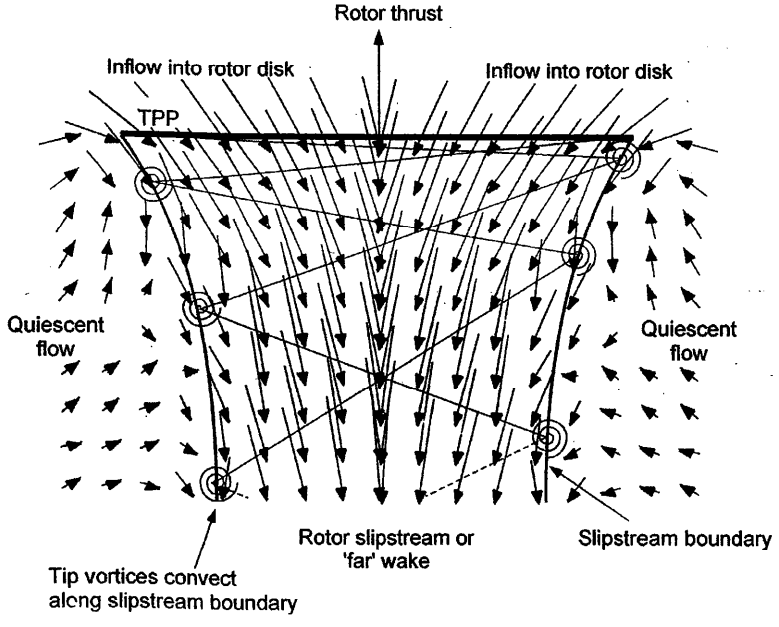

Figure 2.4 Measurements of the velocity field in a diametric plane near and below a two-bladed rotor operating in hover. Data source: Leishman et al. (1995)

With the physical picture of the hovering rotor flow now apparent, it is possible to approach a mathematical solution to this problem. Consider the application of the three basic conservation laws (conservation of mass, momentum, and energy) to the rotor and its flow field. The conservation laws will be applied in a quasi–one-dimensional integral formulation to a control volume surrounding the rotor and its wake. This approach permits us to perform a first level analysis of the rotor performance (e.g., its thrust and power), but without actually having to consider the details of the flow environment, that is without having to consider what is happening locally at each blade section. This approach, which is called *momentum theory*, was first developed by Rankine (1865) for use in the analysis of marine propellers. The theory was developed further by W. Froude (1878) and R. E. Froude (1889), Lanchester (1915), and Betz (1920a,b; 1922). Momentum theory was formally generalized by Glauert (1935) – see entry in Durand (1935). The main difference between the Froude and Rankine theories is in the treatment of the rotor disk as a series of elementary rings, versus the treatment of the disk as a whole. In either case, one fundamental assumption in the basic momentum theory is that the rotor can be idealized as an infinitesimally thin *actuator disk* over which a pressure difference exists. The concept is equivalent to considering an infinite number of blades of zero thickness, a concept first suggested by W. Froude. The actuator disk supports the thrust force that is generated by the rotation of the rotor blades about the shaft and their action on the air. Power is required to generate this thrust, which is supplied in the form of a torque to the rotor shaft. Work done on the rotor leads to a gain in kinetic energy of the rotor slipstream and this is an unavoidable energy loss that is called *induced* power.

2.2.2 *Conservation Laws of Aerodynamics*

In the general approach to the problem, it will be assumed that the flow through the rotor is one-dimensional, quasi-steady, incompressible and inviscid. Consider first an *ideal fluid*, that is, one that generates no viscous shear between fluid elements. Therefore, induced losses are the sole source of losses in the fluid, with other losses resulting from the action of viscosity being assumed negligible, at least for now. Furthermore, assume that the flow is quasi-steady, in that the flow properties at a point do not change with time. Finally, assume that the flow is one-dimensional, and so the properties across any plane parallel to the rotor plane are constant; that is, the fluid properties change only with axial (vertical) position relative to the rotor.

Consider the hover problem. Let the control volume surrounding the rotor and its wake have surface area S, as shown in Fig. 2.5. Let $d\vec{S}$ be the unit normal area vector (i.e., the outward facing normal), which by convention always points out of the control volume across the surface S. A general equation governing the conservation of fluid mass applied to this finite control volume can be written as

$$\iint_S \rho \vec{V} \cdot d\vec{S} = 0, \tag{2.1}$$

where $\vec{V}$ is the local velocity and ρ is the density of the fluid. This equation states that the mass flow into the control volume must equal the mass flow out of the control volume. Notice that this is a scalar equation. Similarly, an equation governing the conservation of fluid momentum can be written as

$$\vec{F} = \iint_S p d\vec{S} + \iint_S (\rho \vec{V} \cdot d\vec{S}) \vec{V}. \tag{2.2}$$

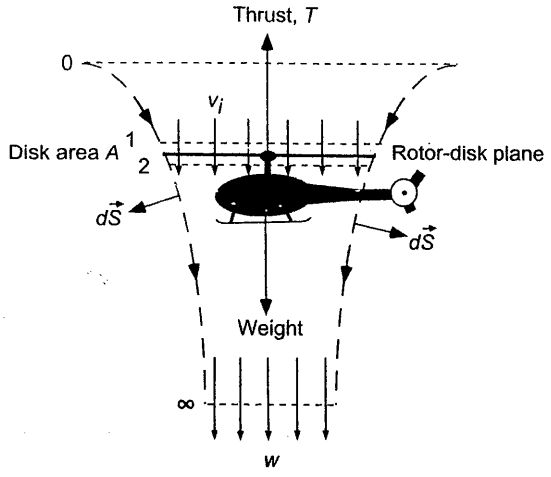

Figure 2.5 Flow model for momentum theory analysis of a rotor in hovering flight.

For an unconstrained flow, the net pressure force on the fluid inside the control volume is zero. This point has been considered by Glauert (1935), although it is not so obvious. Therefore, the net force on the fluid, $\vec{F}$, is simply equal to the rate of change with time of the fluid momentum across the control surface, S. Although Eq. 2.2 is a vector equation, it can be simplified considerably by the assumptions of quasi–one-dimensional flow. This is essentially a byproduct of assuming a uniform pressure jump over the rotor disk and leads to uniform distributions of velocity across any horizontal cross section within the control volume. Because the force on the fluid is supplied by the rotor, by Newton's third law the fluid must exert an equal and opposite force on the rotor. This force is the rotor thrust, T. Finally, an equation governing the conservation of energy in the flow can be written as

$$W = \iint_S \frac{1}{2}(\rho \vec{V} \cdot d\vec{S})|\vec{V}|^2. \tag{2.3}$$

This equation states simply that the work done on the fluid by the rotor manifests as a gain in kinetic energy of the fluid in the rotor slipstream per unit time. It is also a scalar equation.

2.2.3 *Application to a Hovering Rotor*

These general equations of fluid mass, momentum, and energy conservation may now be applied to the specific problem of a hovering helicopter rotor. The procedures are basically those attributed to Rankine and Froude, as generalized by Glauert (1935) and adopted by others, including Johnson (1980). In Fig. 2.5 let cross section 0 denote the plane far upstream of the rotor, where in the hovering case the fluid is quiescent (i.e., $V_0 = 0$). The rotor disk area is denoted by A. Cross sections 1 and 2 are the planes just above and below the rotor disk, respectively, and the "far" wake[2] is denoted by cross section ∞. At the plane of the rotor, assume that the velocity (the induced velocity or velocity imparted to the mass of air contained in the control volume at the rotor disk) is v_i. In the far wake

[2] Meaning the slipstream is well downstream of the rotor at infinity or in the *vena contracta*, although in practice this may only be less than one rotor radius.

(the *vena contracta*), the velocity will be increased over that at the plane of the rotor and this velocity is denoted by w.

From the assumption that the flow is quasi-steady and by the principle of conservation of mass, the mass flow rate, $\dot{m}$, must be constant within the boundaries of the rotor wake (control volume). Therefore, the mass flow rate is

$$\dot{m} = \iint_{\infty} \rho \vec{V} \cdot d\vec{S} = \iint_{2} \rho \vec{V} \cdot d\vec{S}, \tag{2.4}$$

and the 1-D incompressible flow assumption reduces this equation to

$$\dot{m} = \rho A_{\infty} w = \rho A_2 v_i = \rho A v_i. \tag{2.5}$$

The principle of conservation of fluid momentum gives the relationship between the rotor thrust, T, and the net time rate-of-change of fluid momentum out of the control volume (Newton's second law). The rotor thrust is equal and opposite to the force on the fluid, which is given by

$$-\vec{F} = T = \iint_{\infty} \rho(\vec{V} \cdot d\vec{S})\vec{V} - \iint_{0} \rho(\vec{V} \cdot d\vec{S})\vec{V}. \tag{2.6}$$

Because in hovering flight the velocity well upstream of the rotor is quiescent, the second term on the right-hand side of the above equation is zero. Therefore, for the hover problem, the rotor thrust can be written as the scalar equation

$$T = \iint_{\infty} \rho(\vec{V} \cdot d\vec{S})\vec{V} = \dot{m} w. \tag{2.7}$$

From the principle of conservation of energy, the work done on the rotor is equal to the gain in energy of the fluid per unit time. The work done per unit time, or the power consumed by the rotor, is Tv_i and this results in the equation

$$Tv_i = \iint_{\infty} \frac{1}{2}\rho(\vec{V} \cdot d\vec{S})\vec{V}^2 - \iint_{0} \frac{1}{2}\rho(\vec{V} \cdot d\vec{S})\vec{V}^2. \tag{2.8}$$

In hover, the second term on the right-hand side of the above equation is zero so that

$$Tv_i = \iint_{\infty} \frac{1}{2}\rho(\vec{V} \cdot d\vec{S})\vec{V}^2 = \frac{1}{2}\dot{m} w^2. \tag{2.9}$$

From Eqs. 2.7 and 2.9 it is clear that

$$v_i = \frac{1}{2} w \tag{2.10}$$

or that $w = 2v_i$. This, therefore, gives a simple relationship between the induced velocity in the plane of the rotor, v_i, and the velocity w in the vena contracta.

Rotor Slipstream

Because the flow velocity increases in the wake below the rotor, continuity considerations require that the area of the slipstream must decrease. This is apparent from the empirical observations in Figs. 2.2 and 2.4. It follows from the conservation of fluid mass between the rotor and the vena contracta that

$$\rho A v_i = \rho A_{\infty} w = \rho A_{\infty}(2v_i) = 2\rho A_{\infty} v_i, \tag{2.11}$$

so that in hover the ratio of the cross-sectional area of the fully developed far wake to the area of the rotor disk is

$$\frac{A_\infty}{A} = \frac{1}{2}. \tag{2.12}$$

In other words, based on ideal fluid flow assumptions, the vena contracta is an area that is exactly half of the rotor disk area. Alternatively, by considering the radius of the far rotor wake, r_∞, relative to that of the rotor, R, it is easy to show from mass conservation considerations that

$$r_\infty = \frac{R}{\sqrt{2}}. \tag{2.13}$$

Therefore, the ratio of the radius of the wake to the radius of the rotor is $1/\sqrt{2} = 0.707$. This is called the *wake contraction ratio*. In practice, it has been found experimentally that the wake contraction ratio is not as much as the theoretical value given by the momentum theory; typically it is only about 0.78 compared to 0.707. This is mainly a consequence of the viscosity of the fluid, the reality that a nonuniform inflow will be produced over the disk and a small swirl component of velocity in the rotor wake induced by the spinning rotor blades. Behaviors directly attributable to the viscosity of the fluid are termed *nonideal* effects, and these will be considered in detail later.

Induced Velocity and Rotor Power

It has been shown previously using Eq. 2.7 that momentum theory can be used to relate the rotor thrust to the induced velocity at the rotor disk by using the equation

$$T = \dot{m}w = \dot{m}(2v_i) = 2(\rho A v_i)v_i = 2\rho A v_i^2. \tag{2.14}$$

Rearranging this equation and solving for the induced velocity at the plane of the rotor disk gives

$$v_h \equiv v_i = \sqrt{\frac{T}{2\rho A}} = \sqrt{\left(\frac{T}{A}\right)\frac{1}{2\rho}}. \tag{2.15}$$

The ratio T/A is known as the *disk loading*, which is an extremely important parameter in helicopter analysis. Notice that $v_h \equiv v_i$ is used to represent the induced velocity in hover. This value will be used later as a reference when the axial climb and descending flight conditions are considered.

The power required to hover (or the time rate-of-work done by the rotor on the fluid per unit thrust) is given by

$$P = Tv_i \equiv Tv_h = T\sqrt{\frac{T}{2\rho A}} = \frac{T^{3/2}}{\sqrt{2\rho A}}. \tag{2.16}$$

This power, called *ideal power*, is entirely induced in nature because the contribution of viscous effects have not been considered in the present level of analysis. Alternatively, we can write

$$P = Tv_i = 2\dot{m}v_i^2 = 2(\rho A v_i)v_i^2 = 2\rho A v_i^3. \tag{2.17}$$

From this equation it is noted that the power required to hover will increase with the cube of the induced velocity (or inflow) at the disk. Obviously, to make a rotor hover at a given thrust with minimum induced power, the induced velocity at the disk must be small. Therefore, the mass flow through the disk must be large and this consequently requires a large rotor disk area. This is a fundamental design feature of all helicopters.

Pressure Variation

The pressure variation through the rotor flow field in the hover state can be found from the application of Bernoulli's equation along a streamline above and below the rotor disk. Remember that there is a pressure jump across the disk as a result of energy addition by the rotor, so that Bernoulli's equation cannot be applied between points in the flow across the disk. But the pressure jump is uniform over the rotor disk so the equation can be applied to all streamlines contained within the control volume. For incompressible flow, the Bernoulli equation is an alternative to the energy equation (one of the two is redundant). Applying Bernoulli's equation up to the disk between stations 0 and 1 produces

$$p_0 = p_\infty = p_1 + \frac{1}{2}\rho v_i^2. \tag{2.18}$$

Below the disk, between stations 2 and ∞, the application of Bernoulli's equation gives

$$p_2 + \frac{1}{2}\rho v_i^2 = p_\infty + \frac{1}{2}\rho w^2. \tag{2.19}$$

Because the jump in pressure Δp is assumed to be uniform across the disk, this pressure jump must be equal to the disk loading, T/A, that is,

$$\Delta p = p_2 - p_1 = \frac{T}{A}. \tag{2.20}$$

Therefore, we can write

$$\frac{T}{A} = p_2 - p_1 = \left(p_\infty + \frac{1}{2}\rho w^2 - \frac{1}{2}\rho v_i^2\right) - \left(p_\infty - \frac{1}{2}\rho v_i^2\right) = \frac{1}{2}\rho w^2, \tag{2.21}$$

from which it is seen that the rotor disk loading is equal to the dynamic pressure in the vena contracta. One can also determine the pressure just above the disk and just below the disk in terms of the disk loading. Just above the disk the use of Bernoulli's equation gives

$$p_1 = p_\infty - \frac{1}{2}\rho v_i^2 = p_\infty - \frac{1}{2}\rho\left(\frac{w}{2}\right)^2 = p_\infty - \frac{1}{4}\left(\frac{T}{A}\right), \tag{2.22}$$

and just below the disk we get

$$p_2 = p_0 + \frac{1}{2}\rho w^2 - \frac{1}{2}\rho\left(\frac{w}{2}\right)^2 = p_0 + \frac{3}{4}\left(\frac{T}{A}\right). \tag{2.23}$$

Therefore, the static pressure is reduced by $\frac{1}{4}(T/A)$ above the rotor disk and increased by $\frac{3}{4}(T/A)$ below the disk.

2.3 Disk Loading and Power Loading

A parameter used frequently in helicopter analysis that appears in the preceding equations is the disk loading, T/A, which is denoted by DL. Because for a single rotor helicopter in hover, the rotor thrust, T, is equal to the weight of the helicopter, W, the disk loading is sometimes written as W/A or $W/\pi R^2$. Disk loading is measured in pounds per square foot (lb ft^{-2}) in British (Imperial) units or newtons per square meter (N m^{-2}) in the SI system. One may also use kilograms per square meter (kg m^{-2}) in the SI system. The direct use of the kilogram (kg) as a unit of force is frequently found in engineering practice, particularly in the aerospace field. For the purposes of computing the disk loading for multi-rotor helicopters such as tandems and coaxials, or for tilt-rotors, the convention is to assume that each rotor carries an equal proportion of the aircraft's weight. Values of rotor disk loading for a selection of rotating-wing aircraft are given in the appendix.

The power loading is defined as T/P, which is denoted by PL. Power loading is measured in pounds per horsepower (lb hp^{-1}) in Imperial units, or newtons per kilowatt (N kW^{-1}) or kilograms per kilowatt (kg kW^{-1}) in the SI system. Remember that the induced (ideal) power required to hover is given by $P = Tv_h$. This means that the *ideal power loading* will be inversely proportional to the induced velocity at the disk. To see this, recall that the inflow velocity at the disk v_i can be written in terms of the disk loading as

$$v_h \equiv v_i = \sqrt{\frac{T}{2\rho A}} = \sqrt{\frac{DL}{2\rho}} = \frac{P}{T} = (PL)^{-1}. \tag{2.24}$$

According to Fig. 2.6, the ratio T/P decreases quickly with increasing disk loading (note the logarithmic scale on the abscissa). Therefore, vertical lift aircraft that have a low effective disk loading will require relatively low power per unit of thrust produced (i.e., they will have high ideal power loading) and will tend to be more efficient; that is, the rotor will require less power (and consume less fuel) to generate any given amount of thrust. Calculation of the actual power loading and rotor efficiency, however, requires the consideration of viscous losses.

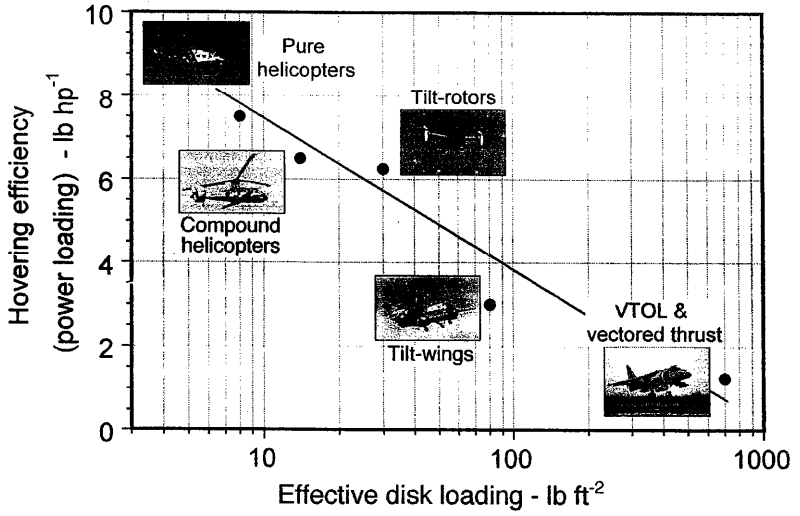

Figure 2.6 Hovering efficiency versus disk loading for a range of vertical lift aircraft.

Helicopters operate with low disk loadings in the region of 5 to 10 lb ft^{-2} or 24 to 48 kg m^{-2}, thus they can provide a large amount of lift for a relatively low power with a power loading up to 5 kg kW^{-1} (50 N kW^{-1} or 10 lb hp^{-1}). Figure 2.6 shows that the helicopter is a very efficient aircraft in hover compared to other vertical takeoff and landing (VTOL) aircraft. Tilt-rotors can be considered a hybrid helicopter/fixed-wing aircraft and have higher rotor disk loadings. Therefore, they are less efficient in hover than a conventional helicopter of the same gross weight but still are much more efficient than other VTOL aircraft without rotating wings.

2.4 Induced Inflow Ratio

The induced inflow velocity, v_i, at the rotor disk can be written as

$$v_h \equiv v_i = \lambda_h \Omega R, \tag{2.25}$$

where the nondimensional quantity λ_h is called the *induced inflow ratio* in hover. The angular or rotational speed of the rotor is denoted by Ω and R is the rotor radius; so the product is simply the tip speed, V_{tip}, which is also sometimes given the symbol $V_{\Omega R}$. The inflow ratio is normally the preferable quantity to use when comparing results from different rotors because it is a nondimensional quantity. For rotating-wing aircraft, it is the convention to nondimensionalize all velocities by the blade tip speed in hovering flight (i.e., by $V_{\text{tip}} = \Omega R = V_{\Omega R}$).

2.5 Thrust and Power Coefficients

Like all branches of engineering, nondimensional coefficients are normally employed in helicopter rotor analysis. Consider the induced velocity, v_i, through the rotor. This can be written in functional form in terms of rotor thrust T, a reference area A such as disk area, a reference velocity V such as blade tip speed V_{tip}, and the density of the flow ρ using

$$v_i = f_1(T, A, V_{\text{tip}}, \rho) \quad \text{or} \quad f_2(T, A, V_{\text{tip}}, \rho, v_i) = 0. \tag{2.26}$$

According to the Buckingham Π method of dimensional analysis [see Anderson (2001)] this means there are five variables ($N = 5$), three fundamental dimensions ($K = 3$, namely: mass,
length, and time) and $N - K = 2$ or two Π products. The functional dependence can, therefore, be written in the form

$$f_3(\Pi_1, \Pi_2) = 0, \tag{2.27}$$

where Π_1 and Π_2 are nondimensional groupings. Choosing the variables ρ, A, and V_{tip} as repeating variables (which are all linearly independent) the two nondimensional Π products can each be written in terms of these repeating variables plus one other variable. Making each grouping dimensionally homogeneous, the first Π product can be written as

$$\Pi_1 = \rho^{-1} A^{-1} V_{\text{tip}}^{-2} T = \frac{T}{\rho A V_{\text{tip}}^2} = C_T, \tag{2.28}$$

which is a thrust coefficient. The second Π product becomes

$$\Pi_2 = \rho^0 A^0 V_{\text{tip}}^{-1} v_i = \frac{v_i}{V_{\text{tip}}} = \lambda_i, \tag{2.29}$$

which is an inflow coefficient. This means that

$$f_3(\Pi_1, \Pi_2) = f_3\left(\frac{T}{\rho A V_{\text{tip}}^2}, \frac{v_i}{V_{\text{tip}}}\right) = f_3(C_T, \lambda_i) = 0 \text{ or } \lambda_i = f(C_T). \tag{2.30}$$

Therefore, in helicopter analysis the rotor thrust coefficient is formally defined as

$$C_T = \frac{T}{\rho A V_{\text{tip}}^2} = \frac{T}{\rho A \Omega^2 R^2}. \tag{2.31}$$

where the reference area is the rotor disk area A and the reference speed is the blade tip speed, ΩR. This definition follows the one used by Glauert (1935). All velocity components are nondimensonalized by tip speed so the inflow ratio λ_i is related to the thrust coefficient in hover by

$$\lambda_h \equiv \lambda_i = \frac{v_i}{\Omega R} = \frac{1}{\Omega R}\sqrt{\frac{T}{2\rho A}} = \sqrt{\frac{T}{2\rho A(\Omega R)^2}} = \sqrt{\frac{C_T}{2}}. \tag{2.32}$$

This is based on the 1-D flow assumption made in the preceding analysis, which means that this value of inflow is assumed to be distributed uniformly over the disk. The rotor power coefficient is defined as

$$C_P = \frac{P}{\rho A V_{\Omega R}^3} = \frac{P}{\rho A \Omega^3 R^3}, \tag{2.33}$$

so that based on momentum theory the power coefficient for the hovering rotor is

$$C_P = \frac{T v_i}{\rho A(\Omega R)^3} = \left(\frac{T}{\rho A(\Omega R)^2}\right)\left(\frac{v_i}{\Omega R}\right) = C_T \lambda_i = \frac{C_T^{3/2}}{\sqrt{2}}. \tag{2.34}$$

Again, this is calculated on the basis of uniform inflow and no viscous losses, so is called the *ideal power* coefficient. The corresponding rotor shaft torque coefficient is defined as

$$C_Q = \frac{Q}{\rho A V_{\Omega R}^2 R} = \frac{Q}{\rho A \Omega^2 R^3}. \tag{2.35}$$

Notice that because power is related to torque by $P = \Omega Q$, then numerically $C_P \equiv C_Q$.

It is important to note that the US customary definition of the thrust, torque, and power coefficients is different to that used in some parts of the world (mainly in Britain, most of Europe, and Russia), where a factor of one half is used in the denominator giving

$$C_T = \frac{T}{\frac{1}{2}\rho A(\Omega R)^2}, \quad C_Q = \frac{Q}{\frac{1}{2}\rho A(\Omega R)^2 R}, \quad \text{and} \quad C_P = \frac{P}{\frac{1}{2}\rho A(\Omega R)^3}. \tag{2.36}$$

This means that the values of thrust, torque, and power coefficients are all a factor of 2 greater than the values obtained with the US customary definition. The US definitions in Eqs. 2.31, 2.33, and 2.35 are used throughout this book.

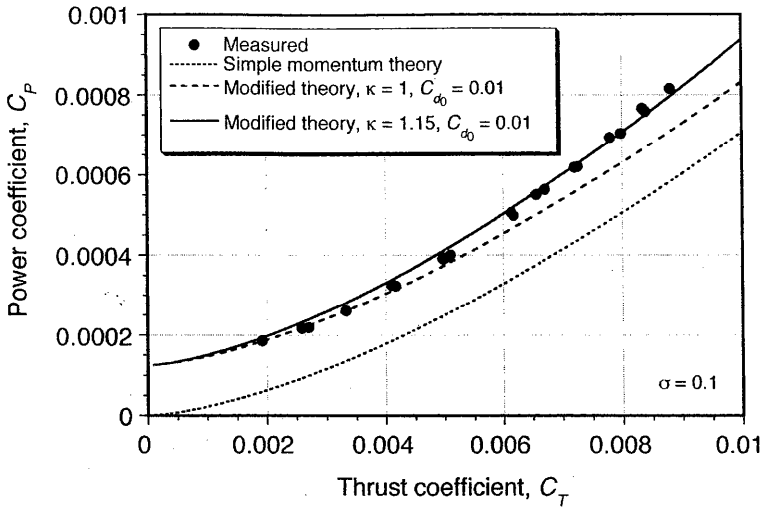

Figure 2.7 Comparison of predictions made with momentum theory to measured power for a hovering rotor. Data source: Bagai & Leishman (1992).

2.6 Comparison of Theory with Measured Rotor Performance

In terms of coefficients it is apparent that the ideal power according to the simple momentum theory can be written as

$$C_P = \frac{C_T^{3/2}}{\sqrt{2}}. \tag{2.37}$$

Figure 2.7 shows a comparison of the simple momentum theory with thrust and power measurements made for a hovering rotor using Eq. 2.37. Notice that the momentum theory underpredicts the actual power required, but the predicted trend that $C_P \propto C_T^{3/2}$ is essentially correct. These differences between the momentum theory and experiment occur because viscous effects (i.e., nonideal effects) have been totally neglected so far.

2.7 Nonideal Effects on Rotor Performance

In hovering flight the induced power predicted by the simple momentum theory can be approximately described by an empirical modification to the momentum result in Eq. 2.34, namely

$$C_{P_i} = \frac{\kappa C_T^{3/2}}{\sqrt{2}}, \tag{2.38}$$

where κ is called an *induced power correction factor* or just an *induced power factor*. This coefficient is derived from rotor measurements (see Section 2.9) or flight tests and it encompasses a number of nonideal, but physical effects, such as nonuniform inflow, tip losses, wake swirl, less than ideal wake contraction, finite number of blades, and so on. For preliminary design, most helicopter manufacturers use their own measurements and experience to estimate values of κ, a typical average value being about 1.15. Values of κ can also be computed directly using more advanced blade element methods (see Chapters 3 and 10), where the effects of the actual flight condition can be more accurately represented. This is

particularly important for high-speed forward flight, where the increasing nonuniformity of the inflow from reverse flow on the retreating blade must be accounted for.

Wake swirl effects serve to reduce the net change of the fluid momentum in the vertical direction and they will decrease the rotor thrust for a given shaft torque (power supplied) or will increase the rotor power required to produce a given thrust. Johnson (1980) shows that as a result of wake swirl the induced power is increased by a factor $[1 + C_T \ln(C_T/2) + C_T/2]^{-1}$; this is less than 1% at the values of C_T typically found on helicopters and can be neglected as a contributor to rotor power requirements. However, see also the discussion of wake swirl in Section 3.3.6.

Proper estimates for the profile power consumed by the rotor requires a knowledge of the drag coefficients of the airfoils that make up the rotor blades; that is, a strip or blade element analysis is required. The airfoil drag coefficient will be a function of both Reynolds number, Re, and Mach number, M, which obviously vary along the span of the blade. A result for the profile power, P_0, can be obtained from an element-by-element analysis of sectional drag forces (i.e., the blade element method – see Chapter 3) and by radially integrating the sectional drag force along the length of the blade using

$$P_0 = \Omega N_b \int_0^R D y dy, \tag{2.39}$$

where N_b is the number of blades and D is the drag force per unit span at a section on the blade at a distance y from the rotational axis. The drag force can be expressed conventionally as

$$D = \frac{1}{2}\rho U^2 c C_d = \frac{1}{2}\rho(\Omega y)^2 c C_d, \tag{2.40}$$

where c is the blade chord. If the section profile drag coefficient, C_d, is assumed to be constant ($= C_{d_0}$) and independent of Re and M (which is not an unrealistic first assumption), and the blade is not tapered in planform (i.e., a rectangular blade), then the profile power integrates out to be

$$P_0 = \frac{1}{8}\rho N_b \Omega^3 c C_{d_0} R^4. \tag{2.41}$$

Converting to a standard power coefficient by dividing through by $\rho A(\Omega R)^3$ gives

$$C_{P_0} = \frac{1}{8}\left(\frac{N_b c R}{A}\right) C_{d_0} = \frac{1}{8}\left(\frac{N_b c R}{\pi R^2}\right) C_{d_0} = \frac{1}{8}\left(\frac{N_b c}{\pi R}\right) C_{d_0} = \frac{1}{8}\sigma C_{d_0}. \tag{2.42}$$

The grouping $N_b c R/A$ (or $N_b c/\pi R$) is known as the *rotor solidity*, which is the ratio of blade area to rotor disk area and is represented by the symbol σ. Typical values of σ for a helicopter rotor range between 0.05 and 0.12, and much use of this solidity parameter is made throughout this book.

Armed with these estimates of the induced and profile power losses, it is possible to recalculate the rotor power requirements by using the modified momentum theory result that

$$C_P = C_{P_i} + C_{P_0} = \frac{\kappa C_T^{3/2}}{\sqrt{2}} + \frac{\sigma C_{d_0}}{8}. \tag{2.43}$$

These alternative results are also shown in Fig. 2.7, as denoted by the "modified theory," which has been calculated by assuming $C_{d_0} = 0.01$. In the first case, it has been assumed that $\kappa = 1.0$ (ideal induced losses), and in the second case, $\kappa = 1.15$ (nonideal losses).

The value of σ for this particular rotor is 0.1. Notice the need to account for nonideal induced losses to give agreement with the measured data. The overall level of correlation thus obtained gives considerable confidence in the modified momentum theory approach for basic rotor performance studies, at least in hover.

2.8 Figure of Merit

There are several difficulties in defining an efficiency factor for a helicopter rotor because many parameters are involved, such as disk area, solidity, blade aspect ratio, airfoil section characteristics, and tip speed. The power loading parameter discussed previously is one measure of rotor efficiency because a helicopter of a given weight should be designed to hover with the minimum power requirements; that is, the ratio T/P should be made as large as possible. However, the power loading is a dimensional quantity and so a standard nondimensional measure of hovering thrust efficiency called the *figure of merit* has been adopted. This quantity is calculated using the simple momentum theory as a reference. The ideas of a figure of merit were first introduced by Renard (1903) and Glauert (1935), but it was introduced in its present form during the 1940s by Richard H. Prewitt of Kellett Aircraft. The figure of merit is equivalent to a static thrust efficiency and defined as the ratio of the ideal power required to hover to the *actual* power required, that is,

$$FM = \frac{\text{Ideal power required to hover}}{\text{Actual power required to hover}} < 1. \tag{2.44}$$

The *ideal* power is given by the simple momentum result in Eq. 2.34. For the ideal case, the figure of merit must always be unity because the momentum theory assumes no viscous losses; hence the ideal power is entirely induced in origin. In reality, viscous effects manifest as both induced and profile contributions, and these are always present in actual power measurements. Therefore, for a real rotor the figure of merit must always be less than unity.

The figure of merit or *FM* can be used as a gauge as to how efficient a given hovering rotor is in terms of generating thrust for a given power. However, to qualify this, it should only be used as a comparative measure between two rotors when the rotors are also compared at the same disk loading, a point made again later. The figure of merit can also be written as

$$FM = \frac{P_{\text{ideal}}}{P_{\text{meas}}} = \frac{C_{T_{\text{meas}}}^{3/2}/\sqrt{2}}{C_{P_{\text{meas}}}} = \frac{C_{T_{\text{meas}}}^{3/2}}{\sqrt{2}\, C_{P_{\text{meas}}}}, \tag{2.45}$$

where the measured value of power coefficient, $C_{P_{\text{meas}}}$, will include both induced effects and all of the other "nonideal" physical effects that have their origin from viscosity.

A representative plot of measured figure of merit versus rotor thrust is shown in Fig. 2.8. It will be apparent that the *FM* reaches a maximum and then remains constant or drops off slightly. This is because of the higher profile drag coefficients ($> C_{d_0}$) obtained at higher rotor thrust and higher blade section AoA. For some rotors, especially those with less efficient airfoils, the curve can exhibit a peak in *FM*, followed by either a progressive or abrupt decrease thereafter. Therefore, the *FM* behavior in the high thrust range will, to some extent, be a function of airfoil shape and airfoil stall type (i.e., gradual or abrupt – see Section 7.9). In practice, *FM* values between 0.7 and 0.8 represent a good hovering performance for a helicopter rotor. State-of-the-art rotors may have figures of merit approaching 0.82 (see Fig. 6.2), although this probably represents the upper limit for a helicopter rotor with conventional technology.

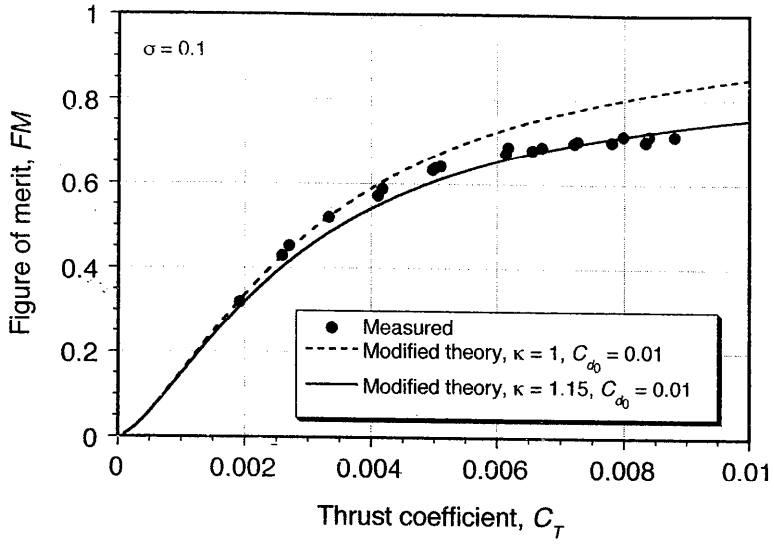

Figure 2.8 Figure of merit predictions made with modified momentum theory to measured results for a hovering rotor. Data source: Bagai & Leishman (1992).

Using the modified form of the momentum theory with the nonideal approximation for the power, the figure of merit can be written as

$$FM = \frac{\text{Ideal power}}{\text{Induced power} + \text{profile power}} = \frac{P_{\text{ideal}}}{\kappa P_{\text{ideal}} + P_0} = \frac{\dfrac{C_T^{3/2}}{\sqrt{2}}}{\dfrac{\kappa C_T^{3/2}}{\sqrt{2}} + \dfrac{\sigma C_{d_0}}{8}}, \tag{2.46}$$

with the results being shown in Fig. 2.8. Notice that at low operating thrusts the figure of merit is small. This is because in Eq. 2.46 the profile drag term in the denominator is large compared to the numerator. As the value of C_T increases, however, the importance of the profile power term decreases relative to the induced term and *FM* increases. This continues until the induced power dominates the profile term and the figure of merit will begin to approach a value of $1/\kappa$, which is shown more clearly in Fig. 2.9. In practice, however, the profile drag contribution decreases this value somewhat. Therefore, the *FM* curve reaches a firm plateau region, which represents the maximum attainable *FM* of the rotor. In practice, at higher values of rotor thrust the profile drag (and power) increases quickly as the blade begin to stall, which will again cause a reduction in *FM*.

It has been mentioned that to be meaningful the figure of merit must only be used as a gauge of rotor efficiency when two or more rotors are compared at the same disk loading. This is because increasing the disk loading, DL $(= T/A)$ will increase the induced power relative to the profile power, producing a higher figure of merit and a potentially misleading comparison between two different rotors. This can be seen if the figure of merit is written dimensionally as

$$FM = \frac{P_{\text{ideal}}}{\kappa P_{\text{ideal}} + P_0} = \frac{1}{\kappa + \dfrac{P_0}{P_{\text{ideal}}}} = \frac{1}{\kappa + \dfrac{\sqrt{2\rho}}{T}\dfrac{P_0}{\sqrt{DL}}}. \tag{2.47}$$

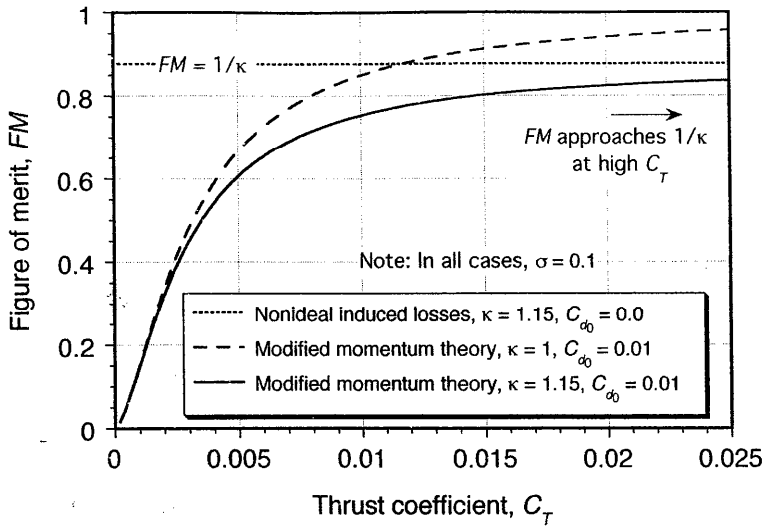

Figure 2.9 Effect of different assumptions on rotor figure of merit.

Therefore, it would be considered inappropriate to compare the values of the figure of merit of two rotors with substantially different disk loadings because the rotor with the higher disk loading will generally always give the higher figure of merit, all other factors being equal (i.e., it would not be meaningful to compare the values of *FM* of a helicopter rotor with its relatively low disk loading to a tilt-rotor with its much higher disk loading). Therefore, caution should always be exercised in the use of *FM* as a means of comparing the efficiency of different rotor systems.

Worked Example 1

In Chapter 1, the primitive helicopter built by Paul Cornu has been described. Each rotor of his machine was approximately 19.7 ft in diameter and the machine had a net gross weight (with pilot) of about 575 lb. Cornu claimed from experiments that 13 hp was required for the rotors to lift this weight. Use momentum theory to verify the power requirements for flight free of the ground.

Assuming each rotor lifted half of the total aircraft weight, then the momentum theory gives a result for net minimum possible power (or ideal power) required to drive both rotors using

$$P_{\text{ideal}} = 2\left(\frac{(W/2)^{3/2}}{\sqrt{2\rho A}}\right), \tag{2.48}$$

where the total take-off weight $W = 575$ lb and where each rotor had a swept disk area, $A = 304$ ft^2. Assuming sea level air density, this gives the ideal shaft power (in horsepower) required to drive both rotors of Cornu's machine as

$$P_{\text{ideal}} = \frac{2}{550}\left(\frac{(575/2)^{3/2}}{\sqrt{2 \times 0.002378 \times 304}}\right) = 14.7 \text{ hp}. \tag{2.49}$$

Therefore, an installed power of at least 14.7 hp would be required for free flight, but only if the rotors were aerodynamically 100% efficient and there were no transmission

losses. Realistically, with the primitive types of rotors used by Cornu, we could expect the aerodynamic efficiency of the rotors to be no more than 50% (a figure of merit of 0.5) and so leading to a power required of about 30 hp. Remember that Cornu also used an inefficient belt and pulley system to drive the rotors from an engine that produced only 24 hp. Therefore, taking into account the aerodynamic efficiency of the rotors and with a conservative estimate of transmission losses, for Cornu to hover his machine free of the ground the installed power required would need to have been about 40 hp. Using an engine with a power output of only 24 hp it is highly unlikely that Paul Cornu's machine ever flew freely in sustained flight, even when accounting for the benefits of ground effect (see Section 5.8) and discounting the losses in efficiency that would be encountered with the slippage of the belt transmission.

Worked Example 2

A tilt-rotor aircraft has a gross weight of 45,000 lb (20,400 kg). The rotor diameter is 38 ft (11.58 m). On the basis of the momentum theory, estimate the power required for the aircraft to hover at sea level on a standard day where the density of air is 0.002378 slugs ft^{-3} or 1.225 kg m^{-3}. Assume that the figure of merit of the rotors is 0.75 and transmission losses amount to 5%.

A tilt-rotor has two rotors, which are each assumed to carry half of the total aircraft weight, that is, $T = 22{,}500$ lb. For each of the rotors, the disk area is, $A = \pi(38/2)^2 = 1134.12$ ft^2. The induced velocity in the plane of the rotor is

$$v_i = \sqrt{\frac{T}{2\rho A}} = \sqrt{\frac{22500}{2 \times 0.002378 \times 1134.12}} = 64.56 \text{ ft s}^{-1}.$$

The ideal power per rotor will be $Tv_i = 22{,}500 \times 64.56 = 1{,}452{,}600$ lb ft s^{-1}. This result is converted into horsepower (hp) by dividing by 550 to give 2,641 hp per rotor. Remember that the figure of merit accounts for the aerodynamic efficiency of the rotors. Therefore, the actual power required per rotor to overcome induced and profile losses will be 2,641/0.75 = 3,521.5 hp, followed by multiplying the result by two to account for both rotors, that is, $2 \times 3{,}521 = 7{,}043$ hp. Transmission losses account for another 5%, so that the total power required to hover is $1.05 \times 7{,}043 = 7{,}395$ hp.

The problem can also be worked in SI units. In this case, $T = 10{,}200 \times 9.81 = 100{,}062$ N. The disk area is, $A = \pi(11.58/2)^2 = 105.32$ m^2. The induced velocity in the plane of the rotor is

$$v_i = \sqrt{\frac{T}{2\rho A}} = \sqrt{\frac{100062}{2 \times 1.225 \times 105.35}} = 19.69 \text{ m s}^{-1}.$$

The ideal power per rotor will be $Tv_i = 100{,}062 \times 19.69 = 1{,}970.2$ kW. The actual power required per rotor to overcome induced and profile losses will be $1{,}970.2/0.75 = 2{,}626.9$ kW followed by multiplying the result by two to account for both rotors, that is, 5,253.8 kW. Transmission losses mean that the total power required to hover will be 5,515.7 kW.

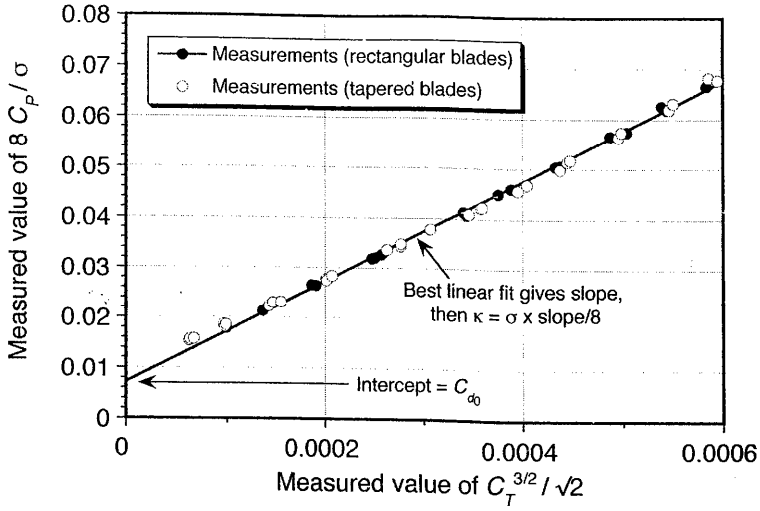

Figure 2.10 Method used to determine the induced power factor and average profile drag coefficient from rotor thrust and power measurements. Data source: Althoff & Noonan (1990).

2.9 Estimating Nonideal Effects from Rotor Measurements

It is often necessary to estimate values for the induced power factor, κ, and the average profile drag coefficients of the blades, C_{d_0}, from rotor thrust and power measurements. These values are then used in various performance estimations. This can be done given measurements of C_T and C_P in sufficient quality and quantity, these normally being made by testing an isolated rotor (i.e., without the airframe) on a hover tower when the rotor is high enough off the ground to be free of ground interference effects. It has been shown that the result in Eq. 2.43 gives a good representation of hover performance, that is,

$$C_{P_{\text{meas}}} = \frac{\kappa C_{T_{\text{meas}}}^{3/2}}{\sqrt{2}} + C_{P_0} = \frac{\kappa C_{T_{\text{meas}}}^{3/2}}{\sqrt{2}} + \frac{\sigma C_{d_0}}{8} \tag{2.50}$$

when using the result for the profile power in Eq. 2.42. Strictly, σ must be viewed the *equivalent* or weighted rotor solidity – see Section 3.4. By plotting $8C_{P_{\text{meas}}}/\sigma$ versus $C_{T_{\text{meas}}}^{3/2}/\sqrt{2}$ as shown in Fig. 2.10, it is apparent that the results lie almost on a perfect straight line. The results can then be fitted in a least squares sense to find the slope (proportional to κ) and the intercept on the y axis (C_{d_0}). From the results in this case for the rotor with rectangular blades and of solidity $\sigma = 0.098$, then $\kappa = 1.233$ and $C_{d_0} = 0.0075$. This latter result is quite reasonable in light of the results for the drag coefficients found for two-dimensional airfoil sections, as shown in Chapter 3 (Fig. 3.14) and also in Chapter 7.

2.10 Induced Tip Loss

The formation of a trailed vortex at the tip of each blade produces a high local inflow over the tip region and effectively reduces the lifting capability there. This physical effect is shown in Fig. 2.11 in terms of the thrust distribution over the blade when compared at the same collective pitch (not at the same thrust). This phenomenon is often referred to as a *tip loss*, in that it represents a loss in lift relative to the finite value of lift that would

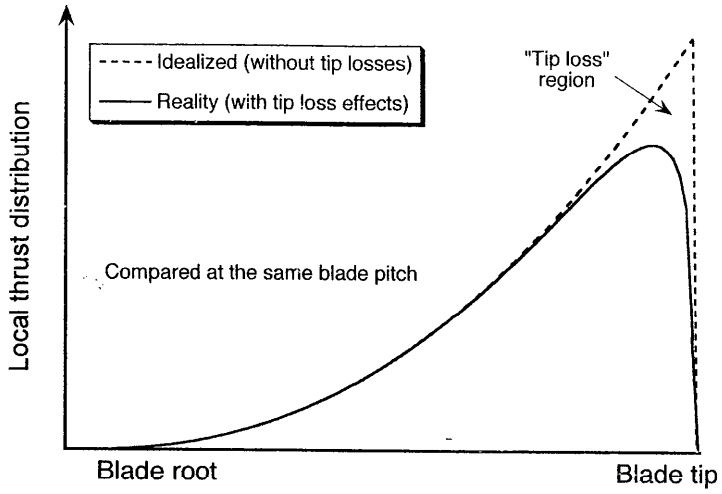

Figure 2.11 The rollup of the tip vortex causes a "tip-loss" effect at the blade tip.

otherwise be produced without the influence of any tip vortices in the flow (i.e., a 2-D assumption).

In performance or preliminary rotor design work, a simple tip-loss factor B can be used to account for this physical effect such that the product BR corresponds to an effective blade radius, $R_e < R$. A tip loss essentially corresponds to a reduction in the rotor disk area by a factor B^2, that is

$$A_e = \pi R_e^2 = \pi (BR)^2 = B^2(\pi R^2) = B^2 A. \tag{2.51}$$

By a simple extension of this concept, the effect of the root cut out (essentially the inner, nonaerodynamic portion of the blade with retention and pitch attachments) can be estimated. If r_0 is the nondimensional radius of the root cut-out, then the effective area of the hovering rotor for momentum theory purposes becomes

$$A_e = \pi B^2 R^2 - \pi r_0^2 R^2, \tag{2.52}$$

or in terms of an area ratio

$$\frac{A_e}{A} = \frac{\pi B^2 R^2 - \pi r_0^2 R^2}{\pi R^2} = B^2 - r_0^2. \tag{2.53}$$

Therefore, it will be apparent that this loss effect will manifest as a higher effective disk loading (i.e., T/A_e instead of T/A) and an increase in the average induced velocity by a factor B^{-1} for a given thrust, with a corresponding increase in induced power.

This is also the essence of Prandtl's approach to modeling tip-loss effects, where an analogy was made between the helical vortex wake below the rotor and a system of parallel vortex sheets – see exposition by Glauert (1935). Prandtl showed that when accounting for the tip loss, the effective blade radius, R_e, is given by

$$\frac{R_e}{R} \approx 1 - \left(\frac{1.386}{N_b}\right) \frac{\lambda_i}{\sqrt{1+\lambda_i^2}}, \tag{2.54}$$

where N_b is the number of blades. For helicopter rotors λ_i is typically less than 0.07; thus λ_i^2 will be small and the preceding equation can be simplified to

$$\frac{R_e}{R} \approx 1 - \left(\frac{1.386}{N_b}\right)\lambda_i. \tag{2.55}$$

A more general tip-loss equation is sometimes used where

$$B = 1 - \frac{1.386\lambda}{N_b} \tag{2.56}$$

and where the inflow ratio is $\lambda = (V_c + v_i)/\Omega R$ and V_c is the climb velocity. For hovering flight with the assumption of uniform inflow it has already been shown that

$$\lambda_i = \sqrt{\frac{C_T}{2}}, \tag{2.57}$$

so that the tip-loss factor is approximated by

$$\frac{R_e}{R} = B = 1 - \left(\frac{1.386}{\sqrt{2}}\right)\frac{\sqrt{C_T}}{N_b} \approx 1 - \frac{\sqrt{C_T}}{N_b}. \tag{2.58}$$

A graph of this result is shown in Fig. 2.12, where the factor B is shown to decrease with decreasing number of blades and also with increasing rotor thrust. The former effect results from blade-to-blade interference, whereas the latter effect has its origin in the spacing of the vortex sheets below the rotor (helical pitch of the wake). In practice, values of B for helicopter rotors are found to range from about 0.95 to 0.98, depending on the number of blades.

Gessow & Myers (1952) suggest an empirical tip-loss factor based on blade geometry alone where

$$B = 1 - \frac{c}{2R} \tag{2.59}$$

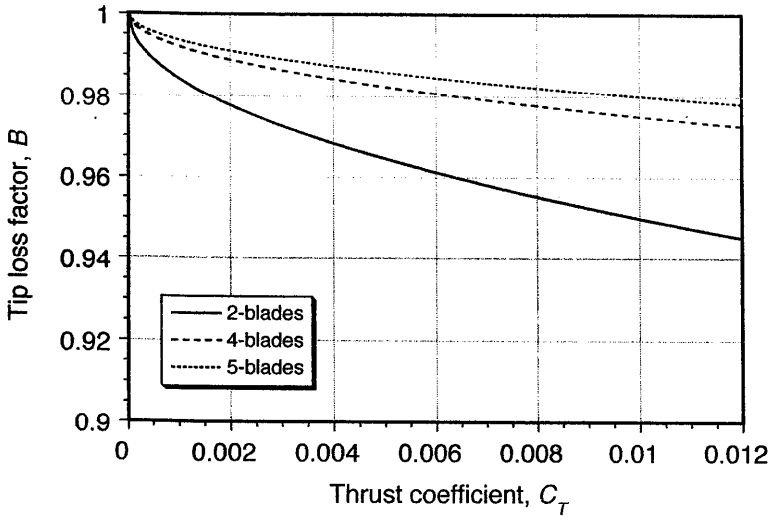

Figure 2.12 The effect of thrust and number of blades on Prandtl's tip-loss factor.

and where c is the tip chord, although it would seem that this result is not general enough to deal with other than rectangular blade tips. Sissingh (1939) has proposed the alternative geometric expression

$$B = 1 - \frac{c_0(1 + 0.7\tau_r)}{1.5R}, \tag{2.60}$$

where c_0 is the root chord of the main blade and τ_r is the blade taper ratio (i.e., the ratio of the tip chord to the root chord). The need to determine B by one of these equations can, however, be avoided if a more general numerical approach to solving for tip-loss effects is used (see Section 3.2.4).

2.11 Rotor Solidity and Blade Loading Coefficient

It will be seen from Eq. 2.46 that the solidity, σ, appears in the expression for figure of merit, *FM*. For a rotor with rectangular blades, the solidity represents the ratio of the lifting area of the blades to the area of the rotor, that is,

$$\sigma = \frac{\text{blade area}}{\text{disk area}} = \frac{A_b}{A} = \frac{N_b c R}{\pi R^2} = \frac{N_b c}{\pi R}. \tag{2.61}$$

If *FM* is plotted for rotors with different values of σ, the behavior is typified by Fig. 2.13. The data have been taken from the classic experiments of Knight & Hefner (1937), for which the thrust and power were measured for rotors with different numbers of blades. While the number of blades also affects rotor performance (see Section 3.3.10) there are no experiments that have examined solidity effects independently of blade number. Results predicted by means of the modified momentum theory are also shown in Fig. 2.13. From the measurements at zero thrust it was deduced that $C_{d_0} = 0.011$, and κ was estimated to be 1.25 and independent of the number of blades. While this value of κ is perhaps on the high side for a modern helicopter rotor, it must be recognized that these measurements were made with untwisted blades and so, as will be shown in Chapter 3, this will produce higher induced flow near the tip and, therefore, the rotor is less efficient with a higher value of κ.

From the results shown in Fig. 2.13 it will be noted that higher values of *FM* are obtained with the *lowest* possible solidity at the same design C_T (i.e., same aircraft gross weight or disk loading). This is hardly an unexpected result from Eq. 2.46 (all other terms such as κ being assumed constant) and simply means that the viscous drag on the rotor is being minimized by reducing the net blade area. However, the minimization of rotor solidity, σ, must be done with extreme caution. This is because reducing blade area must always result in a higher AoA of the blade sections (and higher lift coefficients) to obtain the same values of C_T and disk loading. Therefore, the lowest allowable value of σ must ultimately be limited by the onset of blade stall. This effect is well shown by the results in Fig. 2.13 for the lowest solidity of 0.042, where a progressive departure occurs from the theoretical predictions for $C_T > 0.004$. For a full-scale rotor this would occur at higher values of C_T because of the higher values of maximum lift found at the higher Reynolds numbers on the blades – see Section 7.9.

An alternative format that emphasizes the local lift loading on the blades is to plot the figure of merit versus blade-loading coefficient, C_T/σ. Notice that the blade-loading coefficient can be written as

$$\frac{C_T}{\sigma} = \frac{T}{\rho A(\Omega R^2)}\left(\frac{A}{A_b}\right) = \frac{T}{\rho A_b(\Omega R)^2}, \tag{2.62}$$

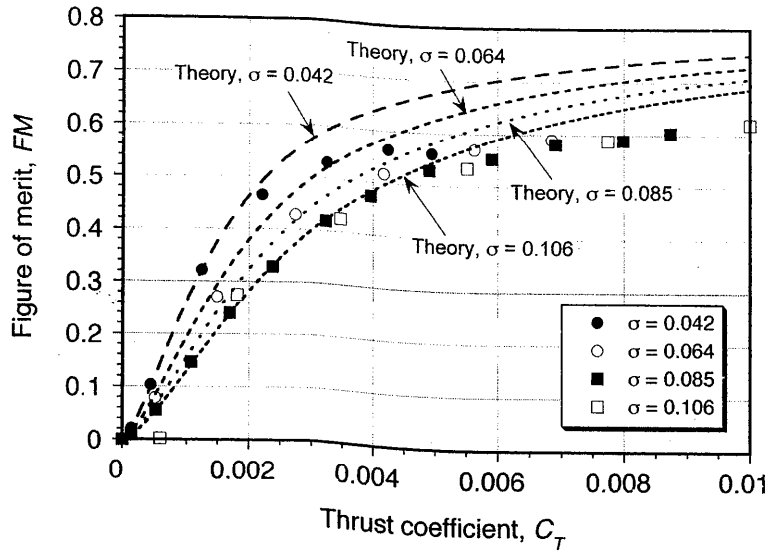

Figure 2.13 Measured and predicted figure of merit versus thrust coefficient for a hovering rotor with different values of solidity. Data source: Knight & Hefner (1937).

where A_b is the area of the blades. These results are shown in Fig. 2.14. Notice that reducing the value of σ results in higher values of C_T/σ for the same operational value of C_T. Although Fig. 2.14 shows the rotor operates at higher values of FM with increased blade loading coefficient, the maximum value is limited by the occurrence of local flow separation on the blades and finally by blade stall. Typically, for a contemporary helicopter rotor, the maximum realizable value of blade loading coefficient without stall is about 0.12–0.14, but the influence of Reynolds number on blade stall must also be considered, especially with subscale rotors, which includes the measured data presented here.

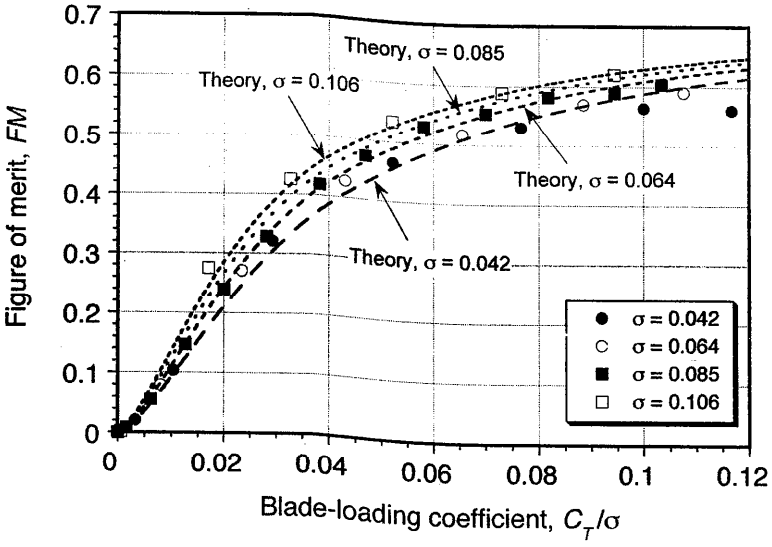

Figure 2.14 Measured and predicted figure of merit versus blade-loading coefficient for a hovering rotor with different solidities. Data source: Knight & Hefner (1937).

The maximum attainable value of C_T/σ will also depend on the distribution of local lift coefficients along the blade, which in turn depends on both the blade twist and the planform. As will be shown in Chapter 3, the local lift coefficients can be related to the blade loading by means of the blade element theory and so the blade twist and blade planform can be designed to delay the effects of stall to higher values of C_T/σ. Nevertheless, it is clear that to maximize the figure of merit the blade sections must always operate close to their maximum lift coefficients (i.e., at the highest possible blade loading without the occurrence of blade stall). It can also be concluded that a rotor that uses airfoils with higher values of maximum-lift coefficient can be designed to have lower solidity. This has the benefits of a lower blade and hub weight, both of which are significant contributors to total helicopter weight. Consequently, there is considerable research emphasis in the helicopter industry to design airfoils with high values of maximum-lift coefficient (see Chapter 7).

Yet another form of presentation that emphasizes solidity effects is shown in Fig. 2.15. It is apparent that the figure of merit can be written in the alternative form

$$FM = \frac{\dfrac{C_T^{3/2}}{\sqrt{2}}}{\dfrac{\kappa C_T^{3/2}}{\sqrt{2}} + \dfrac{\sigma C_{d_0}}{8}} = \frac{1}{\kappa + \dfrac{\sqrt{2}C_{d_0}}{8}\left(\dfrac{C_T^{3/2}}{\sigma}\right)^{-1}}. \tag{2.63}$$

In this case plotting FM versus $C_T^{3/2}/\sigma$ causes the results for all rotors to coalesce essentially into a single performance curve. These results quickly confirm that the performance of a rotor is independent of the number of blades, but only if the performance is compared at the same value of solidity. While this is not strictly true because of secondary influences such as tip-loss effects and Reynolds number influences on C_{d_0} (N_b affects blade chord for a given value of solidity), the results shown in Fig. 2.15 are sufficiently convincing.

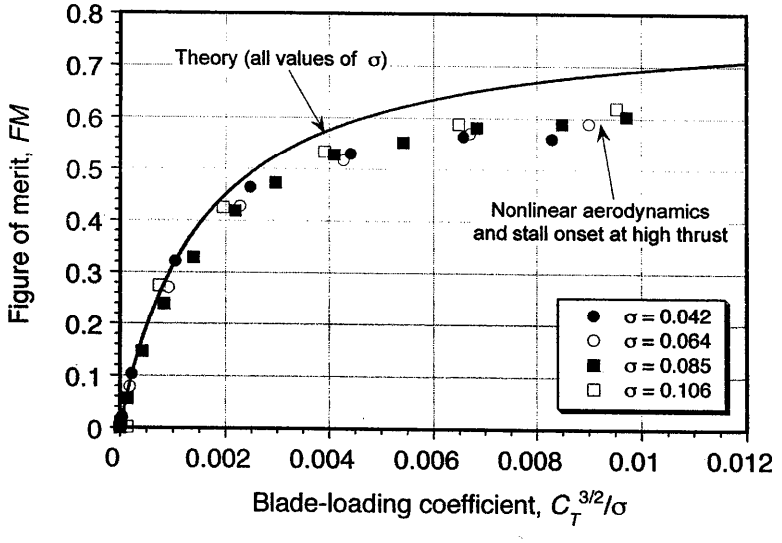

Figure 2.15 Measured and predicted figure of merit versus blade-loading coefficient for a hovering rotor with different solidities. Data source: Knight & Hefner (1937).

2.12 Power Loading

The ratio T/P or the power loading has been previously defined as a rotor efficiency parameter. Helicopters and other rotorcraft are generally designed to hover with the *lowest* possible power required (and hence lowest fuel burn) for a given gross weight, that is, a *high* power loading with a large value of T/P is required. Helicopters spend a good proportion of their flight time in hover or low speed forward flight and the use of the hover condition as an initial design point is clear. However, as will be shown in Chapter 6, optimizing the rotor for maximum hovering efficiency can also have some trade-offs in terms of efficient high-speed forward flight performance.

Power loading is the ratio of the thrust produced to the power required to hover, that is,

$$PL = \frac{W}{P} = \frac{T}{P} = \frac{C_T}{(\Omega R)C_P}. \tag{2.64}$$

This quantity should be as close as possible to the ideal value for best hovering efficiency. Because $T \propto (\Omega R)^2$ but $P \propto (\Omega R)^3$, maximizing the power loading requires a low tip speed (ΩR). On the basis of simple momentum theory considerations, the ratio P/T is given by

$$\frac{P}{T} = \frac{T^{3/2}}{T\sqrt{2\rho A}} = \sqrt{\frac{T}{2\rho A}} = \sqrt{\frac{DL}{2\rho}} = v_i = (PL)^{-1}, \tag{2.65}$$

which, as also shown previously in Eq. 2.24, is related to the disk loading. Therefore, to maximize the power loading (that is to minimize the ratio P/T) the disk loading should be low (i.e., the disk area should be large for a given gross weight to give a low induced velocity *and* the tip speed should be low). Generally, the tip speed is set on the basis of various competing performance requirements for a given rotor size. As shown in Chapter 6, this may include autorotative requirements and rotor noise constraints.

When using the modified momentum theory, the ratio P/T is given by

$$\frac{P}{T} = \kappa\sqrt{\frac{T}{2\rho A}} + \frac{P_0}{T}. \tag{2.66}$$

Alternatively, we can write

$$\frac{P}{T} = \Omega R\frac{C_P}{C_T} = \Omega R\left(\kappa\sqrt{\frac{C_T}{2}} + \frac{C_{P_0}}{C_T}\right) = \frac{\Omega R}{C_T}\left(\kappa\frac{C_T^{3/2}}{\sqrt{2}} + \frac{\sigma C_{d_0}}{8}\right), \tag{2.67}$$

which is a result that depends on the rotor solidity, σ. Equation 2.67 can also be written in terms of the figure of merit, that is,

$$\frac{P}{T} = \frac{\sqrt{DL}}{\sqrt{2\rho}FM} \propto \frac{\sqrt{DL}}{FM} \quad \text{or} \quad PL \propto \frac{FM}{\sqrt{DL}}. \tag{2.68}$$

This means that the best rotor efficiency (maximum power loading) is obtained when the disk loading is a minimum *and* the figure of merit is a maximum.

A representative example of the measured C_T/C_P (which is proportional to power loading at a fixed tip speed) versus thrust is shown in Fig. 2.16 for several values of rotor solidity. By differentiating Eq. 2.67 with respect to C_T, it is easy to show that for a rotor with rectangular blades the operating C_T to give the lowest ratio of T/P is

$$C_T = \frac{1}{2}\left(\frac{\sigma C_{d_0}}{\kappa}\right)^{2/3} \quad \text{for maximum } PL, \tag{2.69}$$

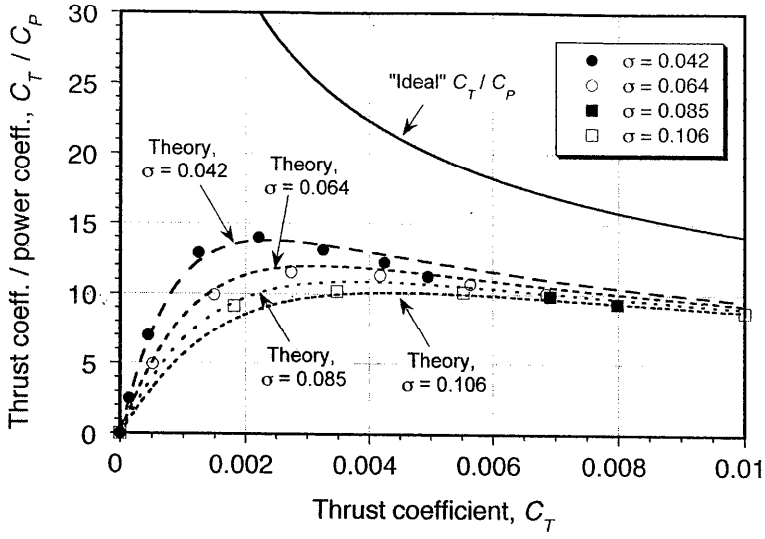

Figure 2.16 Representative measured variation of C_T/C_P versus thrust coefficient for a hovering rotor with different solidities. Data source: Knight & Hefner (1937).

which clearly depends on both the profile and induced effects. Substituting this value into Eq. 2.46, for example, shows that this condition is equivalent to rotor operations at a figure of merit of $2/3\kappa = 0.667\kappa$. Using this result, the disk loading for maximum power loading will be at

$$\frac{T}{A} = \frac{W}{A} = \frac{1}{2}\rho(\Omega R)^2 \left(\frac{\sigma C_{d_0}}{\kappa}\right)^{2/3} \tag{2.70}$$

and for design purposes solving for the rotor radius would determine its optimum value for a given helicopter gross weight, tip speed, and density altitude. However, it is apparent that the conditions for the most efficient operation of the rotor are relatively insensitive to the operating state in that the C_T/C_P (or the T/P) curves in Fig. 2.16 are fairly flat over the normal range of operational thrust coefficients. Therefore, there is some latitude in selecting the rotor radius, which as mentioned previously, may be constrained because of other (nonaerodynamic) factors. See also the discussion in Section 6.4.1.

2.13 Momentum Analysis in Axial Climb and Descent

2.13.1 *Axial Climb*

Adequate climbing flight performance is an important operational consideration for a helicopter and sufficient power reserves must be available to ensure climbing performance is maintained over a wide range of gross weights and operational density altitudes. Again, we can apply the three conservation laws to a control volume surrounding the climbing rotor and its flow field, as shown in Fig. 2.17. As before, consider the problem to be quasi–1-D in that the flow properties will be assumed to vary only in the vertical direction over cross sectional planes parallel to the disk and at each cross section the flow properties are distributed uniformly. In contrast to the hover case where the climb velocity is identically zero, the relative velocity far upstream relative to the rotor will now be V_c. At the plane of the rotor, the velocity will now be $V_c + v_i$, and the slipstream velocity

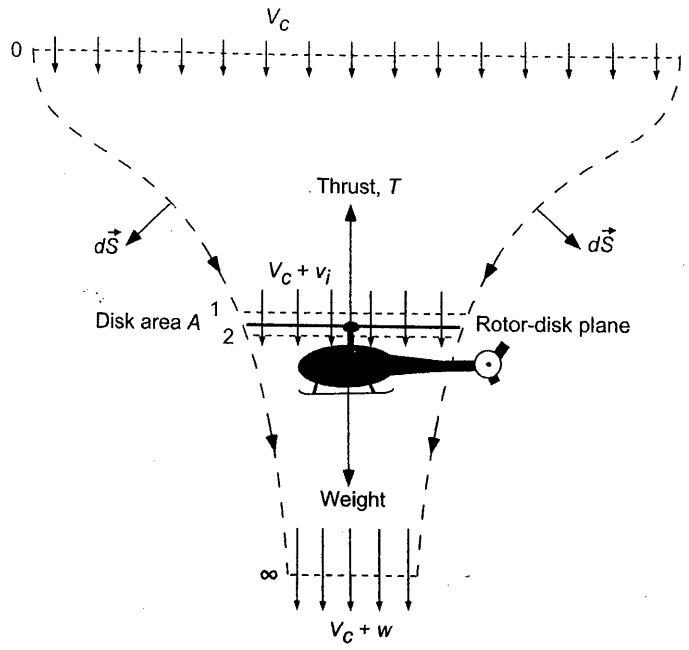

Figure 2.17 Flow model for momentum theory analysis of a rotor in axial climbing flight.

in the vena contracta is now $V_c + w$. By the conservation of mass, the mass flow rate is constant within the boundaries of the wake and so

$$\dot{m} = \iint_{\infty} \rho \vec{V} \cdot d\vec{S} = \iint_{2} \rho \vec{V} \cdot d\vec{S}, \tag{2.71}$$

where $d\vec{S}$ is again the outward pointing normal from the control volume. Therefore, substituting the values for this problem results in

$$\dot{m} = \rho A_{\infty}(V_c + w) = \rho A(V_c + v_i). \tag{2.72}$$

The application of the principle of conservation of momentum gives

$$T = \iint_{\infty} \rho(\vec{V} \cdot d\vec{S})\vec{V} - \iint_{0} \rho(\vec{V} \cdot d\vec{S})\vec{V}. \tag{2.73}$$

Now, in a steady climb the velocity far upstream of the rotor is finite, so that both terms on the right-hand side of the above equation are nonzero. Therefore, in this case

$$T = \dot{m}(V_c + w) - \dot{m}V_c = \dot{m}w. \tag{2.74}$$

Notice that this is the same equation obtained for the rotor thrust in the hover case (Eq. 2.7). Because the work done by the climbing rotor is now $T(V_c + v_i)$, then

$$\begin{aligned} T(V_c + v_i) &= \iint_{\infty} \frac{1}{2}\rho(\vec{V} \cdot d\vec{S})\vec{V}^2 - \iint_{0} \frac{1}{2}\rho(\vec{V} \cdot d\vec{S})\vec{V}^2 \\ &= \frac{1}{2}\dot{m}(V_c + w)^2 - \frac{1}{2}\dot{m}V_c^2 = \frac{1}{2}\dot{m}w(2V_c + w). \end{aligned} \tag{2.75}$$

From these latter two equations, it is readily apparent that $w = 2v_i$, which is the same result as found for the hover case.

The relationship between the rotor thrust and the induced velocity at the rotor disk in hover is

$$v_h \equiv v_i = \sqrt{\frac{T}{2\rho A}} \tag{2.76}$$

and for the climbing rotor it has been shown from Eq. 2.74 that

$$T = \dot{m}w = \rho A(V_c + v_i)w = 2\rho A(V_c + v_i)v_i, \tag{2.77}$$

so that

$$\frac{T}{2\rho A} = v_h^2 = (V_c + v_i)v_i = V_c v_i + v_i^2. \tag{2.78}$$

Dividing through by v_h^2 results in

$$\left(\frac{v_i}{v_h}\right)^2 + \frac{V_c}{v_h}\left(\frac{v_i}{v_h}\right) - 1 = 0, \tag{2.79}$$

which is a quadratic equation in v_i/v_h. This equation has the solution

$$\frac{v_i}{v_h} = -\left(\frac{V_c}{2v_h}\right) \pm \sqrt{\left(\frac{V_c}{2v_h}\right)^2 + 1}. \tag{2.80}$$

Although there are two possible solutions (one positive and one negative), v_i/v_h must always be positive in the climb so as not to violate the assumed flow model. Therefore, the only valid solution becomes

$$\frac{v_i}{v_h} = -\left(\frac{V_c}{2v_h}\right) + \sqrt{\left(\frac{V_c}{2v_h}\right)^2 + 1}. \tag{2.81}$$

The results from this analysis are shown in Fig. 2.18, which is presented in a form first suggested by Hafner (1947). The other root of the quadratic equation lies below the V_c/v_h axis and is physically invalid. It is apparent that as the climb velocity increases the induced velocity at the rotor decreases. This is called the *normal working state* of the rotor, with hover being the lower limit. The branch of the induced velocity curve denoted by the broken line gives a solution to Eq. 2.81 for negative values of V_c (i.e., a descent). However, just as the rotor begins to descend there can be two possible flow directions; this violates the assumed flow model and so this solution is also physically invalid. Yet the measurements follow closely this nonphysical root of the inflow equation, so in practice the momentum theory result can be assumed valid at least for low rates of descent.

2.13.2 *Axial Descent*

The climb flow model cannot be used in a descent (where $V_c \ll 0$) because now V_c is directed upward and so the slipstream will be above the rotor. This will be the case whenever $|V_c|$ is more than twice the average induced velocity at the disk. For cases where the descent velocity is in the range $-2v_h \leq V_c \leq 0$, the velocity at any plane through the rotor slipstream can be either upward or downward. Under these circumstances, a more complicated recirculating (and usually more turbulent and aperiodic) flow pattern may exist at the rotor. Momentum theory cannot be used here because no definitive control volume

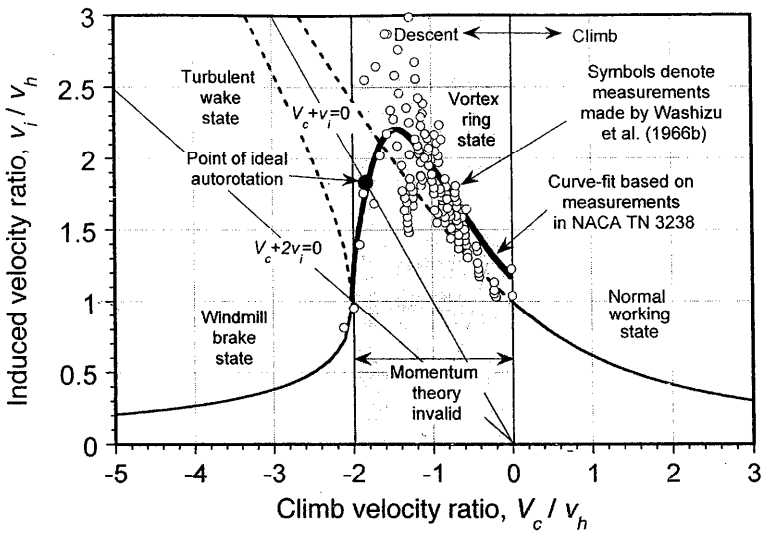

Figure 2.18 Induced velocity variation as a function of climb and descent velocity based on momentum theory (complete induced velocity curve).

surrounding the rotor and its wake can be established – see discussion by Glauert (1935, p. 348). The same argument applies when using the blade element momentum theory (BEMT), which is discussed in Chapter 3. The more complicated operating state where $-2v_h \leq V_c \leq 0$ is discussed in Section 2.13.3.

The assumed flow model and control volume surrounding the descending rotor is shown in Fig. 2.19. To proceed, the assumption must be made that $|V_c| > 2v_h$ so that a well-defined slipstream will always exist above the rotor and encompassing the rotor disk. Far upstream (well below) the rotor, the magnitude of the velocity is the descent velocity, which is equal to $|V_c|$. Notice that to avoid any ambiguity, it will be assumed that the velocity is measured as positive when directed in a downward direction. At the plane of the rotor, the velocity is $|V_c| - v_i$. In the far wake (above the rotor), the velocity is $|V_c| - w$.

By the conservation of mass, the fluid mass flow rate, $\dot{m}$, through the rotor disk is

$$\dot{m} = \iint_{\infty} \rho \vec{V} \cdot d\vec{S} = \iint_{2} \rho \vec{V} \cdot d\vec{S}. \tag{2.82}$$

Therefore, we have

$$\dot{m} = \rho A_{\infty}(V_c + w) = \rho A(V_c + v_i). \tag{2.83}$$

Conservation of fluid momentum gives in this case

$$T = -\left[\iint_{\infty} \rho(\vec{V} \cdot d\vec{S})\vec{V} - \iint_{0} \rho(\vec{V} \cdot d\vec{S})\vec{V}\right], \tag{2.84}$$

with the negative sign arising because the flow direction is now reversed (upward) compared to the climb case. In a steady descent, the velocity far upstream of (below) the rotor must be

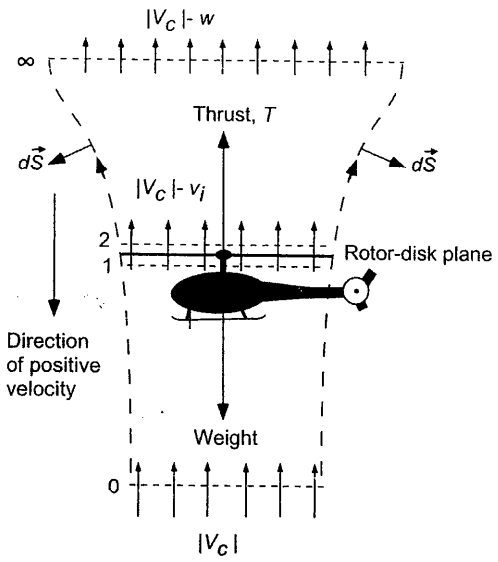

Figure 2.19 Flow model used for momentum theory analysis of a rotor in a vertical (axial) descent.

finite so that both terms on the right-hand side of the above equation are nonzero. Therefore, in this case

$$T = (-\dot{m})(V_c + w) - (-\dot{m})V_c = -\dot{m}w. \tag{2.85}$$

Notice that T is not negative because $\dot{m}$ is negative by means of the assumed sign convention. Because the work done by the rotor in descent is $T(v_i + V_c)$, this gives

$$\begin{aligned} T(v_i + V_c) &= \iint_0 \frac{1}{2}\rho(\vec{V} \cdot d\vec{S})\vec{V}^2 - \iint_\infty \frac{1}{2}\rho(\vec{V} \cdot d\vec{S})\vec{V}^2 \\ &= \frac{1}{2}\dot{m}V_c^2 - \frac{1}{2}\dot{m}(V_c + w)^2 = -\frac{1}{2}\dot{m}w(2V_c + w), \end{aligned} \tag{2.86}$$

which is a negative quantity. Therefore, the rotor is now extracting power from the airstream and this operating condition is known as the *windmill state*, for obvious reasons. More usually it is referred to as the *windmill brake state* because the rotor in this condition decreases or "brakes" the velocity of the flow – see Chapter 13. Using Eqs. 2.85 and 2.86 it is seen, again, that $w = 2v_i$. Note, however, that the net velocity in the slipstream is *less* than $|V_c|$, and so from continuity considerations the wake boundary expands above the descending rotor disk. For the descending rotor

$$T = -\dot{m}w = -\rho A(V_c + v_i)w = -2\rho A(V_c + v_i)v_i. \tag{2.87}$$

Therefore, we can write

$$\frac{T}{2\rho A} = v_h^2 = -(V_c + v_i)v_i = -V_c v_i - v_i^2. \tag{2.88}$$

Dividing through by v_h^2 gives

$$\left(\frac{v_i}{v_h}\right)^2 + \frac{V_c}{v_h}\left(\frac{v_i}{v_h}\right) + 1 = 0, \tag{2.89}$$

which is a quadratic equation in v_i/v_h. This has the solution

$$\frac{v_i}{v_h} = -\left(\frac{V_c}{2v_h}\right) \pm \sqrt{\left(\frac{V_c}{2v_h}\right)^2 - 1}. \tag{2.90}$$

Again, like the climb case, there are two possible solutions for v_i/v_h. One of these solutions produces values of $v_i/v_h > 1$, which violates the assumed flow model in this case. The only valid solution is

$$\frac{v_i}{v_h} = -\left(\frac{V_c}{2v_h}\right) - \sqrt{\left(\frac{V_c}{2v_h}\right)^2 - 1}, \tag{2.91}$$

which is valid for $V_c/v_h \leq -2$. Therefore, it is noted from Fig. 2.18 that as the descent velocity increases the induced velocity decreases and asymptotes smoothly to zero at high descent rates. The other solution to the quadratic, which is denoted by the broken line in Fig. 2.18, violates the assumed flow model and so is a nonphysical solution.

2.13.3 *Region between Hover and Windmill State*

In the region $-2 \leq V_c/v_h \leq 0$ momentum theory is, strictly speaking, invalid because the flow can take on two possible directions and a well-defined slipstream ceases to exist; this means that a control volume cannot be defined that encompasses only the physical limits of the rotor disk. However, the velocity curve can still be defined empirically, albeit only approximately, on the basis of flight tests or other experiments with rotors. Unfortunately descending flight accentuates interactions of the tip vortices with other blades and so the flow becomes rather unsteady and turbulent, and experimental measurements of rotor thrust and power are difficult to make. Also, the average induced velocity cannot be measured directly. Instead, it is obtained indirectly from the measured rotor power and thrust – see Gessow (1948, 1954), Brotherhood (1949), and Washizu et al. (1966b).

The measured rotor power can be written in the assumed form as

$$P_{\text{meas}} = T(V_c + \bar{v}_i) + P_0, \tag{2.92}$$

where P_0 is the profile power and where $\bar{v}_i$ is recognized as only an averaged value of the induced velocity through the disk. Using the result that $P_h = T\bar{v}_h$ we get

$$\frac{V_c + \bar{v}_i}{\bar{v}_h} = \frac{P_{\text{meas}} - P_0}{P_h} = \frac{P_{\text{meas}} - P_0}{T\sqrt{T/2\rho A}} = \frac{(P_{\text{meas}} - P_0)\sqrt{2\rho A}}{W^{3/2}}. \tag{2.93}$$

Therefore, in addition to the measured rotor power P_{meas}, to obtain an estimate for the averaged induced velocity ratio it is necessary to know the rotor profile power. As shown previously by means of Eq. 2.42, one simple estimate for the profile power coefficient of a rotor with rectangular blades is $C_{P_0} = \sigma C_{d_0}/8$, where C_{d_0} is the mean (average) drag coefficient of the airfoil sections comprising the rotor and σ is the rotor solidity.

Because of the high levels of turbulence near the rotor in this operating state, the derived measurements of the average induced velocity contain a relatively large amount of scatter. The smooth curve fit shown in Fig. 2.18 is taken from Gessow (1954) and is a composite

of flight tests and wind tunnel measurements made by Lock et al. (1926), Brotherhood (1949), and Drees & Hendal (1951). Note, however, that the curve follows the nonphysical branch of the induced velocity curve derived on the basis of momentum theory up to about $V_c/v_h \approx -1.5$, after which it drops off precipitously and joins the branch of the curve defined on the basis of the momentum theory result in a descent. The higher values of measured power in hover and at low rates of descent are a result of higher induced power losses, which, as explained previously, are not predicted directly by the simple momentum theory.

Because the nature of the induced velocity curve is not analytically predictable in the range $-2 \leq V_c/v_h \leq 0$, the experimental estimates can be used to find a "best-fit" approximation for v_i at any rate of descent. Various authors, including Young (1978) and Johnson (1980), suggest a linear approximation to the measured curve. Following Young (1978), one approximation is

$$\frac{v_i}{v_h} = \begin{cases} \kappa - \dfrac{V_c}{v_h} & \text{for } -1.5 \leq \dfrac{V_c}{v_h} \leq 0 \\ \kappa\left[7 + 3\dfrac{V_c}{v_h}\right] & \text{for } -2 \leq \dfrac{V_c}{v_h} \leq -1.5, \end{cases} \tag{2.94}$$

where κ is the measured induced power factor in hover. A better approximation to the measured curve is

$$\frac{v_i}{v_h} = \begin{cases} \kappa - \left(\dfrac{3}{4}\right)\dfrac{V_c}{v_h} & \text{for } \dfrac{-8\kappa}{4\kappa+1} \leq \dfrac{V_c}{v_h} \leq 0 \\ \kappa\left[7 + 3\dfrac{V_c}{v_h}\right] & \text{for } -2 \leq \dfrac{V_c}{v_h} < \dfrac{-8\kappa}{4\kappa+1}. \end{cases} \tag{2.95}$$

A continuous approximation to the measured induced velocity curve is the quartic

$$\frac{v_i}{v_h} = \kappa + k_1\left(\frac{V_c}{v_h}\right) + k_2\left(\frac{V_c}{v_h}\right)^2 + k_3\left(\frac{V_c}{v_h}\right)^3 + k_4\left(\frac{V_c}{v_h}\right)^4, \tag{2.96}$$

with $k_1 = -1.125$, $k_2 = -1.372$, $k_3 = -1.718$, and $k_4 = -0.655$, which is valid for the full range $-2 \leq V_c/v_h \leq 0$.

2.13.4 *Power Required in Axial Climbing and Descending Flight*

Notice that because the climb and descent velocity changes the induced velocity at the rotor, the induced power will also be affected. In a climb or descent the power ratio is

$$\frac{P}{P_h} = \frac{V_c + v_i}{v_h} = \frac{V_c}{v_h} + \frac{v_i}{v_h}. \tag{2.97}$$

The two terms on the right-hand side of the above equation are the work done to change the potential energy of the rotor (helicopter) and the work done on the air by the rotor, respectively. The latter induced loss appears as an increase in dynamic pressure and gain in kinetic energy of the rotor slipstream. Using Eq. 2.81 and substituting and rearranging gives

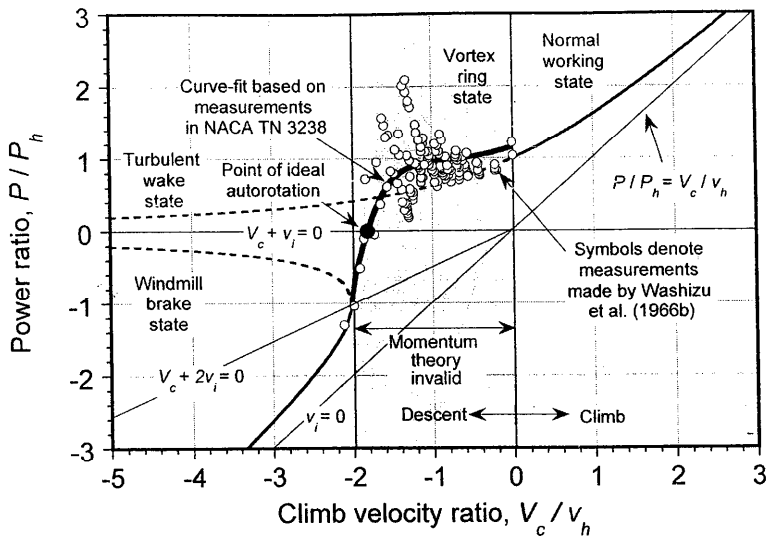

Figure 2.20 Total power required as a function of climb and descent velocity (universal power curve).

the power ratio for a *climb* as

$$\frac{P}{P_h} = \frac{V_c}{2v_h} + \sqrt{\left(\frac{V_c}{2v_h}\right)^2 + 1}, \quad \text{which is valid for } \frac{V_c}{v_h} \geq 0. \tag{2.98}$$

In a *descent*, Eq. 2.91 is applicable, and substituting this into Eq. 2.97 and rearranging gives the power ratio as

$$\frac{P}{P_h} = \frac{V_c}{2v_h} - \sqrt{\left(\frac{V_c}{2v_h}\right)^2 - 1}, \quad \text{which is valid for } \frac{V_c}{v_h} \leq -2. \tag{2.99}$$

Both results are shown in Fig. 2.20, which is usually called the *universal power curve* – a form first suggested by Lock (1947). This graph shows the total rotor power ratio, P/P_h, plotted versus the climb ratio, V_c/v_h. The nonphysical solutions are also shown for reference. Notice that the power required to climb is always greater than the power required to hover. However, as the climb velocity increases the induced power becomes a progressively smaller percentage of the total power required to climb. It is also significant to note that in a descent, at least above a certain rate, the rotor extracts power from the air and uses less power than required to hover (i.e., the rotor now operates like a windmill – see Chapter 13 for more details of this operational state).

2.13.5 *Four Working States of the Rotor in Axial Flight*

A description of the four working states of the rotor were first put forward by Lock and his colleagues (1926, 1928) and are summarized by Glauert (1935) and Hafner (1946). Figures 2.18 and 2.20 show the lines representing $V_c + v_i = 0$ and $V_c + 2v_i = 0$. Johnson (1980) shows that these lines are best used to help demarcate four axial operating states of the rotor. For points above the line $V_c + v_i = 0$, the rotor is absorbing power supplied from the rotor shaft. Below this line, the rotor is extracting power from the relative airstream, which does work on the rotor shaft. To help understand the complicated physical nature of the rotor wake under these conditions, Fig. 2.21 shows flow visualization images of

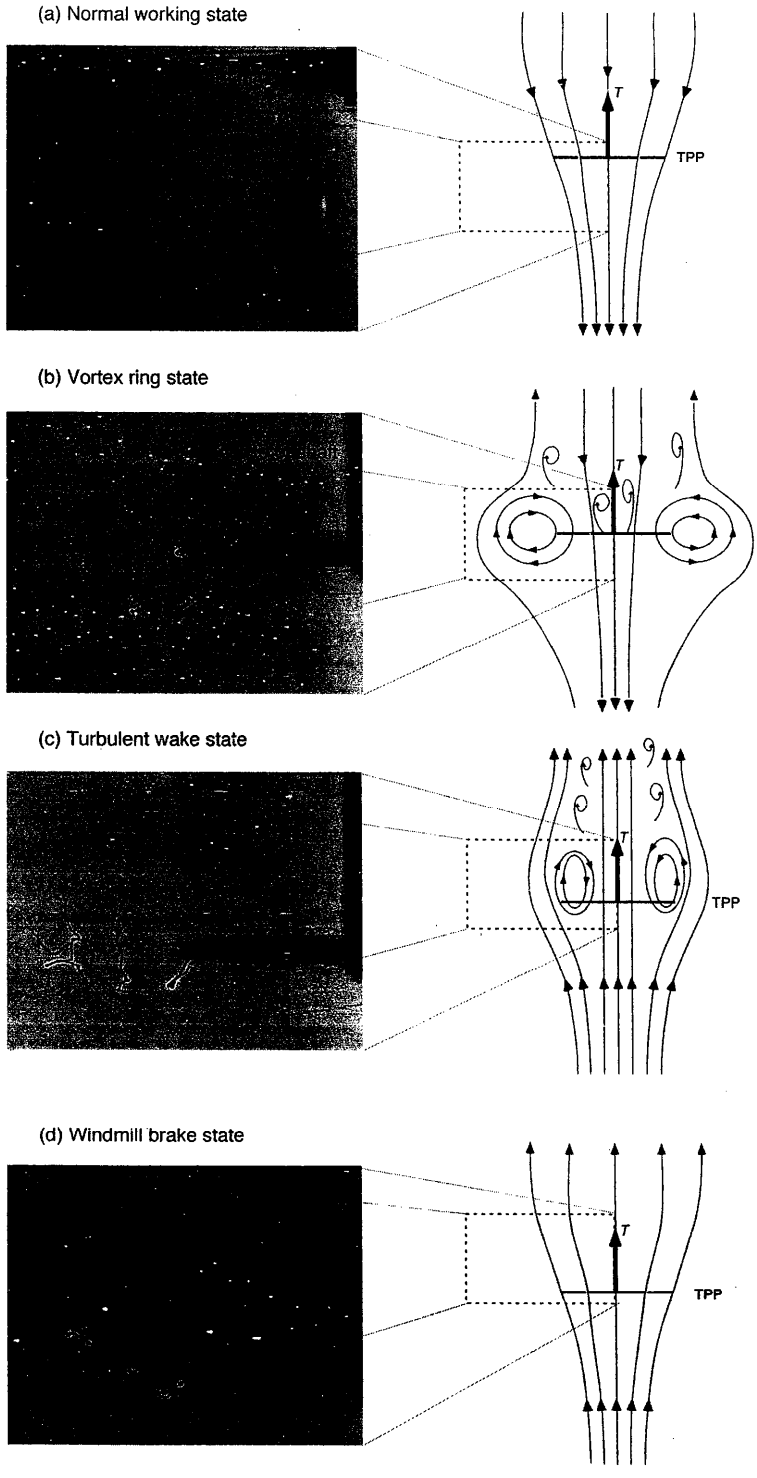

Figure 2.21 The physical nature of the rotor wake in simulated axial descent: (a) Normal working state. (b) Approaching the vortex ring state. (c) Turbulent wake state. (d) Approaching windmill brake state. Flow visualization source: University of Maryland.

the wake at various descent velocities. Unlike some of the earlier work by Lock (1928) where smoke was used to visualize the gross flow structure, the individual blade tip vortices were rendered visible here by means of shadowgraphy, which is a density–gradient method (see Section 10.2.3). Because the flow is nominally axisymmetric, only one side of the rotor is shown for clarity.

1. *Normal Working State:* Figure 2.21(a) shows an image of the flow in the *normal working state*. Here, the tip vortices follow smooth helicoidal-like trajectories. The flow is highly periodic with a smooth slipstream boundary free of any significant disturbances. A schematic of the mean flow is also shown. The normal working state encompasses climb, with the limit being the hover condition.
2. *Vortex Ring State:* For low rates of descent, the tip vortex filaments are convected closer to the plane of the rotor than for the hover case, but they also move radially outward away from the rotor. At higher descent rates, the tip vortices come very close to the rotor plane and considerable unsteadiness (aperiodicity) becomes apparent. This can be seen in Fig. 2.21(b) by the contortions in the tip vortex trajectories and the lack of any distinct slipstream boundary. This is close to the flow condition known as the *vortex ring state*, where the accumulation of tip vortices in the rotor plane begins to resemble a concentric set of vortex rings.
3. *Turbulent Wake State:* As the descent velocity increases further, the wake above the rotor becomes more turbulent and aperiodic and is representative of the flow conditions known as the *turbulent wake state*. This state is shown by Fig. 2.21(c) and represents the initial return to a smooth flow with a well-defined slipstream boundary. The flow is similar to that associated with a bluff body.
4. *Windmill brake State:* At even higher descent velocities, the wake is again observed to develop a more definite slipstream boundary that expands downstream (above) of the rotor. When in this state, the vortical wake structure is found to return to a more regular helical structure, as shown by Fig. 2.21(d). As previously described, this flow condition is known as the *windmill brake state* because the rotor extracts energy from the flow and brakes the flow velocity like a windmill.

2.13.6 *Vortex Ring State*

The vortex ring state (VRS) is worthy of some special further discussion. This is because in the VRS the rotor can experience highly unsteady flow with regions of concurrent upward and downward velocities, and the flow can periodically break away from the rotor disk. This flow state appears to have been first recognized by de Bothezat (1919) and such flows have been visualized and measured in helicopter rotor experiments by Lock et al. (1926), Castles & Gray (1951), Drees & Hendal (1951), Washizu et al. (1966a,b), Azuma & Obata (1968), Moedersheim et al. (1994), and others. An example is shown in Fig. 2.22. Yaggy & Mort (1963) show that the unsteady airloads produced in VRS depend on rotor disk loading and blade twist, confirming the nonlinearity of the VRS problem. Betzina (2001) has conducted experiments in descending flight conditions with a relatively highly loaded rotor, representative of that used on a tilt-rotor. Some dramatic in-flight flow visualization on a helicopter rotor during vertical descent were performed by Brotherhood (1949). Glauert (1926a,b) and Nikolsky & Seckel (1949a,b) were some of the first to conduct a mathematical analysis of the problem. From a piloting perspective, entry into autorotative flight may require transition through the VRS, especially during flight at low airspeeds (see Section 5.7). Because of the flow unsteadiness at the rotor in VRS, it can lead

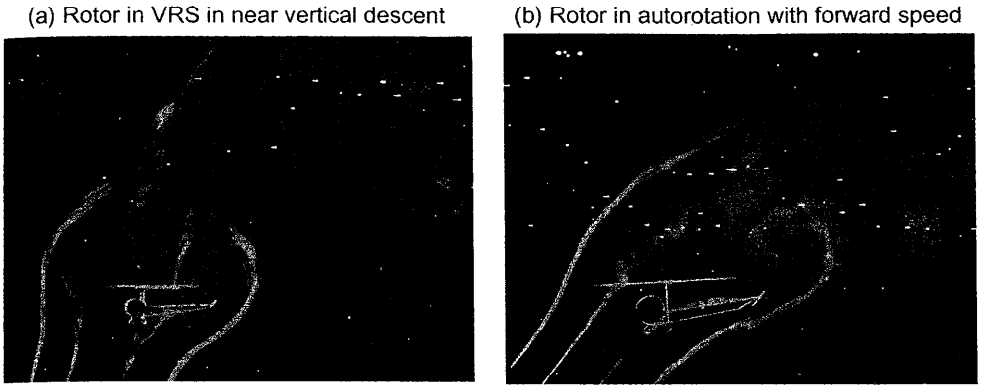

Figure 2.22 Flow visualization at the rotor when it operates in the vortex ring state and in autorotation. Photos from Drees & Hendal (1951).

to significant blade flapping and a loss of rotor control. If the VRS occurs on the tail rotor, such as during sideways flight or hovering in a crosswind, then directional (yaw) control may be seriously impaired. This is a safety of flight issue – see Section 6.9.

2.13.7 *Autorotation*

Notice that from the universal power curve in Fig. 2.20 there is actually a value of V_c/v_h for which zero net power is required for the rotor [i.e., $P = T(V_c + v_i) = 0$ or $P/P_h = 0$]. This condition is called *ideal autorotation* for vertical flight. For a given thrust it is a self-sustained operating state where the energy to drive the rotor comes from potential energy converted to kinetic energy from the relative descent velocity (which is upward relative to the rotor). The principle of autorotation can be seen in nature in the flight of sycamore or maple seeds, which spin rapidly as they slowly descend and are often carried on the wind for a considerable distance. In practice an autorotation is a maneuver that can be used to recover the helicopter to the ground in the event of an engine failure, transmission problems, or loss of the tail rotor. It requires that the pilot let the helicopter descend at a sufficiently high but controlled rate, where the energy to drive the rotor can be obtained by giving up potential energy (altitude) for energy taken from the relative upward flow through the rotor, thereby averting a ballistic fall.

On the basis of assuming the validity of Eq. 2.94, it will be apparent that the power curve crosses the ideal autorotation line $V_c + v_i = 0$ at

$$\frac{V_c}{v_h} = -\left(\frac{7\kappa}{1+3\kappa}\right), \tag{2.100}$$

which gives $V_c/v_h = -1.75$ for an ideal rotor ($\kappa = 1$). In practice, a real (actual) autorotation in axial flight occurs at a slightly higher rate than this, because in addition to induced losses at the rotor, there are also a proportion of profile losses to overcome. In a real autorotation we can write

$$P = \kappa T\,(V_c + v_i) + P_0 = 0. \tag{2.101}$$

Therefore, in a stable autorotation an energy balance must exist where the decrease in potential energy of the rotor TV_c just balances the sum of the induced ($\kappa T v_i$) *and* profile

(P_0) losses of the rotor. Using Eq. 2.101, we see that this condition is achieved when

$$\frac{V_c + v_i}{v_h} = -\frac{P_0}{\kappa T v_h} = -\frac{P_0\sqrt{2\rho A}}{\kappa T^{3/2}} = -\frac{P_0\sqrt{2\rho A}}{\kappa W^{3/2}}, \tag{2.102}$$

which depends primarily on the disk loading. Also, using the definition of figure of merit (and assuming the induced and profile losses do not vary substantially from the hover values), then Johnson (1980) shows that

$$\frac{P_0\sqrt{2\rho A}}{T^{3/2}} = \left(\frac{1}{FM} - \kappa\right). \tag{2.103}$$

Using Eq. 2.94 for the induced velocity with Eq. 2.103 gives the real autorotation condition:

$$\frac{V_c}{v_h} = -\frac{FM^{-1} - \kappa}{1 + 3\kappa} - \frac{7\kappa}{1 + 3\kappa}. \tag{2.104}$$

The first term on the right-hand side of Eq. 2.104 will vary in magnitude from -0.04 to -0.09, depending on the rotor efficiency. Compared to the second term, the extra rate of descent required to overcome profile losses is relatively small. Therefore, on the basis of the foregoing, it is apparent that a real vertical autorotation will occur for values of V_c/v_h between -1.85 and -1.9, that is, according to Fig. 2.20, with the rotor operating in the turbulent wake state. Under these autorotative conditions, the flow above the rotor is known from experimental tests to be relatively turbulent and to resemble that from behind a bluff body (see Question 2.15).

It is interesting to find the effective drag coefficient, $C_{D_{\text{eff}}}$, acting on the rotor in this flow state. We can equate the rotor thrust to its effective drag force using

$$T = W = \frac{1}{2}\rho V_c^2 A C_{D_{\text{eff}}}. \tag{2.105}$$

Now in hover we know that $T = 2\rho A v_h^2$, so solving for $C_{D_{\text{eff}}}$ for the autorotational condition $V_c/v_h \approx -1.9$ gives

$$C_{D_{\text{eff}}} = \frac{4}{(V_c/v_h)^2} \approx \frac{4}{(-1.9)^2} = 1.11. \tag{2.106}$$

This is close to the drag coefficient of bluff bodies [see Hoerner (1965), where $C_D = 1.11$ for a disk, $C_D = 1.2$ for a closed hemisphere and $C_D = 1.33$ for an open hemisphere], which means that aerodynamically the rotor produces a resultant force equivalent to a parachute when in the autorotative state.

It is found that with a helicopter, autorotations must be performed at relatively high rates of descent. Using the result that $v_h \approx 14.49\sqrt{T/A}$, where T/A is in lb/ft^2, gives $V_c \approx -26.81\sqrt{T/A}$ ft s^{-1} for autorotation at sea level conditions, which for a representative disk loading of 10 lb ft^{-2} leads to a vertical rate of descent of about 5,000 ft min^{-1}! However, it is shown in later in Section 5.6 that with some additional forward speed, the power required at the rotor is considerably lower than in the hover case. Because autorotations involve an energy balance, the autorotative rate of descent can be reduced by about half with some forward airspeed, although in practice this is still a relatively high rate. Consequently, in an autorotation the proper recovery of the helicopter requires a high level of skill from the pilot. As the helicopter approaches the ground, the rotational kinetic energy

stored in the rotor can be used to arrest the rate of descent. To do this, the pilot will flare the helicopter using cyclic pitch (which helps to increase rotor rpm and stored rotational kinetic energy in the rotor) and then progressively increase the collective pitch so that the helicopter will settle onto the ground with minimum vertical and forward velocity. At this point, the rotational kinetic energy stored in the rotor will have been nearly exhausted and the rpm will have decayed to a low value. Clearly, the autorotative characteristics of the helicopter affect safety of flight and so autorotational capability becomes an important design issue. Autorotational flight performance is addressed further in Chapters 3, 5, and 6.

2.14 Momentum Analysis in Forward Flight

Under forward flight conditions the rotor moves through the air with an edgewise component of velocity that is parallel to the plane of the rotor disk. Because helicopter rotors are required to produce both a lifting force (to overcome the weight of the helicopter) and a propulsive force (to propel the helicopter forward), the rotor disk must be tilted forward at an AoA relative to the oncoming flow. Under these conditions the axisymmetry of the flow through the rotor is lost. Despite the inherently more complicated nature of the rotor flow in forward flight, the simple momentum theory can be extended to encompass these conditions on the basis of certain assumptions.

The following treatment of rotor performance in forward flight was first derived by Glauert (1928, 1935). An adaptation of Glauert's flow model is shown in Fig. 2.23, where the analysis is performed with respect to an axis aligned with the rotor disk. The mass flow rate, $\dot{m}$, through the actuator disk is now

$$\dot{m} = \rho A U, \tag{2.107}$$

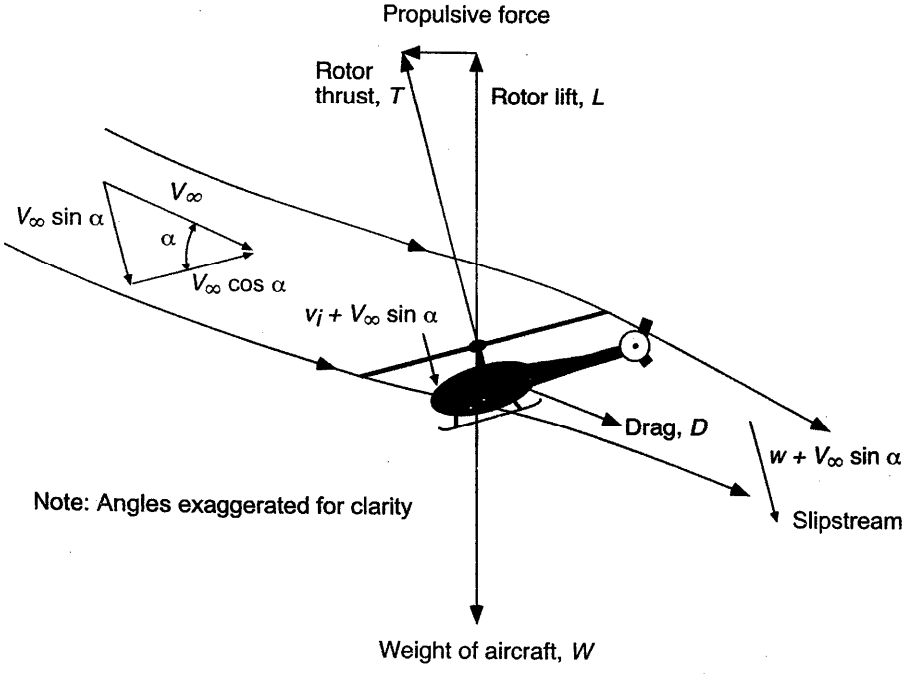

Figure 2.23 Glauert's flow model for the momentum analysis of a rotor in forward flight.

where U is the resultant velocity at the disk and is given by

$$U = \sqrt{(V_\infty \cos\alpha)^2 + (V_\infty \sin\alpha + v_i)^2} = \sqrt{V_\infty^2 + 2V_\infty v_i \sin\alpha + v_i^2}. \tag{2.108}$$

Glauert makes note that there is no rigor in this assumption for the resultant velocity other than it allows the forward flight theory to reduce to the correct limits in hovering and forward flight – a point also noted by Squire (1948). The application of the conservation of momentum in a direction normal to the disk gives

$$T = \dot{m}(w + V_\infty \sin\alpha) - \dot{m} V_\infty \sin\alpha = \dot{m} w \tag{2.109}$$

and by the application of conservation of energy, we obtain

$$\begin{aligned} P = T(v_i + V_\infty \sin\alpha) &= \frac{1}{2}\dot{m}(V_\infty \sin\alpha + w)^2 - \frac{1}{2}\dot{m} V_\infty^2 \sin^2\alpha \\ &= \frac{1}{2}\dot{m}\left(2V_\infty w \sin\alpha + w^2\right). \end{aligned} \tag{2.110}$$

Using Eqs. 2.109 and 2.110 we get

$$2wv_i + 2V_\infty w \sin\alpha = 2V_\infty w \sin\alpha + w^2 \tag{2.111}$$

or simply $w = 2v_i$, which is the same result shown previously for the axial flight cases. Therefore,

$$T = 2\dot{m} v_i = 2\rho A U v_i = 2\rho A v_i \sqrt{V_\infty^2 + 2V_\infty v_i \sin\alpha + v_i^2}. \tag{2.112}$$

Notice that for hovering flight, $V_\infty = 0$, so that Eq. 2.112 reduces to

$$T = 2\rho A v_i^2 = 2\rho A v_h^2, \tag{2.113}$$

which confirms that the forward flight result above reduces to the hover result (Eq. 2.14), as required. As forward flight speed increases such that $V_\infty \gg v_i$, then Eq. 2.112 reduces to

$$T = 2\rho A v_i V_\infty, \tag{2.114}$$

which is called Glauert's "high-speed" approximation. This latter result is exactly the lift on an elliptically loaded fixed-wing with a circular planform of radius R, and it should be expected that the results of the momentum theory analysis of the rotor in high-speed forward flight (excluding stall and reverse flow) should agree with fixed-wing theories (see Question 2.16). This is because the rotational speed of the rotor becomes a relatively smaller part of the forward flight velocity and the rotor must act more and more like a regular wing. This can be shown starting from the elliptical form of the spanwise circulation, Γ, on the wing, that is,

$$\Gamma(y) = \Gamma_0 \sqrt{1 - \left(\frac{y}{R}\right)^2}, \tag{2.115}$$

where Γ_0 is the circulation at mid-span ($y = 0$). By using the transformation $y = -R\cos\theta$ this result can be written simply as

$$\Gamma(\theta) = \Gamma_0 \sin\theta. \tag{2.116}$$

The total lift on the wing can be obtained by integration using

$$T = L = \rho V_\infty \int_{-R}^{R} \Gamma(y)\, dy = \rho V_\infty R \int_0^\pi \Gamma(\theta) \sin\theta\, d\theta = \rho V_\infty \Gamma_0 R \left(\frac{\pi}{2}\right). \tag{2.117}$$

For an elliptically loaded wing of eliptical planform then the induced downwash v_i is constant across the span and is related to Γ_0 by

$$v_i = \frac{\Gamma_0}{4R}. \tag{2.118}$$

Rearranging and substituting in Eq. 2.117 gives the lift as

$$L = T = \rho V_\infty R \left(\frac{\pi}{2}\right)(4Rv_i) = 2\rho V_\infty v_i(\pi R^2) = 2\rho A v_i V_\infty, \tag{2.119}$$

which is exactly the result in Eq. 2.114. See also Ormiston (2004) for a more detailed discussion of such equivalent wing concepts and their limitations.

2.14.1 *Induced Velocity in Forward Flight*

In forward flight, it has been shown in Eq. 2.112 that the rotor thrust is given by

$$T = 2\dot{m}v_i = 2(\rho A U)v_i \tag{2.120}$$

or

$$T = 2\rho A v_i \sqrt{(V_\infty \cos\alpha)^2 + (V_\infty \sin\alpha + v_i)^2}. \tag{2.121}$$

Recall from Eq. 2.113 that for hovering flight $v_h^2 = T/2\rho A$, then the induced velocity in forward flight can be written as

$$v_i = \frac{v_h^2}{\sqrt{(V_\infty \cos\alpha)^2 + (V_\infty \sin\alpha + v_i)^2}}. \tag{2.122}$$

The idea of a *tip speed ratio* or *advance ratio*, μ, is now used. By using the velocity parallel to the plane of the rotor, then we define $\mu = V_\infty \cos\alpha / \Omega R$. The inflow ratio is $\lambda = (V_\infty \sin\alpha + v_i)/\Omega R$. This leads to the expression

$$\lambda = \frac{V_\infty \sin\alpha}{\Omega R} + \frac{v_i}{\Omega R} = \mu \tan\alpha + \lambda_i. \tag{2.123}$$

Also, Eq. 2.122 becomes

$$\lambda_i = \frac{\lambda_h^2}{\sqrt{\mu^2 + \lambda^2}}. \tag{2.124}$$

But, it is also known from the hover case that $\lambda_h = \sqrt{C_T/2}$, therefore,

$$\lambda_i = \frac{C_T}{2\sqrt{\mu^2 + \lambda^2}}. \tag{2.125}$$

Finally, the solution for the inflow ratio, λ, is

$$\lambda = \mu \tan\alpha + \frac{C_T}{2\sqrt{\mu^2 + \lambda^2}}. \tag{2.126}$$

While analytic solutions to this equation can be found, in practice a simple numerical procedure is usually used to solve for λ.

2.14.2 *Special Case, $\alpha = 0$*

If the disk AoA is zero ($\alpha = 0$), an exact analytical solution for λ can be determined. This is a physically unrealistic situation because the rotor must always be tilted slightly forward to produce a propulsive force. However, this special solution serves to illustrate the basic form of the induced part of the inflow through the rotor disk in forward flight and also provides a check case for the numerical solution (considered next). With $\alpha = 0$, the induced velocity ratio in forward flight is

$$\lambda_i = \frac{C_T}{2\sqrt{\mu^2 + \lambda_i^2}} = \frac{\lambda_h^2}{\sqrt{\mu^2 + \lambda_i^2}}. \tag{2.127}$$

Squaring both sides of the above equation and rearranging gives

$$\lambda_i^4 + \mu^2\lambda_i^2 - \lambda_h^4 = 0. \tag{2.128}$$

Dividing by λ_h^4 gives

$$\left(\frac{\lambda_i}{\lambda_h}\right)^4 + \left(\frac{\mu}{\lambda_h}\right)^2\left(\frac{\lambda_i}{\lambda_h}\right)^2 - 1 = 0, \tag{2.129}$$

which is a quadratic in $(\lambda_i/\lambda_h)^2$. This quadratic has the solution

$$\frac{\lambda_i}{\lambda_h} = \left[\sqrt{\frac{1}{4}\left(\frac{\mu}{\lambda_h}\right)^4 + 1} - \frac{1}{2}\left(\frac{\mu}{\lambda_h}\right)^2\right]^{1/2}. \tag{2.130}$$

This result is shown in nondimensional form in Fig. 2.24. Notice that the induced velocity decreases quite quickly with increasing forward flight velocity. The asymptotic

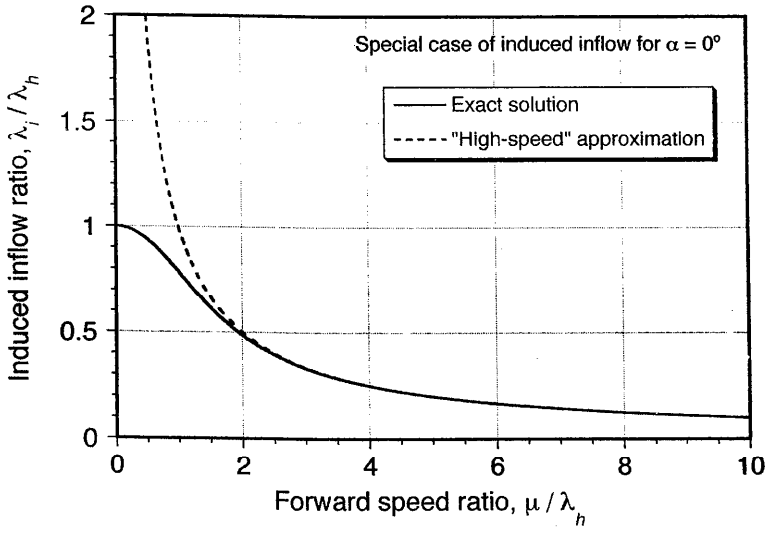

Figure 2.24 Induced inflow ratio at the rotor disk λ_i/λ_h as a function of forward speed ratio μ/λ_h for $\alpha = 0$.

approximation is obtained by letting $\mu \gg \lambda$, so that in high-speed forward flight Eq. 2.127 gives

$$\frac{\lambda_i}{\lambda_h} \to \frac{\lambda_h}{\mu} \quad \text{or that} \quad \lambda_i = \frac{C_T}{2\mu} \text{ (Glauert's high-speed approximation)}, \tag{2.131}$$

which is denoted by the broken line in Fig. 2.24. For most purposes, this approximation is satisfactory for $\mu/\lambda_h > 2$, which in practice is the case for $\mu > 0.1$.

2.14.3 *Numerical Solution to Inflow Equation*

Because α can never be zero in any practical case, Eq. 2.126 is usually solved numerically. While analytic solutions of the inflow equation for $\alpha \neq 0$ are possible, proper selection of the correct root from a set of multiple complex roots make the approach academic and of little practical engineering use. There are two common numerical approaches: 1. A simple fixed-point iteration or 2. A Newton–Raphson iteration. The algorithm for the fixed-point iteration is extremely simple. It consists of a loop to iteratively compute new estimates of λ until a termination criterion has been met. Equation 2.126 can be written as the iteration equation

$$\lambda_{n+1} = \mu \tan\alpha + \frac{C_T}{2\sqrt{\mu^2 + \lambda_n^2}}, \tag{2.132}$$

where n is the iteration number. The starting value for λ_0 is usually the hover value (i.e., $\lambda_0 = \lambda_h = \sqrt{C_T/2}$). The error estimator is

$$\epsilon = \left\| \frac{\lambda_{n+1} - \lambda_n}{\lambda_{n+1}} \right\|. \tag{2.133}$$

Normally, convergence is said to occur if $\epsilon < 0.0005$ or 0.05%. One normally finds that between 10 and 15 iterations are required with the fixed-point iteration approach (Fig. 2.25). However, under some conditions, especially at lower advance ratios, a larger number of iterations may be necessary.

One can also use a Newton–Raphson procedure to solve for λ. The advantage here is that for the price of computing a simple first derivative the convergence is much more rapid. In this case, the iteration scheme is

$$\lambda_{n+1} = \lambda_n - \left[\frac{f(\lambda)}{f'(\lambda)}\right]_n, \tag{2.134}$$

where n is the iteration number. Equation 2.126 may be rearranged in the form $f(\lambda) = 0$ giving

$$f(\lambda) = \lambda - \mu\tan\alpha - \frac{C_T}{2\sqrt{\mu^2 + \lambda^2}} = 0. \tag{2.135}$$

Differentiating this expression to find $f'(\lambda)$ gives

$$f'(\lambda) = 1 + \frac{C_T}{2}\left(\mu^2 + \lambda^2\right)^{-3/2}\lambda. \tag{2.136}$$

Although the Newton–Raphson method can be sensitive to the starting value (initial conditions), in most cases the hover value $\lambda_0 = \lambda_h$ works well, with only 3–4 iterations

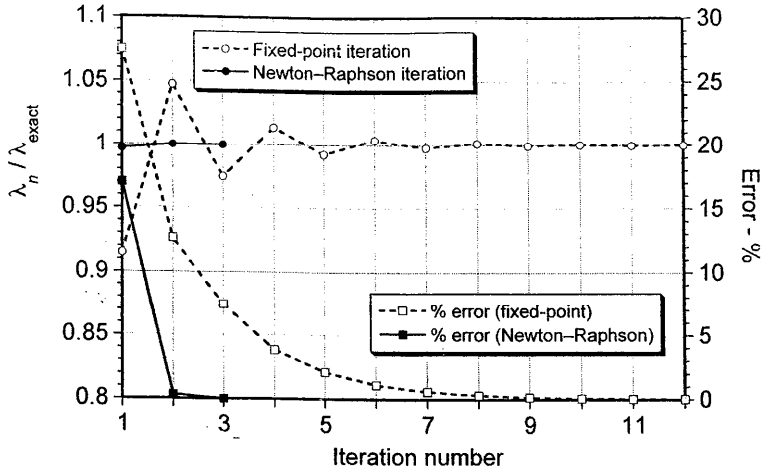

Figure 2.25 The solution of the inflow equation is obtained iteratively, with rapid convergence.

being required to reach the tolerance compared to up to 10 or more iterations using fixed-point iteration, as shown in Fig. 2.25. However, the computing costs with either method are essentially trivial on a computer. See also Questions 2.17 and 2.18.

Results for the inflow ratio λ/λ_h as computed using the iterative scheme are plotted in Fig. 2.26 for several different values of α (both positive and negative) and over a range of values of μ/λ_h typical of a helicopter. Notice that the induced part of the total inflow decreases with increasing advance ratio and the total inflow becomes dominated by the $\mu \tan \alpha$ term at higher advance ratios. Notice also that negative disk angles ultimately produce a negative inflow (upflow) through the disk, which means that the rotor is approaching a zero power required state or the autorotational condition (see Section 2.14.6).

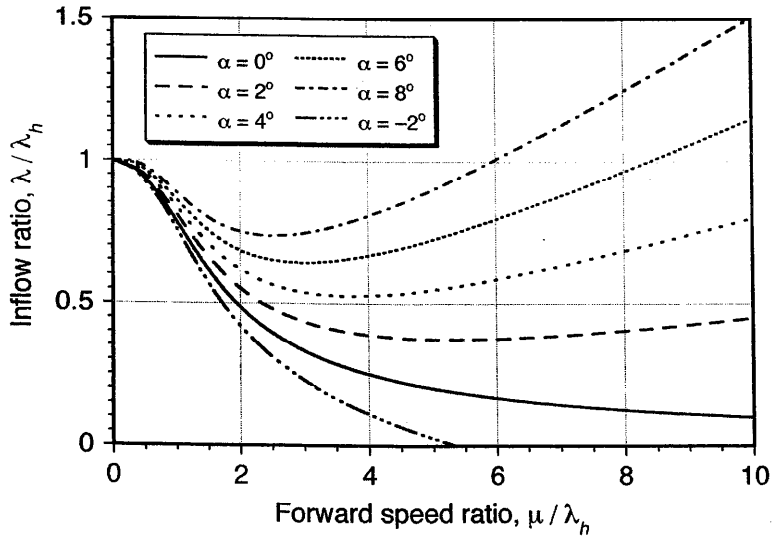

Figure 2.26 Inflow ratio λ/λ_h as a function of forward speed ratio μ/λ_h for several rotor disk angles of attack.

2.14.4 *General Form of the Inflow Equation*

The inflow equation given by Eq. 2.126 needs to be written in a more general form for climbing or descending flight. In this case the inflow ratio can be rewritten as

$$\lambda = \mu_x \tan\alpha + \frac{C_T}{2\sqrt{\mu_x^2 + \lambda^2}} + \mu_y. \tag{2.137}$$

where $\mu_x = V_\infty \cos\alpha / \Omega R$ and $\mu_y = V_\infty \sin\alpha / \Omega R$ can be recognized as the advance ratios defined parallel and perpendicular to the rotor disk, respectively. It will be apparent that this latter equation can be written simply as

$$\lambda = \mu \tan\alpha + \frac{C_T}{2\sqrt{\mu^2 + \lambda^2}} + \lambda_c \cos\alpha. \tag{2.138}$$

2.14.5 *Validity of the Inflow Equation*

The inflow equation as given by Eq. 2.126 or Eq. 2.137 is widely employed for practical calculations involving rotors in climbing and descending flight in both axial and forward flight. However, a nonphysical solution will always be obtained if there is a descent (upward) component of velocity normal to the rotor disk that is between 0 and $2v_i$ (i.e., if $-2v_i \leq V_\infty \sin\alpha \leq 0$ in level flight). Under these conditions there can always be two possible directions for the flow and there can be no well-defined slipstream boundary as was assumed in the physical model. Therefore, the momentum theory cannot be applied under these conditions. For example, this can occur when the rotor disk is at steep angles of attack.

With the numerical solution several things may occur if these restrictions are ignored. First, the simple fixed-point iteration method may not converge. This will always be the case for axial flight ($\mu = 0$) when $-2 \leq V_c/v_i \leq 0$. Second, the fixed-point iteration method may converge, but to a nonphysical solution. In such cases caution should be exercised and the results should probably not be used unless validated by other means. The Newton–Raphson method will generally converge under all conditions, but again the solutions will be nonphysical in the range $-2v_i \leq V_\infty \sin\alpha \leq 0$. The Newton–Raphson method is also sensitive to the initial conditions and may converge to different nonphysical solutions if inappropriate initial conditions are used. Generally it is assumed that $\lambda_0 = \sqrt{C_T/2}$ and this will be satisfactory when the rotor is in the normal working state. However, this initial condition will cause the method to fail for descents (i.e., $V_c < 0$). Here, convergence of the Newton–Raphson method to the proper physical result can generally be ensured if $\lambda_0 = -|\lambda_c|$. Overall, results from the numerical solution to the inflow equation should be used with sensible cross checks to the analytic results wherever possible.

2.14.6 *Rotor Power Requirements in Forward Flight*

The rotor power in forward flight is given by the equation

$$P = T(V_\infty \sin\alpha + v_i) = TV_\infty \sin\alpha + Tv_i \tag{2.139}$$

assuming no viscous losses at this stage. The first term on the right-hand side of the above equation is the power required to propel the rotor forward and also to climb. The second

term is the induced power. As for the axial flight case, we may reference the rotor power in forward flight to the hover result and so

$$\frac{P}{P_h} = \frac{P}{Tv_h} = \frac{T(V_\infty \sin\alpha + v_i)}{Tv_h} = \frac{V_\infty \sin\alpha + v_i}{v_h} = \frac{\lambda}{\lambda_h}. \tag{2.140}$$

Therefore, the form of the power curve simply mimics the inflow curves shown previously in Fig. 2.26. Notice that the power requirements decrease significantly to a minimum value and then increase again. This is a fundamental characteristic of a helicopter and the behavior[3] is examined in much further detail in Chapter 5. The behavior was first noticed in early experiments by Maxim (1897), Riabouchinsky (1906), and Beliner (1908) (see page 16). The results also depend on the disk angle of attack, which must always be tilted forward slightly for propulsion (see Fig. 2.23). Recall that

$$\lambda = \mu\tan\alpha + \frac{C_T}{2\sqrt{\mu^2+\lambda^2}} = \mu\tan\alpha + \frac{\lambda_h^2}{\sqrt{\mu^2+\lambda^2}}. \tag{2.141}$$

Therefore,

$$\frac{\lambda}{\lambda_h} = \frac{P}{P_h} = \frac{\mu}{\lambda_h}\tan\alpha + \frac{\lambda_h}{\sqrt{\mu^2+\lambda^2}}. \tag{2.142}$$

The first term on the right-hand side of the above equation is the extra power to meet propulsion and climb requirements, whereas the second term is the induced power. As mentioned previously, the evaluation of the propulsive power requires a knowledge of the rotor disk angle of attack, which in turn requires a knowledge of the helicopter's drag, D. Assuming straight-and-level flight, the disk angle of attack, α, can be calculated from a simple force equilibrium (see Fig. 2.23). For vertical equilibrium $T\cos\alpha = W$ and for horizontal equilibrium $T\sin\alpha = D\cos\alpha \approx D$. Therefore,

$$\tan\alpha = \frac{D}{W} = \frac{D}{L} \approx \frac{D}{T}, \tag{2.143}$$

which is expressed in terms of the helicopter's overall lift-to-drag ratio. Therefore, the power equation in straight-and-level flight can be written as

$$\frac{P}{P_h} = \frac{\mu}{\lambda_h}\left(\frac{D}{T}\right) + \frac{\lambda_h}{\sqrt{\mu^2+\lambda^2}}. \tag{2.144}$$

The determination of D, however, requires a knowledge of both the drag on the rotor and the drag on the airframe, the latter of which is called *parasitic drag*. The rotor drag must be estimated using blade element theory. The AoA of the disk relative to the oncoming flow will change in a climb or descent, thereby altering the power required. In this case, the power ratio can be written as

$$\frac{P}{P_h} = \lambda_c\cos\alpha + \frac{\mu}{\lambda_h}\tan\alpha + \frac{\lambda_h}{\sqrt{\mu^2+\lambda^2}}, \tag{2.145}$$

where λ_c is climb velocity ratio. In each case, the disk AoA can be solved for on the basis of a free-flight force equilibrium (even if this is only approximate).

[3] From a piloting perspective the decrease in power requirements for flight found when moving from hover cause an excess power available and so the helicopter will climb. Pilots often call this climbing behavior "translational lift," but the term is a misnomer because unless significant acceleration is involved, rotor lift equals helicopter weight and the helicopter climbs by virtue of the excess power available not from excess lift generation.

2.15 Other Applications of the Momentum Theory

The momentum theory analysis has found use in the analysis of other helicopter rotor designs, including contrarotating coaxials, tandems, and ducted fans. The former are now discussed, with the ducted fan problem being discussed later in relation to a fan-in-fin rotor or fenestron concept in Section 6.10.1.

2.15.1 *Coaxial Rotor Systems*

One advantage of the contrarotating coaxial rotor design is that the net size of the rotor(s) is reduced (for a given helicopter gross weight) because each rotor now provides vertical thrust. In addition, no tail rotor is required for anti-torque purposes, so that all power can be devoted to providing useful vertical lift and performance. However, the two rotors and their wakes interact with one another (e.g., Fig 1.38), producing a somewhat more complicated flow field than is found with a single rotor, and this interacting flow incurs a loss of net rotor system aerodynamic efficiency. Coleman (1993) gives a good summary of coaxial helicopter rotors and a comprehensive list of relevant citations on performance, wake characteristics and methods of analysis.

Following Payne (1959), consider a simple momentum analysis of the hovering coaxial rotor problem. Assume that the rotor planes are sufficiently close together and that each rotor provides an equal fraction of the total system thrust, $2T$, where $T = W/2$. The effective induced velocity of the rotor system will be

$$(v_i)_e = \sqrt{\frac{2T}{2\rho A}}. \tag{2.146}$$

Therefore, the induced power is

$$(P_i)_{\text{tot}} = 2T(v_i)_e = \frac{(2T)^{3/2}}{\sqrt{2\rho A}}. \tag{2.147}$$

However, if we treat each rotor separately then the induced power for either rotor will be Tv_i and for the two separate rotors

$$P_i = \frac{2T^{3/2}}{\sqrt{2\rho A}}. \tag{2.148}$$

If the interference-induced power factor κ_{int} is considered to be the ratio of Eqs. 2.147 and 2.148 then

$$\kappa_{\text{int}} = \frac{(P_i)_{\text{tot}}}{P_i} = \left(\frac{(2T)^{3/2}}{\sqrt{2\rho A}}\right)\left(\frac{2T^{3/2}}{\sqrt{2\rho A}}\right)^{-1} = \sqrt{2}, \tag{2.149}$$

which is a 41% increase in induced power relative to the power required to operate the two rotors in complete isolation.

This simple momentum analysis of the problem has been shown to be overly pessimistic when compared with experimental measurements for closely spaced coaxial rotors – see Harrington (1951) and the review by Coleman (1993). The main reason for the overprediction of induced power is related to the actual (finite) spacing between the two rotors. Generally, on coaxial designs the rotors are spaced sufficiently far apart that the lower rotor operates in the vena contracta of the upper rotor. This is justified from the flow visualization results of Taylor (1950), for example. Based on ideal flow considerations, this

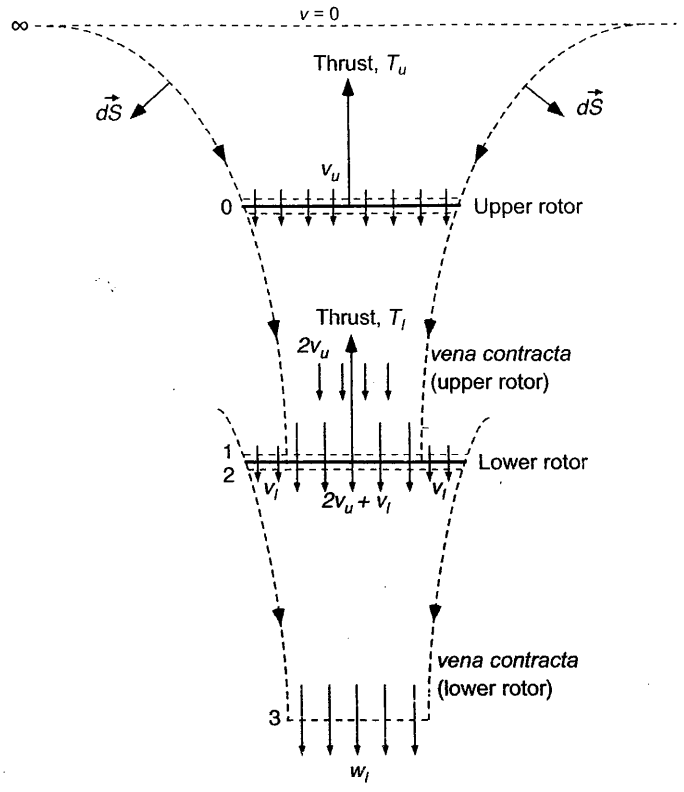

Figure 2.27 Flow model for a coaxial rotor analysis, where the lower rotor is considered to operate in the fully developed slipstream of the upper rotor.

means that only half of the area of the lower rotor operates in an effective climb velocity induced by the upper rotor.

This problem can be tackled by means of the simple momentum theory and the application of the mass, momentum, and energy conservation equations in integral form. We will assume that the performance of the upper rotor is not influenced by the lower rotor. The induced velocity at the upper rotor is

$$v_u = \sqrt{\frac{T}{2\rho A}} = v_h, \tag{2.150}$$

where A is the disk area and T is the thrust on the upper rotor. The vena contracta of the upper rotor is an area of $A/2$ with velocity $2v_u$. Therefore, at the plane of the lower rotor there is a velocity of $2v_u + v_l$ over the inner one-half of the disk area – see Fig. 2.27.

Over the outer one-half of the disk area, the induced velocity is v_l. Assume that the velocity in the fully developed slipstream of the lower rotor (plane 3) is uniform with velocity w_l. The mass flow rate through the upper rotor is $\rho A v_u$, so that the momentum exiting in the slipstream of the upper rotor is $(\rho A v_u)2v_u = 2\rho A v_u^2$. This is the momentum of the fluid into the lower rotor. The mass flow rates over the inner and outer parts of the lower rotor are $\rho(A/2)(2v_u + v_l)$ and $\rho(A/2)v_l$, respectively. Therefore,

$$\dot{m} = \rho\frac{A}{2}(2v_u + v_l) + \rho\left(\frac{A}{2}\right)v_l = \rho A\,(v_u + v_l)\,. \tag{2.151}$$

The momentum flow out of plane 3 is $\dot{m}w_l$, so the thrust on the lower rotor is

$$T_l = \rho A\,(v_u + v_l)\,w_l - 2\rho A v_u^2. \tag{2.152}$$

The work done by the lower rotor is

$$P_l = T_l(v_u + v_l), \tag{2.153}$$

and this is equal to the gain in kinetic energy of the slipstream. Therefore,

$$\begin{aligned} T_l(v_u + v_l) &= \frac{1}{2}\rho A\,(v_u + v_l)\,w_l^2 - \frac{1}{2}\rho\left(\frac{A}{2}\right)(2v_u)(2v_u)^2 \\ &= \frac{1}{2}\rho A\,(v_u + v_l)\,w_l^2 - 2\rho A v_u^3. \end{aligned} \tag{2.154}$$

Assuming $T_l = T_u = T$, then $T = 2\rho A v_u^2$, then from Eq. 2.152 we get

$$T_l = T = \frac{1}{2}\rho A(v_u + v_l)w_l, \tag{2.155}$$

and from Eq. 2.154 we get

$$T(2v_u + v_l) = \frac{1}{2}\rho A(v_u + v_l)w_l^2. \tag{2.156}$$

Using Eqs. 2.155 and 2.156 gives $w_l = 2v_u + v_l$ and substituting this into Eq. 2.155 and remembering that $T = 2\rho A v_u^2$ gives

$$4\rho A v_u^2 = \rho A\,(v_u + v_l)\,w_l = \rho A\,(v_u + v_l)\,(2v_u + v_l)\,. \tag{2.157}$$

Rearranging as a quadratic in terms of v_l and solving gives

$$v_l = \left(\frac{-3 + \sqrt{17}}{2}\right) v_u = 0.5616 v_u. \tag{2.158}$$

The power for the upper rotor is $P_u = T v_u = T v_h$ and for the lower rotor $P_l = T(v_u + v_l) = 1.5616 T v_h$. Therefore, for both rotors the total power is $2.5616 T v_h$. This is compared to $2T v_h$ when the rotors are operating in isolation. This means that the induced power factor from interference, κ_{int}, is given by

$$\kappa_{\text{int}} = \frac{(P_i)_{\text{coax}}}{(2P_i)_{\text{isolated}}} = \frac{2.5616 T v_h}{2T v_h} = 1.281, \tag{2.159}$$

which is a 28% increase compared to a 41% increase when the two rotors have no vertical separation (see Questions 2.19 and 2.20). This is closer to the values deduced from experiments for which $\kappa_{\text{int}} \approx 1.16$ [see, for example, Dingeldein (1954)] but the theory still overpredicts the interference value. When the coaxial is operated at equal rotor torque (see Question 2.20), it can be shown that the induced power factor is given by

$$\kappa_{\text{int}} = \frac{2P_u}{(T_u + T_l)v_u} = 2\sqrt{2}\left(\frac{T_u}{T_l}\right)^{3/2}\left(1 + \frac{T_u}{T_l}\right)^{-3/2} = 1.281, \tag{2.160}$$

which is the same result as for the thrust balanced case when compared to two isolated rotors operated at the same thrust. When compared to two isolated rotors at the thrusts needed for a torque balance, then $\kappa_{\text{int}} = 1.266$.

Figure 2.28 shows the power versus thrust relationship of single and coaxial rotors operating in hover; the measurements are taken from Harrington (1951) and Dingeldein

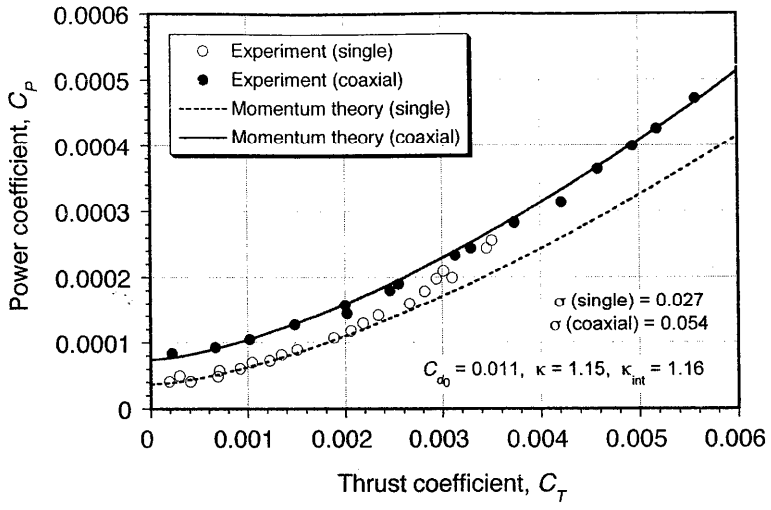

Figure 2.28 Hover performance predictions for a coaxial rotor compared to measurements. Data source: Harrington (1951) and Dingeldein (1954).

(1954). The corresponding plot of figure of merit versus C_T/σ is shown in Fig. 2.29. The power for the single two-bladed rotor was calculated from momentum theory using

$$P = \frac{\kappa T^{3/2}}{\sqrt{2\rho A}} + \rho A(\Omega R)^3\left(\frac{\sigma C_{d_0}}{8}\right) \tag{2.161}$$

and for the coaxial using

$$P = \frac{\kappa_{\text{int}}\,\kappa(2T)^{3/2}}{\sqrt{4\rho A}} + \rho A(\Omega R)^3\left(\frac{2\sigma C_{d_0}}{8}\right), \tag{2.162}$$

with $\kappa = 1.15$ and $\kappa_{\text{int}} = 1.16$. The agreement between momentum theory and the measurements is good and confirms that the coaxial rotor operates as two isolated rotors but with an interference effect accounted for by κ_{int}. In this case the performance of both the single and coaxial rotors is stall-limited because of their relatively low solidity and also the lower blade chord Reynolds numbers at this reduced tip speed test (see Chapter 7), but the momentum theory shows what would be possible if stall was not present. Clearly the coaxial achieves a somewhat lower maximum figure of merit compared to a single rotor, all other factors being equal (i.e., when compared at the same disk loading, solidity and tip speed).

To properly compare the relative efficiency of a single and coaxial rotor system they must be compared at the same equivalent disk loading, that is, each rotor operates at the same approximate value of T/A (or C_T/σ for a given radius and tip speed). Under these conditions the figure of merit of the coaxial can be written as

$$FM = \frac{\dfrac{C_T^{3/2}}{\sqrt{2}}}{\dfrac{\kappa_{\text{int}}\kappa C_T^{3/2}}{\sqrt{2}} + \dfrac{\sigma C_{d_0}}{8}}, \tag{2.163}$$

where $\kappa_{\text{int}} = 1$ for an isolated single rotor. Because the lower rotor of a coaxial operates in the slipstream of the upper rotor its net induced velocity is always higher for a given value

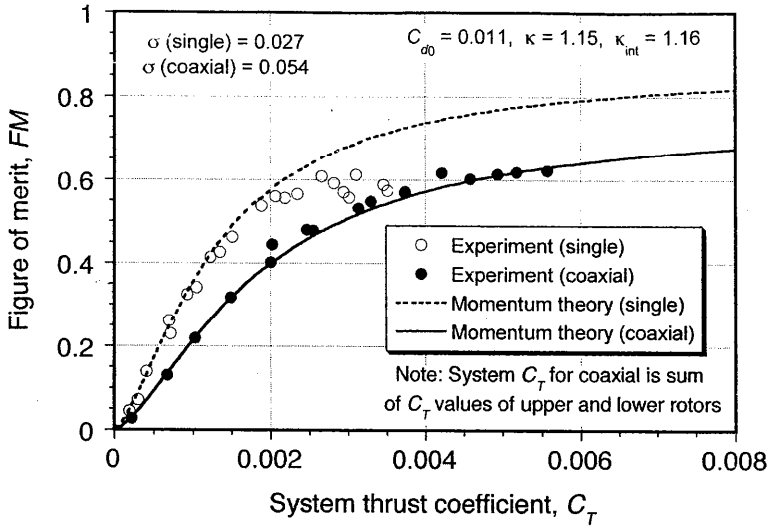

Figure 2.29 Figure of merit for a coaxial rotor compared to measurements. Data source: Dingeldein (1954).

of thrust and $\kappa_{int} > 1$ (where the values of κ_{int} depend on the assumptions made) and so the net system efficiency is lower. Representative results are shown in Fig. 2.30 where it is clear that at a typical operating state the *FM* for a coaxial when operated at the same blade loading coefficient is related approximately to the corresponding *FM* of a single by a factor κ_{int}. Other physical factors that seem to affect coaxial rotor performance include a thrust recovery effect through the removal of swirl losses in the downstream wake, although this effect seems only important at very high values of disk loading such as used on propellers. See also Andrew (1981), Saito & Azuma (1981), and Zimmer (1985) for more details on coaxial rotor performance.

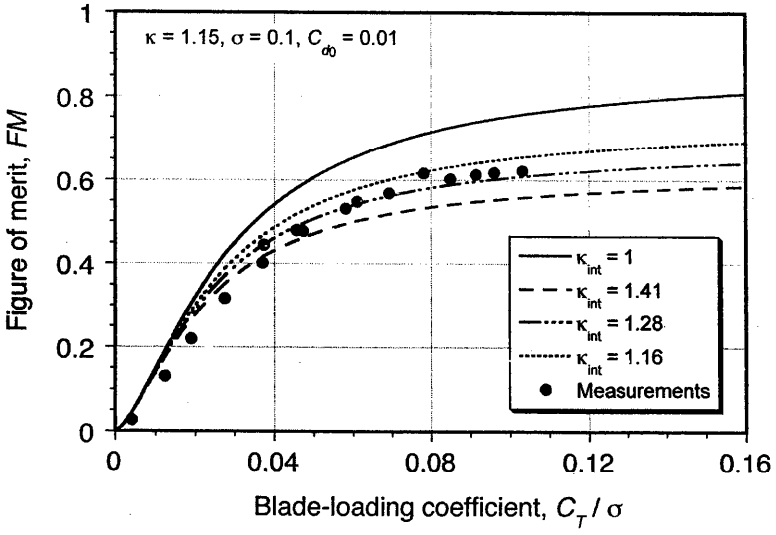

Figure 2.30 Hovering figure of merit for a coaxial rotor is less than a single rotor when operated at the same equivalent disk (or blade) loading.

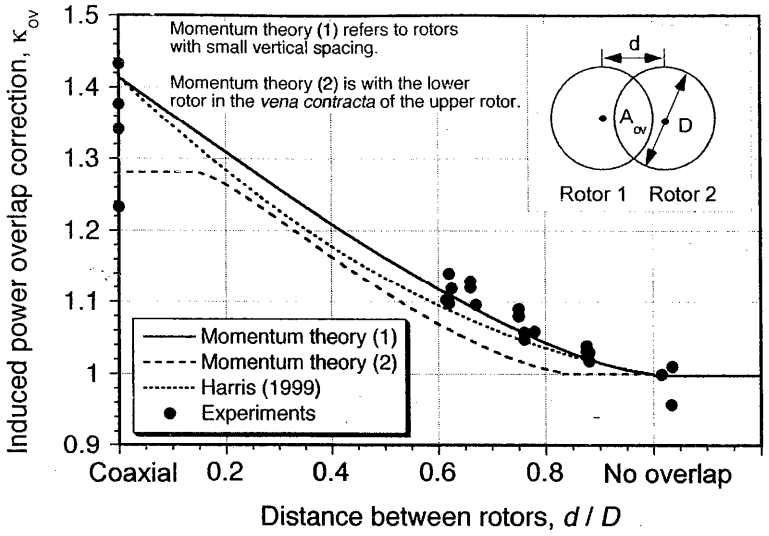

Figure 2.31 Tandem rotor overlap induced power correction in hover as derived from momentum theory and compared to measurements. Data sources: Dingeldein (1954) and Stepniewski & Keys (1984).

2.15.2 *Tandem Rotor Systems*

The basic momentum analysis can also be extended to overlapping tandem rotors. Tandem rotor designs are sometimes used for heavy-lift helicopters because like the coaxial design all of the rotor power can be used to provide useful lift. However, like a coaxial design, the induced power of partly overlapping tandem rotors is found to be higher than that of the two isolated rotors (Fig. 2.31). This is because one of the rotors must operate in the slipstream of the other rotor, resulting in a higher induced power for the same thrust. The tandem rotor problem is discussed extensively by Stepniewski (1955) and Stepniewski & Keys (1984). Other results for twin rotor performance are given by Fail & Squire (1947) and Sweet (1960).

The analysis of overlapping rotors from the perspective of momentum theory is normally based on the ideas of overlapping areas – see Payne (1959). Let $A_{ov} = mA$ be the overlap area according to the inset shown in Fig. 2.31 and also Fig. 2.32. The rotors are assumed to have no vertical spacing, which is Case 1 shown in Fig. 2.32. By means of the geometry of the problem it can be shown that

$$m' = \frac{A_{ov}}{A} = \frac{2}{\pi}\left[\theta - \frac{d}{D}\sin\theta\right], \quad \text{where } \theta = \cos^{-1}\left(\frac{d}{D}\right). \tag{2.164}$$

Let T_1 and T_2 be the thrusts on the two rotors, which may be unequal. Therefore, $m(T_1 + T_2)$ is the thrust on the overlapped region. Based on uniform inflow assumptions then the induced power of the rotors consumed by each of the areas is

$$P_1 = \frac{(1-m')T_1^{3/2}}{\sqrt{2\rho A}}, \quad P_2 = \frac{(1-m')T_2^{3/2}}{\sqrt{2\rho A}}, \quad \text{and} \quad P_{ov} = \frac{m'(T_1+T_2)^{3/2}}{\sqrt{2\rho A}}, \tag{2.165}$$

where the total power is $(P_i)_{tot} = P_1 + P_2 + P_{ov}$. If the rotors are isolated, then $m' = 0$ and the total system power will be

$$P_i = P_1 + P_2 = \frac{(T_1^{3/2} + T_2^{3/2})}{\sqrt{2\rho A}}. \tag{2.166}$$

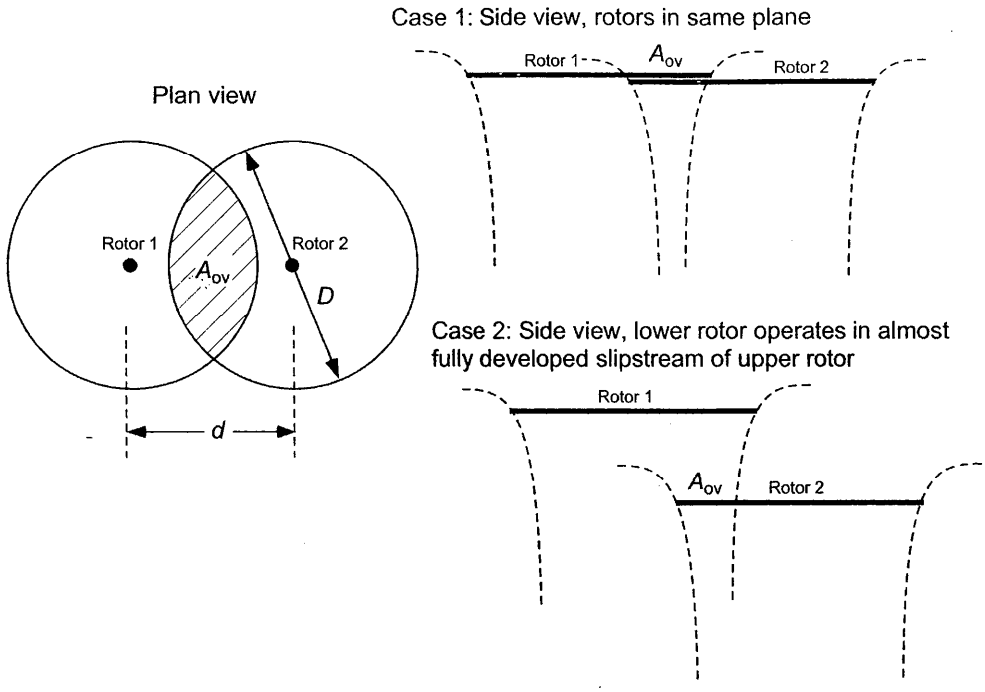

Figure 2.32 Flow models used for tandem rotor analysis. (a) Case 1: Rotors in same plane. (b) Case 2: Lower rotor operates in fully developed slipstream of upper rotor.

Proceeding as for the coaxial case, the induced power factor can be considered as the ratio

$$\frac{(P_i)_{\text{tot}}}{P_i} = \kappa_{\text{ov}} = \frac{(1-m')T_1^{3/2} + (1-m')T_2^{3/2} + m'(T_1+T_2)^{3/2}}{T_1^{3/2} + T_2^{3/2}}. \tag{2.167}$$

Therefore, the total induced power required to hover for a tandem overlapping design can be expressed as

$$P_i = \kappa_{\text{ov}}\, \kappa T \sqrt{\frac{T}{4\rho A}}, \tag{2.168}$$

where A is the disk area of any one of the two rotors and T is the total system thrust as generated by both rotors. If it is assumed that each rotor carries an equal fraction of the total thrust ($T_1 = T_2$) then

$$\frac{(P_i)_{\text{tot}}}{P_i} = \kappa_{\text{ov}} = 1 + (\sqrt{2}-1)m' = 1 + 0.4142\, m', \tag{2.169}$$

where m' is given by Eq. 2.164. Harris (1999) suggests an approximation to κ_{ov}, where

$$\kappa_{\text{ov}} \approx \left[\sqrt{2} - \frac{\sqrt{2}}{2}\left(\frac{d}{D}\right) + \left(1 - \frac{\sqrt{2}}{2}\right)\left(\frac{d}{D}\right)^2\right]. \tag{2.170}$$

The assumptions made in the derivation of the previous equations are not critical, as it can be shown that if each rotor carries a different fraction of the total thrust then κ_{ov} is only slightly higher than if an equal fraction is assumed (see Question 2.21). Notice that in Eq. 2.169 as $m' \to 1$, which is a coaxial, then $\kappa_{\text{ov}} \to \sqrt{2}$, as before. When the rotors are completely separated with no overlap ($m' = 0$), then $\kappa_{\text{ov}} \to 1$, as is required for isolated

rotor performance. The result of Eq. 2.169 is plotted in Fig. 2.31 in terms of the spacing ratio d/D, where d is the spacing between the two rotor axes and D is the rotor diameter. As d becomes larger and the rotors are more separated, the induced power overlap correction factor approaches unity.

An alternative analysis is to consider a situation where the lower rotor of the tandem operates in the fully contracted slipstream of the upper rotor – see Case 2 of Fig. 2.32. Here the overlap area is affected by the contracting wake from the upper rotor and m' must be determined by numerical integration. When the rotors are in the same plane then m' is given by Eq. 2.164. The analysis proceeds using as similar flow model to that shown previously in Fig. 2.27. Using the conservation of momentum, the thrust on the upper and lower rotors are

$$T_u = (\rho A v_u)(2v_u) \tag{2.171}$$

and

$$T_l = (\dot{m}w)_l - (\dot{m}w)_u. \tag{2.172}$$

The mass flow rates through the two rotors are

$$\dot{m}_u = m'\rho A(2v_u) \quad \text{and} \quad \dot{m}_l = (1-m')\rho A v_l + m'\rho A(v_l + 2v_u). \tag{2.173}$$

Assuming the thrust on the upper and lower rotor are equal gives

$$\left[(1-m')\rho A v_l + m'\rho A(v_l + 2v_u)\right]w_l - \left[m'\rho A(2v_u)\right](2v_u) = (\rho A v_u)(2v_u), \tag{2.174}$$

which after simplification becomes

$$\frac{v_u^2(4m'+2)}{w_l} = (v_l + 2m'v_u). \tag{2.175}$$

From the conservation of energy

$$P_l = T\left[(1-m')v_l + m'(v_l + 2v_u)\right] = \left(\frac{1}{2}\dot{m}w^2\right)_l - \left(\frac{1}{2}\dot{m}w^2\right)_u, \tag{2.176}$$

which can be simplified to get

$$T(v_l + 2m'v_u) = \frac{1}{2}\rho A(v_l + 2m'v_u)w_l^2 - 4\rho m' A v_u^3. \tag{2.177}$$

Equation 2.171 can now be substituted into Eq. 2.177 to get

$$2v_u^2(v_l + 2m'v_u) = \frac{1}{2}(v_l + 2m'v_u)w_l^2 - 4m'v_u^3. \tag{2.178}$$

Part of the second term in Eq. 2.178 can be replaced by Eq. 2.175 to give

$$2v_u^2(v_l + 2m'v_u) = \left(\frac{w_l^2}{2}\right)\left(\frac{v_u^2(4m'+2)}{w_l}\right) - 4m'v_u^3. \tag{2.179}$$

Equation 2.179 can be expanded, followed by dividing through by v_u^2, to give

$$2v_u^2 v_l + 4m'v_u^3 = 2m'v_u^2 w_l + v_u^2 w_l - 4m'v_u^3. \tag{2.180}$$

This can be further simplified to give the slipstream velocity at the lower rotor as

$$w_l = \frac{8m'v_u + 2v_l}{(2m'+1)}. \tag{2.181}$$

Equation 2.181 can now be substituted back into Eq. 2.175 to get

$$v_u^2(4m' + 2) = \left(\frac{8m'v_u + 2v_l}{2m' + 1}\right)(v_l + 2m'v_u), \tag{2.182}$$

which on expanding out becomes

$$\left(\frac{16m'^2}{2m' + 1} - 4m' - 2\right)v_u^2 + \left(\frac{12m'}{2m' + 1}\right)v_u v_l + \left(\frac{2}{2m' + 1}\right)v_l^2 = 0. \tag{2.183}$$

This is a quadratic equation, which can be solved using the known numerical value of m'. Equation 2.183 can now be solved to give v_l in terms of v_u as $v_l = G(m')v_u$. The power required by the tandem rotor system is

$$P_{\text{total}} = T_u v_u + T_l(v_l + m'2v_u). \tag{2.184}$$

By inserting the result $v_l = G(m')v_u$ the total power is

$$P_{\text{total}} = T\left(G(m') + 1 + 2m'\right)v_u. \tag{2.185}$$

Using Eq. 2.171 such that $v_u = \sqrt{T/2\rho A}$, then Eq. 2.185 becomes

$$P_{\text{total}} = \frac{(G(m') + 1 + 2m')T^{3/2}}{\sqrt{2\rho A}}. \tag{2.186}$$

Finally, the interference factor is calculated using

$$\kappa_{\text{ov}} = \frac{P_{\text{total}}}{2P_{\text{iso}}} = \frac{G(m') + 1 + 2m'}{2}. \tag{2.187}$$

The results obtained using this latter equation are also shown in Fig. 2.31.

The dependency of κ_{ov} on rotor overlap has been measured experimentally using subscale rotor models. The amount of these data is relatively scarce compared to single rotor data, but the available results have been collated by Stepniewski & Keys (1984) from several sources including Sweet (1960) and Boeing-Vertol experiments. Their results showing the relationship between κ_{ov} and the overlap d/D have been reproduced in Fig. 2.31. It is apparent that the momentum theory result gives good agreement with the measurements, although the approximate result given by Harris (1999) underpredicts κ_{ov}. For tandem rotor designs, such as the CH-46 and CH-47 models, d/D is approximately 0.65, giving κ_{ov} of about 1.13. Unfortunately, because the interference effects are related to the vertical spacing between the rotors as well as the degree of overlap, the results shown in Fig. 2.31 indicate some variance. Also, Dingeldein (1954) shows results that suggest κ_{ov} to be less than unity when the rotors are just separated such that $d/D > 1$; that is, a favorable interference effect exists – see data in Fig. 2.31. Apart from this anomaly, the correlation of Eq. 2.169 or Eq. 2.187 with the measured data is sufficiently good to enable the momentum theory to be used for at least the preliminary estimation of tandem and coaxial rotor performance.

In forward flight, both coaxials and tandem rotors systems appear to behave very much like two single rotors but with one or the other of the rotors operating in the fully developed downwash of the other rotor – see Dingeldein (1954). Stepniewski & Keys (1984) discuss induced power interference effects and tandem rotor performance in forward flight. See also the discussion in Section 5.5.11 for forward flight performance predictions of coaxial and tandem rotors.

2.16 Chapter Review

The theories and results described in this chapter have shown that using certain assumptions and approximations, the application of the conservation laws of aerodynamics in an integral form has permitted an understanding of the factors that influence the basic performance of the helicopter rotor. The so-called momentum theory has allowed a quantification of the thrust and power of a lifting rotor, and it has been shown how these quantities are related to the downwash (inflow) velocity through the rotor. The momentum method has permitted a preliminary evaluation of rotor performance in hover, climb, and descent. It has been shown that the disk loading is a key parameter governing rotor performance, and the need for a low disk loading is essential to give a helicopter good hovering efficiency. The ideas of power loading and figure of merit have been introduced as quantities that can help in designing the rotor as well as to compare the relative efficiency and performance of two different rotor designs.

To account for various nonideal effects that have their origin in the viscosity of the air, it has been shown how the basic momentum theory can be modified empirically to give a methodology that is in substantially better quantitative agreement with experimental measurements of rotor performance, while still retaining the simplicity of the overall method. The basic momentum theory has also been extended to forward flight, for which numerical solutions are generally required to solve for the inflow through the rotor disk. These numerical techniques have been examined, along with the identification of limitations in their use. Finally, the ideas embodied in momentum theory have been extended to coaxial and partly overlapping rotors such as tandems. It has been shown why there are rotor-on-rotor interference effects associated with these designs, which can reduce the net aerodynamic performance of the rotor system.

Despite the advantages of momentum theory in providing clarity of insight into the basic aspects of the helicopter rotor problem, it has many limitations. For example, it provides no information about the distribution of loads over the blade or as to how the rotor blades should be designed (i.e., the planform, twist, thickness distribution, airfoil sections.) to produce a given performance. Furthermore, the effects of blade motion (i.e., flapping) on the rotor behavior have not yet been considered. However, these are limitations that can be overcome by using more advanced methods based on a blade element analysis of the rotor blades, which is considered in the next and subsequent chapters.

2.17 Questions

2.1. Show that for a hovering rotor with blades that operate at constant lift and drag coefficients, the thrust on the rotor is proportional to the square of the tip speed, and the power is proportional to the cube of tip speed.

2.2. The induced velocity, v_i, at the rotor plane in hover is known to be a function of the rotor tip speed, V, the rotor thrust, T, the rotor disk area, A, and air density, ρ. By means of dimensional analysis show that the functional form for v_i can be written as $\lambda_i = f(C_T)$.

2.3. Using Bernoulli's equation instead of the general energy equation, show that the induced velocity in the fully contracted wake of a rotor climbing with a vertical velocity is twice the induced velocity in the rotor plane.

2.4. The simple momentum theory assumes that the jump in pressure across the disk of a hovering rotor is the same everywhere. By considering an elemental annulus of the rotor disk, prove that this is consistent with a distribution of lift across the rotor disk that varies linearly from zero at the rotational axis of the rotor.

2.5. One difference between an actuator disk and a real rotor is that the aerodynamically active parts of real rotor blades do not extend all the way to the rotational axis – the so-called root cut-out. This is because of the need to attach the blades to the hub and also provide flap and lead–lag hinges, as well as a feathering (pitch) bearing. For a root cut-out of 25% of radius and a tip-loss factor $B = 0.97$, estimate the additional effect of the root cut-out on the induced power factor of a hovering rotor.

2.6. For a hovering rotor, momentum theory gives a result for the ideal contraction ratio of the wake. In practice, experimental observations show that the wake contraction is not as much as the ideal value. Why? Show by means of simple momentum theory that a wake contraction that is less than the ideal will result in a higher induced power for the same total thrust. Find an expression for the induced power ratio (actual power relative to ideal at a constant thrust) in terms of a measured wake radial contraction ratio of 0.78.

2.7. Calculate and plot the values of the slipstream velocities in the fully contacted wake of a hovering rotor at sea-level as a function of disk loading, T/A. Assuming a figure of merit of 0.75, compute and plot the power loading versus disk loading.

2.8. A helicopter with a gross weight of 3,000 lb (1,363.6 kg), a main rotor radius of 13.2 ft (4.0 m), and a rotor tip speed of 680 ft/s (207.3 m/s) has 275 hp (205 kW) delivered to the main rotor shaft. For hovering conditions at sea level, compute: (a) the rotor disk loading, (b) the ideal power loading, (c) the thrust and torque coefficients, and (d) the figure of merit and actual power loading.

2.9. For the helicopter in the previous question, the tail rotor radius is 2.3 ft (0.701 m) and the tail rotor is located 15.3 ft (4.66 m) from the main rotor shaft. Calculate the thrust and power required by the tail rotor for hovering conditions at sea level. Assume that the *FM* of the tail rotor is 0.70.

2.10. A helicopter is hovering in a steady cross wind at a gross weight of 3,000 lb (1,360.8 kg). This helicopter has 275 hp (205 kW) delivered to the main rotor shaft. The tail rotor radius is 2.3 ft (0.701 m) and has an induced power factor of 1.15. The tail rotor is located 15.3 ft (4.66 m) from the main rotor shaft. Determine the crosswind conditions (velocity and direction) in which the tail rotor effectiveness may be reduced or lost. If the center of gravity is assumed to lie on the rotor shaft axis, determine the feasible yawing angular velocity that the pilot can demand that may also result in a loss of tail rotor effectiveness.

2.11. An inventor claims to have built a "flying car" that can hover, where the lifting force is provided by two ducted fans. The car weighs 2,200 lb (1,000 kg) and has a 200 hp (149.14 kW) engine. The ducted fans are 7 ft (2.13 m) in diameter. Is hovering flight possible? [Hint: A ducted fan can be considered to have an effective disk area that is twice that of an unducted rotor.]

2.12. A preliminary design of a tandem rotor helicopter with a gross weight of 19,500 lb (8,845.2 kg) suggests a rotor diameter of 45 ft (13.72 m), a blade chord of 20 inches (0.508 m), three blades, and a rotor tip speed of 700 ft/s (213.43 m/s). Estimate the total shaft power required to hover if the induced power factor for the front rotor is 1.20 and that for the rear rotor is 1.15. The rotor airfoil to be used has a zero lift drag coefficient of 0.01. Estimate the installed power if transmission losses amount to 5% and the helicopter must demonstrate a vertical rate of climb of 1,000 ft/min (304.9 m/min) at sea level.

2.13. A tilt-rotor has a gross weight (mass) of 25,500 kg. The rotor diameter is 12 m. On the basis of the simple momentum theory, estimate the power required for

the helicopter to hover at sea level on a standard day. Assume that the figure of merit of the rotors is 0.80 and transmission losses amount to 5%. If each of the two turbo-shaft engines delivers 4,500 kW, estimate the maximum vertical rate of climb at sea level.

2.14. Given a helicopter of weight, $W = 6{,}000$ lb (2,727.3 kg), calculate the power required in hover and up to 600 ft/min axial rate-of-climb. The radius of the main rotor is 20 ft and the rotor has a figure of merit of 0.75. Assume sea level conditions. Plot your results in the form of power required versus climb velocity. Discuss the factors that will determine the maximum vertical climb rate of a helicopter.

2.15. Find the effective drag coefficient, C_D, acting on a rotor that is in vertical autorotation at $V_c/v_h \approx -1.85$. Compare your result to the published drag coefficients of standard bluff-body shapes, and comment.

2.16. Using classical lifting-line theory, show that the lift on an elliptically loaded fixed-wing with a circular planform of radius R in a free stream of velocity V_∞ is given by $L = 2\rho A v_i V_\infty$, where A is the wing area, and v_i is the induced downwash over the wing.

2.17. Compare the results from the iterative solution of the inflow equation to the exact analytical inflow equation for the case of axial flight (i.e., $\mu = 0$). Use both the fixed-point iterative method and the Newton–Raphson method. Determine the conditions (if any) under which these iterative methods fail.

2.18. Starting from the momentum theory result for the induced flow at the rotor disk in forward flight, program numerical solutions to this equation using both the fixed-point iterative method and the Newton–Raphson method. Plot some example graphs of inflow ratio versus advance ratio for a series of rotor angles of attack. Explore the effect of the initial guess for λ on the solution.

2.19. In a coaxial rotor design, the rotors are spaced sufficiently far apart such that the lower rotor operates in the fully developed slipstream of the upper rotor. Show by means of the momentum theory that the induced power factor resulting from interference is 1.28 compared to 1.41 when the rotors have no vertical separation. Assume that the thrusts of both rotors are equal.

2.20. In a coaxial rotor design, the rotors are spaced sufficiently far apart such that the lower rotor operates in the fully developed slipstream of the upper rotor. Show that by means of the momentum theory and on the basis of equal torque (power) that the induced power factor resulting from interference is 1.28 compared to 1.41 when the rotors have no vertical separation.

2.21. Using the momentum analysis for an overlapping rotor configuration with unequal rotor thrusts, find an expression for the overlap induced power factor κ_{ov} in terms of the overlap area $A_{ov} = m'A$ where

$$m' = \frac{2}{\pi}\left[\cos^{-1}\left(\frac{d}{D}\right) - \left(\frac{d}{D}\right)\sqrt{1-\left(\frac{d}{D}\right)^2}\right],$$

and where the rotors are assumed to have no vertical spacing. Assume that the total system thrust is expressed as $2T = \tau T_1 + (2-\tau)T_2$. Plot the results as a function of horizontal rotor separation distance d/D for several values of τ, and comment on the results.

Bibliography

Althoff, S. L. and Noonan, K. W. 1990. "Effect of Blade Planform Variation on a Small-Scale Hovering Rotor," NASA TM 4146, AVSCOM TM 89-B-009.

Anderson, J. D. 2001. *Fundamentals of Aerodynamics*, 3rd Edition, McGraw-Hill, New York, NY.

Andrew, M. J. 1981. "Coaxial Rotor Aerodynamics in Hover," *Vertica*, 5, pp. 163–172.

Azuma, A. and Obata, A. 1968. "Induced Flow Variation of the Helicopter Rotor Operating in the Vortex Ring State," *J. of Aircraft*, 5 (4), pp. 381–386.

Bagai, A. and Leishman, J. G. 1992. "A Study of Rotor Wake Developments and Wake–Body Interactions in Hover Using Wide-Field Shadowgraphy," *J. of the American Helicopter Soc.*, 37 (4), pp. 48–57.

Berliner, E. 1908. "The Berliner Helicopter," *Aeronautics*, Vol. 3.

Betz, A. 1920a. *Z. Flugtech. u Motorluftschiffahrt*, 11, pp. 105.

Betz, A. 1920b. "Development of the Inflow Theory of the Propeller," NACA TN 24.

Betz, A. 1922. "The Theory of the Screw Propeller," NACA TN 83.

Betzina, M. D. 2001. "Tilt-rotor Descent Aerodynamics: A Small-Scale Experimental Investigation of Vortex Ring State," 57th Annual Forum of the American Helicopter Soc., Washington, DC, May 9–11.

Brotherhood, P. 1949. "Flow through a Helicopter Rotor in Vertical Descent," ARC R & M 2735.

Castles, W. and Gray, R. B. 1951. "Empirical Relation Between Induced Velocity, Thrust and Rate of Descent of a Helicopter Rotor as Determined by Wind Tunnel Tests on Four Model Rotors," NACA TN 2474.

Coleman, C. P. 1993. "A Survey of Theoretical and Experimental Coaxial Rotor Aerodynamic Research," 19th European Rotorcraft Forum, Como, Italy, Sept. 14–16.

Cierva, J. de la and Rose, D. 1931. *Wings of Tomorrow: The Story of the Autogiro*, Brewer, Warren & Putnam, New York, NY.

de Bothezat, G. 1919. "The General Theory of Blade Screws," NACA Report 29.

Dingeldein, R. C. 1954. "Wind Tunnel Studies of the Performance of Multirotor Configurations," NACA Technical Note 3236.

Drees, J. M. and Hendal, W. P. 1951. "Airflow Patterns in the Neighborhood of Helicopter Rotors," *Aircraft Engineering*, 23 (266), pp. 107–111.

Durand, W. F. (ed.) 1935. *Aerodynamic Theory*, Vol. IV, Divisions J-M, Springer-Verlag, Berlin. Reprinted by Peter Smith, Glouster, MA, 1976.

Fail, R. and Squire, H. B. 1947. "24-ft Wind Tunnel Tests of Model Multi-Rotor Helicopters," RAE Report No. Aero 2207.

Froude, R. E. 1889. "On the Part Played in Propulsion by Differences of Fluid Pressure," *Transactions of the Institute of Naval Architects*, 30, p. 390.

Froude, W. 1878. "On the Elementary Relation Between Pitch, Slip and Propulsive Efficiency," *Transactions of the Institute of Naval Architects*, 19, pp. 47–57.

Gessow, A. 1948. "Flight Investigation of Effects of Rotor Blade Twist on Helicopter Performance in the High Speed and Vertical Autorotative Descent Conditions," NACA TN 1666.

Gessow, A. 1954. "Review of Information on Induced Flow of a Lifting Rotor," NACA TN 3238.

Gessow, A. and Myers, G. C., Jr. 1952. *Aerodynamics of the Helicopter*, Macmillan Co. (republished by Frederick Ungar Publishing, NY, 1967), pp. 73–75.

Glauert, H. 1926a. "The Analysis of Experimental Results in the Windmill Brake and Vortex Ring States of an Airscrew," ARC R & M 1026.

Glauert, H. 1926b. "A General Theory of the Autogiro," ARC R & M 1111.

Glauert, H. 1928. "On the Horizontal Flight of a Helicopter," ARC R & M 1157.

Glauert, H. 1935. "Airplane Propellers," In Division L of *Aerodynamic Theory*, ed. W. F. Durand, Springer Verlag, Berlin, Germany. Reprinted by Peter Smith, Glouster, MA, 1976.

Hafner, R. 1946. "Developments in Rotating Wing Aircraft," Bulletins of the Helicopter Assoc. of Great Britain, Oct.. pp. 8–29.

Hafner, R. 1947. "Rotor Systems and Control Problems of the Helicopter," Anglo-American Aero. Conf., Sept.

Harrington, R. D. 1951. "Full-Scale Tunnel Investigation of the Static Thrust Performance of a Coaxial Helicopter Rotor," NACA Technical Note 2318.

Harris, F. D. 1999. "Twin Rotor Hover Performance," *J. of the American Helicopter Soc.*, 44 (1), pp. 34–37.

Hoerner, S. F. 1965. *Fluid Dynamic Drag*, Published by the Author, Hoerner Fluid Dynamics, Vancouver, WA.

Johnson, W. 1980. *Helicopter Theory*, Princeton University Press, Princeton, NJ.

Knight, M. and Hefner, R. A. 1937. "Static Thrust of the Lifting Airscrew," NACA TN 626.

Lanchester, F. W. 1915. "A Contribution to the Theory of Propulsion and the Screw Propeller," *Transactions of the Institute of Naval Architects*, 57, pp. 98–116.

Leishman, J. G., Baker, A., and Coyne, A. 1995. "Measurements of Rotor Tip Vortices Using Three-Component Laser Doppler Velocimetry," American Helicopter Soc. Aeromechanics Specialists Meeting, Fairfield, CT, Oct. 11–13.

Lock, C. N. H. 1928. "Photographs of Streamers Illustrating the Flow Around an Airscrew in the Vortex Ring State," ARC R & M 1167.

Lock, C. N. H. 1947. "Note on the Characteristic Curve for an Airscrew or Helicopter," ARC R & M 2673.

Lock, C. N. H., Bateman, H., and Townend, H. C. H. 1926. "An Extension of the Vortex Theory of Aircrews with Applications to Aircrews of Small Pitch, Including Experimental Results," ARC R & M 1014.

Maxim, H. S. 1897. "Screw Propellers Working in Air," *Aeronautical Annual* of 1889, The Royal Aeronautical Soc. of Great Britain.

Moedersheim, E., Daghir, M., and Leishman, J. G. 1994. "Flow Visualization of Rotor Wakes Using Shadowgraph and Schlieren Techniques," 20th European Rotorcraft Forum, Amsterdam, The Netherlands, 4–6 Oct.

Nikolsky, A. A. and Seckel, E. 1949a. "An Analytical Study of the Steady Vertical Descent in Autorotation of Single-Rotor Helicopters," NACA TN 1906.

Nikolsky, A. A. and Seckel, E. 1949b. "An Analysis of the Transition of a Helicopter from Hovering to Steady Autorotative Vertical Descent," NACA TN 1907.

Ormiston, R. A. 2004. "Induced Power of the Helicopter Rotor," 60th Annual Forum of the American Helicopter Soc. International, Baltimore, MD, June 7–10.

Payne, P. R. 1959. *Helicopter Dynamics and Aerodynamics*, The MacMillan Company, New York, NY, pp. 90–98.

Rankine, W. J. M. 1865. "On the Mechanical Principles of the Action of Propellers," *Transactions of the Institute of Naval Architects*, 6, pp. 13–39.

Renard, C. 1903. "Sur la Qualité des Hélices Sustentatrices," *Comptes Rendus*, 37, p. 907.

Riabouchinsky, D. 1906. "Recherches sur l'hélice aérienne se Mouvant Dans un Courant Aérien Dirigé Perpendiculairement à l'axe de l'hélice," Bulletin de l'Institut Aérodynamique de Koutchinio I, 13.

Saito, S. and Azuma, S. 1981. "A Numerical Approach to coaxial Rotor Aerodynamics," 7th European Rotorcraft Forum, Garmisch-Partenkirchen, Germany, Sept. 8–11.

Sissingh, G. 1939. "Contribution to the Aerodynamics of Rotating-Wing Aircraft," NACA TM 921.

Squire, H. B. 1948. "Some Aerodynamic Problems of the Helicopter," *J. of the Helicopter Association of Great Britain*, 1 (3), pp. 35–48.

Stepniewski, W. Z. 1955. "A Simplified Approach to the Aerodynamic Rotor Interference of Tandem Helicopter," American Helicopter Soc. West Coast Region Meeting, Sept. 21–22.

Stepniewski, W. Z. and Keys, C. N. 1984. *Rotary-Wing Aerodynamics*, Dover, New York, NY. Vol. II, Chapter 5.

Sweet, G. E. 1960. "Hovering Measurements for Twin-Rotor Configurations With and Without Overlap," NASA Technical Note D-534.

Taylor, M. K. 1950. "A Balsa-Dust Technique for Air-Flow Visualization and Its Application to Flow Through Model Helicopter Rotors in Static Thrust," NACA Technical Note 2220.

Washizu, K., Azuma, A., Koo, J. and Oka, T. 1966a. "Experimental Study on the Unsteady Aerodynamics of a Tandem Rotor Operating in the Vortex Ring State," 22nd Annual Forum of the American Helicopter Soc., Washington, DC.

Washizu, K. Azuma, A., Koo, J. and Oka, T. 1966b. "Experimental on a Model Helicopter Rotor Operating in the Vortex Ring State," *J. of Aircraft*, 3 (3), pp. 225–230.

Yaggy, P. F. and Mort, K. W. 1963. "Wind-Tunnel Tests of Two VTOL Propellers in Descent," NASA TN D-1766, March.

Young, C. 1978. "A Note of the Velocity Induced by a Helicopter Rotor in the Vortex Ring State," RAE Technical Report 78125.

Zimmer, H. 1985. "The Aerodynamic Calculation of Counter Rotating Coaxial Rotors," 11th European Rotorcraft Forum, London, England, Sept. 10–13.

CHAPTER 3

Blade Element Analysis

Whatever progress the airplane might make, the helicopter will come to be taken up by advanced students of aeronautics.

Thomas Edison (circa, 1920)

3.1 Introduction

The blade element theory (BET) forms the basis of most modern analyses of helicopter rotor aerodynamics because it provides estimates of the radial and azimuthal distributions of blade aerodynamic loading over the rotor disk. The BET assumes that each blade section acts as a quasi–2-D airfoil to produce aerodynamic forces (and moments). Tip loss and other empirical factors may be applied to account for three-dimensional effects. Rotor performance can be obtained by integrating the sectional airloads at each blade element over the length of the blade and averaging the result over a rotor revolution. Therefore, unlike the simple momentum theory, the BET can be used as a basis to help design the rotor blades in terms of the blade twist, the planform distribution and perhaps also the airfoil shape to provide a specified overall rotor performance.

The idea of the BET was apparently first suggested by Drzewiecki (1892, 1920) for the analysis of airplane propellers, although Glauert (1935) indicates that in the nineteenth century F. W. Lanchester also made contributions to solving the problem – see Lanchester (1915). At the beginning of the twentieth century, there was considerable scientific debate about the proper theoretical aerodynamic analysis of propellers and helicopter rotors, mainly between Stefan Drzewiecki and Louis Bréguet – see Liberatore (1998). The principles of blade element theory assume no mutual influence of adjacent blade elements sections; these sections are idealized as 2-D airfoils. However, the effects of a nonuniform "induced inflow" across the blade (its source from the rotor wake) is accounted for through a modification to the angle of attack (AoA) at each blade element. Unless we make some simple analytic assumption for the distribution of induced velocity over the disk, such as a uniform or linear distribution, the blade element calculation is quite a formidable undertaking because it must more precisely represent the highly nonuniform velocity field induced by the vortical wake trailed from each blade, as well as to account for the influence of all the blades and possibly airframe components. However, if the induced velocity can be calculated, or even approximated, then the net thrust and power and other forces and moments acting on the rotor can be readily obtained.

In an extension to the basic approach, the BET and momentum theories were linked together by Reissner (1910, 1937, 1940), de Bothezat (1919), and Glauert (1935) to define the induced velocity or induced AoA distribution. A similar approach for hovering helicopter rotors was developed by Gustafson & Gessow (1946) and Gessow (1948), and the approach is reviewed in Gessow & Myers (1952). The BET was extended to explicitly include the influence of the vortical wake (and the other blades) through an induced AoA component

as calculated by means of the Biot–Savart law. These basic ideas were first pursued at the beginning of the twentieth century by Joukowski – see Tokaty (1971), Glauert (1922), Bienen & von Kármán (1924), and Lock et al. (1925). Betz (1919, and appendix therein by Prandtl) and Goldstein (1929) developed a prescribed vortex wake theory for lifting propellers. This work was later extended by Theodorsen (1948). The early work with the technique as it applies to propellers is reviewed by Glauert (1935). Knight & Hefner (1937) were among the first to apply blade element and prescribed vortex wake principles to the calculation of the helicopter rotor problem. Coleman et al. (1945), Castles & De Leeuw (1954), and Castles & Durham (1956) later extended this work to helicopters operating in forward flight.

Figure 3.1 shows a sketch of the flow environment and aerodynamic forces at representative blade element on the rotor. The aerodynamic forces are assumed to arise solely from the velocity and AoA normal to the leading edge of the blade section. The effect of the radial component of velocity, U_R, on the lift is usually ignored in accordance with the independence principle; see Jones & Cohen (1957). However, the U_R component will affect the drag on the blade in forward flight and should be included in this case. The measured 2-D aerodynamic characteristics of the airfoil as a function of AoA can be assumed for

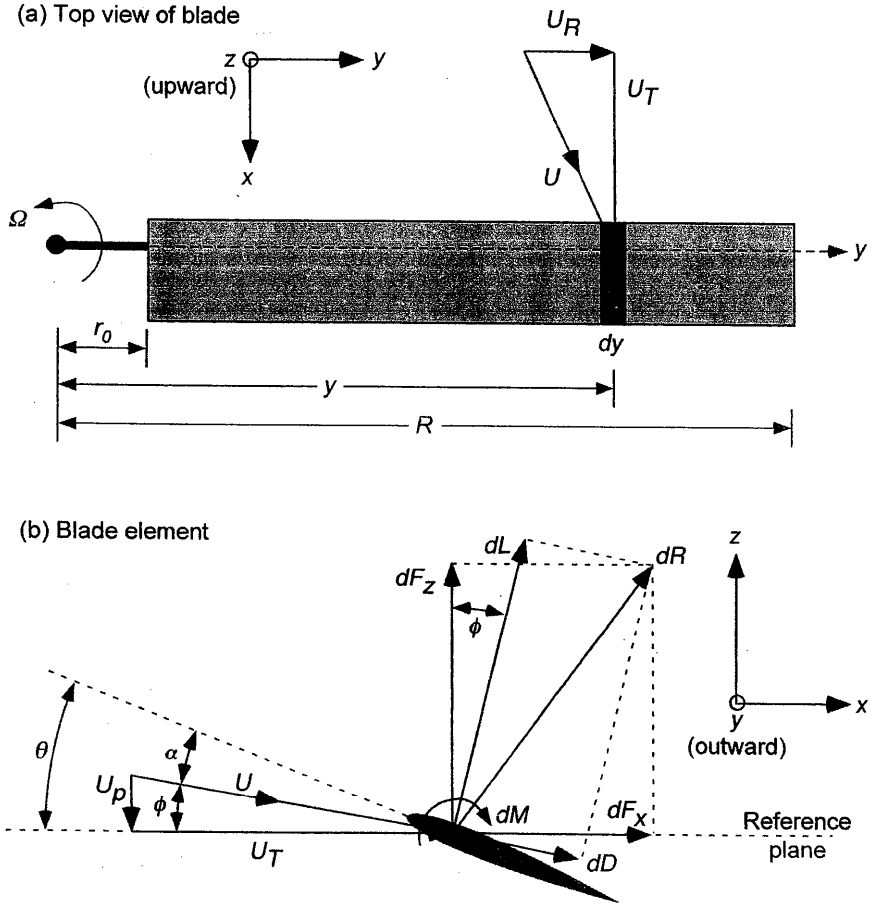

Figure 3.1 Incident velocities and aerodynamic environment at a typical blade element.

the purposes of calculating the resultant lift and pitching moment on each blade element. Such results are available in the published literature for a large number of airfoils and over a wide range of operating conditions (see Chapter 7). The inflow angle of attack, ϕ, arises, primarily because of the velocity induced by the rotor and its wake. Therefore, the induced velocity serves to modify the direction of the relative flow velocity vector and so alters the AoA at each blade element from its 2-D value. This inflow velocity also inclines the local lift vectors, which by definition act perpendicular to the resultant velocity vector at the blade element and, therefore, provides a source of induced drag (drag resulting from lift) and is the source of induced power required at the rotor shaft.

3.2 Blade Element Analysis in Hover and Axial Flight

The blade element approach for the analysis of helicopter rotors has been well established in the prior literature – see Payne (1959), Bramwell (1976), Johnson (1980), and Prouty (1986). The resultant local flow velocity at any blade element at a radial distance y from the rotational axis has an out-of-plane component $U_P = V_c + v_i$ normal to the rotor as a result of climb and induced inflow and an in-plane component $U_T = \Omega y$ parallel to the rotor because of blade rotation, relative to the disk plane. The resultant velocity at the blade element is, therefore,

$$U = \sqrt{U_T^2 + U_P^2}. \tag{3.1}$$

The relative inflow angle (or induced angle of attack) at the blade element will be

$$\phi = \tan^{-1}\left(\frac{U_P}{U_T}\right) \approx \frac{U_P}{U_T} \text{ for small angles.} \tag{3.2}$$

Thus, if the pitch angle at the blade element is θ, then the aerodynamic or effective AoA is

$$\alpha = \theta - \phi = \theta - \frac{U_P}{U_T}. \tag{3.3}$$

The resultant incremental lift dL and drag dD per unit span on this blade element are

$$dL = \frac{1}{2}\rho U^2 c C_l \, dy \quad \text{and} \quad dD = \frac{1}{2}\rho U^2 c C_d \, dy, \tag{3.4}$$

where C_l and C_d are the lift and drag coefficients, respectively. The lift dL and drag dD act perpendicular and parallel to the resultant flow velocity, respectively. Notice that the quantity c is the *local* blade chord. Using Fig. 3.1 these forces can be resolved perpendicular and parallel to the rotor disk plane giving

$$dF_z = dL\cos\phi - dD\sin\phi \quad \text{and} \quad dF_x = dL\sin\phi + dD\cos\phi. \tag{3.5}$$

Therefore, the contributions to the thrust, torque, and power of the rotor are

$$dT = N_b dF_z, \quad dQ = N_b dF_x y \quad \text{and} \quad dP = N_b dF_x \Omega y, \tag{3.6}$$

where N_b is the number of blades comprising the rotor. Notice that in the hover or axial flight condition, the aerodynamic environment is (ideally) axisymmetric and the airloads

are independent of the blade azimuth angle. Substituting the results for dF_x and dF_z from Eq. 3.5 gives

$$dT = N_b(dL\cos\phi - dD\sin\phi), \tag{3.7}$$
$$dQ = N_b(dL\sin\phi + dD\cos\phi)y, \tag{3.8}$$
$$dP = N_b(dL\sin\phi + dD\cos\phi)\Omega y. \tag{3.9}$$

For helicopter rotors the following simplifying assumptions can be made:

1. The out-of-plane velocity U_P is much smaller than the in-plane velocity U_T, so that $U = \sqrt{U_T^2 + U_P^2} \approx U_T$. This is a valid approximation except near the blade root, but the aerodynamic forces are small here anyway.
2. The induced angle ϕ is small, so that $\phi = U_P/U_T$. Also, $\sin\phi = \phi$ and $\cos\phi = 1$.
3. The drag is at least one order of magnitude less than the lift, so that the contribution $dD\sin\phi$ (or $dD\phi$) is negligible.

Applying these simplifications to the preceding equations results in

$$dT = N_b dL, \tag{3.10}$$
$$dQ = N_b(\phi dL + dD)y, \tag{3.11}$$
$$dP = N_b\Omega(\phi dL + dD)y. \tag{3.12}$$

Proceeding further, it is convenient to introduce nondimensional quantities by dividing lengths by R and velocities by ΩR. Hence, $r = y/R$, and $U/\Omega R = \Omega y/\Omega R = y/R = r$. Also, $dC_T = dT/\rho A(\Omega R)^2$, $dC_Q = dQ/\rho A(\Omega R)^2 R$, and $dC_P = dP/\rho A(\Omega R)^3$. The inflow ratio can be written as

$$\lambda = \frac{V_c + v_i}{\Omega R} = \frac{V_c + v_i}{\Omega y}\left(\frac{\Omega y}{\Omega R}\right) = \frac{U_P}{U_T}\left(\frac{y}{R}\right) = \phi r. \tag{3.13}$$

Therefore, the increment in thrust coefficient is

$$\begin{aligned} dC_T &= \frac{N_b dL}{\rho A(\Omega R)^2} = \frac{N_b\left(\frac{1}{2}\rho U_T^2 c C_l\, dy\right)}{\rho(\pi R^2)(\Omega R)^2} \\ &= \frac{1}{2}\left(\frac{N_b c}{\pi R}\right) C_l\left(\frac{y}{R}\right)^2 d\left(\frac{y}{R}\right) \\ &= \frac{1}{2}\left(\frac{N_b c}{\pi R}\right) C_l r^2\, dr. \end{aligned} \tag{3.14}$$

As described in Chapter 2, the grouping $N_b c/\pi R$ is known as the rotor solidity, σ. For a rectangular blade (c = constant), this is the ratio of the rotor blade area to the rotor disk area:

$$\sigma = \frac{\text{Blade area}}{\text{Disk area}} = \frac{A_b}{A} = \frac{N_b c R}{\pi R^2} = \frac{N_b c}{\pi R}.$$

Therefore, the rotor thrust coefficient increment is simply

$$dC_T = \frac{1}{2}\sigma C_l r^2\, dr. \tag{3.15}$$

This is one of the most fundamental equations for rotating-wing analysis by means of the BET. By a similar approach, it can be shown that the rotor–torque coefficient increment is

$$dC_Q \equiv dC_P = \frac{dQ}{\rho A(\Omega R)^2 R} = \frac{N_b(\phi dL + dD)y}{\rho(\pi R^2)(\Omega R)^2 R} = \frac{1}{2}\left(\frac{N_b c}{\pi R}\right)(\phi C_l + C_d) r^3\, dr$$
$$= \frac{1}{2}\sigma\,(\phi C_l + C_d) r^3\, dr, \tag{3.16}$$

which will be noted to represent the sum of an induced part and a profile part.

3.2.1 *Integrated Rotor Thrust and Power*

To find the total C_T and C_Q, the incremental thrust and power quantities derived above must be integrated along the blade from the root to the tip. For a rectangular blade, the thrust coefficient is

$$C_T = \frac{1}{2}\sigma \int_0^1 C_l r^2\, dr, \tag{3.17}$$

where the limits of integration are $r = 0$ at the root to $r = 1$ at the tip. For the corresponding torque or power coefficient

$$C_Q \equiv C_P = \frac{1}{2}\sigma \int_0^1 (\phi C_l + C_d) r^3\, dr = \frac{1}{2}\sigma \int_0^1 (\lambda C_l r^2 + C_d r^3)\, dr, \tag{3.18}$$

using the general result that $\phi = \lambda / r$ from Eq. 3.13.

To evaluate C_T and C_P it is necessary to predict the spanwise variation in the inflow, λ, as well as the sectional aerodynamic force coefficients, C_l and C_d. If 2-D aerodynamics are assumed, then $C_l = C_l(\alpha, Re, M)$ and $C_d = C_d(\alpha, Re, M)$, where Re and M are the local Reynolds number and Mach number, respectively (see Chapter 7). Also, $\alpha = \alpha(V_c, \theta, v_i)$ and $v_i = v_i(r)$. Because these effects cannot, in general, be expressed as simple analytic results, it is necessary to numerically solve the integrals for C_T and C_P. However, with certain assumptions and approximations, it is possible to find closed-form analytical solutions. These solutions are very useful because they serve to illustrate the fundamental form of the results in terms of the operational and geometric parameters of the rotor. They also provide exact check cases for the numerical solutions to the blade element theory.

3.2.2 *Thrust Approximations*

Based on steady linearized aerodynamics, the local blade lift coefficient can be written as

$$C_l = C_{l_\alpha}(\alpha - \alpha_0) = C_{l_\alpha}(\theta - \alpha_0 - \phi), \tag{3.19}$$

where C_{l_α} is the 2-D lift-curve-slope of the airfoil section(s) comprising the rotor, and α_0 is the corresponding zero-lift angle. For an incompressible flow, C_{l_α} would have a value close to the thin-airfoil result of 2π per radian. Although C_{l_α} will take a different value at each blade station because it is a function of local incident Mach number and Reynolds number, an average value for the rotor can be assumed without serious loss of accuracy (i.e., $C_{l_\alpha} =$ constant). Also, unless otherwise stated, it will be assumed that α_0 can be combined into θ.

Therefore, C_{l_α} can be taken outside of the integral sign giving

$$C_T = \frac{1}{2}\sigma \int_0^1 C_l r^2 \, dr = \frac{1}{2}\sigma C_{l_\alpha} \int_0^1 (\theta - \phi) r^2 \, dr, \tag{3.20}$$

and using the result that $\phi = \lambda / r$, then the thrust coefficient can be written as

$$C_T = \frac{1}{2}\sigma C_{l_\alpha} \int_0^1 (\theta r^2 - \lambda r) \, dr. \tag{3.21}$$

Untwisted Blades, Uniform Inflow

For a blade with zero twist, θ = constant = θ_0. Also, for uniform inflow velocity, which is assumed in simple momentum theory, λ = constant. Therefore, in this case the thrust coefficient is given by

$$\begin{aligned} C_T &= \frac{1}{2}\sigma C_{l_\alpha} \int_0^1 (\theta_0 r^2 - \lambda r) \, dr = \frac{1}{2}\sigma C_{l_\alpha} \left[\frac{\theta_0 r^3}{3} - \frac{\lambda r^2}{2} \right]_0^1 \\ &= \frac{1}{2}\sigma C_{l_\alpha} \left[\frac{\theta_0}{3} - \frac{\lambda}{2} \right]. \end{aligned} \tag{3.22}$$

To find the direct relationship between C_T and the blade pitch, we can use the relationship between C_T and λ as is given by the simple momentum theory in Chapter 2 (i.e., $\lambda_i \equiv \lambda_h = \sqrt{C_T/2}$). Therefore,

$$C_T = \frac{1}{2}\sigma C_{l_\alpha} \left[\frac{\theta_0}{3} - \frac{1}{2}\sqrt{\frac{C_T}{2}} \right]. \tag{3.23}$$

This equation must be solved iteratively to find C_T for a given value of θ_0. Alternatively, solving directly for the pitch angle, θ_0, in terms of an assumed thrust gives

$$\theta_0 = \frac{6C_T}{\sigma C_{l_\alpha}} + \frac{3}{2}\sqrt{\frac{C_T}{2}}. \tag{3.24}$$

The first term is the blade pitch required to produce thrust, and the second term is the additional pitch required to compensate for the inflow resulting from that thrust.

Figure 3.2 shows results for the thrust versus collective pitch for four rotors of different solidity. The experimental data are taken from the experiments of Knight & Hefner (1937), who tested subscale rotors with no blade twist. These rotors involved increasing the number of blades to arrive at larger solidity, but there are no experiments that have examined solidity effects independently of blade number. The effect of number of blades (other than solidity) on the rotor aerodynamics, however, is small. For the purposes of these calculations, C_{l_α} was set to a value of 5.73/radian, which represents a small reduction of the 2-D thin-airfoil result of 2π/radian because of finite airfoil thickness and Reynolds number effects. The agreement between Eq. 3.23 and the measurements is found to be good, although there is a slight overprediction of the thrust because so far the nonuniformity of the inflow and nonideal effects, such as tip loss, have not been accounted for in the theory.

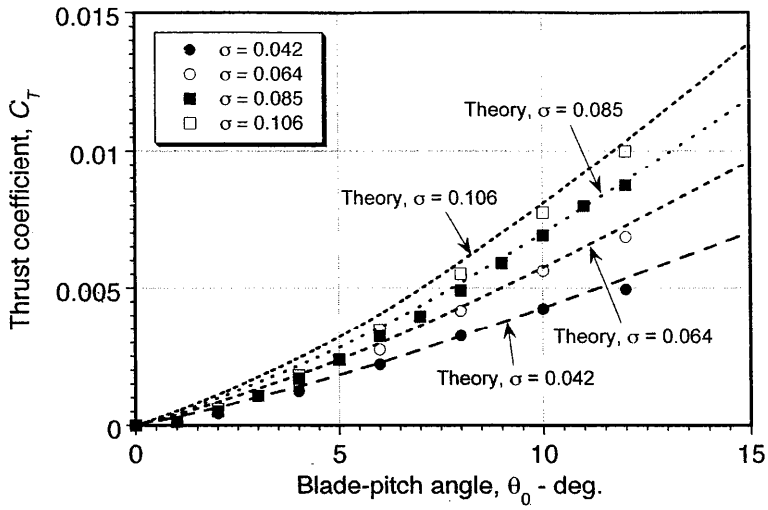

Figure 3.2 Variation in rotor thrust coefficient with collective pitch for rotors with different solidities. Data source: Knight & Hefner (1937).

Linearly Twisted Blades, Uniform Inflow

All helicopter rotor blades use some amount of spanwise twist in their shape, although in different forms and with different amounts. As will be shown, the use of blade twist provides the rotor with several important performance advantages. Many helicopter rotor blades are designed with a linear twist, so that θ takes the form $\theta(r) = \theta_0 + r\theta_{tw}$, where θ_{tw} is the blade twist rate per radius of the rotor (i.e., in degrees per rotor radius or the equivalent in degrees per unit length of blade). Using this variation in $\theta(r)$, we get

$$\begin{aligned} C_T &= \frac{1}{2}\sigma C_{l_\alpha}\int_0^1 [(\theta_0 + r\theta_{tw})r^2 - \lambda r]dr \\ &= \frac{1}{2}\sigma C_{l_\alpha}\left[\frac{\theta_0 r^3}{3} + \frac{\theta_{tw} r^4}{4} - \frac{\lambda r^2}{2}\right]_0^1, \\ &= \frac{1}{2}\sigma C_{l_\alpha}\left[\frac{\theta_0}{3} + \frac{\theta_{tw}}{4} - \frac{\lambda}{2}\right]. \end{aligned} \tag{3.25}$$

If the reference blade-pitch angle (or collective pitch) is taken at 3/4-radius (known as $\theta_{0.75}$, or sometimes just as θ_{75}), then $\theta(r) = \theta_{75} + (r - 0.75)\theta_{tw}$ and

$$\begin{aligned} C_T &= \frac{1}{2}\sigma C_{l_\alpha}\int_0^1 \{[\theta_{75} + (r - 0.75)\theta_{tw}]r^2 - \lambda r\}dr \\ &= \frac{1}{2}\sigma C_{l_\alpha}\int_0^1 (\theta_{75}r^2 + \theta_{tw}r^3 - 0.75\theta_{tw}r^2 - \lambda r)\, dr \\ &= \frac{1}{2}\sigma C_{l_\alpha}\left[\frac{\theta_{75}}{3} + \frac{\theta_{tw}}{4} - \frac{\theta_{tw}}{4} - \frac{\lambda}{2}\right] \\ &= \frac{1}{2}\sigma C_{l_\alpha}\left[\frac{\theta_{75}}{3} - \frac{\lambda}{2}\right]. \end{aligned} \tag{3.26}$$

Comparing this latter equation with Eq. 3.22 shows an interesting result, namely that a blade with linear twist has the same thrust coefficient as one of constant pitch when θ is set to the pitch the twisted blade defined at the 3/4-radius [see also Gessow & Myers (1952) and Johnson (1980)].

3.2.3 *Torque–Power Approximations*

According to the BET, the incremental power coefficient on the rotor can be written as

$$dC_P \equiv dC_Q = \frac{\sigma}{2}(\phi C_l + C_d) r^3 \, dr. \tag{3.27}$$

Using the result that $\lambda = \phi r$ and expanding out Eq. 3.27 gives

$$\begin{aligned} dC_P &= \frac{\sigma}{2}\phi C_l r^3 \, dr + \frac{\sigma}{2} C_d r^3 \, dr \\ &= \frac{\sigma}{2} C_l \lambda r^2 \, dr + \frac{\sigma}{2} C_d r^3 \, dr \\ &= dC_{P_i} + dC_{P_0}, \end{aligned} \tag{3.28}$$

where dC_{P_i} is the induced power and dC_{P_0} is the profile power. Recall from Eq. 3.15 that the incremental thrust coefficient can be written as $dC_T = \frac{1}{2}\sigma C_l r^2 dr$ so that $dC_{P_i} = \lambda dC_T$. Therefore,

$$dC_P = \lambda dC_T + dC_{P_0} \tag{3.29}$$

and the total power coefficient is

$$C_P = \int_{r=0}^{r=1} \lambda dC_T + \int_0^1 \frac{1}{2}\sigma C_d r^3 dr. \tag{3.30}$$

By assuming uniform inflow and $C_d = C_{d_0}$ = constant, then after integration we obtain

$$C_P = \lambda C_T + \frac{1}{8}\sigma C_{d_0}. \tag{3.31}$$

But in hover with uniform inflow then we know that $\lambda = \sqrt{C_T/2}$, and so

$$C_P = \frac{C_T^{3/2}}{\sqrt{2}} + \frac{1}{8}\sigma C_{d_0}. \tag{3.32}$$

Under these assumptions it is apparent that the first term in this latter equation reduces to the simple momentum theory result given previously in Chapter 2, as it should. The second term is the extra power predicted by the BET that is required to overcome profile drag of the rotor blades, which was a concept first introduced in Eq. 2.42.

3.2.4 *Tip-Loss Factor*

The ideas of a so-called tip-loss factor have been introduced in Chapter 2 and can be used to account for the effects on the rotor thrust and induced power because of the locally high induced velocities produced at the blade tips by the trailed tip vortices. The basic form of the BET permits a finite lift to be produced at the blade tip, which, of course, is physically unrealistic. The Prandtl tip-loss factor B is used to represent this loss of blade lift and can be considered as an "effective" blade radius, $R_e = BR$. In practice, B is found to take a value between 0.95 and 0.98 for most helicopter rotors.

When the tip loss is included in the calculation of rotor thrust using the BET, one approach is to consider the outer portion of the blade, $R - R_e$, to be incapable of carrying lift. This is the approach suggested by Gessow (1948) and Gessow & Myers (1952) and followed by Payne (1959), Johnson (1980), and others. In this case the result for the lift is given by integrating the segment lift over the effective blade span as

$$C_T = \int_0^B \frac{\sigma}{2} C_l r^2 \, dr = \int_0^B \frac{\sigma C_{l_\alpha}}{2} \left(\theta r^2 - \lambda r\right) \, dr. \tag{3.33}$$

For untwisted blades ($\theta = \theta_0$) and uniform inflow assumptions ($\lambda = \sqrt{C_T/2}$), this becomes

$$C_T = \frac{1}{2}\sigma C_{l_\alpha} B^2 \left[\frac{\theta_0 B}{3} - \frac{\lambda}{2}\right], \tag{3.34}$$

which can be compared to the result given previously in Eq. 3.22 with no tip losses (or Eq. 3.34 with $B = 1$). For a rotor with a twist distribution of the form $\theta = \theta_{\text{tip}}/r$ (as will be shown, this is known as "ideal" twist), then

$$\begin{aligned} C_T &= \frac{\sigma C_{l_\alpha}}{2} \int_0^B \left(\theta_{\text{tip}} - \lambda\right) r \, dr = \frac{\sigma C_{l_\alpha}}{2} \left[\left(\theta_{\text{tip}} - \lambda\right)\frac{r^2}{2}\right]_0^B \\ &= \frac{\sigma C_{l_\alpha}}{4} B^2 \left[\theta_{\text{tip}} - \lambda\right]. \end{aligned} \tag{3.35}$$

In either of Eq. 3.34 or Eq. 3.35 because B is between 0.95 and 0.98, we find a 6–10% reduction in rotor thrust resulting from tip-loss effects for a given blade-pitch setting under the stated assumptions.

Strictly speaking, the tip-loss equation deduced from the Prandtl theory as first discussed in Chapter 2 should be applied to the calculation of an increased inflow (for the same total thrust). Therefore, to assume that the outboard part of the blade, $R - R_e$, is ineffective in carrying lift is not the correct interpretation of Prantdl's theory. This fact has also been pointed out by Bramwell (1976). The correct interpretation is to consider that for the same thrust the induced inflow will be increased to a value

$$v_h = \sqrt{\frac{T}{2\rho A_e}} = \sqrt{\frac{T}{2\rho(AB^2)}} = \frac{1}{B}\sqrt{\frac{T}{2\rho A}}; \tag{3.36}$$

that is, v_h (or λ_h) is increased by a factor B^{-1} compared to the case with no assumed tip losses. For untwisted blades and uniform inflow with tip losses alone, the thrust becomes

$$C_T = \frac{1}{2}\sigma C_{l_\alpha} \left[\frac{\theta_0}{3} - \frac{\lambda}{2B}\right], \tag{3.37}$$

which can be compared to Eq. 3.34 with the alternative interpretation of tip loss. For ideal twist and uniform inflow, the thrust now becomes

$$C_T = \frac{\sigma C_{l_\alpha}}{4} \left[\theta_{\text{tip}} - \frac{\lambda}{B}\right] \tag{3.38}$$

compared to the result in Eq. 3.35, which will overpredict the effects of tip loss.

Because of tip-loss effects, a real rotor will always have a higher overall average induced velocity compared to that given by momentum theory and so the induced power will also be increased relative to the simple momentum result. Tip loss constitutes an additional source

of nonuniform inflow, and would normally be factored into the value of κ. Using the BET, the induced power can be written as

$$C_{P_i} = \int_{r=0}^{r=1} \lambda dC_T = \int_0^1 \frac{1}{2}\sigma\lambda C_l r^2 \, dr, \tag{3.39}$$

where λ must be calculated for each element. Using untwisted rectangular blades and uniform inflow assumptions, then with a tip loss the total power can be approximated by

$$C_P = \frac{1}{2}\sigma C_{l_\alpha}\kappa\lambda\left[\frac{\theta_0}{3} - \frac{\lambda}{2B}\right] + \frac{1}{8}\sigma C_{d_0}, \tag{3.40}$$

where the induced power factor κ includes the effects of both tip loss *and* nonuniform inflow over the remainder of the blade. As suggested in Chapter 2 by the simple momentum analysis, κ approximately equals 1.25 for the rotor used in this case. In general, we can write that

$$\kappa = \frac{1}{B} + \kappa_\lambda + \kappa_0, \tag{3.41}$$

where κ_λ accounts for the effects of nonuniform inflow and κ_0 accounts for other miscellaneous induced losses. Figure 3.3 shows the variation in power required versus collective pitch for four rotors with increasing solidity. Again, the data are taken from Knight and Hefner (1937). The calculations have used a tip-loss factor, $B = 0.97$, $\kappa = 1.25$, and $C_{d_0} = 0.011$. The result in Eq. 3.40, with the stated assumptions, correlates well with the measured data but now shows a slight underprediction at the higher collective pitch angles. For the most part, this is because of the higher drag coefficients associated with boundary layer thickening and the onset of blade stall, the effects of which tend to increase the profile power above that obtained by assuming a constant profile drag coefficient.

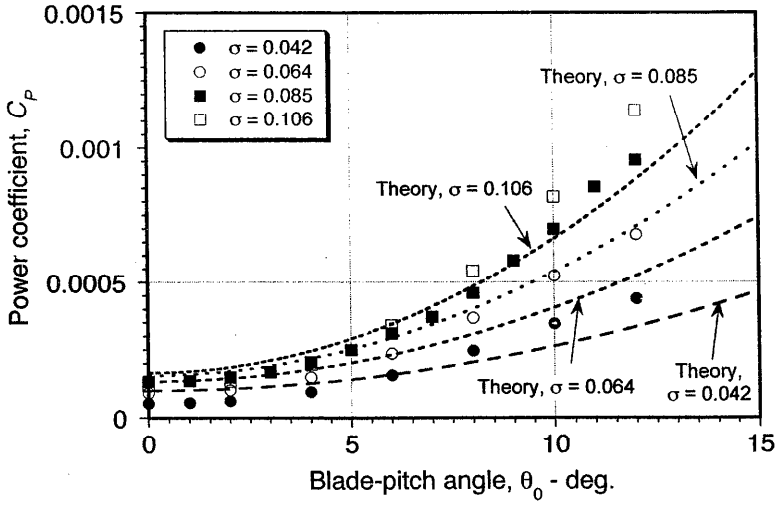

Figure 3.3 Variation in rotor power coefficient with collective pitch for rotors with different solidities. Data source: Knight & Hefner (1937).

3.3 Blade Element Momentum Theory (BEMT)

The blade element momentum theory (BEMT) for hovering rotors is a hybrid method that was first proposed for helicopter use by Gustafson & Gessow (1946) and Gessow (1948) and combines the basic principles from both the blade element and momentum theory approaches. The principles involve the invocation of the equivalence between the circulation and momentum theories of lift. With certain assumptions, the BEMT allows the inflow distribution along the blade to be estimated.

Consider first the application of the conservation laws to an annulus of the rotor disk, as shown in Fig. 3.4. This is the essence of Froude's original differential theory for propellers in axial motion. This annulus is at a distance y from the rotational axis, and has a width dy. The area of this annulus is, therefore, $dA = 2\pi y\ dy$. The incremental thrust, dT, on this annulus may be calculated on the basis of simple momentum theory and with the 2-D assumption that successive rotor annuli have no mutual effects on each other. As might be expected, this approach has good validity except near the blade tips. The removal of this 2-D restriction requires a considerably more advanced treatment of the problem using a vortex wake theory. However, a good approximation to the tip-loss effect on the inflow distribution can be made using Prandtl's "circulation-loss" function, which will be discussed in Section 3.3.10. Tokaty (1971) gives a good historical overview of the origins of the blade element and blade element momentum theories.

On the basis of simple one-dimensional momentum theory developed in Chapter 2, we may compute the incremental thrust on the rotor annulus as the product of the mass flow rate through the annulus and twice the induced velocity at that section. In this case the mass flow rate over the annulus of the disk is

$$d\dot{m} = \rho dA(V_c + v_i) = 2\pi\rho(V_c + v_i)y\ dy, \tag{3.42}$$

so that the incremental thrust on the annulus is

$$dT = 2\rho\,(V_c + v_i)\,v_i dA = 4\pi\rho\,(V_c + v_i)\,v_i y\ dy. \tag{3.43}$$

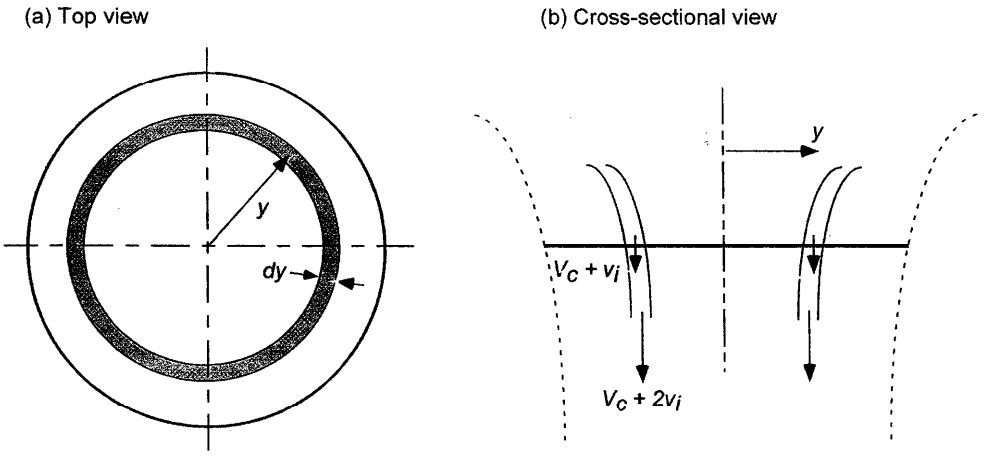

Figure 3.4 Annulus of rotor disk as used for a local momentum analysis of the hovering rotor. (a) Top view. (b) Cross-sectional view.

This has also been known as the Froude–Finsterwalder equation. It is more convenient to work in nondimensional quantities so that

$$dC_T = \frac{dT}{\rho(\pi R^2)(\Omega R)^2} = \frac{2\rho(V_c + v_i)v_i dA}{\rho\pi R^2(\Omega R)^2}$$
$$= \frac{2\rho(V_c + v_i)v_i(2\pi y\, dy)}{\rho\pi R^2(\Omega R)^2} = 4\frac{(V_c + v_i)}{\Omega R}\left(\frac{v_i}{\Omega R}\right)\left(\frac{y}{R}\right)d\left(\frac{y}{R}\right)$$

or simply

$$dC_T = 4\lambda\lambda_i r\, dr. \tag{3.44}$$

Therefore, the incremental thrust coefficient on the annulus can be written as

$$dC_T = 4\lambda\lambda_i r\, dr = 4\lambda(\lambda - \lambda_c) r\, dr \tag{3.45}$$

because $\lambda_i = \lambda - \lambda_c$. The induced power consumed by the annulus is

$$dC_{P_i} = \lambda dC_T = 4\lambda^2\lambda_i r\, dr = 4\lambda^2(\lambda - \lambda_c) r\, dr. \tag{3.46}$$

This assumes no swirl in the wake, which is justified in Section 3.3.6. Consider first the hovering state where $\lambda_c = 0$. The incremental thrust and power contributions of the annulus are given by

$$dC_T = 4\lambda^2 r\, dr \quad \text{and} \quad dC_{P_i} = 4\lambda^3 r\, dr, \tag{3.47}$$

which are given by Glauert (1935). The total thrust coefficient of the rotor is

$$C_T = \int_{r=0}^{r=1} dC_T = 4\int_0^1 \lambda^2 r\, dr \tag{3.48}$$

and the corresponding induced power coefficient is

$$C_{P_i} = \int_{r=0}^{r=1} \lambda dC_T = 4\int_0^1 \lambda^3 r\, dr. \tag{3.49}$$

3.3.1 *Assumed Radial Distributions of Inflow on the Blades*

The foregoing results are valid for any radial form of induced velocity distribution across the disk. Assume for illustrative purposes that the inflow can be prescribed and expressed in the simple form

$$\lambda(r) = \lambda_{\text{tip}} r^n \quad \text{for } n \geq 0. \tag{3.50}$$

Then using Eq. 3.48 leads to

$$C_T = 4\int_0^1 \lambda^2 r\, dr = 4\lambda_{\text{tip}}^2 \int_0^1 r^{2n+1}\, dr = \frac{4\lambda_{\text{tip}}^2}{2n+2} = \frac{2\lambda_{\text{tip}}^2}{n+1}. \tag{3.51}$$

Solving for λ_{tip} gives

$$\lambda_{\text{tip}} = \sqrt{n+1}\sqrt{\frac{C_T}{2}}. \tag{3.52}$$

The induced power coefficient is

$$C_{P_i} = 4\int_0^1 \lambda^3 r\, dr = 4\lambda_{\text{tip}}^3 \int_0^1 r^{3n+1}\, dr = \frac{4\lambda_{\text{tip}}^3}{3n+2}, \tag{3.53}$$

and substituting the result from Eq. 3.52 gives

$$C_{P_i} = \frac{2(n+1)^{3/2} C_T^{3/2}}{(3n+2)\sqrt{2}}. \tag{3.54}$$

It has been shown previously that the induced power can be written as

$$C_{P_i} = \frac{\kappa C_T^{3/2}}{\sqrt{2}}, \tag{3.55}$$

and so in this case the induced power factor, κ, is

$$\kappa = \frac{2(n+1)^{3/2}}{(3n+2)}. \tag{3.56}$$

Notice that for $n = 0$ (uniform inflow) then $\kappa = 1$ (ideal case). For $n > 0$, then $\kappa > 1$, and as the value of n increases κ increases as the inflow becomes more heavily biased toward the blade tips.

3.3.2 *Radial Inflow Equation*

Although it is clear from the foregoing that if the inflow can be determined, considerable information about the rotor performance can be obtained. The issue is now to devise an approach that can solve for the inflow directly, without making any assumptions as to its magnitude or form. One solution can be obtained using a hybrid blade element and momentum approach using the principles of the equivalence between the circulation theory of lift the momentum theory of lift. From the BET it has been shown in Eq. 3.15 that the incremental thrust produced on an annulus of the disk is

$$dC_T = \frac{1}{2}\sigma C_l r^2\, dr = \frac{\sigma C_{l_\alpha}}{2}\left(\theta r^2 - \lambda r\right) dr. \tag{3.57}$$

Equating the incremental thrust coefficients from the momentum and blade element theories (using Eqs. 3.45 and 3.57) we find that

$$\frac{\sigma C_{l_\alpha}}{2}\left(\theta r^2 - \lambda r\right) = 4\lambda\left(\lambda - \lambda_c\right) r, \tag{3.58}$$

which gives

$$\frac{\sigma C_{l_\alpha}}{8}\theta r - \frac{\sigma C_{l_\alpha}}{8}\lambda = \lambda^2 - \lambda_c \lambda \tag{3.59}$$

or

$$\lambda^2 + \left(\frac{\sigma C_{l_\alpha}}{8} - \lambda_c\right)\lambda - \frac{\sigma C_{l_\alpha}}{8}\theta r = 0. \tag{3.60}$$

This quadratic equation in λ has the solution

$$\lambda(r, \lambda_c) = \sqrt{\left(\frac{\sigma C_{l_\alpha}}{16} - \frac{\lambda_c}{2}\right)^2 + \frac{\sigma C_{l_\alpha}}{8}\theta r} - \left(\frac{\sigma C_{l_\alpha}}{16} - \frac{\lambda_c}{2}\right). \tag{3.61}$$

Consider hovering conditions where $\lambda_c = 0$, then Eq. 3.61 simplifies to

$$\lambda(r) \equiv \lambda_{i(r)} = \frac{\sigma C_{l_\alpha}}{16}\left(\sqrt{1 + \frac{32}{\sigma C_{l_\alpha}}\theta r} - 1\right). \tag{3.62}$$

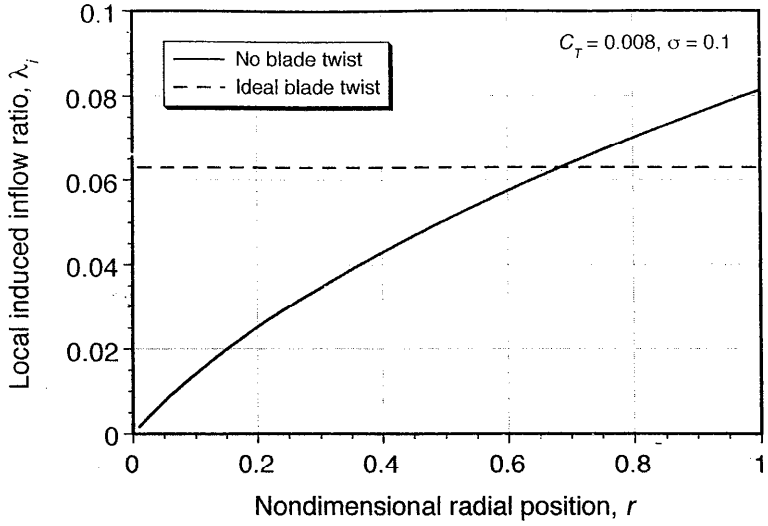

Figure 3.5 Distribution of inflow for an ideally twisted blade as predicted by the BEMT compared to an untwisted blade.

Equation 3.62 allows for a solution of the inflow as a function of radius for any given blade pitch, blade twist distribution, planform (chord distribution), and airfoil section (through the effect of lift-curve-slope C_{l_α} and zero-lift angle α_0 via θ). When the inflow is obtained, the rotor thrust and induced power may then be found by integration across the rotor disk using Eqs. 3.48 and 3.49.

For an untwisted blade of constant chord and uniform airfoil section, the distribution of inflow as predicted by Eq. 3.62 is shown in Fig. 3.5, and is compared with the uniform inflow at the same thrust coefficient. For the untwisted blade the distribution of inflow is concentrated toward its tips (i.e., $n = 1$ in Eq. 3.50). Clearly, the combination of blade geometric parameters for the results shown in Fig. 3.5 is nonideal because as shown by Eq. 3.56 the induced power will be higher than the minimum possible with uniform inflow ($n = 0$). We must now proceed to examine how the blade geometric properties could be adjusted to give a more uniform inflow and, therefore, to minimize the induced power requirements for the rotor.

3.3.3 *Ideal Twist*

Gessow (1948) showed that if $\theta r = \text{constant} = \theta_{\text{tip}}$ there is a special solution to the inflow equation in Eq. 3.62 that gives uniform inflow, that is,

$$\theta(r) = \frac{\theta_{\text{tip}}}{r}. \tag{3.63}$$

This twist distribution is called *ideal twist* and is shown in Fig. 3.6. This solution lays down the goal for a rotor blade design because the uniform inflow case must always correspond to the minimum induced power for the rotor when operating in hover or in axial climb. Unfortunately, the hyperbolic form of pitch angle or twist distribution given by Eq. 3.63 is physically unrealizable as $r \to 0$. However, because of the hub and root cutout, in a practical sense the blade pitch variation here does not matter anyway. Figure 3.6 shows that

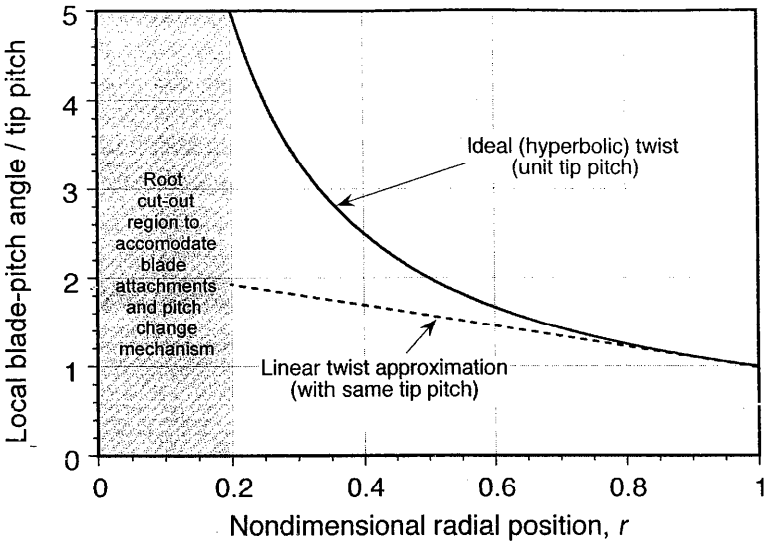

Figure 3.6 Radial distribution of blade twist in ideal case.

a linear twist distribution is reasonably close to the ideal case over the outer part of the blade.

A careful examination of airplane propellers will show that they are highly twisted and, in fact, closely conform to the ideal blade twist given by Eq. 3.63. For helicopter rotors, such high amounts of twist over the blade span is nonoptimum for the entire flight envelope. This is because the rotor must also operate in forward flight, and high values of blade twist can lead to less efficient lift and propulsion generation from the advancing side of the disk at high advance ratios. Nevertheless, because helicopters spend a substantial part of operating time in hover and low speed forward flight, there are considerable performance benefits to be realized by incorporating some blade twist.

With ideal twist the performance of the rotor can now be recalculated. If θr = constant = θ_{tip}, then

$$C_T = \frac{\sigma C_{l_\alpha}}{2} \int_0^1 (\theta_{\text{tip}} - \lambda) r \, dr = \frac{\sigma C_{l_\alpha}}{2} \left(\frac{\theta_{\text{tip}}}{2} - \frac{\lambda}{2} \right). \tag{3.64}$$

Using Eq. 3.13 gives $\lambda = r\phi = \phi_{\text{tip}}$ = constant, and so the preceding equation can also be written as

$$C_T = \frac{\sigma C_{l_\alpha}}{4} (\theta_{\text{tip}} - \phi_{\text{tip}}) = \frac{\sigma C_{l_\alpha}}{4} \alpha_{\text{tip}}. \tag{3.65}$$

Using Eqs. 3.61 and 3.63 gives

$$\lambda(r) = \frac{\sigma C_{l_\alpha}}{16} \left(\sqrt{1 + \frac{32\theta_{\text{tip}}}{\sigma C_{l_\alpha}}} - 1 \right) = \text{constant} = \sqrt{\frac{C_T}{2}}. \tag{3.66}$$

A solution for the blade pitch angle can be found from

$$\theta_{\text{tip}} = \frac{4C_T}{\sigma C_{l_\alpha}} + \sqrt{\frac{C_T}{2}} \quad \text{or} \quad \theta_{\text{tip}} = \frac{4C_T}{\sigma C_{l_\alpha}} + \lambda. \tag{3.67}$$

The first term in either of the previous equations can be thought of as a mean blade pitch to produce thrust, and the second term is an additional blade-pitch angle that is required to compensate for the induced inflow produced by the generation of that thrust.

One can also prove that the ideal twist distribution gives a special result, namely a linear (triangular) lift distribution over the blade, which is consistent with uniform disk loading. Recall that the incremental thrust distribution is given by

$$dC_T = \frac{\sigma C_{l_\alpha}}{2}(\theta_{\text{tip}} - \lambda)r\, dr. \tag{3.68}$$

Because λ is a constant, the thrust distribution on the blade varies in proportion to r (i.e., it is a linear distribution). Another way of writing the preceding equation is just

$$dC_T = \frac{\sigma C_{l_\alpha}}{2}\alpha_{\text{tip}} r\, dr = \frac{\sigma}{2} C_{l_{\text{tip}}} r\, dr. \tag{3.69}$$

Therefore, the total thrust on the rotor with ideal blade twist is

$$C_T = \frac{\sigma}{4} C_{l_{\text{tip}}} = \frac{\sigma}{4} C_{l_\alpha} \alpha_{\text{tip}}. \tag{3.70}$$

3.3.4 *BEMT: Numerical Solution*

In most practical applications the equations of the BEMT are solved numerically. This allows the maximum flexibility to incorporate arbitrary radial variations in twist, planform, and so on. In the numerical approach, the blade must be discretized into a series of small elements of span Δr. For hovering flight, the inflow is now obtained using the discretized equation

$$\lambda(r_n) = \frac{\sigma C_{l_\alpha}}{16}\left(\sqrt{1 + \frac{32}{\sigma C_{l_\alpha}}\theta(r_n) r_n} - 1\right), \tag{3.71}$$

where $n = 1, N$ is the element location (station) and r_n and $\theta(r_n)$ are the radius and pitch angle at the mid-span of each of the N stations, respectively.[1] For climbing flight then Eq. 3.61 must be solved. When the inflow is determined using Eq. 3.71, the incremental thrust at each segment can be found using

$$\Delta C_{T_n} = \frac{\sigma C_{l_\alpha}}{2}\left(\theta(r_n)\, r_n^2 - \lambda(r_n)\, r_n\right) \Delta r. \tag{3.72}$$

The total thrust on the rotor is then obtained by numerically integrating over the blade. The simplest approach is to use the rectangle rule, which is equivalent to considering the inflow and thrust to be constant over each segment. In this case

$$C_T = \sum_{n=1}^{N} \Delta C_{T_n}, \tag{3.73}$$

which will be adequate for most purposes unless only a few stations are used. The corresponding induced torque (or power) can be obtained using

$$C_P \equiv C_Q = \sum_{n=1}^{N} \lambda_n\, \Delta C_{T_n}. \tag{3.74}$$

[1] Typically, a minimum of 20 elements must be used to ensure an adequate numerical resolution of the inflow and spanwise loading, but 40 elements or more is desirable.

It is normally desirable to compare results for different rotors at the same value of C_T. Therefore, for rotors with different twist or planforms, the blade (collective) pitch, θ_0, required to obtain the required value of thrust coefficient, say $C_{T_{\text{req}}}$, must be obtained iteratively starting from an assumed value for θ_0. For this, we can use as a basis the simple relationships found previously between the blade pitch and C_T. For example, for a blade with linear twist and with the assumption of uniform inflow, it was shown that

$$C_T = \frac{1}{2}\sigma C_{l_\alpha}\left(\frac{\theta_0}{3} + \frac{\theta_{\text{tw}}}{4} - \frac{1}{2}\sqrt{\frac{C_T}{2}}\right), \tag{3.75}$$

or rearranging and solving for θ_0 gives

$$\theta_0 = \frac{6C_T}{\sigma C_{l_\alpha}} - \frac{3}{4}\theta_{\text{tw}} + \frac{3}{2}\sqrt{\frac{C_T}{2}}. \tag{3.76}$$

Therefore, one simple iterative scheme based on a bisection method of correcting the collective pitch from iteration j to $j+1$ is

$$\theta_0^{(j+1)} = \theta_0^{(j)} + \left[\frac{6(C_{T_{\text{req}}} - C_T^{(j)})}{\sigma C_{l_\alpha}} + \frac{3\sqrt{2}}{4}\left(\sqrt{C_{T_{\text{req}}}} - \sqrt{C_T^{(j)}}\right)\right] \tag{3.77}$$

starting from the initial value

$$\theta_0^{(0)} = \frac{6C_{T_{\text{req}}}}{\sigma C_{l_\alpha}} - \frac{3}{4}\theta_{\text{tw}} + \frac{3\sqrt{2}}{4}\sqrt{C_{T_{\text{req}}}}. \tag{3.78}$$

Using this approach, the collective pitch is found to converge rapidly to provide the required value of C_T for any arbitrary rotor geometry, typically within two to four iterations.

3.3.5 *Distributions of Inflow and Airloads*

Using the numerical implementation of the BEMT, the distribution of inflow and lift on a blade with any distribution of twist (and planform) can be readily determined. Representative results for λ and dC_T/dr are shown in Figs. 3.7(a) and (b), respectively, for a rectangular blade with different linear twist rates and at a constant value of thrust. For reference purposes, the distribution corresponding to ideal twist is also shown, which gives a uniform inflow and a linear variation of lift from the root to the tip. Notice that the lift on the untwisted blade is parabolic. With moderate values of twist, the lift distribution becomes more linear, with an off-loading at the tip and a greater loading being produced inboard, and more closely resembles that obtained in the ideal blade twist case. For very high values of blade twist exceeding 20°, the tip is off-loaded to the point that the inflow becomes more nonuniform again and the rotor thereby becomes aerodynamically less efficient.

The corresponding local lift coefficient distribution over the blade is found using

$$C_l(r_n) = C_{l_\alpha}\left(\theta(r_n) - \frac{\lambda(r_n)}{r_n}\right), \tag{3.79}$$

with representative results being shown in Fig. 3.8 for different amounts of linear twist. For a rotor with constant blade chord and the ideal twist distribution $\theta = \theta_{\text{tip}}/r$ the local lift

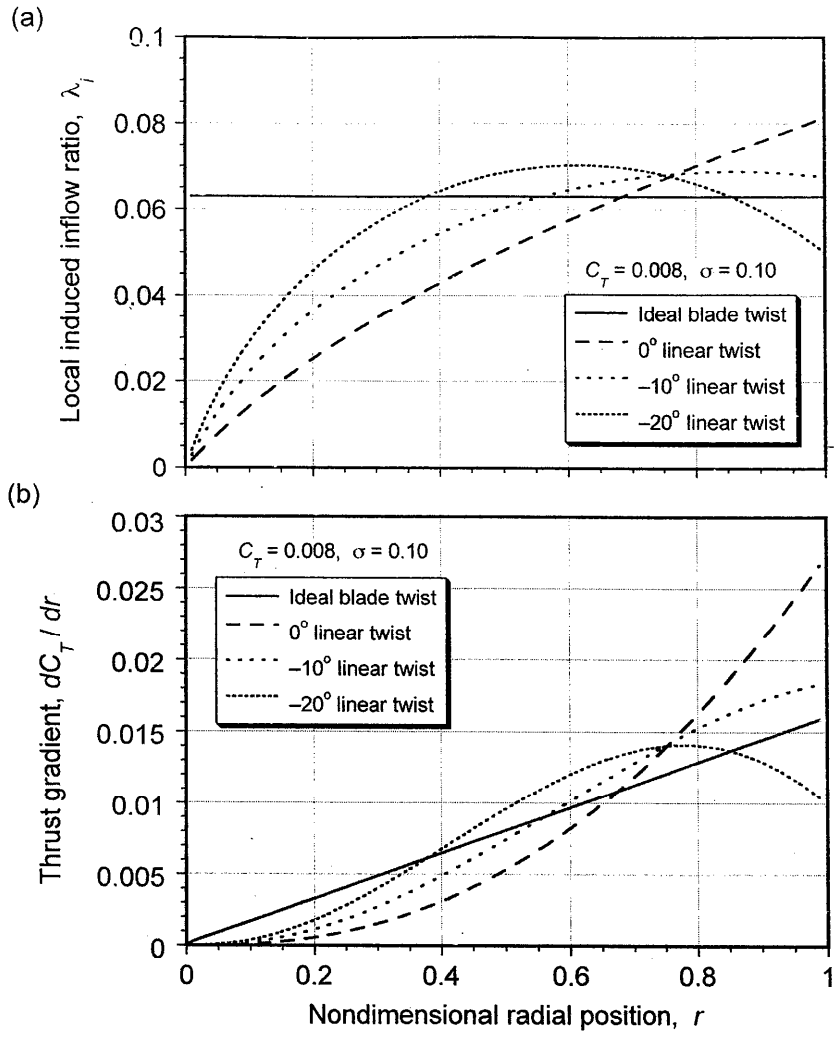

Figure 3.7 BEMT predictions of spanwise distributions of inflow and thrust on a rotor blade for different linear twist rates. Results are compared at a constant total thrust. (a) Inflow ratio. (b) Thrust per unit span.

coefficient can be determined analytically. The incremental thrust coefficient is given by the standard BET equation

$$dC_T = \frac{\sigma C_{l_\alpha}}{2}\left(\theta - \frac{\lambda}{r}\right) r^2\, dr = \frac{\sigma C_{l_\alpha}}{2}\left(\frac{\theta_{\text{tip}}}{r} - \frac{\lambda}{r}\right) r^2\, dr. \tag{3.80}$$

In the ideal case λ is a constant, so that the AoA along the blade must be

$$\alpha(r) = \frac{\theta_{\text{tip}} - \lambda}{r} = \frac{\alpha_{\text{tip}}}{r}. \tag{3.81}$$

This confirms that the blade loading distribution is triangular, that is,

$$\frac{dC_T}{dr} = \frac{\sigma C_{l_\alpha}}{2}\alpha_{\text{tip}} r. \tag{3.82}$$

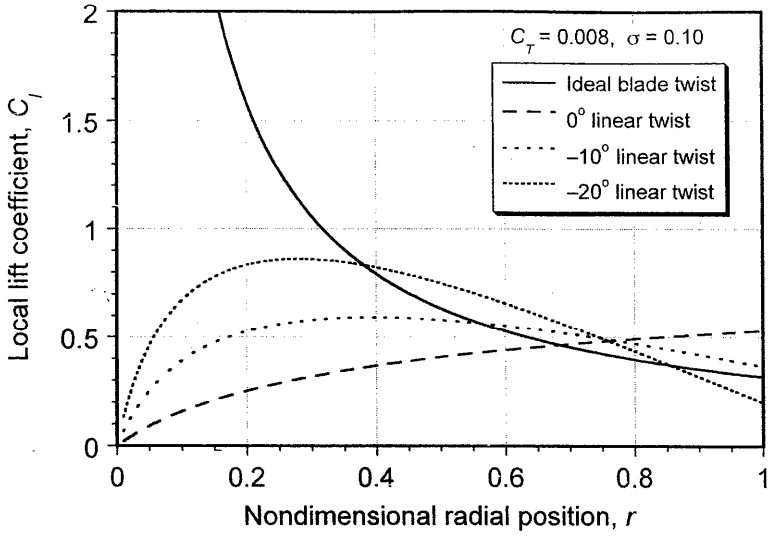

Figure 3.8 BEMT predictions of lift coefficient distribution on a rotor blade for different linear twist rates. Results are compared at a constant total rotor thrust.

As previously shown, besides uniform inflow, the ideal twist distribution also gives uniform disk loading. For the ideal rotor (with constant chord, ideal twist, uniform inflow) integration along the blade leads to

$$C_T = \frac{\sigma C_{l_\alpha}}{4}\left(\theta_{\text{tip}} - \lambda\right) = \frac{\sigma C_{l_\alpha}}{4}\alpha_{\text{tip}}. \tag{3.83}$$

Remember that simple momentum theory gives a value of $\lambda = \sqrt{C_T/2}$ in hover. Therefore, the blade pitch angle is $\theta_{\text{tip}} = \alpha_{\text{tip}} + \lambda$ so that

$$\theta_{\text{tip}} = \frac{4C_T}{\sigma C_{l_\alpha}} + \sqrt{\frac{C_T}{2}}. \tag{3.84}$$

The local blade AoA can also be written as

$$\alpha(r) = \frac{\alpha_{\text{tip}}}{r} = \frac{4C_T}{\sigma C_{l_\alpha}}\left(\frac{1}{r}\right). \tag{3.85}$$

Then the corresponding local blade-lift coefficient is

$$C_l(r) = C_{l_\alpha}\alpha = \frac{4C_T}{\sigma}\left(\frac{1}{r}\right), \tag{3.86}$$

which is plotted in Fig. 3.8. This result shows that for a rectangular blade with ideal twist (minimum possible induced power), the lift coefficients become very large at the root end of the blade; thus drag coefficients will increase and rotor performance will ultimately be limited by the onset of stall. Besides the fact that C_l (and C_d) increases rapidly when moving inboard from the tip, there can only be one blade station on the blade operating at its best lift-to-drag ratio. Therefore, anything less than the best C_l/C_d must always result in a higher profile power consumption from the rotor than would otherwise be possible.

This effect can be seen more clearly if representative lift-to-drag ratios of 2-D airfoils are examined, as shown in Fig. 3.9. In this case, the best C_l/C_d of the airfoil sections occurs at an AoA between 5 and 10° (denoted as α_1), and this operating condition should be the design goal at all blade stations to achieve minimum profile power. The AoA for the

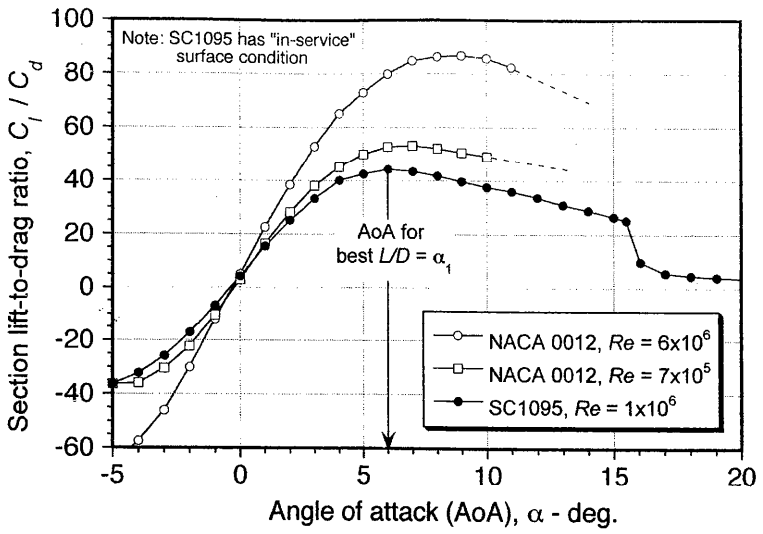

Figure 3.9 Representative lift-to-drag ratio of a 2-D airfoil at low angles of attack and low Mach numbers. Data source: Loftin & Smith (1949) and Leishman (1996).

best C_l/C_d is a function of Mach number as well as Reynolds number and surface finish (roughness) – see Chapter 7. A hovering rotor that is designed to minimize both the induced power and the profile power is called an *optimum hovering rotor* – see Section 3.3.7.

3.3.6 *Effects of Swirl Velocity*

Before considering this optimum rotor, however, it is important to consider the significance of the wake swirl in determining the aerodynamic environment at the blade elements. For a helicopter the wake swirl is a function of rotor operating state (mainly thrust, as discussed on page 69), but swirl is generally small and practice has shown that for a helicopter the swirl can be ignored without any significant effects on predicted blade loads or rotor performance. The most complete and comprehensive exposition of the swirl effects on rotor performance is given by Glauert (1935), but Nikolsky (1951) also gives a good summary. In the generalized differential momentum theory, the thrust and torque on an annulus of the rotor in the hover state are, respectively,

$$dT = 4\pi\rho v_i^2 y\, dy \quad \text{and} \quad dQ_i = 4\pi\rho v_i \Omega a' y^3\, dy, \tag{3.87}$$

where a' is known as the wake rotational interference factor. In terms of a' the work done by the rotor over the annulus is

$$(1 - a')\Omega dQ_i = v_i dT. \tag{3.88}$$

In the case were the wake swirl is ignored (i.e., $a' = 0$), then these results reduce to the two equations used previously, i.e.,

$$dT = 4\pi\rho v_i^2 y\, dy \quad \text{and} \quad \Omega dQ_i = dP_i = 4\pi\rho v_i^3 y\, dy. \tag{3.89}$$

In nondimensional form these are also the same as those used before, that is,

$$dC_T = 4\lambda_i^2 r\, dr \quad \text{and} \quad dC_{P_i} = 4\lambda_i^3 r\, dr. \tag{3.90}$$

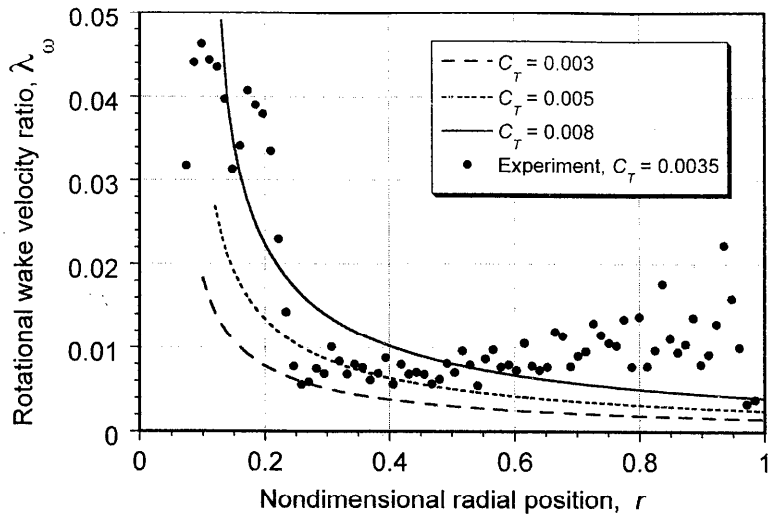

Figure 3.10 Representative distribution of swirl in the wake of a hovering rotor. Data source: LDV measurements from the University of Maryland.

When the wake swirl is included, then the equations become

$$dC_T = 4\lambda_i^2 r\, dr \tag{3.91}$$

and

$$dC_{P_i} = 4\lambda_i a' r^3\, dr \tag{3.92}$$

and with the additional equation

$$(1 - a')a'r^2 = \lambda_i^2. \tag{3.93}$$

These are the equations of Glauert's generalized differential momentum theory.

To illustrate the relative magnitude of the induced swirl for a helicopter, it is convenient to assume that λ_i is distributed uniformly as in the ideal case, in which case Eq. 3.93 can be solved for a'. Results are shown in Fig. 3.10 for several representative rotor-thrust coefficients. The nondimensional swirl velocity λ_ω is simply $a'r$. Time-averaged measurements made in the wake of a two-bladed hovering rotor are also shown and, while there is significant scatter because of the low velocities being measured, the magnitude and distribution are in general agreement with the theory. Notice that the swirl values are small over a large part of the blade (less than 2% of tip speed) but increase more rapidly toward the blade root. This region, however, is of little importance aerodynamically. There is some increase in swirl velocity near the blade tip, which is part of the signature of the tip vortex. Therefore, as a contributor to the resultant velocity and AoA at the blade element it is clear that the effects of the swirl in defining the aerodynamic environment for a helicopter rotor is small, but not completely negligible.

3.3.7 *The Optimum Hovering Rotor*

Minimum induced power requires uniform inflow over the disk. The corresponding condition for minimum profile power requires that each blade station operate at the AoA

for maximum C_l/C_d (i.e., at $\alpha = \alpha_1$ as shown in Fig. 3.9). For minimum induced power then $\theta = \theta_{tip}/r$, and if each element of the blade is to operate at α_1 then

$$dC_T = \frac{\sigma C_{l_\alpha}}{2}\left(\frac{\theta_{tip}}{r} - \frac{\lambda}{r}\right) r^2\, dr = \frac{\sigma C_{l_\alpha}}{2}\alpha_1 r^2\, dr. \tag{3.94}$$

Also, it has been shown previously from the BEMT that for an annulus of the disk

$$dC_T = 4\lambda^2 r\, dr. \tag{3.95}$$

Equating Eqs. 3.94 and 3.95 and solving for λ gives

$$\lambda = \sqrt{\frac{\sigma r C_{l_\alpha}\alpha_1}{8}} = \sqrt{\frac{\sigma_{tip} C_{l_\alpha}\alpha_1}{8}}, \tag{3.96}$$

which is constant over the disk, as required. If it is assumed that α_1 is the same for all the airfoils along the blade span and independent of Reynolds number and Mach number, then for uniform inflow the product σr in Eq. 3.96 must be a constant, that is,

$$\sigma r = \left(\frac{N_b}{\pi R}\right) cr = \text{constant}, \tag{3.97}$$

which requires a local chord distribution over the blade to be given by

$$c(r) = \frac{c_{tip}}{r} \quad \text{and} \quad \sigma(r) = \frac{\sigma_{tip}}{r}. \tag{3.98}$$

Therefore, for each section of the blade to operate at the optimum lift-to-drag ratio, the local blade solidity, $\sigma(r)$ or blade chord, $c(r)$ must vary hyperbolically with span, as shown by Fig. 3.11. Clearly this distribution is physically unrealizable but can be adequately approximated by a linear taper over the outer part of the blade. Because of the hub and root cut-out, the chord variation as $r \to 0$ does not matter anyway. Furthermore, as seen from Fig. 3.9, operating the airfoils at angles of attack that are few degrees less or greater than α_1 does not result in a serious degradation of C_l/C_d. Therefore, the use of some planform taper, while not exactly hyperbolic or applied over the whole blade, will generally always have a beneficial effect on hovering rotor performance.

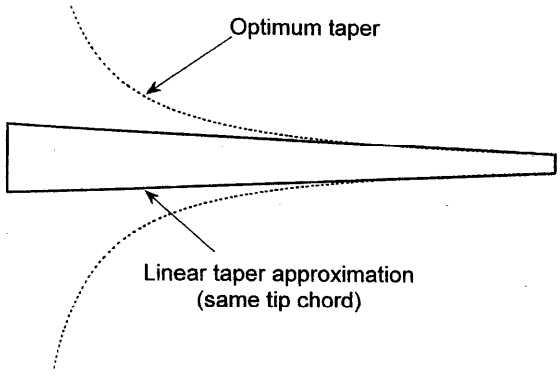

Figure 3.11 Radial distribution of blade chord for an optimum rotor and a linear approximation.

The blade twist required for uniform inflow *and* for a constant AoA along the blade can be found from

$$\alpha = \left(\theta - \frac{\lambda}{r}\right) = \alpha_1 = \text{constant} \tag{3.99}$$

or

$$\theta(r) = \alpha_1 + \frac{\lambda}{r} = \alpha_1 + \sqrt{\frac{\sigma_{\text{tip}} C_{l_\alpha} \alpha_1}{8}} \left(\frac{1}{r}\right). \tag{3.100}$$

In this case, the rotor thrust distribution is still linear across the disk from the root to the tip (corresponding to the uniform pressure jump), with the total thrust being given by

$$C_T = \frac{1}{2} C_{l_\alpha} \int_0^1 \sigma \alpha_1 r^2 \, dr = \left(\frac{\sigma_{\text{tip}} C_{l_\alpha}}{4}\right) \alpha_1. \tag{3.101}$$

Therefore, the *local* solidity (or sometimes known as the *chord* solidity) of the optimum rotor can be written as

$$\sigma(r) = \left(\frac{4C_T}{C_{l_\alpha} \alpha_1}\right) \frac{1}{r} \tag{3.102}$$

and the blade twist as

$$\theta(r) = \alpha_1 + \frac{\lambda}{r} = \alpha_1 + \sqrt{\frac{C_T}{2}} \left(\frac{1}{r}\right), \tag{3.103}$$

which are both hyperbolic variations. This is the "optimum" hovering rotor originally referred to by Gessow (1948). Notice that the final optimum blade design depends on C_T.

It is common for linear blade twist and taper planform variations to be employed on helicopter rotor blades, and this is found sufficiently close to the optimum defined on the basis of the BEMT. For example, Fig. 3.12 shows the effects on the spanwise distribution of lift coefficient for different values of linear taper. The results are compared at the same

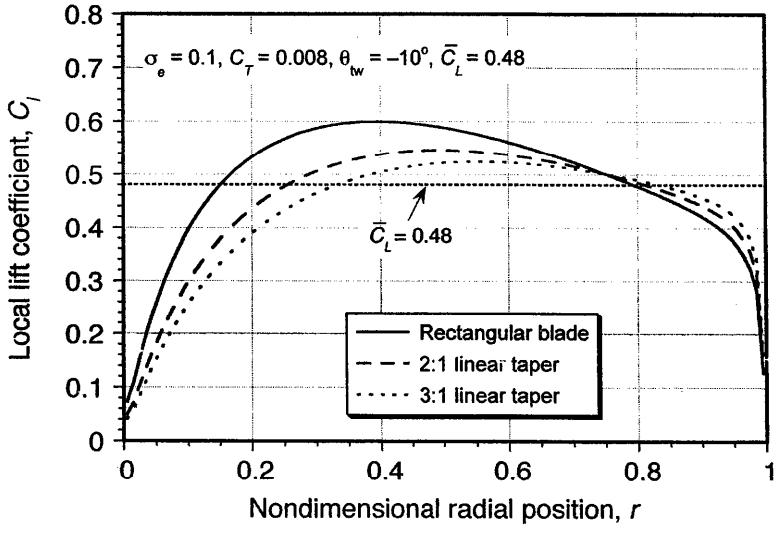

Figure 3.12 Effect of blade taper on the lift coefficient distribution over a blade with constant twist.

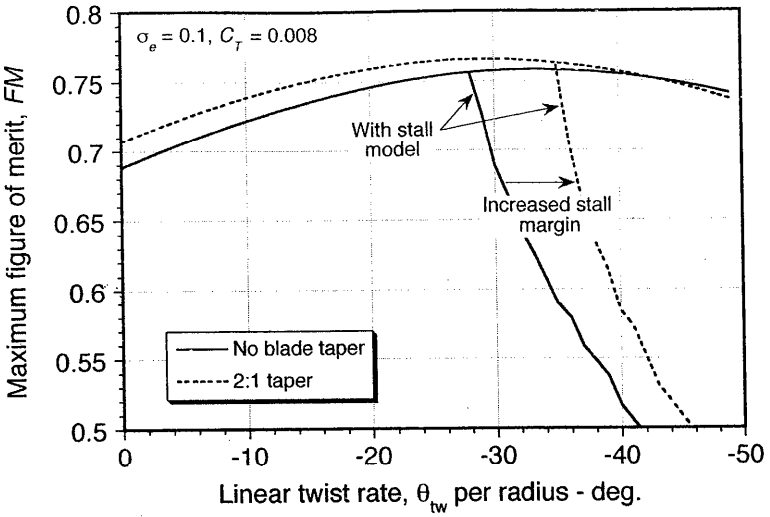

Figure 3.13 Effect of blade twist and taper on rotor figure of merit.

thrust-weighted solidity. For a linearly tapered blade, this means that the solidity at 75% blade radius is the same in all cases – see Section 3.4. Without taper the lift coefficients at the root of the blade are relatively high and cannot operate at the best C_l/C_d ratio for the airfoil section so C_{P_0} would be higher than otherwise possible. As C_T is increased, the rotor performance will be limited by the onset of stall at the blade root. From Fig. 3.12 we see that with the introduction of a moderate amount of taper the values of C_l become much more uniform, with the values of C_l being significantly reduced at the blade root along with a mild increase in C_l at the tip. This reduces the profile power component, and so the rotor can be operated at the same thrust but with an improved figure of merit.

The point is expounded further by the results shown in Fig. 3.13, where the figure of merit is plotted versus the twist rate for a rotor with rectangular blades and one with linearly tapered blades. A mild amount of taper clearly gives a notable increase in *FM*. In either case, the rotor ultimately becomes limited by the onset of stall, but the use of blade taper clearly allows the rotor to operate with a higher stall margin. This also allows a higher possible collective pitch, a higher attainable rotor thrust, and better overall hovering efficiency.

3.3.8 *Circulation Theory of Lift*

Although discussed in more detail in Chapter 10, another interesting result of the foregoing is that with a linear lift loading distribution, the local "bound" circulation on the blade is constant. The link between lift per unit length of span and the distribution of circulation on the blade, $\Gamma(y)$, is given by the Kutta–Joukowski theorem, so that

$$dL = \rho(\Omega y)\Gamma\, dy = \frac{1}{2}\rho(\Omega y)^2 c C_l\, dy \quad \text{or simply that} \quad C_l = \frac{2\Gamma}{\Omega y c}. \tag{3.104}$$

Therefore, using Eq. 3.69

$$dC_T = \frac{N_b\rho(\Omega y)\Gamma\, dy}{\rho A(\Omega R)^2} = \frac{N_b\Gamma r\, dr}{\Omega\pi R^2} = \frac{\sigma C_{l_{tip}}}{2} r\, dr, \tag{3.105}$$

so that

$$\Gamma(r) = \frac{\sigma C_{l_{\text{tip}}} \Omega \pi R^2}{2N_b} = \frac{cRC_{l_{\text{tip}}} \Omega}{2} = \text{constant}, \tag{3.106}$$

confirming that ideal twist gives uniform inflow, a linear distribution of lift (thrust) *and* a constant "bound" circulation over the blade.

A link can also be made between the momentum theory of lift and the vortex theory (considered in Chapter 10). With a uniform circulation along the blade span, Helmholtz's theorem requires a single vortex of the same strength to trail from the blade tips. This vortex strength can be related to the blade loading as follows. The lift per unit span along the blade is

$$dL = \rho(\Omega y)\Gamma \, dy. \tag{3.107}$$

Because Γ is constant, then the lift on one blade is

$$L = \rho\Omega\Gamma \int_0^R y \, dy = \rho\Omega\Gamma R^2/2. \tag{3.108}$$

The total rotor thrust is $T = N_b L$, and in coefficient form we have

$$C_T = \frac{N_b \Gamma}{2(\pi R^2)\Omega}. \tag{3.109}$$

Using the result for the solidity that $\sigma = N_b c/\pi R$, we get

$$\frac{C_T}{\sigma} = \frac{\Gamma}{2\Omega c R} \tag{3.110}$$

or

$$\Gamma = 2\Omega R c \left(\frac{C_T}{\sigma}\right), \tag{3.111}$$

or nondimensionally that

$$\hat{\Gamma} = \frac{\Gamma}{\Omega R c} = 2\left(\frac{C_T}{\sigma}\right). \tag{3.112}$$

Remember that this result is for an "ideal" rotor operating in hover. However, the result provides a simple connection between the rotor operating state and the strength (circulation) of the tip vortex filaments that are trailed into the rotor wake – see Chapter 10.

3.3.9 *Power Estimates for the Rotor*

For a real rotor, the nonuniformity of λ over the disk means that the induced power must be calculated by numerically integrating the equation

$$C_{P_i} = \int_{r=0}^{r=1} \lambda \, dC_T \approx \sum_{n=1}^{N} \lambda_n \Delta C_{T_n} \tag{3.113}$$

using the actual induced velocity distribution computed using the BEMT. This equation also allows the calculation of the induced power factor, κ, for different twist distributions, that is,

$$\kappa = \frac{C_{P_i}}{C_T^{3/2}/\sqrt{2}}. \tag{3.114}$$

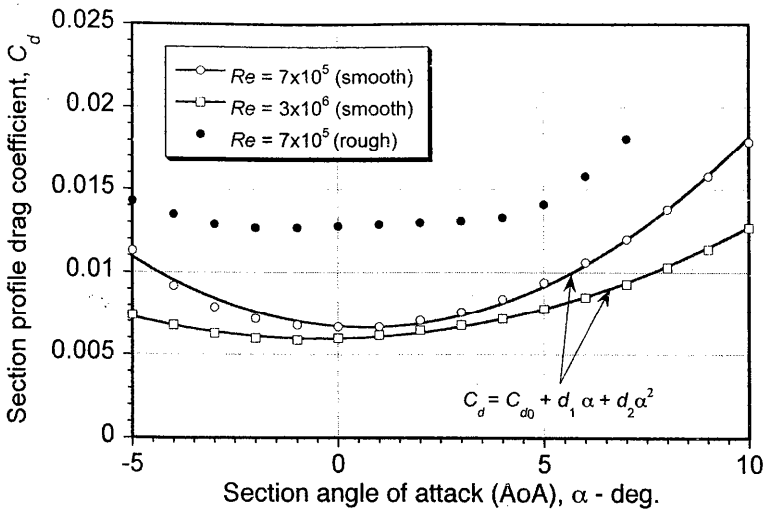

Figure 3.14 Representative 2-D drag coefficient variation for an airfoil as a function of angle of attack. Data source: Loftin & Smith (1949).

For a more accurate calculation of the rotor profile power, we must consider the variation in sectional drag coefficient with blade section AoA – see Bailey & Gustafson (1944). For most airfoils the sectional drag coefficient below stall[2] can be approximated by

$$C_d = C_{d_0} + d_1\alpha + d_2\alpha^2, \tag{3.115}$$

as shown in Fig. 3.14. Clearly, the coefficients of this expression are also a function of airfoil section, Mach number, Reynolds number, and surface finish, and the behavior cannot easily be generalized. In practice, it is found sufficiently accurate to use 2-D airfoil measurements for the Reynolds and Mach numbers corresponding to those at 75% radius on the rotor. Yet, caution should be exercised when analyzing subscale rotors. If measurements for the airfoil in question are not available at low Reynolds number, then catalogs of airfoil data such as those compiled by Althaus (1972) and Miley (1982) are often useful in estimating the anticipated effects.

The profile part of the rotor power is given by

$$C_{P_0} = \frac{\sigma}{2}\int_0^1 C_d r^3\, dr. \tag{3.116}$$

Proceeding on the basis that Eq. 3.115 is valid, then substituting gives

$$\begin{aligned} C_{P_0} &= \frac{\sigma}{2}\int_0^1 \left[C_{d_0} + d_1(\theta - \phi) + d_2(\theta - \phi)^2\right] r^3\, dr \\ &= \frac{\sigma}{2}\int_0^1 \left[C_{d_0} + d_1\left(\theta - \frac{\lambda}{r}\right) + d_2\left(\theta - \frac{\lambda}{r}\right)^2\right] r^3\, dr. \end{aligned} \tag{3.117}$$

[2] Measurements of 2-D section drag are often made by measuring the velocity in the wake of the airfoil, followed by a momentum balance using the conservation laws in integral form. This, however, is a technique valid only below stall where there are no viscous losses from rotation of the fluid (see Section 7.8 and Question 7.9).

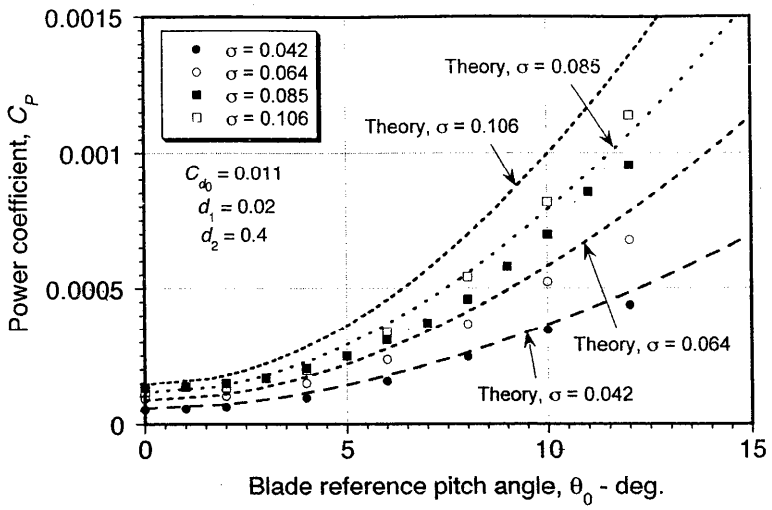

Figure 3.15 Predicted power coefficient collective pitch using higher-order profile drag variation. Data source: Knight & Hefner (1937).

Now, for ideally twisted blades, λ = constant and $\theta r = \theta_{\text{tip}}$ so that

$$C_{P_0} = \frac{\sigma C_{d_0}}{8} + \frac{\sigma d_1}{6}\left(\theta_{\text{tip}} - \lambda\right) + \frac{\sigma d_2}{4}\left(\theta_{\text{tip}} - \lambda\right)^2$$
$$= \frac{\sigma C_{d_0}}{8} + \left(\frac{2d_1}{3C_{l_\alpha}}\right) C_T + \left(\frac{4d_2}{\sigma C_{l_\alpha}^2}\right) C_T^2, \tag{3.118}$$

with the latter equation being obtained using the result that

$$\theta_{\text{tip}} - \lambda = \frac{4C_T}{\sigma C_{l_\alpha}}. \tag{3.119}$$

By including the higher-order approximation for the airfoil drag, improvements in rotor power prediction at higher values of C_T are usually obtained. Results from the experiments of Knight & Hefner (1937) are shown again in Fig. 3.15, but with the modified drag expression. Notice the better agreement than that shown previously in Fig. 3.3 when a constant drag coefficient was assumed, although power is perhaps now somewhat overpredicted for higher solidities and shows the limitations of this approximate approach.

3.3.10 *Prandtl's Tip-Loss Function*

The idea of a tip-loss factor, B, has already been introduced. Instead of assuming a value for B it is possible to compute tip-loss effects on the basis of a method devised by Prandtl – see Betz (1919). Prandtl provided a solution to the problem of the loss of lift near the tips resulting from the induced effects associated with a finite number of blades. This theory contains all the elements of a model that was developed later by Goldstein (1929) and Lock (1930) but has several simplifications that make it attractive for helicopter rotor analysis. Prandtl replaced the curved helical vortex sheets of the rotor wake by a series of 2-D vortex sheets, the assumption here being that the radius of curvature at the blade tips is large. This is a satisfactory assumption for helicopter rotors but is less so for propellers.

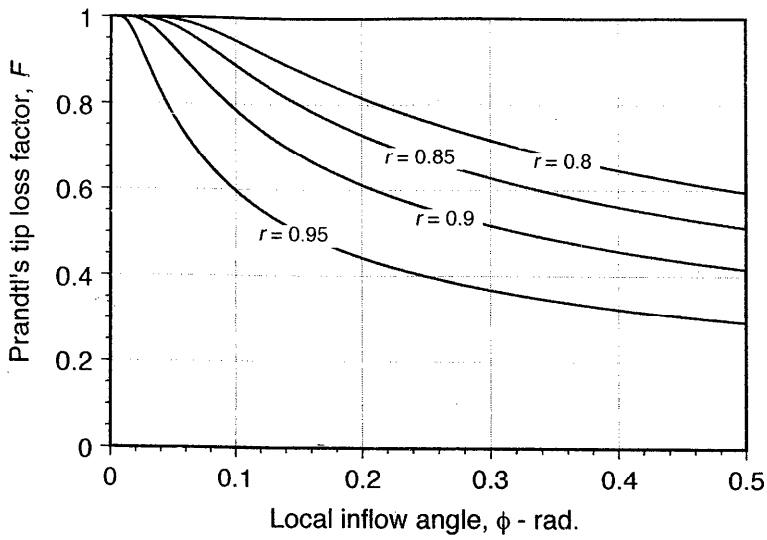

Figure 3.16 Variation of Prandtl tip-loss function versus local flow angle for a two-bladed rotor.

Prandtl's final result can be expressed in terms of a correction factor, F, where

$$F = \left(\frac{2}{\pi}\right)\cos^{-1}\left(\exp(-f)\right), \tag{3.120}$$

where f is given in terms of the number of blades and the radial position of the blade element, r, by

$$f = \frac{N_b}{2}\left(\frac{1-r}{r\phi}\right) \tag{3.121}$$

and ϕ is the induced inflow angle ($= \lambda(r)/r$).

Prandtl's F function is plotted in Fig. 3.16 versus the local inflow angle, ϕ, for a two-bladed rotor. The basic effect of the F function is to increase the induced velocity over the tip region and reduce the lift generated there. The Prandtl function is, therefore, sometimes referred to as a "circulation loss" function. Prandtl's F function is plotted versus the radial position of the blade element in Fig. 3.17 for two- and four-bladed rotors, and for different values of the inflow angle, ϕ. The gradual reduction in the function as the tip is approached represents the basic induced effects of the vortex wake. Notice that F is a function of the number of blades and always has lower values for rotors with fewer blades. This is because the total bound circulation is distributed over fewer blades and the induced effects in the rotor wake are higher. For the limiting case where $N_b \to \infty$, which approximates an actuator disk, the circulation is distributed uniformly over the disk and $F \to 1$.

In the application of the Prandtl tip-loss method, the function F can also be interpreted as a reduction factor applied to the change in fluid velocity as it passes through the control volume. The tip-loss effect can be incorporated into the BEMT as follows. For hovering flight Eq. 3.44 is now modified by the use of the Prandtl factor, F, to give

$$dC_T = 4F\lambda^2 r\, dr. \tag{3.122}$$

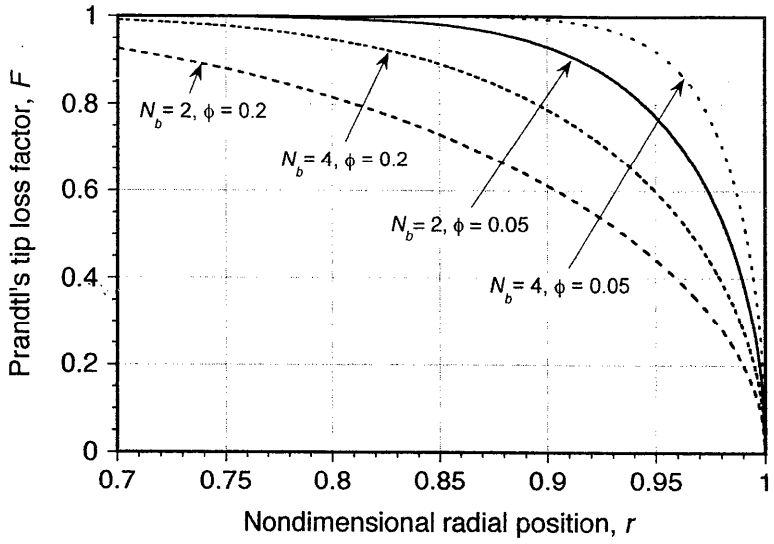

Figure 3.17 Variation of Prandtl tip-loss function versus radial position for two- and four-bladed rotors.

Also, from the BET it has been shown previously that

$$dC_T = \frac{\sigma C_{l_\alpha}}{2}\left(\theta r^2 - \lambda r\right) dr. \tag{3.123}$$

Equating the incremental thrust coefficients from the momentum and blade element theories gives

$$\frac{\sigma C_{l_\alpha}}{2}\left(\theta r^2 - \lambda r\right) = 4F\lambda^2 r \tag{3.124}$$

or

$$\lambda^2 + \left(\frac{\sigma C_{l_\alpha}}{8F}\right)\lambda - \frac{\sigma C_{l_\alpha}}{8F}\theta r = 0. \tag{3.125}$$

This quadratic has the solution

$$\lambda(r) = \frac{\sigma C_{l_\alpha}}{16F}\left(\sqrt{1 + \frac{32F}{\sigma C_{l_\alpha}}\theta r} - 1\right). \tag{3.126}$$

Because F is a function of λ, this equation cannot be solved immediately because λ is initially unknown. Therefore, it is solved iteratively by first calculating λ using $F = 1$ (corresponding to an infinite number of blades) and then finding F from Eq. 3.120 and recalculating λ from the numerical solution to Eq. 3.126. Convergence is rapid and is obtained in three or four iterations.

The resulting effect of the application of Prandtl's F function on the blade-thrust distribution is shown in Fig. 3.18 for an untwisted blade. These comparisons have been performed at the same value of thrust obtained without using the tip-loss effect. Notice that the primary effect of the tip loss is to reduce the thrust production over the immediate tip region. This loss of thrust has to be compensated by a slightly greater blade pitch, which increases the angles of attack further inboard to produce the same total rotor thrust. Generally it is found that the use of a larger number of blades tends to improve the efficiency of the

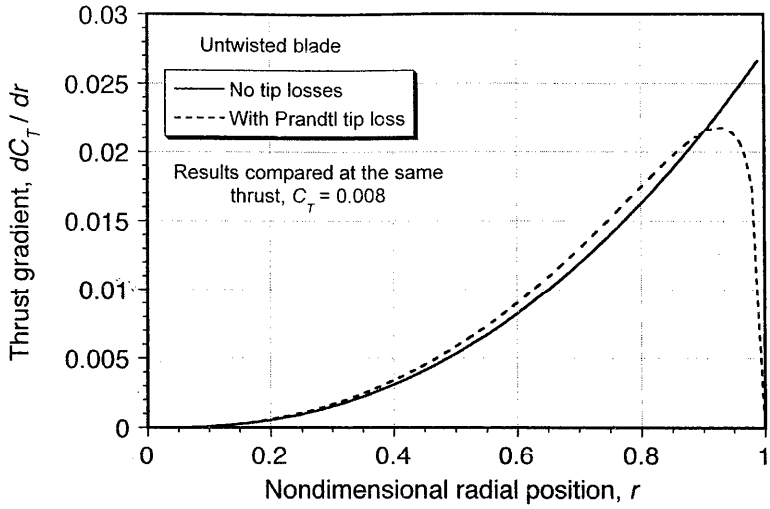

Figure 3.18 Spanwise variation of blade thrust using the Prandtl tip-loss function.

rotor (increases the figure of merit) for a given solidity and disk loading because the induced tip-loss effects tend to decrease with increasing number of blades (see Questions 3.2 and 3.3).

The ideas of tip loss can also be extended to model the loss of lift at the root of the blade. In this case the value of f in Eq. 3.120 becomes

$$f = \frac{N_b}{2}\left(\frac{r}{(1-r)\phi}\right). \tag{3.127}$$

The tip and root losses can be combined into a single function using

$$f = f_{\text{root}}\, f_{\text{tip}}, \tag{3.128}$$

where f_{root} is given by Eq. 3.127 and f_{tip} by Eq. 3.121. Generally the effects of including root loss effects are small on the calculation of total rotor thrust and power because the inboard parts of the blade operate at relatively low dynamic pressures. However, the effects are usually more apparent when examining the spanwise distribution of airloads in coefficient form.

An example using the BEMT with both tip and root losses is shown in Fig. 3.19 for the case of a tilt-rotor operating in the hover mode. Tilt-rotor blades have large amounts of twist, which are more optimal for forward flight performance in propeller mode compared to helicopter mode. The results in this case show how the inboard sections of this rotor operate at relatively high lift coefficients compared to a typical helicopter (see the results in Fig. 3.8) and so more accurate nonlinear aerodynamic modeling here is important in this case, despite the lower dynamic pressures. The BEMT results are compared in Fig. 3.19 with the results of a more advanced blade element theory (BET) combined with a free-vortex model of the rotor wake (see Section 10.7.6). Clearly the use of the BEMT by itself gives reasonable agreement with the BET results, but the introduction of the Prandtl tip- and root-loss effects into the BEMT clearly gives much better results. (The results are all compared at the same total C_T.) Remember that the purpose of the Prandtl tip-loss function is to *approximately* model the high induced losses produced by the trailing vorticity generated from the tip and

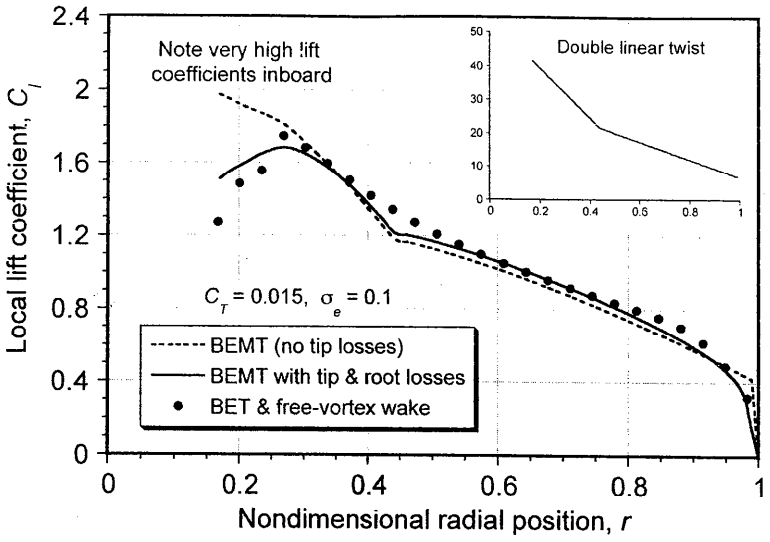

Figure 3.19 Spanwise variation of local lift coefficient for a tilt-rotor using the BEMT incorporating Prandtl losses compared to a more advanced vortex wake analysis.

root side edges of the blade, flow physics that are included in the more advanced vortex wake model. Overall the results in Fig. 3.19 show that the BEMT is an effective tool for at least the preliminary analysis of the spanwise distribution of airloads, especially bearing in mind the negligible computational cost of this type of method.

3.3.11 *Blade Design and Figure of Merit*

On the basis of the predictions of profile power from the blade element analysis, the figure of merit can be written as

$$FM = \frac{C_{P_{\text{ideal}}}}{C_{P_i} + C_{P_0}}, \tag{3.129}$$

where $C_{P_{\text{ideal}}} = C_T^{3/2}/\sqrt{2}$ and C_{P_i} can be written in terms of the induced power factor, κ as $C_{P_i} = \kappa C_T^{3/2}/\sqrt{2}$. From the numerical approach to the BEMT theory, and incorporating Prandtl's tip-loss function, we can readily obtain the results for C_{P_i}, C_{P_0}, κ, and FM as a function of collective pitch or C_T, and the results can then be compared for different blade twist rates and/or planforms. It has been shown previously that blade twist primarily affects the induced power. Results showing the effects of blade twist on the induced power factor, κ versus rotor thrust coefficient are given in Fig. 3.20. The values of κ have been computed for a four-bladed rotor. Notice that there are significant reductions in induced power (and gains in FM) to be made by the addition of nose-down blade twist. Up to $-20°$ of blade twist is considered optimal, with further increases in nose-down twist rate giving only minor returns within the operational values of C_T for a helicopter. The use of high blade twist rates is nonoptimal for forward flight because such blades tend to generate lower lift on the advancing blade compared to a design with less twist – see discussion in Section 6.4.5.

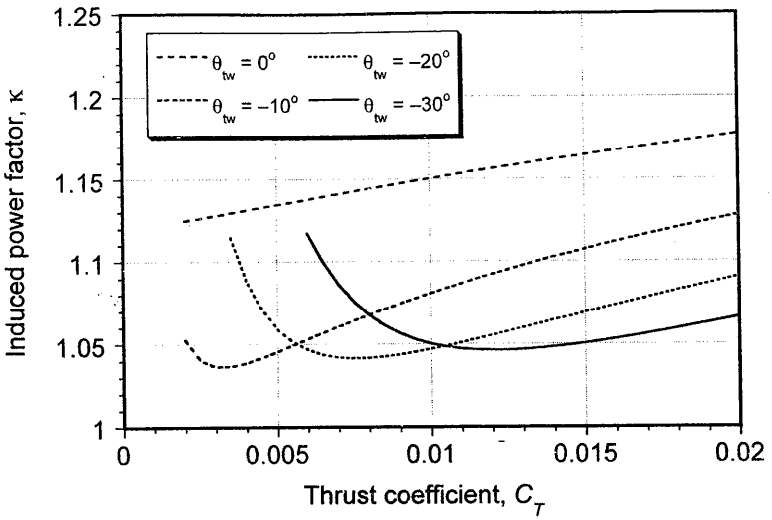

Figure 3.20 BEMT predictions of induced power factor for a four-bladed rotor with linear twist using Prandtl's tip-loss function.

The profile power also affects the *FM*. Using the higher-order drag variation, we have for the rotor with ideally twisted blades that

$$FM = \frac{\dfrac{C_T^{3/2}}{\sqrt{2}}}{\dfrac{\kappa C_T^{3/2}}{\sqrt{2}} + \left[\dfrac{\sigma C_{d_0}}{8} + \left(\dfrac{2\sigma d_1}{3C_{l_\alpha}}\right)\dfrac{C_T}{\sigma} + \left(\dfrac{4\sigma d_2}{C_{l_\alpha}^2}\right)\left(\dfrac{C_T}{\sigma}\right)^2\right]}. \tag{3.130}$$

Notice that the profile power contribution to the *FM* is affected by the rotor solidity, σ. Therefore, it is apparent that to maximize the figure of merit the profile part of the power must be kept as low as possible, which suggests a low value of solidity. The increasing drag of the blades at higher values of C_T means the onset of stall must be delayed to high angles of attack, which means maintaining the blade loading coefficient C_T/σ to lower values. This requires the use of sufficient rotor solidity to maintain sectional C_l's below stall also with sufficient margins in overall C_T/σ for normal flight maneuvers without rotor stall.

3.3.12 *BEMT in Climbing Flight*

The BEMT may be used to estimate the blade airloads during vertically climbing flight. This problem is of some interest because of the changes in the spanwise distribution in lift and so forth that take place. In climbing flight the BEMT requires the use of the Eq. 3.61, that is,

$$\lambda(r, \lambda_c) = \sqrt{\left(\frac{\sigma C_{l_\alpha}}{16F} - \frac{\lambda_c}{2}\right)^2 + \frac{\sigma C_{l_\alpha}}{8F}\theta r} - \left(\frac{\sigma C_{l_\alpha}}{16F} - \frac{\lambda_c}{2}\right), \tag{3.131}$$

which in this case has been modified with the use of the Prandtl tip-loss factor. The numerical solution proceeds as before for the hovering rotor. However, notice that a solution for the blade pitch must also be obtained for each climb rate because thrust also equals weight in the climb (but neglecting airframe download and vertical-drag effects).

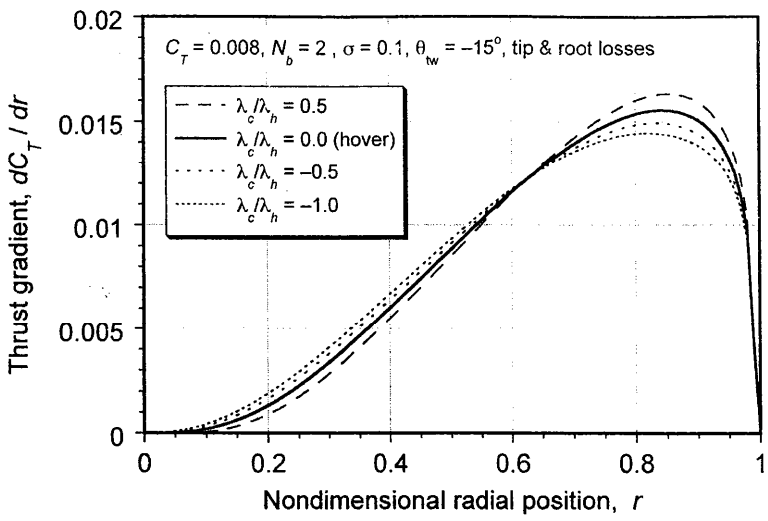

Figure 3.21 BEMT predictions of spanwise thrust for a two-bladed rotor with linear blade twist in vertically climbing and descending flight.

Representative results are shown in Fig. 3.21 for both climbing and descending conditions at the same C_T compared to the hover result. The results show how the spanwise distribution of thrust becomes more heavily biased outboard in climbing flight, with the opposite effect in descending flight. This also changes the distributions of lift coefficient, torque, and so on. While the validity of the BEMT does not strictly extend to descending flight when moving from hover, for the same reasons that the simple momentum theory does not apply here, the solution has credibility as long as the descent velocities are small.

Because the climb (or descent) affects the spanwise distribution of airloads it is of interest to examine the changes in the induced power factor that take place. Normally it is acceptable to assume that κ does not change with flight condition, but much has to do with the actual rotor design. Representative results are shown in Fig. 3.22 for the same rotor in climbing and descending flight but with different amounts of blade twist. The results are obtained by finding the induced power from the BEMT normalized by the induced power from the simple momentum theory. Clearly the value of κ may increase or decrease with climb velocity, depending on the blade twist.

For a rotor that has close to ideal blade twist (which in this case is $\theta_{tw} \approx -20°$ at the defined operating condition of $C_T = 0.008$) either climbing or descending flight changes the spanwise distribution of airloads further from the ideal and the values of κ increase. For a blade with less than near optimum twist, notice from the results in Fig. 3.22 how κ actually decreases as the rotor descends compared to a rotor with large amounts of blade twist (such as a tilt-rotor). This has particularly important implications for the design of autogiro rotors (see Chapter 12); because the flow is upward through the rotor in autorotation little or no twist will give better efficiency (i.e., lower autorotative rate of descent, shallower aft disk tilt in level flight, and overall better lift-to-drag ratio for the rotor). For blades with large amounts of twist, it is apparent that κ improves somewhat in a climb but increases more quickly in a descent. Overall, however, the results show that the variations of κ with climb or descent velocity are fairly modest and for many forms of performance analyses it will be acceptable to assume that κ = constant.

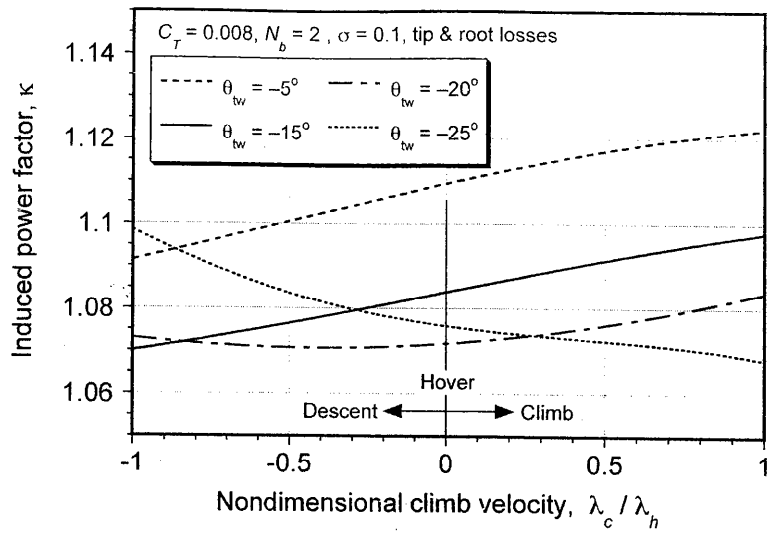

Figure 3.22 BEMT predictions of induced power factor in vertically climbing and descending flight.

3.3.13 *Further Comparisons of BEMT with Experiment*

Results showing predictions made by the complete BEMT with measured thrust and power data for a hovering rotor are given in Fig. 3.23 for a four-bladed rotor of solidity 0.1 and with −13 degrees of linear blade twist. Compared to the modified momentum theory, now only a model for the profile drag losses must be assumed; all the induced losses resulting from nonuniform inflow and Prandtl tip losses are now calculated directly from the more complete BEMT method. Figure 3.23 shows that with the assumption that C_d = constant, the more complete BEMT underpredicts the power, and consequently it will

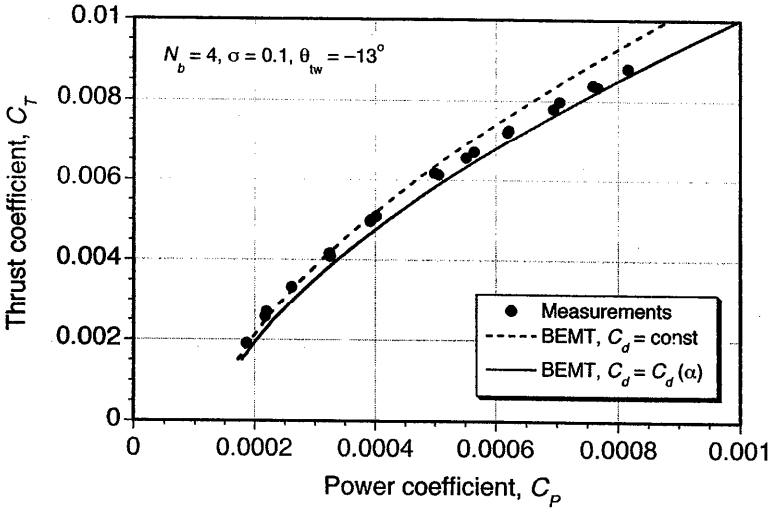

Figure 3.23 Comparison of the BEMT with and without higher-order profile drag terms versus measured thrust and power data (performance polar) for a four-bladed hovering rotor. Data source: Bagai & Leishman (1992).

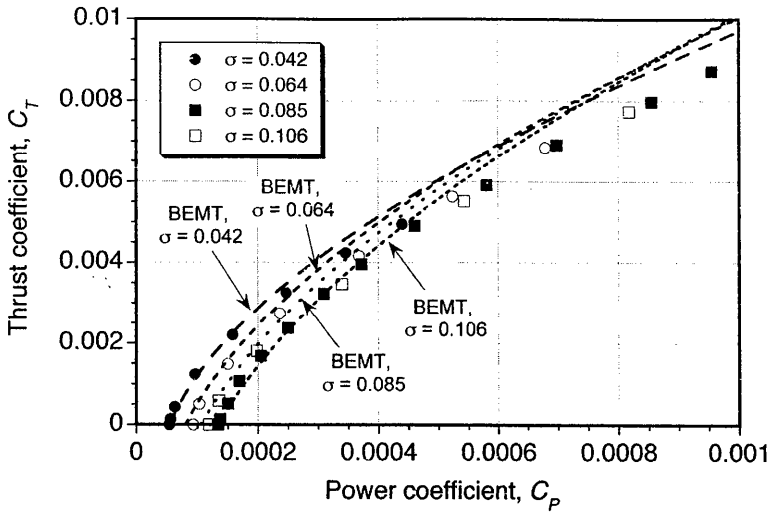

Figure 3.24 Comparison of the BEMT with measured thrust and power data (performance polar) for hovering rotors of different solidity. Data source: Knight & Hefner (1937).

tend to overpredict the figure of merit. The addition of the higher-order drag terms using Eq. 3.115 rectifies this, and the agreement with the measured data is much better.

Figure 3.24 shows a comparison of the complete BEMT with the measurements of thrust and power for a hovering rotor made by Knight & Hefner (1937). Again, the higher-order drag curve using Eq. 3.115 gives good agreement with the measurements. The only discrepancy is at higher values of C_T (> 0.005) where the rotor begins to stall and Eq. 3.115 is insufficient to model the drag behavior. There are also some additional effects of elastic blade twist here, which tend to twist the blade nose-down at the higher blade pitch angles and so aerodynamically offload the tip region.

Measurements of thrust and power in the axial climb condition are relatively rare. Flight test results have been given by Gustafson & Gessow (1945) and others, although it is difficult to estimate fuselage vertical drag and also to separate wake distortion effects resulting from the fuselage from the measured rotor thrust and shaft power in flight tests. These factors make comparisons of flight test results with the BEMT relatively difficult. Such issues are reviewed by Harris (1987), but as Prouty (1986) and others have shown, reasonable climb performance estimation can be expected from the momentum theory if appropriate empirical corrections are taken into account.

Felker & McKillip (1994) have measured isolated rotor performance on subscale rotors tested on a track facility. The thrusting rotor was mounted horizontally on a carriage and moved at constant velocity in still air, thereby simulating a steady climb. The thrust and power were measured with a balance system for constant collective pitch at several axial climb velocities. The measured thrust and power coefficient as a function of climb velocity, λ_c/λ_h or V_c/v_h, are shown in Fig. 3.25 and are compared with results obtained using the BEMT. Because data were acquired at a constant collective pitch, increasing climb velocity reduces the blade element angles of attack resulting in a decrease in rotor thrust. Notice that although the BEMT predicts the thrust behavior well, it tends to underpredict the thrust somewhat at the higher climb velocities. For the lower collective pitch, the maximum underprediction is about 7%; and at the higher collective pitch it is about 4%. Because estimated uncertainties in the measurements are about 5%, the agreement of the BEMT with the measurements can be considered good. The corresponding predictions of power

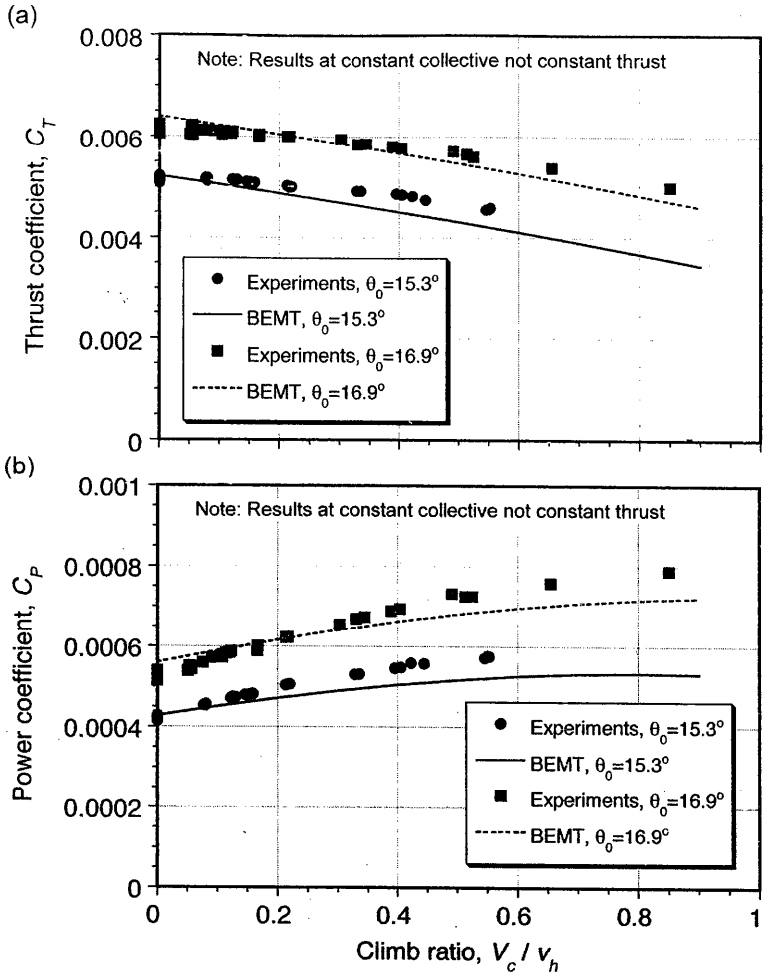

Figure 3.25 Comparison of the BEMT with measured thrust and power data for a climbing rotor. (a) Thrust versus climb ratio. (b) Power versus climb ratio. Data source: Felker & McKillip (1994).

are shown in Fig. 3.25(b), where the climbing work done by the rotor, $C_T\lambda_c$, has been added to the measurements. Again the agreement between the BEMT and experiment is good, except at the higher climb velocities where there is a maximum underprediction of no more than 10%.

3.3.14 *Compressibility Corrections to Rotor Performance*

The assumption that the lift-curve-slope of the blade airfoil sections and the drag coefficients are independent of Mach number is questionable. To examine the effects of compressibility on C_T, consider a correction to the lift-curve-slope of each blade element according to Glauert's rule in which

$$C_{l_\alpha}(M) = \frac{C_{l_\alpha}|_{M=0.1}}{\sqrt{1-M^2}}, \tag{3.132}$$

where $C_{l_\alpha}|_{M=0.1}$ is the measured 2-D lift-curve-slope of the airfoil at $M = 0.1$. The local blade Mach number will be

$$M(y) = \frac{U_T}{a} = \frac{\Omega y}{a}. \tag{3.133}$$

Therefore, the lift-curve-slope correction in terms of the tip Mach number will be

$$\frac{1}{\sqrt{1-M^2}} = \frac{1}{\sqrt{1-\left(\frac{\Omega}{a}\right)^2 y^2}} = \frac{1}{\sqrt{1-M_{\text{tip}}^2 r^2}}, \tag{3.134}$$

where M_{tip} is the tip Mach number. Because $dC_T = \frac{1}{2}\sigma C_l r^2\, dr$ then we may write

$$dC_T = \frac{1}{2}\sigma \frac{C_{l_\alpha}|_{M=0.1}}{\sqrt{1-M_{\text{tip}}^2 r^2}}(\theta r^2 - \lambda r)dr. \tag{3.135}$$

If we still assume ideal twist, and that the inflow remains uniformly distributed, then

$$dC_T = \frac{1}{2}\sigma C_{l_\alpha}|_{M=0.1}(\theta_{\text{tip}} - \lambda)\frac{r}{\sqrt{1-M_{\text{tip}}^2 r^2}}\, dr. \tag{3.136}$$

The total blade thrust is then

$$\begin{aligned} C_T &= \frac{1}{2}\sigma C_{l_\alpha}|_{M=0.1}(\theta_{\text{tip}} - \lambda)\int_0^1 \frac{r}{\sqrt{1-M_{\text{tip}}^2 r^2}}\, dr \\ &= \frac{1}{2}\sigma C_{l_\alpha}|_{M=0.1}(\theta_{\text{tip}} - \lambda)\left[\frac{1}{1+\sqrt{1-M_{\text{tip}}^2}}\right] \\ &= \frac{1}{4}\sigma K C_{l_\alpha}|_{M=0.1}(\theta_{\text{tip}} - \lambda), \end{aligned} \tag{3.137}$$

where the factor K is given by

$$K = \frac{2}{1+\sqrt{1-M_{\text{tip}}^2}}. \tag{3.138}$$

We see that as $M_{\text{tip}} \to 0$ then $K \to 1$ and the incompressible result given previously in Eq. 3.64 is obtained. If it assumed that an averaged compressible lift-curve-slope can be used for the entire rotor then

$$C_{l_\alpha} = \frac{C_{l_\alpha}|_{M=0.1}}{\sqrt{1-(r_e M_{\text{tip}})^2}}, \tag{3.139}$$

where r_e is an effective radius. It can be shown that $r_e = 1/\sqrt{2} = 0.707$ when $M_{\text{tip}} \to 0$, increasing to a value of $r_e = 0.75$ for $M_{\text{tip}} = 0.8$. This is in close agreement with Payne (1959), who suggests using an effective lift-curve-slope at 70% radius, which is probably accurate enough for $M_{\text{tip}} < 0.6$. Peters & Ormiston (1975) suggest using the value of the lift-curve-slope at 75% radius, which is realistic for the normal operational tip Mach numbers of most helicopters. Generally, the effects of compressibility will increase the rotor thrust coefficient by about 10% for a given collective pitch setting. However, tip relief effects (a 3-D effect) tends to reduce these compressibility effects somewhat (see discussion in Section 5.4.3).

Compressibility effects become more important for helicopter rotors when they are operated in forward flight, and especially where the advancing blade tip Mach numbers approach transonic conditions. In forward flight conditions, the idea of a mean lift-curve-slope corrected for compressibility becomes less applicable, and compressibility corrections must be included inside the thrust integral and for other quantities – that is, compressibility modeling must be considered separately at each blade element, and the net effect is obtained by numerical integration. This is the essence of the approach used in nearly all forms of modern helicopter analysis.

3.4 Equivalent Blade Chords and Weighted Solidity

For blades that are nonrectangular in planform the local solidity $\sigma(r)$ varies along the blade span. In this case, to find the thrust coefficient we must use

$$C_T = \frac{1}{2}\int_0^1 \sigma(r) r^2 C_l \, dr, \tag{3.140}$$

where the local solidity of the blade appears *inside* the integral sign. Because the chord varies along the blade span, then the rotor solidity must be written as

$$\sigma_{\text{rotor}} = \frac{\text{Blade area}}{\text{Rotor area}} = \int_0^1 \sigma(r) \, dr. \tag{3.141}$$

For a rectangular blade, the rotor solidity and the local solidity are, of course, identical.

As discussed by Gessow & Myers (1952), the purpose of *weighted* solidities is to help compare the performance of several rotors that may have different blade planforms, for example, rotors with different amounts of taper. The main idea is to generate an equivalent rectangular rotor blade that takes into account the fundamental aerodynamic effects of varying blade chord. The concept, however, is not applicable strictly when applied to other than simple planform shapes. The weighted solidity concept is similar to the mean geometric and aerodynamic chords used in fixed-wing analysis, where an equivalent rectangular wing is derived. In helicopter analyses, two forms of weighted solidities may be used, namely, thrust weighted solidity and power (or torque) weighted solidity. Before defining these quantities, it is instructive to recall the concepts of mean chords used in fixed-wing analyses.

3.4.1 *Mean Wing Chords*

For a fixed (nonrotating) wing, the lift L on the wing of area S and total lift coefficient C_L is given by

$$L = \frac{1}{2}\rho V_\infty^2 S C_L = \frac{1}{2}\rho V_\infty^2 \int_{-s}^{s} c C_l \, dy, \tag{3.142}$$

where C_l is the local section lift coefficient, c is the local chord, and s is the semi-span – see Houghton & Carpenter (1993). We note that the wing area can be written as

$$S = \int_{-s}^{s} c \, dy = 2\int_0^s c \, dy = 2\bar{c}\int_0^s dy, \tag{3.143}$$

where $\bar{c}$ is known as the standard mean chord or the geometric mean chord. Using this definition then

$$C_L \bar{c} \int_0^s dy = \int_0^s c C_l \, dy. \tag{3.144}$$

If an ideal, elliptically loaded wing with elliptical chord is assumed, then C_l is constant along the wing, and so $C_l = C_L$. This gives

$$\bar{c} = \frac{\int_0^s c \, dy}{\int_0^s dy} = \frac{1}{s} \int_0^s c \, dy = \int_0^1 c \, d(y/s), \tag{3.145}$$

which is the usual definition of mean chord used for fixed wings.

3.4.2 *Thrust Weighted Solidity*

Now consider the rotor case. The rotor-thrust coefficient can be written as

$$C_T = \frac{1}{2} \int_0^1 \sigma r^2 C_l \, dr = \frac{1}{2} \sigma_e \int_0^1 r^2 C_l \, dr. \tag{3.146}$$

Assuming constant C_l, as in the case of the fixed wing, gives

$$\int_0^1 \sigma r^2 \, dr = \sigma_e \int_0^1 r^2 \, dr = \frac{\sigma_e}{3}. \tag{3.147}$$

Therefore, based on this assumption the equivalent thrust weighted solidity is

$$\sigma_e = 3 \int_0^1 \sigma(r) r^2 \, dr \tag{3.148}$$

or the equivalent chord is

$$c_e = \frac{3\pi R}{N_b} \int_0^1 \sigma(r) r^2 \, dr. \tag{3.149}$$

This parameter takes into account the primary aerodynamic effect of varying planform, weighting the effects at the tip more heavily than stations further inboard. McVeigh & McHugh (1982) suggest a modification to the weighted solidity definition to take account of tip sweep. In this case, Eq. 3.148 is modified to read

$$\sigma_e = 3 \int_0^1 \sigma(r) r^2 \cos^2 \Lambda(r) \, dr, \tag{3.150}$$

where σ is now measured perpendicular to the local 1/4-chord line and Λ is the local sweep angle of the 1/4-chord from the blade reference axis. The proper validity of this latter expression, however, has not been confirmed.

3.4.3 *Power–Torque Weighted Solidity*

The rotor power or torque coefficient can be written as

$$C_P = C_Q = \int_{r=0}^{r=1} \lambda dC_T + \frac{1}{2} \int_0^1 \sigma(r) r^3 C_d \, dr = \int_{r=0}^{r=1} \lambda dC_T + \frac{1}{2} \sigma_e \int_0^1 r^3 C_d \, dr. \tag{3.151}$$

Assuming constant C_d and uniform inflow then the equivalent power–torque weighted solidity is

$$\sigma_e = 4\int_0^1 \sigma(r)r^3\,dr. \tag{3.152}$$

The torque weighted solidity is analogous to the activity factor used in propeller design. It is also used in wind turbine design but rarely in helicopter design. Again, McVeigh & McHugh (1982) suggest a modification to the weighted solidity if swept tip blades are used so that

$$\sigma_e = 4\int_0^1 \sigma(r)r^3\cos^2\Lambda(r)\,dr. \tag{3.153}$$

3.4.4 *Weighted Solidity of the Optimum Rotor*

With the optimum taper distribution, the profile power coefficient can be established. However, to do this properly we must compare the results at the same *weighted solidity*. In terms of thrust weighted solidity, σ_e, the optimum planform leads to

$$\sigma_e = 3\int_0^1 \sigma r^2\,dr = 3\int_0^1 \left(\frac{\sigma_{\text{tip}}}{r}\right)r^2\,dr = \frac{3}{2}\sigma_{\text{tip}}. \tag{3.154}$$

The profile power coefficient at the same weighted solidity is now

$$C_{P_0} = \int_0^1 \frac{\sigma}{2}r^3 C_{d_0}\,dr = \frac{(2/3)\sigma_e C_{d_0}}{6} = \frac{\sigma_e C_{d_0}}{9}, \tag{3.155}$$

which is about 11% lower than for a rotor with rectangular blades. The figure of merit for the optimum rotor becomes

$$FM = \frac{\dfrac{C_T^{3/2}}{\sqrt{2}}}{\dfrac{\kappa C_T^{3/2}}{\sqrt{2}} + \dfrac{\sigma_e C_{d_0}}{9}}, \tag{3.156}$$

which is a good 2–5% higher than for a rectangular rotor with ideal twist, and this difference can translate into substantial payload gains (see Question 6.8).

3.4.5 *Weighted Solidities of Tapered Blades*

The equivalent solidities for rotors with taper or other planform variation can now be computed. One must be cautious, however, in that the rotor planforms must not be too radically different. This is because the definition of weighted solidity, although based on the blade planform, has a hidden assumption in that the C_l distribution over the blade is assumed to be nominally constant. If this is not the case, then the definition breaks down. Consider a linearly tapered blade that can be described by $\sigma(r) = \sigma_0 + \sigma_1 r$, where σ_0 and σ_1 are constants. The thrust weighted solidity is given by

$$\sigma_e = 3\int_0^1 \sigma r^2\,dr = 3\int_0^1 (\sigma_0 + \sigma_1 r)r^2\,dr = 3\left[\frac{\sigma_0 r^3}{3}\right]_0^1 + 3\left[\frac{\sigma_1 r^4}{4}\right]_0^1$$

$$= \sigma_0 + \frac{3}{4}\sigma_1 = \text{ solidity at 3/4 (75\%) blade radius.}$$

The corresponding power–torque weighted solidity is given by

$$\begin{aligned}\sigma_e &= 4\int_0^1 \sigma r^3\,dr = 4\int_0^1 (\sigma_0 + \sigma_1 r) r^3\,dr \\ &= 4\left[\frac{\sigma_0 r^4}{4}\right]_0^1 + 4\left[\frac{\sigma_1 r^5}{5}\right]_0^1 \\ &= \sigma_0 + \frac{4}{5}\sigma_1 = \text{ solidity at 4/5 (80\%) blade radius.}\end{aligned}$$

Similar results can be obtained for blades with taper extending only over part of the span (see Question 3.12). In this case, the integral for the equivalent weighted solidity must be split into two parts, where the inboard portion of the blade has a constant chord c_r from the root to a point $r = r_1$ (i.e., where $\sigma = \sigma_r$) and then a linear taper from r_1 to the tip at $r = 1$ where the chord is c_t (i.e., $\sigma = \left(\frac{\sigma_t - \sigma_r}{1 - r_1}\right)(r - 1) + \sigma_t$). Then for this blade the equivalent thrust weighted solidity is given by

$$\sigma_e = (\sigma_r - \sigma_t) r_1^3 + \left(\frac{\sigma_t - \sigma_r}{1 - r_1}\right)\left(-\frac{1}{4} + r_1^3 - \frac{3}{4} r_1^4\right) + \sigma_t. \tag{3.157}$$

3.4.6 *Mean Lift Coefficient*

Another parameter that is useful in rotor analyses is the mean lift coefficient, $\bar{C}_L$. The mean lift coefficient[3] is defined to give the same thrust coefficient as

$$C_T = \frac{1}{2}\int_0^1 \sigma r^2 C_l\,dr \tag{3.158}$$

when the entire blade is assumed to be operating at $C_l = \bar{C}_L$. Thus,

$$C_T = \frac{1}{2}\int_0^1 \sigma r^2 \bar{C}_L\,dr = \frac{1}{2}\bar{C}_L \int_0^1 \sigma r^2\,dr = \frac{1}{6}\sigma \bar{C}_L \tag{3.159}$$

or simply that the mean lift coefficient is

$$\bar{C}_L = 6\left(\frac{C_T}{\sigma}\right) = C_{l_\alpha}\bar{\alpha}. \tag{3.160}$$

Therefore, the quantity $\bar{C}_L / C_{l_\alpha}$ can be viewed as a mean AoA of the blades, $\bar{\alpha}$. Because the values of blade loading coefficient, C_T/σ, for a contemporary helicopter rotor will vary between 0.08 and 0.12, it is found that $\bar{C}_L$ is the range 0.5 to 0.8, and so $\bar{\alpha}$ for hovering flight will vary from about 5 to 8 degrees. Remember that, like the weighted solidity factors, the mean lift coefficient is derived on the basis of uniform C_l. In practice, however, for any rotor an estimate of the mean lift coefficient remains a good overall indicator of the average working state of the blades.

[3] Normally in aerodynamics we use lower case subscripts to denote sectional values and subscripts in capitals to mean total or integrated quantities.

Based on the simple corrected momentum theory developed in Chapter 3, notice that the figure of merit can be written in terms of $\bar{C}_L$ as

$$FM = \frac{\lambda_h C_T}{\kappa \lambda_h C_T + \dfrac{\sigma C_{d_0}}{8}} = \frac{1}{\kappa + \dfrac{3}{4}\dfrac{C_{d_0}}{\bar{C}_L}\dfrac{1}{\lambda_h}}, \tag{3.161}$$

which simply confirms what is known all along, in that the use of airfoils with a high average lift-to-drag ratio is required for good hover performance (see also Question 3.7).

3.5 Blade Element Analysis in Forward Flight

For a helicopter, the rotor must provide both a lifting force (in opposition to the aircraft weight) and a propulsive force (to overcome the rotor and airframe drag) in forward flight. In forward flight, the rotor moves almost edgewise through the air, and the blade sections must encounter a periodic variation in local velocity (Fig. 2.1). This gives rise to a number of complications in the aerodynamics of the rotor, including the effects of blade flapping, significant compressibility effects, unsteady effects, nonlinear aerodynamics, and the possibility of stall, reverse flow, and so on, and the complex induced velocity from the rotor wake (see Chapter 10). All these effects are difficult to model. However, using the BET with certain simplifying assumptions, the leading terms of the rotor aerodynamic forces can be obtained – see Chapter 4. These solutions are very instructive and also provide closed form expressions that can be used for validation or as "sanity checks" when analyzing the results from more comprehensive mathematical models of the rotor aerodynamics. The use of such checks is considered good engineering practice.

3.5.1 *Determining Blade Forces*

The same blade element assumptions and approximations previously used for the axisymmetric flight case can also be considered as valid in forward flight. As before, the velocity at the blade element with a pitch angle θ is decomposed into an out-of-plane (perpendicular) velocity component, U_P, and a tangential (in-plane) component, U_T, perpendicular to the leading edge of the blade, both relative to the rotor disk plane, as shown previously in Fig. 3.1. The resultant velocity is

$$U = \sqrt{U_T^2 + U_P^2} \approx U_T \tag{3.162}$$

because U_P is generally small relative to U_T over most of the blade. The relative inflow angle (or induced angle of attack) at the blade section is

$$\phi = \tan^{-1}\left(\frac{U_P}{U_T}\right) \approx \frac{U_P}{U_T} \text{ for small angles.} \tag{3.163}$$

Therefore, the aerodynamic AoA of the blade element is given by

$$\alpha = \theta - \phi. \tag{3.164}$$

The resultant incremental lift dL per unit span on the blade element is given by

$$\begin{aligned} dL &= \frac{1}{2}\rho U^2 c C_l \, dy = \frac{1}{2}\rho U_T^2 c C_{l_\alpha}(\theta - \phi)\, dy \\ &= \frac{1}{2}\rho U_T^2 c C_{l_\alpha}\left(\theta - \frac{U_P}{U_T}\right) dy = \frac{1}{2}\rho c C_{l_\alpha}(\theta U_T^2 - U_P U_T)\, dy \end{aligned} \tag{3.165}$$

and the incremental drag is

$$dD = \frac{1}{2}\rho U^2 c C_d \, dy, \tag{3.166}$$

which act perpendicular and parallel to the resultant flow velocity at the section, respectively. Resolving these forces perpendicular and parallel to the rotor disk gives

$$dF_z = dL\cos\phi - dD\sin\phi \approx dL = \frac{1}{2}\rho c C_{l_\alpha}(\theta U_T^2 - U_P U_T)\, dy \tag{3.167}$$

and

$$\begin{aligned} dF_x &= dL\sin\phi + dD\cos\phi \approx \phi dL + dD \\ &= \frac{1}{2}\rho c C_{l_\alpha}\left(\theta U_P U_T - U_P^2 + \frac{C_d}{C_{l_\alpha}}U_T^2\right) dy. \end{aligned} \tag{3.168}$$

In forward flight the blade element velocity components are periodic at the rotor rotational frequency. As for the hover case, there is an in-plane velocity component because of blade rotation about the rotor shaft, but now there is a further free-stream (translational) part such that

$$U_T(y, \psi) = \Omega y + V_\infty \sin\psi = \Omega y + \mu\Omega R \sin\psi. \tag{3.169}$$

The out-of-plane component consists of three parts. The first is a component comprising the inflow velocity, as in the hover case. The other two components result from perturbations in velocity at the blade element that are produced by blade motion (i.e., flapping). With reference to Fig. 3.26, a perturbation in velocity $y\dot{\beta}$ is produced as a result of the blade flapping velocity about a hinge, with another perturbation $\mu\Omega R\beta\cos\psi$ produced because of blade flapping displacements (coning). The origin of blade flapping is considered in detail in Chapter 4. Therefore, the velocity perpendicular to the disk can be written as

$$U_P(y, \psi) = (\lambda_c + \lambda_i)\Omega R + y\dot{\beta}(\psi) + \mu\Omega R\beta(\psi)\cos\psi. \tag{3.170}$$

Also, there is a radial velocity component parallel to the span axis of the blade and this is given by

$$U_R(\psi) = \mu\Omega R\cos\psi. \tag{3.171}$$

In the BET the aerodynamic effects resulting from this radial velocity are neglected. This is in accordance with the independence principle of sweep, which states that the aerodynamics result only because of the velocity components and AoA perpendicular to the leading edge

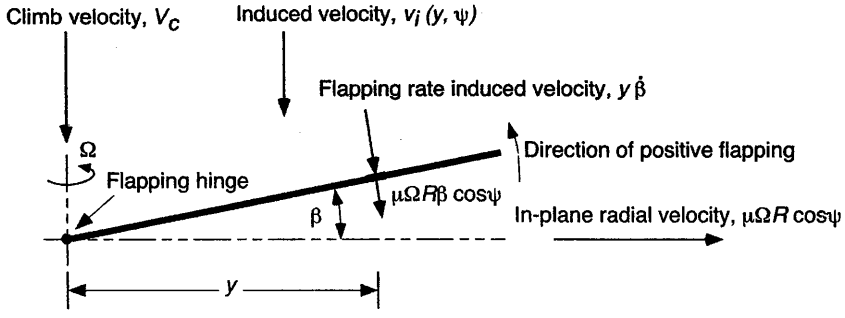

Figure 3.26 Perturbation velocities on the blade resulting from blade flapping velocity and rotor coning.

of the blade (see discussion in Chapter 9). However, the effects of the radial velocity component along the blade may need to be considered when estimating the rotor drag.

In nondimensional form, the three preceding equations can be written as

$$\frac{U_T}{\Omega R} = \left(\frac{y}{R} + \mu \sin\psi\right) = (r + \mu \sin\psi), \tag{3.172}$$

$$\frac{U_P}{\Omega R} = \left(\lambda + \frac{y\dot{\beta}}{\Omega R} + \mu\beta\cos\psi\right) = \left(\lambda + \frac{r\dot{\beta}}{\Omega} + \mu\beta\cos\psi\right), \tag{3.173}$$

$$\frac{U_R}{\Omega R} = \mu\cos\psi. \tag{3.174}$$

3.5.2 *Definition of the Approximate Induced Velocity Field*

Besides accounting for the effects of blade pitch and flapping motion, the blade element method in forward flight requires an estimate of the induced velocity field, which is no longer axisymmetric. This is not known a priori because it is based on a knowledge of the rotor wake (Chapter 10), which in turn depends on the rotor thrust, the blade flapping and overall trim state (i.e., blade collective and cyclic pitch angles), and the distribution of airloads over the blades. The effects of the individual tip vortices tend to produce a highly nonuniform inflow over the rotor disk, and the calculation of these effects is a formidable undertaking. Nevertheless, the performance of the rotor can be analyzed with the aid of simpler models that represent the basic effects on the inflow resulting from the rotor wake. These models are called "inflow" models and can be formulated on the basis of experimental results or more advanced vortex theories. Because of their simplicity, inflow models have found great utility in many problems in helicopter rotor aerodynamics, aeroelasticity, and flight dynamics.

Linear Inflow Models

A remarkable in-flight experiment to measure the time-averaged-induced velocity over the rotor disk in forward flight was made by Brotherhood & Stewart (1949). Based on measurements of the angular displacements of smoke streamers introduced upstream of the rotor, the longitudinal inflow variation was determined to be approximately linear. Some interesting aspects of the vortical wake can also be seen in the experiments [see also photo in Bramwell (1976), p. 131]. Similar results documenting the approximately linear longitudinal variation in the inflow were deduced by Heyson & Katsoff (1957). Since then, many experiments have confirmed the complicated nature of the inflow. During the transition from hover into level forward flight, that is, within the range $0.0 \leq \mu \leq 0.1$, the induced velocity in the plane of the rotor is the most nonuniform, it being strongly affected by the presence of discrete tip vortices that sweep downstream near the rotor plane. In higher speed forward flight ($\mu > 0.15$), the time-averaged longitudinal inflow becomes more linear and can be approximately represented by the variation

$$\lambda_i = \lambda_0\left(1 + k_x\frac{x}{R}\right) = \lambda_0(1 + k_x r\cos\psi), \tag{3.175}$$

which is a form first suggested by Glauert (1926) – see Fig. 3.27. The coefficient λ_0 is the mean (average) induced velocity at the center of the rotor as given by the standard

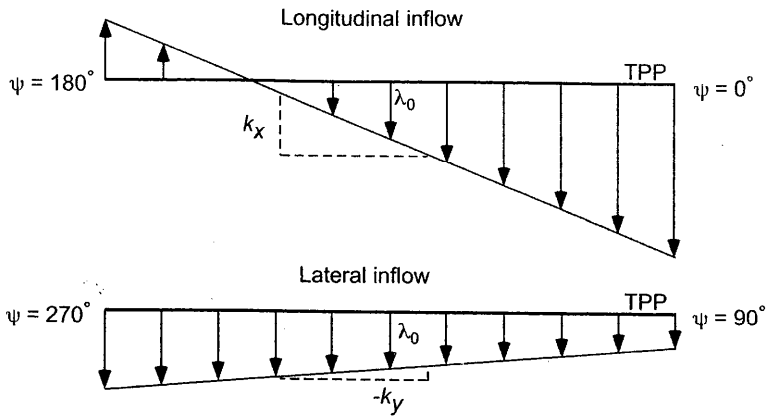

Figure 3.27 A linear inflow model approximation over the rotor disk approximates the physical distribution.

(uniform) momentum theory where

$$\lambda_i = \lambda_0 = \frac{C_T}{2\sqrt{\mu^2 + \lambda_i^2}}. \tag{3.176}$$

Glauert suggested that $k_x = 1.2$, so that there is a small upwash at the leading edge of the rotor and an increase in downwash relative to the average value all along the trailing edge. This, of course, is similar to the chordwise downwash variation generated by a fixed-wing. A variation of Glauert's result is to consider both a longitudinal and lateral variation in the inflow. In this case

$$\lambda_i = \lambda_0\left(1 + k_x\frac{x}{R} + k_y\frac{y}{R}\right) = \lambda_0\left(1 + k_x r\cos\psi + k_y r\sin\psi\right). \tag{3.177}$$

Here k_x and k_y can be viewed as weighting factors and represent the deviation of the inflow from the uniform value predicted by the simple momentum theory. From experiments with trimmed rotors, it is generally found that the inflow is heavily biased toward the rear of the disk and weakly biased toward the retreating side.

Various attempts have been made to directly calculate k_x (and k_y). One estimate can be found using an adaptation of linear momentum theory, as described by Payne (1959) and Johnson (1980) (see also Question 3.14). Weighting factors can also be estimated using rigid cylindrical vortex wake theories – see Coleman et al. (1945) and Johnson (1980) for a summary. One approximation for k_x used by Coleman et al. (1945) is

$$k_x = \tan\left(\frac{\chi}{2}\right), \text{ where the } \textit{wake skew angle} \text{ is } \chi = \tan^{-1}\left(\frac{\mu_x}{\mu_z + \lambda_i}\right), \tag{3.178}$$

and where μ_x and μ_z are advance ratios defined parallel and perpendicular to the rotor disk (see Section 2.14.4 and Fig. 3.28). It is apparent that the skew angle increases rapidly with advance ratio, and for $\mu > 0.2$ the wake is relatively flat. Notice that for high-speed forward flight, k_x approaches unity according to the above expression and does not represent the small region of upwash that is usually measured at the leading edge of the disk. Another parsimonious linear inflow model frequently employed in basic rotor analyses is attributed

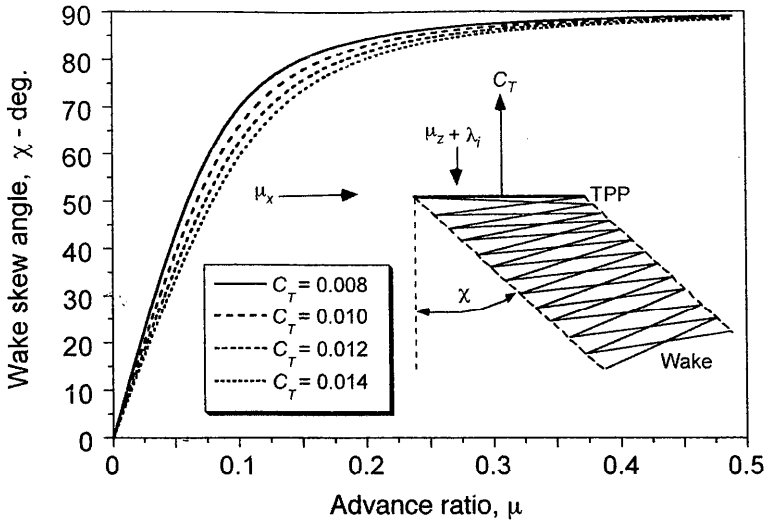

Figure 3.28 Typical variation in rotor wake skew angle with thrust and advance ratio.

to Drees (1949). In this model, the coefficients of the linear part of the inflow are obtained from another variation of vortex theory – see Johnson (1980) for a good summary. The inflow coefficients are given by

$$k_x = \frac{4}{3}\left(\frac{1 - \cos\chi - 1.8\mu^2}{\sin\chi}\right) \quad \text{and} \quad k_y = -2\mu. \tag{3.179}$$

Drees's model gives $k_x = 0$ for $\mu = 0$, a maximum value of 1.11 at $\mu \approx 0.2$, and k_x slowly decreases thereafter. Like all of the other linear inflow models, Drees's model is easy to implement in rotor analyses and gives a reasonably good description of the rotor inflow. Various other authors have suggested values for the coefficients in the Glauert model, which are summarized in Table 3.1. Payne (1959) suggests a value for k_x based on the numerical results of Castles & De Leeuw (1954), which approaches 4/3 at high advance ratios, and in light of the experimental evidence appears to be one of the better representations of the longitudinal inflow distribution. Overall, the Drees (1949), Payne (1959), and Pitt & Peters (1981) models are found to give the best representation of the inflow gradient as functions of the wake skew angle and the advance ratio when compared to the experimental evidence.

Table 3.1. *Various Estimated Values of First Harmonic Inflow*

Author(s)	k_x	k_y
Coleman et al. (1945)	$\tan(\chi/2)$	0
Drees (1949)	$(4/3)(1 - \cos\chi - 1.8\mu^2)/\sin\chi$	-2μ
Payne (1959)	$(4/3)[\mu/\lambda/(1.2 + \mu/\lambda)]$	0
White & Blake (1979)	$\sqrt{2}\sin\chi$	0
Pitt & Peters (1981)	$(15\pi/23)\tan(\chi/2)$	0
Howlett (1981)	$\sin^2\chi$	0

Inflow Model of Mangler & Squire

Another inflow model that has found some use in rotor analyses is that developed by Mangler (1948), Squire (1948), and Mangler & Squire (1950). The method uses the incompressible, linearized, Euler equations to relate the pressure field across the disk to an inflow. The solutions conveniently satisfy Laplace's equation, so that the effects of different forms of loading can be combined by superposition. This theory is partially summarized by Bramwell (1976) and Stepniewski & Keys (1984). Mangler & Squire assume that the loading on the rotor disk can be expressed as a linear combination of two fundamental forms: Type–1, which is an elliptical loading, and Type–3, which is a loading that vanishes at the edges and center of the disk. The pressure loading can be written as

$$\Delta p_m \propto r^{m-1}\sqrt{1-r^2}, \qquad m = 1, 3, \tag{3.180}$$

with r being the distance from the rotational axis. These two pressure distributions correspond to extreme forms of the disk loading, which in the real case will typically comprise a combination of these two loadings, depending on the blade twist and flight conditions.[4] The resulting inflow can be described by the Fourier series

$$\lambda_i = \left(\frac{2C_T}{\mu}\right)\left[\frac{c_0}{2} + \sum_{n=1}^{\infty}(-1)^n c_n(r,\alpha)\cos n\psi\right], \tag{3.181}$$

where α is the disk angle of attack. The coefficients in this equation depend on the assumed form of the disk loading. For Type–1 loading then

$$c_0 = \frac{3}{4}\nu \quad \text{and} \quad c_1 = -\frac{3\pi}{16}\sqrt{1-\nu^2}\left(\frac{1-\sin\alpha}{1+\sin\alpha}\right)^{1/2}, \tag{3.182}$$

where $\nu^2 = 1 - r^2$. For even values of $n \geq 2$,

$$c_n = (-1)^{\frac{n-2}{2}}\left(\frac{3}{4}\right)\left(\frac{\nu+n}{n^2-1}\right)\left(\frac{1-\nu}{1+\nu}\right)^{\frac{n}{2}}\left(\frac{1-\sin\alpha}{1+\sin\alpha}\right)^{\frac{n}{2}}, \tag{3.183}$$

and for odd values of $n \geq 3$, $c_n = 0$. The inflow obtained from this loading is approximately linearly distributed longitudinally across the rotor disk. For Type–3 loading, the coefficients are

$$c_0 = \frac{15}{8}\nu(1-\nu^2), \tag{3.184}$$

$$c_1 = -\frac{15\pi}{256}(5-9\nu^2)\sqrt{1-\nu^2}\left(\frac{1-\sin\alpha}{1+\sin\alpha}\right)^{1/2}, \tag{3.185}$$

$$c_3 = \frac{45\pi}{256}(1-\nu^2)^{3/2}\left(\frac{1-\sin\alpha}{1+\sin\alpha}\right)^{3/2}. \tag{3.186}$$

For even values of $n \geq 2$,

$$c_n = (-1)^{\frac{n-2}{2}}\left(\frac{15}{8}\right)\left[\left(\frac{\nu+n}{n^2-1}\right)\left(\frac{9\nu^2+n^2-6}{n^2-9}\right) + \left(\frac{3\nu}{n^2-9}\right)\right] \times \left(\frac{1-\nu}{1+\nu}\right)^{\frac{n}{2}}\left(\frac{1-\sin\alpha}{1+\sin\alpha}\right)^{\frac{n}{2}}, \tag{3.187}$$

and for odd values of $n \geq 5$, $c_n = 0$.

[4] Type–1 ($m = 1$) elliptic loading is consistent with Glauert's so-called high-speed approximation to the rotor problem, as discussed in Chapter 2.

For Type-1 disk loading, the inflow is exactly linear for $\alpha = 0$ and is only a weak function of α. Type-3 disk loading gives a more nonuniform distribution of inflow, with zero at the center of the disk. Both forms of the assumed disk loading give a lateral distribution of inflow that is symmetric with respect to the longitudinal axis of the rotor. Bramwell (1976) uses Glauert's high-speed approximation to the inflow and replaces the leading $2C_T/\mu$ term in Eq. 3.181 by $4\lambda_0$, where λ_0 is the mean inflow from momentum theory. This implies that the Mangler & Squire theory is valid through hover, but clearly it is not because it violates the high-speed assumptions made in the original work that $v_i \ll V_\infty$. Therefore, the theory should be used only for advance ratios greater than about 0.1.

When applying Mangler & Squire's theory, it can be assumed that the loading on the rotor is described by a linear combination of the Type–1 and Type–3 loadings, that is,

$$\Delta p = w_1 \Delta p_1 + w_3 \Delta p_3, \qquad w_1 + w_2 = 1. \tag{3.188}$$

This is the main disadvantage of theory, which requires the aerodynamic loading on the rotor to be known or assumed a priori. Based on downwash measurements behind a rotor, Fail & Eyre (1954) show that the downwash behind the advancing side of the rotor corresponds to Type-1 loading, whereas from behind the retreating blade the downwash corresponds closely to Type-3 loading. It would seem, however, that at high rotor advance ratios, say greater than 0.5, the onset of reverse flow and retreating blade stall begin to invalidate these loading assumptions – see Ormiston (2004).

The results from the various inflow models described above are compared with inflow measurements over the rotor disk in Fig. 3.29. These data are taken from Elliott et al. (1988), which were measured one chord above the rotor plane using a LDV system. Because this experiment used both a rotor and a fuselage, the measured results cannot be considered entirely representative of an isolated rotor. The rotor was trimmed such that the TPP was perpendicular to the rotor shaft, with a forward shaft tilt, α_s, of $-3°$ (disk AoA of 3°). Figure 3.29 shows that the inflow along the longitudinal axis of the rotor is reasonably well described by linear inflow models such as that of Drees, or with the Type-1 loading in the Mangler & Squire model. The main discrepancies are at the leading and trailing edges of the disk, and also near the rotor hub.

Using a simple average of Type-1 and Type-3 loadings ($w_1 = w_3 = 0.5$), Mangler & Squire's theory gives a somewhat better description of the longitudinal inflow, especially over the back of the rotor. Strictly speaking the coefficients of the Mangler & Squire theory are obtained by solving for the rotor loading (Δp) at the given trim state by means of the BET. Vortex theory (described in Section 10.7) does much better at the leading and trailing edges of the disk and agrees with the linear inflow model over the remainder of the disk. The somewhat larger discrepancies found between all of the theories and the measurements with increasing advance ratio are almost certainly a result of perturbations to the velocity field caused by the rotor hub and also the fuselage below the rotor. Because the mean rotor inflow decreases slightly with increasing advance ratio and the fuselage perturbations increase, the net effect is that a larger fraction of the total inflow is affected by the presence of the fuselage (see Section 11.2.1). Such effects are not easy to calculate but at least must be carefully recognized as a contributing factor to most rotor inflow measurements. The lateral distribution of inflow across the disk is found to be relatively uniform compared to the longitudinal variation but decreases rapidly near the edges of the disk. Outside the edges of the disk, there is an upwash velocity. Drees's model is not unrealistic, but Mangler & Squire's theory gives a much better description of the inflow near the edges of the disk and agrees closely with the results from vortex theory. Again, the influence of the fuselage and rotor hub are responsible for some of the discrepancies seen between theory and experiment.

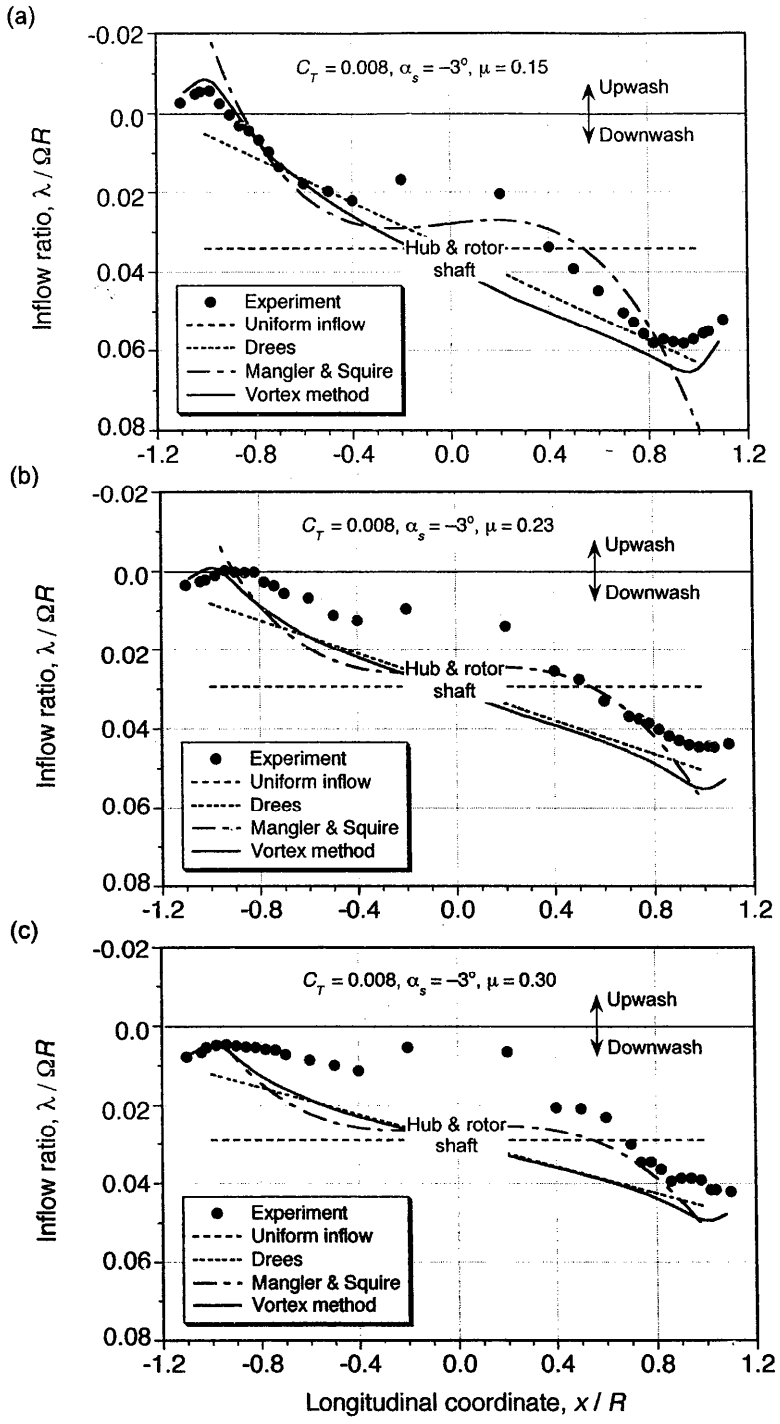

Figure 3.29 Measured variations in the longitudinal and lateral time-averaged inflow across the disk in forward flight compared to inflow models. Measurements made one chord above TPP. (a) Longitudinal inflow at $\mu = 0.15$. (b) Longitudinal inflow at $\mu = 0.23$. (c) Longitudinal inflow at $\mu = 0.30$. (d) Lateral inflow at $\mu = 0.15$. (e) Lateral inflow at $\mu = 0.23$. (f) Lateral inflow at $\mu = 0.30$. Data source: Elliott et al. (1988).

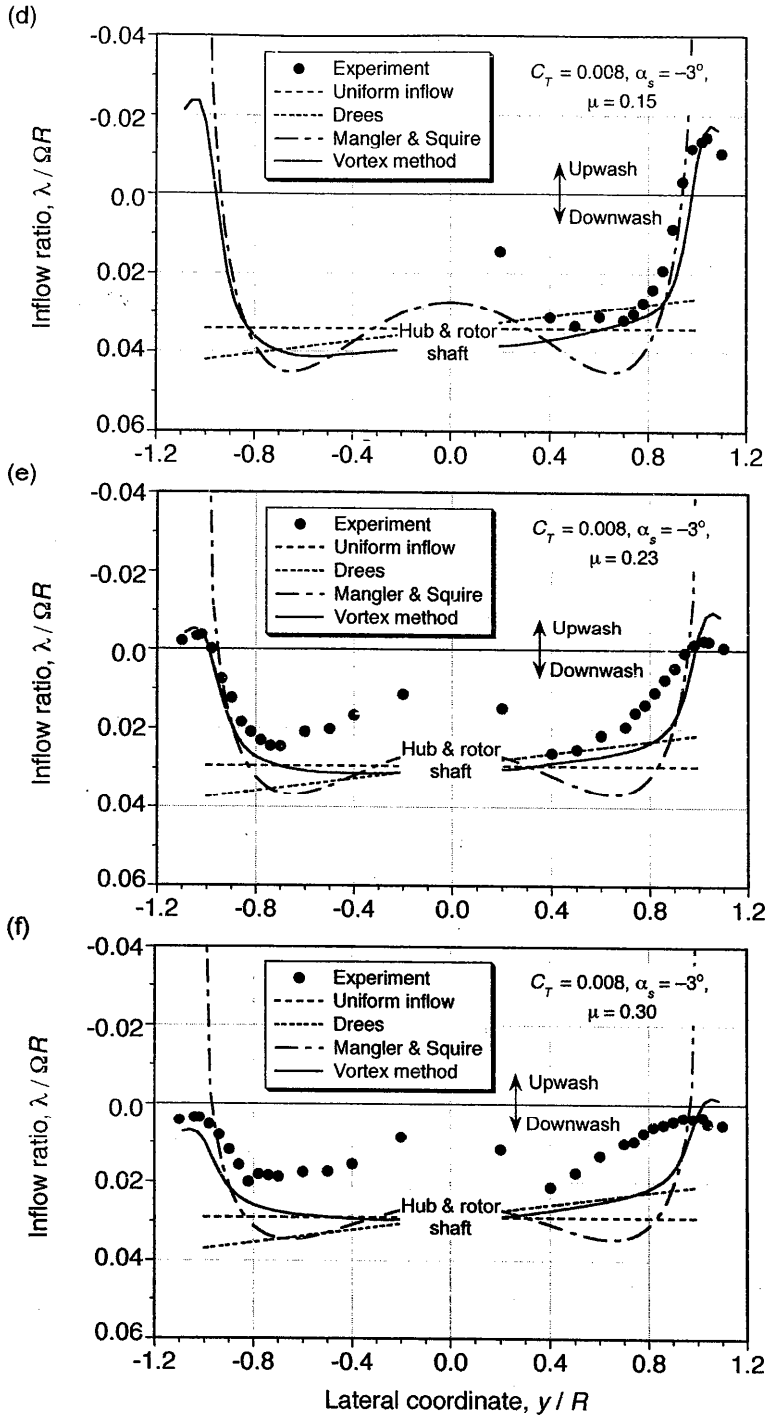

Figure 3.29 (*Continued*)

Examples of the predicted AoA over the rotor disk in forward flight are shown in Fig. 3.30 using four levels of inflow modeling, ranging from uniform inflow to a free-vortex wake prediction (see Chapter 10). In all cases, the rotor was trimmed (see Section 4.14) to meet the same thrust requirement and to ensure that the rotor tip path plane was at the same orientation. Notice in each case the highly nonuniform AoA over the rotor disk. While there are some differences in the AoA distribution when going from a uniform to a linear inflow model, it is the Mangler & Squire model that first begins to pick up the larger nonuniformities in AoA on the retreating side of the disk. Even here, however, the differences are not large

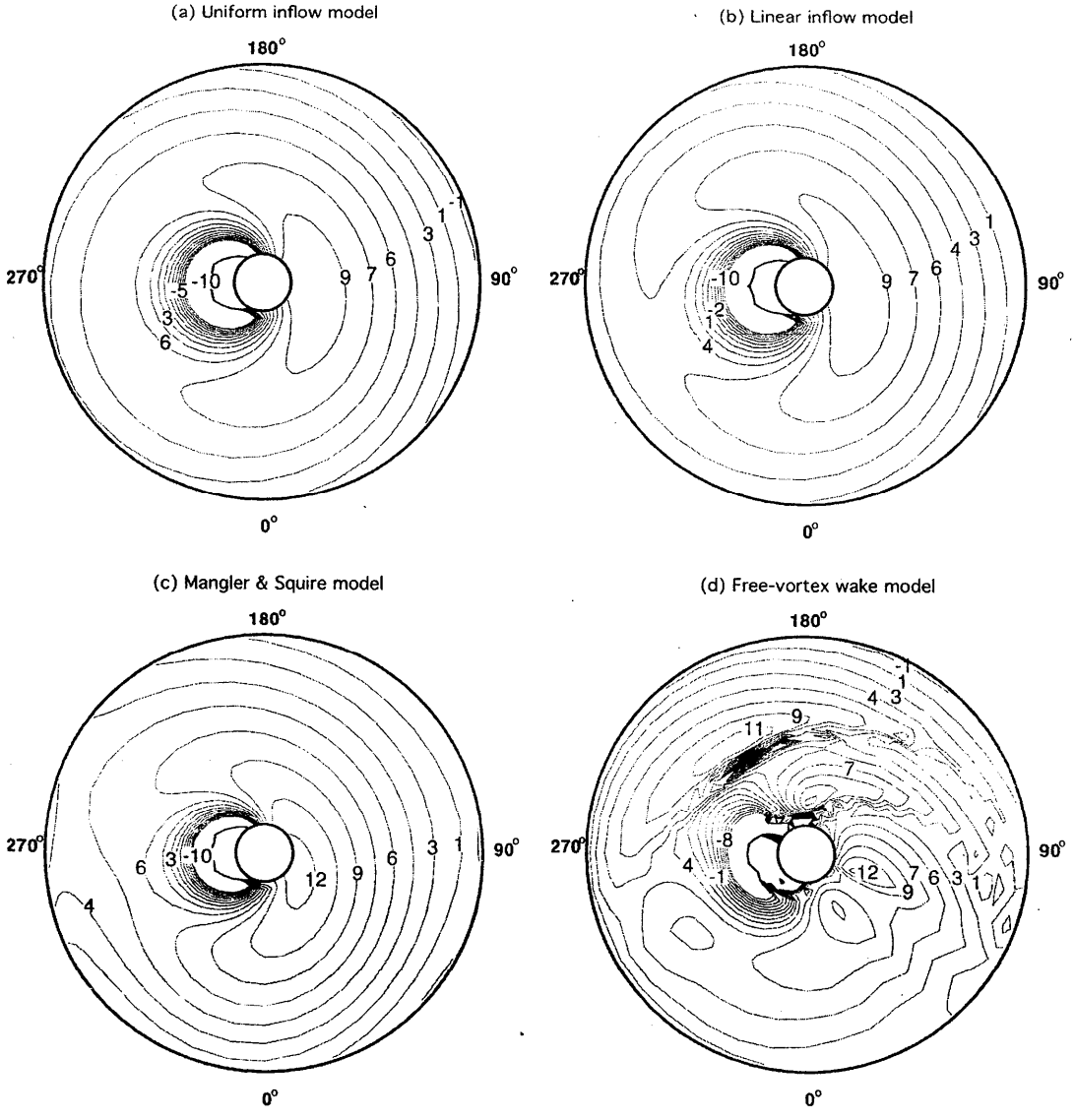

Figure 3.30 Predictions of the AoA over the rotor disk in forward flight using four levels of inflow modeling. (a) Uniform inflow model. (b) Linear inflow model. (c) Mangler & Squire inflow model. (d) Free-vortex wake model. $C_T = 0.008$, $\mu = 0.25$, $\alpha_s = 8°$. Calculations courtesy of Shreyas Ananthan.

compared to linear inflow assumptions. The reverse flow region (see Fig. 5.9) is evident here. The free-vortex model resolves the individual tip vortices in the wake, which in this case appear as ridges of tightly packed AoA contours in the second and third quadrants of the disk (see later in Fig. 10.13). It is here that the fidelity of vortex wake models start to come into their own for blade airloads predictions, despite their much higher computational cost.

Ormiston (1972) describes a more general inflow formulation in the spirit of Mangler & Squire's approach, where the rotor loading and inflow are solved more consistently. For a simple uniform bound circulation distribution on the blades, the inflow results appear substantially similar to those obtained with Mangler & Squire's theory. See also Ormiston (2004). Other more recent developments of the actuator disk inflow model are described by Peters et al. (1987) and Peters & He (1989, 1995). In this theory, the acceleration potential and inflow distribution are expressed in the form of an infinite series of shape functions. When these are substituted into the incompressible, linearized Euler equations, a set of first-order ordinary differential equations are obtained. An aerodynamic loading model is required to solve the equations, which is based on a standard blade element approach. These more recent inflow methods are still in a state of ongoing development (see Section 10.9) but have been shown to give improvements in predictive capability for many rotor problems, especially those involving rotor aeroelasticity. An advantage is that they avoid the need to explicitly model the complicated nature of the true vortex wake and so are computationally less demanding than say, methods based on vortex theory.

3.6 Chapter Review

The blade element theory (BET) is a powerful tool for the aerodynamic analysis of helicopter rotors. It forms the basis for nearly all modern computational methods used for rotor performance, airloads, and aeroelastic analyses. The basic ideas consist of representing the airloads on 2-D sections of the blades, and integrating their effect to find the performance of the rotor as a whole. This allows tremendous flexibility in the rotor analysis and also allows the effects of airfoil shape to be examined, along with the effects of the Reynolds number and the Mach number, and even some elementary effects associated with nonlinear aerodynamics and stall.

On the basis of certain assumptions, it has been shown how the combined blade element momentum theory (BEMT) can provide analytic results about how to design the rotor in terms of optimum blade planform and blade twist distribution to enable maximum hovering efficiency. Whereas the simple momentum theory shows that the rotor should be designed for low disk loading, the blade element approach allows the trade-offs associated with the interrelated effects of disk loading, blade tip speed, blade loading, blade twist, and blade planform to be examined. While the BEMT theory is by no means complete, it paves the way for initial studies in rotor design to meet some specified set of requirements. It is the ability to help *design* the rotor from the onset that gives these methods great practical utility, and they can also be used as check cases for other and more advanced types of methods.

In forward flight, the BET allows for the calculation of the nonaxisymmetric airloads over the rotor disk. Besides the need to account for the effects of blade flapping motion (which are considered next in Chapter 4), this chapter has also introduced the ideas that more accurately representing the effects of the rotor wake is one key to the successful use of the BET. The use of other than uniform inflow models provides a better representation of the effects of the rotor wake and a better overall physical picture of the rotor aerodynamics problem. While inflow models are not completely rigorous, especially at low forward flight speeds, they give

reasonable descriptions of the induced velocity field over the rotor disk and may be well suited for the analysis of many rotor problems. Their computational simplicity allows for easy integration into blade element based rotor models and may allow for the inclusion of unsteady aerodynamic effects as well (see Chapter 8). However, it must be remembered that in many situations where the individual tip vortices come close to the disk (especially in low speed forward flight, during maneuvers, or in descents) the induced velocity distribution is considerably more complicated than can be prescribed by these simple inflow models. The use of prescribed- or free-vortex methods provides the fidelity necessary under these conditions, albeit at much greater computational expense (see Chapter 10).

However, before the rotor problem in forward flight can be fully enunciated, it is necessary to consider properly the effects of the rotor blade motion on the aerodynamic forces. Because the aerodynamics and blade motion are intrinsically coupled, they must be solved simultaneously as a system. This then allows the calculation of rotor trim, that is, the control inputs required to orient the rotor in a direction to meet vehicle lift, propulsion, and control requirements. These issues are considered in the following chapters.

3.7 Questions

3.1. A rotor has a rectangular blade planform, a solidity of 0.1, ideal blade twist, and operates in hover at a thrust coefficient of 0.008. By numerical means, using the combined blade-element momentum theory (BEMT), compare the predicted inflow ratio across the span of the blade with the exact (analytic) result. Show also the radial distributions of thrust, induced torque, and lift coefficient, and compare with the solutions obtained using the exact theory. Finally, compare the numerical calculations of the integrated thrust and induced power with the exact results for this rotor over the range $0.0 \leq C_T \leq 0.010$.

3.2. Using the blade-element momentum theory (BEMT), implement Prandtl's tip-loss function. For a rotor of solidity 0.1 and with no blade twist, show the effects of the tip-loss effect on the induced inflow, thrust distribution, lift coefficient distribution, and torque distribution across the blade span. Neglect profile drag. Compare the results for rotors with two and four blades at a thrust coefficient of 0.008. Also, calculate the induced power factor for the two rotors, with and without the tip-loss effect, and comment on your results.

3.3. Using the blade-element momentum theory (BEMT), show the effect of increasing linear twist on the variations in inflow, thrust, induced power, profile power, and lift coefficient across the span of a rotor with four blades of rectangular planform and solidity 0.1, and operating at a thrust coefficient of 0.008. Assume $C_{d_0} = 0.01$. Include Prandtl tip-loss effects. All of the results should be compared at a constant thrust (disk loading).

3.4. For the same rotor parameters as used in the previous question, compute the power required to hover versus thrust for different values of linear blade twist. Also compute the figure of merit and induced power factor versus thrust coefficient. Assume that the profile drag is given by $C_d = 0.01 + 0.025\alpha + 0.65\alpha^2$. Show your results graphically. Include the Prandtl tip-loss function. Comment on your results.

3.5. Tapering the blade planform can have a powerful impact on the profile power of the rotor. Using the blade-element momentum theory (BEMT), show the effect of increasing taper on the variations in inflow, thrust, power, and lift coefficient

across the span of a rotor with two blades of linearly tapered planform and with a thrust weighted solidity of 0.1. The blades have 10 degrees of linear nose-down twist. Consider blade taper ratios of 1:1, 2:1, and 3:1. Include Prandtl tip-loss effects. Remember that all of the results should be compared at a constant thrust (disk loading) and thrust weighted solidity. Determine an optimum combination of twist and taper that will give a maximum figure of merit.

3.6. Explain and discuss the potential benefits to be gained by using blade twist, planform taper, low solidity, large radius, and low rotational speed for the main rotor of a heavy lift helicopter that is designed to operate primarily in hover. Discuss any disadvantages associated with these design factors.

3.7. Assuming an optimum hovering rotor, rewrite an expression for the figure of merit in terms of rotor tip speed, disk loading, and airfoil lift-to-drag ratio. Comment on your result.

3.8. A manufacturer has developed a growth version of an existing helicopter that has a higher gross weight. This new aircraft has a main rotor that has the same rotor disk area, but with a higher solidity. Explain qualitatively, quantitatively, or both, what benefits and/or trade-offs may be expected with reference to the hover, forward flight, and maneuver capabilities of the new helicopter.

3.9. Given that the inflow distribution over a rotor with rectangular untwisted blades is approximately triangular, and assuming no tip-loss effects: (a) Compute the variation with radius of inflow angle and section AoA for such a rotor. (b) Derive the relation between the blade element lift coefficients and C_T/σ. (c) Derive an expression for the hovering power of such a rotor in terms of C_T/σ and C_{d_0}.

3.10. The inflow distribution over a rotor operating in hover with no tip losses is assumed to be linear; that is, $\lambda = \lambda_{\text{tip}} r$, where λ_{tip} is the value of the inflow at the tip. By considering a momentum balance on successive annuli of the rotor disk, show that the induced power factor for such a rotor is $4\sqrt{2}/5$.

3.11. What is the purpose of using "equivalent" solidities in helicopter rotor performance studies? Explain the potential pitfalls in using such "equivalent" factors with rotors.

3.12. A blade has an inboard portion of constant chord c_r from the root to a point $r = r_1$, and then a linear taper from r_1 to the tip at $r = 1$ where the chord c_t. Show that the equivalent thrust weighted solidity for this blade is given by

$$\sigma_e = (\sigma_r - \sigma_t) r_1^3 + \left(\frac{\sigma_t - \sigma_r}{1 - r_1}\right)\left(-\frac{1}{4} + r_1^3 - \frac{3}{4} r_1^4\right) + \sigma_t.$$

3.13. For helicopter operations at high speed, it is possible that a "reverse flow" region can exist at the root end of the blade on the retreating side of the rotor disk. Show that the reverse flow region on the rotor disk is a circle of diameter μ with a center located at $(r, \psi) = (\mu/2, 3\pi/2)$.

3.14. By considering a local momentum analysis of a uniformly loaded rotor disk in high-speed forward flight, show that the induced inflow can be written in the form $v_i = v_0 [1 + Kr \cos\psi]$, where the inflow gradient $K = \left(\sqrt{1 - r^2}\right)^{-1}$ and v_0 is the velocity at the center of the disk.

Bibliography

Althaus, D. 1972. "Stuttgarter Profilkatalog I," Institut für Aerodynamik und Gasdynamik der Universität Stuttgart.

Bagai, A. and Leishman, J. G. 1992. "A Study of Rotor Wake Developments and Wake–Body Interactions in Hover using Wide-Field Shadowgraphy," *J. of the American Helicopter Soc.*, 37 (4), pp. 48–57.

Bailey, F. J. and Gustafson, F. B. 1944. "Charts for Estimation of the Characteristics of a Helicopter Rotor in Forward Flight," NACA ACR L4H07.

Betz, A. 1919. *Schraubenpropeller mit geringstem Energieverlust*, Göttinger Nachrichten, p. 193.

Bienen, T. and von Kármán, T. 1924. *Z. Ver. deutsch. Ing.*, 68, p. 1237.

Bramwell, A. R. S. 1976. *Helicopter Dynamics*, Edward Arnold, London.

Brotherhood, P. and Stewart, W. 1949. "An Experimental Investigation of the Flow through a Helicopter Rotor in Forward Flight," ARC R & M 2734.

Castles, W., Jr. and De Leeuw, J. H. 1954. "The Normal Component of the Induced Velocity in the Vicinity of a Lifting Rotor and Some Examples of Its Application," NACA Report 1184.

Castles, W., Jr. and Durham, H. L., Jr. 1956. "Distribution of Normal Component of Induced Velocity in Lateral Plane of a Lifting Rotor," NACA TN 3841.

Coleman, R. P., Feingold, A. M, and Stempin, C. W. 1945. "Evaluation of the Induced Velocity Fields of an Idealized Helicopter Rotor," NACA ARR L5E10.

de Bothezat, G. 1919. "The General Theory of Blade Screws," NACA TR 29.

Drees, J. M. 1949. "A Theory of Airflow Through Rotors and Its Application to Some Helicopter Problems," *J. of the Helicopter Association of Great Britain*, 3 (2), July–Sept., pp. 79–104.

Drzewiecki, S. 1892. Bulletin de l'Association Technique Maritime.

Drzewiecki, S. 1920. *Théorie Générale de l'Hélice*, Paris.

Elliott, J. W., Althoff, S. L. and Sailey, R. H. 1988. "Inflow Measurements Made with a Laser Velocimeter on a Helicopter Model in Forward Flight," In three volumes: Volume I: Rectangular Planform at an Advance Ratio of 0.15," NASA TM 100545. Volume II: Rectangular Planform at an Advance Ratio of 0.23," NASA TM 100546. Volume III: Rectangular Planform at an Advance Ratio of 0.30," NASA TM 100547.

Fail, R. A. and Eyre, R. C. W. 1954. "Downwash Measurements Behind a 12-ft Diameter Helicopter Rotor in the 24-ft Wind Tunnel," ARC R & M 2810.

Felker, F. F. and McKillip, R. M. 1994. "Comparisons of Predicted and Measured Rotor Performance in Vertical Climb and Descent," 50th Annual Forum of the American Helicopter Soc., Washington DC, May 11–13.

Gessow, A. 1948. "Effect of Rotor-Blade Twist and Plan-Form Taper on Helicopter Hovering Performance," NACA Technical Notice 1542.

Gessow, A. and Myers, G. C., Jr. 1952. *Aerodynamics of the Helicopter*, Macmillan Co., Republished by Frederick Ungar Publishing, New York, NY, 1967, Chapter 4.

Glauert, H. 1922. "An Aerodynamic Theory of the Airscrew," ARC R & M 786.

Glauert, H. 1926. "A General Theory of the Autogiro," ARC R & M 1111.

Glauert, H. 1935. "Airplane Propellers," In Division L of *Aerodynamic Theory*, edited by W. F. Durand, Springer Verlag, Berlin, Germany. Reprinted by Peter Smith, Glouster, MA, 1976.

Goldstein, L. 1929. "On the Vortex Theory of Screw Propellers," *Proc. of the Royal Soc.*, 123 (792), pp. 440–465.

Gustafson, F. B. and Gessow, A. 1945. "Flight Tests on the Sikorsky HNS-1 (Army YR-4B) Helicopter," NACA MR L5D09a.

Gustafson, F. B. and Gessow, A. 1946. "Effect of Rotor Tip Speed on Helicopter Rotor Performance and Maximum Forward Speed," NACA ARR No. L6A16.

Harris, F. D. 1987. "Rotary Wing Aerodynamics: Historical Perspectives and Important Issues," American Helicopter Soc. Specialists' Meeting on Aerodynamics and Aeroacoustics, Fort Worth, TX, Feb. 25–27.

Heyson, H. H. and Katsoff, S. 1957. "Induced Velocities Near a Lifting Rotor with Nonuniform Disk Loading," NACA Technical Report 1319.

Houghton, E. L. and Carpenter P. W. 1993. *Aerodynamics for Engineering Students*, John Wiley & Sons, New York, NY.

Howlett, J. J. 1981. "UH-60A Blackhawk Engineering Simulation Program: Vol. 1–Mathematical Model," NASA CR-66309.

Johnson, W. 1980. *Helicopter Theory*, Princeton University Press, Princeton, NJ, Chapter 4.

Jones, R. T. and Cohen, D. 1957. "Aerodynamics of Wings at High Speeds," Vol. VII of *High Speed Aerodynamics and Jet Propulsion*, Section A, Chapter 1, Aerodynamic Components of Aircraft at High Speeds. A. F. Donovan & H. R. Lawrence (eds.), Princeton University Press, Princeton, NJ, pp. 36–48.

Knight, M and Hefner, R. A. 1937. "Static Thrust of the Lifting Airscrew," NACA TN 626.

Lanchester, F. W. 1915. "A Contribution to the Theory of Propulsion and the Screw Propeller," *Trans. Inst. Naval Architects*, 57, p. 98.

Leishman, J. G. 1996. "Experimental Investigation into the Aerodynamic Characteristics of Helicopter Rotor Airfoils with Ballistic Damage," ARL-CR-295.

Liberatore, E. K. 1998. *Helicopters before Helicopters*, Krieger Publishing, Malabar, FL, pp. 60–61, 249.

Lock, C. N. H. 1930. "The Application of Goldstein's Theory to the Practical Design of Airscrews," ARC R & M 1377.

Lock, C. N. H., Bateman, H., and Townend, H. 1925. "An Extension of the Vortex Theory of Airscrews with Applications to Airscrews of Small Pitch and Including Experimental Results," ARC R & M 1014.

Loftin, L. K. and Smith, H. A. 1949. "Aerodynamic Characteristics of 15 NACA Airfoil Sections at Seven Reynolds Numbers from 0.7×10^6 to 9×10^6," NACA Technical Notice 1945.

Mangler, K. W. 1948. "Calculation of the Induced Velocity Field of a Rotor," Royal Aircraft Establishment, Report Aero 2247.

Mangler, K. W. and Squire, H. B. 1950. "The Induced Velocity Field of a Rotor," ARC R & M 2642.

McVeigh, M. A. and McHugh, F. J. 1982. "Recent Advances in Rotor Technology at Boeing Vertol," 38th Annual Forum of the American Helicopter Soc., Anaheim, CA, May 4–7.

Miley, S. J. 1982. "A Catalog of Low Reynolds Number Airfoil Data for Wind Turbine Applications," US Department of Energy, Wind Energy Division, RFP-338, UC-60.

Nikolsky, A. 1951. *Helicopter Analysis*, John Wiley & Sons, Inc., New York, NY.

Ormiston, R. A. 1972. "An Actuator Disk Theory for Rotor Wake Induced Velocities," AGARD-CP-111, Aerodynamics of Rotary Wings.

Ormiston, R. A. 2004. "Induced Power of the Helicopter Rotor," 60th Annual Forum of the American Helicopter Soc. International, Baltimore, MD, June 7–10.

Payne, P. R. 1959. *Helicopter Dynamics and Aerodynamics*, Pitman & Sons, London.

Peters, D. A. and He, C. J. 1989. "Correlation of Measured Induced Velocities with a Finite-State Wake Model," 45th Annual Forum of the American Helicopter Soc., Boston, MA, May 22–24.

Peters, D. A. and He, C.-J. 1995. "Finite-State Induced Flow Models Part II: Three-Dimensional Rotor Disk," *J. of Aircraft*, 32 (2), pp. 323–333.

Peters, D. A. and Ormiston, R. A. 1975. "Flapping Response Characteristics of Hingeless Rotor Blades by a Generalized Harmonic Balance Method," NASA TN D-7856.

Peters, D. A., Boyd, D. D., and He, C. J. 1987. "Finite-State Induced-Flow Model for Rotors in Hover and Forward Flight," 43rd Annual Forum of the American Helicopter Soc., St. Louis, MO, May 18–20.

Pitt, D. M. and Peters, D. A. 1981. "Theoretical Prediction of Dynamic Inflow Derivatives," *Vertica*, 5, pp. 21–34.

Prouty, R. W. 1986. *Helicopter Performance, Stability, and Control*, Prindle, Weber & Schmidt, PWS Engineering, Boston, pp. 97–101.

Reissner, H. 1910. *Z. Flugtech. Motorluftschiffahrt*, 1, pp. 257–309.

Reissner, H. 1937. "On the Vortex Theory of the Screw Propeller," *J. Aeronaut. Sciences*, 5 (1), pp. 1–6.

Reissner, H. 1940. "A Generalized Vortex Theory of the Screw Propeller and Its Application," NACA TN 750.

Squire, H. B. 1948. "Some Aerodynamic Problems of the Helicopter," *J. of the Helicopter Association of Great Britain*, 1 (3), pp. 35–48.

Stepniewski, W. Z. and Keys, C. N. 1984. *Rotary-Wing Aerodynamics*, Dover, New York, NY, Part 1, Chapter 5.

Theodorsen, T. 1948. *Theory of Propellers*, McGraw-Hill, New York, NY.

Tokaty, G. A. 1971. *A History and Philosophy of Fluid Mechanics*, Foulis & Co., Henley-on-Thames, England.

White, F. and Blake, B. B. 1979. "Improved Method of Predicting Helicopter Control Response and Gust Sensitivity," 35th Annual Forum of the American Helicopter Soc., Washington DC, May 21–23.

CHAPTER 4

Rotating Blade Motion

It is sufficient to say that it [the dissymmetry of lift on the rotor] is completely eliminated by the articulation of the rotor blades, which no longer set up a powerful inherent force which must be overcome in order to control the craft.

Juan de la Cierva (1931)

4.1 Introduction

The interdependent coupling of the aerodynamic forces produced on the rotor blades and the resulting blade motion is the key to understanding the behavior of the blade response and in developing a means of giving the pilot positive control over the rotor system. A distinctive feature of helicopter rotors is that articulation in the form of flapping and lead–lag hinges is incorporated at the root of each blade. These may be mechanical hinges, or modern rotor hub designs may use semi-rigid or hingeless flexures that allow motion about a "virtual" hinge location. In either case, the hinges allow each blade to independently flap and lead or lag with respect to the hub plane under the action of varying aerodynamic lift and drag loads (Fig. 4.1). The idea of a flapping hinge for a rotor was first patented by Bartha & Madzer (1913). However, the flapping hinge was first successfully used on an aircraft by Juan de la Cierva with his autogiros (see Chapter 12). The addition of a lead–lag hinge allows in-plane motion of the blade in response to the Coriolis accelerations and forces that are produced when the radius of gyration of the blade changes by virtue of flapping. A pitch bearing is also incorporated into the blade design to allow the blades to *feather*, providing an ability to change their pitch. This can be done collectively (together) on all blades, thereby changing the magnitude of the rotor thrust, or cyclically, that is, with respect to blade azimuth, thereby changing the phasing of the aerodynamic loads over the disk. The latter allows the rotor disk to tilt so as to reorient the rotor thrust vector and provide the pilot with pitch and roll control of the helicopter.

In hovering flight, the flow field is azimuthally axisymmetric and so each blade encounters exactly the same aerodynamic environment. The blades flap up and lag back with respect to the hub and reach a steady equilibrium position under the action of these steady (nonazimuthally varying) aerodynamic and centrifugal forces. The blades will "cone" up to form a static balance between the blade aerodynamic forces and the centrifugal forces, and the rotor disk plane takes on some orientation in inertial space. The centrifugal forces are dominant and so the coning angles on helicopter rotors always remain relatively small (a few degrees). In addition, the aerodynamic drag forces on the blades cause them to lag back. Because the drag forces are only a fraction of the lift forces and are overpowered by the centrifugal forces, the lag angle displacements are even smaller than the coning angles.

As the helicopter moves into forward flight, the asymmetry of the onset flow and dynamic pressure over the disk produces aerodynamic forces that are functions of blade azimuth position (i.e., cyclically varying airloads are now produced). The flapping hinge allows each blade to freely flap up and down in a periodic manner with respect to azimuth angle

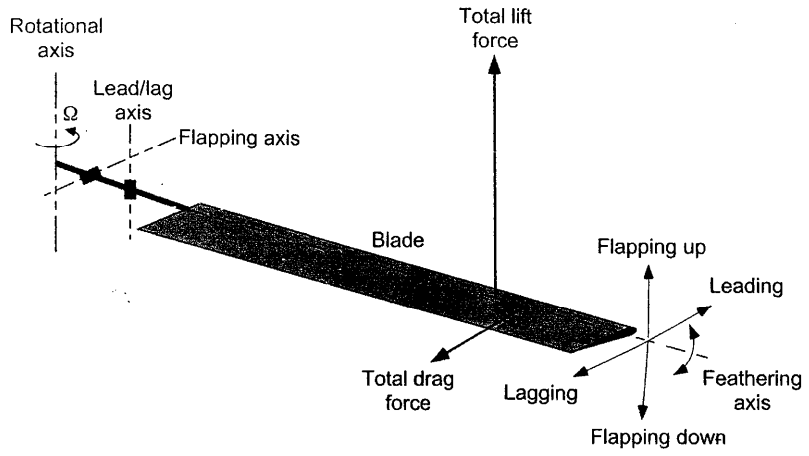

Figure 4.1 Schematic showing flapping, lead–lag and feathering motion of a rotor blade.

under the action of these varying aerodynamic loads. The blades reach an equilibrium condition again when the local changes in angle of attack (AoA) and the aerodynamic loads produced as a result of blade flapping are sufficient to compensate for the local changes in the airloads resulting from variations in dynamic pressure. In the words of Cierva, the blades were "free to move in a sort of flapping motion wherever they liked according to the effects of the air upon them." The rotor disk, therefore, naturally wants to takes up a new orientation in space, although this may not be the desired orientation. Positive control of the blade pitch is required to cyclically adjust the magnitude and phasing of the aerodynamic loads to bring the rotor to a desired orientation.

Some of the first theoretical studies of blade flapping and rotor response were undertaken in Great Britain by Lock (1927), Glauert (1928), and Squire (1936), motivated initially by the success of the autogiro. In the United States, Wheatly (1934), Sissingh (1939, 1941), Bailey (1941), and Wald (1943) were responsible for most of the initial work in understanding rotor blade flapping behavior in forward flight. Nikolsky (1944, 1951) gave one of the first formal treatments of the various problems in rotor dynamics and the effect on rotor performance. Bramwell (1976) and Johnson (1980) give the most thorough textbook expositions of rotating blade dynamics and rotor response. Loewy (1969), Reichert (1973), Friedmann (1977, 2004), and Chopra (1990) give good reviews of the complicated coupled dynamics and the various aeroelastic problems associated with helicopter rotors from a research perspective.

4.2 Types of Rotors

There are basically four types of helicopter rotor hubs in use. These are the teetering design, the articulated design, the hingeless design and the bearingless design. A teetering rotor has two blades that are hinged at the rotational axis (i.e., on the shaft) and uses no independent flap or lead–lag hinges. The well-known Bell (Young) design shown in Fig. 4.2(a) is an example of a teetering rotor design. The blades are connected together, so that as one blade flaps up the other flaps down like a seesaw or teeter board. A separate pitch or feathering bearing on each blade allows for cyclic and collective pitch capability. A stabilizer bar may be included, which acts like a gyroscope maintaining its orientation in space and introduces a flapping–blade cyclic pitch feedback, which gives the helicopter

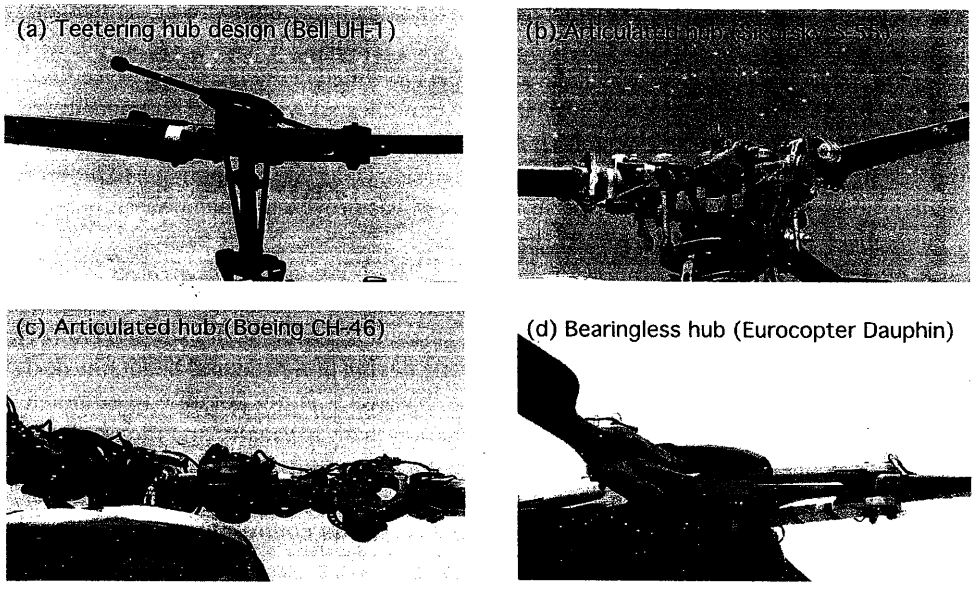

Figure 4.2 Various types of rotor hubs. (a) Bell teetering hub design. Notice the bob weights attached to the stabilizer bar. (b) An articulated hub, in this case with coincident flapping and lag hinges. (c) An articulated hub, with the lag hinge outboard of both the flap and feathering bearing. (d) A bearingless hub, where the mechanical hinges are replaced by flexures.

increased flight stability. The teetering design has the advantage of being mechanically simple with a low parts count and it is easy to maintain. One disadvantage of the design is that it can have a relatively high parasitic drag in forward flight, in part because of the stabilizer bar. On later teetering rotor designs, the stabilizer bar has been removed.

A variation of the teetering design is the underslung teetering hub, an example being used on the Bell-Huey series of helicopters. Here, the blades are given a precone angle so that a downward (negative) bending component resulting from the centrifugal forces produced by blade rotation eliminates the upward (positive) bending moment at the hub resulting from the aerodynamic loads. However, any precone displacement will move the center of gravity of the rotor system above the axis of the teetering hinge, and this can introduce an undesirable coupling into the rotor system through Coriolis effects. To prevent this, the rotor is underslung below the teetering hinge to minimize the center of gravity movement relative to the shaft. A problem, however, that has arisen with underslung teetering rotor designs is mast bumping, which occurs when the rotor is lightly loaded (such as in a push-over maneuver) and excessive blade flapping causes the blade hub to contact the rotor shaft. While snubbers are used to help prevent this, repetition of the problem can result in damage to the rotor shaft. Another variation of the teetering design, called the gimbaled hub, is used on tilt-rotor aircraft such as the V-22 Osprey, where the three blades and the hub are attached to the rotor shaft by means of a gimbal or universal joint.

A large number of helicopters use conventional or fully articulated rotor hubs. Here, mechanical flap and lead–lag hinges are provided on each blade along with a feathering bearing. Different helicopters use various sequences of hinges and bearings, and this affects the dynamics of the rotor system. Many Sikorsky helicopters use coincident flap and lead–lag hinges, with the feathering bearing located further outboard [see Fig. 4.2(b)].

The Boeing CH-46 and CH-47 helicopters use a lead–lag hinge outboard of the feathering bearing [see Fig. 4.2(c)]. In both cases, because of the relatively low drag and aerodynamic damping in the lead–lag plane, mechanical dampers are fitted at the lag hinges. Needless to say, the articulated rotor design is mechanically complicated with many component parts and is relatively expensive to maintain. It is also heavy and produces relatively high drag in forward flight. Nevertheless, the fully articulated design is the classic approach to providing blade articulation on a helicopter and in practice it has proven mechanically reliable but with relatively high maintenance costs because of the large number of parts.

A hingeless rotor design eliminates the flap and lead–lag hinges by using a flexure to accommodate blade motion. A feathering bearing is still used to allow for pitch changes on each blade. The advantage of a hingeless design is that it is mechanically simple. However, because blade articulation is achieved by the elastic flexing of a structural beam, the design of such rotors is rather complicated. In addition, because it is not possible to completely isolate the flapping motion from the lead–lag motion there is usually significant flap–lag coupling to contend with. Major advantages of the hingeless hub design include mechanical simplicity with a low parts count and low aerodynamic drag. In addition, the relatively stiff hub design gives the helicopter a powerful response to control inputs and increased maneuvering capability.

Bearingless hub designs are a relatively new innovation. In addition to eliminating the mechanical flap and lead–lag hinges, the bearingless hub also eliminates the feathering bearing. All three degrees of motion are obtained by bending, flexing, and twisting of the hub structure. Needless to say, obtaining the required stiffnesses is only possible by means of new fatigue-resistant composite materials such as glass, carbon, and Kevlar, which can be arranged so that load paths, stiffnesses, and couplings can all be controlled. Designing a bearingless hub is difficult and requires a detailed (i.e., finite-element based) structural dynamic analysis. While retaining all the advantages of a hingeless design, bearingless hubs can be particularly susceptible to aeromechanical instabilities as a result of low in-plane damping of the lead–lag blade motion.

4.3 Equilibrium about the Flapping Hinge

Consider now the mathematical analysis of a rotating flapping blade. Figure 4.3 shows a rigid (aeroelastically stiff) rotor blade flapping about a hinge located at a distance eR from the rotational axis. The equilibrium position of the blade is determined by the balance of aerodynamic and centrifugal forces (CF). The contributions from the gravitational forces on the blade are small relative to the other forces and can be neglected. Furthermore, because the centrifugal forces are much larger than the aerodynamic forces, the flapping (coning) angle β is usually quite small (between 3° and 6° is typical for a helicopter rotor).

Assume first for simplicity that the flapping hinge is at the rotational axis, that is, $e = 0$. For other than teetering rotor designs (see Section 4.13.1), the flapping hinge is always offset a small distance from the rotational axis, but this does not alter the fundamental physics of the blade dynamics problem. The rotational speed about the axis is Ω radians per second and is constant. Assume a uniform mass per unit length of the blade, m. Consider a small element of the blade of length dy. The mass of this element is mdy. The forces on the element are aerodynamic and centrifugal. The contribution of this small element to the centrifugal force acting in a direction parallel to the plane of rotation is

$$d(F_{CF}) = (mdy)y\Omega^2 = m\Omega^2 y\, dy. \tag{4.1}$$

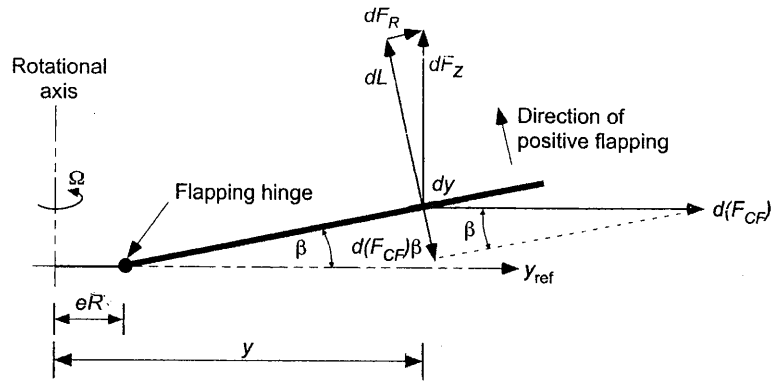

Figure 4.3 Equilibrium of blade aerodynamic and centrifugal forces about the flapping hinge.

Therefore, the total centrifugal force acting on the blade is

$$F_{CF} = \int_0^R m\Omega^2 y \, dy = \frac{m\Omega^2 R^2}{2} = \frac{M\Omega^2 R}{2}, \tag{4.2}$$

where the mass of the uniform blade is M $(= mR)$. Notice that the centrifugal forces increase linearly in proportion to blade mass and length and are also proportional to Ω^2. If the blade is coned up at some angle β, then the contribution of this small element to the CF acting in a direction perpendicular to the blade is

$$d(F_{CF}) \sin\beta = (m dy) y\Omega^2 \sin\beta \approx my\Omega^2 \beta \, dy. \tag{4.3}$$

The moment about the flapping hinge (at the rotational axis) as a result of the centrifugal forces produced by all the elements is, therefore,

$$\begin{aligned} M_{CF} &= \int_0^R m\Omega^2 y^2 \beta \, dy = m\Omega^2 \beta \int_0^R y^2 \, dy \\ &= \frac{m\Omega^2 \beta R^3}{3} = \frac{M\Omega^2 \beta R^2}{3} = \frac{2}{3} F_{CF} R\beta. \end{aligned} \tag{4.4}$$

The aerodynamic moment about the flap hinge, M_β, depends on the distribution of lift, L, across the blade, that is,

$$M_\beta = -\int_0^R Ly \, dy. \tag{4.5}$$

Notice that the negative sign indicates that the aerodynamic moment is in the opposite direction to the centrifugal moment. The rotating blade will reach an equilibrium position where the CF moment about the hinge is equal and opposite to the aerodynamic moment about the hinge. Therefore, the equilibrium equation can be written as

$$M_\beta + M_{CF} = 0 \tag{4.6}$$

and so the equilibrium or *coning angle* β_0 will be given by

$$\beta_0 = \frac{3\int_0^R Ly \, dy}{M\Omega^2 R^2}. \tag{4.7}$$

This result is valid for any form of the aerodynamic loading over the blade. Also, the flapping hinge has been assumed to lie at the rotational axis of the rotor. For a parabolic distribution

of loading of lift over the blade (no blade twist), the center of lift will be located at 3/4 blade radius so that

$$M_\beta = -\frac{3}{4}R \times \text{blade lift.} \tag{4.8}$$

A rotor with ideal twist and uniform inflow will produce a linear (triangular) lift loading, which has a center of lift located at 2/3 blade radius, that is,

$$M_\beta = -\frac{2}{3}R \times \text{blade lift.} \tag{4.9}$$

Therefore, it is clear that this latter case will produce a smaller aerodynamic moment about the hinge for the same total blade lift. For the case where the blade lift is distributed in a triangular manner across the blade (ideal twist) the coning angle β_0 is determined from

$$\frac{2}{3}R \times \text{blade lift} - \frac{2}{3}R\, F_{CF}\, \beta = 0 \tag{4.10}$$

or in general for given lift distribution

$$\beta_0 = \frac{\text{blade lift}}{\text{centrifugal force}}. \tag{4.11}$$

The important point to remember is that the coning angle increases in proportion to rotor thrust and decreases inversely with centrifugal forces. In other words, increasing either blade mass or rotor speed will decrease the coning angle.

In practice the flapping hinge is not normally at the rotational axis (except for teetering rotors) but is offset by a small distance, eR. Typically, $e < 0.15$. In this case, the aerodynamic moment about the flap hinge, M_β, is

$$M_\beta = -\int_{eR}^{R} Ly\, dy. \tag{4.12}$$

Also, the CF moment about the hinge is

$$\begin{aligned} M_{CF} &= \int_{eR}^{R} m\Omega^2 y^2 \beta\, dy = \frac{m\Omega^2 \beta R^3 (1 - e^3)}{3} \\ &= \frac{M\Omega^2 \beta R^2 (1 + e)}{3} + O(e^2), \end{aligned} \tag{4.13}$$

where $M = mR(1 - e)$. Therefore, in this case the coning angle will be given by

$$\beta_0 = \frac{3\int_{eR}^{R} Ly\, dy}{M\Omega^2 R^2 (1 + e)}. \tag{4.14}$$

4.4 Equilibrium about the Lead–Lag Hinge

The equilibrium of the blade about the lead–lag hinge is also determined by a balance of centrifugal and aerodynamic moments. In this case, the aerodynamic moments are generated by the aerodynamic drag of the blade as it rotates. The lag angle, ζ, is defined as positive in the lagging direction (Fig. 4.4). The centrifugal force on the blade element is

$$d(F_{CF}) = m\Omega^2 y\, dy \tag{4.15}$$

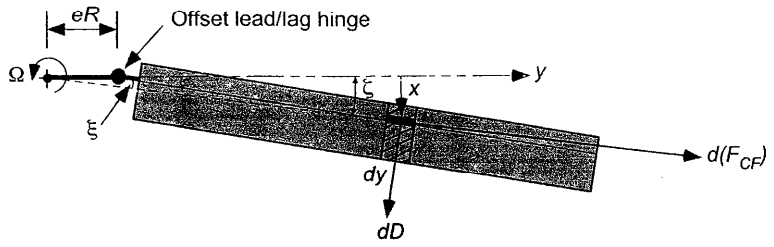

Figure 4.4 Blade with an offset lead–lag hinge.

and the component of this force perpendicular to the axis of the blade, which tends to rotate the blade toward zero lag angle, is

$$d(F_{CF}) = m\Omega^2 y\, dy\, \zeta. \tag{4.16}$$

Therefore, with a very small hinge offset the lag moment will be

$$M_\zeta \approx \int_0^R m\Omega^2 \zeta y^2\, dy. \tag{4.17}$$

The aerodynamic forces acting on the blade in the plane of rotation include both induced drag and profile drag components. To keep the following analysis as simple as possible, it will be assumed that the resultant of all these drag forces is denoted by F_D and acts at a distance y_D from the lead–lag hinge. The equation of equilibrium is therefore

$$F_D y_D = M_\zeta = \int_0^R m\Omega^2 \zeta y^2\, dy = \frac{m\Omega^2 R^3 \zeta}{3} = \frac{M\Omega^2 R^2 \zeta}{3} \tag{4.18}$$

or

$$\zeta_0 = \frac{3F_D y_D}{M\Omega^2 R^2}. \tag{4.19}$$

Like the coning angle, this equation indicates that, for a constant aerodynamic loading, the mean lag angle is inversely proportional to both blade mass and to Ω^2.

Again, in practice, like the flapping hinge, the lead–lag hinge is also offset from the rotational axis. Notice that the lag hinge offset may be different from the flap hinge offset. In this case, the centrifugal force as a result of lag about the offset hinge is

$$F_{CF} = \int_{eR}^R m\Omega^2(\zeta - \xi) y\, dy. \tag{4.20}$$

From the geometry of the problem shown in Fig. 4.4, it can be shown that

$$\xi = \zeta\left(1 - \frac{eR}{y}\right). \tag{4.21}$$

Therefore, the centrifugal moment about the hinge is

$$\begin{aligned} M_\zeta &= \int_{eR}^R m\Omega^2(\zeta - \xi) y^2\, dy = \int_{eR}^R m\Omega^2 \zeta eRy\, dy \\ &= \frac{M\Omega^2 \zeta eR(1+e)}{2}, \end{aligned} \tag{4.22}$$

where the blade mass is $mR(1-e)$ and this shows that the centrifugal force acts at a distance $R(1+e)/2$ from the rotational axis (i.e., at the center of gravity of the blade, y_{cg}).

The resultant of the aerodynamic forces because of blade drag is denoted by F_D and acts at a distance y_D from the hinge axis. The shear force on the lead–lag hinge because of the aerodynamic and centrifugal forces must be equal to the shaft torque, Q, divided by the hinge offset, eR. The equation of force equilibrium is, therefore,

$$F_D \cos\zeta - \int_{eR}^{R} m\Omega^2 y \sin\xi \, dy = \frac{Q}{eR}. \tag{4.23}$$

This equation indicates that, for a given rotor, the mean drag angle of the blades will essentially be a function of Q/Ω^2.

4.5 Equation of Motion for a Flapping Blade

In hovering flight, the solution for β is a constant ($= \beta_0$) independent of ψ and this angle is called the coning angle. Under forward flight conditions as a result of the cyclically (azimuthally) varying airloads, the blade flaps up and down in a periodic manner with respect to azimuth. Consider Fig. 4.5, which shows the line of action of the aerodynamic forces, the centrifugal forces, and the inertial forces acting on a small element of the blade span. Define the moment to be positive in a direction such as to reduce β. The centrifugal moment about the hinge is

$$d(M_{CF}) = (m dy) y^2 \Omega^2 \beta = m y^2 \Omega^2 \beta \, dy. \tag{4.24}$$

The inertial moment about the hinge is

$$d(I) = (m dy) y^2 \ddot{\beta} = m y^2 \ddot{\beta} \, dy \tag{4.25}$$

and the aerodynamic moment about the hinge is

$$d(M_\beta) = -Ly \, dy, \tag{4.26}$$

where the sign of the latter term is noted. It will be assumed that there is no hinge offset, that is, $e = 0$. Therefore, the equation of motion can be derived by summing the moments about the flap hinge giving

$$\int_0^R d(M_{CF}) + \int_0^R d(I) + \int_0^R d(M_\beta) = 0. \tag{4.27}$$

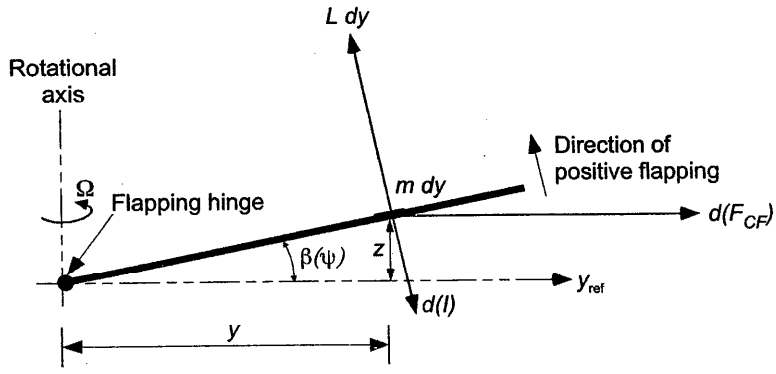

Figure 4.5 Forces acting on an element of a flapping blade.

Introducing the relevant expressions for $d(M_{CF})$, $d(I)$, and $d(M_\beta)$ gives

$$\int_0^R m\Omega^2\beta y^2\,dy + \int_0^R m\ddot{\beta}y^2\,dy - \int_0^R Ly\,dy = 0. \tag{4.28}$$

Collecting terms results in

$$\left(\int_0^R my^2\,dy\right)\left(\ddot{\beta} + \Omega^2\beta\right) = \int_0^R Ly\,dy. \tag{4.29}$$

The mass moment of inertia of the blade about the flap hinge is

$$I_b = \int_0^R my^2\,dy. \tag{4.30}$$

Thus the equation of flapping motion in Eq. 4.29 can be written as

$$I_b\ddot{\beta} + I_b\Omega^2\beta = \int_0^R Ly\,dy. \tag{4.31}$$

Noting that $\psi = \Omega t$ results in the following transformations

$$\dot{\beta} = \frac{\partial\beta}{\partial t} = \Omega\frac{\partial\beta}{\partial\psi} = \Omega\overset{*}{\beta} \quad \text{and} \quad \ddot{\beta} = \frac{\partial^2\beta}{\partial t^2} = \Omega^2\frac{\partial^2\beta}{\partial\psi^2} = \Omega^2\overset{**}{\beta}. \tag{4.32}$$

We can then write the flapping equation as

$$I_b\Omega^2\frac{\partial^2\beta}{\partial\psi^2} + I_b\Omega^2\beta = \int_0^R Ly\,dy \tag{4.33}$$

or in short-hand notation simply as

$$\overset{**}{\beta} + \beta = \frac{1}{I_b\Omega^2}\int_0^R Ly\,dy \tag{4.34}$$

Now, consider the aerodynamic forces. At any blade element of chord c at a radial distance y from the rotational axis it can be readily shown using the blade element theory (Section 3.5) that with uniform inflow the aerodynamic force per unit length is

$$L = \frac{1}{2}\rho U_T^2 cC_l = \frac{1}{2}\rho U_T^2 cC_{l_\alpha}\left(\theta - \frac{\dot{\beta}y}{U_T} - \frac{v_i}{U_T}\right), \tag{4.35}$$

so the aerodynamic moment about the hinge will be

$$\begin{aligned}\int_0^R Ly\,dy &= \frac{1}{2}\rho\Omega^2 cC_{l_\alpha}\int_0^R y^3\left(\theta - \frac{\dot{\beta}}{\Omega} - \frac{v_i}{\Omega y}\right)dy \\ &= \frac{1}{8}\rho\Omega^2 cC_{l_\alpha}R^4\left(\theta - \frac{\dot{\beta}}{\Omega} - \frac{4\lambda_i}{3}\right).\end{aligned} \tag{4.36}$$

The Lock number is defined as

$$\gamma = \frac{\rho C_{l_\alpha} cR^4}{I_b}, \tag{4.37}$$

which can be viewed as a measure of the ratio of aerodynamic forces to inertial forces. For a typical helicopter rotor, the value of the Lock number varies from 5 to 10. Notice, however, that its value depends on the density of the air and so will be affected by changes

in density altitude (see Section 5.2). The equation governing the behavior of the flapping blade becomes

$$\ddot{\beta} + \beta = \frac{\rho C_{l_\alpha} c R^4}{I_b}\left(\frac{1}{8}\right)\left(\theta - \dot{\beta} - \frac{4\lambda_i}{3}\right), \tag{4.38}$$

which on rearrangement gives

$$\ddot{\beta} + \left(\frac{\gamma}{8}\right)\dot{\beta} + \beta = \frac{\gamma}{8}\left(\theta - \frac{4\lambda_i}{3}\right). \tag{4.39}$$

This is the flapping equation for a *centrally hinged* blade, that is, one that is hinged at the rotational axis with $e = 0$. A more general form is to leave the aerodynamic force (moment) on the right-hand side unintegrated, in which case

$$\ddot{\beta} + \beta = \gamma \bar{M}_\beta, \tag{4.40}$$

where

$$\bar{M}_\beta = \frac{1}{\rho C_{l_\alpha} c R^4 \Omega^2}\int_0^R Ly\, dy. \tag{4.41}$$

Notice the similarity of Eq. 4.40 with the equation of motion of a single degree-of-freedom spring–mass–damper system, that is, $m\ddot{x} + c\dot{x} + kx = F$, where x is the displacement, m is the mass, c is the damping, and k is the spring stiffness. This system has an undamped natural frequency of $\omega_n = \sqrt{k/m}$. Therefore, by analogy with Eq. 4.40 the undamped natural frequency of the flapping blade about a hinge located at the rotational axis is once per revolution (1/rev) or $\omega_n = \Omega$ rad/s.

Consider first the case where the rotor operates in a vacuum, in which case there are no aerodynamic forces present. The flapping equation reduces to

$$\ddot{\beta} + \beta = 0. \tag{4.42}$$

It is easy to show that this equation has the general solution

$$\beta = \beta_{1c}\cos\psi + \beta_{1s}\sin\psi, \tag{4.43}$$

where β_{1c} and β_{1s} are arbitrary coefficients. Thus, in the absence of aerodynamic forces, the rotor takes up an arbitrary orientation in inertial space. In effect, the rotor acts like a gyroscope. The introduction of aerodynamic forces produces an aerodynamic flapping moment about the hinge, which causes the rotor to *precess* to a new orientation until the aerodynamic damping (which is contained inside the $\bar{M}_\beta$ term) causes equilibrium to be obtained once again.

In forward flight, the aerodynamic forces provide the forcing to the flapping blade at multiples of the rotor frequency. This aerodynamic excitation is primarily at 1/rev. The blade flapping motion with respect to the rotor hub can be represented as an infinite Fourier series of the form

$$\begin{aligned}\beta(\psi) &= \beta_0 + \beta_{1c}\cos\psi + \beta_{1s}\sin\psi + \beta_{2c}\cos 2\psi + \beta_{2s}\sin 2\psi + \cdots \\ &= \beta_0 + \sum_{n=1}^{\infty}(\beta_{nc}\cos n\psi + \beta_{ns}\sin n\psi),\end{aligned} \tag{4.44}$$

where the time scale has been nondimensionalized with respect to rotor time such that the dimensionless period is 2π radians. The Fourier coefficients may be evaluated from the flapping displacements using

$$\beta_0 = \frac{1}{2\pi}\int_0^{2\pi} \beta \, d\psi, \tag{4.45}$$

$$\beta_{nc} = \frac{1}{\pi}\int_0^{2\pi} \beta \cos n\psi \, d\psi, \tag{4.46}$$

and

$$\beta_{ns} = \frac{1}{\pi}\int_0^{2\pi} \beta \sin n\psi \, d\psi. \tag{4.47}$$

Assuming uniform inflow and linearly twisted blades, we can evaluate the aerodynamic flapping moment about the hinge analytically using the blade element theory where

$$\bar{M}_\beta = \frac{1}{\rho c l_\alpha c R^4 \Omega^2}\int_0^R y dF_z \tag{4.48}$$

$$= \frac{1}{2}\int_0^1 r\left[\left(\frac{U_T}{\Omega R}\right)^2 \theta - \left(\frac{U_P}{\Omega R}\right)\left(\frac{U_T}{\Omega R}\right)\right] dr. \tag{4.49}$$

After substituting the results for U_T and U_P obtained previously in Section 3.5, and also assuming uniform inflow and linearly twisted blades, we get

$$\begin{aligned}\bar{M}_\beta = {} & \theta\left(\frac{1}{8} + \frac{\mu}{3}\sin\psi + \frac{\mu^2}{4}\sin^2\psi\right) \\ & + \theta_{tw}\left(\frac{1}{10} + \frac{\mu}{4}\sin\psi + \frac{\mu^2}{6}\sin^2\psi\right) - \lambda\left(\frac{1}{6} + \frac{\mu}{4}\sin\psi\right) \\ & - \dot{\beta}\left(\frac{1}{8} + \frac{\mu}{6}\sin\psi\right) - \beta\mu\cos\psi\left(\frac{1}{6} + \frac{\mu}{4}\sin\psi\right)\end{aligned} \tag{4.50}$$

and this result can then be substituted into Eq. 4.40 to compute β.

Some interesting characteristics of the resulting flapping equation are as follows:

1. In forward flight, that is, when $\mu \neq 0$, the equation has periodic coefficients. This does not allow an analytical closed-form solution of the flapping equation.
2. The flap damping term, which is the coefficient associated with the $\dot{\beta}$ term in Eq. 4.50 for $\bar{M}_\beta$, is

   $$\frac{\gamma}{8}\left(1 + \frac{4}{3}\mu\sin\psi\right),$$

   which is of aerodynamic origin (all the terms multiplied by the Lock number γ come from the aerodynamics) and is usually very high. For the case of hover and for the natural frequency of 1/rev, the corresponding damping ratio is $\gamma/16$. For a Lock number $\gamma = 8$ this means that the damping is 50% of the critical value; thus the blade flapping motion is stable and well damped.
3. Finally, notice that the flapping equation has been derived with respect to the plane defined by the hub of the rotor, and so both the flap angle β and the pitch control angle θ will generally be functions of the azimuth angle ψ.

The general flapping equation of motion cannot be solved analytically in closed form for the general case of $\mu \neq 0$. Therefore, two options present themselves:

1. *Solve the equation numerically.* The equation can be integrated for given values of collective pitch θ_0, lateral cyclic θ_{1c}, longitudinal cyclic θ_{1s}, and inflow λ_i. The selection of the initial conditions for the flapping is not very important because even extreme initial conditions will simply cause a numerical transient that will disappear after a few numerical iterations because of the high damping present in the blade flapping motion. The main problem with the numerical solution is that it does not provide any insight into how the blade flapping response is affected by the various rotor geometry parameters and operational flight conditions.
2. *Find a periodic solution.* In this case the problem is to find a steady-state, periodic solution, in the form of a Fourier series. Obviously this solution is not adequate for transient situations such as during a maneuver, but it allows the identification of the relationships between the flapping response and the various problem parameters.

Assuming the solution for the blade flapping motion to be given by the first harmonics only, that is,

$$\beta(\psi) = \beta_0 + \beta_{1c}\cos\psi + \beta_{1s}\sin\psi \tag{4.51}$$

and harmonically matching constant and periodic (sine and cosine) terms on both sides of the derived flapping equation gives

$$\beta_0 = \gamma\left[\frac{\theta_0}{8}\left(1+\mu^2\right) + \frac{\theta_{tw}}{10}\left(1+\frac{5}{6}\mu^2\right) + \frac{\mu}{6}\theta_{1s} - \frac{\lambda}{6}\right], \tag{4.52}$$

$$\beta_{1s} - \theta_{1c} = \frac{\left(-\frac{4}{3}\mu\beta_0\right)}{\left(1+\frac{1}{2}\mu^2\right)}, \tag{4.53}$$

$$\beta_{1c} + \theta_{1s} = \frac{-\frac{8}{3}\mu\left[\theta_0 - \frac{3}{4}\lambda + \frac{3}{4}\mu\theta_{1s} + \frac{3}{4}\theta_{tw}\right]}{\left(1-\frac{1}{2}\mu^2\right)}. \tag{4.54}$$

Notice that by setting $\mu = 0$ (hovering flight) in the above equations the following results are obtained:

$$\beta_{1s} - \theta_{1c} = 0 \quad \text{or} \quad \beta_{1s} = \theta_{1c}, \tag{4.55}$$

$$\beta_{1c} + \theta_{1s} = 0 \quad \text{or} \quad \beta_{1c} = -\theta_{1s}. \tag{4.56}$$

This shows that there is an equivalence between pitching motion and flapping motion. If the cyclic pitch motion is assumed to be

$$\theta = \theta_0 + \theta_{1c}\cos\psi + \theta_{1s}\sin\psi, \tag{4.57}$$

then the flapping response will be

$$\beta = \beta_0 + \theta_{1c}\sin\psi - \theta_{1s}\cos\psi \tag{4.58}$$

$$= \beta_0 + \theta_{1c}\cos\left(\psi - \frac{\pi}{2}\right) + \theta_{1s}\sin\left(\psi - \frac{\pi}{2}\right). \tag{4.59}$$

Therefore, because of the dynamic behavior of the blade, the flapping response lags the blade pitch (aerodynamic) inputs by $\pi/2$ or 90°, which is a resonant condition[1] and is independent of any damping. Also, notice the one-to-one correspondence between a unit of pitch and a unit of flapping. This means that when the pilot inputs a unit of cyclic pitch, the rotor will respond with a unit of flapping. Strictly speaking this behavior is for a rotor with a flapping hinge at the rotational axis, but even with a hinge offset the underlying physics and rotor response is essentially similar. The effect of a hinge offset on the flapping problem will be considered in Section 4.7.

4.6 Physical Description of Blade Flapping

The basic physics of blade flapping are relatively elementary, although on an actual helicopter during flight, the combined harmonics of the flapping displacements result in a more complicated blade motion. To this end, it is convenient to explain the net blade motion in terms of the contributing elements. This is the approach followed by Gessow & Myers (1952).

4.6.1 *Coning Angle*

The coefficient β_0 is the average or mean part of the flapping motion that is independent of time or blade azimuth, ψ. In hovering flight, $\beta(\psi) = \beta_0$, which, as mentioned previously, is called the coning angle. The presence of a coning angle has been pointed out to be the angle that results from the moment balance about the flapping hinge as a result of the centrifugal and aerodynamic forces. Because the centrifugal loads remain constant for a given rotor speed, the coning angle varies with both the magnitude and distribution of lift across the blade. For example, a higher gross weight of the helicopter requires a higher blade lift to hover, which tends to increase the aerodynamic moment about the hinge, resulting in a higher blade coning angle. Also, it is already known from the previous discussion in Chapter 3 that the inflow velocity has an effect on the blade spanwise loading. As the magnitude of the inflow increases, for a given overall total rotor thrust the blade must become more highly lift loaded toward the tips. This produces a higher aerodynamic moment about the hinge and, therefore, a higher coning angle. Because the time-averaged inflow (induced velocity) through the rotor disk changes with forward speed, the rotor coning angle will mimic the variation in mean inflow through the disk with forward speed, as discussed in Section 2.14.6.

4.6.2 *Longitudinal Flapping Angle*

The coefficient β_{1c} represents the amplitude of the pure cosine flapping motion (Fig. 4.6). This represents a longitudinal or fore aft tilt of the rotor tip path plane. In forward flight, the rotor disk has a natural tendency to tilt back (longitudinally) because of the dissymmetry in lift produced between the advancing and retreating sides of the disk. As a result of the higher dynamic pressure on the advancing side of the disk, the blade lift is increased over that obtained at $\psi = 0°$ and $\psi = 180°$. Therefore, as the blade rotates into the advancing side of the disk, the excess lift causes the blade to flap upward, which decreases its lift. This behavior is shown more clearly in Fig. 4.7.

[1] For a single degree-of-freedom linear, time-invariant system excited at its natural frequency, there will always be a phase lag of 90° between the input and the output.

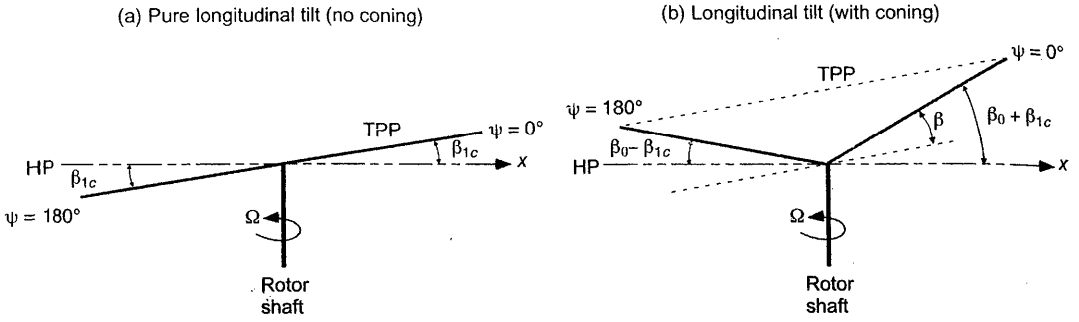

Figure 4.6 Pure longitudinal flapping of the rotor, with positive displacements shown.

Over the front of the disk the dynamic pressure reduces progressively and the blade reaches a maximum *displacement* with $\dot{\beta} = 0$ at $\psi = 180°$. As the blade rotates into the retreating side of the rotor disk, the deficiency in dynamic pressure causes the blade to flap downward. This downward flapping motion increases the AoA at the blade element, which tends to increase blade lift over the lift that would have been obtained without flapping motion. This upward and downward flapping of the blade tends to reduce and increase the AoA at the blade elements by an amount

$$\Delta\alpha(y, \mu) = -\tan^{-1}\left(\frac{y\dot{\beta}}{\Omega y + \mu\Omega R}\right) = -\tan^{-1}\left(\frac{r\overset{*}{\beta}}{r + \mu}\right). \tag{4.60}$$

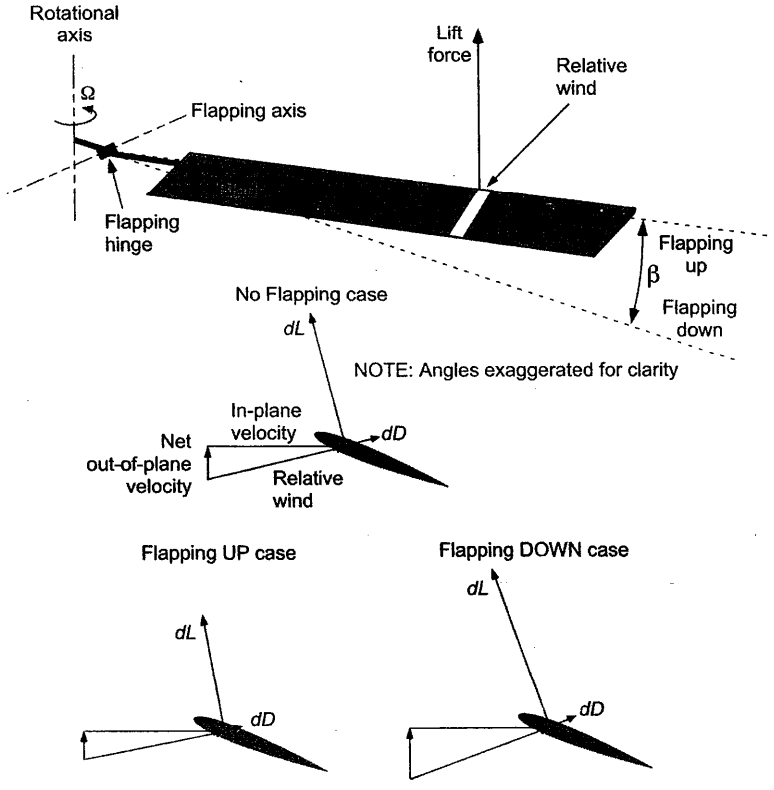

Figure 4.7 The effect of flapping serves to reduce or increase the lift on the blade.

For example, as a result of the flapping upward ($\dot{\beta} > 0$), the blade lift tends to decrease relative to the lift that would have been produced without a flapping hinge. Conversely, for flapping downward, the blade lift tends to increase relative to the lift that would be produced without the flapping hinge.

The upshot of all this flapping motion is that the rotor blades reach an equilibrium condition again when the local changes in AoA and aerodynamic loads as a result of blade flapping become sufficient to compensate for local changes in the airloads resulting from variations in dynamic pressure between the advancing and retreating sides of the disk. For the situation described previously, in the final equilibrium condition the disk will be tilted back longitudinally with respect to the hub (i.e., a $-\beta_{1c}$ flapping motion). Remember that the forcing function in this case is phased such that the maximum aerodynamic force occurs at $\psi = 90°$, but because of the dynamic behavior of the rotor blade, the maximum flapping displacement occurs $\pi/2$ or 90° later at $\psi = 180°$. This is of fundamental importance because it allows an understanding of what happens to the rotor flapping under the action of aerodynamic loads that are phased differently with respect to the rotor azimuth.

4.6.3 *Lateral Flapping Angle*

The coefficient β_{1s} represents the amplitude of the pure sine motion (see Fig. 4.8). This represents the lateral or left–right tilt of the tip path plane. In addition to the natural tendency for the disk to tilt back with a change in forward flight speed, the disk also has a tendency to tilt laterally to the right. This effect arises because of blade flapping displacement (coning). For the coned rotor, the blade AoA is decreased when the blade is at $\psi = 0°$ and increased when $\psi = 180°$. Again, another source of periodic forcing is produced, but now this is phased 90° out of phase compared to the effect discussed previously. However, because of the 90° force–displacement lag of blade, in this case it results in a lateral tilt of the rotor disk to the right when viewed from behind (i.e., a $-\beta_{1s}$ motion). Notice that in the hypothetical case with no coning, the blades see the same increase in AoA at $\psi = 0°$ and 180° and there will be no lateral tilt.

4.6.4 *Higher Harmonics of Blade Flapping*

The coefficients β_{2c}, β_{2s}, and so on, represent the amplitudes of the higher harmonics of the blade motion. In practice, these are found to be very small and of no substantial significance but appear as a slight warping or wobbling of the rotor tip path plane. For

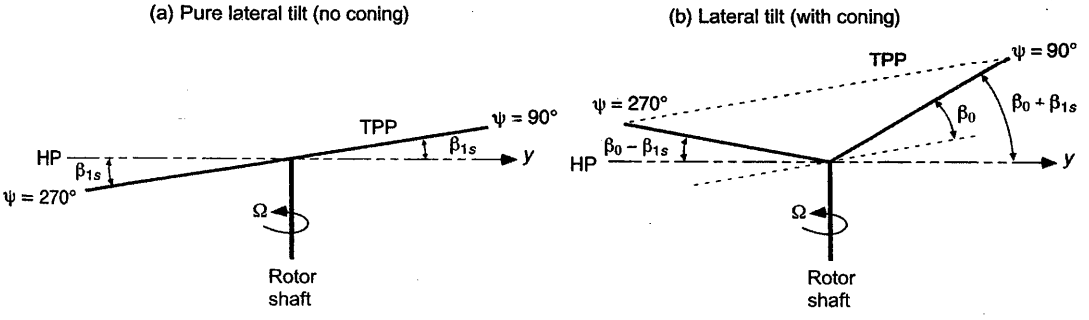

Figure 4.8 Pure lateral flapping of the rotor, with positive displacements shown.

rotor trim and performance evaluation it is considered acceptable engineering practice to neglect all harmonics above the first. However, the effects of higher harmonic flapping on the vibration and aeroelastic stability characteristics of the rotor are important.

4.7 Dynamics of Blade Flapping with a Hinge Offset

The analysis of a blade with a hinge offset is similar to the foregoing, but there are some important quantifiable differences. The blade is assumed to be rigid and hinged at a distance eR from the rotational axis. The forces acting on an element of the blade are as follows:

1. Inertia force $m(y - eR)\ddot{\beta}dy$ acting at a distance $(y - eR)$ from the hinge.
2. Centrifugal force $my\Omega^2\, dy$ acting at a distance $(y - eR)\beta$ from the hinge.
3. Aerodynamic lift forces $L\, dy$ acting at a distance $(y - eR)$ from the hinge.

Taking moments about the flapping hinge gives the equation of motion

$$\int_{eR}^{R} m(y-eR)^2\ddot{\beta}\, dy+\int_{eR}^{R} m\Omega^2 y(y-eR)\beta\, dy-\int_{eR}^{R} L(y-eR)\, dy = 0. \quad (4.61)$$

In this case, the mass moment of inertia about the flapping hinge is

$$I_b = \int_{eR}^{R} m(y - eR)^2\, dy, \quad (4.62)$$

so that the flapping equation becomes

$$I_b\left\{\ddot{\beta} + \Omega^2\left(1 + \frac{eR\int_{eR}^{R} m(y - eR)dy}{I_b}\right)\beta\right\} = \int_{eR}^{R} L(y - eR)dy. \quad (4.63)$$

Dividing through by Ω^2 gives

$$I_b\left(\overset{**}{\beta} + \nu_\beta^2\beta\right) = \frac{1}{\Omega^2}\int_{eR}^{R} L(y - eR)dy, \quad (4.64)$$

where ν_β is the nondimensional flapping frequency in terms of the rotational speed, that is,

$$\nu_\beta^2 = 1 + \frac{eR\int_{eR}^{R} m(y - eR)dy}{I_b}. \quad (4.65)$$

Again, the physical analogy with a spring–mass–damper system can be drawn. Evaluation of Eq. 4.65 shows that the undamped natural frequency of the uniform system is now

$$\nu_\beta = \omega_n = \sqrt{1 + \frac{3e}{2(1 - e)}} \approx \sqrt{1 + \frac{3}{2}e}, \quad (4.66)$$

the proof of which is the basis for Question 4.1. The behavior is shown in Fig. 4.9. Typically, the value of e varies from 4 to 6% for an articulated blade (although higher for hingeless

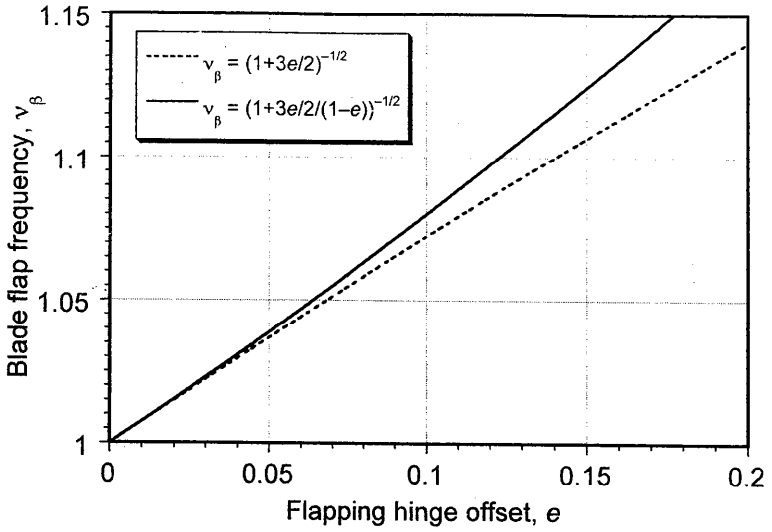

Figure 4.9 The blade flapping frequency varies with the hinge offset.

or semi-rigid rotors), so that the natural frequency of the rotor is only slightly greater than Ω or 1/rev. This also means that the phase lag between the forcing and the rotor flapping response must be less than 90° and the flapping displacements also now depend on aerodynamic damping. In this case, the flapping equation is

$$\overset{**}{\beta} + \nu_\beta^2 \beta = \gamma \bar{M}_\beta, \tag{4.67}$$

where ν_β is the rotating flapping frequency in terms of rotational speed. (Remember that $\nu_\beta = 1$ for a hinge at the rotational axis.) Therefore, in hover the flapping response to cyclic pitch inputs is given by

$$\beta_{1c}\left(\nu_\beta^2 - 1\right) + \beta_{1s}\frac{\gamma}{8} = \frac{\gamma}{8}\theta_{1c}, \tag{4.68}$$

$$\beta_{1s}\left(\nu_\beta^2 - 1\right) - \beta_{1c}\frac{\gamma}{8} = \frac{\gamma}{8}\theta_{1s}. \tag{4.69}$$

This gives for the longitudinal flapping angle

$$\beta_{1c} = \frac{-\theta_{1s} + \left(\nu_\beta^2 - 1\right)\dfrac{8}{\gamma}\theta_{1c}}{1 + \left[\left(\nu_\beta^2 - 1\right)\dfrac{8}{\gamma}\right]^2}, \tag{4.70}$$

and for the lateral flapping angle

$$\beta_{1s} = \frac{\theta_{1c} + \left(\nu_\beta^2 - 1\right)\dfrac{8}{\gamma}\theta_{1s}}{1 + \left[\left(\nu_\beta^2 - 1\right)\dfrac{8}{\gamma}\right]^2}. \tag{4.71}$$

In this case, the forcing frequency (1/rev) is less than the natural flapping frequency (off resonance condition) and it can be shown that the phase lag, ϕ, will be less than 90° as given by

$$\phi = \tan^{-1}\left(\frac{\gamma\left(1-\frac{8e}{3}\right)}{8\left(\nu_\beta^2-1\right)}\right) \approx \tan^{-1}\left(\frac{\gamma/8}{\nu_\beta^2-1}\right), \tag{4.72}$$

which is a result considered in Question 4.7. For hingeless rotors, which have a relatively high effective hinge offset, the phase lag is about 75–80°.

4.8 Blade Feathering and the Swashplate

The blade pitch (or feathering) motion can be described as the Fourier series

$$\theta(r,\psi) = \theta_{tw}r + \theta_0 + \theta_{1c}\cos\psi + \theta_{1s}\sin\psi + \cdots + \theta_{nc}\cos n\psi + \theta_{ns}\sin n\psi + \cdots, \tag{4.73}$$

where r is the nondimensional radial position on the blade. Blade-pitch motion comes from two sources, namely

1. Commanded input from the helicopter control system. This is done by means of a *swashplate*, the orientation of which is controlled by the pilot. The control inputs produced by the swashplate consist of the collective pitch θ_0 and the *first* harmonics of the Fourier series: the lateral cyclic θ_{1c} and the longitudinal cyclic θ_{1s}. The collective pitch controls the average blade pitch angle and, therefore, the blade lift and average total rotor thrust. The cyclic pitch controls the orientation or tilt of the rotor disk and so the direction of the rotor thrust vector.
2. Elastic deformations (twist) of the blade and control system. The elastic (torsional) deformations of the blade, and although small, they are significant. However, these can be neglected at the present level of analysis.

The swashplate is the key to effecting pitch control to the rotor blades, for which a photo is shown in Fig. 4.10 and a schematic in Fig. 4.11. The swashplate has rotating and nonrotating disks concentric with the rotor shaft. A set of bearings between the two disks allows the upper disk to rotate with the rotor while the lower is nonrotating. Both disks can be slid up and down the shaft in response to collective inputs and the swashplate can also be tilted to an arbitrary orientation in response to cyclic inputs from the pilot's controls. A minimum of three pushrods or actuators are required to position the swashplate relative to the rotor shaft, which is connected (either mechanically or hydraulically) to the flight control system. The upper swashplate has a set of lugs that are connected to the blades, with one lug for each blade. The blade pitch motion itself is induced about a pitch or feathering bearing. A pitch horn is attached to the blade outboard of the pitch bearing. A pitch link is attached to the pitch horn and the upper (rotating) part of the swashplate in such a way that as the upper plate rotates, the vertical displacement of the pitch link produces blade pitch motion. The novel part of the helicopter swashplate is the ability to tilt the plate to an arbitrary orientation, which requires a gimbal or spherical bearing between the swashplate and the rotor shaft. This allows a first harmonic blade-pitch input with any phase angle. The earliest swashplate mechanisms for helicopter applications are documented in patents by Crocco in 1906, Yurev in 1910, and Hafner in 1922. See Prouty & Curtiss (2003) for a good review of other helicopter rotor control systems, including the swashplate.

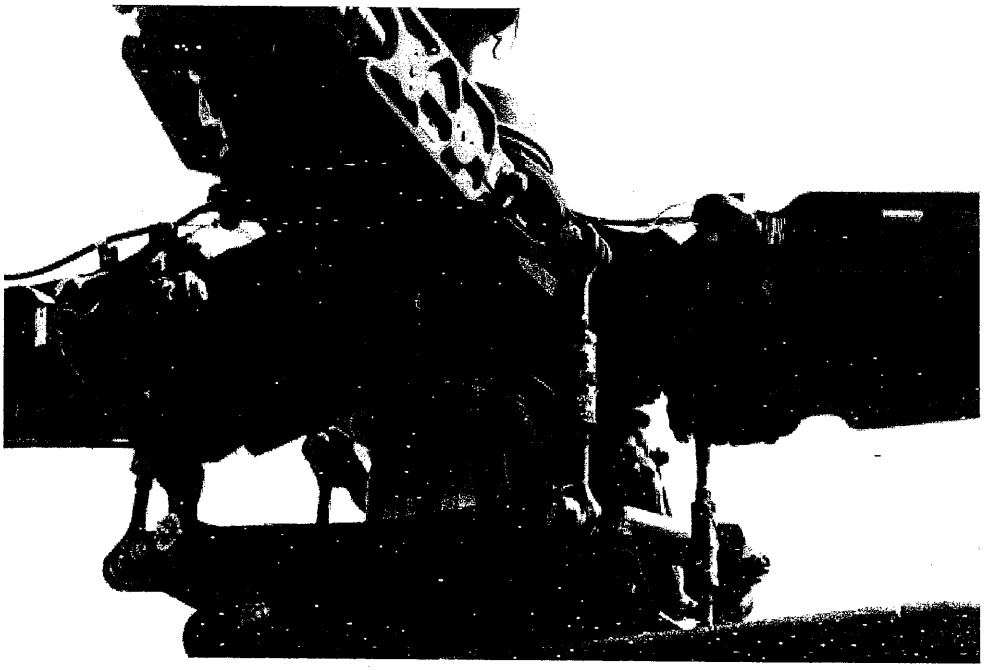

Figure 4.10 Photograph of the hub, pitch links, and swashplate mechanism on an AH-64.

As shown in Fig. 4.12, the vertical motion of the swashplate results in a vertical motion of the pitch link and a collective pitch change to the blades. This either increases or decreases the rotor thrust. The fore and aft tilt of the swashplate translates into a once-per-revolution cyclic pitch on each rotor blade. This produces a once-per-revolution aerodynamic forcing, which causes the rotor blades to flap and the rotor to precess to a new orientation in space, thereby tilting the thrust vector. The system is really fundamentally very simple; an aerodynamic forcing is applied at or close to the natural frequency of the flapping blade and the blades respond so that a unit of cyclic pitch input results in (almost) a unit of flapping response.

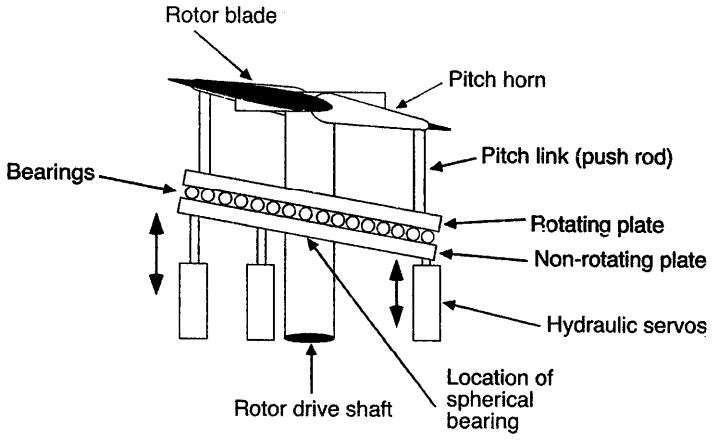

Figure 4.11 Schematic of the swashplate and blade pitch attachments.

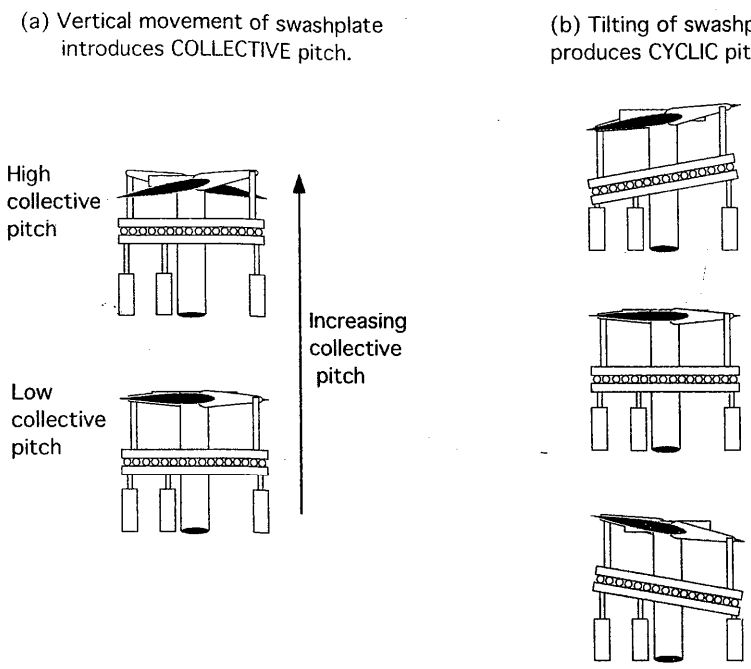

Figure 4.12 The movements of the swashplate result in changes in blade pitch. (a) Collective pitch. (b) Cyclic pitch.

Notice that for a centrally hinged rotor system, the term θ_{1c} controls the lateral orientation of the rotor disk and θ_{1s} controls the longitudinal orientation. Remember that for a rotor with a centrally located flapping hinge there is an exact 90° force–displacement phase-lag. In the case of pure θ_{1c} (cosine) cyclic motion, the maximum applied aerodynamic force occurs at $\psi = 0°$ and so the maximum flapping displacement occurs 90° later at $\psi = 90°$. Therefore, the application of a θ_{1c} pitch displacement causes the rotor to tilt laterally to the left, which is equivalent to a β_{1s} flapping motion and, therefore, this is called *lateral cyclic*. By a similar argument, the application of a θ_{1s} pitch displacement causes the disk to tilt back longitudinally, which is equivalent to a $-\beta_{1c}$ flapping displacement, and this is called *longitudinal cyclic*.

For a contrarotating coaxial rotor system, both rotors must be tilted. Therefore, the pitch angles of both sets of rotors must be connected together through two swashplates so that they tilt in unison. Figure 4.13 gives some idea of the mechanical complexity of the control linkages to do this. Nevertheless, the different aerodynamic environments found on both rotors results in considerable differential flapping. This requires significant spacing between the rotors to ensure that the blades do not collide. The much larger rotor mast and exposed rotor flight control linkages, therefore, result in a high parasitic drag in forward flight. This is one major disadvantage of the coaxial rotor configuration.

4.9 Review of Rotor Reference Axes

There are several physical planes that can be used to describe the equations of motion of the rotor blades. These reference planes or axes systems have evolved as a matter of convenience, and each has advantages over others for certain types of analysis. However,

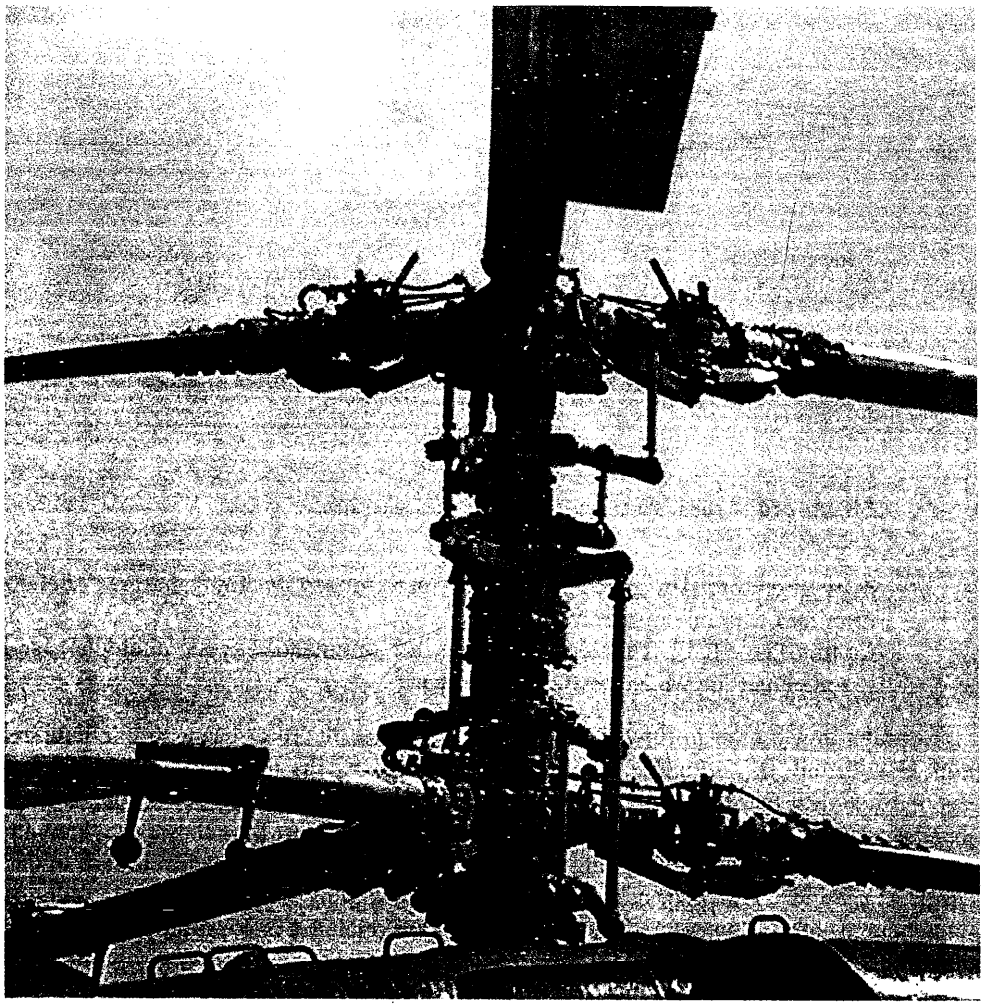

Figure 4.13 Hub of a coaxial rotor system showing the high level of mechanical complexity.

it is always possible to transform an analysis from one reference axis to another, as required. Figure 4.14 schematically shows the various reference planes and axes that are often used in helicopter analyses. These planes are:

1. Hub Plane (HP): The rotor hub plane is perpendicular to the rotor shaft. In the HP, an observer would see both blade flapping and feathering (pitch changes) during forward flight. While this plane is the most complicated for analysis of the rotor, it has the advantage of being linked to a physical part of the aircraft. The HP is often used for blade dynamic and flight dynamic analyses.
2. No Feathering Plane (NFP): This plane was first introduced by Gessow & Myers (1952). The NFP is a plane where an observer sees no variation in cyclic pitch, that is both θ_{1c} and θ_{1s} are zero. However, the observer will still see a cyclic variation in blade flapping angle. Normally, this plane is used for performance analyses.
3. Tip Path Plane (TPP): This is the plane whose boundary is described by the blade tips. Therefore, an observer will see no variation in flapping, that is, both β_{1c} and

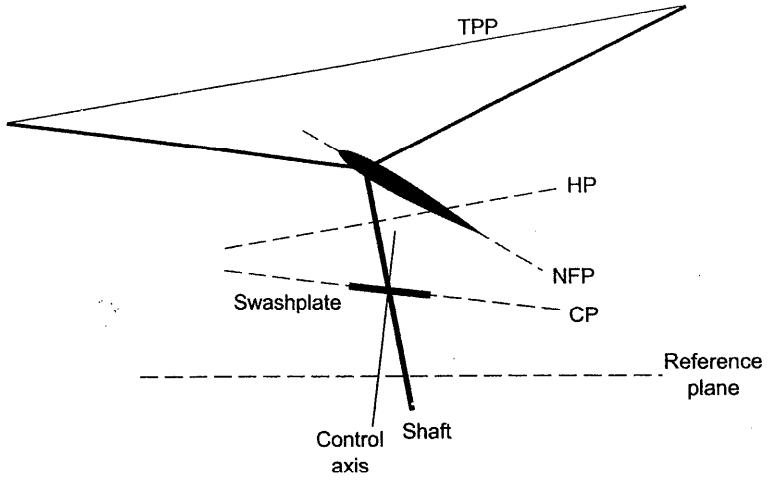

Figure 4.14 Schematic of rotor reference axes and planes.

β_{1s} will be zero. This plane is commonly used for aerodynamic analyses, such as rotor inflow or other wake models.

4. Control Plane (CP): This plane represents the commanded cyclic pitch plane and is sometimes known as the swashplate plane.

Consider now a rotor in forward flight and assume that the rotor has a simple flapping motion with only β_{1c} – that is, the rotor tilts forward by the amount β_{1c} as shown in Fig. 4.15. Notice that the relative amount of blade flapping versus feathering depends on the axis system to which the blade motion is being referenced. At $\psi = 0°$ we see that with respect to the NFP the blade flapping is full up, but the blade pitch is neutral (zero in this case). At $\psi = 90°$, with respect to the NFP the blade flapping is now zero, again with the pitch being neutral. However, at this azimuth the blade pitch is a maximum with respect to the TPP.

Now consider a more general case where the disk is tilted both forward and to the left. Again, as shown by Fig. 4.16, we see that the amount of blade feathering versus flapping depends on the axis system used to view the blade motion. Therefore, in light of this and the previous example, it is apparent that the amount of blade pitch (feathering) with respect to the TPP is equal to the amount of blade flapping with respect to the NFP. Fore and aft (longitudinal) flapping or β_{1c} with respect to the NFP is equivalent to lateral feathering (pitch) with respect to the TPP. Therefore, there is an equivalence of flapping and feathering motion. Strictly speaking, this equivalence is only true for a teetering type of rotor (where the flapping hinge is exactly at the rotational axis), but the equivalence is strong for all types of helicopter rotors. The results of this example are summarized in Table 4.1.

In the transformation from one plane to another, it will be apparent that

$$\beta_{1c} + \theta_{1s} = \text{constant} = (\beta_{1c})_{\text{NFP}} = (\theta_{1s})_{\text{TPP}} \,. \tag{4.74}$$

Also, we have that

$$\beta_{1s} - \theta_{1c} = \text{constant} = (\beta_{1s})_{\text{NFP}} = -(\theta_{1c})_{\text{TPP}} \,. \tag{4.75}$$

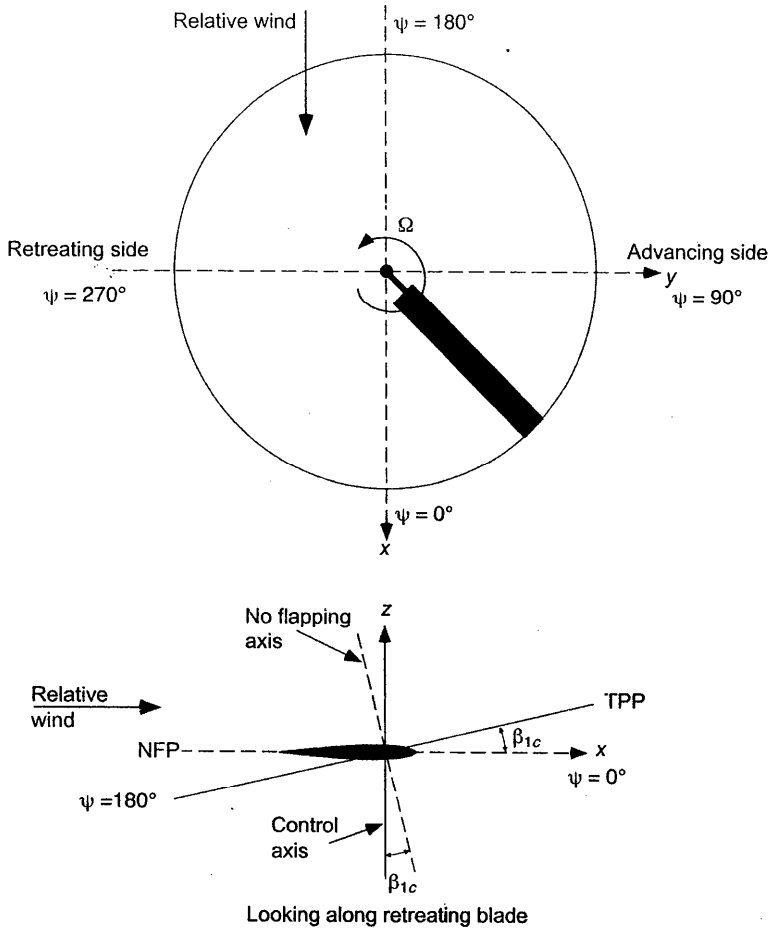

Figure 4.15 Rotor blade with simple flapping motion showing equivalence of flapping and feathering.

Using the above relationships, it is possible to transfer any analysis from one reference system to another, that is, from the TPP to the NFP or vice versa. For example, the angles of attack in the TPP are related to those in the NFP by

$$(\alpha)_{\text{TPP}} = (\alpha)_{\text{NFP}} - (\beta_{1c} + \theta_{1s}) . \tag{4.76}$$

Table 4.1. *Summary of Blade Motion with Respect to NFP and TPP*

ψ	With respect to NFP	With respect to TPP
0°	Flapping = max up	Pitch = zero
90°	Flapping = zero	Pitch = max
180°	Flapping = max down	Pitch = zero
270°	Flapping = zero	Pitch = min

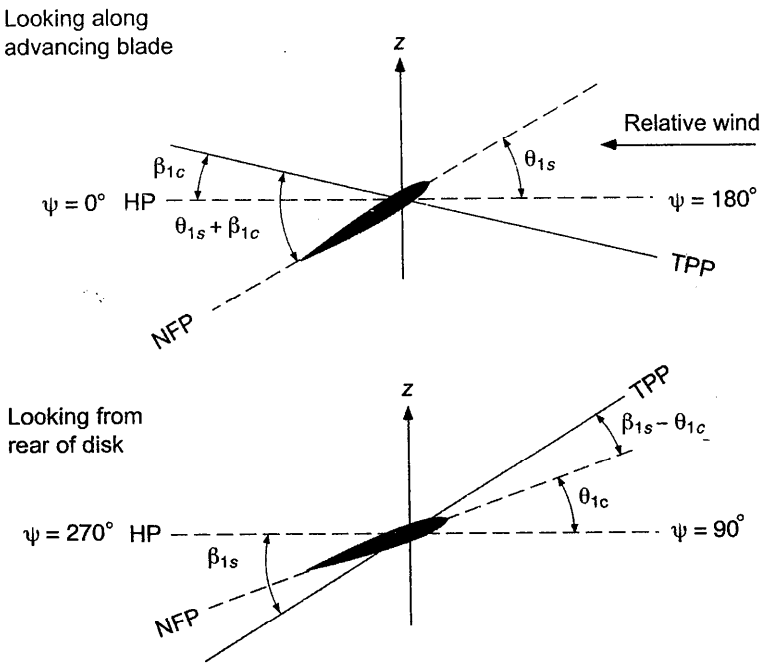

Figure 4.16 General case of rotor blade undergoing flapping and pitching (feathering).

4.10 Dynamics of a Lagging Blade with a Hinge Offset

The blade is assumed to be rigid and undergoes a simple lagging in the plane of rotation about a hinge located at a distance eR from the rotational axis. The various forces acting on the blade are now:

1. The inertia force $m\ddot{x}\,dy = m(y - eR)\ddot{\zeta}\,dy$, acting at a distance $(y - eR)$ about the lag hinge.
2. The centrifugal force $m\Omega^2 y\,dy$ acting at a distance eRx/y from the rotational axis, where $x = (y - eR)/\zeta$.
3. The aerodynamic drag force $D\,dy$ acting at a distance $(y - eR)$ from the hinge axis.

Taking moments about the lag hinge gives

$$\int_{eR}^{R} m(y - eR)^2\ddot{\zeta}\,dy + \int_{eR}^{R} m\Omega^2 y(y - eR)\frac{eR}{y}\zeta\,dy - \int_{eR}^{R} D(y - eR)dy = 0. \tag{4.77}$$

The mass moment of inertia I_ζ about the lag hinge is

$$\int_{eR}^{R} m(y - eR)^2\,dy = I_\zeta. \tag{4.78}$$

Therefore, the equation of motion for lagging about the lead–lag hinge can be written as

$$I_\zeta\left(\overset{**}{\zeta} + \nu_\zeta^2\zeta\right) = \frac{1}{\Omega^2}\int_{eR}^{R} D(y - eR)dy, \tag{4.79}$$

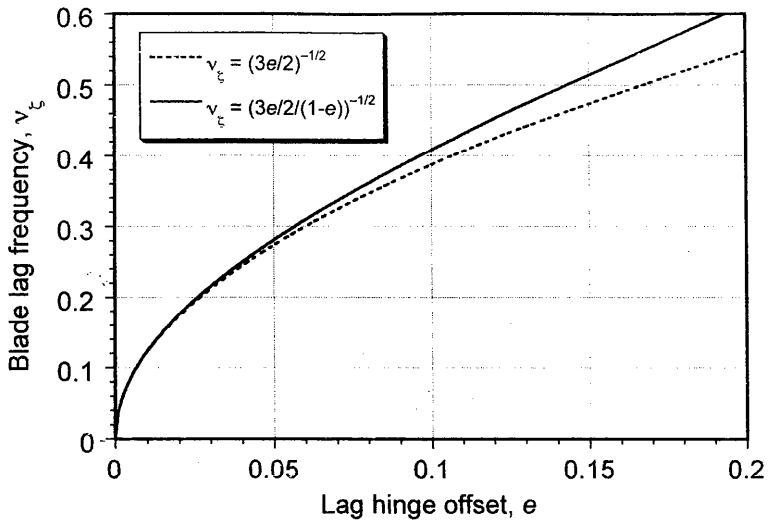

Figure 4.17 The blade lagging frequency varies with the hinge offset.

where ν_ζ is the nondimensional lag frequency in terms of the rotational speed, as determined from

$$\nu_\zeta^2 = \frac{eR\int_{eR}^{R} m(y - eR)dy}{I_\zeta}. \tag{4.80}$$

Notice that $\nu_\zeta = 0$ if there is no hinge offset. Evaluation of Eq. 4.80 gives the lag frequency with a hinge offset as

$$\nu_\zeta = \sqrt{\frac{3}{2}\left(\frac{eR}{R - eR}\right)} \approx \sqrt{\frac{3}{2}e}, \tag{4.81}$$

which is shown graphically in Fig. 4.17. Because the centrifugal restoring moment about the lag hinge is much smaller than in flapping, the corresponding uncoupled natural frequency of the lag motion is much smaller. For articulated rotors, the uncoupled rotating lag frequency varies from about 0.2 to 0.3Ω (see also Question 4.9). For hingeless designs, the value of ν_ζ is much higher, typically from 0.6 to 0.8Ω.

Notice that the lag motion of the blade is lightly damped. Besides the fact that the lead–lag displacements about the hinge are small, they only produce aerodynamic forces through changes in velocity and dynamic pressure normal to the leading edge of the blade. This has a much smaller effect than the aerodynamic forces produced by changes in AoA induced by blade flapping motion. Also, the drag forces acting on the blades are almost two orders of magnitude less than the lift forces. Therefore, because of the low inherent damping it is found that the blade lag motion is very susceptible to driving various types of aeroelastic and aeromechanical instabilities on the rotor.

One important example of an aeromechanical instability associated with blade lag motion is *ground resonance*, where the blade lag motion and the in-plane motion of the fuselage become coupled to produce a catastrophic aeromechanical instability. Ground resonance is associated with the out of pattern in-plane motion of the blades (see Fig. 4.18) and a coupling with the dynamics of the undercarriage and wheels of the helicopter when on the ground. When the motion of the center of gravity is in the same direction of rotor rotation it is

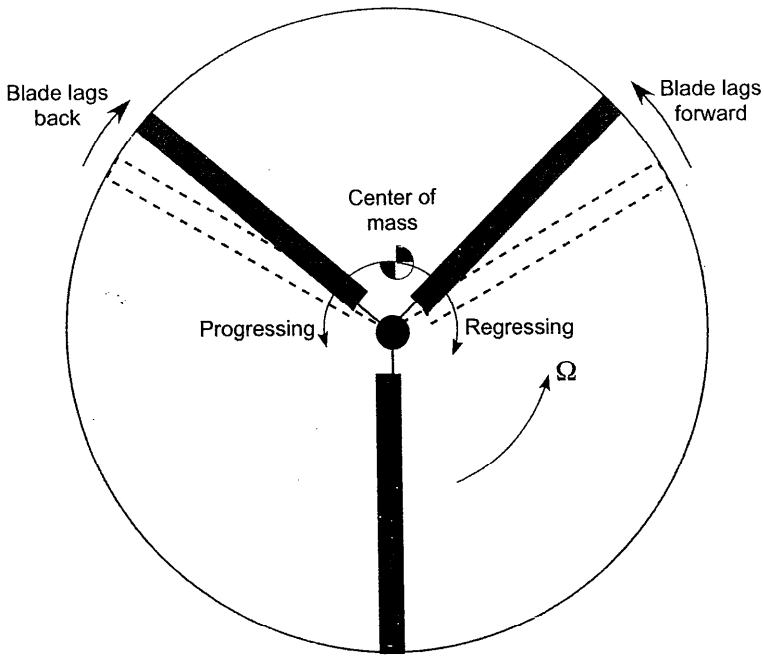

Figure 4.18 Ground resonance is a potentially catastrophic aeromechanical instability of the rotor resulting from an out-of-pattern in-plane lead–lag motion of the blades and its coupling with airframe motion on its landing gear.

called the *progressive* lag mode, and when in the opposite direction it is called the *regressive* lag mode. The problem of ground resonance occurs when the frequency of the regressive lag mode corresponds to an airframe frequency. This causes the net center of gravity of the rotor system to spiral outward away from the rotor hub, initially resulting in a severe shaking of the machine and quickly leading to a catastrophic resonance. "Sympathetic" pilot inputs through the flight controls can provide the initial excitation to the rotor system, although taxiing the machine over rough ground can also be a culprit. A related problem is called *air resonance*, which occurs in flight when the regressive lag mode couples with the fuselage roll and pitch motions, and this too can also be disastrous. This is the reason why most helicopter rotors have mechanical lag dampers, which provide artificial damping to suppress the occurrence of aeromechanical phenomena. If the lag frequency is larger than the rotational frequency (i.e., for a stiff in-plane rotor blade), then there is no possibility of ground or air resonance instability. Coleman & Feingold (1958) developed the first mathematical theory to predict and cure the problem of ground resonance, although even here several aerodynamic approximations are involved. A good summary of the theory of ground resonance is also given by Bramwell (1976) and Johnson (1980).

4.11 Coupled Flap–Lag Motion

It will be apparent from the foregoing that, in practice, the blade flapping and lead–lag motion are coupled. Now consider the analysis of the problem where the blade simultaneously undergoes two types of motion with both flapping and lead–lagging about their respective hinges. This type of model is a good representation of a blade with a high torsional stiffness. For simplicity, it will be assumed that the flapping and lead–lagging hinges are coincident. In this case, note that the flapping and lead–lag motions are coupled as

a result of Coriolis and aerodynamic forces. Coriolis effects introduce an important coupling between blade flapping or out-of-plane motion and lead–lag or in-plane motion. The Coriolis effect is an additional inertial force, first described by Gustave-Gaspard Coriolis in 1835. Coriolis showed that in a rotating frame of reference, an inertial force must be included into the general equations of motion. On a rotor, Coriolis forces will appear whenever there is a radial lengthening or shortening of the blade about the rotational axis, which will be a result of blade flapping or bending. Coriolis effects produce forces in the plane of rotation of the rotor.

A more complete description of the various forces acting on the rotor can now be obtained. For the flapping motion, the forces acting on the blade element are as follows:

1. Inertia force $m(y - eR)\ddot{\beta}\, dy$ acting at a distance $(y - eR)$ about the flap hinge.
2. Centrifugal force $m\Omega^2 y\, dy$ acting act a distance $(y - eR)\beta$ from the flap hinge.
3. Coriolis force $2m(y - eR)\Omega\dot{\zeta}\, dy$ acting at a distance $(y - eR)\beta$ from the flap hinge.
4. Aerodynamic lift forces $L\, dy$ acting at a distance $(y - eR)$ from the flap hinge.

For the lag motion (see Fig. 4.4), the various forces acting on the blade element are as follows:

1. Inertia force $m(y - eR)\ddot{\zeta}\, dy$ acting at a distance $(y - eR)$ about the lag hinge.
2. Centrifugal force $m\Omega^2 y\, dy$ acting act a distance $(y-eR)eR/y\zeta$ from the lag hinge.
3. Coriolis force $2m(y - eR)\beta\Omega\, dy$ acting at a distance $(y - eR)$ from the lag hinge.
4. Aerodynamic drag forces $D\, dy$ acting at a distance $(y-eR)$ from the lag hinge.

Taking the moment of the forces about the flapping hinge gives

$$\int_{eR}^{R} m(y - eR)^2\ddot{\beta}\, dy + \int_{eR}^{R} m\Omega^2 y(y - eR)\beta\, dy - \int_{eR}^{R} 2m\Omega(y - eR)^2\beta\dot{\zeta}\, dy - \int_{eR}^{R} L(y - eR)dy = 0, \tag{4.82}$$

so that the coupled equation of motion of the blade becomes

$$I_b\left(\ddot{\beta} + \nu_\beta^2\Omega^2\beta - 2\Omega\dot{\zeta}\beta\right) = \int_{eR}^{R} L(y - eR)dy, \tag{4.83}$$

where the flapping frequency can be found from

$$\nu_\beta^2 = 1 + \frac{eR\displaystyle\int_{eR}^{R} m(y - eR)dy}{I_b}. \tag{4.84}$$

This reduces to the correct result that $\nu_\beta \to 1$ as $e \to 0$. Taking the moment of the forces about the lead–lag hinge gives

$$\int_{eR}^{R} m(y - eR)^2\ddot{\zeta}\, dy + \int_{eR}^{R} m\Omega^2 eR(y - eR)\zeta\, dy + \int_{eR}^{R} 2m\Omega(y - eR)^2\beta\dot{\beta}\, dy - \int_{eR}^{R} D(y - eR)dy = 0, \tag{4.85}$$

so that the coupled equation of motion for the blade becomes

$$I_\zeta\left(\ddot{\zeta} + \nu_\zeta^2\Omega^2\zeta + 2\Omega\dot{\beta}\beta\right) = \int_{eR}^{R} D(y - eR)dy, \tag{4.86}$$

where the lagging frequency can be found from

$$\nu_\zeta^2 = \frac{eR\int_{eR}^{R} m(y - eR)dy}{I_\zeta}, \tag{4.87}$$

which, again, reduces to the correct result that $\nu_\zeta \to 0$ as $e \to 0$. It is of particular significance to note how the flap–lag equations are coupled through the Coriolis acceleration terms.

4.12 Coupled Pitch–Flap Motion

A rotor can use pitch–flap coupling using a δ_3 hinge to reduce cyclic flapping. This idea is often used on tail rotors to avoid having to use a lead–lag hinge, hence saving weight. As shown in Fig. 4.19, this is achieved by placing the pitch link/pitch horn connection to lie off the flap hinge axis. The kinematics are such that if the blade flaps by an amount β, the pitch angle is reduced by an angle $\beta \tan \delta_3$. Therefore, the pitch angle θ on the right-hand side of the flapping equation (Eq. 4.39) can be replaced by $\theta - \beta \tan \delta_3$, which gives

$$\ddot{\beta} + \frac{\gamma}{8}\dot{\beta} + \left(1 + \frac{\gamma}{8}\tan\delta_3\right)\beta = \frac{\gamma}{8}\left(\theta - \frac{4\lambda_i}{3}\right), \tag{4.88}$$

where uniform inflow has been assumed. This means that the flapping frequency is increased to

$$\nu_\beta = \sqrt{1 + \frac{\gamma}{8}\tan\delta_3} \tag{4.89}$$

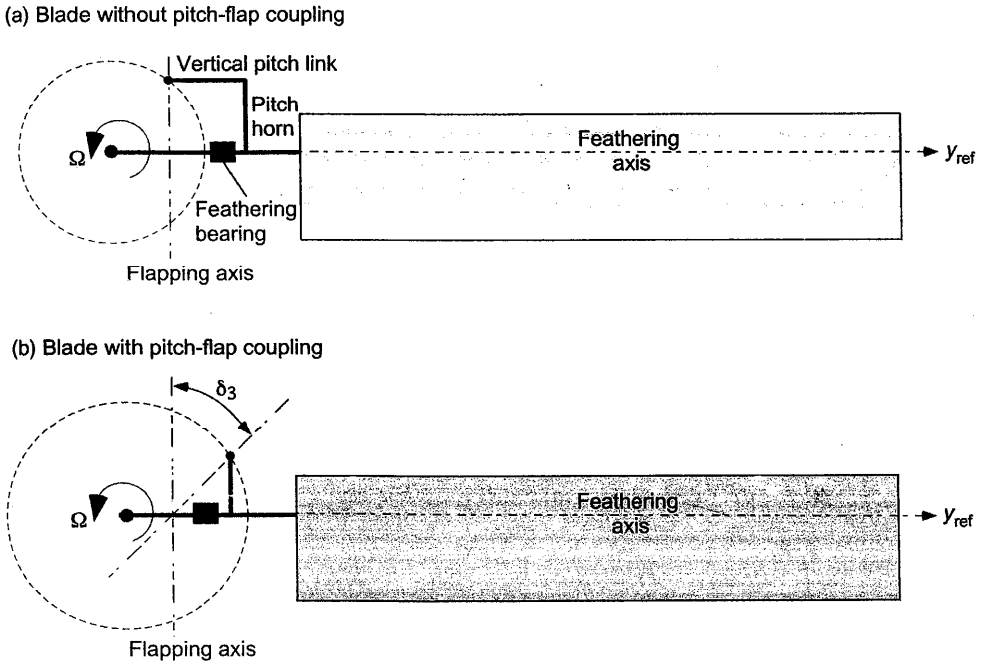

Figure 4.19 Schematic showing introduction of pitch–flap coupling on a blade through a δ_3 hinge.

(a) BK-117 2-bladed teetering tail rotor

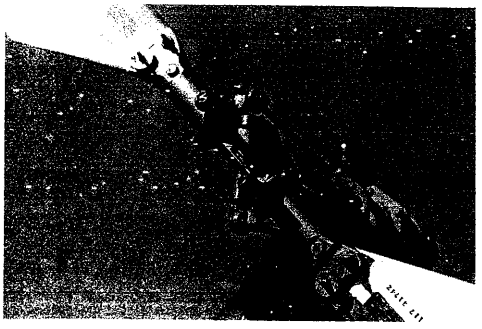

(b) EH-101 4-bladed tail rotor with "spider" pitch mechanism

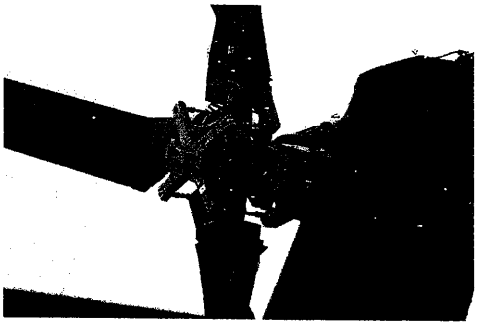

Figure 4.20 Tail rotor designs typically incorporate a large δ_3 angle. (a) BK-117 tail rotor. (b) EH-101 tail rotor.

and the coning angle now becomes

$$\beta_0 = \frac{\gamma\left(\theta_0 - \frac{4}{3}\lambda_i\right)}{8 + \gamma \tan\delta_3}, \tag{4.90}$$

which relative to the case without pitch–flap coupling is reduced for a given collective pitch. On tail rotors, the δ_3 angle is close to 45°, which makes the effect significant. Two examples of tail rotors sporting a δ_3 hinge are shown in Fig. 4.20.

4.13 Other Types of Rotors

4.13.1 *Teetering Rotor*

The teetering (or seesaw) rotor design has already been mentioned; the two interconnected blades form a single structure and have a flapping hinge located on the shaft axis. The teetering design uses no independent flap or lead–lag hinges. An example is shown in Fig. 4.20(a) and is illustrated schematically in Fig. 4.21. The blades may have a built-in precone angle, β_p, which reduces lift-induced steady bending loads. A δ_3 angle may be included, which as previously mentioned, reduces cyclic flapping and Coriolis effects. A separate pitch or feathering bearing on each blade allows for cyclic and collective pitch capability.

The dynamic flapping motion of the teetering rotor is obtained by considering simultaneously the equilibrium of forces on both blades. Consider the flapping moments about the

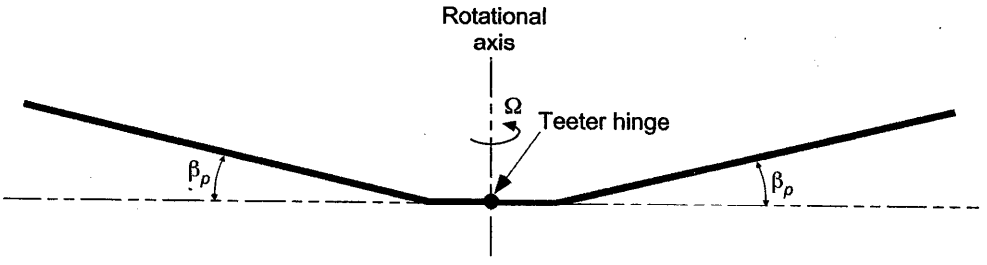

Figure 4.21 A teetering rotor design has two interconnected blades that behave as a single rotating system.

teeter hinge. Each blade has a contribution to the moment, which is equivalent to twice the moment produced by any one blade. This means that

$$2\left(\overset{**}{\beta} + \beta - \gamma \bar{M}_\beta\right) = 0, \tag{4.91}$$

so the equation of motion of the teetering rotor system becomes

$$\overset{**}{\beta} + \nu_\beta^2 \beta = \gamma \bar{M}_\beta, \tag{4.92}$$

where the natural frequency is $\nu_\beta = 1$. It is apparent, therefore, that a teetering rotor behaves like an articulated rotor with no hinge offset.

Consider now the flapping response of the teetering design. With reference to Fig. 4.21, then for one blade the flapping motion is

$$\beta_1(\psi) = \beta_0 + \sum_{n=1}^{\infty} (\beta_{nc} \cos n\psi + \beta_{ns} \sin n\psi), \tag{4.93}$$

and for the other blade, which is located at $\psi + \pi$, the flapping motion is

$$\beta_2(\psi) = 2\beta_p - \beta_1 = \beta_0 + \sum_{n=1}^{\infty} \left[\beta_{nc} \cos n(\psi + \pi) + \beta_{ns} \sin n(\psi + \pi)\right]. \tag{4.94}$$

This latter equation may be written as

$$\beta_2(\psi) = 2\beta_p - \beta_1 = \beta_0 + \sum_{n=1}^{\infty} (-1)^n (\beta_{nc} \cos n\psi + \beta_{ns} \sin n\psi). \tag{4.95}$$

Substituting Eq. 4.93 into Eq. 4.95 and equating trigonometric coefficients gives

$$\beta_2(\psi) = \beta_p + \sum_{n \text{ odd}}^{\infty} (\beta_{nc} \cos n\psi + \beta_{ns} \sin n\psi). \tag{4.96}$$

This means that for the teetering rotor the coning angle is equal to the precone angle β_p and also that only the odd harmonics of flapping are present; the even harmonics cancel and the effects are reacted as structural stresses internal to the rotor hub. Because the harmonics of $n \geq 3$ are small they may be neglected. Only the first harmonics of flapping remain, which control the orientation of the rotor tip path plane. This means that all the solutions obtained for the articulated rotor also apply to the teetering rotor, but only if they are referred to the axis of no feathering or NFP.

4.13.2 *Semi-Rigid or Hingeless Rotors*

In the semi-rigid type of hub design, the flap and lag hinges are replaced by flexures (Fig. 4.22), which are normally built out of advanced composite materials. This eliminates the complexity, weight, and maintenance that is associated with the use of mechanical hinges and bearings. There are many different types of semi-rigid or hingeless hub designs. If the feathering bearing is also replaced by a flexible element, it is called a bearingless hub design.

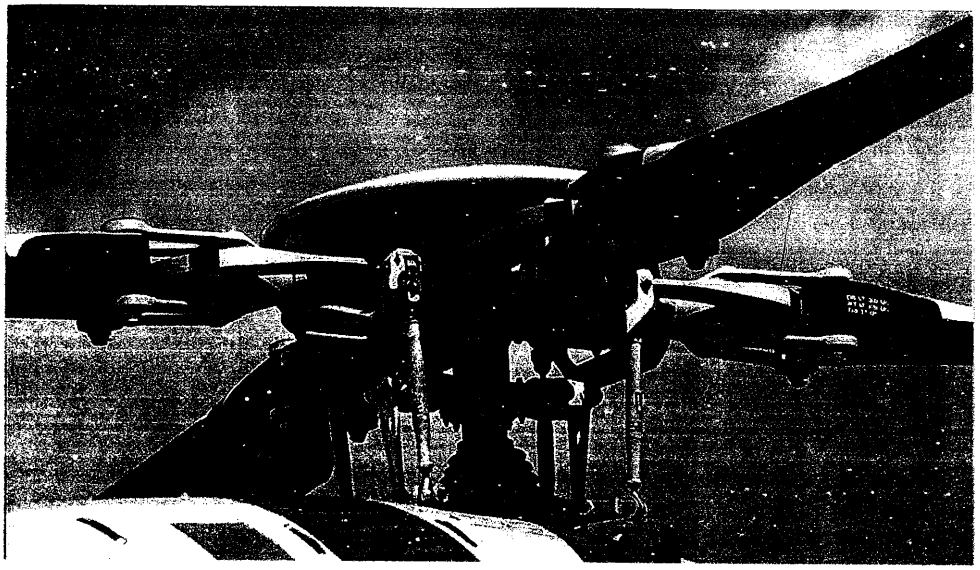

Figure 4.22 A bearingless hub design where flapping, lagging, and feathering take place about flexures.

The analysis of the semi-rigid blade proceeds by assuming that the flexure provides an equivalent spring stiffness k_β at an equivalent hinge offset e. In this case, the equation of motion becomes

$$\int_{eR}^{R} m(y - eR)^2 \ddot{\beta} dy + \int_{eR}^{R} m(y - eR)\beta\Omega^2 y dy + k_\beta(\beta - \beta_p) = \int_{eR}^{R} F_z(y - eR)dy, \tag{4.97}$$

where all the symbols have their usual meaning and β_p is the pre-cone angle. This pre-cone angle is designed into the hub and blade to reduce the steady flapping moments about the hinge (like the underslung teetering design) and typically would be about 2–3°. The foregoing equation can be written in conventional form as

$$\overset{**}{\beta} + \nu_\beta^2 \beta = \gamma M_\beta + \frac{\omega_0^2}{\Omega^2}\beta_p, \tag{4.98}$$

where ω_0 is the nonrotating flapping frequency as given by $\omega_0 = \sqrt{k_\beta / I_\beta}$. The natural frequency of flapping is

$$\nu_\beta = \sqrt{1 + \frac{3e}{2} + \frac{\omega_0^2}{\Omega^2}}, \tag{4.99}$$

where it has been assumed that $I_\beta \approx I_b$. Notice that the flapping frequency is now affected by both the CF forces and the elastic bending stiffness of the hub. If $\omega_0 = 0$, then the result reduces to that for an articulated rotor.

The equivalent hinge offset and flap stiffness can be determined approximately by comparing the deflected slope of the blade at the root to a point further out on the blade (normally 75% radius), as shown in Fig. 4.23. The majority of the curvature is in the hub region at

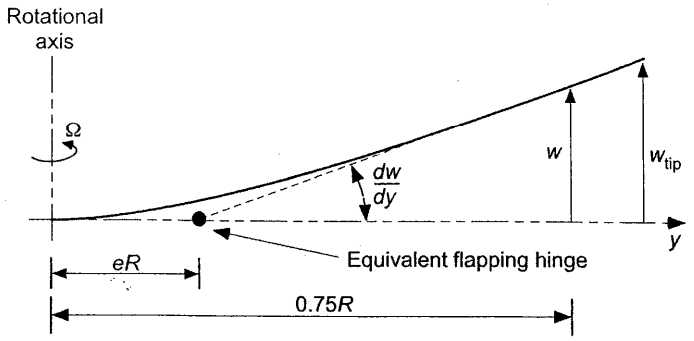

Figure 4.23 Method for finding the equivalent hinge offset and spring stiffness of a hingeless blade design.

the flexure and the remainder of the blade is essentially straight. The equivalent offset e is given by

$$e = 1 - \frac{w_{\text{tip}}}{R\left(\frac{dw}{dy}\right)_{y=0.75R}} \tag{4.100}$$

and the effective spring stiffness is

$$k_\beta = I_\beta \Omega^2 \left(\nu_\beta - 1 - \frac{3e}{2}\right). \tag{4.101}$$

A similar approach can be used for the lagging direction. This means that the analysis of the hingeless rotor design can proceed using all the same methods of analysis used for the articulated rotor, but with a corrected effective hinge offset and flapping frequency.

4.14 Introduction to Rotor Trim

The trim solution involves the calculation of the blade pitch control settings, rotor disk orientation (blade flapping) and overall helicopter orientation for the prescribed flight conditions. Controlling the position of the helicopter in free-flight requires the adjustment of the forces and moments about all three axes. For a conventional helicopter there are three independent controls used for this purpose:

1. *Collective pitch:* This input (θ_0) increases the main rotor blade pitch angles by the same amount, and, therefore, this changes the magnitude of the rotor thrust. The collective is changed by a lever that is held in the pilot's left hand, with an upward pulling motion required for an increase in thrust. Increasing collective pitch also requires an increase in power. On some helicopters this requires the pilot to open the throttle (increasing fuel flow to the engine), which is operated by a twist-grip at the end of the collective lever. However, on most helicopters the fuel-flow is controlled by an engine governor, which automatically maintains rotor rpm at the regulated value as rotor torque required increases or decreases.
2. *Lateral and longitudinal cyclic pitch:* These inputs impart a once-per-revolution cyclic pitch change to the blades. Lateral cyclic (θ_{1c}) is applied such that the rotor disk can be tilted left and right. This changes the orientation of the rotor–thrust

vector, producing both a side force and a rolling moment about the center of gravity of the helicopter. Longitudinal cyclic (θ_{1s}) imparts a once-per-revolution cyclic pitch change to the blades such that the rotor disk can be tilted fore and aft. Like the lateral cyclic, this changes the orientation of the rotor thrust vector, in this case producing both a longitudinal force and pitching moment. Both lateral and longitudinal cyclic are controlled by the pilot using a cyclic stick (similar to the conventional stick on a fixed-wing aircraft), which is held in the pilot's right hand.

3. *Yaw:* This is controlled by using the tail rotor thrust. The pilot has a set of floor mounted pedals, which are operated by the pilot's feet, just like a rudder on a fixed-wing aircraft. By pushing the pedals in the required direction, the collective pitch, θ_{TR}, on the tail rotor is changed, producing a change in tail rotor thrust and, therefore, causing the nose to yaw right or left.

As will be appreciated, there is a considerable amount of crosscoupling of the forces and moments on the helicopter when the pilot applies the controls. The relevant equations describing the behavior of the helicopter are complicated and interdependent, and there is no simple solution to this problem. For example, a change in rotor thrust produced by pulling up on the collective will require a higher power and will create a larger torque reaction on the fuselage. This, in turn, will require a yaw correction to be made to keep the helicopter tracking in a straight line. These and other so-called cross-coupling effects are unavoidable on a helicopter, but much can be done to minimize their effects and reduce the workload for the pilot by appropriate mixing of the control inputs. On early helicopters this was done mechanically, but now these effects can be handled electronically by an on-board flight control system.

There are two basic types of trim solution that are of interest to helicopter engineers: "propulsive" or "free-flight" trim and "wind-tunnel" trim. Wind-tunnel trim is used when testing model rotors in the wind tunnel and is somewhat different from free-flight trim because only force equations are used. For propulsive trim, the solution simulates the free-flight conditions of the helicopter, and moment equations must be included. For a specified helicopter gross weight, altitude, center of gravity location, forward speed and flight path angle, the trim solution must numerically evaluate the rotor controls, namely the collective pitch angle θ_0; the cyclic pitch angles θ_{1c} and θ_{1s}; the rotor disk orientation, which is described by β_0, β_{1c} and β_{1s}; and the vehicle orientation, which is described by the inertial angles (pitch angle, θ_F, roll angle, ϕ_F) and the aerodynamic angles (angles of attack, α, and sideslip, β) and the tail rotor collective pitch, θ_{TR}.

There are many possible forms of trim solution, and several levels of approximations and assumptions are used. In all cases, the free-flight trim solution is obtained from a set of vehicle equilibrium equations. These are usually simplified by using small-angle assumptions, although, for some flight conditions, such as turns where the angles are large, such assumptions become increasingly questionable – see Chen & Jeske (1981). Some trim solutions neglect the lateral equilibrium equation and this is justified because a lateral tilt of the rotor disk does not substantially change the rotor or fuselage aerodynamics. The trim solution can be approached from two perspectives. One approach is to use the blade element theory with certain assumptions for the wake inflow to calculate analytic results for the blade flapping and control angles. This gives a good first estimate of the rotor trim state. Another approach is to use a less restrictive solution for the blade aerodynamics (which may include nonuniform inflow and nonlinear aerodynamics) and to calculate the rotor trim state numerically – see Section 10.7.6. In either case, an iterative approach is required.

4.14.1 *Equations for Free-Flight Trim*

Figure 4.24 shows the forces and moments acting on the helicopter in free-flight. In the treatment of the trim problem, it is useful to decompose each of the components according to its origin. For example, the moment can be written in terms of the contributions from the main rotor (MR), fuselage (F), horizontal tail (HT), vertical tail (VT), tail rotor (TR), and other sources (O) as

$$M = M_{MR} + M_F + M_{HT} + M_{VT} + M_{TR} + M_O \tag{4.102}$$

and similarly for the other force and moment components. The hub plane (HP) is used as the reference plane. The flight path (FP) angle is θ_{FP}. It will be assumed that there is

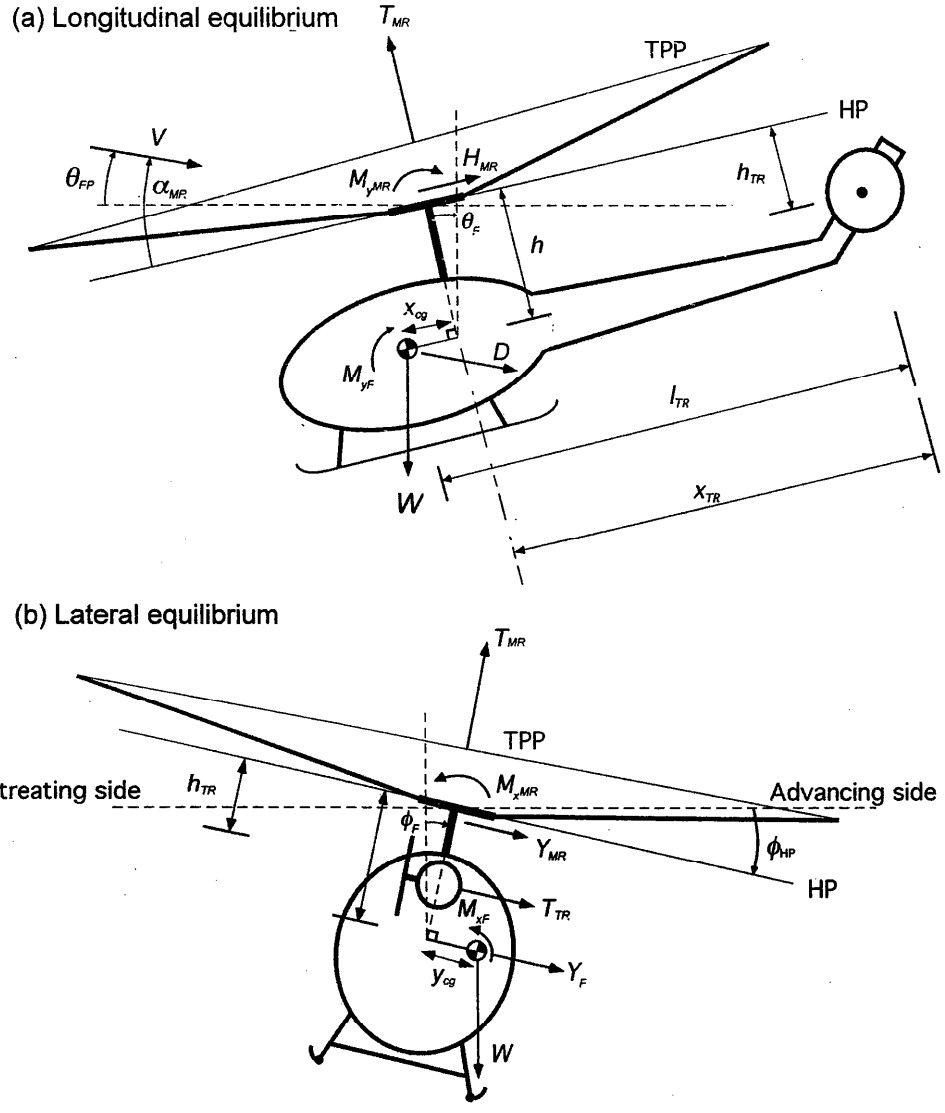

Figure 4.24 Forces and moments acting on a helicopter in free-flight. (a) Longitudinal forces and moments. (b) Lateral forces and moments.

no side-slip angle, therefore the fuselage side force (Y_F) can be assumed negligible. Also, it will be assumed for simplicity that there are no contributions from the horizontal and vertical tails. For vertical force equilibrium

$$W - T_{MR}\cos\theta_F\cos\phi_F + D\sin\theta_{FP} - H_{MR}\sin\theta_F + Y_{MR}\sin\phi_F + Y_{TR}\sin\phi_F = 0. \tag{4.103}$$

For longitudinal force equilibrium a balance of forces results in

$$D\cos\theta_{FP} + H_{MR}\cos\theta_F - T_{MR}\sin\theta_F\cos\phi_F = 0. \tag{4.104}$$

For lateral force equilibrium the tail rotor thrust, T_{TR}, must be included to give

$$Y_{MR}\cos\phi_F + T_{TR}\cos\phi_F + T_{MR}\cos\theta_F\sin\phi_F = 0. \tag{4.105}$$

For pitching moment equilibrium about the hub

$$M_{y_{MR}} + M_{y_F} - W(x_{cg}\cos\theta_F - h\sin\theta_F) - D\cos\theta_F(h\cos\theta_F + x_{cg}\sin\theta_F) = 0. \tag{4.106}$$

For rolling moment equilibrium about the hub

$$M_{x_{MR}} + M_{x_F} + T_{TR}h_{TR} + W(h\sin\phi_F - y_{cg}\cos\phi_F) = 0. \tag{4.107}$$

Finally, torque equilibrium about the shaft gives

$$Q_{MR} - Y_{TR}l_{TR} = 0. \tag{4.108}$$

Using small-angle assumptions, the equilibrium equations can be reduced to the set

$$\begin{aligned} W - T_{MR} &= 0,\\ D + H_{MR} - T_{MR}\theta_F &= 0,\\ Y + T_{TR} + T_{MR}\phi_F &= 0,\\ M_{y_{MR}} + M_{y_F} + W(h\theta_F - x_{cg}) - hD &= 0,\\ M_{x_{MR}} + M_{x_F} + W(h\phi_F - y_{cg}) + T_{TR}h_{TR} &= 0,\\ Q_{MR} - T_{TR}l_{TR} &= 0. \end{aligned}$$

The rotor thrust is simply the average of the blade lift during one revolution multiplied by the number of blades. Mathematically, this is stated as

$$T_{MR} = \frac{N_b}{2\pi}\int_0^{2\pi}\int_0^R dF_z\,d\psi. \tag{4.109}$$

The thrust coefficient can therefore be written as

$$C_{T_{MR}} = \frac{\sigma C_{l_\alpha}}{2}\frac{1}{2\pi}\int_0^{2\pi}\int_0^1\left[\left(\frac{U_T}{\Omega R}\right)^2\theta - \left(\frac{U_P}{\Omega R}\right)\left(\frac{U_T}{\Omega R}\right)\right]dr\,d\psi. \tag{4.110}$$

Because of the complexity of the expressions for U_P, U_T, and θ, this equation must usually be solved numerically. However, by assuming uniform inflow, that is, $\lambda(r,\psi) = \lambda =$ constant, $C_d = C_{d_0}$, $c =$ constant, and linear blade twist, we can obtain the result for the rotor thrust coefficient analytically. The result can be shown to be

$$C_{T_{MR}} = \frac{\sigma C_{l_\alpha}}{2}\left[\frac{\theta_0}{3}\left(1 + \frac{3}{2}\mu^2\right) + \frac{\theta_{tw}}{4}(1+\mu^2) + \frac{\mu}{2}\theta_{1s} - \frac{\lambda}{2}\right]. \tag{4.111}$$

In addition, the rotor torque, side force, drag force, and moments about the respective axes can be computed by a similar process. The rotor drag force (also known as the H-force) is given by

$$H_{MR} = \frac{N_b}{2\pi}\int_0^{2\pi}\int_0^R [dF_x \sin\psi + dF_R \cos\psi]\, d\psi \tag{4.112}$$

or, in coefficient form,

$$C_{H_{MR}} = \frac{\sigma C_{l_\alpha}}{2}\frac{1}{2\pi}\int_0^{2\pi}\int_0^1 \left\{\sin\psi\left[\left(\frac{U_P}{\Omega R}\right)\left(\frac{U_T}{\Omega R}\right)\theta - \left(\frac{U_P}{\Omega R}\right)^2\right]\right.$$
$$\left. - \beta\cos\psi\left[\left(\frac{U_T}{\Omega R}\right)^2\theta - \left(\frac{U_P}{\Omega R}\right)\left(\frac{U_T}{\Omega R}\right)\right] + \frac{C_{d_0}}{C_{l_\alpha}}\left(\frac{U_T}{\Omega R}\right)^2\sin\psi\right\} dr\, d\psi. \tag{4.113}$$

The rotor side force (also known as the Y-force) is given by

$$Y_{MR} = \frac{N_b}{2\pi}\int_0^{2\pi}\int_0^R [-dF_x\cos\psi + dF_R\sin\psi]\, d\psi. \tag{4.114}$$

The rotor torque is given by

$$Q_{MR} = \frac{N_b}{2\pi}\int_0^{2\pi}\int_0^R y\, dF_x\, d\psi. \tag{4.115}$$

The rotor rolling moment is given by

$$M_{x_{MR}} = \frac{N_b}{2\pi}\int_0^{2\pi}\int_0^R y\, dF_z \sin\psi\, d\psi. \tag{4.116}$$

Finally, the rotor pitching moment is given by

$$M_{y_{MR}} = -\frac{N_b}{2\pi}\int_0^{2\pi}\int_0^R y\, dF_z\cos\psi\, d\psi. \tag{4.117}$$

Closed-form expressions for the latter quantities can also be derived.

Additional equations may be necessary. For example, two more equations should be added to determine the trim value of main rotor inflow λ_{MR} and tail rotor inflow λ_{TR}. These inflow equations should be solved together with all the other trim equations. For this purpose it is convenient to rewrite them so that all the terms are on one side of the equal sign. Using simple momentum theory for the main rotor (MR) gives

$$\lambda_{MR} - \mu_{MR}\tan\alpha_{MR} - \frac{C_{T\,MR}}{2\sqrt{\mu_{MR}^2 + \lambda_{MR}^2}} = 0, \tag{4.118}$$

where $\mu_{MR}\cos\alpha_{MR} = V/\Omega_{MR}R_{MR}$ and α_{MR} is the disk AoA, for which setting $\alpha_{MR} = \alpha$ is usually reasonable. For the tail rotor (TR),

$$\lambda_{TR} - \mu_{TR}\tan\alpha_{TR} - \frac{C_{T\,TR}}{2\sqrt{\mu_{TR}^2 + \lambda_{TR}^2}} = 0, \tag{4.119}$$

where $\mu_{TR} = V\cos\alpha_{TR}/\Omega_{TR}R_{TR}$ and α_{TR} is the disk AoA of the tail rotor (this will be zero if there is no side-slip angle).

The vehicle equilibrium equations, along with the inflow equations, can then be written in the form $\mathbf{F}(\mathbf{X}) = 0$, where $\mathbf{X}$ is a vector of rotor trim unknowns defined as

$$\mathbf{X} = [\theta_0 \ \theta_{1c} \ \theta_{1s} \ \lambda_{MR} \ \lambda_{TR} \ \theta_F \ \phi_F]^T, \tag{4.120}$$

4.14.2 *Typical Trim Solution Procedure for Level Flight*

In the trim process, the rotor collective and cyclic pitch controls must be adjusted to control the orientation of the rotor to provide trim, control and propulsion requirements. For wind-tunnel trim, the rotor cyclic controls are calculated from a prescribed rotor shaft angle (say, equivalent to θ_F). In a wind tunnel, the model rotor is controlled by a conventional swashplate and the operator remotely "flies" the model rotor very much in the way of an actual helicopter. However, because the rotor is rigidly attached to a support system, the operator must ensure that large amounts of cyclic flapping do not occur as the wind speed is increased. This is done by constantly controlling the orientation of the swashplate to eliminate cyclic flapping with respect to the rotor shaft. A typical free-flight trim simulation is more complicated because it must satisfy the vehicle equilibrium equations and involves the following steps:

1. Calculate the main rotor thrust and weight coefficients from

$$C_{T_{MR}} \approx C_W = \frac{W}{\rho\pi R^2(\Omega R)^2}. \tag{4.121}$$

2. Calculate the net helicopter power coefficient (see Chapter 5) using

$$C_{P_{MR}} = \frac{\kappa C_{T_{MR}}^2}{2\mu} + \frac{\sigma C_{d_0}}{8}\left(1 + 4.65\mu^2\right) + \frac{1}{2}\left(\frac{f}{A}\right)\mu^3 + \lambda_c C_{T_{MR}}, \tag{4.122}$$

which is valid for $\mu > 0.1$. For lower advance ratios, we should use the more complete expression

$$C_{P_{MR}} = \frac{\kappa C_{T_{MR}}^2}{2\sqrt{\mu^2 + \lambda^2}} + \frac{\sigma C_{d_0}}{8}\left(1 + 4.65\mu^2\right) + \frac{1}{2}\left(\frac{f}{A}\right)\mu^3 + \lambda_c C_{T_{MR}}, \tag{4.123}$$

where the iterative numerical procedures to solve the general inflow equation that have been discussed in Section 2.14.3 can be used to determine λ.

3. Calculate the tail rotor thrust from the torque balance using

$$\frac{Y_{TR}}{W} = \frac{C_{Q_{MR}}}{C_{T_{MR}}}\frac{R}{l_T} = \frac{C_{P_{MR}}}{C_{T_{MR}}}\frac{R}{l_T}. \tag{4.124}$$

4. Calculate the inflow, λ_{TPP} using

$$\lambda_{\text{TPP}} = \frac{C_{T_{MR}}}{2\sqrt{\mu^2 + \lambda^2}} + \frac{1}{2}\left(\frac{f}{A}\right)\frac{\mu^3}{C_{T_{MR}}} + \mu\frac{C_{H_{\text{TPP}}}}{C_{T_{MR}}}. \tag{4.125}$$

For the first iteration we can use

$$\lambda_{\text{TPP}} = \frac{C_{T_{MR}}}{2\mu} + \frac{1}{2}\left(\frac{f}{A}\right)\frac{\mu^3}{C_{T_{MR}}}. \tag{4.126}$$

5. Calculate the drag and side forces using Eqs. 4.113 and 4.114. For the first iteration, set $C_{H_{\text{TPP}}} = C_{Y_{\text{TPP}}} = 0$.
6. Calculate β_{1c}, β_{1s}, θ_F, and ϕ_F.

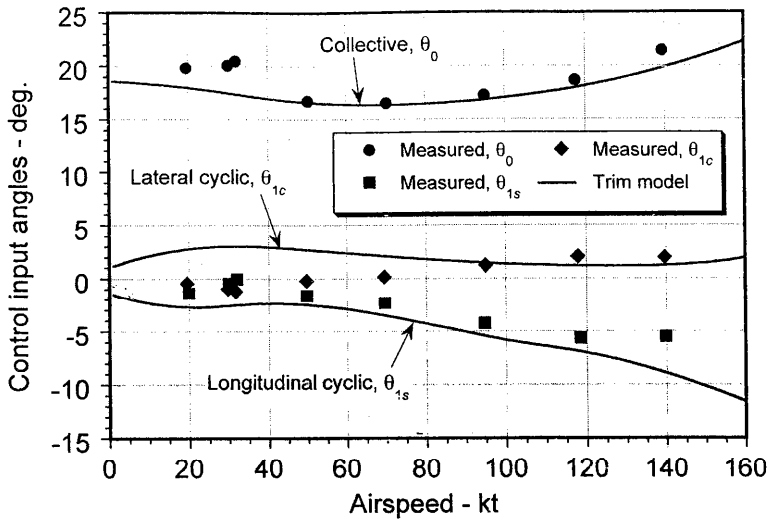

Figure 4.25 Representative variations in collective and cyclic pitch inputs to trim a rotor in forward flight. Propulsive trim calculation. Data source: Ballin (1987). (Calculation courtesy of Rendy Cheng.)

7. Calculate θ_0, θ_{1s}, β_0, and θ_{1c}.
8. Go back to step 3 and recalculate the values.
9. Iterate and monitor the control angles until convergence is achieved.

Representative variations in the control input angles, θ_0, θ_{1c}, and θ_{1s} versus forward speed for a conventional helicopter, as computed from a typical free-flight trim solution, are shown in Fig. 4.25. The results must be considered representative only but are typical of the inputs that would be required on any single rotor helicopter. An example helicopter, which resembles the UH-60, was used for these calculations. Experimental measurements of control angles are also shown, which are taken from Ballin (1987). Remember that as the rotor transitions from hover to forward flight, a primary effect is the dissymmetry in lift between the advancing and retreating blades. The excess of lift on the advancing blade causes the blade to flap upward, reaching a maximum displacement over the front of the disk. Conversely, the reduced dynamic pressure on the retreating blade causes the blade to flap downward over the rear of the disk. The net effect is that the rotor disk naturally wants to tilt back (i.e., a negative longitudinal flapping or $-\beta_{1c}$). Therefore, to prevent this longitudinal flapping, the cyclic pitch controls must be adjusted to bring the rotor disk back to an orientation that will meet propulsion (to overcome vehicle drag) and control requirements. Notice that the θ_{1s} component of cyclic pitch (longitudinal cyclic) controls the longitudinal flapping; thus an increasingly negative value of θ_{1s} (of magnitude approximately equal to $-\beta_{1c}$) must be imposed by using forward stick.

The effects of blade coning cause a lateral flapping response. When a blade passes over the front of the disk, the effects of the forward flight velocity cause an increase in AoA because it acts as an upwash. At the rear of the disk, the effects of the free stream cause a decrease in AoA. Therefore, there is a once-per-revolution (1/rev) forcing function generated as a result of blade coning, and the response to this forcing causes a negative lateral disk tilt (to starboard). The amount of lateral tilt is proportional to the rotor coning angle, which in turn depends on inflow for a given rotor thrust. To counteract this effect, a positive value of lateral cyclic (θ_{1c}) must be applied using left stick. A small additional amount

of lateral cyclic must also be applied to counter the thrust and moments produced by the tail rotor, which will vary with the anti-torque requirements. Also, some lateral cyclic is required to compensate for the nonuniformity of the longitudinal inflow over the rotor disk in forward flight (see Section 3.5.2). Because of these coupled effects, the amount of lateral cyclic required for trim does not show a strong trend in one direction unlike the longitudinal cyclic. See Harris (1972) for a systematic study of inflow effects on rotor flapping response.

4.15 Chapter Review

A basic understanding of the dynamic behavior of the rotor blades in response to the changing aerodynamic loads has been the objective of this chapter. The blades have two primary degrees of freedom: flapping and lagging, which take place about either mechanical or virtual hinges near the blade root. A third degree of freedom allows pitch or feathering of the blade, which can be applied in both a collective and cyclic sense. Despite the fact that helicopter blades are relatively flexible, centrifugal effects cause stiffening and the basic physics of the blade dynamics can be explained by assuming them as rigid. In hovering flight the airloads do not vary with azimuth, therefore the blades flap up and lag back with respect to the hub and reach a steady equilibrium position under a simple balance of aerodynamic and centrifugal forces. However, in forward flight the fluctuating airloads cause continuous flapping motion and give rise to aerodynamic, inertial and Coriolis forces on the blades that result in a dynamic behavior with an amplitude and phase response. The flapping hinge allows the effects of the cyclically varying airloads to reach an equilibrium with airloads produced by the blade flapping motion. It has also been shown that the flapping motion is highly damped by the aerodynamic forces so the blades flap and the rotor tilts almost immediately in response to control inputs.

A rotor blade has a flapping natural frequency that is equal to its rotational frequency (or nearly so). Because the rotor is excited by the aerodynamic loads primarily at 1/rev, this means that there is a 90° phase lag between the aerodynamic forcing and the blade flapping response. It has been shown how collective and cyclic pitch can be used to change the magnitude and phasing of the aerodynamic loads over the disk. This is the key to changing the flapping of the rotor and the orientation of the rotor plane, thereby effecting a means of control for the helicopter. The ideas of controlling the orientation of the rotor are formally embodied in a procedure known as "trim." While there are many forms of numerical solution to the trim problem, the basic procedure is the same: to adjust the control inputs to give resultant forces and moments on the helicopter that will satisfy a specified equilibrium and propulsive force condition. The evaluation of the various forces and moments acting on the helicopter is by no means trivial. However, under certain assumptions and with sufficient labor, many of the results can be obtained analytically in closed form. This allows the identification of the relationships between the solution and various problem parameters and will be useful for many problems related to the preliminary design of the helicopter.

4.16 Questions

4.1. A rigid rotor blade with a uniform mass distribution has its flapping hinge located at a distance e from the rotational (shaft) axis. If the shaft is rotating at an angular velocity Ω, calculate the natural frequency of the blade about the flapping hinge. Show all the steps in your derivation. Assume $e/R \ll 1$.

4.2. Derive expressions for the mean coning angle, β_0, of a hovering rotor blade that has a uniform mass per unit length m and a concentrated mass M at its tip. Zero hinge offset can be assumed. Assume that the thrust on the blade varies linearly with radius.

4.3. (a) Name and explain the functions of the three principal degrees-of-freedom of a rotor blade. (b) Describe the differences between (i) an articulated rotor system, (ii) a hingeless rotor system, and (iii) a bearingless rotor system. What are the principal advantages of one versus the other?

4.4. A rotor in a given flight condition has the following flapping motion with respect to the control axis (control plane): $\beta(\psi) = 6° - 4° \cos\psi - 4° \sin\psi$. (a) Sketch a side view and rear view of the rotor. (b) How much is the TPP inclined in the fore and aft direction? Forward or backward? (c) How much is the TPP inclined laterally? Is the advancing or retreating blade high? (d) What angle does the blade make with the control plane at $\psi = 0°, 90°, 180°, 270°$. (e) At what azimuth angle is the flapping angle greatest? What is the flapping angle at this point?

4.5. If the flapping motion of a centrally hinged blade with uniform mass distribution in forward flight is represented as $\beta = \beta_0 + \beta_{1c} \cos\psi + \beta_{1s} \sin\psi$, prove that the thrust moment (that is the flapping moment created by the blade thrust) about the flapping hinge is constant around the disk (i.e., independent of ψ).

4.6. By considering the blade thrust, blade weight, centrifugal force, and blade inertia of a centrally flapping untwisted untapered blade, find an expression for the coning angle of the blade in forward flight. Assume uniform inflow.

4.7. Starting from the equation of motion of a flapping blade with a hinge offset operating in hover, show that the flapping response lags the aerodynamic forcing by an angle

$$\phi = \tan^{-1}\left(\frac{\gamma/8}{(\nu_\beta^2 - 1)}\right),$$

where all the symbols have their usual meanings.

4.8. A tail rotor uses pitch-flap coupling via a δ_3 hinge to reduce cyclic flapping. Find a relationship between the coning angle and the collective pitch, and the effect on the flapping frequency. Assume zero flapping hinge offset and uniform inflow.

4.9. Calculate and plot, as a function of hinge offset, the natural frequency about the lag hinge of a blade that is twice as heavy per unit length at the root compared to the tip, where e is the lag hinge offset.

4.10. Explain why, in reality, the variation of inflow through a helicopter rotor in forward flight is highly nonuniform. Itemize and explain the sources of this nonuniformity.

4.11. If the time-averaged inflow is assumed linearly distributed longitudinally and laterally over the disk, qualitatively describe the effects of this nonuniform inflow on the rotor flapping response, compared to the uniform inflow case with the same mean value of inflow.

4.12. If the coning angle of a blade is given by

$$\beta_0 = \frac{\frac{1}{2}\rho C_{l_\alpha} c R^4 \left[\frac{\theta_0}{4}(1+\mu^2) + \frac{\lambda}{3}\right]}{I_b},$$

then write the above expression in terms of the Lock number, γ. What does this factor represent?

4.13. A helicopter is flying along with its physical shaft aligned with the tip path plane axis. The angle of attack of the rotor is 10° and the longitudinal flapping angle is 5°. Assume that the flapping hinges are located on the rotational axis. Determine: (a) the value of the longitudinal cyclic pitch required to maintain this flight condition, (b) the inclination of the rotor shaft with respect to the vertical, and (c) the longitudinal flapping with respect to the rotor shaft.

Bibliography

Bailey, F. J. 1941. "A Simplified Theoretical Method of Determining the Characteristics of a Lifting Rotor in Forward Flight," NACA Report 716.

Ballin, M. G. 1987. "Validation of a Real-Time Engineering Simulation of the UH-60 Helicopter," NASA TM-88360.

Bartha, M. and Madzer, J. 1913. "Schraubenflügelanordnung für Luftschraubenpaare," Patent No. 249,702.

Bramwell, A. R. S. 1976. *Helicopter Dynamics*, Edward Arnold, London.

Chen, R.T.N. and Jeske, J.A. 1981. "Kinematic Properties of the Helicopter in Coordinated Turns," NASA Technical Paper 1773.

Chopra. I. 1990. "Perspectives in Aeromechanical Stability of Helicopter Rotors," *Vertica*, 14 (4), pp. 457–508.

Cierva. J. de la and Rose, D. 1931. *Wings of Tomorrow: The Story of the Autogiro*, Brewer, Warren & Putnam, NY.

Coleman, R. P. and Feingold, A. M. 1958. "Theory of Self-Excited Mechanical Oscillations of Helicopter Rotors With Hinged Blades," NACA Report 1351.

Friedmann, P. P. 1977. "Recent Developments in Rotary-Wing Aeroelasticity," *J. of Aircraft*, 14 (11), pp. 1027–1041.

Friedmann, P. P. 2004. "Rotary-Wing Aeroelasticity: Current Status and Future Trends," *AIAA Journal*, 42 (10), pp. 953–972.

Gessow, A. and Myers, G. C., Jr. 1952. *Aerodynamics of the Helicopter*, Macmillan Co., Republished by Frederick Ungar Publishing, New York, NY, 1967.

Glauert, H. 1928. "On the Horizontal Flight of a Helicopter," ARC R & M 1157.

Harris, F. D. 1972. "Articulated Rotor Blade Flapping Motion at Low Advance Ratios," *J. of the American Helicopter Soc.*, 17 (1), pp. 41-48.

Johnson, W. 1980. *Helicopter Theory*, Princeton University Press, Princeton, NJ.

Lock, C. N. H. 1927. "Further Development of Autogyro Theory," ARC R & M 1127.

Loewy, R. G. 1969. "Review of Rotary Wing V/STOL Dynamics and Aeroelastic Problems," *J. of the American Helicopter Soc.*, 14 (3), pp. 3–24.

Nikolsky, A. 1944. *Notes on Helicopter Design Theory*, Princeton University Press, Princeton, NJ.

Nikolsky, A. 1951. *Helicopter Analysis*, John Wiley & Sons, Inc., New York, NY.

Prouty, R. W. and Curtiss, H. C. 2003. "Helicopter Control Systems: A History," *J. of Guidance, Control, and Dynamics* 26 (1), pp. 12–18.

Reichert, G. 1973. "Basic Dynamics of Rotors," AGARD-LS-63.

Sissingh, G. 1939. "Contribution to the Aerodynamics of Rotating Wing Aircraft," NACA TM 921.

Sissingh, G. 1941. "Contribution to the Aerodynamics of Rotating Wing Aircraft, Part 2." NACA TM 990.

Squire, H. B. 1936. "The Flight of a Helicopter," ARC R & M 1730.

Wald, Q. 1943. "A Method for Rapid Estimation of Helicopter Performance," *J. Aeronautical Sciences*, 10 (4), April, pp. 131–135.

Wheatly, J. B. 1934. "An Aerodynamic Analysis of the Autogyro Rotor and Comparison between Theory and Experiments," NACA TR 487.

CHAPTER 5

Helicopter Performance

The future of the helicopter . . . therefore lies not in competition with the airplane, but in its ability to perform certain functions which the airplane cannot undertake.

Dr. Alexander Klemin (1925)

5.1 Introduction

The aerodynamic tools described in the previous chapters can now be used to analyze the basic performance of the helicopter. By the term *helicopter performance* we mean the estimation of the installed engine power required for a given flight condition, determination of maximum level flight speed, evaluation of the ceiling (in and out of ground effect), or the estimation of the endurance or range of the helicopter. Both the momentum and blade element methods will allow for good estimates of total rotor thrust, power, and figure of merit in hover and can be used with confidence to predict overall rotor performance in forward flight. In addition, the performance of the helicopter during maneuvers, in descending autorotational flight, in flight in or near the vortex ring state, and during flight operations when operating near the ground will be considered in this chapter.

5.2 The International Standard Atmosphere

An important point to remember is that the rotor performance and the performance of the helicopter as a whole is a function of the air density in which it is actually flying. This makes it problematic to predict or compare aircraft performance metrics unless the data are corrected to some standard condition. For example, decreasing density (increasing altitude and/or temperature) will result in a greater power required for the same aircraft gross takeoff weight (GTOW). To remedy this problem, the International Standard Atmosphere (ISA) has been established, which gives the height in a standard atmosphere corresponding to the properties of the air in which the aircraft is flying. The standards[1] are defined in Minzner et al. (1959), the ICAO (1964), and NASA (1966), where a *standard day* at sea level is an air temperature, T_0, of 15°C (59°F, 288.16°K, 518.4°R) with a barometric pressure, p_0, of 2116.4 lb/ft^2 or 101,301 N/m^2 or 29.92 in (980 mm) of mercury or 1013.2 millibars.

The pressure in the atmosphere is a function of altitude (elevation), h, and the air density is a function of both altitude and temperature. The pressure in the standard atmosphere is defined relative to the standard conditions as

$$\frac{p}{p_0} = \delta = \left(1 - 6.876 \times 10^{-6} h\right)^{5.265}, \tag{5.1}$$

where h is in feet, and the density is defined by

$$\frac{\rho}{\rho_0} = \sigma = \left(1 - 6.876 \times 10^{-6} h\right)^{4.265}. \tag{5.2}$$

[1] The ICAN standard may be used in many European countries.

In the lower atmosphere where helicopters normally fly (say, below 20,000 ft or 6,000 m), the standard value of air density can be closely approximated by the equation

$$\frac{\rho}{\rho_0} = \exp\left(\frac{-0.0297h}{1000}\right), \tag{5.3}$$

where h is expressed in feet and $\rho_0 = 0.002378$ slugs/ft^3. In SI units the corresponding equation is

$$\frac{\rho}{\rho_0} = \exp\left(\frac{-0.0296h}{304.8}\right), \tag{5.4}$$

where h is expressed in meters and $\rho_0 = 1.225$ kg/m^3. These expressions are useful for initial evaluations of the effects of altitude on helicopter and engine performance.

Up to 36,000 ft (11 km) altitude, the pressure, p, and the temperature, T, are related by

$$\frac{dp}{p} = \frac{dT}{T}\frac{1}{R}\left(\frac{dh}{dT}\right), \tag{5.5}$$

where the standard lapse rate dT/dh is 6.51°K (or 6.51°C) per km of altitude or 3.57°R (or 3.57 °F) per 1,000 ft of altitude. The temperature in the standard atmosphere is a linearly decreasing function of altitude and can be expressed by

$$T = 59 - 3.57(h/1000) \quad \text{in units of °F}, \tag{5.6}$$

where h is expressed in feet, or

$$T = 15 - 1.983(h/304.8) \quad \text{in units of °C}, \tag{5.7}$$

where h is expressed in meters, or

$$T = 15 - 0.001981h = 15 - Bh \quad \text{in units of °C}, \tag{5.8}$$

where $B = 0.00198$ is the lapse rate in °C per foot and the altitude h is in feet.

Integrating Eq. 5.5 from sea level using the standard lapse rate gives a relationship between temperature and pressure, and using the equation of state the corresponding density of the air can be determined. The *pressure altitude*, h_p, is the height at which a given pressure is found in the standard atmosphere. This is given by

$$h_p = \frac{T_0}{B}\left[1 - \left(\frac{p}{p_0}\right)^{0.1903}\right] = \frac{518.4}{0.00357}\left[1 - \left(\frac{p}{p_0}\right)^{0.1903}\right]. \tag{5.9}$$

The result can be converted from feet to meters by multiplying by 0.3048. The altimeters used in all aircraft are calibrated according to Eq. 5.9. The *density altitude* in feet, h_ρ, is defined using the ambient density in the relation

$$h_\rho = \frac{T_0}{B}\left[1 - \left(\frac{\rho}{\rho_0}\right)^{0.235}\right] = \frac{518.4}{0.00357}\left[1 - \left(\frac{\rho}{\rho_0}\right)^{0.235}\right]. \tag{5.10}$$

While it is the density altitude that affects the performance of the helicopter, the advantage of using pressure altitude is that it is a function of the ambient pressure alone, and the value of h_p can be read directly off the altimeter in the aircraft. This is done by setting the value in the altimeter Kohlsman (reference) window to the standard sea level pressure

Table 5.1. *Useful Values for the International Standard Atmosphere*

Altitude (ft)	Altitude (m)	Temperature (°F)	Temperature (°C)	Density ratio (ρ/ρ_0)	Pressure ratio (p/p_0)
0	0	59.0	15.2	1.0000	1.0000
1,000	304	55.4	13.2	0.9771	0.9644
2,000	609	51.9	11.2	0.9428	0.9298
3,000	914	48.3	9.3	0.9151	0.8962
4,000	1,219	44.7	7.3	0.8881	0.8637
5,000	1,524	41.2	5.3	0.8617	0.8320
6,000	1,828	37.6	3.3	0.8359	0.8014
7,000	2,133	34.0	1.3	0.8106	0.7716
8,000	2,428	30.4	-0.6	0.7860	0.7428
9,000	2,743	26.9	-2.6	0.7620	0.7128
10,000	3,048	23.3	-4.6	0.7385	0.6877
11,000	3,352	20.1	-6.6	0.7155	0.6614
12,000	3,657	16.52	-8.6	0.6932	0.6360

of $p_0 = 29.92$ inches or 1,013.2 millibars (equivalent to 2,116.4 lb/ft^2 or 101,301 N/m^2). Density altitude, however, must be computed from measurements of pressure altitude corrected for nonstandard ambient temperature. The density ratio can be obtained from

$$\sigma = \frac{\rho}{\rho_0} = \frac{T_0}{(T + 273.16)}\left(1 - \frac{Bh_p}{T_0}\right)^{5.256} = \frac{288.16}{(T + 273.16)}\left(1 - \frac{0.001981\, h_p}{288.16}\right)^{5.256}, \tag{5.11}$$

where the pressure altitude, h_p, is in feet and T is in °C or using

$$\sigma = \frac{\rho}{\rho_0} = \frac{518.4}{(T + 459.4)}\left(1 - \frac{0.001981\, h_p}{288.16}\right)^{5.256}, \tag{5.12}$$

where h_p is in feet and T is in °F. Pressure altitude and density altitude are identical if the temperature conforms to standard conditions. As a rule of thumb, density altitude exceeds pressure altitude by about 60 ft per °F (30 ft per °C) that the temperature exceeds the standard value.

A convenient table of values for the standard atmosphere is given in Table 5.1. For example, on a standard day the density ratio will be 1.0 at sea level and 0.888 at 4,000 ft. On a very hot day with a pressure (indicated) altitude of 4,000 ft but with an outside air temperature of 30°C (86°F), which corresponds to approximately 23°C or 41°F over standard conditions, the density ratio will be 0.82. This corresponds to a density altitude of approximately 6,400 ft. Performance charts in a helicopter flight manual may be expressed in terms of either pressure altitude or density altitude, although pressure altitude is the more common form. Because the aircraft altimeter will read pressure altitude, a simple altitude conversion chart is provided to the pilot to allow rapid conversions to density altitude for a given ambient temperature, as required.

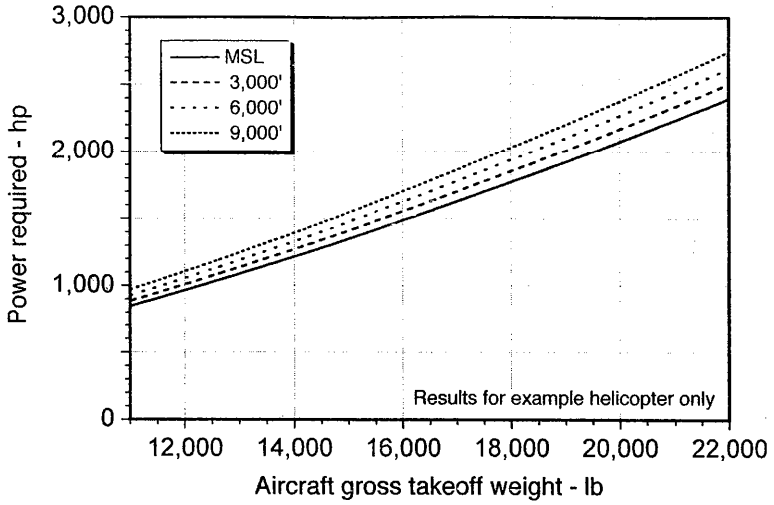

Figure 5.1 Example showing the power required to hover versus helicopter weight for various density altitudes.

5.3 Hovering and Axial Climb Performance

It has already been shown in Chapter 3 that the rotor power required in hover can be estimated from the equation

$$P = P_i + P_0 = \frac{\kappa W^{3/2}}{\sqrt{2\rho A}} + \rho A(\Omega R)^3\left(\frac{\sigma C_{d_0}}{8}\right) = \left(\frac{1}{FM}\right)\frac{W^{3/2}}{\sqrt{2\rho A}}, \tag{5.13}$$

or in nondimensional form simply as

$$C_P = C_{P_i} + C_{P_0} = \frac{\kappa C_W^{3/2}}{\sqrt{2}} + \frac{\sigma C_{d_0}}{8} = \left(\frac{1}{FM}\right)\frac{C_W^{3/2}}{\sqrt{2}}, \tag{5.14}$$

where $C_W(\approx C_T)$ is the weight coefficient, κ is the induced power factor of the rotor, C_{d_0} is the average profile drag coefficient of the blade sections, and FM is the figure of merit of the rotor.

Note from Eq. 5.13 that the hover power required is a function of aircraft gross weight and ambient density. The basic effect of density altitude on hovering performance is illustrated in Fig. 5.1. The results are for a representative helicopter closely resembling the UH-60, for which the basic parameters of this aircraft are given in Table 5.2. The empty weight of

Table 5.2. *Parameters for Example Helicopter*

Parameter	Symbol	Main Rotor	Tail Rotor
Radius (ft)	R	27.0	5.5
Chord (ft)	c	1.7	0.80
Solidity	σ	0.082	0.19
Number of blades	N_b	4	4
Tip speed (ft s^{-1})	ΩR	725	685
Induced power factor	κ	1.15	1.15
Profile drag coefficient	C_{d_0}	0.008	0.008

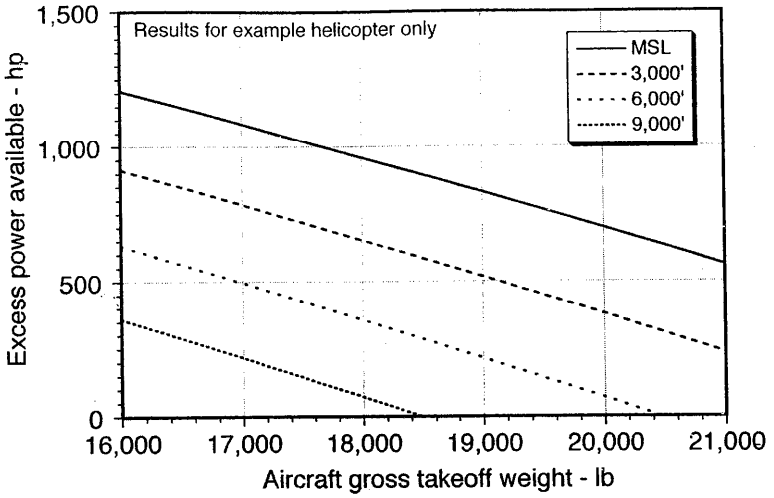

Figure 5.2 Excess hover power available as a function of GTOW and density altitude.

the aircraft is 11,000 lb (5,000 kg). Notice from Fig. 5.1 that as much as 20% greater power will be required to hover at a density altitude of 9,000 ft versus that required at sea level conditions. The induced power factor κ or figure of merit FM is not substantially affected by density altitude. While the power required to hover increases with increasing density altitude, the engine power available also decreases – see Section 5.5.5. For a reciprocating engine a reasonable approximation can be found by multiplying the power available at mean sea level (MSL) by the density ratio found at that altitude relative to MSL with a nonstandard temperature correction. For a turboshaft engine the power output at altitude follows a more complicated relationship but is approximately proportional to the atmospheric pressure ratio with a nonstandard temperature correction.

Representative results for the example helicopter that show the decrease in excess power with aircraft gross weight for various density altitudes are given in Fig 5.2. At any given altitude the decrease in excess power is almost proportional to the extra aircraft weight. The excess power available with altitude ultimately becomes zero, and this defines the hover ceiling. For a maximum GTOW of 20,000 lb (9,100 kg) the hover ceiling for the example helicopter is about 7,000 ft ($\approx$ 2,100 m), which means that the aircraft cannot hover above this altitude at this weight. The helicopter, however, will be able to fly at considerably higher altitudes with some forward speed – see Section 5.5.9.

The power required for any vertical rate of climb, V_c, can be estimated by solving for the induced velocity using the momentum theory result given previously in Chapter 2, namely

$$\frac{v_i}{v_h} = -\frac{V_c}{2v_h} + \sqrt{\left(\frac{V_c}{2v_h}\right)^2 + 1} \approx 1 - \frac{V_c}{2v_h} \quad \text{for low rates of climb,} \tag{5.15}$$

where v_h is the hover induced velocity. The maximum rate of climb is then obtained by solving for V_c using

$$\frac{P_h + \Delta P}{P_h} = \frac{V_c}{2v_h} + \sqrt{\left(\frac{V_c}{2v_h}\right)^2 + 1} \approx 1 + \frac{V_c}{2v_h} \quad \text{for low rates of climb,} \tag{5.16}$$

where ΔP is the excess power available over and above that required for hover. Note that the climb velocity does not depend on excess rotor thrust but on an excess of power. It will

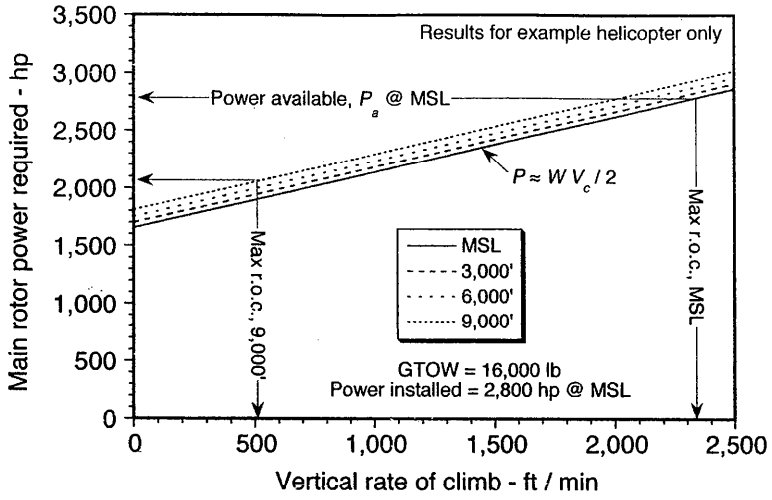

Figure 5.3 Power required to climb as a function of GTOW and density altitude.

be apparent that for low to moderate rates of climb $\Delta P \approx T V_c/2$, or that $V_c \approx 2\Delta P/W$ in axial (vertical) flight. Because of increased inflow through the rotor disk, higher values of collective pitch will be required in a climb. Normally it is convention in performance work for the rate of climb to be expressed in terms of feet per minute, mainly because the rate of climb indicator in the aircraft will be calibrated this way. See also Section 6.6.2 for further discussion on climb performance.

Representative results for the maximum possible climb velocity for the example helicopter at a GTOW = 16,000 lb (7,256 kg) are shown in Fig. 5.3. Notice the significant decrease in the maximum possible climb velocity with increasing density altitude. High values of density altitude can be encountered during "hot and high" operations, and it is important for the pilot to recognize that a potentially serious performance degradation may occur under these conditions.

5.4 Forward Flight Performance

For a helicopter in forward flight, the total power required at the rotor, P, can be expressed by the equation

$$P = P_i + P_0 + P_p + P_c, \tag{5.17}$$

where P_i is the induced power, P_0 is the profile power required to overcome viscous losses at the rotor, P_p is the parasitic power required to overcome the drag of the helicopter, and P_c is the climb power required to increase the gravitational potential of the helicopter. Consider the equilibrium of forces on a single rotor helicopter in a climbing forward flight situation, as shown in Fig. 5.4. In the figure θ_{FP} is the flight path angle, so that for small angles the climb velocity, $V_c = V_\infty \theta_{FP}$. For small angles, satisfying vertical equilibrium gives the equation

$$T \cos(\alpha_{\text{TPP}} - \theta_{FP}) = W \approx T. \tag{5.18}$$

Satisfying horizontal equilibrium leads to

$$T \sin(\alpha_{\text{TPP}} - \theta_{FP}) = D_{FP} \cos\theta_{FP}. \tag{5.19}$$

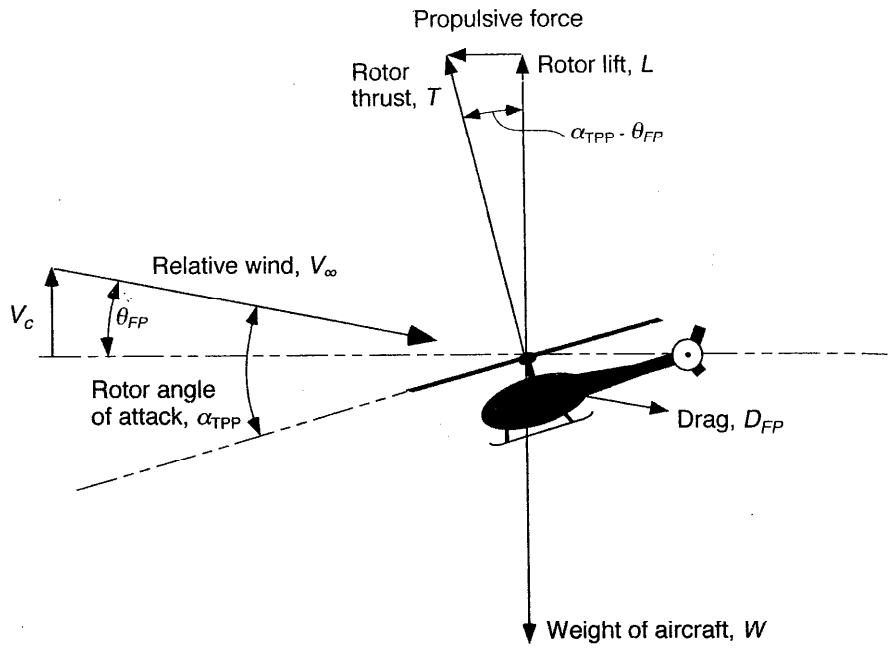

Figure 5.4 Equilibrium of forces on a helicopter in forward flight.

Assuming D_{FP} is independent of the angle of climb, then this latter equation simplifies to

$$T(\alpha_{\text{TPP}} - \theta_{FP}) = D. \tag{5.20}$$

Rearranging and solving for the disk AoA, α_{TPP}, gives

$$\alpha_{\text{TPP}} = \theta_{FP} + \frac{D}{W}. \tag{5.21}$$

Now, consider the power to undertake a climb (and also to propel the helicopter forward). This part of the power is

$$\begin{aligned} TV_\infty \sin\alpha_{\text{TPP}} &\approx TV_\infty\alpha_{\text{TPP}} = WV_\infty\left(\theta_{FP} + \frac{D}{W}\right) \\ &= WV_\infty\theta_{FP} + DV_\infty = WV_c + DV_\infty. \end{aligned} \tag{5.22}$$

The term WV_c is known as the climb power, P_c. The term DV_∞ is known as the *parasitic power*, P_p, because this is energy lost to viscous effects.

5.4.1 *Induced Power*

It is already known from the simple 1-D momentum theory described in Chapter 2 that the induced power of the rotor, P_i, can be approximated as

$$P_i = \kappa T v_i. \tag{5.23}$$

If the forward velocity is sufficiently high, say $\mu > 0.1$, then the induced velocity can be approximated by the asymptotic result predicted by Glauert's "high-speed" flight formula

given by Eq. 2.114. Therefore, the power equation can be written more simply as

$$P = \frac{\kappa T^2}{2\rho A V_\infty} + P_0 + P_p + W V_c, \tag{5.24}$$

where κ is the now familiar empirical correction to account for a multitude of aerodynamic phenomena, mainly those resulting from tip losses and nonuniform inflow. The value of κ cannot necessarily be assumed independent of advance ratio, but the use of a mean value between 1.15 and 1.25 is usually sufficiently accurate for preliminary predictions of rotor power requirements. The previous equation shows the origin of the constituent terms that comprise the basic power requirements of the helicopter in forward flight. Note that in coefficient form the induced power can be written as

$$C_{P_i} = \frac{\kappa C_T^2}{2\sqrt{\lambda^2 + \mu^2}} \approx \frac{\kappa C_T^2}{2\mu} \text{ for larger } \mu. \tag{5.25}$$

5.4.2 *Blade Profile Power*

Glauert (1926) and Bennett (1940) were among the first to formally establish estimates of profile power using the blade element theory. The profile power coefficient with a uniform blade chord is

$$C_{P_0} = \frac{\sigma C_{d_0}}{4\pi} \int_0^{2\pi} \int_0^1 \left(\frac{U}{\Omega R}\right)^3 dr\, d\psi, \tag{5.26}$$

where U is the resultant velocity at the element and C_{d_0} is the profile drag coefficient of the airfoils that make up the rotor blades. The inclusion of the radial component of the velocity at the blade element means $U^2 = U_T^2 + U_R^2$, where $U_R = \Omega R \mu \cos\psi$. Neglecting the radial flow component U_R such that $U = U_T = \Omega R(r + \mu \sin\psi)$ gives

$$C_{P_0} = \frac{\sigma C_{d_0}}{4\pi} \int_0^{2\pi} \int_0^1 (r + \mu \sin\psi)^3\, dr\, d\psi. \tag{5.27}$$

Expanding and integrating gives

$$\begin{aligned} C_{P_0} &= \frac{\sigma C_{d_0}}{4\pi} \int_0^{2\pi} \int_0^1 \left(r^3 + 3r^2\mu \sin\psi + 3r\mu^2 \sin^2\psi + \mu^3 \sin^3\psi\right) dr\, d\psi \\ &= \frac{\sigma C_{d_0}}{8}(1 + 3\mu^2). \end{aligned} \tag{5.28}$$

The results from the analysis of Glauert (1926) and Bennett (1940) show that the profile drag can be approximated as

$$C_{P_0} = \frac{\sigma C_{d_0}}{8}(1 + K\mu^2), \tag{5.29}$$

where the numerical value of K varies from 4.5 in hover to 5 at $\mu = 0.5$, depending on the various assumptions and/or approximations that are made. In practice, usually average values of K are used that are independent of advance ratio. Bennett (1940) used an average value of $K = 4.65$, while Stepniewski (1973) suggests $K = 4.7$. Either value will be acceptable for basic performance studies at the advance ratios typical of conventional helicopters, that is, for $\mu < 0.5$. At higher advance ratios, experimental evidence suggests that profile power grows more quickly than given by Eq. 5.29, as shown in Fig. 5.5. This is a result of radial and reverse flow, as well as compressibility effects on the rotor.

5.4.3 *Compressibility Losses and Tip Relief*

Gessow & Crim (1956) have estimated the additional effects of compressibility on the overall rotor profile power requirements when the tip of the advancing blade approaches and exceeds the drag divergence Mach number M_{dd} of the airfoil sections. Their results were obtained using blade element theory combined with 2-D airfoil section characteristics. By fitting a curve to their results, Johnson (1980) suggests that the extra rotor profile power with compressibility effects can be approximated by

$$\frac{\Delta C_{P_0}}{\sigma} = \begin{cases} 0.007(\Delta M_{dd}) + 0.052(\Delta M_{dd})^2 & \text{for } M_{1,90} \geq M_{dd} \\ 0 & \text{for } M_{1,90} < M_{dd}, \end{cases} \tag{5.30}$$

where ΔM_{dd} is the amount the advancing blade tip Mach number exceeds the drag divergence Mach number of the airfoil section, that is, $\Delta M_{dd} = M_{1,90} - M_{dd}$, where $M_{1,90}$ is the tip value at $r = 1$ and $\psi = 90°$. Values for M_{dd} must be obtained from tests on 2-D airfoils (see Chapter 7). Generally, it is found that the drag on an airfoil remains nominally constant and independent of Mach number until M_{dd} is reached. The result of the Gessow & Crim correction to the profile power is shown in Fig. 5.5 when added to Eq. 5.29, where it is apparent that this model overpredicts the profile power. However, by making allowance for so-called *tip relief* effects (see next) by increasing the effective drag divergence Mach number of sections near the tip, the agreement with the measured results is better. See also Norman & Sultany (1965).

Similar techniques can be developed to account separately for the effects of stall on rotor power – see Gustafson & Myers (1946), Gustafson & Gessow (1947), and Amer (1955). While these techniques are by no means exact, they allow a relatively simple estimate of compressibility and blade stall effects on rotor performance predictions and so are suitable for preliminary design purposes.

Harris (1987) suggests another approximation for the profile power increase from compressibility effects with blades of different thickness-to-chord ratios (t/c). The result is

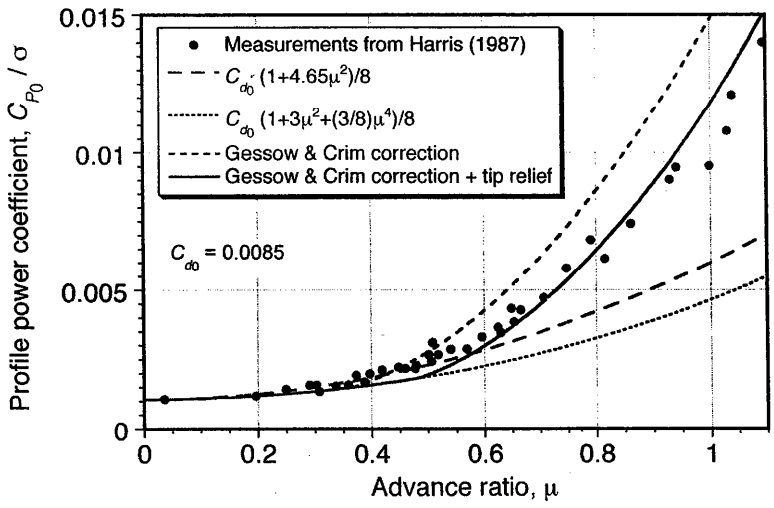

Figure 5.5 Predictions of main rotor power in forward flight will be underestimated at high advance ratios without accounting for compressibility effects. Data source: Harris (1987).

based on transonic similarity rules by using

$$\frac{\Delta C_{P_0}}{\sigma} = \begin{cases} 0.3\,(1+\mu)^{5/2}\,(t/c)^{5/2}\,(\tilde{M}+1)^2 & \text{for } M_{1,90} \geq M_{dd} \\ 0 & \text{for } M_{1,90} < M_{dd}, \end{cases} \tag{5.31}$$

where

$$\tilde{M} = \frac{(M_{1,90})^2 - 1}{1.79(M_{1,90})^{4/3}(t/c)^{2/3}}. \tag{5.32}$$

A more detailed analysis of compressibility effects on the rotor must represent the actual nonlinear airfoil characteristics as functions of Mach number through stall at each blade element, including 3-D effects, followed by integrating numerically to find the effects on rotor thrust and power. Some allowance for an effect known as tip-relief should normally be included in any such power calculation. Tip relief accounts for the relaxation of compressibility effects at the edge of a lifting surface of finite span, and approximations for the effect can also be developed based on transonic similarity rules. The effect was first noted in experiments on propellers, which showed that losses in propulsion efficiency did not occur until the tip Mach numbers well exceeded the drag divergence Mach number of the blade tip sections estimated from 2-D considerations. One practical analysis of tip-relief effects is given by Prouty (1971, 1986), although several approximations are involved. See also LeNard (1972) and LeNard & Boehler (1973).

The region of the rotor disk affected by compressibility effects is shown in Fig. 5.6 and can be defined by finding where the incident Mach number of the flow that is normal to the leading of the blade exceeds the drag divergence Mach number M_{dd}. For an unswept blade the incident Mach number is

$$M_{r,\psi} = M_{\Omega R}\,(r + \mu \sin\psi), \tag{5.33}$$

where $M_{\Omega R}$ is the hover tip Mach number. This means that the region of the disk affected by compressibility effects is defined by

$$M_{\Omega R}\,(r + \mu \sin\psi) \geq M_{dd} \quad \text{or that} \quad r + \mu \sin\psi \geq \frac{M_{dd}}{M_{\Omega R}}. \tag{5.34}$$

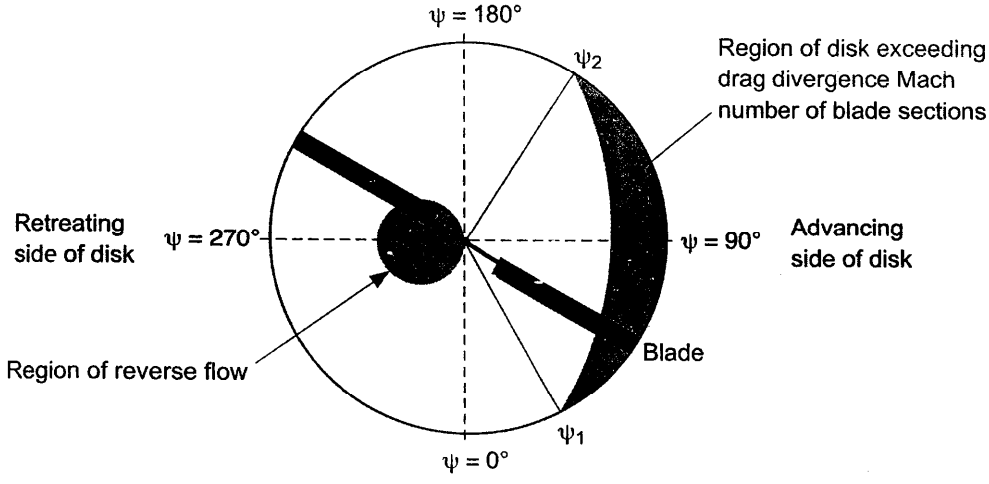

Figure 5.6 The region of the disk where the blade sections reach high Mach numbers.

The azimuth angle for the onset of drag divergence (ψ_1) can be obtained by setting $r = 1$ so that

$$\psi_1 = \sin^{-1}\left[\frac{1}{\mu}\left(\frac{M_{dd}}{M_{\Omega R}} - 1\right)\right]. \tag{5.35}$$

The symmetry of the problem suggests that the tip section leaves the drag divergence zone at $\psi_2 = 180° - \psi_1$. The parts of the blade in the drag divergence region can be found using

$$r_{dd} = \left(\frac{M_{dd}}{M_{\Omega R}} - \mu \sin\psi\right) \quad \text{for } \psi_1 \le \psi \le \psi_2. \tag{5.36}$$

The increment in profile power associated with this region on the disk will be

$$\frac{\Delta C_P}{\sigma} = \frac{1}{4\pi}\int_{\psi_1}^{\psi_2}\int_{r_{dd}}^{1}(r + \mu\sin\psi)^3\,\Delta C_d r\,dr\,d\psi, \tag{5.37}$$

where ΔC_d is the extra drag on the blade section when it exceeds the drag divergence Mach number M_{dd}. For the NACA 0012 airfoil, Prouty (1986) suggests that this be approximated by

$$\Delta C_d(M) = \begin{cases} 12.5(M - 0.74)^3 & \text{for } M \ge 0.74 \\ 0 & \text{otherwise.} \end{cases} \tag{5.38}$$

For lower Mach numbers the drag stays fairly constant (see also Fig. 7.43). As shown in Fig. 5.7, this model gives good agreement with 2-D drag measurements.

Tip relief effects can be accounted for in the blade element theory (BET) using an effective local Mach number M_{eff} at each blade element in the tip region that exceeds the drag divergence Mach number, that is, $M_{r,\psi} > M_{dd}$. One method suggested by Prouty (1986) is to define the effective Mach number as

$$M_{\text{eff}}(r) = M_{r,\psi}\left[\frac{M_{dd2}}{M_{dd3}} + \left(1 - \frac{M_{dd2}}{M_{dd3}}\right)(1 - r)\,AR_{\text{blade}}\right], \tag{5.39}$$

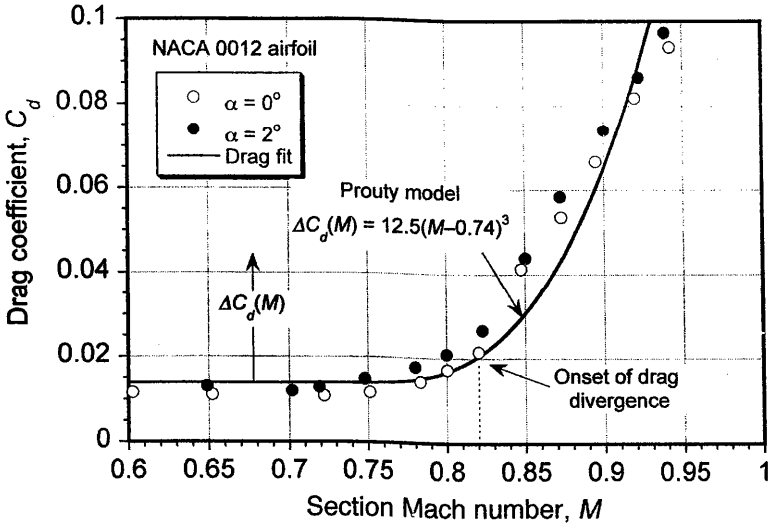

Figure 5.7 Sectional drag increases rapidly after the drag divergence Mach number is exceeded. Data source: NACA 0012 airfoil from Ferri (1945).

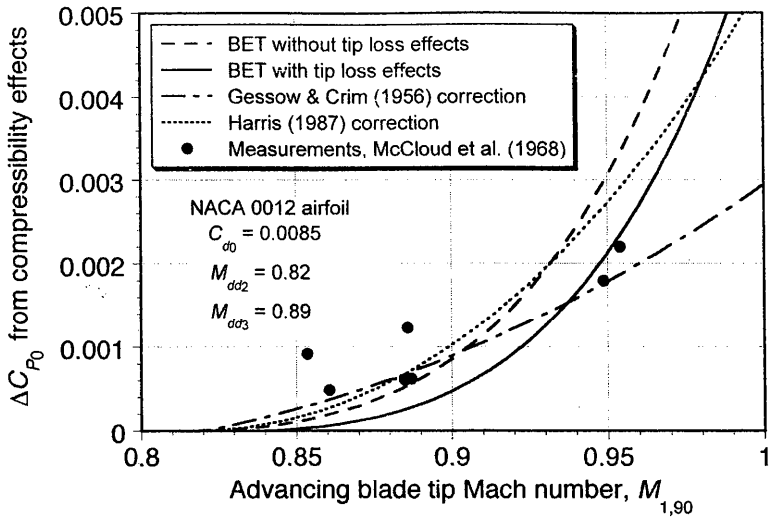

Figure 5.8 Profile power increases rapidly at high advancing tip Mach numbers but is offset to some extent by tip relief effects.

where M_{dd2} is the 2-D value of the drag divergence Mach number (i.e., from the data in Fig. 5.7) and M_{dd3} is the 3-D value with tip relief. In most cases it is found from finite wing measurements that M_{dd3} exceeds M_{dd2} by 10–15%. The parameter AR_{blade} is the aspect ratio of the blade (i.e., R/c). Equation 5.39 is used in Eq. 5.37 to compute the relieving effects of the 3-D flow about the extreme tip of the blade.

The results in Fig. 5.8 show that at high advancing tip Mach numbers the profile power increases rapidly, although it is offset to some extent by tip relief effects. It would appear that the corrections suggested by Gessow & Crim (Eq. 5.30) and Harris (Eq. 5.31) give reasonable results bearing in mind the relative simplicity of these equations. Notice that M_{dd} is also a function of AoA of the airfoil section (see Chapter 7) and the thrust on the rotor. The relationship between M_{dd} and the rotor mean lift coefficient can be approximated empirically – see Stepniewski & Keys (1984) and Prouty (1986). The effects of a swept tip serve to further modify these results, but can be accounted for approximately by using an incident Mach number that is normal to the leading edge of the blade. In such a case the incident Mach number is

$$M_{r,\psi} = M_{\Omega R}\,(r + \mu \sin\psi)\cos\Lambda, \tag{5.40}$$

where Λ is the local sweep angle. See also Section 6.4.6 on swept tips.

5.4.4 *Reverse Flow*

At higher rotor advance ratios, a considerable amount of reverse flow will exist on the retreating side of the rotor disk, that is, the blade sections operate with the trailing edge into the relative wind. This reverse flow region on the rotor disk is illustrated by Fig. 5.9. The locus of the region where $U_T = 0$ means that

$$U_T = 0 = \Omega R\,(r + \mu \sin\psi), \tag{5.41}$$

which has the simple solution $r = -\mu \sin\psi$. Therefore, the region of reverse flow where $U_T \leq 0$ covers a circular region of the disk of diameter μ, with the circle centered at

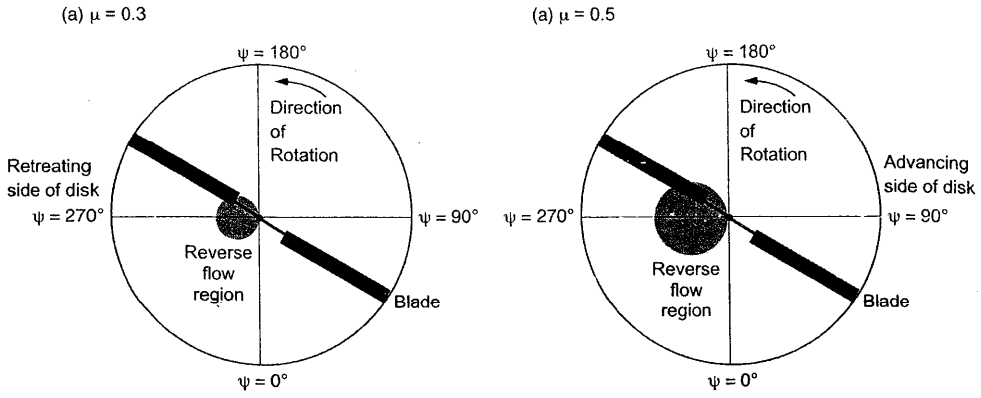

Figure 5.9 With increasing advance ratio, the region of reverse flow covers an increasingly large proportion of the retreating side of the rotor disk. (a) $\mu = 0.3$. (b) $\mu = 0.5$.

$(r, \psi) = (\mu/2, 270°)$. In this reverse flow region the sign of both U_T and the sectional drag contribution to the rotor drag changes (see Section 7.11.6), and so this must be accounted for in the radial and azimuthal integration to find the rotor power and drag coefficients. For a conventional helicopter the maximum feasible advance ratio is about 0.5, which means that the inboard 50% of the retreating blade operates in reverse flow. Autogiros, however, may operate at much higher μ – see Chapter 12.

The effects of reverse flow can be included by changing the sign of the drag in the region defined by $r = -\mu \sin\psi$ on the retreating side of the disk. This may be treated by writing the integral in the profile power equation as the sum of two parts, that is

$$C_{P_0} = \frac{\sigma C_{d_0}}{4\pi} \int_0^{2\pi} \int_0^1 (r + \mu \sin\psi)^3 dr\, d\psi - \frac{\sigma C_{d_0}}{2\pi} \int_\pi^{2\pi} \int_0^{-\mu \sin\psi} (r + \mu \sin\psi)^3 dr\, d\psi, \tag{5.42}$$

where the first integral has been previously evaluated in Eq. 5.28 and the second integral is the increment that accounts for the proper sign on the drag inside the reverse flow region (see Question 5.4). If the drag coefficient is assumed to be unchanged in the reverse flow region, then after integration the profile power coefficient becomes

$$C_{P_0} = \frac{\sigma C_{d_0}}{8} \left(1 + 3\mu^2 + \frac{3}{8}\mu^4\right). \tag{5.43}$$

This result is a fairly common approximation that can be used in a rotor performance analysis and Fig. 5.5 suggests its validity is good to about $\mu = 0.4$. Doubling the drag coefficient in the reverse flow region (see results in Section 7.11.6) will increase the coefficient of the μ^4 term to 3/4. The equivalent rotor drag force coefficient corresponding to Eq. 5.43 is

$$C_H = \frac{\sigma C_{d_0}}{8} \left(2\mu + \frac{1}{2}\mu^3\right) \tag{5.44}$$

when including reverse flow. When radial flow is included then

$$C_{P_0} = \frac{\sigma C_{d_0}}{8} \left(1 + 4\mu^2\right) \tag{5.45}$$

and with radial *and* reverse flow then

$$C_{P_0} = \frac{\sigma C_{d_0}}{8}\left(1 + 4\mu^2 + \frac{5}{8}\mu^4\right). \tag{5.46}$$

Harris (1966) and Johnson (1980) summarize how various other assumptions affect the profile power, including the effects of reverse flow and modified drag coefficients in yawed and reverse flow. The validity of some of these assumptions, however, are questionable at higher advance ratios and larger advancing tip Mach numbers and do not necessarily lead to more accurate models of the profile power. For example, because the blade stalls in the reverse flow region, the assumption that $C_d = C_{d_0}$ (or even $C_d =$ constant) is clearly invalid there (see Section 7.11.6). Generally, however, the effects of the various other assumptions are small, except for radial flow and drag effects in yawed flow, which Johnson (1980) suggests must be included to give an accurate calculation of rotor power. In this case numerical evaluation of the blade element integral is required. But the main advantage of this numerical approach is that more realistic models of the airfoil drag as a function of angle of attack (AoA), including stall, dynamic stall, yawed and radial flow, and compressibility effects can be included into the rotor performance predictions.

5.4.5 *Parasitic Power*

The parasitic power, P_p, is a power loss as a result of viscous shear effects and flow separation (pressure drag) on the airframe, rotor hub, and so on. Because helicopter airframes are much less aerodynamic than their fixed-wing counterparts (for the same weights), this source of drag can be very significant. We can write the parasitic power as

$$P_p = \left(\frac{1}{2}\rho V_\infty^2 S_{\text{ref}} C_{D_f}\right) V_\infty, \tag{5.47}$$

where S_{ref} is some reference area and C_{D_f} is the drag coefficient based on this reference area. In nondimensional form, this becomes

$$C_{P_p} = \frac{1}{2}\left(\frac{S_{\text{ref}}}{A}\right)\mu^3 C_{D_f} = \frac{1}{2}\left(\frac{f}{A}\right)\mu^3, \tag{5.48}$$

where A is the rotor disk area and f $(= C_{D_f} S_{\text{ref}})$ is known as the *equivalent wetted area* or *equivalent flat-plate area*. This parameter accounts for the drag of the hub, fuselage, landing gear, and so on, in aggregate. The concept of equivalent wetted area comes from noting that while the drag coefficient can be written in the conventional way as

$$C_{D_f} = \frac{D_f}{\frac{1}{2}\rho V_\infty^2 S_{\text{ref}}}, \tag{5.49}$$

where S_{ref} is a reference area, the definition of S_{ref} may not be unique. Thus an equivalent wetted area is used, which is defined as

$$f = \frac{D_f}{\frac{1}{2}\rho V_\infty^2}. \tag{5.50}$$

This avoids any confusion that may arise through the definition of S_{ref}. It is found that values of f range from about 10 ft^2 (0.93 m^2) on smaller helicopters to as much as 50 ft^2 (4.65 m^2) on large utility helicopter designs. The concept of equivalent flat-plate area is discussed further in Section 6.6.1.

Another approach represents the parasitic drag of the helicopter relative to a value measured at a reference speed of 100 units (ft/s, kts, etc.) at sea level conditions. The drag at any airspeed and altitude is then calculated using

$$D = D_{100}\left(\frac{V}{100}\right)^2 \sigma, \tag{5.51}$$

where $\sigma = \rho/\rho_0$ as given by Eq. 5.11 or Eq. 5.12.

5.4.6 *Climb Power*

The climb power is equal to the time rate of increase of potential energy. If the potential energy is denoted as E, then $E = Wh$. The rate of increase of potential energy is $W\dot{h} = TV_c = WV_c$, where W is the aircraft weight and V_c is the climb velocity. The climb power coefficient can be written as $C_{P_c} = \lambda_c C_W$. The effect of the fuselage vertical drag is normally taken into account when estimating the climb power, and this is discussed further in Section 6.6.2.

5.4.7 *Tail Rotor Power*

The power required by the tail rotor typically varies between 3 and 5% of the main rotor power in normal flight, and up to 20% of the main rotor power at the extremes of the flight envelope. It is calculated in a similar way to the main rotor power, with the thrust required being set equal to the value necessary to balance the main rotor torque reaction on the fuselage. The use of vertical tail surfaces to produce a side force in forward flight can help to reduce the power fraction required for the tail rotor, albeit at the expense of some increase in parasitic and induced drag. If the distance from the main rotor shaft to the tail rotor shaft is x_{TR}, the tail rotor thrust required will be

$$T_{TR} = \frac{(P_i + P_0 + P_p)}{\Omega\, x_{TR}}, \tag{5.52}$$

where Ω is the angular velocity of the main rotor. This assumes that there is no off-loading of the tail rotor by the fin. The interference between the main rotor and the tail rotor, and between the tail rotor and the vertical fin, is usually neglected in preliminary analysis. However, the effects of the main rotor wake may be accounted for by an increase in the induced power factor, κ, to take into account the generally higher nonuniform inflow at the tail rotor location. The loss of tail rotor efficiency because of the vertical fin can be approximately accounted for by results discussed in Section 6.9.4. Although the tail rotor power consumption is relatively low, interference effects may increase the power required by up to 20%, depending on the tail rotor and fin configuration.

The tail rotor power required is initially high in hover, but quickly decreases as airspeed builds up and the main rotor torque requirements decrease. In high-speed forward flight, the tail rotor power required increases again as the main rotor torque increases to overcome parasitic drag. However, this can be offset to some extent by an aerodynamic side force that is produced on a vertical fin, such as by using a fixed incidence or using a cambered airfoil section. Because of the relatively low amount of power consumed by the tail rotor, for first estimates of performance the power required can be expressed as a fraction of the total main rotor power, with a good estimate being 5%.

5.4.8 *Total Power*

In light of the forgoing, the total power coefficient for the helicopter in forward flight can be written in the form

$$C_P \equiv C_Q = \frac{\kappa C_T^2}{2\sqrt{\lambda^2+\mu^2}} + \frac{\sigma C_{d_0}}{8}(1+K\mu^2) + \frac{1}{2}\left(\frac{f}{A}\right)\mu^3 + \lambda_c C_W + C_{P_{TR}}. \quad (5.53)$$

The tail rotor power must always be added to obtain a proper estimate of total helicopter power requirements. For larger values of μ, then $\lambda \ll \mu$, so that Glauert's formula allows Eq. 5.53 to be simplified to

$$C_P \equiv C_Q = \frac{\kappa C_T^2}{2\mu} + \frac{\sigma C_{d_0}}{8}(1+K\mu^2) + \frac{1}{2}\left(\frac{f}{A}\right)\mu^3 + \lambda_c C_W + C_{P_{TR}}. \quad (5.54)$$

Representative results of net power required for the example helicopter in straight-and-level flight is shown in Fig. 5.10. A gross takeoff weight of 16,000 lb (7,256 kg) and an operating altitude of 5,200 ft (1,585 m) has been assumed. The rotor disk AoA was calculated at each airspeed to satisfy the horizontal force equilibrium (see Fig. 2.23), which, although not a complete trim calculation, provides reasonably acceptable results. An analysis of the predicted components of the total rotor power are also shown, including that of the tail rotor. The equivalent flat-plate area, f, of the helicopter is 23.0 ft^2 (2.137 m^2). For both the main and tail rotors, it is assumed that $\kappa = 1.15$ and $C_{d_0} = 0.008$. The distance between the main and tail rotor shafts, x_{TR}, is 32.5 ft (9.9 m).

Note from Fig. 5.10 that the induced and propulsive part of the power initially decreases with increasing airspeed but increases again as the disk is progressively tilted forward to meet greater propulsion requirements. This is because the rotor must do increasing work to overcome rotor profile and airframe parasitic losses. It is not sufficient to assume induced losses are only a result of lift generation, so induced losses decrease rapidly with airspeed to a point and then start to increase again as losses associated with propulsive forces. Unless

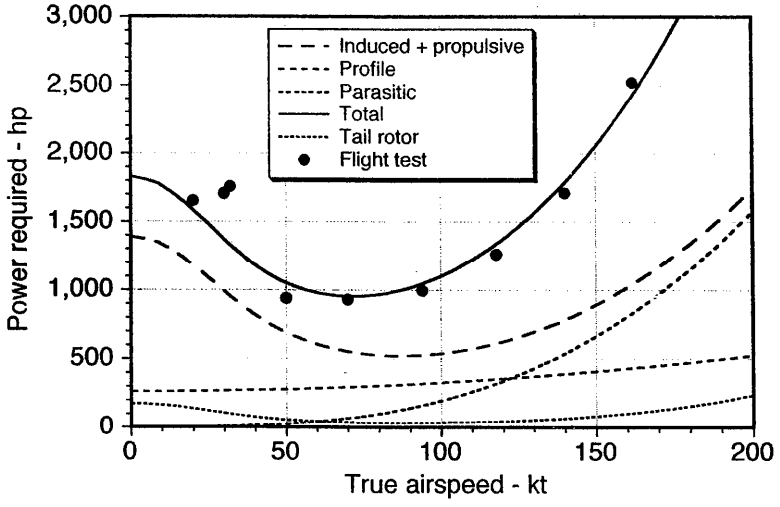

Figure 5.10 Predictions of main rotor power in forward flight. Data source: Ballin (1987).

the problem is being solved for a free-flight trim (solving for the TPP to obtain vertical horizontal equilibrium of the helicopter) then the power curves do not represent a real flight condition. It can be seen that the power required for high-speed forward flight increases dramatically at higher airspeeds because the parasitic losses are proportional to μ^3. The rate of power growth is even higher when reverse flow and compressibility losses on the rotor are considered. However, the airframe drag makes a major contribution to the total power required in high-speed flight, and much can be done to expand the flight envelope by designing a more streamlined airframe. Unfortunately, because of various design constraints, this is not always an easy process. However, as discussed in Section 6.6.1, noticeable reductions in overall parasitic drag can be made by fairing-in the rotor hub to the fuselage, particularly by using streamlining downstream of the hub.

5.5 Performance Analysis

5.5.1 *Effect of Gross Weight*

Clearly the power required in forward flight will be a function of helicopter weight. Because a relatively small weight fraction of fuel is carried relative to total weight, it is convenient to represent the performance results in terms of gross take of weight (GTOW). Representative results showing the effect of GTOW on the rotor power required are given in Fig. 5.11 for the example helicopter at mean sea level (MSL) conditions. Note that with increasing GTOW, the excess power available becomes progressively less, but it is particularly affected at lower airspeed where the induced power requirement constitutes a greater fraction of the total power. In this case, the power available at MSL is 2,800 hp and for a turboshaft engine this stays relatively constant with airspeed. The airspeed obtained at intersection of the power required curve with the power available curve gives the maximum level flight speed; however, the maximum speed may be limited by the onset of power creep from compressibility effects or high blade loads associated with rotor stall before this point is reached.

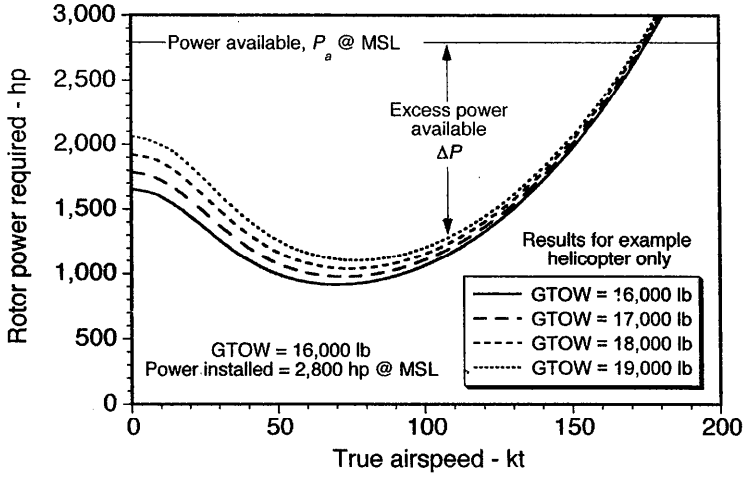

Figure 5.11 Predictions of main rotor power in forward flight at different gross takeoff weights.

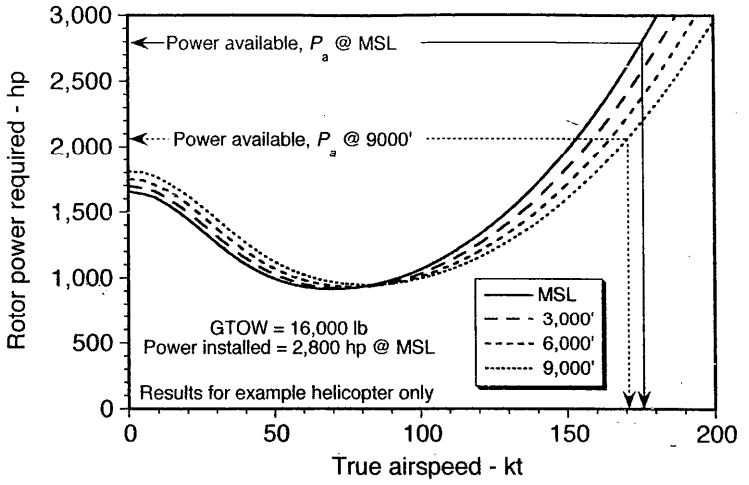

Figure 5.12 Predictions of main rotor power in forward flight at different density altitudes.

5.5.2 *Effect of Density Altitude*

As discussed at the beginning of this chapter, an important operational consideration is the effect of altitude on overall helicopter performance. As shown in Fig. 5.12, increasing density altitude increases the power required in hover and at lower airspeeds. At higher airspeeds, the result of lower air density results in a smaller power requirement because of the reduction in parasitic drag. However, a higher density altitude will also affect the engine power available. As shown in Fig. 5.12, at 9,000 ft the power available is about 25% less than that available at MSL conditions, resulting in a large decrease in the excess power available at any airspeed relative to that at MSL.

5.5.3 *Lift-to-Drag Ratios*

The lift-to-drag ratio (L/D) of the helicopter or just the rotor alone can also be calculated from the power required curves. This is useful for comparison of the forward flight efficiency with another rotor, another helicopter, or a fixed-wing aircraft. Because the rotor provides both propulsive and lifting forces, the lift force is $T\cos\alpha_{TPP}$. The effective drag can be calculated from the power expended (i.e., $D = P/V_\infty$). For the rotor alone the power is $P = P_i + P_0$, and for the complete helicopter $P = P_i + P_0 + P_P + P_{TR}$. Therefore, for the rotor alone the lift-to-drag ratio is

$$\frac{L}{D} = \frac{T\cos\alpha_{TPP}}{(P_i + P_0)/V_\infty} \approx \frac{WV_\infty}{P_i + P_0}. \tag{5.55}$$

For the complete helicopter the lift-to-drag ratio is

$$\frac{L}{D} = \frac{T\cos\alpha_{TPP}}{(P_i + P_0 + P_p + P_{TR})/V_\infty} \approx \frac{WV_\infty}{P_i + P_0 + P_p}. \tag{5.56}$$

Representative results for the lift-to-drag ratio for the example helicopter in forward flight are shown in Fig. 5.13. It is apparent that the L/D increases rapidly as induced power requirements decrease, reaches a maximum, then drops off as the parasitic power

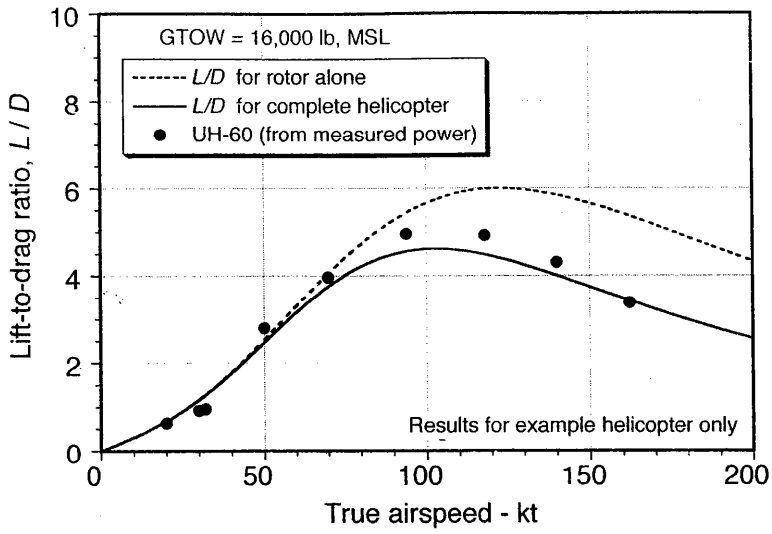

Figure 5.13 Example of equivalent lift-to-drag ratios for rotor and complete helicopter.

requirements rapidly increase. The maximum lift-to-drag ratio of the rotor is about 6, which is typical of most modern helicopters and is also typical of a low aspect ratio fixed wing. The maximum lift-to-drag ratio of the complete helicopter is about 4.5, which gives some idea as to the considerable effect of the airframe drag in the overall cruise efficiency of the helicopter. A typical L/D ratio for a fixed-wing aircraft of the same gross weight will be about 3–4 times this value. Note that the maximum lift-to-drag ratio for this example occurs at about 100 kts, which will be the airspeed to fly for maximum range. The lift-to-drag ratio of the rotor and helicopter will also be a function of the density altitude at which it is flying.

5.5.4 *Climb Performance*

The general power equation can be used to estimate the climb velocity, V_c, that is possible at any given airspeed. Rearranging Eq. 5.53 in dimensional form in terms of V_c leads to

$$V_c = \frac{P - \left(P_{TR} + P_0 + P_p + \dfrac{\kappa T^2}{2\rho A V_\infty}\right)}{T}. \tag{5.57}$$

It is realistic to assume that for low rates of climb or descent the rotor induced power, P_i, the profile power, P_0, and the airframe drag, D, remain nominally constant. In this case we can easily solve for the climb velocity to get

$$V_c = \frac{P - P_{\text{level}}}{T} = \frac{\Delta P}{T} = \frac{\Delta P}{W}. \tag{5.58}$$

Note that P_{level} is simply the net power required to maintain level flight conditions at the same forward speed. If the installed power available is P_a (which may vary with flight condition) then it will be seen that the power available to climb varies with forward flight

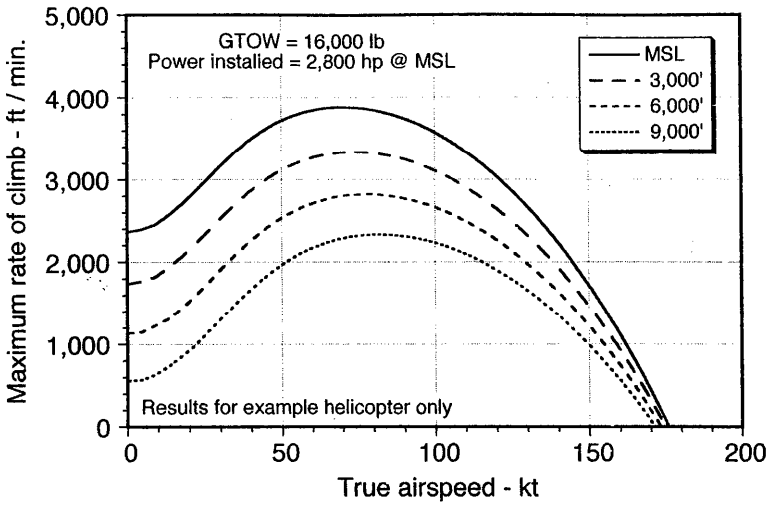

Figure 5.14 Maximum possible rate of climb as a function of airspeed for different density altitudes.

speed. The climb velocity can then be obtained from

$$V_c = \frac{P_a - (P_i + P_0 + P_p + P_{TR})}{T} = \frac{\Delta P}{W}, \tag{5.59}$$

where ΔP is the excess power available at that combination of airspeed and altitude.

Calculations of the maximum rate of climb as a function of flight speed and density altitude are shown in Fig. 5.14 for the example helicopter. These curves mimic the excess power available curves because the climb (or descent) velocity is determined simply by the excess (or decrease) in power required, ΔP, relative to steady level flight conditions. This excess is determined also by the power available from the engine (see next). Pilots often call the tendency of the helicopter to climb when translating from the hover condition as "translational lift." However, the term is a misnomer because the helicopter climbs because of the excess power available and not because of any extra rotor lift. As shown by Fig. 5.14, the rate of climb performance is substantially affected by density altitude.

5.5.5 *Engine Fuel Consumption*

For many performance problems, such as the calculation of range and endurance, a knowledge of the engine fuel burn is required. From the power required curves the fuel consumption can be estimated for a given type of engine. Engine performance data are often expressed in terms of a specific fuel consumption *SFC* (in units of lb $hp^{-1}hr^{-1}$ or kg $kW^{-1}hr^{-1}$) versus shaft power (in units of hp or kW). These curves are a function of atmospheric conditions, so a series of curves are required for different altitudes and operating temperatures. For a normally aspirated (nonsupercharged) reciprocating (piston) engine, the power curves vary almost linearly with density ratio, σ. One common approximation is

$$P_{\text{alt}} \approx P_{\text{MSL}} \left(\frac{1.133\sigma - 0.133}{\sqrt{\theta}} \right), \tag{5.60}$$

where P_{alt} is the power available at altitude and P_{MSL} is the power available at mean sea level conditions. The value of the density ratio σ and the temperature ratio θ can be found from the equations describing the properties of the standard atmosphere given in Section 5.2. For a turboshaft engine the power output decreases almost linearly with density altitude so that a good approximation is

$$P_{alt} \approx (1 - Kh_\rho) \approx P_{MSL}\left(\frac{\delta}{\theta}\right), \tag{5.61}$$

where K is a constant that depends on the particular engine and δ is the pressure ratio at that altitude.

Normalizing both the power and the *SFC* by $\delta\theta^{1/2}$ is found to give a single unique relationship for a turboshaft engine [see Stepniewski & Keys (1984)]. Notional results for a turboshaft engine in the 2,000 hp class are given in Fig. 5.15. Notice that the *SFC* is a function of power output but quickly approaches a nearly constant value as the engine reaches its maximum continuous rated power output. Clearly the engine operates more efficiently under these conditions.

Because helicopters will operate with the engines operating at close to their rated power for much of the flight, a first level approximation is to assume that the *SFC* remains independent of power output. Of course, a better approximation is to calculate the actual fuel flow rate from the *SFC* curve for the engine. By multiplying the *SFC* by the power output it will be apparent that the fuel flow rate $\dot{W}_F$ is a linear function of power output (Fig. 5.15). This relationship can be generalized as

$$\frac{\dot{W}_F}{\delta\sqrt{\theta}} = A_E + B_E\left(\frac{P}{\delta\sqrt{\theta}}\right), \tag{5.62}$$

where the coefficients A_E and B_E depend on the characteristics of a particular engine.

The result in Eq. 5.62 can be easily incorporated into the performance analysis of the helicopter. It is also a useful result when examining engine selection and trading off fuel burn versus number of engines. Clearly a greater number of engines is desirable for safety of flight considerations, but more engines will also affect net fuel burn. This is apparent

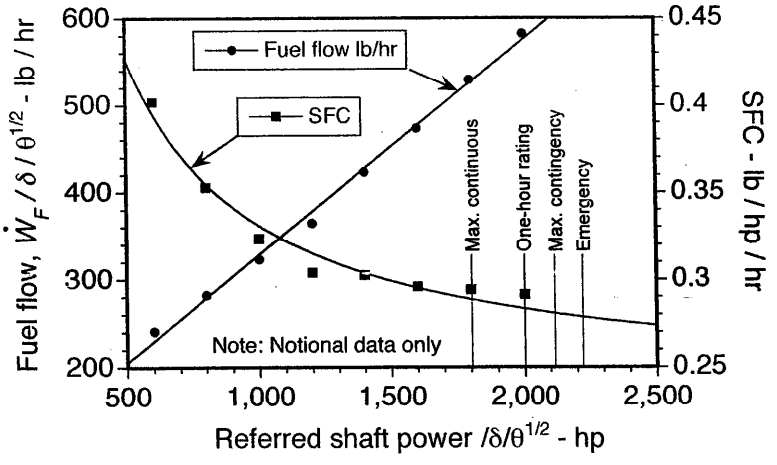

Figure 5.15 Normalized specific fuel consumption and fuel flow for a notional turboshaft engine.

when considering a helicopter with N_E engines that must produce a net power P for flight, then each engine will produce a power of P/N_E. This means that the fuel burn (fuel flow) will be

$$\frac{\dot{W}_F}{\delta\sqrt{\theta}} = N_E\left[A_E + B_E\left(\frac{P}{N_E\delta\sqrt{\theta}}\right)\right] = N_E A_E + B_E\left(\frac{P}{\delta\sqrt{\theta}}\right), \tag{5.63}$$

which on comparing with Eq. 5.62 shows that the fuel flow will always be greater by a factor of approximately $(1 - N_E)A_E$ for a multi-engine installation. Therefore, the design will normally use the fewest number of engines that is consistent with safety of flight and other considerations. Modern helicopters in the medium- to heavy-weight category will use either two or three engines, although smaller helicopters will generally use only one engine to constrain empty aircraft weight and reduce operational costs.

5.5.6 *Speed for Minimum Power*

On the basis of the preceding analysis, it is clear that many of the performance characteristics of the helicopter in forward flight may be estimated directly from curves of excess power available and fuel burn relative to that required for straight-and-level flight at the same airspeed. For example, the maximum possible rate of climb is obtained at the speed for minimum power in level flight (this speed is often denoted by V_{mp} or V_y). It can be seen from Fig. 5.11 or Fig. 5.12 that this situation occurs at a fairly low airspeed, usually in the range 60–80 kts.

The speed V_{mp} will also be the optimum speed to fly for minimum autorotative rate of descent. At this airspeed the power required by the rotor is a minimum, and for an autorotation at this airspeed the pilot will need to give up the least amount of potential energy (altitude) per unit time. Thus, on the basis of the form of the power required curve it can be deduced that in the event of a mechanical failure in the hover condition, it is beneficial for the pilot to translate some of the stored potential energy into translational (forward flight) kinetic energy because the autorotative rate of descent under these conditions will be lower. However, if a mechanical failure occurs close to the ground, this transition may not be possible. For this reason, the normal operational envelope of a helicopter is restricted to an acceptable combination of altitude and airspeed that always allows safe autorotational landings to be performed (see Section 5.6.1).

In addition to being the speed to fly for maximum rate of climb and minimum autorotative rate of descent, V_{mp} also determines the speed to give the best endurance, that is, to obtain maximum loiter time on station for surveillance, search, and so on. To obtain maximum endurance the fuel burn per unit time must be a minimum. Now, the weight of fuel burned W_F in a given time t is given in terms of SFC (lb hp^{-1} hr^{-1}) as

$$W_F = SFC \times P\,t, \tag{5.64}$$

so the endurance (in appropriate units) for a given amount of fuel is

$$t = \frac{W_F}{SFC \times P}. \tag{5.65}$$

Clearly this time is maximized at the best SFC and lowest power required for flight. Figure 5.16 shows representative fuel burn curves for the example helicopter. Because the engine SFC curve is fairly flat over the range of power settings where engines will operate in practice (Fig. 5.15), the fuel burn is proportional to power at a given pressure altitude and temperature, and the speed for minimum fuel burn coincides with the speed for minimum

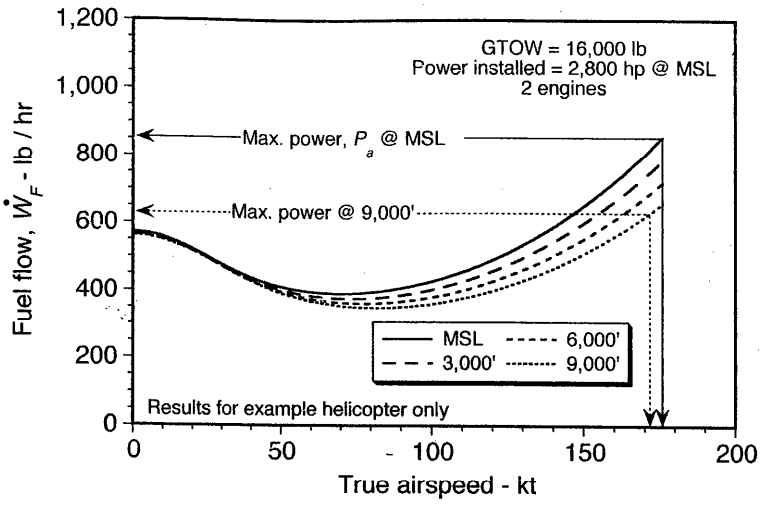

Figure 5.16 Representative fuel burn versus airspeed plots for the example helicopter.

power. For the unusual case of engine operations at very low power settings, however, the *SFC* increases quickly and these two speeds will not necessarily be equal.

To estimate the value of V_{mp}, the approximation previously derived in Eq. 5.53 for the helicopter power can be used, namely

$$C_P \equiv C_Q = \frac{\kappa C_T^2}{2\mu} + \frac{\sigma C_{d_0}}{8}(1 + K\mu^2) + \frac{1}{2}\left(\frac{f}{A}\right)\mu^3 + \lambda_c C_W. \tag{5.66}$$

At lower airspeeds the rotor profile power is small and builds slowly with the square of airspeed. Therefore, the minimum power is essentially determined by the variation in induced power and the parasitic power at these lower air speeds [see Johnson (1980)]. It can be assumed that $C_T \approx C_W$ and so

$$C_P \approx \frac{\kappa C_W^2}{2\mu} + \frac{1}{2}\left(\frac{f}{A}\right)\mu^3. \tag{5.67}$$

Differentiating this expression with respect to μ gives

$$\frac{dC_P}{d\mu} = -\frac{\kappa C_W^2}{2\mu^2} + \frac{3}{2}\left(\frac{f}{A}\right)\mu^2, \tag{5.68}$$

which equals zero for a minimum. Therefore,

$$\frac{\kappa C_W^2}{2\mu^2} = \frac{3}{2}\left(\frac{f}{A}\right)\mu^2 \quad \text{or} \quad \mu = \left(\frac{\kappa C_W^2}{3f/A}\right)^{1/4} \tag{5.69}$$

for maximum endurance. Also, recall that $\lambda_h = \sqrt{C_W/2}$ so that

$$\mu = \lambda_h \left(\frac{4\kappa}{3f/A}\right)^{1/4} = \sqrt{\frac{C_W}{2}}\left(\frac{4\kappa}{3f/A}\right)^{1/4} \tag{5.70}$$

or

$$V_y = V_h \left(\frac{4\kappa}{3f/A}\right)^{1/4} = \sqrt{\frac{W}{2\rho A}}\left(\frac{4\kappa}{3f/A}\right)^{1/4}. \tag{5.71}$$

Note that, in general, this speed will increase with increasing density altitude, that is, with both increases in altitude and temperature. In addition, it will be apparent that this airspeed is proportional to the square-root of disk loading and helicopter weight.

5.5.7 *Speed for Maximum Range*

The range of the helicopter is the distance it can fly for a given takeoff weight and for a given amount of fuel. In all cases contingency fuel allowances (i.e., reserves) must be taken into account, depending on the mission profile and whether visual or instrument flight rules apply. The range can be written as $R = Vt$ so in terms of SFC and a given amount of fuel, a first approximation to the range is

$$R = \frac{V W_F}{SFC \times P}. \tag{5.72}$$

Typically, the fuel burn versus airspeed curves mimic the power required curves if the engines operate at the power settings where their SFC curves are relatively flat, as shown in Figs. 5.15 and 5.16. Therefore, as a first approximation the speed to fly to give the best range is obtained when the ratio V/P is a maximum or the ratio P/V is a minimum, that is, when the helicopter is operated at the best lift-to-drag ratio. For no-wind conditions this speed is graphically obtained from a line drawn through the origin and tangent to the P versus V (or torque versus V) curve, as shown in Fig. 5.17. As can be seen that this airspeed is usually at a somewhat higher airspeed than that required for maximum endurance. Notice that this speed will change with both the weight of the helicopter and with the atmospheric conditions.

The speed to fly for maximum range, V_{mr}, is also determined essentially by the variation in induced power and the parasitic power. Therefore, the ratio of P/V can be approximated

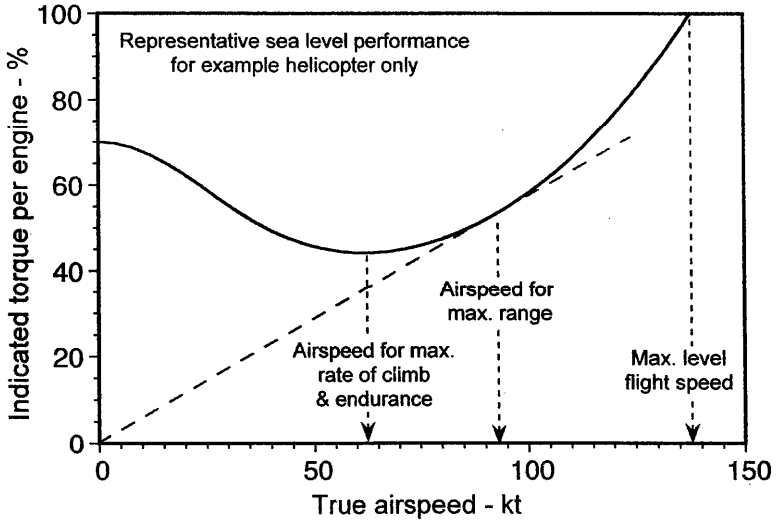

Figure 5.17 Determination of speed to fly for maximum rate of climb, maximum range, and maximum level flight speed from representative torque (power) curve.

by the expression

$$\frac{C_P}{\mu} \approx \frac{\kappa C_W^2}{2\mu^2} + \frac{1}{2}\left(\frac{f}{A}\right)\mu^2. \tag{5.73}$$

Differentiating this latter expression with respect to μ gives

$$\frac{d(C_P/\mu)}{d\mu} = -\frac{\kappa C_W^2}{\mu^3} + \left(\frac{f}{A}\right)\mu, \tag{5.74}$$

which equals zero for a minimum. Therefore,

$$\mu = \left(\frac{\kappa C_W^2}{f/A}\right)^{1/4} \tag{5.75}$$

for maximum range or

$$V_{\text{mr}} = V_h\left(\frac{4\kappa}{f/A}\right)^{1/4} = \sqrt{\frac{W}{2\rho A}}\left(\frac{4\kappa}{f/A}\right)^{1/4}. \tag{5.76}$$

Note that, like the speed for maximum range, this speed will also increase with increasing density altitude and with the square-root of aircraft weight.

A more accurate estimate of range will take into account the actual *SFC* curves and fuel flow rates at the particular power settings for the altitude and temperature at which the helicopter is actually flying. From the representative results shown in Fig. 5.18, it is apparent that the maximum range condition that P/V is a minimum is obtained when a line drawn from the origin of the axes is tangent to the fuel flow curve. The resulting fuel flows (in units of lb hr^{-1} or kg hr^{-1}) for different conditions (see Fig. 5.16) can then be used to find the specific range (in terms of distance flown per unit of fuel). Such results would normally be plotted as specific range versus true airspeed for different density altitudes. Determination of maximum endurance (see Section 5.20) also requires an accurate determination of the fuel flow curves.

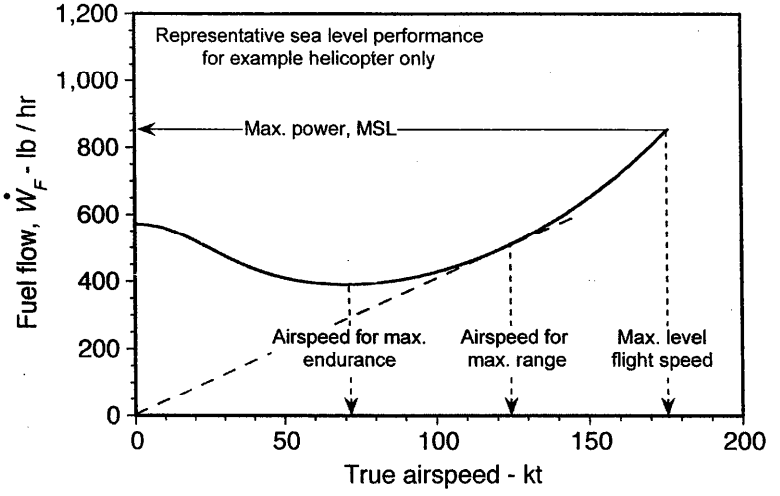

Figure 5.18 Representative fuel burn versus airspeed plots for the example helicopter.

5.5.8 *Range–Payload and Endurance–Payload Relations*

Range–payload and endurance–payload curves provide information of the effects of aircraft range and endurance when trading off payload for fuel. The specific mission for the aircraft must be defined, although most flight plans will involve a flight from point A to point B, as shown in Fig. 5.19. As previously explained, the engine characteristics must be taken into account to determine both the maximum endurance and maximum range. Fuel flow curves must be derived versus indicated airspeed and gross weight, and these depend on whether the helicopter is powered by reciprocating or turboshaft engines. Generally, the fuel flow curves versus airspeed (at a given density altitude) are fairly flat and so this alternative form of defining the performance curves closely follows the shapes of the power curves. McCormick (1995) lays down the basic range analysis for an aircraft, which can be adapted for the helicopter. The fuel burn, W_F, with respect to distance, R, will be

$$\frac{dW_F}{dR} = \frac{P \times (SFC)}{V}, \tag{5.77}$$

where SFC is the specific fuel consumption of the engine(s). The power required, P, varies with gross weight and density altitude and, as already shown, the SFC depends on power and density altitude. Because the weight decreases as fuel is burned, Eq. 5.77 must be integrated numerically to find the range. Fuel burned during takeoff, climb, and descent is factored into the calculation, along with a mandated fuel reserve in minutes of flying time. However, because the fuel weight is normally a small fraction of the total gross weight of the helicopter (usually, but not always) then Eq. 5.62 can be evaluated fairly accurately at the point in the cruise where the aircraft weight is equal to the initial gross weight (gross takeoff weight, W_{GTOW}) less half the initial fuel weight, that is, at the point where $W = W' = W_{GTOW} - W_F/2$, where W_F is the initial fuel weight. In this case the range, R, of the helicopter when cruising at speed V is given by

$$R = \int_{W_{GTOW}}^{W_{GTOW}-W_F} \frac{V}{P \times (SFC)} dW \approx W_F \left[\frac{V}{P \times (SFC)}\right]_{W=W'} \tag{5.78}$$

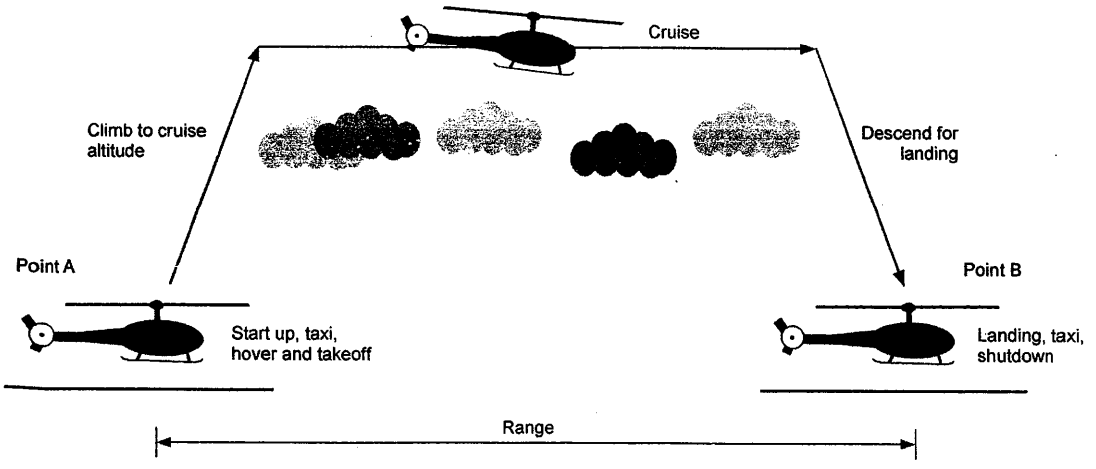

Figure 5.19 A representative mission profile for a helicopter.

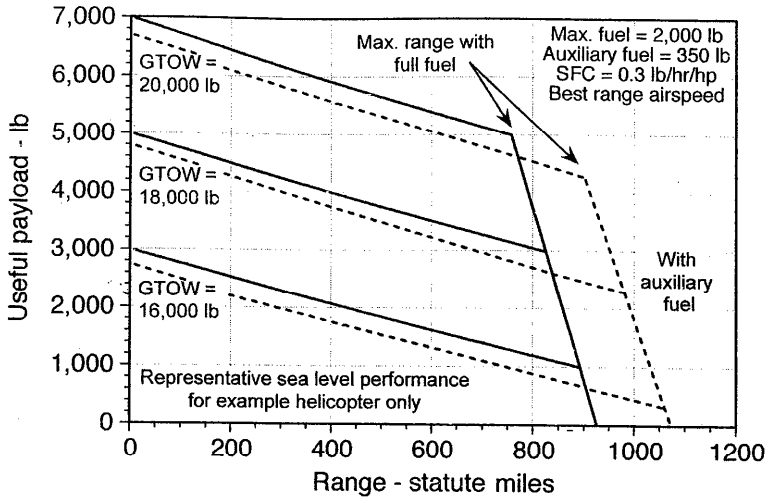

Figure 5.20 A representative payload–range curve for example the helicopter.

less an allowance for the other contingency factors described previously. By a similar process, the estimated endurance, E, will be given by

$$E = W_F \left[\frac{1}{P \times (SFC)} \right]_{W=W'} \tag{5.79}$$

Generally, it is sufficiently accurate to estimate endurance by dividing the useable fuel on-board by the average fuel flow rate, as given by Eq. 5.72.

An example of a payload–range curve is shown in Fig. 5.20. The detailed nature of the range and endurance curves are obtained by numerical calculation and then confirmed by the manufacturer by flight testing. Some helicopters may be able to be fitted with long-range fuel tanks, for which ferry operations over considerable distances are possible, but with reduced payload. All of this payload–range information is presented to the pilot in the form of performance charts, and these are included in the aircraft flight manual. The pilot can use these charts for flight planning at the combination of aircraft weight and atmospheric conditions. Stepniewski & Keys (1984) give good examples of payload–range and payload–endurance curves and provide step-by-step procedures for determining the curves for specific mission profiles.

5.5.9 *Maximum Altitude or Ceiling*

The maximum attainable altitude or *ceiling* that the helicopter can fly at is determined by the power available at the rotor and the power required for flight at a given weight. The power required will increase with increasing density altitude and simultaneously the engine power output will decrease with altitude. The altitude at which the power required is equal to the power available is defined as the ceiling. Recall that the power required in forward flight can be approximated by the equation

$$P_{\text{req}} = \frac{\kappa T^2}{2\rho A V_\infty} + P_0 + P_p + P_{TR} + W V_c \tag{5.80}$$

and including a suitable allowance for transmission losses. The power available at altitude for a turboshaft engine is given by Eq. 5.61. The absolute maximum ceiling of the helicopter

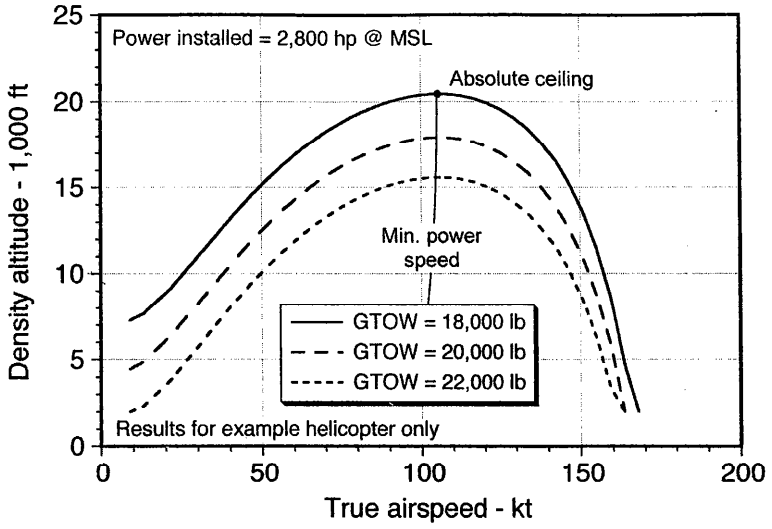

Figure 5.21 Maximum altitude or ceiling is a function of true airspeed and gross weight.

will be obtained at the speed for minimum power when $P_{req} = P_{alt}$. Because this condition is approached asymptotically, the altitude at which this occurs can be determined by setting the rate of climb V_c arbitrarily to the low value of 1 fts^{-1} (0.3 ms^{-1}) and solving Eq. 5.80 for the density altitude at which this condition is reached. This is called the service ceiling.

Results showing the service ceiling as a function of true airspeed for the example helicopter at different gross weights are given for standard atmospheric conditions in Fig. 5.21. This type of plot is often referred to as an operational flight envelope – see Fig. 6.38 for general operational flight envelopes of several rotorcraft configurations. It is apparent that the ceiling curves mimic the excess power available or maximum rate of climb curves, as would be expected. The ceiling that the helicopter can reach may be further qualified by specifying in ground effect (IGE) or out of ground effect (OGE) conditions – see Section 5.8. This is because operations IGE will reduce power required and so can help to augment the operational ceiling, a useful behavior when operating out of high altitude or mountainous terrain. However, the useful flight envelope may be further restricted by structural limitations that must be clearly defined to avoid inadvertent operations that may overstress the rotor – see Stepniewski & Keys (1984).

5.5.10 *Factors Affecting Maximum Attainable Forward Speed*

Conventional helicopters are relatively low speed machines compared to their fixed-wing counterparts. The maximum flight speed will be determined by a combination of one or more of the following: 1. Installed engine power, 2. Airframe parasitic drag, 3. Gearbox (transmission) torque limits, and 4. Rotor stall and/or compressibility effects. Early helicopters were powered by reciprocating engines and were mostly limited in performance because of the lack of installed power. Reciprocating engines have relatively poor power-to-weight ratios and become extremely heavy when large amounts of power are required. A reciprocating engine, on average, has a power-to-weight ratio of about 0.5 hp/lb (0.82 kW/kg), whereas a modern turboshaft engine has at least three times as much. Above a certain aircraft gross weight, it is inefficient to use reciprocating engines on helicopters.

As a result, on modern helicopters turboshaft engines are almost universally used because of their superior power-to-weight ratios. However, turboshaft engines have high acquisition and operating costs and are not usually found on small training helicopters. On turboshaft-powered helicopters, performance limits are dictated by allowable transmission torque. When it is necessary to transmit large amounts of torque to the rotor shaft, the transmission system becomes relatively heavy because of structural strength requirements, and so there is usually a torque limit imposed to minimize overall transmission weight. In this case, helicopter performance charts are usually presented in terms of indicated engine power or shaft torque versus indicated airspeed (e.g., Fig. 5.17).

Airframe drag constitutes a substantial impediment to high-speed flight. Therefore, the minimization of airframe drag has become a major issue in the design of a modern helicopter. Over the past thirty years there have been progressive improvements toward reducing airframe drag and improving forward flight speeds and reducing fuel burn. A major drag producer at high forward speed is the rotor hub, especially because the blade hinges and controls are mostly all exposed to the airstream. Careful contouring of the fuselage in this region can significantly help reduce hub drag and control the extent and intensity of the separated wake behind the hub. More recently, there has been a shift to the use of hingeless or bearingless rotor hubs. Besides being mechanically simpler than conventional articulated rotor hubs, these types of hub designs are also aerodynamically cleaner and have a much lower equivalent flat-plate area.

On many helicopters, the maximum forward flight performance is limited by the aerodynamics of the rotor itself. This is because of the occurrence of one of two possible factors. First, high power (or torque) is required to overcome compressibility effects generated on the advancing side of the rotor disk. Second, retreating blade stall can produce sufficiently high blade loads and vibration levels to limit the flight speed. Compressibility effects manifest as wave drag as a result of the onset of transonic flow and the generation of shock waves. The intensity of the supercritical (transonic) flow may also progress to a point where the shock waves are sufficiently strong to promote rapid thickening of the local boundary layer, and it may even produce shock induced separation and stall. The approach of the rotor into these conditions is usually accompanied by a relatively gradual increase in power required or so-called power "creep" (see Section 5.4.3) with mild increases in vibration. However, the occurrence of retreating blade stall is often more sudden in its occurrence and is accompanied by high rotor vibration levels.

Finally, it will be apparent that an expansion of the flight boundary of helicopters to high flight speeds is limited by not only aerodynamic constraints, but also by aeroelastic and structural constraints as well. Usually, high stresses or intolerable fatigue loadings of the various structural components are limiting factors, particularly on the hub and pitch links. These vibratory stresses result from the generation of large unsteady aerodynamic loads on the rotor system, which is simply an undesirable outcome of pushing the rotor to its aerodynamic limits. The complex nature of these loads reflects the need to understand the highly unsteady aerodynamic flow field produced within the rotor disk, which is discussed in detail in Chapter 8.

5.5.11 *Performance of Coaxial and Tandem Dual Rotor Systems*

The hovering performance of coaxial and tandem rotors has been previously discussed in Section 2.15.1. By accounting for the induced interference effects between the rotors, it has been shown that the relationship between power and thrust can be adequately

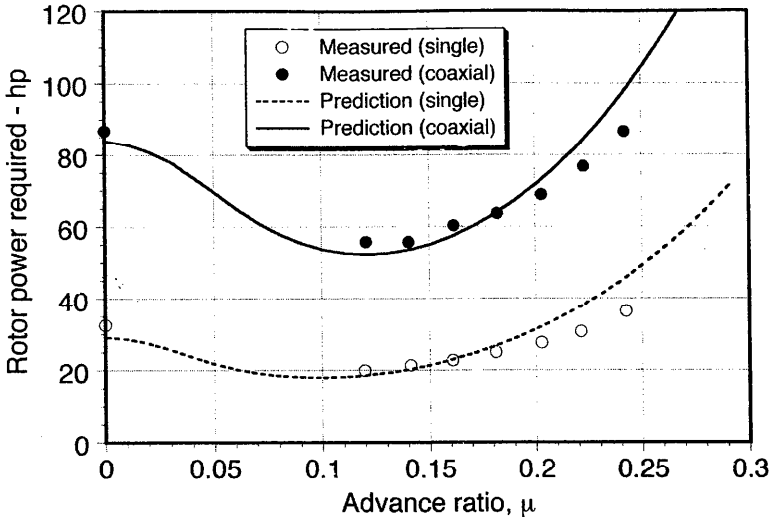

Figure 5.22 Predictions of power in forward flight for single and coaxial rotor system compared to measurements. Data source: Dingeldein (1954).

estimated using a variation of the simple momentum theory. The power required for a coaxial rotor system operating in forward flight at a constant thrust coefficient and over a range of advance ratios is shown in Fig. 5.22. The experimental data are taken from Dingeldein (1954). The predictions were made using the extension of simple momentum theory to forward flight, with the effects of profile losses accounted for through the blade element theory, in the same manner used previously for the single rotor. The single rotor had a solidity of 0.027 and the coaxial rotor had a solidity of 0.054. An equivalent flat-plate parasitic drag area of 10 ft^2 was used to define the propulsive force component, along with $C_{d_0} = 0.01$, $\kappa = 1.15$, and $\kappa_{int} = 1.16$, the latter being derived from the hover case and assumed to be valid also for forward flight.

For both the single and coaxial rotors, the predictions in Fig. 5.22 compare favorably with the measurements, although there is a slight over prediction of power at the highest advance ratios. It is clear that for the coaxial configuration, there is a higher overall power requirement than for an equivalent single rotor. This is because of the interference effects between the two rotors. Also, the higher overall parasitic drag of the two hubs and dual control linkages (see Fig. 4.13) make a coaxial rotor aerodynamically less efficient than a single rotor system. However, this negative aspect can be outweighed by the overall reduced rotor size and compactness of the coaxial rotor helicopter design.

The forward flight performance obtained with a tandem rotor configuration is shown in Fig. 5.23, along with a breakdown of the power required separately for the front and rear rotors. There is no rotor overlap for this particular tandem configuration, with the rotor shafts being separated by 103% of the rotor diameter. Each rotor had a solidity of 0.027. The equivalent flat-plate area drag was 2 ft^2. Note that the performance of the front rotor was almost identical to that of the single rotor, suggesting that in this case there is little or no interference produced on the forward rotor by the rear rotor during forward flight. This, however, may not be a general result that is independent of rotor spacing or relative difference in rotor height. Prediction of performance by means of the momentum/blade element theory is, therefore, of the quality expected based on previous studies with single rotors. The power

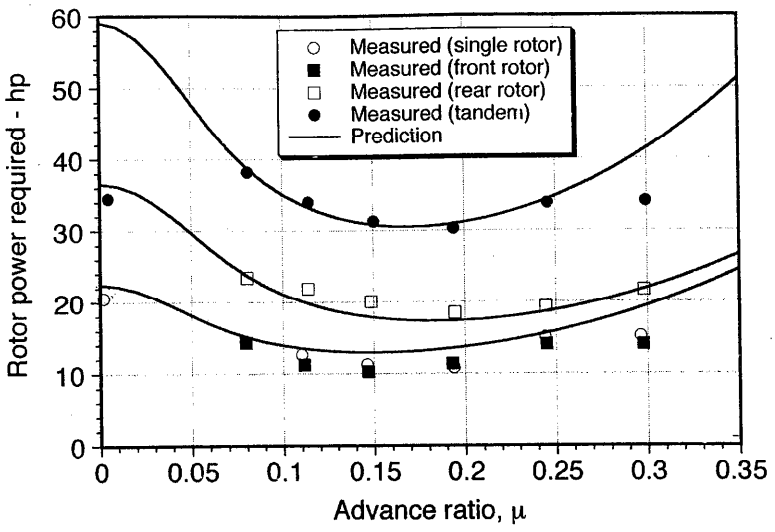

Figure 5.23 Predictions of power in forward flight for a tandem rotor system compared to measurements. Data source: Dingeldein (1954).

required for the rear rotor is considerably higher because it operates in the downwash generated by the front rotor[2] – see Heyson (1954). By computing the downwash from the front rotor, this can be used to redefine the flow environment encountered by the rear rotor. The induced power for the combination becomes

$$P_i = T_F v_{i_F} + \kappa_{ov} T_R v_{i_R}, \tag{5.81}$$

where T_F and T_R are the thrusts of the front and rear rotor, respectively. An induced power interference factor, κ_{ov}, equal to 1.14 (see Section 2.15.2) was assumed for the rear rotor, for which the power required can then be estimated. For advance ratios of 0.1 and above, Fig. 5.23 shows that there is a good agreement between the predictions and the measurements. Note that because of the effects of the forward rotor, the minimum power required for the rear rotor is attained at a much higher advance ratio. Combining the results for the two rotors gives the power required for the tandem configuration. Agreement between prediction and experiment is generally good, except for low advance ratios approaching hover where the experimental results show a favorable interference effect. Based on the results shown previously in Section 5.5.11, this favorable effect seems unique to this tandem configuration and would not necessarily be expected for substantially overlapping tandem rotors.

5.6 Autorotational Performance

The autorotation maneuver has been discussed in Section 2.13.7 and is defined as a self-sustained rotation of the rotor without the application of any shaft torque from the engine (i.e., $C_Q \approx 0$). Under these conditions, the power to drive the rotor comes from the relative airstream upward through the rotor as the helicopter descends through the air.

[2] On tandems such as the CH-46 or CH-47 the rear rotor is placed substantially higher than the front rotor to minimize these interference effects.

Autorotation is used as a means of recovering the safe flight helicopter in the event of a catastrophic mechanical failure, such as engine, transmission, or tail rotor failure. The ability to autorotate is, therefore, a safety of flight issue. Under established autorotative conditions, there is an energy balance where the decrease in aircraft potential energy per unit time is equal to the power required to sustain the rotor speed. In other words, the pilot gives up altitude at a controlled rate in return for energy to turn the rotor to keep it producing thrust. Recall from Section 2.13.7 that an autorotation at low forward flight speeds will take place in the turbulent wake state where the flow is not smooth and leads to a certain amount of unsteadiness at the rotor. At higher forward speeds the flow through the rotor tends to be smoother in the autorotational condition.

Consider now the flow environment encountered at a blade element on the rotor during a descent, as shown in Fig. 5.24. Although most autorotations are conducted with some forward speed, first consider a vertical autorotative descent with no forward speed. In an autorotation, the inflow angle ϕ must be such that there is no net in-plane force and, therefore, no contribution to rotor torque, that is, for this station on the blade,

$$dQ = (D - \phi L)y\, dy = 0. \tag{5.82}$$

However, this is a condition that can only exist at most at two radial stations on the blade. In general, some stations on the rotor will absorb power from the relative airstream and some will consume power such that the net power at the rotor shaft is approximately zero. With

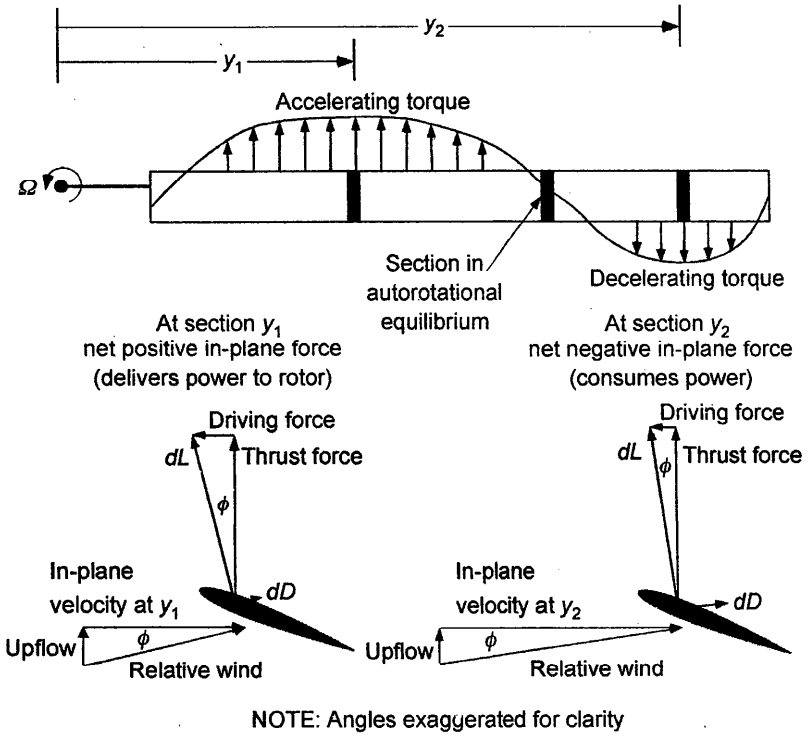

Figure 5.24 In autorotation, different parts of the rotor consume power or produce power. Adapted from Bennett (1947).

the assumption of uniform inflow over the disk, the induced AoA is given by

$$\phi = \tan^{-1}\left(\frac{|V_c + v_i|}{\Omega y}\right). \tag{5.83}$$

It follows that the induced angles of attack over the inboard stations of the blade are high, and near the tip ϕ is low. Therefore, we find that at the inboard part of the blade the net AoA results in a forward inclination of the sectional lift vector and is such that in this region there is now a negative induced drag component that is greater than the profile drag. Therefore, this blade element absorbs power from the airstream to the rotor. At the tip of the blade where ϕ is low, these sections consume power because, as a result of the forward inclination of the lift vector, the propulsive component is insufficient to overcome the profile drag. The effect is summarized in Fig. 5.24. The consequences are that after initial autorotational equilibrium is obtained, variations in rotor thrust, inflow, and so on, will cause rotor rpm (Ω) to adjust itself automatically until autorotational equilibrium is again obtained. Generally, autorotation is a stable equilibrium point because if Ω increases, ϕ will decrease and the region of accelerating torque will decrease inboard, and this tends to decrease rotor rpm. Conversely, if the rotor rpm decreases then ϕ will increase and the region of accelerating torque will grow outward.

Consider the autorotation diagram shown in Fig. 5.25, where the blade section C_d/C_l is plotted versus AoA at the blade section. This is a form originally used by Wimperis (1928). Both Nikolsky (1944) and Gessow & Myers (1952) describe rotor equilibrium at the blade element in terms of this interpretation, which is relatively useful for a further understanding

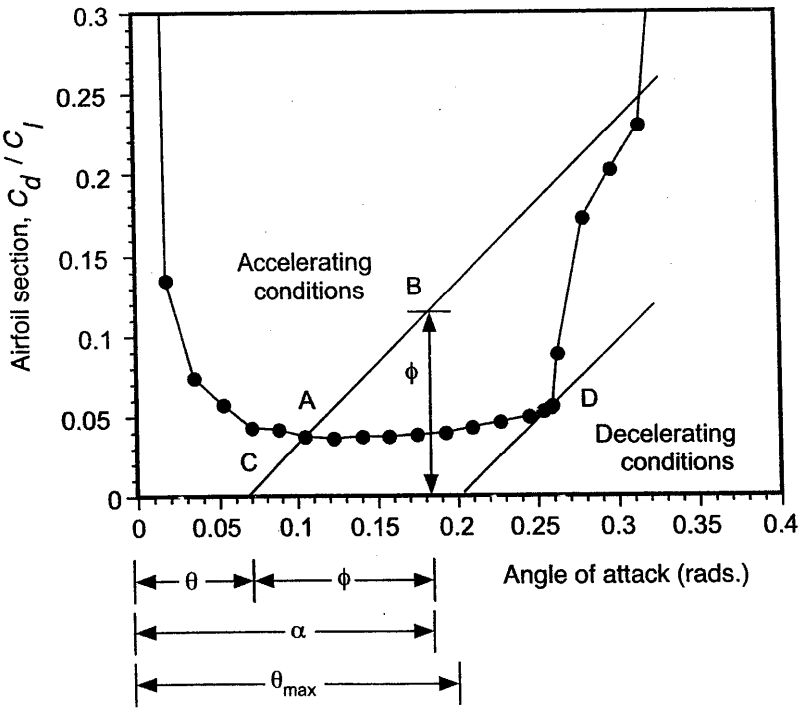

Figure 5.25 Autorotative diagram used to describe equilibrium conditions at the blade element. Adapted from Gessow & Myers (1952).

of the phenomenon. For a single section in equilibrium recall that

$$C_d - \phi C_l = 0 \quad \text{or} \quad \frac{C_d}{C_l} = \phi = \alpha - \theta, \tag{5.84}$$

where θ is the blade pitch angle. For a given value of blade pitch angle, θ, and inflow angle ϕ, the previous equation represents a series of points that form a straight line, which is plotted on Fig. 5.25. The intersection of this line with the measured C_d/C_l data at point A corresponds to the equilibrium condition where $\phi = C_d/C_l$. Above this point, say at point B, $\phi > C_d/C_l$; so this represents an accelerating torque condition. Point C is where $\phi < C_d/C_l$; this represents a decelerating torque condition. Note that above a certain pitch angle, say $\theta_{\max}$, equilibrium is not possible and so for operation at point D stall will occur causing the rotor rpm to decay.

Establishing stable autorotational flight requires a certain level of skill from the pilot. The rotor rpm and the rate of descent can be controlled by the pilot by means of judicious adjustment of the collective pitch setting. The cyclic pitch is used to control the airspeed. The collective controls the mean blade pitch (and hence the mean aerodynamic angles of attack at the blade sections) and, therefore, the blade mean lift, drag, and rotor rpm. In an autorotation the collective pitch is always held at a low value. The inboard parts of the rotor blades always operate at high angles of attack during the autorotative descent. Therefore, the pilot must ensure that the collective pitch angle is kept low enough to prevent stall propagating out from the blade root region, which will tend to quickly decrease rotor rpm because of the high profile drag associated with stall.

The initial stages of the autorotative maneuver are the most critical. During these initial stages, the pilot must sharply lower the collective pitch setting from the normal flight value to prevent blade stall and a rapid decay in rotor rpm. Both military and civil certification requirements impose a finite time delay (usually a few seconds) to account for normal pilot reaction time before the collective pitch is lowered; thus there is always some safety margin imposed in all helicopter designs – see Prouty (1986). However, in most cases the pilot must still react sufficiently quickly to ensure that the rotor rpm does not decay below acceptable margins, this usually being only a matter of seconds.

How quickly the rotor rpm decays is a function of the power required at the time of failure and the rotational kinetic energy of the rotor. Stewart & Sissingh (1949), Newman (1994), and Johnson (1980) give a good summary of this problem, although an approximate but accurate analysis is given by McCormick (1956). The equation of motion for the decay of the rotor rotational speed with time t after the removal for the shaft torque at time $t = 0$ is

$$I_R \frac{d\Omega}{dt} = Q = -Q_0 \left(\frac{\Omega}{\Omega_0}\right)^2, \tag{5.85}$$

where I_R is the net inertia of the rotor system and the subscript 0 refers to time $t = 0$. This assumes that the helicopter does not reach an appreciable rate of descent or that the collective pitch is changed. The minus sign on the right-hand side of the foregoing equation denotes a decelerating torque. Integrating Eq. 5.85 by means of separation of variables gives

$$\int_{\Omega_0}^{\Omega} \frac{d\Omega}{\Omega^2} = -\frac{Q_0}{I_R \Omega_0^2} \int_0^t dt, \tag{5.86}$$

which after rearrangement gives the solution for the rotor rpm decay as

$$\frac{\Omega}{\Omega_0} = \frac{1}{1 + \dfrac{Q_0 t}{I_R \Omega_0}} = \frac{1}{1 + \dfrac{t}{\tau}} \tag{5.87}$$

and the corresponding buildup in rate of descent is

$$V_d(t) = gt\left(\frac{t}{t + I_R\Omega_0/Q_0}\right) = gt\left(\frac{t}{t+\tau}\right) \tag{5.88}$$

The time constant τ is

$$\tau = \frac{I_R\Omega_0}{Q_0} = \frac{I_R\Omega_0^2}{Q_0\Omega_0} = \frac{2KE_0}{P_0}. \tag{5.89}$$

Notice that KE_0 is simply the rotational kinetic energy of the rotor at $t = 0$. This means that rotors with higher initial levels of stored kinetic energy and lower power requirements (i.e., rotors with the lowest disk loading) will have the slowest rate of rpm decay after the removal of shaft torque and the slowest initial rate of descent. See also Section 5.6.3.

Generally, values of τ are found to vary from as low as about 1.5 seconds for the biggest and heaviest helicopters to about 4 seconds for the smallest and lightest helicopters. This means that for a typical helicopter the time for the rotor rpm to decay significantly is at most only a few seconds, and so the pilot's reaction to engine or transmission failure must be almost immediate. In the first instance, this will require a rapid reduction of collective pitch. In the second instance, the pilot will generally use cyclic pitch to seek the forward flight airspeed that will give the lowest autorotational rate of descent.

The safe rpm range in autorotation for most helicopters is usually between 80 and 120% of the normal rotor rpm, which is controlled by the pilot primarily by using collective pitch. If the rpm becomes too low, the rotor will begin to stall and excessive blade flapping will also occur because of reduced centrifugal effects on the blades. Conversely, if the rotor rpm becomes too high, then structural overload becomes a concern.

5.6.1 *Autorotation in Forward Flight*

The autorotative energy balance in forward flight is basically the same as for vertical flight. However, because of the forward flight velocity there is a loss of axial symmetry in the induced velocity and angles of attack over the rotor disk. This tends to move the distribution of parts of the rotor disk that consume power and absorb power, as shown in Fig. 5.26. The stalled region may become biased toward the retreating side of the disk. However, the basic physics of the autorotational problem remains unchanged. Estimates of the autorotative rate of descent in forward flight can be made using the power equation given in terms of the momentum and blade element theories. While at low airspeeds autorotation takes place in the turbulent wake state, which is not strictly amenable to analysis by momentum theory without empirical correction, with some forward speed the flow state becomes much smoother. This means that the standard power equation can give results that are sufficiently accurate for engineering estimates of the rate of descent in autorotation as long as averaged flow properties are considered.

In an autorotation $C_Q = 0$, so that to a first approximation (and neglecting the tail rotor) to the rate of descent and finding the speed to fly for minimum rate of descent we can use a rearrangement of the power equation (e.g., Eq. 5.53) to give

$$-\lambda_c \equiv \lambda_d \approx -\frac{\kappa C_W}{2\sqrt{\mu^2+\lambda^2}} - \frac{\sigma C_{d_0}}{8C_W}(1 + K\mu^2) - \frac{1}{2C_W}\left(\frac{f}{A}\right)\mu^3. \tag{5.90}$$

This equation applies down to descent angle and high rotor disk AoA, where the induced velocity through the rotor then needs to be modeled empirically – see also Section 12.8. The result for the rate of descent would normally be expressed in ft/min so that $V_d = 60\lambda_d\Omega R$.

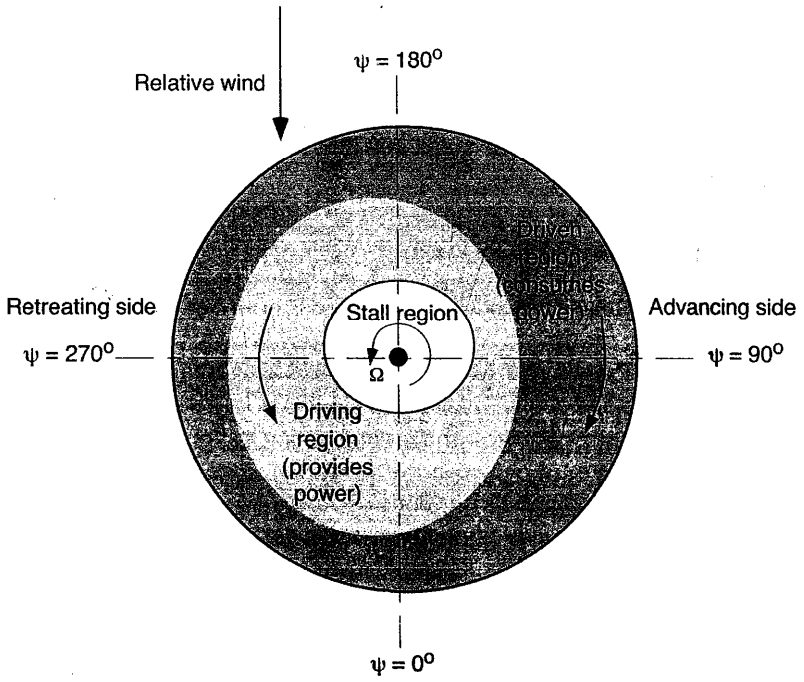

Figure 5.26 Autorotative torque distribution over the rotor disk in forward flight.

Representative results for the autorotative rate of descent in forward flight based on the use of the power equation are shown in Fig. 5.27. The shape of the curve mimics the power (or torque) required curve for steady level flight, as shown previously in Fig. 5.10 – see also Gessow & Myers (1947) and Wheatley (1932). Note the extremely high rates required at very low airspeeds, but for near V_{mp} (airspeed for minimum power under normal flight conditions), the rate of descent is reduced to about half the value required in axial (vertical) flight. Therefore, should a problem arise that requires the pilot to put the aircraft

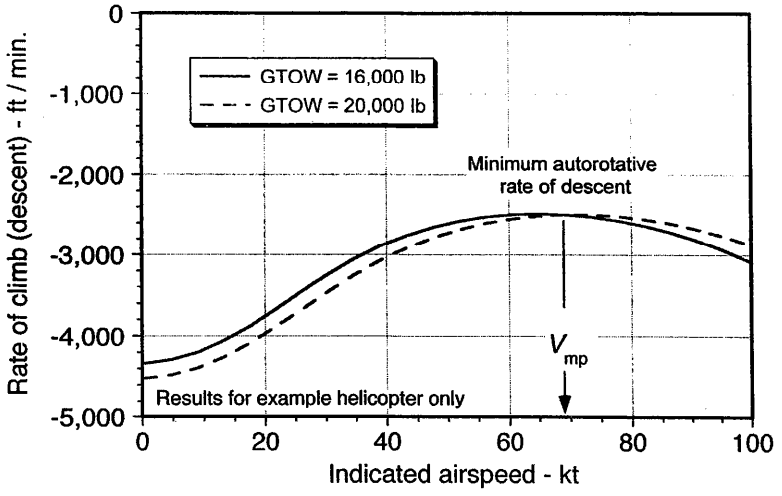

Figure 5.27 Estimates of rate of descent in autorotation for example helicopter.

into an autorotation, the airspeed should be immediately increased or decreased to V_{mp} to enable the lowest possible rate of descent. For example, if there is a mechanical problem in high-speed forward flight, the pilot would immediately pull back on the stick (application of longitudinal cyclic), to gain some additional altitude (zoom-climb) and lose airspeed, before quickly lowering the collective and entering the autorotation before the rotor rpm begins to decay.

Autorotations performed at or near V_{mp} will give the pilot more time to diagnose and even try to correct a possible engine problem. When established at the minimum rate of descent, the pilot will also have the maximum possible time to select a suitable landing site. It is likely that an actual autorotation will have to be performed away from the vicinity of an airport, and maximizing the time to complete the descent is essential for choosing a suitable landing area. Although the autorotative rate of descent is always high, the actual autorotative entry is a relatively safe and benign maneuver from the pilot's perspective when sufficient altitude is available. The final stages of the autorotation happen more quickly, however, and require great piloting skill. At about 50 ft (17 m) from the ground, the pilot must begin to decelerate the helicopter. This is done by slowly pulling up on the collective pitch (increasing blade pitch angles and so initially increasing rotor thrust), while simultaneously pulling back on the cyclic to flare the helicopter, increase the disk AoA, and reduce forward speed. As the collective pitch is increased, the unpowered rotor rpm will reduce quickly and so the pilot must ensure that the collective is brought in progressively and at a rate that still allows the rpm of the unpowered rotor to stay within acceptable values to produce thrust and prevent blade stall. Increasing the disk AoA to give the helicopter a steep nose-high attitude in the flare will tend to maintain rotor rpm as the component of forward velocity normal to the disk plane now helps to maintain the rotor in autorotation. The probability of success or otherwise of the resulting attempt at autorotation depends on many factors, including the exact pitch and roll angle of the helicopter when engine or mechanical failure occurred, overall pilot workload and the need to maneuver the helicopter as much as possible "into wind" to minimize ground speed at touchdown, and the need to find a suitable landing site free of obstructions.

It will be apparent that the time constant τ in Eq. 5.89 will also govern the decay of the rotor rpm as the pilot raises the collective pitch and uses cyclic pitch to flare the helicopter. Because a reduction in rotor rpm also decreases rotor thrust, the consideration of rotor stall margins are also important here. Because rotor thrust is essentially proportional to Ω^2 the lowest acceptable rotor rpm (Ω_{stall}) can be determined by using

$$\left(\frac{\Omega_{stall}}{\Omega}\right) = \sqrt{\frac{C_T/\sigma}{(C_T/\sigma)_{stall}}} = \sqrt{\frac{C_T/\sigma}{C_T/\sigma + \Delta(C_T/\sigma)_{stall}}}, \tag{5.91}$$

where the $\Delta(C_T/\sigma)_{stall}$ is the *stall margin* in terms of blade loading coefficient. Even though the stall margin on most helicopters at high gross weights is relatively modest, the allowable decay in rotor rpm during the flare maneuver is fairly generous while still avoiding stall. However, even without blade stall as an issue, the rotor rpm must also be maintained to avoid excessive blade flapping from flapwise blade inertia loads, especially as the helicopter touches down. There have been several serious accidents during the autorotative maneuver as a result of the pilot allowing low rotor rpm and so producing excessive blade flapping, which can cause the blades to strike the airframe. The overall objective for the pilot is to cushion the rate of descent such that the helicopter touches down with a rate of descent of less than about 10 ft s^{-1} (≈ 3 ms^{-1}) with minimal forward speed.

5.6.2 *Height–Velocity (H–V) Curve*

In a survey of helicopter accidents conducted by Harris et al. (2000), it was found that out of 8,436 accidents, 2,408 accidents occurred because of the loss of engine power. Out of these 2,408 accidents, about half were a result of fuel exhaustion. Nine hundred thirty-five accidents resulted in substantial damage to the helicopter and 445 helicopters were completely destroyed. Besides the tragic loss of lives, such statistics are certainly not acceptable from an engineering standpoint and clearly emphasize the need for better helicopter designs with adequate single engine out performance and safe autorotational landing capability.

The flight conditions that will allow safe entry to an autorotation and recovery of the helicopter are summarized in the form of height–velocity or "H–V" curves. These are often called "deadman's" curves, for obvious reasons. Figure 5.28 shows representative examples of the H–V curves for single-engine and multi-engine helicopters, which are typical of the information included in the aircraft flight manual. The curves that define the "avoid" regions are established though systematic test flights prior to certification of the helicopter. The tests are conducted at altitude relative to a virtual "floor" by incrementally approaching the

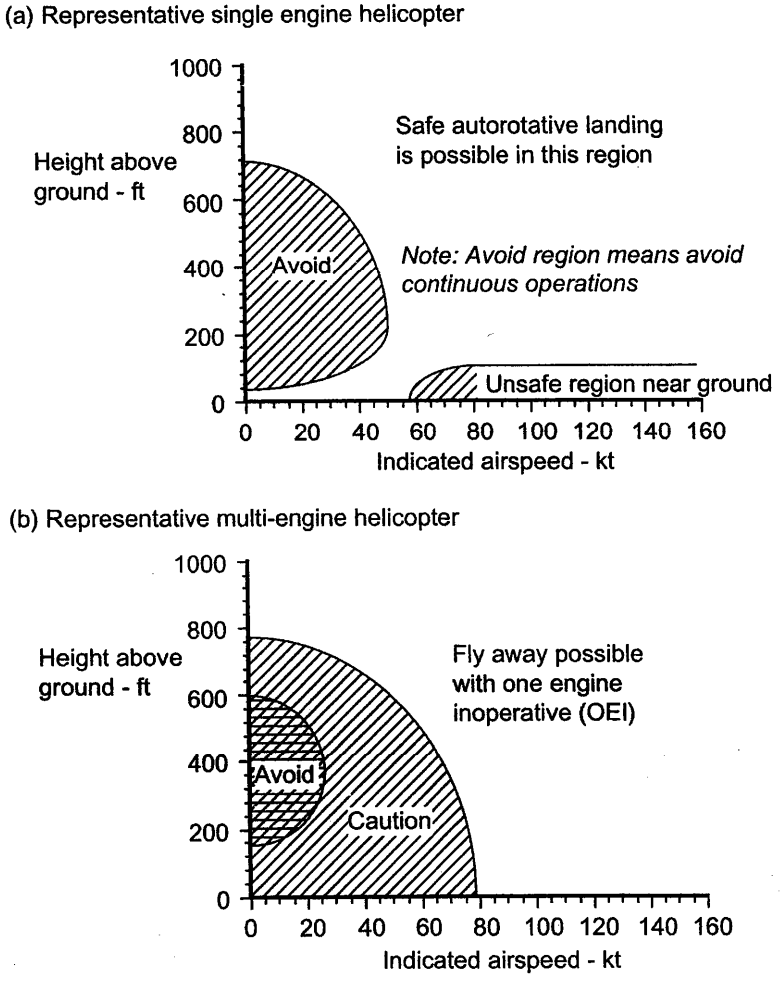

Figure 5.28 Representative height–velocity curves for single-engine and multi-engine helicopters. (a) Single-engine. (b) Multi-engine.

combinations of airspeed and altitude where acceptable autorotational capability becomes questionable on the basis of pilot opinions, that is, a difficulty rating. The engineering results are then corrected for different helicopter gross weights and density altitudes, and charts made for the flight manual. For flight anywhere outside the avoid region the pilot should be able to safely recover the helicopter through an autorotative maneuver in the event of a flight emergency. While flight in the avoid region is not prohibited, its boundaries dictate the conditions where sustained flight operations should be avoided less there be an engine failure.

The actual size and shape of the H–V curve depends on many factors, including the characteristics of the helicopter, its gross weight, and operational density altitude [see Pegg (1968)]. As shown in Section 2.13.7, the disk loading T/A is the primary factor influencing the autorotative rate of descent. The number of engines installed in the helicopter will also affect the shape of curves because flight operations (but at reduced performance) are possible, so multiple curves may be defined for single- and multi-engine operations. Note that for a single engine helicopter there are two unsafe regions defined by the H–V curve. The avoid region at low altitude and high airspeeds determines the minimum altitude below which translational kinetic energy cannot be converted into potential energy by means of a zoom-climb prior to entering the autorotation. This boundary is also marked to prevent unsafe operations close to the ground. The most important avoid region is obviously, however, at low airspeeds.

The bottom part of the H–V curve is defined as the lowest height from which a successful autorotation can be performed from a full-power climb out, with some prescribed allowance for pilot reaction time, that is, the time between the power failure and the reduction in collective pitch. Military and civil requirements usually differ, so that the limits of the curve will also vary with the model of helicopter. The FARs require a 1-second delay, whereas the military require 2 seconds to allow for the typically higher workload of military pilots. To establish the lowest portion of the H–V diagram (zero airspeed) it is normally assumed that this is the height above which a vertical power off landing cannot be made with damaging the aircraft. Under these conditions the pilot will rapidly increase collective pitch to cushion the landing at the expense of a rapid decay in rotor rpm. The top portion of the H–V curve is established for level flight power conditions, again by including some prescribed pilot reaction time. If a power or mechanical failure occurred at this combination of altitude and low airspeed the pilot would normally dive the helicopter to gain airspeed at the expense of altitude while attempting to maintain rotor rpm with collective, followed by a flare with aft cyclic pitch as the ground is approached. Emergency descents from points near to the "avoid" region always requires a high level of piloting skill.

Reducing the size of the avoid region is obviously desirable from an operational point of view but is generally difficult from an engineering perspective. Helicopters with low disk loading will tend to have a much smaller avoid regions; hence the autorotative characteristics of the helicopter usually enter into the basic sizing and design of the rotor (see Section 6.4.1). Increasing the stored rotational kinetic energy by adding blade mass is one possibility, but this is not desirable as it will be at the expense of higher blade stresses and a lower payload. For a multi-engine helicopter the unsafe or avoid region shrinks considerably, as shown in Fig. 5.28(b). For twin-engine helicopters, the avoid region diminishes to the point where there is only a slight chance that a fly-away or safe autorotation could not be performed. For three-engine helicopters the avoid region essentially disappears in the event of a single engine failure. However, there will always be some avoid regions marked on the H–V diagram in the event of a tail rotor failure, which will require an autorotation to be performed no matter how many engines are installed.

5.6.3 *Autorotation Index*

It is clear that the autorotative performance of a helicopter depends on several interrelated factors. These include the rotor disk loading (which affects the descent rate), the stored kinetic energy in the rotor system (which influences the probability of success of entry and completion of the autorotational maneuver), as well as subjective "difficulty rating" flight assessments by pilots. To help select the rotor diameter during predesign studies, an "autorotative index" is often used. Although various types of indices have been used [see White et al. (1982) for a summary] the autorotation index is basically a stored energy factor. One form of the index can be defined in terms of the ratio of the kinetic energy of the main rotor to the gross weight of the aircraft, that is,

$$AI = \frac{I_R \Omega^2}{2W}, \tag{5.92}$$

which is used by Bell – see Wood (1976). An alternative autorotative index used by Sikorsky, which is weighted by disk loading [see Fradenburgh (1984)] is

$$AI = \frac{I_R \Omega^2}{2WDL}. \tag{5.93}$$

These indices may be modified to reflect the effects of higher density altitudes by using, for example, with the latter index

$$AI = \frac{I_R \Omega^2}{2WDL}\left(\frac{\rho}{\rho_0}\right). \tag{5.94}$$

Figure 5.29 shows the autorotative index for several helicopters, which have been calculated using Eq. 5.93 based on published information for each helicopter. These indices are of great use in the sizing of the main rotor or in examining the effects on autorotative characteristics with increasing gross weight or density altitude. Note that the absolute values of the index are of no significance by themselves, but the relative values provide a means

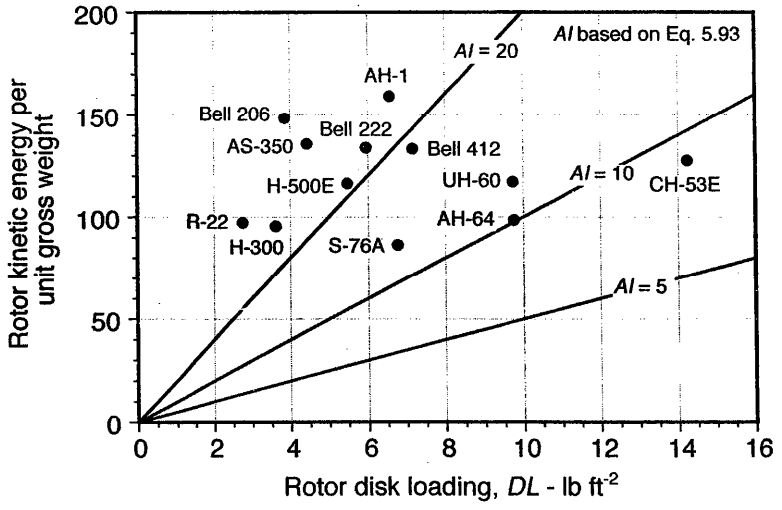

Figure 5.29 Autorotative indices derived for several helicopters at standard sea level conditions. Data source: Various published helicopter specifications.

of comparing the autorotative performance of a new helicopter design against another helicopter with already acceptable autorotative characteristics. An index of about 20 would normally be considered acceptable for single-engine helicopters. A multi-engine helicopter can have a lower index and still have safe flight characteristics in the event of a single engine failure because any initial decay in rotor rpm is soon picked up by increasing torque from the remaining engine(s).

The autorotative characteristics of the helicopter may also be expressed in terms of equivalent hover time – see Wood (1976). This is the time that the stored kinetic energy in the rotor system can supply sufficient equivalent power to hover before the rotor rpm decays to the point that stall occurs (see previous discussion on page 245). This "equivalent time" parameter seems to correlate well with pilot opinion of autorotative characteristics – see Prouty (1986) for a summary. Based on the results of Wood (1976), a helicopter with an equivalent hover time of 3 or more seconds is ideal but rarely possible, but a goal for a new helicopter will be to design for at least half of this value to assure sufficient margins in autorotational capability to be safe for an average pilot.

5.7 Vortex Ring State (VRS)

The phenomenon of vortex ring state (VRS) has been previously mentioned in Section 2.13.6. Under descending flight conditions at high rates or at steep descending flight path angles, helicopter rotors can begin to operate in this adverse flight condition. For VRS to occur, the upward component of velocity normal to the rotor disk plane must be a substantial fraction of the average induced velocity downward through the rotor disk. In the VRS the wake vorticity produced by the blades cannot convect away from the rotor. Instead, the wake accumulates near the rotor plane, clumping or bundling together forming a violent, unsteady flow condition that is analogous to flight in a "vortex ring" – see Fig. 2.21. An early effort to analyze the VRS problem for a helicopter rotor was made by de Bothezat (1919).

Entry into the VRS manifests as rotor thrust fluctuations and also an increase in the average rotor-shaft torque (power required), the latter which is necessary to overcome the higher induced aerodynamic losses associated with rotor operations inside its own blade wake. Most helicopters do not have a lot of excess power available at low airspeeds, so the extra power required to overcome these additional induced losses can be of sufficient magnitude to negate the decreased rotor power requirements associated with giving up altitude (potential energy). Therefore, when in the VRS, the application of high rotor torque (power) may be required to maintain equilibrium flight, even though the aircraft is rapidly descending. This scenario is often referred to by pilots as "power settling" or "settling with power" and can be a safety of flight issue – see Varnes et al. (2000). These latter terms, however, are not accurate descriptors of VRS conditions because such "settling" issues can also occur under operational flight conditions when VRS is clearly not present, such as when a helicopter transitions from hover into forward flight while in ground effect (see Section 5.8) or climbs out of ground effect at high gross weights or high density altitudes.

5.7.1 *Quantification of VRS Effects*

Washizu et al. (1966) have quantified the increased induced power measured during equilibrium descent through the VRS in terms of a power loss factor, κ, where

$$\kappa = \frac{P_i}{T v_i} = \frac{C_{P_i}}{C_T \lambda_i} \tag{5.95}$$

where P_i is the induced part of the rotor power and v_i refers to the average induced velocity through the rotor as given by the simple momentum theory (see Chapter 2). The induced velocity can be determined from an estimate of the induced power, which is obtained from the measurements of total shaft power by assuming that the profile power, P_0, is a function of the rotor thrust alone and does not depend on V_c, that is, in an approach similar to that given in Section 2.13.3 to define the induced power curve in the region where momentum theory is invalid. However, this approach is only approximate and stall effects (which may be produced as a result of the high angles of attack inboard on the blades at high rates of descent) may need to be accounted for. The induced power can then be calculated by subtracting the profile power and loss of potential energy per unit time from the total measured power using $C_{P_i} = C_P - C_{P_0} - \lambda_c C_T$, from which the average induced velocity ratio can be obtained from $\lambda_i = C_{P_i}/C_T$. The induced power loss factor then follows from Eq. 5.95 and is essentially a measure of the extra induced power required by the rotor as compared to the momentum theory solution to produce thrust as it descends into its own vortical wake.

The measured values in Fig. 5.30 show the variation of κ as a function of descent velocity, where it is noted that a maximum induced loss occurs for this helicopter rotor configuration around a nondimensional descent rate of $V_d/v_h \approx 1.2$ ($V_c/v_h \approx -1.2$). This is consistent with flow visualization and other experimental evidence shown in Section 2.13.6, which suggests that this condition is deeply into the VRS. It is clear also that in autorotation, which is where $V_d/v_h \approx 1.9$, the rotor returns to having a fairly low induced power factor.

The VRS is accompanied by an extremely unsteady (aperiodic) flow field surrounding the rotor. This behavior is illustrated by the experimental results of Yaggy & Mort (1963), as shown in Fig. 5.31, where the measured rotor thrust fluctuations for a rotor in vertical descent are plotted as a percentage of its mean thrust. At low rates of descent notice that the data essentially collapse to a single curve for all values of disk loading. Because rotor thrust fluctuations in VRS are produced by interactions with its own wake as it comes close to the rotor, then the amplitude of the fluctuations should be related to the mean thrust.

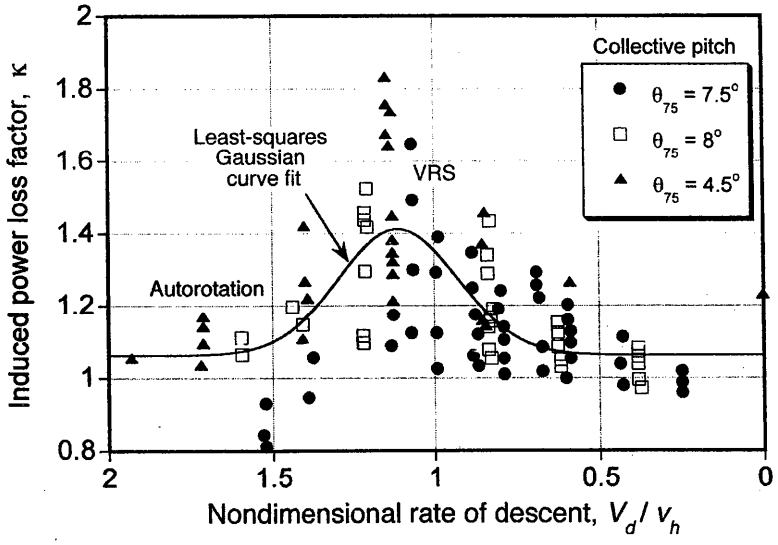

Figure 5.30 Measured induced power factor in vertical descending flight through the vortex ring state. Data source: Washizu et al. (1966).

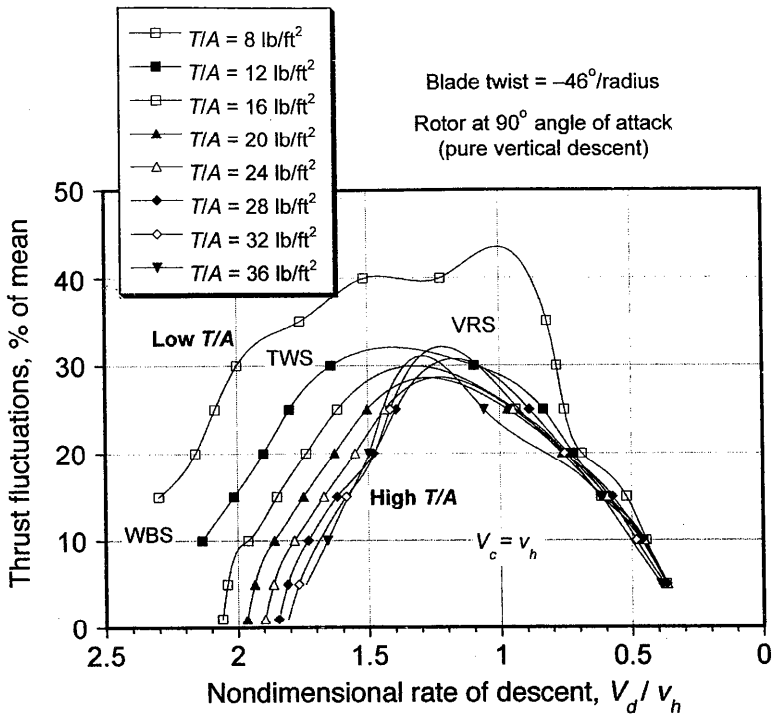

Figure 5.31 Measured rotor thrust fluctuations in vertical descending flight through the vortex ring state for different values of disk loading. Data source: Yaggy & Mort (1963).

Therefore, a correlation with disk loading at low rates of descent is to be expected. Notice that the thrust fluctuations build up rapidly as the vertical rate of descent increases, reaching a maximum at $V_d/v_h \approx 1.2$. Thereafter, the fluctuations decrease rapidly as the rotor enters into the turbulent brake state (TWS) and then the windmill brake state (WBS), where the wake is now expanding above the rotor (see also Fig. 14.18).

The experimental results in Fig. 5.31 show a marked dependence on disk loading near VRS, a point discussed by Brown et al. (2002). Disk loading and blade loading (the latter which is related to mean lift coefficients and so to stall proximity) are proportional for a given rotor, and so the observed change in rotor loads with disk loading suggests that the measured data probably contains some evidence of blade stall. This effect is much less clear from the results of Washizu et al. (1966) or Betzina (2001) because there are insufficient data to allow for an interpolation of points to constant values of disk loading. Nearly all of the VRS data in the literature have been obtained from subscale model rotor tests at fixed collective pitch. This makes it difficult to isolate the effects of blade loading on the rotor aerodynamics in the VRS, so to predict how VRS may differ for different rotor configurations (i.e., rotors with different geometric characteristics). However, in nearly all cases the peak amplitude of the unsteady thrust fluctuations lies close to the conditions where the rate of descent is equal to the induced velocity through the rotor.

Yaggy & Mort (1963) also show that a rotor with larger blade twist exhibits larger thrust fluctuations in the VRS. Blade twist affects the distribution of induced velocity over the disk, the position of the tip vortices in the wake and, therefore, the points over the disk that first approach VRS conditions. Leishman et al. (2002) also made this point based on theoretical arguments of wake stability and the onset of wake breakdown in descending

flight. Therefore, it would seem that attempts to generalize the behavior of a rotor as it approaches VRS without reference to the interdependent effects of disk loading or geometric parameters (such as blade planform and blade twist) would be inappropriate.

As previously mentioned, the conditions leading to the onset of the VRS may be obtained under a number of different flight conditions, including situations in forward flight where the rate of descent is low but the disk AoA is high. For example, this situation could be obtained operationally during certain types of maneuvers, such as descending pull-ups at moderate to high airspeeds. Unfortunately, there are fewer experimental results for these conditions. Yet, both the flow visualization of Drees & Hendal (1951) and the thrust fluctuations measurements of Yaggy & Mort (1963) and Betzina (2001) suggest that the strongest unsteady VRS conditions can be obtained at high rates of descent but with some small forward speed (i.e., a small edgewise component of flow velocity parallel to the disk). The problem, however, is the accurate determination of the induced velocity through the rotor under these conditions.

For an inclined descent when the AoA of the disk is α_{TPP}, the velocity components normal and parallel to the rotor disk are $-V_c \sin\alpha_{TPP}$ and $V_c \cos\alpha_{TPP}$, respectively. The results for the induced velocity through the rotor are shown in Fig. 5.32 for a range of AoA. It is interesting that the measurements follow the same trend as given by the momentum theory (Section 2.14.4), although this should not be construed as an endorsement of its applicability in this regime. Momentum theory does, however, underpredict the value of the induced velocity and clearly does not predict the inherent unsteady fluctuations, which is of course a fundamental characteristics of the rotor flow state when in the VRS. Notice that the fluctuations drop off quickly as the disk AoA decreases below 50° and is consistent with piloting experience on helicopters, which shows that a forward speed component causes the rotor to quickly exit the VRS. The results in both Figs. 5.30 and 5.32 are useful in that they provide the analyst with at least some quantifiable basis for estimating the rotor power requirements in steeply descending flight and possibly determining the flight conditions that may result in the phenomenon of "power settling" for a specific type of helicopter.

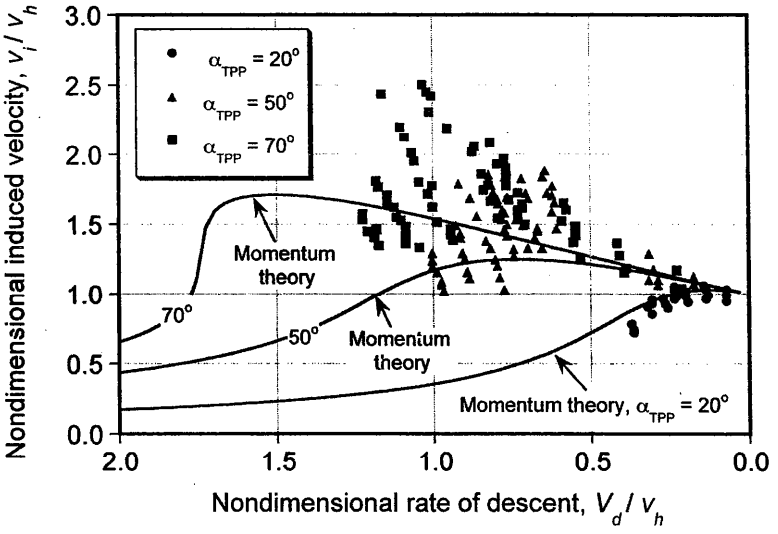

Figure 5.32 Estimated induced velocity in inclined descending flight. Data source: Washizu et al. (1966).

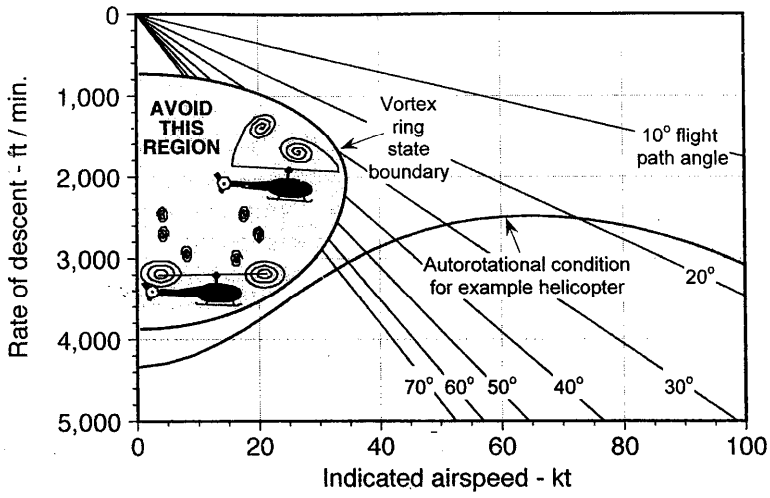

Figure 5.33 The boundary where vortex ring state is encountered is limited to low airspeeds and high rates of descent. Notional data only – does not represent any particular helicopter.

5.7.2 *Implications of VRS on Flight Boundary*

The adverse conditions associated with VRS mostly occur within a boundary confined to a part of the flight envelope at low forward airspeeds and at steep angles of descent or high rates of descent – see Fig. 5.33. Such results, however, are not general and the VRS boundary is known to be helicopter specific. In all cases, however, the unsteady flow conditions obtained during flight in or near VRS may result in highly unsteady blade airloads, significant rotor vibrations and unpredictable, aperiodic blade flapping. The blade flapping can lead to substantial loss of control effectiveness and high piloting workload. The rotor thrust fluctuations (see Fig. 5.31) usually lead to low-frequency vertical vibrations and an unpleasant bouncing of the helicopter. While operation in the VRS is obviously undesirable, it can be entered inadvertently through poor piloting technique. Recovery is usually attained quickly, however, by the application of cyclic control inputs to cause some increase in forward or sideward airspeed to sweep the recirculating wake away from the rotor disk.

Instrumented flight tests documenting the VRS behavior of helicopters are sparse, mainly because it is a difficult flight condition to sustain any form of equilibrium flight. The flight tests of Brotherhood (1949), Stewart (1951), and Scheiman (1964) have documented the highly unsteady blade loads and high rotor power requirements found during flight in the VRS. Several researchers have conducted laboratory tests with rotors operating in the VRS, although few detailed flow field measurements have actually been obtained. This has been paralleled by some limited modeling efforts to predict the flight boundaries for the onset of VRS, mostly using forms of the classical momentum theory – see Wolkovitch (1972), Heyson (1975), Peters & Chen (1982), Newman et al. (2001), and Prasad et al. (2004). While momentum theory seems to predict a reasonable lower bound of the time-averaged induced velocity at the rotor disk and also the average induced power requirements, but it is not a rigorous approach to the problem. Momentum theory based models are deficient in predicting the conditions leading to VRS because of the ambiguity in defining a single flow direction and a well-defined slipstream boundary over which to apply the governing

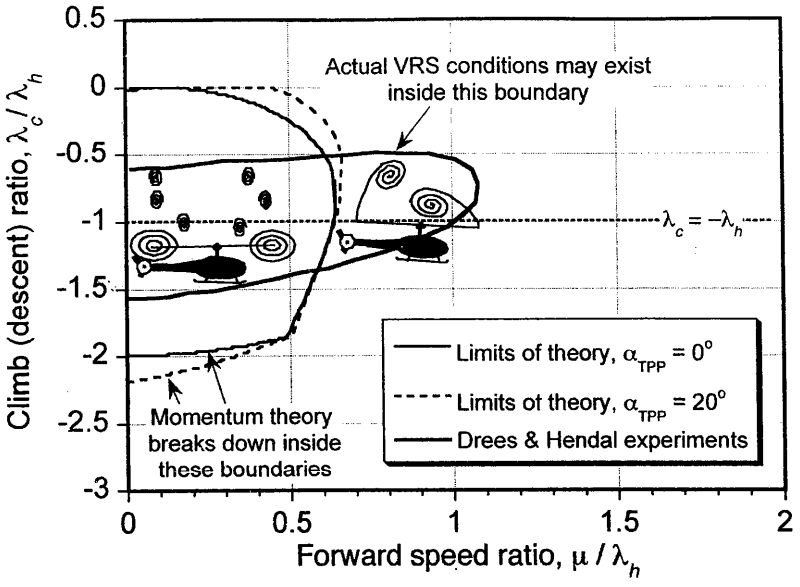

Figure 5.34 The vortex ring state boundary exists within a domain where the classical momentum theory is strictly invalid.

equations, this issue already having been discussed in Chapter 2. This problem is illustrated in Fig. 5.34 in terms of the combination of normalized rates of descent and forward flight velocity over which momentum based theories become strictly invalid, along with the VRS boundary estimated from the classic experiments of Drees & Hendal (1951).

Another limitation with the momentum theory is that it does not provide any indication as to the effects of rotor geometric parameters (e.g., number of blades, rotor solidity, blade planform, or twist) or rotor configuration (e.g., conventional, side-by-side, tandem overlapping etc.) on the VRS problem. This is a significant deficiency that must be treated by alternative mathematical models of VRS, such as based on vortex theory – see, for example, Leishman et al. (2002). It would seem that because VRS is a nonlinear function of rotor disk loading, amongst a host of other operational and geometric parameters, it would seem unwise to generalize results obtained from tests on one rotor or any given helicopter in an attempt to predict the behavior of another helicopter. The inherent flow complexity of the VRS would seem to pose a good practical problem for advanced computational fluid dynamics methods, although the challenge has not yet been taken up except using vorticity transport methods (see Sections 14.3 and 14.10.7). One difficulty is in preserving the fidelity of the wake to older wake ages, the wake dynamics being inherent to the problem of VRS. Further discussion of the VRS problem using free-vortex methods is made in Section 10.10.

5.8 Ground Effect

Helicopter performance is affected by the presence of the ground or any other boundary that may alter or constrain the flow into the rotor or constrain the development of the rotor wake. The effect has long been recognized, but the aerodynamics of the rotor under these conditions are still not fully understood. "Ground effect" is of concern both in actual flight operations as well as in the wind tunnel or hover tower testing of rotors.

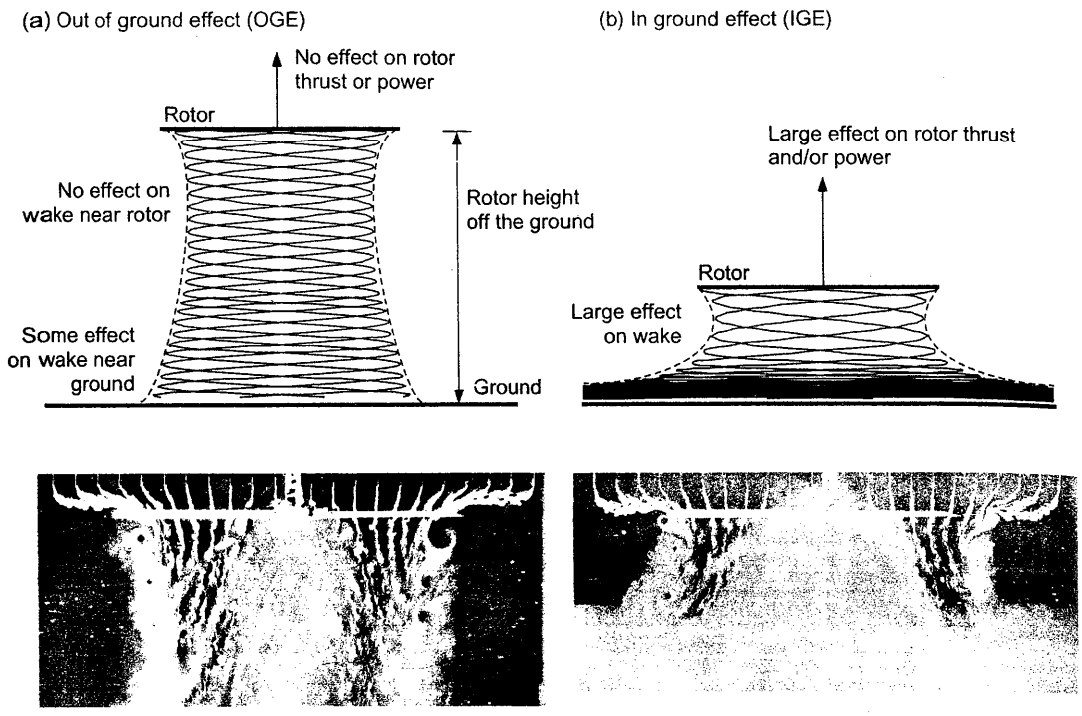

Figure 5.35 The behavior of the wake from a hovering rotor: (a) Out of ground effect (OGE). (b) In ground effect (IGE). (Flow visualization photos courtesy of Sikorsky Aircraft.)

5.8.1 *Hovering Flight Near the Ground*

Consider a rotor hovering in close proximity to the ground, as shown in Fig. 5.35. Because the ground must be a streamline to the flow, the rotor slipstream tends to rapidly expand as it approaches the surface. This alters the slipstream velocity, the induced velocity in the plane of the rotor, and, therefore, the rotor thrust and power. Similar effects are obtained both in hover and forward flight, but the effects are strongest in the hovering state. Other visualization of the flow of hovering rotors operating in ground effect are shown by Taylor (1950) and Light & Norman (1989). Systematic studies of rotors operating in ground effect were first conducted by Knight & Hefner (1941).

When the hovering rotor is operating in ground effect, the rotor thrust is found to be increased for a given power. A representative plot of the thrust ratio in hover versus height from the ground is shown in Fig. 5.36. This plot has been derived from several experiments with rotors operating at different blade loadings, as discussed by Zbrozek (1947) and others, including Betz (1937), Knight & Hefner (1941), Cheeseman & Bennett (1955), Fradenburgh (1960, 1972), Stepniewski & Keys (1984), and Prouty (1985). Hayden (1976) gives a comprehensive summary of flight test measurements of ground effect using the standardized technique of Lewis (1972). The results suggest significant effects on hovering performance for heights less than one rotor diameter. The results are also dependent somewhat on blade loading (or mean lift coefficient), blade aspect ratio, and blade twist. Yet, within the bounds dictated by most helicopters a universal behavior seems a good approximation for engineering estimates of the phenomenon. Besides the effects on actual helicopter performance, these results provide useful guidelines for laboratory testing of rotors in hovering flight,

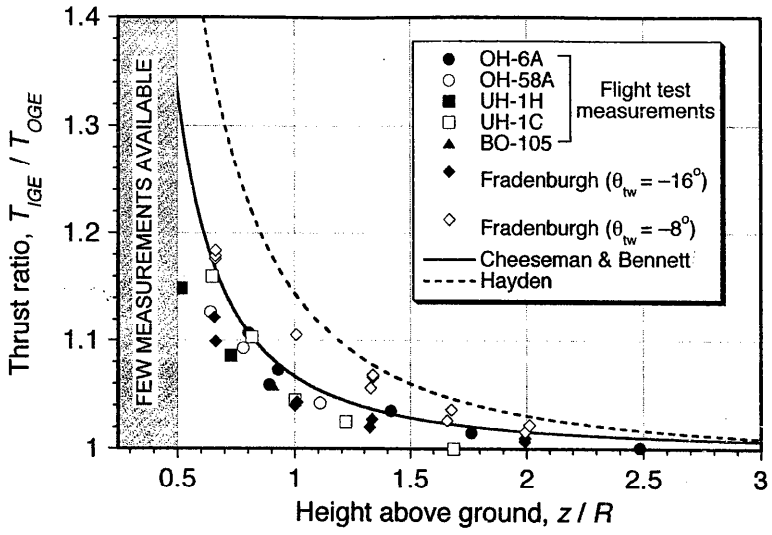

Figure 5.36 Increase in rotor thrust versus distance from the ground for a variety of helicopters. Data sources: Fradenburgh (1972) and Hayden (1976).

where a minimum distance of at least $2R$ from the ground is required to ensure performance measurements that are free of interference effects.

The problem of ground effect can also be viewed as a reduction in power for a given thrust. Most of the power reduction is induced in nature, but there is also some small reduction in profile power because the blade angles are operating at a somewhat lower AoA to produce the same thrust. Because of ground effect there is an important operational advantage to be gained, namely that the lower power required will allow the helicopter to hover in ground effect (IGE) at a higher gross weight or density altitude than would be possible out of ground effect (OGE). The extra thrust or reduction in power requirements that is felt near the ground will also "cushion" the descent of the helicopter when landing.

Ground effect in hovering flight has been examined analytically, albeit approximately, by means of the method of images. Cheeseman & Bennett (1955) replaced the rotor by a simple source with an image source to simulate ground effect and obtained some analytic relationships for the effects of the ground. Knight & Hefner (1941) and Rossow (1985) have used a vortex cylinder model. Based on Cheeseman & Bennett's analysis, ground effect on the rotor thrust can be expressed by the equation

$$\left[\frac{T}{T_\infty}\right]_{P=\text{const}} = \frac{1}{1 - \dfrac{(R/4z)^2}{1 + (\mu/\lambda_i)^2}}, \tag{5.96}$$

where z is the height off the ground and λ_i is the induced velocity at the rotor. This equation has a validity of $z/R \geq 0.5$. Incorporating the effect of blade loading they obtained

$$\left[\frac{T}{T_\infty}\right]_{P=\text{const}} = \frac{1}{1 - \dfrac{\sigma C_{l_\alpha} \lambda_i}{4C_T} \dfrac{(R/4z)^2}{1 + (\mu/\lambda_i)^2}}, \tag{5.97}$$

although C_T/σ has a secondary effect. For hovering flight and neglecting any blade-loading effects this latter result simply becomes

$$\left[\frac{T}{T_\infty}\right]_{P=\text{const}} = \frac{1}{1-(R/4z)^2}. \tag{5.98}$$

Figure 5.36 shows that this equation gives good agreement with the experimental measurements. Because ground effect can be expressed in terms of the increase in thrust at a constant power, then $\lambda_{IGE}\, C_{T_{IGE}} = \lambda_{OGE}\, C_{T_{OGE}}$ or

$$\frac{\lambda_{IGE}}{\lambda_{OGE}} = \frac{T_{OGE}}{T_{IGE}} = k_G. \tag{5.99}$$

Alternatively, the influence of ground effect in hover can be viewed as a reduction in the rotor induced velocity (at a constant thrust and height above the ground) by a factor k_G such that

$$\left[\frac{\text{Power required IGE}}{\text{Power required OGE}}\right]_{T=\text{const}} = \left[\frac{P_{IGE}}{P_{OGE}}\right]_{T=\text{const}} = \left[\frac{C_{p\ IGE}}{C_{p\ OGE}}\right]_{T=\text{const}} = k_G. \tag{5.100}$$

This means that up to a 25% reduction in the induced velocity and the induced power is possible with the Cheeseman & Bennett model.

Using a relatively simple model, Betz (1937) has suggested the effect on the rotor power at a constant thrust to be modeled by the equation

$$\left[\frac{P_{IGE}}{P_{OGE}}\right]_{T=\text{const}} = k_G = \frac{2z}{R}. \tag{5.101}$$

Hayden (1976) has used flight test measurements to find the influence of the ground in hover. The profile part of the total power was assumed to be isolated from the induced effect such that only the induced effect is influenced by the ground, that is,

$$P = P_0 + k_G(P_i)_{IGE}, \tag{5.102}$$

where k_G is derived from a curve fit to the experimental data using

$$k_G = \frac{1}{A + B(2R/z)^2} \tag{5.103}$$

with $A = 0.9926$ and $B = 0.0379$. As shown by Fig. 5.36, when viewed in terms of an increase in thrust for a given power, Hayden's result is found to slightly overpredict the rotor thrust. In all cases it is apparent that the effects of the ground on the rotor performance become negligible for rotors hovering greater than three rotor radii above the ground.

5.8.2 *Forward Flight Near the Ground*

The effects of the ground on rotor performance in forward flight are also significant, but here the flow state near the rotor tends to be even more complicated. The typical behavior is shown in Fig. 5.37, which is adapted from the work of Curtiss et al. (1984, 1987). At low forward speeds, a region of flow recirculation is formed upstream of the rotor near the ground. This phenomena has negligible effects on performance but may throw loose surface material up into the air that may be reingested by the rotor. As forward speed increases, this recirculation develops into a small vortical flow region between the

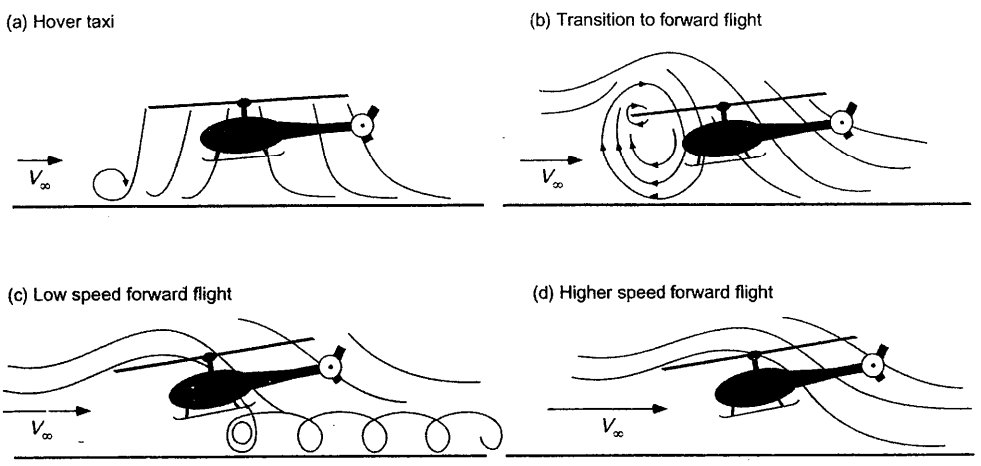

Figure 5.37 Flow characteristics for a rotor in forward flight near the ground: (a) hover taxi. (b) transition to forward flight. (c) low speed forward flight. (d) higher speed forward flight. Adapted from Curtiss et al. (1984, 1987).

ground and around the leading edge of the rotor. This vortex has been documented both in wind-tunnel experiments and helicopter operations in the field. For helicopters operating in a dusty or snowy environment the flow recirculation upstream of the rotor becomes particularly evident. This recirculation increases the inflow through the forward part of the rotor disk, and, as a consequence, the induced power requirements will increase above that required for hover IGE. The pilot, therefore, experiences a form of "power settling" unless collective pitch is increased to maintain altitude as the aircraft transitions into forward flight. Above a critical advance ratio, which depends on aircraft weight (rotor thrust) and proximity to the ground, a well-defined horseshoe vortex (ground vortex) is formed under the leading edge of the rotor near the ground. With further increases in airspeed, this phenomenon disappears as the rotor wake is skewed back by the oncoming flow. Ground effect is usually considered negligible for $V_\infty > 2v_h$ or for advance ratios greater than about 0.10. See also Section 14.10.6 for a further discussion of ground effect on rotor aerodynamics.

A representative set of results of rotor power in forward flight for operations in both IGE and OGE is shown in Fig. 5.38, which is reproduced from the wind-tunnel measurements of Sheridan & Weisner (1977). The advantages of ground effect are apparent for hover and very low airspeeds, where the effects indicate considerable power reductions compared to flight OGE. Note that for operation IGE the power increases rapidly as the helicopter transitions from the hover state. This is because of the formation and influence of flow recirculation at the leading edge of the rotor disk, as previously alluded to, which causes the rotor to experience a higher induced inflow than for hovering flight IGE. This increases slightly the power requirements, as previously mentioned. Similar types of results showing the same effects have been obtained by Cheeseman & Bennett (1955) on the basis of flight tests.

Similar rotor–ground plane interference effects are noted in wind tunnel tests on rotors, where the effects of the tunnel floor (as well as the ceiling and side walls, if present) can alter the induced flow through the rotor. Ganzer & Rae (1960) and Lehman & Besold (1971) have studied the effects experimentally. If the objective is to simulate free-air conditions with the rotor, then the presence of the walls on rotor performance cannot be easily discounted,

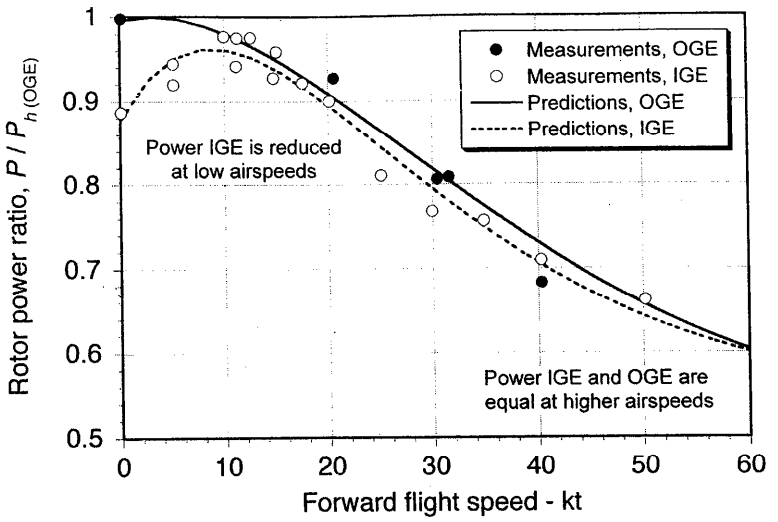

Figure 5.38 Measurements and predictions of rotor power versus forward speed when operating near the ground. Data source: Sheridan & Weisner (1977).

especially at low airspeeds. For tunnel dimensions that are at least twice the diameter of the rotor, the effects of the wind tunnel walls are small for advance ratios greater than 0.1. Generally, it must always be assumed that the effects of the tunnel walls will lead to some flow recirculation at lower advance ratios (say, $\mu < 0.1$) making reliable free-air measurements of rotor performance difficult or impossible, even if suitable corrections could be derived – see also Philippe (1990). Measurement of the wall pressure signatures allows the investigator to monitor interference effects and help define the lowest allowable wind speed for a given rotor thrust and/or advance ratio that can be tested without the results being contaminated by wall interference effects. Deviations of the wall pressures from their static values will be a sensitive indicator of such interference effects, although correcting the rotor measurements is a more difficult problem. It would seem that minimizing the interference effects in the first place is the best strategy for testing helicopter rotors, which suggests the use of large wind tunnels or wind tunnels with open working sections.

Other studies of the flows associated with rotors operating IGE have used both vortex methods and grid-based computational fluid dynamic (CFD) methods. A free-vortex wake model is described by DuWalt (1966) who assumed an axisymmetric, periodic wake. Ground effect was simulated by modeling the problem as a mirror image wake below the ground plane, and studies were conducted for varying rotor heights and advance ratios. Similar types of models have been developed by Saberi & Maisel (1987), Quackenbush & Wachspress (1989), Graber et al. (1990), Itoga et al. (1999), and Griffiths & Leishman (2002). While predictions of wake behavior in hover and in forward flight has been demonstrated, relatively limited success has been achieved in correctly predicting rotor performance IGE when compared to experimental results. This reflects the inherent complexity and strongly viscous nature of the rotor IGE flow problem. The use of most forms of CFD methods do not yet have seen to have reached the maturity for predicting rotor performance IGE, but approaches such as that discussed by Moulton et al. (2004) at least seem promising for predicting the effects of the rotor downwash at regions below the rotor, which is important for several operational reasons. The best current quantitative levels of predictive success for ground effect problems using CFD have been achieved using vorticity transport models – see Section 14.3.

5.9 Performance in Maneuvering Flight

Maneuver requirements will set the ultimate flight capability for a helicopter. Therefore, the prediction of the rotor airloads under maneuvering conditions forms an essential part of the overall design process. Yet this is a difficult task made even more complicated by the generally nonlinear aerodynamics of the rotor, and the complex kinematics of the rotor and the helicopter under most types of maneuvering flight conditions – see Padfield (1996) for an overview of the issues. Limiting aerodynamic factors in maneuvers may include stall and the effects of the wake, which can induce vibratory airloads from blade vortex interactions. The proper prediction of helicopter maneuvering performance is an illusive goal that will challenge helicopter analysts for years to come.

Maneuver issues are of particular importance for military helicopters – see Lappos (1984). A modern military helicopter may be required to perform maneuvers consisting of high load factor turns and pull-ups, steep turns and rollovers (see Fig. 5.39), arrested high rates of descent in combat landing zones, and quick pop-up–pop-down maneuvers for battlefield observation – see Thomson & Bradley (1990). Rotor stall issues are often a key consideration under these conditions because of the extra thrust demanded from the rotor, and sufficient stall margins must be incorporated into the rotor design. Both military and civil requirements will dictate the rotor capabilities that must be demonstrated without the rotor stalling. Maneuvers cause the rotor flapping response to lag with respect to the maneuver rates of the helicopter, which can also affect blade angles of attack and stall margins – see discussion in Section 6.9.3. Consideration of rotor noise levels and retention of good helicopter handling qualities have also become important factors in the design of helicopters with good maneuver capabilities.

The ability of a helicopter to maneuver (such as a pull-up or sustained horizontal turn) depends, in part, on the excess thrust possible from the rotor and the excess power available

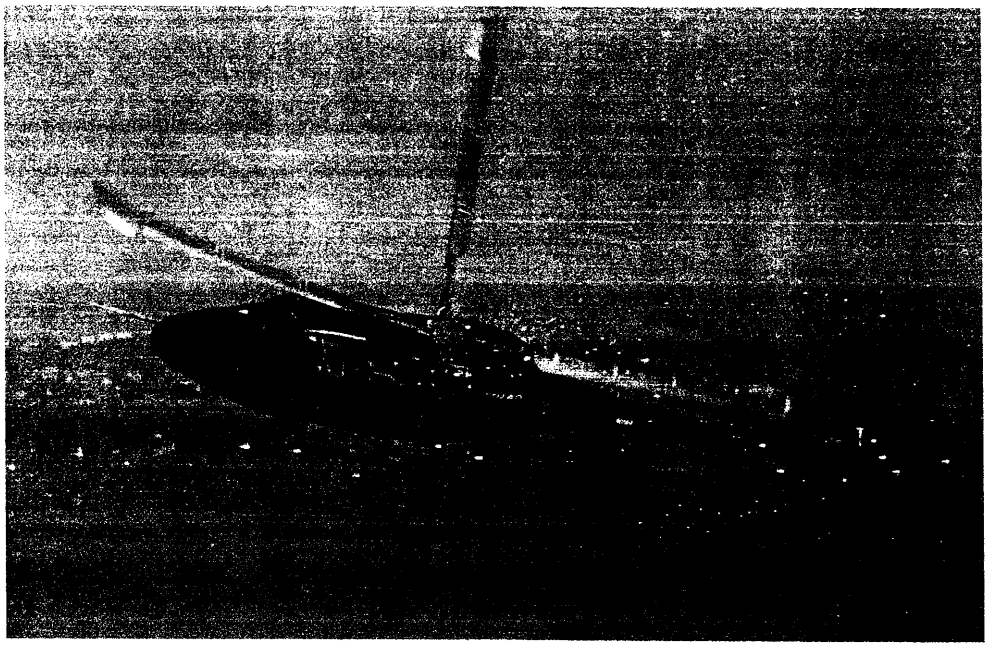

Figure 5.39 A Lynx helicopter executing a steep banked turn maneuver. (Photo courtesy of Agusta–Westland via F. John Perry.)

over and above that required for level, unaccelerated flight. The load factor on the rotor, n, can be defined as the net thrust of the rotor divided by the gross weight of the helicopter, that is, $n = T/W$. The ability to produce a given load factor on the rotor depends on: 1. The ability of the helicopter to actually sequence a maneuver with the use of normal flight controls; 2. The effective management of potential, translational kinetic, and rotor rotational kinetic energy by the pilot through the use of flight controls; 3. The excess energy or power available at that airspeed (i.e., having excess translational kinetic energy or an engine with sufficient power margin); 4. The ability of the rotor to actually use that excess power and produce a load factor without stalling (i.e., the rotor must be designed to have sufficient stall margin); and 5. The structural strength and aeroelastic margins of the rotor at the higher accelerations and load factors associated with maneuvering flight. Therefore, the ability of the rotor to produce and sustain a load factor can be viewed as one measure of the ability of the helicopter to maneuver. The problem of defining a load factor, however, can be a relatively complicated one for a helicopter when all the kinematic relationships of AoA, sideslip and bank angle are taken into account; the load factor measured by an accelerometer on the aircraft is not necessarily the same as the load factor being produced by the rotor – see Chen & Jeske (1981).

5.9.1 *Steady Maneuvers*

For steady (nontransient) maneuvers, the forces acting on the helicopter can be assumed to act in equilibrium. A classic problem is a level banked turn, which is considered by Saunders (1975) and Prouty (1986). By assuming the helicopter to act as a point mass, the centripetal acceleration required to perform a turn with a flight path of radius R_{turn} will be $V_\infty^2/R_{\text{turn}}$, where V_∞ is the true airspeed. With reference to Fig. 5.40(a), the rotor thrust required must overcome both weight W and centrifugal force F_{CF} giving

$$T = \sqrt{W^2 + F_{\text{CF}}^2} = \sqrt{W^2 + \left(\frac{W}{g}\frac{V_\infty}{R_{\text{turn}}}\right)^2}. \tag{5.104}$$

This result, of course, assumes that the tail rotor makes a negligible contribution to the problem. The load factor on the rotor is, therefore,

$$n = \frac{T}{W} = \sqrt{1 + \left(\frac{V_\infty^2}{gR_{\text{turn}}}\right)^2}, \tag{5.105}$$

where n is the rotor load factor ($n = 1$ in level, unaccelerated flight) and g is acceleration under gravity. The bank angle required [refer to Fig. 5.40(b)] will be

$$\phi = \cos^{-1}(1/n) \tag{5.106}$$

and so for equilibrium the rotor thrust, T, is

$$T = W/\cos\phi. \tag{5.107}$$

These equations allow the rotor thrust to be determined, albeit approximately, for any bank angle and, therefore, for any turning radius of the flight path. Notice that the bank angle required to perform a given radius of turn will also be a function of the speed of the helicopter along its flight path, which is a key factor in determining the load factor for a given radius of turn.

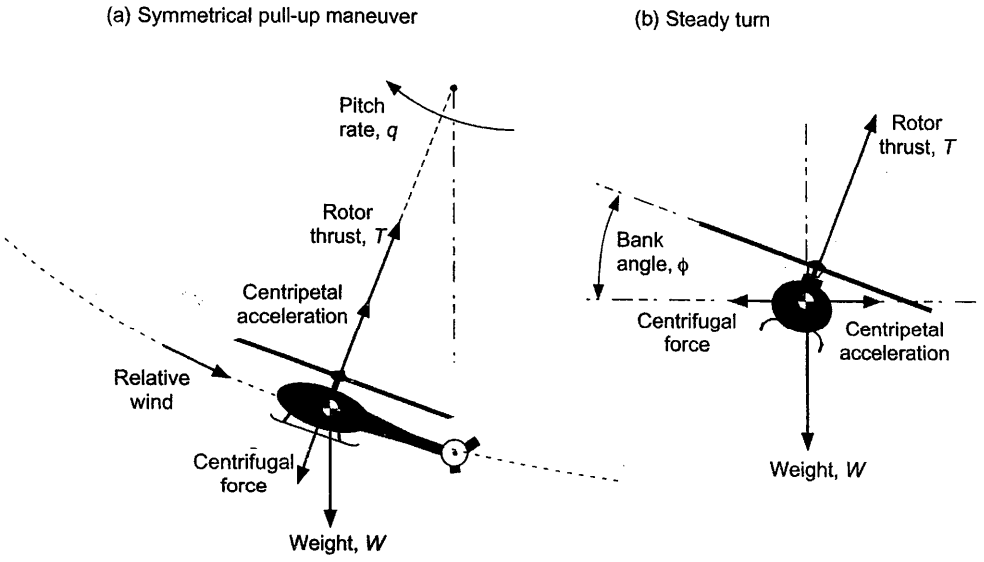

Figure 5.40 Forces acting on a helicopter in (a) a symmetrical pull-up maneuver and, (b) a coordinated turn.

The power required in turning flight with bank angle ϕ can be determined using the performance model based on momentum theory, as described in Section 5.4. In coefficient form, the total power can now be written as

$$C_P = \frac{\kappa(C_T/\cos\phi)^2}{2\sqrt{\lambda^2+\mu^2}} + \frac{\sigma C_{d_0}}{8}(1+K\mu^2) + \frac{1}{2}\left(\frac{f}{A}\right)\mu^3 + C_{P_{TR}}, \tag{5.108}$$

where $C_{P_{TR}}$ is the contribution from the tail rotor.[3] Notice that it is only the induced part of the power (the thrust dependent term) that is affected by the bank angle, ϕ, assuming that the turn is coordinated and there is no slip (yaw) angle. For modest bank angles, say up to $\phi = 30°$, there are only mild effects on power requirements. However, for steep bank angles the power required may exceed that available and the maneuver capability could be power limited. This is particularly apparent at high density altitudes, where maneuver performance will almost certainly be limited because of either reduced excess power available or by reaching rotor stall limits. Roll rate (or pitch rate for that matter) has only a secondary and transient effect on rotor power required because rate affects primarily the distribution of thrust over the rotor disk and not its magnitude.

5.9.2 *Transient Maneuvers*

The analysis of the transient (nonsteady) maneuver of a helicopter can be approached using energy methods – see Schillings et al. (1990), Lappos (1984), and Ebert & Lappos (1985). The instantaneous energy state of the helicopter, E, can be written as a sum of its potential energy, translational kinetic energy and the rotational kinetic energy stored in the rotor, that is,

$$E = Wh + \frac{1}{2}\left(\frac{W}{g}\right)V_\infty^2 + \frac{1}{2}I_R\Omega^2, \tag{5.109}$$

[3] To a first approximation this can be assumed to be a fixed fraction of the main rotor power.

where W is the weight of the aircraft, h is its altitude relative to a datum (normally the ground), V_∞ is true airspeed, I_R is the rotor inertia, and Ω is the rotational speed of the rotor. The time rate of transfer of energy between these three different energy states of the helicopter is equivalent to the power required to change the energy level. This transfer of excess power provides a measure of maneuver capability and the rate of transfer of power is a measure of its potential agility (i.e., the quickness of the maneuver). By differentiating Eq. 5.109 with respect to time this gives

$$\frac{dE}{dt} = W\frac{dh}{dt} + \left(\frac{W}{g}\right)V_\infty\frac{dV_\infty}{dt} + I_R\Omega\frac{d\Omega}{dt} = \Delta P_{\text{energy level}}. \tag{5.110}$$

The net excess power available can be written as a contribution from the engine(s) and from the rate of change of energy level associated with changes in the flight condition, that is, the net excess power available is

$$\Delta P = \Delta P_{\text{engine}} + \Delta P_{\text{energy level}}, \tag{5.111}$$

where ΔP can be viewed as the net excess power available over and above that required for equilibrium flight at any one flight condition (i.e., at any given altitude, airspeed, rotor rpm and maneuver state). For example, any excess power available can be used to increase potential energy (gain more altitude), to increase kinetic energy (gain more airspeed), to increase the rotor energy (increase rotor rpm) or otherwise change the flight condition. The signs and magnitude of the various energy rates define the nature of the changes that are possible to the flight condition of the helicopter. For most normal flight conditions the rotor rpm is automatically governed to allow only small variations, but an overspeed (but not much of an underspeed) of the rotor can be allowed under some conditions.

The energy to produce extra rotor thrust to perform an accelerated maneuver comes from either excess shaft power available or from the conversion of one energy state to another. Rotor overspeeds can also be used for this purpose ($T \propto \Omega^2$), but rarely is this done in practice because of the risk of overstressing the rotor. Rotor overspeeds, however, are often used during the final transient stages of an emergency autorotative maneuver, where the pilot will flare the helicopter to a steep nose-high attitude to gain excess rotor rpm to aid in a safe touchdown – see page 248.

For a conventional helicopter the rotor thrust T can be estimated from the product of the gross weight of the aircraft W and the rotor load factor n. Consider a helicopter undergoing a simple pull-up maneuver, as shown in Fig. 5.40(a). The normal acceleration, a, is

$$a = (n-1)g = \ddot{z} + qV_\infty. \tag{5.112}$$

The potential load factor also depends partly on the ability to produce a normal (vertical) acceleration $\ddot{z}$ through the application of blade pitch. The helicopter must have, therefore, an excess power available at the rotor shaft over and above that required for level, unaccelerated flight at the same conditions (i.e., at the same airspeed, weight, and density altitude). Notice that the potential load factor also depends on the energy level through the flight velocity V_∞ and the ability to actually produce a pitch rate q through the application of flight control inputs.

The excess power available ΔP over and above that power required P at a given airspeed V_∞ is available to produce extra rotor thrust ΔT and, therefore, to produce an acceleration. In horizontal flight (or conditions that may be nearly so) the equation of motion is

$$T - W = \Delta T = \left(\frac{W}{g}\right)a = \left(\frac{W}{g}\right)(\ddot{z} + qV_\infty). \tag{5.113}$$

The load factor on the helicopter is then

$$n = 1 + \left(\frac{\ddot{z} + qV_\infty}{g}\right) = 1 + \frac{\Delta T}{W}. \tag{5.114}$$

The ability to produce this load factor depends on the stall margin of the rotor, which in this case can be defined in terms of the value of C_T/σ that will produce stall relative to the $1g$ level flight value, that is,

$$M_{\text{sm}} = n\frac{\left(\frac{C_T}{\sigma}\right)_{1g}}{\left(\frac{C_T}{\sigma}\right)_{\text{stall}}}. \tag{5.115}$$

If $M_{\text{sm}} > 1$ then the rotor stall boundary will be exceeded before the power limit is reached. Therefore, an excess power available is no guarantee of maneuver capability, and both power and rotor stall margins must be addressed.

The load factors possible with a conventional helicopter are shown in Fig. 5.41, where a helicopter was flown in various transient maneuvers such as decelerating pull-ups and turns at different airspeeds in an attempt to define its transient maneuver envelope – see Lappos & Padfield (1994). The demonstrated (flight-tested) load factors are limited at low airspeeds by the low translational kinetic energy and by the relatively low excess power margin of the conventional helicopter. This type of comparison can, for now, be considered only qualitative in nature but it serves to illustrate how the shape of the measured maneuver envelope at low flight speeds mimics the excess engine power available (power margin) curve – see discussion in Section 5.5.4. It is reasonable to assume that this behavior is typical of any conventional helicopter (i.e., one without benefits of lift or thrust compounding).

At intermediate forward flight speeds the transient maneuver capability is less dependent on the excess engine power available because the power margin is greater as rotor induced losses are lower, and also because the higher translational kinetic energy of the helicopter

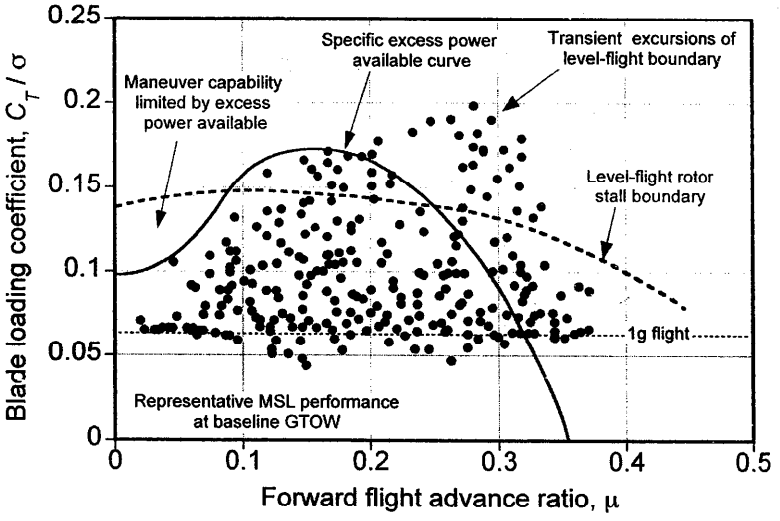

Figure 5.41 Transient load factors for a representative helicopter based on excess power available and sustainable pitch rate. Demonstrated capability may exceed the rotor stall margin at moderately high airspeeds. Adapted from Lappos & Padfield (1994).

allows for a transfer of energy (see Eq. 5.110). Flight test results indicate that in some cases these transient load factors may be of the order of $3g$ and are likely to well-exceed the normal static stall boundary of the rotor and approach its structural limits. Some part of these overshoots in the static stall envelope can be attributed to the delay in the onset of stall that is associated with the favorable effects of pitch rate on stall – a phenomenon recognized by Brown & Schmidt (1963) and discussed in detail in Chapter 9. There are also gyroscopic effects on the rotor during maneuvers, which affects the blade flapping response (see Section 6.9.3). The corresponding changes in blade section AoA can add or subtract from the stall margins depending on the nature of the maneuver (rolls to the left or right, etc.).

The potential maneuver capability from the excess engine power available can be estimated with reference to the engine power required versus power available curves. The excess rotor power available ΔP_{eng} can be related to the potential of increasing rotor thrust, ΔT. In low-speed flight (i.e., near to hovering flight), it is sufficient to assume the hover result relating rotor power required to rotor thrust using the momentum theory, that is,

$$P = \left(\frac{1}{FM}\right)\frac{T^{3/2}}{\sqrt{2\rho A}}, \tag{5.116}$$

where A is the rotor disk area, FM is the rotor figure of merit, and ρ is the air density at the actual operational flight conditions. Differentiating the power equation with respect to thrust gives

$$\frac{dP}{dT} = \left(\frac{3}{2FM}\right)\sqrt{\frac{T}{2\rho A}}. \tag{5.117}$$

Linearizing the problem by assuming the excess thrust and engine power are a fraction of those required at the level, unaccelerated flight condition means the excess power can be written as

$$\Delta P = \left(\frac{dP}{dT}\right)\Delta T, \tag{5.118}$$

or the extra rotor thrust capability found by

$$\Delta T = \Delta P / \left(\frac{dP}{dT}\right). \tag{5.119}$$

Using Eq. 5.113 shows that the acceleration is related to the extra rotor thrust by

$$a = \ddot{z} + qV_\infty = \frac{\Delta T}{(W/g)} = \frac{\Delta T\, g}{W}. \tag{5.120}$$

The potential load factor capability is then

$$n = 1 + \left(\frac{\ddot{z} + qV_\infty}{g}\right) = 1 + \frac{\Delta T}{W} = 1 + \frac{\Delta P}{W}\left(\frac{dT}{dP}\right). \tag{5.121}$$

Using the result from Eq. 5.117, and assuming that the increase in thrust is relatively small compared to the thrust required for level, unaccelerated flight at that gross weight and

density altitude gives the potential load factor as

$$n \approx 1 + \frac{2}{3}\left(\frac{\Delta P_{\text{eng}}}{P}\right), \tag{5.122}$$

where it is assumed that all of the excess engine power available can, in fact, be used to generate an extra rotor thrust (i.e., the rotor is not stall limited before being power limited). Therefore, Eq. 5.122 confirms the hypothesis made earlier that the ability to produce a maneuver load factor on the aircraft depends on the specific excess power available. This particular result is valid at low airspeeds where the translational kinetic energy is low and where the shape of the excess power available curve closely mimics the actual maneuver capability of the helicopter.

This problem can also be examined by assuming that the power required by the rotor is approximated by the forward flight result

$$P = \frac{\kappa T^2}{2\rho A V_\infty} + P_0 + P_p, \tag{5.123}$$

where P_0 is the profile power required and P_p is the parasitic power. The first term in Eq. 5.124 is the induced power required as given by Glauert's approximation (Eq. 2.114). The profile and parasitic terms are primarily a function of flight speed V_∞. The profile term is nominally constant in low-speed flight, and the parasitic term increases only slowly when in low-speed forward speed. Therefore

$$P \approx \frac{\kappa T^2}{2\rho A V_\infty} + \frac{1}{2}\rho f V_\infty^3. \tag{5.124}$$

By differentiation of Eq. 5.124, the approximate change in power required with respect to a change in rotor thrust can be written as

$$\frac{dP}{dT} = \frac{\kappa T}{\rho A V_\infty}. \tag{5.125}$$

As before, linearizing the problem by assuming the excess power (and thrust) is a fraction of the power available means the excess power can be written in terms of the excess thrust. Using the result in Eq. 5.125 by assuming that the change in rotor thrust is a fraction of the thrust required at that aircraft weight, gives the potential load factor as

$$n \approx 1 + \frac{1}{2}\left(\frac{\Delta P_{\text{eng}}}{P}\right). \tag{5.126}$$

These results help quantify the effects of excess engine power available on the potential maneuver capability of the helicopter, which approximately mimics the curve of excess power available relative to level flight. However, it is clear that the maneuver capability depends on many interrelated parameters, including the translational kinetic energy of the helicopter, the kinematics of its flight trajectory, and the stall margins of the rotor.

5.10 Factors Influencing Performance Degradation

The performance of a helicopter can be degraded under different circumstances. The accumulation of dirt and dead insects on the leading edges of the blades can degrade both main and tail rotor performance, although these effects are relatively mild. Estimates of such effects on rotor performance can be obtained by increasing the value of C_{d_0} in

accordance with measured effects of roughness on 2-D airfoil sections (see Section 7.9.1). The operation of the helicopter in dusty or desert environments can lead to blade erosion, and this can have much more deleterious effects on rotor performance. A C_{d_0} allowance of up to 50% can be used to represent such effects in rotor performance estimation. Aerodynamic degradation of the rotor performance from battle damage can be an issue for military helicopters, but such effects are much more difficult to predict (see Section 7.14). Nevertheless, an assessment of degraded effects on rotor performance is essential for assessing operational risks to military helicopters in a combat environment.

Icing is a particularly significant factor that can degrade rotor performance. For good utility, helicopters must be designed to operate in an all-weather environment, of which flight in extremely cold conditions are not uncommon. However, icing can occur under other atmospheric conditions, and there is a risk whenever visible moisture is present in the air. Under certain conditions, ice accumulation on the rotor and airframe may occur. Icing characteristics of helicopters are similar in some respects to airplanes, and ice may accumulate on windshields, engine inlets, the leading edges of the empennage, antennas, Pitot probes, and so on. Icing can result in a serious performance degradation and may also affect flight control capability. The field as applied to helicopters is comprehensively reviewed by Flemming (2002).

Ice accumulation may increase the parasitic drag of the airframe. Engine inlet icing may reduce engine power and in extreme cases can cause engine surge–stall. However, airframe, engine inlet, and windshield icing can be dealt with effectively by electrical deicing. Empennage icing and the associated aerodynamic degradation is usually less important for helicopters than for airplanes because icing may only affect trim, and on most helicopters the rotor itself has ample flight control capability to compensate for this. Icing on the rotor, however, can have serious consequences, with a significant degradation in aerodynamic capability – see Flemming et al. (1987). Because the type and accumulation of ice normally varies in a 3-D manner along the blade span, and may be different from blade to blade, icing can be accompanied by significant rotor vibrations. Modern helicopters may be capable of flight into icing conditions with suitable deicing protection, but most helicopters are not certified for flight onto known icing conditions because of the amount of flight certification tests and high costs incurred by the manufacturer. Icing protection on the rotor is provided by electrically heated deicing mats that are molded into the composite blades during manufacture [see Rauch & Quillien (2003)], but Coffman (1987) discusses other concepts.

Steady 2-D airfoil testing in special icing wind tunnels has allowed measurements of ice accumulation at the leading edge of rotor airfoils, which have shown substantial degradation on aerodynamic performance – see Flemming & Lednicer (1985). Unsteady tests on airfoils, which are designed to more accurately simulate the time-varying flow environment at the rotor, have suggested different ice shapes may accumulate, with smoother profiles because of the continuously varying AoA. Tests with subscale rotors in special icing tunnels has been conducted to more accurately assess the susceptibility of helicopters and their rotor systems to icing – see Korkan et al. (1984) and Flemming & Saccullo (1991). These icing shapes can be used to cast molds to modify the blades of other model rotors, which are then tested in dry-air tunnels in an attempt to measure the effects on rotor performance. Scaling issues (such as Reynolds number effects and heat transfer) that are associated with ice accumulation on model rotors are, however, not well understood. Therefore, confidence levels in extrapolating wind tunnel results to estimate the impact of icing on the full-size rotors is not yet acceptable. Various mathematical models have also been developed to assess the effects of icing on rotor performance both empirically [see Korkan et al. (1984)] and by

using modern CFD approaches [see Narramore et al. (2002)]. However, validation is lacking because of the limited amount of existing flight test data, and so predictive confidence levels with CFD alone remain lower than required to satisfy the certification authorities. Actual in-flight icing tests are often augmented by artificial tests to cover the full flight envelope of the helicopter – see Ramage (2004). Computational methods continue to be developed, however, to enable better predictions of the aerodynamic characteristics with ice accreted on the entire rotorcraft with the ultimate goal of reducing significantly the amount of required certification flight testing [see Narramore et al. (2003)].

5.11 Chapter Review

This chapter has addressed some elementary analyses and predicted results that define the overall performance characteristics of the helicopter in hover, climb, forward flight, and during certain types of maneuvers. It has been shown that these performance characteristics can be derived, in part, by using relatively parsimonious mathematical models for the rotor aerodynamics that have their origin in the momentum and blade element theories given in previous chapters. Good estimates of rotor profile power can be made on the basis of blade element theory, perhaps allowing for radial, yawed, and reversed flow effects and also for compressibility losses at high speeds. Airframe drag has been discussed, and the modeling of these effects has been introduced through the ideas of an equivalent wetted or flat-plate parasitic area. Airframe drag increases rapidly on a helicopter in higher-speed forward flight, eventually becoming one limiting factor in defining its maximum speed capability. The resulting models give good approximations to the rotor power required and performance of the helicopter over the substantial part of the operational flight envelope. The results can be used to estimate performance as functions of helicopter weight and operational factors such as its density altitude. Performance issues such as the speed to fly for maximum range or endurance have been discussed, and it has been shown how these results follow directly from a knowledge of the power required curves.

However, the performance of modern helicopters is mostly limited by other aerodynamic factors, such as blade stall and compressibility effects on the rotor. While compressibility effects show up as progressive increases in power required in high-speed forward flight, the onset of blade stall is more critical because it is a source of high unsteady blade loads and increases in vibration. Both compressibility and stall effects are difficult to model without resorting to more thorough types of analyses that model the aerodynamics at a more fundamental level, such as using the blade element approach. These phenomena and methods for their approximation will be considered in the following chapters.

Helicopter performance when operating near the ground or in a wind tunnel has also been discussed. The complexity of the recirculating flow near the ground is such that this particular aerodynamic problem is not amenable to easy solution and the problem must be modeled semi-empirically. An introduction to the maneuvering flight capability of helicopters has been given based on simple kinematics for steady maneuvers and using an energy approach for the transient case. It is apparent that much can be demanded from the modern military helicopter, which must be able to maneuver effectively. Clearly the most important aspect of maneuverability is the ability of the helicopter to produce extra rotor thrust over and above that required for flight at the original equilibrium flight condition. The extra rotor thrust, however, may be limited because of installed power limitations, transmission torque limits, blade stall, rotor rpm limits, or structural loading limits. Finally, potential performance degradation effects from the effects of airframe and rotor icing has been reviewed.

5.12 Questions

5.1. For the helicopter specified by the parameters listed in the table below, estimate the power required to hover for several values of the density altitude at a gross weight of 16,000 lb. The distance between main and tail rotor shafts, x_{tr}, is 32.5 ft. Assume that transmission power losses amount to 10%. If the power available (installed power) is 3,000 hp at MSL on a standard day, estimate the hover ceiling (as a density altitude) at this gross weight.

Parameter	Symbol	Main Rotor	Tail Rotor
Rotor radius (ft)	R	27.0	5.5
Blade chord (ft)	c	1.7	0.80
Solidity	σ	0.082	0.19
Number of blades	N_b	4	4
Tip speed (ft s^{-1})	$V_{tip}(=\Omega R)$	725	685
Induced power factor	κ	1.15	1.15
Profile drag coefficient	C_{d_0}	0.008	0.008

5.2. Sketch a representative total power curve for a helicopter in forward flight at sea level. Draw in and label the breakdown of the constituent parts comprising this power curve, and explain the source of each part. Show also how you can use this type of power required curve (at a given altitude and gross weight) to determine: the vertical rate of climb, the speed for maximum endurance, the speed for maximum range, the maximum forward speed, and the maximum rate of climb in forward flight.

5.3. A helicopter is operating in level forward flight at 210 fts^{-1} under the following conditions: shaft power supplied = 655 hp, W = 6,000 lb, ρ = 0.00200 slugs/ft^3. The rotor parameters are R = 19 ft, σ = 0.08, ΩR = 700 fts^{-1}, k = 1.15, C_{d_0} = 0.01. (i) How much power is required to overcome induced losses? (ii) How much power is required to overcome profile losses? (iii) What is the equivalent flat-plate area, f? (iv) If the installed power is 800 hp, estimate the maximum rate of climb possible at this airspeed.

5.4. By means of the blade element theory in forward flight show that by including the effects of reverse flow on the drag, the profile power coefficient can be written as

$$C_{P_0} = \frac{\sigma C_{d_0}}{8}\left(1 + 3\mu^2 + \frac{3}{8}\mu^4\right).$$

Neglect the radial component of velocity. Compare this result to the predicted power obtained without reverse flow.

5.5. An understanding of the vortex ring state is necessary to explain certain aspects of helicopter performance. Describe, with the aid of a diagram(s), what is the mechanism behind the vortex-ring state. Under what flight conditions is the vortex ring state important to a pilot and why?

5.6. What is meant by autorotation? Explain the circumstances when an autorotation maneuver might be necessary with a helicopter. What characteristics of the helicopter affect the autorotative performance? By means of a blade element diagram, carefully show and explain why: (a) The mean flow velocity must be vertically upwards through the rotor for autorotation to occur. (b) The blade pitch angles must

be low in an autorotation compared to hover or climb. Show where and explain why in an autorotation the rotor blades will absorb power from the airstream at some blade locations and consume power at other blade stations.

5.7. Estimate the autorotative rate of descent in forward flight at sea level conditions for a small light-weight helicopter with the following characteristics: Weight = 1370 lb, rotor radius = 12.6 ft, rotor solidity = 0.30, tip speed = 700 ft/s.

5.8. Describe the procedure a pilot would follow if the engine of a single engine helicopter failed in hover. How might the procedure differ if: (a) two engines were installed and one engine failed, (b) the tail rotor failed. Estimate the autorotative rates of descent of three substantially different (in terms of gross weight) single-rotor helicopters of your choosing. Comment on your results.

5.9. Draw and explain the main features of the height–velocity diagram for a single-engine/single-rotor helicopter. Explain if and/or how these curve(s) will change for: (a) a single-rotor/twin-engine helicopter, (b) a tandem-rotor helicopter, (c) a single-rotor system with a high overall rotational inertia, and (d) a higher density altitude.

5.10. An understanding of "ground effect" is necessary to explain certain trends in helicopter behavior. Describe the mechanism of ground effect in hover. How does ground effect influence the performance of the helicopter during the transition from hover to forward flight?

Bibliography

Amer, K. B. 1955. "Effect of Blade Stalling and Drag Divergence on Power Required by a Helicopter Rotor at High Forward Speed," 11th Annual National Forum of the American Helicopter Soc., Washington DC.

Ballin, M. G. 1987. "Validation of a Real-Time Engineering Simulation of the UH-60 Helicopter," NASA TM-88360.

Bennett, J. A. J. 1940. "Rotary Wing Aircraft," *Aircraft Engineering*, 12 (131–138), Jan.–Aug., pp. 7–9, 40–42, 65–67, 109–112, 139–141, 174–176, 208–209, 237–241, 246.

Bennett, J. A. J. 1947. "Limitations in Helicopter Design," *J. of the Helicopter Association of Great Britain*, 1 (1), pp. 24–43.

Betz, A. 1937. "The Ground Effect on Lifting Propellers," NACA TM 836.

Betzina, M. D. 2001. "Tilt-rotor Descent Aerodynamics: A Small-Scale Experimental Investigation of Vortex Ring State," American Helicopter Soc. 57th Annual Forum, Washington, DC, May 9–11.

Brotherhood, P. 1949. "Flow Through the Helicopter Rotor in Vertical Descent," British ARC R & M 2735, July.

Brown, E. L. and Schmidt, P. S. 1963. "The Effect of Helicopter Pitching Velocity on Rotor Lift Capability," *J. of the American Helicopter Soc.*, 8 (4), pp. 1–6.

Brown, R. E., Leishman, J. G., Newman, S., and Perry, F. J. 2002. "Blade Twist Effects on Rotor Behavior in the Vortex Ring State," 28th European Rotorcraft Forum, Bristol, England, Sept. 17–20.

Cheeseman, I. C. and Bennett, W. E. 1955. "The Effect of the Ground on a Helicopter Rotor in Forward Flight," ARC R & M 3021.

Chen, R. T. N. and Jeske, J. A. 1981. "Kinematic Properties of the Helicopter in Coordinated Turns," NASA TP-1773, April.

Coffman, H. J. 1987. "Helicopter Rotor Icing Protection Methods," *J. of the American Helicopter Soc.*, 32 (2), pp. 34–39.

Curtiss, H. C., Erdman, W., and Sun, M. 1987. "Ground Effect Aerodynamics," *Vertica*, 11 (1/2), pp. 29–42.

Curtiss, H. C., Sun, M., Putman, W. F., and Hanker, E. J. 1984. "Rotor Aerodynamics in Ground Effect at Low Advance Ratios," *J. of the American Helicopter Soc.*, 29 (1), pp. 48–55.

de Bothezat, G. 1919. "The General Theory of Blade Screws," NACA TR 29.

Dingeldein, R. C. 1954. "Wind Tunnel Studies of the Performance of a Multirotor Configurations," NACA Technical Note 3236.

Drees, J. M. and Hendal, W. P. 1951. "Airflow Patterns in the Neighborhood of Helicopter Rotors," *Aircraft Engineering*, 23 (266), pp. 107–111.

DuWaldt, F. A. 1966. "Wakes of Lifting Propellers (Rotors) in Ground Effect," Cornell Aeronautical Laboratory, Report CAL No. BB-1665-S-3, Nov.

Ebert, F. J. and Lappos, N. D. 1985. "Application of Helicopter Air-to-Air Combat Test (AACT) Data to Current LHX Concerns," 41st Annual Forum of the American Helicopter Soc., Ft. Worth, TX, May 15–17.

Ferri, A. 1945. "Completed Tabulation in the United States of Tests of 24 Airfoils at High Mach Numbers," NACA WR L-143. Also, ACR No. L5E21.

Flemming, R. T. 2002. "The Past Twenty Years of Icing Research and Development at Sikorsky Aircraft," AIAA Paper 2002-0238, 40th Aerospace Sciences Meeting, Reno, NV, Jan. 14–17.

Flemming, R. J. and Lednicer, D. A. 1985. "High Speed Ice Accretion on Rotorcraft Airfoils," NASA Contractor Report 3910.

Flemming, R. J., Shaw, R. J., and Lee, J. D. 1987. "The Performance Characteristics of Rotorcraft Airfoils With Simulated Ice," *J. of the American Helicopter Soc.*, 32 (2), pp. 67–77.

Flemming, R. T. and Saccullo, A. 1991. "Tests of a Model Main Rotor in the NASA Lewis Research Center Icing Research Tunnel," NASA CR 189071.

Fradenburgh, E. A. 1960. "The Helicopter and the Ground Effect Machine," *J. American Helicopter Soc.*, 5 (4), pp. 26–28.

Fradenburgh, E. A. 1972. "Aerodynamic Factors Influencing Overall Hover Performance," AGARD-CP-111.

Fradenburgh, E. A. 1984. "A Simple Autorotational Flare Index," *J. American Helicopter Soc.*, 29 (3), pp. 73–74.

Ganzer, V. M. and Rae, W. H. 1960. "An Experimental Investigation of the Effect of Wind Tunnel Walls on the Aerodynamic Performance of a Helicopter Rotor," NASA TN D-415.

Gessow, A. and Crim, A. D. 1956. "A Theoretical Estimate of the Effects of Compressibility on the Performance of a Helicopter Rotor in Various Flight Conditions," NACA TN 3798.

Gessow, A. and Myers, G. C., Jr. 1947. "Flight Tests of a Helicopter in Autorotation, Including a Comparison with Theory," NACA TN 1267.

Gessow, A. and Myers, G. C., Jr. 1952. *Aerodynamics of the Helicopter*, Macmillan Co., Republished by Frederick Ungar Publishing, New York, NY, 1967, p. 121.

Glauert, H. 1926. "On the Horizontal Flight of a Helicopter," ARC R & M 1730.

Graber, A., Rosen, A., and Seginer, A. 1990. "An Investigation of a Hovering Rotor in Ground Effect," Proceedings of the 16th European Rotorcraft Forum, Glasgow, Sept. 18–20.

Griffiths, D. A. and Leishman, J. G. 2002. "Dual-Rotor Interference and Ground Effect Using a Free-Vortex Wake Model," 58th Annual Forum of the American Helicopter Soc. International, Montréal Canada, June 11–13.

Gustafson, F. B. and Gessow, A. 1947. "Effect of Blade Stalling on the Efficiency of a Helicopter Rotor as Measured in Flight," NACA TN 1250.

Gustafson, F. B. and Myers, G. C., Jr. 1946. "Stalling of Helicopter Blades," NACA Rep. 840.

Harris, F. D. 1966. "Preliminary Study of Radial Flow Effects on Rotor Blades," *J. of the American Helicopter Soc.*, 11 (3), pp. 1–21.

Harris, F. D. 1987. "Rotary Wing Aerodynamics – Historical Perspective and Important Issues," National Specialists' Meeting on Aerodynamics and Aeroacoustics, American Helicopter Soc., Arlington, TX, Feb. 25–27.

Harris, F. D., Kasper, E. F., and Iseler, L. E. 2000. "US Civil Rotorcraft Accidents through 1997," NASA/TM-2000-20597 USAAMCOM-TR-00-A-006, Dec.

Hayden, J. S. 1976. "The Effect of the Ground on Helicopter Hovering Power Required," 32th Annual National V/STOL Forum of the American Helicopter Soc., Washington DC, May 10–12.

Heyson, H. H. 1954. "Preliminary Results from Flow Field Measurements around Single and Tandem Rotors in the Langley Full-Scale Tunnel," NACA TN 3242.

Heyson, H. H. 1975. "A Momentum Analysis of Helicopters and Autogyros in Inclined Descent, with Comments on Operational Restrictions," NASA TN D-7917, Oct.

International Civil Aviation Organization (ICAO). 1964. *Manual of the ICAO Standard Atmosphere.*

Itoga, N., Nagashima, T., Iboshi, N., Kawakami, S., Prasad, J. V. R., and Peters, D. A. 1999. "Numerical Analysis of Ground Effect for a Lifting Rotor Hovering at Close Proximity to Inclined Flat Surface," American

Helicopter Soc. Specialists' Meeting on Advanced Helicopter Technology and Disaster Relief, Gifu, Japan, April 21–23.

Johnson, W. 1980. *Helicopter Theory*, Princeton University Press, Princeton, NJ, pp. 216–221.

Klemin, A. 1925. "An Introduction to the Helicopter," NACA TM 340.

Korkan, K. D., Cross, E. J., and Cornell, C. C. 1984. "Experimental Study of Performance Degradation of a Model Helicopter Main Rotor with Simulated Ice Shapes," AIAA Paper 84-0184, 22nd AIAA Aerospace Sciences Meeting, Reno, NV, Jan. 9–12.

Knight, M. and Hefner, R. A. 1941. "Analysis of Ground Effect on the Lifting Airscrew," NACA TN 835.

Lappos, N. D. 1984. "Insights into Helicopter Air Combat Maneuverability," 40th Annual Forum of the American Helicopter Soc., Arlington, VA, May 16–18.

Lappos, N. and Padfield, G. 1994. "Designing Helicopters for Agility," In: AGARD AR-314 *Operational Agility*.

Lehman, A. F. and Besold, J. A. 1971. "Test Section Size Influence on Model Helicopter Rotor Performance," USAAVLABS TR 71-6.

Leishman, J. G., Bhagwat, M. J., and Ananthan, S. 2002. "The Vortex Ring State as a Spatially and Temporally Developing Wake Instability," American Helicopter Soc. International Specialists Meeting on Aerodynamics, Acoustics, and Test and Evaluation, San Francisco, CA, Jan. 23–25.

LeNard, J. M. 1972. "A Theoretical Analysis of the Tip Relief Effect on Helicopter Rotor Performance," USAAM-RDL Technical Report 72-7.

LeNard, J. M. and Boehler, G. D. 1973. "Inclusion of Tip Relief in the Prediction of Compressibility Effects on Helicopter Rotor Performance," USAAMRDL Technical Report 73-71.

Lewis, R. B. 1972. "Army Helicopter Performance Trends," *J. American Helicopter Soc.*, 17 (2), pp. 15–23.

Light, J. S. and Norman, T. 1989. "Tip Vortex Geometry of a Hovering Helicopter Rotor in Ground Effect," 45th Annual Forum of the American Helicopter Soc., Boston, MA, May 22–24.

McCloud, J. L. III, Biggers, J. C., and Stroub, R. H. 1968. "An Investigation of Full-Scale Helicopter Rotors at High Advance Ratios and Advancing Tip Mach Numbers," NASA TN D-4632, July.

McCormick, B. W. 1956. "On the Initial Vertical Descent of a Helicopter Following Power Failure," *J. of the Aeronautical Sciences*, 23 (12), pp. 1125–1126.

McCormick, B. W. 1995. *Aerodynamics, Aeronautics, and Flight Mechanics*, John Wiley & Sons, Inc., New York, NY, Chapter 7.

Minzner, R. A., Champion, K. S. W., and Pond, H. L. 1959. "The ARDC Model Atmosphere," AF CRC-TR-59-267.

Moulton, M., O'Malley, J. A., and Ranjagopalan, G. 2004. "Rotorwash Prediction Using an Applied Computational Fluid Dynamics Tool," 60th Annual Form of the American Helicopter Soc., Baltimore, MD, June 7–10.

Narramore, J. C., Tran, P., Baruzzi, G. S., Habashi, W. G., Akel, I., and Balage, S. 2003. "Ice Accretion Computations of Full Tiltrotor Configurations," 59th Annual National Forum of the American Helicopter Soc., Phoenix, AZ, May 6–8.

Narramore, J. C., Tran, P., Habashi, W. G., Balage, S., and Baruzzi, G. S. 2002. "Reducing Icing Certification Flight Tests Through Second Generation 3-D CFD Based Technologies," 58th Annual National Forum of the American Helicopter Soc., Montréal, Canada, June 11–13.

NASA. 1966. "US Standard Atmosphere Supplements," NASA CR-88870.

Newman, S. 1994. *The Foundations of Helicopter Flight*, Edward Arnold, London, pp. 122–127.

Newman, S. J., Brown, R., Perry, J., Lewis, S., Orchard, M., and Modha, A. 2001. "Comparative Numerical and Experimental Investigations of the Vortex Ring Phenomenon in Rotorcraft," 57th Annual Forum of the American Helicopter Soc. International, Washington DC, May 9–11.

Nikolsky, A. 1944. *Notes on Helicopter Design Theory*, Princeton University Press, Princeton, NJ, p. 55.

Norman, D. C. and Sultany, D. J. 1965. "An Empirical Method for Calculating the Power Required Due to Compressibility on a Single Rotor Helicopter," *J. of the American Helicopter Soc.*, 10 (3), pp. 30–36.

Padfield, G. D. 1996. *Helicopter Flight Dynamics: The Theory and Application of Flying Qualities and Simulation Modeling*," AIAA Education Series, Washington, DC.

Pegg, R. J. 1968. "An Investigation of the Helicopter Height–Velocity Diagram Showing Effects of Density Altitude and Gross Weight," NASA TN D-4536.

Peters, D. A. and Chen, S-Y. 1982. "Momentum Theory, Dynamic Inflow, and the Vortex-Ring State," *J. of the American Helicopter Soc.*, 27 (3), pp. 18–24.

Philippe, J. J. 1990. "Considerations on Wind-Tunnel Testing Techniques for Rotorcraft," AGARD-R-781.

Prasad, J. V. R., Chen, C., Basset, P. M., and Kolb, S. 2004. "Simplified Modeling and Non-Linear Analysis of a Helicopter Rotor in Vortex Ring State," 30th European Rotorcraft Forum, Marseilles, France, Sept. 14–16.

Prouty, R. W. 1971. "Tip Relief for Drag Divergence," *J. American Helicopter Soc.*, 16 (4), pp. 61–62.

Prouty, R. W. 1985. "Ground Effect and the Helicopter," AIAA Paper 85-4034, AIAA/AHS/ASEE Aircraft Design Systems and Operations Meeting, Colorado Springs, CO, Oct. 14–16.

Prouty, R. W. 1986. *Helicopter Performance, Stability, and Control*, PWS Engineering Publishing, Boston, MA.

Quackenbush, T. R. and Wachspress, D. A. 1989. "Enhancements to a New Free Wake Hover Analysis," NASA CR 177523, April.

Ramage, A. I. 2004. "Artificial Icing Trials on the EH-101," 30th European Rotorcraft Forum, Marseilles, France, Sept. 14–16.

Rauch, P. and Quillien, C. 2003. "Advanced Technologies for High Performance NH90 Blades," 59th Annual Forum of the American Helicopter Soc. International, Phoenix AZ, May 6–8.

Rossow, V. J. 1985. "Effect of Ground and/or Ceiling Planes on Thrust of Rotors in Hover," NASA Technical Memorandum 86754.

Saberi, H. A. and Maisel, M. D. 1987. "A Free-Wake Rotor Analysis Including Ground Effect," 43rd Annual Forum of the American Helicopter Soc., St. Louis, MO, May 18–20.

Saunders, G. H. 1975. "Dynamics of Helicopter Flight," John Wiley & Sons, Inc., New York, NY, pp. 138–142.

Scheiman, J. 1964. "A Tabulation of Helicopter Rotor-Blade Differential Pressures, Stresses, and Motions Measured in Flight," NASA TM X-952, March.

Sheridan, P. F. and Wiesner, W. 1977. "Aerodynamics of Helicopter Flight Near the Ground," 33rd Annual Forum of the American Helicopter Soc., Washington DC, May 9–11.

Shillings, J. J., Roberts, B. J., Woods, T. L., and Wernicke, K. G. 1990. "Maneuver Performance Comparison Between the XV-15 and an Advanced Tiltrotor Design," *J. of the American Helicopter Soc.*, 25 (2), pp. 4–15.

Stepniewski, W. Z. 1973. "Basic Aerodynamics and Performance of the Helicopter," In: AGARD Lecture Series LS-63.

Stepniewski, W. Z. and Keys, C. N. 1984. *Rotary-Wing Aerodynamics*, Dover Publications, New York, NY. Part II, Chapters 2 and 3.

Stewart, W. 1951. "Helicopter Behaviour in Vortex Ring Conditions," British ARC R & M 3117, Nov.

Stewart, W. and Sissingh, G. J. 1949. "Notes on Helicopter Rotor Behavior after Engine Failure in Hovering Flight," ARC R & M No. 2659.

Taylor, M. K. 1950. "A Balsa-Dust Technique for Air-Flow Visualization and Its Application to Flow through Model Helicopter Rotors in Static Thrust," NACA Technical Note 2220.

Thomson, D. G. and Bradley, R. 1990. "Modelling and Classification of Helicopter Combat Manoeuvres," Proceedings of ICAS Congress, Stockholm, Sweden, Sept.

Varnes, D. J., Duren, R. W., and Wood, E. R. 2000. "An Onboard Warning System to Prevent Hazardous Vortex Ring State Encounters," 26th European Rotorcraft Forum, The Hague, The Netherlands, Sept. 26–29.

Washizu, K., Azuma, A., Kōo, J., and Oak, T. 1966. "Experiments on a Model Helicopter Rotor Operating in the Vortex Ring State," *J. of Aircraft*, 3 (3), pp. 225–230.

Wheatley, J. B. 1932. "Lift and Drag Characteristics and Gliding Performance of an Autogiro as Determined in Flight," NACA Report No. 434.

White, G. T., Logan, A. H., and Graves, J. D. 1982. "An Evaluation of Helicopter Autorotation Assist Concepts," 38th Annual Forum of the American Helicopter Soc., Anaheim, CA, May 4–7.

Wimperis, H. E. 1928. "The Rotating Wing in Aircraft," ARC R & M 1108.

Wolkovitch, J. 1972. "Analytical Prediction of Vortex-Ring Boundaries for Helicopters in Steep Descents," *J. of the American Helicopter Soc.*, 17 (3), pp. 13–19.

Wood, T. L. 1976. "High Energy Rotor System," 32nd Annual V/STOL Forum of the American Helicopter Soc., Washington DC, May 10–12.

Yaggy, P. F. and Mort, K. W. 1963. "Wind-Tunnel Tests of Two VTOL Propellers in Descent," NASA TN D-1766, March.

Zbrozek, J. 1947. "Ground Effect on the Lifting Rotor," British ARC R & M 2347.

CHAPTER 6

Aerodynamic Design of Helicopters

We built the first helicopter by what we hoped was intelligent guess. It was time of crystal ball.

Igor Alexis Sikorsky (1957)

6.1 Introduction

There are many fundamental issues, some of them conflicting, in the aerodynamic design of the modern helicopter. Helicopter designers are concerned with overall aircraft performance, rotor and airframe loads, vibration levels, external and internal noise, stability and control characteristics, and aircraft handling qualities. Specific emphasis in this chapter is placed on the general elements and features contributing to the aerodynamic design of helicopter main rotors and related components. However, many of the issues and arguments are applicable to other types of rotorcraft as well. The first part of this chapter outlines the basic sizing and overall optimization methodology of helicopter main rotors. This ultimately leads to the further consideration of rotor airfoil sections and the need for good airfoil designs, the trade-offs in blade planform design, and the role of tip shape in the efficient design of the modern rotor. While helicopter design is often synonymous with rotor aerodynamics, the aerodynamics of the fuselage has received considerable attention in recent years and now constitutes an important part in the overall design process of the modern helicopter. The general issues associated with the selection of anti-torque producing devices such as conventional tail rotors and other concepts are also discussed. Finally, some significant aerodynamic design issues associated with human powered helicopters and micro air vehicles are outlined.

6.2 Overall Design Requirements

Both the conceptual preliminary and detailed design processes comprise a highly interactive effort among aerodynamicists, structural dynamicists, aeroelasticians, material specialists, weight engineers, flight dynamicists, and other specialists. Prouty (1986) gives a good overview of the basic helicopter design process, particularly for military machines. The helicopter design must start with a clear set of specifications, which are defined based on the needs of a potential customer, or more so in the case of military machines, the needs to meet a specific mission requirement. Design technology for the civilian market is driven mostly by customers who emphasize reduced acquisition and operating costs, increased safety, reduced cabin noise and increased passenger comfort, and better overall mechanical reliability and maintainability. Because many of the helicopters in civilian use will operate from heliports and in populated areas, there is also an increasing emphasis on design for reduced external noise. The military have somewhat different requirements. They tend to demand much more in the way of flight performance, speed and maneuver capabilities, and damage tolerance, so the design of military helicopters is often much more difficult and expensive. Military planners also constantly emphasize the need of operational

flexibility and adaptability and the need for long operational life with components that can be continuously upgraded. Vulnerability of the helicopter and the survivability of crew and passengers in a combat situation are also issues important to the military. Today, increasing emphasis is being placed on the dual use of military and civilian technology, which is simply the efficient integration of these traditionally separate design technologies. This has benefits for both the customer and the manufacturer.

The general design requirements for a new helicopter will include (not in any order of priority): 1. Hover capability, including both in and out of ground effect operations; 2. Maximum payload in different types of roles or missions; 3. Range and/or endurance under different conditions; 4. Cruise, maximum level flight speed and maximum "dash" speed; 5. Climb performance, both vertically and with forward speed; 6. "Hot and high" performance, icing, and other environmental effects; and 7. Maneuverability and agility (for military helicopters). One general objective for the manufacturer will be to design the smallest and lightest helicopter to minimum cost. A challenge in minimizing costs is to lower the design cycle time, and this is where the role of analysis and improved mathematical models becomes useful. However, the design must proceed on the basis of many constraints, which may limit the number of design choices. These constraints may include (not in any order of priority): 1. Maximum allowable main rotor disk loading; 2. Maximum allowable overall physical size of the helicopter; 3. One engine inoperative performance; 4. Autorotative capability at maximum gross weight; 5. Maximum allowable noise (both civil and military); 6. Various civil certification or military acceptance requirements; 7. Crashworthiness and survivability requirements; 8. Maintenance issues; 9. Radar cross section and detectability (for military helicopters); and 10. Vulnerability (for military helicopters).

The various requirements for a new helicopter design will be initially specified by the customer. These are then negotiated with the manufacturer and written into a sales contract. Often the "customer" will be the military forces, which will invite various competing manufacturers to respond to a "Request for Proposal" or RFP. Less often, the manufacturer will risk its own resources to develop a new design in anticipation of a production contract. In the design of the new helicopter, performance guarantees will be made to the customer based on various agreed metrics such as hover capability, payload, range and endurance, and cruise speed. In addition, the performance of the machine with one engine inoperative may be included in the guaranteed performance. Methods for determining compliance with the specified performance by means of predictions, analyses and flight testing will be detailed in the contract. Because any failure of the manufacturer to achieve the negotiated performance may result in substantial cost and other penalties, the manufacturer needs to have high levels of confidence that the performance guarantees can indeed be met.

The basic procedure that a manufacturer will follow in establishing a performance guarantee is based on statistical confidence levels of results obtained from both mathematical models and flight tests. A good summary of some of the key flight testing activities conducted during the certification of a modern twin-engine helicopter is given by Ockier (2003). Confidence values can be assigned to predictions based on the established accuracy of a given mathematical model. Typically, most models will have been in use by the manufacturer for some time and will be well-validated based on correlation with idealized laboratory experiments, ground and wind tunnel tests of sub- and full-scale rotor systems, as well as flight tests. This will allow the manufacturer to establish good statistical bounds on the confidence levels for the predictions. For example, methodologies validated with reference to a prototype or a similar helicopter will allow a high confidence level to be accessed. In contrast, a completely new helicopter with an advanced rotor design or new blade tip shape may have more uncertainties in the design, and confidence levels in any predictive

methodology will be lower. This, however, is where the benefits of fundamental research and development become useful, and significant payoffs can be realized by producing a much more advanced and competitive helicopter design.

6.3 Conceptual and Preliminary Design Processes

The methodology used in a conceptual or preliminary design study is an iterative process that begins with input specifications, such as the required payload and range of the helicopter. A series of performance and rotor sizing calculations based on these requirements are then undertaken using the elementary rotor theory described in previous chapters. The use of momentum theory in its various incarnations is very useful in this regard. Assessments of propulsive efficiency, lift-to-drag ratio, transmission power conversion efficiency, rotor tip speed, rotor figure of merit, and so on, are then performed. After these calculations are complete, a series of weight calculations are performed for the various components that make up the helicopter (rotor, blades, hub, airframe, engines, transmission, etc.). These weights are usually based on empirical equations, with the coefficients in these equations defined based on correlations to historical data. Next, these component weights are used to sum up the empty weight, the fuel weight for the mission is estimated, and the performance of the helicopter is recalculated. The updates are then substituted into the various weight equations and the process runs iteratively until convergence is achieved. Capital acquisition and direct operating costs are then evaluated.

The basic design methodology is depicted in Fig. 6.1. The logical sequence of this process allows trade studies to be performed and perhaps compared with other rotorcraft configurations. The intent is ultimately to select the best design that will meet the specified requirements at minimum cost. The conceptual and preliminary design process is then followed by a detailed design study at which the elements of the helicopter and its performance are examined in considerable detail. This is done using analysis, ground and wind tunnel testing, construction of a prototype, and finally flight testing. All of these steps involve considerable engineering time and large amounts of money. Flight testing is generally a protracted affair, often involving many months or even years of systematic testing before the helicopter is finally handed off to the customer.

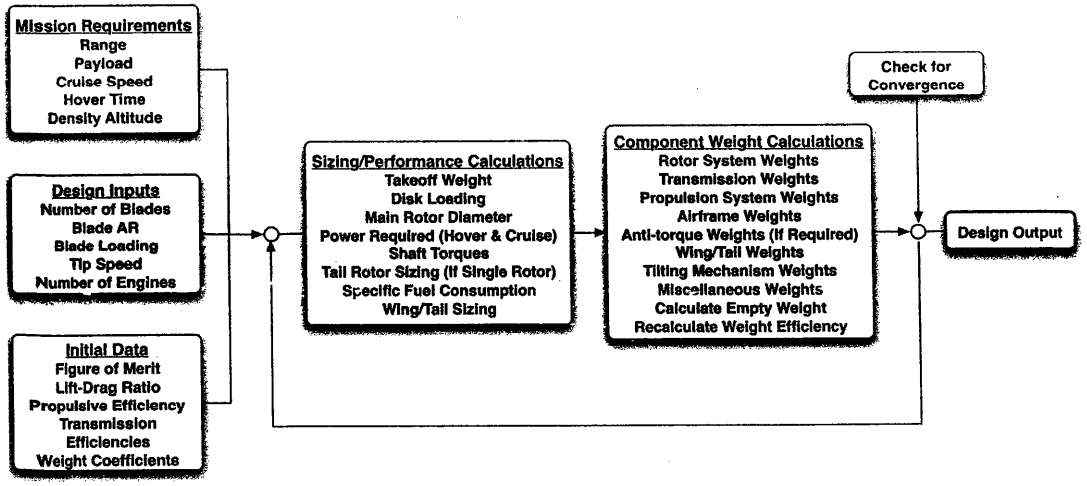

Figure 6.1 Flowchart showing the conceptual design process for a generic rotorcraft.

6.4 Design of the Main Rotor

Arguably, the main rotor is *the* single most important component of the helicopter. Good overviews of the design of modern rotor systems are given by JanakiRam et al. (2003) and Rauch & Quillien (2003). Proper design of the rotor is critical to meeting the performance specifications that have been laid down for the helicopter as a whole. The design of the tail rotor is similar to that of the main rotor, but because it has a different set of design constraints it will be discussed separately. There is still a great deal of activity in developing an improved understanding of helicopter rotor aerodynamics and in developing new and improved mathematical models that will more faithfully predict the flow physics and help design more aerodynamically efficient rotors of lighter weight. One should always bear in mind that small, systematic improvements in rotor efficiencies can potentially result in significant increases in the payload capability, maneuver margins, or the forward flight speeds of modern helicopters.

Rotor design efficiency is often measured by figure of merit (see Section 2.8), although its use as a comparative metric is restricted to rotors operated at the same equivalent disk loading. A historical record of measured main rotor figure of merit versus year of initial development is shown in Fig. 6.2, the data (in part) being compiled by Carlson (2002). It is clear that improvements in aerodynamic design have lead to state-of-the-art values of *FM* approaching 0.82. While substantial gains have been obtained over the years, the slow asymptotic nature of the faired curve suggests that further increases in the *FM* of helicopter rotors may require much more revolutionary developments in its aerodynamic performance. Potentially, this can be obtained through better integrated aerodynamic optimization of the rotor, such with the use of fully 3-D aerodynamic design techniques combined (perhaps) with the use of forms of active flow control (see page 401). It would seem that values of *FM* approaching 0.85 may be feasible, although much work remains before such goals are realizable. The current interest in hovering small remotely piloted helicopters and micro air vehicles (see Section 6.14) suggests that at this scale the rotors may have *FM* values that are close to half of those obtained with full-scale rotors, and clearly there is considerable opportunity for improvement here.

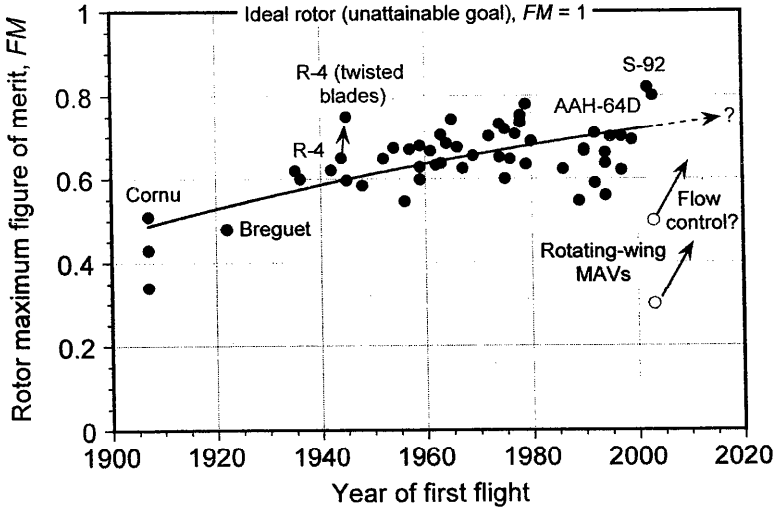

Figure 6.2 Main rotor figure of merit versus year of development show sustained improvements in aerodynamic efficiency, although future gains may be more elusive.

The conceptual and preliminary design of the main rotor must encompass the following key aerodynamic considerations:

1. General sizing: This will include a determination of rotor diameter, disk loading and rotor tip speed. There are several important trade-offs in performance and other characteristics with variations in all of these parameters.
2. Blade planform: This will include chord, solidity, number of blades, and blade twist. The optimal blade planform and twist distribution for hover may not be optimum for high-speed forward flight. The consideration of other than a rectangular tip shape may be part of the preliminary design.
3. Airfoil section(s): These play an important role in meeting overall performance requirements. On most modern rotors, the use of different airfoils at various stations along the blade will be a likely design choice to maximize rotor performance.

6.4.1 *Rotor Diameter*

There are several conflicting factors that must be examined when determining the main rotor diameter. As shown previously in Chapters 2 and 5, both good hover performance and safe autorotational capabilities call for a large rotor diameter. The advantages of a larger rotor diameter are lower disk loadings, lower average induced velocities, and lower induced power requirements. It was shown in Section 2.12 that based on the modified momentum theory the operating thrust coefficient, C_T, to give the best power loading was

$$C_T = \frac{1}{2}\left(\frac{\sigma C_{d_0}}{\kappa}\right)^{2/3} \quad \text{for best } PL, \tag{6.1}$$

which depends on airfoil section, rotor solidity and induced power factor. Using this result, the disk loading for minimum power loading will be

$$DL = \frac{T}{A} \approx \frac{W}{A} = \frac{1}{2}\rho(\Omega R)^2\left(\frac{\sigma C_{d_0}}{\kappa}\right)^{2/3}. \tag{6.2}$$

This equation determines the optimum radius of the rotor to maximize power loading at a given gross weight. Solving for the main rotor radius gives

$$R = \sqrt{\frac{W}{\pi DL}} \quad \text{for a conventional single rotor design} \tag{6.3}$$

and

$$R = \frac{1}{\sqrt{2}}\sqrt{\frac{W}{\pi DL}} \quad \text{for a coaxial or dual rotor design,} \tag{6.4}$$

where it is assumed that for design purposes each rotor of the dual rotor helicopter carries one half of the total weight of the aircraft. It has also been shown that

$$PL = \frac{T}{P} \propto \frac{FM}{DL}, \tag{6.5}$$

which means for a given disk loading the rotor(s) should also be operated at the highest possible figure of merit. However, Fig. 2.16 has shown that the most efficient power loading (compared to the ideal value) is relatively insensitive to the operating state of the rotor, in that the power loading curve is fairly flat over the normal range of operational thrust coefficients. Therefore, there is some latitude in selecting rotor radius, which may be constrained

because of factors other than pure aerodynamic considerations. For example, if the helicopter is required to operate off loose terrain such as gravel or sand, the design may require the disk loading to be limited so that the downwash velocities remain low enough not to stir up any of the loose surface material. This usually means the use of a relatively high rotor diameter. A large diameter also means a larger inertia and stored rotational kinetic energy, which is essential for safe autorotational characteristics (see Section 5.6). Initial sizing studies of the main rotor must always consider autorotational capability, which will require some minimum rotor inertia if the helicopter is to meet the military acceptance criteria or civilian certification requirements. Both single and multiengine helicopters must demonstrate safe autorotative landing capability at maximum gross weights. Often the initial rotor design is guided by previous rotor designs that are known to meet the autorotative specifications necessary for certification. An autorotative index of the form that was discussed in Section 5.6.3 may be used as a means of quantifying the potential autorotative characteristics of a proposed new rotor design.

Usually a much smaller rotor diameter must ultimately be used than would be desired for best hovering efficiency (for a given blade area and tip speed) so as to meet overall helicopter size, weight, cost, gearbox torque limitations, speed, maneuverability requirements, and storage or transportation requirements for the helicopter. A smaller rotor will have a smaller and lighter hub and a lower overall parasitic drag, and so this will be more efficient for cruising flight. Smaller rotors also permit a more compact net helicopter design, which is useful for several operational reasons, including storage and transportation by sea and air. In addition, a smaller rotor diameter minimizes the static deflection or "droop" of the nonrotating blades. The static droop can increase quickly for larger rotor diameters and may cause problems when starting and stopping the rotor, especially in gusty wind conditions where the low centrifugal forces on the blades may lead to "blade sailing," causing the rotor blades to flap and flex and perhaps impact the airframe. In most cases, the blade radius is usually kept to less than about 40 ft (12 m) otherwise the extra structure necessary to increase the blade stiffness will incur a significant weight penalty.

Figure 6.3 gives a summary of main rotor radius versus gross weight for a selection of helicopters (see appendix). Plotting the data on a logarithmic scale accentuates the

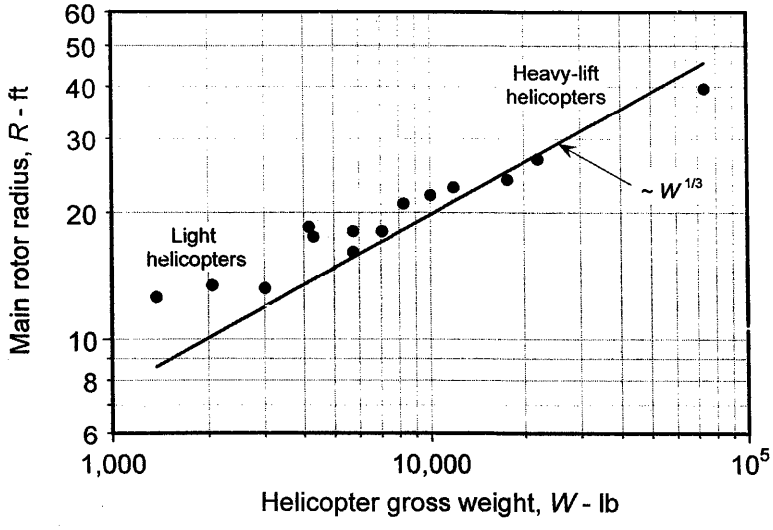

Figure 6.3 General trends in main rotor size (radius) versus helicopter gross weight.

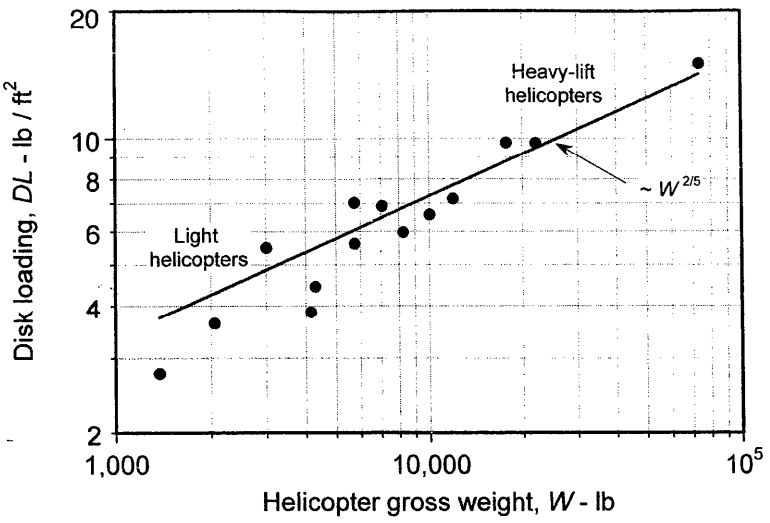

Figure 6.4 General trends of main rotor disk loading versus helicopter gross weight.

strong correlation between the quantities. This plot shows that the helicopter weight grows much faster than the rotor size. The well-known "square–cube" scaling law gives a simple explanation for this behavior. For geometrically similar aircraft, the overall area of the aircraft increases with the square of a characteristic length, say l, and its volume by the cube of this length; so the weight of the aircraft, W, should also increase with the cube power of a characteristic length, that is, $W \propto l^3$ or $l \propto W^{1/3}$. Therefore, for a helicopter $R \propto W^{1/3}$, which indeed is the trend shown in Fig. 6.3.

The corresponding trend of rotor disk loading versus gross weight is shown in Fig. 6.4. Remember that the disk loading must be kept as low as possible to maximize hovering performance, although with the larger and heavier helicopters this comes at some price. Because of the various other nonaerodynamic constraints posed in the design, such as the minimization of rotor weight and greater torque requirements, a large rotor diameter is not always practical. Generally, the manufacturer will try to find the smallest rotor diameter that will meet all of the specifications laid down for that helicopter. The square–cube law would suggest that $T/A \propto W^{1/3}$, but the results shown in Fig. 6.4 indicate a slightly more rapid increase such that $T/A \propto W^{2/5}$ because of the nonaerodynamic constraints. Therefore, the corresponding power loading will be proportional to $W^{-1/5}$.

6.4.2 *Tip Speed*

A high rotor tip speed helps to maintain the local velocities and decrease the angles of attack on the retreating blade, thereby delaying the onset of blade stall for a given blade area and advance ratio. A high tip speed also gives the rotor a high level of stored rotational kinetic energy for a given radius and helps reduce design weight. Because $P = \Omega Q$, a high tip speed reduces the rotor torque required for a given power and allows a lighter gearbox and transmission design. However, there are two important factors that work against the use of a high tip speed: compressibility effects and noise. Compressibility effects manifest as increased rotor power requirements. If the drag divergence Mach number of the tip sections is exceeded, the sectional drag (and thus rotor power) increases dramatically – see Section 5.4.3. Therefore, reducing the tip speed permits a higher flight speed to be achieved

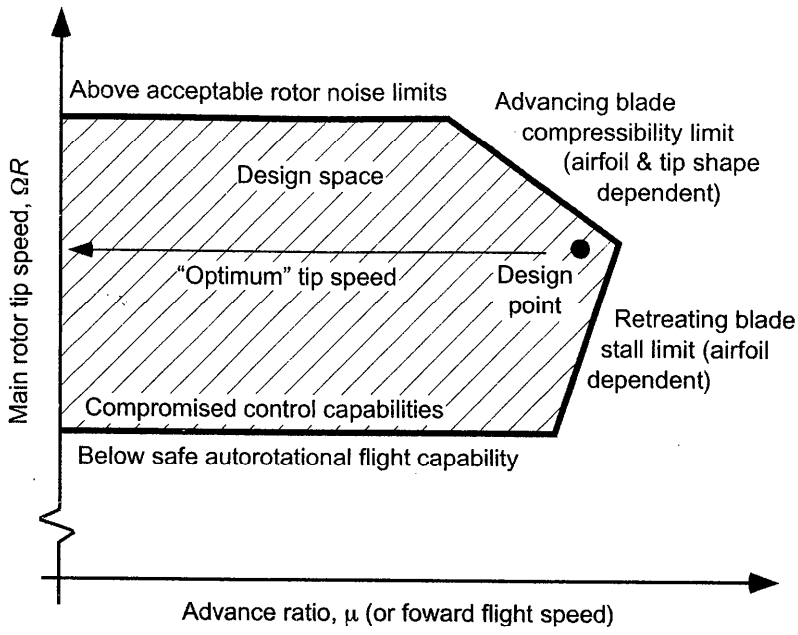

Figure 6.5 Aerodynamic, noise, and autorotative constraints imposed on the selection of rotor tip speed. Adapted from Prouty (1998) and other sources.

before compressibility effects become important. The use of a thinner airfoil at the blade tip and/or a swept tip shape can help significantly to delay the onset of compressibility effects to a higher advance ratio. Rotor noise increases rapidly with increasing tip Mach number. At low tip speeds, the noise resulting from the steady and harmonic loading on the blades is dominant. At higher tip speeds, the noise caused by blade thickness effects becomes an important contributor to the overall sound pressure, and the noise signature can become increasingly obtrusive.

Figure 6.5 shows what would be considered the range of acceptable tip speeds for conventional helicopters. The challenge for new rotor designs is to extend both the stall and compressibility limits to a higher forward flight speed. Yet, this is not easily achieved. The usual design constraints of maintaining good hover performance and acceptable autorotational characteristics (stored kinetic energy in the rotor system) severely limit the range of acceptable rotor tip speeds. However, the development of modern high-lift airfoil sections for rotors has permitted a reduction in rotor tip speed and, therefore, rotor noise levels, without compromising other aspects of the rotor performance. The use of thinner and/or "supercritical-like" airfoils and swept tips can also help alleviate compressibility effects – see Section 6.4.6. For many rotor designs, the autorotative kinetic energy limit may be an issue – see Section 5.6.3. Although this can be improved by adding rotor mass, the corresponding decrease in payload and the increase in blade and hub loads because of the higher centrifugal forces are usually unacceptable. In light of the foregoing, these issues tend to set the lowest possible allowable main rotor tip speed to about 680 ft/s (207 m/s) for a conventional helicopter.

Systematic experimental measurements of rotor performance (thrust, power, figure of merit) at different operational tip speeds (or tip Mach numbers) and rotor solidities are relatively scarce. Figure 6.6 shows the effects of rotor tip Mach number on the figure of merit as a function of rotor solidity. While there is clearly scatter in the data, the results

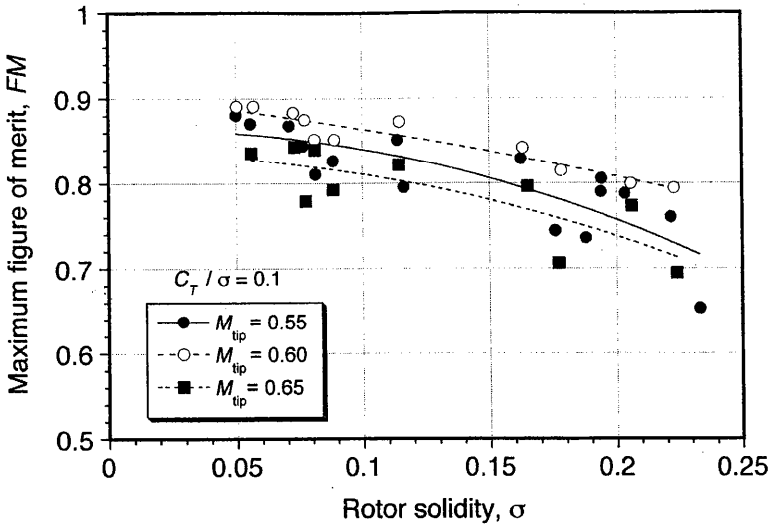

Figure 6.6 Measured figure of merit variation versus rotor solidity for different main rotor tip Mach numbers. Data source: Department of the Army, Engineering Design Handbook (1974).

confirm that operation at lower blade tip Mach numbers and lower rotor solidities is very desirable if hovering performance is to be maximized. At higher tip Mach numbers the rotor performance degrades because of the increasing compressibility losses. However, it must be recalled that rotor operation at low tip speeds will compromise forward flight performance because of the need for the retreating blade to operate at higher angles of attack and closer to the stall, all other factors being equal. In addition, the need to allow sufficient stall margin in the rotor design, especially for helicopters designed for high maneuverability and agility (see Section 5.9), requires the use of a higher main rotor tip speed.

6.4.3 *Rotor Solidity*

Rotor solidity, σ, has been defined previously as the ratio of total blade area to the disk area (i.e., $\sigma = N_b c/\pi R$). Values of σ for contemporary helicopters vary from about 0.06 to 0.12. Smaller helicopters generally tend to have lower solidity rotors. It has been shown in Chapter 3 that the mean rotor lift coefficient is given in terms of the blade loading coefficient, C_T/σ, by $\bar{C}_L = 6(C_T/\sigma)$. Typical values of $\bar{C}_L$ for helicopters range from about 0.4 to 0.7.

Selecting the rotor solidity during the design process requires a careful consideration of blade stall limits, that is the mean lift coefficient where the rotor performance will be stall limited. Certification or acceptance requirements dictate the load-factors and bank angles that must be demonstrated without the rotor stalling. Normally civil helicopters require a minimum of 1.15 g or a 30° bank angle without evidence of stall at the maximum gross weight of the helicopter. Military requirements tend to be much more severe, however. Rotors that are designed for high forward flight speeds and/or high maneuverability requirements require a higher solidity for a given diameter and tip speed. Obviously, a rotor that uses airfoil sections with high maximum lift coefficients can be designed to have a lower solidity, all other factors being equal. Alternatively, the use of high-lift airfoil sections permits a lower tip speed for the same solidity. Because rotor noise is considerably

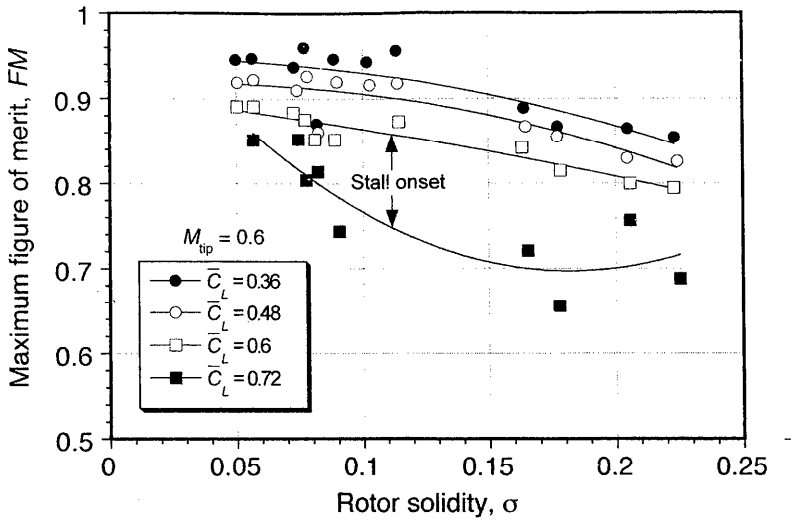

Figure 6.7 Measured figure of merit variation at different mean lift coefficients versus rotor solidity for a constant tip Mach number of 0.6. Data source: Department of the Army, Engineering Design Handbook (1974).

reduced when the rotor is operated at lower tip speeds, the development of high-lift airfoils that operate efficiently over the diverse range of conditions found within the rotor environment has always been an important design goal for the helicopter industry – see Section 7.9.

Figure 6.7 shows experimental results for the variation in figure of merit versus rotor solidity at different mean lift coefficients. These results simply reaffirm that one way to minimize profile power is to keep the rotor solidity as low as possible. However, this approach must be done with caution because decreasing the solidity reduces the blade lifting area, increases the blade loading coefficients, and elevates the local and mean blade lift coefficients for a given rotor thrust. In other words, decreasing the rotor solidity decreases the *stall margin*, which is the margin between the average values of the operational lift coefficients and the maximum lift coefficient of rotor as a whole. For example, consider rotor operation at a nominal mean lift coefficient, $\bar{C}_L$, of 0.6, as shown in Fig. 6.7. Then for a given value of solidity, operation of the rotor at a higher $\bar{C}_L$ results in a substantial degradation in rotor performance. This degradation is alleviated by increasing the solidity of the rotor, which helps reduce the local lift coefficients and improve the lift-to-drag ratios of the airfoil sections. Because the onset of stall sets the performance limits of a rotor, it is also very important to provide some additional stall margin in the rotor design to allow for normal maneuvers and gusts typical of turbulent air. The specified margin, which will vary for different helicopter designs, generally tends to set the lowest allowable solidity to which the rotor can be designed. For example, a highly maneuverable combat helicopter will always require a larger stall margin than a civilian transport machine. This is obtained, however, only with increased blade weight and higher overall rotor weight.

The onset of retreating blade stall in forward flight also limits the rotor performance. In forward flight, the rotor must provide both lifting and propulsive forces, the latter of which depends largely on the parasitic drag of the airframe but the rotor drag is also important. The stall inception boundary in forward flight can be most easily observed from strain-gauge

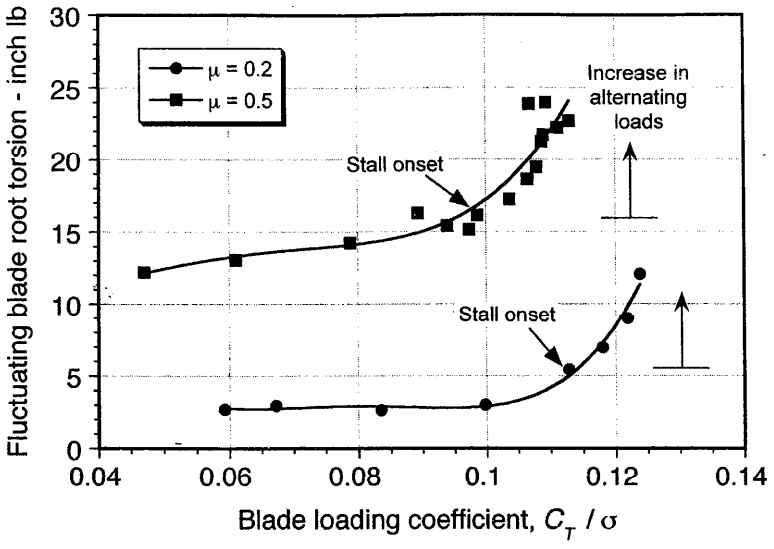

Figure 6.8 Retreating blade stall inception in forward flight deduced from blade root torsion loads. Data source: McHugh (1978).

measurements of blade-pitch link and/or blade torsion loads. When stall occurs on the rotor, the mean (average) and alternating aerodynamic pitching moments increase dramatically. Representative measurements of the fluctuating component of the blade root torsion loads are shown in Fig. 6.8 as a function of C_T/σ at two advance ratios of 0.2 and 0.5. At low advance ratios the blade root torsion loads are relatively low, but as C_T/σ reaches about 0.11, there is a more rapid increase as the rotor begins to show some evidence of stall. As the advance ratio increases, stall inception occurs at progressively lower values of C_T/σ. At $\mu = 0.5$, the stall onset is more sudden and shows large increases in the fluctuating loads because of the onset of dynamic stall on the retreating blade. These fluctuating loads will manifest as high structural stresses in the blade and hub, and higher control forces, accompanied by significant increases of vibration levels. Stall will also cause longitudinal blade flapping, tilting the disk back (a β_{1c} blade motion) and decreasing propulsive force, therefore setting a natural barrier to further increases in forward speed. Higher control forces and the higher than normal vibration levels on the helicopter will serve as a warning to the pilot that the limits of the normal operational flight envelope of the rotor are being reached.

As already mentioned, propulsive force considerations also influence the selection of rotor solidity. In forward flight the function of the rotor is to provide a vertical lift force to overcome airframe weight as well as to provide a forward acting propulsive force. The overall envelope is summarized by Fig. 6.9, which is one type of representation of blade loading (or mean lift coefficient) versus propulsive force. The disk must be progressively tilted forward to provide this forward thrust (propulsion) component, and so stall onset will be obtained at progressively lower values of mean lift coefficient. Notice also that rotor noise issues become important in high-speed forward flight, particularly a form known as high-speed impulsive or HSI noise. Propulsive requirements can be reduced by minimizing the parasitic drag of the airframe or by thrust and/or lift compounding. While offering some advantages over a conventional helicopter, compound helicopter designs also suffer from many disadvantages as well – see Section 6.11.1.

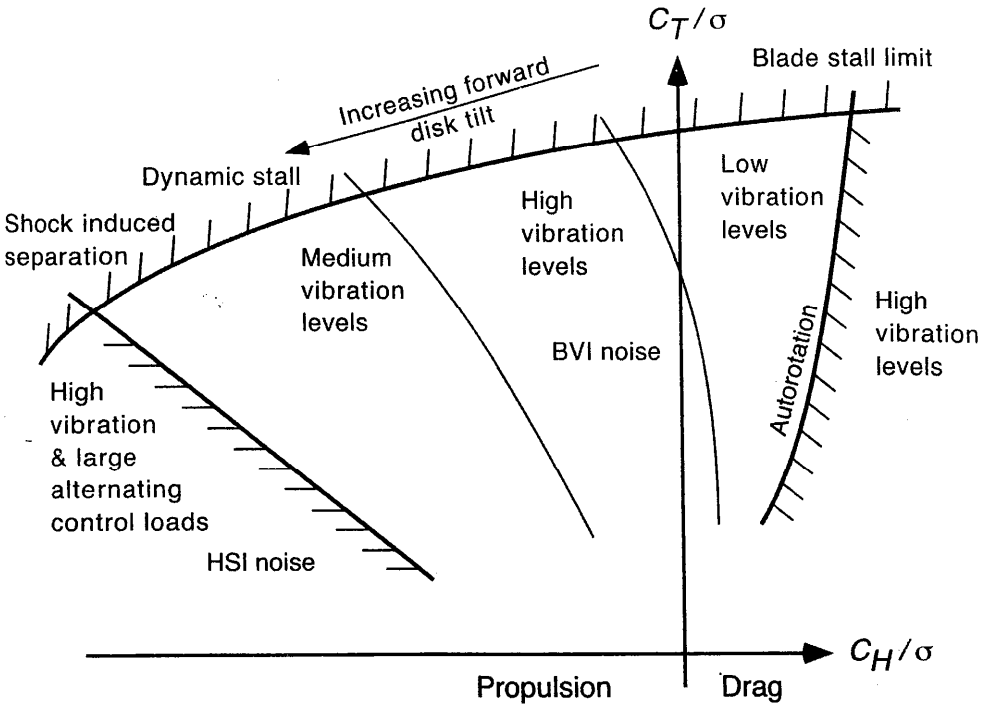

Figure 6.9 Propulsive limits for a conventional helicopter. Adapted from Vuillet (1990) and other sources.

6.4.4 *Number of Blades*

The selection of the number of blades for a rotor (for a given blade area or solidity) is usually based on dynamic rather than aerodynamic criteria, that is, it is based on the minimization of vibratory loads, which is easier for rotors that use a larger number of blades. Fewer blades, however, will usually reduce blade and hub weight, minimize hub drag, and may give better reliability and maintainability because of a lower parts count. Lighter weight helicopters usually have two blades, whereas heavier helicopters generally have four, five, seven or even eight blades. As shown in Section 3.2.4, aerodynamically the induced tip-loss effects are reduced by increasing the number of blades, but the effects on induced power are relatively small for the high aspect ratio blades typical of helicopter rotors.

Knight & Hefner (1937) and Landgrebe (1972) have conducted systematic tests of blade number and solidity on rotor performance. Knight & Hefner tested subscale rotors with two, three, four, and five blades with no twist and at fairly low tip speeds. Landgrebe tested subscale rotors with two, four, six, and eight blades, linear twist, and at full-scale tip Mach numbers. All of the tests were done by adding blades to the rotor hub so the results cannot distinguish independently the effects of solidity from the number of blades. However, an analysis of these data suggest that hover performance is primarily affected by rotor solidity; the number of blades are secondary. Following Knight & Hefner (1937), the primary rotor behavior can be analyzed by the use of the blade element theory. From Section 3.2, the rotor-thrust coefficient is given by

$$C_T = \frac{1}{2}\sigma \int_0^1 C_l r^2 \, dr = \frac{1}{2}\sigma C_{l_\alpha} \int_0^1 (\theta - \phi) r^2 \, dr. \tag{6.6}$$

Also, $\phi(r) = \lambda/r$, and for a linearly twisted blade $\theta(r) = \theta_{75} + \theta_{tw}(r - 0.75)$. Therefore

$$C_T = \frac{1}{2}\sigma C_{l_\alpha} \int_0^1 \left[(\theta_{75} + (r - 0.75)\theta_{tw})r^2 - \lambda r\right] dr$$
$$= \frac{1}{2}\sigma C_{l_\alpha} \left(\frac{\theta_{75}}{3} - \frac{\lambda}{2B}\right) \tag{6.7}$$

when including tip losses alone through the factor B. Assuming uniform inflow, the corresponding power can be written as

$$C_P = C_{P_i} + C_{P_0}$$
$$= \lambda C_T + C_{P_0}$$
$$= \frac{\lambda}{2}\sigma C_{l_\alpha} \left(\frac{\theta_{75}}{3} - \frac{\lambda}{2B}\right) + C_{P_0}. \tag{6.8}$$

Incorporating other nonideal induced losses (other than tip loss) such that $\lambda = \kappa\sqrt{C_T/2}$ and dividing through by σ^3 gives

$$\frac{C_P}{\sigma^3} - \frac{C_{P_0}}{\sigma^3} = \frac{\Delta C_P}{\sigma^3} = \frac{C_{l_\alpha}\kappa}{2\sqrt{2}}\sqrt{\frac{C_T}{\sigma^2}} \left(\frac{\theta_{75}}{3\sigma} - \frac{\kappa}{2\sqrt{2}B}\sqrt{\frac{C_T}{\sigma^2}}\right). \tag{6.9}$$

Therefore, if the results from rotor experiments are plotted in the form of $(C_P - C_{P_0})/\sigma^3$ versus C_T/σ^2, then this should remove the primary effect of solidity from the measurements. As shown by Figure 6.10, the results from both sets of measurements show good correlation with the result given by Eq. 6.9, confirming that the effect of blade number on rotor performance is indeed secondary. The modified results are based on the assumption that $\kappa = 1.25$, $B = 0.97$ and a higher-order approximation for the profile power, both effects having been discussed previously in Section 3.3.9. Note that the latter assumption gives a small but significant improvement in the correlation at high values of thrust where

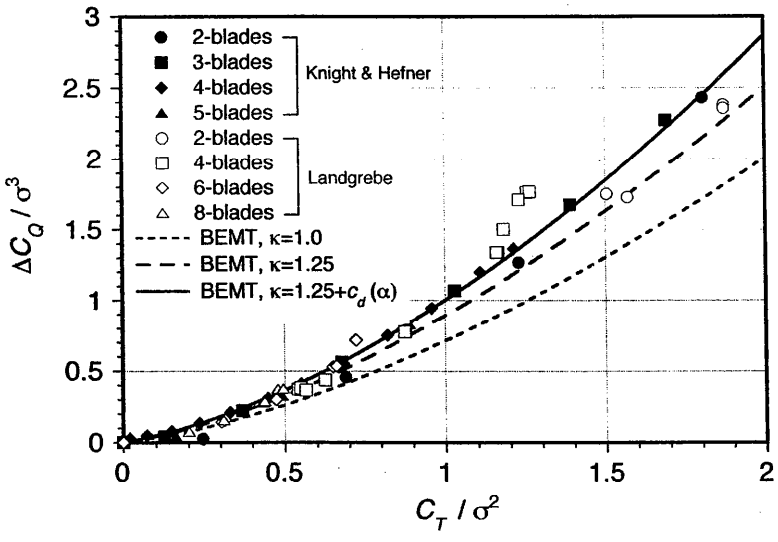

Figure 6.10 Correlation curve suggested by Knight & Hefner (1937) of C_Q/σ^3 versus C_T/σ^2 showing negligible effect of blade number on hovering rotor performance.

nonlinear drag effects begin to become important as the boundary layer thickens and the blade sections approach stall.

In subscale rotor experiments the effects of blade number can be masked by other effects, including those associated with the effects of Reynolds number and Mach number. The effects of Reynolds number can be particularly significant on small-scale rotors with small chords and tip Reynolds numbers that are often below 10^6 – see Section 7.9.1. Increasing the number of blades while maintaining the solidity of the rotor will decrease the blade chord and decrease the Reynolds numbers. Based on 2-D arguments this will tend to result in slightly higher values of the profile drag coefficient and, therefore, will give a small but finite reduction in the figure of merit.

A larger number of blades also leads to weaker tip vortices (for the same overall rotor thrust), thus potentially reducing the intensity of any airloads produced by blade–vortex interactions (all other factors being assumed equal). However, with more blades, the number of potential blade–vortex interactions over the disk will be increased (see Section 10.4.2). This can affect both the frequency and directivity of propagated noise, and the problem becomes far too complicated to make generalizations as to the expected trends. Furthermore, from the perspective of noise generation, a higher number of blades results in a smaller chord and lower "thickness" noise associated with each blade. However, even though the strengths of the tip vortices may be reduced by using a larger number of blades (at a constant thrust), the blades are closer azimuthally. Because the tip vortices are convected vertically only relatively slowly in hover and remain almost in the plane of the rotor, the following blades may more closely interact with the vortices from previous blades. Such a phenomenon has been encountered on hovering rotors with five or seven blades and can significantly affect predictions of induced power – see Clark & Leiper (1970).

6.4.5 *Blade Twist*

The proper use of blade twist (washout) can significantly improve the figure of merit of the rotor, a result found early on in helicopter development after the development of basic aerodynamic theory. This is reflected in Fig. 6.2 by the significant gain in the *FM* for the early Sikorsky R-4 helicopter by using redesigned blades with twist. Based on the combined blade element momentum theory (BEMT) discussed in Section 3.3, it has been shown that negative (nose down) twist can redistribute the lift over the blade and help reduce the induced power, but only to a point. Therefore, proper use of blade twist can significantly improve the figure of merit in hover. In Section 3.3.11 the effect of blade twist on the induced power factor has been shown based on analytical results. Paul & Zincone (1977) have shown the effects of blade twist on the maximum figure of merit deduced from full-scale rotor tests; these results are reproduced in Fig. 6.11. In general, the results confirm the theory in that the figure of merit of highly twisted rotors is nearly always better than that for moderately twisted rotors when operating at the same disk loading.

In forward flight, rotors with a high nose-down blade twist (say, greater than 15°) may suffer some performance loss. This is because of the reduced angles of attack can be produced on the tip of the advancing blade, resulting in a loss of rotor thrust and propulsive force. The problem has been explored by Keys et al. (1987). Results documenting the problem are shown in Fig. 6.12 in terms of power required (relative to hover power) versus advance ratio. Although not severe, some degradation in high-speed cruise performance is noted with the higher blade twist. Blades with very large twist rates, while offering performance benefits in hover, may suffer reduced or even negative lift production on the advancing blade tip and are obviously to be avoided. A survey of existing rotor designs

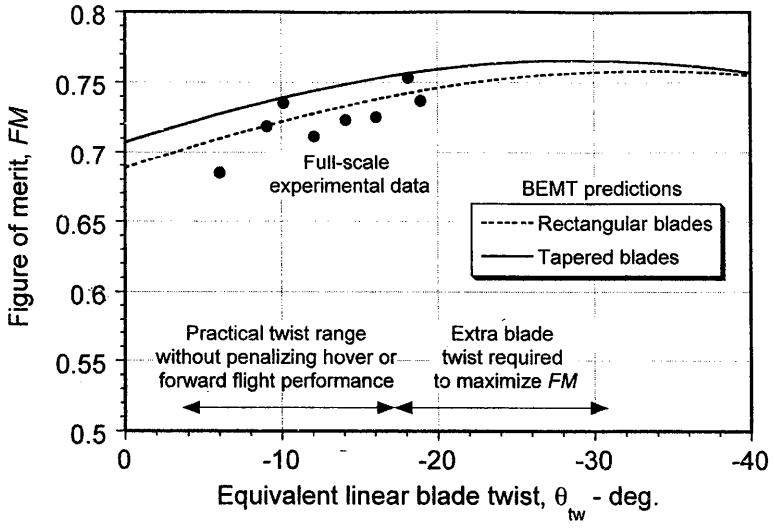

Figure 6.11 Effect of blade twist on hovering figure of merit. Measurements from Paul & Zincone (1977).

shows that most helicopter blades incorporate a negative linear twist between 8° and 15°, with only a few exceptions. This twist range is a compromise between maximizing the *FM* of the rotor in hover at its design point (typically maximum hover gross weight), while simultaneously avoiding any detrimental effects on forward flight performance. Clearly, however, some gains in *FM* are possible if large values of blade twist can be tolerated. In the quest for high-speed forward flight capability of the helicopter, some manufacturers have used a nonlinear twist or double linear blade twist, where the effective twist rate is reduced or reversed near the blade tip. This helps give the helicopter better forward flight

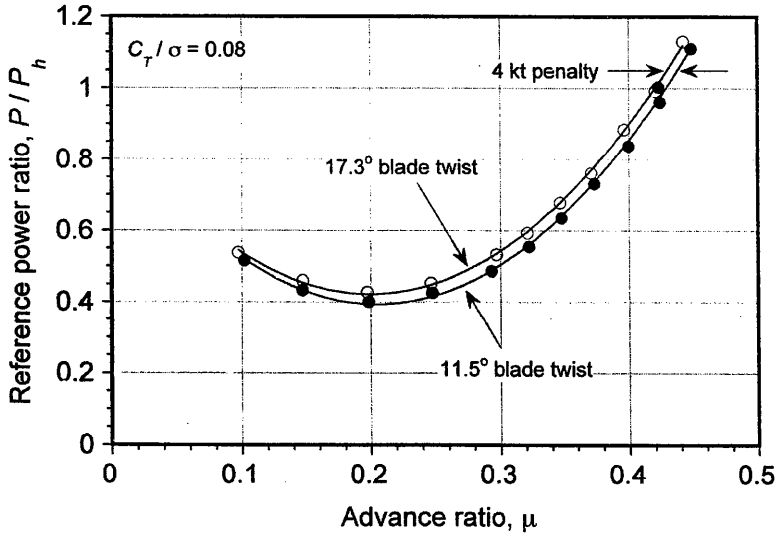

Figure 6.12 A loss of performance with highly twisted rotor blades may be expected in forward flight. Data source: Keys et al. (1987).

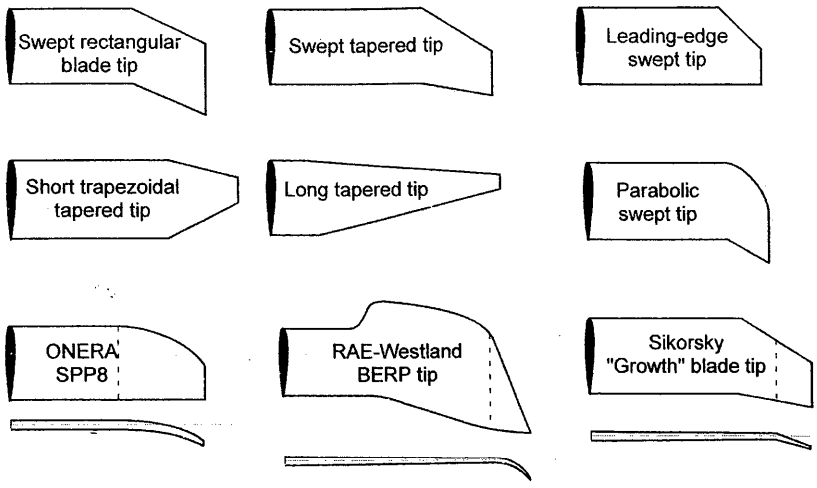

Figure 6.13 Some advanced main rotor blade tip designs. Note: Not to scale.

performance while retaining most of the hover performance and thus offers another good compromise for the rotor design.

6.4.6 *Blade Planform and Tip Shape*

The tips of the blades play a very important role in the aerodynamic performance of the helicopter rotor. The blade tips encounter the highest dynamic pressure and highest Mach numbers and strong trailed tip vortices are produced there. A poorly designed blade tip can have serious implications on the rotor performance. Figure 6.13 shows some blade tip designs that have been used or proposed for helicopter rotors. There are several common designs, comprising those with taper, those with sweep, and those with a combination of sweep and taper. Some blade tips may also use anhedral, which, as shown by Balch (1984) and others, can improve the figure of merit of the rotor. A good analysis of the effects of anhedral is given by Desopper et al. (1986, 1988), Vuillet et al. (1989), and Tung & Lee (1994). An example of a state-of-the-art tip shape is that on the "advanced growth blade" designed by Sikorsky for the S-92 and later models of the UH-60. This unique tip incorporates all three geometric parameters, sweep, taper, and anhedral. Other special tip designs such as that used on the Westland/RAE BERP blade incorporate somewhat more radical variations in sweep, planform, and anhedral.

It is known from the analysis in Section 3.4 that blade planform can also have an important effect on the blade lift distribution and, therefore, on the rotor performance. Usually, small amounts of taper over the blade tip region can help to significantly improve the figure of merit (*FM*) in hover. This is confirmed in Fig. 6.14, which is taken from the subscale rotor experiments of Althoff & Noonan (1990). The benefits, however, seem to be lost for larger amounts of taper, most likely because of the higher profile drag coefficients associated with operation at small tip chord Reynolds numbers (see Fig 7.4). Nevertheless, the experimental results confirm the previous observations from the BEMT that a maximum figure of merit for the rotor can, in part, be obtained by using both a combination of blade twist and taper. The type and amount of taper and twist, however, needs to be factored into the overall rotor design and operational specifications. A 2:1 taper over the tip region seems about optimum for a helicopter blade.

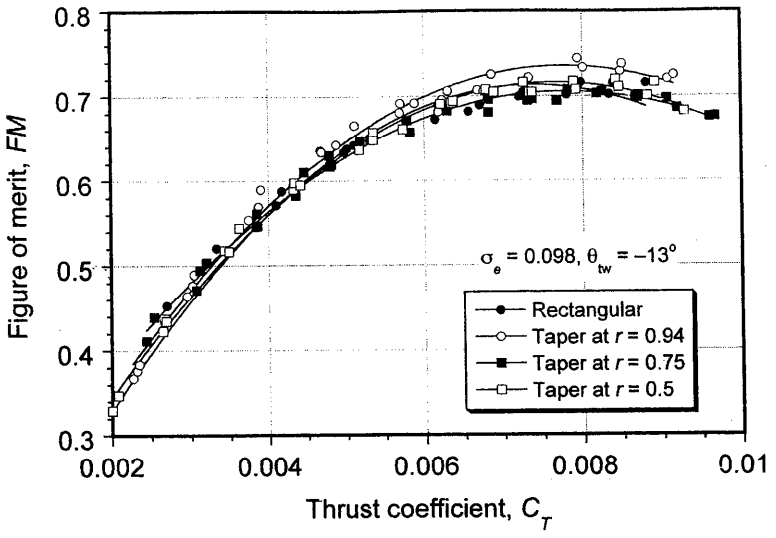

Figure 6.14 Measured effect of blade taper on the figure of merit of a hovering rotor. Data source: Althoff & Noonan (1990).

Sweeping the leading edge of the blade reduces the Mach number normal to its leading edge, thus allowing the rotor to attain a higher advance ratio before compressibility effects manifest as an increase in sectional drag and an increase in net rotor power required. The use of sweep also affects tip vortex formation, its location after it has been trailed from the blade, and its overall structure – see, for example, the results of Rorke et al. (1972), Balcerak & Felker (1973), Spivey (1968), Spivey & Morehouse (1970), Carlin & Farrance (1990), Sigl & Smith (1990), Smith & Sigl (1995), and Martin & Leishman (2002). However, the problem of rotor tip vortex formation and the effects of tip shape on the vortex characteristics, such as the velocity profile and the diffusive characteristics, is still the subject of ongoing research; systematic studies of the tip vortex characteristics generated by rotors with different tip shapes have not yet been accomplished. It is likely, however, that this is an area where research may lead to improved tip shapes and rotor blades optimized for lower induced drag.

Blade tips with a constant sweep angle and those with a progressively varying sweep angle have been used. Many modern helicopters (for example, the UH-60 Blackhawk and the AH-64 Apache) use some simple constant sweepback on the blade tip. The amount of sweep is usually kept low enough ($< 20°$) so that there are no inertial couplings introduced into the blade dynamics by an aft center of gravity or by aerodynamic couplings caused by a more rearward center of pressure. A constant sweep angle offers simplicity in design and construction, but may result in higher than desirable aerodynamic torsional couplings because of the rearward location of the local center of lift.

A blade tip with a progressive sweep angle can be designed on the basis of a simple 2-D blade element analysis. One criteria is to choose a sweep angle that is just sufficient to maintain a constant incident Mach number normal to the leading edge. The velocity normal to the leading edge, U_n, is given by

$$U_n = \Omega R\,(r + \mu \sin\psi)\cos\Lambda, \tag{6.10}$$

where Λ is the local sweep angle of the blade 1/4-chord axis (see inset in Fig. 6.15). The incident Mach number, $M_{r,\psi}$, is then

$$M_{r,\psi} = \frac{\Omega R}{a}\,(r + \mu \sin\psi)\cos\Lambda = M_{\Omega R}\,(r + \mu \sin\psi)\cos\Lambda, \tag{6.11}$$

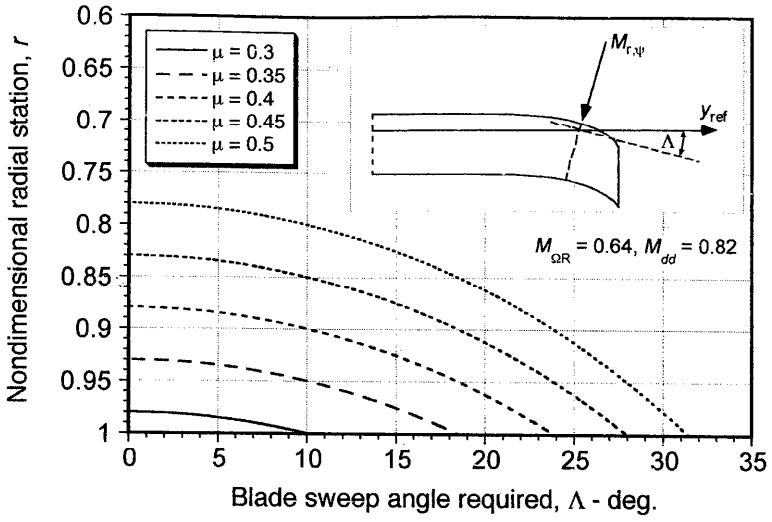

Figure 6.15 Example of sweep angle required to maintain the incident Mach number normal to the blade equal to a constant for a given advance ratio.

where a is the sonic velocity and $M_{\Omega R}$ is the hover tip Mach number. Consider the design point as the advancing blade, that is, where $\psi = 90°$, and ignore any unsteady effects associated with the problem. If the local Mach number is to be maintained below the drag divergence Mach number, M_{dd}, then the sweep angle required to do this is given by

$$\Lambda = \cos^{-1}\left(\frac{M_{dd}}{M_{\Omega R}(r+\mu)}\right). \tag{6.12}$$

For example, assume a typical hover tip Mach number of 0.64, and an airfoil with $M_{dd} = 0.82$. Then the sweep angle required to ensure that $M_{r,\psi}$ at each section remains just below M_{dd} is

$$\Lambda = \cos^{-1}\left(\frac{1.281}{r+\mu}\right). \tag{6.13}$$

The results are plotted in Fig. 6.15, where it will be seen that the 1/4-chord sweep angle is a smooth, almost parabolic, curve. With increasing advance ratio the amount of sweep required increases substantially and the sweep initiation point moves inboard on the blade. However, the amount of sweep that can actually be used or tolerated on a given helicopter blade clearly depends on structural dynamic issues as well, and such effects must be carefully examined. See also Questions 6.9 and 6.10.

McVeigh & McHugh (1982) have conducted experiments with subscale rotors to study the effects of tip shape on overall rotor performance and cruise lift-to-drag ratio. It was shown that the combined use of improved airfoil sections and tapered tip shapes can help minimize profile power and significantly improve overall cruise efficiency of the rotor. The effects of tip shapes were examined for four rotors having rectangular, swept, swept-tapered, and tapered tips. All rotors were tested at the same lift, propulsive force and trim state, which provides a proper datum for performance comparisons. Figure 6.16 reproduces a summary of the results from McVeigh & McHugh (1982). The tapered tip was found to give about 10% higher equivalent L/D ratio compared to the rectangular blade, but interestingly enough the rectangular blade gave a better maximum cruise L/D ratio than either of the swept or swept tapered blades. This is because both the advancing and retreating blade characteristics of

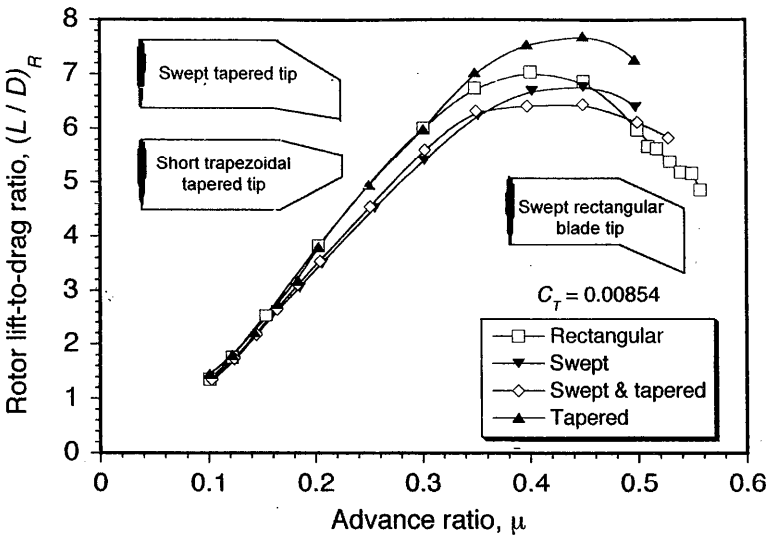

Figure 6.16 Equivalent lift-to-drag ratios for a rotor with different tip shapes. Data source: McVeigh & McHugh (1982).

the tip shape are important, and an integrated performance metric such as L/D ratio does not allow one to distinguish separately between these characteristics. While sweepback alone clearly has the advantage of delaying the onset of compressibility effects to higher advance ratios, the sweep may also promote early flow separation on the retreating blade at lower angles of attack. Therefore, there can be a performance penalty associated with a swept tip.

Yeager et al. (1987) and Singleton et al. (1990) have examined the performance of a tapered blade versus a blade with a simple swept tip and have found improvements in performance, with lower power requirements up to advance ratios of 0.4. Noonan et al. (1992) have examined the effects of blade taper alone on forward flight performance. Generally, small amounts of taper are desirable and help to improve rotor performance, at least up to advance ratios of 0.3. Larger amounts of taper yield much smaller improvements. Yeager et al. (1997) have tested a "BERP-like" (see Section 6.3.8) subscale rotor under similar controlled conditions and have compared the results to a rectangular blade with the same airfoil section. These and the other results confirm that a sophisticated swept tip design is by no means a panacea; each tip design must be assessed on the performance gains to be expected over the full operational envelope as well as within the overall requirements and constraints imposed by the rotor design process.

6.4.7 *Airfoil Sections*

The choice of airfoil sections for helicopter rotors requires special consideration because significant improvements in rotor performance can be realized with the optimal selection of airfoil shapes. This is of such fundamental importance to helicopter design that Chapter 7 is devoted to a basic understanding of the subject. Early helicopters used derivatives of NACA 0012 or NACA 230-series airfoils, which gave a reasonable compromise in overall performance. These can be considered as "first-generation" airfoil sections – see Fig. 6.17. Later, helicopters began to use a variety of airfoils sections that were optimized to match the aerodynamic requirements of each station along the blade. This is required

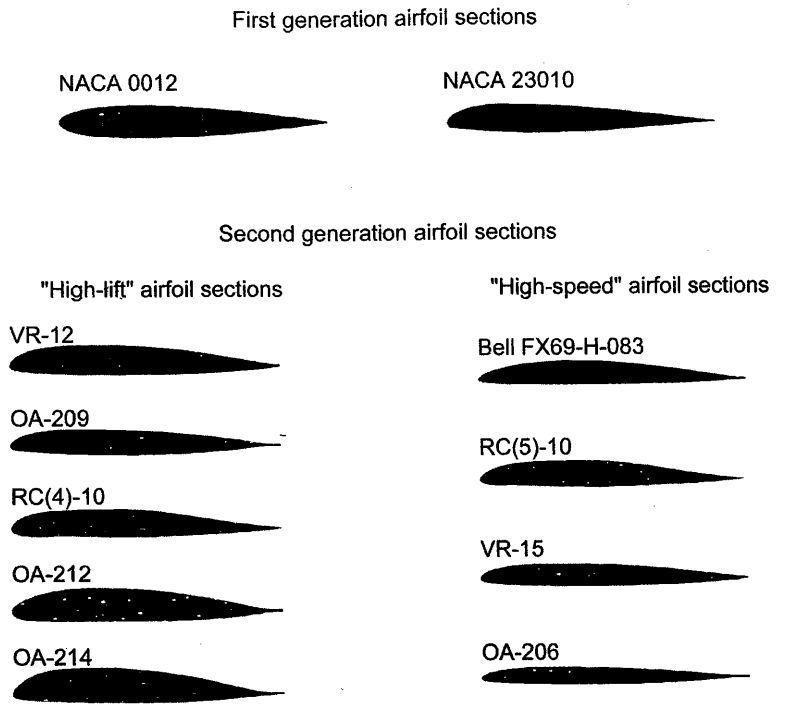

Figure 6.17 Airfoil sections for helicopters have been specifically developed to meet the aerodynamic conditions actually encountered on the rotor.

because during each rotor revolution, the airfoil sections on helicopter rotors encounter a wide diversity of operating conditions. For example, for a representative blade station (say at 75% blade radius) the aerodynamic environment in which this section operates in hover and forward flight are different. On the advancing side of the rotor disk the blade sections may reach high subsonic speed and in high-speed forward flight they may penetrate into the transonic flow regime. This causes wave drag, and if the shock strengths become sufficiently severe, shock induced flow separation and stall may be produced.

On the retreating side of the disk, the blade tip sections operate at subsonic speeds, but at much higher angles of attack, eventually close to stall. Therefore, the blade sections must be thin enough to maximize the drag divergence Mach number, while simultaneously they must have some minimum thickness and incorporate some camber to give a relatively high $C_{l_{max}}$ but still maintain low pitching moments throughout. No single airfoil profile will meet all these requirements and the airfoil(s) must be designed to reach a compromise between the requirements of all flight conditions, both at low and high airspeeds and also at high thrusts. Margins for maneuvering flight and turbulent air conditions must be factored in to the design to allow for sufficient performance. In general, the goal is to find airfoil sections that balance the advancing blade requirements (high drag divergence Mach number) with those of the retreating blade (high maximum lift at low Mach numbers), while maintaining a good overall lift-to-drag ratio throughout. This will help to maximize rotor efficiency throughout the flight envelope.

While rotor efficiency is often viewed simply as a hovering efficiency, forward flight efficiency (i.e., the effective lift-to-drag ratio of the rotor) is also important. But consider first the hovering efficiency. The airfoil requirements can be examined by rewriting the

figure of merit in another form to that shown previously. For a rotor with rectangular blades then

$$FM = \frac{\dfrac{C_T^{3/2}}{\sqrt{2}}}{\dfrac{\kappa C_T^{3/2}}{\sqrt{2}} + \dfrac{\sigma C_{d_0}}{8}} = \frac{1}{\kappa + \dfrac{\sqrt{2}\sigma C_{d_0}}{8C_T^{3/2}}}. \tag{6.14}$$

The mean lift coefficient of the rotor is $C_L = 6(C_T/\sigma)$ and it will be assumed that all the sections operate at the same $C_d = C_D$, an approximate but useful assumption. In terms of C_L and C_D the figure of merit becomes

$$FM = \frac{1}{\kappa + \dfrac{3\sqrt{2}\sqrt{6}}{4\sqrt{\sigma}}\left(\dfrac{C_D}{C_L^{3/2}}\right)} = \frac{1}{\kappa + \dfrac{2.6}{\sqrt{\sigma}}\left(\dfrac{C_L^{3/2}}{C_D}\right)^{-1}}. \tag{6.15}$$

Therefore, the figure of merit will be a maximum when all of the airfoils comprising the rotor blades operate at their best values of the ratio $C_l^{3/2}/C_d$ – see also Question 6.1. This result has been pointed out by many authors, including Gessow & Myers (1952), Prouty (1986), and Stepniewski & Keys (1984). While in practice not all the airfoils on the blade can operate at the same condition because of the varying Mach number and Reynolds number along the blade span, the forgoing result does show the need for good airfoil designs, in general, to obtain maximum hovering rotor efficiency.

This requirement is summarized in Fig. 6.18, where Eq. 6.15 has been rearranged to solve for $C_l^{3/2}/C_d$ as a function of the induced power factor κ for several values of rotor FM. It is clear that to achieve a state-of-the-art rotor design the induced losses should be low (by means of appropriate blade twist) and the value of $C_l^{3/2}/C_d$ for the airfoils should be large (through appropriate airfoil design and blade solidity selection). It would seem that values of FM of 0.80 or higher are only possible with an extremely careful rotor design (using optimal

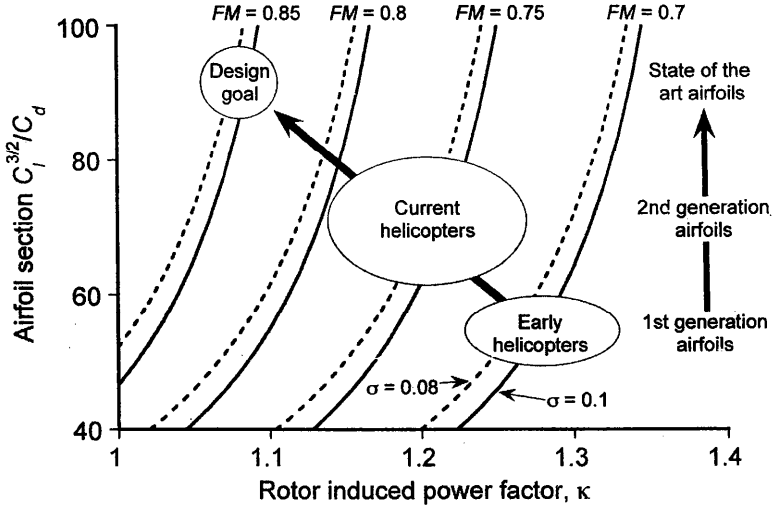

Figure 6.18 Maximum hovering efficiency is obtained by using low solidity rotors and by designing for low induced losses with good airfoil designs. Adapted from Stepniewski & Keys (1984).

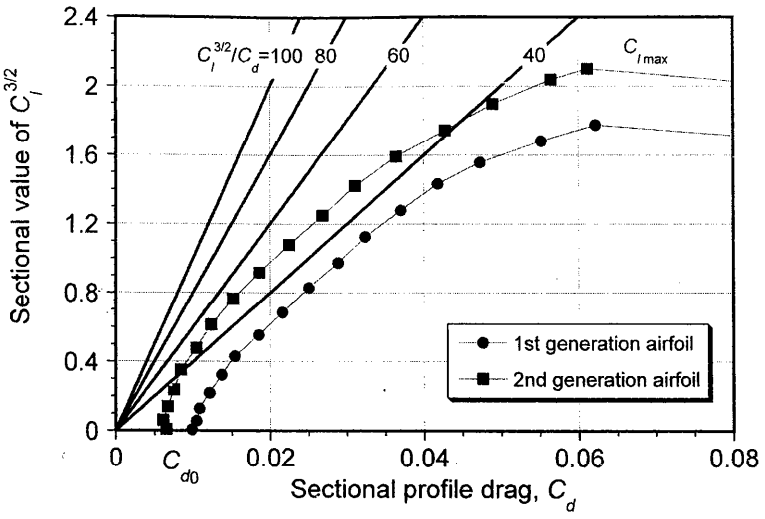

Figure 6.19 A form of 2-D drag polar for an airfoil showing that much higher values of $C_l^{3/2}/C_d$ are only possible through reductions in profile drag *and* increases in maximum lift coefficient.

blade twist, planform and tip shape) and also by using very advanced airfoils, perhaps with flow control devices to delay the onset of stall (see page 401). It is apparent, however, that after the airfoils reach high maximum values of $C_l^{3/2}/C_d$ (say over 80), further gains in rotor figure of merit through airfoil design improvements alone are very much harder to come by.

A form of drag polar for two representative helicopter rotor airfoils is shown in Fig. 6.19. One airfoil represents a first generation airfoil section with relatively modest performance and the other is a second generation airfoil with lower profile drag and a better value of maximum C_l, that is, $C_{l_{max}}$. Also shown are lines of constant $C_l^{3/2}/C_d$ from 40 (a modest but realistic airfoil performance) to 100 (an excellent but perhaps unrealistic performance). It is clear from Fig. 6.19 that improvements in $C_l^{3/2}/C_d$ come about by decreasing profile drag to as low a value as possible while simultaneously increasing the maximum attainable lift coefficient to as high a value as possible. It is for this reason that helicopter designers have strived for many decades to develop high-lift/low-drag airfoils that retain these characteristics over a wide range of operational Mach numbers – see Chapter 7. It is also apparent from Fig. 6.19 that the maximum values of $C_l^{3/2}/C_d$ are obtained over a good range of operating lift coefficients, usually in the range $0.7 \leq C_l \leq 1.2$, and so the rotor can operate at its maximum efficiency over a fairly wide range of disk loadings. This is a clearly beneficial result, so the rotor does not become as much of a "point" design. Delaying the onset of stall and the drag rise at higher lift coefficients obviously helps to further maintain rotor efficiency. However, it is not realistic to expect on a practical rotor that the best values of $C_l^{3/2}/C_d$ can be achieved simultaneously at all blade sections, nor that 2-D airfoil measurements are entirely representative of the aerodynamic behavior of the airfoils on the rotor. Yet the results in Fig. 6.18 indicate the general design goals.

Clearly, one way to help minimize profile power and maximize figure of merit in hover is to consider the use of an extremely low drag airfoil. As shown in Section 7.8, the airfoil profile drag consists of two parts, namely pressure drag and viscous (or shear stress) drag. The pressure drag can be minimized by using relatively thin airfoil sections, although the use of thin airfoils has some disadvantages as well, mainly because of the possibilities of

achieving fairly low maximum lift coefficients. The viscous drag component, represented approximately by the coefficient C_{d_0}, can be minimized by carefully controlling the airfoil pressure distribution and maximizing the chordwise extent of laminar flow, at least for a range of low to moderate lift coefficients. This is called a natural laminar flow (NLF) section. Unfortunately, there are other aspects of airfoil performance, such as the need for low pitching moments and high maximum lift, that usually preclude the use of special low drag or NLF airfoil sections on rotor blades. Also, environmental factors tend to produce insect accretion and blade erosion at the blade leading edge, which can cause premature boundary layer transition and reduce the run of laminar flow in any case. In some circumstances surface roughness can adversely alter other aspects of the airfoil characteristics such as by lowering $C_{l_{max}}$ and/or changing the stall characteristics.

A powerful parameter affecting the profile power of the rotor is the airfoil thickness. Using 2-D airfoil measurements given by Abbott & von Doenhoff (1949), the zero-lift sectional drag coefficient for the NACA symmetric series can be approximated by the equation

$$C_{d_0} \approx 0.007 + 0.025\left(\frac{t}{c}\right), \tag{6.16}$$

where t/c is the thickness-to-chord ratio. The result is valid in the range $0.06 \leq t/c \leq 0.24$. The effects of Mach number compound the behavior of the drag, but at moderate angles of attack below the drag divergence Mach number the effects of compressibility are small and are more sensitive to Reynolds number. Assume, for example, that a blade tapers in thickness from an airfoil with a 12% thickness-to-chord ratio at the root to an 8% ratio at the tip. Therefore, using Eq. 6.16 the drag coefficient can be written as

$$C_{d_0}(r) = 0.007 + 0.025(0.12 - 0.04r) = 0.01 - 0.001r. \tag{6.17}$$

The profile power coefficient can now be estimated using the blade element model where

$$C_{P_0} = \frac{1}{2}\sigma \int_0^1 C_{d_0} r^3 dr = \frac{1}{2}\sigma \int_0^1 (0.01 - 0.001r) r^3 dr. \tag{6.18}$$

Evaluation of this expression gives a value of $\frac{1}{8}\sigma(0.0092)$ compared to the value $\frac{1}{8}\sigma(0.01)$ without the use of thickness variations (i.e., an 8% reduction in profile power). Typically, this would translate into an increase in figure of merit of between 1 and 2%. For a given rotor power or shaft torque, this would offer a 0.5–1.5% increase in overall vertical lifting capability (see also Question 6.8). This is significant; measurements by McVeigh & McHugh (1982) show a 5% gain in rotor figure of merit and a 25% gain in equivalent lift-to-drag ratio in forward flight through the use of advanced airfoil sections designed for lower profile drag and higher drag divergence Mach numbers.

The effects of Reynolds number variation of rotor profile power and figure of merit can also be estimated using this blade element approach. Based on the results shown in Section 7.3.2 it is apparent that the effects of Reynolds number on profile drag can be approximated from turbulent boundary layer theory by

$$C_{d_0} = 0.1166\, Re^{-0.2}, \tag{6.19}$$

although McCroskey suggests the empirical result

$$C_{d_0} = 0.0044 + 0.018\, Re^{-0.15} \quad \text{for } Re > 5 \times 10^5, \tag{6.20}$$

which is based on an average of more than 40 different wind tunnel tests with the NACA 0012 airfoil, and this equation seems to offer a slightly better approximation in the higher Reynolds number regime (see Fig. 7.4). This suggests an increase in rotor profile power of about 15% when reducing the tip Reynolds number from 10^7 to 5×10^5. Reducing further the Reynolds numbers to the values typical of micro air vehicles or MAVs (see Section 6.14 and Fig. 7.4) would suggest values of C_{d_0} in the range of 0.03 with a corresponding fourfold increase in rotor profile power requirements. One approximation for low Re is to use the scaling

$$C_{d_0} = C_{d_{\text{ref}}} \frac{Re_{\text{ref}}}{Re}^{-0.4} . \tag{6.21}$$

These high values of drag help explain the relatively poor hovering efficiency and low values of figure of merit of current rotating-wing MAVs (see Fig. 6.2 and Section 6.14) and the need for vast improvements in airfoil efficiency at low Reynolds numbers if these types of MAVs are to become more viable.

Consider now the effects of airfoil performance on the efficiency of the rotor in forward flight, which is explained by Stepniewski & Keys (1984). Consider the power requirements for the rotor in forward flight based on the results given previous in Chapter 5. For flight at some forward speed V_∞ (but high enough that Glauert's approximation to the induced inflow is valid) and assuming the rotor thrust is equal to the weight of the helicopter, then the main rotor power required is the sum of its induced and profile losses, namely

$$P = \frac{\kappa W^2}{2\rho A V_\infty} + \rho A(\Omega R)^3 \frac{\sigma C_D}{8}\left(1 + 4.65\mu^2\right), \tag{6.22}$$

where C_D is assumed to represent the average profile drag coefficients of the airfoils on the blades. All of the other symbols have their usual meanings. We seek a result for the effective lift-to-drag ratio of the rotor, $(L/D)_R$, in the forward flight condition in terms of airfoil properties. The rotor L/D ratio can be approximated by $L/(P/V_\infty) = W/(P/V_\infty)$ – see Section 5.5.3. Therefore the ratio of D/L can be found using the standard form of the power equation to get

$$\left(\frac{L}{D}\right)_R^{-1} = \frac{P/V_\infty}{W} = \frac{\kappa W}{2\rho A V_\infty^2} + \frac{\rho A(\Omega R)^3}{V_\infty W}\frac{\sigma C_D}{8}\left(1 + 4.65\mu^2\right). \tag{6.23}$$

Proceeding further it is convenient to write the rotor thrust in terms of a mean operating lift coefficient C_L, which working on the assumption that all blade sections operate at the same C_l (as shown in Section 3.4.6) is given approximately by

$$C_L = 6\left(\frac{C_T}{\sigma}\right) = \frac{6}{\sigma}\left(\frac{W}{\rho A(\Omega R)^2}\right). \tag{6.24}$$

With this result $(D/L)_R$ for the rotor can be written as

$$\left(\frac{L}{D}\right)_R^{-1} = \left(\frac{D}{L}\right)_R = \frac{\kappa\,\sigma\,C_L}{12\mu^2} + \frac{3}{4\mu}\frac{C_D}{C_L}\left(1 + 4.65\mu^2\right). \tag{6.25}$$

Differentiating Eq. 6.25 with respect to C_L to find the value that will give the best $(L/D)_R$ gives

$$C_{L_{\text{best}}} = 3\sqrt{\frac{(1 + 4.65\mu^2)\mu}{\kappa\,\sigma}}\sqrt{C_D} \tag{6.26}$$

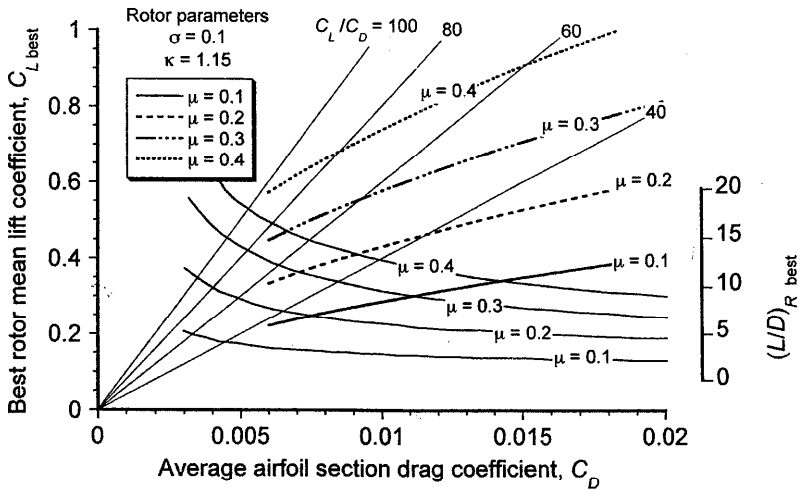

Figure 6.20 Efficient rotor operation in high-speed forward flight demands the use of airfoil sections with very high average lift-to-drag ratios. Adapted from Stepniewski & Keys (1984).

and substituting Eq. 6.26 into Eq. 6.25 gives the best lift-to-drag ratio of the rotor as

$$\left(\frac{L}{D}\right)_{R_{\text{best}}} = \left[\left(\frac{\sqrt{\kappa\,\sigma}}{2\mu}\right)\sqrt{(1+4.65\mu^2)/\mu}\sqrt{C_D}\right]^{-1}. \tag{6.27}$$

As might be expected, the result for the net rotor efficiency comes out in terms of the average drag coefficients of the airfoils comprising the rotor.

The results are summarized by the composite set of curves in Fig. 6.20 in terms of the mean operational lift coefficient required to reach the best L/D ratio (for a rotor of given solidity) at a given advance ratio versus the mean drag coefficient, C_D, of the airfoil sections. The corresponding results for the best L/D ratio of the rotor are also shown. It is assumed that the induced factor κ is known a priori. To understand this plot consider a given airfoil family with a known average value of C_D. The results show that for efficient flight at higher speeds the rotor must be operated at a relatively larger mean lift coefficients, which clearly requires airfoils with very good lift-to-drag ratios. The need for very high-speed flight (i.e., $\mu > 0.4$) demands airfoil sections with extremely good average characteristics, that is, with 2-D sectional lift-to-drag ratios approaching 80. It will be apparent that for a helicopter of given weight operating at a given μ the value of C_L can only be reduced by increasing rotor solidity (Eq. 6.26), although this must always be at the expense of blade weight and some loss of hovering efficiency. These results, however, illustrate rather nicely some aspects of the design trade-offs when developing a truly high-speed rotor system, where it is clear that only so much performance can be gained from airfoil section developments and increases in rotor solidity. To further improve cruise efficiency at high speeds requires that the high average C_L/C_D of the blades be maintained by simultaneously delaying both the onset of advancing blade compressibility effects and retreating blade stall.

6.5 Case Study: The BERP Rotor

The British Experimental Rotor Program (BERP) blade has been alluded to previously and is worthy of special consideration because its design encompasses some of

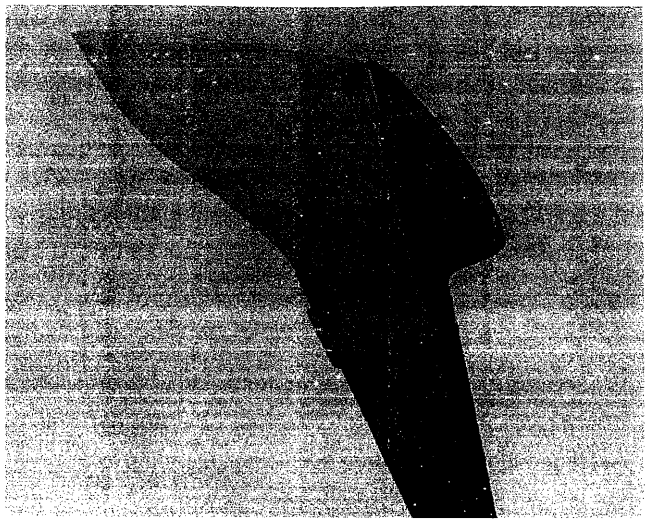

Figure 6.21 Photograph of the BERP blade as used on the Westland Lynx. (Courtesy of Westland–Agusta.)

the issues discussed in the previous section. The BERP rotor was designed specifically to meet the conflicting aerodynamic requirements of the advancing and retreating blade conditions, either of which can limit the C_L/C_D of the blades and the performance of the rotor in high-speed forward flight. The technical details of the BERP research program are described by Perry (1987), Perry et al. (1998), and Wilby (1998). This research paid off in 1986 when a Westland Lynx attained the world absolute speed record for a conventional helicopter.

As shown in Fig. 6.21, the BERP rotor blade is distinctive because of its unique tip shape. However, the aerodynamic improvements shown with the BERP rotor are the result of several innovations in both airfoil design and tip shape design. The BERP blade uses a number of high performance airfoils based on the RAE family (see Fig. 6.22). The main lifting airfoil is the RAE 9645, which is located on the blade from 65 to 85% radius. This airfoil has a maximum lift coefficient of about 1.55, which is high compared to even second-generation helicopter airfoil sections – see Dadone (1976) and Wilby (1998). However, this high lift coefficient is obtained at the expense of higher pitching moments. These pitching

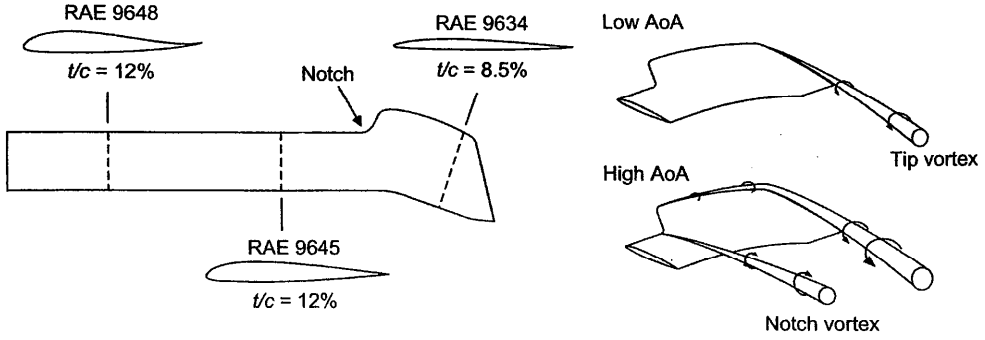

Figure 6.22 Distribution of airfoil sections on the BERP blade and high angle of attack performance. Adapted from Perry (1987).

moments are offset by the RAE 9648 airfoil, which is reflexed and located inboard of 65% radius where the demands of high maximum lift are not so important. The tip region uses the RAE 9634 airfoil, which has a relatively low thickness-to-chord ratio to give a high drag divergence Mach number. The RAE 9634 airfoil is also cambered in such a way as to give a weak shock wave and low pitching moments.

A distinctive feature of the BERP blade is the use of high sweepback over the tip region, which as mentioned previously, is an effective means of reducing compressibility effects and delaying their effects on the rotor to a higher advance ratio. On the BERP blade a progressively increasing sweepback angle is used over the outboard 16% of blade radius. Because the Mach number varies linearly along the blade, the amount of sweep that is necessary can be minimized by keeping the Mach number normal to the leading edge approximately constant – see Section 6.4.6. What is different for the BERP blade is that the area distribution in the tip region is configured to ensure that the center of lift is located close to the elastic axis of the blade. This is done primarily by offsetting the location of the local 1/4-chord axis forward starting at 86% radius. This offset also produces a discontinuity in the leading edge of the blade, which is referred to as a "notch."

It must be recognized that while a swept tip geometry will generally always reduce profile power and delay the onset of increased power requirements to higher advance ratios, it will not necessarily improve the performance of the blade at high angles of attack on the retreating side of the disk. In fact, results have been previously shown in Fig. 6.16 that a swept tip blade may have inferior forward flight characteristics compared to a standard (unswept) blade tip. The BERP blade is specifically designed to perform as a swept tip at high Mach numbers and low angles of attack, but it is also designed to operate at very high angles of attack without stalling. This latter attribute is obtained, in part, through the generation of stable vortex flows that enhance lift and delay the onset of gross flow separation over the tip region to extremely high angles of attack (see Fig. 6.22). This mechanism is promoted by giving the airfoils in this region a small leading edge nose radius. As the AoA of the blade is increased, this vortex begins to develop from a point further forward along the leading edge into the less highly swept region. At a sufficiently high angle of attack, the vortex will initiate close to the forward most part of the leading edge near the notch region. Experimental evidence by Duque & Brocklehurst (1990) have shown that a second notch vortex is also formed, which is trailed streamwise across the blade. This vortex acts like an aerodynamic fence and retards the flow separation region from encroaching into the tip region. Numerical calculations by Duque (1992) have shown that in high-speed flight this notch also helps to further reduce the strength of shock waves on the tip, acting as a form of "tip relief" – see Section 5.4.3. Further increases in AoA make little change to the flow structure until a very high AoA is reached (in the vicinity of 22°) when the flow will finally break down and separate. For a conventional tip planform, flow breakdown would be expected to occur at about 12° local angle of attack.

The performance of the BERP rotor is confirmed by the results shown in Fig. 6.23, which is based on actual flight tests using the Lynx helicopter – see Perry et al. (1998). The results are shown in terms of blade loading coefficient versus advance ratio. Clearly the BERP rotor demonstrates a significant increase in the operational flight envelope. Further results are shown by Perry et al. (1998), who compared the BERP rotor with other rotor blades in terms of hovering performance and the maximum thrust capability in forward flight. Despite some controversy about comparing rotor performance in forward flight on the basis of weighted solidities [see Amer (1989) and Perry (1989)] the performance gains of the BERP rotor are convincing and clearly demonstrate the benefits of a careful synthesis of both improved airfoil design and blade planform shape in the design of better helicopter rotors suitable

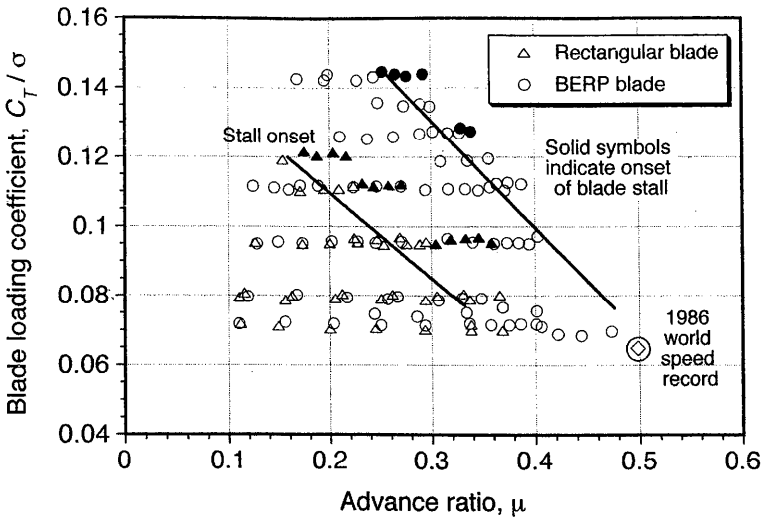

Figure 6.23 Flight envelope of the Lynx with standard rectangular blades and BERP blades. Data source: Perry et al. (1998).

for high-speed forward flight. The latest derivatives of the BERP blade have used some anhedral over the tip region, which provides some additional gains in performance. The success of the BERP program has seen the blades retrofitted to the fleet of military Lynx helicopters, and the design is also used on the EH-101 helicopter.

6.6 Fuselage Aerodynamic Design Issues

The fuselage is the largest airframe component on a helicopter, so its aerodynamic characteristics will have a significant impact on the performance of the helicopter as a whole. Functional constraints such as the need for rear loading doors means that the shapes that are typical of helicopter fuselage designs are often prone to flow separation and high drag. In addition, the airframe often operates in the main rotor wake, which changes the aerodynamic characteristics compared to those obtained without the rotor. These effects make the understanding and prediction of airframe aerodynamics extremely complicated, to the point that the whole of Chapter 11 is devoted to the subject.

6.6.1 *Fuselage Drag*

The parasitic drag of the fuselage affects cruise speed and fuel consumption of the helicopter. Williams & Montana (1975) and Keys & Wiesner (1975) have emphasized the need for low fuselage drag in the design of helicopters for improved performance. The drag of a helicopter fuselage may be up to one order of magnitude higher than that of a fixed-wing aircraft of the same gross weight. One reason is because of the rotor shaft, hub, and blade attachments, which may account for 30% or more of the total fuselage drag – see Sheehy & Clark (1975) and Sheehy (1977). Another major contributor is the fuselage after-body or bluff-body drag, which may account for 20% of the total fuselage drag. Drag is also caused by flow separation in the region where the main fuselage tapers to the tail boom. Sedden (1982) has shown that large drag penalties result when using fuselage shapes with large rear fuselage upsweep angles, because these can promote flow separation and

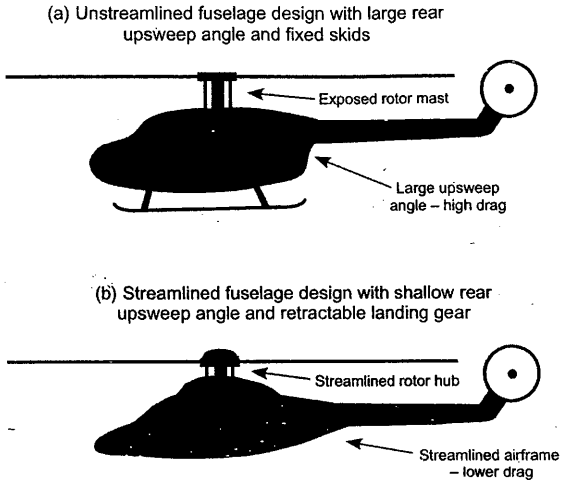

Figure 6.24 Reductions in fuselage parasitic drag are obtained through streamlining. (a) Utility type fuselage. (b) Streamlined fuselage.

the formation of two strong trailing vortices. See also Epstein et al. (1994) for details of this phenomenon.

There are, however, many constraints that can limit the design of the fuselage shape and consequently the lowest possible drag of the fuselage. Much depends on the operational needs for the machine. For example, as shown in Fig. 6.24 an executive transport helicopter can be designed to have a more streamlined fuselage compared to a utility helicopter, which may need to have a rear access door. In either case, it is found that the fuselage shape should be more circular than square to keep drag as low as possible. Using a fairing over the top of the fuselage can help reduce drag from the main rotor shaft and control linkages. See also Montana (1975, 1976). Replacing the skids with a retractable undercarriage can reduce drag considerably. However, a fixed wheeled undercarriage will have higher drag than skids. The use of active flow separation control concepts seems a prime candidate for a future means of fuselage drag reduction – see Section 9.12.

In view of the complicated interacting viscous dominated flows that can exist over helicopter fuselages, predictive capabilities for pressure and skin friction drag are not yet mature. Current capabilities for design are based on synthesis of component drag using experimental data or by using a combination of experimental data and potential flow theory. Classical panel methods have found considerable use in routine helicopter fuselage design – see Section 14.7 for details. These methods are based on the assumption of small disturbance potential flow, with the basic approach being described by Hess (1990). A modern treatment of the various types of panel methods is given by Maskew (1982), Morino (1985), and Katz & Plotkin (1991). Large computer codes that use panel methods are commercially available and are in widespread use in the helicopter industry. Sophisticated computational fluid dynamics methods such as Navier–Stokes and Reynolds-Averaged Navier–Stokes (RANS) are still in the development stage – see Section 14.2.1. Even if enormous computer memory and storage requirements can be overcome, they are relatively far from being practical for use in routine helicopter fuselage design studies. Another problem with Navier–Stokes methods is the efficient generation of grids, and especially the proper coupling of structured and unstructured grids. However, rapid progress in grid generation techniques and solution

algorithms is being made. See, for example, Berry et al. (1994), Chaffin & Berry (1994), Duque & Dimanlig (1994), and Duque (1994).

To supplement numerical predictions of fuselage aerodynamics, semi-empirical drag prediction methods are in widespread use in the helicopter industry. Based on component testing in the wind tunnel, and with some additional engineering judgment, these approaches can give very reliable estimates of fuselage drag. An estimate of the fuselage parasitic equivalent wetted or flat-plate area, f (introduced in Section 5.4.5), can be determined from a knowledge of the drag coefficients of the various components that make up the helicopter using an equation of the form

$$f = \sum_n C_{D_n} S_n, \tag{6.28}$$

where S_n is the area on which the definition of C_D is based. This may be either the wetted area or the projected frontal area of the component. Initial drag estimates will assume no mutual interference effects from individual components, but despite this approximation the approach is found to give a reasonable initial estimation for the fuselage drag. More refined values of f are obtained by component testing of isolated fuselage and rotor/fuselage models in the wind tunnel – see, for example, Bosco (1972), Wilson (1984), Philippe et al. (1985), and Wilson (1990). Component interference effects can then be incorporated into the drag estimate. Further refinements need actual flight tests because wind tunnel models cannot simulate accurately the effects of full-scale Reynolds numbers, or drag producing details such as antennas, leakage through doors, and other gaps. In this case, estimates of drag are derived indirectly from rotor power measurements. The whole process, although somewhat empirical, gives quite reliable estimates of the parasitic drag.

An analysis of the individual items contributing to the parasitic drag of a typical helicopter is given in Table 6.1. These results are not for any one helicopter design per se and must be considered only as representative. It will be apparent that a major source of the overall drag is the rotor hub and blade attachments, which may account for up to 30–50% of the total parasite drag on fully articulated rotor blade designs. Sheehy & Clark (1975), Sheehy (1977), Sedden (1979), and Prouty (1986) give a good summary of various sources of published rotor hub drag data. Considerable turbulence may also be produced behind the hub, which

Table 6.1. *Typical Breakdown of Parasitic Drag Components of a Representative Helicopter. After Prouty (1986)*

Component	% of Total
Fuselage	30
Nacelles	6
Rotor hub & shaft	35
Tail rotor hub	4
Main landing gear	6
Tail landing gear	4
Horizontal tail	1
Vertical tail	1
Rotor/fuselage interference	7
Exhaust system	3
Miscellaneous	3
Total	100

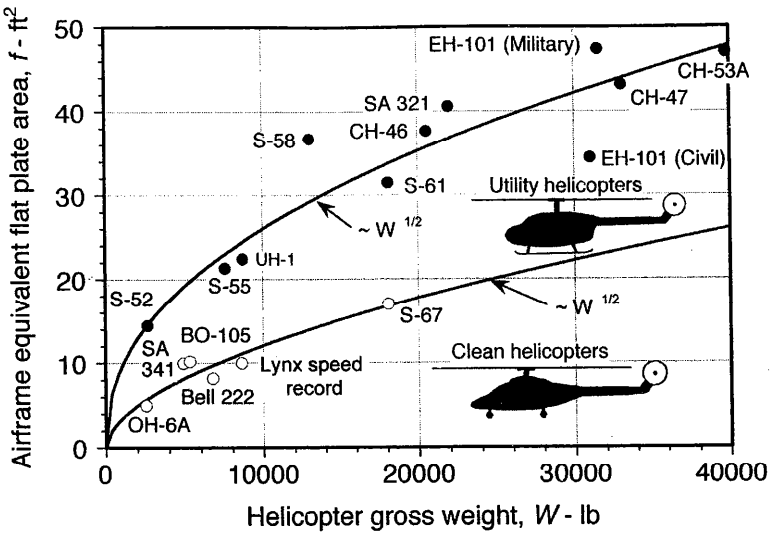

Figure 6.25 Equivalent flat-plate (wetted) areas for a selection of helicopter designs.

can have an influence on the magnitude and frequency of the airloads produced on the tail boom and empennage; see Berry (1997) for a discussion of hub turbulence measurements. Further discussion of this important issue is made in Chapter 11. Streamlining the fuselage on the top of the airframe near the hub can help reduce the drag of the rotor shaft, the exposed controls, and the hub. However, it is only with the use of modern hingeless or bearingless rotors that hub drag reductions are possible, with values of f/A for a bearingless rotor being about half those of an articulated design. Cler (1989) describes a fully faired hub design, although this is impractical for most helicopters.

The equivalent total flat-plate areas of helicopter airframes range from less than 10 ft^2 (0.93 m^2) on smaller helicopters to as much as 50 ft^2 (4.65 m^2) on large utility helicopter designs, as shown in Fig. 6.25. Heavy-lift crane designs may have twice these values (>100 ft^2 or 9.3 m^2 being typical). The measured data have been obtained from a variety of sources, including Rosenstein & Stanzione (1981). The results suggest that values of f/A typically will fall between 0.004 for clean helicopter designs and up to 0.025 for first-generation or heavy-lift transport helicopters. Again, notice that the drag curves are approximately proportional to $(\text{weight})^{1/2}$, which follows the "square–cube" law mentioned previously. Obviously, the addition of external hardware or stores on military helicopters tends to dramatically increase its equivalent wetted area, thereby significantly increasing power required and reducing forward flight performance. Conversely, a general drag clean up of the airframe can result in substantial increases in climb and forward flight speed capability, as well as in reduced fuel burn and improved overall operational economics.

6.6.2 *Vertical Drag and Download Penalty*

It is normally assumed that the total thrust, T, required by the main rotor is equal to the weight of the helicopter, W. However, there is usually an extra increment in power required because of the download or vertical drag, D_v, on the helicopter fuselage that results from the action of the rotor slipstream velocity (i.e., now the rotor thrust will be $T+\Delta T = W+D_v$). See Wilson (1975) for a good summary of the basic problem. Typically, the vertical download on the fuselage can be up to 5% of the gross takeoff weight, but it

can be much higher for some rotorcraft designs such as compounds or tilt-rotors that have large wings situated in the downwash field below the rotor. In its simplest form, the vertical drag can be accounted for by assuming an equivalent drag area f_v or a drag coefficient C_{D_v} based on a reference area, say S_{ref}. This means that the extra rotor thrust to overcome this drag will be

$$\Delta T = D_v = \frac{1}{2}\rho \bar{v}^2 f_v, \tag{6.29}$$

where $\bar{v}$ is the average velocity in the rotor slipstream.

In the first instance, the simple momentum theory can be used to estimate $\bar{v}$. It is known that the rotor wake contracts very rapidly below the rotor, so that the airframe can be assumed to operate in the fully developed vena contracta; in the hover condition this velocity is twice the induced velocity at the disk. In a vertical climb, the induced velocity at the rotor will be given using Eq. 5.15, which for normal rates of climb is approximately

$$\frac{v_i}{v_h} = 1 - \frac{V_c}{2v_h}. \tag{6.30}$$

Because the wake velocity $\bar{v}$ is given by $\bar{v} = V_c + 2v_i$, then using Eq. 6.30 it is apparent that $\bar{v} = 2v_h$, that is, $\bar{v}$ is independent of climb velocity V_c. This means that the rotor thrust will be

$$T = W + D_v = W + \frac{1}{2}\rho \bar{v}^2 f_v = W + 2\rho v_h^2 f_v = W + T\left(\frac{f_v}{A}\right). \tag{6.31}$$

Rearranging and solving for the rotor thrust T gives

$$T = \left(\frac{W}{1 - f_v/A}\right) = \left(\frac{W}{1 - S_{\text{ref}}\, C_{D_v}/A}\right). \tag{6.32}$$

From this result, the net rotor power requirements can be easily calculated using

$$P = \frac{W}{1 - f_v/A}\left(\frac{V_c}{2} + \sqrt{\frac{W}{2\rho A(1 - f_v/A)}}\right) + P_0, \tag{6.33}$$

which is valid for low to moderate rates of climb, assuming the validity of Eq. 6.30. It will be apparent, fortunately, that because $f_v/A < 0.1$ then the airframe drag makes only a modest additional contribution to the total power requirements in climbing flight.

Because of the bluff-body nature of the flow about the fuselage, estimates of the vertical drag can only be reliably obtained from wind tunnel testing of isolated fuselage models. Precautions should be taken to properly represent the nonuniformity of the rotor downwash, as well as Reynolds number effects on the fuselage, the latter which can be difficult to simulate on subscale models.

In the second instance the vertical drag on the fuselage can be calculated by estimating the drag coefficient of individual 2-D fuselage cross sections (i.e., a strip approach), as shown schematically in Fig. 6.26, which is suggested by Stepniewski & Keys (1984). The vertical drag of the entire fuselage can then be obtained by successively testing 2-D cross sections of the fuselage to determine the pressure distributions and then finding the net drag on the fuselage by summation. For example, the incremental vertical drag on any one segment of the fuselage of length dl and width w will be

$$dD_v = \frac{1}{2}\rho \bar{v}^2 C_{D_v} w\, dl, \tag{6.34}$$

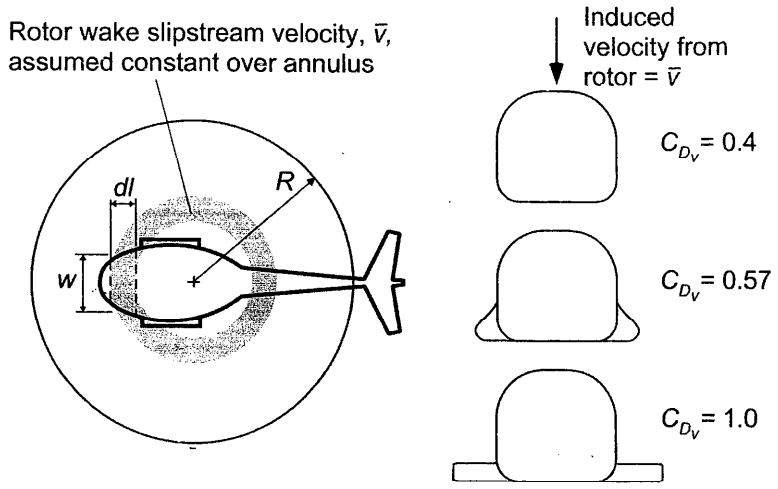

Figure 6.26 Strip analysis of the fuselage for the estimation of vertical drag.

where $\bar{v}$ is the local downwash velocity (from the fully developed rotor wake) at the element and C_{D_v} is the drag coefficient. The net vertical drag will be given by

$$D_v = \sum dD_v, \tag{6.35}$$

where it is recognized that C_{D_v} and $\bar{v}$ will vary between cross sections. Generally, it is found that helicopter fuselage cross-sectional drag coefficients average out at about 0.5, although the addition of sponsons or stub-wings can increase the drag coefficients to over unity. Wilson & Kelly (1983, 1986) give results for a variety of fuselage cross-sectional shapes, which have been estimated from wind tunnel tests. Drag coefficients for various other bluff-body shapes resembling fuselage cross sections can be found in Delany & Sorensen (1953) and Hoerner (1965).

Note that the strip method of fuselage drag estimation requires an estimate for distribution of the induced velocity in the wake below the rotor. A good first estimate can be made by means of the BEMT discussed previously in Chapter 3. However, because the fuselage also influences the rotor in a reciprocal way, accurate estimates of the interference effects on $\bar{v}$ are difficult to obtain. The effect of the fuselage is also known to affect the rotor performance, increasing the thrust as the fuselage is brought closer to the rotor – see for example Sheridan (1978), Sheridan & Smith (1979), and Fradenburgh (1972). Because of these effects, and the fact that 3-D effects have also been neglected, the strip method described above tends to be rather crude, at least in theory. Yet, in practice the method has been shown to give fairly reliable estimates of the extra rotor thrust required to overcome fuselage drag in climbing flight.

6.6.3 *Vertical Drag Recovery*

When determining in ground effect (IGE) hover capability of the helicopter, the vertical fuselage drag must be corrected to account for a favorable effect that occurs in this regime. This is referred to as vertical drag recovery or *airframe download recovery* and offsets the download obtained on the fuselage from the rotor when the helicopter is hovering very near to the ground. This behavior results from a change in static pressure in the wake below the airframe. Measured results documenting this phenomenon are given

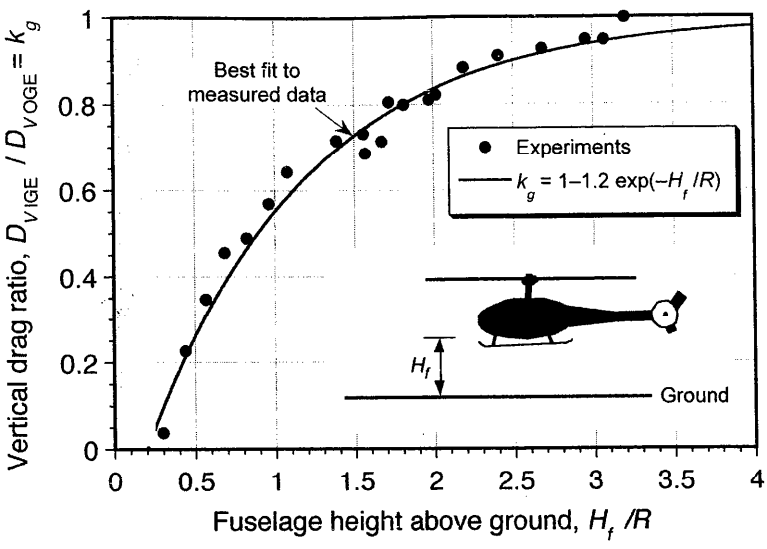

Figure 6.27 A change in static pressure below the airframe as it approaches the ground results in a favorable reduction in airframe download. Data source: Stepniewski & Keys (1984).

by Fradenburgh (1972) and Stepniewski & Keys (1984). The decrease in effective fuselage vertical drag is found to be significant for hovering heights of less than one rotor diameter. The results of measurements are shown in Fig. 6.27 in terms of the download ratio in ground effect to that out of ground effect (OGE). It is apparent that the behavior can be modeled approximately by

$$\frac{D_{vIGE}}{D_{vOGE}} = k_g \approx 1 - 1.22\exp(-H_f/R) \quad \text{for} \quad H_f/R \geq 0.25. \tag{6.36}$$

6.6.4 *Fuselage Side-Force*

During hovering flight, the tail rotor provides the anti-torque thrust to maintain yaw equilibrium. However, in sideward flight or when hovering over a fixed point above the ground in a crosswind, an aerodynamic side-force will also be produced on the fuselage. For most helicopters this side-force is small enough to have a minimal impact on the handling qualities and operational envelope. For a rotor turning in the conventional direction (counterclockwise when viewed from above), the aerodynamic side-force on the fuselage and tail boom will be opposite to the direction of the tail rotor thrust when the helicopter is in starboard sideward flight or has a starboard crosswind component. On some helicopters this effect can affect directional (yaw) control and in some cases may even limit the operational flight envelope – see Amer & Gessow (1955) for the first study. In particular, this can be an issue on military helicopters, which must often demonstrate high-speed sideward flight capability for combat tactics, or for naval helicopters in particular, which must often operate in confined locations in gusty crosswind conditions.

The aerodynamic side-force on the fuselage is found to be accentuated by certain tail boom shapes, which can produce a sizable circulatory lift force in the direction *opposite* to the anti-torque requirement when the sideward velocity is combined with the main rotor downwash. To counter this undesirable effect, Brocklehurst (1985) and Wilson et al. (1988)

have suggested the use of a strake that runs longitudinally along the one side (usually the port side) of the tail boom – see Section 11.2.4 for a detailed discussion. This strake forces the flow to separate, spoiling the aerodynamic side-force on the tail boom, thereby restoring or improving the normal operational flight envelope of the helicopter. See also Kelly et al. (1993).

6.7 Empennage Design

The empennage on a helicopter consists of the vertical and horizontal stabilizer and related fuselage structure. A stabilizer is simply a fixed surface that produces an aerodynamic lifting force (positive or negative). The primary purpose of a stabilizer is to enhance stability about a particular axis (pitch, yaw), although there are secondary aerodynamic characteristics of stabilizers that are important design considerations for helicopters. These problems are often associated with component interaction aerodynamics – see Chapter 11.

6.7.1 *Horizontal Stabilizer*

The primary purpose of a horizontal stabilizer is to give the helicopter stability in pitch. Both the helicopter rotor and its fuselage have an inherent negative stability derivative in pitch and the stabilizer helps to give the helicopter better overall handling qualities. The fuselage itself has a powerful negative stability because of the typically large surface area of the airframe forward of the center of gravity – see Prouty (1985). The selection of the size and position of the horizontal stabilizer on the tail has proven to be one of the most difficult challenges facing helicopter designers. In addition to aerodynamic, structural, weight and stability and control trade-offs, there are important aerodynamic interactional effects between the rotor wake and the tail region – see Section 11.3.1.

Prouty & Amer (1982) describe how there are basically three types of horizontal stabilizer designs used on helicopters: a forward mounted stabilizer, an aft mounted low stabilizer, and a T-tail design. Using a forward fixed stabilizer will generally avoid any sudden changes in download caused by wake impingement because it will remain inside the rotor wake boundary from hover up until a fairly high forward flight speed is reached. Many Bell helicopter designs use this forward stabilizer position. However, because the reduced moment arm, the surface must be larger (and heavier) compared to a stabilizer mounted further back along the tailboom. The stabilizer, however, may have a capability of being used for trim augmentation in that the pitch angle may be linked into the longitudinal cyclic. In hovering flight the rotor wake produces a vertical download on forward mounted horizontal stabilizers, which usually represents a significant performance penalty. The Bell designs also use an inverted airfoil for the stabilizer, which creates a download in forward flight to keep the fuselage at an angle of attack for lowest parasitic drag. It is also designed to stall when the helicopter is in steep autorotation to avoid producing an upthrust and an undesirable nose-down pitching moment on the fuselage.

A stabilizer that is mounted low down near the end of the tail has good structural efficiency, with all the loads being carried directly into the tail boom. However, this stabilizer design tends to produce interactional aerodynamic issues and trim during transition from low-speed flight into hover or vice versa, where the main rotor wake may suddenly move forward over the empennage location and so produce a nose-down pitching moment on the helicopter – see Section 11.3.1. Also, the unsteady separated flow from the upper fuselage and rotor hub tends to reduce the efficiency of this type of stabilizer design so that the lifting area needs to be greater than for one that could be located away from the wake. On military

helicopters, clearance issues between the tail and the ground may be important and can preclude this particular design choice. Nevertheless, as evidenced by the large number of helicopters with this low mounted horizontal stabilizer configuration, it is a popular design choice for small to medium size helicopters.

In the T-tail design, the horizontal stabilizer is mounted at the top of the vertical fin. This moves the stabilizer away from the rotor wake for most flight conditions, and so it can be smaller in area to give the same overall stability. However, the design is structurally inefficient because of the higher overall weight of the vertical fin required to carry the stabilizer loads, and also because of various low-frequency structural vibration modes that can be excited by the main and/or tail rotors. On a low or forward set stabilizer, it may be necessary to have different incidence (pitch) settings for the port and starboard sides to account for the gradients in downwash in the rotor wake. With a T-tail design, there are often twisting moments that may limit the maximum area of the stabilizer. Often a compromise is drawn by using a stabilizer mounted to only one side of the fin, such as used on many of the Sikorsky machines. See Prouty & Amer (1982), Prouty (1983), Hansen (1988), and Main & Mussi (1990) for further information on stabilizer design.

A stabilator is a stabilizer that has a variable incidence (pitch) capability. It can help give better overall handling qualities over a wider range of flight conditions than is possible with a stabilizer of fixed pitch, including hovering flight. The stabilator is set to large positive pitch angles in hovering flight to help reduce download effects and is reduced to low pitch values in cruise flight. The pitch angle is set automatically by a flight control computer using airspeed and other measurements, although manual override can be used to give the pilot control of the stabilator below certain airspeeds. A stabilator is mechanically relatively complicated compared to a stabilizer because it requires a pitch change mechanism, and is also a structurally inefficient design choice because of its higher weight. However, sometimes it can be the best choice to meet the demanding flight envelope of military helicopters. For example, a stabilator design is used on both the AH-64 and UH-60 helicopters.

6.7.2 *Vertical Stabilizer*

The primary purpose of a vertical stabilizer or fin is to provide stability in yaw. While the tail rotor itself provides considerable yaw stability, the vertical stabilizer may also be required to provide sufficient aerodynamic side-force to offset the tail rotor thrust in forward flight and to provide sufficient anti-torque to allow continued flight in the event of the loss of the tail rotor – see Horst & Reschak (1975). This side-force can be provided by using an airfoil section with a relatively large amount of camber. Alleviating the tail rotor thrust in high-speed flight by means of a side force on the fin is usually desirable to minimize tail rotor flapping and cyclic loads and to maximize component fatigue life. With sufficient forward speed and some side-slip angle, the side-force can be great enough to allow continued flight without the tail rotor, although this flight condition is difficult to achieve in practice.

The vertical stabilizer also forms a structural mount for the tail rotor. Because the flows will strongly interact, the tail rotor can be considered to be an integral part of the fin and empennage assembly. The size of the vertical stabilizer directly and adversely affects tail rotor performance. A smaller stabilizer will reduce the adverse effects on tail rotor efficiency, but this must be balanced against the effects on yaw stability and other design requirements including sideward flight. Because of the need for side forces on the fin to be low when the helicopter is operating in hovering flight with a crosswind, the trailing edge of the fin may often be blunt because this tends to help reduce adverse fin forces at large angles of

attack. The special complications associated with the design of the tail rotor itself means the aerodynamics of the tail rotor and the interactions with the fin must be discussed separately – see Section 6.9.

6.8 Role of Wind Tunnels in Aerodynamic Design

Wind tunnel testing of subscale rotors and airframes is an important technique for estimating the performance of full-size helicopters. The various techniques are discussed by Harris (1973) and Philippe (1990). Wind tunnel tests allow good estimates of rotor thrust and airframe drag and also help to design out complicated effects prior to first flight, including any adverse rotor–airframe interactional effects – see Chapter 11. To reduce Reynolds number uncertainties and minimize risk, large- or full-scale testing is desirable – see also Section 7.3.4. While the wind tunnel testing of a full-scale rotor or a complete helicopter is an enormously expensive and time consuming undertaking, it can be much less expensive than remedying a persistent problem after the helicopter has flown. Wind tunnel testing with close to full-scale rotors gives the analyst the opportunity to measure results exactly as they would be found on the actual helicopter, without the uncertainties of Reynolds number or other issues that would be apparent on subscale models. Yet very few wind tunnels in the world are capable of full-scale or large subscale rotor experiments. Full-scale rotors are routinely tested on hover towers by helicopter manufacturers, but this gives only limited knowledge of their overall performance.

The need for measurements of rotor thrust and power is essential in any model test, these usually being obtained using strain-gauge balances. The use of blade and airframe instrumentation for on- and off-surface measurements are usually a goal in either hover or wind tunnel testing, although such data are not always available simultaneously from any one tunnel entry. The issues of repeatability of the test conditions and rotor operating state then become a concern. The difficulties in obtaining off-surface measurements in the wake of the rotor cannot be underestimated (see Chapter 10), and for comprehensive tests on large or full-scale rotors, this often requires an international effort by specialists from several organizations. As a consequence, most helicopter rotor and rotor–airframe testing has been done at a smaller scale, which may range from 1/4 to 1/8 scale. Such tests are often on simpler and more generic airframe configurations, perhaps with aeroelastically stiff (rigid) blades to better isolate specific interactional aerodynamic phenomena – see Chapter 11. This gives the analyst the best opportunity to precisely define the geometry of the problem and to study the flow physics of specific phenomena with greater confidence. These tests can provide the analyst with a comprehensive data suite of on- and off-surface measurements (along with estimates of tunnel wall interference effects), and so are ideally suited for the validation of computational models of the flow field. Unfortunately, few tests have provided coincident measurements of on-surface loads and off-surface flow properties, and the lack of such data continues to impede the validation of computational aerodynamic models.

The testing of geometrically and aeroelastically scaled rotor models gives much information about the actual capabilities of the full-scale rotor system. Combined with geometrically scaled airframe models such as that shown in Fig. 6.28, the net system performance can be measured to a high level of fidelity and the measurements used confidently to validate various levels of performance predictions. Despite the enormous costs, pressure measurements on the blade surface are extremely useful for the validation of comprehensive rotor analyses. This helps gain better confidence levels in these analyses for use in the design of future rotors. However, the complications of elastic blade deformations on the full-size helicopter makes it difficult to isolate specific aerodynamic phenomena, and such tests are

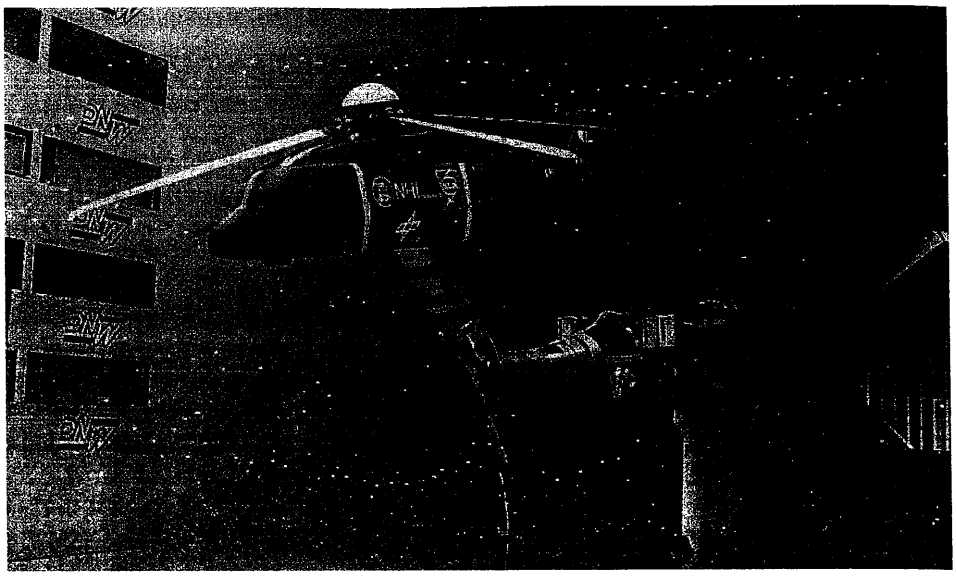

Figure 6.28 A geometrically scaled rotor and airframe of the NH-90 helicopter tested in a large wind tunnel.

less useful for generating high-fidelity measurements that can be used for the validation of flow models. As better Navier–Stokes-based CFD methods and turbulence models become increasingly capable and reliable, the role of wind tunnel testing on larger scale rotor configurations must clearly shift back toward the generation of high-fidelity measurements on simpler configurations but at close to full-scale flight Reynolds numbers. In this regard, the closure (or constant threat of) of large subsonic wind tunnels suitable for helicopter studies continues to be a major concern to both the research and manufacturing community.

6.9 Design of Tail Rotors

The vast majority of helicopters in production are of the single main rotor with tail rotor configuration. The primary purpose of the tail rotor is threefold. First, the tail rotor provides an anti-torque force to counter the torque reaction of the main rotor on the fuselage. Second, the tail rotor gives yaw stability and provides the pilot with directional control about the yaw axis. Third, the aerodynamics of the tail rotor provide the helicopter with a significant *weathercock stability*. For example, if the helicopter is yawed nose-left, then the tail rotor will experience an effective climb. If the collective pitch is held constant, then this will result in a decrease of thrust (a result of the higher inflow) and a restoring moment about the yawing axis. Similarly, if the helicopter yaws nose-right, the tail rotor experiences an effective descent, with an increase in thrust, and again, a restoring moment is produced. This weathercock stability is a useful characteristic of tail rotors, but it can also make helicopters less maneuverable.

The tail rotor has to operate in a relatively complex aerodynamic environment and its operation is affected by the main rotor wake, the main rotor hub and the empennage. However, to be effective it must produce thrust with the relative flow coming from essentially any direction. This means that the aerodynamic design requirements for the tail rotor are different in some respects from those of the main rotor. For these reasons, it is known to be difficult to design a tail rotor that will meet all the various interdependent aerodynamic,

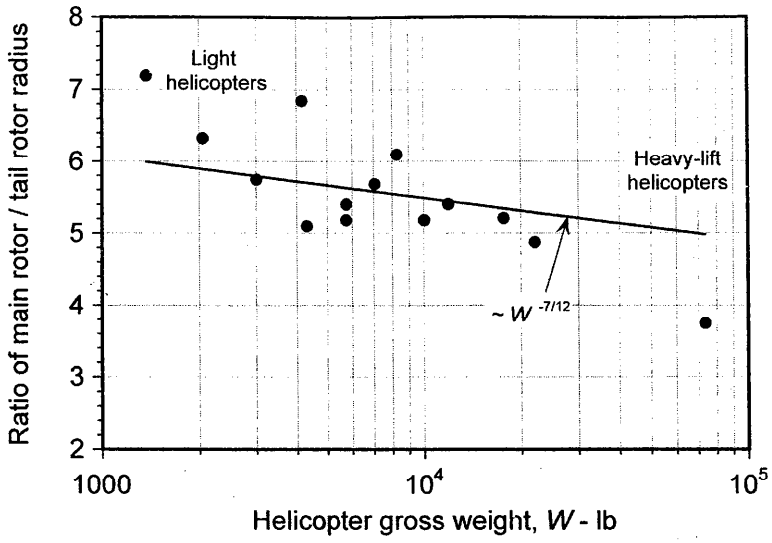

Figure 6.29 General trends of main rotor size to tail rotor size versus helicopter gross weight.

control, stability, weight, and structural requirements. See Lynn (1970), Cook (1978), Byham (1990), and Newman (1994) for a detailed overview of tail rotor design issues.

6.9.1 *Physical Size*

Consider the physical characteristics of typical tail rotors on production helicopters, as listed in the appendix. A comparison of the size of the tail rotor to the main rotor shows that it is roughly one sixth the diameter of the main rotor. Because the ratio decreases with gross weight, the size of the tail rotor grows more rapidly than the size of the main rotor with increasing gross weight, as shown in Fig. 6.29. Note that for machines with fenestrons, the size of the fenestron can be much smaller than that of a conventional tail rotor. Again, the trends (for conventional tail rotors) can be explained with the aid of the square–cube law. It has been shown previously that the main rotor power (or torque) required is $\propto W^{3/2}$. Also, because the size of the helicopter (and length of the tail moment arm) grows with $W^{1/3}$ so the anti-torque force requirement should be $\propto W^{7/6}$. Because tail rotor disk loading remains relatively independent of helicopter gross weight (for good efficiency), the size of the tail rotor should be $\propto W^{-7/12}$. This trend is in general agreement with the data shown in Fig. 6.29. Note also that the tail rotor tip speed is approximately the same as the main rotor tip speed. This means that the rotational speeds of tail rotors are roughly six times the main rotor frequency, and this has particularly important consequences on rotor noise levels. While the noise energy produced by the tail rotor is only a fraction of that produced by the main rotor, the higher frequencies generated by the tail rotor can be more discernible to the human ear (see Section 8.19).

6.9.2 *Thrust Requirements*

The primary purpose of the tail rotor is to provide a sideward force on the airframe in a direction and of sufficient magnitude to counter the main rotor torque reaction. The tail rotor also provides the pilot with directional (yaw) control. Roughly, the tail rotor consumes up to about 10% of the total power for the helicopter, although allowances of up to 20% may

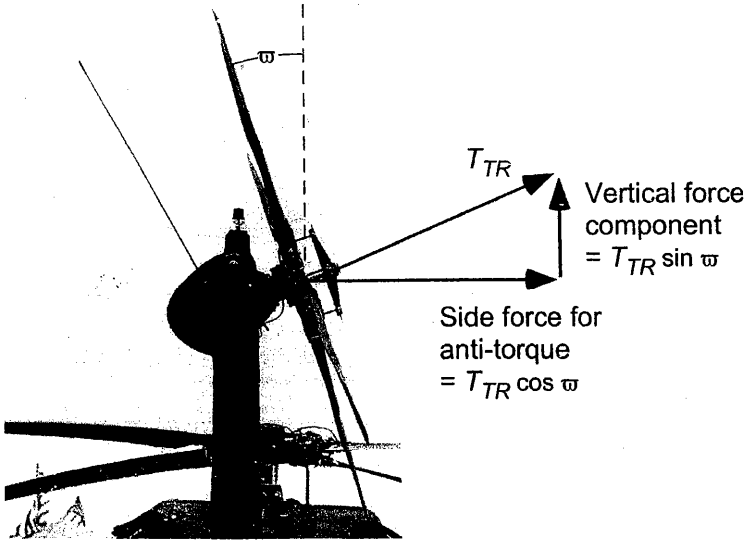

Figure 6.30 A canted tractor tail rotor design, which provides both side and vertical forces.

be made for design purposes to ensure sufficient maneuvering and transient capabilities. This is power that is completely lost, because unless the tail rotor is canted, as on the UH-60 Blackhawk (Fig. 6.30), it provides no useful lifting force. The purpose of the canted tail design is to widen the allowable center of gravity of the helicopter. This design, however, introduces an adverse coupling between yaw and pitch, but this effect can be minimized by a flight control system.

The direction of the anti-torque force depends on the direction of rotation of the main rotor. For a rotor turning in the conventional direction (counterclockwise direction when viewed from above), the tail rotor thrust is to the right (starboard). The magnitude of this thrust, as well as its power consumption, depends on the reaction torque from the main rotor, Q_{MR}, and the location of the tail rotor from the center of gravity (i.e., the moment arm l_{MR}). In addition, there are inertial effects that the tail rotor must overcome during yawing maneuvers. In this case, the tail rotor thrust can be found from

$$Q_{MR} + I_{zz}\ddot{\Psi} = T_{TR}l_{TR} \tag{6.37}$$

where $\ddot{\Psi}$ is the yaw acceleration and I_{zz} is the mass moment of inertia of the helicopter about the yaw axis.

The tail rotor thrust is controlled by the pilot's feet by pushing on a set of floor mounted pedals. For example, for a rotor turning in the conventional direction pushing on the left pedal increases tail rotor thrust (positive to starboard) and the helicopter will yaw nose left about its center of gravity. The tail rotor must also provide the specified yaw acceleration in the maximum specified crosswind conditions, taking into consideration possible losses in efficiency because of aerodynamic interference effects between the tail rotor and the vertical fin – see Section 6.9. Furthermore, when the main rotor thrust or power is increased, for example, to climb, the reaction torque, Q_{MR}, on the fuselage is increased. This means that the tail rotor thrust must also increase to balance this torque reaction. Therefore, when the pilot increases the collective pitch to climb, foot pressure must be applied to the appropriate pedal to keep the nose pointed straight in the desired direction of flight.

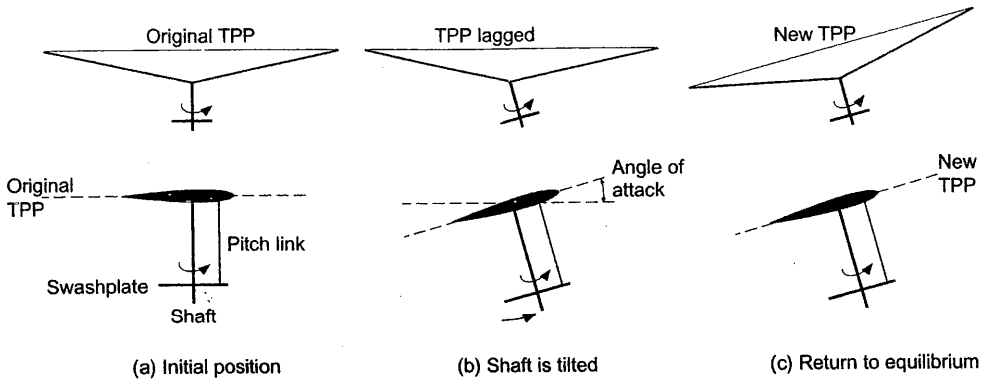

Figure 6.31 Sequence of events following a tilt of the rotor shaft. (a) Initial position. (b) Intermediate position with TPP unchanged. (c) Final equilibrium position.

6.9.3 *Precessional Stall Issues*

A problem that has occurred on tail rotors that can limit its thrust is a phenomenon known as precessional stall – see Lynn (1970). The tail rotor has no cyclic pitch and so it is free to flap in response to the changing aerodynamic forces. The tail rotor is subjected to higher effective angular rates than the main rotor as a result of yawing maneuvers, these rates being relatively large during turns about a point in hovering flight (so-called "spot-turns"). As described in Chapter 4, the rotor basically acts like a gyroscope so that when its shaft axis is suddenly tilted as the helicopter yaws the tail rotor initially maintains its orientation in inertial space – see Fig. 6.31. However, the tilting of the rotor shaft produces a change in blade pitch with respect to the original orientation of the tip-path-plane (TPP) and so a cyclic variation in blade lift is produced. This lift acts to create blade flapping and so begin to precess the rotor. The rotor plane, therefore, will align itself so that it once again becomes perpendicular to the rotor shaft. This realignment occurs rather quickly, certainly within one rotor revolution.

If the tail rotor shaft undergoes continuous angular displacements such as would be produced by the helicopter undergoing a yawing motion, the rotor disk will continuously try to realign itself. Because the realignment does not happen immediately, eventually the time rate of change of shaft displacement can become sufficiently high that the rotor TPP lags behind the shaft plane by a finite angle – see Fig. 6.32. The additional flapping moment on the blades resulting from gyroscopic effects on a rotor with pitch rate q and roll rate p is

$$M_g = -2I_b\Omega q \sin\psi - 2I_b\Omega p \cos\psi, \tag{6.38}$$

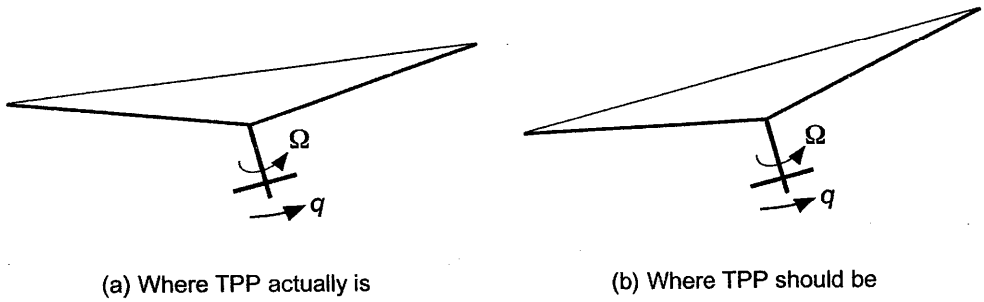

Figure 6.32 A lag in tilt of the TPP is produced when the shaft is tilted at a finite rate.

which is derived in Gessow & Crim (1955) and Brown & Schmidt (1963). Solving the equation of motion for a flapping blade (Eq. 4.5) with these additional terms gives the flapping response of the rotor. For a combination of pitch rate q and roll rate p about the rotor y (lateral) and x (longitudinal) axes respectively, the *lag* in the blade flapping displacements (relative to where the TPP would be under steady conditions) are

$$\begin{Bmatrix} \Delta\beta_{1c} \\ \Delta\beta_{1s} \end{Bmatrix} = \begin{bmatrix} \dfrac{16}{\gamma(1-\mu^2/2)} & \dfrac{-1}{1+\mu^2/2} \\ \dfrac{1}{1+\mu^2/2} & \dfrac{16}{\gamma(1-\mu^2/2)} \end{bmatrix} \begin{Bmatrix} q/\Omega \\ p/\Omega \end{Bmatrix}, \tag{6.39}$$

which is for a rotor with no hinge offset, where γ is the Lock number (see page 179) and μ is the advance ratio of the rotor. It can be assumed for the tail rotor that a yaw rate $\dot{\Psi} \equiv q$. This means that for a nose right yaw rate the tail rotor experiences an effective nose up pitch rate, causing a longitudinal lag in the blade flapping response combined with some smaller lateral flapping response.

The upshot is that when the angular rates (the yaw rate in this case) become sufficiently large, the blades will experience substantial changes in angles of attack that would be necessary to produce the aerodynamic forces to precess the tail rotor. For high enough rates, therefore, the flapping tail rotor blades will operate at such large angles of attack that they will approach stalled conditions. Because stall occurs as the tail rotor attempts to create aerodynamic forces to cause blade flapping and precess the orientation of the rotor plane, this phenomenon is called *precessional stall.* Precessional stall, therefore, can limit the anti-torque and directional (yaw) control of the tail rotor, and so can set a limit to overall helicopter performance. Lynn (1970) describe how this phenomenon may reduce attainable yaw rates. The situation is, of course, exacerbated when the helicopter is operating at high weights and/or high density altitudes whenever the tail rotor is operating under demanding thrust requirements and the blades are generating high lift coefficients.

In forward flight the tail rotor blades are already undergoing some flapping motion as a result of the dissymmetry in lift between the advancing and retreating sides of the disk. Therefore, by means of Eq. 6.39, it is apparent that relatively smaller angular yaw rates could produce precessional stall onset. Tail rotors typically have lower Lock numbers than the main rotor and, according to Eq. 6.39, the precessional effects will be relatively stronger, all other factors being equal. The onset of precessional stall can be reduced by using blades with increased Lock number (a byproduct of increased blade weight and flapping inertia) or by using rotor airfoils with larger $C_{l_{max}}$ capability. Extra blade weight, however, is certainly not desirable and higher $C_{l_{max}}$ is difficult to obtain without increasing torsional blade moments and control forces (see Section 7.7).

6.9.4 *"Pushers" versus "Tractors"*

Tail rotors may be either of the pusher or tractor variety and can be located either on the left- or right-hand side of a vertical fin. All designs suffer from interference effects between the rotor and the fin, these effects being a function of the tail rotor size or disk area, A, fin area, S, and spacing of the rotor plane from the fin. The effects are summarized by Lynn (1970), and representative measurements are reproduced in Fig. 6.33 in terms of net anti-torque producing side-force versus fin/rotor separation distance. The results are shown for various ratios of fin area to tail rotor disk area, S/A. In the pusher style the wake of the tail rotor is convected away from the vertical tail. This means that the vertical fin only

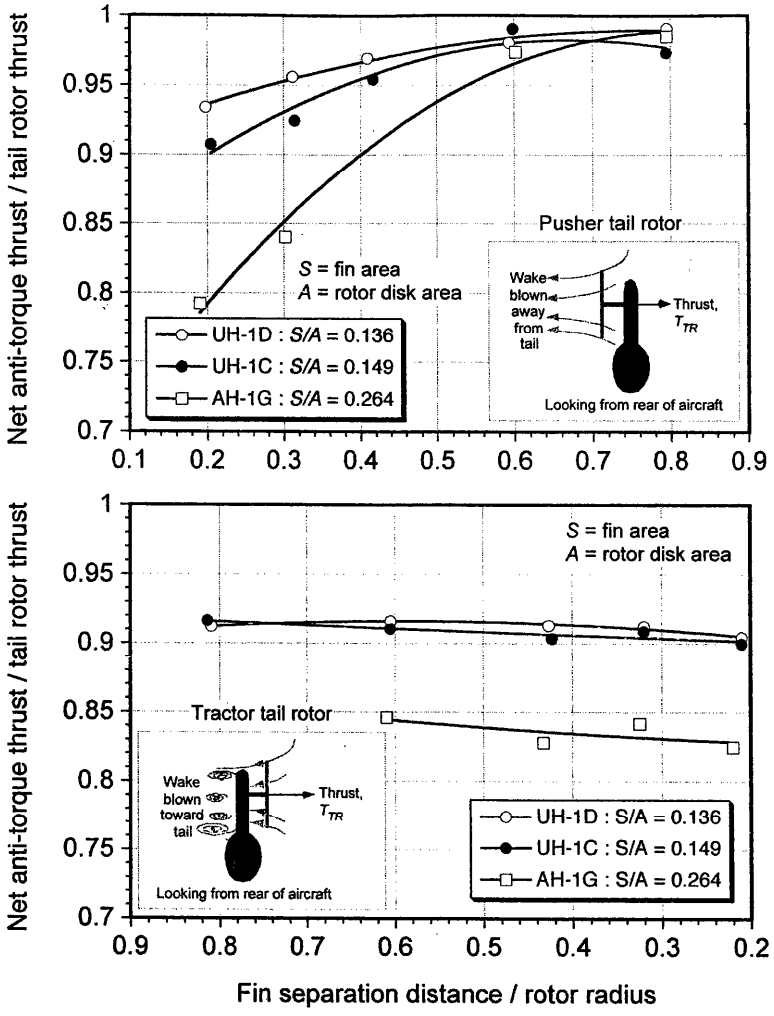

Figure 6.33 Effects of rotor/fin separation distance on net anti-torque producing side force. Data source: Lynn (1970).

distorts the inflow into the tail rotor, the consequences of which are a nonuniform inflow and higher induced power requirement. It can also be a source of 2/rev ($2N_b$) vibratory airloads. In contrast, the tractor design has the vertical fin located inside the high-energy region from the tail rotor wake. While this "blockage" effect tends to increase the tail rotor thrust, there is also a significant force applied to the vertical tail that is in the opposite direction to the anti-torque thrust requirement. It is found, however, that the net effect is a decrease in thrust compared to what would be obtained if the rotor was operating in isolation. In both cases, the interference effects become greater with larger fins and/or smaller rotors. A majority of modern helicopters use a pusher tail rotor design because this configuration tends to have a higher overall anti-torque producing efficiency.

6.9.5 *Design Requirements*

As for the main rotor, the power required to drive the tail rotor depends on the disk loading. Whereas a larger diameter may be preferable for low induced power requirements,

this is outweighed by several factors. First, a larger diameter usually means a heavier design and this is undesirable, mainly because of adverse effects on the helicopter's center of gravity location. Second, to meet certification requirements it is usually desirable that the tail rotor disk loading and induced velocities be high enough so that sideward flight of at least 35 kts is possible without the tail rotor entering into the vortex ring state. Both of these constraints dictate the use of a relatively small tail rotor with a high disk loading.

Tail rotors typically have two or four blades, and it has been shown in Section 6.4.4 that for a rotor there is no particular aerodynamic advantage of one number over the other. Only collective pitch is required because there is no need to control the orientation of the tail rotor disk plane. Tail rotor blades may have some built-in twist to help minimize induced power requirements. However, the amount of blade twist is usually very small compared to the main rotor to avoid losses in efficiency and the possibilities of stall when the tail rotor is operating in an effective descent, such as when hovering in crosswinds or in sideward flight. Although some blade designs may use cambered airfoil sections, the tail rotor blades found on many helicopters use symmetric airfoils because of their reasonable overall performance and low pitching moments. While the higher maximum lift obtained with cambered airfoils can help reduce rotor solidity and thereby minimize tail rotor size and weight, this can be outweighed by their larger pitching moments (which lead to higher control forces) and poorer performance when operating at negative angles of attack. Generally, tail rotors are designed to operate at tip speeds that are comparable to those of the main rotor. Lower tip speeds are desirable to minimize noise. However, for a given thrust, tail rotors operating at lower tip speeds require higher solidity to prevent blade stall. A lower tip speed also increases the torque requirement. Both of these factors will increase the weight of the drive system.

A secondary effect of the anti-torque side-force is the tendency for the helicopter to drift sideways. This is corrected for by the main rotor, which is tilted slightly to the left (by means of cyclic pitch inputs) so that a component of the main rotor thrust produces an equal and opposite side-force. This is the reason why it will be noticed that a helicopter will tend to hover with one wheel (or skid) lower than the other. On larger helicopters, the main rotor shaft is physically tilted slightly (as part of the design, thereby introducing a pretilt) so that the pilot does not require as much cyclic pitch input to counter the tail rotor side-force. The tail rotor thrust and the component of the main rotor side-force act together, producing a couple, and thereby, a rolling moment about the center of gravity (c.g.). To reduce this moment, the tail rotor is located vertically up on the tail structure at a location so that the line of action of its thrust vector is close to the c.g. of the helicopter.

6.9.6 *Representative Tail Rotor Designs*

Examples of modern tail rotor assemblies are shown in Fig. 6.34. Some tail rotors may be very simple two-bladed teetering assemblies (e.g., Fig. 4.20), whereas others may be relatively sophisticated bearingless or hingeless designs. Common amongst all tail rotors is the lack of any cyclic pitch; only collective pitch is used because control of the tail rotor disk orientation is not required. Nevertheless, the tail rotor must be provided with flapping so that the blades may be allowed to respond to the changing aerodynamic environment. Lead–lag hinges are not used to save weight and reduce mechanical complexity. Instead, a large amount of δ_3 or pitch–flap coupling is built into the tail rotor design. This provides a means of allowing the blades to pitch cyclically in such a way as to minimize blade flapping produced by the changing aerodynamic loads (see Section 4.12). In addition, a set of preponderance weights may be attached to the tail rotor pitch horns. These are a set of weights that lie out of the plane of rotation and rely on centrifugal forces to help keep the

(a) Four bladed tractor (UH-60) (b) Four bladed pusher (AH-64)

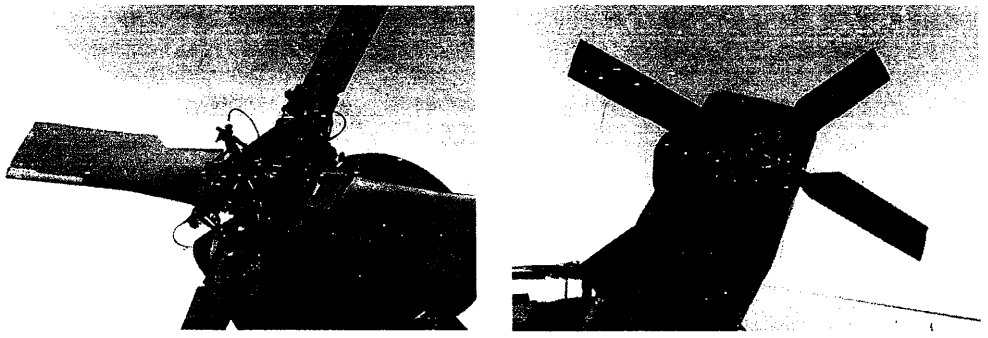

Figure 6.34 Representative tail rotor assemblies (a) UH-60 bearingless tail rotor. (b) AH-64 twin teetering tail rotor

control forces to within manageable limits. Preponderance weights are usually only found on tail rotors that use highly cambered airfoil sections so as to help minimize moments transferred to the pitch control system.

6.10 Other Anti-Torque Devices

Besides the conventional tail rotor, other types of anti-torque devices are used on modern helicopters. These are the fenestron (or fan-in-fin or fantail) and the NOTAR concepts. All have relative advantages and disadvantages compared to a conventional tail rotor.

6.10.1 *Fan-in-Fin*

Shrouded or ducted fan anti-torque designs, which are known as "fenestrons," "fan-in-fin," or "fantail" designs, have been frequently considered over conventional tail rotors, especially for smaller and lighter helicopters. A photograph and schematic of a fan-in-fin design is shown in Fig. 6.35. Details of the design of such anti-torque devices are given by Mouille (1970, 1979), Mouille & Dámbra (1986), Vuilet & Morelli (1986), Vialle & Arnaud (1993), and Abrego & Bulaga (2002). Fan-in-fin designs typically are found to have lower power requirements than an open tail rotor to produce the same amount of thrust. Alternatively, this means the fan-in-fin design can give the same anti-torque and yaw authority with a smaller and perhaps lighter design compared to a conventional tail rotor. See also Davidson et al. (1972) for the design trades.

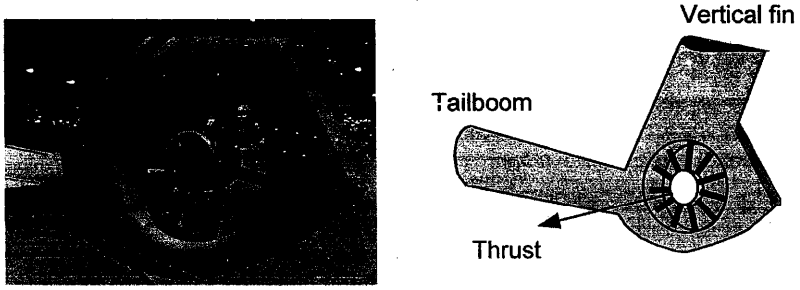

Figure 6.35 The fan-in-fin or fenestron tail rotor, as used on the SA-365 Dauphin.

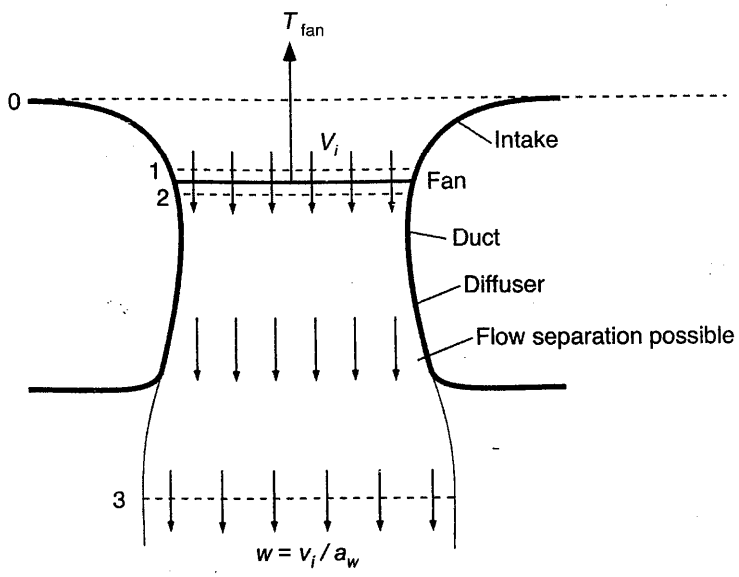

Figure 6.36 Flow model assumed for fan-in-fin analysis using momentum theory.

The theoretical analysis of the ducted rotor (propeller or fan) has been approached by Kruger (1949) and Kuchemann & Weber (1953), with experimental work by Mort (1965), and Mort & Gamse (1967). The momentum theory discussed in Chapter 2 can be extended to the analysis of a fan-in-fin design, with the flow model being shown in Fig. 6.36. Far upstream of the fan, the velocity can be assumed to be zero. At the plane of the fan, the induced velocity is v_i. By the principle of conservation of mass, the mass flow rate, $\dot{m}$, is constant through the system so that

$$\dot{m} = \rho A v_i = \rho(a_w A)w, \tag{6.40}$$

where, by virtue of the duct design the area of the slipstream flow at the outlet is $a_w A$ with the velocity at the duct outlet being w and with a_w being a wake contraction parameter. This gives the relationship that $w = v_i/a_w$. By means of conservation of momentum the thrust on the duct and fan is

$$T = T_{\text{duct}} + T_{\text{fan}} = \dot{m}w = (\rho A v_i)w = \frac{\rho A v_i^2}{a_w}, \tag{6.41}$$

or

$$v_i = \sqrt{\frac{a_w T}{\rho A}} = \sqrt{\frac{T}{2\rho A_{\text{eff}}}}, \tag{6.42}$$

where $A_{\text{eff}} = A/2a_w$. Applying the Bernoulli equation between stations 0 and 1 gives

$$p_0 = p_1 + \frac{1}{2}\rho v_i^2, \tag{6.43}$$

and between stations 2 and 3 gives

$$p_2 + \frac{1}{2}\rho v_i^2 = p_0 + \frac{1}{2}\rho w^2. \tag{6.44}$$

Using Eqs. 6.43 and 6.44 gives for the thrust on the fan:

$$T_{\text{fan}} = (p_2 - p_1)A = \frac{1}{2}\rho w^2 A. \tag{6.45}$$

Using Eqs. 6.41 and 6.45 gives

$$\frac{T_{\text{fan}}}{T} = \frac{\frac{1}{2}\rho A w^2}{\rho A v_i w} = \frac{w}{2v_i} = \frac{1}{2a_w}. \tag{6.46}$$

Using Eqs. 6.42 and 6.46, we obtain the induced power consumed by the fan:

$$(P_i)_{\text{fan}} = T_{\text{fan}} v_i = \left(\frac{T}{2a_w}\right)\sqrt{\frac{a_w T}{\rho A}} = \frac{T^{3/2}}{\sqrt{4a_w \rho A}} \tag{6.47}$$

or

$$\frac{(P_i)_{\text{fan}}}{(P_i)_{TR}} = \frac{1}{\sqrt{2a_w}}, \tag{6.48}$$

where $(P_i)_{TR}$ refers to a conventional (unducted) tail rotor. The latter equation gives an interesting result, in that it shows that if the shape of the duct is controlled so that the rotor wake does not contract as much as would occur naturally with a conventional tail rotor (for which in the ideal case, $a_w = 0.5$, $A_{\text{eff}} = A$), less power will be required to produce a given total thrust. In the case where $a_w = 1$ (the assumption of no wake contraction so that $A_{\text{eff}} = A$) a ducted fan of the same area will consume $1/\sqrt{2}$ of the power of a conventional tail rotor (i.e., 30% less power for the same net thrust). Alternatively, a ducted fan of half the disk area of a conventional tail rotor (i.e., a diameter reduced by a factor $1/\sqrt{2}$) will produce the same thrust and consume the same power. Generally, however, because the length of the duct must be relatively short to minimize structural weight and drag penalties in forward flight, the potential gains in efficiency are not as large as suggested by the above analysis. Losses introduced by drive shafts also reduce any potential gains in efficiency. However, the lower tip-loss effects associated with a fan-in-fin design give a further reduction in induced power requirements. Overall, the fan-in-fin design offers some overall advantages compared to a conventional tail rotor for anti-torque and directional control.

The fan rotor design may also be approached from the principles of the blade element momentum theory (BEMT) discussed in Section 3.3. Equating the contributions to section thrust made from the momentum and blade element theories (using Eqs. 3.45 and 3.57), then we can write for the ducted fan that the incremental thrust is

$$dC_T = \frac{2}{a_w}\lambda^2 r dr = \frac{1}{2}\sigma C_l r^2 dr, \tag{6.49}$$

where the mass flow through the duct and fan is controlled by the effective wake contraction ratio a_w. This is a function of duct design as well as the gap between the fan blades and the duct. Stator vanes are usually used to straighten the outlet flow and recover swirl losses, which are higher because of the higher rotor rpm. With the assumption for a value for a_w (a common assumption for a fan is to use a_w=1.25), then the inflow λ can be solved by finding a solution to a modified form of the inflow equation, namely

$$\lambda(r) = \frac{a_w \sigma C_{l_\alpha}}{8}\left[\sqrt{1 + \frac{16}{a_w \sigma C_{l_\alpha}}\theta r} - 1\right]. \tag{6.50}$$

Clearly, the optimum blade twist for a fan is of the same hyperbolic form needed for an unducted rotor. In some cases fan rotor designs may have large blade twist angles compared to a conventional tail rotor, and it may be inadequate to assume small angle approximations to find λ. In this case the inflow equation can be solved numerically. Starting from Eq. 6.49 then the inflow distribution over the disk can be found using

$$\lambda(r) = \sqrt{a_w \sigma (C_l \cos\phi - C_d \sin\phi) r/4}. \tag{6.51}$$

Because C_l and C_d are functions of the blade section angle of attack, $\theta - \phi$, which is in turn a function of λ at each section, then the foregoing equation must be solved iteratively. Convergence, however, is found to be rapid. Thereafter, the sectional airloads can be determined and net rotor thrust and power follows by radial integration along the blade.

In forward flight the fan-in-fin is shielded from the external flow and the main rotor wake and, consequently, its performance is usually more predictable. Although as shown by Basset & Brocard (2004), even here empirical corrections to the momentum theory approach must be used because of the streamline inlet distortion produced by the duct. The vertical fin surrounding the fan is designed to provide a side force in forward flight and so most of the anti-torque. The aerodynamics of "sense of rotation" and the interference effects of the fin assembly, which are important for conventional tail rotors, are less important for the fan-in-fin design. However, the possibility of flow separation at the inlet lip of the shroud must be kept in mind, and usually the lip is carefully contoured to avoid such effects. Flow separation at the inlet to a ducted fan-in-fin can lead to a loss of thrust and/or thrust fluctuations that is consistent with some loss of effectiveness as a directional control producing device (instantaneous thrust) although not necessarily as an anti-torque device (average thrust).

From a safety perspective, the shrouded nature of the fan-in-fin reduces the possibilities of blade strikes during low-altitude flight operations and also the risk of injury to personnel on the ground. The larger number of blades on a fan-in-fin design increases the frequency of the rotor noise and this can appear in the helicopter noise spectrum over a range of frequencies to which the human ear is more sensitive. However, at greater distances these higher frequency sounds are more readily absorbed in the atmosphere. Efforts to reduce the noise of fan-in-fin designs through phase modulation using unequal blade spacing have made the fan-in-fin sound subjectively less noisy – see Vialle & Arnaud (1993).

6.10.2 *NOTAR Design*

The use of jet thrust for anti-torque is not a new one, having been used on the Cierva–Weir W-9 in 1945 and also in other designs. However, the design required high power and directional sensitivity was poor. The idea was also used on prototype helicopters built by Hiller in the US and Nord in France. The NO TAil Rotor or NOTAR concept uses a similar yet different approach to anti-torque and yaw control. The design is discussed by Logan (1978) and Sampatacos et al. (1983), and is reviewed by Winn & Logan (1990). Here, anti-torque capability comes from a *circulation control* concept, which results in a distributed side-force along the entire tail boom assembly. As shown in Fig. 6.37, a high-velocity jet (or jets) of air from a pressurized tail boom is blown tangential to the surface out of narrow slots that run lengthwise on one side of the tail boom. In combination with the downwash velocity produced by the main rotor, these jets cause the flow to remain attached to the tail boom surface by means of the *Coanda effect*. Downstream of the slots, a powerful suction pressure is produced on one side of the tail boom and a side (anti-torque) force results. The magnitude of this side-force depends on the jet velocity out of the slot. This is controlled by adjusting the pressure inside the tail boom by means of a variable pitch fan and compressor. A small auxiliary nozzle at the end of the tail boom provides a pressurized jet to improve yaw control rates and overcome the inherent lag in the circulation control system. The nozzle in the jet thruster is rotated by the conventional action of the pilot's foot pedals.

In forward flight, the circulation control becomes less effective as the main rotor downwash moves further along the tail boom. Fixed aerodynamic stabilizers and the jet thruster

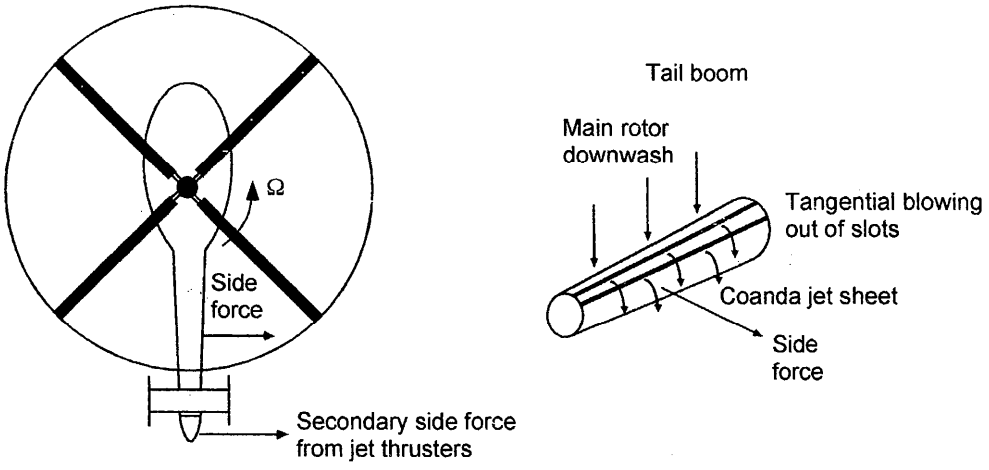

Figure 6.37 The NOTAR anti-torque system

combine to produce the necessary anti-torque and yaw control. The NOTAR concept has proved attractive to operators because of its low noise, safety for ground personnel, and freedom from blade strikes when operating in confined locations. Also, for a military helicopter this system is attractive because of the absence of a vulnerable tail rotor assembly, and it has a high level of redundancy in the event of any tail boom damage.

6.11 High-Speed Rotorcraft

Vertical lift aircraft that use compounding or have tilt-rotor or tilt-wing capability are referred to as high-speed rotorcraft. Not only are these aircraft capable of vertical takeoff and landing, but they can attain much higher speeds than conventional helicopters. They are, however, not necessarily more efficient (say, in terms of effective lift-to-drag ratio) nor are they as economic because they generally always have a higher empty weight fraction (i.e., lower payload), as well as higher capital and operating costs.

6.11.1 *Compound Helicopters*

A compound helicopter involves a lifting wing in addition to the main rotor (lift compounding) or the addition of a separate source of thrust for propulsion (thrust compounding) – see the review of Lynn & Drees (1967). The idea is to enhance the basic performance metrics of the helicopter, such as lift-to-drag ratio, propulsive efficiency, and maneuverability. The general benefit can be an expansion of the flight envelope compared to a conventional helicopter (see Fig. 6.38). While there are no compound helicopter designs in current production (although many prototype designs have been built), except for some of the Russian designs that may have an element of lift compounding, most helicopter manufacturers at one time or another have investigated auxiliary propulsion or lifting wings to off-load the rotor and expand the flight envelope. However, there are major drawbacks in this compound design in terms of increase in empty weight and loss of payload capability, download penalties in hover, reduced vertical rate of climb and higher operating costs.

One of the first experimental compound helicopter designs was the McDonnell XV-1. This was a pressure jet driven rotor, with a wing and a pusher propeller. After a vertical takeoff, the power was shifted from the tip jets to the propeller and the rotor continued to turn in autorotation. In 1954 the aircraft was flown at speeds approaching 175 kts (201 mph,

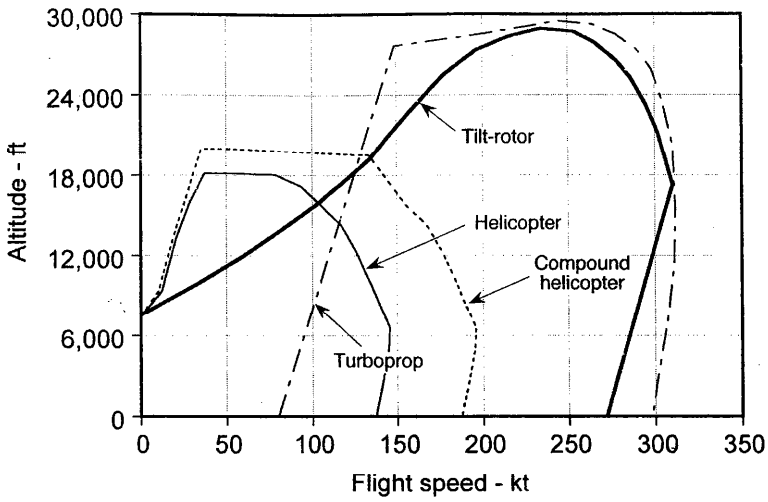

Figure 6.38 Representative speed-altitude flight envelopes of a conventional helicopter versus a compound design, a fixed-wing turboprop, and a tilt-rotor.

324 km/h). The Sikorsky NH-3A was based on the S-61 and used a wing mounted with two turbo-jets for auxiliary propulsion. It achieved speeds of up to 230 kts (265 mph, 388 km/h) – see Fradenburgh & Chuga (1968). The Bell UH-1 compound also had a wing and two turbojets and reached a speed of 275 kts in level flight. The Fairey company built a number of tip-jet driven compound machines, with the last and largest being the Rotodyne (see page 715). This 33,000 lb (15,000 kg) aircraft was powered by two turboprops, which also supplied compressed air for the tip jets. In 1959 the machine set a world speed record in its class of 167 kts (192 mph, 309 km/h). The Piasecki Pathfinder (Fig. 6.39) was a compound

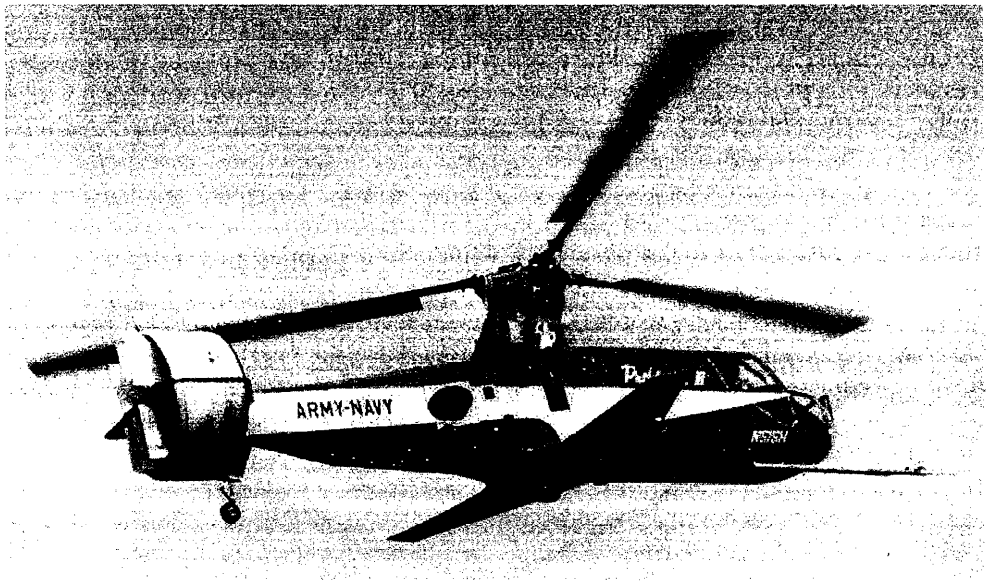

Figure 6.39 The Piasecki Pathfinder was a successful compound helicopter concept from the 1960s but it remained in the experimental phase.

that used a rotor off-loaded by a small, low-mounted fixed wing when the craft transitioned into forward flight. The ducted fan ("ring-tail") at the tail, with vertical vanes in the duct, provided anti-torque and directional control. The 16H-1A Pathfinder II was a bigger and more powerful version, with a cabin large enough for eight seats. This machine reached level flight speeds of 195 kts (224 mph, 361 km/h). This US Navy and US Army evaluation program provided a wealth of valuable information on compound rotorcraft technology and operations, much of which was later used in the development of the Lockheed AH-56 Cheyenne (Fig. 1.39), which used a wing and a pusher propeller mounted to the tail. Today, the Piasecki Company continues to examine compound helicopter concepts. In the early 1970s, Boeing-Vertol flew the tandem Model 347 with relatively large wings, the technical motivation for which is discussed in detail by Stepniewski & Keys (1984).

The ideas of compounding have received renewed attention by some manufacturers, with some revived ideas being discussed by Humpherson (1998). Orchard & Newman (1999a,b; 2000) have considered some of the unique design issues associated with the optimization of a modern compound helicopter concept. It remains to be seen, however, if the compound helicopter design will reemerge as a viable rotating-wing design concept for the twenty-first century.

6.11.2 *Tilt-Rotors*

Based on Bell's experience with the XV-3 (see page 48), the Bell XV-15 tilt-rotor was designed and first flown in 1977. It has proven a reliable research aircraft, from which much knowledge has been gained about tilt-rotor technology. The much larger V-22 tilt-rotor (Fig. 1.40) flew in 1989 and in 2005, after a lengthy development phase, it was in low-rate production. The V-22 is designed to fullful many of the missions that are possible with a conventional helicopter, but with the added advantage of much higher flight speed capability. However, it must be borne in mind that the tilt-rotor design is a hybrid, and a performance compromise, between a helicopter and a conventional airplane. The Agusta-Bell Model 609 tilt-rotor was designed in the late 1990s for the civilian market.

The aerodynamic design of the tilt-rotor poses many additional challenges over that of the conventional helicopter. The smaller rotor diameter means that in hover the disk loadings of a tilt-rotor are much higher than those of a helicopter of the same gross weight. The efficiency of the rotor is also lowered because of the very high blade twist, a feature required to ensure good propulsive efficiency in airplane mode. In addition, when in hover the wings of the tilt-rotor operate in the downwash from the rotors, which produces a large download on the aircraft and decreases the payload it can carry. The fixed wings also influence rotor performance, and the combined effect degrades the hovering efficiency (figure of merit) compared to a helicopter of the same gross weight – see McVeigh et al. (1991). Various techniques are used to minimize these interactional aerodynamic effects, including 90-degree deflections of the wing flaps – see Stepniewski & Keys (1984) and Wood & Peryea (1991). In fixed-wing mode, when the rotors act as propellers, they are rather less efficient because the disk loading is too low and profile losses are higher than would be achieved with a conventional propeller. Rosenstein (1986) and McVeigh et al. (1997) give good overviews of the numerous aerodynamic design trade-offs for tilt-rotors.

The tilt-rotor has two sets of flight controls, one set for helicopter mode and another for fixed-wing mode. In helicopter mode, the rotors of a tilt-rotor are controlled with normal cyclic and collective pitch controls. Yaw is controlled by differential cyclic, just like a tandem rotor machine such as the CH-47. During transition from helicopter mode to fixed-wing mode, the aerodynamic environment encountered by the rotors becomes extremely

complex and high airloads can be produced. The relationship between the airspeed and the rotor tilt angle must conform to a relatively narrow envelope for safe operation and this is controlled with the aid of the fight control system. In airplane mode the rotors act as conventional propellers, with all of the vertical lift forces being produced by the wing. In this mode, control is achieved with the use of conventional aerodynamic surfaces, namely the flaperons, elevator, and rudder. Despite the complexity and high costs of the tilt-rotor it has the potential to play a unique role in vertical flight aviation that a conventional helicopter cannot. It has not yet, however, advanced to the level of military or civil success enjoyed by the modern helicopter.

6.11.3 *Other High-Speed Concepts*

Most of the major US helicopter manufacturers have undertaken studies of *high-speed rotorcraft concepts*. Similar studies have been conducted by some European manufacturers. The general requirements call for a rotorcraft capable of efficient hover capability that can cruise at over 400 kts, which is about twice as fast as is attainable with a conventional helicopter. Most concepts would be classified as convertible aircraft or *convertiplanes*. The primary advantage of any convertiplane concept is the ability to balance efficient hovering flight capabilities with efficient cruise and good range but without incurring large weight and cost penalties. Despite much research, there is no other high-speed or convertible rotorcraft concept currently flying other than tilt-rotors. Some of the high-speed rotorcraft designs considered have included the following:

1. *The ABC concept*: In the 1960s, Sikorsky Aircraft announced the XH-59A research aircraft using the Advancing Blade Concept (ABC). This was a compound concept with auxiliary propulsion and a rigid coaxial rotor system that was designed to alleviate the problem of retreating blade stall by allowing a more symmetric distribution of lateral airloads over the rotor disk. Chaney (1969) gives a good overview of the aerodynamic issues. During flight testing, the machine reached a maximum speed of 263 kts (487 kph). For the time, it was the only rotorcraft to have approached such speeds without lift compounding.
2. *The X-wing concept:* This design employs a unique rotor system that uses circulation control. The blades consist of thick elliptical airfoils, and air is blown at high velocity out of the leading or trailing edges to create lift by means of the Coanda effect – see Cheeseman (1968) and Williams (1976). A complicated pneumatic blowing system was required for cyclic blowing in forward flight. As airspeed built, the rotor system was designed to be slowed down and stopped, forming an X-wing configuration. The full-scale rotor was tested in a wind tunnel in the early 1980s, but it was never flown because of various technical issues and escalating costs.
3. *The variable diameter rotor concept:* This is another Sikorsky concept, which looks similar to a conventional helicopter but the blades telescope in length during flight to increase or decrease the disk area. The design is discussed by Fradenburgh et al. (1973) and Fradenburgh (1992). A system of clutches inside the rotor hub controls the extension and retraction process. This technique allows for low rotor disk loadings and maximum efficiency in hover, whereas the smaller diameter rotor allows for a higher cruise efficiency. A similar design has been considered for a tilt-rotor, where the rotor diameter is reduced for airplane mode – see Studebaker & Matuska (1993). The system has been successfully flown in the wind tunnel but not yet on a full-scale aircraft.

4. *Rotor–wing concept:* This is a high solidity stoppable rotor system with three blades. The rotor is slowed down and stopped in forward flight, with two blades pointing upstream forming forward swept wings, whereas the third blade points downstream and lies over the fuselage. The concept is similar to the ill-fated X-wing circulation-controlled rotor of the 1980s. See Rutherford et al. (1993) for a history of such stopped rotor designs.
5. *Quad tilt-rotor:* A quad tilt-rotor concept has been proposed in 1999 by Bell with a fuselage the approximate size of a large fixed-wing cargo airplane. Design features of the quad tilt-rotor include the use of two wings, one forward and one aft. Each wing has an engine and proprotor mounted at its tip. The civil version of the concept has been designed to carry up 100 passengers at 300 kts.
6. *Folding, stowed, or trailed rotor systems:* In this concept the rotor is stopped, the blades folded back into the fuselage, and the lift is transferred to fixed wings. Various aeroelastic effects are possible during the stopping and stowing process and these are difficult to contend with; see Celniker et al. (1965) and Deckert & McCloud (1968). The high capital and maintenance costs of the system, as well as the high weight of the folding and blade storage system, means that this type of machine is not a particularly attractive design option.
7. *Shrouded rotor designs:* The idea here is to use a relatively large ducted fan, integral to a wing, to provide the vertical lift. As the aircraft gains speed, power is transferred from the fan to pure propulsion, shutters cover the fan, and the wing provides all the lift. The concept, however, is not new, having being used on the Ryan XV-5 in the 1960s. This aircraft demonstrated successful transitions from hover to forward flight and back, flying at speeds of up to 330 kts (577 kph).
8. *Slowed rotor concepts:* By reducing rotor rpm in flight, this alleviates compressibility effects on the advancing blade and allows higher flight speeds. However, all rotor systems experience a loss of flapping rigidity with reduction in rotor rpm, so only about a 20–30% reduction in rpm seems possible before aeroelastic issues become critical. Nevertheless, some aerodynamic benefits at very high advance ratios seem possible, including better rotor lift-to-drag ratios. See also Celniker et al. (1965).
9. *Gyroplane concepts:* The gyroplane concept takes advantage of the vertical takeoff capabilities of the helicopter but the higher speed of a compound but with the rotor operating in the autorotative state. The ideas were explored in the 1950s by McDonnell with the XV-1 and by Fairey with the Gyrodyne and Rotodyne (see page 715). One advantage of a gyroplane is reduced capital and operating costs compared to a conventional shaft driven helicopter. It would appear that renewed interest in this concept may lead to its further development in the twenty-first century.
10. *Morphing concepts:* There have been many convertiplane concepts proposed over the years. More recently, the Mono Tilt-Rotor (MTR) has been proposed as an innovative convertiplane concept. Its capabilities are predicated on the combination of a single coaxial rotor system and sophisticated kinematics that morph the aircraft topology for efficient flight operations. As yet only developed in conceptual form [see Preator et al. (2004)], the MTR design fully integrates an efficient coaxial rotor, a folding lifting wing system and a cargo handling system that is capable of rapidly and economically moving different types of mission tailored payloads.

6.12 Smart Rotor Systems

A "smart" structure is one that involves distributed actuators and sensors, along with a computer to analyze responses and apply displacements or strains to change the characteristics of the structure in an adaptive and beneficial way. Smart structures make it possible to aerodynamically alter the properties of rotors in a desirable way so as to reduce vibrations, improve performance, and enhance other performance factors. Such alterations would include the use of actively controlled aerodynamic surfaces on the rotor, such as with trailing-edge flaps (Fig. 6.40) or an all-movable blade tip or with strain producing actuators embedded in the blade to create elastic deformations. The field is reviewed by Chopra (1997, 2000). While the technology is not yet mature, various concepts are developing quickly, and it is likely that a full-scale helicopter rotor incorporating one or more new smart technologies will fly early in the twenty-first century.

Much of the work in this field has so far focused on building and testing dynamically scaled smart rotor models. The actuation concepts are presently difficult to build at full-scale without excessive weight and power penalties, but this will change as further research is conducted. Many of these rotor models consist of controllable twist blades, incorporating embedded piezoelectric elements or trailing-edge flaps (Fig. 6.40), actuated by piezoceramic or magnetostrictive actuators. The performance of the actuation systems seems to be degraded dramatically at higher rotational speeds because of high dynamic pressure, centrifugal forces, and frictional moments on the actuation mechanisms. For trailing-edge flap designs, a compact torsional actuation technique is required, and several approaches have been examined. For controllable twist designs, banks of piezoceramic elements are embedded under the skin of the blade on the top and bottom surface. To induce sufficient

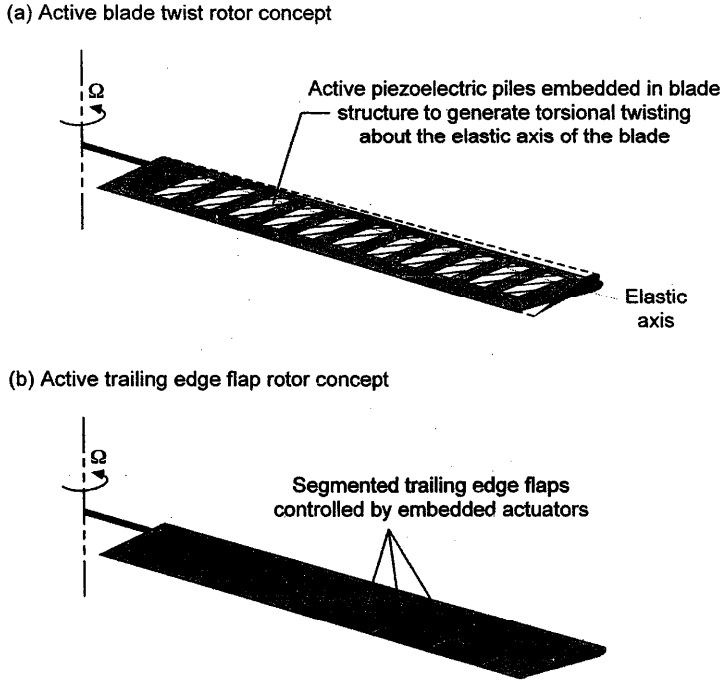

Figure 6.40 Schematics of two "smart" rotor blade concepts: (a) Active blade twist using embedded piezoelectric piles. (b) Actively controlled trailing edge flaps.

blade twist for active control of rotor vibration or noise, a large number of distributed piezoceramic elements are required. Although this system involves no moving parts, it incurs a significant weight penalty and gives an undesirable increase in blade stiffness. There are also structural integrity issues.

Straub (1995) and Straub & Merkley (1995) have carried out a feasibility study of using smart structures technology for primary as well as active control of a full-scale helicopter rotor. It was concluded that the concept of blade twist and profile camber control using embedded actuators is not practical with the types smart materials currently available. Servoflap control systems using on-blade smart material actuators appeared conceptually feasible for primary and active controls. Shen et al. (2003) have examined the idea of trailing edge flaps for the primary flight control of an ultralight helicopter. So far there has been limited research towards the development of analytical tools need for a smart rotor design. Recently, however, there has been some effort to develop a coupled actuator-flap-rotor dynamic analysis, but it is far from being as comprehensive as would be required for confident design use. The development of unsteady aerodynamic models for this purpose have also undergone substantial development – see Section 8.18 – and the proper modeling of unsteady aerodynamic effects is vital to the predictive success of analytical tools for smart rotor systems. While it is clear that the smart rotor technology is not yet mature, either from a theoretical or practical perspective, various concepts are developing quickly and it is likely that a full-scale helicopter incorporating one or more of these technologies will fly within the next few years. It would seem, however, that full flight certification of actively controlled rotors for use in production helicopters is a longer way off.

6.13 Human-Powered Helicopter

The problem of designing a human-powered helicopter (HPH) is not a new one, with some good theoretical studies being performed by Kendall, (1959), Naylor (1959), and Shenstone & Whitby (1959). In 1981, the American Helicopter Society (AHS) first offered a $20,000 prize [see Sopher (1997)] for the first successful controlled flight of a HPH. As of 2005, the prize remains unclaimed. The AHS's requirements for the HPH dictate that the machine must lift itself and the pilot off the ground without the use of any stored energy devices, climb to a height of 3 m (9.84 ft) and be in flight for 1 minute while maintaining horizontal flight position within a 10 m (32.81 ft) square. A slow descent is allowed after the maximum height is reached. There have been two notable attempts to do this – one in Japan [see Naito (1990) and Fig. 6.41] and one in the United States at California Polytechnic Institute [see Mouritsen (1990)]. Both of the machines were driven by tip mounted propellers, very much like the early Brennan machine (see Fig. 1.13) so requiring no anti-torque devices, and had rotor diameters of over 100 ft (30.48 m). The pilot delivered power from a chain and sprocket system through a cable transmission to the propellers. The current flight record by the US team is 8 seconds at a maximum altitude of 0.203 m (8 in) and the Japanese team holds the duration record of 19 seconds, both attempts which are far from meeting the AHS's requirements. In the late 1990s, there were only two active HPH projects, one at the University of Michigan and the other at the University of British Columbia.

Patterson (1986) gives a good overview of the technical and practical issues in building a HPH. While the choice of strong lightweight materials and the construction of a suitable HPH is one technical barrier, much of the problem has to do with the limits of human physiology. For an endurance of 1 minute an athletic human can be expected to deliver a power of between 0.67 hp and 0.8 hp (500–600 W) and perhaps up to a peak of 1.34 hp

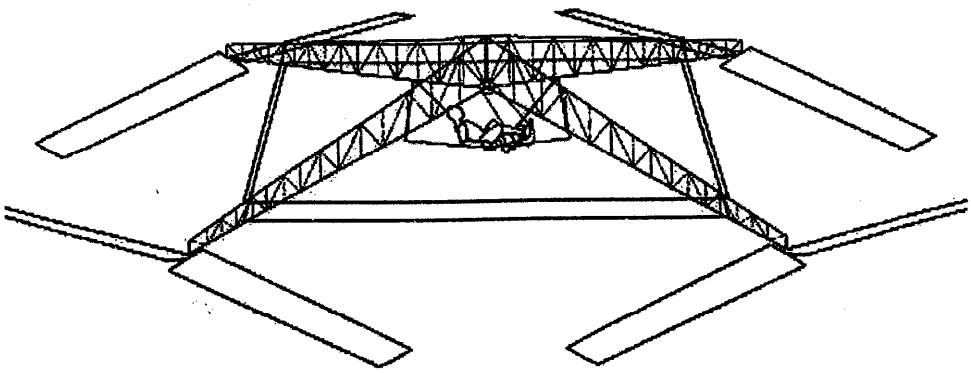

Figure 6.41 An example of a human power helicopter concept, in this case the Yuri I design built at Nihon University in Japan.

(1,000 W) for a duration of 10 seconds. This means that a net possible energy expenditure of a human before exhaustion is about 34.1 BTU (36 kJ). Based on these power expectations it is possible to proceed with the conceptual design of a rotor to accomplish the AHS's requirements. The design problem has been recently considered in some detail by Filippone (2002). The minimum power to hover a vehicle of weight W out of ground effect (OGE) will be given by the modified momentum theory (Chapter 2) where

$$P_{OGE} = \frac{1}{FM}\frac{W^{3/2}}{\sqrt{2\rho A}} = \frac{1}{FM}\frac{W^{3/2}}{\sqrt{2\rho\pi R^2}}. \tag{6.52}$$

Because the most optimistic average power output is known ($P_{\text{avail}} = 0.8$ hp) the foregoing equation can be rearranged to solve for the rotor radius R giving

$$R = \frac{1}{FM}\frac{1}{\sqrt{2\pi\rho}}\frac{W^{3/2}}{P_{\text{avail}}}. \tag{6.53}$$

Assuming a net aircraft and pilot weight of 200 lb (optimistic) and a rotor a figure of merit of 0.75 (also optimistic, even with the benefits of ground effect) operated at sea level conditions, then solving for the rotor radius gives more than 77 ft. It is probably unrealistic to build such a large single rotor with blades that are both lightweight and have sufficient strength and structural rigidity, although the attempt has been made. Multirotor machines may offer better prospects in this regard. Furthermore, because such a rotor will have blades that turn at a low rpm, the tip Reynolds numbers will be low and the viscous drag on the blades will be relatively high. It would seem unlikely, therefore, that such a rotor with a FM of 0.75 is realizable. However, it is interesting that if it were possible, such a rotor would have a disk loading of only 0.0107 lb/ft^2 and an average induced velocity, v_h, of about 3 ft/s.

Filippone (2002) considers the possibility of two or more crew to power a HPH because this will double the effective power available. This is a variation of the engine selection problem previously introduced in Section 5.5.5. Yet because the crew weight will at least double, Eq. 6.53 shows that that the rotor radius will have to increase by at least a factor of 1.41 to maintain a low disk loading, and so empty airframe will also increase (i.e., an increase of the empty weight fraction.) This is a direct result of the square–cube law (see Section 6.4.1). The various trades, however, require further study for multirotor HPH configurations.

Any HPH must have a large diameter rotor operating in close proximity to the ground, so the issue of ground effect (see Section 5.8) on rotor performance must be carefully

considered. Fradenburgh (1960) reports on measurements made with rotor height/diameter (h/D) ratios as low as 0.05, and Prouty (1985) gives a summary of other ground effect measurements. Reductions in induced velocity IGE of more than 60% seem possible for a large rotor in very close proximity to the ground. This favorable IGE effect will result in a lower effective disk loading (higher effective disk area) and so a smaller rotor can be built to meet the same requirements. The rapid loss in the benefits of IGE operation, however, are found for $h/D > 0.4$. Therefore, for the HPH to remain IGE throughout its flight for good aerodynamic efficiency, a balance between the choice of rotor diameter and hovering IGE benefits must be sought.

Proceeding further by assuming such a rotor could be built and hovered in ground effect, it is interesting to evaluate whether sufficient human energy is available to climb a HPH to 3 m and then to hover there (i.e., further out of ground effect) for a period of time. The power to climb vertically can be established from the results in Chapter 2. Assuming low rates of climb then the extra power required to overcome induced losses and also increase potential energy will be

$$P_{\text{req}} = P_{\text{hover}}\left(1 + \frac{V_c}{2v_h}\right) = P_{\text{hover}} + \Delta P_{\text{req}}, \tag{6.54}$$

where V_c is the climb velocity and ΔP_{req} is the excess power required to climb. The extra energy expended during this process is

$$E = \int \Delta P_{\text{req}}\, dt = P_{\text{hover}} \int \left(\frac{V_c}{2v_h}\right) dt = \frac{P_{\text{hover}} V_c t}{2v_h}, \tag{6.55}$$

if V_c is assumed to be constant. This means that the excess energy available to climb to the required altitude can either be expended quickly by climbing at a higher rate or slowly by climbing at a low rate. If the maximum extra power that is humanly possible is assumed to be 0.25 hp (0.186 kW) for a duration of 10 seconds (equivalent to an energy of 1.768 BTU or 1.86 kJ) then a maximum climb velocity of about 1.85 ft/s (0.56 m/s) is possible, reaching the required altitude in about 5 seconds. A subsequent hover for 55 seconds would consume at least 31 BTU (32.6 kJ), clearly to the point of human exhaustion. Alternatively, a slower climb over 60 seconds will need a climb velocity of only 0.164 ft/s (0.05 m/s) using a total energy of about 34.8 BTU (36.7 kJ), but this again is right at the limits of human endurance. Even if such a flight could be performed by a super-athlete, the final stages of the flight will require the aircraft to descend and possibly autorotate to the ground. Of interest is that because of the extremely low induced velocity through the rotor, even a modest rate of descent may take the rotor into the vortex ring state. This will require the machine to have good control capability, although it would seem that with kinesthetic (weight shifting) alone this may be insufficient.

In conclusion, it would seem that the design of a HPH to meet the AHS's requirements is feasible but probably not yet practical. This is in part because of the enormous size and structural difficulties in building rotor to give the low power requirements that are necessary to match the physiological capabilities of even the most athletic, super-fit human. Also, it would seem that the assumed aerodynamic efficiencies of such large, slow turning rotors are unlikely to be realizable, even operating IGE. Some means of effective flight control will also be required for such a vehicle to stay within the within the defined 10 m (32.81 ft) box, although it would seem that apart from some allowance for kinesthetic control this aspect of the problem has received little attention from designers. The design of a HPH, however, will continue to be a problem that will fascinate generations of engineers for many years to come.

6.14 Hovering Micro Air Vehicles

A micro air vehicle (MAV) has been defined variously as an aircraft having a maximum dimension of 15 cm ($\approx$ 6 in) to as much as 40 cm ($\approx$ 16 in). MAVs are being designed to meet the requirements of various military missions at affordable cost. While having the obvious advantage of small scale and correspondingly low radar cross section, MAVs can potentially provide for reconnaissance capability advantages with rapid deployment and real-time data acquisition capability, with stealth and relatively low noise. Being able to operate autonomously is obviously an added capability of much military value. These capabilities can offer the modern military increased situational awareness and greater combat effectiveness with fewer casualties.

There are two VTOL types of MAV configurations that received interest, those based on rotating-wings and those with flapping (reciprocating) wings. As shown in Fig. 6.42, all existing MAV designs fall well short of the desired empty weight, payload and endurance objectives because they have not yet shown credible aerodynamic efficiency [see Bohorquez et al. (2003) and Tarascio & Chopra (2003)] or sufficiently good specific fuel consumption. Rotating-wing MAVs operate at blade chord Reynolds numbers that may be three orders of magnitude lower than full-scale helicopters. This produces thick boundary layers on the blades and results in large values of profile drag (see Fig. 7.4 as well as Sections 6.4.7 and 7.13). The resulting poor lift-to-drag ratios of the blade sections decrease substantially the net rotor efficiency (the figure of merit). In concert with this effect is the typically high induced power requirements associated with MAV-scale rotors. Specific problems of engine efficiency at this scale must be also considered, including increased friction and thermal losses and significantly decreased overall engine efficiency. In addition, for internal combustion engines there are carbureation and fuel-air mixing issues associated with low intake Reynolds numbers.

The underlying reason for high induced aerodynamic losses from a rotating-wing MAV can be seen in the structure of the rotor wake, an example of which is shown in Fig. 6.43.

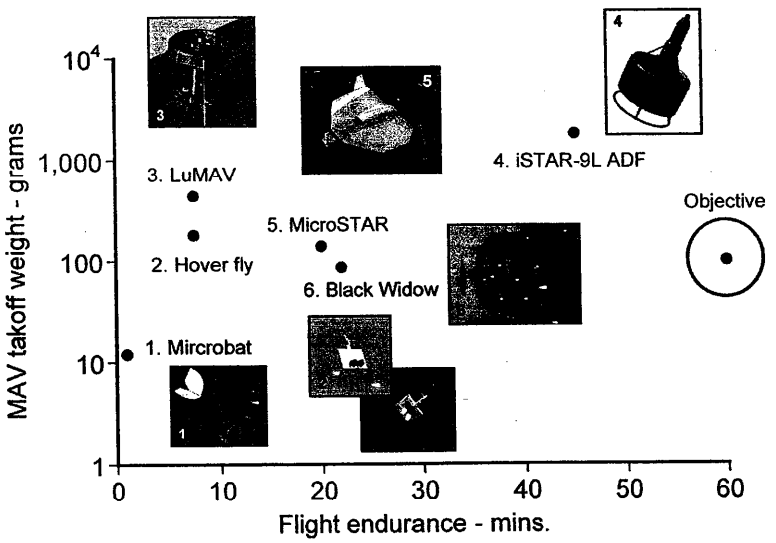

Figure 6.42 The domain of weight–endurance for some hovering MAV designs. Adapted from Tarascio & Chopra (2003).

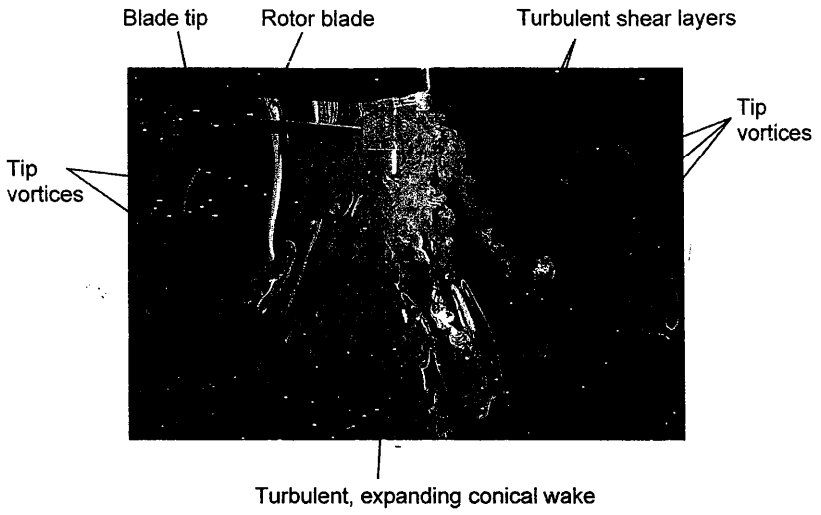

Figure 6.43 Smoke flow visualization of the wake generated by a small rotating-wing MAV with a 6 inch (2.36 cm) diameter rotor. Source: University of Maryland.

The wake was visualized using smoke and laser sheet illumination (see Section 10.2.2). While the helicoidal wake structure is qualitatively similar to that found on rotors at much larger scale (see Figs. 2.2, 2.4, and 10.5), with clear evidence of the tip vortices on the periphery of the wake boundary, the most noticeable difference at this small scale is the very thick, turbulent vortex sheets in the rotor wake. These sheets are formed by the merging of the thick boundary layers on the upper and lower surfaces of the blade sections, which operate at Reynolds numbers of less than 10^4. These sheets are then convected downward in the wake below the rotor, undergoing a stretching and folding process. The net result is a relatively wide, conical, turbulent inner wake region that occupies a substantial fraction of the slipstream area. This means that an increased mass flow is necessary to produce the same change in vertical momentum of the fluid through the control volume surrounding the rotor and its wake. The net result for the MAV is larger induced losses to generate a given thrust, a higher effective disk loading, and much reduced hovering efficiency.

The measured hovering performance of this MAV is shown in Fig. 6.44 in terms of figure of merit (*FM*) as a function of blade loading coefficient. Notice the relatively low value of maximum *FM* obtained by the MAV (about 0.5) compared to a larger rotor (about 0.75), even at subscale. This loss of performance can be modeled within the context of the momentum theory with a nonideal wake contraction, as discussed for the ducted fan in Section 6.10.1. The ideal induced power coefficient for the MAV can be written as

$$C_{P_{\text{ideal}}} = \frac{C_T^{3/2}}{\sqrt{4a_w}}, \tag{6.56}$$

where a_w is the wake contraction parameter. Note that $a_w = 0.5$ for an ideal rotor with a 2:1 wake area contraction and $a_w = 1$ for an ideal ducted fan with no wake contraction. In the case of the MAV, $a_w < 0.5$ and is probably close to 0.25 based on the flow visualization shown in Fig. 6.43. Using Eq. 6.56 allows the figure of merit for the MAV to written

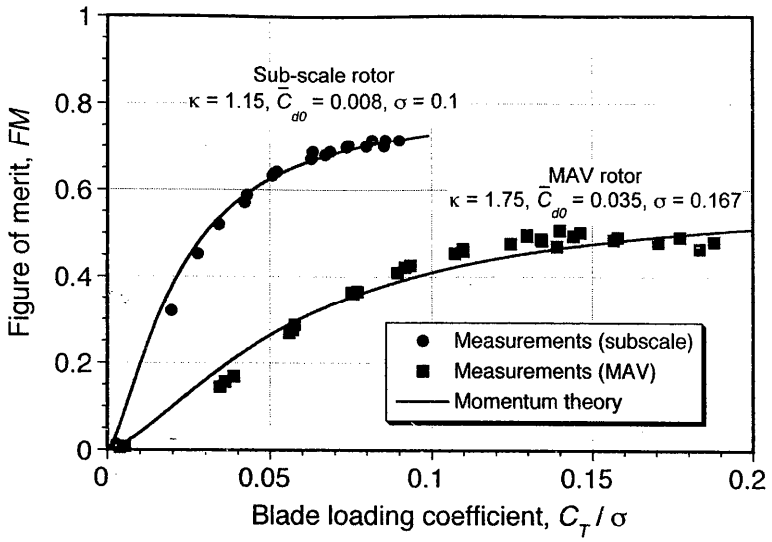

Figure 6.44 Measured hovering figure of merit for a small rotating-wing MAV with a 6-inch (2.36 cm) diameter rotor. Source: University of Maryland and courtesy of Benjamin Hein.

in the conventional way as

$$FM = \frac{C_{P_{\text{ideal}}}}{\kappa C_{P_{\text{ideal}}} + \dfrac{\sigma \bar{C}_{d_0}}{8}} = \frac{\dfrac{\kappa C_T^{3/2}}{\sqrt{2}}}{\dfrac{\kappa C_T^{3/2}}{\sqrt{2}} + \dfrac{\sigma \bar{C}_{d_0}}{8}}. \tag{6.57}$$

In this case the value of κ is about 1.75 based on the asymptotic value of the measured *FM* curve, and $\bar{C}_{d_0} \approx 0.035$ based on low Reynolds number airfoil data (Fig. 7.4). Figure 6.44 shows that the momentum theory compares well with the measurements, but only if the wake contraction parameter, a_w, is set to about 0.25. This confirms that because of the thick viscous wake losses the MAV rotor behaves as if it were being operated at a much higher disk loading, and combined with a high induced power factor and large profile drag, this gives the MAV relatively poor efficiency compared to a rotor operated at larger scale. This makes the value of rotating-wing MAVs less attractive because they require higher power with the result of reduced payload, range, and endurance. It is likely that future advances in understanding extremely low Reynolds number aerodynamics will lead to the improved viability of the rotating wing MAV concept. Already novel ideas such as blade surface heating–cooling or the application of Gurney flaps are showing some promising results but with dubious gains in net vehicle performance – see Kim et al. (2003) and Nelson & Koratkar (2004). One key to improved performance obviously lies within the viscous dominated wake structure and the need to reduce induced losses not just profile losses.

As a consequence of these poor efficiencies, the flapping wing MAV concept has received some attention [see Woods et al. (2001)], and this seems to offer the potential of developing MAVs with improved hovering performance capability at these very low flight Reynolds numbers. The reasons are apparent from studies of autorotating seeds [Azuma & Yasuda

(1989)] and also measurements on flapping wings themselves – see review by Sane (2003). While showing only average lift-to-drag ratios in the range of 2 to 4, the ability to generate maximum lift coefficients of 2 or more is of considerable significance for low Reynolds number flight. However, it would be naive to conclude that somehow flapping wings were more aerodynamically efficient than a rotor and, therefore, are more well-suited for low Reynolds number flight. The physics of flapping wing aerodynamics is extremely complicated because it involves unsteady aerodynamic effects, large regions of flow separation and the production of highly vortical flows; see Sane (2003), Lehmann (2004), Singh et al. (2005), and Ramaşamy et al. (2005). An example of flow visualization that was conducted on a small flapping wing vehicle is shown in Fig. 6.45, which clearly reveals leading-edge and mid-chord vortical structures that augments wing lift. These are not stable structures and are cast off the wing continuously for much of the flapping cycle. A stronger "starting vortex" is cast off as the wing rotates about its pitch axis (supination) and as it changes its direction for the second half of the flapping cycle. The process is repeated when the wing direction reverses again at the other end of the stroke (pronation). This vortical shedding process in many ways resembles the problem of dynamic stall, which is discussed in Chapter 9, although the low aspect ratios of typical flapping wings makes the problem considerably more 3-D than found even on helicopter rotor blades. The flapping process also continuously trails a pair of tip and root vortices into the wake that are laid down as a set of folded, interacting wake structures, a structure it seems that is difficult to generalize. Żbikowski (2002) suggests that some prediction capability of the unsteady aerodynamic forces on flapping wings might be achieved using unsteady thin airfoil theory (such as the methods given in Chapter 8), but the extremely nonlinear nature of the problem clearly offers considerable opportunities for new research.

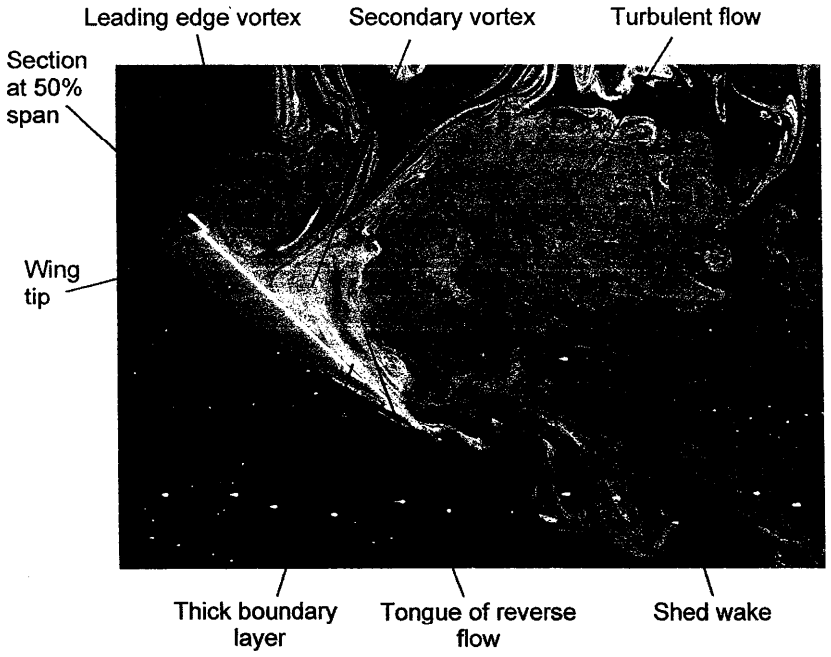

Figure 6.45 Flow visualization of a hovering flapping wing vehicle reveals a complex vortical structure that augments wing lift. Source: University of Maryland.

6.15 Chapter Review

This chapter has reviewed many of the aerodynamic issues important in the design of the modern helicopter. It has been noted that there are several trade-offs in the basic sizing and overall optimization methodology of helicopter main rotors. The final design is always a compromise to meet the needs of a particular set of customer or mission requirements. The use of improved airfoil sections and advanced tip shapes generally helps to improve overall rotor performance, allowing higher figures of merit and better cruise efficiency. The computational tools for rotor design are now at a high level of maturity, although significant empiricism must generally still be relied on.

The aerodynamics of the helicopter fuselage and empennage are complicated in themselves, mainly because of the extensive regions of separated flow that can exist. This is complicated further by the aerodynamic interactions that exist between the main rotor and the fuselage, a subject considered in detail in Chapter 11. Predictions of airframe drag is still beyond the state of the art, but can be reliably estimated through component testing of the fuselage and rotor in the wind tunnel and verified by flight testing experience. Besides the main rotor and the airframe, the design of the empennage and tail rotor are key elements in the successful design of the helicopter. Because of the various aerodynamic interactions and the trade-offs in weight and stability, the sizing and positioning of the horizontal stabilizer on the tail has proven to be one of the most difficult challenges facing helicopter designers. The special issues associated with tail rotors have been shown to be extremely important to the design of the modern helicopter. The tail rotor operates in a complicated flow environment, with its operation being affected strongly by the main rotor wake, an issue also discussed in Chapter 11. Many other factors need to be considered to ensure that the tail rotor operates effectively as an anti-torque and directional control device over the full operational flight envelope of the helicopter. Other anti-torque devices such as the fenestron and NOTAR have proved viable alternatives to the conventional tail rotor.

Some concepts for compounds and "high-speed" helicopters have been reviewed. While many ideas have been put forth over the past fifty years, there are no high-speed rotorcraft other than tilt-rotors currently flying. The aerodynamic and aeroelastic problems of high-speed helicopters have proved difficult to solve cost effectively. However, with the advent of new technologies such as smart structures to help control aerodynamic forces and vibration levels on the rotor, it is likely that a further expansion in the operational flight envelope of conventional helicopters will occur.

The unique problem of designing a human-powered helicopter has also been discussed. While perhaps feasible, albeit at the expense and practical difficulties of building a truly enormous and lightweight rotor, it does not seem likely that even the most athletic human has the energy or endurance that can power a helicopter rotor for any significant time. This does not mean, however, the the task is impossible. Finally, the emerging area of hovering micro air vehicles has been mentioned. Current MAVs fall short of anticipated performance because of the low Reynolds numbers and relatively high viscous drag forces. However, this is a relatively new area of research and further developments in aerodynamic understanding will likely lead to much improved MAV designs.

6.16 Questions

6.1. Starting from an expression for the figure of merit for an optimum hovering rotor, show that the figure of merit is a maximum when the blade sections are operating at the highest values of $C_l^{3/2}/C_d$.

6.2. Based on the modified momentum theory, show that the operating thrust coefficient, C_T, to give the lowest power in hover (best power loading) is

$$C_T \text{ for best } PL = \frac{1}{2}\left(\frac{\sigma C_{d_0}}{\kappa}\right)^{2/3}.$$

Also, show that this condition corresponds to a figure of merit of $2/3\kappa$.

6.3. Discuss in detail the reasons why the modern helicopter is still essentially a low-speed aircraft. Discuss how a main rotor system might be designed so that a helicopter can achieve higher overall forward flight speeds and a possible expansion of the maneuvering envelope. Identify any potential trade-offs with any design option.

6.4. The design of a highly maneuverable helicopter requires some special considerations that include aerodynamic issues. Discuss the various interdisciplinary design issues that you feel are important.

6.5. The Cierva company designed a heavy-lift helicopter with three main rotors, with a layout such that the rotors were arranged at the corners of an equilateral triangle (two rotors at the back in a lateral arrangement, and one rotor at the front), with all three rotors turning in the same direction. How is torque reaction compensated for, and how would the aircraft be controlled?

6.6. When designing a hovering rotor for maximum aerodynamic efficiency with the disk loading fixed, should a designer choose a high or low value of tip speed? To further increase the rotor figure of merit, should the designer choose a high or low solidity, and why? If the rotor was to be powered by ramjets located at the blade tips, so that it had to operate at a high tip speed, should the designer choose a high or low solidity, and why?

6.7. You are asked to design a rotor for a large helicopter whose primary mission is to lift logs and heavy construction equipment in the mountains. If the gross weight is 100,000 lb, rotor diameter is 120 ft, average operating altitude is 15,000 ft, and rotor tip speed is 650 ft/s, calculate the tip chord (assuming seven blades), equivalent rotor solidity, and mean rotor lift coefficient for the helicopter. How much power would be required to hover out of ground effect at the design condition? Choose and obtain data on an appropriate airfoil.

6.8. In a hypothetical helicopter rotor design, the use of blade taper has been shown to increase the figure of merit of the main rotor by 1%. Estimate the percentage increase in vertical lifting and payload capability of the helicopter with all other factors being assumed constant.

6.9. In the design of a swept tip rotor blade, it is desired to introduce only as much sweep angle as necessary to keep the Mach number incident to the leading-edge of the blade equal to a constant, say M_c, over the tip region. Because of unsteady flow effects, the critical azimuth angle for the design is taken to be at $\psi = 100°$. Find an expression for the sweep angle as a function of r, the hover tip Mach number $M_{\Omega R}$, the design mach number M_c, and the advance ratio, μ. If $M_{\Omega R} = 0.65$ and $M_c = 0.8$, plot the sweep angle required as a function of radial blade station for a series of advance ratios.

6.10. In the design of a swept tip rotor blade, it is desired to introduce only as much sweepback as necessary to keep the Mach number incident to the leading-edge of the blade equal to a constant, say M_c, over the tip region. In addition, the location

of the 1/4-chord axis of the blade is to be moved forward by a value $eR = 0.02$ at the point of sweep initiation so as to minimize the torsional moments on the blade that would be associated with the sweepback. Based on 2-D strip considerations, calculate and show the resulting blade geometry for a design advance ratio of 0.5. Assume that the critical azimuth angle for the design is taken to be at $\psi = 90°$, and that $M_{\Omega R} = 0.65$ and $M_c = 0.8$.

6.11. Discuss the relative merits of the compound helicopter design. In your discussion, consider propulsive and lift compounding as both separate and combined means of compounding. Why do you think a true compound helicopter has never been put into production?

6.12. It is required to improve the tail rotor authority of an existing helicopter design. The design of the rotor blades is to be changed, but without modifying the blade pitch attachments, hub, pitch links, and so on. Define the requirements, outline any conflicting issues, and suggest possible means of tackling this problem.

6.13. Examine the person/power/weight trade offs in the design of a human-powered helicopter. Examine the claim that the best possible flight performance can only be achieved with one person.

6.14. Estimate the figure of merit curves for a rotating wing micro air vehicle in the 1 lb (0.5 kg) weight class. Use any sensible assumed values for the induced power factor and profile drag coefficient. Based on the rotor design conditions that will be required for high hovering efficiency, determine the rotor operating conditions that will allow for maximum hovering flight endurance.

Bibliography

Abbott, I. H. and von Doenhoff, A. E. 1949. *Theory of Wing Sections, Including a Summary of Airfoil Data*, McGraw-Hill Book Co., Inc., New York, NY. Also Dover Publications, New York, NY, 1959.

Abrego, A. I. and Bulaga, R. W. 2002. "Performance Study of a Ducted Fan System," American Helicopter Soc. Specialists Meeting on Aerodynamics, Acoustics, and Test and Evaluation, San Francisco, CA, Jan. 23–25.

Althoff, S. L. and Noonan, K. W. 1990. "Effect of Blade Planform Variation on a Small-Scale Hovering Rotor," NASA TM 4146, AVSCOM TM 89-B-009.

Amer, K. B. 1989. "High Speed Rotor Aerodynamics," *J. of the American Helicopter Soc.*, 34 (1), pp. 63–66.

Amer, K. B. and Gessow, A. 1955. "Charts for Estimating the Tail-Rotor Contribution to Helicopter Directional Stability and Control in Low-Speed Flight," NACA Report 1216.

Azuma, A. and Yasuda, K. 1989. "Flight Performance of Rotary Seeds," *J. of Experimental Biology*, 138, pp. 23–54.

Balcerak, J. C. and Felker, R. F. 1973. "Effect of Sweep Angle on the Pressure Distributions and Effectiveness of the Ogee Tip in Diffusing a Line Vortex," NASA CR 132355.

Balch, D. A. 1984. "Impact of Main Rotor Tip Geometry on Main Rotor/Tail Rotor Interactions in Hover," 40th Annual Forum of the American Helicopter Soc., Arlington, VA, May 16–18.

Basset, P. M. and Brocard, M. 2004. "Fenestron Model for Improving the Helicopter Yaw Dynamics Flight Simulation," 30th European Rotorcraft Forum, Marseilles, France, Sept. 14–16.

Bernhard, A. and Chopra, I. 1996. "Development of a Smart Moving Blade Tip Activated by a Piezo-Induced Bending-Torsion Coupled Beam," SPIE North American Symposium on Smart Structures and Materials, San Diego, CA, Feb. 25–29.

Berry, J. D. 1997. "Unsteady Velocity Measurement Taken Behind a Model Helicopter Rotor Hub in Forward Flight," NASA TM-4738.

Berry, J. D., Chaffin, M. S., and Duque, E. 1994. "Helicopter Fuselage Aerodynamic Predictions: Navier–Stokes and Panel Method Solutions and Comparison with Experiment," American Helicopter Soc. Aeromechanics Specialists Conference, San Francisco, CA, Jan. 19–21.

Bohorquez, P., Samual, P., Sirohi, J., Pines, D., Rudd, L., and Perel, R. 2003. "Design, Analysis and Performance of a Rotary Wing Micro Air Vehicle," *Journal of the American Helicopter Soc.*, 48 (2), pp. 80–90.

Bosco, A. 1972. "Aerodynamics of Helicopter Components Other Than Rotors," In: AGARD-CP-111.

Brocklehurst, A. 1985. "A Significant Improvement to the Low Speed Control of the Sea King Helicopter Using a Tail Boom Strake," 11th European Rotorcraft Forum, London, Sept. 10–13.

Brown, E. L. and Schmidt, P. S. 1963. "The Effect of Helicopter Pitching Velocity on Rotor Lift Capability," *J. of the American Helicopter Soc.*, 8 (4), pp. 1–6.

Byham, G. M. 1990. "An Overview of Conventional Tail Rotors," RAeS Conference on Helicopter Yaw Control Concepts, London, February/March.

Carlin, G. and Farrance, K. 1990. "Results of Wake Surveys on Advanced Rotor Planforms," 46th Annual Forum of the American Helicopter Soc., Washington DC, May 21–23.

Carlson, R. M. 2002. "Helicopter Performance–Transportation's Latest Chromosome: The 21st Annual Alexander A. Nikolsky Lecture," *J. of the American Helicopter Soc.*, 47 (1), pp. 3–17.

Celniker, L., Carlson, R. M., and Donham, R. E. 1965. "Stopped and Slow Rotor Aircraft Configuration," SAE Paper 650806, National Aeronautics & Space Engineering & Manufacturing Meeting, Los Angeles, CA, Oct. 4–8.

Chaffin, M. S. and Berry, J. D. 1994. "Navier–Stokes and Potential Theory Solutions for a Helicopter Fuselage and Comparison with Experiment," NASA Technical Memorandum 4566, ATCOM Technical Report 94-A-013.

Chaney, M. C. 1969. "The ABC Helicopter," *J. of the American Helicopter Soc.*, 14 (4), pp. 10–19.

Cheeseman, I. C. 1968. "Circulation Control and Its Application to Stopped Rotor Aircraft," *Aeronautical J.*, 72, pp. 635–646.

Chopra, I. 1997. "Status of Application of Smart Structures Technology to Rotorcraft Systems," RAeS Proceedings of Innovation in Rotorcraft Technology, June 24–25.

Chopra, I. 2000. "Status of Application of Smart Structures Technology to Rotorcraft Systems," *J. of the American Helicopter Soc.*, 45 (4), pp. 228–252.

Clark, D. R. and Leiper, A. C. 1970. "The Free Wake Analysis, A Method for the Prediction of Helicopter Rotor Hovering Performance," *J. of the American Helicopter Soc.*, 15 (1), pp. 3–12.

Cler, A. 1989. "High Speed Dauphin Fuselage Aerodynamics," 15th European Rotorcraft Forum, Amsterdam, The Netherlands, Sept. 12–15.

Cook, C. V. 1978. "Tail Rotor Design and Performance," *Vertica*, 2, pp. 163–181.

Dadone, L. 1976. "US Army Helicopter Design Datcom, Volume 1, Airfoils," US Army Air Mobility Research and Development Laboratory.

Davidson, J. K., Havey, C. T., and Sherrieb, H. E. 1972. "Fan-in-Fin Anti-torque Concept Study," USAAMRDL TR 72-44, July.

Deckert. W. H. and McCloud, J. L. 1968. "Considerations of the Stopped Rotor V/STOL Concept," *J. of the American Helicopter Soc.*, 13 (1), pp. 27–43.

Delany, N. K. and Sorensen, N. E. 1953. "Low Speed Drag of Cylinders of Various Shapes," NACA TN-3038.

Department of the Army. 1974. "Engineering Design Handbook: Helicopter, Part 1–Preliminary Design," AMCP 706-201, US Army Materiel Command.

Desopper, A., Lafon, P., Philippe, J. J., and Ceroni, P. 1986. "Ten Years of Rotor Flow Studies at ONERA: State of the Art and Future Studies," 42nd Annual Forum of the American Helicopter Soc., Washington DC, June 2–4.

Desopper, A., Lafon, P., Philippe, J. J., and Prieur, J. 1988. "Effect of an Anhedral Sweptback Tip on the Performance of a Helicopter Rotor," 44th Annual Forum of the American Helicopter Soc., Washington DC, June 16–18. Also, 13th European Rotorcraft Forum, Arles, France, Sept. 8–11.

Duque, E. P. N. 1992. "Numerical Analysis of the British Experimental Rotor Program Blade," *J. of the American Helicopter Soc.*, 37 (1), pp. 46–54.

Duque, E. P. N. 1994. "A Structured/Unstructured Embedded Grid Solver for Helicopter Rotor Flows," 50th Annual Forum of the American Helicopter Soc., Washington, DC, May 11–13.

Duque, E. P. N. and Dimanlig, A. C. B. 1994. "Navier–Stokes Simulation of the RAH-66 (Comanche) Helicopter," American Helicopter Soc. Aeromechanics Specialists Conference, San Francisco, CA, Jan. 19–21.

Duque, E. P. N. and Brocklehurst, A. 1990. "Experimental and Numerical Study of the British Experimental Rotor Program Blade," Paper AIAA 90-3008, 8th AIAA Applied Aerodynamics Conference, Portland, OR, Aug. 20–22.

Epstein, R. J., Carbonaro, M. C., and Caudron, F. 1994. "Experimental Investigation of the Flowfield about an Upswept Afterbody," *J. of Aircraft*, 31 (6), pp. 1281–1290.

Filippone, A. 2002. "The Human Powered Helicopter," *Aeronautical J.*, 106 (1065), pp. 613–618.

Fradenburgh, E. A. 1960. "The Helicopter and the Ground Effect Machine," *J. American Helicopter Soc.*, 5 (4), pp. 26–28.

Fradenburgh, E. A. 1972. "Aerodynamic Factors Influencing Overall Hover Performance," In: AGARD-CP-111.

Fradenbergh, E. A. 1992. "Wind-Tunnel Tests of a Variable Diameter Rotor," 48th Annual Forum of the American Helicopter Soc., Washington DC, June 3–5.

Fradenburgh, E. A. and Chuga, G. M. 1968. "Flight Program on the NH-3A Research Helicopter," *J. of the American Helicopter Soc.*, 13 (1), pp. 44–62.

Fradenburgh, E. A., Murrill, R. J., and Kiely, E. F. 1973. "Dynamic Model Wind Tunnel Tests of a Variable-Diameter, Telescoping-Blade Rotor System (TRAC Rotor)," USAAMRDL TR 73-32.

Gessow, A. and Crim, A. D. 1955. "A Method for Studying the Transient Blade Flapping Behavior of Lifting Rotors at Extreme Operating Conditions," NACA Technical Note 3366, Jan.

Gessow, A. and Myers, G. C., Jr. 1952. *Aerodynamics of the Helicopter*, Macmillan Co. (republished by Frederick Ungar Publishing, NY, 1967).

Hansen, K. 1988. "Handling Qualities, Design and Development of the CH-53E, UH-60A and S-76 Helicopters," RAeS Conference on Handling Qualities and Control, London, Nov. 15–17.

Harris, F. D. 1973. "Aerodynamic and Dynamic Rotary Wing Model Testing in Wind Tunnels and Other Facilities," In: *Helicopter Aerodynamics and Dynamics*, AGARD LS-63.

Hess, J. L. 1990. "Panel Methods in Computational Fluid Dynamics," *Annual Review of Fluid Mechanics*, 22, pp. 255–274.

Hoerner, S. F. 1965. *Fluid Dynamic Drag*, Published by the Author, Hoerner Fluid Dynamics, Vancouver, WA.

Horst, T. J. and Reschak, R. J. 1975. "Designing to Survive Tail Rotor Loss," 31st Annual National Forum of the American Helicopter Soc., Washington DC, May 13–15.

Humpherson, D. V. 1998. "Compound Interest–A Dividend for the Future, Revisited," 54th Annual Forum of the American Helicopter Soc., Washington DC, May 20–22.

JanakiRam, R., Smith, R., Charles, B., and Hassan, A. 2003. "Aerodynamic Design of a New Affordable Main Rotor for the Apache Helicopter," 59th Annual Forum of the American Helicopter Soc. International, Phoenix AZ, May 6–8.

Katz, J. and Plotkin, A. 1991. *Low Speed Aerodynamics–From Wing Theory to Panel Methods*, McGraw-Hill, New York, NY.

Kelly, H. L., Crowell, C. A., Yenni, K. R., and Lance, M. B. 1993. "Flight Investigation of the Effect of Tail Boom Strakes on Helicopter Directional Control," NASA TP-3278 ATCOM TR-93-A-003.

Kendall, E. R. 1959. "Is Man-Powered Rotating-Wing Flight a Future Possibility?" *J. of the Helicopter Association of Great Britain*, 13 (2), pp. 100–129.

Keys, C. and Wiesner, R. 1975. "Guidelines for Reducing Helicopter Parasitic Drag," In: *Rotorcraft Parasitic Drag*, 31st Annual Forum of the American Helicopter Soc., Washington DC, May 13–15.

Keys, C., Tarzanin, F., and McHugh, F. 1987. "Effect of Twist on Helicopter Performance and Vibratory Loads," 13th European Rotorcraft Forum, Arles, France, Sept. 8–11.

Kim, J., Rusak, Z., and Koratkar, N. 2003. "Small-Scale Airfoil Aerodynamic Efficiency Improvement by Surface Temperature and Heat Transfer," *AIAA J.*, 41 (11), pp. 2105–2113.

Knight, M. and Hefner, R. A. 1937. "Static Thrust of the Lifting Airscrew," NACA TN 626.

Kruger, W. 1949. "On Wind Tunnel Tests and Computations Concerning the Problem of Shrouded Propellers," NACA TM 1202.

Kuchemann, D. and Weber, J. 1953. *Aerodynamics of Propulsion*, McGraw-Hill, New York, NY.

Landgrebe, A. J. 1972. "Wake Geometry of a Hovering Helicopter Rotor and Its Influence on Rotor Performance," *J. of the American Helicopter Soc.*, 17 (4), pp. 3–15.

Lehmann, F-O. 2004. "The Mechanisms of Lift Enhancement in Insect Flight," *Naturwissenschaften*, 99, pp. 101–122.

Logan, A. H. 1978. "Evaluation of a Circulation Control Tail Boom for Yaw Control," USARTL TR 78-10.

Lynn, R. R. 1970. "Tail Rotor Design," *J. of the American Helicopter Soc.*, 15 (4), pp. 2–30.

Lynn, R. R. and Drees, J. M. 1967. "Promise of Compounding," *J. of the American Helicopter Soc.*, 12 (1), pp. 1–20.

Main, B. J. and Mussi, F. 1990. "EH-101: Development Status Report," 16th European Rotorcraft Forum, Glasgow, Scotland, Sept. 18–20.

Martin, P. and Leishman, J. G. 2002. "Trailing Vortex Measurements in the Wake of a Hovering Rotor with Various Tip Shapes," 58th Annual Forum of the American Helicopter Soc. International, Montréal Canada, June 11–13.

Maskew, B. 1982. "Prediction of Subsonic Aerodynamic Characteristics: A Case for Low-Order Panel Methods," *J. of Aircraft*, 19 (2), pp. 157–163.

McHugh, F. J. 1978. "What Are the Lift and Propulsive Limits at High Speed of the Conventional Rotor?" 34th Forum of the American Helicopter Soc., Washington DC, May 15–17.

McVeigh, M. A. and McHugh, F. J. 1982. "Recent Advances in Rotor Technology at Boeing Vertol," 38th Annual Forum of the American Helicopter Soc., Anaheim, CA, May 4–7.

McVeigh, M. A., Grauer, W. K., and Paisley, D. J. 1991. "Rotor-Airframe Interactions on Tilt-Rotor Aircraft," *J. of the American Helicopter Soc.*, 35 (3), pp. 43–51.

McVeigh, M. A., Liu, J., and O'Toole, S. J. 1997. "V-22 Osprey Aerodynamic Development–A Progress Review," *Aeronautical J.*, 101 (1006), pp. 231–244.

Montana, P. S. 1975. "Experimental Investigation of Three Rotor Hub Fairing Shapes," David W. Taylor Naval Ship Research and Development Center, Report ASED 333.

Montana, P. S. 1976. "Experimental Evaluation of Analytically Shaped Helicopter Rotor Hub-Pylon Configurations," David W. Taylor Naval Ship Research and Development Center, Report ASED 355

Morino L., ed. 1985. *Computational Methods in Potential Aerodynamics*, Springer-Verlag, Berlin.

Mort, K. W. 1965. "Performance Characteristics of a 4-Foot Diameter Ducted Fan at Zero Angle of Attack for Several Fan Blade Angles," NASA TN D-3122, 1956.

Mort, K. W. and Gamse, B. 1967. "A Wind-Tunnel Investigation of a 7-Foot Diameter Ducted Propeller," NASA TN D-4142.

Mouille, R. 1970. "The Fenestron Shrouded Tail of the SA.341 Gazelle," *Journal of the American Helicopter Soc.*, 15 (4), pp. 31–37.

Mouille, R. 1979. "Ten Years of Aerospatiale Experience with the Fenestron and Conventional Tail Rotor," 35th Annual Forum of the American Helicopter Soc., Washington DC, May 21–23.

Mouille, R. and Dámbra, F. 1986. "The Fenestron, a Shrouded Tail Rotor Concept for Helicopters," 42nd Annual Forum of the American Helicopter Soc., Washington DC, May 21–23.

Mouritsen, S. 1990. "An Aerodynamic and Design Analysis of the Human Powered Helicopter," Paper SAWE 1924, 49th Conference of the Soc. of Allied Weight Engineers, Chandler, AZ.

Naito, A. A. 1990. "A Study of Human Powered Helicopter in Japan," Paper SAWE 1925, 49th Conference of the Soc. of Allied Weight Engineers, Chandler, AZ.

Narramore, J. C. and Brand, A. G. 1992. "Navier–Stokes Correlations to Fuselage Wind Tunnel Test Data," 48th Annual Forum of the American Helicopter Soc., Washington DC, June 3–5.

Naylor, C. H. 1959. "Is Man-Powered Rotating Wing Flight a Future Possibility," *J. of the Helicopter Association of Great Britain*, 13 (5), pp. 294–304.

Nelson, J. and Koratkar, N. 2004. "Effect of Trailing Edge Gurney Flaps in Aerodynamic Efficiency of Micro-Rotorcraft," 60th Annual Forum of the American Helicopter Soc. International, Baltimore, MD, June 7–10.

Newman, S. 1994. *The Foundations of Helicopter Flight*, Edward Arnold, London, Chapter 11.

Noonan, K. R., Althoff, S. L., Samak, D. K., and Green, M. D. 1992. "Effect of Blade Planform Variation on the Forward Flight Performance of Small-Scale Rotors," NASA Technical Memorandum 4345.

Ockier, C. J. 2003. "Flight Testing of the Eurocopter EC145," 59th Annual Forum of the American Helicopter Soc. International, Phoenix AZ, May 6–8.

Orchard, M. N. and Newman, S. J., 1999a. "The Compound Helicopter–Why Have We Not Succeeded Before?" *Aeronautical J.*, 103 (1028), pp. 489–495.

Orchard, M. N., and Newman, S. J. 1999b. "A Generic Compound Helicopter Model," 25th European Rotorcraft Forum, Rome, Sept. 14–16.

Orchard, M. N., and Newman, S. J. 2000. "Some Design Issues for the Optimization of the Compound Helicopter Configuration," 56th Annual Forum of the American Helicopter Soc., Virginia Beach, VA, May 2–4.

Patterson, W. B. 1986. "The Design and Test of a Human Powered Helicopter," 42nd Annual Forum of the American Helicopter Soc., Washington DC, June 2–5.

Paul, W. F. and Zincone, R. 1977. "Advanced Technology Applied to the UH-60A and S-76 Helicopters," 3rd European Rotorcraft and Powered Lift Forum, Aix-en-Provence, France, Sept. 7–9.

Perry, F. J. 1987. "The Aerodynamics of the World Speed Record," 43rd Annual Forum of the American Helicopter Soc., St. Louis, MO, May 18–20.

Perry, F. J. 1989. "The Contribution of Planform Area to the Performance of the BERP Rotor," *J. of the American Helicopter Soc.*, 34 (1), pp. 64–66.

Perry, F. J., Wilby, P. G., and Jones, A. F. 1998. "The BERP Rotor–How Does it Work and What Has it Been Doing Lately?" *Vertiflite*, 44 (2), pp. 44–48.

Philippe, J. J. 1990. "Considerations on Wind Tunnel Testing Techniques for Rotorcraft," In *Aerodynamics of Rotorcraft*, AGARD-R-781.

Philippe, J. J., Roesch, P, Dequin, A. M., and Cler, A. 1985. "A Survey of Recent Developments in Helicopter Aerodynamics," In: AGARD LS-139.

Preator, R., Leishman, J. G., and Baldwin, D. G. 2004. "Conceptual Design Studies of a Mono Tiltrotor (MTR) Architecture," 60th Annual Forum of the American Helicopter Soc. International, Baltimore, MD, June 7–11.

Prouty, R. W. 1983. "Development of the Empennage Configuration of YAH-64 Advanced Attack Helicopters," USAAVRADCOM-TR-82-D-22.

Prouty, R. W. 1985. "Ground Effect and the Helicopter," AIAA Paper 85-4034, AIAA/AHS/ASEE Aircraft Design Systems and Operations Meeting, Colorado Springs, CO, Oct. 14–16.

Prouty, R. W. 1986. *Helicopter Performance, Stability, and Control*, PWS Engineering Publishing, Boston, MA. Chapter 10.

Prouty, R. W. 1998. *Military Helicopter Design Technology*, 2nd Edition, Krieger Publishing Co., Malabar, FL.

Prouty, R. W. and Amer, K. B. 1982. "The YAH-64 Empennage and Tail Rotor–A Technical History," 38th Annual Forum of the American Helicopter Soc., Anaheim, CA, May 4–7.

Ramasamy, M., Leishman, J. G., and Singh, B. 2005. "Wake Structure Diagnostics of a Flapping Wing MAV," SAE Paper 2005-01-3198, International Powered Lift Conference, Grapevine, TX, Oct. 3–6.

Rauch, P. and Quillien, C. 2003. "Advanced Technologies for High Performance NH90 Blades," 59th Annual Forum of the American Helicopter Soc. International, Phoenix AZ, May 6–8.

Rorke, J. B., Moffitt, R. C., and Ward, J. F. 1972. "Wind Tunnel Simulation of Full Scale Vortices," 28th Annual National Forum of the American Helicopter Soc., Washington DC, May.

Rosenstein, H. 1986. "Aerodynamic Development of the V-22 Tilt-Rotor," 12th European Rotorcraft Forum, Garmisch-Partenkirchen, Germany, Sept. 22–25.

Rosenstein, H. and Stanzione, K. 1981. "Computer-Aided Helicopter Design," 37th Annual Forum of the American Helicopter Soc., Washington DC, May 17–20.

Rutherford, J. W., Bass, S. M., and Larsen, S. D. 1993. "Canard Rotor/Wing: A Revolutionary High-Speed Rotorcraft Concept," AIAA Paper 93-1175, AIAA/AHS/ASEE Aerospace Design Conference, Irvine, CA, Feb. 16–19.

Sampatacos, E. P., Morger, K. M., and Logan, A. H. 1983. "NOTAR–The Viable Alternative to a Tail Rotor," AIAA Paper 83-2527, AIAA Aircraft Design, Systems and Technology Meeting, Ft. Worth, TX, Oct. 17–19.

Sane, S. P. 2003. "The Aerodynamics of Insect Flight," *J. of Experimental Biology*, 206, pp. 4191–4208.

Sedden, J. 1979. "An Analysis of Helicopter Rotorhead Drag Based on New Experiments," 5th European Rotorcraft and Powered Lift Forum, Amsterdam, The Netherlands, Sept. 4–7.

Sedden, J. 1982. "Aerodynamics of the Rear Fuselage Upsweep," 8th European Rotorcraft Forum, Aix-en-Province, France, Aug. 31–Sept. 3.

Sheehy, T. W. 1977. "A General Review of Helicopter Rotor Hub Drag Data," *J. of the American Helicopter Soc.*, 22 (2), pp. 2–10.

Sheehy, T. W. and Clark, D. R. 1975. "A General Review of Helicopter Rotor Hub Drag Data," In: *Rotorcraft Parasitic Drag*, 31st Annual Forum of the American Helicopter Soc., Washington DC, May 13–15.

Shen, J., Chopra, I., and Johnson W. 2003. "Performance of Swashplateless Ultralight Helicopter Rotor with Trailing-Edge Flaps for Primary Flight Control," 59th Annual Forum of the American Helicopter Soc. International, Phoenix, AZ, May 6–8.

Shenstone, B. S. and Whitby, R. H. 1959. "Man-Powered Helicopters," *J. of the Helicopter Association of Great Britain*, 13 (5), pp. 305–315.

Sheridan, P. F. 1978. "Interactional Aerodynamics of the Single Rotor Helicopter Configuration," Final Report. USARTL-TR-78-23A.

Sheridan, P. F. and Smith, R. P. 1979. "Interactional Aerodynamics: A New Challenge of Helicopter Technology," 35th Annual National Forum of the American Helicopter Soc., Washington DC, May 21–23.

Sigl, D. G. and Smith, D. E. 1990. "Flow Over and Behind Various Rotor Blade Tip Shapes: Wind Tunnel Test Data Report," NASA CR 182000.

Sikorsky, I. A. 1957. Quote from comments made by "Professor" I. I. Sikorsky, Chief Aerodynamicist of the Sikorsky Aircraft Corporation, in reference to the VS-300 developments in 1939. See also Gablehouse (1969) *Helicopters and Autogiros,* Lippincott Co., Philadelphia & New York.

Singh, B., Ramasamy, M., Chopra, I., and Leishman, J. G. 2005. "Insect-Based Flapping Wings for Micro Hovering Air Vehicles: Experimental Investigations," American Helicopter Soc. International Specialist's Meeting on Unmanned Rotorcraft, Chandler, AZ, Jan. 18–20.

Singleton, J. D., Yeager, W. T., and Wilbur, M. L. 1990. "Performance Data from a Wind-Tunnel Test of Two Main-Rotor Blade Designs for a Utility-Class Helicopter," NASA Technical Memorandum 4183.

Smith, D. G. and Sigl, D. E. 1995. "Helicopter Tip Shapes for Reduced Blade Vortex Interaction," AIAA Paper 95-0192, 33rd Aerospace Sciences Meeting and Exhibit, Reno, NV, Jan. 9–12.

Sopher, R. 1997. "The AHS Igor Sikorsky Human Powered Helicopter Competition," *Vertiflite*, 43 (3), pp. 32–35.

Spivey, R. F. 1968. "Blade Tip Aerodynamics–Profile and Planform Effects," 24th Annual National Forum of the American Helicopter Soc., Washington DC, May.

Spivey, W. A. and Morehouse, C. G. 1970. "New Insights into the Design of Swept-Tip Rotor Blades." 26th Annual National Forum of the American Helicopter Soc., Washington DC, June 16–18.

Stepniewski, W. Z. and Keys, C. N. 1984. *Rotary-Wing Aerodynamics*, Dover Publications, New York, NY, Vol. II

Straub, F. K. 1995. "A Feasibility Study of Using Smart Materials for Rotor Control," *Smart Materials and Structures*, 5 (1), pp. 1–10.

Straub, F. K. and Merkley, D. J. 1995. "Design of a Servo-Flap Rotor for Reduced Control Loads," *Smart Materials and Structures*, 5 (1), pp. 68–75.

Studebaker, K. and Matuska, D. 1993. "Variable Diameter Tilt-Rotor Wind Tunnel Test Results," 49th Annual Forum of the American Helicopter Soc., St. Louis, MO, May 19–21.

Tarascio, M and Chopra, I. 2003. "Design and Development of a Thrust Augmented Emtomopter: An Advanced Flapping Wing Micro Hovering Air Vehicle," 59th Annual Forum of the American Helicopter Soc. International, Phoenix, AZ, May 6–8.

Tung, C. and Lee, S. 1994. "Evaluation of Hover Performance Prediction Codes," 50th Annual Forum of the American Helicopter Soc., Washington DC, May 11–13.

Vialle, M. and Arnaud, G. 1993. "A New Generation of Fenestron Fan-in-Fin Tail Rotors on EC 135," 19th European Rotorcraft Forum, Cernobbo (Como), Italy, Sept. 14–16.

Vuillet, A. and Morelli, F. 1986. "New Aerodynamic Design of the Fenestron for Improved Performance," 12th European Rotorcraft Forum, Garmisch-Partenkirchen, Germany, Sept. 22–25.

Vuillet, A., Allongue, M., Philippe, J. J., and Desopper, A. 1989. "Performance and Aerodynamic Development of the Super Puma Mk II Main Rotor with New SPP8 Blade Tip Design," 15th European Rotorcraft Forum, Amsterdam, The Netherlands, Sept. 12–15.

Vuillet, A. 1990. "Rotor and Blade Aerodynamic Design," In: AGARD R-781.

Wilby, P. G. 1998. "Shockwaves in the Rotor World–A Personal Perspective of 30 Years of Rotor Aerodynamic Research in the UK," *Aeronautical J.*, 102 (1013), pp. 113–128.

Williams, R. and Montana, P. S. 1975. "A Comprehensive Plan for Drag Reduction," In: *Rotorcraft Parasitic Drag*, 31st Annual Forum of the American Helicopter Soc., Washington DC, May 13–15.

Williams, R. M. 1976. "Application of Circulation Control Rotor Technology to a Stopped Rotor Aircraft Design," *Vertica*, 1, pp. 3–15.

Wilson, F. T. 1984. "Design and Testing of a Large Scale Helicopter Model in the RAE 5 Metre Pressurised Wind Tunnel," 10th European Rotorcraft Forum, The Hague, The Netherlands, Aug. 28–31.

Wilson, F. T. 1990. "Fuselage Aerodynamic Design Issues and Rotor/Fuselage International Aerodynamics–Part 1: Practical Design Issues," In: AGARD-R-781.

Wilson, J. C. 1975. "Rotorcraft Low-Speed Download Drag Definition and Its Reduction," In: *Rotorcraft Parasitic Drag*, 31st Annual Forum of the American Helicopter Soc., Washington DC, May 13–15.

Wilson, J. C. and Kelley, H. L. 1983. "Measured Aerodynamic Forces on Three Typical Helicopter Tail Boom Cross Sections," *J. of the American Helicopter Soc.*, 28 (4), pp. 68-71.

Wilson, J. C. and Kelley, H. L. 1986. "Aerodynamic Characteristics of Several Current Helicopter Tail Boom Cross Sections Including the Effect of Spoilers," NASA TP-2506, AVSCOMTR-85-B-3.

Wilson, J. C., Kelly, H. L., and Donahue, C. C. 1988. "Development in Helicopter Tailboom Strake Application," RAeS Conference on Helicopter Handling Qualities and Control, London, Nov. 15–17.

Winn, A. L. and Logan, A. H. 1990. "The MDHC NOTAR System," RAeS Conference on Helicopter Yaw Control Concepts, London, Feb.–March.

Wood, T. L. and Peryea, M. A. 1991. "Reduction of Tilt-Rotor Download," 47th Annual Forum of the American Helicopter Soc., Phoenix, AZ, May 6–8.

Woods, M. I., Henderson, J. F., and Lock, G. D. 2001. "Energy Requirements For the Flight of Micro Air Vehicles," *The Aeronautical J.*, 105 (1045), pp. 135–146.

Yeager, W. T, Jr., Mantay, W. R., Singleton, J. D. Wilbur, M. L., Cramer, R. G., and Singleton, J. D. 1987. "Wind-Tunnel Evaluation of an Advanced Main-Rotor Blade Design for a Utility-Class Helicopter," NASA Technical Memorandum 89129.

Yeager, W. T, Jr., Noonan, K. W., Singleton, J. D. Wilbur, M. L., and Minick, P. H. 1997. "Performance and Vibratory Loads Data from a Wind-Tunnel Test of a Model Helicopter Main-Rotor Blade with a Paddle-Type Tip," NASA TM-4754, ARL TR-1283, ATCOM TR-97-A-006.

Żbikowski, R. 2002. "On Aerodynamic Modelling of an Insect-Like Flapping Wing in Hover for Micro Air Vehicles," *Philosophical Transactions of the Royal Society of London, Series A: Mathematical, Physical and Engineering Sciences*, 360 (1791), pp. 273–290.

CHAPTER 7

Aerodynamics of Rotor Airfoils

> It [the Göttingen-429] is a reasonably efficient airfoil, although others give greater lift and a great many different curves [airfoil shapes] are used for designing airplanes. But, the important advantage of this particular type is that its center of lift or pressure is approximately the same at all angles which it may assume in flight. This is not true of other types of airfoil, so that center of pressure travel is a factor to be reckoned with in using them.
>
> Juan de la Cierva (1931; in reference to the twisting moment produced on autogiro blades by a cambered airfoil.)

7.1 Introduction

The goal of this chapter is to review the aerodynamics of airfoils and to discuss their potential impact on helicopter rotor performance. An improved understanding and predictive capability of rotor airfoil characteristics will always lead to an improved analysis capability of existing rotor designs and may ultimately lead to new rotors optimized for greater performance in both hover and forward flight. The selection of airfoil sections for helicopter rotors is more difficult than for a fixed-wing aircraft because they are not point designs; that is, the AoA and Mach number vary continuously at all blade elements on the rotor and one airfoil section cannot meet all the various aerodynamic requirements.

On early helicopters, little attention was paid to the selection of airfoil section because there were just too many other technical problems to solve. Although the NACA had developed some special helicopter airfoils in the late 1940s, it was not until the middle of the 1960s that airfoil sections specifically tailored to meet the special requirements of helicopters became more widely used by manufacturers. Since then, the major helicopter manufacturers and research organizations have developed various families of improved airfoil profiles for use on helicopter rotors. Each airfoil profile within the family will have specific aerodynamic and geometric attributes optimized for different radial positions on the blade. The construction of a blade with multiple airfoil sections along its length is made easier today, mainly because of computer aided design and composite materials manufacturing technology, which makes the design and production costs comparable to one with a single airfoil.

Historically, the best airfoils are obtained through an evolutionary process, where both theory and experiment go hand in hand to meet specific operating requirements. The tools to help design airfoils that have specific aerodynamic characteristics have been available since the 1920s. The development of the thin-airfoil theory by Munk (1922, 1924) and Glauert (1947) led to an understanding of how camber affected the chordwise pressure loading. This allowed the effects of camber to be isolated from thickness, but the effects combined as required by linear superposition. The problem of defining the airfoil pressure distribution for an airfoil of arbitrary shape was tackled semi-analytically by Theodorsen & Garrick (1932). The design of practical airfoil shapes was further aided by methods representing airfoil thickness, such as the conformal transformation method developed by

Prandtl & Tiejens (1934). This made it possible to compute pressure distributions and lift characteristics, at least for some specially shaped "Joukowski" airfoils. The detailed aerodynamic properties of Joukowski airfoils were studied in the late 1920s at Göttingen, Germany and by the NACA – see Schrenk (1927) and von Mises (1959). Abbott et al. (1945) developed a numerical method to predict chordwise pressure distributions and airfoil characteristics based on an extension of thin-airfoil theory, where the increment in loading distribution associated with camber could be combined with the loading from thickness and angle of attack (AoA).

By the 1960s, surface singularity or "panel methods" coupled with boundary layer displacement corrections were available for airfoil design – see Section 14.7 for details. Much of the pioneering work with panel methods was done by Rubbert (1964) and by Hess & Smith (1967). Inverse panel methods allowed airfoils to be designed meet specific aerodynamic requirements. Kennedy & Marsden (1978) were one of the first to develop such methods. Generally, the airfoil designs were optimized for maximum lift. Eppler & Somers (1980) discuss an alternative method for inverse airfoil design using conformal mapping with boundary layer corrections. Hicks & McCroskey (1980) discuss the numerical optimization of a helicopter airfoil, with experimental validation. The advent of numerical methods for transonic airfoil design also meant that for the first time helicopter airfoil shapes could be more carefully designed to meet advancing blade requirements. Sloof et al. (1975) and Narramore & Yen (1982, 1997) discuss transonic airfoil design methods for helicopter rotors.

While most airfoil designs have been conducted for 2-D flows, the complicated flow near the tip of a helicopter blade demands 3-D prediction methods as well. Caradonna and colleagues (1972, 1976, 1978) were major contributors to 2-D and 3-D transonic flow prediction methods for helicopter blades using finite-difference methods. The advent of finite-difference solvers for the Euler and Navier–Stokes equations has led to increasing sophistication in airfoil design tools – see, for example, McCroskey & Baeder (1985), Malone et al. (1989), Bezard (1992), and Narramore (1994). However, the extreme operating conditions and often highly unsteady flow environment found on helicopters means that rotor airfoils must still be tested in a wind tunnel to fully and accurately assess their aerodynamic performance, mainly because modern computational methods have not yet matured to a level where turbulent flow separation and stall effects can be predicted with acceptable accuracy.

7.2 Helicopter Rotor Airfoil Requirements

A representative variation in the operating lift coefficient, C_l, versus incident Mach number, M, for a section near the tip of a helicopter rotor blade in forward flight is illustrated in Fig. 7.1. Two flight conditions are shown. Superimposed on each figure is the approximate static stall boundary for a first-generation airfoil, such as the NACA 0012. One condition is where the rotor operational limits are determined by advancing blade compressibility effects. The other condition is where the rotor limits are determined by retreating blade stall. Notice that in either case the advancing blade operates at low AoA but at high subsonic or transonic conditions, whereas the retreating blade operates at low Mach numbers and high lift coefficients. Overall, it will be seen that this airfoil section operates throughout at a condition close to the boundary where flow separation may occur. Because the onset of flow separation may ultimately limit rotor performance, there has been a great deal of emphasis in rotor design on maximizing the lifting capability of rotor airfoil sections to

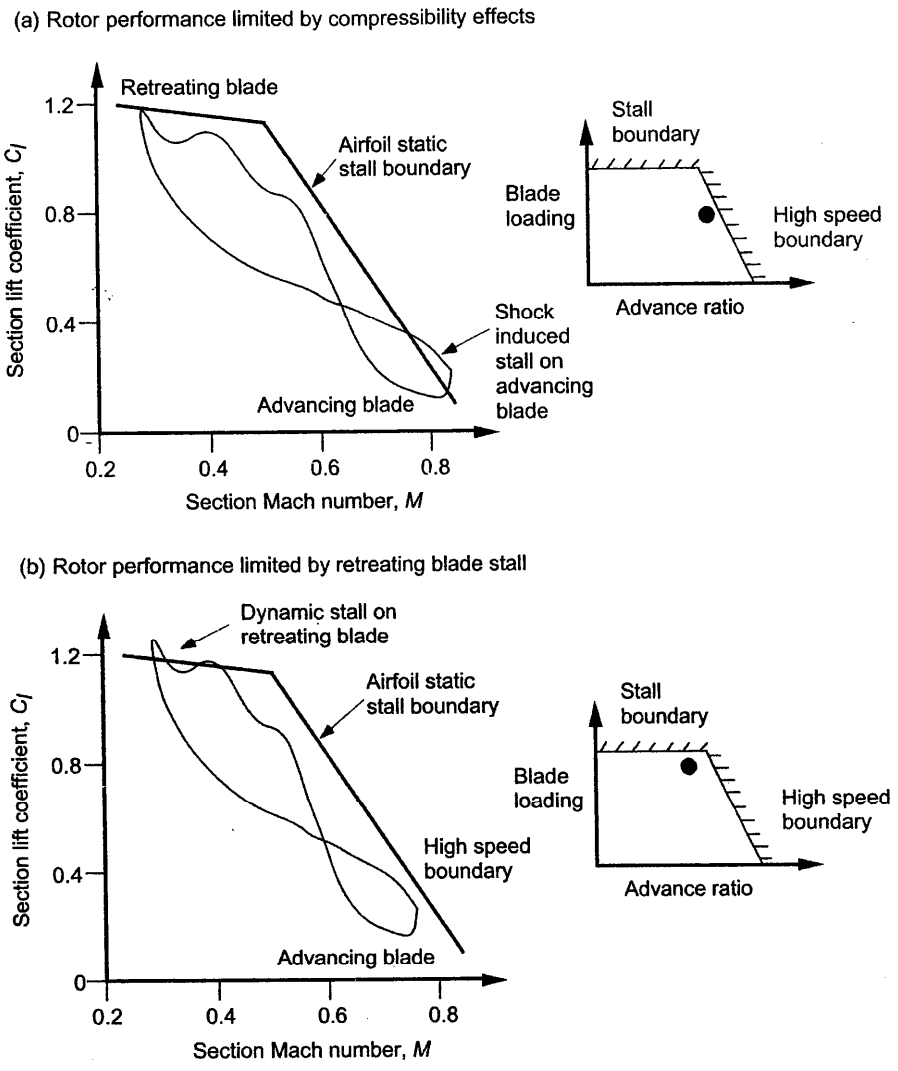

Figure 7.1 Representative operating conditions and maximum lift coefficient versus Mach number boundary for a helicopter rotor section. The rotor limits may be determined by either: (a) advancing blade compressibility effects, or (b) retreating blade stall.

simultaneously alleviate both compressibility effects and retreating blade stall. The rotor design point, therefore, must recognize the influence of both effects as limiting factors, as well as allow sufficient margin from the stall/compressibility boundary for perturbations in AoA and Mach number associated with maneuvering flight and turbulent air.

The general requirements for a good helicopter rotor airfoil are as follows:

1. A high maximum lift coefficient, $C_{l_{max}}$. This will allow a rotor with lower solidity and lighter weight, or will permit flight at higher rotor thrusts and under higher maneuver load factors.
2. A high drag divergence Mach number. This will permit flight at high forward speeds without prohibitive power loss or increase in noise levels.

3. A good lift-to-drag ratio over a wide range of Mach number. This will give the rotor a low profile power consumption and the helicopter a low autorotative rate of descent.
4. A low pitching moment. This will help minimize blade torsion moments, minimize vibrations, and keep control loads to reasonable values.

In airfoil design, it turns out that many of these requirements are conflicting in that they cannot all be simultaneously achieved with the use of a single airfoil shape. However, much can be done to maximize one or more of the airfoil performance attributes without drastically compromising another. To do this, however, requires an understanding of the key (and interrelated) effects of factors such as airfoil shape, AoA, Reynolds number, and Mach number on the aerodynamic performance.

7.3 Reynolds Number and Mach Number Effects

Two of the most well known parameters used in aerodynamics are the *Reynolds number* and the *Mach number*. For an airfoil, its size is described by a characteristic length based on the chord, c. When the airfoil is moving through a fluid of viscosity μ, density ρ, and sonic velocity a, and with a speed V_∞ at some relative orientation to the flow, then the method of *dimensional analysis* shows that the force on the airfoil, F, can be written in functional form as

$$\frac{F}{\rho V_\infty^2 c^2} = C_F = f\left(\frac{\rho V_\infty c}{\mu}, \frac{V_\infty}{a}\right) = f\,(Re, M)\,. \tag{7.1}$$

The combinations $\rho V_\infty c/\mu$ and V_∞/a are called the Reynolds number (denoted by Re) and Mach number (denoted by M), respectively. Unfortunately, these parameters have both independent and interdependent influences, which complicates the understanding of the problem of finding their effects on the aerodynamic force.

7.3.1 *Reynolds Number*

The physical significance of the Reynolds number is that it represents the ratio of the inertial forces to the viscous forces in the fluid. This can be seen by writing the Reynolds number as

$$Re = \frac{\rho V_\infty c}{\mu} = \frac{\rho V_\infty c(V_\infty c)}{\mu(V_\infty c)} = \frac{\rho V_\infty^2 c^2}{\mu(V_\infty/c)c^2} \equiv \frac{\text{Inertial force}}{\text{Viscous force}}. \tag{7.2}$$

On the numerator, $\rho V_\infty^2 c^2$ has units of force and so it represents an inertial force. The coefficient of viscosity, μ, is the shear force per unit area per unit velocity gradient. The denominator, therefore, is a viscous force. For an ideal fluid, the Reynolds number is effectively infinite. However, when viscous forces are dominant, the Reynolds number is small in value. For helicopters the range of Reynolds numbers encountered by the rotor is significant, and Reynolds number effects on its aerodynamics are significant.

The aerodynamic characteristics of rotor airfoils must be assessed at their actual operational Reynolds numbers and Mach numbers. Figure 7.2 illustrates the operational Reynolds number and Mach number ranges typical of helicopter rotors, both at full scale and model (sub) scale. The maximum lift coefficient, $C_{l_{max}}$, can be used as one indicator of the significance of viscous effects. At the low end of the practical Reynolds number range for rotors (i.e., for chord Reynolds numbers in the range $10^5 < Re < 10^6$), most airfoils have

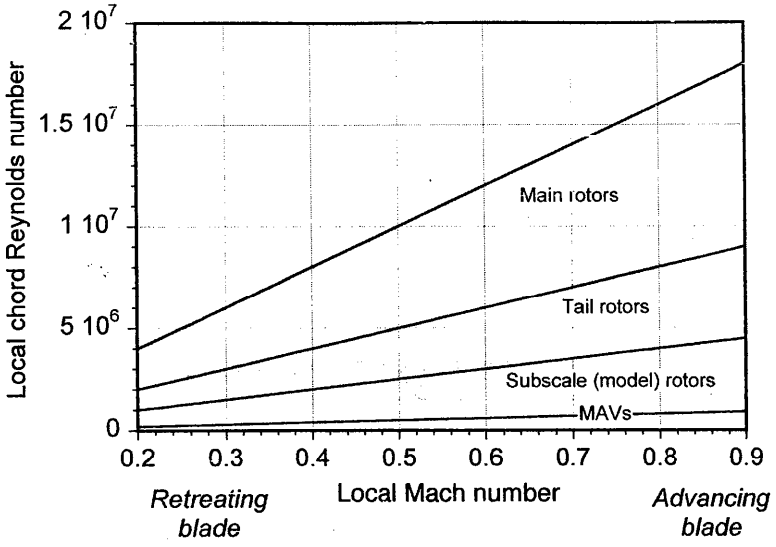

Figure 7.2 Representative ranges of Reynolds number and Mach number found on helicopter rotors.

relatively low values of $C_{l_{max}}$. This is because the viscous forces are more dominant, the boundary layer is thicker, and the flow will separate more readily from the airfoil surface, all other factors being equal. In the range $Re = 1 \times 10^6$ to 3×10^6 the greatest changes in $C_{l_{max}}$ generally occur. For $Re > 4 \times 10^6$ any changes in $C_{l_{max}}$ are found to be more gradual. Clearly, Fig. 7.2 shows that subscale rotor models and tail rotors will fall into the range where the airfoil characteristics can be sensitive to Reynolds number. In particular, for subscale rotors the chord Reynolds numbers on the retreating blade are typically below 10^6 and, therefore, are more susceptible to viscous effects. This is important when assessing the performance characteristics obtained from subscale rotor tests and extrapolating the results to estimate full-scale rotor performance. Notice that the blade Reynolds numbers found on rotating-wing types of micro air vehicles (see Section 6.14) will fall well below those of even the smallest helicopter rotors, and are generally well below 10^5.

It will be apparent that on the rotor blade the Reynolds number and Mach number are related by the velocity, V. For example, the Reynolds number can be written in terms of the Mach number as

$$Re = \left(\frac{\rho a c}{\mu}\right) M. \tag{7.3}$$

At standard sea level conditions this becomes

$$Re = 23.26 \times 10^6 M \text{ per foot of chord,} \tag{7.4}$$

or in SI units

$$Re = 7.096 \times 10^6 M \text{ per meter of chord.} \tag{7.5}$$

This means that for a typical helicopter, with a main rotor blade chord of between 0.5 ft and 1.5 ft (0.15 m to 0.46 m), on the advancing blade at a point where the Mach number is 0.7 the Reynolds number will be as high as $0.81–2.44 \times 10^7$, and on the retreating blade at a point where the Mach number is 0.3 the Reynolds number will be only as low as $0.35–1.05 \times 10^7$.

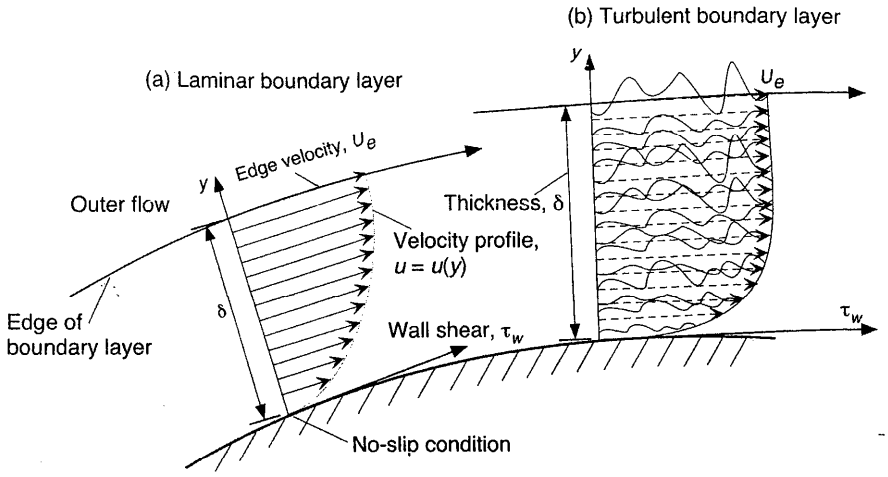

Figure 7.3 Development of a boundary layer on a solid surface.

7.3.2 *Concept of the Boundary Layer*

At low angles of attack, the effects of viscosity are confined to a thin region near the surface of the airfoil known as the *boundary layer*. Historically, the concept of the boundary layer was first proposed by Prandtl (1928) in his seminal work on the subject. Real fluids do not slip at a solid boundary and there will be no relative motion between the fluid and the surface of the airfoil. Therefore, there is a region close to the airfoil where the velocity rises from zero at the surface to the external flow velocity, U_e. This boundary layer region is generally very thin, being a small fraction of the airfoil chord. The concept is illustrated in Fig. 7.3. On an airfoil operated at higher Reynolds numbers the boundary layer will generally vary from practically zero thickness near the leading edge to a few percentages of the chord at the trailing edge. At lower Reynolds numbers the boundary layer can be much thicker, which will result also in the airfoil having a higher a profile drag.

Boundary layers are found to be of two main types: *laminar* or *turbulent*. A third type can be considered to be *transitional*, although this is not a steady boundary layer flow and is difficult to characterize. A comparison of the profile shapes of a laminar and turbulent boundary layer is also shown in Fig. 7.3. The parameter δ is the boundary layer thickness, which is defined as the value of y for which 99% of the external flow velocity is recovered (i.e., $u = 0.99U_e$). The flow in a laminar boundary layer is smooth and free of any mixing of fluid between successive layers, whereas the flow in a turbulent boundary layer is characterized by significant mixing between layers of the fluid. This produces a momentum transfer through the boundary layer, and so the distribution of velocity in a turbulent boundary layer is characterized by larger velocities closer to the airfoil surface. Also, for the same reasons, a turbulent boundary layer has a greater thickness compared with a laminar boundary layer that develops under the same pressure gradient. See Schlichting (1979) and Young (1989).

Viscous stresses are produced whenever there is relative motion between adjacent fluid elements, and these stresses produce a resistance that tends to retard the motion of the fluid. The viscous shear stress, τ, is related to the absolute viscosity, μ, by Newton's formula

$$\tau = \mu \frac{\partial u}{\partial y}, \tag{7.6}$$

where $\partial u/\partial y$ is the rate at which the flow velocity increases perpendicular to the airfoil surface. (Note that the partial derivative is used in this equation because u can vary not only with y but also in other directions.) Thus, as implied by the shape of the boundary layer velocity profile in Fig. 7.3, the shear stress, τ_w, produced on the surface of an airfoil will be greater with a turbulent boundary layer than for a laminar one because

$$\tau_w = \mu \left(\frac{\partial u}{\partial y} \right)_{y=0}. \tag{7.7}$$

The development of a laminar boundary layer in a zero pressure gradient flow can be computed exactly. This result was first obtained by Blasius (1908), with an improved solution by Kuo (1953). In Blasius's solution the local skin friction coefficient, c_f, on one side of a flat-plate is

$$c_f = \frac{\tau_w}{\frac{1}{2}\rho V_\infty^2} = 0.664\ Re_x^{-0.5}, \tag{7.8}$$

where Re_x is the Reynolds number based on the distance from the leading edge of the plate. The net shear stress drag coefficient of the plate will be

$$C_d = \frac{2}{c}\int_0^c c_f\, dx = 1.328\ Re^{-0.5}, \tag{7.9}$$

where c is the chord of the plate. This result is plotted in Fig. 7.4; however, very few airfoils follow the Blasius result because at Reynolds numbers above about 5×10^5 the boundary layer usually becomes turbulent even at low angles of attack. The reason for this is that at Reynolds numbers above a certain minimum value, natural flow disturbances (although often caused prematurely by surface roughness) can cause a *transition* from a laminar to a turbulent boundary layer. Helicopter airfoils will typically exhibit laminar flow only over a few percentages of the chord. For a fully developed turbulent boundary layer on a flat-plate, the skin friction coefficient c_f on one side of the plate is found to be close to

$$c_f = 0.0583\ Re_x^{-0.2}, \tag{7.10}$$

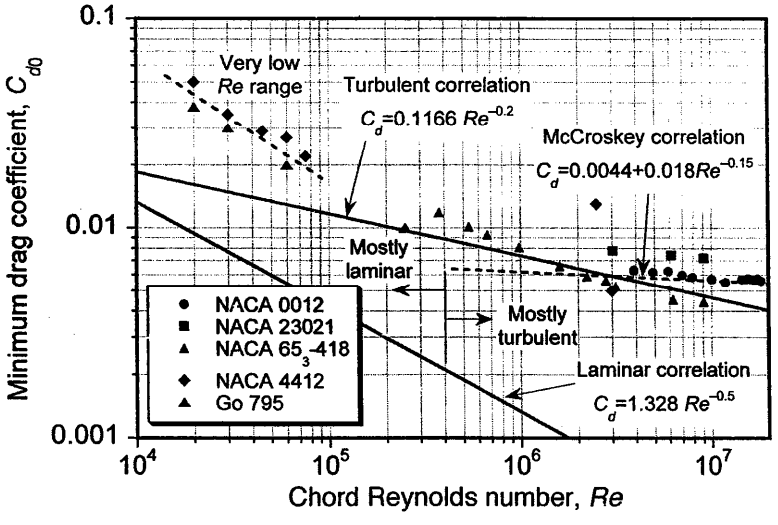

Figure 7.4 Viscous drag of a flat plate compared to minimum drag coefficients of several airfoils. Data source: Abbott & von Doenhoff (1949) and Simons (1986).

so that

$$C_d = \frac{2}{c}\int_0^c c_f\, dx = 0.1166\, Re^{-0.2}. \tag{7.11}$$

The validity of the latter expression is limited to a Re range between 10^5 and 10^9. Below $Re = 5 \times 10^5$ the boundary layer can normally be assumed to be laminar unless artificially tripped. The drag of a flat-plate with a fully turbulent boundary layer is also plotted in Fig. 7.4 and is compared to the measured minimum drag coefficients of several airfoils. The results suggest that the turbulent flat-plate solution is a good approximation to the viscous (shear) drag on airfoils over the practical range of Reynolds numbers to be found on helicopters, that is, above about 10^6. In this case it will be sufficient to assume that

$$C_d = C_{d_{\text{ref}}}\left(\frac{Re}{Re_{\text{ref}}}\right)^{-0.2} \tag{7.12}$$

where Re_{ref} is the reference Reynolds number for which a reference value of drag $C_{d_{\text{ref}}}$ is known. The empirical equation (Eq. 6.20) suggested by McCroskey (1977) offers an improved correlation for airfoils with fully developed turbulent boundary layers at the higher Reynolds numbers. At very low Reynolds numbers, say below 10^5, the laminar boundary layer separates more readily and the profile drag of typical airfoils are much larger that either laminar or turbulent boundary layer theory would suggest. Airfoil behavior in this Reynolds number regime is important for many classes of micro air vehicles (see Section 6.14). In this case, changing the scaling coefficient from 0.2 to 0.4 in Eq. 7.12 is good approximation based on the results shown in Fig. 7.4 at very low Re.

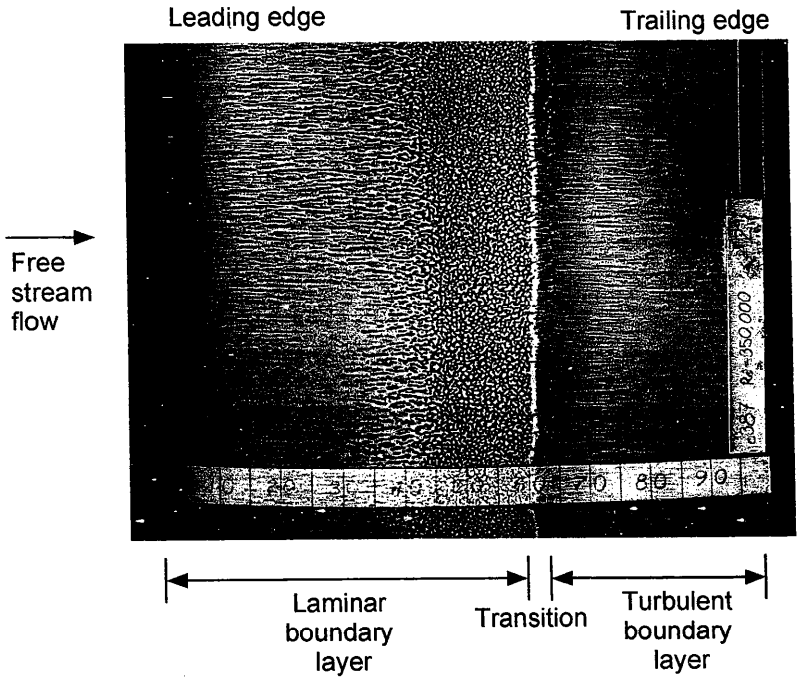

Figure 7.5 Surface flow visualization on a airfoil at low AoA showing the transition from a laminar to turbulent boundary layer. Eppler 387 airfoil, $Re = 350,000$, $\alpha = 2°$. (Photo courtesy of Michael Sellig.)

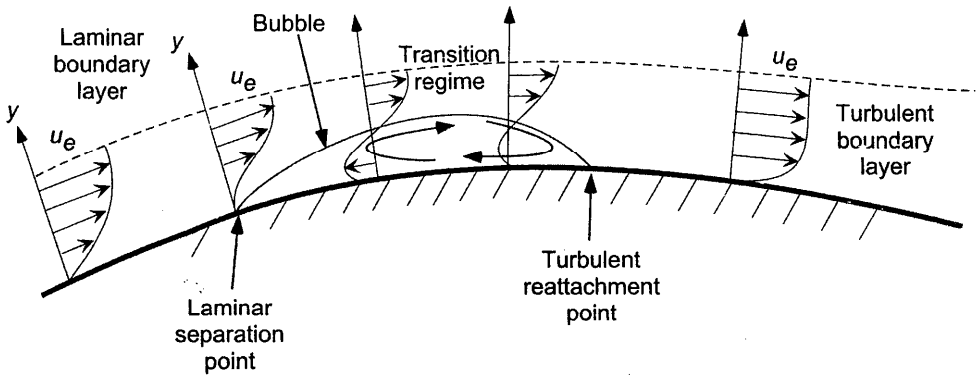

Figure 7.6 Schematic showing the structure of a laminar separation bubble. Adapted from Ward (1963).

Note also that a turbulent boundary layer will be thicker than a laminar one. If δ is defined as the value where $u = 0.99U_e$ then for a laminar boundary layer

$$\delta \simeq 5.2x\ Re^{-0.5}, \tag{7.13}$$

and for a turbulent boundary layer

$$\delta \simeq 0.37x\ Re^{-0.2}. \tag{7.14}$$

Therefore, in addition to a higher viscous shear on the airfoil surface the presence of a turbulent boundary layer will result in a greater wake momentum deficit and a higher overall profile drag compared to an airfoil with a fully laminar boundary layer.

The significance of the two boundary layer states on an airfoil at low AoA and relatively low Reynolds number is illustrated in Fig. 7.5. The flow was visualized by means of the surface oil flow technique (see also Fig. 7.31). For these conditions the forward 60% of the airfoil has a laminar boundary layer. The low surface shear stress here allows the oil to accumulate, especially near mid-chord, where the boundary layer approaches the point of separation. After laminar separation occurs, the flow will temporarily leave the airfoil surface but undergo a transition process and immediately reattach again as a turbulent boundary layer. This can leave a small region of recirculating separated flow that is known as a *laminar separation bubble*, as shown schematically in Fig. 7.6. The presence of laminar separation bubbles can also be observed by a small constant pressure region in the measurement of the chordwise pressure distribution near the leading edge of the airfoil. With surface oil flow visualization, the bubble is evidenced by an accumulation of oil – see Fig. 7.5 and later in Fig. 7.30. The formation of laminar separation bubbles is common for the types of airfoils and Reynolds numbers found on helicopter rotors. Further details on laminar separation bubbles are given by Ward (1963), Horton (1967), and Liebeck (1992).

It is found that the developing boundary layer on an airfoil is sensitive to the pressure gradient. In the boundary layer, a simplified form of the Navier–Stokes equations applies – see Section 14.2.1. In this case the equations are written in a classic form as

$$\frac{\partial u}{\partial x} + \frac{\partial v}{\partial y} = 0 \quad \text{(continuity)}, \tag{7.15}$$

$$u\frac{\partial u}{\partial x} + v\frac{\partial u}{\partial y} = -\frac{1}{\rho}\frac{\partial p}{\partial x} + \nu\frac{\partial^2 u}{\partial y^2} \quad (x\text{-component of momentum}), \tag{7.16}$$

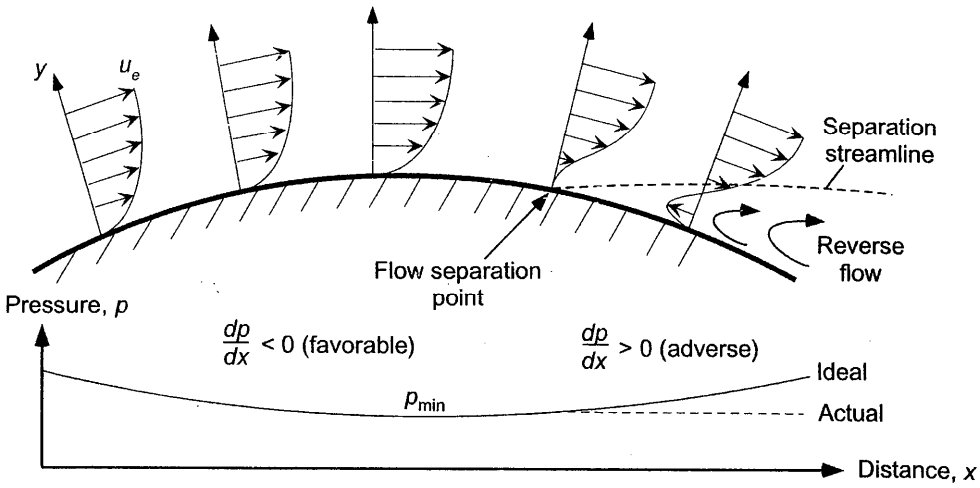

Figure 7.7 Development of the boundary layer in a simple external pressure gradient.

$$-\frac{\partial p}{\partial y} = 0 \quad \text{(pressure gradient normal to surface).} \tag{7.17}$$

The pressure gradient is denoted by $\partial p/\partial x$ along the surface. When the gradient is positive or adverse, that is, one in which $\partial p/\partial x > 0$, the pressure force is in the direction that tries to decelerate the flow. The resulting force on the fluid is particularly strong near the surface of the airfoil where the velocity is low; therefore $\partial u/\partial y$ near $y = 0$ becomes smaller the longer the adverse pressure gradient persists. This effect is shown in Fig. 7.7. At some distance downstream a point is reached where $\tau_w \to 0$ and the direction of the flow reverses near the surface. This point is called the flow *separation point*, because the flow breaks away and leaves the surface, altering the entire disposition of the flow. Under these conditions, the concept of the boundary layer breaks down and a recirculating flow (wake) is left downstream of the separation point; downstream of separation the effects of viscosity influence an extensive region of the flow. Flow separation is one of the least well understood and poorly modeled phenomena in fluid mechanics, even under steady 2-D conditions. In unsteady (external) flows, the onset of flow separation is more complicated and there can be significant regions of flow reversal within the boundary layer even in the absence of separation – see McCroskey (1977). On rotating blades there are additional centrifugal and Coriolis acceleration terms acting on the 3-D boundary layer, which can affect stall behavior – see Section 13.12.2.

Turbulent boundary layers are much less susceptible to separation than laminar boundary layers because of the higher mixing and interlayer momentum transfer of the fluid. At higher Reynolds numbers, the pressure rise required to separate a turbulent boundary layer may be an order of magnitude larger than that required to separate a laminar boundary layer. On rotor airfoils, which tend to have relatively sharp leading edges and peak suction pressures close to the leading edge, a steep adverse pressure gradient is found over most of the chord, and a laminar boundary layer can only exist for a very short distance from the stagnation point (typically, 2–15% chord). At low angles of attack, the turbulent boundary layer will generally extend all the way to the trailing edge of the airfoil. At higher angles of attack, the increasing intensity of the adverse pressure gradients will ultimately cause the turbulent boundary layer to begin to separate – see Thwaites (1960). Many rotor airfoils stall by the process of progressive turbulent trailing edge flow separation, whereby the separation

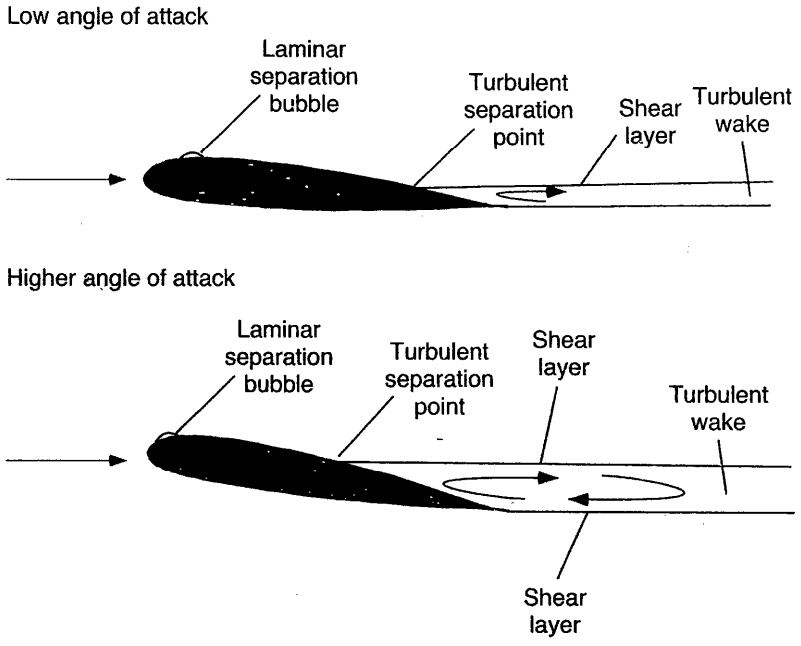

Figure 7.8 Development of trailing edge flow separation on an airfoil.

point starts at the trailing edge and moves forward on the chord with increasing AoA. This process is shown schematically in Fig. 7.8. When the airfoil forces and moments are plotted versus AoA, the onset of progressive trailing edge flow separation has a deleterious effect on the airfoil performance compared to that obtained with fully attached flow (see Section 7.9).

7.3.3 *Mach Number*

The ratio of the speed of the flow to that of the speed of sound is called the *Mach number* and can be interpreted physically as a ratio of inertia forces in the fluid to forces resulting from compressibility. The speed of sound is the speed at which pressure disturbances are propagated through the air and is given by $a = \sqrt{\gamma RT}$ where $\gamma = 1.4$ is the ratio of specific heats for air, R is the gas constant, and T is absolute temperature. The speed of sound is approximately 1,117 ft s^{-1} (340 m s^{-1}) at sea level on a standard day – see Section 5.2. When an airfoil travels at low speeds relative to the speed of sound, pressure disturbances travel at relatively high speeds in all directions. This causes the flow approaching the airfoil to change its velocity and pressure very gradually. The flow, therefore, can be considered incompressible. Notice that for an truly incompressible flow $a = \infty$, so that $M = 0$. When the airfoil travels at higher speeds relative to the speed of sound, disturbances cannot travel as far from the airfoil in a given time. This means that the flow approaching the airfoil undergoes more sudden changes. Under these conditions there are measurable changes to the characteristics of the airfoil, such as increased lift coefficient and a movement of the aerodynamic center. If the airfoil approaches and exceeds sonic speeds, then disturbances cannot be propagated upstream and discontinuous changes in the flow properties take place at the airfoil. Under these conditions there are large nonlinear changes in the airfoil characteristics.

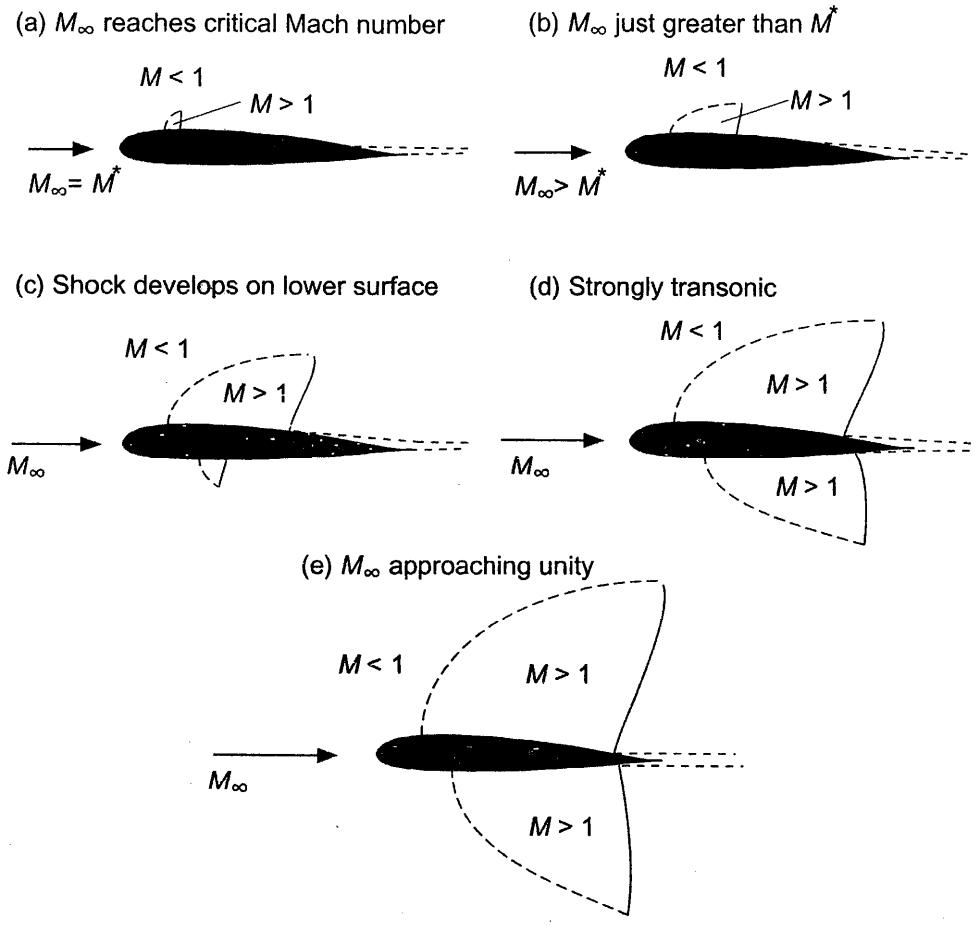

Figure 7.9 Development of supersonic flow pockets on an airfoil for increasing free-stream Mach number. (a) M_∞ = critical Mach number, M^*. (b) $M_\infty > M^*$ with developing shock wave. (c) Shock wave develops on lower surface. (d) Lower surface shock wave moves quickly toward trailing edge. (e) M_∞ approaching unity.

When the air flows past an airfoil, the local velocity at the surface outside the boundary layer may be greater or less than the free-stream velocity. The highest velocities occur near the leading edge and over the upper surface of the airfoil. If the free-stream velocity is low enough, the flow velocity remains *subsonic* everywhere. Such flows are relatively easy to analyze because the governing equations are linear. At higher free-stream velocities, however, the acceleration of the flow will eventually cause regions of supersonic flow. This is a mixed or *transonic* flow, which although predominantly subsonic, has an embedded supersonic pocket, as illustrated by Fig. 7.9. This problem is much more difficult to analyze because of the nonlinear nature of the equations governing the flow.

The value of the free-stream Mach number, M_∞, where the flow first becomes locally sonic ($M = 1$) is called the *critical Mach number*, M^*. The value of M^* will also depend on the AoA of the airfoil. Further increases in M_∞ cause the extent of the supersonic region to grow, and the region becomes terminated by a *shock wave* that is initially almost perpendicular to the airfoil surface. Across the shock wave there is a rapid increase in pressure and also an entropy change whereby energy is converted to heat resulting in

a form of profile drag known as *wave drag*. The interaction of the shock wave and the boundary layer results in an increase in skin friction drag. Moreover, the high adverse pressure gradients found in the vicinity of the shock wave make boundary layer thickening inevitable and this will be accompanied by an increase in profile drag.

With increasing Mach number (or AoA) the shock wave will strengthen, move aft, and become more oblique to the airfoil surface. At some point, depending on the AoA and airfoil shape, the flow on the lower surface also becomes supersonic, resulting in a second supersonic pocket and terminating shock wave. With further increases in M_∞, the lower surface shock wave moves quickly toward the trailing edge; this is followed by the rapid aft movement of the upper surface shock wave. If at any point during this process the shock wave becomes sufficiently strong, then the high adverse pressure gradients will cause the boundary layer to separate causing a loss of lift and an increase in drag known as *shock induced stall*. Liepman (1946) and Pearcy (1955) give good fundamental discussions on shock wave/boundary layer interactions.

In Fig. 7.1 it has already been shown that rotor airfoils operate in a relatively diverse aerodynamic regime during each revolution of the rotor, ranging from low subsonic speeds at the root of the blade to transonic flow conditions at the blade tips. Compressibility effects can manifest before sonic speed is reached locally on the airfoil. Even when the free-stream Mach number is quite low, say about 0.3 on the retreating blade, the high angles of attack found under dynamic (unsteady) conditions mean that a supercritical (locally supersonic) flow region can exist near the leading edge of the airfoil. Consequently, compressibility issues need to be addressed very carefully to ensure that the selected airfoil sections will perform satisfactorily under the actual flight conditions found on a helicopter rotor.

7.3.4 *Model Rotor Similarity Parameters*

The effects of Reynolds number and Mach number becomes particularly important when studying the performance of subscaled rotors, and especially when attempting to use these results to predict the performance of the full-scale rotor. See Section 6.8 for a summary, but the problems are discussed in considerable detail by Philippe (1990). The dimensions of most wind tunnels do not permit the testing of model rotors much above 1/4-scale. There are, however, some special wind tunnels that permit the testing of larger rotor models. For example, the DNW tunnel in the Netherlands has a 32×32 ft (9.75×9.75 m) section where 40% subscale rotor models may be tested. In another large wind tunnel at NASA Ames Research Center, which has both 40×80 ft (12.2×24.4 m) and 80×120 ft (24.4×36.6 m) working sections, full-scale rotors may be tested.

For a rotor in forward flight, the speed similarity parameter is the advance ratio $\mu = V_\infty / \Omega R$. Normally, the advance ratio is fairly easy to simulate in a wind tunnel environment by a suitable choice of rotor tip speed and V_∞. To simulate the aerodynamic effects, the Reynolds numbers and Mach numbers on the model rotor must be as close as possible to the full-scale values. In practice, this is not easy to achieve. For example, consider the attainment of full-scale tip Mach numbers on a 1/5-scale rotor. If the rotational frequency of the full-scale rotor is Ω, then for Mach number scaling the rotational frequency of the model must be 5Ω. Yet, the Reynolds numbers for the model will still be a factor of 1/5 those on the full-scale rotor. Thus, the model rotor may operate with Reynolds numbers that are in the sensitive regime, that is, in Reynolds number regimes where the aerodynamic characteristics of the blade sections show a higher sensitivity to Reynolds number. The inability of model rotors to achieve tip Reynolds numbers above 10^6 is a serious factor when trying to extrapolate airloads and rotor performance measurements to full-scale.

Table 7.1. *Relative Scaling Parameters for a 1/5-Scale Rotor in Air and Freon*

Scaling factors	Air	Freon-12
Mach number	1.0	1.0
Lock number	1.0	1.0
Advance ratio	1.0	1.0
Froude number	5.0	1.0
Reynolds number	0.2	0.53
Time	0.2	0.446
Angular velocity	5.0	2.24
Linear velocity	1.0	0.448
Force	0.04	0.0334
Moment	0.008	0.00667
Power	0.04	0.01419
Mass	0.008	0.0334

Some of the problems in matching Reynolds numbers and Mach numbers on models have been overcome by changing the test gas from air to Freon. However, the use of Freon as a test medium is expensive and can be used only in very specialized wind tunnels. Freon will allow full-scale tip Mach numbers to be achieved with a rotational frequency of 2Ω with a 1/5-scale rotor. Furthermore, the properties of Freon allow the Reynolds numbers to be as high as 0.53 those of full-scale. The general scaling parameters for a 1/5-scale model in air and Freon are summarized in Table 7.1, which is from Philippe (1990).

7.4 Airfoil Shape Definition

The importance of the airfoil shape on the rotor behavior was well known to Juan de la Cierva – see Cierva & Rose (1931). Cierva originally used a symmetric airfoil section on his Autogiros, but he later changed the airfoil to a highly cambered 17% thick section for better performance. While having a higher stalling AoA, this airfoil also had a higher pitching moment, which resulted in blade twisting and control problems and finally led to a crash of a Cierva Model C-30 Autogiro – see Beavan & Lock (1939). This event, and the generally low torsional stiffness of early wood and fabric helicopter blades, led to the almost universal use of symmetric airfoil sections on helicopters produced prior to 1960. Although symmetric airfoils offered a reasonable overall compromise in terms of maximum lift coefficient, low pitching moments and high drag divergence Mach numbers, they were by no means optimal for attaining maximum performance from the rotor. However, it was not until the early 1960s that a more serious effort came about to improve airfoil sections for use on helicopters.

As early as 1920, a number of different research institutions had begun to examine the characteristics of various airfoils and organize the results into families of airfoils, basically in an effort to determine the profile shapes that were best suited for specific applications. In the United States, NACA conducted a comprehensive and systematic study of the effect of airfoil shape on aerodynamic characteristics. Existing cambered airfoils such as the Clark-Y and Göttingen 398 sections were known from early experiments to have good aerodynamic characteristics. These airfoils were used by NACA as a basis and were found to have geometrically similar shapes when the camber was removed and the airfoils were reduced to the same thickness-to-chord ratio. NACA then followed a procedure where a

given airfoil could be constructed of a *thickness shape* that was distributed around a *camber line*. This allowed the systematic construction of several families of airfoil sections. The use of linearized methods such as thin-airfoil theory also enabled the chordwise aerodynamic loading associated with camber and thickness to be studied, allowing means of designing airfoils to meet specific purposes. The various families of airfoils developed by NACA were then tested in the wind tunnel to document the effects of varying the important geometrical parameters on the airfoil lift, drag, and pitching moment characteristics as a function of AoA, Reynolds number, and Mach number. Variables found to have important effects on the airfoil characteristics included the maximum camber and its distance aft of the leading edge and the leading edge nose curvature (nose radius) of the airfoil. A summary of the results are documented in considerable detail by Abbott et al. (1945) and Abbott & von Doenhoff (1949).

Two of the most popular airfoils used on many early helicopters were the symmetric NACA 0012 and NACA 0015 sections. These airfoils were found to have low pitching moments about the 1/4-chord and good low-speed as well as high-speed (transonic) performance, giving a relatively high maximum lift and a high drag divergence Mach number. Because these airfoils were also relatively thick, the stiffness of the blade could be maintained while keeping blade weight to a minimum. The upper and lower surfaces of the NACA four-digit symmetrical sections (or thickness envelopes) are described by the polynomial

$$\pm \frac{y_t}{c} = \bar{y}_t = 5\bar{t}[0.29690\sqrt{\bar{x}} - 0.12600\bar{x} - 0.35160\bar{x}^2 + 0.28430\bar{x}^3 - 0.10150\bar{x}^4], \tag{7.18}$$

where $t/c = \bar{t}$ = maximum thickness as a fraction of chord. For example, for the NACA 0012 airfoil $\bar{t} = 0.12$. The corresponding leading edge radius of the airfoil is $r_t = 1.1019\bar{t}^2$. The center for the leading edge radius is found by drawing a straight line through the end of the chord at the origin of the axes and moving a distance along the x axis that is equal to the leading edge radius. The nose radius is then inscribed and faired onto the upper and lower surfaces of the airfoil. The resulting shape is shown in Fig. 7.10(a). The analytic form of the construction lends itself easily to computer generation of the airfoil coordinates – see, for example, Ladson et al. (1995).

A similar approach is used for cambered airfoils, but the mean line (camber line) is used for laying out the airfoil shape. The camberline can be specified as $y_c = y_c(x_c)$. If the slope of the camberline makes an angle θ with the chord line, then the airfoil shape is obtained by plotting the thickness distribution at right angles to the slope of the camberline. This will give the upper (x_u, y_u) and lower coordinates (x_l, y_l) of the airfoil:

$$\bar{x}_u = \bar{x} - \bar{y}_t \sin\theta \quad \text{and} \quad \bar{y}_u = \bar{y}_c + \bar{y}_t \cos\theta, \tag{7.19}$$

$$\bar{x}_l = \bar{x} + \bar{y}_t \sin\theta \quad \text{and} \quad \bar{y}_l = \bar{y}_c - \bar{y}_t \cos\theta, \tag{7.20}$$

where $\theta = \tan^{-1}(dy_c/dx_c)$. In effect, the shape is being defined as a tangent to a series of circles of radius y_t with centers on the camberline. For cambered airfoils, the center for the leading edge radius is found by drawing a straight line through the end of the chord at the origin of the axes but with slope equal to the slope of the camberline at $\bar{x} = 0.005$, and then moving along this line a distance that is equal to the leading edge radius. Because of the form of the geometric construction of cambered airfoils, the leading edge part of the nose radius protrudes very slightly forward of the origin at $x = 0$. As with the symmetric airfoils, the nose radius is then inscribed and faired onto the upper and lower surfaces.

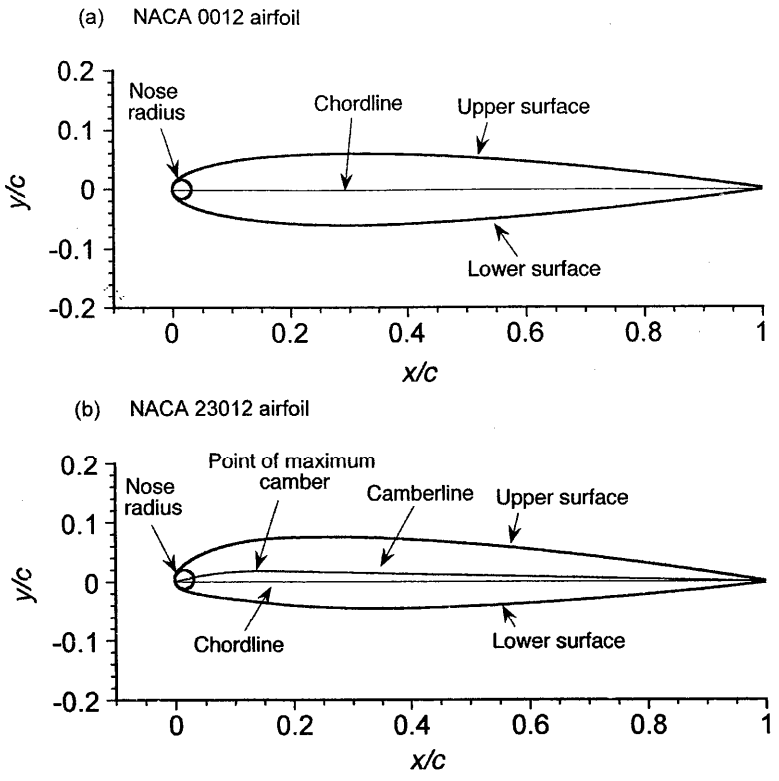

Figure 7.10 NACA airfoil construction with inscribed nose radius. (a) NACA four-digit 0012 airfoil. (b) NACA five-digit 23012 airfoil section.

Various series of mean lines were developed by the NACA, and some of the resulting sections (and derivatives) can be found on modern helicopter blades. Many mean lines, such as the three-digit mean lines, are defined by two equations derived to produce shapes having progressively decreasing camber line slope from the leading edge to the trailing edge. The slope of the camberline is zero at the point of maximum camber (denoted by p) and is constant aft of point m over the trailing edge. The equations for these mean lines are

$$\bar{y}_c = \frac{1}{6}k_1\left[\bar{x}^3 - 3m\bar{x}^2 + m^2(3-m)\bar{x}\right] \quad \text{from } \bar{x} = 0 \text{ to } \bar{x} = m, \tag{7.21}$$

$$\bar{y}_c = \frac{1}{6}k_1 m^3(1-\bar{x}) \quad \text{from } \bar{x} = m \text{ to } \bar{x} = 1. \tag{7.22}$$

Values of p were selected to give five positions of maximum camber, and values of k_1 were selected to give a design lift coefficient of 0.3. The various values of p, m, and k_1 for the three-digit camberlines are given in Table 7.2. Figure 7.10(b) shows the graphical construction of the NACA 23012 section, which has been used as a baseline for many modern helicopter airfoil sections. It is derived from the 230 mean line plus the 0012 thickness distribution, and it has a maximum camber at 15% chord and a thickness-to-chord ratio of 12%.

Modifications to the four-digit and five-digit series of NACA airfoil sections include reflex camber to produce zero pitching moment [see Jacobs & Pinkerton (1935)] and changes in the nose radius and position of thickness to improve $C_{l_{max}}$ capability [see Stack

Table 7.2. *Numerical Values for Three-Digit Camberlines Used in the NACA Five-Digit Airfoil Construction. Source: Abbott & von Doenhoff (1949)*

Mean Line	p	m	k_1
210	0.05	0.0580	361.4
220	0.10	0.1260	51.64
230	0.15	0.2025	15.957
240	0.20	0.2900	6.643
250	0.25	0.3910	3.230

& von Doenhoff (1934)]. The latter sections have seen some use on helicopter rotor and are denoted by a two-digit suffix, such as the NACA 0012-64 and NACA 23012-64. The first integer after the dash indicates the relative magnitude of the nose radius, with a standard nose radius denoted by 6 and a sharp radius by 0. The second digit indicates the position of maximum thickness in tenths of chord.

An early series of special helicopter sections was designed at NACA by Tetervin (1943) and Stivers & Rice (1946). These airfoils, which have NACA 3-H-00 through NACA 10-H-00 series designators, were designed to have lower overall drag over a useful range of lift coefficients but still retain relatively low pitching moments. These airfoils are also discussed by Gessow & Myers (1952).

Another set of NACA airfoils that has seen some use in helicopter applications is the six-digit series. These airfoils were designed to achieve lower drag, higher drag divergence Mach numbers, and higher values of maximum lift. The shapes of these airfoils is such that they are conducive to maintaining an extensive region of laminar flow over the leading edge region and, thereby, lowering skin friction drag, at least over a range of AoA that is limited to low lift coefficients. This is achieved by using camberlines that have a uniform loading from the leading edge to a distance $\bar{x} = a$, and thereafter the loading decreases linearly to zero at the trailing edge. The favorable pressure gradients tend to give the airfoils lower drag compared to other airfoils, but these characteristics are easily spoiled by surface contaminants or other transition causing disturbances. There are many designator combinations used in the six-digit number system. For example, consider the NACA 64_3-215 $a = 0.5$ section. In this case, the number 6 denotes the airfoil series, and the 4 denotes the position of minimum pressure in tenths of chord for the basic symmetric section. The 3 denotes the range of lift coefficient in tenths above and below the design lift coefficient for which low drag may be obtained. The 2 after the dash indicates a design lift coefficient of 0.2, and 15 denotes a 15% thickness-to-chord ratio. These and many other airfoil designators are explained by Abbott & von Doenhoff (1949).

7.5 Airfoil Pressure Distributions

7.5.1 *Pressure Coefficient*

In measurements or calculations of the flow about airfoils, the surface pressure data are conventionally presented in terms of the *pressure coefficient* C_p. In incompressible flow, the definition of C_p follows from *Bernoulli's equation*, that is,

$$p_\infty + \frac{1}{2}\rho_\infty V_\infty^2 = p + \frac{1}{2}\rho_\infty V^2, \tag{7.23}$$

where p and V are the local pressure and velocity, and p_∞ and V_∞ are the corresponding free-stream conditions at infinity (i.e., far upstream of the airfoil). Using the standard abbreviation for the dynamic pressure, $q_\infty = \frac{1}{2}\rho_\infty V_\infty^2$, we can define the pressure coefficient as

$$C_p = \frac{p - p_\infty}{q_\infty} = 1 - \left(\frac{V}{V_\infty}\right)^2. \tag{7.24}$$

For an incompressible flow, $C_p = 1$ at a stagnation point (i.e., where $V = 0$). Also, it will be apparent that $C_p = 0$ far from the airfoil where $V = V_\infty$.

For compressible flow, the pressure coefficient is defined in terms of the Mach number. The dynamic pressure can be expressed in terms of M_∞ as follows:

$$q_\infty = \frac{1}{2}\rho_\infty V_\infty^2 = \frac{1}{2}\frac{\gamma p_\infty}{\gamma p_\infty}\rho_\infty V_\infty^2 = \frac{\gamma}{2} p_\infty \left(\frac{\rho_\infty}{\gamma p_\infty}\right) V_\infty^2. \tag{7.25}$$

Also, because $a_\infty^2 = \gamma p_\infty / \rho_\infty$, the above equation becomes

$$q_\infty = \frac{\gamma}{2} p_\infty \frac{V_\infty^2}{a_\infty^2} = \frac{\gamma}{2} p_\infty M_\infty^2, \tag{7.26}$$

and the pressure coefficient can be written as

$$C_p = \frac{2}{\gamma M_\infty^2}\left(\frac{p}{p_\infty} - 1\right), \tag{7.27}$$

which is simply an alternative form of the pressure coefficient for compressible flow. Most airfoil pressure distributions are plotted using this definition of C_p.

7.5.2 *Critical Pressure Coefficient*

With this definition of pressure coefficient we can define the critical condition when the minimum pressure reaches the sonic pressure p^* and $M_\infty = M^*$. The critical pressure coefficient is

$$C_p^* = \frac{2}{\gamma (M^*)^2}\left(\frac{p^*}{p_\infty} - 1\right). \tag{7.28}$$

Using the energy equation applied to isentropic flow along a streamline gives

$$\frac{V_\infty^2}{2} + \frac{a_\infty^2}{\gamma - 1} = \frac{V^2}{2} + \frac{a^2}{\gamma - 1}, \tag{7.29}$$

and for the condition when $V = a = a^*$ then

$$\frac{(M^*)^2}{2} + \frac{1}{\gamma - 1} = \left(\frac{a^*}{a_\infty}\right)^2 \left(\frac{1}{2} + \frac{1}{\gamma - 1}\right), \tag{7.30}$$

or

$$\left(\frac{a^*}{a_\infty}\right)^2 = (M^*)^2\left(\frac{\gamma - 1}{\gamma + 1}\right) + \frac{2}{\gamma + 1}. \tag{7.31}$$

But because

$$\frac{p^*}{p_\infty} = \left(\frac{a^*}{a_\infty}\right)^{2\gamma/(\gamma-1)}, \tag{7.32}$$

then substituting into Eq. 7.28 gives

$$C_p^* = \frac{2}{\gamma(M^*)^2}\left[\left(\frac{\gamma-1}{\gamma+1}(M^*)^2 + \frac{2}{\gamma+1}\right)^{\gamma/(\gamma-1)} - 1\right]. \tag{7.33}$$

Note that C_p^* is the pressure coefficient at the point on the airfoil when sonic conditions are first achieved, that is, $M_\infty = M^*$. This point is generally not known a priori and is usually predicted on the basis of the minimum pressure coefficient found from incompressible flow. For this, the well-known Kármán–Tsien relation [see Abbott & von Doenhoff (1949)] can be used where the compressible value C_{p_M} is related to the incompressible value C_{p_i} using

$$C_{p_M} = C_{p_i}\left[\beta + \left(\frac{M_\infty^2}{1+\beta}\right)\left(\frac{C_{p_i}}{2}\right)\right]^{-1}. \tag{7.34}$$

7.5.3 *Synthesis of Chordwise Pressure*

The ideas of synthesizing the distribution of chordwise pressure on the basis of contributions from camber and thickness envelopes are discussed by Abbott & von Doenhoff (1949). The velocity distribution about the airfoil, v/V_∞, can be considered to be composed of three separate and independent contributions that are combined subsequently by linear superposition. These components of loading are: 1. A distribution of velocity v_t/V_∞ corresponding to that of the basic thickness form at zero AoA. 2. A distribution of velocity v_c/V_∞ corresponding to the camberline when operating at its ideal AoA. The ideal AoA corresponds to $-\alpha_0$, where α_0 is the AoA for zero-lift. 3. A distribution of chordwise loading or the "additional" loading v_a/V_∞. This loading closely corresponds to the thin-airfoil result for a flat-plate at AoA, although Abbott & von Doenhoff give tabulated values of v_a/V_∞ for airfoils with finite thickness as obtained from other theoretical methods.

The local loading is equal to the difference in velocity between the upper and lower surfaces of the airfoil. In accordance with the principles of vortex sheets and thin-airfoil concepts, the velocity increment on one side of the airfoil surface is equal to the velocity decrement on the other surface. Therefore, the pressure coefficient can be obtained from

$$C_p = 1 - \left(\frac{v_t}{V_\infty} \pm \frac{v_c}{V_\infty} \pm \frac{v_a}{V_\infty}\right)^2. \tag{7.35}$$

Values for v_t and v_c can be read directly from the tables in Abbott & von Doenhoff (1949). Values of v_c will be tabulated for a specified design lift coefficient. The additional loading is a function of airfoil thickness, and is usually tabulated for a lift coefficient of 1.0. Because the results will usually be required for lift coefficients other than 1.0, they must be scaled by multiplying the values of the additional loading v_a by $f(\alpha)$ where

$$f(\alpha) = \frac{C_l - C_{l_i}}{C_{l_0}}, \tag{7.36}$$

and where C_{l_i} is the ideal lift coefficient, C_l is the desired lift coefficient, and C_{l_0} is the lift coefficient for which the values of v_a were tabulated.

The perturbation velocity distributions for a large number of camberlines and thickness envelopes are tabulated by Abbott & von Doenhoff (1949), and the method of superposition offers a simple and convenient way of constructing estimates of chordwise pressure for any derived airfoil shape. More importantly, however, the technique provides key elements for

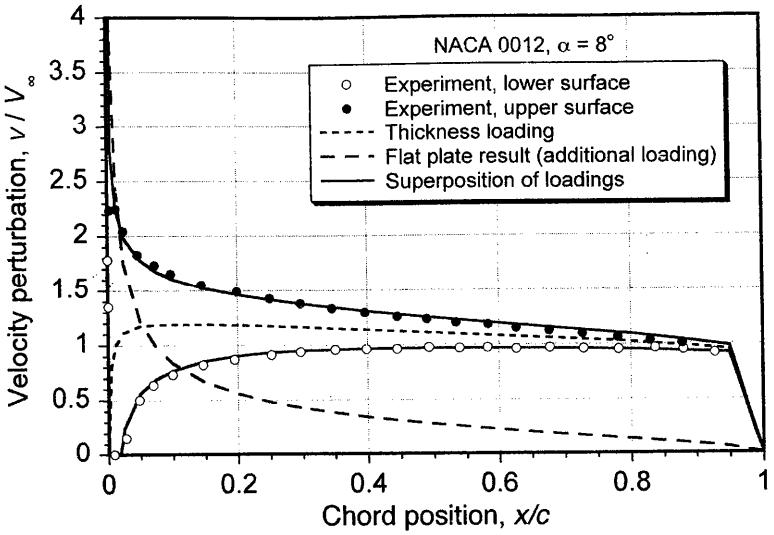

Figure 7.11 Predicted velocity distributions about a NACA 0012 airfoil in low speed (subsonic) flow, $M_\infty = 0.38$, using the NACA method of linear superposition. Data source: Bingham & Noonan (1982).

the understanding of how airfoil shape affects the aerodynamic characteristics. An example of the technique is shown in Fig. 7.11, where the velocity distribution across the chord of a NACA 0012 airfoil is plotted in terms of the constituent parts. We see that the technique gives good agreement with the measurements. However, the technique is obviously restricted to low (subsonic) speeds and low angles of attack where the assumption of linearity can be justified (see also Question 7.4).

In the first instance, the effects of compressibility on the pressure distribution can be predicted using the Glauert rule, which gives the pressure distribution at any Mach number C_{p_M} in terms of the incompressible value C_{p_i} using

$$C_{p_M} = \frac{C_{p_i}}{\beta}, \tag{7.37}$$

which is restricted to conditions below the critical Mach number where linearity in the airloads can be assumed.

7.5.4 *Measurements of Chordwise Pressure*

Representative measurements of chordwise pressure distributions about an airfoil at various angles of attack below stall in a subsonic flow are shown in Fig. 7.12. Although there is a stagnation region over the lower leading edge region where C_p is positive, over most of the airfoil C_p is negative. Note that as the AoA is increased from zero, the pressure reduction on the upper surface increases both in intensity and extent. The high adverse pressure gradients downstream of the leading edge make the boundary layer thicker, and ultimately when the adverse pressure gradients become too large, the boundary layer will separate from the surface causing stall.

With the formation of regions of supercritical (locally supersonic) flow, such as found toward the tip of a rotor blade, the airfoil pressure distribution changes considerably. Measurements of the pressure distribution about an airfoil in a developing transonic flow are

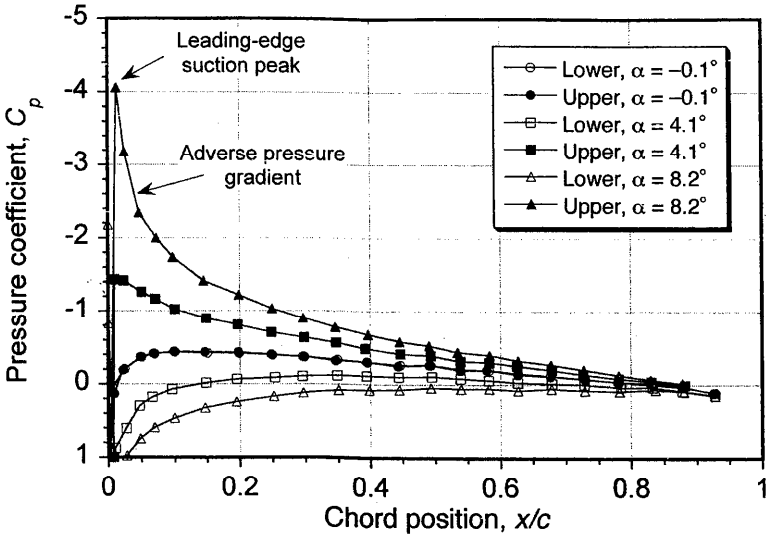

Figure 7.12 Representative pressure distributions about a NACA 0012 airfoil in low speed (subsonic) flow, $M_\infty = 0.38$. Data source: Bingham & Noonan (1982).

plotted in Fig. 7.13 for a condition where the flow is just supercritical ($M_\infty = 0.68$) and also for a supercritical condition ($M_\infty = 0.77$). The large adverse pressure gradients found near the leading edge in the subsonic case now move further aft to near the mid-chord of the airfoil, which is a result of the formation of a supersonic flow region and a shock wave. The adverse pressure gradients near the shock wave make the boundary layer on the surface more susceptible to thickening and separation, resulting in higher drag. When the shock wave becomes stronger, flow separation will occur at the foot of the shock and the airfoil will ultimately stall if the AoA is increased any further.

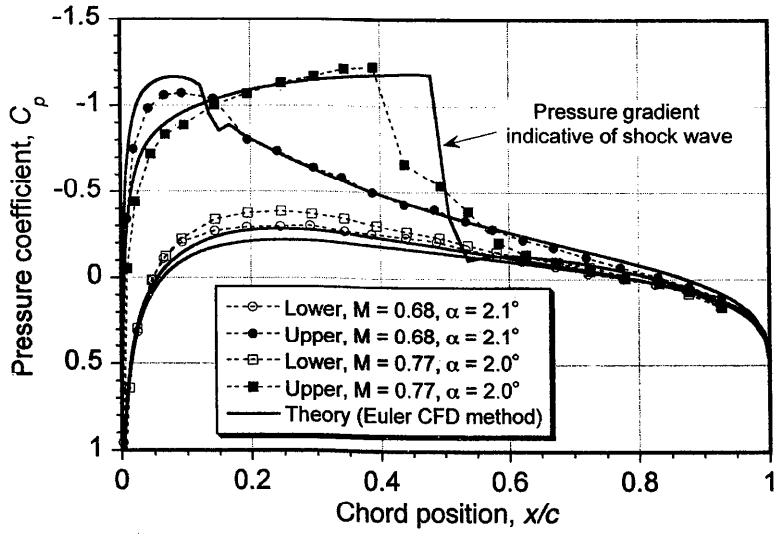

Figure 7.13 Representative chordwise pressure distribution about an airfoil in a developing transonic flow. NACA 0012, $\alpha \approx 2°$, with $M_\infty = 0.68$ and $M_\infty = 0.77$. Data source: Bingham & Noonan (1982).

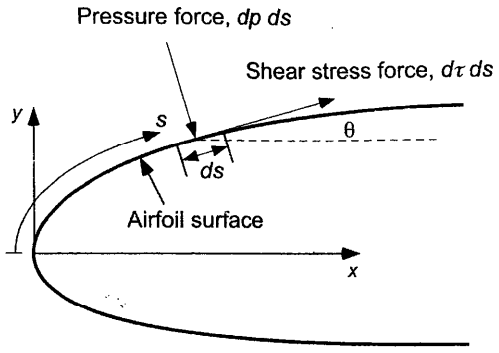

Figure 7.14 Pressure and shear forces acting on an element of the airfoil surface.

7.6 Aerodynamics of a Representative Airfoil Section

The resultant forces and moments acting on a typical section of the blade are the net result of the action of the distributed pressure and viscous shear forces, as shown schematically by Fig. 7.14. These forces and moments are obtained by integrating the local values of pressure and shear stress acting normal and parallel to the surface around the airfoil. The forces can be resolved into a wind-axis system (lift and drag) or a chord-axis system (normal force and chord force), as shown in Fig. 7.15. The lift force per unit length, L, acts normal to the velocity, V_∞, and the drag, D, is parallel to V_∞. Alternatively, this lift force can be decomposed into the sum of two other forces as shown in Fig. 7.15: the normal force, N, which acts normal to the airfoil chord, and the leading edge suction force or axial chord force, A, which points upstream and acts parallel to the chord.

7.6.1 *Integration of Distributed Forces*

Surface shear contributions to the normal force and the pitching moment are small and can usually be neglected. For the axial and drag forces, the shear stress contribution has a measurable effect and should always be included. If we consider the pressure forces

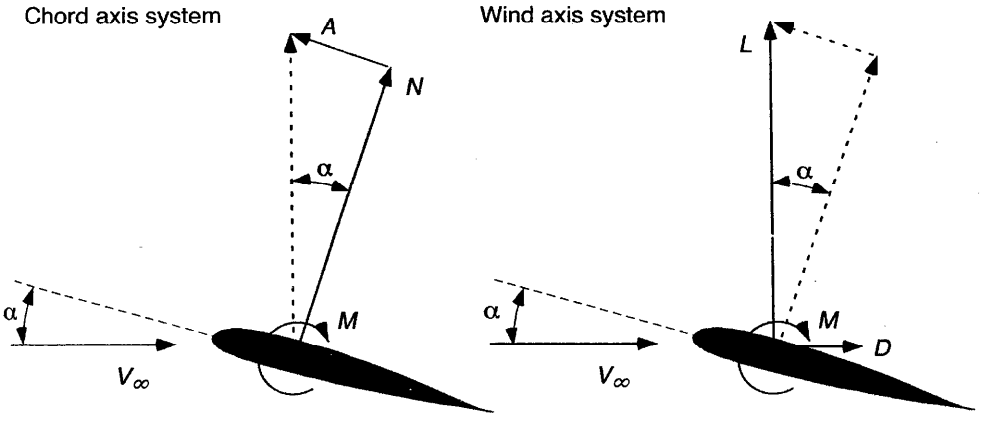

Figure 7.15 Decomposition of distributed surface pressure into resultant forces and moments on an airfoil.

alone, then on the upper surface

$$dN_u = -p_u ds_u \cos\theta_u, \quad \text{and} \quad dA_u = -p_u ds_u \sin\theta_u, \tag{7.38}$$

where θ is the local surface slope. On the lower surface

$$dN_l = p_l ds_l \cos\theta_l, \quad \text{and} \quad dA_l = p_l ds_l \sin\theta_l. \tag{7.39}$$

Integrating gives the normal and leading edge suction (axial) forces, respectively

$$N = -\int_{LE}^{TE} p_u \cos\theta \, ds_u + \int_{LE}^{TE} p_l \cos\theta \, ds_l, \tag{7.40}$$

$$A = -\int_{LE}^{TE} p_u \sin\theta \, ds_u + \int_{LE}^{TE} p_l \sin\theta \, ds_l, \tag{7.41}$$

and the moment about the leading edge by

$$M_{LE} = \int_{LE}^{TE} (p_u x \cos\theta + p_l y \sin\theta) ds_u - \int_{LE}^{TE} (-p_l x \cos\theta + p_u y \sin\theta) ds_l. \tag{7.42}$$

The lift and the pressure drag are obtained by resolving the chordwise (axial) and normal forces through the AoA α to give

$$L = N\cos\alpha + A\sin\alpha, \tag{7.43}$$

$$D = N\sin\alpha - A\cos\alpha. \tag{7.44}$$

The corresponding force and moment coefficients are defined as

$$C_n = \frac{N}{q_\infty c}, \quad C_a = \frac{A}{q_\infty c}, \quad C_m = \frac{M}{q_\infty c^2}, \quad C_l = \frac{L}{q_\infty c}, \quad \text{and} \quad C_d = \frac{D}{q_\infty c}, \tag{7.45}$$

where c is the airfoil reference chord. For a thin-airfoil this gives the normal, suction, and moment coefficients in terms of the pressure coefficient C_p:

$$C_n = \frac{1}{c}\int_0^c (C_{p_l} - C_{p_u}) dx = \frac{1}{c}\int_0^c \Delta C_p dx = \int_0^1 \Delta C_p d\bar{x}, \tag{7.46}$$

$$C_a = \frac{1}{c}\int_0^c \left(\frac{dy_l}{dx} C_{p_l} - \frac{dy_u}{dx} C_{p_u}\right) dx, \tag{7.47}$$

$$C_{m_{LE}} = -\frac{1}{c^2}\int_0^c (C_{p_l} - C_{p_u}) x dx = -\frac{1}{c^2}\int_0^c \Delta C_p x dx = -\int_0^1 \Delta C_p \bar{x} d\bar{x}. \tag{7.48}$$

The normal force coefficient can generally be used interchangeably with the lift coefficient in the low AoA regime. This can be seen by resolving the normal force and axial chord forces in the lift direction, that is

$$C_l = C_n \cos\alpha + C_a \sin\alpha. \tag{7.49}$$

Also, for 2-D potential flow we notice that $C_a = C_n \tan\alpha$ (which follows from the fact that $C_d = 0$), so that

$$C_l = C_n \cos\alpha + C_n \tan\alpha \sin\alpha = C_n \cos\alpha + O(\alpha^2) \approx C_n. \tag{7.50}$$

For low to moderate angles of attack (i.e., for angles of attack less than 15°) C_l and C_n have almost the same numerical values.

7.6.2 *Pressure Integration*

The accuracy with which the values of C_n, C_a, and C_m can be measured (or computed) depends on the number and location of the pressure points over the airfoil surface. A typical subsonic pressure distribution is shown in Fig. 7.16 and is compared to theory based on a standard panel method solution. The agreement is good, and any slight differences can likely be attributed to experimental uncertainty and wind tunnel interference effects. For subsonic flows, the suction peak and high adverse pressure gradients occur near the leading edge, so that there must be a bias of pressure points in the leading edge region to minimize

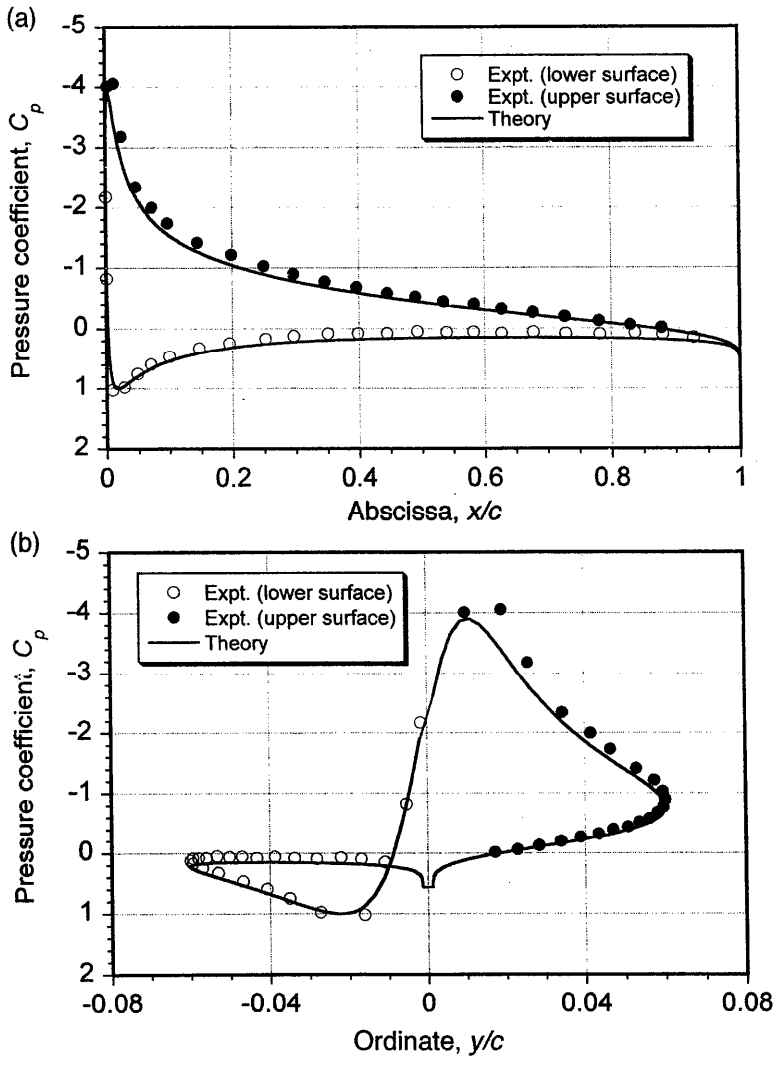

Figure 7.16 Representative airfoil pressure distributions in subsonic flow. (a) C_p versus chord dimension, x/c. (b) C_p versus ordinate, y/c. NACA 0012, $\alpha = 8.2°$. Data source: Bingham & Noonan (1982).

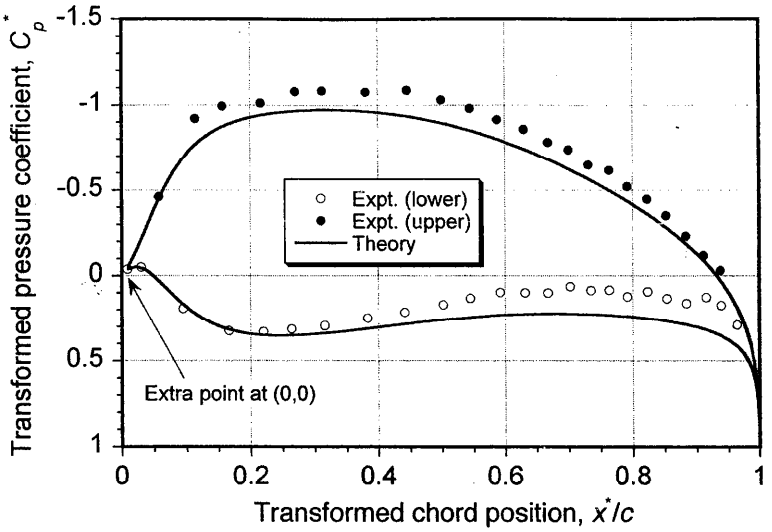

Figure 7.17 Transformation of chordwise pressure distribution to aid in numerical integration. NACA 0012, $\alpha = 8.2°$. Data source: Bingham & Noonan (1982).

errors in the integration process to find the forces and moments. At higher subsonic speeds and when transonic flow develops over the airfoil, the largest pressure gradients occur downstream of the leading edge, usually near any shock waves. Therefore, the pressure points must be relocated to this region to adequately resolve the pressure distribution and maintain the accuracy in the calculation of the integrated loads. While numerically this can be easily done by respecifying the locations where C_p is to be calculated, in an experiment this is not usually possible because relocating pressure instrumentation on a wing or airfoil section can be expensive or impractical. Note from Fig. 7.16(b) that the integration with respect to airfoil thickness becomes particularly difficult if the suction peak and pressure gradients are not adequately resolved.

Special interpolation methods can sometimes be used to maintain accuracy in the calculation of total forces and moments from discrete pressure points, as long as this is done with caution. One way of improving the accuracy with sparse numbers of points in the leading edge region is to apply a transformation to the measured or computed pressure distribution. One such transformation is

$$C_p^* = 2C_p\sqrt{x/c} \quad \text{and} \quad x^*/c = \sqrt{x/c}, \tag{7.51}$$

which is used by St. Hillaire et al. (1979) and McCroskey et al. (1982). The transformed variables C_p^* and x^*/c are then plotted in the conventional way. This transformation has the effect of providing a better definition of the leading edge pressure peak, as shown by Fig. 7.17, and also generating an additional point at $(x^*/c, C_p^*) = (0, 0)$. The coefficients C_n and $C_{m_{LE}}$ are given in terms of the transformed variables by

$$C_n = \int_0^1 \Delta C_p^* \, d(x^*/c) \quad \text{and} \quad C_{m_{LE}} = -\int_0^1 \Delta C_p^* (x^*/c)^2 d(x^*/c). \tag{7.52}$$

7.6.3 *Representative Force and Moment Results*

The data plotted in Fig. 7.18 show the low speed lift force coefficient, 1/4-chord pitching moment coefficient, and drag coefficient variations as functions of AoA for the

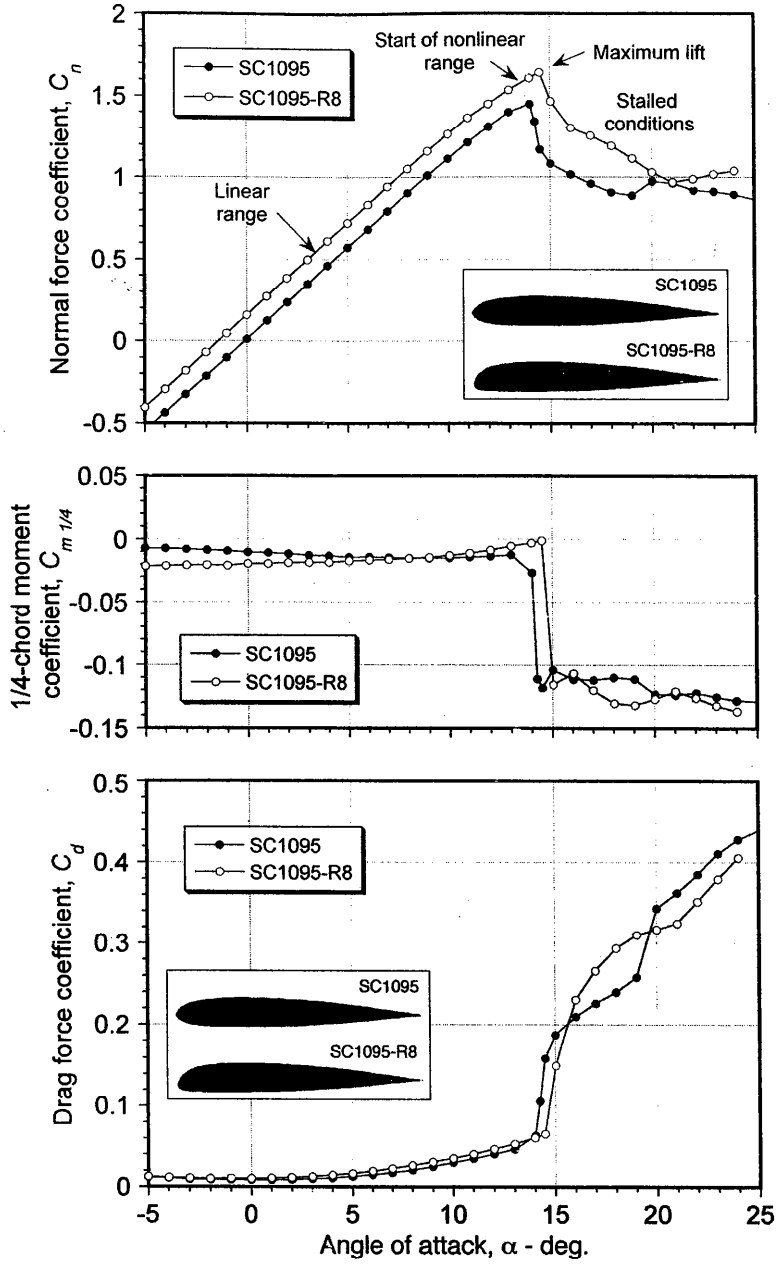

Figure 7.18 Variation of C_n, C_m, and C_d with AoA for the SC1095 and SC1095-R8 airfoils at $M = 0.3$ and $Re = 3 \times 10^6$. Source: Leishman (1996).

SC1095 and SC1095-R8 airfoils at $M = 0.3$.[1] The results are shown over an extended AoA that ranges from fully attached flow, where the lifting characteristics of an airfoil below stall are not substantially influenced by the presence of the boundary layer, to the fully stalled conditions where the flow has detached from the upper surface of the airfoil.

[1] The SC1095-R8 has a modified nose shape and a slightly smaller thickness-to-chord ratio than the SC1095. For this reason, it is sometimes referred to as the SC1094-R8 – see Flemming (1982).

Below stall the resultant pressure forces on the airfoil are only slightly affected by the thickness and camber of the airfoil (provided they are small) and this is usually the case for most rotor airfoils. The lift on the airfoil section is proportional to its AoA and the local dynamic pressure. The lift per unit span of the blade can be written as

$$L = \frac{1}{2}\rho_\infty V_\infty^2 c C_l = \frac{1}{2}\rho_\infty V_\infty^2 c C_{l_\alpha}(\alpha - \alpha_0), \tag{7.53}$$

where C_{l_α} is the lift-curve-slope and is measured in per degree or per radian AoA. In coefficient form then

$$C_l = C_{l_\alpha}(\alpha - \alpha_0) \quad \text{in the low } \alpha \text{ range}, \tag{7.54}$$

where α_0 is the AoA for zero lift or the zero-lift angle. The above relation comes under the category of *linearized* aerodynamics. For a real fluid, the lift varies linearly with AoA and is within about 10% of the above relation up to an angle of about 10–15°, depending on the Mach number and Reynolds number. Figure 7.18 shows that above a certain angle, the lift decreases and the pitching moment becomes increasingly negative (nose-down). This is a result of the onset of flow separation on the upper surface of the airfoil, which moves the center of pressure aft on the chord.

The effects of compressibility manifest as an increase in the effective AoA, which increases the lift on the airfoil. In other words, the effects of increasing Mach number appear as an increase in lift-curve-slope. In linearized subsonic flow, this increase in lift-curve-slope is given mathematically by the Prandtl–Glauert or Glauert rule [see Glauert (1927, 1947)], where

$$C_{l_\alpha}(M_\infty) = \frac{2\pi}{\sqrt{1 - M_\infty^2}} = \frac{2\pi}{\beta}, \tag{7.55}$$

where 2π is the lift-curve-slope in incompressible flow and the Glauert factor is $\beta = \sqrt{1 - M_\infty^2}$, with M_∞ as the free-stream Mach number. The Glauert correction factor is found to give good agreement with experimental measurements of the lift-curve-slope of airfoils of thin to moderate thickness-to-chord ratio, and will be a sufficiently accurate correction to apply in practice. An example is shown in Fig. 7.19 where the lift-curve-slope for several airfoils in the NACA 00-series is plotted versus Mach number. The agreement with the Glauert factor is generally good for thinner airfoils (in accordance with its derivation) and/or up until the critical Mach number, M^*. Beyond this, the developments of shock waves and their interactions with the boundary layer produce a reduction in the lift-curve-slope throughout the transonic range.

Kaplan (1946) suggests an improvement to the Glauert correction using the rule

$$C_{l_\alpha}(M_\infty) = \frac{2\pi}{\beta} + \frac{2\pi\,(t/c)}{1 + (t/c)}\left[\frac{1}{\beta}\left(\frac{1}{\beta} - 1\right) + \frac{1}{4}(\gamma + 1)\left(\frac{1}{\beta^2} - 1\right)^2\right], \tag{7.56}$$

where the second term represents the effects of thickness-to-chord ratio t/c. The Kaplan rule, however, tends to overpredict the magnitude of $C_{l_\alpha}(M_\infty)$ when compared to measurements and suggests a small further increase in C_{l_α} with increases in airfoil thickness. In practice the theoretical value of the lift-curve-slope can replaced by $2\pi\eta_l$ (where η_l can be viewed as an efficiency factor) to account for such effects.

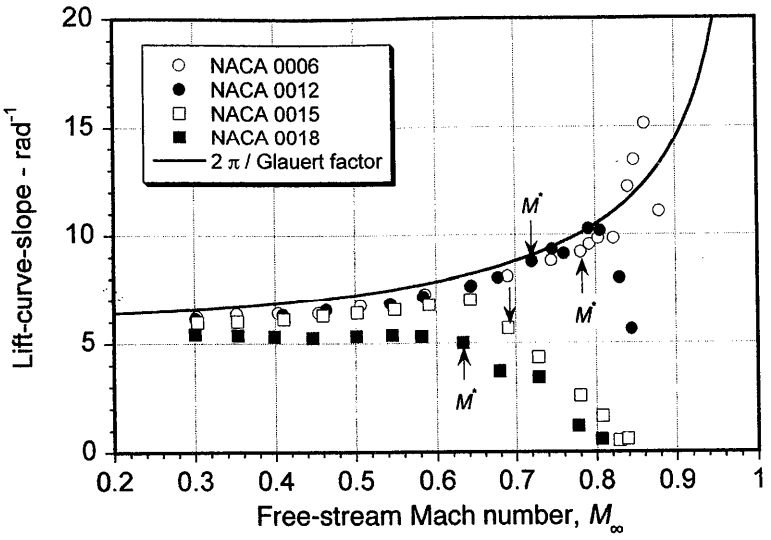

Figure 7.19 Comparison of measured lift-curve-slope for the NACA 00-series with predictions made by using Glauert factor. Data source: Riegels (1961).

7.7 Pitching Moment and Related Issues

Because the pitching moment can be sensitive to small changes in the chordwise pressure distribution, its variation with AoA can be difficult to compute accurately. It may be estimated experimentally by direct measurement from a balance or by the integration of chordwise pressure about some reference point, as described previously. In either case, the pitching moment coefficient depends on the reference point chosen. For helicopter work, the 1/4-chord point is normally used. Converting from one reference point to another uses the rules of statics. For example, assume the normal force and pitching moment are known at a point a distance x_a from the leading edge of the airfoil and it is desired to find the pitching moment about another point, say at a distance x behind the leading edge (see Fig. 7.20). Taking moments about the airfoil leading edge in each case gives

$$M_x = M_a + N(x - x_a). \tag{7.57}$$

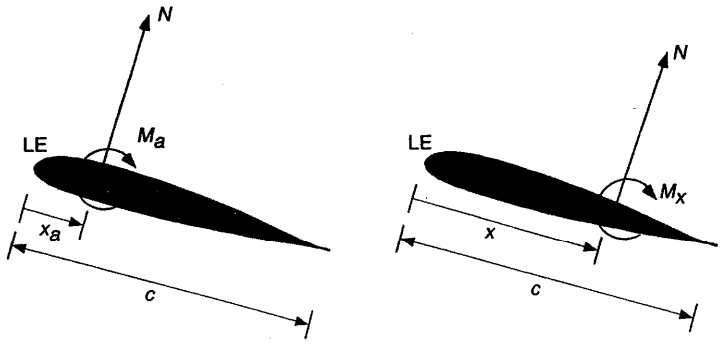

Figure 7.20 Equivalent point loadings on an airfoil.

Converting to coefficient form by dividing by $\frac{1}{2}\rho_\infty V_\infty^2 c^2$ gives

$$C_{m_x} = C_{m_a} + C_n\left(\bar{x} - \bar{x}_a\right). \tag{7.58}$$

As an example, if the known pitching moment is about the leading edge, $C_{m_{LE}}$, then $\bar{x}_a = 0$ and the above equation becomes

$$C_{m_x} = C_{m_{LE}} + \bar{x}C_n. \tag{7.59}$$

7.7.1 *Aerodynamic Center*

There is one special point on an airfoil for which it is found that C_m is constant and independent of the AoA. This point is called the *aerodynamic center*. For angles of attack up to a few degrees below the stalling angle it is a fixed point on the chord and is relatively close to 1/4-chord. For a flat-plate airfoil in inviscid, incompressible flow, the aerodynamic center is theoretically on the 1/4-chord axis. However, the thickness of the airfoil and viscous effects because of the development of a boundary layer usually cause the aerodynamic center to move a few percentages further forward or aft of the 1/4-chord.

The aerodynamic center on an airfoil can be found with a knowledge of the normal force coefficient and the moment coefficient about any other known point. If the aerodynamic center is assumed to lie at a distance x_{ac} behind the leading edge, then

$$C_{m_a} = C_{m_{ac}} + C_n\left(\frac{x_a}{c} - \frac{x_{ac}}{c}\right) = C_{m_{ac}} + C_n\left(\bar{x}_a - \bar{x}_{ac}\right). \tag{7.60}$$

Differentiating the above equation with respect to C_n gives

$$\frac{dC_{m_a}}{dC_n} = \frac{dC_{m_{ac}}}{dC_n} + \left(\bar{x}_a - \bar{x}_{ac}\right). \tag{7.61}$$

By definition, the aerodynamic center is that point about which the moment is independent of C_n and so the first term on the right hand side is zero. Therefore,

$$\bar{x}_{ac} = \bar{x}_a - \frac{dC_{m_a}}{dC_n}. \tag{7.62}$$

We can obtain dC_{m_a}/dC_n by using the result

$$\frac{dC_{m_a}}{dC_n} = \frac{dC_{m_a}}{d\alpha}\frac{d\alpha}{dC_n}, \tag{7.63}$$

or if C_{m_a} is plotted versus C_n and the slope of the best straight line is found, then the aerodynamic center can be determined by using Eq. 7.62.

Representative results are shown in Fig. 7.21. In the attached flow regime, the data lie on a straight line, the slope of which gives the offset of the aerodynamic center from the 1/4-chord axis. For the SC1095 airfoil at this Mach number and Reynolds number, the aerodynamic center is located at approximately 25.6% chord, and for the SC1095-R8 the aerodynamic center is at 24.7% chord.

The effects of compressibility tend to move the aerodynamic center further aft of the 1/4-chord, and for supersonic flow the aerodynamic center is situated near 50% chord. The measured behavior of the NACA 00-series airfoils is shown in Fig. 7.22, where it is apparent that the aerodynamic center initially tends to drift slightly forward with increasing Mach number. The explanation for this behavior lies in the effects of the pressure distribution on the developing boundary layer. Higher Mach numbers tend to form a pressure distribution

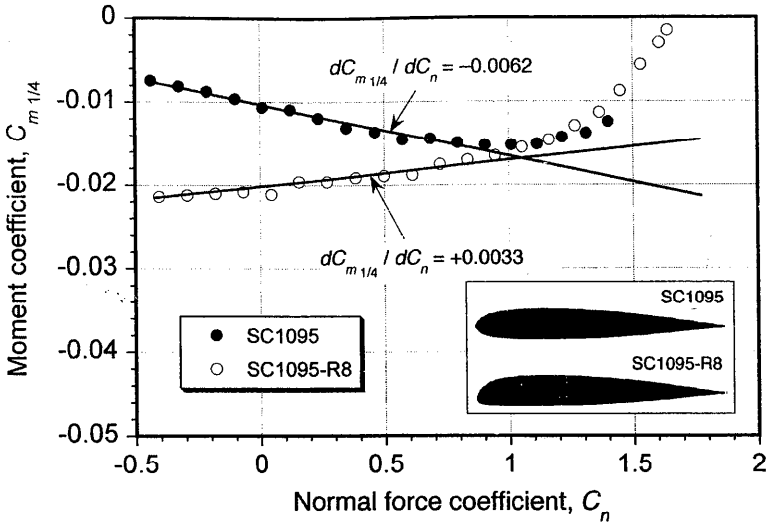

Figure 7.21 Variation of $C_{m_{1/4}}$ with C_n for SC1095 and SC1095-R8 airfoils at $M_\infty = 0.3$. Data source: Leishman (1996).

that resembles one about an airfoil with a higher thickness ratio. Thin airfoils, such as the NACA 0006, tend to have an aerodynamic center that remains close to the theoretical flat-plate value of 1/4-chord. Also, because of the higher critical Mach number of thin sections, the onset of shock waves is delayed and so the aft movement of the aerodynamic center occurs at relatively higher subsonic Mach numbers. When shock waves do occur (see Fig. 7.9), the movement of the aerodynamic center is dictated by the relative position of the upper and lower surface shock waves. Because these positions will be a function of both airfoil shape and AoA, a simple generalization of the aerodynamic center position in the transonic regime is usually not possible.

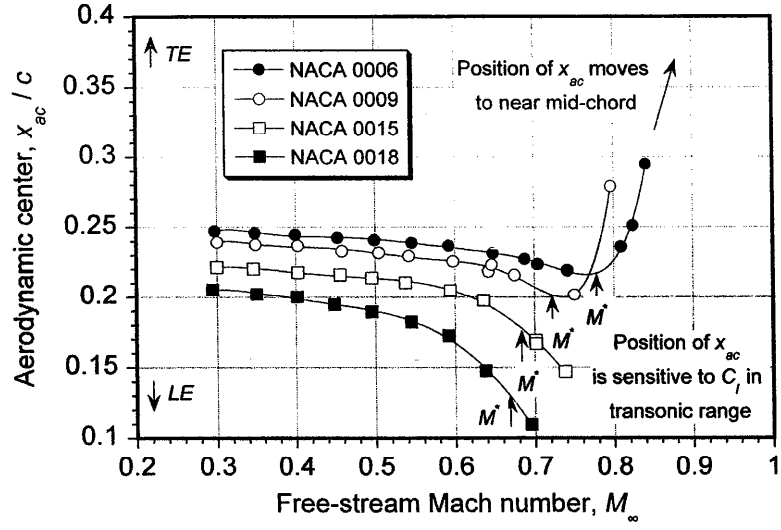

Figure 7.22 Variation of aerodynamic center with Mach number for NACA 00-series airfoil sections. Data source: Riegels (1961).

7.7.2 *Center of Pressure*

As shown previously by means of Fig. 7.15, the net aerodynamic loads on an airfoil may be represented by a normal force, an axial force (leading edge suction or chord force), and a pitching moment. For each value of the normal force a single point can be determined about which the pitching moment is zero. Therefore, the loading on the airfoil can be replaced only by normal and axial (chord) forces acting at this point, which is called the *center of pressure*. The aerodynamic center is a fixed point on the airfoil at a given Mach number and below stall, but the center of pressure moves to different locations on the chord with changes in AoA. For example, we may find the center of pressure, x_{cp}, on an airfoil using the normal force and pitching moment about the 1/4-chord. Using Fig. 7.20 with $x_a = c/4$ and $x = x_{cp}$, we take moments about the leading edge to obtain

$$M_{LE} = \left(M_{1/4} - N\right)\frac{c}{4} = -Nx_{cp}, \tag{7.64}$$

and in coefficient form this becomes

$$C_{m_{1/4}} = C_n\left(\frac{1}{4} - \bar{x}_{cp}\right), \tag{7.65}$$

so that the center of pressure is given by

$$\bar{x}_{cp} = \frac{1}{4} - \frac{C_{m_{1/4}}}{C_n}. \tag{7.66}$$

The coefficient $C_{m_{1/4}}$ is generally negative, so that the center of pressure will be behind the aerodynamic center. This effect is shown in Fig. 7.23, where it will also be noticed that the center of pressure moves forward and approaches the aerodynamic center (which is near 1/4-chord) for higher values of C_n, but below stall. After the airfoil stalls, the center of pressure stabilizes and approaches mid-chord. This reflects the form of the pressure distribution over the upper surface of the airfoil, which is much more uniform when the flow is separated.

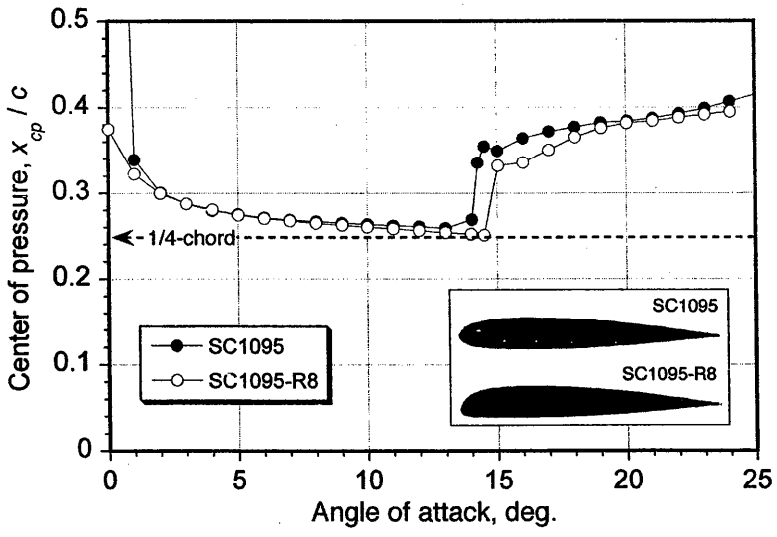

Figure 7.23 Variation of center of pressure for the SC1095 and SC1095-R8 airfoils at $M_\infty = 0.3$. Data source: Leishman (1996).

Table 7.3. *Variation in Lift and Moment Coefficients for Example Airfoil*

AoA (deg.)	−2	0	2	4	6	8	10
C_l	−0.16	0.06	0.28	0.50	0.72	0.94	1.16
$C_{m_{1/3}}$	−0.03	−0.01	0.01	0.03	0.05	0.07	0.09

Consider an example to illustrate the forgoing concepts of aerodynamic center and center of pressure. If the results of the lift coefficient and the pitching moment about 1/3-chord as a function of AoA are given in Table 7.3 then it is possible to determine the position of the aerodynamic center and the variation of the center of pressure as a function of AoA. In addition, it is possible to determine the lift-curve-slope, the zero-lift AoA and the zero-lift pitching moment.

By inspection, we see that the lift-curve-slope, C_{l_α}, is exactly 0.11 per degree. We can write a simple linear relationship for the lift-coefficient that $C_l = C_{l_\alpha}(\alpha - \alpha_0)$ where α_0 is the zero-lift angle. It is easy to determine α_0 from any known value of C_l. For example, when $\alpha = 0$ then from the table $C_l = 0.06$ so that $\alpha_0 = -0.06/0.11 = -0.45°$. By inspection, the slope of the $C_{m_{1/3}}$ by α curve is exactly 0.01 per degree. We can find the zero-lift pitching moment coefficient by using the equation

$$C_{m_0} = C_{m_{1/3}} - \left(\frac{dC_{m_{1/3}}}{d\alpha}\right)(\alpha - \alpha_0). \tag{7.67}$$

Using the result, for example, that $C_{m_{1/3}} = -0.01$ when $\alpha = 0$ gives that

$$C_{m_0} = -0.01 - 0.01\big(0.0 - (-0.45)\big) = -0.0145. \tag{7.68}$$

The position of the aerodynamic center can be found from the lift and pitching moment about any known point using Eq. 7.62. In this case, we use the equation

$$\bar{x}_{ac} = \frac{1}{3} - \left(\frac{dC_{m_{1/3}}}{dc_l}\right) = \frac{1}{3} - \left(\frac{dC_{m_{1/3}}}{d\alpha}\right)\left(\frac{d\alpha}{dC_l}\right). \tag{7.69}$$

Substituting in the appropriate values leads to $\bar{x}_{ac} = 0.333 - 0.01/0.11 = 0.242$. Finally, the center of pressure can be found from the equation

$$\bar{x}_{cp} = \frac{1}{3} - \frac{C_{m_{1/3}}}{C_l}, \tag{7.70}$$

the results from which are given in Table 7.4. Notice again that the center of pressure comes closer to the aerodynamic center for larger values of C_l (but below stall).

7.7.3 *Effect of Airfoil Shape on Pitching Moment*

The effect of the airfoil shape on the pitching moment characteristics is of utmost concern for the design of helicopter rotors. As mentioned earlier, experiences with cambered airfoils on early autogiros resulted in significant blade twisting and high control loads. For

Table 7.4. *Variation in Center of Pressure for Example Airfoil*

AoA (deg.)	−2	0	2	4	6	8	10
$\bar{x}_{cp}$	0.146	0.500	0.298	0.273	0.264	0.259	0.256

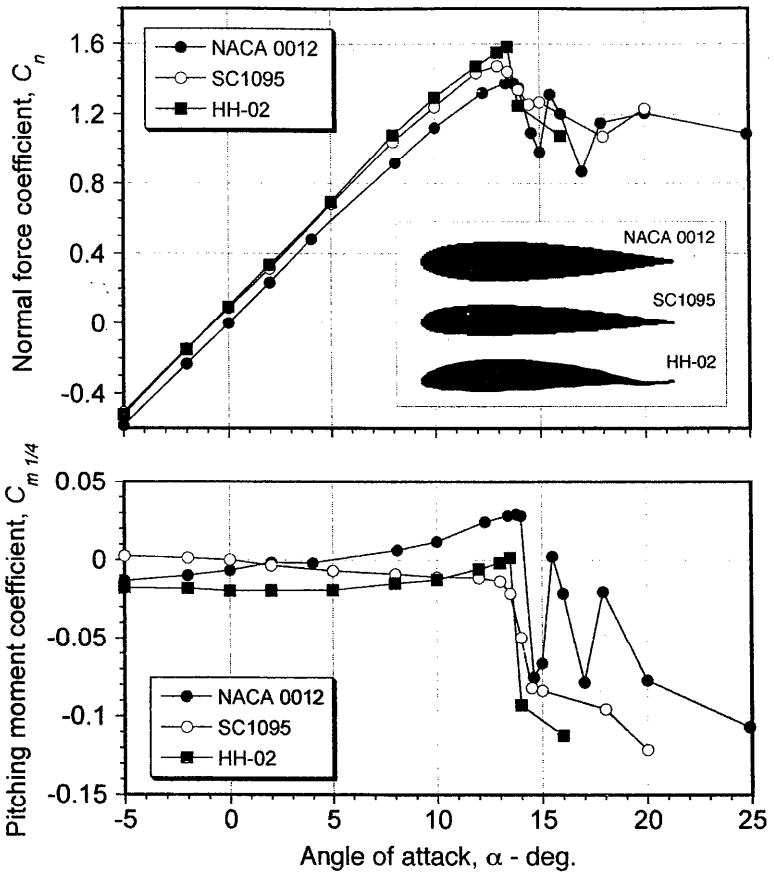

Figure 7.24 Comparison of lift and pitching moments on symmetric and cambered airfoils at $M_\infty = 0.3$. Data source: McCroskey et al. (1982).

many years, this led to the exclusive use of conservative, low pitching moment (symmetrical) sections on nearly all helicopters. Today, blades are torsionally stiffer because they are made of composite materials and control systems can also be made stiffer without a weight penalty. This has allowed the better high lift capabilities of cambered airfoils to be utilized on modern helicopter blades.

Figure 7.24 shows lift and pitching moment results for a NACA 0012 in comparison with two cambered helicopter rotor airfoils, one with a relatively small amount of camber (the SC1095) and one with a larger amount of camber (the HH-02). Both the NACA 0012 and SC1095 airfoils have relatively low zero-lift pitching moments, C_{m_0}, whereas the HH-02 has a higher pitching moment. The actual moments that can be tolerated on a given rotor blade depends on structural and other requirements, as well as the type of hub and control system. Traditionally, various individual airfoils have been developed based on the minimization of C_{m_0}. But by allowing radially varying airfoil sections on the blade, pitching moment limits placed on the airfoil section itself can be relaxed somewhat; the main requirement is that the resultant moment that is reacted by the blade and control system be minimized as much as possible. As described in Chapter 6, this is sometimes accomplished by using a reflex cambered airfoil at the inboard sections of the blade where the need for a high maximum lift coefficient is not as stringent.

The effect of camber and chordwise position of maximum camber can be readily studied using the thin-airfoil theory (see Section 14.8 for the equations). The NACA four-digit airfoils have a camberline that can be conveniently expressed in terms of two parabolic arcs that are tangent at the position of maximum camber. The camberline is defined by

$$\bar{y}_c = \frac{m}{p^2}(2p\bar{x} - \bar{x}^2) \quad \text{for } \bar{x} \le p, \tag{7.71}$$

$$\bar{y}_c = \frac{m}{(1-p)^2}[(1-2p) + 2p\bar{x} - \bar{x}^2] \quad \text{for } \bar{x} \ge p, \tag{7.72}$$

where m is the maximum camber and p is the position of maximum camber, both as fractions of the chord. For example, the NACA 2412 airfoil has 2% camber at 40% chord with a thickness ratio of 12%. To use the thin-airfoil theory, the slope of the camberline is required. Differentiating the expressions for y_c gives

$$\frac{d\bar{y}_c}{d\bar{x}} = \frac{2m}{p^2}(p - \bar{x}) \quad \text{for } \bar{x} \le p, \tag{7.73}$$

$$\frac{d\bar{y}_c}{d\bar{x}} = \frac{2m}{(1-p)^2}(p - \bar{x}) \quad \text{for } \bar{x} \ge p, \tag{7.74}$$

and converting to an angular coordinate using $\theta = \cos^{-1}(1 - 2\bar{x})$ gives

$$\frac{d\bar{y}_c}{d\bar{x}} = \frac{m}{p^2}(2p - 1 + \cos\theta) \quad \text{for } \theta \le \theta_p, \tag{7.75}$$

$$\frac{d\bar{y}_c}{d\bar{x}} = \frac{m}{(1-p)^2}(2p - 1 + \cos\theta) \quad \text{for } \theta \ge \theta_p. \tag{7.76}$$

The thin-airfoil theory gives the pitching moment about the 1/4-chord as $C_{m_{1/4}} \equiv C_{m_0} = -\pi(A_1 - A_2)/4$, where

$$\begin{aligned} A_1 &= \frac{2}{\pi}\int_0^{\pi} \frac{d\bar{y}_c}{d\bar{x}} \cos\theta d\theta \\ &= \frac{2m}{\pi p^2}\left[(2p-1)\sin\theta_p + \frac{1}{4}\sin 2\theta_p + \frac{\theta_p}{2}\right] \\ &\quad - \frac{2m}{\pi(1-p)^2}\left[(2p-1)\sin\theta_p + \frac{1}{4}\sin 2\theta_p - \frac{1}{2}(\pi - \theta_p)\right], \end{aligned} \tag{7.77}$$

$$\begin{aligned} A_2 &= \frac{2}{\pi}\int_0^{\pi} \frac{d\bar{y}_c}{d\bar{x}} \cos 2\theta d\theta \\ &= \left(\frac{m}{\pi p^2} - \frac{m}{\pi(1-p)^2}\right)\left[(2p-1)\sin 2\theta_p + \sin\theta_p - \frac{1}{3}\sin^3\theta_p\right]. \end{aligned} \tag{7.78}$$

The results are summarized in Fig. 7.25 where the zero-lift pitching moment coefficient is plotted versus the point of maximum camber, p. Notice that forward camber has a much smaller effect on the pitching moment compared to camber applied near the trailing edge of the airfoil. Generally, the thin-airfoil theory will tend to slightly overpredict the pitching moment because of viscous effects, but the trends are correct.

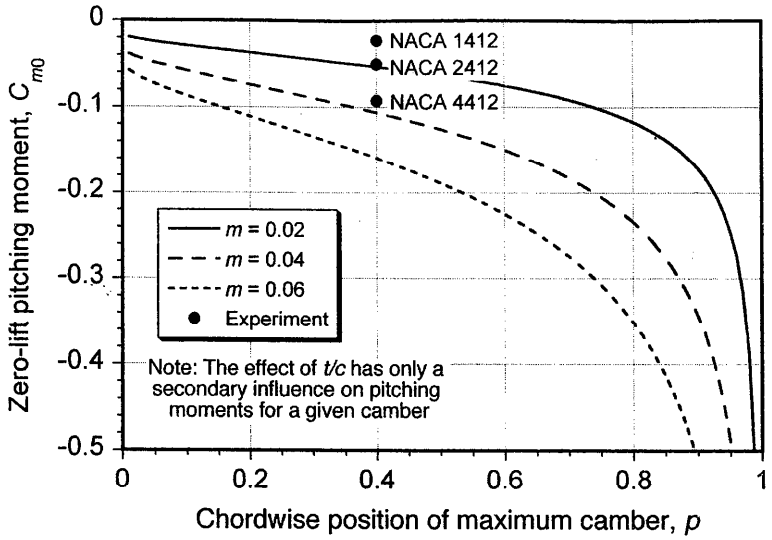

Figure 7.25 Effect of chordwise position of maximum camber on pitching moment for the NACA 4-digit airfoils. Data source: Abbott & von Doenhoff (1949).

7.7.4 *Use of Trailing Edge Tabs*

On helicopter airfoils, trailing edge tabs are frequently used to help negate the pitching moment produced by positive camber over the leading edge nose region, while retaining the benefits of a high maximum lift achieved by the use of camber. An example is the HH-02 shown previously in Fig. 7.24. As shown in Fig. 7.25, the mean camberline near the trailing edge affects significantly the pitching moment, and also the zero lift angle of the section is altered. On early helicopter rotors, trailing edge tabs were used to move the aerodynamic center further aft to help control or delay the onset of torsional flutter. Today, this is done by better airfoil design. Furthermore, an aft aerodynamic center is desirable as less nonstructural mass has to be installed in the blade to achieve the proper net moment balance about the elastic axis of the blade for aeroelastic stability reasons.

By means of the thin-airfoil theory (Section 14.8) the contributions to the lift and moment from the tab can be obtained for a given tab size and angle of deflection. The problem was first examined experimentally by Wenzinger (1935). Assume that the ratio of the tab chord to the airfoil chord is given by E, as shown in Fig. 7.26, and the tab deflection angle is η. An upward deflection of a tab makes the ordinates of the mean camberline more positive in the trailing edge region. As a consequence, the zero lift angle becomes more positive, and the lift and net pitching moment are reduced for a given AoA. The curvature of the camberline is zero for $\bar{x} \leq (1 - E)$ and takes a value η for $\bar{x} > (1 - E)$. Thin airfoil theory gives for the A_0 coefficient

$$A_0 = -\frac{1}{\pi}\int_0^{\pi} \frac{dy}{dx} d\theta = -\frac{1}{\pi}\int_{\theta_t}^{\pi} \eta d\theta = \left(\frac{\theta_t}{\pi} - 1\right)\eta, \tag{7.79}$$

where θ_t is the value of θ at the tab, that is, $\theta_t = \cos^{-1}(2E - 1)$. In a similar way, A_1 and A_2 can be evaluated as

$$A_1 = \frac{2\eta}{\pi}\sin\theta_t \qquad \text{and} \qquad A_2 = \frac{\eta}{\pi}\sin\theta_t. \tag{7.80}$$

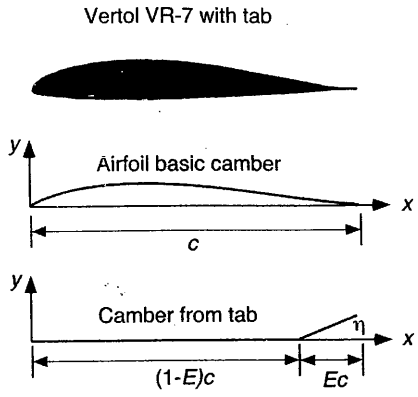

Figure 7.26 Airfoil with a trailing-edge tab and thin airfoil model.

The incremental lift and moment from tab deflection can, therefore, be written as

$$\frac{dC_l}{d\eta} = -2(\pi - \theta_t - \sin\theta_t) \quad \text{and} \quad \frac{dC_{m_{1/4}}}{d\eta} = -\frac{1}{2}\sin\theta_t(\cos\theta_t - 1). \tag{7.81}$$

Figure 7.27 shows the results of tab deflection on the lift and moment as a function of the ratio of the tab to airfoil chord. Experimental results, which have been collated by Prouty (1986), correlate reasonably well with the predictions made by thin-airfoil theory. The larger tabs have the ability to produce sizable pitching moments, but without any significant penalty in terms of maximum lift. There are no significant drag penalties associated with trailing edge tabs (or flaps) provided the tab deflection remains below 5°. If the deflection angle is significant, the adverse pressure gradients found in the region where the tab in initiated will lead to boundary layer thickening and a reduction of maximum lift and increase in profile drag. On contemporary rotors, small trailing-edge tabs are often apparent and are there to help track the rotor, but they are built into only a small part of the blade span.

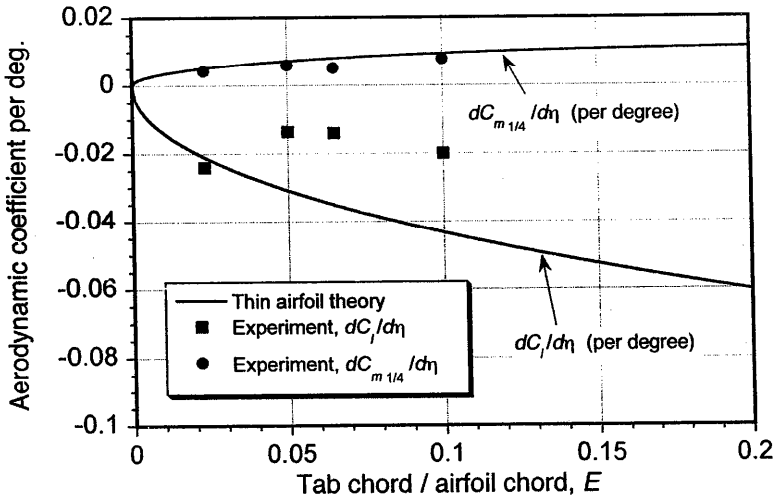

Figure 7.27 Effects of trailing-edge tabs on lift and pitching moment. Positive upward tab deflection. Data source: Collated results by Prouty (1986).

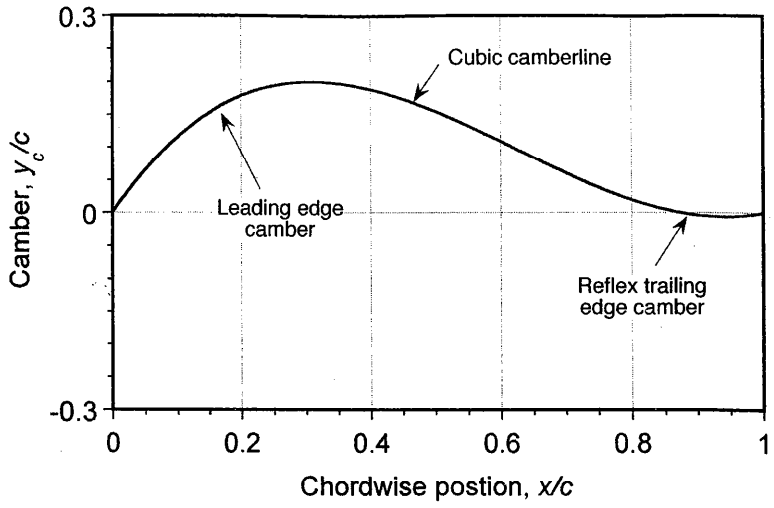

Figure 7.28 A reflexed cubic camberline with $m = 0.2$ designed for zero pitching moment.

7.7.5 *Reflexed Airfoils*

A more elegant way to control the pitching moment of an airfoil is to use *reflex camber*. Generally, for a given airfoil, the addition of reflex camber to an airfoil with camber in the nose region gives a significant reduction in C_m with only a minor reduction in maximum lift capability and a small drag penalty. Many authors have investigated low pitching moment reflexed airfoils based on cubic camberlines – see Glauert (1947) and Houghton & Carpenter (1993). A cubic camberline may be expressed as

$$\bar{y}_c = m\, a\, \bar{x}(\bar{x} + b)(\bar{x} - 1), \tag{7.82}$$

where m is the maximum camber as a fraction of chord, and a and b are general coefficients. While this equation describes a family of camberlines, of specific interest in this case are the values of a and b that will produce a camberline with zero pitching moment. We may define a specific cubic camberline such that $d\bar{y}_c/d\bar{x} = 0$ at $\bar{x} = p$ and $\bar{y}_c/m = 1$ at $\bar{x} = p$. This leads to the two simultaneous equations

$$ap^3 + a(b-1)p^2 - abp = 1 \quad \text{and} \quad 3ap^2 + 2a(b-1)p - ab = 0, \tag{7.83}$$

which can be solved for a and b under the assumption that $C_{m_{1/4}} = 0$ (i.e., $A_1 - A_2 = 0$ using the thin-airfoil theory). The results for A_1 and A_2 are given by

$$A_1 = -\left(\frac{a}{2} + ab\right)m \quad \text{and} \quad A_2 = \frac{3a}{8}m, \tag{7.84}$$

and by satisfying $A_1 - A_2 = 0$ we find that $a = 8.28$ and $b = 0.875$ with $p = 0.31$. The resulting shape is shown in Fig. 7.28 for $m = 0.2$. It is apparent that only a small amount of reflex at the trailing edge is required to negate the pitching moment produced by the positive camber near the leading edge. Many modern helicopter rotor designs take advantage of the low pitching moment benefits produced by reflex cambered airfoils.

7.8 Drag

Drag forces on airfoils operating in attached flow are typically nearly two orders of magnitude less than the lift forces at the same AoA. There are two sources of drag:

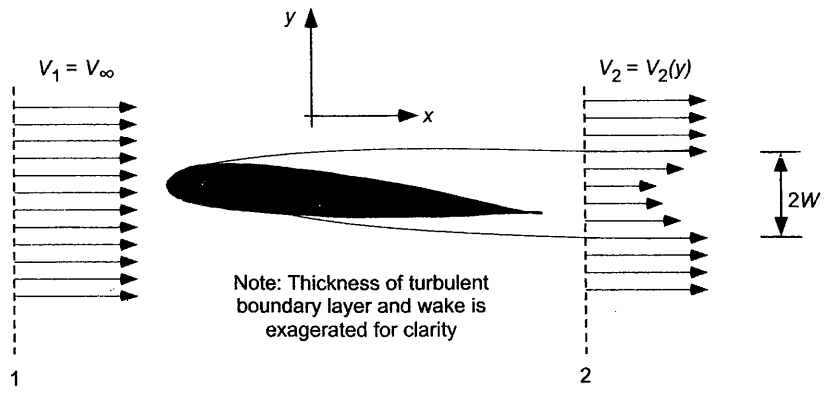

Figure 7.29 Measurement of drag by wake momentum deficit approach.

1. Pressure drag, and 2. Viscous shear drag. The sum of these is called profile drag. In addition, at higher Mach numbers there is a source of drag known as wave drag, which is important whenever a shock wave forms of the airfoil. Pressure drag may be estimated by the integration of pressure with respect to airfoil thickness as previously described. However, for this to be accurate a good concentration of pressure points is required in the region of high suction pressure (usually the leading edge region). The problem is complicated, however, with the formation of supercritical flow and a shock wave. Alternatively the drag may be measured with a force balance. This has the advantage of measuring both the pressure and viscous shear drag. However, the measurements must be properly corrected for any 3-D effects associated with the airfoil configuration in the test facility.

One common way of estimating the steady drag on a 2-D airfoil section is to estimate the momentum loss in the wake of the airfoil by measuring the velocity profile downstream of its trailing edge, as shown in Fig. 7.29. This is sometimes called the "wake rake" technique. By placing a control volume around the airfoil section and its wake, we can use the momentum equations in integral form to find the time rate of change of momentum into and out of the control volume. This will give a force on the fluid as it passes through the control volume, and by Newton's third law, this force is equal and opposite to the (drag) force on the airfoil.

By looking at the change of momentum in the streamwise direction, it can be shown that

$$\int_1 V_\infty(\rho V_\infty dy_1) = D + \int_2 V_2(\rho V_2 dy_2). \tag{7.85}$$

The two integrals can both be expressed in terms of y_2 by using conservation of mass through the stream tube $\rho V_\infty dy_1 = \rho V_2 dy_2$. Therefore, the drag force may be written as

$$D = \int_2 \rho V_2(V_\infty - V_2)dy_2. \tag{7.86}$$

Good accuracy has been demonstrated with this method if the measurement plane is about 15% chord downstream from the trailing edge of the airfoil. (See also Question 7.9.) However, this technique is only valid for angles of attack below stall. When significant flow separation exists above the airfoil, the technique becomes less valid because of other rotational losses that do not appear as a loss of momentum in the downstream wake. In these circumstances, the drag must be measured with a force balance or from pressure integration around the airfoil surface. However, the sectional drag can be measured reliably by means of this wake rake or wake survey technique at low angles of attack (which gives a measure of both the viscous *and* pressure drag) and by pressure integration to obtain the pressure

drag component alone. The total or profile drag is then the sum of the viscous drag and the pressure drag. The wake rake technique, however, cannot measure the unsteady drag, this only being possible by the integration of unsteady surface pressures.

7.9 Maximum Lift and Stall Characteristics

As previously noted, at higher angles of attack the adverse pressure gradients produced on the upper surface of the airfoil result in a progressive increase in the thickness of the boundary layer and cause some deviation from the linear lift versus AoA behavior (see Fig. 7.8). Eventually, the flow will separate causing stall. On many airfoils, the onset of flow separation and stall occurs gradually with increasing AoA, but on some airfoils, particularly those with sharp leading edges, the flow separation may occur quite suddenly. In the stalled flow regime, the flow over the upper surface of the airfoil is characterized by a region of fairly constant static pressure. The pitching moment about the 1/4-chord is much more negative (nose-down) because with the almost constant pressure over the upper surface the center of pressure is now close to mid-chord. Less lift is generated by the airfoil because of the reduction in circulation and loss of suction near the leading edge, and the drag is greater. In addition, under these separated flow conditions, steady flow no longer prevails, with turbulence and vortices being shed alternately from the leading and trailing edges of the airfoil into the wake. Measurements will generally show fairly large fluctuating forces and moments on the airfoil under stalled flow conditions.

One of the most important characteristics used to judge the performance of an airfoil is the maximum static lift capability. This is a quantity that is not easily predicted, even with state-of-the-art computational methods, and reliance must be placed on experimental measurements. However, even from an experimental perspective, absolute values of $C_{l_{max}}$ are difficult to guarantee with high precision, and especially between tests performed in different wind tunnels. This is mainly because of the uncertainties associated with the testing technique, the aspect ratio of the wing or airfoil specimen, tunnel wall interference effects, and different turbulence intensities in different wind tunnels. McCroskey (1987) gives a good overview of the problem. However, it appears that if airfoil measurements are performed in a consistent manner and to uniform data accuracy standards, such as those defined by Steinle & Stanewsky (1982), the measurements can be considered reliable. However, the formation of test specific 3-D stall developments near maximum lift are difficult to avoid – see Moss & Murdin (1965). See also Prouty (1975) for a survey of rotor airfoil measurements.

Most of the understanding about the aerodynamics of helicopter airfoil sections comes from "2-D" testing in a wind tunnel. However, there are some special considerations that must be understood and appreciated when attempting to interpret the 2-D characteristics of airfoil sections. These issues are especially important when comparing the relative performance of different airfoils. Usually in 2-D testing, the test airfoil (wing) is made to fully span one dimension of the wind tunnel, that is, across the height or width of the test section. This has the effect of making the specimen appear to be of infinite (high) aspect ratio. The pressures around the airfoil at mid-span are measured using pressure taps connected to a scanning valve and a pressure sensor, or by individual pressure sensors directly. At the mid-span, 3-D effects and wind tunnel wall interference effects are much smaller. Alternatively, the test airfoil may often be placed in a 2-D insert, as shown in Fig. 7.30. This reduces the span of the test airfoil, while still maintaining nominally 2-D flow.

Note that no matter what aspect ratio is used for the wing, 3-D separation will ultimately occur – an effect first studied by Moss & Murdin (1965). If this 3-D effect is severe, then

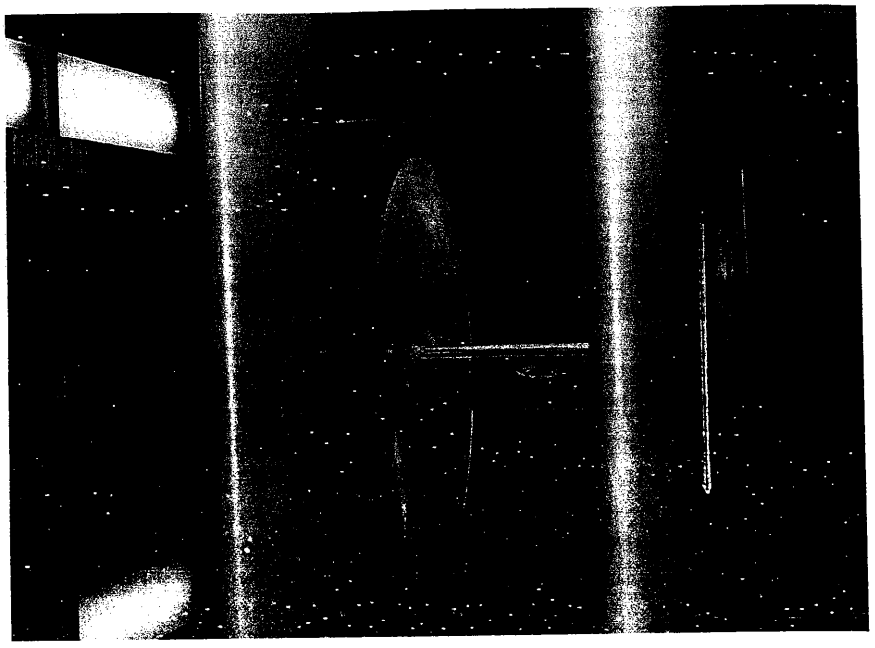

Figure 7.30 Sectional airfoil characteristics may be measured using 2-D airfoil testing, in this case involving the use of a special insert installed in the wind tunnel.

it will almost certainly affect the airfoil characteristics at the mid-span measuring station. Thus, some knowledge of the 3-D stall development on the test airfoil is always essential, especially when comparing the aerodynamic behavior of different airfoils near maximum lift. Figure 7.31 shows a helicopter blade section being tested in a 2-D insert. The flow is rendered visible by surface oil flow in which titanium dioxide power has been dissolved; this gives a white flow pattern on the black painted surface of the airfoil. The photo shows

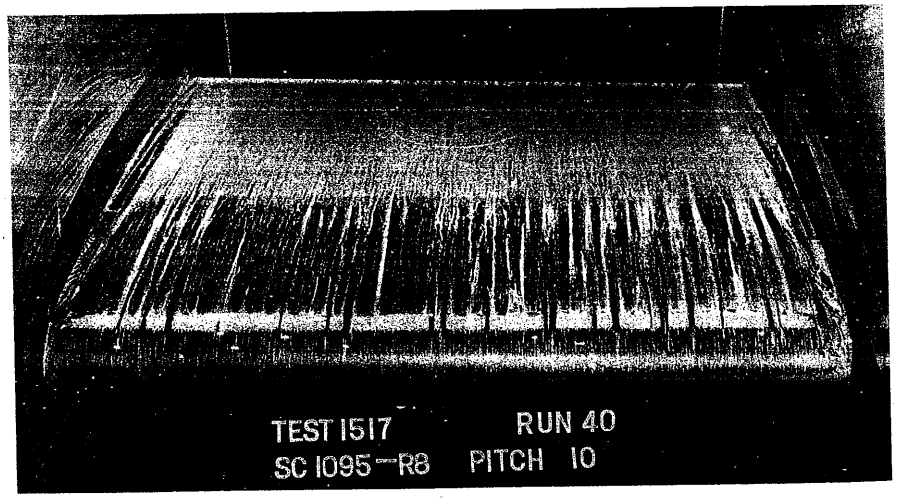

Figure 7.31 Airfoil specimen being tested in a 2-D insert. The flow is rendered visible by surface oil flow visualization showing that a laminar separation bubble forms near the leading edge of the airfoil.

the leading edge of the airfoil (looking downstream). Note the "scarf" vortex wrapped around the junction between the airfoil and the wall, which tends to keep the flow attached there. The small region of laminar flow is terminated by a laminar separation bubble, which is evident from the accumulation of oil in a narrow band spanwise along the airfoil (see also Fig. 7.5). This bubble has been burst in places by small imperfections in the surface of the airfoil, which causes premature transition to a turbulent boundary layer. The results reinforce how laminar boundary layers are extremely sensitive to disturbances. Downstream of the laminar separation bubble, the boundary layer is fully turbulent. The surface shear stress decreases toward the trailing edge, so the boundary layer ultimately begins to separate from the surface. For this airfoil, the stall mechanism was by means of the trailing edge stall mechanism; that is, the progressive movement of the turbulent trailing edge separation point forward toward the leading edge of the airfoil for increasing AoA.

Abbott & von Doenoff (1949) have documented a summary of airfoil section measurements made at Reynolds numbers of 3 to 9 million and Mach numbers up to 0.2. These Reynolds numbers are close to the range encountered by the retreating blade on a full-scale helicopter rotor and provide a consistent basis from which to review the stall characteristics of airfoils, in general. The maximum lift that can be developed by an airfoil when operating at a steady AoA is related to the type of stall characteristic of that airfoil. At low speeds, airfoils generally fall into three static stall categories, as identified by McCullough & Gault (1953) and Gault (1957). These types are thin-airfoil stall, leading edge stall, and trailing edge stall. The results show that thin-airfoil and leading edge stalls can be fairly sensitive to changes in airfoil shape, whereas trailing edge stall is insensitive. Most conventional helicopter rotor airfoils fall into the category of trailing edge or leading edge stall types at low to moderate Mach numbers. It is also common for a *mixed stall* behavior to occur on some airfoils, which is a stall characteristic that is not clearly one type or another.

The three low speed static stall characteristics can be illustrated by comparing the lift and moment results for a given family of airfoils that have different thickness-to-chord ratios. For example, Fig. 7.32 shows results for the NACA 63 series airfoil section for thickness-to-chord ratios of 6%, 12%, 15%, and 21%. *Thin airfoil stall* occurs on the NACA 63-006 airfoil. The sharp nose radius produces high adverse pressures near the leading edge, which results in separation of the laminar boundary layer at low angles of attack. Initially the flow reattaches as a turbulent boundary layer, but as the AoA is increased the turbulent reattachment point moves aft producing a *long separation bubble*. The formation of the bubble often causes a slight nonlinearity in the lift-curve-slope at moderate angles of attack, say between 3° and 7°. Ultimately, the boundary layer fails to reattach and the airfoil stalls. Thin airfoil stall occurs mainly at low Reynolds numbers and, as shown by Fig. 7.32, it involves a fairly gentle lift stall characteristic with a break in the moment curve at low AoA. This is followed by a progressive increase in nose-down pitching moment as the separation bubble envelops more of the upper surface of the airfoil. Airfoils that exhibit thin-airfoil stall also tend to show considerable hysteresis in the airloads, and different results can be obtained depending on whether the AoA is set in the wind tunnel before turning on the flow or vice versa. The former tends to replicate flow reattachment from stalled conditions. This problem is called *static stall hysteresis*.

The NACA 63-012 airfoil exhibits what is known as *leading edge stall*. This airfoil achieves a much higher value of maximum lift, followed by an abrupt stall leading to sharp breaks in the lift and moment curves. The leading edge stall mechanism involves the participation of a *laminar separation bubble* in the leading edge region, as previously discussed and shown in Fig. 7.6. Transition to a turbulent boundary layer occurs at this bubble. While the airfoil is sufficiently thin to promote laminar separation, the adverse

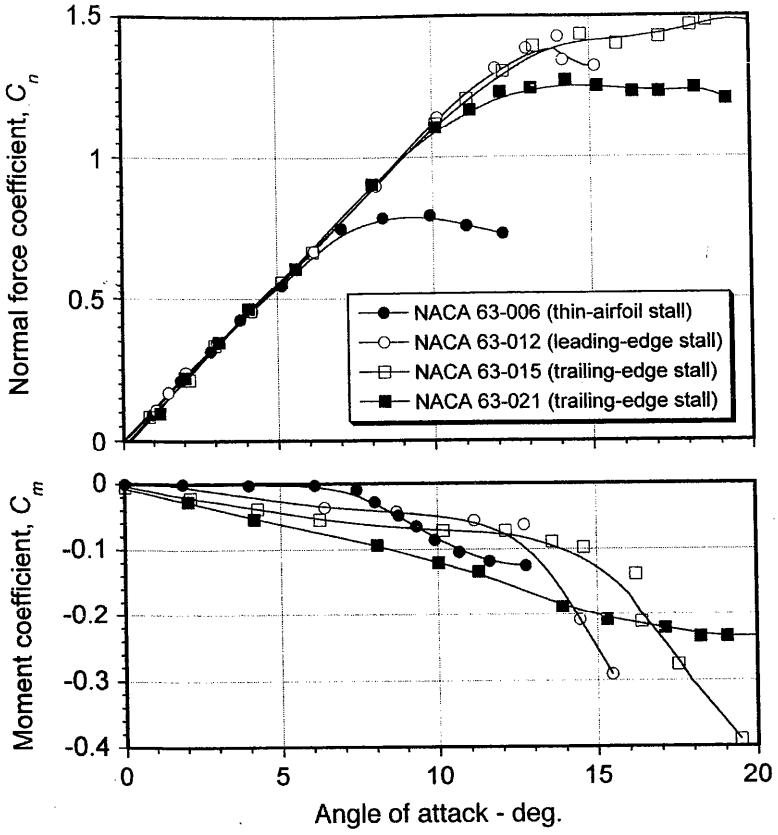

Figure 7.32 Lift and pitching moment characteristics of the NACA 63-series airfoil sections with different thickness-to-chord ratios. Data source: Abbott & von Doenhoff (1949).

pressure gradients are mild enough to cause the transitional turbulent boundary layer to reattach forming this bubble, which is typically 2–3% of chord and is normally situated immediately downstream of the leading edge suction peak in the region of steepest adverse pressure gradient. As the AoA is increased, this bubble moves forward on the chord toward the leading edge. Eventually, the adverse pressure gradient becomes more severe, preventing the turbulent boundary layer from reattaching to the surface, and the bubble can be said to "burst." Alternatively, the bubble may remain present and the turbulent boundary layer may separate abruptly immediately downstream of the bubble. This is called leading edge stall by the *reseparation* mechanism – see Evans & Mort (1959). Because both bubble burst and reseparation result in a sudden change in the flow pattern around the airfoil, it is often difficult to discern the actual flow separation mechanism. It can usually be determined with the aid of flow visualization, which can confirm the existence of a laminar separation bubble in the post stall regime. At the Reynolds numbers of practical interest on full-scale helicopter rotors, reseparation is the common flow mechanism for leading edge stall.

The third type of static stall shown in Fig. 7.32, which is exhibited by the relatively thicker NACA 63-015 and the very thick NACA 63-021 airfoil, is called *trailing edge stall.* This is a fairly common stall mechanism found with the higher t/c ratios and larger camber values typical of some modern rotor airfoils, and it is caused by the relatively gradual movement of the turbulent flow separation point from the trailing edge toward the leading edge. Trailing edge stall produces a progressive rounding of lift behavior near maximum

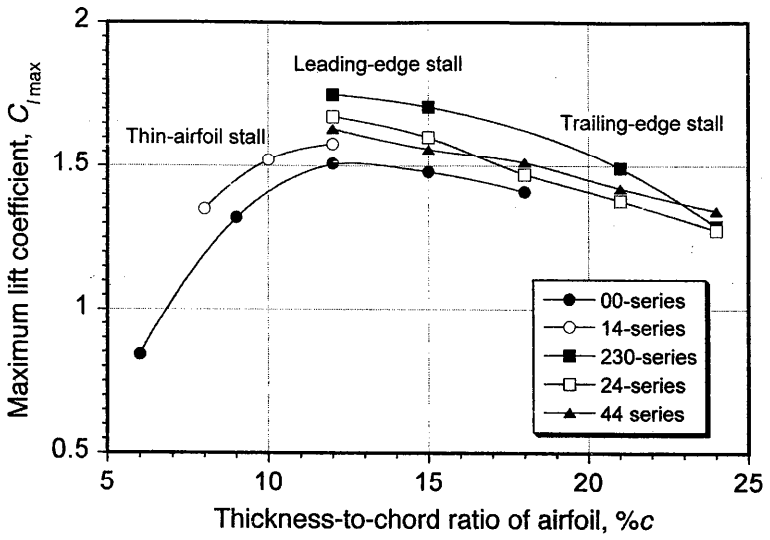

Figure 7.33 Summary of results showing combined effect of thickness and camber on $C_{l_{max}}$. Data source: Abbott & von Doenhoff (1949).

lift with a gentle pitching moment break. Another characteristic of the trailing edge stall mechanism is that the pitching moments exhibit a pronounced nose-up tendency just prior to maximum lift. For lower t/c ratios a high value of maximum lift is still produced on airfoils that exhibit trailing edge stall, although generally not as high as for airfoils that exhibit leading edge stall. With increasing t/c, the maximum lift decreases rapidly with trailing edge separation occurring at progressively lower angles of attack. Some airfoils can experience abrupt trailing edge stall, particularly at higher Reynolds numbers, which manifest as a rapid forward movement of the trailing edge separation point and in the absence of supporting evidence, such as pressure distributions and flow visualization, can be easily confused with leading edge stall.

In light of the foregoing, it is apparent that several potential design methods can be used to increase the $C_{l_{max}}$ of an airfoil. One method is simply to change the airfoil thickness, such as using a NACA 0012 over a NACA 0009. Figures 7.33 and 7.34 summarize the experimental results for the NACA airfoils. There are clearly significant advantages in using some thickness to avoid the formation of a long laminar separation bubble, but there is no substantial benefits in terms of $C_{l_{max}}$ for $t/c > 15\%$, unless thicker airfoils are needed to meet blade structural requirements near the blade root. Another method is to introduce forward camber for a given airfoil thickness, such as using the NACA 23012 rather than the NACA 0012. These results are summarized in Fig. 7.34. This latter modification gives a more gradual curvature to the airfoil at the leading edge, resulting in a less adverse pressure gradient at a given AoA or lift coefficient. As shown in both Figs. 7.33 and 7.34, all of the cambered airfoils exhibit higher values of $C_{l_{max}}$ compared to the symmetric NACA 00-series, but this will be at the expense of some increase in pitching moment (see Fig. 7.25).

7.9.1 *Effects of Reynolds Number*

At low Mach numbers, variations in Reynolds number will affect both the type of stall and the maximum lift coefficient. A fundamental study of the relationships was first made by Jacobs & Sherman (1937). Increasing the Reynolds number increases the inertial effects in the flow, which will dominate over the viscous effects and, all other factors being

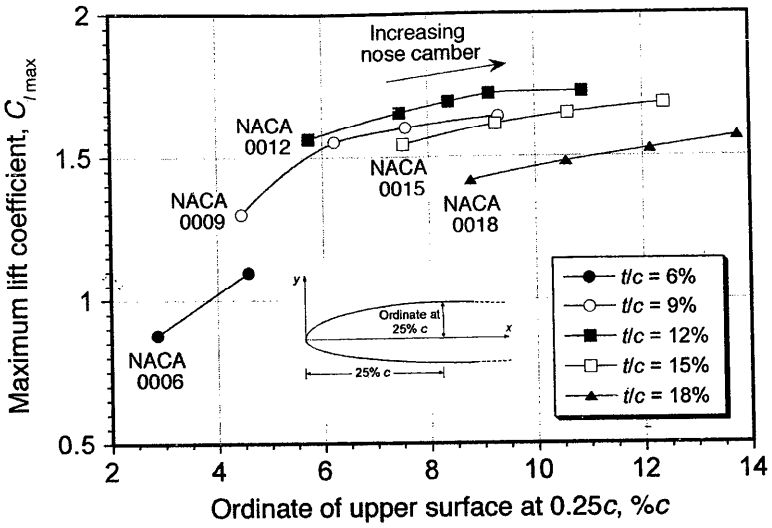

Figure 7.34 Results showing effect of nose camber on $C_{l_{max}}$. Data source: Jacobs et al. (1937).

equal, will thin the boundary layer and delay the onset of flow separation to higher values of AoA and lift coefficient. Figure 7.35 shows the effects of increasing Reynolds number for the NACA 63- and 64-series airfoils. The main trend is an increase in $C_{l_{max}}$, but at a very small rate after a certain value of Re is reached. The main difficulty in assessing the effects of Reynolds number is the interdependent effects of Mach number. The Mach number, M_∞, may be written in terms of the Reynolds number, Re, as

$$M_\infty = \left(\frac{\mu}{\rho\, a}\right)\frac{Re}{c}, \tag{7.87}$$

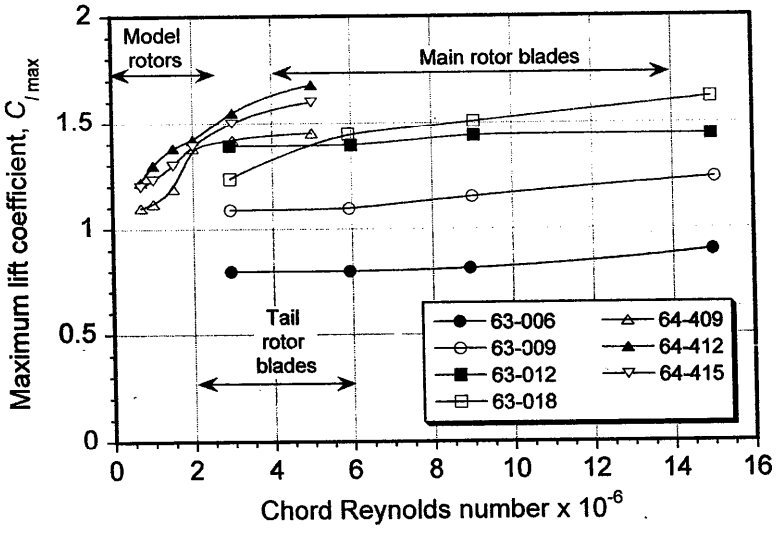

Figure 7.35 Effect of Reynolds number on the maximum lift coefficient of the NACA 63-series and 64-series airfoils. Data source: Racisz (1952).

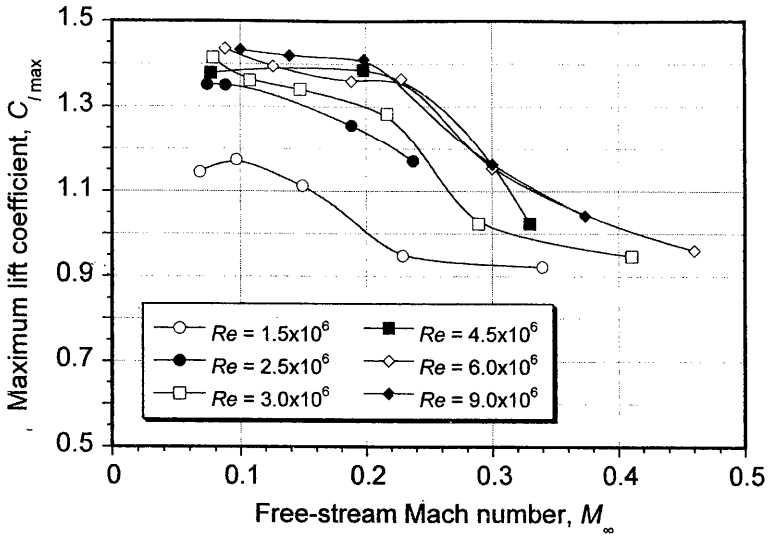

Figure 7.36 Results of independent Reynolds number and Mach number variations on the $C_{l_{max}}$ of a NACA 64-210 airfoil. Data source: Racisz (1952).

where c is the airfoil chord. Unless special (pressurized) wind tunnels are used where the Reynolds number can be varied completely independently of Mach number, Eq. 7.87 shows that a change in free-stream Mach number will always be accompanied by a change in Reynolds number and vice versa.

Up to Mach numbers of about 0.4, the effects of varying Reynolds number on the maximum lift and stall characteristics can be significant. For example, results showing the independent Mach number and Reynolds number variation on the maximum lift of a NACA 64-210 airfoil section are given in Fig. 7.36. These data show that the Reynolds number has a strong influence on the maximum lift capability at a given Mach number, with larger Reynolds number leading to higher values of $C_{l_{max}}$ for a given Mach number. At higher free-stream Mach numbers the effects of Reynolds number are secondary compared to the effects of compressibility, as confirmed by the fact that curves for each Reynolds number show a converging trend. These effects of interdependent Reynolds number and Mach number should be borne in mind when analyzing results from subscale rotor tests, where the blade Reynolds numbers may be one-quarter or less of the full-scale rotor values.

In addition to the effects of Reynolds number and airfoil shape, any roughness on the leading edge of the airfoil may also affect the stall type. Surface roughness causes premature transition from a laminar to a turbulent boundary layer, thereby increasing the effective Reynolds number. Generally, prematurely tripping the boundary layer will always make the airfoil exhibit a trailing edge (gradual) stall, whereby the point of turbulent separation moves forward on the chord with increasing AoA. In wind tunnel experiments, standard roughness is applied to the airfoils in the form of carborundum grains or other standardized approaches – see, for example, Loftin (1945) and Abbott & von Doenhoff (1949). In the case of an airfoil that initially exhibits thin-airfoil stall, leading edge roughness will eliminate the laminar separation bubble and will always give the airfoil a gradual turbulent trailing edge stall characteristic (see Fig. 7.37). As shown by the NACA 63-006 airfoil, this is usually accompanied by a mild increase in $C_{l_{max}}$. However, the application of standard roughness to an airfoil that initially exhibits leading edge stall will cause the boundary layer to be more susceptible to turbulent boundary layer separation at a lower AoA. Therefore, as shown by

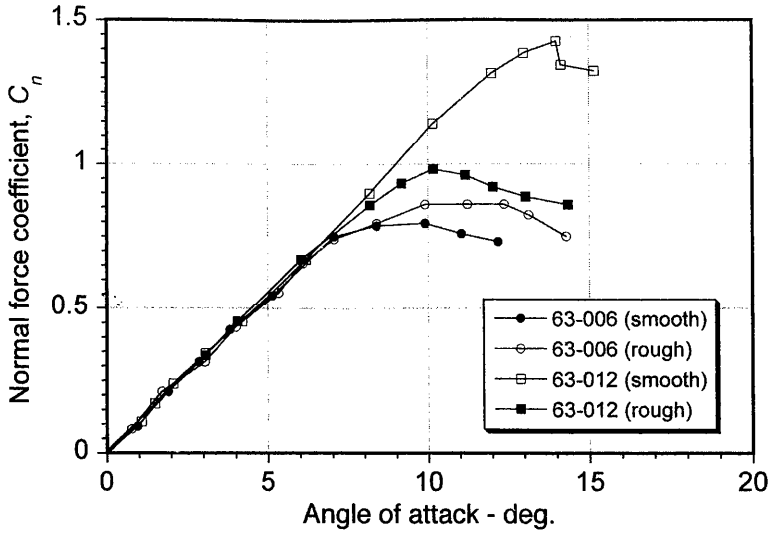

Figure 7.37 Effect of leading edge roughness on the low-speed lift and stall characteristics of the 63-006 and 63-012 airfoils: Data source: Abbott & von Doenhoff (1949).

the 63-012 airfoil, this results in a gradual trailing edge stall characteristic and a significant loss of maximum lift capability.

7.9.2 *Effects of Mach Number*

As described previously, airfoil characteristics at Mach numbers above about 0.3 are affected by the compressible nature of a real flow. As an example, the effects of Mach number on the lift and pitching moment characteristics of a NACA 0012 are shown in Fig. 7.38. Two effects are immediately noticeable. First, there is an increase in the lift-curve-slope with increasing Mach number. This is the well-known Glauert effect, as discussed previously in Section 7.6.3. Physically, the effect occurs because pressure disturbances cannot propagate as far upstream in a given time as the Mach number increases. This increases the streamline curvature near the leading edge of the airfoil and manifests as an increase in the effective AoA. Second, the value of maximum lift coinciding with the break in the pitching moment curve tends to decrease with increasing Mach number. This is because of the onset of flow separation produced by the high adverse pressure gradients near the leading edge at low free-stream Mach numbers or near the shock wave at higher Mach numbers.

To explain airfoil behavior at higher Mach numbers, consider the presentations given in Figs. 7.39 and 7.40. Figure 7.39 shows results of the upper surface pressure distribution on the NACA 0012 for a range of angles of attack at a free-stream Mach number of 0.64. As the AoA is increased from 0 to 2°, the flow at the leading edge of the airfoil becomes mildly supercritical (locally supersonic). Under these conditions the flow returns to subsonic conditions by passing through a shock wave before reaching the trailing edge. With increasing AoA, the extent of supercritical flow increases and the shock wave moves further aft on the chord and strengthens. However, as the AoA reaches 6° the shock wave becomes more oblique to the airfoil surface and starts to move forward. The pressure behind the shock also decreases as reflected in the "break" in the pitching moment shown in Fig. 7.38. This indicates the onset of flow separation. However, the flow reattaches again some distance

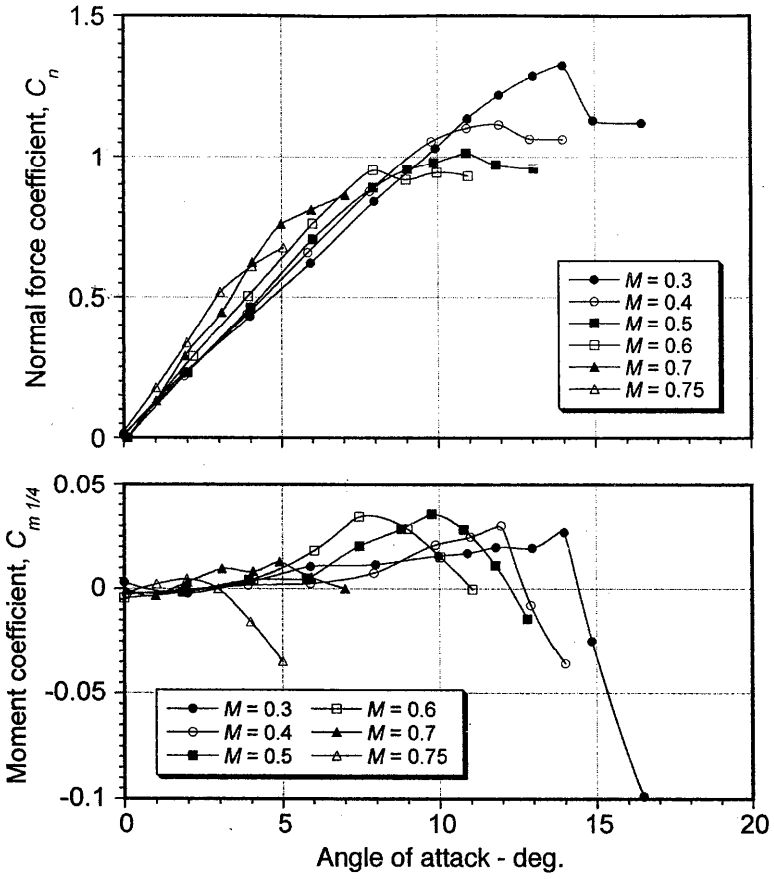

Figure 7.38 Effect of Mach number on the static lift and pitching moment characteristics of a NACA 0012 airfoil. Data source: Wood (1979).

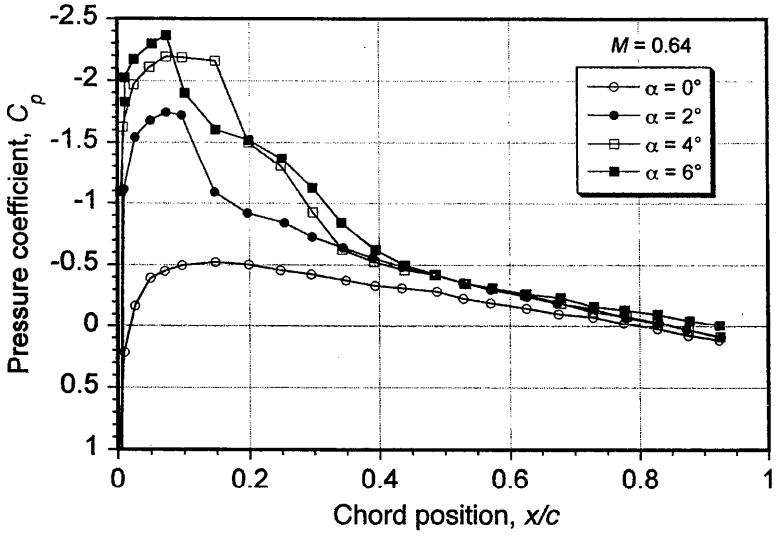

Figure 7.39 Effect of increasing AoA on the upper surface pressure distribution of a NACA 0012 airfoil at $M_{\infty} = 0.64$. Data source: Bingham & Noonan (1982).

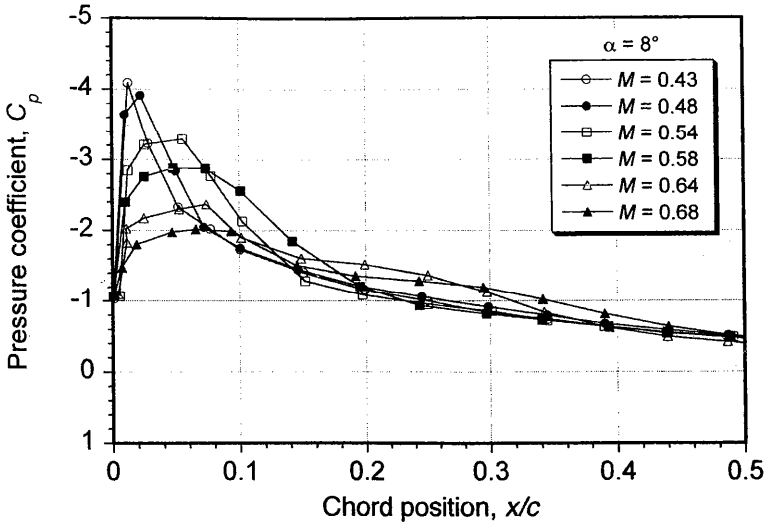

Figure 7.40 Effect of increasing free-stream Mach number on the upper surface pressure distribution of a NACA 0012 airfoil at a constant AoA of 8°. Data source: Bingham & Noonan (1982).

downstream of the shock wave, in effect producing a turbulent separation bubble. This bubble is conceptually similar to a laminar separation bubble and contains a region of low velocity, constant pressure, recirculating flow. During this process, the lift coefficient shows a departure from the linear C_l versus α behavior but continues to increase with increasing AoA.

Figure 7.40 shows the upper surface pressure distribution over the leading edge region of the NACA 0012 for a series of increasing values of free-stream Mach number when the airfoil is held at a constant AoA of 8°. As M_∞ is increased from 0.43 to 0.48, the subsonic form of the pressure distribution changes as the flow near the leading edge becomes mildly supercritical and the steepest adverse gradient moves aft to about 20% chord. With further increases in M_∞, the shock wave strengthens and moves further aft as the extent of supercritical flow increases. Eventually at $M_\infty = 0.64$, the shock becomes sufficiently strong to produce flow separation, which causes the shock to move forward on the chord and to become more oblique to the airfoil surface. Again, the flow reattaches forming a turbulent separation bubble. Further increases in M_∞ causes the bubble to lengthen, and eventually the boundary layer will fail to reattach, producing complete flow separation over the upper surface of the airfoil. This is called *shock induced stall.*

Figure 7.41 shows the effect of Mach number on the maximum value of lift of the airfoil for nominally attached flow. Because the lift continues to increase after the onset of flow separation, these values have been derived by determining the value of C_l corresponding to the break in the pitching moment curve (i.e., the initial onset of flow separation), which will also be coincident with a rapid increase in drag. For lower values of M_∞ the curves are relatively flat and the airfoils retain their maximum lift, although the effects of compressibility clearly cause the values of $C_{l_{max}}$ to decrease with increasing Mach number. For values of M_∞ greater than about 0.5, the onset of supercritical flow causes the maximum values of lift to quickly decrease for further increases in M_∞, at least for the NACA 0012 and NACA 23015 airfoils. At the lower Mach numbers, the camber of the NACA 23015 airfoil increases the value of $C_{l_{max}}$ relative to the NACA 0012, but this advantage is lost at the higher

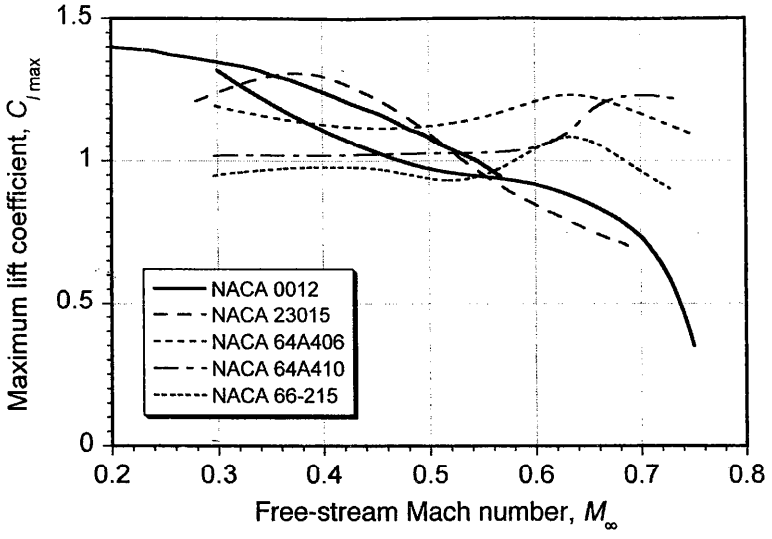

Figure 7.41 Composite results showing effect of Mach number on $C_{l_{max}}$ coinciding with pitching moment break for several conventional and supercritical-like airfoil sections. Data sources include: Racisz (1952), Stivers (1954), Benson et al. (1973), and Wood (1979).

Mach numbers because the camber and slightly greater thickness gives the NACA 23015 airfoil a lower critical Mach number. For the higher Mach numbers, the range of angles of attack over which the airfoils can operate without some flow separation is considerably reduced.

While most airfoils show a steady reduction of maximum lift coefficient with increasing Mach number, not all airfoils behave this way. Figure 7.41 also shows the $C_{l_{max}}$ behavior of the NACA 64-series and 66-series airfoils. While the values of $C_{l_{max}}$ attainable by this airfoil at low Mach numbers is inferior to either of the NACA 0012 or 23015 airfoils, there is a beneficial effect on $C_{l_{max}}$ at the higher Mach numbers. The NACA 66-215 and 64-series airfoils have a point of maximum camber fairly far aft, and so these airfoils exhibit a higher critical Mach number and a favorable effect on the strength of the developing shock wave. This is similar to the behavior of *supercritical* airfoils, the ideas of which have been introduced previously. Improved airfoils for transonic flow applications were originally devised by NASA – see Whitcomb & Clark (1965) and Whitcomb (1976). To achieve this behavior, the leading edge geometry (thickness and camber) must be shaped to produce a longer run of supersonic flow but a weaker recovery shock. These conditions, however, can generally only be obtained for very specific combinations of angles of attack and Mach numbers. For other "off-design" operating conditions these airfoils usually suffer lift and drag penalties. Supercritical airfoils have been used for many years on jet transport aircraft, and "supercritical-like" sections are used as tip sections on some helicopters. At subsonic speeds, supercritical airfoils can exhibit higher leading edge suction peaks and are likely to encourage stall at lower angles of attack compared to conventional airfoils and thus would not be suitable for the inboard parts of helicopter blades.

As previously discussed, the effects of compressibility initially cause the aerodynamic center to migrate slightly forward with increasing Mach number. As the flow becomes supercritical and then transonic, the aerodynamic center shifts more quickly rearward resulting in the *Mach tuck* phenomenon – see Abbott & von Doenhoff (1945), Dadone & Fukushima (1975), and Prouty (1986). Mach tuck manifests as a rapid increase in nose-down pitching

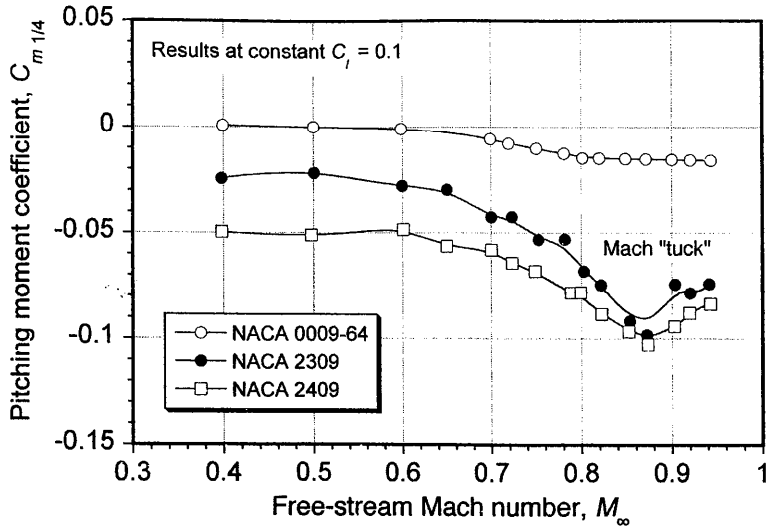

Figure 7.42 Effect increasing free-stream Mach number on the pitching moment at constant lift coefficient for several NACA series airfoils. Data source: Ferri (1945)

moment for a relatively small change in Mach number. If Mach tuck occurs on the advancing tip of a rotor, then it may produce high blade and control loads and may effectively limit the helicopter's forward flight speed. For most airfoils, the onset of Mach tuck appears at a slightly higher Mach number after drag divergence as the shock waves begin to strengthen and move more rapidly aft on the airfoil surface.

Because it is possible for the rotor to exceed the tip drag divergence Mach number under various flight regimes such as during dives and certain maneuvers, it is obviously desirable to minimize the nose-down pitching moment trend to as high a Mach number as possible. The data in Fig. 7.42, taken from Ferri (1945), compare pitching moment results at a constant $C_l = 0.1$. Figure 7.42 shows that the nose-down trend in the pitching moment is minimized for symmetric airfoils. Experiments have shown that camber applied further to the rear of the airfoil generally results in more severe "tuck" problems than for an airfoil with nose camber. The increased pitching moment is caused by changes in the relative chordwise pressure distributions on the upper and lower surfaces of the airfoil that result from the development of supercritical flow and shock waves. Thus supercritical airfoil design techniques are often used to minimize the strength of the shock wave and can delay the Mach tuck problem on the airfoil to higher free-stream Mach numbers.

Figure 7.1 has shown that the tip of the advancing blade operates at low lift but at high Mach numbers. Therefore, from a rotor power consumption point of view the drag characteristics of the airfoil when it operates at high Mach numbers are also important. Figure 7.43 shows the drag characteristics of several airfoils as a function of M_∞. In the low Mach number range, the drag stays nominally constant or may decrease slightly because of an interdependent effect of increasing Reynolds number. It is only when the critical Mach number is reached that the drag shows a more rapid rise. This drag rise occurs at progressively lower Mach numbers as the thickness-to-chord ratio of the airfoil is increased. A similar effect is obtained by increasing the AoA. The effect of camber also decreases the critical Mach number and so reduces the Mach number at which the drag rise occurs compared to symmetric airfoils of the same thickness-to-chord ratio.

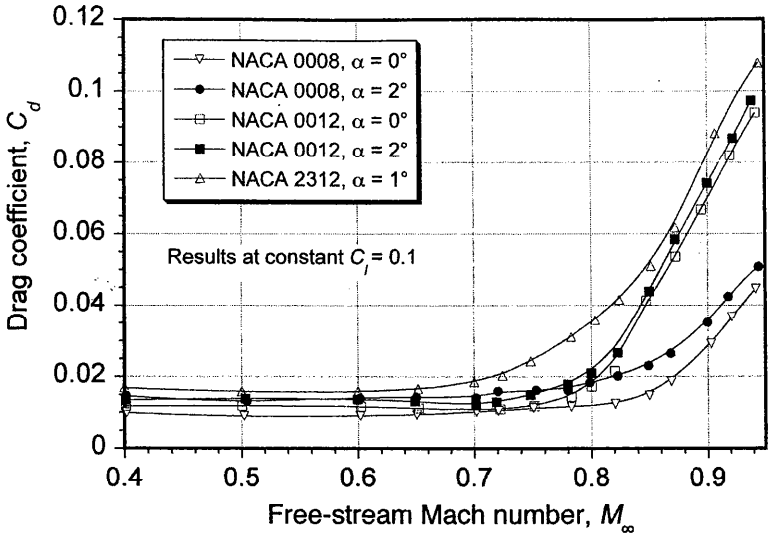

Figure 7.43 Effect of increasing free-stream Mach number on the drag of several NACA series airfoils. Data source: Ferri (1945)

The value of M_∞ at which the drag coefficient begins to rapidly increase is known as the *drag divergence Mach number*, M_{dd}. Physically, drag divergence occurs because of an entropy loss through the shock wave coupled with additional pressure drag as a result of boundary layer thickening and shock induced separation. Nitzberg & Crandall (1949) discuss the phenomenon in detail. The value of M_{dd} is often defined in as the Mach number for which $dC_d/dM_\infty > 0.1$ or, alternatively, the Mach number for which the drag coefficient becomes twice its incompressible value [see Prouty (1986)] at the same C_l or α. The drag divergence Mach numbers of airfoils at zero lift are plotted in Fig. 7.44 as a function of

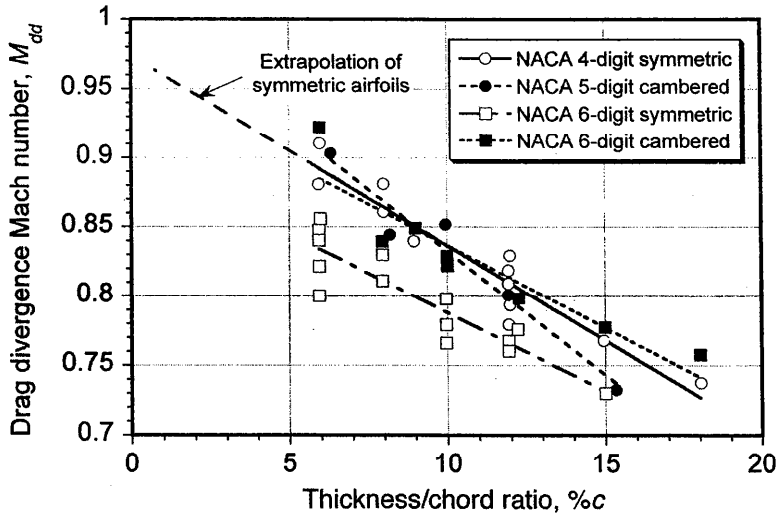

Figure 7.44 Drag divergence Mach numbers of several NACA series airfoils at zero lift. Data source: Collated information by Prouty (1986).

thickness-to-chord ratio. It can be readily observed that thinner airfoils have a much higher drag divergence Mach number and so will be the best choice for the blade tip region.

7.10 Advanced Rotor Airfoil Design

Several research programs have been undertaken with a view of improving helicopter performance by careful design and optimization of rotor airfoils. With appropriate design of both the airfoil sections and the blade geometry itself, conventional helicopters can now operate at flight speeds approaching 200 kts (370 km/h) without the rotor being limited by significant stall or compressibility effects. To achieve these speeds by expansion of the flight boundary, it is necessary to vary the airfoil section along the blade to give optimal performance for the extreme in the operating regimes encountered at that blade station.

Programs of airfoil development have been conducted by many of the major helicopter manufacturers and government research organizations. As previously discussed, the NACA 0012 airfoil represents a good compromise between high maximum lift, low pitching moment, and high drag divergence Mach number performance. As shown in Fig. 7.44, reducing the thickness-to-chord ratio of the airfoil gives a marked improvement to the high Mach number performance through a reduction in the drag divergence Mach number. This allows a higher forward flight speed to be obtained with the rotor prior to the onset of increased rotor torque demands. Alternatively, for a given operational forward speed the rotor tip speed can be increased without incurring penalties of drag divergence and flow separation, and so rotor solidity could be reduced, thereby saving weight. However, reducing blade thickness limits the maximum lift capability of the airfoil at low Mach numbers, and this can adversely impact the retreating blade performance of the rotor. Therefore, generally the airfoil section thickness must be maintained to give a compromised high Mach number performance, whereas the high-lift performance is much improved by adding leading edge camber. As shown previously in Figs. 7.33 and 7.34, the maximum lift capability of an airfoil improves rapidly with the addition of some nose camber, although at the expense of some modest increase in pitching moment.

Unfortunately, the addition of camber also affects the shock strength on the airfoil lower surface at higher Mach numbers, causing a reduction in the drag divergence Mach number. Nevertheless, Perry (1987) explains how careful addition of leading edge camber can restore the $C_{l_{max}}$ performance back to the levels of at least the NACA 0012 when operated at the same Mach number, whilst still retaining the higher drag divergence Mach number. The high-lift capability can only be improved further by using camber more toward the rear of the airfoil, but as shown previously in Fig. 7.25, this is at the expense of a more significant increase in pitching moment. On the retreating side of the rotor disk, the high pitching moments that are associated with cambered airfoils can normally be tolerated as the dynamic pressure is relatively low. Yet, on the advancing side, the dynamic pressure is larger, and so the blade pitching moments can be significant enough to manifest in high control loads, and possibly result in flight envelope restrictions. The final design of the airfoil section is usually a compromise in this regard.

The evolution of the Boeing (Vertol) VR airfoil series is shown in Fig. 7.45 – see Dadone and Fukushima (1975) and Dadone (1978, 1982, 1987). The VR-12 and the VR-15 airfoils represent the best compromise in terms of maximum lift capability at the lower Mach numbers typical of the retreating blade whilst also maximizing the drag divergence Mach number and meeting hover requirements and control load limitations. These sections were designed with the aid of numerical methods using a potential flow/boundary layer interaction analysis

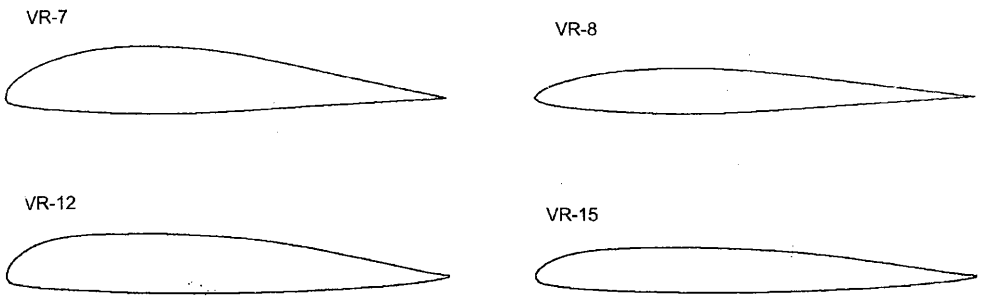

Figure 7.45 Boeing VR-series of helicopter airfoil development.

and a viscous transonic analysis. These analyses were previously validated against experimental measurements on other airfoil shapes so that they could be used with confidence in the airfoil design process.

The ONERA has conducted a systematic development of helicopter airfoil sections [see Thilbert & Gallot (1977)]. These airfoil shapes are designated as the OA- family, for which a selection is shown in Fig. 7.46. The philosophy behind the design of these airfoil shapes also follows that of high $C_{l_{max}}$ capability at low Mach numbers and a higher drag divergence Mach number. The OA-206 is an example of a thin supercritical-like section, which exhibits a higher drag divergence Mach number and gives potentially large improvements in advancing blade performance. The OA-209 is an example of an airfoil that is a compromise between advancing and retreating blade requirements, with gains in $C_{l_{max}}$ relative to the NACA 0012 at low Mach numbers and with some modest increase in the drag divergence Mach number. Recall that a high $C_{l_{max}}$ capability is required only on the outboard sections of the blade (between 50 and 80% of radius) and maximum lifting performance is relaxed further inboard. Thus, some reflex camber can be used on the inboard sections to generate lower pitching moments, that is, the OA-212 and OA-213 airfoils.

The Royal Aircraft Establishment and Westland Helicopters have conducted a systematic development of helicopter sections since the late 1960s. A good review of this work is given by Wilby (1979, 1998). The first airfoil in the series, the RAE (NPL) 9615, used nose camber to give a moderate increase in $C_{l_{max}}$ compared to the NACA 0012, with a small increase in drag divergence Mach number. Both improvements were made with only a small increase in pitching moment. Later airfoils that were developed included the 12% thick RAE 9645 (see Fig. 6.22), which has more aft camber and gives a 30% increase in $C_{l_{max}}$ relative to the NACA 0012. The RAE 9648 is a 12% thick reflexed airfoil, which gives a significant nose-up pitching moment whilst retaining most of the high-lift advantages of the RAE 9645. The RAE 9634 airfoil is a thinner 8% thick section, which is designed to minimize transonic

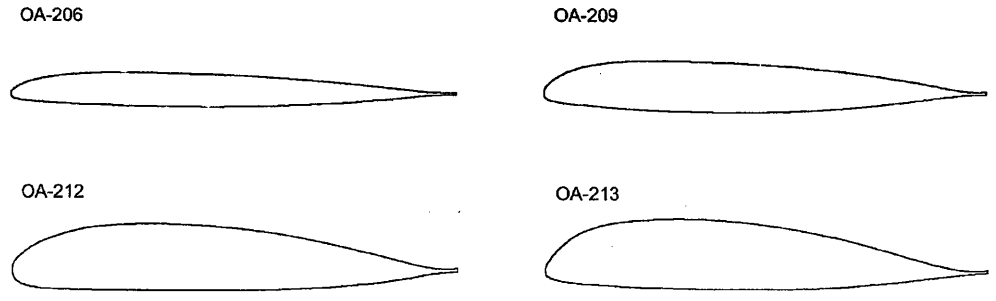

Figure 7.46 The ONERA OA-series of helicopter airfoils.

flow effects by giving a higher drag divergence Mach number and to delay the nose-down pitching moment (Mach tuck) trend to as high a Mach number as possible.

A series of high-lift low pitching moment airfoils have been devised by the US Army and NASA for helicopter applications. These are designated as the NASA RC-series – see Bingham (1975) and Bingham & Noonan (1982). The RC(3) airfoil families use a careful combination of nose camber, trailing edge reflex camber and a supercritical type thickness distribution to extract the highest static $C_{l_{max}}$ from the airfoil whilst retaining a very low pitching moment and a high drag divergence Mach number. The NASA RC(4) and RC(5) series were designed by Noonan (1990) for high maximum lift coefficients and are suitable for the inboard part of the blade – see Fig. 6.17. The RC(5) family has a lower thickness than the RC(4) family forward of the point of maximum thickness. The RC(6) series is described by Noonan (1991) and is a development of the RC(3) series designed for application at the tip of the blade.

It is in the more precise design optimization of airfoils to meet the 3-D unsteady flow environment at the rotor where future research challenges lie in airfoil design. This will see benefits from advanced computational fluid dynamic (CFD) models based on the Navier–Stokes equations – see Chapter 14. Design for maximum lift and low drag is important for all helicopter airfoils, but CFD methods have not yet matured to a level where turbulent flow separation and stall effects can be predicted with acceptable accuracy. The future, however, will see helicopter airfoils designed more specifically to meet the highly unsteady, 3-D flow requirements in which they really operate. This may provide an exciting opportunity to finally realize desired airfoil performance levels (Fig. 7.47) and so to produce significant gains in rotor efficiency and overall helicopter performance. Until then, the extreme operating conditions and often highly unsteady flow environment found on helicopters means that rotor airfoils must be tested in a wind tunnel to fully assess both their steady and unsteady

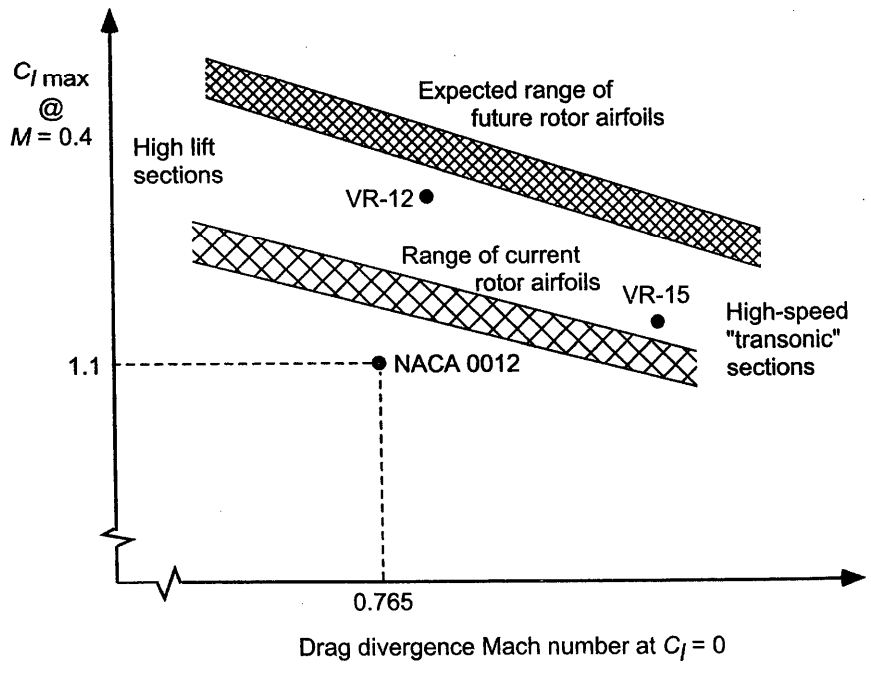

Figure 7.47 The design of new helicopter airfoils will continue to require the synergistic use of modeling and experiment to realize desired performance gains.

aerodynamic performance. Wind tunnel tests are very expensive and time consuming, but they will always form an essential part of validating CFD models used for airfoil design.

The use of passive or active flow control devices may offer further gains in airfoil (and rotor) performance, perhaps increasing the rotor FM by 5–10% and expanding the forward flight and maneuver boundaries of the helicopter. One tried approach is to design the airfoils for natural laminar flow (NLF) over a significant portion of the leading edge region by favorably altering the pressure gradients, in principle lowering skin friction drag at lower lift coefficients. The resulting shapes, however, are usually ill-suited for helicopter rotors because they give a lower critical Mach number and/or higher pitching moments. Anyway, the natural erosion of the leading edge of the blade during service also tends to promote an earlier transition to a turbulent boundary layer, so any gains with NLF are still lost. Laminar flow on better suited rotor airfoils may be increased by using vortex generators [see Kerho & Kramer (2003)] or by applying boundary layer suction or heating/cooling to the surface. The idea here is to suppress the natural growth of unstable disturbances in the laminar boundary layer that eventually lead to transition. While demonstrated on fixed-wings [see Joslin (1998)], suction has not yet been used on helicopter rotors because of the weight and complexity of using pumps, valving, tubing, and so on. Receptivity control, which attempts to cancel out natural disturbances in the boundary layer, also offers some promise in increasing the extent of laminar flow on the blades. Such an approach, however, has many practical challenges in its implementation [see Saric et al. (1998)] and especially so for helicopter rotors. The use of zero-mass flow synthetic jets [see Amitay et al. (1998) and Hassan et al. (2002)] may also lead to enhanced rotor performance by increasing airfoil maximum lift and decreasing drag. There are also good possibilities for using these devices for airframe drag reduction. In general, active flow concepts are likely to see much future interest in the quest for better helicopter performance.

7.11 Representing Static Airfoil Characteristics

The details of the airfoil pressure distribution and the variation with Mach number are important for airfoil design and airfoil selection purposes. However, in helicopter rotor performance and airloads analysis the details of the pressure distributions are usually not required because these are too expensive and time consuming to compute on a routine basis. More often it is required to mathematically model the airfoil characteristics in terms of lift, pitching moment and drag coefficients as functions of AoA. These models can then be incorporated into a blade element model, such as the approach introduced in Chapter 3, and in the "comprehensive" rotor models discussed in Section 14.11. Computational tools have not yet evolved to the point where the nonlinear performance of the airfoil at high angles of attack near stall and at high subsonic and transonic Mach numbers near drag divergence can be obtained with confidence. Therefore, reliance is placed on experimental measurements. These experimental measurements of the airfoil characteristics are usually obtained at discrete values of AoA from measurements in 2-D wind tunnel tests.

7.11.1 *Linear Aerodynamic Models*

In the low AoA regime, and at subsonic Mach numbers, the airloads can be adequately modeled using the equations

$$C_n \approx C_l = c_0 + c_1\alpha, \tag{7.88}$$

$$C_m = m_0 + m_1\alpha, \tag{7.89}$$

$$C_d = d_0 + d_1\alpha + d_2\alpha^2, \tag{7.90}$$

where c_0, c_1, m_0, m_1, d_0, d_1, and d_2 are empirically derived coefficients obtained through curve fitting to the airfoil measurements. It is very important to recognize that these polynomials can only be used to represent airfoil characteristics below stall; they are totally invalid with significant amounts of flow separation or in the stalled flow regime.

The aerodynamic significance of the constants $c_0, c_1, m_0, m_1, d_0, d_1$, and d_2 are not always recognized but can be readily established. Usually it is desirable to express the airloads in terms of well-known (measurable) aerodynamic parameters, such as lift-curve-slope and zero lift angle. The usual way of representing the lift is by using the equation

$$C_l = C_{l_\alpha}(\alpha - \alpha_0), \tag{7.91}$$

where C_{l_α} is the lift-curve-slope and α_0 is the zero lift AoA. Expanding gives

$$C_l = C_{l_\alpha}\alpha - C_{l_\alpha}\alpha_0 = c_0 + c_1\alpha. \tag{7.92}$$

Therefore, $c_0 = -C_{l_\alpha}\alpha_0$ and $c_1 = C_{l_\alpha}$. The pitching moment about the 1/4-chord is represented by

$$C_m = C_{m_0} + \left(\frac{1}{4} - \frac{x_{ac}}{c}\right) C_l, \tag{7.93}$$

where C_{m_0} is the zero lift moment and x_{ac} is the position of the aerodynamic center from the leading edge. Substituting for C_l and expanding gives

$$C_m = C_{m_0} + \left(\frac{1}{4} - \frac{x_{ac}}{c}\right) C_{l_\alpha}\alpha - \left(\frac{1}{4} - \frac{x_{ac}}{c}\right) C_{l_\alpha}\alpha_0, \tag{7.94}$$

which is in the form of

$$C_m = m_0 + m_1\alpha. \tag{7.95}$$

Therefore, the coefficient m_0 includes a combination of the usual aerodynamic parameters C_{m_0}, C_{l_α}, as well as x_{ac}. The coefficient m_1 is a term that represents the offset of the aerodynamic center from the 1/4-chord axis. The pressure drag can be obtained by resolving the components of the normal force and chord force through the AoA using

$$C_{d_p} = C_n \sin\alpha - C_a \cos\alpha. \tag{7.96}$$

The total drag (profile drag) is obtained by adding the contribution from viscous shear to the pressure drag. (This is roughly C_{d_0} at low angles of attack.) Therefore, the total drag can be written as

$$C_d = C_{d_0} + C_n \sin\alpha - C_a \cos\alpha. \tag{7.97}$$

For real (viscous) flows, the chord force coefficient is no longer given by $C_a = C_n \tan\alpha$ because the effects of viscosity limit the leading edge suction to some value that is less than the inviscid value. This effect can be modeled by using a leading edge suction recovery factor, η_a such that C_a is now given by

$$C_a = \eta_a C_n \tan\alpha. \tag{7.98}$$

Typically, η_a is close to but less than one. Thus, the pressure drag becomes

$$\begin{aligned} C_d &= C_{d_0} + C_n \sin\alpha - \eta_a C_n \tan\alpha \cos\alpha \\ &= C_{d_0} + C_n (1 - \eta_a) \sin\alpha. \end{aligned} \tag{7.99}$$

For small angles, $\sin\alpha \approx \alpha$ and $C_n \approx C_l = C_{l_\alpha}(\alpha - \alpha_0)$ so that the total drag is

$$\begin{aligned} C_d &= C_{d_0} + C_{l_\alpha}(1-\eta_a)(\alpha-\alpha_0)\alpha \\ &= C_{d_0} + C_{l_\alpha}(1-\eta_a)\alpha^2 - C_{l\alpha}(1-\eta_a)\alpha\alpha_0 \\ &= C_{d_0} - (C_{l_\alpha}(1-\eta_a)\alpha_0)\alpha + (C_{l_\alpha}(1-\eta_a))\alpha^2, \end{aligned} \tag{7.100}$$

which is of the form

$$C_d = d_0 + d_1\alpha + d_2\alpha^2. \tag{7.101}$$

This equation, like the previous equations for the lift and moment, is valid only in the regimes where the flow is fully attached. Note that $d_1 = 0$ for a symmetric airfoil ($\alpha_0 = 0$).

7.11.2 *Nonlinear Aerodynamic Models*

In the high AoA regime, flow separation and stall occur and the airloads become highly nonlinear functions of AoA. Therefore, the mathematical representation of the airfoil characteristics in this regime becomes more difficult. Usually this cannot be easily accomplished by using simple polynomial curve fits to the test data. However, mathematically representing the nonlinear airfoil characteristics by means of analytic functions or equations can still be accomplished in several different ways. These methods need to be relatively parsimonious because they will be included inside the blade element models used for the rotor analysis; this means that computational efficiency is always paramount simply because of the very large number of times such models are accessed during a typical rotor calculation.

7.11.3 *Table Look-Up*

One common way of representing nonlinear airfoil characteristics is to store the measured airfoil data as tables. Generally, one table must be provided for each Mach number. A computer program can be written to manipulate these data and to extract interpolated values of C_l (or C_n), C_m, and C_d for any specified AoA and Mach number. This is a procedure used by large comprehensive rotor analyses, and it is also used for flight simulation work where there may be a need for real-time evaluation of the blade airloads and so brevity of calculation is paramount, but without accepting a large loss of physical accuracy.

Representative experimental results for C_l versus α for a rotor airfoil at Mach numbers of 0.3, 0.4, and 0.5 are shown in Fig. 7.48. The results for the intermediate Mach number of 0.4 were found by linear interpolation between the results at $M_\infty = 0.3$ and $M_\infty = 0.5$. It will be seen that, in the low α range, the results are accurate, but for conditions near stall less reliable results may be produced. If the measurements are spaced at sufficiently small increments in Mach number, then the resulting interpolated data using this kind of scheme is normally viable.

7.11.4 *Direct Curve Fitting*

Curve fitting the airfoil characteristics using higher-order polynomials is another possible way of representing the nonlinear airfoil characteristics in the high AoA regime. Various strategies are possible, but caution should be used. For example, the lift

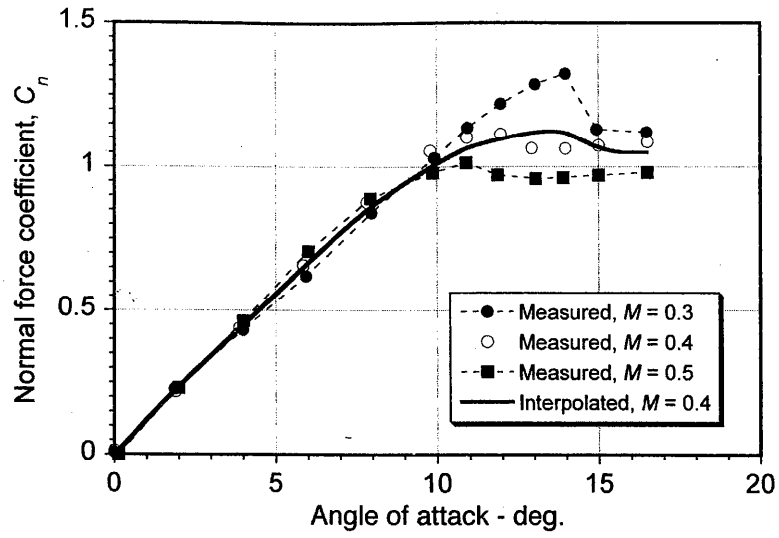

Figure 7.48 Interpolated static lift coefficient versus AoA characteristics using table look-up.

may be represented using

$$C_l = \sum_n a_n \alpha^n. \tag{7.102}$$

Generally, as low an order of polynomial as possible would be used. Typically, $N = 3$ gives a reasonable approximation. Alternatively, a ratio of polynomials of the form

$$C_l = \sum_{n=1}^{N} a_n \alpha^{2n-1} \left(1 + \sum_{m=1}^{M} b_m \alpha^{2m}\right)^{-1} \tag{7.103}$$

will often prove acceptable. In each case, the coefficients in the series are obtained in a least-squares sense.

As shown in Fig. 7.49, comparisons of direct curve fitting techniques with test data are reasonably adequate but tend to underpredict the magnitude of the airloads near maximum lift and also change the nature of the stall characteristic. This is typical whenever the airloads change rapidly with respect to AoA. However, single polynomial representations generally do not work well over an extended range of AoA.

Alternatively, the representation of the airfoil characteristics can be broken into smaller ranges of AoA. For example, one curve can be used below stall, and another curve(s) in the post stall regime, while requiring that the curves be piecewise continuous. This method has some difficulties, however, especially when interpolating the curve fit coefficients and break points between Mach numbers. Also, the conditional branching in the computer program consumes more time, which may not be acceptable in some applications, especially real-time flight simulation work where computational speed is paramount.

7.11.5 *Beddoes Method*

Another method, originally devised by Beddoes (1983), uses the Kirchhoff or Helmholtz solution for the lift on a flat-plate with a fixed separation point to model the

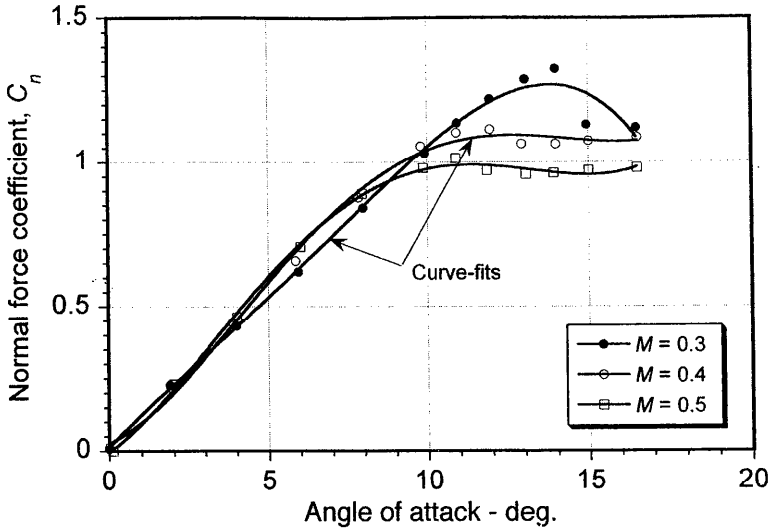

Figure 7.49 Curve-fitting static lift coefficient versus AoA characteristics using a higher-order polynomial in α.

nonlinear airfoil characteristics. In the Kirchhoff–Helmholtz model, the lift or normal force coefficient on the airfoil, C_n, is approximated by the equation

$$C_n = 2\pi \left(\frac{1+\sqrt{f}}{2} \right)^2 \alpha, \tag{7.104}$$

where 2π is the normal force-curve-slope for incompressible flow, f is the trailing edge separation point (nondimensionalized with respect to chord), and α is the AoA – see Thwaites (1960). Thus, if the separation point can be determined (the difficult part), it is easy to compute the normal force coefficient. The expression in Eq. 7.104 may also be extended to encompass compressible flows where 2π is replaced by the force-curve-slope at the appropriate Reynolds number and Mach number [i.e., $C_{n_\alpha}(Re, M_\infty)$], and α is measured relative to the zero lift angle, that is,

$$C_n = C_{n_\alpha}(Re, M_\infty) \left(\frac{1+\sqrt{f}}{2} \right)^2 (\alpha - \alpha_0). \tag{7.105}$$

To practically implement this procedure, the relationship between the separation point, f, and the AoA, α, must be obtained. These data are not generally known; however, an "effective" trailing edge separation point, f, can be deduced from the experimental measurements of the static C_n variation with α by rearranging Eq. 7.105 to solve directly for f, that is,

$$f = \left(2\sqrt{\frac{C_n}{C_{n_\alpha}(\alpha - \alpha_0)}} - 1 \right)^2. \tag{7.106}$$

The resulting curves are given by Beddoes (1983) and have been recalculated in Fig. 7.50 for the NACA 0012 airfoil over a range of Mach numbers.

After the values of f have been found, the lift at any AoA can be found by interpolating the values of f and finding the corresponding nonlinear value of C_n using Eq. 7.105. Beddoes (1983) shows that the f versus α curves all have a characteristic shape for all

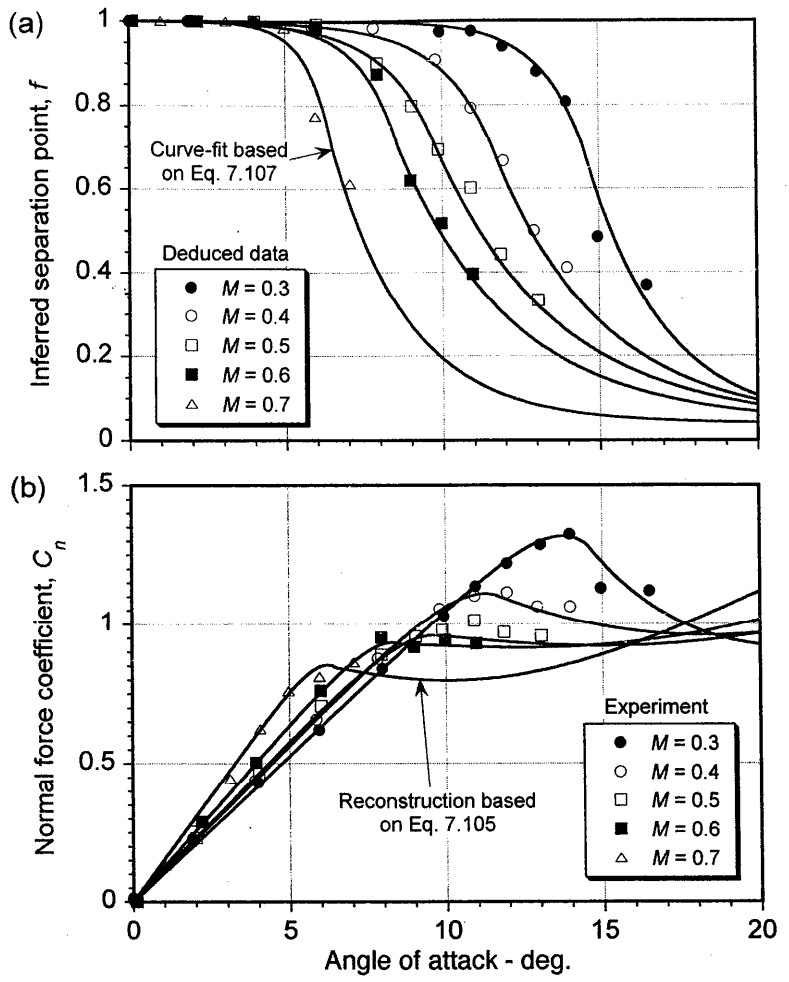

Figure 7.50 Reconstructions of static airfoil characteristics using the Beddoes method. (a) Position of effective separation point. (b) Reconstruction of the nonlinear lift.

Mach numbers, which turns out to be extremely convenient because the variations can then be generalized empirically in a fairly simple manner using the curve fits

$$f = \begin{cases} 1 - 0.3\exp\left(\dfrac{(\alpha - \alpha_0) - \alpha_1}{S_1}\right) & \text{if } \alpha \le \alpha_1, \\ 0.04 + 0.66\exp\left(\dfrac{\alpha_1 - (\alpha - \alpha_0)}{S_2}\right) & \text{if } \alpha > \alpha_1. \end{cases} \tag{7.107}$$

The coefficients S_1 and S_2 define the static stall characteristic, that is, whether the stall occurs progressively or abruptly. The value of α_1 defines the break point corresponding to $f = 0.7$. This point is defined only as a matter of convenience; however, the value of α when $f \approx 0.7$ closely corresponds to the static stall AoA. The coefficients S_1 and S_2 and α_1 are easily determined for different Mach numbers from the static lift data. Their values are read from a data table, with values for intermediate Mach numbers being performed using interpolation, as required – see Beddoes (1983).

The pitching moment as a function of AoA can also be found from Kirchhoff–Helmholtz theory. However, in practice the resulting equation is found inadequate and Beddoes has suggested several empirical relations. From the airfoil static data, the center of pressure at any AoA may be determined from the ratio C_m/C_n (allowing for the zero lift moment C_{m_0}). The variation can be plotted versus the corresponding value of the separation point and curve fitted using a low-order polynomial. One suitable curve fit is to use the form

$$\frac{C_{m_{1/4}}}{C_n} = k_0 + k_1(1 - f) + k_2 \sin(2\pi f^m), \tag{7.108}$$

where $k_0 = (0.25 - x_{ac})$ is the aerodynamic center offset from the 1/4-chord. The constant k_1 gives the direct effect on the center of pressure as a result of the growth of the separated flow region, and the constant k_2 helps describe the shape of the moment break at stall. Again, the values of k_0, k_1, k_2, and m can be obtained using a least-squares fit to the measured center of pressure.

7.11.6 *High Angle of Attack Range*

An understanding of the aerodynamic behavior of airfoils in the high AoA regime is important for predicting the adverse effects produced in the reverse flow regime on the rotor. In the reverse flow region, the AoA increases through stall beyond 90° as the direction of the relative flow vector now changes from the trailing edge toward the leading edge of the airfoil. Although the velocities and dynamic pressure are low in this region, the low maximum lift coefficients and high drag coefficients associated with flow separation may result in a higher overall parasitic power penalty (see also Section 5.5.10).

The aerodynamics of airfoils at extreme angles of attack beyond the normal static stall angle and in reversed flow have been measured by Lock & Townend (1925), Anderson (1931), Naumann (1942), Critzos et al. (1955), and Leishman (1996). All measurements are at low Mach numbers. Representative results are reproduced in Fig. 7.51, which shows the lift, pitching moment, and drag characteristics as a function of AoA. Although the airfoil shape makes some difference to the nature of the stall characteristic at positive and negative angles of attack and in reverse flow, when the flow becomes fully separated the results become mostly independent of airfoil shape and are close to the values for a flat-plate.

In the high AoA range, the quasi-steady lift coefficient can be modeled using

$$C_l = A \sin 2(\alpha - \alpha_0), \tag{7.109}$$

where $A = 1.1$ for the NACA 0012 and $A = 1.25$ for the SC1095 when determined in a least-squares sense, with α being measured in degrees. An average value of 1.175 would seem reasonable for use with an arbitrary airfoil where the force coefficients are not known. For either airfoil, the center of pressure in the post stall regime moves close to mid-chord when $\alpha = 90°$ (i.e., $\bar{x}_{cp} = 0.5$). For the ranges $20° \leq (\alpha - \alpha_0) \leq 160°$ and $-160° \leq (\alpha - \alpha_0) \leq -20°$ the center of pressure varies approximately linearly with α and can be represented by

$$\bar{x}_{cp} = 0.33 + 0.0019(\alpha - \alpha_0) \quad \text{for } 20° \leq (\alpha - \alpha_0) \leq 160°, \tag{7.110}$$

$$\bar{x}_{cp} = 0.33 - 0.0019(\alpha - \alpha_0) \quad \text{for } -160° \leq (\alpha - \alpha_0) \leq -20°. \tag{7.111}$$

Alternatively, the pitching moment in the post stall regime can be modeled directly using

$$C_m = B \sin(\alpha - \alpha_0) + C \sin 2(\alpha - \alpha_0), \tag{7.112}$$

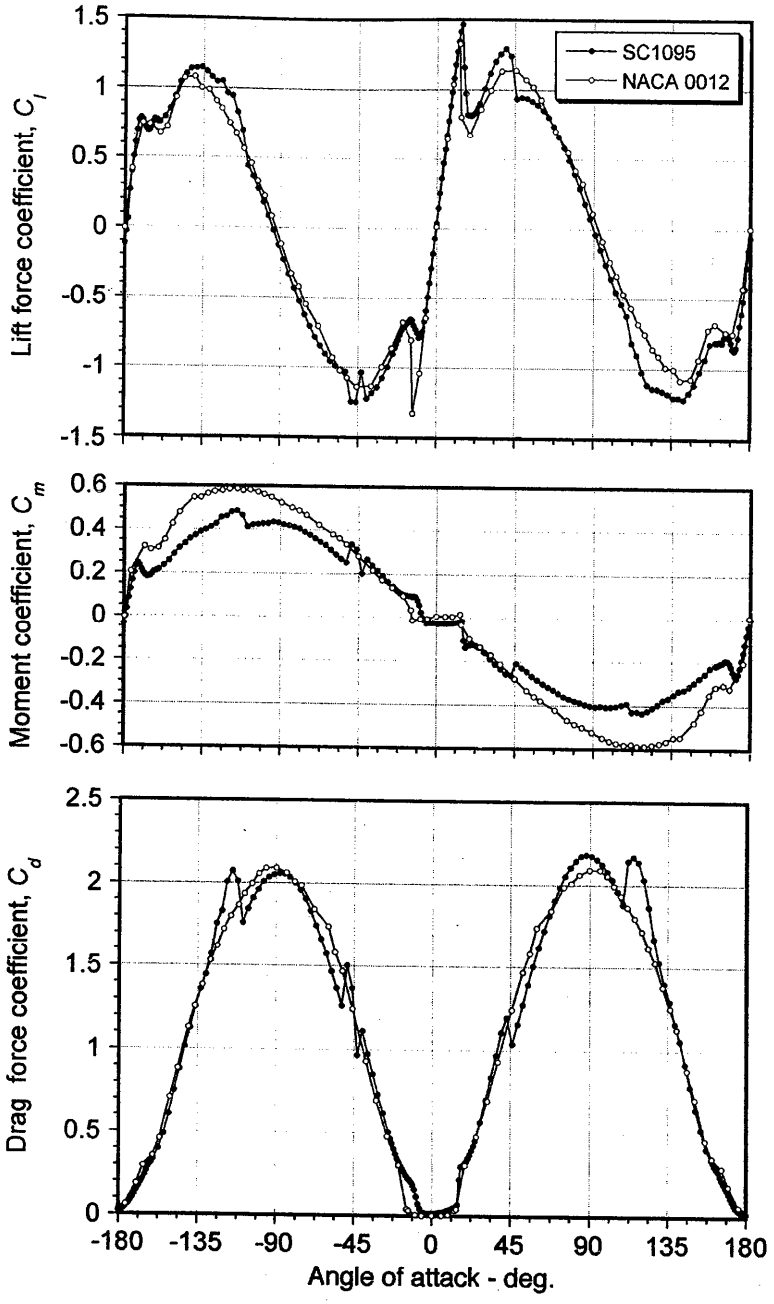

Figure 7.51 Measurements of lift, pitching moment, and drag for a complete 360° range of AoA at low Mach number. Data source: Critzos et al. (1955) and Leishman (1996).

where $B = -0.5$ and $C = 0.11$ are the averages for the two airfoils, which would seem appropriate choices for an arbitrary airfoil. Finally, the drag can be modeled using

$$C_d = D + E\cos 2(\alpha - \alpha_0), \tag{7.113}$$

with $D = 1.135$ and $E = -1.05$ for both airfoils.

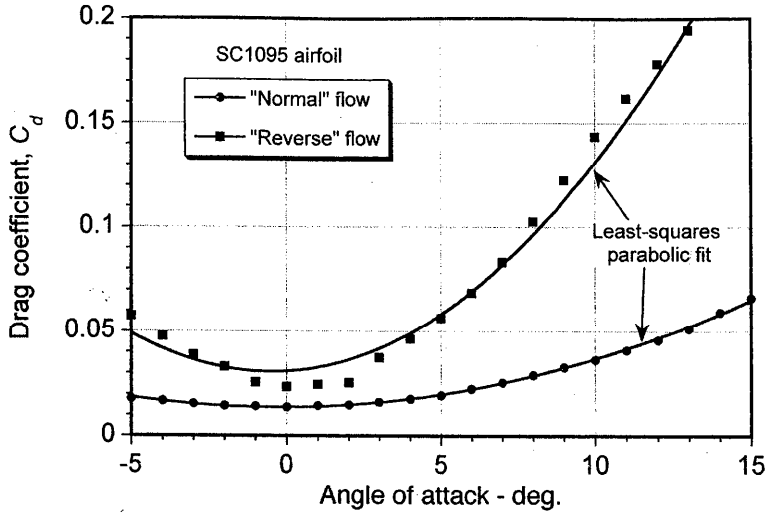

Figure 7.52 Measurements of sectional drag coefficient in normal and reverse flow. Data source: Leishman (1996).

It becomes harder to model empirically the aerodynamic characteristics in the reverse flow regime. This can be seen if the drag coefficient in "normal" and "reverse" flow is examined in detail, as shown in Fig. 7.52. While the drag in normal flow is accurately represented by a simple parabolic fit, this is less applicable for the case of reverse flow. Notice that in this case the minimum drag is approximately double the minimum drag in normal flow. Also, notice that the drag increases much more rapidly as the AoA is increased to either positive or negative values. Because the drag in reverse flow exhibits a "bucket" region, it is apparent that a parabolic fit to the measured data is less accurate in this case.

The forgoing discussion is based on the assumption that the flow in the reverse flow region is quasi-steady, but this may not necessarily be representative of the actual flow state on the rotor. This is because the flow in the reverse flow region is actually dynamic (unsteady) in nature, and the flow may not have time to adjust to the quasi-steady values. For a typical helicopter it can be shown that the aerodynamic time scales are between 2 and 6 semi-chords of airfoil travel through the flow in the reverse flow region. Based on known results from unsteady airfoil measurements [see Green (1995) and the results in Chapter 8], these time scales are short to allow the flow to readjust, even if the angles of attack were to become low enough to promote flow reattachment with reverse flow. For this reason, it is more accurate to calculate the airloads in the reverse flow region by means of a *dynamic stall* model (see Section 9.5.1). However, in the absence of such a model or other information then if the flow is stalled it would be sufficient to assume that $C_l = 0$, $\bar{x}_{cp} = 0.5$, and $C_d = 2.05$ in the reverse flow region when using the blade element method. (Note: $C_d \approx 2$ for a flat-plate at $\alpha = 90°$.)

7.12 Circulation Controlled Airfoils

Circulation controlled (CC) airfoils rely upon the Coanda effect to generate high lift independently of AoA. The Coanda effect has been introduced previously in Section 6.10.2 and is the tendency of a fluid issuing from a tangentially ejected jet to travel close to a

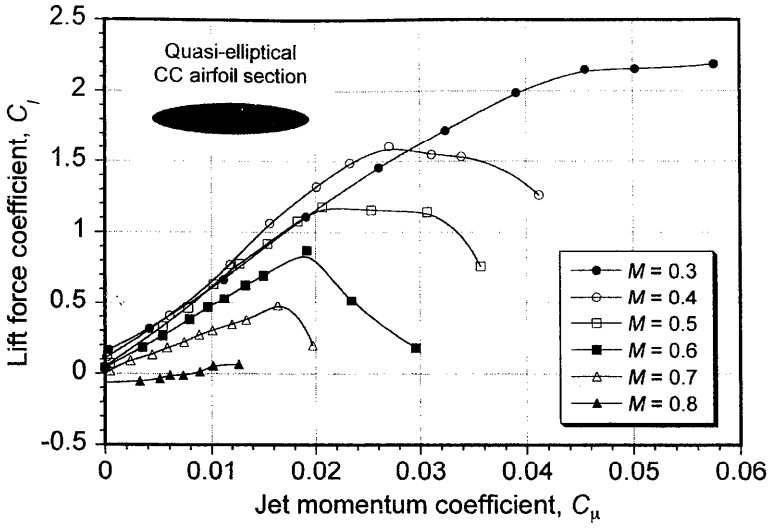

Figure 7.53 Effect of jet blowing on the lift of a circulation controlled airfoil. Data source: Publications of David W. Taylor Research and Development Center.

surface contour, even if the surface curvature diverges from the jet axis – see Newman (1961). Usually CC airfoils are elliptical or quasi-elliptical in shape, with well-rounded, almost blunt trailing edges. A balance of centrifugal force and reduced static pressure causes the thin jet to adhere to the blunt trailing edge. The jet is usually obtained by pressurizing a plenum inside the airfoil and ejecting flow out of a thin slot. Because of the high lift coefficients that can be attained with CC airfoils (often in excess of 2) they have been envisioned or applied for use on both fixed-wing and rotating-wing aircraft – see Wood & Neilsen (1986) and Reader et al. (1978).

Representative results for a CC airfoil at several free-stream Mach numbers are shown in Fig. 7.53 in terms of the jet momentum coefficient defined by

$$C_\mu = \frac{\dot{m} V_j}{\frac{1}{2}\rho V_\infty^2 c}, \tag{7.114}$$

where $\dot{m}$ is the mass flow through the slot and V_j is the jet velocity. At lower values of blowing the jet initially acts as an effective form of boundary layer control through flow entrainment on the upper surface of the airfoil. At higher blowing coefficients boundary layer control yields to super-circulation. At some point downstream of the slot the reduced static pressure and centrifugal force balance is ultimately lost (usually near where the jet velocity becomes sonic) and the jet detaches from the Coanda surface. This defines the maximum lift of the CC airfoil. The location of the jet detachment depends mainly on the strength of the jet, the slot geometry, the curvature of the Coanda surface, as well as the characteristics of the boundary layer prior to the slot.

The ideas of circulation control for application to a rotor were first investigated in depth by Cheeseman & Seed (1967). In the early 1980s, Kaman built and flight tested a CC rotor system on a HH-2D Seasprite, although only in hover and in low speed forward flight. Other applications of CC technology to rotorcraft are the ill-fated X-wing (see Linden & Biggers (1985) and Section 6.11.3) as well as the very successful NOTAR anti-torque system (see Section 6.10.2). However, while offering considerable possibilities when applied to rotor (either for either direct lift production or secondary lift control using higher harmonic

lift), the behavior of CC airfoils operating in a rotor environment is not well understood. In forward flight, a CC rotor encounters a time-varying flow environment in which both the AoA and local onset velocity vary periodically with azimuth position. Because the geometric pitch of the blade is generally held constant, jet blowing must be cyclically adjusted to for trim and control. This necessitates the modulation of the blade plenum pressure, and therefore, the jet blowing as a function of azimuth position. This is a highly unsteady aerodynamics problem.

The first theoretical work of CC airfoil aerodynamics was made by Kind (1968), Kind & Maull (1968), Dunham (1968), Dvorak & Kind (1979), and Soliman (1984). Dvorak & Kind (1979) incorporated integral and finite-difference boundary layer/jet mixing models into an external potential flow (surface singularity) model. Shrewsbury (1986) has used Navier–Stokes methods in the analysis of circulation controlled airfoils. Englar (1975) has shown results for pulsed blowing on a circulation controlled elliptical airfoil. Schmidt (1978) carried out experiments to examine the unsteady aerodynamic effects on an airfoil with a Coanda surface, reporting a transportation lag effect between the duct pressure and the blowing, as well as a decrease in lift augmentation ratio with increasing blowing frequency. A detailed bibliography of CC aerodynamics research through 1980 is given by Englar & Applegate (1984). The results of CC airfoil research as it applies to rotorcraft has been reviewed by Abramson et al. (1985).

Lorber et al. (1989) have investigated the unsteady aerodynamic behavior of an oscillating jet flap at a constant AoA and over a range of Mach numbers, albeit at limited blowing levels and at very low reduced frequencies. Ghee & Leishman (1990, 1992) and Zandieh & Leishman (1993) have investigated the behavior of a CC circular cylinder with periodic jet blowing operating in a steady free-stream. This work has also shown significant phase lags exist between the application of blowing and the buildup of the airloads. Furthermore, under some conditions unsteady blowing may cause sudden jet detachment, whereas this may not occur with steady blowing under the same free-stream conditions.

Computational work on modeling the behavior of CC airfoils under unsteady conditions is relatively scarce. Raghavan et al. (1988) and Sun & Wang (1989) used a surface singularity–boundary layer method for CC airfoils operating in an unsteady free-stream flow and with unsteady blowing, showing that CC airfoils will exhibit both a lift attenuation and a phase lag with respect to the blowing. While CC is clearly attractive because of the potentially high lift capability, the behavior of CC airfoils in an unsteady rotor environment is still not well understood. Nevertheless, CC airfoil concepts continue to be suggested for use on rotorcraft, but none have yet proved successful or practical.

7.13 Very Low Reynolds Number Airfoil Characteristics

There has been much recent interest in understanding rotating wing airfoil characteristics at very low Reynolds numbers because of the generally low performance of existing micro air vehicles or MAVs (see Müller (2001) and discussion by Bohorquez et al. (2003), and also Section 6.14). The flow over airfoils at Reynolds numbers of less than 10^5 are generally more complicated that those at higher Reynolds numbers because of stronger viscous effects, and as yet these effects are not well understood. The main problems include: 1. The susceptibility of a laminar boundary layer to separate under only mild adverse pressure gradients; 2. The formation of long laminar separation bubbles; 3. The thick boundary layers, high drag, and low maximum lift coefficients; and 4. The increased sensitivity of airfoil characteristics to surface condition and free-stream turbulence. Furthermore, at these low Reynolds numbers the airfoil characteristics tend to vary in a highly nonlinear manner with

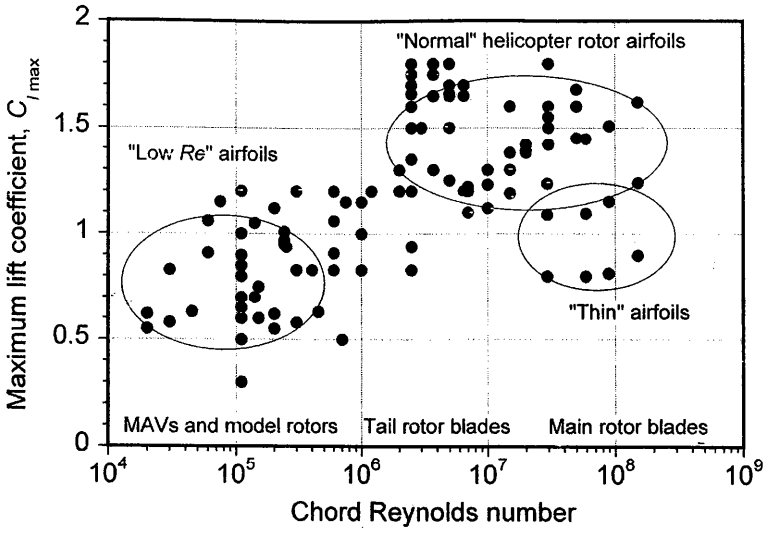

Figure 7.54 At very low chord Reynolds numbers of less than 10^5 nearly all airfoils have relatively low values of maximum lift coefficient. Consolidated data source: Woods et al. (2001).

respect to AoA, making modeling attempts much more challenging. It is in this regime that fundamental research in experimental fluid mechanics and modeling efforts using advanced numerical solutions to the Navier–Stokes equations are beginning to make an impact – see Müller (2001).

Besides the generally higher drag coefficients of airfoils that operate at low Reynolds numbers (see Fig. 7.4) this is accompanied by low maximum lift coefficients of 1.0 or less and low lift-to-drag ratios of 10 or less. This seriously impacts the overall flight performance of rotating-wing based MAVs – see Bohorquez et al. (2003) and Martin (2005). The results shown in Fig. 7.54 are consolidated data from many sources of low Reynolds number measurements that have been compiled by Woods et al. (2001) and show that values of $C_{l_{max}}$ may be on average about half of the values found at higher Reynolds numbers, but perhaps with some exceptions. It would seem also that at these Reynolds numbers the aerodynamic performance of crude flat-plate types of airfoils are often surprisingly better that conventional airfoil profiles, raising many questions about what a low Reynolds number airfoil should really look like, especially for a rotor. The impact of higher airfoil drag coefficients and lower maximum lift coefficients generally translates into much lower values of rotor figure of merit; measured values of FM for rotating wing MAVs are typically in the range of 0.3 to 0.4 compared to values approaching 0.82 for a modern full-scale helicopter rotor (Fig. 6.2). However, the ability to generate maximum lift coefficients of more than 1.5 on rotating wings at very low Reynolds numbers seems possible based on the studies of Azuma & Yasuda (1989). For further information on the aerodynamics of airfoils at very low Reynolds numbers; see AGARD (1985), RAeS (1986), and Müller (2001).

7.14 Effects of Damage on Airfoil Performance

Ballistic vulnerability is an important consideration for military helicopters because they generally fly lower and slower than fixed-wing aircraft. Therefore, to minimize unexpected attrition of helicopter forces, any performance degradation must be minimized

and, if possible, prevented to ensure continued success on the battlefield. Compared to fixed-wing aircraft, however, helicopters have a much lower degree of system redundancy because the rotor itself provides all of the lift, propulsion and control. This means that any damage inflicted to the main or tail rotor systems is more likely to have serious consequences. Increased emphasis on improving survivability for US military helicopters has led to the Joint Live Fire (JLF) test program. These simulated live fire tests have helped to identify any especially vulnerable airframe components and aircraft subsystems early in the development cycle, so that potential problems can be rectified without incurring weight or cost penalties; see Foulk (1976) and Atkinson & Ball (1995).

While the use of modern composite materials give a high level damage tolerance to rotor blades, ballistic damage may still present significant problems in regard to the aerodynamic performance. A quantitative understanding of the aerodynamic effects of ballistic damage on the rotor system is, therefore, essential for the development and/or improvement of mathematical models representing these degraded aerodynamic effects in rotor analyses and to help assess reasonable risks in carrying on with a mission after the helicopter has been hit by a projectile. Unfortunately, the aerodynamic effects of blade damage will be a function of many interrelated parameters, including the location (chordwise and spanwise), physical nature of the damage and extent of damage. This makes the aerodynamic effects difficult to generalize. Yet it is clear that damage inflicted to the outboard sections of the blade are going to be aerodynamically more important on a rotor because of the high dynamic pressure in this area. At a minimum, a small damaged area on the blade may dramatically decrease section lift and increase drag. This will result in a loss of rotor thrust, increased rotor power requirements, the possibilities of premature blade stall, high control forces, and/or increased vibration levels. Even a minor performance degradation resulting from damage may incur much higher fuel consumption, and may seriously limit the ability of the helicopter to complete its assigned mission.

Some of the earliest recorded tests on the aerodynamic effects of ballistic damage was performed at NACA – see NACA (1936). This work examined the effects of machine gun and cannon fire on the lift and drag properties of fabric covered aircraft wings. More systematic experimental investigations were carried out by Reece (1952a,b). The results, which included measurements of the drag increase incurred by different damaged configurations, became the basis for later studies by Chang & Stearman (1980) and Westkaemper (1980). However, it is difficult to properly quantify ballistic damage effects on the aerodynamic characteristics of helicopter rotor blades because of the very 3-D and time-varying flow environment. Helicopter blade sections are often quite different physically and aerodynamically to those used on fixed-wing aircraft, so it may not be appropriate to extrapolate any known results to helicopters. Eastman (1993) has made some attempt to assess the aerodynamic effects on a UH-60 main rotor blade subject to ballistic damage. Leishman (1993, 1996) has made experimental measurements of the aerodynamic characteristics of series of helicopter blade sections with both simulated and actual ballistic damage. Other measurements on damaged airfoil sections have been conducted by Erwin & Render (2000).

These tests have all revealed that ballistic damage significantly degraded the aerodynamic characteristics of the blade section, with a loss in lifting performance, changes in the pitching moment characteristics and a substantial increase in sectional drag. For example, Fig. 7.55 shows the measured aerodynamic characteristics of an undamaged SC1095-R8 airfoil section relative to two damaged specimens; one with simulated damage toward the leading edge and the other with damage near the trailing edge. The leading edge damaged blade section had a circular hole cut through the blade spar, whereas the damage at the

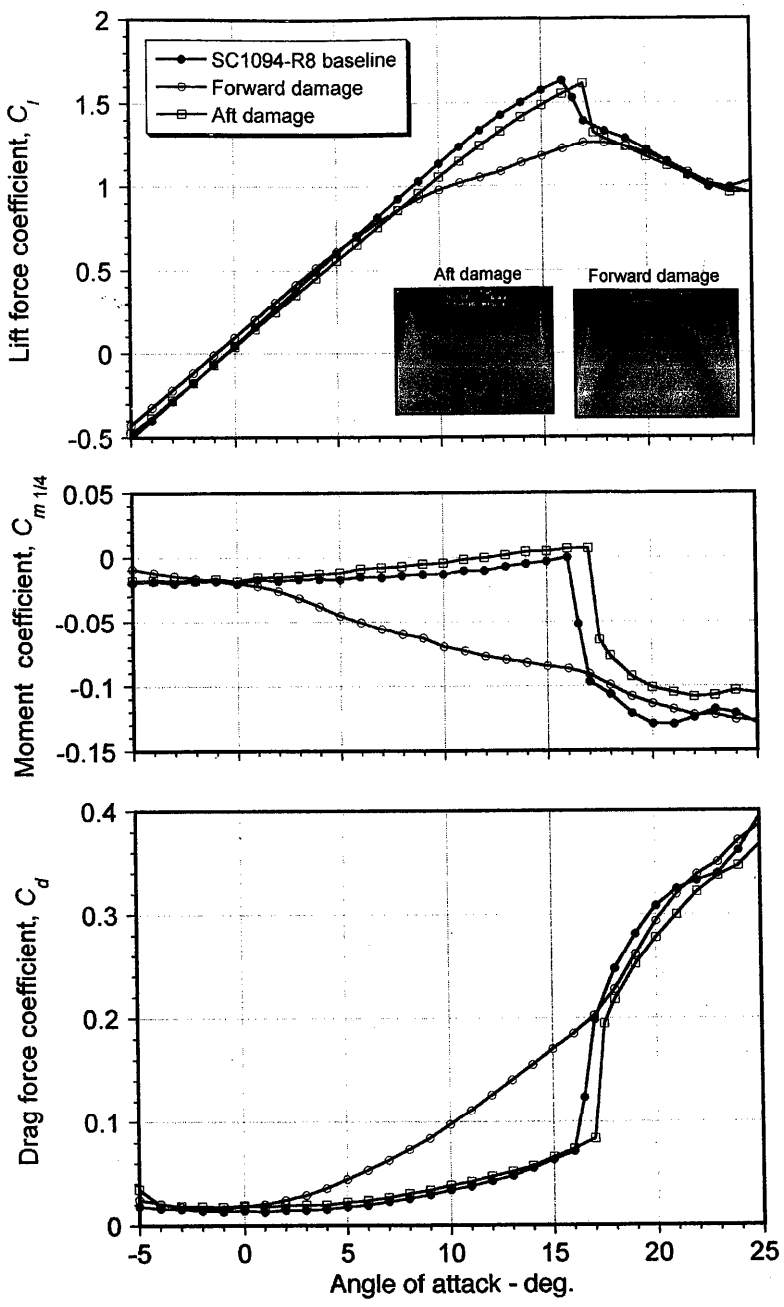

Figure 7.55 Comparison of the lift, moment and drag coefficients of an undamaged airfoil section versus two specimens with simulated damage at the leading- and trailing-edges, respectively. Mach number = 0.3, Reynolds number = 2×10^6. Data source: Leishman (1996).

trailing edge was cut into the paper honeycomb structure. It is apparent that damage near the leading edge of the section is more critical in terms of its effects on the aerodynamics than damage at the trailing edge. Notice that with leading edge damage, the lift-curve-slope decreases dramatically at approximately 6 degrees, yet the lift still continues to increase linearly after this point until stall occurs. This elbow in the lift-curve-slope is most likely

the result of increased flow from the lower surface up through the hole to the upper surface at higher angles of attack, that is, a "jet in a crossflow effect" – see Erwin & Render (2000). Flow visualization (inset in Fig. 7.55) has shown that this tends to fix the point of flow separation over the range from lower angles of attack through the stall angle. For increasing angles of attack this separation extends over large parts of the blade chord and span. Interestingly, while reaching a lower maximum lift coefficient than either the baseline or the specimen with trailing edge damage, the final stall AoA is at least 3° higher. The pitching moment variation suggests that leading edge damage caused an aft movement of the aerodynamic center, which would probably not result in any adverse aeroelastic effects on the rotor. However, the drag for the forward damaged blade section is much larger than the baseline, growing from 1.4 times the baseline value at lower angles of attack to more than 2.5 times at higher angles of attack. This would have a very major effect on rotor performance and blade loads.

7.15 Chapter Review

This chapter has described some basic aerodynamic characteristics of airfoil sections and has provided a basis for assessing the potential impact of airfoil design and selection on helicopter rotor performance. Methods of geometrically defining airfoils have been described following the NACA approach of combining camberlines and thickness envelopes. This is justified because many of the airfoils used on current helicopter rotors have their origin in the NACA sections. Also, the ideas of combining loading distributions associated with thickness and camber allow the primary effects of geometric shape on the chordwise loading and overall aerodynamic characteristics to be assessed. However, the primary discussion in this chapter has been centered around published measurements of static airfoil characteristics. These results, while from more than one primary source, allow a good basis from which to compare airfoil behavior, and for the most part are considered relatively unbiased by the wind tunnel test facility or by testing techniques. For these latter reasons, it has not been considered fruitful to dwell on the relative merits of airfoils designed by the various competing helicopter manufacturers.

Airfoils designed for helicopter applications have traditionally been obtained through a long evolutionary process, in which various levels of theory and experimental measurements have been combined in the pursuit of airfoil shapes with higher values of maximum lift, better lift-to-drag ratios, lower pitching moments, and higher drag divergence Mach numbers. It has been shown that, in general, these requirements are conflicting, making the design of general purpose rotor airfoils extremely challenging. Instead, various families of airfoils have been developed and optimized to meet the specific needs of different parts of the rotor blade. For example, airfoils with high camber and moderate thickness, which give high values of maximum lift, are used between 60 and 85% of blade radius. Much thinner airfoils, perhaps even those with supercritical-like shapes, give relatively high drag divergence Mach numbers and have been designed for the tip region of the blade ($>85\%R$). The use of different airfoils along the blade is made easier today because of computer-aided design and composite manufacturing capability, which involves only small additional costs over a blade made with a single airfoil section.

The principles of integrating surface pressure and shear stress distributions to obtain lift, drag and pitching moment coefficients on airfoils have been reviewed. Representative airfoil characteristics have been discussed, along with the limits of conventional linearized theories in predicting this behavior. Because of the importance of low pitching moments in the design of helicopter airfoils, the principles of defining the aerodynamic center and center of pressure have been reviewed. The influence of Reynolds number and Mach number on airfoil

characteristics have been highlighted. Although these parameters have both dependent and interdependent effects on airfoil behavior, it has been possible to isolate the basic effects and assess their significance on maximum lift and other important airfoil characteristics. Because the design of airfoils with high values of maximum lift can result in smaller and lighter rotors with lower solidity, the geometric shape of the airfoil and other factors affecting maximum lift have been discussed in detail.

While an improved understanding of airfoil characteristics will usually lead to an improved analysis capability of existing rotor designs, and may lead to new rotors optimized for greater performance in both hover and high-speed forward flight, the performance of the rotor cannot be completely parameterized on the basis of static (steady) considerations alone. Therefore, in the next two chapters, the important role of unsteady aerodynamics on the problem of airfoil behavior are discussed.

7.16 Questions

7.1. Write a computer program to plot the geometry of the NACA four-digit airfoil sections. In particular, plot the shape of the NACA 0018 airfoil section. Using an enlarged plot, clearly show the location of the nose radius and how it is faired into the lower and upper surfaces.

7.2. Use the 230 camberline to construct the coordinates of the NACA 23018 airfoil section. Clearly show the construction of the nose radius relative to the camberline and in relation to the lower and upper surfaces of the airfoil, and show how the nose radius protrudes slightly forward of $\bar{x} = 0$.

7.3. Construct the family of airfoils: 22015, 23015, and 25015. By means of thin-airfoil theory, compute the zero-lift AoA and pitching moment coefficient for this series of airfoils. Comment on your results.

7.4. Consider the family of airfoils: NACA 24006, 24012, and 24018. Use linear superposition principles and the tabulated results in Abbott & von Doenhoff to show the effects of thickness on the distribution of chordwise pressure. Compare the results at the same mean lift coefficient of 1.0. Comment on your results.

7.5. The upper and lower surface pressure coefficients on a particular airfoil at a particular AoA are assumed to be approximated by the functions

$$C_{p_u}(\bar{x}) = -(100\bar{x}^{3/4}\ \exp(-(30\bar{x} - 1)) + 0.75\bar{x}^{1/7}(1 - \bar{x})),$$
$$C_{p_l}(\bar{x}) = 10\bar{x} \quad \text{for } 0 \le \bar{x} \le 0.1,$$
$$C_{p_l}(\bar{x}) = 1.11(1 - \bar{x}) \quad \text{for } 0.1 \le \bar{x} \le 1.$$

The airfoil geometry as a fraction of chord is given by the piecewise continuous functions

$$\bar{y}(\bar{x}) = \pm 0.06\sqrt{(1 - \tfrac{1}{9}(8\bar{x} - 3)^2)} \quad \text{for } 0 \le \bar{x} \le 3/5,$$
$$\bar{y}(\bar{x}) = \pm 0.12(1 - \bar{x}) \quad \text{for } 3/5 \le \bar{x} \le 1.$$

Plot the pressure distribution with respect to chord and with respect to thickness. Estimate numerically, and for different numbers of points (say, 10, 50, 100, 200): (a) the normal force coefficient, (b) the chord force (leading edge suction) coefficient, (c) the pitching moment coefficient about the leading edge, and (d) the pitching moment coefficient about 27% chord.

7.6. Test results for a new helicopter airfoil section show that the normal force coefficient and the pitching moment coefficient about the 1/4-chord vary with the AoA as given in the following table for Mach numbers of 0.3, 0.5, and 0.7. For each Mach number, find the lift-curve-slope in the low AoA range, the zero-lift angle of attack, the aerodynamic center, and the zero-lift moment coefficient. Comment on your results.

$M_\infty = 0.3$				$M_\infty = 0.5$				$M_\infty = 0.7$			
α	C_n	α	C_m	α	C_n	α	C_m	α	C_n	α	C_m
−10.0	−0.690	−16.0	0.199	−10.0	−0.690	−16.0	0.199	−10.0	−0.730	−16.0	0.199
−8.0	−0.610	−16.0	0.198	−8.0	−0.600	−16.0	0.184	−8.0	−0.640	−16.0	0.130
−6.0	−0.530	−8.0	−0.012	−6.0	−0.510	−8.0	−0.0104	−6.0	−0.720	−8.0	−0.0068
−4.0	−0.312	−7.0	−0.011	−4.0	−0.350	−7.0	−0.0114	−4.0	−0.420	−7.0	−0.0252
−3.0	−0.201	−5.0	−0.0091	−3.0	−0.229	−5.0	−0.0100	−3.0	−0.270	−5.0	−0.0335
−2.0	−0.093	−3.0	−0.0081	−2.0	−0.108	−3.0	−0.0095	−2.0	−0.120	−3.0	−0.0243
−1.5	−0.039	−2.5	−0.0071	−1.5	−0.047	−2.5	−0.0091	−1.5	−0.045	−2.5	−0.0243
−1.0	0.058	−1.0	−0.0060	−1.0	0.014	−1.0	−0.0092	−1.0	0.030	−1.0	−0.0151
0.0	0.125	0.0	−0.0050	0.0	0.135	0.0	−0.0071	0.0	0.180	0.0	−0.0140
1.0	0.232	2.0	−0.0040	1.0	0.254	2.0	−0.0040	1.0	0.333	2.0	−0.0050
2.0	0.339	4.0	−0.0010	2.0	0.374	4.0	−0.0009	2.0	0.486	4.0	−0.0093
3.0	0.447	6.5	0.0010	3.0	0.493	6.5	0.0042	3.0	0.639	6.5	−0.0323
3.5	0.500	12.0	0.0058	3.5	0.553	12.0	−0.0100	3.5	0.708	12.0	−0.0121
4.0	0.554	15.5	0.0045	4.0	0.612	15.5	−0.0489	4.0	0.770	15.5	−0.0122
6.0	0.768	16.0	−0.0610	6.0	0.851	16.0	−0.0610	6.0	0.875	16.0	−0.0610
8.0	0.983			8.0	1.060			8.0	0.857		
10.0	1.180			10.0	1.210			10.0	0.903		
12.0	1.360			12.0	1.220			12.0	0.963		
14.0	1.540			14.0	1.250			14.0	1.022		
16.0	1.650			16.0	1.207			16.0	1.081		
17.0	1.653			17.0	1.189			17.0	1.105		

7.7. An 11 cm chord model of the airfoil refered to in the previous question is to be tested in a 30 cm-by-25 cm high-speed pressurized wind tunnel. The airfoil completely spans the larger dimension of the working section and can be pivoted about the 1/4-chord axis driven by an actuator system. To achieve high Reynolds numbers, the wind tunnel operates at 5 atmospheres and the temperature in the working section is $320°K$. *Estimate* the design loads for the model support structure and actuator system. Comment on your results.

7.8. When testing a new airfoil section for helicopter applications, the lift variation at $M_\infty = 0.4$ shows an abrupt break at an AoA of 13.5°. What static stall mechanism may be displayed by this airfoil? Describe the various steps that would be taken to confirm the stall type.

7.9. The drag on an airfoil (at low angles of attack) can be estimated by measuring the streamwise velocity in the wake behind the airfoil in a plane normal to the chord. The resulting distribution of velocity can be approximated by the equation

$$\frac{v(y)}{V_\infty} = \left[1 - \frac{1}{2}\cos\left(\frac{\pi y}{2W}\right)\right],$$

where $2W$ is the total width of the wake normal to the airfoil chord. Using the "momentum deficiency" approach (application of momentum conservation equation in integral form to a control volume surrounding the airfoil and its wake), find an expression for the drag coefficient C_d in terms of the measured wake width W.

Bibliography

Abbott, I. H. and von Doenhoff, A. E. 1949. *Theory of Wing Sections, Including a Summary of Airfoil Data*, McGraw-Hill Book Co., Inc., New York, NY. (Reprinted by Dover Publications, New York, NY, 1959.)

Abbott, I. H., von Doenhoff, A. E., and Stivers, L. S., Jr. 1945. "Summary of Airfoil Data," NACA Rep. No. 824.

Abramson J., Rogers E. O., and Schwartz A. W. 1985. "Applied Aerodynamics of CC Airfoils and Rotors," 41st Annual Forum of the American Helicopter Soc., Ft. Worth, TX, May 15–17.

AGARD. 1985. "Low Reynolds Number Vehicles," AGARDograph AG-288.

Amitay, M.,-Smith, B. L., and Glezer, A. 1998. "Aerodynamic Flow Control Using Synthetic Jet Technology," AIAA Paper 98-0208, 36th Aerospace Sciences Meeting and Exhibit, Reno, NV, Jan. 12–15.

Anderson, R. F. 1931. "The Aerodynamic Characteristics of Six Commonly Used Airfoils over a Large Range of Positive and Negative Angles of Attack," NACA TN 397.

Atkinson, D. B. and Ball, R. E. 1995. "A History of the Survivability Design of Military Aircraft," AIAA Paper 95-1421, 36th Annual AIAA/ASME/ASCE/AHS/ASC Structures, Structural Dynamics, and Materials Conference, New Orleans, LA, April 10–11.

Azuma, A. and Yasuda, K. 1989. "Flight Performance of Rotary Seeds," *J. of Experimental Biology*, 138, pp. 23–54.

Beavan, J. A. and Lock, C. N. H. 1939. "The Effect of Blade Twist on the Characteristics of the C.30 Autogyro," ARC R & M 1727.

Beddoes, T. S. 1983. "Representation of Airfoil Behavior," *Vertica*, 7 (2), pp. 183–197.

Benson, R. G., Dadone, L. U., Gormont, R. E., and Kohler, G. 1973. "Influence of Airfoils on Stall Flutter Boundaries of Articulated Helicopter Rotors." *J. of the American Helicopter Soc.*, 18 (1), pp. 36–46.

Bezard, H. 1992. "Rotor Blade Design by Numerical Optimization and Unsteady Calculations," 48th Annual Forum of the American Helicopter Soc., Washington DC, June 3–5.

Bingham, G. J. 1975. "An Analytical Evaluation of Airfoil Sections for Helicopter Rotor Applications," NASA TN D-7796.

Bingham, G. J. and Noonan, K. W. 1982. "Two-Dimensional Aerodynamic Characteristics of Three Rotorcraft Airfoils at Mach Numbers from 0.35 to 0.90," NASA TP-2000, AVRADCOM TR-82-B-2.

Blasius, H. 1908. "Grenzschichten in Flüssigkeiten mit kleiner Rewing," *z. Math. Phys.*, 56. (Available as NACA TM 1256.)

Bohorquez, P., Samuel, P., Sirohi, J., Pines, D., Rudd, L., and Perel, R. 2003. "Design, Analysis and Performance of a Rotary Wing Micro Air Vehicle," *J. of the American Helicopter Soc.*, 48 (2), pp. 80–90.

Caradonna, F. X. and Isom, M. P. 1972. "Subsonic and Transonic Potential Flow over Helicopter Rotor Blades," *AIAA J.*, 10 (12), pp. 1606–1612.

Caradonna, F. X. and Isom, M. P. 1976. "Numerical Calculation of Unsteady Transonic Potential Flow over Helicopter Rotor Blades," *AIAA J.*, 14 (4), pp. 482–487.

Caradonna, F. X. and Philippe, J. J. 1978. "The Flow over a Helicopter Blade Tip in the Transonic Regime," *Vertica*, 2 (1), pp. 43–60.

Chang, J. H. and Stearman, R. O. 1980. "The Effects of Warhead-Induced Damage on the Aeroelastic Characteristics of Lifting Surfaces," Vol. 1–Aeroelastic Effects, AFOSR-TR-80-1039.

Cheeseman, I. C. and Seed, A. R. 1967. "The Application of Circulation Control by Blowing to Helicopter Rotors," *J. of the Royal Aeronautical Soc.*, 71, July, pp. 451–467.

Cierva, J. de la and Rose, D. 1931. *Wings of Tomorrow: The Story of the Autogiro*, Brewer, Warren & Putnam, New York, NY.

Critzos, C. C., Heyson, H. H., and Boswinkle, R. W. 1955. "Aerodynamic Characteristics of NACA 0012 Airfoil Section at Angles of Attack from 0° to 180°," NACA TN 3361.

Dadone, L. U. 1978. "Rotor Airfoil Optimization: An Understanding of the Physical Limits," 34th Annual Forum of the American Helicopter Soc., Washington DC, May 15–17.

Dadone, L. U. 1982. "The Role of Analysis in the Aerodynamic Design of Advanced Rotors," In: AGARD CP 334.

Dadone, L. U. 1987. "Future Directions in Helicopter Rotor Development," American Helicopter Soc. Aeroacoustics Specialists' Meeting, Arlington, TX, Feb. 25–27.

Dadone, L. U. and Fukushima, T. 1975. "A Review of Design Objectives for Advanced Helicopter Rotor Airfoils," American Helicopter Soc. Northeast Region Symp., Hartford, CT.

Dunham, J. 1968. "A Theory of Circulation Control by Slot Blowing Applied to a Circular Cylinder," *J. of Fluid Mechanics*, 33 (3), pp. 495–514.

Dunham, J. 1970. "Experiments Toward a Circulation-Controlled Lifting Rotor: Part I–Wind Tunnel Tests," *J. of the Royal Aeronautical Soc.*, 74, Jan., pp. 91–103.

Dvorak, F. A. and Kind, R. J. 1979. "Analysis Method for Viscous Flow Over Circulation Controlled Airfoils," *J. of Aircraft*, 16 (1), pp. 23–28.

Eastman, L. 1993. "UH-60A Dynamic Main Rotor Blade Ballistic Vulnerability Assessment," United Technologies Report SER-701981.

Englar, R. J. 1975. "Subsonic Two-Dimensional Wind Tunnel Investigations of the High Lift Capability of Circulation Control Wing Sections," David Taylor Naval Ship Research and Development Center Report ASED-274, April.

Englar, R. J. and Applegate, C. A. 1984. "Circulation Control–A Bibliography of DTNSRDC Research and Selected Outside References," David W. Taylor Research and Development Center Report DTNSRDC-84/052, Sept.

Erwin, A. J. and Render, A. J. 2000. "The Influence of Mid-Chord Battle Damage on the Aerodynamic Characteristics of Two Dimensional Wings," *Aeronautical J.*, 104 (1033), pp. 153–161.

Eppler, R. and Somers, D. M. 1980. "A Computer Program for the Design and Analysis of Low-Speed Airfoils, Including Transition," NASA TM-80210 (Supplement NASA TM-81862).

Evans, W. T. and Mort, K. W. 1959. "Analysis of Computed Flow Parameters for a Set of Sudden Stalls in Low Speed Two-Dimensional Flow," NASA TN D-85.

Ferri, A. 1945. "Completed Tabulation in the United States of Tests of 24 Airfoils at High Mach Numbers," NACA WR L-143. Also ACR No. L5E21.

Flemming, R. J. 1982. "An Experimental Evaluation of Advanced Rotorcraft Airfoils in the NASA Ames Eleven-Foot Wind Tunnel," NASA CR-166587.

Foulk, J. B. 1976. "Survivability of the Army/Sikorsky YUH-60A Helicopter," Preprint No. 1011, 32nd Annual National V/STOL Forum of the American Helicopter Soc., Washington DC, May 10–12.

Gault, D. E. 1957. "A Correlation of Low Speed Airfoil Section Stalling Characteristics with Reynolds Number and Airfoil Geometry," NACA TN 3963.

Gessow, A. and Myers, G. C. Jr. 1952. *Aerodynamics of the Helicopter*, Macmillan Co., New York, NY, 1967, pp. 244–249. (Republished by Frederick Ungar Publishing, New York, NY.)

Ghee, T. A. and Leishman, J. G. 1990. "Effects of Unsteady Blowing on the Lift of a Circulation Controlled Cylinder,"*J. of the American Helicopter Soc.*, 34 (3), pp. 90–93.

Ghee, T. A. and Leishman, J. G. 1992. "Unsteady Circulation Control Aerodynamics of a Circular Cylinder with Periodic Jet Blowing,"*AIAA J.*, 30 (2), pp. 289–299.

Glauert, H, 1927. "The Effect of Compressibility on the Lift of an Aerofoil," ARC R & M 1095.

Glauert, H, 1947. *The Elements of Airscrew and Aerofoil Theory,* Cambridge University Press, Cambridge, UK.

Green, R. B. and Galbraith, R. A. McD. 1995. "Dynamic Recovery to Fully Attached Aerofoil Flow from Deep Stall," *AIAA J.*, 33 (8), pp. 1433–1440.

Hassan, A. A., Nagib, H., and Wygnanski, I. 2002. "Oscillatory Jets–Benefits and Numerical Modeling Issues," 58th Annual Forum of the American Helicopter Soc., June 11–13, Montréal, Canada.

Houghton, E. L. and Carpenter, P. W. 1993. *Aerodynamics for Engineering Students*, John Wiley & Sons, Inc., New York, NY, Chapter 4.

Hess, J. L. and Smith, A. M. O. 1967. "Calculation of Potential Flow About Arbitrary Bodies," *Progress in Aero. Sciences*, 8 (1), Pergamon Press.

Hicks, R. M. and McCroskey, W. J. 1980. "An Experimental Evaluation of a Helicopter Rotor Section Designed by Numerical Optimization," NASA TM 78622.

Horton, H. P. 1967. "A Semi-Empirical Theory for the Growth and Bursting of Laminar Separation Bubbles," ARC C & P 1073.

Jacobs, E. N. Pinkerton, R. M., and Greenberg, H. 1935. "Tests in the Variable-Density Wind Tunnel of Related Airfoils Having the Maximum Camber Unusually Far Forward," NACA Report 537.

Jacobs, E. N. and Sherman, A. 1937. "Airfoil Section Characteristics as Affected by Variations of the Reynolds Number," NACA TR 586.

Joslin, R. D. 1998. "Aircraft Laminar Flow Control," *Annual Review of Fluid Mechanics*, 30 (198), pp. 1–29.

Kaplan, C. 1946. "Effect of Compressibility at High Subsonic Velocities on the Lifting Force Acting on an Elliptic Cylinder," NACA TN 1118.

Kennedy, J. L. and Marsden, D. J. 1978. "A Potential Flow Design Method for Multi-Component Airfoil Sections," *J. of Aircraft*, 15 (1), pp. 47–52.

Kerho, M. F. and Kramer, B. R. 2003. "Enhanced Airfoil Design Incorporating Boundary Layer Mixing Devices," AIAA Paper 2003-0211, 41st AIAA Aerospace Sciences Meeting & Exhibit, Reno, NV, Jan. 6–9.

Kind, R. J. 1968. "A Calculation Method for Circulation Control by Tangential Blowing Around a Bluff Trailing Edge," *Aeronautical Quarterly*, 19, Aug., pp. 205–223.

Kind, R. J. and Maull, D. J. 1968. "An Experimental Investigation of a Low-Speed Circulation Controlled Aerofoil," *Aeronautical Quarterly*, 19, May, pp. 170–182.

Kuo, Y. H. 1953. "On the Flow of an Incompressible Viscous Fluid Past a Flat Plate at Moderate Reynolds Numbers," *J. of Mathematics & Physics*, 32, pp. 83–100.

Ladson, C. L., Brooks, C. W., Hill, A. S., and Sproles, D. W. 1995. "Computer Program to Obtain Ordinates for NACA Airfoils," NASA Technical Memorandum 4741.

Liebeck, R. H. 1992. "Laminar Separation Bubbles and Airfoil Design at Low Reynolds Numbers," AIAA Paper 92-2735-CP, AIAA 10th Applied Aerodynamics Conference, Palo Alto, CA, June 22–24.

Leishman, J. G. 1993. "Aerodynamic Characteristics of a Helicopter Rotor Airfoil as Affected by Simulated Ballistic Damage," United States Army Research Laboratory, Report ARL-CR-66, April.

Leishman, J. G. 1996. "Experimental Investigation into the Aerodynamic Characteristics of Helicopter Rotor Airfoils with Ballistic Damage," United States Army Research Laboratory, Report ARL-CR-295, April.

Liepman, H. W. 1946. "The Interaction Between Boundary Layer and Shock Waves in Transonic Flow," *J. of the Aeronautical Sciences*, 13 (912), pp. 623–637.

Linden, A. W. and Biggers, J. C. 1985. "X-Wing Potential for Navy Applications," 41st Annual Forum of the American Helicopter Soc., Ft. Worth, TX, May 15–17.

Lock, C. N. H. and Townend, H. C. H. 1925. "Lift and Drag of Two Aerofoils Measured over 360° Range of Incidence," ARC R & M 958.

Loftin, L. K. 1945. "Effects of Specific Types of Surface Roughness on Boundary-Layer Transition," NACA ACR L5J29a (Wartime Report No. L-48).

Lorber, P. F., Carta, F. O., and Carlson, R. G. 1989. "The Aerodynamics of an Oscillating Jet Flap," *J. of the American Helicopter Soc.*, 34 (2), pp. 24–32.

Malone, J. B., Narramore, J. C., and Sankar, L. N. 1989. "An Efficient Airfoil Design Method Using the Navier–Stokes Equations," AGARD FPD Specialists' Meeting on Computational Methods for Aerodynamic Design (Inverse) and Optimization, Loen, Norway, May 22–23.

Martin, P. B. 2005. "Rotor Blade Airfoil Design for High-Altitude VTOL UAVs," American Helicopter Soc. Specialists' Meeting on Unmanned Rotorcraft: Design, Control & Testing, Chandler, AZ, Jan. 18–20.

McCroskey, W. J. 1977. "Some Current Research in Unsteady Fluid Dynamics," *J. of Fluids Engineering*, 99 (1), pp. 8–39.

McCroskey, W. J. 1987. "A Critical Assessment of Wind Tunnel Results for the NACA 0012 Airfoil," AGARD Fluid Dynamics Panel Symp. on Aerodynamic Data Accuracy and Quality: Requirements and Capabilities on Wind Tunnel Testing, Naples, Italy, Sept. 28–Oct. 2. See also NASA Technical Memorandum 100019.

McCroskey, W. J., McAlister, K. W., Carr, L. W., and Pucci, S. L. 1982. "An Experimental Study of Dynamic Stall on Advanced Airfoil Sections," 1, 2 & 3, NASA TM-84245.

McCroskey, W. J. and Baeder, J. D. 1985. "Some Recent Advances in Computational Aerodynamics for Helicopter Applications," NASA TM-86777.

McCullough, G. B. and Gault, D. E. 1953. "Examples of Three Types of Stall," NACA TN 2502.

Moss, G. F. and Murdin, P. M. 1965. "Two Dimensional Low-Speed Tunnel Tests on the NACA 0012 Section Including Measurements Made during Pitching Oscillations at the Stall," ARC C & P 1145.

Munk, M. M. 1922. "General Theory of Thin Wing Sections," NACA TR 142.

Munk, M. M. 1924. "Elements of the Wing Section Theory and of the Wing Theory," NACA TR 191.

Müller, T. J. (Ed.) 2001. *Fixed and Flapping Wing Aerodynamics for Micro Air Vehicles*, AIAA Progress in Aeronautics and Astronautics, Vol. 195, Reston, VA.

NACA. 1936 "Effects of Machine Gun and Cannon Fire on the Lift and Drag Properties of Airplane Wings," Report for Aberdeen Proving Ground by NACA Langley Research Center, June.

Narramore, J. C. 1994. "Computational Fluid Dynamics Development and Validation at Bell Helicopter," In: AGARD CP-552.

Narramore, J. C. and Yen, J. G. 1982. "A New Transonic Airfoil Design Method and Its Application to Helicopter Rotor Airfoil Design," 38th Annual Forum of the American Helicopter Soc., Anaheim, CA, May 4–7.

Narramore, J. C. and Yen, J. G. 1997. "Computing Nonlinear Airfoil Characteristics at High Mach Numbers," American Helicopter Soc. Technical Specialists' Meeting on Rotorcraft Acoustics and Aerodynamics, Williamsburg, Oct. 28–30.

Naumann, A. 1942. "Pressure Distribution on Wings in Reversed Flow," NACA TM 1011.

Newman, B. G. 1961. "The Deflection of Plane Jets by Adjacent Boundaries–Coanda Effect," *Boundary Layer and Flow Control*, edited by Lachmann, Vol. 1, Pergamon Press, pp. 232–264.

Nitzberg, G. E. and Crandall, S. 1949. "A Study of Flow Changes Associated With Airfoil Section Drag Rise at Supercritical Speeds," NACA TN 1813.

Noonan, K. W. 1990. "Aerodynamic Characteristics of Two Rotorcraft Airfoils Designed for Application to the Inboard Region of a Main Rotor Blade," NASA TP-3009, AVSCOM TR-90-B-005.

Noonan, K. W. 1991. "Aerodynamic Characteristics of a Rotorcraft Airfoil Designed for the Tip Region of a Main Rotor Blade," NASA Technical Memorandum 4264, AVSCOM Technical Report 91-B-003.

Pearcy, H. H. 1955. "Some Effects of Shock-Induced Separation of Turbulent Boundary Layer in Transonic Flow Past Aerofoils," ARC R & M 3108.

Perry, F. J. 1987. "The Aerodynamics of the World Speed Record," 43rd Annual Forum of the American Helicopter Soc., St. Louis, MO, May 18–20.

Philippe, J. J. 1990. "Considerations on Wind Tunnel Testing Techniques for Rotorcraft," In: *Aerodynamics of Rotorcraft*, AGARD-R-781

Prandtl, L. 1928. "Motion of Fluids with Very Little Viscosity," NACA TN 452. Paper originally presented to the 3rd Int. Mathematical Congress, Heidelberg, Germany, 1904.

Prandtl, L. and Tietjens, O. G. 1934. *Fundamentals of Hydro- and Aeromechanics*, United Engineering Trustees, Inc. Published by Dover, New York, NY, 1957.

Prouty, R. W. 1975. "A State-of-the-Art Survey of Two-Dimensional Airfoil Data." *J. of the American Helicopter Soc.*, 20 (4), 14–25.

Prouty, R. W. 1986. *Helicopter Performance, Stability, and Control*, PWS Engineering Publishing, Boston, MA. Chapter 6.

Racisz, S. F. 1952. "Effects of Independent Variations of Mach Number and Reynolds Number on the Maximum Lift Coefficients of Four NACA 6-Series Airfoil Sections," NACA TN 2824.

RAeS. 1986. *Aerodynamics at Low Reynolds Number* $10^4 < Re < 10^6$ *International Conference*, London, England, Oct.

Raghavan, V., Chopra, I., and Pai, S. 1988. "Circulation Control Airfoils in an Unsteady Flow," *J. of the American Helicopter Soc.*, 33 (4), pp. 28–37.

Reader, K. R., Kirkpatrick, D. G., and Williams, R. M. 1978. "Status Report on Advanced Development Program Utilizing Circulation Control Rotor Technology," 4th European Rotorcraft Forum, Stresa, Italy, Sept. 13–15.

Reece, J. W. 1952a. "Investigation of Characteristics of Airflow within Aircraft Structures–Phase b(1)," Cornell Aeronautical Laboratory, Inc., Report No. V-699-D-17, April.

Reece, J. W. 1952b. "Interpretation of the Drag Changes Measured in the Wind Tunnel Tests of a Holed Wing," Cornell Aeronautical Laboratory, Inc., Report No. G1- 634-G-1, March 1952.

Riegels, F. W. 1961. *Aerofoil Sections–Results from Wind-Tunnel Investigations and Theoretical Foundations*, translated from the German by D. G. Randall, Butterworths, London, England.

Rubbert, P. E. 1964. "Theoretical Characteristics of Arbitrary Wings by a Nonplanar Vortex Lattice Method," Boeing Co. Report D6-9244.

Saric, W. S., Carrillo, R. B., and Reibert, M. S. 1998. "Leading Edge Roughness as a Transition Control Mechanism," AIAA Paper 1998-781, 36th Aerospace Sciences Meeting and Exhibit, Reno, NV, Jan. 12–15.

Schlichting, H. 1979. *Boundary Layer Theory*, 7th Edition., McGraw-Hill, New York, NY.

Schmidt, L. V. 1978. "Unsteady Aerodynamics of a Circulation Controlled Airfoil," 4th European Rotorcraft Forum, Stresa, Italy, Sept. 13–15.

Schrenk, O. 1927. "Systematic Investigation of Joukowski Wing Sections," NACA TM 422.

Shrewsbury, G. 1986. "Numerical Evaluation of Circulation Control Airfoil Performance Using Navier–Stokes Methods," AIAA Paper 86-0286, 24th AIAA Aerospace Sciences Meeting, Reno, NV, Jan. 6–9.

Simons, M. 1986. "The Use of Wind Tunnel Data in the Design of Radio Controlled Contest Sailplanes," Paper 20, RAeS Conference on Low Reynolds number Aerodynamics, London, England, Oct. 15–18.

Sloof, J. W., Wortmann, F. X., and Duhon, J. M. 1975. "The Development of Transonic Airfoils for Helicopters," 31st Annual National Forum of the American Helicopter Soc., Washington DC, May 13–15.

Solimon, M. M., Smith, R. V., Cheeseman, I. C., "Modeling Circulation Control by Blowing," AGARD CP 365, 1984.

Stack, J. and von Doenhoff, A. E. 1934. "Tests of 16 Related Airfoils at High Speeds," NACA Report 492.

Steinle, F. and Stanewsky, E. 1982. "Wind Tunnel Flow Quality and Data Accuracy Requirements," AGARD Advisory Report 184.

Stivers, L. S., Jr. 1954. "Effects of Subsonic Mach Number on the Forces and Pressure Distributions on Four NACA 64A-Series Airfoil Sections at Angles of Attack as High as 28°," NACA TN 3162.

Stivers, L. S., Jr. and Rice, F. J., Jr. 1946. "Aerodynamic Characteristics of Four NACA Airfoil Sections Designed for Helicopter Rotor Blades," NACA RB L5K02.

St. Hillaire, A. O., Carta, F. O., Fink, M. R., and Jepson, W. D. 1979. "The Influence of Sweep on the Aerodynamic Loading of a NACA 0012 Airfoil," Vol. 1–Technical Report, NASA CR 3092.

Sun, M. and Wang, W. 1989. "Method for Calculating the Unsteady Flow of an Elliptical Circulation-Control Airfoil," *J. of Aircraft*, 26 (10), pp. 907–913.

Tetervin, N. 1943. "Tests in the NACA Two-Dimensional Low-Turbulence Tunnel of Airfoil Sections Designed to Have Small Pitching Moments and High Lift-Drag Ratios," NACA CB 3I13.

Theodorsen, T. and Garrick, I. E. 1932. "General Potential Theory of Arbitrary Wing Sections," NACA TR 452.

Thibert, J. J. and Gallot, J. 1977. "A New Airfoil Family for Rotor Blades," 3rd European Rotorcraft and Powered Lift Aircraft Forum, Aix-en-Provence, France, Sept. 7–9.

Thwaites, B. 1960. *Incompressible Aerodynamics*, Oxford University Press, Oxford, England.

von Mises, R. 1945. *Theory of Flight*, McGraw-Hill, New York, NY. Republished 1959 by Dover Publications, Inc., New York, NY.

Ward, J. W. 1963. "The Behaviour and Effects of Laminar Separation Bubbles on Aerofoils in Incompressible Flow," *J. of the Royal Aeronautical Soc.*, 67 (636), pp. 783–789.

Wenzinger, C. J. 1935. "Pressure Distribution over an Airfoil Section with a Flap and Tab," NACA Report 574.

Westkaemper, J. C. and Chandrasekharan, R. M. 1980. "The Effects of Warhead-Induced Damage on the Aeroelastic Characteristics of Lifting Surfaces," Vol. 2–Aerodynamic Effects, AFOSR-TR-80-1040, 1980.

Whitcomb, R. T. 1976. "Advanced Transonic Aerodynamic Technology," NASA CP 2001 *Advances in Engineering Science*, Vol. 4.

Whitcomb, R. T. and Clark, L. R. 1965. "An Airfoil Shape for Efficient Flight at Supercritical Mach Numbers," NASA TM X-1109.

Wilby, P. G. 1979. "The Aerodynamic Characteristics of Some New RAE Blade Sections and their Potential Influence on Rotor Performance," 5th European Rotorcraft Forum, Amsterdam, The Netherlands, Sept. 4–7.

Wilby, P. G. 1998. "Shockwaves in the Rotor World–A Personal Perspective of 30 Years of Rotor Aerodynamic Research in the UK," *The Aeronautical J.*, 102 (1013), pp. 113–128.

Wood, M. E. 1979. "Results from Oscillatory Pitch Tests on the NACA 0012 Blade Section," Aircraft Research Association, Bedford, UK, ARA Memo 220.

Wood, N. J. and Neilsen, J. N. 1986. "Circulation Control Airfoils as Applied to Rotary-Wing Aircraft," *J. of Aircraft*, 23 (3), pp. 865–875.

Woods, M. I., Henderson J. F., and Lock, G. D. 2001. "Energy Requirements for the Flight of Micro Air Vehicles," *The Aeronautical J.*, 105 (1045), pp. 135–149.

Young, A. D. 1989. *Boundary Layers*, AIAA Education Series, Washington DC.

Zandieh, A. and Leishman, J. G. 1993. "Boundary Layer Effects on a Circular Cylinder with Unsteady Blowing," *AIAA J.*, 31 (10), pp. 1769–1776.

CHAPTER 8

Unsteady Airfoil Behavior

The addition of the dimension "time" to steady aerodynamics has far-reaching effects, both practical and theoretical. There is the practical necessity for coping with many important problems involving nonsteady phenomena such as flutter, buffeting, transient flows, gusts, dynamic response in flight, maneuvers, and stability. Apart from the many applications, theoretical nonsteady aerodynamics embraces and sheds light on the realm of steady aerodynamics and introduces interesting new methods.

I. E. Garrick (1957)

8.1 Introduction

The confidence levels in the design of new helicopters are greatly improved by the ability to predict accurately the aerodynamic behavior of the rotor system at all corners of the operational flight envelope. One difficulty and uncertainty in this process is to fully account for *unsteady* aerodynamic effects, especially when the helicopter is in high-speed forward flight and during flight maneuvers. In the previous chapter, the quasi-steady aerodynamic characteristics of rotor airfoils have been discussed in detail. Yet, these attributes alone are not necessarily the best indicator as to whether a given airfoil will operate successfully in the rotor environment or will meet the requirements of a given rotor design. The next level of consideration is to examine unsteady aerodynamic effects and to strive to assess their potential impact on the prediction of the airloads and performance of helicopter rotors.

In the context of rotor airloads prediction, the mathematical modeling of unsteady airfoil behavior is one of formidable complexity. While the absence of significant flow separation reduces somewhat the complexity of the problem, a complete understanding of unsteady airfoil behavior even in attached flow has not yet been obtained. The additional problem of dynamic flow separation[1] is still the subject of ongoing research, and completely satisfactory predictive models of the problem have not yet been developed. This is particularly true for the rotor case, where the rotor blades encounter a broad spectrum of unsteady effects from a number of different sources. The most obvious are the excursions in AoA resulting from blade flapping and pitch control inputs. The additional effects of the rotor wake, with its embedded concentrated tip vortices, lead to regions of the rotor disk that can experience large perturbations in AoA over very short time scales. The problems are compounded by the 3-D effects found at the blade tips, which can be locally transonic during forward flight. Therefore, the problems of defining accurately the unsteady aerodynamic flow field on the rotor is really rather formidable.

The principal focus of the present chapter is to describe the key physical features and techniques for modeling the unsteady aerodynamic effects found on airfoils operating under nominally attached flow conditions away from stall. The essential physics of nonsteady airfoil problems can be observed from idealized 2-D experiments, and interpretations of

[1] This is called "dynamic stall" and is discussed in detail in Chapter 9.

the behavior can be supported by theoretical or numerical models. The "classical" unsteady aerodynamic theories describing the observed behavior have formed the basis for many types of rotor analyses. The tools for the analysis of 2-D, incompressible, unsteady aerodynamic problems were laid down by 1940, with the extension to compressible flows complete by 1950. The most authoritative source documenting these theories is Bisplinghoff et al. (1955). Lomax and his colleagues (1952, 1968) have provided a basis from which to develop linearized unsteady aerodynamic models applicable to compressible flows. The mathematical elegance and computational simplicity of these linearized approaches are attractive to the helicopter rotor analyst. Although there have been a plethora of "new" unsteady aerodynamic theories developed over the years for helicopter applications, most still have their roots in the classical theories. Also, while the classical theories assume linearity in the airloads, the assumption of linearity can probably be justified for many of the problems encountered on the rotor, in practice. The proof of this latter statement is not always easy to justify, mostly because of other uncertainties in the problem such as those resulting from the rotor wake. The advent of nonlinear methods based on CFD solutions to the Euler and Navier–Stokes equations has provided new results that help the rotor analyst justify and define the limits of the parsimonious, linear models and may give guidance in developing improved and more practical unsteady aerodynamic models for future use in helicopter rotor blade airloads prediction, aeroelastic analysis, and rotor design.

8.2 Sources of Unsteady Aerodynamic Loading

Figure 8.1 summarizes the various sources of unsteady effects that may affect the blade airloads. The AoA environment of a typical blade element is the resultant of a combination of forcing from collective and cyclic blade pitch, twist angle, elastic torsion, blade flapping velocity, and elastic bending. The induced downwash effects from the trailed wake system and the locally high velocity field perturbations produced by discrete tip vortices are also of primary importance, and their effects on the airloads must be considered if the unsteady aerodynamics effects on the rotor are to be fully understood and predicted.

At the blade element level, the various effects described in Fig. 8.1 can be decomposed into perturbations to the local AoA and velocity field, as shown in Fig. 8.2. At low angles of attack with fully attached flow, the various sources of unsteady effects manifest primarily as moderate amplitude and phase variations relative to the quasi-steady airloads. However, at higher angles of attack when time-dependent flow separation from the airfoil may be involved, a phenomenon that has become known as *dynamic stall* may occur. This phenomenon is manifest by large overshoots in the values of the lift, drag, and pitching moment relative to the quasi-steady stall values. Dynamic stall is also accompanied by much larger phase variations in the unsteady airloads as a result of significant hysteresis in the flow developments; that is, the values of the airloads at the same AoA may be very different depending on whether the flow is separating or reattaching. As will be discussed in Chapter 9, the amplitude and phase effects produced by the stalled airloads can lead to various aeroelastic problems on the rotor that may seriously limit its performance compared to that assumed or predicted on the basis of making quasi-steady flow assumptions.

8.3 Concepts of the Blade Wake

The wake from the rotating blade comprises, in part, a vortical shear layer or vortex sheet, with a concentrated vortex formed at the blade tip. The vortex sheet is comprised of vorticity with vectors aligned mainly normal to and parallel to the trailing edge of the

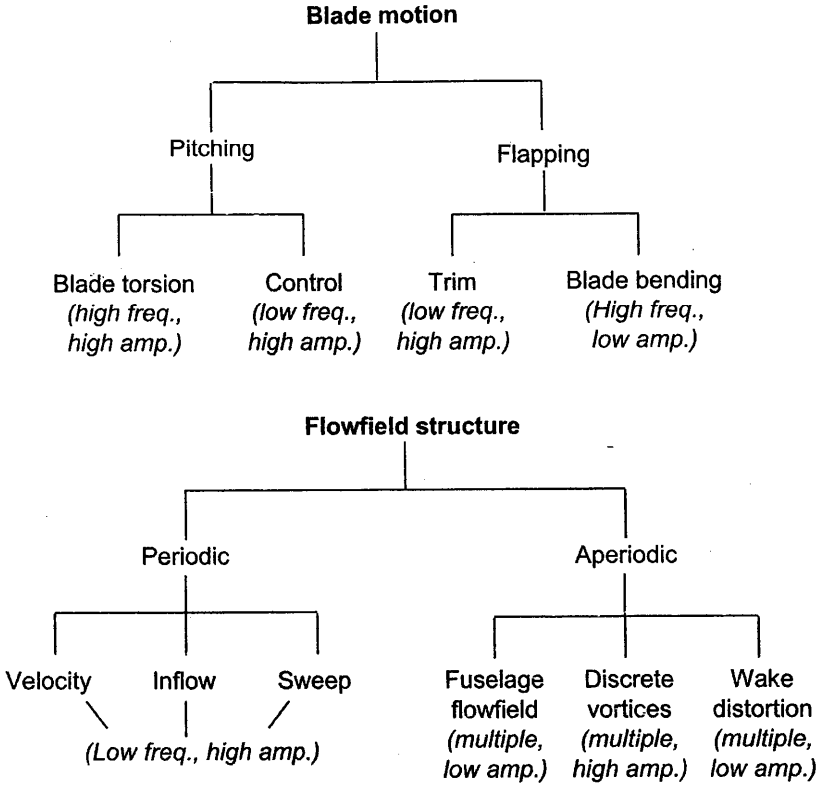

Figure 8.1 Possible sources of unsteady aerodynamic loading on a helicopter rotor. Adapted from Beddoes (1980).

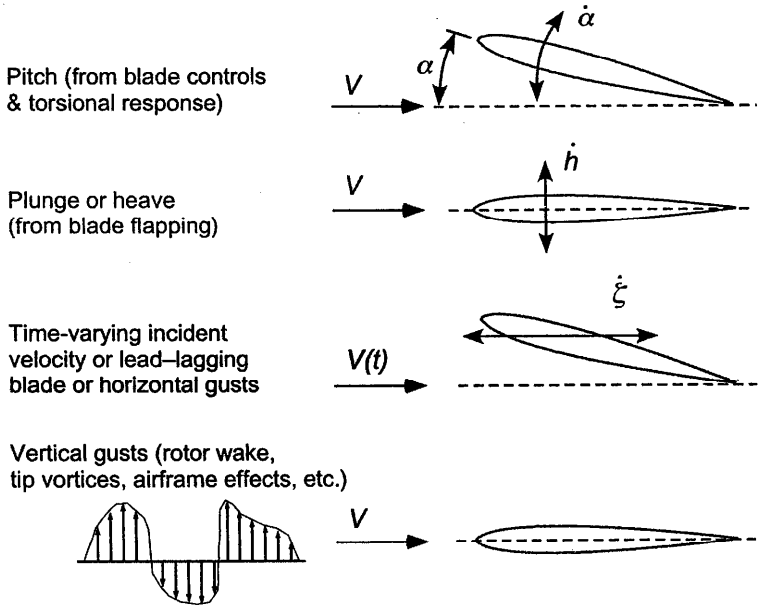

Figure 8.2 Decomposition of unsteady aerodynamic forcing terms at the blade element level.

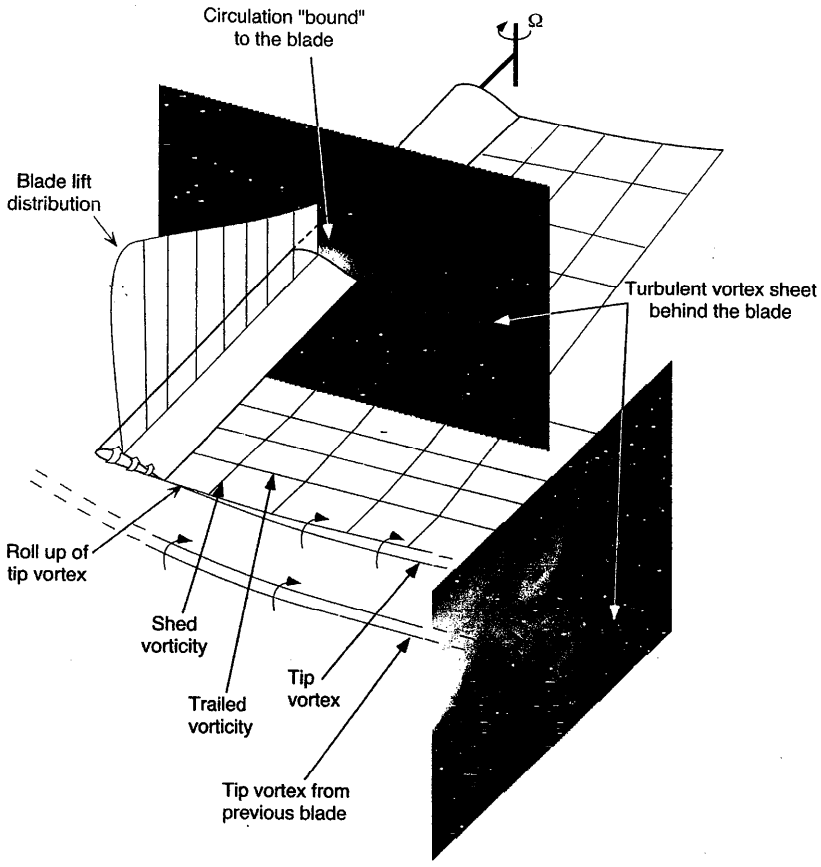

Figure 8.3 Schematic showing the wake and tip vortex rollup behind a single blade and the interaction with the vortex from another blade.

blade, as shown in Fig. 8.3, which is a schematic reconstruction of the wake behind a rotor blade using both flow field measurements and flow visualization. The strength of the former component (the trailed vorticity) is related to the spanwise gradient of lift (circulation, Γ) on the blade (i.e., to $\partial\Gamma/\partial r$), whereas the latter component (the shed vorticity) is related to the time rate of change of lift on the blade (i.e., to $\partial\Gamma/\partial t$). Experiments with rotors have shown that the blade tip vortices are almost fully rolled-up within only a few degrees of blade rotation. Because the aerodynamic loading on the blades is biased toward their tips, the tip vortex is of high overall strength with significant induced velocities.

While the fundamental process of the blade wake and tip vortex formation is similar to that found with a fixed wing, one obvious difference with helicopter tip vortices is that they are curved and so they experience a self-induced effect. Another complication with helicopter rotors is that the wakes and tip vortices from other blades can lie close to each other and to the plane of blade rotation and so have large induced effects on the blade lift distribution. Because of these self- and mutually induced effects, the problem of calculating the detailed airloads over the rotor disk is quite formidable. Miller (1964) has examined the higher harmonics of the rotor loading in forward flight and has concluded that the effects of the trailed wake (tip vortices) are generally more important than the shed wake; only for very low advance ratios or for hover do the effects of the "returning" shed wake or the shed

wake from other blades seem to be important. However, the effects of the "near" shed wake (that is, the wake vorticity immediately behind each blade) on the blade from which it was generated were found to be important under all flight regimes. These observations suggest that the overall aerodynamic environment at the blade (specifically, the quasi-steady angle of attack at the blade element) is determined mainly by the trailed wake (tip vortex) system. In general, *unsteady* aerodynamic effects are relatively local and are a consequence of the time history of the vorticity contained in the shed wake immediately behind each blade. Such observations often permit simplified forms of mathematical analysis to be pursued, without substantial loss of accuracy in predicting the unsteady airloads on the rotor.

8.4 Reduced Frequency and Reduced Time

One important parameter used in the description of unsteady aerodynamics and unsteady airfoil behavior is the *reduced frequency*. This parameter is used to characterize the *degree of unsteadiness* of the problem. It can be shown that the reduced frequency appears when nondimensionalizing the Navier–Stokes equations. Alternatively, it can be shown using dimensional analysis that the resultant force F on an airfoil of chord c, oscillating at angular frequency ω in a flow of velocity V, can be written in functional form as

$$\frac{F}{\rho V^2 c^2} = f\left(\frac{\rho V c}{\mu}, \frac{V}{a}, \frac{\omega c}{V}\right) = f\,(Re, M, k), \tag{8.1}$$

the proof of which is the basis of Question 8.1. As noted previously in Section 7.3, the resultant force, F, depends on the Reynolds number, Re, and the Mach number, M, but now the reduced frequency, k, of the flow is a third parameter to be considered. The reduced frequency is normally defined in terms of the airfoil semi-chord, $b = c/2$, so that

$$k = \frac{\omega b}{V} = \frac{\omega c}{2V}. \tag{8.2}$$

For $k = 0$, the flow is steady. For $0 \leq k \leq 0.05$, the flow can be considered quasi-steady; that is, unsteady effects are generally small, and for some problems they may be neglected completely. Usually flows with characteristic reduced frequencies of 0.05 and above are considered unsteady, and the unsteady terms in the governing equations cannot be routinely neglected. Problems that have characteristic reduced frequencies of 0.2 and above are considered highly unsteady, and the unsteady terms, such as those associated with acceleration effects, will begin to dominate the behavior of the airloads.

For a helicopter rotor in forward flight the reduced frequency at any blade element is an ambiguous parameter because the local sectional velocity (which appears in the denominator of the reduced frequency expression) is constantly changing. However, a first-order approximation for k can give useful information about the degree of unsteadiness found on a rotor and the necessity of modeling unsteady aerodynamic effects in any form of analysis. Consider first the unsteady effects induced by rigid blade flapping, for which it has been shown in Section 4.7 that the first flap frequency is about 1.05Ω for an articulated rotor. Then the reduced frequency, k_{75}, at the 75% radius location ($r = 0.75$) will be

$$k_{75} = \frac{1.05\Omega c}{2 \times 0.75\Omega R} = \frac{2.8c}{R}, \tag{8.3}$$

assuming for simplicity that the local velocity at the blade element is just the rotational velocity, $r\Omega R$. For a helicopter rotor with a blade aspect ratio $R/c > 10$, then $k_{75} > 0.07$, which

is in the unsteady range. Also, because the reduced frequencies increase further inboard on the blade owing to the lower values of local sectional velocity, k may become relatively large. Consider further the first elastic torsion mode, which is typically about 3–4Ω. In this case, at the tip the reduced frequency associated with airloads generated by torsional displacements is in excess of 0.2. At these reduced frequencies, there is a significant amplitude and phasing introduced into the airloads by the effects of the unsteady aerodynamics, and the modeling of unsteady aerodynamics is critical if erroneous predictions of the airloads are to be avoided.

It should be appreciated that the previous reduced frequency calculations are only very approximate and serve only to illustrate the *potential* significance of unsteady effects and the need to model such effects in predicting the airloads in rotor problems. For quantification of more transient problems, the concept of a single reduced frequency in terms of characterizing the degree of unsteadiness of the problem begins to lose its significance. Under these circumstances it is normal to use *reduced time*, s, where

$$s = \frac{1}{b}\int_0^t V dt = \frac{2}{c}\int_0^t V dt, \tag{8.4}$$

which represents the relative distance traveled by the airfoil through the flow in terms of airfoil semi-chords during a time interval t. It has been found useful to characterize many of the events occurring in unsteady aerodynamics, such as dynamic stall or blade encounters with blade tip vortices, in terms of a reduced time parameter.

8.5 Unsteady Attached Flow

A prerequisite in any unsteady aerodynamic theory is the ability to model accurately the unsteady airloads at the blade element under attached flow conditions. In the first instance, the most elementary level of approximation is to consider incompressible, 2-D flow. This avoids the need to model the wake from other blades (a problem considered in detail in Chapter 10) and allows convenient analytical and semi-analytical mathematical solutions to be incorporated into the rotor analysis. However, the helicopter rotor analyst is still faced with several compromises. First, the assumptions and limitations of any model must be properly assessed and understood. For example, neglecting the compressibility of the flow is not readily justified for rotor problems. This justification requires that not only must the local free stream Mach number be low, but the frequency of the source of unsteady effects must be small compared to the sonic velocity, that is, the product $\omega c/a \ll 1$, where a is the speed of sound. This means that the characteristic reduced frequency must also be small. The reduced frequency can be written as $k = \omega c/2Ma$, so that $Mk \ll 1$ to justify the assumption of incompressible flow. Second, any model must be written in a mathematical form that can be coupled into the structural dynamic model of the rotor system. For example, in some cases it may be desirable to write the aerodynamic model at each blade element as sets of ordinary differential equations. Third, because the blade element unsteady aerodynamic model is contained within radial and azimuthal integration loops, computational time considerations are important, and this alone can limit the allowable level of sophistication possible with any mathematical model of unsteady aerodynamics.

The most fundamental approach to the modeling of unsteady aerodynamic effects is through an extension of steady, 2-D thin-airfoil theory. This gives a good level of analysis of the problem and provides considerable insight into the physics responsible for the underlying unsteady behavior. Results for unsteady airfoil problems have been formulated in both the time domain and the frequency domain, primarily by Wagner (1925), Theodorsen (1935),

Küssner (1935), and von Kármán & Sears (1938). These solutions all have the same roots in incompressible, unsteady thin-airfoil theory and give exact analytic (closed-form) solutions for the pressure distribution (hence, the forces and pitching moments) for different forcing conditions (i.e., for perturbations in AoA or an imposed nonuniform vertical distribution of chordwise velocity). While these methods are valid for 2-D and incompressible flows, and were primarily intended for fixed-wing aeroelastic applications, they have also formed the foundation for several extensions to subsonic compressible flow and also to specific types of rotating-wing problems. For example, one extension of Theodorsen's theory was developed by Loewy (1957), which is a solution that approximates the effects of the shed wake vorticity below the rotor, as laid down by the blade and by other blades.

The unsteady compressible (subsonic) thin-airfoil problem has also received considerable attention – see, for example, Lomax et al. (1952) and Lomax (1968). Even though in some cases the local flow may have an incident Mach number that may be low, the product Mk must still be much less than unity if the incompressibility of the flow is to be justified. Because the governing equation in a compressible flow is the hyperbolic wave equation compared to the elliptic nature of Laplace's equation for incompressible flow [see Karamcheti (1966)], unsteady aerodynamic theories cannot be obtained in a corresponding exact, convenient analytical form. There are, however, some limited exact solutions and numerical solutions available. These can be used to great advantage in the development of semi-analytic or semi-empirical methods for unsteady subsonic compressible flows, which are formulated in the spirit of the classical incompressible theories but are still computationally practical enough to be included within helicopter rotor analyses.

8.6 Principles of Quasi-Steady Thin-Airfoil Theory

The unsteady airfoil problem can be tackled initially starting from the classical, incompressible, steady, thin-airfoil theory, which is described in Section 14.8. This is equivalent to setting all the unsteady terms in the governing flow equations equal to zero and will be called the *quasi-steady* problem. At the most elementary level it is convenient to think of oscillatory motion of the airfoil. This motion can be decomposed into contributions associated with AoA (which is equivalent to a pure plunging motion) and contributions associated with pitching (which includes contributions from both AoA and pitch rate) – see Fig. 8.4.

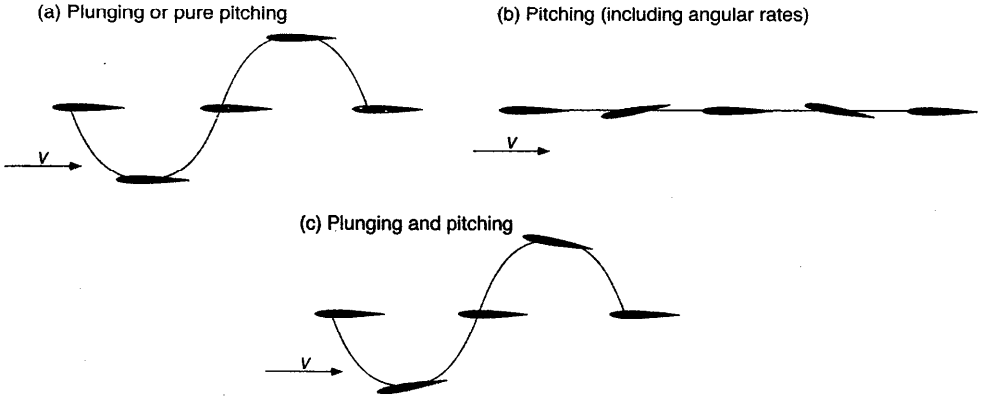

Figure 8.4 Unsteady oscillatory forcing can be considered to have contributions from both plunging and pitching motion, including rate terms.

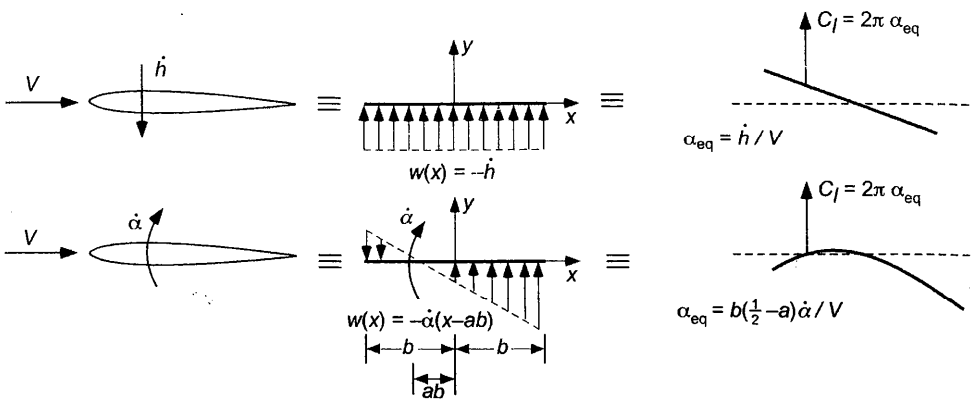

Figure 8.5 Velocity perturbation normal to chord and effective induced camber for plunge velocity and pitch rate about an axis located at 1/4-chord.

The unsteady motion of the airfoil produces a distribution of perturbation velocity normal to the chord, for which a solution to the vortex sheet strength on the airfoil, γ_b, can be found to maintain flow tangency on the chordline. An angle of attack, α, or plunge velocity, $\dot{h}$, produces a uniform velocity perturbation w that is normal to the chord, as shown in Fig. 8.5. For an AoA perturbation, $w(x) = V\alpha = \text{constant}$. Similarly, for a steady plunge velocity, $w(x) = -\dot{h} = \text{constant}$. The pitch-rate term produces a linear variation in normal perturbation velocity. For a pitch rate imposed about an axis at a semi-chords from the mid-chord, then $w(x) = -\dot{\alpha}(x - ab)$, so that the induced camber is a parabolic arc, as also shown in Fig. 8.5.

The quasi-steady contribution to the airloads follows directly from thin-airfoil theory (Section 14.8) using the following solutions for the Fourier harmonics:

$$A_0 = \alpha - \frac{1}{\pi}\int_0^\pi \left(\frac{w}{V}\right) d\theta \quad \text{and} \quad A_n = \frac{2}{\pi}\int_0^\pi \left(\frac{w}{V}\right) \cos n\theta d\theta, \tag{8.5}$$

where $x = -b\cos\theta$ based on a coordinate system at mid-chord. The results for this problem are summarized in Table 8.1. The quasi-steady lift and pitching moment are then

$$C_l = 2\pi\left[\alpha + \frac{\dot{h}}{V} + b\left(\frac{1}{2} - a\right)\frac{\dot{\alpha}}{V}\right], \tag{8.6}$$

$$C_{m_{0.25}} = -\frac{\pi}{4}\frac{\dot{\alpha}b}{V}, \tag{8.7}$$

and

$$C_{m_{0.5}} = \left[-\frac{\pi}{4} + \frac{1}{2}\left(\frac{1}{2} - a\right)\right]\frac{\dot{\alpha}b}{V}. \tag{8.8}$$

For a pitching axis at the 1/4-chord ($a = -1/2$), the term inside the square brackets in Eq. 8.6 will be seen to be the effective AoA at the 3/4-chord. If $a = 1/2$ then no lift is produced by pitch rate about 3/4-chord, and for this reason the 3/4-chord point is sometimes called the rear neutral point. Also, note that the pitching moment about the 1/4-chord resulting from the pitch rate contribution is independent of the pitch axis location, a (see Question 8.2).

Table 8.1. *Coefficients for the Quasi-Steady Airfoil Problem Using Thin-Airfoil Theory*

Coefficient	A_0	A_1	A_2
α	α	0	0
$\dot{h}$	$\dot{h}/V$	0	0
$\dot{\alpha}$	$-\dot{\alpha}ab/V$	$\dot{\alpha}b/V$	0

8.7 Theodorsen's Theory

Theodeorsen's theory, which is widely used by fixed-wing analysts, forms one root for many of the unsteady aerodynamic solution methods used for helicopter analysis. The problem of finding the airloads on an oscillating airfoil was first tackled by Glauert (1929), but was properly solved by Theodorsen (1935). Theodorsen's approach gives a solution to the unsteady airloads on a 2-D harmonically oscillated airfoil in inviscid, incompressible flow, and subject to small disturbance assumptions. The basic model is shown in Fig. 8.6. Both the airfoil and its shed wake are represented by a vortex sheet, with the shed wake extending as a planar surface from the trailing edge downstream to infinity. The shed wake comprises countercirculation that is shed at the airfoil trailing edge and is convected downstream at the free stream velocity. The assumption of a planar wake is justified if the AoA disturbances remain relatively small. As with the standard quasi-steady thin-airfoil theory, the bound vorticity, γ_b, can sustain a pressure difference and, therefore, a lift force. The wake vorticity, γ_w, however, must be force free with zero net pressure jump over the sheet.

Theodorsen's problem was to obtain the solution for the loading, γ_b, on the airfoil surface under harmonic forcing conditions. The governing integral equation is

$$w(x,t) = \frac{1}{2\pi}\int_0^c \frac{\gamma_b(x,t)}{(x-x_0)}dx + \frac{1}{2\pi}\int_c^\infty \frac{\gamma_w(x,t)}{(x-x_0)}dx, \tag{8.9}$$

where w is the downwash on the airfoil surface. This equation must be solved subject to invoking the Kutta condition at the trailing edge [i.e., $\gamma_b(c,t) = 0$]. There is also a connection to be drawn between the change in circulation about the airfoil and the circulation shed into

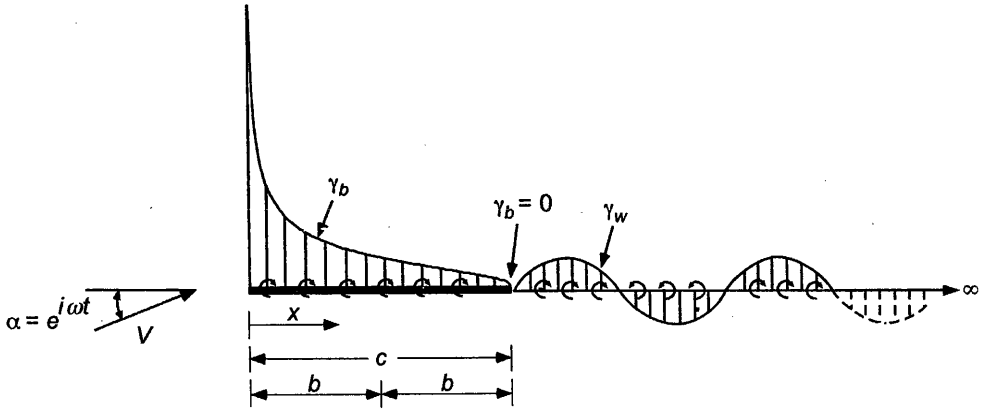

Figure 8.6 Mathematical model of a harmonically oscillated thin airfoil used by Theodorsen.

the wake. Conservation of circulation requires that

$$\gamma_w(c,t)dx = -\frac{d\Gamma(t)}{dt}dt. \tag{8.10}$$

Assuming that the shed vortices are convected at the free stream velocity, V, this gives $dx = Vdt$ and so

$$V\gamma_w(c,t) = -\frac{d\Gamma(t)}{dt}, \tag{8.11}$$

where the airfoil circulation $\Gamma(t)$ is given by

$$\Gamma(t) = \int_0^c \gamma_b(x,t)dx. \tag{8.12}$$

This wake vorticity changes the downwash velocity over the airfoil and, therefore, the loads on the airfoil are also affected. So long as the circulation about the airfoil is changing with respect to time, circulation is continuously shed into the wake and will continuously affect the aerodynamic loads on the airfoil. In the limit as the forcing becomes zero, the shed wake vorticity cast off the trailing edge of the airfoil becomes zero, and the remaining circulation in the wake convects downstream to infinity. In this case, the problem is modeled by the standard quasi-steady thin-airfoil theory.

The unsteady problem posed above is certainly not trivial to solve, but for simple harmonic motion the solution is given by Theodorsen (1935) in a form that represents a transfer function between the forcing (angle of attack) and the aerodynamic response (pressure distribution, lift, and pitching moment). Theodorsen's approach is summarized by Bisplinghoff et al. (1955) and by another approach attributed to Schwarz. See also Bramwell (1976) and Johnson (1980) for a good exposition of the theory. For a general motion, where an airfoil of chord $c = 2b$ is undergoing a combination of pitching (α, $\dot{\alpha}$) and plunging (h) motion in a flow of steady velocity V, Theodorsen gives for the lift

$$L = \pi\rho V^2 b\left[\frac{b}{V^2}\ddot{h} + \frac{b}{V}\dot{\alpha} - \frac{b^2}{V^2}a\ddot{\alpha}\right] + 2\pi\rho V^2 b\left[\frac{\dot{h}}{V} + \alpha + \frac{b\dot{\alpha}}{V}\left(\frac{1}{2} - a\right)\right]C(k), \tag{8.13}$$

where a is the pitch axis location relative to the mid-chord of the airfoil and is measured in terms of semi-chords. The corresponding moment about mid-chord is

$$M_{1/2} = -\rho b^2\left[\pi\left(\frac{1}{2} - a\right)Vb\dot{\alpha} + \pi b^2\left(\frac{1}{8} + a^2\right)\ddot{\alpha} - a\pi b\ddot{h}\right] + 2\rho Vb^2\pi\left(a + \frac{1}{2}\right)\left[V\alpha + \dot{h} + b\left(\frac{1}{2} - a\right)\dot{\alpha}\right]C(k). \tag{8.14}$$

The first set of terms in Eqs. 8.13 and 8.14 result from flow acceleration effects (i.e., a *noncirculatory* or *apparent mass* effect). The second terms arise from the creation of circulation about the airfoil (i.e., a *circulatory* effect). The circulatory term $C(k) = F(k) + iG(k)$ is a complex valued transfer function known as *Theodorsen's function*, which accounts for the effects of the shed wake on the unsteady airloads.

The noncirculatory or apparent mass terms arise from the $\partial\phi/\partial t$ term contained in the unsteady Bernoulli equation (Kelvin's equation) [see Karamcheti (1966)] and account

for the pressure forces required to accelerate the fluid in the vicinity of the airfoil. For example, for a thin-airfoil of chord $c = 2b$ moving normal to its surface at velocity $w(t)$, the noncirculatory fluid force, F^{nc}, acting on the surface is

$$F^{nc} = -M_a \frac{dw}{dt}. \tag{8.15}$$

The term M_a is known as the *apparent mass* and in this case is given by

$$M_a = \pi \rho b^2 = \pi \rho \frac{c^2}{4}, \tag{8.16}$$

which can be identified with the $\ddot{h}$ term in Eq. 8.13. Other apparent mass forces and pitching moments will be produced for different types of forcing – see Bisplinghoff et al. (1955) for a further discussion.

In coefficient form, Theodorsen's results in Eqs. 8.13 and 8.14 can be expressed as

$$C_l = \pi b \left(\frac{\dot{\alpha}}{V} + \frac{\ddot{h}}{V^2} - \frac{ba\ddot{\alpha}}{V^2} \right) + 2\pi C(k) \left[\frac{\dot{h}}{V} + \alpha + b\left(\frac{1}{2} - a \right) \frac{\dot{\alpha}}{V} \right], \tag{8.17}$$

$$C_{m_{1/2}} = \frac{\pi}{2} \left[\frac{ba\ddot{h}}{V^2} - \frac{b^2}{V^2} \left(\frac{1}{8} + a^2 \right) \ddot{\alpha} \right] + \pi \left(a + \frac{1}{2} \right) \times \left[\frac{\dot{h}}{V} + \alpha + b\left(\frac{1}{2} - a \right) \frac{\dot{\alpha}}{V} \right] C(k) - \frac{\pi}{2} \left[\left(\frac{1}{2} - a \right) \frac{b\dot{\alpha}}{V} \right]. \tag{8.18}$$

The last term in the pitching moment expression is a circulatory term, albeit a quasi-steady term not associated with the $C(k)$ function. Furthermore, the effects of an aerodynamic center offset from the 1/4-chord should be added to the pitching moment by multiplying the circulatory value of the lift by the offset distance – see previous discussion in Section 7.7.1.

Theodorsen's function $C(k)$ is expressed in terms of Hankel functions, H, with the reduced frequency k as the argument, where

$$C(k) = F(k) + iG(k) = \frac{H_1^{(2)}(k)}{H_1^{(2)}(k) + iH_0^{(2)}(k)}. \tag{8.19}$$

The Hankel function is defined as $H_\nu^{(2)} = J_\nu - iY_\nu$, with J_ν and Y_ν being Bessel functions of the first and second kind, respectively. Implicitly recognizing that each Bessel function has an argument k, then the real or in-phase ($\Re$) part and imaginary or out-of-phase part ($\Im$) can be written as

$$\Re C(k) = F = \frac{J_1(J_1 + Y_0) + Y_1(Y_1 - J_0)}{(J_1 + Y_0)^2 + (J_0 - Y_1)^2} \tag{8.20}$$

and

$$\Im C(k) = G = -\frac{Y_1 Y_0 + J_1 J_0}{(J_1 + Y_0)^2 + (J_0 - Y_1)^2}. \tag{8.21}$$

Theodorsen's function is plotted in Fig. 8.7. The amplitude and phase of Theodorsen's function are given by

$$|C(k)| = \sqrt{F^2 + G^2} \quad \text{and} \quad \phi = \tan^{-1}\left(\frac{G}{F} \right), \tag{8.22}$$

respectively.

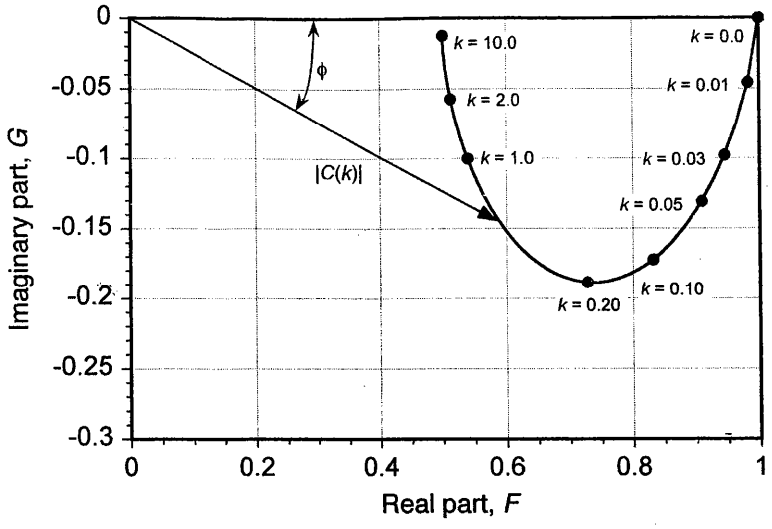

Figure 8.7 Theodorsen's function plotted as real and imaginary parts.

It will be appreciated from Fig. 8.7 that Theodorsen's function serves to introduce an amplitude reduction and phase lag effect on the *circulatory* part of the lift response compared to the result obtained under quasi-steady conditions. The basic effect can be seen if a pure oscillatory variation in AoA is considered, that is, $\alpha = \bar{\alpha}e^{i\omega t}$. In this case[2] the circulatory part of the airfoil lift coefficient is given by

$$C_l = 2\pi\bar{\alpha}\, C(k) = 2\pi\bar{\alpha}\left[F(k) + iG(k)\right]. \tag{8.23}$$

Representative results from the Theodorsen model are shown in Fig. 8.8. For $k = 0$ the steady-state lift behavior is obtained, that is C_l is linearly proportional to α. However, as k is increased, the lift plots develop into hysteresis loops, and these loops rotate such that the amplitude of the lift response (half of the peak-to-peak value) decreases with increasing reduced frequency. These loops are circumvented in a counterclockwise direction such that the lift is lower than the steady value when α is increasing with time and higher than the steady value when α is decreasing with time (i.e., there is a phase lag). Notice that for infinite reduced frequency the circulatory part of the lift amplitude is half that at $k = 0$ and there is no phase lag angle.

8.7.1 *Pure Angle of Attack Oscillations*

It is now possible to consider the effects of both the circulatory and the noncirculatory contributions to the unsteady lift. Consider first a pure harmonic variation in α, that is, $\alpha = \bar{\alpha}e^{i\omega t}$. Substituting into the expression for the lift given by Eq. 8.13 yields

$$L = 2\pi\rho V^2 b\left[C(k) + i\frac{\omega b}{2V}\right]\bar{\alpha}e^{i\omega t}. \tag{8.24}$$

[2] Notice that this case does not represent an oscillating airfoil in AoA because the pitch-rate terms are not included.

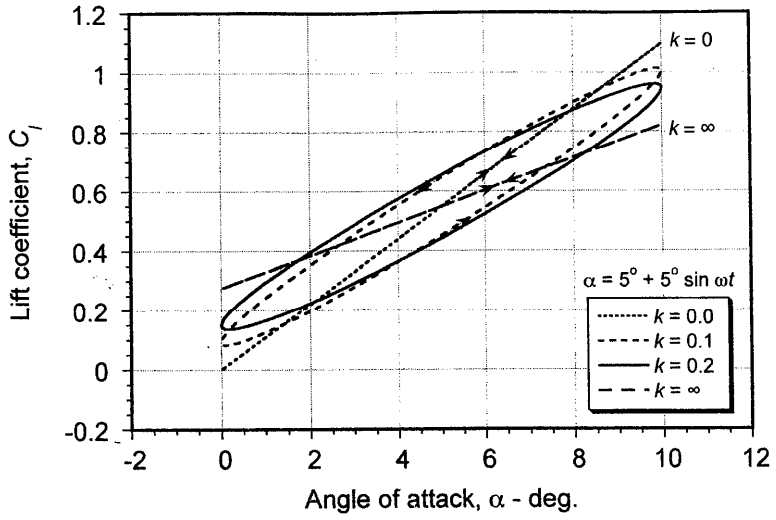

Figure 8.8 The effects of Theodorsen's function on the circulatory part of the unsteady lift response for a sinusoidal variation in angle of attack.

In terms of the lift coefficient, the result is

$$C_l = \frac{L}{\rho V^2 b} = \Big[\, 2\pi(F + iG) + i\pi k \Big] \bar{\alpha} e^{i\omega t}. \tag{8.25}$$

The term inside the square brackets can be considered the lift transfer function, which accounts for the difference between the unsteady and quasi-steady airloads. The first term inside the brackets is the circulatory term, and the second term is the apparent mass contribution. Notice that the apparent mass contribution is proportional to the reduced frequency and leads the forcing by a phase angle of $\pi/2$. If the result is normalized by $2\pi|\bar{\alpha}|$ then

$$\frac{|C_l|}{2\pi|\bar{\alpha}|} = (F + iG) + i\frac{k}{2}. \tag{8.26}$$

The equivalent result for the pitching moment about mid-chord is

$$\frac{|C_{m_{1/2}}|}{|\bar{\alpha}|} = -i\frac{\pi k}{2} \tag{8.27}$$

and where the moment about the 1/4-chord is obtained by a transformation using

$$C_{m_{1/4}} = C_{m_{1/2}} - \frac{C_l}{4}. \tag{8.28}$$

The results for the unsteady lift are shown in Fig. 8.9, where the significance of the apparent mass contribution to both the amplitude and phase can be appreciated. At lower values of reduced frequency (say, $k < 0.1$) the noncirculatory or apparent mass forces are small, and the circulatory terms dominate the solution. At higher values of reduced frequency, the apparent mass forces clearly dominate. By setting $C(k) = 1$, that is, $F = 1$ and $G = 0$ in Eq. 8.26, the effects of the shed wake are removed and the quasi-steady result is obtained.[3]

[3] The apparent mass contributions to the forces and pitching moments, which are proportional to the instantaneous motion, are often included as part of the quasi-steady result. If they are not, then the standard quasi-steady thin-airfoil result is obtained.

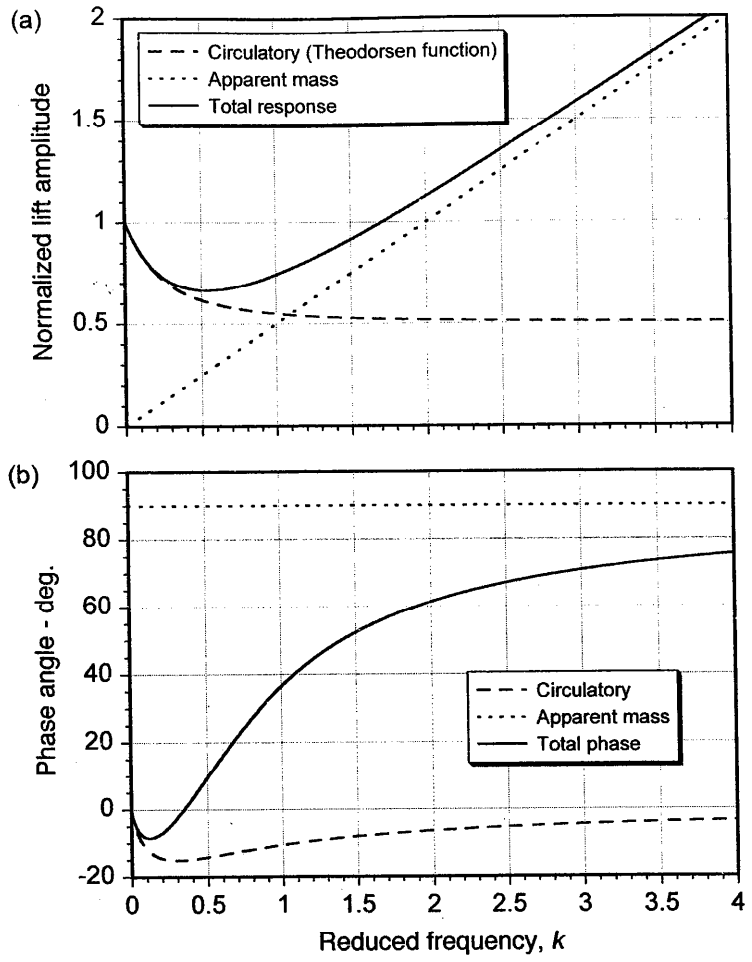

Figure 8.9 Circulatory and apparent mass contributions to the normalized unsteady lift response for a pure sinusoidal AoA oscillation. (a) Lift amplitude. (b) Phase of lift.

8.7.2 *Pure Plunging Oscillations*

Consider now a harmonic plunging motion, such as would be contributed by blade flapping. Here, the forcing is $h = \bar{h}e^{i\omega t}$ so that $\dot{h} = i\omega\bar{h}e^{i\omega t}$ and $\ddot{h} = -\omega^2\bar{h}e^{i\omega t}$. Substituting into the expression for the lift given by Eq. 8.13 and solving for the lift coefficient gives

$$C_l = \left[2\pi k(iF - G) - \pi k^2 \right] \frac{\bar{h}}{b} e^{i\omega t}. \tag{8.29}$$

Again, the complete term inside the square brackets can be considered as the lift transfer function. Notice that for this problem the circulatory part of the lift response leads the forcing displacement h by a phase angle of $\pi/2$. Also, the apparent mass force leads the circulatory part of the response by a phase angle of $\pi/2$ or the forcing by a phase angle of π. The corresponding pitching moment about mid-chord for this case is

$$C_{m_{1/2}} = \left(\frac{\pi}{4}\right) k^2 \frac{\bar{h}}{b} e^{i\omega t}. \tag{8.30}$$

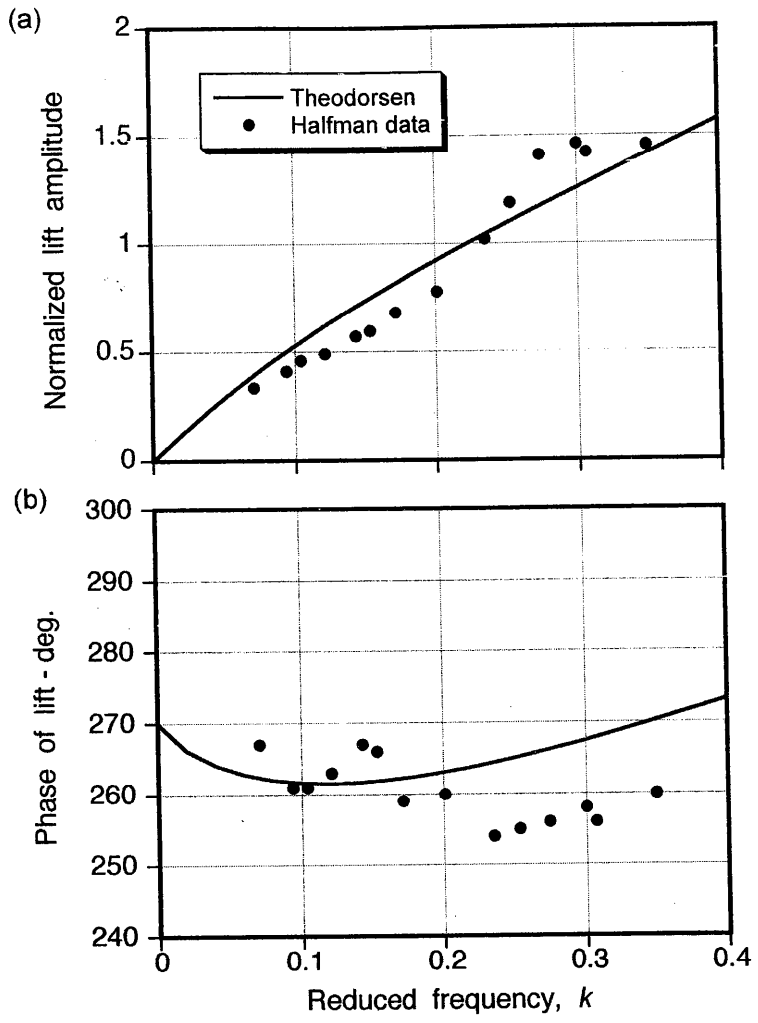

Figure 8.10 Theodorsen's theory compared to measurements of first harmonic unsteady lift for an airfoil oscillating in plunge. (a) Lift amplitude. (b) Phase of lift.

A comparison of Theodorsen's result with experimental data for an airfoil oscillating in plunge is shown in Figs. 8.10 and 8.11. The results are plotted as a the first harmonic normalized amplitude of the lift and pitching moment about the 1/4-chord and their corresponding phase angles as functions of reduced frequency. The experimental results are taken from Halfman (1951), where measurements were made on an oscillating NACA 0012 airfoil. These tests were conducted for Mach numbers less than 0.1 and a Reynolds number of approximately 10^6. It is significant, however, that a relatively high reduced frequency of 0.4 was attained in the experiment. Figure 8.10 shows that there is good agreement between Theodorsen's theory and Halfman's measurements. Notice the sign of the lift phase angle, which changes from a lag (less than 270° or minus 90°) to a lead (greater than minus 90°) at higher reduced frequencies as the noncirculatory effects become more dominant. Notice also in Fig. 8.11 that the phase of the pitching moment shows a significant digression from the results obtained with the baseline Theodorsen theory, which predicts a phase lag of 180°. However, this behavior can be explained by the fact that the aerodynamic center

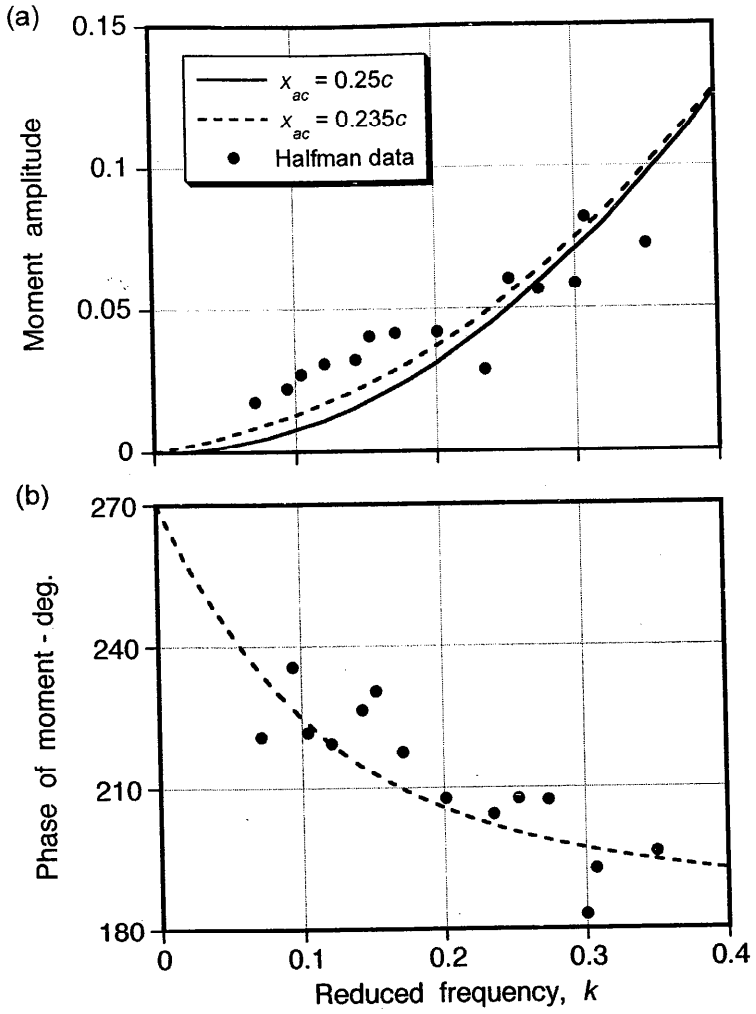

Figure 8.11 Theodorsen's theory compared to measurements of first harmonic unsteady pitching moment for an airfoil oscillating in plunge. (a) Pitching moment amplitude about 1/4-chord. (b) Phase of pitching moment.

location is not at the 1/4-chord; the results in this case suggest an aerodynamic center for this airfoil and test conditions that is located at 23.5% chord.

8.7.3 *Pitching Oscillations*

For harmonic pitch oscillations, additional terms involving pitch rate $\dot{\alpha}$ appear in the equations for the aerodynamic response. The forcing is now given by $\alpha = \bar{\alpha}e^{i\omega t}$, and the pitch rate by $\dot{\alpha} = iw\bar{\alpha}e^{i\omega t}$. In this case, the lift coefficient is

$$C_l = 2\pi\left(F[1+ik] + G[i-k]\right)\bar{\alpha}e^{i\omega t} + \pi k\left(i - \frac{k}{2}\right)\bar{\alpha}e^{i\omega t}. \tag{8.31}$$

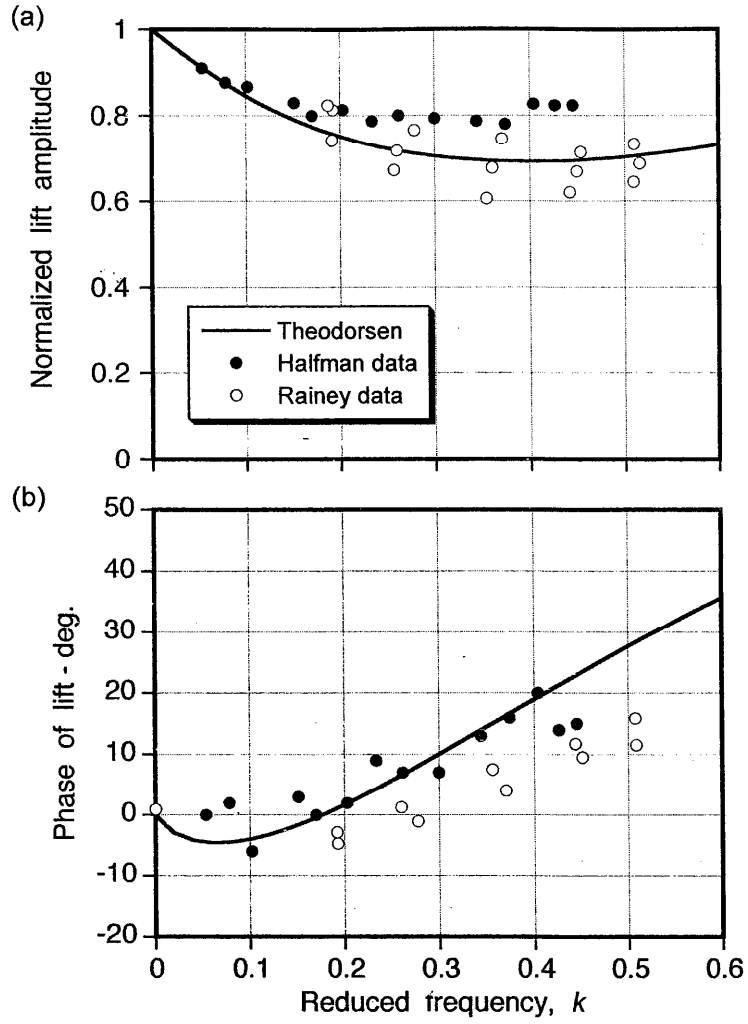

Figure 8.12 Theodorsen's theory compared to measurements of first harmonic unsteady lift for an airfoil oscillating in pitch. (a) Lift amplitude. (b) Phase of lift.

The corresponding pitching moment about mid-chord is

$$C_{m_{1/2}} = \frac{\pi}{2}k\left(\frac{3}{8}k - i\right)e^{i\omega t}. \tag{8.32}$$

The results from these predictions are compared with experimental measurements in Figs. 8.12 and 8.13, again in terms of the normalized lift and pitching moment amplitude about the 1/4-chord (using Eq. 8.28) and their corresponding phase angles versus reduced frequency. In addition to the low Mach number results of Halfman (1951), this figure shows data measured by Rainey (1957), which are for a Mach number of about 0.3 and a Reynolds number of 5.3×10^6. It is significant in the latter case that a reduced frequency of up to 0.6 was obtained in the experiment, which gives a good opportunity to examine the validity of the linearized incompressible aerodynamic theory at higher reduced frequencies. As shown in Fig. 8.12, the lift amplitude initially decreases with increasing k because of the effects of the shed wake. The amplitude begins to increase again for $k > 0.5$ as the apparent mass

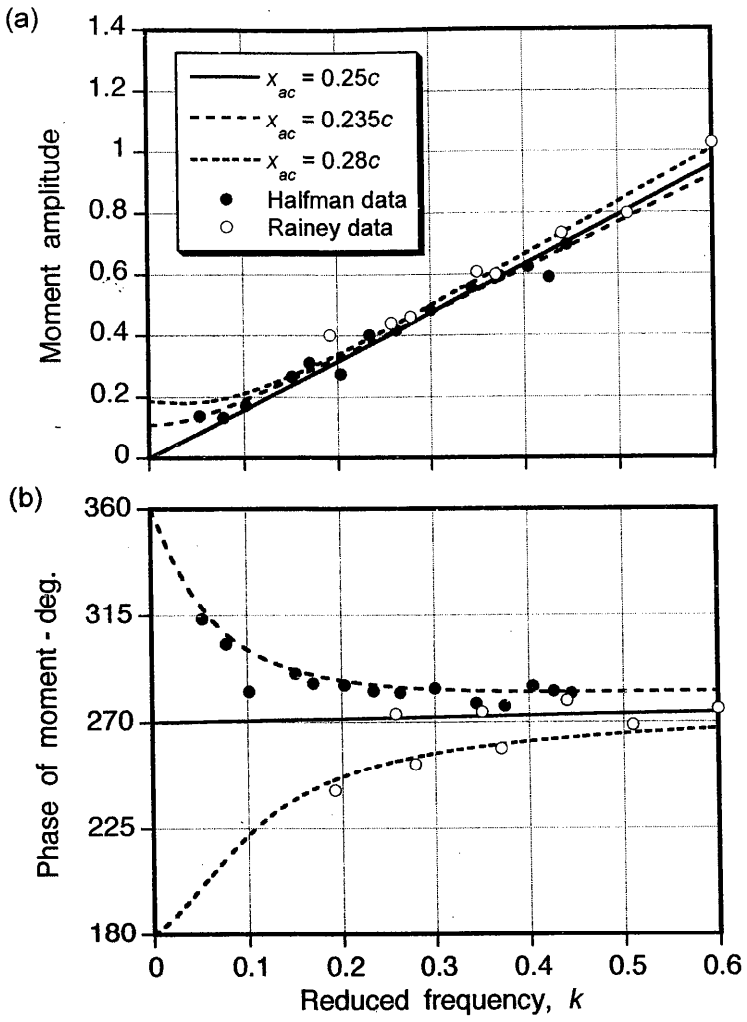

Figure 8.13 Theodorsen's theory compared to measurements of first harmonic unsteady pitching moment for an airfoil oscillating in pitch. (a) Pitching moment amplitude about 1/4-chord. (b) Phase of pitching moment.

forces begin to dominate the airloads. This is also shown by the phase angle, which exhibits an increasing lead for $k > 0.3$. For the lift amplitude, Theodorsen's theory compares well with Rainey's results. The agreement with Halfman's results are not quite as good for the lift amplitude but are better in phase. In Fig. 8.13 it is apparent that the amplitude of the 1/4-chord pitching moment increases quickly with increasing k, with the agreement of theory and experiment being excellent. Again, the phase of the pitching moment response shows a behavior that can be explained in terms of shift of the aerodynamic center from the 1/4-chord. As for the plunging case, Halfman's data suggest an aerodynamic center at 23.5% chord. Rainey's data, however, suggest that the aerodynamic center is further back at 28% chord. Overall, the correlation obtained between Theordorsen's theory and experimental measurements for airfoils oscillating in pitch and plunge is quite good, giving considerable support to the validity of Theodorsen's theory, at least for low Mach numbers and up to moderate values of reduced frequency.

8.8 The Returning Wake: Loewy's Problem

Theodorsen's theory has represented an isolated 2-D thin-airfoil with the wake convected downstream to infinity. For rotorcraft work, this is perhaps a questionable assumption because the rotor blade sections may encounter the wake vorticity from previous blades as well as the returning wake from the blade in question. This fact was acknowledged by Loewy (1957) and by Jones (1958) who set up a model of a 2-D blade section with a returning shed wake, as shown in Fig. 8.14.

This returning wake can be modeled with planar 2-D vortex sheets, just as in Theodorsen's method, but now with a series of sheets below the airfoil with vertical separation, h, that depend on the mean induced velocity through the rotor disk and the number of rotor blades. Loewy (1957) has shown that in this case the lift on the blade section can be expressed by replacing Theodorsen's function by

$$C'\left(k, \frac{\omega}{\Omega}, h\right) = \frac{H_1^{(2)}(k) + 2J_1(k)W}{H_1^2(k) + iH_0^{(2)}(k) + 2(J_1(k) + iJ_0(k))W}, \tag{8.33}$$

where $C'(k)$ is known as the Loewy function, with argument of reduced frequency k. For a single blade, the complex valued W function is given by

$$W\left(\frac{kh}{b}, \frac{\omega}{\Omega}\right) = \left(e^{kh/b}e^{i2\pi(\omega/\Omega)} - 1\right)^{-1}. \tag{8.34}$$

If ω/Ω = an integer, then all the shed wake effects are in phase. Notice from Eqs. 8.33 and 8.34 that as $h \to \infty$ then $W \to 0$ and $C'(k) \to C(k)$, and Loewy's function approaches

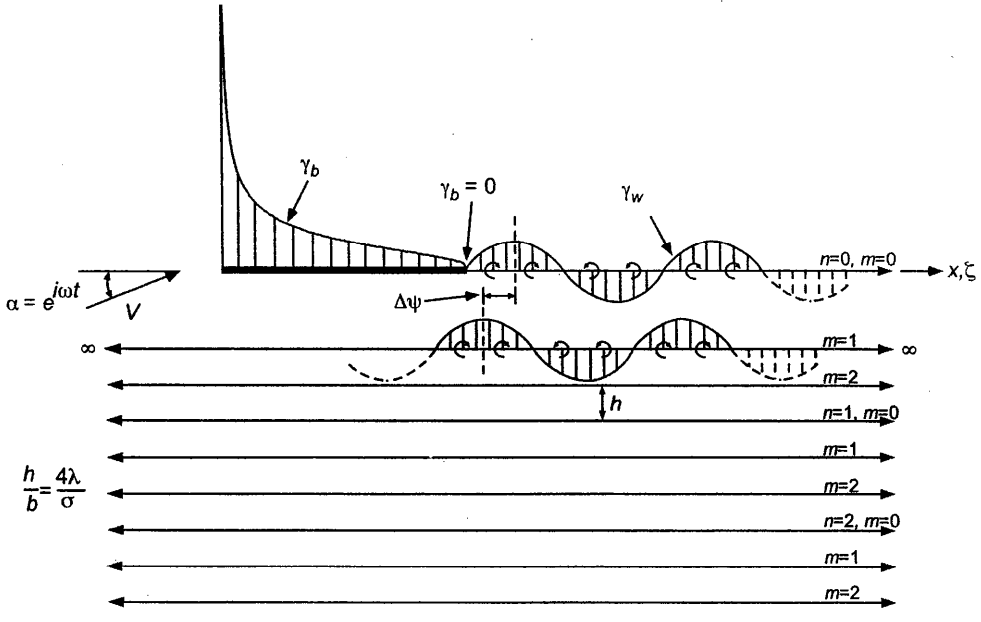

Figure 8.14 Schematic of Loewy's problem showing the "returning" nature of the shed wake.

Theodorsen's result, as it should. For a rotor with N_b blades, the W function is modified to read

$$W\left(\frac{kh}{b}, \frac{\omega}{\Omega}, \Delta\psi, N_b\right) = \left(e^{kh/b} e^{i2\pi(\omega/N_b\Omega)e^{i(\Delta\psi)\omega/\Omega}} - 1\right)^{-1}, \tag{8.35}$$

where the parameter $\omega/N_b\Omega$ now controls the wake phasing.

The wake spacing ratio h/b can be determined from the spacing of the helical vortex sheets that are laid down below the rotor. If an average induced velocity $v_i = \lambda\Omega R$ is assumed, then during a single rotor revolution the shed wake generated by a single blade will be at a distance $h = (2\pi/\Omega)v_i$ below the rotor. For multiple blades, the spacing will be $(2\pi)v_i/(\Omega N_b)$, that is,

$$\frac{h}{b} = \frac{\lambda\Omega R 2\pi}{\Omega N_b b} = \frac{4\lambda}{\sigma}, \tag{8.36}$$

with σ as the rotor solidity. For $\Delta\psi = 0$, which means that the only phase shift in the wake vorticity results from the spacing between the blades, then

$$W\left(\frac{kh}{b}, \frac{\omega}{\Omega}, 0, N_b\right) = \left(e^{kh/b} e^{i2\pi(\omega/N_b\Omega)} - 1\right)^{-1}. \tag{8.37}$$

Representative results from Loewy's theory for a one-bladed rotor are shown in Fig. 8.15, where we see that the main consequence of including the shed vorticity below the blade is that it serves to amplify or attenuate the unsteady lift response, depending on the reduced frequency, wake spacing, and wake phase. The most important effects are for lower reduced frequencies, with oscillations at the harmonics of the rotor rotational frequency. Using typical helicopter values of $\lambda \approx 0.05$ and $\sigma = 0.1$ gives $h/b \approx 2$. Therefore, for a helicopter rotor the Loewy function predicts that $|C'| \approx 0.5$ over most of the reduced frequency range, which is an important effect. This can lead to lower damping of blade flapping and flapwise elastic bending modes and will increase the vibratory response of the blade to harmonic airloads. However, it is only for very low advance ratios or for hover that the Loewy effect seems important. Daughaday et al. (1959) have conducted indirect validation of the Loewy effect from measured blade flap bending moments and transient flapping decay data. The reduction in flap damping at frequencies that were multiples of the rotor rotational frequency was verified. Other verifications of the Loewy effect and the implications for rotor aeroelasticity have been made by Ham et al. (1958), Silviera & Brooks (1959), and Anderson & Watts (1975). Hammond & Pierce (1972) have considered a development of the Loewy problem for subsonic compressible flow. Whereas the effects of compressibility are small for ω/Ω near unity, larger differences are noted for $\omega/\Omega < 1$. No equivalent analytic theory to the Loewy problem is available for forward flight; the only option is to solve the problem numerically through discrete vortex wake tracking, a problem discussed in Chapter 10.

8.9 Sinusoidal Gust: Sears's Problem

Von Kármán & Sears (1938) analyzed the problem of a thin-airfoil moving through a sinusoidal vertical gust field. This is also a frequency domain solution. The gust can be considered as an upwash velocity that is uniformly convected by the free stream, as shown

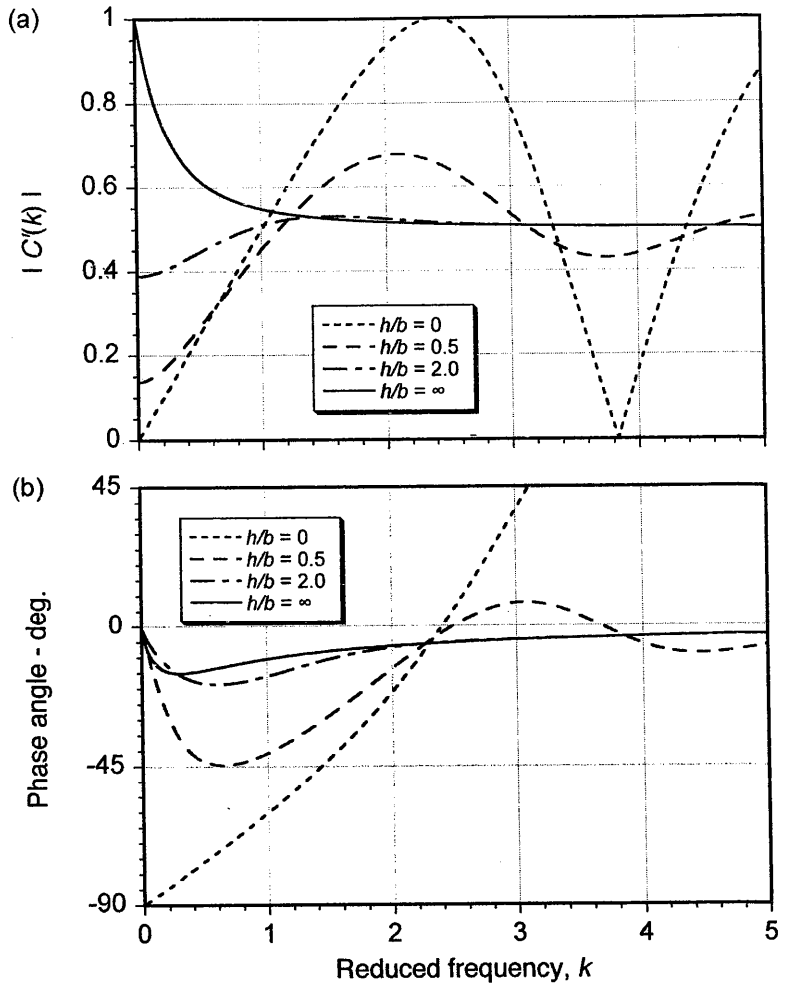

Figure 8.15 Loewy's function for a one-bladed rotor with different wake spacings and ω/Ω = integer. (a) Lift amplitude. (b) Phase of lift.

in Fig. 8.16. The forcing function in this case is

$$w_g(x,t) = \sin\left(\omega_g t - \frac{\omega_g x}{V}\right)$$
$$= \sin\omega_g t \cos\left(\frac{\omega_g x}{V}\right) - \cos\omega_g t \sin\left(\frac{\omega_g x}{V}\right), \tag{8.38}$$

where ω_g is the gust frequency. There are two cases of interest. First, if the gust is referenced to the airfoil leading edge then $x = 0$ and so Eq. 8.38 simply becomes $w_g(t) = \sin\omega_g t$. Second, if the gust is referenced to the mid-chord, then $x = b = c/2$ and the forcing becomes $w_g(t) = \cos k_g \sin\omega_g t - \sin k_g \cos\omega_g t$, which is equivalent to a phase shift (see also Question 8.6). The mid-chord was the reference point used in the original work of

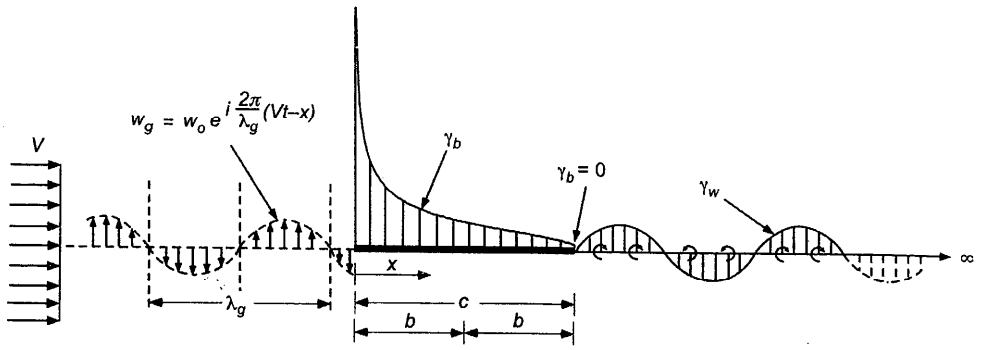

Figure 8.16 Model of a thin airfoil encountering a sinusoidal vertical gust (Sears's problem).

von Kármán & Sears (1938). In this case, the final result for the lift coefficient can be written as

$$C_l = 2\pi\left(\frac{w_0}{V}\right)S(k_g)e^{i2\pi V/\lambda_g}, \tag{8.39}$$

where $S(k_g)$ is known as Sears's function. The gust encounter frequency is given by

$$k_g = \frac{2\pi b}{\lambda_g}, \tag{8.40}$$

where λ_g is the wavelength of the gust (see Fig. 8.16). Sears's function can also be computed exactly in terms of Bessel functions and is given by

$$S(k_g) = \big(J_0(k_g) - iJ_1(k_g)\big)C(k_g) + iJ_1(k_g) \tag{8.41}$$

or in terms real and imaginary parts as

$$\Re S(k_g) = F(k_g)J_0(k_g) + G(k_g)J_1(k_g), \tag{8.42}$$

$$\Im S(k_g) = G(k_g)J_0(k_g) - F(k_g)J_1(k_g) + J_1(k_g). \tag{8.43}$$

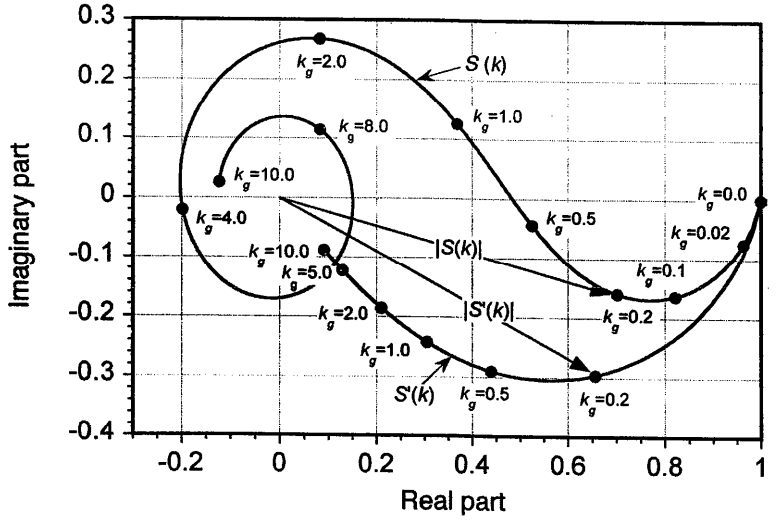

Figure 8.17 Real and imaginary parts of Sears's function, as referenced to the mid-chord and also to the leading edge of the airfoil.

If the gust is referenced to the leading edge of the airfoil, the result must be transformed, as described previously. This function will be called S' and can be written as

$$\Re S'(k_g) = \Re S \cos k_g + \Im S \sin k_g, \tag{8.44}$$

$$\Im S'(k_g) = -\Re S \sin k_g + \Im S \cos k_g, \tag{8.45}$$

which is equivalent to a frequency dependent phase shift. The two results are plotted in Fig. 8.17. Notice that the peculiar spiral shape of the S transfer function arises only when the gust front is referenced to the mid-chord of the airfoil. If the gust response is computed relative to the leading edge, then the S' transfer function is obtained. In application, the gust front reference point is frequently confused in the published literature. While the differences are small at low reduced frequencies, the errors will be significant for $k_g > 0.2$.

The Sears function and the Theodorsen function are compared in Fig. 8.18 in terms of amplitude and phase angle as a function of reduced frequency. At low reduced frequencies the functions converge, but for $k > 0.1$ the differences become increasingly large. Notice

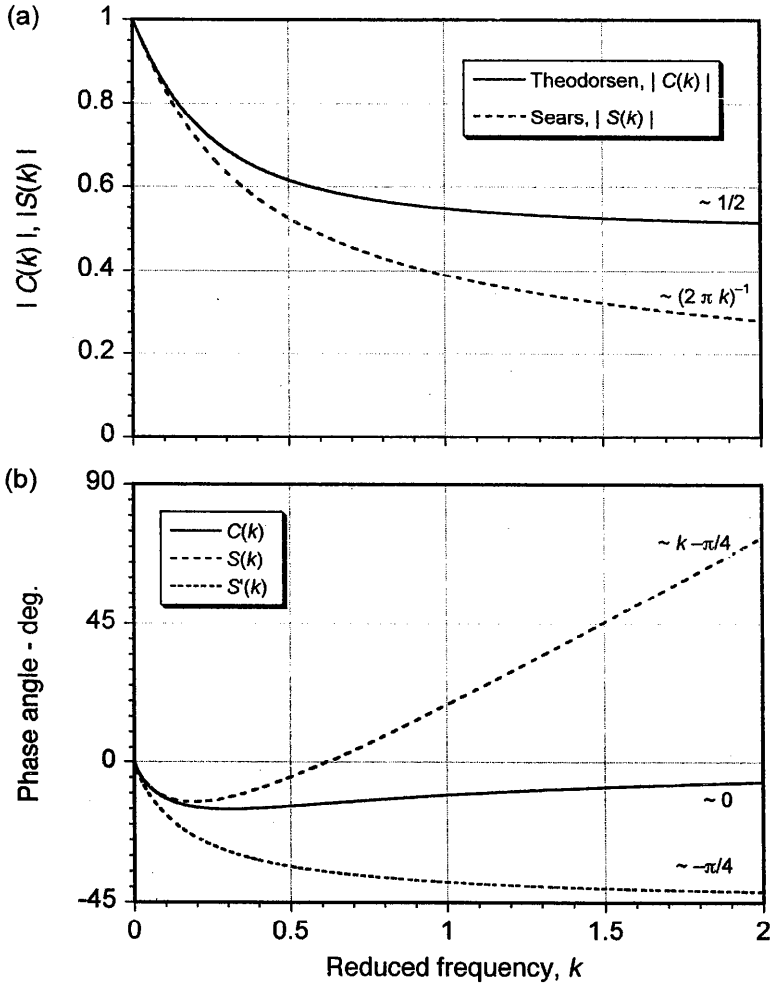

Figure 8.18 The Theodorsen and Sears functions in terms of amplitude and phase angle as a function of reduced frequency. (a) Amplitude. (b) Phase.

that as $k \to \infty$ then $|C(k)| \to 1/2$, and the corresponding phase angle $\to 0$. For Sears's function, the asymptotic behavior is $|S(k_g)| \propto 1/\sqrt{2\pi k_g}$. When referenced to the mid-chord, then phase angle is proportional to $k_g - \pi/4$, or $-\pi/4$ if the leading edge of the airfoil is used as the reference point.

8.10 Indicial Response: Wagner's Problem

Theodorsen's lift deficiency approach has found use in many problems in both fixed-wing and helicopter aeroelasticity. However, for a rotor analysis Theodorsen's theory is somewhat less useful because the nonsteady value of velocity at the blade elements, $V = U_T(y, \psi)$, means that the argument k (the reduced frequency) is, strictly speaking, an ambiguous parameter. Therefore, a theory formulated in the time domain is more general and is usually more useful. Wagner (1925) has obtained a solution for the so-called *indicial* lift on a thin-airfoil undergoing a transient step change in AoA in an incompressible flow.[4] The transient chordwise pressure loading is given by

$$\frac{\Delta C_p(\bar{x}, s)}{\alpha} = \frac{4}{V}\delta(t)\sqrt{(1-\bar{x})\bar{x}} + 4\phi(s)\sqrt{\frac{1-\bar{x}}{\bar{x}}}, \tag{8.46}$$

where $\phi(s)$ is called Wagner's function and, by analogy with the Theodorsen function, accounts for the effects of the shed wake. As defined previously in Eq. 8.4, the variable s represents the distance traveled by the airfoil in semi-chords. The first term in Eq. 8.46 is the apparent mass contribution, which for a step input appears as a Dirac-delta function $\delta(t)$. The corresponding result for an indicial change in pitch rate about the leading edge is given by

$$\frac{\Delta C_p(\bar{x}, t)}{q} = \frac{\delta(t)}{V}(1+2\bar{x})\sqrt{(1-\bar{x})\bar{x}} + \left(3\phi(s) - 1\right)\sqrt{\frac{1-\bar{x}}{\bar{x}}} + 4\sqrt{(1-\bar{x})\bar{x}}. \tag{8.47}$$

Again, the first term is an apparent mass term, with the second term being circulatory in nature and is affected by the shed wake. The third term is a quasi-steady term, with an analogous term also appearing in Theodorsen's result.

Wagner's function, $\phi(s)$, is known exactly [see, for example, Lomax (1968)] and is plotted in Fig. 8.19. Notice that the noncirculatory or apparent mass loading is responsible for the initial infinite pulse at $s = 0$. Thereafter, the function builds asymptotically from one half to a final value of unity as $s \to \infty$. In Wagner's problem, the aerodynamic center is at mid-chord at $s = 0$ and moves immediately to the 1/4-chord for $s > 0$. The resulting variation in the lift coefficient for a step change in angle of attack, α, can be written as

$$C_l(t) = \frac{\pi c}{2V}\delta(t) + 2\pi\alpha\phi(s), \tag{8.48}$$

where $2\pi\alpha$ is the steady-state lift coefficient, as given by steady thin-airfoil theory.

For rotor analyses, the indicial lift response makes a useful starting point in the development of a general time domain unsteady aerodynamic theory. If the indicial response is known, then the unsteady loads to arbitrary changes in AoA can be obtained through the superposition of indicial aerodynamic responses using the Duhamel integral. Consider a general system in response to a general forcing function $f(t)$, $t \geq 0$. If the indicial response

[4] By definition, an indicial function is the response to a disturbance that is applied instantaneously at time zero and held constant thereafter, that is, a disturbance given by a step function. In this case, $w = 0$ for $t < 0$ and $w = V\alpha$ for $t > 0$.

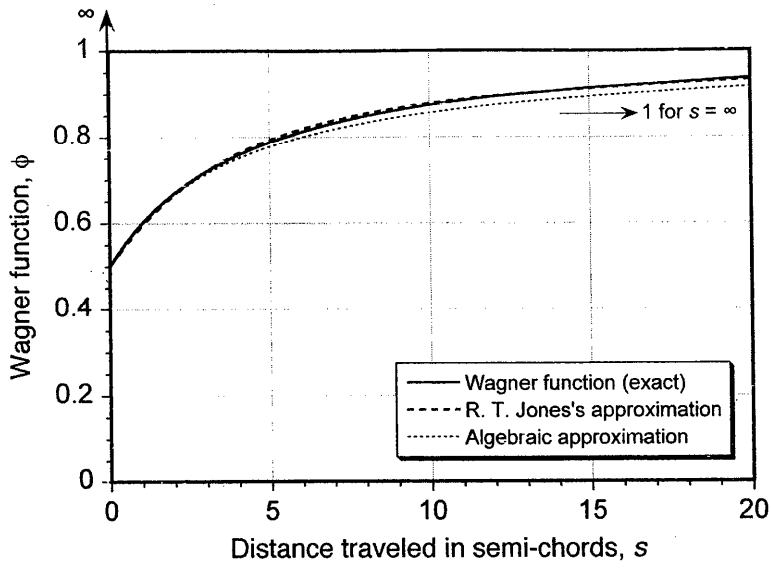

Figure 8.19 Wagner's function for a step change in angle of attack.

ϕ of the system is known, then the output $y(t)$ of the system can be written in terms of Duhamel's integral as

$$y(t) = f(0)\phi(t) + \int_0^t \frac{df}{dt}\phi(t-\sigma)d\sigma. \tag{8.49}$$

See Section 8.14 and Bisplinghoff et al. (1955) or von Kármán & Biot (1940) for details. In Eq. 8.49, σ is simply a dummy time variable of integration, and the first term is related to the initial condition from which subsequent inputs are applied. By analogy with Eq. 8.49, the circulatory part of the lift coefficient, C_l^c, in response to an arbitrary variation in AoA can now be written in terms of the Wagner function as

$$C_l^c(t) = 2\pi\left(\alpha(0)\phi(s) + \int_0^s \frac{d\alpha(\sigma)}{dt}\phi(s-\sigma)d\sigma\right) = 2\pi\alpha_e(t), \tag{8.50}$$

where α_e simply represents an effective AoA and contains within it all of the time history effects on the lift because of the influence of the shed wake. Notice that if V = constant, then $s = 2Vt/c$. In addition, the appropriate apparent mass terms must be added to get the total lift. For incompressible flow, however, the apparent mass terms are proportional to the instantaneous motion, so they all conveniently appear outside the Duhamel integral.

The Duhamel integral in Eq. 8.50 can be solved analytically or numerically. Analytical solutions are mostly restricted to simple forcing functions, and numerical methods must be employed in the general case. The main difficulty in solving Duhamel's integral is, however, with the Wagner function itself. Although the Wagner function is known exactly, its evaluation is not in a convenient analytic form. Therefore, it is usually replaced by a simple exponential or algebraic approximation. When this is done, a whole series of practical numerical tools for computing the unsteady aerodynamics can be unleashed. One approximation to the Wagner function, attributed to R. T. Jones (1938, 1940), is written as a two term exponential series with four coefficients, that is,

$$\phi(s) \approx 1.0 - 0.165e^{-0.0455s} - 0.335e^{-0.3s}, \tag{8.51}$$

as shown in Fig. 8.19. This approximation is found to agree with the exact solution to an accuracy that is within 1%. Another approximation to the Wagner function is attributed to W. P. Jones (1945); here

$$\phi(s) \approx 1.0 - 0.165e^{-0.041s} - 0.335e^{-0.32s}. \tag{8.52}$$

In each case it will be noted that $A_1 + A_2 = 0.5$, according to Wagner's exact result.

The main advantage of using the exponential approximation is that it has a simple Laplace transform. While the exponential behavior of the Wagner function is not an exact representation of the physical behavior, it is usually sufficiently accurate for practical calculations.[5] An alternative algebraic approximation to the Wagner function suggested by Garrick (1938) is

$$\phi(s) \approx \frac{s+2}{s+4}, \tag{8.53}$$

which, although not as accurate as the exponential approximation except in the limit as $s \to \infty$, it agrees with both the exact solution and with the exponential approximation to within 2% accuracy.

8.11 Sharp-Edged Gust: Küssner's Problem

In a rotor flow field, the rotor wake (and specifically the tip vortices) produces a highly nonuniform induced velocity field across the plane of the rotor disk. Therefore, a typical blade element encounters a nonuniform vertical upwash/downwash as it rotates in this field. It is, therefore, important to distinguish properly the effects on the airloads arising from AoA changes from blade motion (in effect, a plunging and pitching motion at the blade element) from the effects resulting from the rotor wake–induced velocity field (in effect, a vertical gust velocity normal to the blade element). This distinction has important effects on the resulting airloads and should not be overlooked in the mathematical modeling of helicopter rotor problems.

The problem of finding the transient lift response on a thin-airfoil entering a sharp-edged vertical gust (that is, a vertical upwash velocity) was first tackled by Küssner (1935) and properly solved by von Kármán and Sears (1938). In this problem, the upwash velocity, w_g, is defined relative to an axis at the leading edge as

$$w_g = \begin{cases} 0 & \text{if } \bar{x} > Vt/c \\ w_0 & \text{if } \bar{x} \leq Vt/c \end{cases} \tag{8.54}$$

as shown in Fig. 8.20. Recall that, in Wagner's problem, the AoA changes instantaneously over the whole chord at $s = 0$. In Küssner's problem, however, the quasi-steady AoA changes progressively as the airfoil penetrates into the gust front. At $s = 2$, the airfoil becomes fully immersed in the gust. The resulting variation in the lift coefficient can be written in a similar way to Wagner's solution such that

$$C_l(t) = 2\pi\left(\frac{w_0}{V}\right)\psi(s), \tag{8.55}$$

[5] For some applications the exponential approximation to the indicial response may not be considered adequate. This is usually because the rate of approach to the asymptotic value is not as correct for the exponential approximation compared to the exact behavior. This effect, however, is more of academic interest rather than of any practical importance.

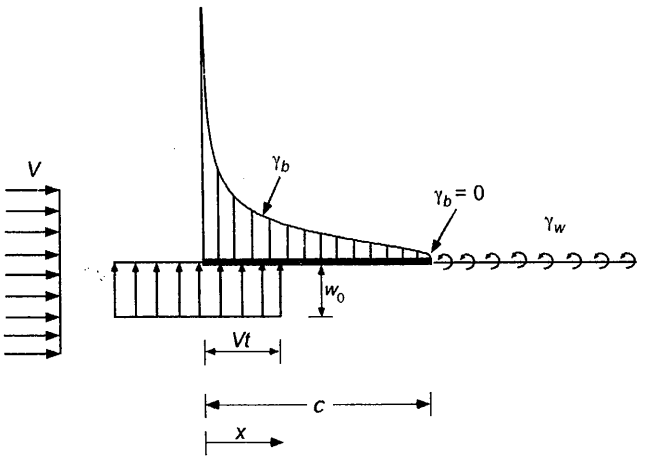

Figure 8.20 Boundary conditions for an airfoil penetrating into a sharp-edged vertical gust.

where $\psi(s)$ is known as Küssner's function and is plotted in Fig. 8.21. Compared to the Wagner function, which has an initial value of one-half, it will be seen that the Küssner function builds from an initial value of zero and asymptotes to unity for $s \to \infty$. Küssner's function is also known exactly, albeit not in a convenient analytic form. Von Kármán & Sears (1938) also showed that the aerodynamic center always acts at the 1/4-chord of the airfoil for all s. This is perhaps a surprising result, but it has been verified experimentally – see Sears & Sparks (1941).

The Küssner function can be used with the Duhamel superposition integral to find the lift response to an arbitrary vertical upwash field, where the lift coefficient can now be obtained using

$$C_l(t) = \frac{2\pi}{V}\left(w_g(0)\psi(s) + \int_0^s \frac{dw_g(\sigma)}{dt}\psi(s-\sigma)d\sigma\right). \tag{8.56}$$

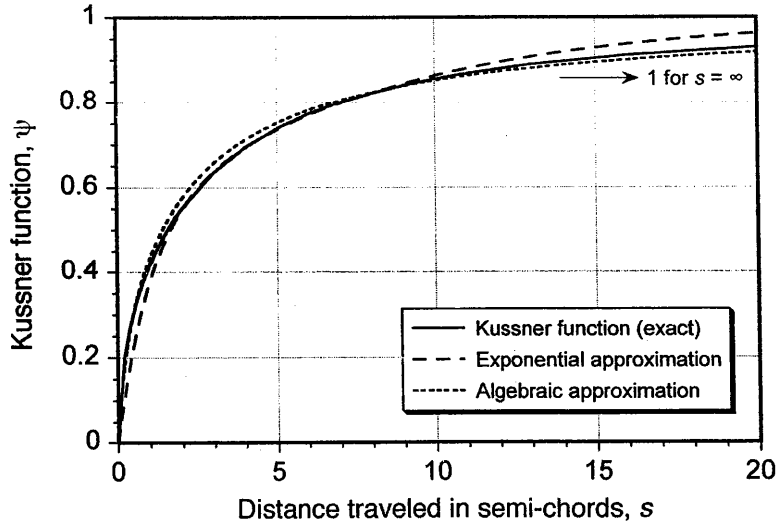

Figure 8.21 Küssner's function for the penetration of a sharp-edged vertical gust.

Notice that this equation is analogous to the result for the lift resulting from arbitrary variations in angle of attack, as given previously in Eq. 8.50, but with a different indicial function being used. To enable practical calculations using Duhamel superposition, the Küssner function, like the Wagner function, is usually replaced by an exponential approximation. One approximation is given by Sears & Sparks (1941) as

$$\psi(s) \approx 1 - 0.5e^{-0.13s} - 0.5e^{-1.0s}, \tag{8.57}$$

which is shown in Fig. 8.21. Alternatively, an algebraic approximation that is sometimes used for the Küssner function is

$$\psi(s) \approx \frac{s^2 + s}{s^2 + 2.82s + 0.80}, \tag{8.58}$$

which is given by Bisplinghoff et al. (1955). Neither approximation represents the correct vertical tangent of the ψ curve at $s = 0$, but this is of no practical significance.

8.12 Traveling Sharp-Edged Gust: Miles's Problem

Results for the lift on a thin 2-D airfoil encountering traveling (in-plane convecting) vertical sharp-edged gusts in incompressible flow have been obtained by Miles (1956) in terms of a gust speed ratio, λ:

$$\lambda = \frac{V}{(V + V_g)}, \tag{8.59}$$

where V is the velocity of the airfoil and V_g is the component of the gust convection velocity in the chord plane of the airfoil. The usual assumption made in most rotor aerodynamic analyses is that the wake (tip vortices and corresponding induced velocity field) are stationary (nonconvecting) with respect to the rotor (i.e., rigid wake assumption), so that $\lambda = 1$ at all the blade elements over the rotor disk. However, the self-induced velocities generated by the vortex wake system results in a continuously changing and nonuniform convection of the induced velocity field with respect to the rotor, and this may produce values of λ less than or greater than unity.

Miles (1956) showed that as the propagation speed of the traveling gust front, V_g, increased from zero to ∞ (λ decreases from 1 to 0), the solution for the unsteady lift changes from the Küssner result to the Wagner result, with a variety of intermediate transitional results being obtained. Miles's results were later generalized by Drischler & Diederich (1957) who obtained continuous semi-analytical forms for both the lift and pitching moment gust functions. The problem has also been solved by Leishman (1997) using the reverse flow theorems. All approaches make use of either algebraic or exponential approximations to the Wagner function to facilitate numerical solutions.

Consider a 2-D airfoil traveling with velocity V and subject to a vertical sharp-edged gust field of magnitude w_0 convecting with velocity $V_g = (\lambda^{-1} - 1)V$, as shown in Fig. 8.22. Notice that when the gust field is stationary, $\lambda = 1$, and when the field is traveling toward the airfoil at infinite speed, $\lambda = 0$. For the sharp-edged gust, the primary boundary condition is that the downwash, w, is zero on the part of the airfoil that has not reached the gust front. This means that for a downstream traveling gust referenced to the leading edge then

$$w_g = \begin{cases} 0 & \text{if } \bar{x} > \bar{x}_0 = V\lambda^{-1}\, t/c = s/2\lambda, \\ w_0 & \text{if } \bar{x} < \bar{x}_0 = V\lambda^{-1}\, t/c = s/2\lambda, \end{cases} \tag{8.60}$$

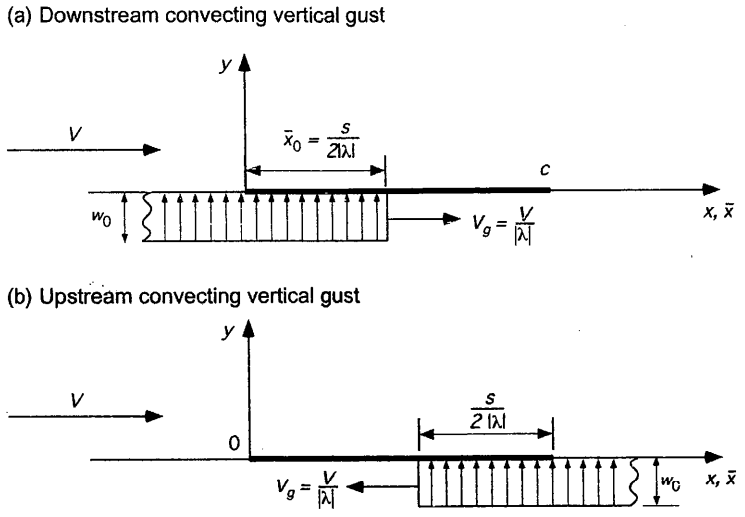

Figure 8.22 Boundary conditions for an airfoil encountering a convecting sharp-edged vertical gust.

and for an upstream traveling gust then

$$w_g = \begin{cases} 0 & \text{if } \bar{x} < \bar{x}_0 = 1 - V|\lambda|^{-1}\, t/c = 1 - s/2|\lambda|, \\ w_0 & \text{if } \bar{x} > \bar{x}_0 = 1 - V|\lambda|^{-1}\, t/c = 1 - s/2|\lambda|. \end{cases} \tag{8.61}$$

The gust problem is shown schematically in Fig. 8.22. In either case, it will be seen that, like the Küssner problem, the quasi-steady AoA on the airfoil changes progressively as a function of time as the airfoil penetrates into the gust front. For a stationary gust $\lambda = 1$, and under incompressible flow assumptions, this is equivalent to solving Küssner's problem. For $\lambda = 0$, this is equivalent to solving Wagner's problem.

One approach to solving the convecting gust problem involves using the reciprocal or reverse flow theorems – see Flax (1952, 1953), Brown (1949), Jones (1951), Heaslet & Spreiter (1952), and Leishman (1997). The main utility of reverse flow theorems is that they build from known solutions for airfoil flows and obviate the need to start each new problem from first principles. They are ideally suited to solving various indicial problems, both analytically and numerically. For example, the reverse flow theorems have been used by Leishman (1994) and Hariharan & Leishman (1996) to calculate the indicial responses of airfoils with flaps. General forms of the aerodynamic reverse flow theorems have been established by Heaslet & Spreiter (1952). The first theorem states that: "The lift in steady or indicial motion of one airfoil having arbitrary twist and camber is equal to the integral over the planform of the product of the local AoA and the loading per unit AoA at the corresponding points on a second flat-plate airfoil of identical planform but moving in the reverse direction." In application, consider two airfoils, one moving in a forward direction and the other in a reverse direction. The first airfoil (the unknown problem) has an arbitrary AoA distribution $\alpha_1(x_1)$, which could be produced by a vertical gust field (or a flap). The second airfoil is a flat plate at constant angle of attack, $\alpha_2 = \text{constant}$, which is assumed to have a known aerodynamic loading over the chord. The boundary conditions are $\alpha_1 = \alpha_1(x_1)$, $\alpha_2 = \text{const}$. The first reverse flow theorem gives the result that

$$\alpha_2 C_{l_1} = \int_1 \alpha_2 \Delta C_{p_1} dx_1 = \int_2 \alpha_1 \Delta C_{p_2} dx_2. \tag{8.62}$$

In other words, the lift coefficient on the first airfoil can be found from the loading on the second airfoil by integrating the known solution and the local chordwise AoA using

$$C_{l_1} = \int_2 \alpha_1 \left(\frac{\Delta C_{p_2}}{\alpha_2} \right) dx_2. \tag{8.63}$$

This relatively simple but powerful technique allows some remarkable simplifications in solving both steady and transient airfoil problems. The utility of the theorems, however, extends only to the integrated forces and pitching moments on the airfoil and not to pressure distributions, which may be required for some problems.

For $M = 0$, the chordwise pressure loading for an indicial change in AoA is given by Eq. 8.46. By using the reverse flow theorems, the time-varying (indicial) lift on the airfoil for a traveling sharp-edged vertical gust can be obtained by integration of this known solution over the appropriate part of the airfoil affected by the gust front, but when the airfoil is moving in the reverse direction. For the downstream traveling vertical gust, this is equivalent to integrating the known flat-plate loading from the trailing edge to the leading edge of the gust front at $\bar{x}_0$ (see Fig. 8.22). For the upstream traveling gust, the known loading must be integrated from the leading edge of the airfoil up to $\bar{x}_0$. It will be immediately apparent that different results, both quasi-steady and unsteady, will be produced for downstream versus upstream traveling vertical gusts.

For incompressible flows, the noncirculatory part of the unsteady lift can be written in terms of the instantaneous upwash over the airfoil. For a traveling sharp-edged vertical gust, results can be obtained analytically by integrating the first term of Eq. 8.46 with the boundary conditions given in Eqs. 8.60 and 8.61. For a downstream traveling gust the noncirculatory lift can be shown to be

$$\frac{C_l^{nc}(t)}{(w_0/V)} = \frac{1}{2}\frac{\partial}{\partial t}\left(\frac{\sin 2\theta_0}{2} - \theta_0 + \pi \right), \tag{8.64}$$

where $\theta_0 = \cos^{-1}(1 - 2\bar{x}_0)$, so that $\theta_0 = 0$ at the time when the gust front is at the airfoil leading edge and $\theta_0 = \pi$ at the trailing edge. For the upstream traveling sharp-edged vertical gust, the corresponding result for the noncirculatory lift is

$$\frac{C_l^{nc}(t)}{(w_0/V)} = \frac{1}{2}\frac{\partial}{\partial t}\left(\theta_0 - \frac{\sin 2\theta_0}{2} \right). \tag{8.65}$$

Equations 8.64 and 8.65 can be evaluated numerically at discrete values of time as the gust front proceeds over the airfoil, with the time derivatives being evaluated by means of finite differences.

Unlike the apparent mass terms, the circulatory parts of the unsteady lift depend on the prior time history of the gust field, and so the lift must be obtained numerically by Duhamel superposition (see Section 8.14.1 for details). For a downstream traveling gust, the quasi-steady part of the circulatory lift can be obtained analytically by integration of the second term in Eq. 8.46 with the application of the appropriate boundary conditions. For the downstream traveling sharp-edged gust, it can be shown (see Question 8.12) that

the quasi-steady circulatory lift is

$$\frac{C_l^{qs}}{(w_0/V)} = 2(\pi - \theta_0 - \sin\theta_0) \tag{8.66}$$

or, in terms of equivalent angle of attack,

$$\frac{C_l^{qs}}{(w_0/V)} = 2\pi\alpha^{qs} = 2\pi\left(1 - \frac{\theta_0}{\pi} - \frac{\sin\theta_0}{\pi}\right). \tag{8.67}$$

For the upstream traveling sharp-edged gust, the equivalent quasi-steady AoA is

$$\alpha^{qs} = \left(\frac{\theta_0}{\pi} + \frac{\sin\theta_0}{\pi}\right)\left(\frac{w_0}{V}\right). \tag{8.68}$$

The net unsteady circulatory lift is then determined numerically by Duhamel superposition with the instantaneous or quasi-steady equivalent AoA and the Wagner function using Eq. 8.50. The calculation of the corresponding unsteady pitching moments proceeds by a similar process. This problem, however, is somewhat more difficult to solve because a second reverse flow theorem and the chordwise loading as a result of pitch rate must be used in addition to the AoA result – see Leishman (1997).

Results for the unsteady lift and pitching moment for downstream traveling sharp-edged gusts are shown in Fig. 8.23. For $\lambda = 0$ ($V_g = \pm\infty$), the results lead to the Wagner function. For $\lambda = 1$ ($V_g = 0$), the results reduce to the Küssner function. For intermediate values of λ, notice that a different series of results are obtained as the gust propagation speed increases from zero ($\lambda = 1$). The noncirculatory term is responsible for the very large peaks in the lift that are produced as λ decreases. The lift reaches a maximum at the point when the airfoil is about half way into the gust. It can be seen that the magnitudes of these peaks are often larger than the steady-state lift coefficient of 2π per radian angle of attack. For vertical gusts that move with the wing at velocities less than 0 ($\lambda > 1$), the noncirculatory part of the lift is small and the circulatory lift grows only very slowly with time. The corresponding pitching moment shows a change in the sign of the center of pressure for λ greater or less than one. For the stationary gust ($\lambda = 1$), the center of pressure remains at the 1/4-chord throughout the motion, a result proved analytically by von Kármán & Sears (1938). As the gust speed approaches infinity, the peak in the pitching moment approaches $-\pi\delta(t)$ with the center of pressure moving to mid-chord. For receding vertical gusts, the center of pressure moves in front of the 1/4-chord.

Results for upstream traveling vertical gusts are shown in Fig. 8.24. Again, for quickly traveling gusts the results approach the Wagner function. For progressively slower gusts, large peaks in the lift and pitching moment appear as a result of the noncirculatory contributions to the airfoil loading. Notice that the noncirculatory terms are the same for any value of $|\lambda|$ but that the total transient value of the lift is higher than for a downstream traveling gust. The reasons for this will be apparent from a comparison of Eqs. 8.67 and 8.68, which simply prove that a gust affecting the trailing edge of the airfoil will have a larger effect on the circulatory lift than a gust affecting the same percentage of the leading edge. For the same reasons, a trailing edge flap deflection is more effective in producing a change in lift than a leading edge flap.

8.13 Time-Varying Incident Velocity

The previously described unsteady airfoil solutions have considered the local free stream velocity to be constant. However, in forward flight a typical blade element on a rotor

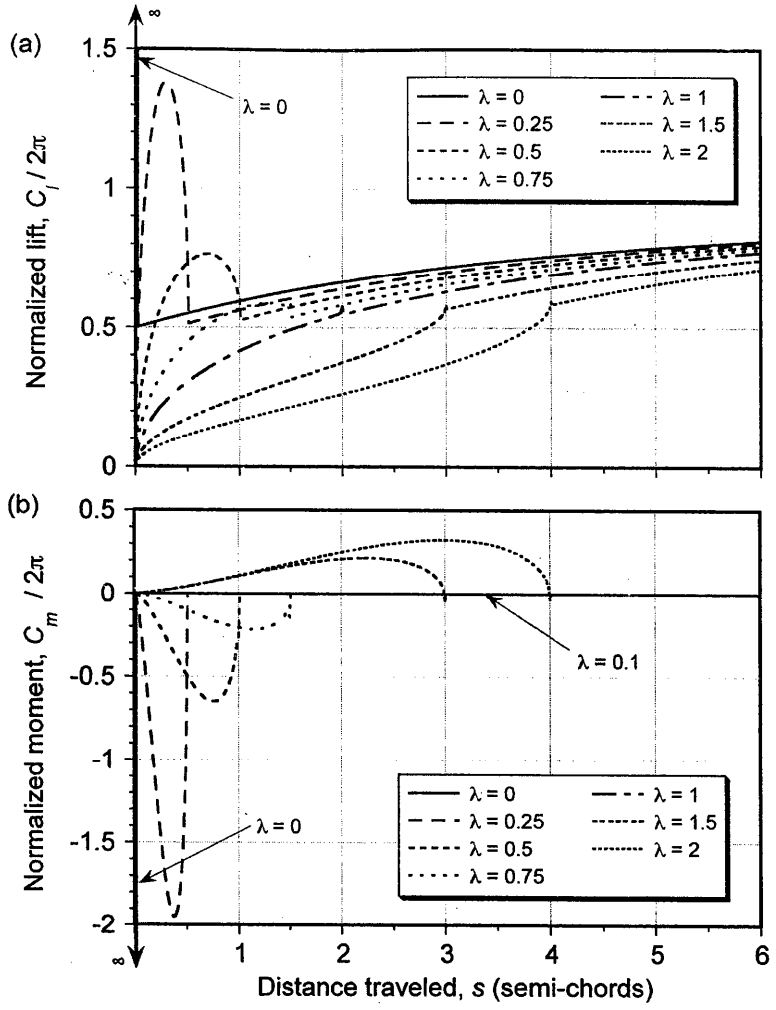

Figure 8.23 Airloads produced for a series of downstream moving sharp-edged vertical gusts. (a) Lift. (b) Pitching moment about 1/4-chord.

will encounter a time-varying incident velocity because $V = U_T(y, \psi) = \Omega y + \mu\Omega R \sin\psi$. Under these conditions, there are additional unsteady aerodynamic effects to be considered. These effects include both noncirculatory and circulatory contributions. With a time-varying incident flow velocity, the shed wake behind the airfoil is convected at a nonuniform velocity (see Fig. 8.25), and this causes several complications in the mathematical treatment of the induced velocity effects. Isaacs (1945, 1946) derived a closed form solution for the additional unsteady aerodynamic effects of a harmonically varying free stream velocity. Greenberg (1947) published a similar theory, but made a high frequency assumption about the shed wake behind the airfoil to obtain a solution in terms of the Theodorsen function alone. An approximate theory for this problem was also developed by Kottapalli (1985), in which small "lead–lag" airfoil oscillation amplitudes with respect to the mean velocity were assumed. Johnson (1980) has also discussed the general problem of a varying velocity on unsteady airloads. Using the same assumptions made by Isaacs, complete expressions are given for the lift and pitching moment on an airfoil executing harmonic plunge and pitch motion about

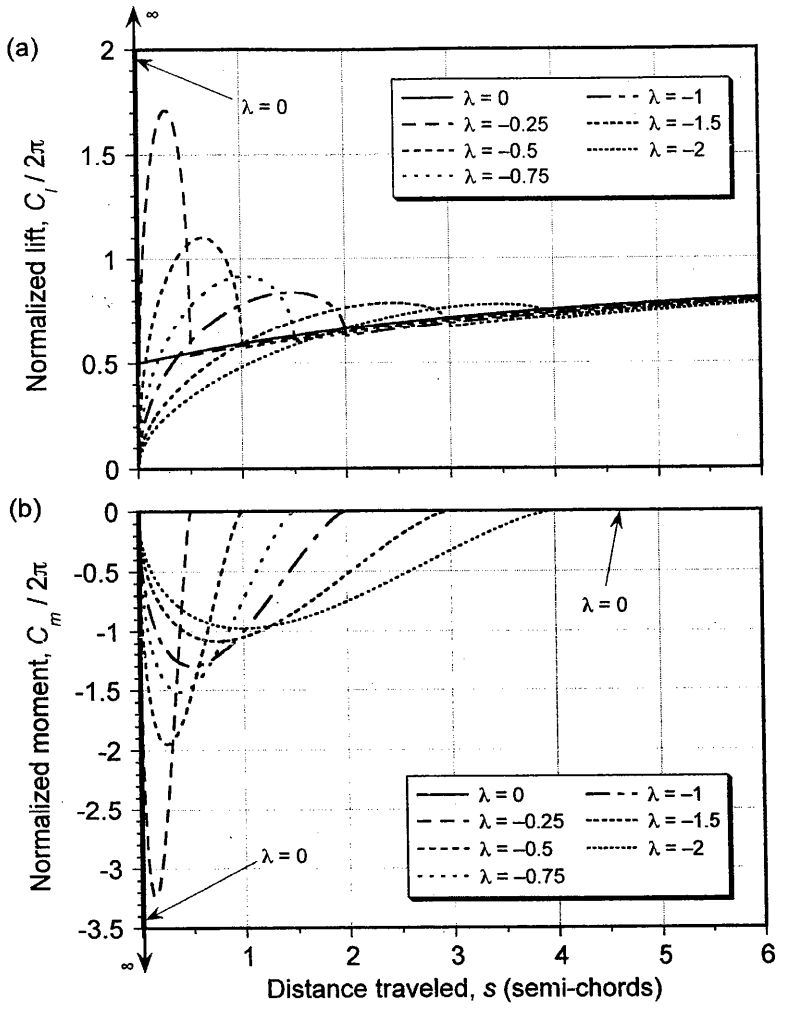

Figure 8.24 Airloads produced for a series of upstream moving vertical gusts. (a) Lift. (b) Pitching moment about 1/4-chord.

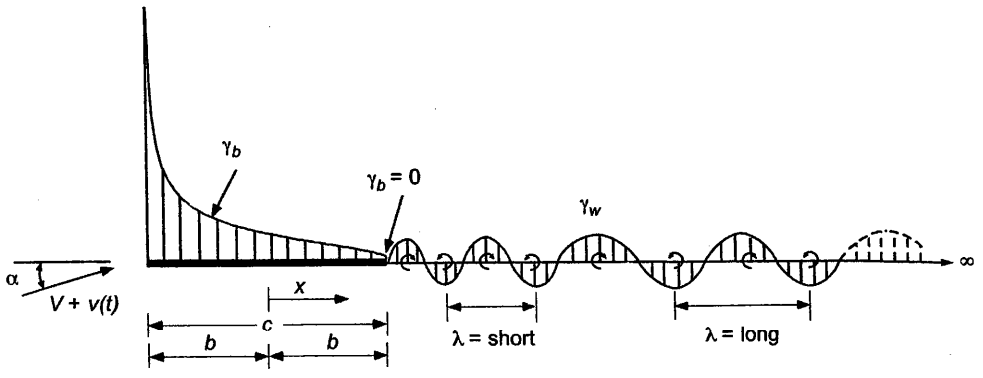

Figure 8.25 A time-varying free-stream velocity results in a nonuniform convection speed of the shed wake.

an arbitrary pitch axis. Essentially, Johnson's conclusion is that the approximation using the Theodorsen function with the local reduced frequency is appropriate for flow oscillation amplitudes of up to 70% of the mean velocity. For small flow oscillation amplitudes, the Theodorsen function calculated with the reduced frequency argument based on the mean velocity will be accurate enough, which effectively means neglecting the unsteady free stream effects.

The theoretical problem of a time-varying free stream velocity on the unsteady aerodynamic response has been examined by van der Wall & Leishman (1994), both from the classical frequency domain approach and also from the time domain. This work reemphasizes that one of the significant effects of an oscillating incident flow velocity is a nonuniform convection velocity of the shed wake vorticity behind the airfoil. Van der Wall & Leishman (1994) compare and contrast five theories representing the effect of the unsteady incident velocity variations: Isaacs's theory, Greenberg's theory, Theodorsen's theory combined with unsteady incident velocity, Kottapalli's theory, and the Duhamel superposition with the Wagner function. They found that, strictly speaking, all of the theories represent the case of a fore–aft moving airfoil instead of an unsteady incident velocity; this latter case should be more correctly viewed as a propagating horizontal gust field. A helicopter rotor blade section in forward flight encounters both unsteady sectional velocity (the superposition of rotation and forward flight velocity components), but in addition there is a fore–aft motion through the blade lead–lag degree of freedom. However, it was found that in the range of reduced frequencies encountered by a helicopter blade, the results obtained from all the various theories are essentially equivalent. Therefore, the interpretation of an unsteady free stream as equivalent to fore–aft motion of the airfoil can be viewed as a good approximation for the helicopter case. All of the theories cited above lead to the same noncirculatory expressions, and all were found to reduce to Theodorsen's theory (or equivalent) when the varying part of the incident flow oscillation amplitude becomes zero.

As mentioned previously, in the time domain the effect of a time-varying velocity in an incompressible flow can be modeled using Duhamel superposition with the Wagner function. Again, the appropriate apparent mass forces must be included in the solution, even though they will be small for the frequencies and amplitudes of the fluctuating velocity typically found on a helicopter. In this case

$$C_l(t) = \frac{\pi b}{V^2}\left(\ddot{h} + \frac{d(V\alpha)}{dt} - ab\ddot{\alpha}\right) + \frac{2\pi}{V}\left(V\alpha(0)\phi(s) + \int_0^s \frac{d(V\alpha)(\sigma)}{dt}\phi(s-\sigma)d\sigma\right). \tag{8.69}$$

The distance traveled through the flow is now proportional to the area under the velocity versus time curve as given by Eq. 8.4. Van der Wall & Leishman have compared results obtained with this time domain method with Isaac's frequency domain results, where the agreement is essentially exact.

Results calculated using Eq. 8.69 are shown in Fig. 8.26 for the lift on an airfoil at a constant angle of attack, α, experiencing a harmonic oscillation of velocity of the form $V(t) = V_\infty(1 + \lambda \sin \omega t)$ at a reduced frequency, k, of 0.2 with $\lambda = 0, 0.2, 0.4, 0.6$, and 0.8. The Duhamel integral was solved by means of a finite-difference approximation using the numerical scheme discussed in Section 8.14.1. The lift in Fig. 8.26 is shown as a fraction of the quasi-steady lift, $(C_l)_{qs} = 2\pi\alpha$. Also shown in this figure are results computed by means of a CFD method based on solutions to the Euler equations. It will be seen from Fig. 8.26 that at a given time the primary effect of unsteadiness is either an increase or attenuation

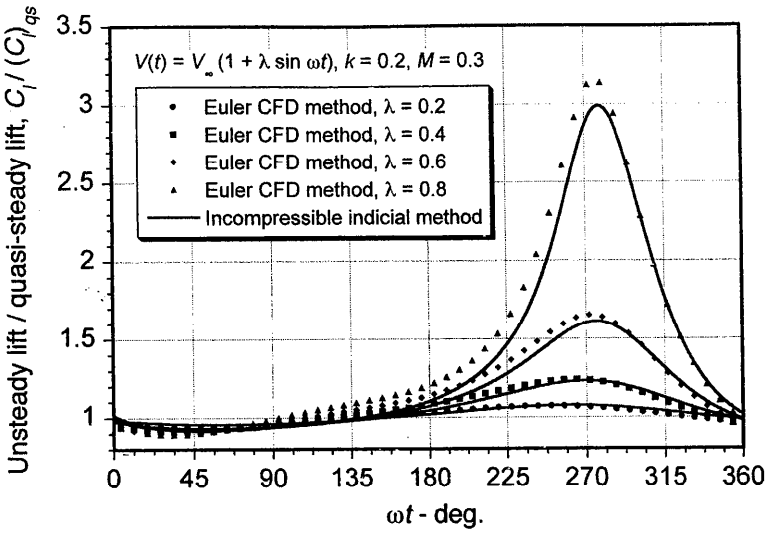

Figure 8.26 The effects of a nonsteady free-stream velocity on the unsteady lift for an airfoil with a constant angle of attack. (CFD calculations courtesy of Arun Jose.)

of the unsteady lift compared to the quasi-steady result, which is a result already noted for oscillations in angle of attack. For $0° < \omega t < 90°$, the local velocity (and thus the product $V\alpha$) is increasing. Here, the shed circulation has the opposite sign to the airfoil circulation and so the unsteady lift is less than the quasi-steady value. The higher local velocity here means that the shed wake is further away from the airfoil in a given time, and this effect contributes to a more rapid buildup in the circulatory lift compared to the case where the wake convection speed would be assumed uniform. For $90° \leq \omega t < 270°$, the local velocity is decreasing. Here, the shed circulation has the same sign as the airfoil circulation, which tends to increase the lift over the quasi-steady value. Furthermore, for $180° \leq \omega t < 360°$ a velocity lower than the mean incident velocity means that the shed wake is closer to the airfoil; this then enhances the basic unsteady effect and the lift quickly becomes much greater than the quasi-steady values. Finally for $270° \leq \omega t < 360°$, the local velocity is increasing again. With the change in sign of the wake circulation and the increasing wake convection velocity, the lift drops quickly to become close to the quasi-steady value again. Notice that in Fig. 8.26 there is good agreement between the incompressible theory and the CFD method,[6] despite the slight phase differences. Other theoretical work on modeling unsteady free stream velocity effects is given by Ashley et al. (1952) and Friedmann & Yuan (1977). The extension of this problem to subsonic compressible flow is not without its difficulties, but one approach is discussed later in Section 8.17.

8.14 General Application of the Indicial Response Method

As described previously, if the indicial aerodynamic response(s) can be determined, then these solutions form a powerful means of finding the unsteady aerodynamic forces and pitching moments in the time domain in response to arbitrary variations in AoA and/or in-flow velocity by using Duhamel superposition. The effects of a time-varying incident flow

[6] The Euler CFD method is computationally expensive, being approximately five orders of magnitude greater than the cost of the solution obtained using Duhamel superposition.

velocity may also be handled by means of this approach. There are two main difficulties with this method, however. The first is to determine the indicial response functions themselves. While they are known exactly for incompressible flow (e.g., Wagner and Küssner functions), they are not known exactly for subsonic compressible flow. Nevertheless, there are various techniques that can be used to find and approximate forms of the indicial response from aerodynamic transfer functions obtained from experimental measurements. Second, numerical methods must be devised to enable the superposition process to be conducted accurately and computationally efficiently.

The indicial method is based on the fundamental principle that the flow can be linearized with respect to the forcing function. For example, a generalized unsteady force coefficient acting on the airfoil, say $C_f(t)$, can be assumed to be a smooth, nonlinear function of angle of attack, α. About some mean value of angle of attack, say α_m, this allows C_f to be expressed as the first-order Taylor series expansion

$$C_f(t) = C_f(\alpha = \alpha_m, t = 0) + \left.\frac{\partial C_f}{\partial \alpha}\right|_{\alpha=\alpha_m} \Delta\alpha. \tag{8.70}$$

This approximation will become more exact as the step $\Delta\alpha \to 0$. If C_f is a *linear* function of α, then Eq. 8.70 is already exact. If $\partial C_f/\partial\alpha$ is a linear time invariant response such that it does not depend on α and so depends only on the time after the step input is applied, then the linear result for C_f is

$$C_f(t) = C_f(t = 0) + \frac{dC_f}{d\alpha}(t)\Delta\alpha = C_f(t = 0) + \phi_f(t)\Delta\alpha, \tag{8.71}$$

where $\phi_f(t)$ is called the linear *indicial response* of C_f, in this case to a step input in α.

For arbitrary inputs in α, then as shown previously the value of C_f can then be expressed in terms of the Duhamel superposition (or convolution) integral as

$$C_f(t) = \frac{dC_f}{d\alpha}\alpha(0)\phi_f(t) + \frac{dC_f}{d\alpha}\int_0^t \frac{d\alpha}{dt}(\sigma)\phi_f(t-\sigma)d\sigma, \tag{8.72}$$

where the first term is a short time transient. The evaluation of the Duhamel integral, therefore, produces an aerodynamic quantity that contains all of the prior time-history information of what has happened to the aerodynamic response since the initial time. Equation 8.72 is solved numerically (see Section 8.14.1) and different approaches can be formulated. Notice that in the limit of steady flow, Eq. 8.72 reduces to the trivial result that

$$C_f = \left(\frac{dC_f}{d\alpha}\right)\alpha = \text{constant}, \tag{8.73}$$

which is fully consistent with linearized, steady airfoil theory.

The time-varying value of the lift coefficient, $C_l(t)$, can be expressed as a function of angle of attack, $\alpha(t)$, in terms of the Duhamel integral as

$$C_l(t) = C_{l_\alpha}\left[\alpha(t_0)\phi(s) + \int_{s_0}^{s} \frac{d\alpha}{dt}(\sigma)\phi(s-\sigma)d\sigma\right] = C_{l_\alpha}\alpha_e(t), \tag{8.74}$$

where $\phi(s)$ is indicial response to a unit step input α and C_{l_α} is the lift-curve-slope (= 2π/radian for incompressible flow). If the integral is evaluated, then the term $\alpha_e(t)$ can be

viewed as an effective AoA in that it contains all the time history information.[7] Equation 8.74 is usually solved numerically for discrete values of time. For a discretely sampled system at times $s = s, \sigma_i, \ldots, \sigma_2, \sigma_1, s$, then $\alpha_e(s)$ can be written using Eq. 8.74 as

$$\begin{aligned}\alpha_e(s) &= \alpha(s_0)\phi(s) + \sum_{i=1}^{\infty} \frac{d\alpha}{ds}(\sigma_i)\phi(s-\sigma_i)\Delta\sigma_i \\ &= \alpha(s_0)\phi(s) + \alpha'(\sigma_1)\phi(s-\sigma_1)\Delta\sigma_1 + \alpha'(\sigma_2)\phi(s-\sigma_2)\Delta\sigma_2 + \cdots \\ &\quad + \alpha'(\sigma_i)\phi(s-\sigma_i)\Delta\sigma_i + \cdots,\end{aligned} \tag{8.75}$$

with the summation extending over all inputs that have acted up to the instant s. Therefore, the result for $\alpha_e(s)$ requires the storage of $\alpha'(s), \alpha'(\sigma_1), \ldots, \alpha'(\sigma_i)$ at all previous time steps and the repeated reevaluation of the indicial function for each $s - \sigma_i$ at each new time step. Obviously, in most cases information at a large number of previous time steps must be retained. Also, the indicial response function is not always known in a convenient simple analytic form, such as with the Wagner and Küssner functions, so a relatively large number of numerical operations must be performed. This is not helpful for a helicopter rotor calculation, but, fortunately, there are alternative approaches to solving this numerical problem.

8.14.1 *Recurrence Solution to the Duhamel Integral*

If a general two term exponentially growing indicial function is assumed such that

$$\phi(s) = 1 - A_1 e^{-b_1 s} - A_2 e^{-b_2 s}, \tag{8.76}$$

then the Duhamel integral in Eq. 8.74 can be written numerically as

$$\begin{aligned}\alpha_e(s) &= \alpha(s_0)\phi(s) + \int_{s_0}^{s} \frac{d\alpha}{ds}(\sigma)\phi(s-\sigma)d\sigma \\ &= \alpha(s_0)(1 - A_1 e^{-b_1 s} - A_2 e^{-b_2 s}) \\ &\quad + \int_{s_0}^{s} \frac{d\alpha}{ds}(\sigma)(1 - A_1 e^{-b_1(s-\sigma)} - A_2 e^{-b_2(s-\sigma)})d\sigma \\ &= \alpha(s_0) - A_1\alpha(s_0)e^{-b_1 s} - A_2\alpha(s_0)e^{-b_2 s} + \int_{s_0}^{s} d\alpha(s) \\ &\quad - A_1 \int_{s_0}^{s} \frac{d\alpha}{ds}(\sigma)e^{-b_1(s-\sigma)}d\sigma - A_2 \int_{s_0}^{s} \frac{d\alpha}{ds}(\sigma)e^{-b_2(s-\sigma)}d\sigma.\end{aligned} \tag{8.77}$$

Notice that the terms $A_1\alpha(s_0)e^{-b_1 s}$ and $A_2\alpha(s_0)e^{-b_2 s}$ containing the initial value of α are short-term transients and can be neglected. Therefore, the Duhamel integral can be rewritten as

$$\alpha_e(s) = \alpha(s) - X(s) - Y(s), \tag{8.78}$$

[7] Notice that the result in Eq. 8.74 can also be extended to finite wings, where ϕ represents the indicial aerodynamic response of the entire wing as opposed to a single 2-D section – see Jones (1940) and Lomax (1968).

which is in the notation used by Beddoes (1976, 1984), where the X and Y terms are given by

$$X(s) = A_1 \int_{s_0}^{s} \frac{d\alpha}{ds}(\sigma) e^{-b_1(s-\sigma)} d\sigma, \tag{8.79}$$

$$Y(s) = A_2 \int_{s_0}^{s} \frac{d\alpha}{ds}(\sigma) e^{-b_2(s-\sigma)} d\sigma. \tag{8.80}$$

Assuming a continuously sampled system with time step Δs (which may be nonuniform) and that $s_0 = 0$, then we have at the next time step $s + \Delta s$

$$X(s + \Delta s) = A_1 \int_{0}^{s+\Delta s} \frac{d\alpha}{ds}(\sigma) e^{-b_1(s+\Delta s-\sigma)} d\sigma. \tag{8.81}$$

Splitting the integral into two parts gives

$$X(s + \Delta s) = A_1 e^{-b_1 \Delta s} \int_{0}^{s} \frac{d\alpha}{ds}(\sigma) e^{-b_1(s-\sigma)} d\sigma + A_1 \int_{s}^{s+\Delta s} \frac{d\alpha}{ds}(\sigma) e^{-b_1(s+\Delta s-\sigma)} d\sigma \tag{8.82}$$

$$= X(s) e^{-b_1 \Delta s} + A_1 \int_{s}^{s+\Delta s} \frac{d\alpha}{ds}(\sigma) e^{-b_1(s+\Delta s-\sigma)} d\sigma$$

$$= X(s) e^{-b_1 \Delta s} + I. \tag{8.83}$$

Notice that this new value, $X(s+\Delta s)$, is a one-step recursive formula in terms of the previous value, $X(s)$, and a new increment, I, over the new period. Consider now the evaluation of the I term:

$$I = A_1 \int_{s}^{s+\Delta s} \frac{d\alpha}{ds}(\sigma) e^{-b_1(s+\Delta s-\sigma)} d\sigma = A_1 e^{-b_1(s+\Delta s)} \int_{s}^{s+\Delta s} \frac{d\alpha}{ds}(\sigma) e^{b_1 \sigma} d\sigma$$

$$= A_1 e^{-b_1(s+\Delta s)} \int_{s}^{s+\Delta s} \frac{d\alpha}{ds}(\sigma) f(\sigma) d\sigma \tag{8.84}$$

with $f(\sigma) = e^{b_1 \sigma}$. At this point, several simplifying assumptions can be made. Introducing a simple backward-difference approximation for $d\alpha/ds$ at time $s + \Delta s$ gives

$$\left.\frac{d\alpha}{ds}\right|_{s+\Delta s} = \frac{\alpha(s + \Delta s) - \alpha(s)}{\Delta s} = \frac{\Delta \alpha_{s+\Delta s}}{\Delta s}, \tag{8.85}$$

which has an error of order $\alpha''(s + \Delta s)\Delta s$. Alternatively, we could use

$$\left.\frac{d\alpha}{ds}\right|_{s+\Delta s} = \frac{3\alpha(s + \Delta s) - 4\alpha(s) + \alpha(s - \Delta s)}{2\Delta s}, \tag{8.86}$$

which has an error of order $\alpha'''(s + \Delta s)(\Delta s)^2$, although this scheme requires the storage of α at two previous time steps. The remaining part of the integral involving $f(\sigma)$ can be evaluated exactly and I becomes

$$I = A_1 \left(\frac{\Delta \alpha_{s+\Delta s}}{\Delta s} \right) \left(\frac{1 - e^{-b_1 \Delta s}}{b_1} \right) \tag{8.87}$$

when using Eq. 8.85. Now, if $b_1 \Delta s$ is small so that $b_1^2(\Delta s)^2$ and higher powers can be neglected, then

$$\frac{1 - e^{-b_1 \Delta s}}{b_1} \approx \Delta s. \tag{8.88}$$

Therefore, we obtain the relatively simple result that

$$I = A_1 \left(\frac{\Delta \alpha_{s+\Delta s}}{\Delta s} \right) \Delta s = A_1 \Delta \alpha_{s+\Delta s}. \tag{8.89}$$

It will be seen that this latter result is equivalent to setting $f(\sigma) = \text{constant} = e^{b_1(s+\Delta s)}$ over the sample period (i.e., using the rectangle rule of integration) and has a local error of order $(\Delta s)^2$. When Eq. 8.89 is introduced into Eq. 8.83, this gives the recurrence formula

$$X(s + \Delta s) = X(s) e^{-b_1 \Delta s} + A_1 \Delta \alpha_{s+\Delta s} \tag{8.90}$$

or

$$X(s) = X(s - \Delta s) e^{-b_1 \Delta s} + A_1 \Delta \alpha_s. \tag{8.91}$$

Proceeding in a similar fashion for the Y term in Eq. 8.80 gives

$$\alpha_e(s) = \alpha(0) + \int_0^s d\alpha(s) - X(s) - Y(s) = \alpha(s) - X(s) - Y(s), \tag{8.92}$$

where the $X(s)$ and $Y(s)$ terms are given by the one-step recursive formulas that will be denoted by Algorithm D-1:

$$X(s) = X(s - \Delta s) e^{-b_1 \Delta s} + A_1 \Delta \alpha_s, \tag{8.93}$$

$$Y(s) = Y(s - \Delta s) e^{-b_2 \Delta s} + A_2 \Delta \alpha_s. \tag{8.94}$$

Notice that recursive functions X and Y contain all the time history information of the unsteady aerodynamics and are simply updated once at each time step, thereby providing numerically efficient solutions to the unsteady lift for arbitrary variations in α. Obviously, the above results can be extended to other modes of forcing and to any number of exponential terms that may be used to represent the indicial function. The error in this algorithm results mostly from the approximation used in Eq. 8.88, and it can be shown that the relative error in the integral is

$$\epsilon = 2 - \frac{b_1 \Delta s}{1 - e^{-b_1 \Delta s}} - \frac{b_2 \Delta s}{1 - e^{-b_2 \Delta s}}. \tag{8.95}$$

Generally, to obtain errors of less than 5%, each of the products $b_1 \Delta s$ and $b_2 \Delta s$ must be less than 0.05. This requires a relatively small time step and may not always be practical in many helicopter rotor problems.

The main reason for adopting an algorithm of this latter form is that there is a significant computational overhead associated with the repetitive numerical evaluation of the formula for I containing the exponential function in Eq. 8.87 versus using the simpler result that $I = A_1 \Delta \alpha_{t+\Delta t}$; the relative computational cost is a savings of about one order of magnitude (see Fig. 8.27) over using the exact solution. Bearing in mind these algorithms are intended for use in various helicopter rotor analyses where the recurrence formulas may be evaluated tens or hundreds of thousands of times, an order of magnitude extra overhead just to get an exact solution is certainly significant. However, this is at the expense of notable errors

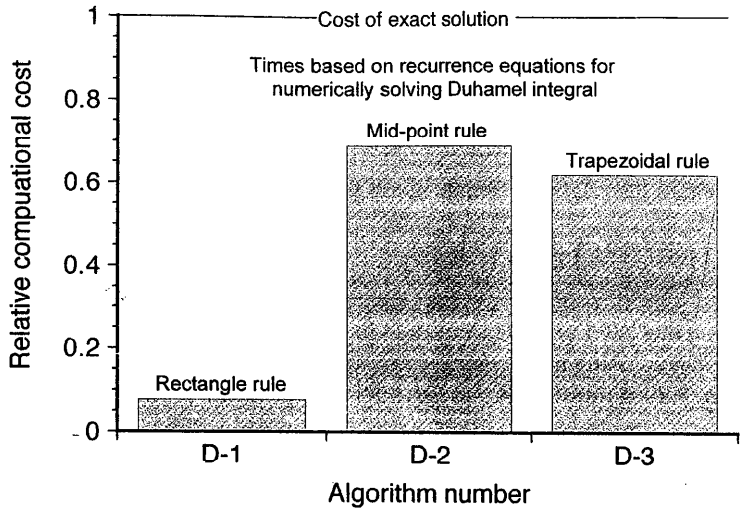

Figure 8.27 Relative computational cost of the numerical solution of Duhamel integral using different numerical methods. Cost is evaluated relative to exact solution.

for practical values of the sampling time step, and the motivation for developing alternative algorithms that are still numerically efficient but have lower numerical errors becomes clear.

If Δs (or the products $b_1\Delta s$ or $b_2\Delta s$) is large, another approximation based on the midpoint rule can be used. In this case let $f(\sigma) \approx f(s + \Delta s/2)$, and thus

$$\begin{aligned} I &= A_1 e^{-b_1(s+\Delta s)} \left(\frac{\Delta\alpha_{s+\Delta s}}{\Delta s}\right) \int_s^{s+\Delta s} f(\sigma)d\sigma \\ &= A_1 e^{-b_1(s+\Delta s)} \left(\frac{\Delta\alpha_{s+\Delta s}}{\Delta s}\right) e^{b_1(s+\Delta s/2)}\Delta s \\ &= A_1 \Delta\alpha_{s+\Delta s}\, e^{-b_1\Delta s/2}. \end{aligned} \tag{8.96}$$

This gives a method that will be denoted as Algorithm D-2:

$$X(s) = X(s - \Delta s)e^{-b_1\Delta s} + A_1\Delta\alpha_s\, e^{-b_1\Delta s/2}, \tag{8.97}$$

$$Y(s) = Y(s - \Delta s)e^{-b_2\Delta s} + A_2\Delta\alpha_s\, e^{-b_2\Delta s/2}. \tag{8.98}$$

This recurrence algorithm was first used by Beddoes (1984). This method has a local error of order $(\Delta s)^3$, and the relative error in the integral can be shown to be

$$\epsilon = 2 - \frac{b_1\Delta s\, e^{-b_1\Delta s/2}}{1 - e^{-b_1\Delta s}} - \frac{b_2\Delta s\, e^{-b_2\Delta s/2}}{1 - e^{-b_2\Delta s}}. \tag{8.99}$$

In this case, Eq. 8.99 suggests that errors of less than 1% from an exact solution will be obtained if both $b_1\Delta s$ and $b_2\Delta s$ are less than 0.25, which is a much more practically realizable option in a helicopter rotor analysis, despite a notable increase in computational cost. It is, however, still less expensive than the exact solution. See Question 8.8 for a solution to this numerical problem using the trapezoidal rule (Algorithm D-3).

8.14.2 *State-Space Solution for Arbitrary Motion*

For some applications, it is more convenient if the unsteady aerodynamic model is written in the form of differential equations (i.e., in state-space or state-variable form). The differential equations describing the unsteady aerodynamics can then be directly appended to the structural dynamic equations governing the airfoil or blade motion. One advantage of this approach is that the stability of an aeroelastic problem for a wing section or rotor blade can then be obtained by formulating it as an eigenvalue problem or using a Floquet stability analysis [see Johnson (1980)]. Alternatively, the problems can be studied by time integration of the governing equations using standard numerical algorithms.

One of the most fundamental concepts associated with the description of any dynamic system, aerodynamic or otherwise, is the *state* of the system. The state describes the internal behavior of that system and is simply the information required at a given instant in time to allow the determination of the outputs from the system given future inputs. In other words, the state of the system determines its present condition; it is represented by a set of appropriately chosen variables describing the internal mechanics of the system. These variables are called the state variables and define an n-dimensional vector space $\mathbf{x}$ called the state-space in which one coordinate is defined by each of the state variables $x_1, x_2, ..., x_n$. A general nth order differential system with m inputs and p outputs may be represented by n first-order differential equations

$$\dot{\mathbf{x}} = \mathbf{A}\mathbf{x} + \mathbf{B}\mathbf{u} \tag{8.100}$$

with the output equations

$$\mathbf{y} = \mathbf{C}\mathbf{x} + \mathbf{D}\mathbf{u}, \tag{8.101}$$

where $\dot{x} = dx/dt$; $\mathbf{u} = u_i$, $i = 1, 2, ..., m$ are the system inputs, and the $\mathbf{y} = y_i$, $i = 1, 2, ..., p$ are the system outputs. $\mathbf{x} = x_i$, $i = 1, 2, ..., n$ are the states of the system. See Franklin et al. (1994) for more information about this approach.

The state equations describing the behavior of a 2-D unsteady airfoil can be obtained through direct application of Laplace transform methods to the indicial response. Consider the indicial lift response, ϕ, which is to be approximated by the exponential function given previously by Eq. 8.76. This function can be written in the time domain as

$$\phi(t) = 1.0 - A_1 e^{-b_1\left(\frac{2V}{c}\right)t} - A_2 e^{-b_2\left(\frac{2V}{c}\right)t}. \tag{8.102}$$

Initially, let $\phi(0) = 0 = 1 - A_1 - A_2$. Then the corresponding impulse response, $h(t)$, is given by

$$h(t) = A_1 b_1 \left(\frac{2V}{c}\right) e^{-b_1\left(\frac{2V}{c}\right)t} + A_2 b_2 \left(\frac{2V}{c}\right) e^{-b_2\left(\frac{2V}{c}\right)t}. \tag{8.103}$$

The Laplace transform of the impulse response is

$$\mathcal{L}[h(t)] = \frac{A_1 b_1 \left(\frac{2V}{c}\right)}{p + b_1\left(\frac{2V}{c}\right)} + \frac{A_2 b_2 \left(\frac{2V}{c}\right)}{p + b_2\left(\frac{2V}{c}\right)}, \tag{8.104}$$

which can be rearranged to yield the transfer functions as the Padé approximant

$$\mathcal{L}[h(t)] = \frac{(A_1 b_1 + A_2 b_2)\left(\frac{2V}{c}\right) p + (A_1 + A_2)(b_1 b_2)\left(\frac{2V}{c}\right)^2}{p^2 + (b_1 + b_2)\left(\frac{2V}{c}\right) p + (b_1 b_2)\left(\frac{2V}{c}\right)^2}. \tag{8.105}$$

From this transfer function, the lift response to an input $\alpha(t)$ can be directly written in state-space form as

$$\begin{Bmatrix} \dot{x}_1 \\ \dot{x}_2 \end{Bmatrix} = \left(\frac{2V}{c}\right) \begin{bmatrix} -b_1 & 0 \\ 0 & -b_2 \end{bmatrix} \begin{Bmatrix} x_1 \\ x_2 \end{Bmatrix} + \begin{Bmatrix} 1 \\ 1 \end{Bmatrix} \alpha(t), \tag{8.106}$$

and the output equation for the lift coefficient is

$$C_l(t) = C_{l_\alpha} \left(\frac{2V}{c}\right) \begin{bmatrix} A_1 b_1 & A_2 b_2 \end{bmatrix} \begin{Bmatrix} x_1 \\ x_2 \end{Bmatrix}, \tag{8.107}$$

with C_{l_α} being recognized as the lift-curve-slope of the airfoil. These equations are in the form of Eqs. 8.100 and 8.101, where in this case the matrix **D** is equal to zero. An alternative realization of the system is the form

$$\begin{Bmatrix} \dot{x}_1 \\ \dot{x}_2 \end{Bmatrix} = \begin{bmatrix} 0 & 1 \\ -b_1 b_2 \left(\frac{2V}{c}\right)^2 & -(b_1 + b_2)\left(\frac{2V}{c}\right) \end{bmatrix} \begin{Bmatrix} x_1 \\ x_2 \end{Bmatrix} + \begin{Bmatrix} 0 \\ 1 \end{Bmatrix} \alpha(t), \tag{8.108}$$

and the corresponding equation for the lift coefficient is

$$C_l(t) = C_{l_\alpha} \begin{bmatrix} b_1 b_2 \left(\frac{2V}{c}\right)^2 & (A_1 b_1 + A_2 b_2)\left(\frac{2V}{c}\right) \end{bmatrix} \begin{Bmatrix} x_1 \\ x_2 \end{Bmatrix}. \tag{8.109}$$

For a nonzero initial condition, such as when using the Wagner function approximation, the form of these equations is only slightly different. In this case

$$\begin{Bmatrix} \dot{x}_1 \\ \dot{x}_2 \end{Bmatrix} = \begin{bmatrix} 0 & 1 \\ -b_1 b_2 \left(\frac{2V}{c}\right)^2 & -(b_1 + b_2)\left(\frac{2V}{c}\right) \end{bmatrix} \begin{Bmatrix} x_1 \\ x_2 \end{Bmatrix} + \begin{Bmatrix} 0 \\ 1 \end{Bmatrix} \alpha(t), \tag{8.110}$$

and the equation for the lift coefficient is

$$\begin{aligned} C_l(t) = C_{l_\alpha} &\begin{bmatrix} (A_1 + A_2) b_1 b_2 \left(\frac{2V}{c}\right)^2 & (A_1 b_1 + A_2 b_2)\left(\frac{2V}{c}\right) \end{bmatrix} \begin{Bmatrix} x_1 \\ x_2 \end{Bmatrix} \\ &+ C_{l_\alpha}(1 - A_1 - A_2)\, \alpha(t). \end{aligned} \tag{8.111}$$

For example, if R. T. Jones's approximation to the Wagner function is used (Eq. 8.51), then after substituting the numerical values of the coefficients we get

$$\begin{Bmatrix} \dot{x}_1 \\ \dot{x}_2 \end{Bmatrix} = \begin{bmatrix} 0 & 1 \\ -0.01375 \left(\frac{2V}{c}\right)^2 & -0.3455 \left(\frac{2V}{c}\right) \end{bmatrix} \begin{Bmatrix} x_1 \\ x_2 \end{Bmatrix} + \begin{Bmatrix} 0 \\ 1 \end{Bmatrix} \alpha(t), \tag{8.112}$$

with

$$C_l(t) = 2\pi \begin{bmatrix} 0.006825 \left(\frac{2V}{c}\right)^2 & 0.10805 \left(\frac{2V}{c}\right) \end{bmatrix} \begin{Bmatrix} x_1 \\ x_2 \end{Bmatrix} + \frac{\pi}{2} \alpha(t), \tag{8.113}$$

where $C_{l_\alpha} = 2\pi$. The extra term $\pi\alpha/2$ on the right-hand side of the above equation arises because of the non-zero initial conditions for the Wagner function, that is, $\phi(0) = 1 - A_1 - A_2 = 1/2$. Conversely, if we apply a unit step input to the above state-space equations and set the initial states to be zero [i.e., $\alpha(t) = 1$ for $t \geq 0$ and $x_1(0) = x_2(0) = 0$], the resulting response is exactly Jones's approximation to the Wagner function (see Question 8.11). In fact, it is clear that the Theodorsen solution, the Wagner solution with Duhamel superposition, and the above state-space model are simply different mathematical realizations of the same aerodynamic system. Friedmann (1985), Dinyavari & Friedmann (1986), and Leishman & Nguyen (1990) describe state-space unsteady aerodynamic models of 2-D airfoil sections using Jones's approximation to the Wagner function for the incompressible flow case. Friedmann (1985) describes a more general, but still approximate, state-space

realization of Loewy's function (Section 8.8). This is done by representing Loewy's exact lift transfer function as a higher-order Padé approximation – see also Vepa (1976).

8.15 Indicial Method for Subsonic Compressible Flow

All rotor aerodynamic problems involve compressibility to some degree. However, for subsonic compressible flow there is no analytic equivalent to Theodorsen's theory, nor to the Wagner or Küssner functions. This is because of the nature of the governing equation, which for the subsonic case is the hyperbolic wave equation versus the elliptic Laplace's equation for incompressible flow [see Karamacheti (1966) and Chapter 14]. Therefore, alternative numerical means of finding the indicial responses must be derived. Because a time domain representation of the unsteady aerodynamics is sought, it is convenient to address the subsonic problem starting from the indicial response. Although this is by no means the only basis from which the problem can be tackled, it has already been shown that the indicial approach gives considerable physical insight into the problem of unsteady aerodynamics.

For a compressible flow, the initial loading on the airfoil after an indicial (step) input comprises a pressure wave system with a compression wave on one surface of the airfoil and an expansion wave on the other. This initial pressure loading on the surface can be computed directly using linear piston theory, which is a local wave equation solution for the unsteady airloads [see Lomax (1968)]. The piston theory gives a result valid for any Mach number, M, but only at the instant after the perturbation has been applied (i.e., at $t = 0$ or $s = 0$). If we consider a small element of an airfoil subject to a downward plunging type motion that produces a change in normal velocity Δw as shown in Fig. 8.28, then piston theory gives the difference in pressure across the surface as $\Delta p = 2\rho a \Delta w$, so that

$$\Delta C_p(x, t = 0) = \frac{2\rho a \Delta w(x)}{\frac{1}{2}\rho V^2} = \left(\frac{4}{M}\right)\frac{\Delta w(x)}{V}. \tag{8.114}$$

Consider now a thin-airfoil undergoing a simultaneous plunging and pitching about the 1/4-chord. Figure 8.5 has shown that the normal velocity on the airfoil is composed of two primary modes: a uniform perturbation in w from the pure AoA contribution plus another uniform perturbation resulting from plunge velocity, $\dot{h}/V$, and another perturbation mode

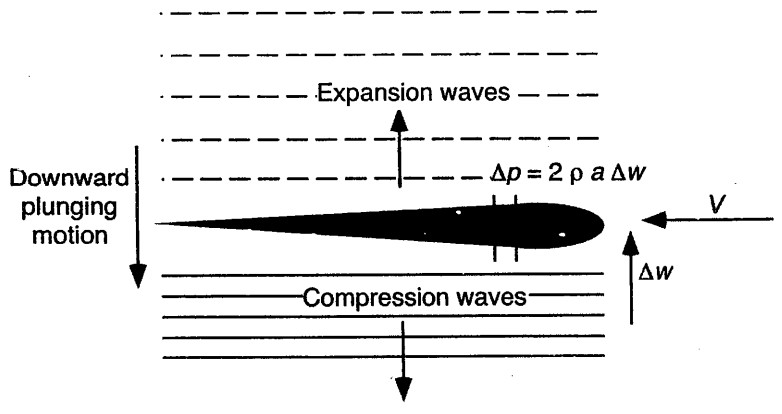

Figure 8.28 In the initial stages on indicial motion the airloads can be calculated using one-dimensional piston theory. Adapted from Lomax (1968).

from the pure pitch rate of the airfoil q $(= \dot{\alpha}c/V)$. By convention it will be assumed that the pitching motion takes place about the 1/4-chord, although the result can be generalized to any pitch axis. For a step change in each mode, applying piston theory and integrating across the chord gives the normal force coefficients[8] at $t = 0$ as

$$\Delta C_{n_\alpha}(0) = \frac{4}{M}\Delta\alpha \quad \text{and} \quad \Delta C_{n_q}(0) = \frac{1}{M}\Delta q \tag{8.115}$$

and the initial moment coefficients about the 1/4-chord as

$$\Delta C_{m_\alpha}(0) = -\frac{1}{M}\Delta\alpha \quad \text{and} \quad \Delta C_{m_q}(0) = -\frac{7}{12M}\Delta q. \tag{8.116}$$

For subsequent time, pressure waves from the airfoil propagate at the local speed of sound and, in the absence of any other forcing, the loading will decay rapidly with time from these initial "noncirculatory" values. For a compressible flow the noncirculatory terms do not appear as an infinite pulse at $s = 0$ as for incompressible flow, but are finite in magnitude and decay more slowly from their initial values. Therefore, it will be appreciated that noncirculatory terms can no longer be assumed proportional to the *instantaneous* blade motion (i.e., to α, $\dot{\alpha}$, $\dot{h}$) as they are for the incompressible case and, like the circulatory terms, they must also depend on the time history of the forcing. Physically this is because for an incompressible flow the pressure waves are propagated at infinite velocity, whereas for a real flow the disturbances propagate at the speed of sound.

Such a transient behavior is difficult to compute in subsonic flow, but some analytic solutions can be obtained for limited values of time after the step input has been applied. Using an analogy of unsteady 2-D subsonic flow with steady supersonic flow, solutions to the wave equation have been evaluated exactly by Lomax et al. (1952) to obtain the chordwise pressure loading on the airfoil in the short period in the range between $0 \le s \le 2M/(M+1)$. For a unit step change in AoA then

$$\frac{\Delta C_p^\alpha(x,\hat{t})}{\alpha} = \Re\left\{\frac{8}{\pi(1+M)}\sqrt{\frac{\hat{t}-x'}{M\hat{t}+x'}} + \frac{4}{\pi M}\left[\cos^{-1}\left(\frac{\hat{t}(1+M)-2(c-x')}{\hat{t}(1-M)}\right)\right.\right.$$
$$\left.\left. - \cos^{-1}\left(\frac{2x'-\hat{t}(1-M)}{\hat{t}(1+M)}\right)\right]\right\}, \tag{8.117}$$

where the domain is $x' = x - M\hat{t}$. This equation is valid for the early period $0 \le \hat{t} \le c/(1+M)$. The symbol $\Re$ refers to the real part where the real parts of the arc cosine of numbers greater than 1 and less than 1 are 0 and π, respectively. Results are shown in Fig. 8.29 for $M = 0.5$. Notice the nature of the chordwise pressure loading as the upstream and downstream moving waves pass over the chord of the airfoil. Even after a very short time, the growth in circulation has been established, but the final value steady state circulation is only obtained after a relatively long time. Stahara & Spreiter (1976) and Singh & Baeder (1997a) show numerical solutions to the same problem using CFD methods.

By integrating the exact chordwise pressure loading solution in Eq. 8.117, the lift (normal force) and pitching moment during the short period $0 \le s \le 2M/(1+M)$ can be determined analytically. The lift coefficient resulting from a step change in AoA is

$$\frac{C_{n_\alpha}(s)}{\alpha} = \frac{4}{M}\left[1 - \frac{1-M}{2M}s\right] \tag{8.118}$$

[8] Notice that in the thin-airfoil solution and also because low angles of attack are assumed, the normal force and lift force are usually used synonymously.

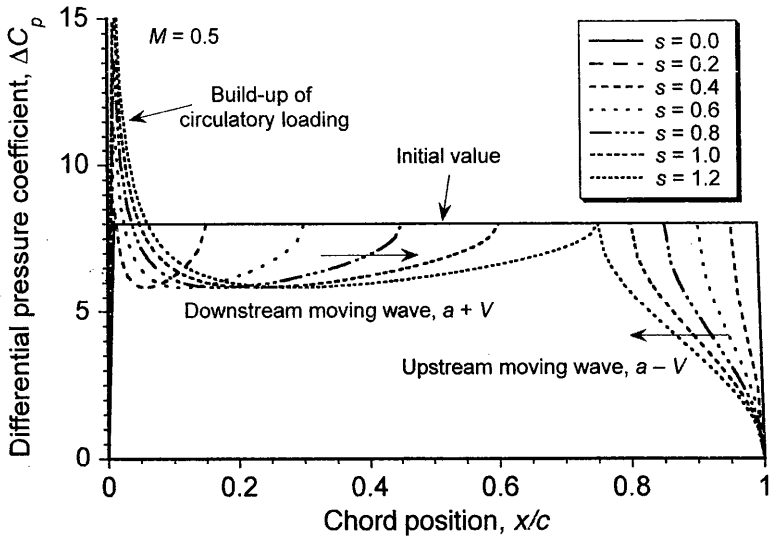

Figure 8.29 Initial stages of transient chordwise loading after a step change in AoA in subsonic flow at $M = 0.5$, showing the decay of the noncirculatory pressure loading and buildup of circulatory loading.

and the pitching moment coefficient about the 1/4-chord from a step in AoA is

$$\frac{C_{m_\alpha}(s)}{\alpha} = -\frac{1}{M}\left[1 - \frac{1-M}{2M}s + \frac{M-2}{4M}s^2\right]. \tag{8.119}$$

Similarly, by using the corresponding chordwise loading for pitch rate, it is found that

$$\frac{C_{n_q}(s)}{q} = \frac{1}{M}\left[1 - \frac{1-M}{2M}s + \left(1 - \frac{M}{2}\right)\frac{s^2}{2M}\right] \tag{8.120}$$

and

$$\frac{C_{m_q}(s)}{q} = \frac{1}{M}\left[-\frac{7}{12} + \frac{5(1-M)}{8M}s - \frac{1-M^2}{8M^2}s^2 + \frac{(1-M)^3 + 4M}{64M^2}s^3\right]. \tag{8.121}$$

8.15.1 *Approximations to the Indicial Response*

The exact results given in Eqs. 8.118–8.121 are only valid for short values of time but they are useful because they provide guidance in developing approximations for the indicial functions for all values of time that are also in a more convenient analytic form to derive recurrence solutions to the Duhamel integral or for state-space realizations (see previously). In the general case, the indicial normal force and 1/4-chord pitching moment response to a step change in angle of attack, α, and a step change in nondimensional pitch

rate about the 1/4-chord, q $(= \dot{\alpha}c/V)$, can be represented by the equations

$$\frac{C_{n_\alpha}(s)}{\alpha} = \frac{4}{M}\phi_\alpha^{nc}(s, M) + \frac{2\pi}{\beta}\phi_\alpha^{c}(s, M), \tag{8.122}$$

$$\frac{C_{m_\alpha}(s)}{\alpha} = -\frac{1}{M}\phi_{\alpha_m}^{nc}(s, M) + \frac{2\pi}{\beta}\phi_\alpha^{c}(s, M)(0.25 - x_{ac}), \tag{8.123}$$

$$\frac{C_{n_q}(s)}{q} = \frac{1}{M}\phi_q^{nc}(s, M) + \frac{\pi}{\beta}\phi_q^{c}(s, M), \tag{8.124}$$

$$\frac{C_{m_q}(s)}{q} = -\frac{7}{12M}\phi_{q_m}^{nc}(s, M) - \frac{\pi}{8\beta}\phi_{q_m}^{c}(s, M), \tag{8.125}$$

where ϕ^{nc} refers to the assumed noncirculatory part of the indicial response and ϕ^c refers to the assumed circulatory part. While it must be remembered that in the subsonic case this decomposition of the total loading is only an idealization, it is convenient for engineering purposes to handle the problem this way. The β term is the Glauert compressibility factor for linearized subsonic flow (i.e., $\beta = \sqrt{1 - M^2}$). In the preceding equations, the initial values of the indicial response functions are given directly by linear piston theory as

$$\frac{C_{n_\alpha}(s=0)}{\alpha} = \frac{4}{M} \quad \text{and} \quad \frac{C_{m_\alpha}(s=0)}{\alpha} = -\frac{1}{M}, \tag{8.126}$$

$$\frac{C_{n_q}(s=0)}{q} = \frac{1}{M} \quad \text{and} \quad \frac{C_{m_q}(s=0)}{q} = -\frac{7}{12M}. \tag{8.127}$$

The final values are given by the steady linearized subsonic theory as

$$\frac{C_{n_\alpha}(s=\infty)}{\alpha} = \frac{2\pi}{\beta} \quad \text{and} \quad \frac{C_{m_\alpha}(s=\infty)}{\alpha} = \frac{2\pi}{\beta}(0.25 - x_{ac}), \tag{8.128}$$

$$\frac{C_{n_q}(s=\infty)}{q} = \frac{\pi}{\beta} \quad \text{and} \quad \frac{C_{m_q}(s=\infty)}{q} = -\frac{\pi}{8\beta}. \tag{8.129}$$

It should be noted that in practical applications the linearized value of the lift-curve-slope, $2\pi/\beta$, can be replaced by the measured value for a given airfoil at the appropriate Reynolds number and Mach number,[9] which is generally denoted by $C_{n_\alpha}(M)$. Additionally, the second term in Eq. 8.123 represents the contribution to the pitching moment resulting from a Mach number dependent offset of the aerodynamic center from the 1/4-chord axis of the airfoil, an effect previously described for the incompressible flow case. As shown in Section 7.7.1, the values of the aerodynamic center, x_{ac}, for a given airfoil can be obtained from static airfoil measurements at the appropriate Mach number. Also notice that the second term of Eq. 8.125 represents the induced camber pitching moment resulting from the pitch rate motion, as given by the quasi-steady thin-airfoil result, as also previously described. Therefore, it will be appreciated that the various indicial response functions, denoted by ϕ, represent the time-dependent behavior of the lift and pitching moment between the initial "piston theory" values at $s = 0$ and the normal quasi-steady values at $s = \infty$.

[9] The effects of the Reynolds number are generally implied, and the functional dependency will be omitted for brevity.

8.15.2 *Indicial Lift from Angle of Attack*

The lift or normal force response to a unit step change in angle of attack, α, can be idealized as the sum of a decaying noncirculatory part, $C_{n_\alpha}^{nc}$, and a growing circulatory part, $C_{n_\alpha}^{c}$, that is

$$C_{n_\alpha}(s) = C_{n_\alpha}^{nc}(s, M) + C_{n_\alpha}^{c}(s, M) \tag{8.130}$$

or in terms of the indicial functions

$$C_{n_\alpha}(s) = \frac{4}{M}\phi_\alpha^{nc}(s, M) + \frac{2\pi}{\beta}\phi_\alpha^{c}(s, M). \tag{8.131}$$

Using reciprocal relations, the noncirculatory component of the loading on the airfoil can be theoretically extracted from the total lift response. This was first done by Mazelsky (1952a). The result can be closely approximated as an exponentially decaying function, and so the noncirculatory part of lift for a unit step change in α may be written as

$$C_{n_\alpha}^{nc}(s, M) = \frac{4}{M}\phi_\alpha^{nc}(s, M) = \frac{4}{M}\exp\left(\frac{-s}{T'_\alpha}\right), \tag{8.132}$$

where $T'_\alpha = T'_\alpha(M) > 0$ is a Mach number dependent time-constant still to be defined. For the growing (circulatory) part of the total indicial response, Mazelsky (1952a,b) appears to have been one of the first investigators to use an exponential approximation of the form

$$\phi^c(s, M) = 1 - \sum_{n=1}^{N} A_n e^{-b_n s}; \quad \sum_{n=1}^{N} A_n = 1, b_n > 0 \tag{8.133}$$

for compressible flow, where the coefficients A_n and b_n will vary as a function of Mach number. These coefficients were obtained indirectly by Mazelsky by relating back into the time domain from numerical results (transfer functions) obtained for oscillating airfoils in the frequency domain. A similar approach has also been suggested by Dowell (1980) to obtain approximations to the indicial response for incompressible flow using Theodorsen's exact result and for compressible flows by using transfer functions numerically computed using CFD solutions to the unsteady flow problem. In general, indicial type CFD calculations are rare in the published literature, but direct indicial and vertical sharp-edged gust solutions have been performed by McCroskey & Goorjian (1983) using CFD methods. A series of more elaborate direct indicial calculations have been performed by Parameswaran & Baeder (1997) who have computed indicial angle of attack, pitch rate and sharp-edged gust results using an Euler/Navier–Stokes CFD method. These solutions provide good check cases for unsteady airfoil problems that cannot be simulated by experimentation nor amenable to exact analytical treatment. However, these CFD solutions are only available at a relatively high computational cost, and even then they are still subject to certain approximations and limitations.

While Mazelsky's exponential approximation in Eq. 8.133 may be acceptable for applications in fixed-wing analyses, it is not entirely convenient for a helicopter rotor analysis. This is because each blade station encounters a different local Mach number as a function of both blade radial location and azimuth angle. Therefore, repeated interpolation of the A_n and b_n coefficients will be required between successive Mach numbers to find the locally effective indicial function. Although relatively simple in concept, there is relatively large computational overhead associated with this process. In addition, it must be recognized that when superposition is applied to find the unsteady lift, each exponential term in the series in Eq. 8.186 contributes an additional state or deficiency function. To this end, Beddoes

(1984) and Leishman (1987a, 1993) have assumed that the circulatory lift can be expressed in terms of a two term growing exponential function, but one that scales directly with Mach number alone. The lift function $\phi_\alpha^c(s, M)$ takes the general form

$$\phi_\alpha^c(s, M) = 1 - A_1 e^{-b_1 \beta^2 s} - A_2 e^{-b_2 \beta^2 s}; \quad A_1 + A_2 = 1, \quad b_1, b_2 > 0, \quad (8.134)$$

where $\beta = \sqrt{1 - M^2}$, and the A and b coefficients are fixed and independent of Mach number.[10] The use of the β^2 term in the indicial function reflects the effects of compressibility (Mach number) on the growth of the circulatory part of the lift (through the effects of the shed wake). This manifests as larger lags in the growth of lift at higher Mach numbers. Such a behavior is well known from a theoretical standpoint [see Osborne (1973)] as well as from experimental observations with oscillating airfoils. Furthermore, in a practical sense, not only is this simple compressibility scaling approach a computationally efficient way of accounting for compressibility effects in the wake, but it is also more accurate than repeated linear interpolation of the coefficients between discrete Mach numbers.

The coefficients A_1, A_2, b_1, and b_2 must be assumed as initially unknown, and although they could be derived in a number of ways, they can be reliably determined by relating back from frequency domain results using experimental measurements for oscillating airfoils in subsonic flow. Such measurements are widely available; see, for example, Liiva et al. (1968), Wood (1979), and Davis & Malcolm (1980). It is possible to reduce the number of coefficients implicit in the indicial representation in Eq. 8.131 from five to four by obtaining an expression for the noncirculatory time constant, T'_α in terms of the coefficients A_1, A_2, b_1, and b_2. Differentiating the approximation in Eq. 8.131 (using Eqs. 8.132 and 8.134) and the exact result in Eq. 8.118, and equating the gradients at $s = 0$ gives the time constant in the s domain as

$$T'_\alpha(M) = \frac{4M}{2(1 - M) + 2\pi\beta M^2(A_1 b_1 + A_2 b_2)}. \quad (8.135)$$

Using the results $T_\alpha = (c/2V)T'_\alpha$ and $M = V/a$ gives the time constant in the t domain as

$$T_\alpha = \left[(1 - M) + \pi\beta M^2(A_1 b_1 + A_2 b_2) \right]^{-1} \frac{c}{a} = \kappa_\alpha T_i, \quad (8.136)$$

where $T_i = c/a$. The advantage of taking this approach is that, regardless of the values of the coefficients A_1, A_2, b_1, and b_2, the noncirculatory constant, T_α, will always be adjusted give the correct initial value and slope of the total indicial response as given by exact linear theory in Eq. 8.118. The continuity between the initial impulsive and succeeding circulatory loading is then obtained using linear superposition, as given by Eq. 8.131.

8.15.3 *Indicial Lift from Pitch Rate*

The indicial lift response to a step change in pitch rate q about the 1/4-chord can also be written as the sum of a noncirculatory part, $C_{n_q}^{nc}$ and a circulatory part, $C_{n_q}^c$, that is

$$C_{n_q}(s) = C_{n_q}^{nc}(s, M) + C_{n_q}^c(s, M) \quad (8.137)$$

[10] This equation can be shown valid up to at least the critical Mach number of the airfoil, beyond which nonlinear effects do not allow such simple generalizations because of the development of transonic flow.

or in terms of the indicial functions

$$\frac{C_{n_q}(s)}{q} = \frac{1}{M}\phi_q^{nc}(s, M) + \frac{\pi}{\beta}\phi_q^c(s, M). \tag{8.138}$$

Numerous references have shown that, for incompressible flow, the chordwise pressure variation on the airfoil is the same as the thin-airfoil loading but is independent of the mode of motion. Therefore, an angular velocity about some point can be considered equivalent to an angular velocity about some other point plus an angle of attack. In particular, the indicial lift for a pitch rate about the 3/4-chord position in incompressible flow is an impulse at $s = 0$ and is exactly zero thereafter. Subsequently, it follows that for incompressible flow $\phi_\alpha^c = \phi_q^c$. In linearized subsonic flow, the circulatory lift lag still remains an intrinsic function of the fluid itself. The chordwise pressure variation remains the same as the steady thin-airfoil loading and is unaffected by the mode of forcing or pitch axis location. Therefore, on a thin airfoil in subsonic flow, the lift always acts at the 1/4-chord point. In view of the foregoing, it is valid to assume $\phi_\alpha^c(s, M) = \phi_q^c(s, M)$ for subsonic compressible flow as well as incompressible flow without any loss of rigor. The circulatory part of the lift from pitch rate about the 1/4-chord, therefore, can be written as

$$\frac{C_{n_q}^c(s)}{q} = \frac{\pi}{\beta}\left(1 - A_1 e^{-b_1\beta^2 s} - A_2 e^{-b_2\beta^2 s}\right) \tag{8.139}$$

The noncirculatory function can be assumed to be of the form

$$C_{n_q}^{nc}(s) = \frac{1}{M}\phi_q^{nc}(s) = \frac{1}{M}\exp\left(\frac{-s}{T_q'}\right). \tag{8.140}$$

Using Eqs. 8.139 and 8.140 and following the same procedure as before where the slopes of the approximating indicial function and the exact result (in this case, Eq. 8.120) are matched at $s = 0$ gives the time constant as

$$T_q = \left(\frac{c}{2V}\right)T_q' = \left[(1 - M) + 2\pi\beta M^2(A_1 b_1 + A_2 b_2)\right]^{-1}\frac{c}{a} = \kappa_q T_i. \tag{8.141}$$

8.15.4 *Determination of Indicial Function Coefficients*

The coefficients A_1, A_2, b_1, and b_2 are used to define the intermediate behavior of the indicial lift approximations. Using experimental results for the total lift and pitching moment response resulting from a prescribed harmonic forcing, such as oscillations in pitch or plunge, we can relate these data back to empirically determine the coefficients of the indicial functions. Experimental data are available from a number of sources. For the most part, they comprise measurements of the unsteady aerodynamic lift and pitching moment as a function of reduced frequency from pitch and plunge oscillations performed under nominally attached flow conditions; that is, in the region where linearized aerodynamics are appropriate. It is essential that the data selected be for attached flow conditions as the presence of nonlinearities that arise from flow separation effects introduces further complications in the validation of the indicial responses. In Beddoes (1984) and Leishman (1993), data were taken mainly from the results of Liiva et al. (1968), Wood (1979), and Davis & Malcolm (1980).

Because the indicial functions have been completely defined as exponential functions of time, they may be easily manipulated using Laplace transforms. If we consider just the

circulatory part of the lift from AoA given by Eqs. 8.131 and 8.134, the Laplace transform of this part of the indicial response function yields

$$C_n^c(p) = C_{n_\alpha}(M)\left(\frac{1}{p} - \frac{A_1 T_1}{1 + T_1 p} - \frac{A_2 T_2}{1 + T_2 p}\right), \tag{8.142}$$

where

$$T_1 = \frac{c}{2V b_1 \beta^2} \quad \text{and} \quad T_2 = \frac{c}{2V b_2 \beta^2}.$$

The Laplace transform of the forcing function (which in this case is a step change in angle of attack) is given by $\alpha(p) = 1/p$. The circulatory lift transfer function can be simplified to

$$\frac{C_n^c(p)}{\alpha(p)} = C_{n_\alpha}(M)\left[(1 - A_1 - A_2) + \frac{A_1}{1 + T_1 p} + \frac{A_2}{1 + T_2 p}\right]. \tag{8.143}$$

Because the initial value of the circulatory indicial response is zero (i.e., $\phi^c(0, M) = 0$), then $(1 - A_1 - A_2) = 0$ and the lift transfer function simplifies further to

$$\frac{C_n^c(p)}{\alpha(p)} = C_{n_\alpha}(M)\left(\frac{A_1}{1 + T_1 p} + \frac{A_2}{1 + T_2 p}\right). \tag{8.144}$$

For the noncirculatory lift from angle of attack, the Laplace transform of the indicial response yields the transfer function

$$\frac{C_n^{nc}(p)}{\alpha(p)} = \frac{4}{M}\left(\frac{T'_\alpha p}{1 + T'_\alpha p}\right), \tag{8.145}$$

and the transfer functions for the other lift components can be derived in a similar way. Therefore, for any forcing function for which a Laplace transform may be easily derived (such as for a sinusoid), the lift and pitching moment response may be derived in explicit form by using inverse Laplace transforms in terms of the assumed form of the indicial response function (see also Questions 8.4–8.7). For example, the lift response to a harmonic pitch oscillation with a reduced frequency k about the 1/4-chord axis of the airfoil may be obtained after some algebra as

$$\Re\, C_{n_\alpha}(k, M) = C_{n_\alpha}(M)\left(\frac{A_1 b_1^2 \beta^4}{b_1^2 \beta^4 + k^2} + \frac{A_2 b_2^2 \beta^4}{b_2^2 \beta^4 + k^2}\right) + \frac{4}{M}\left(\frac{4\kappa_\alpha^2 M^2 k^2}{1 + 4\kappa_\alpha^2 M^2 k^2}\right), \tag{8.146}$$

$$\Im\, C_{n_\alpha}(k, M) = -C_{n_\alpha}(M)\left(\frac{A_1 b_1 \beta^2 k}{b_1^2 \beta^4 + k^2} + \frac{A_2 b_2 \beta^2 k}{b_2^2 \beta^4 + k^2}\right) + \frac{4}{M}\left(\frac{2\kappa_\alpha M k}{1 + 4\kappa_\alpha M^2 k^2}\right), \tag{8.147}$$

$$\Re\, C_{n_q}(k, M) = C_{n_\alpha}(M)\left(\frac{A_1 b_1 \beta^2 k^2}{b_1^2 \beta^4 + k^2} + \frac{A_2 b_2 \beta^2 k^2}{b_2^2 \beta^4 + k^2}\right) - \frac{1}{M}\left(\frac{4\kappa_q M^2 k^2}{1 + 4\kappa_q^2 M^2 k^2}\right), \tag{8.148}$$

$$\Im\, C_{n_q}(k, M) = C_{n_\alpha}(M)\left(\frac{A_1 \beta^4 k}{b_1^2 \beta^4 + k^2} + \frac{A_2 \beta^4 k}{b_2^2 \beta^4 + k^2}\right) + \frac{1}{M}\left(\frac{8\kappa_q^2 M^2 k^3}{1 + 4\kappa_q^2 M^2 k^2}\right), \tag{8.149}$$

where $\Re$ and $\Im$ denote the real and imaginary parts of the aerodynamic response, respectively. The resultant frequency response can be obtained by summing the various contributions to the real and imaginary components. A similar approach can be adopted to find the response

Table 8.2. *Coefficients of Indicial Lift Approximation Deduced from Oscillating Airfoil Experiments*

Data Source	A_1	A_2	b_1	b_2	δ_α	δ_q
Boeing Data	0.636	0.364	0.339	0.249	0.77	0.70
ARA Data	0.625	0.375	0.310	0.312	1.00	1.00
NASA Data	0.482	0.518	0.684	0.235	0.72	0.70
All Data	0.918	0.082	0.366	0.102	0.85	0.73

from harmonic plunge oscillations, which of course, are useful because they do not include any pitch rate (q) terms in the aerodynamic response.

A vector $\mathbf{x}$ can now be defined that consists of the coefficients A_1, A_2, b_1, and b_2 used in the indicial lift function:

$$\mathbf{x}^T = \{A_1\ A_2; b_1\ b_2;\ \delta_\alpha, \delta_q\}. \tag{8.150}$$

The additional factors δ_α and δ_q are empirical values chosen to modify the initial value of the indicial response functions to account for the possibilities of 3-D or finite-span effects present in the airfoil measurements. It has been shown, however, that their values are always close to unity, suggesting that the unsteady airfoil measurements selected are indeed representative of 2-D unsteady flow. The vector in Eq. 8.150 must be chosen to minimize the difference between the explicit solution based on the assumed indicial response approximations and the reference solutions (in this case, experimental results) for the unsteady lift in the frequency domain. If the real and imaginary parts, $F_m(M_i)$ and $G_m(M_i)$, respectively, are known at up to M values of reduced frequency and at each of I values of Mach number, an objective function $\bar{J}(\mathbf{x})$ can be defined as

$$\bar{J} = \sum_{i=1}^{I} J(\mathbf{x}, M_i), \tag{8.151}$$

where

$$J(\mathbf{x}, M_i) = \sum_{m=1}^{M} [F_m(M_i) - \Re C_n(\mathbf{x}, M_i, k_m)]^2 + [G_m(M_i) - \Im C_n(\mathbf{x}, M_i, k_m)]^2 . \tag{8.152}$$

The minimum of the objective function $\bar{J}$ in the parameter space $\mathbf{x}$ will give the best approximation to the known (reference) lift transfer function. Therefore, the objective function minimization algorithm is basically a nonlinear programming problem of minimizing $\bar{J}(\mathbf{x})$ subject to the constraints

$$A_n,\ b_n > 0,\ n = 1, 2 \quad \text{and} \quad 0 \le \delta_\alpha, \delta_q \le 1 \quad \text{and} \quad \sum_{n=1}^{2} A_n = 1. \tag{8.153}$$

The latter equality constraint may be replaced by a penalty function. Notice that although Table 8.2 shows that the different sets of experimental data result in slightly different values of the coefficients A_1, A_2, b_1, and b_2, the differences are of limited practical significance; the quality of the derived indicial functions is as good as the quality of the experimental data.

8.15.5 *Indicial Pitching Moment from Angle of Attack*

A similar process to that described previously can be used to find approximations for the other indicial response functions. The indicial pitching moment response about the 1/4-chord resulting from a step change in angle of attack, α, can also be written as the sum of a noncirculatory part, $C^{nc}_{m_\alpha}$, and a circulatory part, $C^{c}_{m_\alpha}$, that is,

$$C_{m_\alpha}(s) = C^{nc}_{m_\alpha}(s, M) + C^{c}_{m_\alpha}(s, M) \tag{8.154}$$

or in terms of the indicial functions

$$\frac{C_{m_\alpha}(s)}{\alpha} = -\frac{1}{M}\phi^{nc}_{\alpha_m}(s, M) + \frac{2\pi}{\beta}(0.25 - x_{ac})\phi^{c}_{\alpha}(s, M). \tag{8.155}$$

For the noncirculatory part, a convenient general expression for the indicial function is of the form

$$\phi^{nc}_{\alpha_m}(s) = A_3 \exp\left(\frac{-s}{b_3 T'_{\alpha_m}}\right) + A_4 \exp\left(\frac{-s}{b_4 T'_{\alpha_m}}\right). \tag{8.156}$$

One approximation to this function uses the values $A_3 = 1.5$, $A_4 = -0.5$, $b_3 = 0.25$, and $b_4 = 0.1$. Following a similar approach to that used above for the lift, but now using Eq. 8.155, gives the noncirculatory time constant as

$$T_{\alpha_m} = \left(\frac{c}{2V}\right)T'_{\alpha_m} = \left[\frac{A_3 b_4 + A_4 b_3}{b_3 b_4(1 - M)}\right]\frac{c}{a} = \kappa_{\alpha_m} T_i. \tag{8.157}$$

8.15.6 *Indicial Pitching Moment from Pitch Rate*

Finally, for the indicial moment response about the 1/4-chord resulting from a step change in pitch rate q about the 1/4-chord, this can be written as the sum of a noncirculatory part, $C^{nc}_{m_q}$, and a circulatory part, C^{c}_{mq}, that is

$$C_{m_q}(s) = C^{nc}_{m_q}(s, M) + C^{c}_{m_q}(s, M) \tag{8.158}$$

or in terms of the indicial functions

$$\frac{C_{m_q}(s)}{q} = \frac{-7}{12M}\phi^{nc}_{q_m}(s, M) + \frac{-\pi}{8\beta}\phi^{c}_{q_m}(s, M). \tag{8.159}$$

The circulatory part is assumed to be of the form

$$\frac{C^{c}_{m_q}(s)}{q} = \frac{-\pi}{8\beta}\phi^{c}_{q_m} = \frac{-\pi}{8\beta}\left[1 - A_5 \exp(-b_5\beta^2 s)\right], \tag{8.160}$$

where $A_5 = 1.0$ and $b_5 = 5.0$ are found to be satisfactory when using oscillating airfoil measurements as a basis. For the noncirculatory part of the indicial response

$$\frac{C^{nc}_{m_q}(s)}{q} = \frac{-7}{12M}\phi^{nc}_{q_m} = \frac{-7}{12M}\exp\left(\frac{-s}{T'_{m_q}}\right). \tag{8.161}$$

Following the same procedure as before, but using Eq. 8.121, leads to the noncirculatory time constant

$$T_{q_m} = \left(\frac{c}{2V}\right)T'_{q_m} = \left[\frac{7}{15(1 - M) + 3\pi\beta M^2 A_5 b_5}\right]\frac{c}{a} = \kappa_{q_m} T_i. \tag{8.162}$$

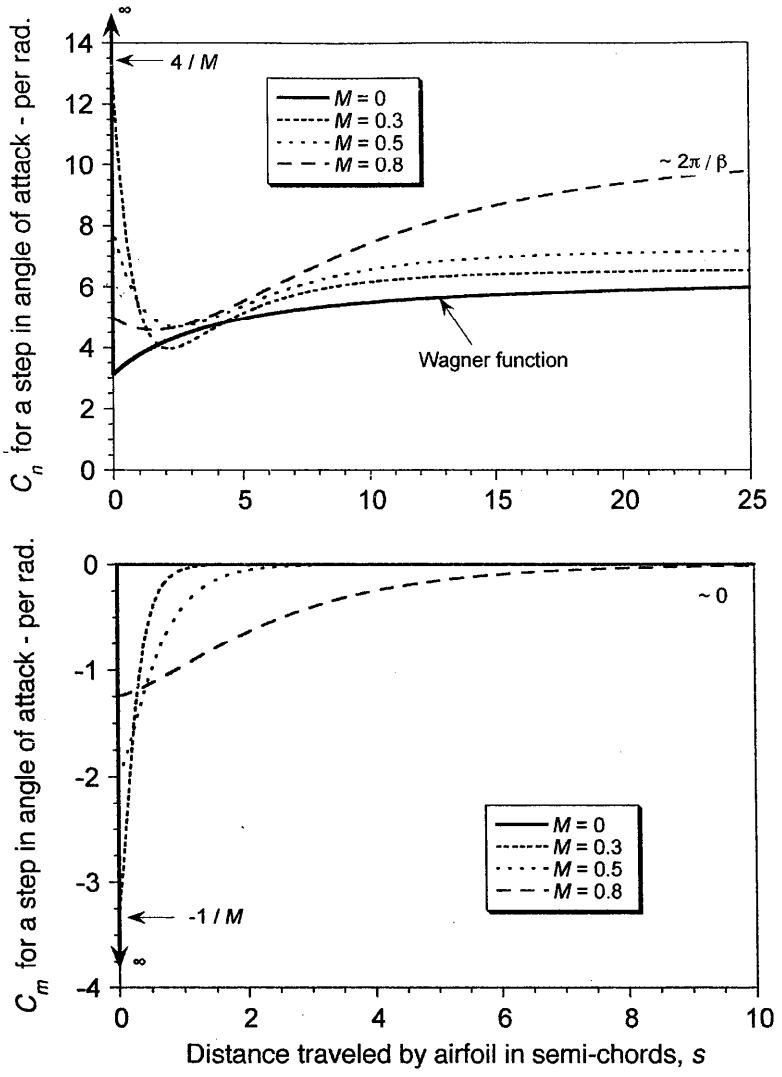

Figure 8.30 Indicial lift and pitching moment resulting from a step change in angle of attack.

Thus, the noncirculatory time constants T_α, T_{α_m}, T_q, and T_{q_m} used in the indicial response functions are now defined in terms of the other (circulatory) coefficients. These functions are only weakly dependent on Mach number in the low subsonic flow regime; however, their values increase rapidly as $M = 1$ is approached but the theory breaks down here anyway.

The four basic indicial functions are plotted in Figs. 8.30 and 8.31 for several Mach numbers to illustrate their behavior. The considerable influence of Mach number compared to the incompressible values should be noted. In application, these subsonic indicial aerodynamic functions are manipulated in exactly the same way as that shown previously for the incompressible case when using the exponential approximation to the Wagner or Küssner functions. For example, in the case of the subsonic lift to an arbitrary variation in α, three recurrence equations or three states instead of two must now be used, with both the circulatory and the noncirculatory terms having a time-history effect.

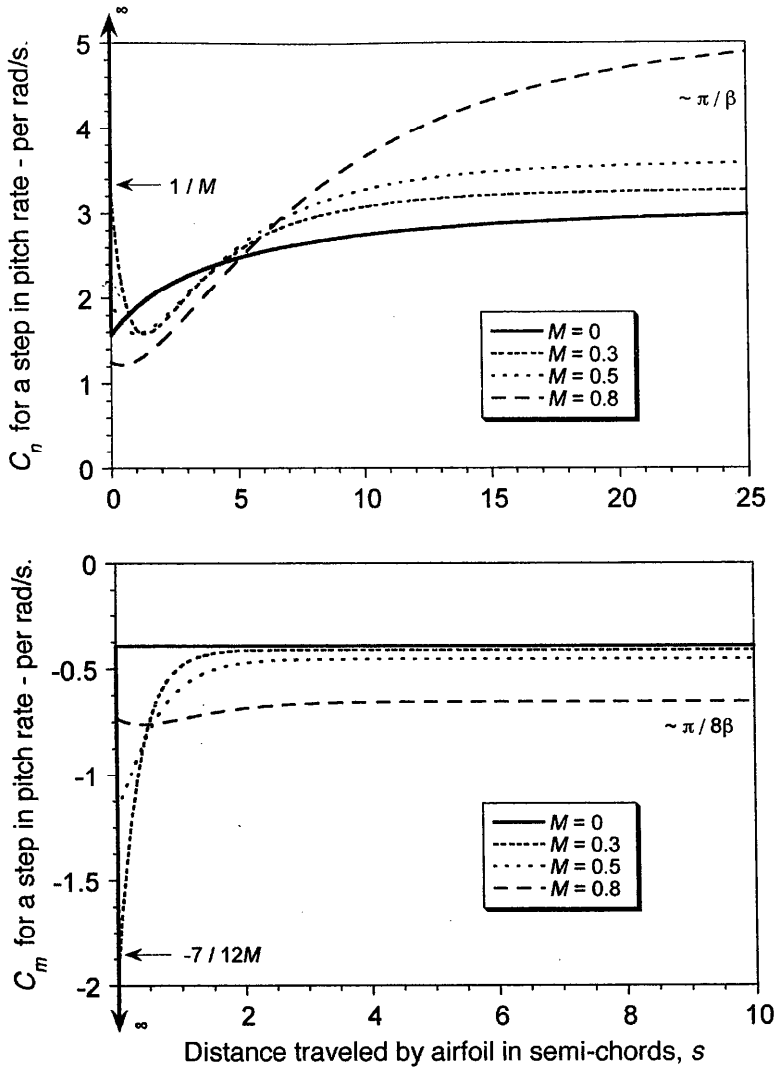

Figure 8.31 Indicial lift and pitching moment resulting from a step change in pitch rate about the 1/4-chord.

8.15.7 *Unsteady Axial Force and Airfoil Drag*

Helicopter rotor blades have a much lower stiffness and effective damping than the wing of a fixed wing aircraft for the in-plane (lead–lag) degree of freedom. Whereas the blade flapping and torsion degrees of freedom are primarily influenced by the lift and pitching moment respectively, the lead–lag degree of freedom is influenced by the drag. Furthermore, the blade lead–lag motion may couple with the flapping or torsion degrees of freedom and may lead to an aeroelastic instability of the blades. For example, this is intrinsic to the problem of ground resonance discussed in Section 4.10. As shown in Chapter 4, these coupling effects result from both the Coriolis forces and the aerodynamic loads. Therefore, for a comprehensive model of the rotor system it is necessary to include an accurate representation of the unsteady aerodynamic loads for all three degrees of freedom (lift, pitching moment, and drag).

For steady flow conditions, the pressure drag coefficient C_{d_p} may be computed by resolving the normal force and axial force (or the leading edge suction force) coefficients through the AoA α using

$$C_{d_p} = C_n \sin\alpha - C_a \cos\alpha, \tag{8.163}$$

as shown in Section 7.11.1. For steady flow the normal force coefficient is given in terms of the force curve slope, $C_{n_\alpha}(M)$, at a given Mach number, M, and the angle of attack, α, as

$$C_n = C_{n_\alpha}(M)\,\alpha. \tag{8.164}$$

The corresponding axial (chord) force coefficient for these conditions is given by

$$C_a = C_{n_\alpha}(M)\,\alpha\,\tan\alpha. \tag{8.165}$$

where α is measured in radians. Now, it is well known that for steady potential flow the pressure drag, C_{d_p}, is identically zero (d'Alembert's paradox), that is,

$$C_{d_p} = C_n \sin\alpha - C_a \cos\alpha = C_{n_\alpha}(M)\alpha\ \sin\alpha - C_{n_\alpha}(M)\alpha\ \tan\alpha\ \cos\alpha = 0. \tag{8.166}$$

However, for a real flow there is a net pressure drag on the airfoil because of viscous effects on the chordwise pressure distribution. As shown Section 7.11.1, the inability of the airfoil to attain 100% leading edge suction is modeled using the recovery factor η_a such that

$$C_a = \eta_a\ C_{n_\alpha}(M)\ \alpha\ \tan\alpha, \tag{8.167}$$

where the value of η_a may be adjusted empirically as necessary to give the best fit with the static axial force and/or drag measurements. Typically, the value of η_a is approximately 0.95.

The viscous (shear stress) drag is represented by the term C_{d_0} and is also a function of Mach number. However, its value is nominally constant for the AoA range below stall. Thus, the total drag in steady flow is given by the sum of the pressure and viscous shear components as:

$$C_d = C_{d_0} + C_{d_p} = C_{d_0} + C_n \sin\alpha - C_a \cos\alpha. \tag{8.168}$$

The unsteady axial force coefficient, $C_a(t)$, depends only on the circulatory component of the loading. This is easily proved by considering the chordwise form of the circulatory and noncirculatory pressure loadings. The circulatory form is given by the standard thin-airfoil theory result, namely

$$\Delta C_p^c(\bar{x}, t) = 4\left(\alpha_e + \frac{\dot{\alpha}_e c}{2V}\right)\sqrt{\frac{1-\bar{x}}{\bar{x}}}. \tag{8.169}$$

The important point here is that the circulatory form has a leading edge pressure singularity, and this form of pressure distribution is obtained no matter what the value of the effective angle of attack, α_e. The noncirculatory form (at time zero) is given by the piston theory result

$$\Delta C_p^{nc}(\bar{x}, t = 0) = \frac{4}{M}\alpha. \tag{8.170}$$

While this initial loading changes with time as pressure waves propagate from the airfoil, no leading edge singularity exists for any time. The general expression for the leading edge suction force is

$$C_a = \frac{\pi}{8} \lim_{\bar{x}\to 0} \{\Delta C_p^2 \bar{x}\}, \tag{8.171}$$

and inserting the circulatory loading gives

$$C_a = \frac{\pi}{8} \lim_{\bar{x}\to 0} \left[16\left(\alpha_e + \frac{\dot{\alpha}_e c}{2V}\right)^2 \left(1 - \frac{\bar{x}}{c}\right)\right] = 2\pi \left(\alpha_e + \frac{\dot{\alpha}_e c}{2V}\right)^2. \tag{8.172}$$

Thus, as a consequence of the above the unsteady axial force may be obtained directly from the steady result by replacing α by the instantaneously effective angle of attack $\alpha_e + \dot{\alpha}_e c/2V$, that is,

$$C_a(t) = \eta_a \, C_n(t) \tan\left(\alpha_e + \frac{\dot{\alpha}_e c}{2V}\right) \approx \eta_a \, C_{n_\alpha}(M) \left(\alpha_e + \frac{\dot{\alpha}_e c}{2V}\right)^2. \tag{8.173}$$

Notice that the noncirculatory loading does not appear in this expression. The unsteady pressure drag (if this is required) is obtained by resolving the total normal force (including noncirculatory terms) and axial force coefficients through the AoA α to obtain

$$C_d(t) = C_n(t) \sin\alpha - C_a(t) \cos\alpha + C_{d_0}. \tag{8.174}$$

See also Leishman (1987b) for further discussion on the modeling of unsteady drag.

8.15.8 *State-Space Aerodynamic Model for Compressible Flow*

By suitably generalizing the indicial response in terms of exponential functions and Mach number as shown previously, the corresponding state-space realization may also be obtained for each component of the loading in a subsonic compressible flow – see Leishman & Nguyen (1990). Firstly, consider the normal force response to continuous forcing in terms of angle of attack. Using the indicial functions given previously, the circulatory normal force response to a variation in AoA can be written in state-space form as

$$\begin{Bmatrix} \dot{x}_1 \\ \dot{x}_2 \end{Bmatrix} = \left(\frac{2V}{c}\right) \beta^2 \begin{bmatrix} -b_1 & 0 \\ 0 & -b_2 \end{bmatrix} \begin{Bmatrix} x_1 \\ x_2 \end{Bmatrix} + \begin{Bmatrix} 1 \\ 1 \end{Bmatrix} \alpha_{3/4}(t), \tag{8.175}$$

with the output equation for the normal force coefficient given by

$$C_n^c(t) = \frac{2\pi}{\beta} \left(\frac{2V}{c}\right) \beta^2 [A_1 b_1 \; A_2 b_2] \begin{Bmatrix} x_1 \\ x_2 \end{Bmatrix}, \tag{8.176}$$

where $2\pi/\beta$ is the lift-curve-slope for linearized compressible flow and $\alpha_{3/4}$ is the AoA at the 3/4-chord, that is,

$$\alpha_{3/4}(t) = \alpha(t) + \frac{q(t)}{2}.$$

Similarly, the noncirculatory normal force from AoA can be written in the state-space representation as

$$\dot{x}_3 = \alpha(t) - \frac{1}{\kappa_\alpha T_i} x_3 = \alpha(t) + a_{33} x_3, \tag{8.177}$$

with the output equation for the normal force coefficient given by

$$C_{n_\alpha}^{nc}(t) = \frac{4}{M}\dot{x}_3. \tag{8.178}$$

The remaining state equations for the pitching moment and pitch rate terms can be derived in a similar way using all of the other indicial response approximations for pitching moments and pitch rate, as given previously. The individual components of aerodynamic loading are then linearly combined to obtain the overall aerodynamic response. For example, the total normal force coefficient is given by

$$C_n(t) = C_n^c(t) + C_{n_\alpha}^{nc}(t) + C_{n_q}^{nc}(t) \tag{8.179}$$

and an analogous equation holds for the pitching moment about the 1/4-chord. Thus, the overall unsteady aerodynamic response can be described in terms of a two-input, two-output system where the inputs are the airfoil AoA and pitch rate and the outputs are the unsteady normal force (lift) and pitching moment. It can be shown that by rearranging the state equations, the inputs and outputs can be represented in the general form

$$\begin{Bmatrix} \dot{x}_1 \\ \dot{x}_2 \\ \dot{x}_3 \\ \dot{x}_4 \\ \dot{x}_5 \\ \dot{x}_6 \\ \dot{x}_7 \\ \dot{x}_8 \end{Bmatrix} = \begin{bmatrix} a_{11} & 0 & 0 & 0 & 0 & 0 & 0 & 0 \\ 0 & a_{22} & 0 & 0 & 0 & 0 & 0 & 0 \\ 0 & 0 & a_{33} & 0 & 0 & 0 & 0 & 0 \\ 0 & 0 & 0 & a_{44} & 0 & 0 & 0 & 0 \\ 0 & 0 & 0 & 0 & a_{55} & 0 & 0 & 0 \\ 0 & 0 & 0 & 0 & 0 & a_{66} & 0 & 0 \\ 0 & 0 & 0 & 0 & 0 & 0 & a_{77} & 0 \\ 0 & 0 & 0 & 0 & 0 & 0 & 0 & a_{88} \end{bmatrix} \begin{Bmatrix} x_1 \\ x_2 \\ x_3 \\ x_4 \\ x_5 \\ x_6 \\ x_7 \\ x_8 \end{Bmatrix} + \begin{bmatrix} 1 & 0.5 \\ 1 & 0.5 \\ 1 & 0 \\ 0 & 1 \\ 1 & 0 \\ 1 & 0 \\ 0 & 1 \\ 0 & 1 \end{bmatrix} \begin{Bmatrix} \alpha \\ q \end{Bmatrix},$$

$$\begin{Bmatrix} C_n \\ C_m \end{Bmatrix} = \begin{bmatrix} c_{11} & c_{12} & c_{13} & c_{14} & 0 & 0 & 0 & 0 \\ c_{21} & c_{22} & 0 & 0 & c_{25} & c_{26} & c_{27} & c_{28} \end{bmatrix} \begin{Bmatrix} x_1 \\ x_2 \\ x_3 \\ x_4 \\ x_5 \\ x_6 \\ x_7 \\ x_8 \end{Bmatrix} + \begin{bmatrix} \frac{4}{M} & \frac{1}{M} \\ \frac{-1}{M} & \frac{-7}{12M} \end{bmatrix} \begin{Bmatrix} \alpha \\ q \end{Bmatrix},$$

which is the form of Eqs. 8.100 and 8.101. The total aerodynamic lift and pitching moment response to an arbitrary time history of α and q can be obtained from the above state equations by integrating numerically using a standard ordinary differential equation solver.

The unsteady axial force (in-plane force) and pressure drag on the airfoil may also be obtained in terms of the state variables. From the output equation, the effective AoA of the airfoil, α_e, because of the shed wake (circulatory) terms can be written in terms of the states x_1 and x_2 as

$$\alpha_e(t) = \beta^2 \left(\frac{2V}{c}\right)(A_1 b_1 x_1 + A_2 b_2 x_2). \tag{8.180}$$

Therefore, as shown previously, the corresponding axial force C_a is given in terms of α_e as

$$C_a(t) = \frac{2\pi}{\beta}\alpha_e^2(t), \tag{8.181}$$

which involves a bilinear combination of the states x_1 and x_2. Thus, as a byproduct of the above system representation for the unsteady lift, the necessary information may be extracted from the system at a given instant of time to obtain the unsteady axial force component. Finally, the instantaneous pressure drag can be obtained by resolving the components of the normal force and chordwise forces through the geometric AoA α using Eq. 8.174.

8.15.9 *Comparison with Experiment*

Whereas the formulation of the subsonic unsteady aerodynamic model in the previous section has been derived, in part, by using experimental measurements in the frequency domain, the validity of the model must be reconfirmed by comparing with experimental results of unsteady forces and pitching moments as functions of time or angle of attack. The unsteady airloads in response to an arbitrary time history of α and q can be obtained by using the previously derived indicial functions with Duhamel superposition in the form of the recurrence equations, or by integration of the state-space equations. Results will now be shown for both a pure plunging oscillation and also for a pitching oscillation; the absence of pitch rate in the plunge oscillations makes it possible to isolate the effects of the pitch rate in the unsteady aerodynamic response. For the plunging case, an equivalent

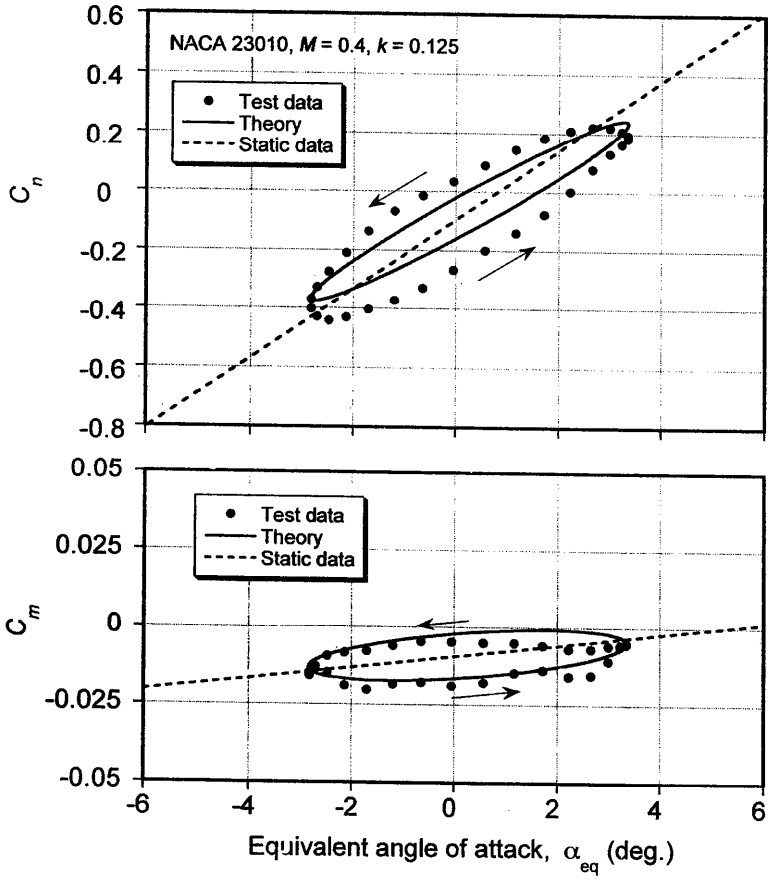

Figure 8.32 Comparison of theory and experiment for the lift and pitching moment coefficients in fully attached flow under oscillatory plunge forcing conditions at $M = 0.4$.

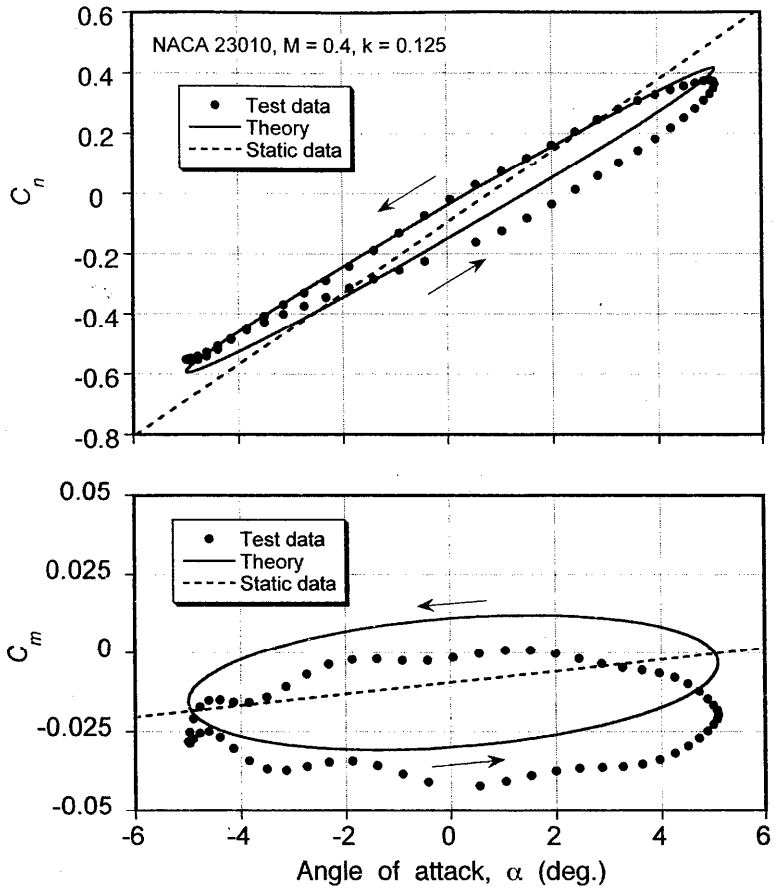

Figure 8.33 Comparison of theory and measurements for the lift and pitching moment coefficients in fully attached flow under oscillatory pitch forcing conditions at $M = 0.4$.

quasi-steady AoA can be defined using

$$\alpha_{eq}(t) = \tan^{-1}\left(\frac{\dot{h}}{V}\right) \approx \frac{\dot{h}}{V}. \tag{8.182}$$

Notice that, unlike the pitch angle, the equivalent AoA in Eq. 8.182 is not a directly measurable quantity because it depends on the free stream velocity, V.

Representative variations in normal (lift) force and 1/4-chord pitching moment coefficients are shown in Fig. 8.32 for harmonic plunge forcing and in Fig. 8.33 for harmonic pitch forcing. In each case, the results obtained from the subsonic unsteady aerodynamic model are compared to experimental measurements made by Liiva et al. (1968). The pitch and plunge data have been selected for approximately the same reduced frequency and mean AoA, although the equivalent amplitude of forcing is slightly different. The results show the expected characteristic elliptical shaped normal force and pitching moment loops symptomatic of attached flow. It is clear that in both cases there is a reduction of the unsteady "lift slopes" compared to the steady case, but with a larger phase lag (width of the hysteresis loop) for the plunging case. The width (amplitude) of the moment loop for the pitching oscillation is much larger than that for the plunge oscillation because of the

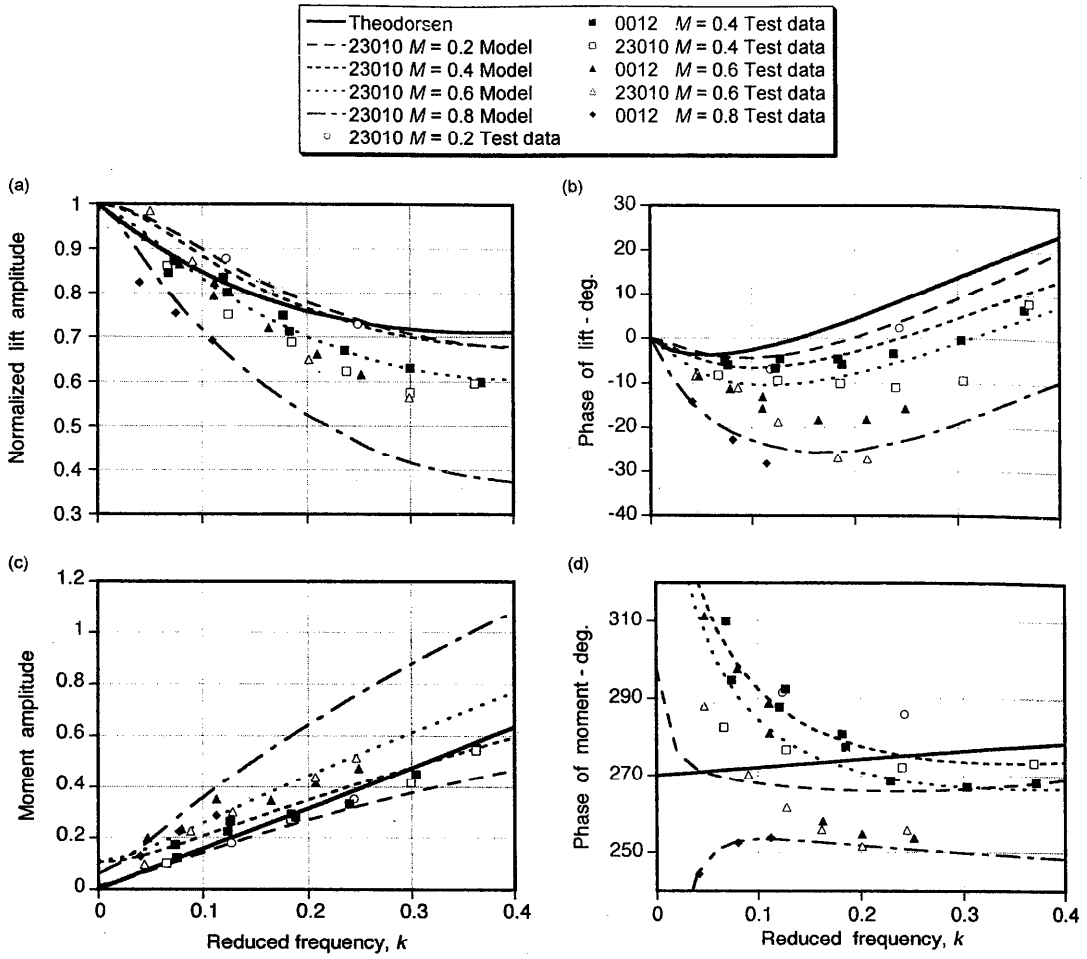

Figure 8.34 Comparison of the compressible unsteady airfoil theory with pitch oscillation measurements at various Mach numbers. (a) Lift amplitude. (b) Phase of lift. (c) Pitching moment amplitude. (d) Phase of pitching moment.

pitch rate contributions.[11] For each mode of forcing, it is apparent that the major axis of the unsteady pitching moment loop is closely aligned with the steady moment slope. This positive slope is a result of the aerodynamic center being slightly forward of the 1/4-chord measurement axis.

Further results showing quality of the predictions of the unsteady lift in compressible flow and the improvement that can be obtained over Theodorsen's theory are given in Fig. 8.34 for pitching oscillations. To summarize as many operating conditions as possible, the results are shown in terms of lift and pitching moment amplitude and corresponding phase angle versus reduced frequency. To put the measurements on a common basis, the amplitudes of the response have been expressed as ratios by normalizing with respect to the measured static lift curve slope. Plunge oscillation data are more scarce, but as mentioned previously, they are particularly useful because of the absence of loading contributions from pitch rate (q) terms. It is clear from the results obtained in Fig. 8.34 that there is a good

[11] Notice that there is some offset in the C_m curves, which has been attributed to thermal drift of the pressure transducers used in the experiment.

correlation between the predicted and measured lift response. This provides considerable support for using this type of unsteady aerodynamic modeling over the Mach number and reduced frequency range appropriate for helicopter applications.

The subsonic compressible flow theory compares more favorably with measurements than Theodorsen's theory, particularly for the phase. The pitching moment is, however, more difficult to predict without the use of empirical results. Notice from Fig. 8.34(d) that there is a gradual divergence of the phase angle as the reduced frequency tends to zero. As described previously in Section 7.7.1, this is attributable to an offset of the aerodynamic center from the 1/4-chord moment reference point, and it emphasizes the need to carefully represent the changing aerodynamic center with Mach number in a rotor simulation if accurate predictions of the unsteady aerodynamic effects are to be obtained.

8.16 Nonuniform Vertical Velocity Fields

In the rotor plane, there are a large number of vortical disturbances that lie in proximity to the blades. This is especially significant on the advancing and retreating sides of the rotor where the blades may interact with tip vortices – see Section 8.16.4. The unsteady forces produced on a rotor blade arise primarily because of the vertical velocity between the wake disturbance (gust field) and the airfoil surface. In linear theory, this is treated as an imposed unsteady upwash field, which must be used to satisfy the boundary conditions of flow tangency on the airfoil surface. As described previously, within the assumptions of linear theory, incompressible flow solutions for the sinusoidal vertical gust problem have been solved by Sears (1940), and exact solutions for the sharp-edged vertical gust problem have been found by Küssner (1935), von Kármán & Sears (1938), and Miles (1956).

8.16.1 *Exact Subsonic Linear Theory*

For the subsonic compressible flow case, the problem of finding the sharp-edged vertical gust response, $\psi(s, M)$, was considered by Lomax (1953) using a similar approach to that described previously to derive the indicial responses from changes in airfoil AoA and pitch rate. The subsonic vertical gust result was also obtained by Heaslet & Sprieter (1952) by means of reciprocal relations. The actual mathematical calculations are fairly involved, but Lomax (1953) has shown that exact analytical expressions for the airfoil pressure distribution can be found for a limited period of time after the vertical gust entry. For the period $0 \leq s \leq 2M/(1+M)$ the lift coefficient is given by

$$\Delta C_n^g(s) = \frac{2s}{\sqrt{M}} \left(\frac{\Delta w_g}{V} \right). \tag{8.183}$$

for a gust velocity perturbation of Δw_g. The corresponding 1/4-chord pitching moment coefficient for the period $0 \leq s \leq 2M/(1+M)$ can also be found, giving

$$\Delta C_m^g(s) = \frac{8s - \left[\dfrac{(M+1)}{M} \right] s^2}{4\sqrt{M}} \left(\frac{\Delta w_g}{V} \right). \tag{8.184}$$

Although these results are valid for less than one-chord length of airfoil travel for all subsonic Mach numbers, these analytic solutions are exact within the underlying assumptions of linearized, subsonic, unsteady thin-airfoil theory.

One interesting result from Eq. 8.183 is that increasing Mach number decreases the *initial* rate of lift production for a given distance traveled during the vertical gust penetration, perhaps not an intuitive result. However, a similar result has been shown previously for the indicial AoA case, where there is an increasing lag in the development of the circulatory lift for higher subsonic Mach numbers – see also Bisplinghoff et al. (1955). Using Eq. 8.183 it can be shown that the lift builds very rapidly during the vertical gust penetration, reaching close to one third of its final value ($2\pi/\beta$) shortly after the airfoil becomes fully immersed in the vertical gust (that is, when $s = 2$).

The position of the center of pressure during the vertical gust penetration is also of interest. Helicopter rotor blades tend to be relatively compliant in torsion compared to the wings of fixed-wing aircraft, and so the variation in airfoil pitching moment about the elastic axis can be very important. For the period $0 \leq s \leq 2M/(1+M)$, the center of pressure can be computed from Eqs. 8.183 and 8.184 giving

$$\bar{x}_{cp}(s, M) = \frac{s}{8}\left[\frac{M+1}{M}\right], \tag{8.185}$$

which shows that $\bar{x}_{cp}$ moves quickly aft to the 1/4-chord location within the short period $s = 2M/(1+M)$. Therefore, for most practical purposes it is sufficient to assume that the aerodynamic center remains at the 1/4-chord throughout the vertical gust penetration. This result is also consistent with the incompressible solution of von Kármán & Sears (1938). For later values of time up to $s = 4M/(1-M^2)$, solutions for the airfoil pressure distribution during the vertical gust penetration takes a more complicated form, and the determination of the lift and pitching moment is only possible by means of numerical methods. For $s > 4M/(1-M^2)$ no exact solutions to the sharp-edged vertical gust problem are possible in subsonic flow by means of the linear theory; consequently other and usually more approximate numerical methods or CFD solutions must be adopted.

8.16.2 *Approximations to the Sharp-Edged Gust Functions*

Mazelsky (1952a) and Mazelsky & Drishler (1952) have obtained exponential approximations to the stationary sharp-edged vertical gust functions at various Mach numbers by means of reciprocal theorems in conjunction with numerical solutions for airloads computed in the frequency domain. A suitable functional approximation for the sharp-edged vertical gust is of the form

$$\psi(s, M) \approx 1 - \sum_{i=1}^{N} G_i e^{-g_i s}, \tag{8.186}$$

where the G_i and g_i coefficients will all be Mach number dependent, and with $\sum_{i=1}^{N} G_i = 1$ and $g_i, i = 1, \ldots, N > 0$. The corresponding lift is given by

$$\Delta C_n^g(t, M) = \frac{2\pi}{\beta}\psi(s, M)\left(\frac{\Delta w_g}{V}\right) = \frac{2\pi}{\beta}\left(1 - \sum_{i=1}^{N} G_i e^{-g_i s}\right)\left(\frac{\Delta w_g}{V}\right). \tag{8.187}$$

It has been shown previously that the circulatory part of the total lift from a step change in AoA in subsonic compressible flow can be approximated by a two-term exponential function, and for all subsonic Mach numbers the results are related through a characteristic time

that can be scaled in terms of Mach number alone. For later values of time the sharp-edged vertical gust and indicial AoA functions must approach each other; thus it is reasonable also to assume a similar behavior for the vertical gust function. It can be approximated by an exponential function of the form

$$\psi(s, M) \approx 1 - \sum_{i=1}^{N} G_i e^{-g_i \beta^2 s}, \quad \sum_{i=1}^{N} G_i = 1, \quad g_i > 0, \tag{8.188}$$

but now the Gs and gs are fixed and considered independent of Mach number. Like the indicial AoA functions given previously, such an approximation can be assumed to be valid up to at least the critical Mach number of the airfoil, beyond which nonlinear effects associated with transonic flow do not allow for such relatively simple generalizations.

The solution for the coefficients in Eq. 8.188 can now be formulated as a least-squares optimization problem with several imposed constraints. In this case, however, there are no equivalent experimental results for airfoils in sinusoidal gust fields. Therefore, direct time domain results obtained using analytic and CFD solutions can be used as a reference to find the gust function approximations in exponential form. To obtain an approximation to the exact linear theory, one constraint can be imposed by matching the time rate of change of the exact solution (Eq. 8.183) and approximate solution (Eq. 8.187) at $s = 0$. This helps constrain the solution to ensure that the exact result will always be closely obtained in the initial stages. This part of the response is particularly important for transient aerodynamic phenomena such as BVI – see Section 8.16.4. Differentiating Eqs. 8.183 and 8.188 with respect to s and equating their gradients at $s = 0$ leads to a definition for the first constraint, namely

$$\sum_{i=1}^{N} G_i g_i = \frac{1}{\pi\sqrt{M\beta}} = \frac{1}{\pi\sqrt{M}\sqrt{1-M^2}} = \text{constant}. \tag{8.189}$$

This result cannot be obtained over the entire subsonic Mach number regime; however, an evaluation of right-hand side of Eq. 8.189 shows that it is numerically close to 0.6 over the practical range $0.2 \leq M \leq 0.8$. As $M \to 0$, the slope tends to infinity at $s = 0$, which is consistent with the exact solution given by von Kármán & Sears (1938). In the latter case, with any common type of exponential approximation to the exact incompressible solution [see, for example, Bisplinghoff et al. (1955)] the gradients cannot be matched as $s \to 0$. In addition, a constraint is imposed for the initial conditions, namely $\sum_{i=1}^{N} G_i - 1 = 0$, and also $G_i,\ g_i,\ > 0, i = 1, 2, \ldots, N$. Also, as $s \to \infty$, the airloads approach the value given by the usual steady-state subsonic linearized airfoil theory [i.e., $C_n^g(s = \infty, M) = 2\pi/\beta$]. In a parallel way to that described previously for the indicial AoA case, a $2N$-dimensional vector of unknown coefficients can now be defined as

$$\mathbf{x}^T = \{G_1\ G_2 \ldots G_N;\ g_1\ g_2 \ldots g_N\}. \tag{8.190}$$

The vector in Eq. 8.190 can be chosen to minimize the differences between the approximating exponential vertical gust function and the exact or any reference solutions over the domain of s and M.

Exact results for the vertical gust response in linearized subsonic flow can be computed using the solutions given by Lomax (1968) and Lomax et al. (1952), but only up to $s = 4M/(1 - M^2)$. For higher Mach numbers this corresponds to finding an exact solution up to about 10 semi-chord lengths of airfoil travel. CFD results for the sharp-edged gust

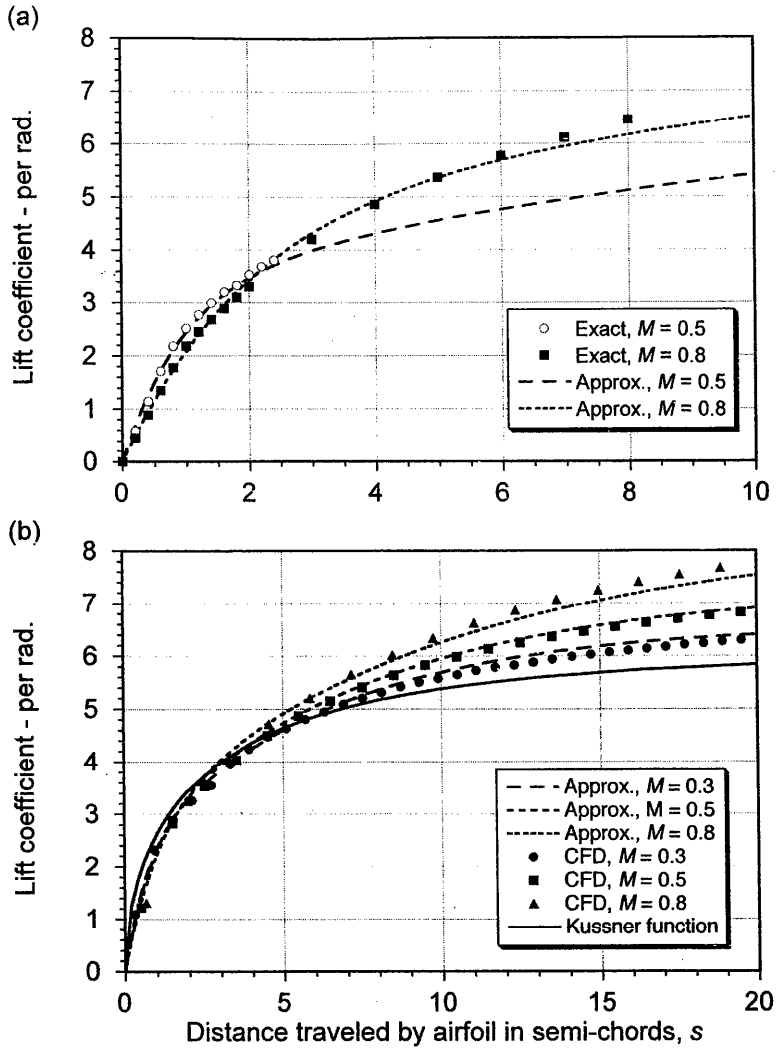

Figure 8.35 Sharp-edged vertical gust indicial lift functions at different Mach numbers. (a) Short values of time. (b) Longer values of time.

problem have been made available by Singh & Baeder (1997b). Notice that the exponential approximations to the gust response, which are shown in Fig. 8.35, match the exact solutions and the CFD solutions almost precisely. It is apparent that although the final values increase with increasing Mach number, the initial growth in lift is less.

The resulting coefficients for the indicial gust functions are given in Table 8.3. Results for the $N = 3$ case at $M = 0.5$ as given by Mazelsky & Drischler (1952) are also tabulated. The coefficients of the generalized subsonic vertical gust function as $M \to 0$ are close to those given by R. T. Jones (1938, 1940) for the incompressible case (the $N = 2$ exponential approximation to the Küssner function) and confirms that the results for the subsonic case are closely approximated by scaling the g coefficients by β^2; that is, the aerodynamic vertical gust responses are related in subsonic flow, albeit approximately, through a characteristic time.

Table 8.3. *Summary of Sharp-Edged Vertical Gust Function Coefficients*

	G_1	G_2	G_3	g_1	g_2	g_3
$\psi(s)$*	0.5	0.5	–	0.130	1.0	–
$\psi(s, M = 0.5)$**	0.390	0.407	0.203	0.0716	0.374	2.165
$\psi(s, M)$ (linear)	0.527	0.473	–	0.100	1.367	–
$\psi(s, M = 0.5)$ (linear)	0.527	0.473	–	0.075	1.025	–
$\psi(s, M)$ (CFD)	0.670	0.330	–	0.1753	1.637	–

* From Bisplinghoff et al. (1955).
** From Mazelsky & Drischler (1952).

8.16.3 *Response to an Arbitrary Vertical Gust*

If the subsonic sharp-edged gust functions are approximated in exponential form, the same techniques used previously to find the total unsteady lift to an arbitrary forcing can be applied. Within the assumptions of the linear theory, a general stationary vertical gust field, $w_g(x, t)$, can be decomposed into a series of sharp-edged vertical gusts of small magnitude. When the approximation to the aerodynamic response for sharp-edged vertical gust is found, then the response to an arbitrary vertical gust field can be found using linear superposition by means of Duhamel's integral. After the initial transient dies out, the response to a continuous vertical gust field may be written analytically as

$$\Delta C_n^g(s) = \frac{2\pi}{\beta}\left[\frac{1}{V}\int_0^s \frac{dw_g}{dt}\psi(s-\sigma, M)d\sigma\right]. \tag{8.191}$$

As described previously, the Duhamel superposition can be performed numerically in various ways, including the state-space (continuous time) form or the one-step recursive formulation (discrete time) form. In the latter case, a finite-difference approximation to the Duhamel integral leads to a solution for the lift that may be constructed from an accumulating series of small vertical gust inputs using

$$\Delta C_n^g(t) = \frac{2\pi}{\beta}\frac{1}{V}\Big[\, w_g(s) - Z_1(s) - Z_2(s)\Big], \tag{8.192}$$

where the terms Z_1 and Z_2 are the deficiency functions. In this case, using Algorithm D-2 given previously in Section 8.14.1, the deficiency functions are given by the one-step recursive formulas

$$Z_1(s) = Z_1(s-\Delta s)E_1 + G_1\big[w_g(s) - w_g(s-\Delta s)\big]E_1^{1/2}, \tag{8.193}$$

$$Z_2(s) = Z_2(s-\Delta s)E_2 + G_2\big[w_g(s) - w_g(s-\Delta s)\big]E_2^{1/2}, \tag{8.194}$$

where $E_1 = \exp(-g_1\beta^2\Delta s)$ and $E_2 = \exp(-g_2\beta^2\Delta s)$.

By applying Laplace transforms to the exponential approximation to the sharp-edged vertical gust function in Eq. 8.188, the lift transfer function relating the output (the lift) to the input (the vertical gust field) can be obtained. From the transfer function, the alternative state-space form of the equations can be written as

$$\begin{Bmatrix} \dot{z}_1(t) \\ \dot{z}_2(t) \end{Bmatrix} = \begin{bmatrix} 0 & 1 \\ -g_1 g_2 \left(\frac{2V}{c}\right)^2 \beta^4 & -(g_1+g_2)\left(\frac{2V}{c}\right)\beta^2 \end{bmatrix} \begin{Bmatrix} z_1(t) \\ z_2(t) \end{Bmatrix} + \begin{Bmatrix} 0 \\ 1 \end{Bmatrix} \frac{\Delta w_g(t)}{V}, \tag{8.195}$$

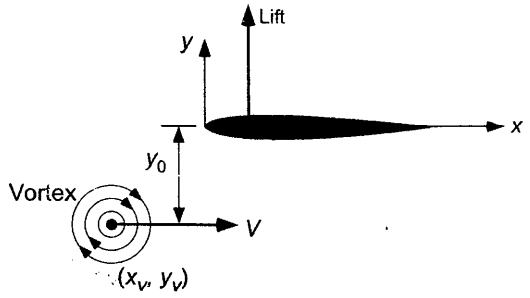

Figure 8.36 Two-dimensional model of the blade–vortex interaction (BVI) problem.

with the corresponding output equation for the total normal force (lift) coefficient for the arbitrary vertical gust field as

$$\Delta C_n^g(t) = \frac{2\pi}{\beta}\left[(g_1 g_2)\left(\tfrac{2V}{c}\right)^2 \beta^4 \quad (G_1 g_1 + G_2 g_2)\left(\tfrac{2V}{c}\right)\beta^2\right]\begin{Bmatrix} z_1(t) \\ z_2(t) \end{Bmatrix}. \tag{8.196}$$

These equations can then be solved using a standard ordinary differential equation solver for any arbitrarily imposed vertical gust field.

8.16.4 *Blade–Vortex Interaction (BVI) Problem*

Blade–vortex interaction (BVI) is one practical example of a helicopter flow with an intense vertical velocity field with high velocity gradients. The 2-D BVI problem, which is shown schematically in Fig. 8.36, has been widely addressed in the literature – see, for example, McCroskey & Goorjian (1983) and Singh & Baeder (1997b). While passing an airfoil at a predetermined distance, a convecting vortex of positive circulation produces a downwash velocity while upstream of the blade (airfoil), and this changes to an upwash as it moves downstream. This situation leads to a rapidly and continuously changing angle of attack, resulting in highly unsteady aerodynamic lift and other airloads. The acoustic pressure (or noise) propagated to an observer from such a blade–vortex encounter is related, as given by the compact source limit, to the time rate of change of this lift (see Section 8.19).

Representative numerical calculations will now be shown for the unsteady loads on a NACA 0012 airfoil interacting with a convecting vortex of nondimensional strength $\hat{\Gamma} = \Gamma/(Vc) = 0.2$. The airfoil is assumed to have zero angle of attack. The interacting vortex was assumed to have a Lamb-like normal velocity distribution (see Eq. 10.9) given by

$$w_g(x, y) = -\frac{\hat{\Gamma}}{2\pi}\frac{(x - x_v)}{r^2}\left[1 - \exp\left(\frac{-r^2}{r_c^2}\right)\right], \tag{8.197}$$

with $r^2 = (x - x_v)^2 + (y - y_v)^2$, where x_v, y_v refer to the position of the vortex relative to a coordinate axis at the leading edge of the airfoil. The reciprocal influence of the airfoil on the vortex convection velocity and trajectory is neglected, and we can assume that the vortex remains undisturbed from the path $y_v = y_0 = -0.26$. As shown by Srinivasan & McCroskey (1987), the effect of vortex trajectory distortion appears to be of secondary importance to the overall airloads except for the transonic case when the vortex may pass close to a shock wave. A viscous core of dimensions $r_c = 0.05c$ was used for the calculations, although the interaction between the airfoil and the vortex is sufficiently spaced in this case that the core radius does not play a role.

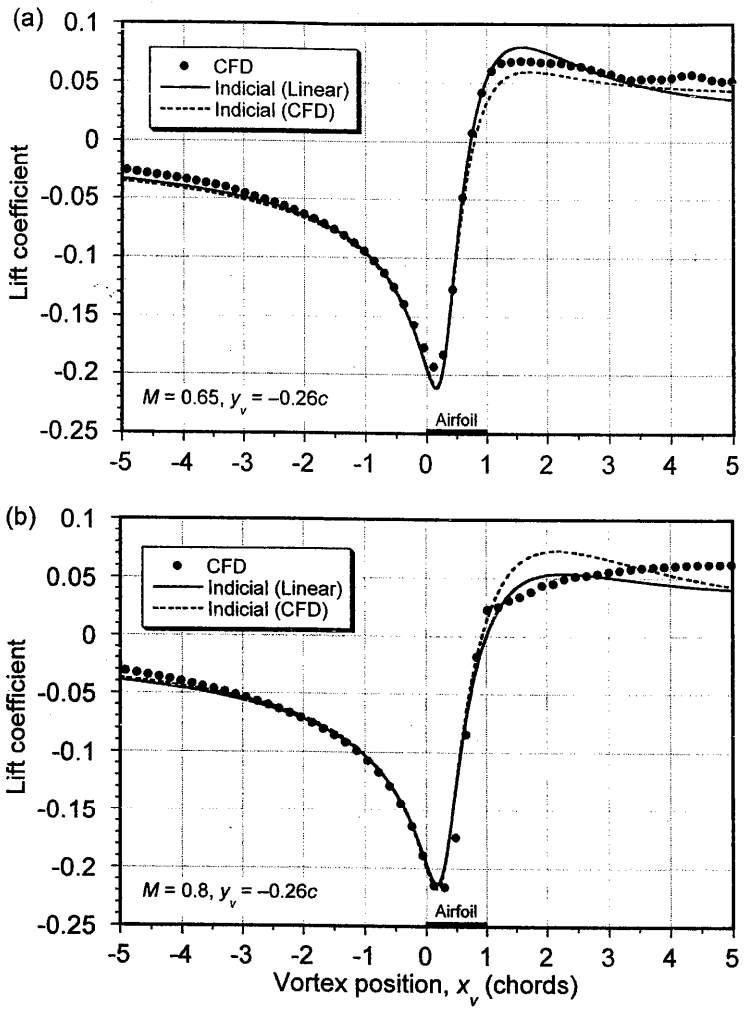

Figure 8.37 Comparison of indicial method with Euler CFD result for the lift during a 2-D vortex-airfoil interaction. $\hat{\Gamma} = 0.2$ and $y_0 = -0.26$. (a) $M = 0.65$ (subsonic). (b) $M = 0.8$ (weakly transonic).

Results for Mach numbers between 0.65 and 0.8 are shown in Fig. 8.37. The results are compared to a CFD solution based on the Euler equations. Notice the good agreement between the indicial approach and the CFD solution, the results essentially confirming the validity of linear theory for this problem. Even for the higher Mach number of 0.8, where some nonlinearities because of the transonic nature of the flow might be expected, the agreement is good, although there is a somewhat larger lift overshoot downstream of the airfoil trailing edge compared to that predicted by the Euler method. The results in Fig. 8.37 also indicate that that the peak-to-peak value of the lift response becomes attenuated with increasing Mach number, which is exactly the opposite to the result obtained using quasi-steady, subsonic airfoil theory or incompressible unsteady airfoil theory. Also, it is apparent that the effects of increasing Mach number introduces a significantly larger phase lag in the lift response, which obviously becomes a critical consideration when accurate noise predictions are an issue (see also Question 8.12).

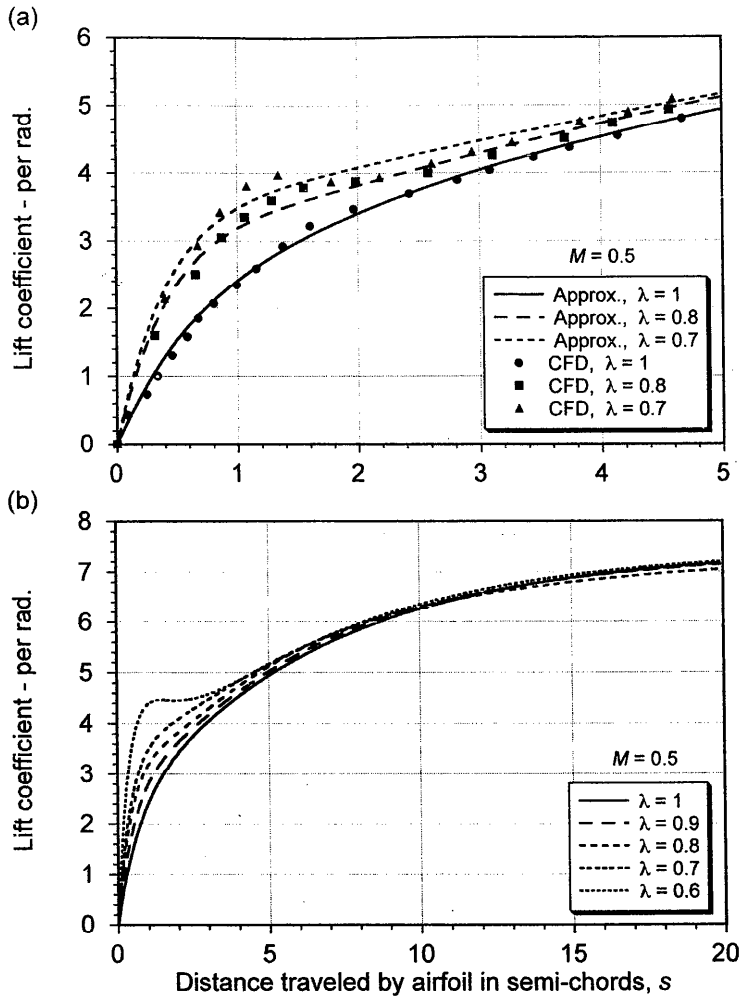

Figure 8.38 Convecting sharp-edged vertical gust indicial lift functions for different gust speed ratios at $M = 0.5$. (a) Short values of time. (b) Longer values of time.

8.16.5 *Convecting Vertical Gusts in Subsonic Flow*

In the subsonic case, the time-varying lift and pitching moment during the penetration of a convecting sharp-edged gust can only be found by numerical means. The problem, however, can be simplified if it is approached by using the reverse flow theorems, as discussed previously; see also Leishman (1997). Results for the lift on the airfoil penetrating a traveling sharp-edged gust at a Mach number of 0.5 are shown in Fig. 8.38 for various gust speed ratios. Results at other Mach numbers are qualitatively similar. Notice that the effect of increasing the gust convection velocity is to increase the rate of buildup of lift, analogous to the incompressible case shown previously in Figs. 8.23 and 8.24. For the subsonic case the center of pressure is always initially forward of the 1/4-chord as the airfoil penetrates into the gust front, but it moves back quickly again after the airfoil becomes fully immersed in the gust. After only a short time, the aerodynamic center is fully at the 1/4-chord.

Lift and pitching moment results for convecting sharp-edged gusts in subsonic flow have also been computed by Singh & Baeder (1997b) using an Euler CFD method. Representative

results for the lift are shown in Fig. 8.38 for a Mach number of 0.5 and for several gust speed ratios. Notice that in the early period where $s < 2M/(1 + M)$, or 0.67 semi-chords at this Mach number, the lift varies almost linearly with time as predicted by the exact subsonic linear theory, the rate of growth increasing with increasing gust convection velocity. The comparisons are excellent and lend significant credibility to the CFD results, which can provide valuable solutions for later values of time where exact analytic solutions are not possible. Like the incompressible results, the CFD results predict an initial lift overshoot for $s > 2M/(1 + M)$ that reaches a peak when the airfoil is about halfway into the gust.

To use the indicial method to examine arbitrary convecting vertical gust problems, the convecting sharp-edged gust solutions must be approximated by exponential functions. One suitable exponential approximation to the lift produced on an airfoil encountering a convecting sharp-edged gust is

$$\frac{C_l(s)}{w_0/V} = C_{l_\alpha}\left(1 - \sum_{i=1}^{N} G_i e^{-g_i s}\right) + G_{(N+1)}e^{-g_{(N+1)}s} - G_{(N+1)}e^{-g_{(N+2)}s}, \qquad (8.198)$$

where all the coefficients will, in general, be Mach number dependent. To satisfy the initial conditions at $s = 0$ then $\sum_{i=1}^{N} G_i = 1$. Also, $g_i > 0$ for $i = 1, \ldots, N + 2$. The transient shown in the lift response at small values of time for fast traveling gusts is represented by the second two terms in Eq. 8.198, where the coefficient G_{N+1} and the differences in the values of the time constants g_{N+1} and g_{N+2} will affect the size and width of this transient. Physically, this transient is a result of the accumulation of pressure waves. In the limit when $\lambda \to 0$, the magnitude of the transient approaches the piston theory value of $4/M$. Results of this procedure are shown in Fig. 8.38 for several gust speed ratios at a Mach number of 0.5. It is seen that while an exact fit to the initial transient at smaller values of λ cannot be obtained, an acceptable level of accuracy is possible for values of λ that are not too far from unity.

The problem of convecting vortices on the unsteady lift and noise generation has been addressed by Singh & Baeder (1997b) and Leishman (1997). Results for the unsteady lift on the airfoil for the same conditions of Fig. 8.37 are shown in Fig. 8.39 for several gust speed

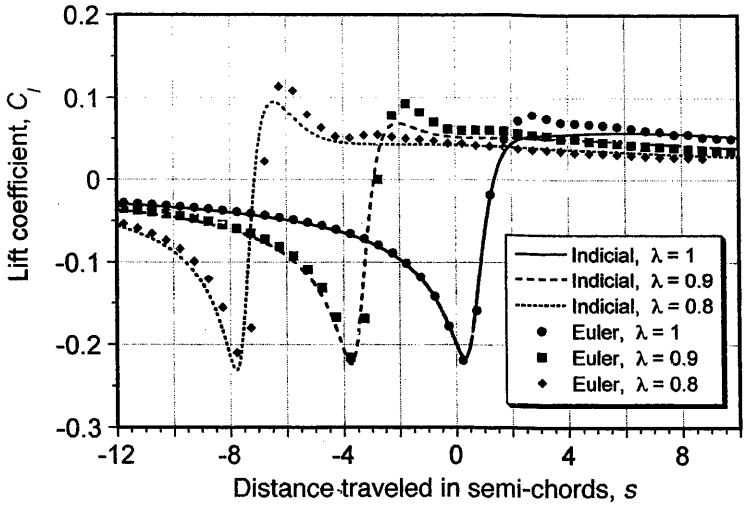

Figure 8.39 Indicial and Euler CFD predictions of unsteady lift for downstream convecting vortices. $\Gamma/V_\infty c = 0.2$, $h = -0.25c$, and $M = 0.5$.

ratios. The results are all referenced to the $\lambda = 1$ case, so that for downstream traveling vortices the BVI encounter occurs progressively earlier in time (or distance). We see that an increase in vortex convection speed (decrease in λ) progressively increases the peak-to-peak value of the unsteady lift, but more importantly, increases the time rate of change of lift. This will be reflected in the corresponding acoustic field, where the BVI sound pulse (see Fig. 8.48) will increase significantly in magnitude even for values of λ not too much lower than unity. Figure 8.39 also shows results for the BVI problem as computed directly using the Euler CFD method; the correlation of the indicial results with the Euler solution is excellent. Overall, these results confirm that the gust speed ratio of the tip vortices in the rotor wake will be a necessary parameter to account for in helicopter blade unsteady airloads and aeroacoustics analyses.

8.17 Time-Varying Incident Mach Number

As previously discussed in Section 8.13, for a rotor in forward flight a blade element will encounter a time-varying incident velocity and Mach number. Under these conditions, there are additional unsteady aerodynamic effects to be considered, including the effects of the nonuniform convection of the shed wake (see Fig. 8.25) as well as noncirculatory effects. If compressibility effects are to be included, the mathematical modeling of the problem becomes relatively difficult because, unlike the incompressible flow case, no exact solution can be found. However, extending the compressible indicial theory from the previous sections it can be shown that for nonsteady variations in Mach number at a constant AoA α that for the circulatory part of the unsteady lift

$$C_l^c(t, M) = \frac{1}{M}\left[\frac{2\pi\alpha M_0}{\beta_0}\phi^c(s) + \int_0^s \frac{2\pi\alpha}{\beta^3}\frac{dM}{d\sigma}(\sigma)\phi^c(s-\sigma)\,d\sigma\right], \tag{8.199}$$

and for the noncirculatory part of the unsteady lift

$$C_l^{nc}(t) = \int_0^s \frac{4\alpha}{M^2}\frac{dM}{d\sigma}(\sigma)\exp\left[-\left(\frac{s-\sigma}{T_\alpha}\right)\right]d\sigma, \tag{8.200}$$

where M_0 is the initial Mach number and all the symbols have their usual meanings as defined in the preceding sections. See Jose & Leishman (2005) for details.

Representative calculated results are shown in Fig. 8.40 for time-dependent free-stream Mach number variations with the airfoil at a constant angle of attack, and are compared with direct CFD calculations based on an Euler method. Notice again the applicability of the indicial method for this type of calculation, which is several orders of magnitude more computationally efficient than the CFD solution, and so is ideal for various forms of helicopter rotor analyses where the treatment of these unsteady effects is necessary. It will be apparent that the unsteady incompressible flow theory (see Section 8.13) fails for these conditions, again emphasizing that the proper treatment of compressibility effects will be necessary if accurate unsteady airloads predictions are to be obtained on the rotor.

8.18 Unsteady Aerodynamics of Flaps

With the advent of smart structures it is now becoming increasingly feasible to use smart compliant airfoil surfaces or several trailing edge mounted flaps on rotor blades

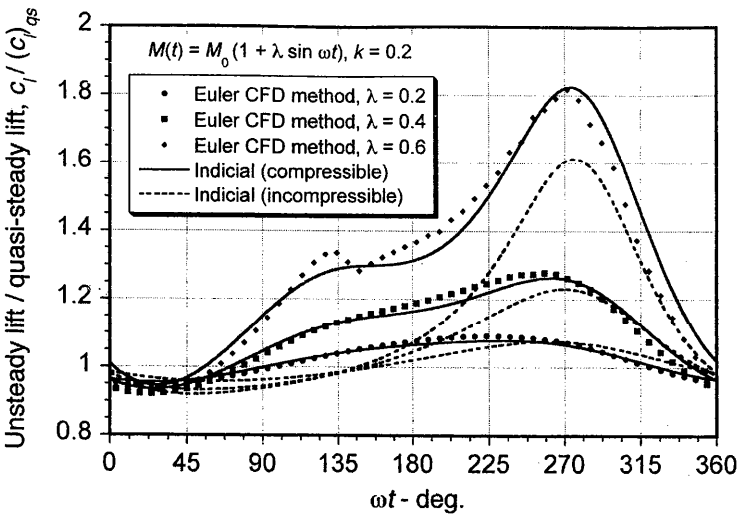

Figure 8.40 The effects of a nonsteady free-stream Mach number variations on the unsteady lift for an airfoil with a constant AoA at a mean value of $M_0 = 0.5$. (CFD calculations courtesy of Arun Jose.)

as a means of individually controlling the aerodynamic environment on each blade – see Section 6.12. Actively controlling the blade airloads as a function of blade azimuth position offers tremendous possibilities in improving helicopter rotor performance, as well as reducing blade loads and vibration levels and perhaps even reducing rotor noise. See Lorber (2000) and Friedmann (2004) for a good summary of what may be possible. However, practical concern of active blade adaptation through the application of flaps, airfoil camber or other chordwise shape changes is the availability of suitable low mass, high force actuators. These actuators must also be mounted inside the rotating blade and must be used to drive the aerodynamic surfaces at relatively high physical and reduced frequencies.

Theoretical studies of these types of moving flap problems using advanced helicopter rotor models require the use of a suitably formulated time-domain theory for the blade section aerodynamics. An unsteady aerodynamic theory is required, first because the local camber actuation frequency may be several multiples of the rotor rotational frequency and, second, because high resolution predictions of both the unsteady airloads and acoustics need to be made. In addition, because the local effective reduced frequencies based on active camber motion may become large, incompressible assumptions may not be adequate despite the exact analytical neatness of the theory.

8.18.1 *Incompressible Flow Theory*

The prediction of unsteady lift, airfoil pitching moment and the hinge moment on an airfoil for a harmonic flap oscillation in incompressible flow has been studied by Küssner & Schwartz (1941), Theodorsen (1935), and Theodorsen & Garrick (1942) by means of unsteady thin airfoil theory. The results are known exactly for the frequency domain and can be reformulated in the time-domain with arbitrary flap motion using Duhamel superposition. Other contributions have been made by Drescher (1952). As shown previously for an incompressible flow, the unsteady lift and moment coefficients on a thin airfoil

can be written as

$$C_n = \frac{\pi b}{V^2}\left(V\dot{\alpha} + \ddot{h} - ba\ddot{\alpha}\right) + 2\pi C(k)\left[\frac{\dot{h}}{V} + \alpha + b\left(\frac{1}{2} - a\right)\frac{\dot{\alpha}}{V}\right] \tag{8.201}$$

and

$$C_m = -\frac{\pi}{2V^2}\left[\left(\frac{1}{8} + a^2\right)\ddot{\alpha} - ab\ddot{h}\right] + \pi\left(a + \frac{1}{2}\right)C(k)\left[\frac{\dot{h}}{V} + \alpha + b\left(\frac{1}{2} - a\right)\frac{\dot{\alpha}}{V}\right] - \frac{\pi}{2V^2}\left[V\left(\frac{1}{2} - a\right)\dot{\alpha}\right]. \tag{8.202}$$

The first term in each of the above equations is the noncirculatory (apparent mass) component. The second group of terms in the equations are all circulatory components, with the Theodorsen function $C(k)$ accounting for the influence of the shed wake vorticity.

With the addition of a trailing edge flap hinged at eb (measured from the mid-chord) there are additional airloads produced that depend on the flap deflection angle, δ, and its time rate-of-change, $\dot{\delta}$ – see Fig. 8.41. These additional terms are

$$C_n^f = \frac{b}{V^2}\left(-VF_4\dot{\delta} - bF_1\ddot{\delta}\right) + 2\pi C(k)\left(\frac{F_{10}\delta}{\pi} + \frac{bF_{11}\dot{\delta}}{2\pi V}\right) \tag{8.203}$$

and

$$C_m^f = -\frac{1}{2V^2}\left[\left(F_7 + (e-a)F_1\right)b^2\ddot{\delta}\right] + \pi\left(a + \frac{1}{2}\right)C(k)\left(\frac{F_{10}\delta}{\pi} + \frac{bF_{11}\dot{\delta}}{2\pi V}\right) - \frac{1}{2V^2}\left\{\left(F_4 + F_{10}\right)V^2\delta + \left[F_1 - F_8 - (e-a)F_4 + \frac{1}{2}F_{11}\right]Vb\dot{\delta}\right\}, \tag{8.204}$$

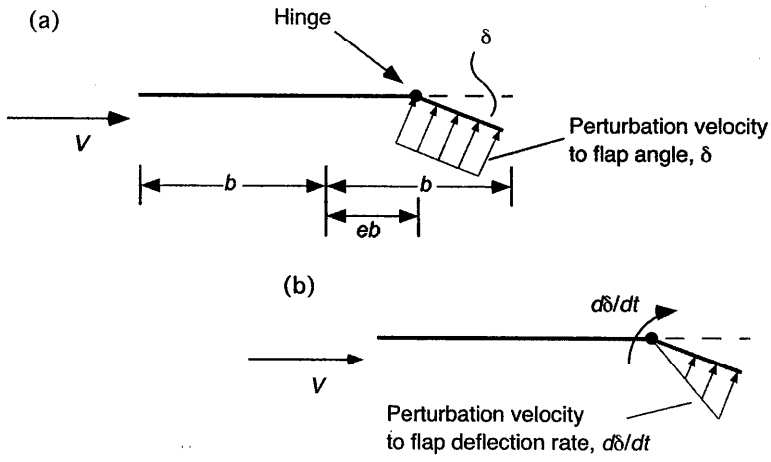

Figure 8.41 Nomenclature for airfoil with a trailing edge flap. Perturbation velocities are produced by trailing edge motion: (a) flap displacement, (b) angular rate about the hinge.

where, again, the first group of terms in each equation are of noncirculatory origin. The addition of the trailing edge flap also gives rise to a hinge moment, which is

$$C_h = -\frac{1}{2V^2}\left(2F_{13}b^2\ddot{\alpha} - F_1 b\ddot{h}\right) - \frac{F_{12}}{2}C(k)\left[\frac{\dot{h}}{V} + \alpha + b\left(\frac{1}{2} - a\right)\frac{\dot{\alpha}}{V}\right]$$
$$-\frac{1}{2V^2}\left\{\left[-2F_9 - F_1 + F_4\left(a - \frac{1}{2}\right)\right]Vb\dot{\alpha}\right\} \tag{8.205}$$

and

$$C_h^f = -\frac{1}{2V^2}\left[-\frac{1}{\pi}F_3 b^2\ddot{\delta}\right] - \frac{F_{12}}{2}C(k)\left[\frac{1}{\pi}F_{10}\delta + b\frac{1}{2\pi}\frac{F_{11}}{V}\dot{\delta}\right]$$
$$-\frac{1}{2V^2}\left[\frac{1}{\pi}V^2(F_5 - F_4F_{10})\delta - \frac{1}{2\pi}Vb\dot{\delta}F_4F_{11}\right], \tag{8.206}$$

where the individual contributions to the hinge moment in response to the airfoil motion and in response to the flap have been written out explicitly. In the above equations, the "F" terms are geometric constants that depend only on the size of the flap relative to the airfoil chord and are listed by Theodorsen (1935) and by Hariharan & Leishman (1996).

Because of the linear assumption in the thin-airfoil theory, the loading contributions from the airfoil and from the flap can be obtained by superposition. Therefore, the lift, pitching moment and hinge moment in response to independent oscillatory airfoil motion and oscillatory flap motion can be written in coefficient form as

$$C_n(t) = C_n^{nc}(t) + 2\pi C(k)\left(\alpha_{qs} + \delta_{qs}\right), \tag{8.207}$$

$$C_m(t) = C_m^{nc}(t) + \pi\left(a + \frac{1}{2}\right)C(k)\left(\alpha_{qs} + \delta_{qs}\right) + C_m^{qs}(t) \tag{8.208}$$

and

$$C_h(t) = C_h^{nc}(t) + \frac{F_{12}}{2}C(k)\left(\alpha_{qs} + \delta_{qs}\right) + C_h^{qs}(t), \tag{8.209}$$

where

$$C_n^{nc}(t) = \frac{\pi b\dot{\alpha}}{V} + \frac{b}{V^2}\left[\pi\ddot{h} - \pi ba\ddot{\alpha} - VF_4\dot{\delta} - bF_1\ddot{\delta}\right], \tag{8.210}$$

$$C_m^{nc}(t) = -\frac{\pi}{2V^2}\left[\left(\frac{1}{8} + a^2\right)\ddot{\alpha} - ab\ddot{h}\right] - \frac{1}{2V^2}\left[F_7 + (e-a)F_1\right]b^2\ddot{\delta}, \tag{8.211}$$

$$C_m^{qs}(t) = -\frac{1}{2V^2}\left\{\pi V\left(\frac{1}{2} - a\right)b\dot{\alpha} + (F_4 + F_{10})V^2\delta\right.$$
$$\left.+\left[F_1 - F_8 - (e-a)F_4 + \frac{1}{2}F_{11}\right]Vb\dot{\delta}\right\}, \tag{8.212}$$

$$C_h^{nc}(t) = -\frac{1}{2V^2}\left(2F_{13}b^2\ddot{\alpha} - F_1 b\ddot{h} - \frac{1}{\pi}F_3 b^2\ddot{\delta}\right), \tag{8.213}$$

and

$$C_h^{qs}(t) = -\frac{1}{2V^2}\left\{\left[-2F_9 - F_1 + F_4\left(a - \frac{1}{2}\right)\right] Vb\dot{\alpha} + \frac{1}{\pi}V^2(F_5 - F_4F_{10})\delta - \frac{1}{2\pi}Vb\dot{\delta}F_4F_{11}\right\}. \tag{8.214}$$

Notice that in these foregoing expressions several terms have been grouped together; α_{qs} is the quasi-steady airfoil AoA and δ_{qs} is the quasi-steady AoA in response to the imposed flap motion as given by

$$\alpha_{qs} = \left[\frac{\dot{h}}{V} + \alpha + b\left(\frac{1}{2} - a\right)\frac{\dot{\alpha}}{V}\right] \quad \text{and} \quad \delta_{qs} = \left[\frac{F_{10}\delta}{\pi} + \frac{bF_{11}\dot{\delta}}{2\pi V}\right]. \tag{8.215}$$

The foregoing equations hold good only for oscillatory motion of the airfoil and/or the flap. However as shown previously the results can be transformed to handle arbitrary motion by means of Duhamel's superposition integral with the Wagner indicial (step) response. In the time domain, the unsteady aerodynamic loads can be written as

$$C_n(t) = C_n^{nc}(t) + 2\pi\left[\alpha_{qs}(0)\phi_W(s) + \int_0^s \frac{d\alpha_{qs}}{d\sigma}\phi(s-\sigma)d\sigma\right] + 2\pi\left[\delta_{qs}(0)\phi_W(s) + \int_0^s \frac{d\delta_{qs}}{d\sigma}\phi(s-\sigma)d\sigma\right], \tag{8.216}$$

$$C_m(t) = C_m^{nc}(t) + C_m^{qs}(t) + \pi\left(a + \frac{1}{2}\right)\left[\alpha_{qs}(0)\phi_W(s) + \int_0^s \frac{d\alpha_{qs}}{d\sigma}\phi(s-\sigma)d\sigma\right] + \pi\left(a + \frac{1}{2}\right)\left[\delta_{qs}(0)\phi_W(s) + \int_0^s \frac{d\delta_{qs}}{d\sigma}\phi(s-\sigma)d\sigma\right], \tag{8.217}$$

and

$$C_h(t) = C_h^{nc}(t) + C_h^{qs}(t) + \frac{F_{12}}{2}\left[\alpha_{qs}(0)\phi_W(s) + \int_0^s \frac{d\alpha_{qs}}{d\sigma}\phi(s-\sigma)d\sigma\right] + \frac{F_{12}}{2}\left[\delta_{qs}(0)\phi_W(s) + \int_0^s \frac{d\delta_{qs}}{d\sigma}\phi(s-\sigma)d\sigma\right], \tag{8.218}$$

where ϕ_W is the Wagner function. This can be written approximately using an exponential function, as shown in Section 8.10. Using these results state-space equivalent arbitrary airfoil motion can then be written as

$$C_{n_\alpha}^c(t) = 2\pi\left[(b_1b_2/2)\left(\frac{V}{b}\right)^2(A_1b_1 + A_2b_2)\left(\frac{V}{b}\right)\right]\begin{bmatrix} z_1(t) \\ z_2(t)\end{bmatrix} + \pi\alpha_{qs}(t), \tag{8.219}$$

$$C_{m_\alpha}^c(t) = \pi\left(a + \frac{1}{2}\right)\left[(b_1b_2/2)\left(\frac{V}{b}\right)^2(A_1b_1 + A_2b_2)\left(\frac{V}{b}\right)\right]\begin{bmatrix} z_1(t) \\ z_2(t)\end{bmatrix} + \frac{\pi}{2}\left(a + \frac{1}{2}\right)\alpha_{qs}(t), \tag{8.220}$$

and

$$C^c_{h_\alpha}(t) = \frac{F_{12}}{2}\left[(b_1b_2/2)\left(\frac{V}{b}\right)^2 (A_1b_1 + A_2b_2)\left(\frac{V}{b}\right)\right]\begin{bmatrix} z_1(t) \\ z_2(t)\end{bmatrix} + \frac{F_{12}}{4}\alpha_{qs}(t), \quad (8.221)$$

where

$$\begin{bmatrix}\dot{z}_1(t) \\ \dot{z}_2(t)\end{bmatrix} = \begin{bmatrix} 0 & 1 \\ -b_1b_2\left(\frac{V}{b}\right)^2 & -(b_1+b_2)\left(\frac{V}{b}\right)\end{bmatrix}\begin{bmatrix} z_1(t) \\ z_2(t)\end{bmatrix} + \begin{bmatrix} 0 \\ 1\end{bmatrix}\alpha_{qs}(t). \quad (8.222)$$

For arbitrary trailing edge flap motion, the state-space form for the unsteady airloads can be written in a similar form. The output equations for the loads are

$$C^c_{n_\delta}(t) = 2\pi\left[(b_1b_2/2)\left(\frac{V}{b}\right)^2 (A_1b_1 + A_2b_2)\left(\frac{V}{b}\right)\right]\begin{bmatrix} z_3(t) \\ z_4(t)\end{bmatrix} + \pi\delta_{qs}(t), \quad (8.223)$$

$$C^c_{m_\delta}(t) = \pi\left(a + \frac{1}{2}\right)\left[(b_1b_2/2)\left(\frac{V}{b}\right)^2 (A_1b_1 + A_2b_2)\left(\frac{V}{b}\right)\right]\begin{bmatrix} z_3(t) \\ z_4(t)\end{bmatrix} + \frac{\pi}{2}\left(a + \frac{1}{2}\right)\delta_{qs}(t), \quad (8.224)$$

and

$$C^c_{h_\delta}(t) = \frac{F_{12}}{2}\left[(b_1b_2/2)\left(\frac{V}{b}\right)^2 (A_1b_1 + A_2b_2)\left(\frac{V}{b}\right)\right]\begin{bmatrix} z_3(t) \\ z_4(t)\end{bmatrix} + \frac{F_{12}}{4}\delta_{qs}(t), \quad (8.225)$$

where

$$\begin{bmatrix}\dot{z}_3(t) \\ \dot{z}_4(t)\end{bmatrix} = \begin{bmatrix} 0 & 1 \\ -b_1b_2\left(\frac{V}{b}\right)^2 & -(b_1+b_2)\left(\frac{V}{b}\right)\end{bmatrix}\begin{bmatrix} z_3(t) \\ z_4(t)\end{bmatrix} + \begin{bmatrix} 0 \\ 1\end{bmatrix}\delta_{qs}(t). \quad (8.226)$$

Notice that the coefficient terms in the foregoing equations for the flap are the same as for the AoA terms. This is because the circulatory lag function itself [i.e., $C(k)$ or ϕ_W] does not depend on the mode of forcing for incompressible flow (i.e., it does not depend on α, $\dot{\alpha}$, δ, or $\dot{\delta}$). Furthermore, the noncirculatory components and the contributions in response to the quasi-steady terms of the lift, pitching moment and the hinge moment are proportional to the instantaneous displacements for an incompressible flow and involve no additional states. They can be computed directly using Eqs. 8.210–8.214. The circulatory lift acts at the aerodynamic center but there are no additional states required to calculate the pitching moment. Therefore, the complete aerodynamic system for the airfoil and flap in an incompressible flow can be represented by a set of four aerodynamic states. Although it is convenient to separate out the circulatory lift in response to airfoil motion from that in response to the flap motion, in a practical application their net effects can be combined so that, in fact, only two states are required to compute the net circulatory airloads.

8.18.2 *Subsonic Flow Theory*

As previously described there are no equivalent exact results that are analogous to Theodorsen's theory or Wagner's solution for the unsteady airloads on airfoils in subsonic compressible flow. Here, both the circulatory and the noncirculatory loads have different time-history effect. As shown in Section 8.15 the initial loading on an airfoil operating in a compressible flow can be computed directly using piston theory. For indicial flap

motion (i.e., displacements and rates – see Fig. 8.41) about a hinge located e semi-chords downstream of mid-chord, the initial values airloads according to piston theory are

$$\Delta C_{n_\delta}(s=0, M) = \frac{2(1-e)}{M}\Delta\delta, \tag{8.227}$$

$$\Delta C_{n_{\dot\delta}}(s=0, M) = \frac{(1-e)^2}{2M}\left(\frac{\Delta\dot\delta c}{V}\right), \tag{8.228}$$

$$\Delta C_{m_\delta}(s=0, M) = -\frac{(1-e)(2+e)}{2M}\Delta\delta, \tag{8.229}$$

$$\Delta C_{m_{\dot\delta}}(s=0, M) = -\frac{1}{12M}\left[(1+e)^3 - (12e-4) - \frac{3}{2}(1-e)^2\right]\left(\frac{\Delta\dot\delta c}{V}\right), \tag{8.230}$$

$$\Delta C_{h_\delta}(s=0, M) = -\frac{(1-e)^2}{2M}\Delta\delta, \tag{8.231}$$

and

$$\Delta C_{h_{\dot\delta}}(s=0, M) = -\frac{(1-e)^3}{6M}\left(\frac{\Delta\dot\delta c}{V}\right). \tag{8.232}$$

These results are valid for any Mach number, but only at $s = 0$ when the perturbation (δ or $\dot\delta$) is applied. The final values of the indicial response are given by the linearized subsonic airfoil theory, so that for indicial flap displacements

$$\Delta C_{n_\delta}(s=\infty, M) = \frac{2F_{10}}{\beta}\Delta\delta, \tag{8.233}$$

$$\Delta C_{n_{\dot\delta}}(s=\infty, M) = \frac{F_{11}}{2\beta}\left(\frac{\Delta\dot\delta c}{V}\right), \tag{8.234}$$

$$\Delta C_{m_\delta}(s=\infty, M) = -\frac{F_4 + F_{10}}{2\beta}\Delta\delta, \tag{8.235}$$

$$\Delta C_{m_{\dot\delta}}(s=\infty, M) = -\frac{2F_1 - 2F_8 - (2e+1)F_4 + F_{11}}{8\beta}\left(\frac{\Delta\dot\delta c}{V}\right), \tag{8.236}$$

$$\Delta C_{h_\delta}(s=\infty, M) = -\frac{(F_5 - F_4F_{10}) + F_{12}F_{10}}{2\pi\beta}\Delta\delta, \tag{8.237}$$

and

$$\Delta C_{h_{\dot\delta}}(s=\infty, M) = -\frac{F_{11}(F_{12} - F_4)}{4\pi\beta}\left(\frac{\Delta\dot\delta c}{V}\right). \tag{8.238}$$

The indicial response functions define the behavior between $s = 0$ and $s = \infty$. The indicial lift, airfoil pitching moment and hinge moment coefficients in response to impulsive flap deflection (about some hinge axis at e) can be written in general functional form as a sum of noncirculatory and circulatory parts, as for the airfoil contributions shown previously, that is,

$$\Delta C_{n_\delta}(s, M, e) = \left[\frac{2(1-e)}{M}\phi^{nc}_{n_\delta}(s, M, e) + \frac{2F_{10}}{\beta}\phi^{c}_{n_\delta}(s, M, e),\right]\Delta\delta, \tag{8.239}$$

$$\Delta C_{n_{\dot\delta}}(s, M, e) = \left[\frac{(1-e)^2}{2M}\phi^{nc}_{n_{\dot\delta}}(s, M, e) + \frac{F_{11}}{2\beta}\phi^{c}_{n_{\dot\delta}}(s, M, e)\right]\left(\frac{\Delta\dot\delta c}{V}\right), \tag{8.240}$$

$$\Delta C_{m_\delta}(s, M, e) = -\left[\frac{(1-e)(2+e)}{2M}\phi^{nc}_{m_\delta}(s, M, e) + \frac{F_4 + F_{10}}{2\beta}\phi^{c}_{m_\delta}(s, M, e)\right]\Delta\delta, \tag{8.241}$$

$$\Delta C_{m_{\dot\delta}}(s, M, e) = -\left\{\frac{1}{12M}\left[(1+e)^3 - (12e-4) - \frac{3}{2}(1-e)^2\right]\phi^{nc}_{m_{\dot\delta}}(s, M, e) + \frac{2F_1 - 2F_8 - (2e+1)F_4 + F_{11}}{8\beta}\phi^{c}_{m_{\dot\delta}}(s, M, e)\right\}\left(\frac{\Delta\dot\delta c}{V}\right), \tag{8.242}$$

$$\Delta C_{h_\delta}(s, M, e) = -\left[\frac{(1-e)^2}{2M}\phi^{nc}_{h_\delta}(s, M, e) + \frac{(F_5 - F_4F_{10}) + F_{12}F_{10}}{2\pi\beta}\phi^{c}_{h_\delta}(s, M, e)\right]\Delta\delta, \tag{8.243}$$

and

$$\Delta C_{h_{\dot\delta}}(s, M, e) = -\left[\frac{(1-e)^3}{6M}\phi^{nc}_{h_{\dot\delta}}(s, M, e) + \frac{F_{11}(F_{12} - F_4)}{4\pi\beta}\phi^{c}_{h_{\dot\delta}}(s, M, e)\right]\left(\frac{\Delta\dot\delta c}{V}\right), \tag{8.244}$$

where the indicial response functions ϕ represent the intermediate behavior of the respective indicial airloads between $s = 0$ and $s = \infty$. The definition of all of these indicial functions is given by Leishman (1994) and Hariharan & Leishman (1996), including the numerical procedures that can be used to manipulate these indicial functions to find the unsteady airloads in response to arbitrary flap motion such as in the recurrence or state-space forms.

8.18.3 *Comparison with Measurements*

The preceding theoretical development applies to flaps that do not lose their effectiveness because of viscous effects. In practice a trailing edge flap may operate in a relatively thick turbulent boundary layer because the flap hinge produces a locally adverse pressure gradient that tends to thicken the boundary layer. This will alter the effective flap camber, reducing the flap effectiveness for a given flap deflection angle – see White & Landahl (1968). In addition, the influence of the flap hinge geometry and the possibility of a gap at the hinge leads to additional viscous effects that may adversely alter the relationship between the flap deflection angle and the aerodynamic forces and moments – see Gray & Davies (1972). To a first order it is possible to account for such effects by the application of flap effectiveness coefficients. However, because the lift, moment, and hinge moment will be influenced to different degrees by viscosity, the effectiveness of each component of the loading must be considered separately. Flap effectiveness coefficients can be derived most accurately by empirical means on the basis of quasi-steady flow considerations; that is, based only on circulatory effects and with regard to measurements of the aerodynamic coefficients at very low reduced frequency with flap angle and gap size. Therefore, the actual aerodynamic forces and moments will be the linear theory values multiplied by constant terms, say ϵ_n, ϵ_m, and ϵ_h, which may be functions of Reynolds and Mach number.

Experimental results for a NACA 64A006 airfoil with an oscillating plain flap are reported by Tijdeman & Schippers (1973). The main emphasis in this work was for the high subcritical and transonic flow cases, but results are given for shock-free flow and weak transonic conditions. Under these conditions nonlinear effects are relatively mild and the results can be expected to provide a useful basis for comparison with the foregoing incompressible and compressible flow theories. Some additional results for an oscillating flap on a NLR 7301 airfoil are given by Zwaan (1982a,b), although these data are more limited. From the equations given previously, the response to a particular harmonic motion of the flap can be derived.

Representative results are shown in Fig. 8.42 for two conditions, one at the lowest Mach number of 0.5 and the other for $M = 0.748$. Also included in these plots are results from the incompressible theory, but with the lift curve slope corrected by the Glauert compressibility factor $1/\beta$. When plotted versus flap displacement angle, as shown in Figs. 8.42(a) and (b), the lift coefficient curve exhibits a characteristic elliptical loop that is similar to that obtained on an airfoil oscillating in angle of attack. A flap lift effectiveness of $\epsilon_n = 0.70$ was determined from the real part of the aerodynamic response at zero frequency and this value was assumed to be constant over the entire Mach number and frequency range. Notice that in Fig. 8.42(a) and (b) the lift loops are circumvented in a counterclockwise direction, corresponding to a phase lag. At higher flap oscillation frequencies, the lift will develop a phase lead as the noncirculatory terms begin to dominate. However, the effects of increasing free-stream Mach number tends to increase the circulatory lag, which means that the lift mostly lags the flap forcing over the range of conditions typically encountered in practice. This is shown for the $M = 0.748$ case in Fig. 8.42(b), where despite the higher reduced frequency the phase lag is considerably greater. Notice that the incompressible results do not correlate as well with the experimental results; the incompressible theory does not predict the phasing correctly at the Mach numbers typical of helicopter rotors.

Figures 8.42(c) and (d) show that the airfoil pitching moment behaves in an almost quasi-steady manner. A value of $\epsilon_m = 0.96$ was found to be applicable for this component of the loading. Here, the pitching moment loops are circumvented in a clockwise sense,

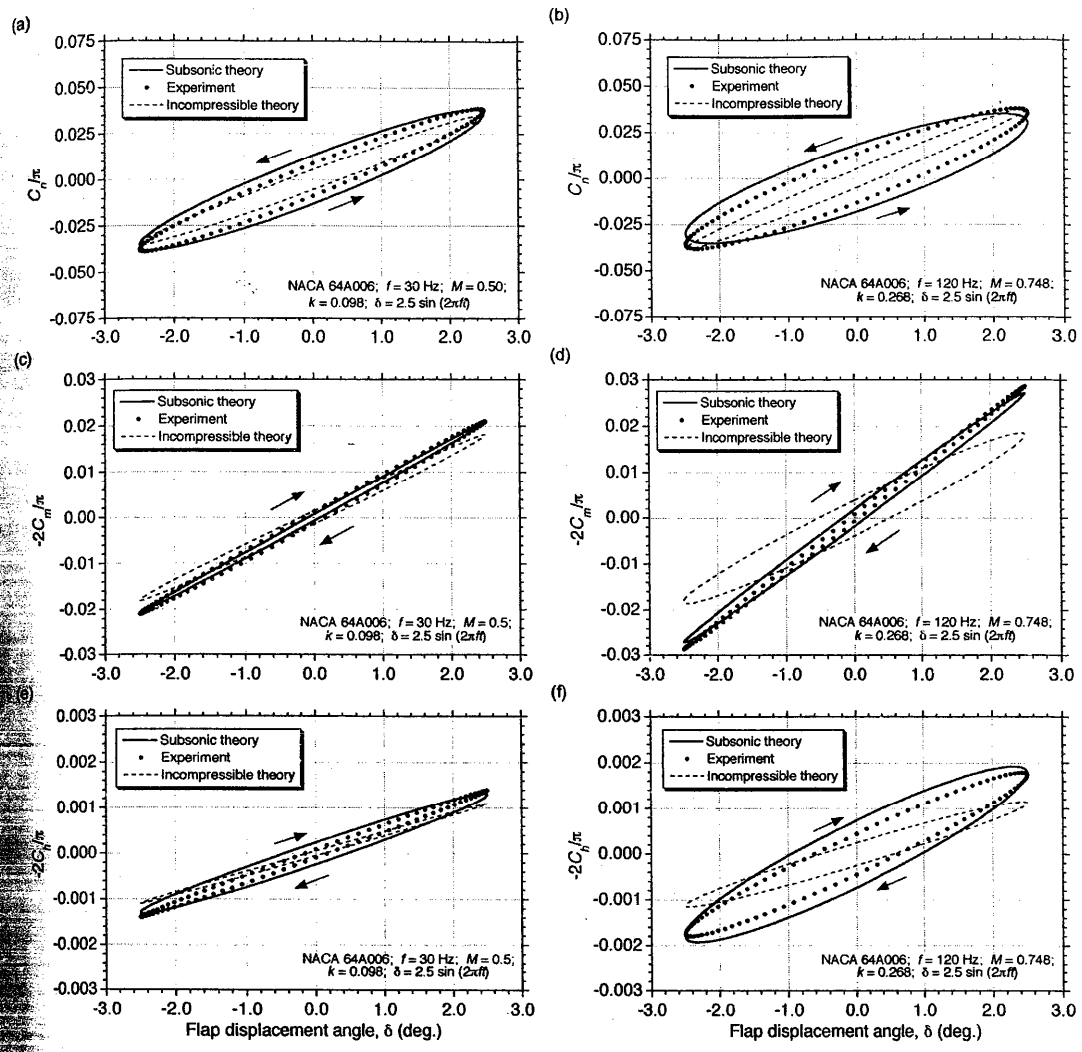

Figure 8.42 Comparison of unsteady airfoil theory with experimental data for an oscillating flap in subsonic flow with schedule $\delta(t) = 2.5° \sin \omega t$. (a) Lift coefficient, $M = 0.5$, (b) Lift coefficient, $M = 0.748$, (c) Pitching moment coefficient, $M = 0.5$, (d) Pitching moment coefficient, $M = 0.748$, (e) Hinge moment coefficient, $M = 0.5$, (f) Hinge moment coefficient, $M = 0.748$. Data source: NACA 64A006 airfoil tests by Tijdeman & Schippers (1973).

but the phase lead is small. In general, there is a weak effect of both Mach number and frequency on the unsteady airfoil pitching moment, and it would be adequately predicted in the general case if quasi-steady conditions were assumed. Figures 8.42(e) & (f) show that the flap hinge moment experiences a considerably more powerful unsteady effect. This component is probably the most difficult quantity to predict accurately because it is sensitive to viscous effects; the flap airloads are strongly influenced by the local geometry and pressure gradients produced near the flap hinge. As discussed previously, such effects are usually corrected for empirically and a hinge moment effectiveness of $\epsilon_h = 0.68$ was inferred from the quasi-steady aerodynamic data for this airfoil section. In this case there is a phase lead

between the response and the forcing, giving loops that are circumvented in a clockwise direction. Again, this is because of the noncirculatory terms, which play an important role in determining the aerodynamic response at higher flap frequencies. In this case, even when the free-stream Mach number is low, the disturbances do not propagate sufficiently quickly relative to the flap motion for the flow to be considered as incompressible.

8.19 Principles of Noise Produced by Unsteady Forces

The intensity and directivity of the noise generated by a helicopter is of considerable importance in both civilian and military operations. The field of aerodynamically generated noise is called *aeroacoustics* and in the case of helicopter rotors it involves several distinct areas of study – see Schmitz (1991) and Brentner & Farassat (2003). Today there are strict certification and community noise constraints that apply to helicopters, especially during takeoffs and landings – see Lowson (1992). There is also a need to abate noise to reduce detectability in military helicopter operations.

One obtrusive source of noise from a helicopter is from the main rotor, which generally occurs at low frequency and high amplitude. It is often referred to as discrete frequency noise. There are two types of discrete frequency noise, namely blade vortex interaction or BVI noise and high-speed impulsive or HSI noise – see Fig. 8.43. The tail rotor (if one is used) is also a contributor to the overall noise spectrum of a helicopter, tail rotor noise being of higher frequency and often appearing over a wider range of frequencies. Engine noise tends to be at higher frequencies. Other types of noise, called broadband noise, comes from a variety of sources such as boundary layer noise, airframe noise, including ingestion of other parts of the wake and turbulence into the rotor. A plethora of models exist to predict helicopter rotor acoustics these ranging from purely empirical methods to wave tracing methods, to blade element type unsteady aerodynamics models coupled with Ffowcs Williams-Hawking's (FW-H) methods, to modern CFD-type methods.

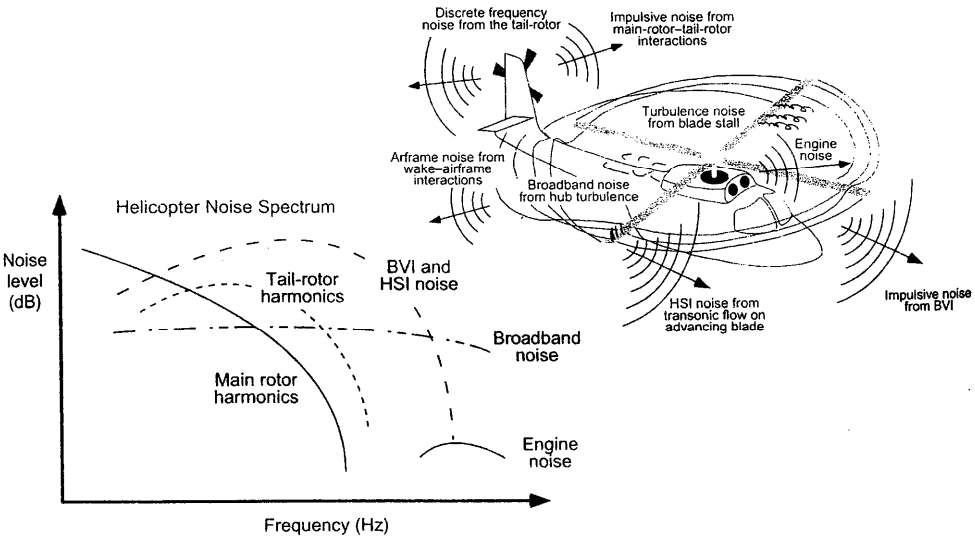

Figure 8.43 Helicopter noise has many different sources and appears at many different frequencies with different intensities. Adapted from Edwards & Cox (2002).

A large proportion of noise is generated by the unsteady aerodynamic forces, such as interactions of the blades with the wake or with discrete tip vortices, the so-called BVI problem, which has been discussed previously in Section 8.16.4. See Widnall (1971), George (1978), Schmitz & Yu (1986), and Schmitz (1991) for detailed discussions of the BVI noise phenomenon. BVI noise can become stronger when the leading edge of the blade becomes parallel to the axis of the tip vortex, which occurs primarily on the advancing and retreating sides of the rotor disk in forward flight. The BVI noise problem can be especially acute during descending low speed forward flight or during maneuvering flight, where the tip vortices tend to lie closer to the rotor.

The highly 3-D unsteady aerodynamics produced by the various BVI events on the blades give rise to multiple noise sources with different directivity and phase relationships. The net sound field, therefore, comprises complicated interfering omnidirectional traveling sound waves, but often highly focused, acoustic wave paths are produced as well. Besides the high computational cost of finding the rotor airloads themselves, which almost certainly will involve the use of unsteady aerodynamic models and free-vortex wake models (see Section 10.7.6). high costs are associated with evaluating the acoustics after the airloads are determined. For example, a typical acoustics calculation may use tens of thousands of observer points to map out the sound field from the rotor, so it becomes very expensive to systematically map out the directivity of the critical regions in the acoustic field. Furthermore, because of the typically pronounced directivity associated with BVI noise there is a very real possibility that localized regions that experience sound focusing effects can be missed, even by using very large numbers of observer points. This may result in misleading comparisons between different rotors and/or at different flight conditions. Overall, the prediction of the noise from a helicopter continues to be an extremely challenging research problem from both a theoretical and applications perspective; see Brentner & Farassat (2003) for a good review of the field.

Because of the complicated wake structure on an helicopter rotor in forward flight, where vortices can lie at many different orientations and inclinations with respect to the blades (see Figs 10.12 and 10.13), it has not yet proven possible to model the aeroacoustics of a helicopter rotor to the fidelity necessary for acceptable predictions without empirical correction, nor with reasonable computing costs. Most aeroacoustic models, however, have been shown to give good noise predictions for idealized problems, such as the interactions of blades with rectilinear-type vortices – see Caradonna et al. (1997) and Sim et al. (1997) for comparisons for idealized problems using different approaches. Several idealized BVI experiments have also been conducted – see Surendraiah (1970), Seath et al. (1987), Kokkalis & Galbraith (1986), Kitaplioglu & Caradonna (1994), and Kitaplioglu et al. (1997), who have provided valuable measurements to validate aeroacoustic predictions.

Most of the recent work on modeling the aeroacoustic effects of BVI, however, has concentrated on complete CFD solutions, an example being given by Strawn (1997). However, complete first-principles based CFD approaches for rotor aeroacoustics are not yet practical, in part, because of significant numerical dissipation and dispersion errors (see Chapter 14). Furthermore, while coupled CFD based methods have provided much insight into various rotor aeroacoustic phenomena they are still only research tools and far too computationally expensive for routine use or for the parametric studies that would be necessary for rotor design. Bearing in mind that any aeroacoustic model must be properly coupled to a structural dynamic model of the rotor blades, and perhaps also to a flight dynamics simulation, there are clearly many limitations on what quantitative level of acoustic predictive capability for helicopters can be genuinely achieved in the shorter term.

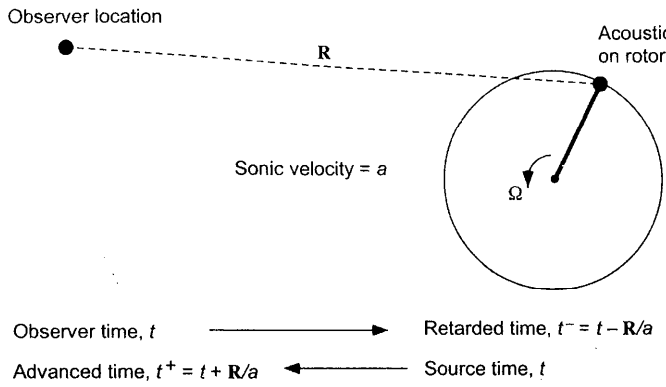

Figure 8.44 Ideas of retarded time and advanced time.

8.19.1 *Retarded Time and Source Time*

A key issue in any acoustic problem is the determination of the time of arrival of sound waves at a given observer location in 3-D space. The evaluation of the acoustic field requires accounting for either the time of emission of a sound wave from a source point relative to the current or observer time (i.e., a *retarded time* calculation), or the time of arrival of a sound wave relative to a given source time (i.e., an *advanced time* calculation). Acoustic waves travel at the speed of sound plus or minus the local velocity of the fluid in which the waves propagate. This may be a nonuniform velocity field, which of course requires that this be known a priori for the acoustics calculation. For example, in a stationary flow the retarded time of the emission of a sound wave after it has traveled a distance **R** to reach the observer at time t is given by

$$\tau = t^- = t - \frac{\mathbf{R}}{a}, \tag{8.245}$$

or in a flow with velocity v in the direction of **R** the retarded time is

$$\tau = t^- = t - \frac{\mathbf{R}}{v + a}. \tag{8.246}$$

Of course, this means that the intensity of the acoustic source on the rotor must not be evaluated at the present time but according what happened at a past or retarded time, as illustrated schematically in Fig. 8.44. This is essentially a temporal mapping process and is fundamental to any type of acoustic calculation. Of course, for a rotor this retarded time problem increases the complexity of the acoustic calculations tremendously because for a given observer time all of the contributions to the sound at each observer point will have different retarded times – see Fig. 8.45. It is the evaluation of all the retarded times for points all over the rotor that adds significantly to the net computational cost of the problem.

Alternatively, to avoid a retarded time calculation the time of arrival of sound waves at the observer can be determined. This means that the future or advanced time of arrival of a wave at a given observer location is calculated using

$$t^+ = t + \frac{\mathbf{R}}{v + a}. \tag{8.247}$$

This approach means that for a given source time all the acoustic waves must be tracked and the net sound field at a point in the acoustic field must be combined according to

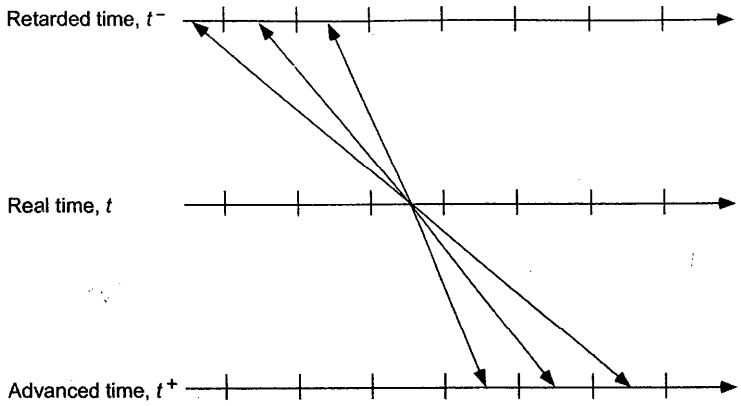

Figure 8.45 Time, retarded time and advanced time are related through a mapping.

the arrival time. This process was used successfully by Leishman (1996, 1999), mainly because of the large computational time savings, especially for maneuvering helicopter problems – see Brentner & Jones (2000). When using either the retarded time or advanced time formulation, the individual contributions from all wave sources from different source times are added together in amplitude and phase at each observer position and time.

8.19.2 *Wave Tracing*

These ideas of source time and arrival time of sound waves are formally embodied in a process known as *wave tracing*. In a fixed reference frame with respect to the rotor the spherical wavelets that propagate radially from each source point proceed at the local speed of sound plus the component of the flow velocity in the propagation direction, that is, say initially in a direction β relative to the blade. For example, for an outward moving source point the initial wavelet trajectory over a period Δt can be formalized as

$$\vec{x} = \begin{Bmatrix} x \\ y \\ z \end{Bmatrix} = \begin{Bmatrix} x_B \\ y_B \\ z_B \end{Bmatrix} + \begin{bmatrix} a\cos(\psi_b + \beta) + u \\ a\sin(\psi_b + \beta) + v \\ (a + w) \end{bmatrix} \Delta t, \tag{8.248}$$

where (x_B, y_B, z_B) is the acoustic source point on the blade, ψ_b is the blade azimuth angle (or time) of the acoustic source point and (u, v, w) can be considered as the local flow velocities relative to a coordinate system at the rotor hub.

For illustration, it is useful to consider a model problem of the sound field radiated by a rotating point source that has a subsonic Mach number, which is typical of the helicopter rotor. This is a simple problem in concept, but is complicated even here. The principles involved, however, contain most of the physics associated with the acoustics of real rotors. Assume that an acoustic source at a given radius rotates at frequency Ω, as shown previously in Fig. 8.44. Assume first that there is no forward motion of the source and no relative flow velocity, so this system corresponds to a helicopter rotor in hover. The results in Fig. 8.46(a) show that the wave fronts coalesce along a spiral and move away from the source point at the speed of sound. With forward speed of the source, in this case with a relative flow from left to right, Fig. 8.46(b) shows that the wave fronts propagate at the speed of sound plus or minus the local flow velocity. In this case upstream moving waves bunch closer together and the downstream moving waves are spread further apart. This is essentially a

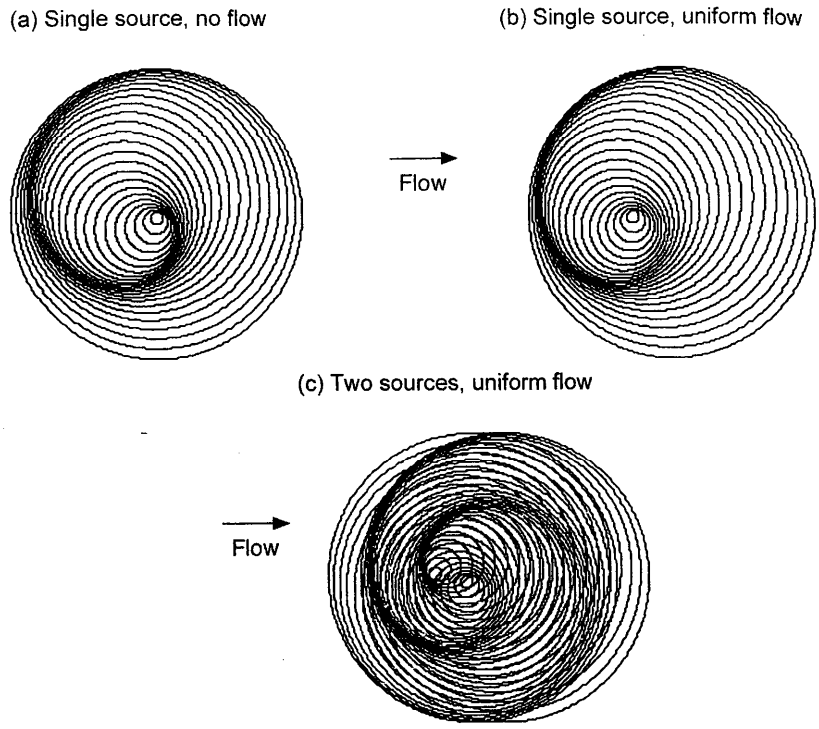

Figure 8.46 Examples of acoustic waves produced by a rotating subsonic source: (a) Single rotating source in stationary flow. (b) Single rotating source in a uniform flow from left to right. (c) A rotating source pair in a uniform flow from left to right.

Doppler effect, which manifests as an increase or decrease of the apparent sound frequency and intensity at upstream or downstream observer locations, respectively. The addition of a second source, as shown in Fig. 8.46(c), makes the problem much more complicated. With the many different potential sound sources on a helicopter rotor, the net sound field tends to be very omnidirectional, but with embedded regions of focused noise.

8.19.3 *Compactness*

When a body is large compared to the wavelength of the sound waves that it generates, interference of wave fronts from different parts of the body produce a complicated sound pattern. This is especially important in the region near the body or in the near field. When the body is small relative to the wavelength scale of the sound it generates or the sound is at high frequency, the phase differences between different source points is small and the body radiates like a point source. In acoustics this relative size of the body at a given frequency is called its *compactness*. Therefore a compact source radiates like a point source, whereas noncompact bodies must be treated in more detail.

In rotorcraft acoustics it is often sufficient to consider unsteady lift producing acoustic sources on the rotor as a series of compact sources. However, some contributions to rotor noise, such as thickness noise and HSI noise, arise because of phase differences between the different times of arrival of sound waves from the leading and trailing edges of the airfoil sections. In these cases, compactness cannot be assumed and the problem is considerably more complicated; see Brentner & Farassat (2003) for a summary.

8.19.4 *Trace or Phase Mach Number*

The acoustic field generated by a helicopter often tends to be highly focused in one specific direction or series of discrete directions. This is because acoustic waves can accumulate along a front. The focusing of acoustic waves depends on the *trace Mach number* of the acoustic source point – see Lowson (1968, 1996), Sim (1995, 1996), and Leishman (1999). It is known that the sound waves that have their origin from clusters of source points with supersonic trace Mach numbers on the rotor arrive simultaneously (or nearly so) at the same observer location, thereby generating an acoustic convergence. This is similar to the problem of wave focusing on a ground plane from supersonic flying aircraft that generate sonic booms – see Onyenonwu (1975a,b).

Consider now in more detail the problem of the noise generated by a BVI source point. It will be assumed that the source is acoustically compact. It has been shown previously in Section 8.16.4 that aerodynamic intensity of a BVI depends on the strength of the tip vortex, the distance from the blade to the tip vortex, and the orientation of the vortex to the blade. (See Section 10.4.2 for the method of calculating the BVI locations over the rotor disk.) The trace Mach numbers of the BVI intersection points between the blade and the axis of the vortex filament inside the rotor disk can, under many conditions, be supersonic. The consequences of this is that the fronts of the spherical sound wavelets generated at the BVI source points on the blades will accumulate along an envelope, similar to a Mach cone generated by a supersonic aircraft. This concept is shown schematically in Fig. 8.47. It is apparent that the principal direction of the sound wave propagation will be normal to the Mach cone.

On a rotor the trace Mach number, M_{tr}, is related to the relative speed of convection of the blade tip vortex axis relative to a blade, V, and the angle of intersection, γ, using

$$M_{tr} = \frac{V}{a \tan \gamma}, \tag{8.249}$$

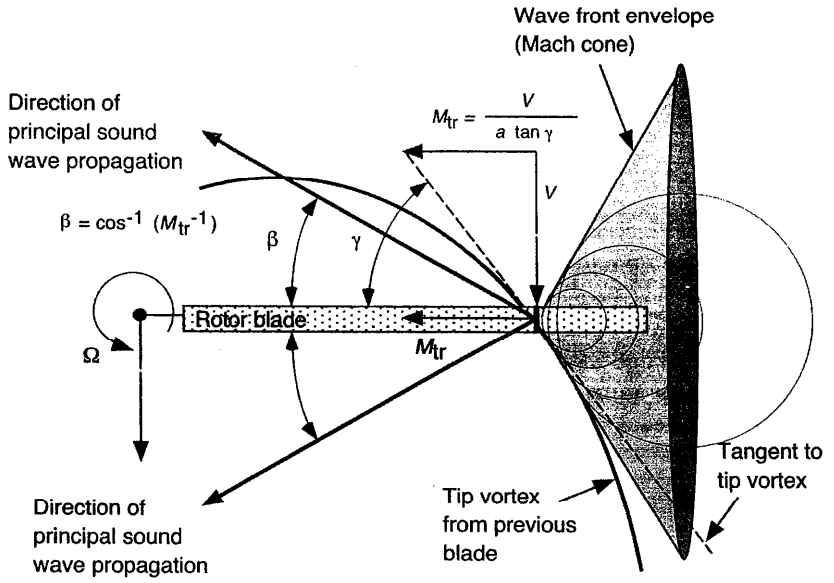

Figure 8.47 Ideas of trace or phase Mach number of an acoustic source point on the rotor.

where a is the sonic velocity. A diagram explaining the basic concept is given in Fig. 8.47 for an axis system moving with the rotor. The velocity, V, in Eq. 8.249 must be modified to account for the additional local in-plane convection speed of the vortex filament, which arises from the self-induced effects of the vortical rotor wake or from any blade motion or aircraft maneuver kinematics. It will be apparent from Eq. 8.249 that the trace Mach number can range from subsonic to supersonic, and the trace velocity vector can be directed outward or inward along the blade axis. If the angle of intersection is small, that is, the blade and vortex axes are almost parallel to each other, then the trace Mach number along the blade axis can be significantly supersonic. Figure 8.47 shows that the accumulated wavelet fronts then will propagate into the acoustic field along a ray cone with a semi-vertical angle β to the instantaneous trace velocity vector, where $\beta = \cos^{-1}\left(M_{\text{tr}}^{-1}\right)$. Because the value of β will vary from point to point on the blade, this effectively forms a series of intersecting ray cones with different vertices and spread angles. The initial conditions of the wavelets are defined by the emission times of all the individual sound fronts that are generated at BVI points with supersonic trace Mach numbers. By numerically computing the positions of the wavelets with respect to time, the pattern of fronts that intersect the plane at any blade angle ψ_b can be determined.

It is usually desirable to examine the rotor acoustics on a horizontal (ground) plane below the rotor in a frame of reference where the observer moves with the rotor. When the ray cones generated from each supersonic BVI source point in the rotor plane intersect the horizontal ground plane they become conics. This planar intercept is termed an *acoustic line* because it forms the locus of any acoustic disturbances from the wave fronts that reach the x–y observer plane from the BVI emission points. Notice that after the wavelet intersects the observer plane, the principal direction of the front is along these acoustic lines. If the wave fronts approximately intersect in regions of high acoustic line density, then sound focusing can be said to occur. In forward flight, the radiation cones become distorted by the local flow velocities, although the means of calculating the acoustic lines is the same. By formulating the orientations and intersections of these acoustic lines, which becomes mostly a problem in analytic geometry, it gives a measure of the qualitative directivity of the dominant sound in the far-field as produced by the BVI events on the rotor. This is the essence of the so-called radiation cone methods originally formalized by Ringler et al. (1991), Sim et al. (1995), and Sim & George (1996).

Depending on the trace Mach number and direction of the trace velocity vector along the blade, the resulting acoustic lines can crowd together or overlap. It is, therefore, possible for sound focusing to occur where the acoustic lines lie close together (high acoustic line density), and in some cases they may converge to form so-called caustics. Ringler et al. (1991) and Sim & George (1996) state that caustics or intersections of ray cones result in wave focusing and the formation of acoustic "hot spots." However, the intersection of acoustic lines (ray cones) is a necessary but not a sufficient condition to produce sound wave focusing. Intersections of acoustic lines as a means of determining locations of focused sound is only meaningful for wavelet fronts (acoustic rays) that have actually reached observer points at the same times, which of course requires either a retarded or advanced time calculation for each wavefront.

8.19.5 *Ffowcs Williams-Hawkings Equation*

The movement of all the acoustic waves in the field are mathematically embodied in the Ffowcs Williams-Hawkings (FW-H) equation – see Ffowcs Williams & Hawkings (1969) for the original derivation. This equation incorporates the fundamental principles of

mass, momentum, and energy conservation through a rearrangement of the Navier–Stokes equations in the form of a wave equation – see also Farassat (1975, 1981), Brentner (1997a), and Brentner & Farassat (2003). There have been many subsequent studies of the FW-H equation, including reformations of the equations into different forms that are suitable for different forms of analysis and for use with different types of numerical techniques.

According to the FW-H equation the acoustic pressure at a point $\vec{x}$ at time t can be written in the form

$$p'(\vec{x},t) = \frac{1}{4\pi}\frac{\partial}{\partial t}\iint_S \left[\frac{\rho v_n}{\mathbf{R}(1-M_\mathbf{R})}\right]_\tau dS + \frac{1}{4\pi a}\frac{\partial}{\partial t}\iint_S \left[\frac{l_\mathbf{R}}{\mathbf{R}(1-M_\mathbf{R})}\right]_\tau dS + \frac{1}{4\pi}\iint_S \left[\frac{l_\mathbf{R}}{\mathbf{R}^2(1-M_\mathbf{R})}\right]_\tau dS. \tag{8.250}$$

where $l_\mathbf{R}$ is the total force on the fluid at each source point on the blade surface S in the direction of the observer and τ is the retarded time. The first term in Eq. 8.250 is the thickness noise, which involves a determination of the perturbation velocity, v_n, which is produced by the blade as it passes through the flow. The second and third terms are called the loading noise. The third term is a near-field term, which does not represent a propagating wave. Notice that first part of the loading noise is related to the time rate of change of the pressure on the blade. In the compact source limit, this is equivalent to the time rate of change of the lift, which for a BVI event is known to have rapid changes (see previously in Fig. 8.37). As shown in Fig. 8.48, the qualitative nature of BVI sound consists of a highly impulsive change in pressure, and this is fundamentally the source of the "thump-thump" noise so commonly produced by helicopters.

In practice, the evaluation of the FW-H equation is performed numerically in a discretized form, for which for rotor applications several variations are possible. A common computer model for helicopter acoustics is the WOPWOP code developed by Brentner (1986), which uses a retarded time formulation. See also Farassat (1975, 1981) and Farassat & Brentner

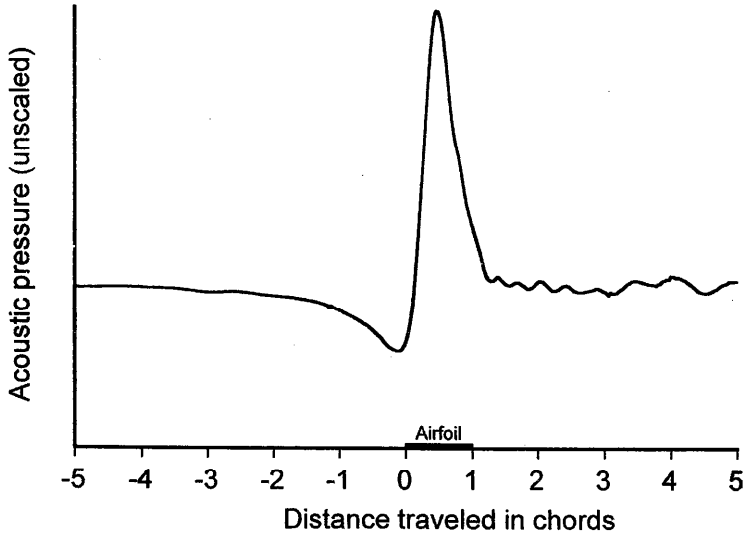

Figure 8.48 Representative acoustic pressure change during a BVI event. Pressure is unscaled because observer location is unspecified.

(1987), Brentner (2000), Brentner & Jones (2000), and Brentner & Farassat (2003) for further details on solving numerically the FW-H equation. The computational cost of solving the FW-H equation for helicopter acoustic problems, however, continues to be relatively large and more advanced numerical methods that are more accurate and computationally faster continue to be pursued, including parallel processing – see Long & Brentner (2000). The use of an advanced time instead of a retarded time formulation also allows computational time savings, that is, the time required to propagate the sound into the field (observer) point is calculated directly from the known emission (source) times. While this gives results at unequally spaced observer times, the data can be readily sorted into discrete bins with the same arrival time, as suggested by Fig. 8.45. A typical observer time step must be about 0.5° of rotor azimuth to obtain sufficient temporal resolution. If the observer time overlaps one discrete bin width, then the acoustic information can be weighted over adjacent bins by applying weighting factors. After the complete noise signal is obtained at the observer location from all the sound sources, the time derivative on the appropriate terms in the FW-H equation are taken using a finite-difference formula.

8.19.6 *BVI Acoustic Model Problem*

Acoustic results for an idealized BVI problem is now considered, the problem of an actual helicopter being far too complicated to explain the fundamental principles. The model is for an interaction of an elastically stiff two-bladed rotor encountering an idealized streamwise vortex parallel to the x axis, with results for both parallel and oblique (offset) cases being considered. The configuration is shown schematically in Fig. 8.49, which has been examined experimentally by Kitaplioglu & Caradonna (1994) who have measured unsteady blade loads and simultaneous acoustics data. The hover tip Mach number was 0.7 and the rotor was operated at an advance ratio of 0.2. The primary BVI event occurred over the front of the rotor disk where the blade axis was effectively parallel to the axis of the generator vortex. While a BVI event may be expected downstream as well, the effects of the hub were shown by means of flow visualization to rapidly diffuse the vortex and effectively eliminated the BVI at $\psi_b = 0$. Experimental data for the parallel interaction case ($y_v = 0.0$) have been made available and have been compared to predictions from various types of aeroacoustic models – see Caradonna et al. (1997).

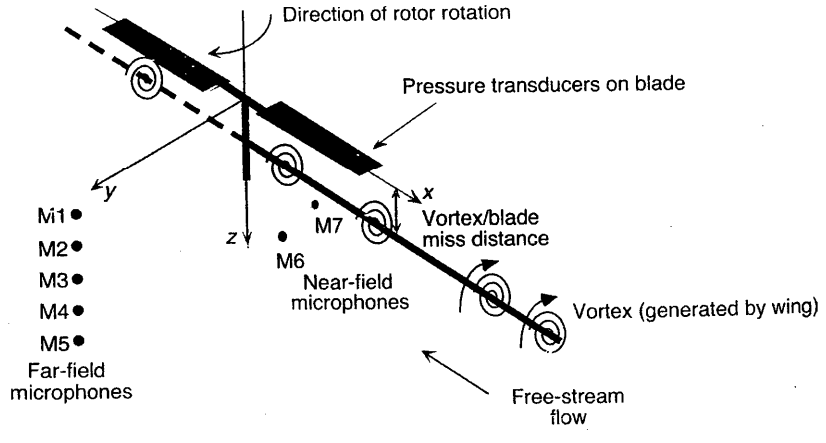

Figure 8.49 Schematic showing the configuration of the idealized BVI experiment.

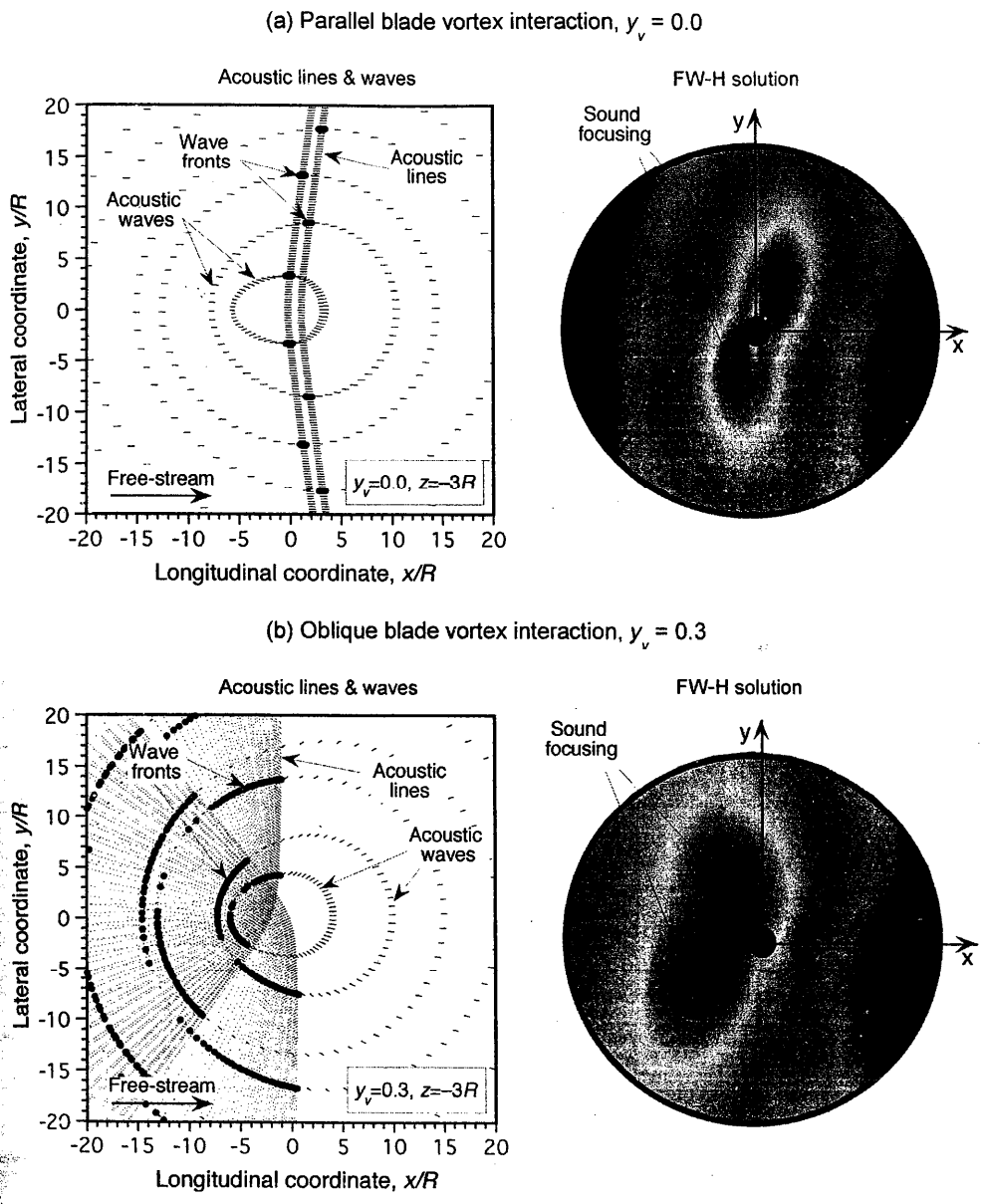

Figure 8.50 Representative acoustic results for a two-bladed rotor encountering an idealized streamwise vortex parallel to the x axis. Acoustic lines from BVI sources with supersonic trace Mach numbers and a FW-H solution are shown. (a) Parallel interaction, with vortex on rotor centerline. (b) Oblique interaction with vortex to starboard off the rotor centerline.

In the first case, acoustic lines from BVI sources on the rotor with supersonic trace Mach numbers are compared in Fig. 8.50 with the FW-H solution for an observer plane three rotor radii below the rotor. The wave tracing technique allows for the rapid calculation of the principal sound directions and arrival times from all of the BVIs with supersonic source points. In the parallel case, which is shown in Fig. 8.50(a), infinite trace Mach numbers occur all along the blade at $\psi_b = (0, \pi)$. The vertex of each ray cone is, therefore, located on the

x axis upstream and downstream of the rotational axis. The ray cones appear as hyperbolic acoustic lines on the horizontal observer plane, with asymptotic slopes $\pm \tan^{-1}(1/\mu M_{\Omega R})$. Wave fronts of focused acoustic energy are formed by the intersection of the closely spaced spherical wavelets generated at each of the BVI source points with supersonic trace Mach numbers. The position of these fronts at successive intervals in time (in this case every 2π radians of rotor revolution) can be tracked by wave tracing. Notice that on the observer plane there are two sets of almost circular wavelets being generated, one from the BVIs occurring at the rear of the disk and the other occurring from the BVIs at the front. These BVI events occur half a rotor revolution apart. It will be seen that the primary wave fronts formed by the intersection of the individual groups of wavelets from each blade travel along the paths defined by the two sets of acoustic lines. Therefore, in the parallel BVI case, the sound wavelets become highly focused in directions perpendicular to the blades at $\psi_b = (0, \pi)$. Notice that the results from the FW-H equation gives an acoustic directivity that is in good agreement with the results from wave tracing.

Both the near-field and far-field acoustics are sensitive to the phasing of the unsteady airloads during the BVI. In addition, the duration and phasing of the BVI event along the blade, the Doppler magnification, and the distance of the event to the microphone location combine to produce the net sound pressure signature at a given time. The thickness sound pressure further combines with the loading term, resulting in small variations in phasing that can significantly affect the net noise signature from the rotor. Comparisons of the sound pressure obtained using theory and experiment are given in Fig. 8.51 for a far-field and near-field microphone location. Notice that the far-field sound pressure consists of two BVI-type pulses, one being generated by each blade as it passes the vortex. The other fluctuations are background noise. The phase of the pulse in time with respect to rotor position depends on the distance to the microphone location. In this case, where the blade and vortex axes

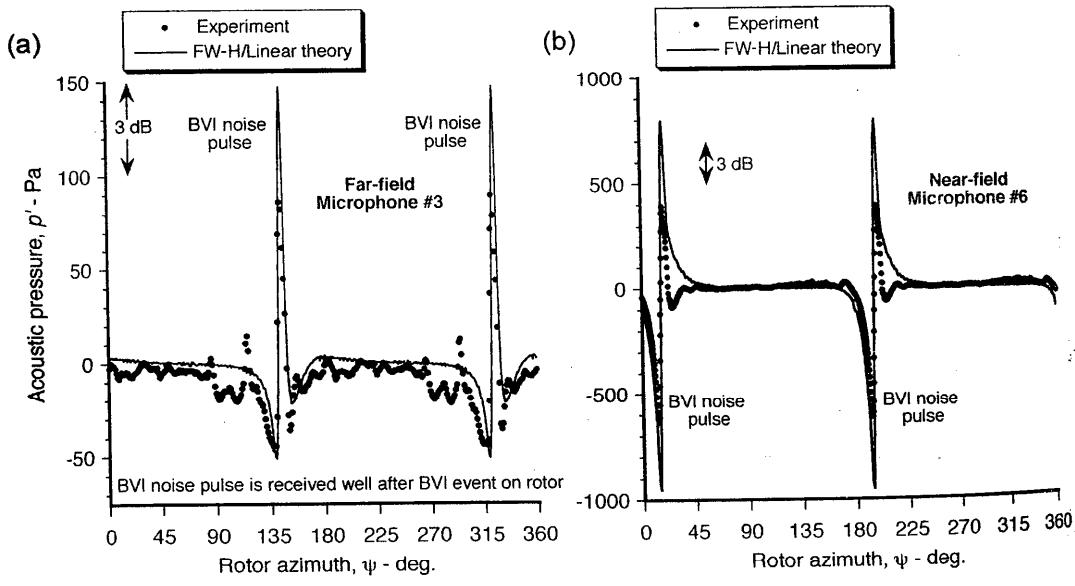

Figure 8.51 Comparison of sound pressures using FW-H/linear method with experimental measurements for the parallel ($y_v = 0.0$) BVI case. (a) Far-field microphone 3. (b) Near-field microphone 6. See Fig. 8.49 for microphone locations. Vortex at $z/c = -0.25$, tip Mach number = 0.7, vortex strength $\Gamma_v = -0.36$.

are parallel, there is essentially one BVI event and all points on the blade produce a sound wave that is in-phase with each other. The agreement of linear theory with experiment is good, both in terms of the peak-to-peak and the character of the acoustic pressure pulse but with an overprediction of peak-to-peak pressure. This seems typical of most computational aeroacoustic methods for reasons that are likely related to nonlinear aerodynamics.

Because the large majority of BVIs on the rotor involve oblique interactions, it is important to understand their aeroacoustic effects. Aerodynamically, the oblique BVI cases produce significant 3-D unsteady airloads. Also, the directivity of the acoustics is somewhat more complicated in this case. The extension of the problem to oblique BVIs provides a good challenge for any aeroacoustic method and, in the first instance, avoids the complexities of the real rotor wake. The obliqueness of the vortex to the blade can be obtained using various offset distances (y_v) between the vortex and the longitudinal axis. When the vortex is offset laterally from the longitudinal x axis, the BVIs with the blades are no longer parallel. This means that there are fewer points along the blade that have supersonic trace Mach numbers. The radial location of the BVIs points in this case can be found using

$$r_v = \left| \frac{y_v}{R \sin \psi_b} \right| \quad \text{for } 0 \leq r_v \leq 1. \tag{8.251}$$

The corresponding trace Mach numbers are

$$M_{\text{tr}}(r_v, \psi_b) = \frac{M_{\Omega R}(r_v + \mu \sin \psi_b)}{\tan \psi_b}, \tag{8.252}$$

where the blade/vortex intersection angle is $\gamma = \psi_b$ and $M_{\Omega R} = \Omega R/a$. It is easily deduced that with increasing values of y_v fewer intersections points will have values of γ that result in supersonic trace Mach numbers. For the special case where $y_v = 0$, the BVIs lie all along the blade at $\psi = (0, \pi)$ and $M_{\text{tr}} = \infty$ so that $\beta = \pi/2$. With reference to Fig. 8.50(b) it can be seen that with a starboard offset of the vortex to $y_v > 0$ the acoustic lines are now directed toward the front of the rotor disk (i.e., into the second and third quadrants). Because of the varying supersonic trace Mach number in the oblique BVI cases, the focused sound waves radiate over a much larger spread angle. Notice that again the results from the FW-H equation predict an acoustic field that is in good agreement with the directivity suggested by the acoustic lines. While the results in Fig. 8.50 represent a discretization of the problem into a finite number of radial blade elements and supersonic source points, each of the solutions in Fig. 8.50(a) and (b) have been computed with the same resolution,[12] and therefore, the concentration of acoustic lines and wavelet fronts can be compared directly.

8.19.7 *Comparison of Aeroacoustic Methods*

There are no measurements for the oblique BVI case of the model problem previously discussed, but results have been computed using two different aeroacoustic methods; one based on FW-H/linear unsteady aerodynamics approach and the other based on CFD – see Strawn (1997). The latter method consists of a CFD solution on and near the rotor blades, followed by an interpolation onto a surface that encloses the rotor. An acoustics integration scheme propagates the acoustic signal to the far-field. This integration scheme is based on a Kirchhoff Ffowcs Williams-Hawkings (KFWH) acoustics formulation. An Euler flow solver (Section 14.2.2) computes the near-blade CFD solution. All nonlinear effects on the acoustic propagation are accurately modeled within the framework of the

[12] Also note, that while the sound wavelets produced by each supersonic source point are nominally circular in form, they have been plotted here discretely and so have a reduced angular resolution.

Euler equations. The KFWH formulation is used to propagate the acoustics signal to the far field. The KFWH formulation begins with a derivation of the FW-H equation for the radiated noise from a surface with arbitrary motion. The resulting integral equation reduces to the classic FW-H equation when the chosen surface coincides with the surface of the rotor blades. It reproduces the classic Kirchhoff formulation when the KFWH surface is far from the rotor blades. In this particular case, the CFD grid consisted of 135-by-50-by-35 points in the chordwise, spanwise, and normal directions to the blade surface, respectively. The grid had a C-H topology (refer to Fig. 14.1), and extended approximately 1.5 blade radii above, below, and beyond the blade tip in the spanwise direction. A constant time-step of 0.25 degrees of blade azimuthal motion was used. The KFWH surface consisted of a total of 86,400 mesh points distributed over a top, bottom, and side grid. The linear method used 50 spanwise elements along the blade and an azimuthal step of 0.5°.

The results are shown Fig. 8.52 for an oblique ($y_v = 0.5$) case. Results for four reference microphones are shown, three of which lie upstream and below the rotor, with the fourth microphone upstream and in the plane of the rotor. Figure 8.52 shows that the agreement obtained between the FW-H/linear and the CFD/KFWH methods is very good at all of the

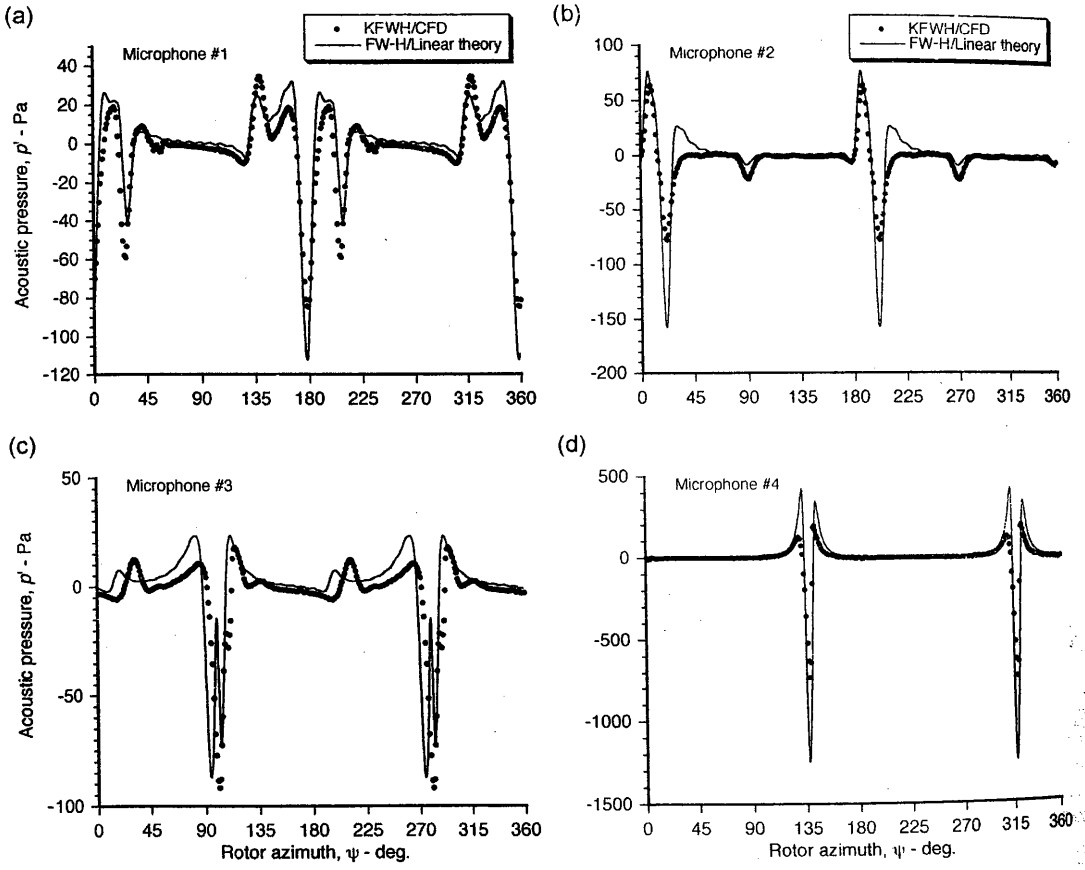

Figure 8.52 Comparison of sound pressures using FW-H/linear aerodynamics method and a Kirchhoff/CFD method for an oblique ($y_v = 0.5$) BVI case. (a) Microphone 1. (b) Microphone 2. (c) Microphone 3. (d) Microphone 4. See Fig. 8.49 for microphone locations. Vortex at $z/c = -0.25$, tip Mach number = 0.76, vortex strength $\Gamma_v = 0.406$.

microphone locations. For the out-of-plane locations, the sound pressure is comprised of contributions from both "loading" and "thickness" sound waves. The in-plane microphone (Microphone 4) receives only the thickness wave, which is exactly the same in both cases (both positive and negative signs of the vortex strength). The agreement between the two computational methods is very good, but the simple source–sink displacement model used in the FW-H/linear method slightly overpredicts the intensity of the thickness sound wave. The out-of-plane microphones receive sound waves from both thickness and loading sources, which results in somewhat more complicated waveforms. In some cases, the sound waves from the various sources arrive just in-phase, and this can result in either constructive or destructive interference depending on the sign (compression or rarefaction) of the BVI wave front. An example of this is shown in Figs. 8.52(b) and (c). This will affect the net directivity in the acoustic field and shows the difficulties in considering just BVI sources alone as contributors to the noise field.

Overall, this type of simple model problem demonstrates the enormous complexity of predicting accurately the noise from an actual helicopter rotor with its plethora of possible BVI locations. However, it seems that if the structure, strength, and location of the tip vortices relative to the blades are known, then aeroacoustic methods have matured to the point where good noise predictions are possible. Of course, on an actual helicopter predicting the spatial and temporal locations of the tip vortices relative to the dynamically flapping and deflecting blades is really the greatest challenge, and one that is still technically beyond the state of the art. This wake problem is considered in detail in Chapter 10. It would seem that until the more thorough and complete integration of more physically representative wake models and tip vortex models into aeroacoustic analyses is completed, the accurate quantitative prediction of rotor noise will always remain an elusive goal.

8.19.8 *Methods of Rotor Noise Reduction*

It will be clear that in the quest to reduce helicopter rotor noise not only does the rotor noise intensity and directivity need to be predicted accurately, but strategies need be devised to either reduce or defocus rotor noise. One approach is to first try to relate the far-field rotor noise levels to their source points on the rotor. This has been recognized by several authors, including Sim et al. (1995), Lowson (1996), and Strawn (1997). Therefore, at least in principle, it may be possible to modify the aerodynamics at specific source points on the rotor and change the propagated noise in a profitable way. This, however, is not an easy goal, and even if possible theoretically by means of calculations and analysis, much work will be needed to actually implement any such proposed system on a helicopter.

The use of higher harmonic cyclic blade pitch [see Brooks et al. (1991) and Yu et al. (1994)] and active trailing edge flaps [see Charles et al. (1994) and Dawson (1995)] have been suggested to modify the unsteady blade airloads and alter the intensity of propagated BVI noise. While some benefits have been realized on actual rotor tests, these approaches have been only "open-loop" processes and so require extensive mapping out of the combinations of conditions where significant noise reductions are actually obtained. These reduced noise flight conditions, unfortunately, often coincide with increases in vibration levels on the rotor, which will never be acceptable. Passive designs such as blade tip sweep and unequal blade spacing have also been proposed to dephase rotor noise sources [see Baeder (1997) and Sullivan et al. (2002)]. Operational techniques such as aircraft trajectory optimization or tip-path-plane AoA control proposed by Schmitz (1998) may offer such benefits in changing vortex/blade miss distances at the rotor. Validation of this approach, however, will require careful predictions of the rotor wake to understand the relative changes in the

wake to flight condition. However, to be successful any approach toward noise reduction still requires a better understanding of the nature and focusing characteristics of the critical sound sources generated by the rotor. The problem of rotor noise reduction continues to be a prime opportunity for future research in helicopter aeroacoustics – see Brentner (1997a,b) and Edwards & Cox (2002).

8.20 Chapter Review

This chapter has described the key physical features of the unsteady aerodynamic effects found on airfoils operating under nominally attached flow conditions and away from stall. Unsteady aerodynamic effects have an important role in the prediction of the airloads and performance of helicopter rotors. The contributions of circulatory and noncirculatory effects to the unsteady airloads have been described, and their effects have been explained through the use of classical unsteady aerodynamic theories. These theories have their origin in thin-airfoil theory, with allowance for a shed vortical wake of nonzero strength downstream of the airfoil. Of primary significance is that unsteady effects manifest as phase differences between the forcing function and the aerodynamic response; these are functions of the reduced frequency, the Mach number and the mode of forcing. While most of the classical unsteady aerodynamic theories are elegant in mathematical form, they are restricted to fully incompressible flows. This is an assumption that is hard to justify for helicopter problems, where both the local Mach numbers and effective reduced frequencies are generally high enough to render incompressible flow assumptions invalid, at least under the strictest terms. However, sometimes even some allowance for unsteady effects provides a better predictive capability than if quasi-steady flow alone is assumed.

For subsonic flows no exact analytic solutions are available for unsteady airfoil problems, at least not over the entire time domain, and numerical solutions must be sought. However, the extension of the classical incompressible methods to subsonic compressible flows can be approached using many of the same fundamental principles as for incompressible flow, albeit using certain levels of approximation. It has been shown that compressibility effects generally manifest as increased phase lags between the forcing function and the unsteady aerodynamic response. For some transient problems, such as blade vortex interactions and unsteady trailing edge flap motions, the treatment of compressibility proves essential if the correct amplitude and phasing of the aerodynamic loads are to be predicted. Validation of the various methods have been conducted with experimental results. Unfortunately, many of the problems of interest are difficult to simulate experimentally, and recourse to indirect validation has been the only choice. However, the recent advent of nonlinear methods based on CFD solutions to the Euler or Navier–Stokes equations has provided a new standard that now helps define the limits of applicability of the classical theories.

The problem of understanding and predicting rotor noise continues to be a challenging one for the analyst. While much progress has been made, the significant reduction of helicopter noise is an illusive goal. To this end, the accurate modeling of unsteady aerodynamic forces on the blades continues to be fundamental to the prediction of rotor noise. While the better use of CFD methods is often held out to be the answer, good acoustic results are still possible within the framework of linear unsteady aerodynamic theories, albeit with proper correction for compressibility effects. These types of models are also amenable for inclusion in comprehensive rotor analysis, such as those including rotor blade dynamics and aeroelastic response, and perhaps also flight dynamics simulations. Acoustic tools such as wave tracing also provide good insight into the acoustic directivity produced by BVI phenomena and can be used to augment FW-H or other solutions in terms of understanding

the significant acoustic sources on the rotor. However, despite many advances in the understanding of problems in aeroacoustics, the key to more faithful unsteady airloads and acoustic predictions really lies in the ability to better define the induced velocity field at the blades produced by the rotor wake, a problem considered in detail in Chapter 10.

8.21 Questions

8.1. Show using dimensional analysis that the resultant force F on an airfoil of chord c oscillating at angular frequency ω in a flow of velocity V, density ρ, sonic velocity a, and viscosity μ, can be written in functional form as

$$\frac{F}{\rho V^2 c^2} = f\left(\frac{\rho V c}{\mu}, \frac{V}{a}, \frac{\omega c}{V}\right) = f\,(Re, M, k)\,.$$

8.2. Use the quasi-steady thin-airfoil theory to compute the instantaneous differential pressure distribution on an airfoil for a series of nondimensional pitch rates, $q = \dot{\alpha}c/V$ about an axis at 1/4-chord. Plot and compare your results at the same value of lift coefficient. Determine and plot the chordwise pressure gradient, again at the same value of lift coefficient. Comment on the results in regard to the likely effect on the boundary layer development.

8.3. According to Theodorsen's theory, how does the unsteady motion of an airfoil affect the lift response? Briefly, explain why frequency domain methods such as Theodorsen's theory cannot be easily applied to to calculate the unsteady airloads on a rotor in forward flight.

8.4. If the Wagner function is assumed to be represented (in general) as the exponential series

$$\phi(s) = 1 - \sum_{j=1}^{N} A_j e^{-b_j s}$$

then show, by the application of Laplace transforms, that it is possible to write an approximation to the Theodorsen function in terms of real and imaginary parts, that is, $C(k) = F(k) + iG(k)$, as

$$F(k) \approx \frac{1}{2} + \sum_{j=1}^{N} \frac{A_j b_j^2}{\left(b_j^2 + k^2\right)},$$

$$G(k) \approx -\sum_{j=1}^{N} \frac{A_j b_j k}{\left(b_j^2 + k^2\right)}.$$

Compare the approximation derived above using the $N = 2$ result for ϕ given by R. T. Jones with Theodorsen's exact solution. Comment on your result.

8.5. If the gust response function for the penetration of a stationary sharp-edged gust is assumed to be represented by the equation

$$\psi(s) \approx 1 - \sum_{j=1}^{N} G_j e^{-g_j s}$$

show that for a pure first sinusoidal gust referenced to the leading-edge of the airfoil the resulting real and imaginary parts of lift response can be written as

$$\Re\, C_l^g(k_g) = 2\pi \left[\sum_{j=1}^{N} \frac{G_j g_j^2}{g_j^2 + k_g^2}\right]$$

and

$$\Im\ C_l^g(k) = -2\pi \left(\sum_{j=1}^{N} \frac{G_j g_j k_g}{g_j^2 + k_g^2} \right),$$

where k_g is the gust reduced frequency. Use an exponential approximation to the Küssner function to estimate the Sears function. Comment on your results.

8.6. Show, by a suitable transformation, that when the sinusoidal gust in the previous problem is referenced to the mid-chord of the airfoil then

$$\Re\ C_n^g(k_g) = 2\pi \left(\cos k_g \sum_{j=1}^{N} \frac{G_j g_j^2}{g_j^2 + k_g^2} - \sin k_g \sum_{j=1}^{N} \frac{G_j g_j k_g}{g_j^2 + k_g^2} \right),$$

$$\Im\ C_n^g(k_g) = -2\pi \left(\cos k_g \sum_{j=1}^{N} \frac{G_j g_j k_g}{g_j^2 + k_g^2} + \sin k_g \sum_{j=1}^{N} \frac{G_j g_j^2 k_g}{g_j^2 + k_g^2} \right).$$

8.7. If the sharp-edged gust function in subsonic flow is assumed to be represented by the equation

$$\psi(s) \approx 1 - \sum_{j=1}^{N} G_j e^{-g_j \beta^2 s}$$

then show that for a pure first harmonic sinusoidal gust referenced to the leading-edge of the airfoil the resulting real and imaginary parts of lift response can be written as

$$\Re\ C_l^g(k_g, M) = \frac{2\pi}{\beta} \left(\sum_{j=1}^{N} \frac{G_j g_j^2 \beta^4}{g_j^2 \beta^4 + k_g^2} \right)$$

and

$$\Im\ C_l^g(k_g, M) = -\frac{2\pi}{\beta} \left(\sum_{j=1}^{N} \frac{G_j g_j \beta^2 k_g}{g_j^2 \beta^4 + k_g^2} \right),$$

where k_g is the gust reduced frequency.

8.8. Program a solution to the Loewy function. Show the results of the lift transfer function and corresponding phase angle for a case where $\omega/\Omega =$ integer, integer $+1/4$, integer $+1/2$, and integer $+3/4$. Use a primary wake spacing parameter $h/b = 4.0$. Discuss your results.

8.9. Program the numerical solution to the Duhamel superposition problem with the $N = 2$ exponential approximation to the Wagner function using the one-step recurrence equations. Use at least two of the numerical methods given in the text. Consider a sinusoidal forcing at various reduced frequencies. Compare the exact results for the time-history of the circulatory lift as obtained using Theodorsen's theory with the numerical results obtained using the recurrence equations. Also, compare the results from the recurrence solutions to the frequency domain approximation to Theodorsen's theory using the Wagner function coefficients. Use several values of the time step, Δs (or points per cycle), to illustrate your answer.

8.10. Starting from a general indicial function in terms of a two term exponentially growing function, use the trapezoidal rule of integration to numerically approximate the Duhamel integral to find the solution to an arbitrary input in the form of one-step recurrence equations.

8.11. For some applications, it is convenient to write the unsteady aerodynamics of a two-dimensional airfoil in the form of differential equations, that is, in state-space form. Program a numerical solution for the unsteady lift in incompressible flow resulting from changes in AoA using the appropriate state-space equations. Use a convenient ordinary differential equation solver of your choice. Compute and plot the lift coefficient for an input comprising: (a) a sinusoidal oscillation. (b) a step input.

8.12. Use the state-space model derived in the previous question to numerically calculate the circulation and the total lift (circulatory lift plus apparent mass lift) on a flat plate airfoil penetrating a stationary (nonconvecting) sharp-edged gust. Use thin-airfoil theory and the first reverse flow theorem to calculate the quasi-steady AoA during the gust penetration.

8.13. Use Duhamel superposition with an exponential approximation to the sharp-edged gust to calculate numerical results for the unsteady lift on a flat plate airfoil interacting with a convecting Lamb-like desingularized vortex of nondimensional strength $\hat{\Gamma} = \Gamma/(Vc) = 0.2$ and core size $r_0 = 0.05$, which convects at a distance $y_v = 0.2$ chords below the airfoil. The airfoil is set to zero angle of attack. Plot your results as a function of vortex position, x_v, for several values of free stream Mach number. Compare your results with the incompressible ($M = 0$) case using Duhamel superposition with the Küssner function.

8.14. Using the results from the previous question, find the time-derivative of the lift, which is an approximation to the acoustic pressure generated by the interaction. Discuss your results.

8.15. Explain the principle of *retarded time* and why it must be evaluated to calculate the sound field generated by a helicopter rotor. Why does the evaluation of retarded time depend on the position of the observer?

8.16. Write an algorithm to evaluate the retarded time of an acoustic source that is received at an observer location at time t. Assume both a quiescent flow and a flow of uniform velocity. Write an equivalent algorithm to calculate the advanced time for the same acoustic source.

Bibliography

Anderson, W. D. and Watts, G. A. 1975. "Rotor Blade Wake Flutter–A Comparison of Theory and Experiment," 31st Annual National Forum of the American Helicopter Soc., Washington DC, May 13–15.

Ashley, H., Dugundji, J., and Nielson, D. O. 1952. "Two Methods for Predicting Air Loads on a Wing in Accelerated Motion," *J. of the Aeronautical Sciences*, 19 (8), pp. 543–552.

Baeder, J. D. 1997. "Passive Design for Isolated Blade-Vortex Interaction Noise," 53rd Annual Forum of the American Helicopter Soc., Virginia Beach, VA, April 29–May 1.

Beddoes, T. S. 1976. "A Synthesis of Unsteady Aerodynamic Effects Including Stall Hysteresis," *Vertica*, 1 (2), pp. 113–123.

Beddoes, T. S. 1980. "Unsteady Flows Associated with Helicopter Rotors," In: AGARD Report 679.

Beddoes, T. S. 1984. "Practical Computation of Unsteady Lift," *Vertica*, 8 (1), pp. 55–71.

Bisplinghoff, R.L., Ashley, H., and Halfman, R.L. 1955. *Aeroelasticity*, Addison-Wesley Publishing Co., Reading, MA.

Bramwell, A. R. S. 1976. *Helicopter Dynamics*, Edward Arnold, London, England, Chapter 8.

Brentner, K. S. 1986. "Prediction of Helicopter Rotor Discrete Frequency Noise–A Computer Program Incorporating Realistic Blade Motions and Advanced Acoustic Formulation," NASA TM-87721, Oct.

Brentner, K. S. 1996. "Numerical Algorithms for Acoustic Integrals–The Devil is in the Details," AIAA Paper No. 96-1706, 2nd AIAA/CEAS Aeroacoustic Conference, State College, PA, May 6–8.

Brentner, K. S. 1997a. "A Superior Kirchhoff Method for Aeroacoustic Noise Prediction: The Ffowcs–Williams Hawkings Equation," 134th Meeting of the Acoustical Soc. of America, San Diego, CA, Dec. 1–5.

Brentner, K. S. 1997b. "Helicopter Rotor Noise Prediction: Background, Current Status, and Future Direction," University of Tennessee Space Institute Seminar, Chattanooga, TN, Dec.

Brentner, K. S. 2000. "Modeling Aerodynamically Generated Sound: Recent Advances in Rotor Noise Prediction, AIAA Paper 2000-0345, 38th AIAA Aerospace Sciences Meeting and Exhibit, Reno, NV, Jan. 10–13.

Brentner, K. S. and Farassat, F. 2003. "Modeling Aerodynamically Generated Sound of Helicopter Rotors," *Progress in Aerospace Sciences*, 39 (2-3), pp. 83–120.

Brentner, K. S. and Jones, H. E. 2000. "Noise Prediction for Maneuvering Rotorcraft," AIAA Paper 2000–2031, 6th AIAA/CEAS Aeroacoustics Conference, Lahaina, HI, June 12–14.

Brooks, T. F., Booth, E. R. Boyd, D. D., Splettstoesser, W. R., Schultz, K. J., Roland, N., Georg, H., and Stregy O. 1991. "HHC study in the DNW to Reduce BVI Noise–An Analysis," International Technical Specialists Meeting on Rotor Acoustics and Rotor Fluid Dynamics, AHS/RAeS, Valley Forge, PA, Oct. 15–17.

Brown, C. E. 1949. "The Reversibility Theorem for Thin Airfoils in Subsonic and Supersonic Flow," NACA TN 1944.

Caradonna, F. X., Kitaplioglu, C., McCluer, Baeder, J. D., Leishman, J. G., Berezin, C., Bridgeman, J., Burley, C. R. Eipstein, R., Lyrintzis, A., Koutsavdis, E., Rahier, G., Jobard J., and J. Rule, J. 1997. "A Review of Methods for the Prediction of BVI Noise. American Helicopter Soc. Technical Specialists' Meeting in Rotorcraft Acoustics and Aerodynamics, Williamsburg, VA, Oct. 28–30.

Charles, B., Hassan, A. A., Sankar L. N., and Tadghighi, H. 1994. "Effects of Leading and Trailing Edge Flaps on the Aerodynamics of Airfoil/Vortex Interaction, *J. of the American Helicopter Soc.*, 39 (2), pp. 35–46.

Daughaday, H., Du Walt, F., and Gates, C. 1959. "Investigation of Helicopter Blade Flutter and Load Amplification Problems," *J. of the American Helicopter Soc.*, 2 (3), pp. 27–46.

Davis, S. S. and Malcolm, G. N. 1980. "Experimental Unsteady Aerodynamics of Conventional and Supercritical Airfoils," NASA TN 81221.

Dawson, S. 1995. "Wind Tunnel Test of an Active Flap Rotor: BVI Noise and Vibration Reduction," 51st Annual Forum of the American Helicopter Soc., Fort Worth, TX, May 9–11.

Dinyavari, M. A. H. and Friedmann, P. P. 1986. "Application of Time-Domain Unsteady Aerodynamics to Rotary-Wing Aeroelasticity," *AIAA J.*, 24 (9), pp. 1424–1432.

Dowell, E. H. 1980. "A Simple Method of Converting Frequency Domain Aerodynamics to the Time Domain," NASA TM-81844.

Drescher, H. 1952. "Untersuchungen an einem symmetrischen Tragflügel mit spaltos angeschlossenem Ruder bei raschen Aenderungen des Ruderausschlags (ebene Strömung), Max-Plank Institute für Strömungsforschung.

Drischler, J. A. and Diederich, F. W. 1957. "Lift and Moment Responses to Penetration of Sharp-Edged Traveling Vertical Gusts, with Application to Penetration of Weak Blast Waves." NACA TN 3956.

Edwards, B. D. and Cox, C. 2002. Revolutionary Concepts for Helicopter Noise Reduction–S.I.L.E.N.T. Program," NASA/CR-2002-211650, May.

Farassat, F. 1975. "Theory of Noise Generation From Moving Bodies with an Application to Helicopter Rotors," NASA TR R 451, Dec.

Farassat, F. 1981. "Linear Acoustic Formulas for Calculation of Rotating Blade Noise," *AIAA J.*, 19 (9), pp. 1122–1130.

Farassat, F. and Brentner, K. S. 1987. "The Uses and Abuses of the Acoustic Analogy in Helicopter Rotor Noise Prediction," AHS Specialists Meeting on Aerodynamics and Aeroacoustics, Arlington, TX, Feb. 25–27.

Ffowcs Williams, J. E. and Hawkings, D. L. 1969. Sound Generation by Turbulence and Surfaces in Arbitrary Motion. *Philosophical Transactions of the Royal Soc. of London*, A264, pp. 321–342.

Flax, A. H. 1952. "General Reverse Flow and Variational Theorems in Lifting-Surface Theory," *J. of the Aeronautical Sciences*, 19 (6), pp. 361–374.

Flax, A. H. 1953. "Reverse-Flow and Variational Theorems for Lifting Surfaces in Nonstationary Compressible Flow," *J. of the Aeronautical Sciences*, 19 (2), pp. 120–126.

Franklin, G. F., Powell, J. D., and Abbas, E. N. 1994. *Feedback Control of Dynamic Systems*, 3rd Edition, Addison-Wesley Publishing Co., Reading, MA, Chapters 2 & 7.

Friedmann, P. P. 1985. "A New Look at Arbitrary Motion Unsteady Aerodynamics and Its Application to Rotary-Wing Aeroelasticity," 2nd Int. Symp. on Aeroelasticity and Structural Dynamics, Aachen, Germany, April 1–3.

Friedmann, P. P. 2004. "Vibration Reduction in Rotorcraft Using Actively Controlled Flaps–Their Evolution and Potential for Improving Rotorcraft Technology," 30th European Rotorcraft Forum, Marseilles, France, Sept. 14–16.

Friedmann, P. and Yuan, C. 1977. "Effect of Modified Aerodynamic Strip Theories on Rotor Blade Aeroelastic Stability," *AIAA J.*, 15 (7), pp. 932–940.

Garrick, I. E. 1938. "On Some Reciprocal Relations in the Theory of Non-Stationary Flows," NACA Report 629.

Garrick, I. E. 1957. "Nonsteady Wing Characteristics," Section F of Aerodynamic Components of Aircraft at High Speeds, Vol. VII of *High Speed Aerodynamics and Jet Propulsion*," A. F. Donovam & H. R. Lawrence, eds., Princeton University Press, Princeton, NJ.

George, A. R. 1978. "Helicopter Noise: State-of-the-Art," *J. of Aircraft*, 15 (11), pp. 707–715.

Glauert, H. 1929. "The Force and Moment on an Oscillating Airfoil," ARC R & M 1242.

Greenberg, J. M. 1947. "Airfoil in Sinusoidal Motion in a Pulsating Stream," NACA TN 1326.

Gray, R. and Davies, D. E. 1972. "Comparison of Experimentally and Theoretically Determined Values of Oscillatory Aerodynamic Control Surface Hinge Moment Coefficients," RAE Technical Report, 72023, March.

Halfman, R. 1951. "Experimental Aerodynamic Derivatives of a Sinusoidally Oscillating Airfoil in Two-Dimensional Flow," NACA TN 2465.

Ham, N. D., Moser, H. H., and Zvara, J. 1958. "Investigation of Rotor Response to Vibratory Aerodynamic Inputs–Experimental Results and Correlation with Theory," Wright Air Development Center, Report WADC TR 58-87, Part 1.

Hammond, C. E. and Pierce, G. A. 1972. "A Compressible Unsteady Aerodynamic Theory for Helicopter Rotors," In: AGARD-CP-111.

Hariharan, N. and Leishman, J. G. 1996. "Unsteady Aerodynamics of a Flapped Airfoil in Subsonic Flow by Indicial Concepts," *J. of Aircraft*, 33 (5), pp. 855–868.

Heaslet, M. A. and Sprieter, J. R. 1952. "Reciprocity Relations in Aerodynamics," NACA Report 1119.

Isaacs, R. 1945. "Airfoil Theory for Flows of Variable Velocity," *J. of the Aeronautical Sciences*, 12 (1), pp. 113–117.

Isaacs, R. 1946. "Airfoil Theory for Rotary Wing Aircraft," *J. of the Aeronautical Sciences*, 13 (4), pp. 218–220.

Johnson, W. 1980. *Helicopter Theory*, Princeton University Press, Princeton, NJ, Chapter 10.

Jones, J. P. 1958. "The Influence of the Wake on the Flutter and Vibration of Rotor Blades," *Aeronautical Quarterly*, 9 (3), pp. 258–286.

Jones, R. T. 1938. "Operational Treatment of the Non-Uniform Lift Theory in Airplane Dynamics," NASA Technical Note 667.

Jones, R. T. 1940. "The Unsteady Lift of a Wing of Finite Aspect Ratio," NACA Report 681.

Jones, R. T. 1951. "The Minimum Drag of Thin Wings in Frictionless Flow," *J. of the Aeronautical Sciences*, 18 (2), pp. 75–81.

Jones, W. P. 1945. "Aerodynamic Forces on Wings in Nonuniform Motion," ARC R & M 2117.

Jose, A., Leishman, J. G., and Baeder, J. D. 2005. "Unsteady Aerodynamic Modeling with Time-Varying Free-Stream Mach Numbers, 61st Annual Forum of the American Helicopter Soc., Grapevine, TX, June 1–3.

Karamcheti, K. 1966. *Principles of Ideal-Fluid Aerodynamics*, John Wiley & Sons, Inc., New York, NY.

Kitaplioglu, C. and Caradonna, F. X. 1994. "Aerodynamics and Acoustics of Blade Vortex Interaction Using an Independently Generated Vortex," American Helicopter Soc. Aeromechanics Specialists Conference, San Francisco, CA, Jan. 19–21.

Kitaplioglu, C., Caradonna, F. X., and Burley, C. L. 1997. "Parallel Blade-Vortex Interactions: An Experimental Study and Comparison with Computation," *J. of the American Helicopter Soc.*, 42 (1), pp. 272–281.

Kokkalis, T. and Galbraith, R. A. McD. 1986. "Description of and Preliminary Results From a New Blade-Vortex Interaction Test Facility," 12th European Rotorcraft Forum, Garmish, Germany, Sept. 22–25.

Kottappalli, S. B. R. 1985. "Unsteady Aerodynamics of Oscillating Airfoils with Inplane Motions, *J. of the American Helicopter Soc.* 30 (1), pp. 62–63.

Küssner, H. G. 1935. "Zusammenfassender Bericht über den instationären Auftrieb von Flügeln," *Luftfahrtforschung*, 13 (12), pp. 410–424.

Küssner, H. G. and Schwartz, L. 1941. "The Oscillating Wing with Aerodynamically Balanced Elevator," NACA Translation TM 991.

Leishman, J. G. 1987a. "Validation of Approximate Indicial Aerodynamic Functions for Two-Dimensional Subsonic Flow," *J. of Aircraft*, 25 (10), pp. 914–922.

Leishman, J. G. 1987b. "A Two-Dimensional Model for Airfoil Unsteady Drag below Stall," *J. of Aircraft*, 25 (7), pp. 665–666.

Leishman, J. G. 1993. "Indicial Lift Approximations for Two–Dimensional Subsonic Flow as Obtained from Oscillatory Measurements," *J. of Aircraft*, 30 (3), pp. 340–351.

Leishman, J. G. 1994. "Unsteady Lift of a Flapped Airfoil by Indicial Concepts," *J. of Aircraft*, 31 (2), pp. 288–297.

Leishman, J. G. 1996. "Aeroacoustics of 2-D and 3-D Blade Vortex Interaction Using the Indicial Method," 52nd Annual Forum of the American Helicopter Soc., Washington DC, June 4–6.

Leishman, J. G. 1997. "Unsteady Aerodynamics of Airfoils Encountering Traveling Gusts and Vortices," *J. of Aircraft*, 34 (6), pp. 719–729.

Leishman, J. G. 1999. "Acoustic Focusing Effects During Parallel and Oblique Blade Vortex Interaction," *J. of Sound and Vibration*, 221 (3), pp. 415–441.

Leishman, J. G. and Nguyen, K. Q. 1990. "A State-Space Representation of Unsteady Aerodynamic Behavior," *AIAA J.*, 28 (5), pp. 836–845.

Liiva, J., Davenport, F. J., Gray, L., and Walton, I. C. 1968. "Two-Dimensional Tests of Airfoils Oscillating Near Stall," USAAVLABS TR 68-13, Vols. I & II.

Loewy, R. G. 1957. "A Two-Dimensional Approximation to the Unsteady Aerodynamics of Rotary Wings," *J. of the American Helicopter Soc.*, 24 (2), pp. 81–92.

Lomax, H. 1953. "Lift Developed on Unrestrained Rectangular Wings Entering Gusts and Subsonic and Supersonic Speeds," NACA Technical Note 2925.

Lomax, H. 1968. "Indicial Aerodynamics," Chapter 6, AGARD Manual on Aeroelasticity.

Lomax, H., Heaslet, M. A., Fuller, F. B., and Sluder, L. 1952. "Two and Three Dimensional Unsteady Lift Problems in High Speed Flight," NACA Report 1077.

Long, L. N. and Brentner, K. S. 2000. "Self-Scheduling Parallel Methods for Multiple Serial Codes with Application to WOPWOP," AIAA Paper 2000-0346, 38th AIAA Aerospace Sciences Meeting and Exhibit, Reno, NV, Jan. 10–13.

Lorber, P. F. 2000. "Active Flap Full Scale Oscillating Blade Section Experiment," American Helicopter Soc. NE Region Technical Specialists' Meeting on Improving Rotorcraft Acceptance through Active Controls Technology, Bridgeport, CT, Oct. 4–5.

Lowson, M. V. 1992. "Progress Towards Quieter Civil Helicopters, *Aeronautical J.*, 96, pp. 209–223.

Lowson, M. V. 1996. "Focusing of Helicopter BVI Noise," *J. of Sound and Vibration*, 190 (3), pp. 477–484.

Lowson, M. V. and Ollerhead, J. B. 1968. "Studies of Helicopter Rotor Noise," USAAVLABS Technical Report 68–60.

Mazelsky, B. 1952a. "Determination of Indicial Lift and Moment of a Two-Dimensional Pitching Airfoil at Subsonic Mach Numbers from Oscillatory Coefficients with Numerical Calculations for a Mach Number of 0.7," NACA TN 2613.

Mazelsky, B. 1952b. "On the Noncirculatory Flow about a Two-Dimensional Airfoil at Subsonic Speeds," *J. of the Aeronautical Sciences*, 19 (12), pp. 848–849.

Mazelsky, B. and Drischler, J. A. 1952. "Numerical Determination of Indicial Lift and Moment Functions of a Two-Dimensional Sinking and Pitching Airfoil at Mach Numbers 0.5 and 0.6," NACA TN 2739.

McCroskey, W. J. and Goorjian, P. M., 1983. "Interactions of Airfoils with Vertical Gusts and Concentrated Vortices in Unsteady Transonic Flow," AIAA Paper 83-1691, 16th Fluid and PlasmaDynamics Conference, Danvers, MA, July 12–14.

Miles, J. W. 1956. "The Aerodynamic Force on an Airfoil in a Moving Gust," *J. of the Aeronautical Sciences*, 23 (11), pp. 1044–1050.

Miller, R. H. 1964. "Unsteady Air Loads on Helicopter Rotor Blades," *J. of the Royal Aeronautical Soc.*, 68 (640), pp. 217–229.

Onyenonwu, R. O. 1975a. "Sonic Boom Signatures and Ray Focusing in General Manoeuvres: 1. Analytical Foundations and Computer Formulation," *J. of Sound and Vibration*, 42 (1), pp. 85–102.

Onyenonwu, R. O. 1975b. "Sonic Boom Signatures and Ray Focusing in General Manoeuvres: 2. Numerical Study," *J. of Sound and Vibration*," 42 (1), pp. 103–114.

Osborne, C. 1973. "Unsteady Thin Airfoil Theory in Subsonic Flow," *AIAA J.*, 11 (2), pp. 205–209.

Parameswaran, V. and Baeder, J. D. 1997. "Indicial Aerodynamics in Compressible Flow–Direct Calculations," *J. of Aircraft*, 34 (1), pp. 131–133.

Rainey, A. G. 1957. "Measurement of Aerodynamic Forces for Various Mean Angles of Attack on an Airfoil Oscillating in Pitch and on Two Finite-Span Wings Oscillating in Bending with Emphasis on Damping in the Stall," NACA Report 1305.

Ringler, T. D., George A. R., and Steele J. B. 1991. "The Study of Blade-Vortex Interaction Sound Generation and Directivity," American Helicopter Soc. International Technical Specialist Meeting, Valley Forge, PA, Oct. 15–17.

Schmitz, F. H. 1991. "Aeroacoustics of Flight Vehicles: Theory and Practice," NASA Reference Publication 1258, Chapter 2. Rotor Noise, pp. 65–149.

Schmitz, F. H. 1998. "Reduction of Blade Vortex Interaction (BVI) Noise through X-Force Control," *J. of the American Helicopter Soc.*, 43 (1), pp. 14–24.

Schmitz, F. W. and Yu, Y. U. 1986. "Helicopter Impulsive Noise: Theoretical and Experimental Status," *J. of Sound and Vibration*, 109 (3), pp. 361–422.

Sears, W. R. 1940. "Operational Methods in the Theory of Airfoils in Nonunform Motion," *J. of the Franklin Institute*, 230, pp. 95–111.

Sears, W. R. and Sparks, B. O. 1941. "On the Reaction of an Elastic Wing to Vertical Gusts," *J. of the Aeronautical Sciences*, 9 (2), pp. 64–81.

Seath, D. D., Kim, J. M., and Wilson, D. R. 1987. "An Investigation of the Parallel Blade-Vortex Interaction in a Low Speed Wind-Tunnel," AIAA Paper 87-1345, 19th Fluid Dynamics, Plasma Dynamics, and Lasers Conference, Honolulu, HI, June 8–10,

Sim. B. W-C. and George, A. R. 1996. "The Propagation of Caustics in Rotorcraft Blade-Vortex Interaction Noise," AIAA Paper 96-1737, 2nd AIAA and CEAS, Aeroacoustics Conference, State College, PA, May 6–8.

Sim, B. W-C., George, A. R., and Yen, S. J. 1995. "Blade-Vortex Interaction Noise Studies Using the Trace Mach Number," American Helicopter Soc. Aeromechanics Specialist Conference, Bridgeport, CT, Oct. 11–13.

Sim, B. W-C., Leishman, J. G., Strawn, R. C., and George, A. R. 1997. "Analytical and Computational Investigations of Oblique Blade-Vortex Interaction Generated Noise," AIAA Paper 97-1706, 3rd AIAA/CEAS Aeroacoustics Conference, Atlanta, GA, May 12–14.

Singh, R. and Baeder, J. D. 1997a. "The Direct Calculation of Indicial Lift Response of a Wing Using Computational Fluid Dynamics," *J. of Aircraft*, 35 (4), pp. 465–471.

Singh, R. and Baeder, J. D. 1997b. "Generalized Moving Gust Response Using CFD with Application to Airfoil–Vortex Interaction," AIAA Paper 97-2208, 15th AIAA Applied Aerodynamics Conference, Atlanta, GA, June 23–25.

Silviera, M. A. and Brooks, G. W. 1959. "Dynamic-Model Investigation of the Damping of Flapwise Bending Modes of Two-Blade Rotors in Hovering and a Comparison with Quasistatic and Unsteady Aerodynamic Theories," NACA TN D-175.

Srinivasan, G.R. and McCroskey, W. J. 1987. "Numerical Simulations of Unsteady Airfoil Interactions," *Vertica*, 11 (1/2), pp. 3–28.

Stahara, S. S. and Spreiter, J. R. 1976. "Research on Unsteady Transonic Flow Theory," NEAR TR-107, Jan. For Office of Naval Research, Arlington, VA.

Strawn, R. C., 1997. "New Computational Methods for the Prediction and Analysis of Helicopter Noise," *J. of Aircraft*, 34 (5), pp. 665–672.

Sullivan, B. M., Edwards, B. D., Brentner, K. S., and Booth, E. A., Jr. 2002. "A Subjective Test of Modulated Blade Spacing for Helicopter Main Rotors," AHS International 58th Annual Forum and Technology Display, Montréal, Canada, June 11–13.

Surendraiah, M. 1970. "An Experimental Study of Rotor Blade-Vortex Interaction," NASA CR-1573.

Tijdeman, H. and Schippers, P. 1973. "Results of Pressure Measurements on an Airfoil with Oscillating Flap in Two-Dimensional High Subsonic and Transonic Flow," National Aerospace Laboratory, The Netherlands, July.

Theodorsen, T. 1935. "General Theory of Aerodynamic Instability and the Mechanism of Flutter," NACA Report 496.

Theodorsen, T. and Garrick, I. E. 1942. "Nonstationary Flow about a Wing-Aileron-Tab Combination, Including Aerodynamic Balance," NACA Report 736, 1942.

van der Wall, B. and Leishman, J. G. 1994. "The Influence of Variable Flow Velocity on Unsteady Airfoil Behavior," *J. of the American Helicopter Soc.*, 39 (4), pp. 288–297.

Vepa, R. 1976. "On the Use of Padé Approximants to Represent Unsteady Acrodynamic Loads for Arbitrary Small Motions of Wings," AIAA Paper 76-17, 14th AIAA Aerospace Sciences Meeting and Exhibit, Washington DC., Jan. 26–28.

von Kármán, Th. and Biot, M. A. 1940. *Mathematical Methods in Engineering*, McGraw-Hill Book Company, Inc., New York and London.

von Kármán, Th. and Sears, W. R. 1938. "Airfoil Theory for Non-Uniform Motion," *J. of the Aeronautical Sciences*, 5 (10), pp. 379–390.

Wagner, H. 1925. "Über die Entstehung des dynamischen Auftriebes von Tragflügeln," *Zeitschrift für Angewandte Mathematik und Mechanik*, 5 (1), pp. 17–35.

White, R. B. and Landahl, M. 1968. "Effect of Gaps on the Loading Distribution of Planar Lifting Surfaces," *AIAA Journal*, 6 (4), pp. 626–631.

Widnall, S. 1971. "Helicopter Noise Due to Blade–Vortex Interaction," *J. of the Acoustical Soc. of America*, 50 (1), Pt. 2, pp. 354–365.

Wood, M. E. 1979. "Results from Oscillatory Pitch Tests on the NACA 0012 Blade Section," ARA Memo 220, Aircraft Research Association, Bedford, UK.

Yu, Y. H., Gmelin, Y. B., Heller, H., Philippe, J. J., Mercker, E., and Preisser, J. S. 1994. "Higher Harmonic Control Aeroacoustics Test–The Joint German/French/US HART Project," Proceedings of 20th European Rotorcraft Forum, Amsterdam, Netherlands, Oct. 4–7.

Zwaan, R. J. 1982a. "NACA 64A006, Oscillating Flap," In: AGARD R–702, A Compendium of Unsteady Aerodynamic Measurements, N. C. Lambourne (ed.).

Zwaan, R. J. 1982b. "NLR 7301 Supercritical Airfoil–Oscillatory Pitching and Oscillating Flap," In: AGARD R-702, A Compendium of Unsteady Aerodynamic Measurements, N. C. Lambourne (ed.).

CHAPTER 9

Dynamic Stall

Fortunately, engineers and technologists do not wait until everything is completely understood before building and trying new devices. Even so, an improved understanding of fundamental unsteady fluid flow processes can serve to stimulate new innovations, as well as improvements in the performance, reliability, and costs of many existing machines. Therefore, research in unsteady fluid dynamics seems assured a lively future in modern industrial societies.

William J. McCroskey (1975)

9.1 Introduction

The phenomenon of dynamic stall has long been known to be a factor that limits helicopter performance. The problem of dynamic stall usually occurs on the rotor at high forward flight speeds or during maneuvers with high load factors and is accompanied by the onset of large torsional airloads and vibrations on the rotor blades – see, for example, Tarzanin (1972), McCroskey & Fisher (1972), McHugh (1978), Bousman (1998), and Isaacs & Harrison (1989). Whereas for a fixed-wing aircraft, stall occurs at low flight speeds, stall on a helicopter rotor will occur at relatively high airspeeds as the advancing and retreating blades begin to operate close to the limits where the flow can feasibly remain attached to the airfoil surfaces. As shown previously by Fig. 7.1, the advancing blade operates at low values of AoA but close to its shock induced flow separation boundary. The retreating blade operates at much lower Mach numbers but encounters very high values of AoA close to stall. Because of the time-varying blade element AoA resulting from blade flapping, cyclic pitch inputs, and wake inflow, the flow separation and stall ultimately occurs on a rotor in a very much more dynamic or time-dependent manner. This stall phenomenon is, therefore, is referred to as "dynamic stall." Despite the fact that the static stall characteristics of airfoils have been discussed extensively in Chapter 7, the problem of flow separation and airfoil stall must now be reassessed from a nonsteady perspective.

Following the general definition given by McCroskey and colleagues (1976, 1982), dynamic stall will occur on any airfoil or other lifting surface when it is subjected to time-dependent pitching, plunging or vertical translation, or other type of nonsteady motion, that takes the effective AoA above its normal static stall angle. Under these circumstances, the physics of flow separation and the development of stall have been shown to be fundamentally different from the stall mechanism exhibited by the same airfoil under static (quasi-steady) conditions (i.e., where $k = 0$). Dynamic stall is, in part, distinguished by a delay in the onset of flow separation to a higher AoA than would occur statically. This initial delay in stall onset is obviously advantageous as far as the performance and operational flight envelope of a helicopter rotor is concerned. However, when dynamic flow separation does occur, it is found to be characterized by the shedding of a concentrated vortical disturbance from the leading edge region of the airfoil. As long as this vortex disturbance stays over the airfoil upper surface, it acts to enhance the lift being produced. Yet, the vortex flow pattern

is not stable, and the vortex is quickly swept over the chord of the blade by the oncoming flow. This produces a rapid aft movement of the center of pressure, which results in large nose-down pitching moments on the blade section and an increase in torsional loads on the blades. This is the main adverse characteristic of dynamic stall that concerns the rotor analyst, for which the effects have proved difficult to predict.

As discussed by Beddoes (1979, 1983) and Wilby (1984, 1996, 1998), the consideration of dynamic stall in the rotor design process will more accurately define the operational and overall performance boundaries of the helicopter. Generally the rotor will be first designed so that the onset of high blade loads, aeroelastic problems, or limits in flight performance are not limiting factors on the basis of linear and nonlinear quasi-steady aerodynamic assumptions (i.e., using the blade element representations described in Chapter 7). Nonlinearities in the airloads associated with dynamic stall can introduce further effects that give rise to dangerously high blade stresses, vibrations, and control loads. One such nonlinear phenomena is called *stall flutter*.[1] Because of the significant hysteresis in the airloads as functions of AoA that takes place during dynamic stall, and also because of the possibilities of lower aerodynamic damping, an otherwise stable elastic blade mode can become unstable if flow separation is present. Therefore, the onset of dynamic stall generally defines the overall lifting, propulsive, and aeroelastic performance limits of a helicopter rotor.

The accurate prediction of the combination of AoA and Mach number on the blade section that will produce dynamic stall onset, as well as the prediction of the subsequent effects of dynamic stall on rotor loads and performance, is not an easy task. The phenomenon of dynamic stall is not fully understood and is still the subject of much research on both experimental and numerical fronts – see Carr (1988). The very large number of publications on the phenomenon (see bibliography for this chapter) illustrates the importance of dynamic stall in the more complete aerodynamic and aeroelastic analysis of the helicopter rotor and the difficulties in both measuring and predicting the phenomenon. The complicated nonlinear physics of dynamic stall means that the behavior can only be completely modeled by means of numerical solutions to the Navier–Stokes equations (using computational fluid dynamics or CFD). This, like other CFD problems that involve unsteady, compressible, separated flows, the solution to dynamic stall problems is a formidable task that is not yet practical, but see the detailed discussion in Section 14.10.1. However, since the early 1990s, the rapid increase in computer resources has enabled considerable progress to be made in modeling dynamic stall by means of CFD approaches – see, for example, Srinivasan et al. (1993), Ekaterinaris et al. (1994), Landgrebe (1994), Barakos et al. (1998), and Spentzos et al. (2004). CFD methods will eventually prevail, but for the most part these methods are currently impractical for routine use in helicopter rotor analyses or design studies. For engineering analyses, the modeling of dynamic stall also remains a particularly challenging problem. To this end, a large number of semi-empirical models have been developed for use in helicopter rotor analysis and design codes. A brief discussion of some of these methods will be described in this chapter, along with a demonstration of their general capabilities in predicting dynamic stall induced airloads. While giving good results, these models are not strictly predictive tools and can really only be used confidently for conditions that are bounded by validation with experimental data. Such data, unfortunately, are not easy to obtain, requiring extensive wind tunnel testing on airfoils and wings, but remains fundamental to the success of such engineering models.

[1] This is different from classical flutter, which involves fully attached flow.

9.2 Flow Morphology of Dynamic Stall

The effects of unsteady motion on unsteady airfoil behavior and dynamic flow separation have been recognized for many years, mainly through studies of oscillating airfoils in wind-tunnel experiments. As mentioned previously, for an increasing AoA it has been observed that the flow remains attached to the upper surface of an airfoil to an AoA much higher than that could be attained quasi-statically, giving a corresponding increase in maximum lift. Kramer (1932) was one of the first investigators to observe the phenomenon. The delay in the onset of flow separation under unsteady conditions is a result of three primary unsteady phenomena. First, during the conditions where the AoA is increasing with respect to time, the unsteadiness of the flow resulting from circulation that is shed into the wake at the trailing edge of the airfoil causes a reduction in the lift and adverse pressure gradients compared to the steady case at the same AoA. This "classical" effect has been described in Section 8.6. Second, by virtue of a kinematic induced camber effect, which has also been described in Section 8.6, a positive pitch rate further decreases the leading edge pressure and pressure gradients for a given value of lift. This can be considered a quasi-steady effect. Ericsson (1967), Carta (1971), Johnson & Ham (1972), Ericsson & Redding (1972), McCroskey (1973), and Beddoes (1978) have given a good summary of these basic effects from the perspective of unsteady airfoil theory. Third, in response to the external pressure gradients, there are also additional unsteady effects that occur within the boundary layer, including the existence of flow reversals in the absence of any significant flow separation – see McAlister & Carr (1979). These unsteady boundary layer effects have been quantitatively examined by Scruggs et al. (1974), Telionis (1975), and McCroskey (1975). Although the behavior of unsteady turbulent boundary layers is still not fully understood, the onset of flow separation on airfoils is generally found to be delayed by unsteady effects such as those associated with increasing pitch rate. Coupled with the aforementioned pressure gradient reductions, the resulting lag in the formation of boundary layer separation causes the onset of dynamic stall to be averted to a significantly higher AoA than would be obtained under quasi-steady conditions.

Ultimately, however, with increasing AoA, the high adverse pressure gradient that builds up near the leading edge under dynamic conditions causes flow separation to occur there. Experimental evidence suggests the formation of a free shear layer that forms just downstream of the leading edge, which quickly rolls up and forms a vortical disturbance. This feature is now known to be a very characteristic aspect of dynamic stall and is shown in the flow visualization images in Fig. 9.1. Not long after it is formed, this vortical disturbance leaves the leading edge region and begins to convect over the upper surface of the airfoil. This induces a pressure wave that sustains lift and produces airloads well in excess of those obtained under steady conditions at the same AoA. A qualitative understanding of this vortex shedding phenomenon was first given by Ham (1968) and McCroskey (1972a,b) and is reviewed by Beddoes (1979). A great number of subsequent experimental studies have provided a much more comprehensive physical understanding of the factors that determine the onset of dynamic stall, including the important influence of compressibility – see Beddoes (1978, 1983), Lorber (1992), and Chandrasekhara & Carr (1990, 1994). However, there have been fewer experimental studies of dynamic stall at the combinations of Reynolds numbers and Mach numbers that would be useful to the helicopter analyst. Fortunately, a few studies have been commissioned to study the effects of compressibility on the quantitative effects of dynamic stall on airfoils operating at or near to full-scale rotor Reynolds numbers – see, for example, Liiva et al. (1968) and Wood (1979). Generally, the results have shown that the qualitative features of the dynamic stall process remain similar

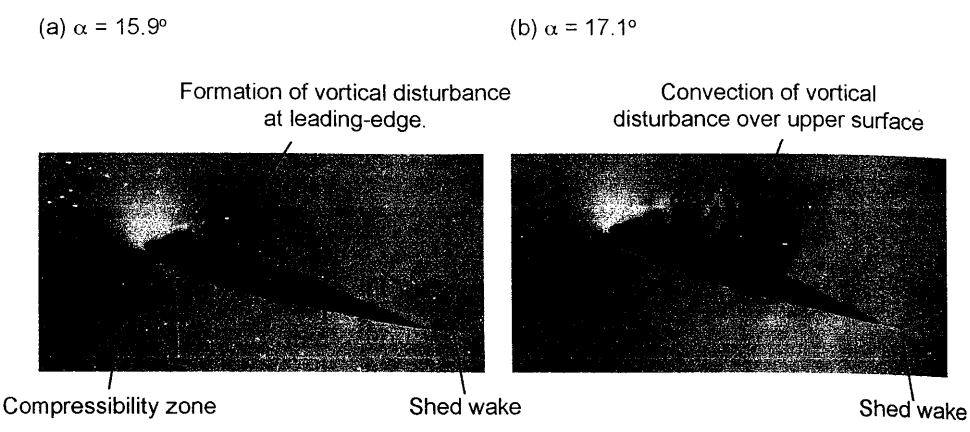

Figure 9.1 Visualization of dynamic stall using schlieren. Source: Chandrasekhara & Carr (1990) and courtesy of M. S. Chandrasekhara.

over a fairly wide range of Mach numbers and also under different types of forcing condition (i.e., for pitching oscillations, plunging oscillations, and ramp or constant angular rate motions). Yet, the quantitative behavior of the airloads shows subtle variations with Mach number, especially for different airfoil shapes and under 3-D conditions. It is these more subtle aspects of the dynamic stall problem that make its accurate prediction difficult for the helicopter rotor analyst.

The various stages of the dynamic stall process are summarized schematically by means of Fig. 9.2. Stage 1 represents the delay in the onset of flow separation in response to a reduction in adverse pressure gradients produced by the kinematics of pitch rate (induced camber), the influence of the shed wake and the unsteady boundary layer response. Stage 2 of the dynamic stall process involves flow separation and the formation of a vortex disturbance that is cast-off from the leading edge region of the airfoil. This vortex disturbance provides additional lift on the airfoil so long as it stays over the upper surface. In some cases, primarily at low Mach numbers, the additional "lift overshoots" produced by this process may be between 50 and 100% higher than the static value of maximum lift. The effective lift-curve-slope may also increase during this process. These, often surprisingly large increments in lift, are also accompanied by significant increases in nose-down pitching moment, which results from an aft moving center of pressure as the vortex disturbance is swept downstream across the chord. The speed at which the vortex convects downstream has been documented to be between one third and one half of the free-stream velocity – see Beddoes (1976) and Galbraith et al. (1986). It will also be seen from Fig. 9.2, that the sudden "break" in the lift coefficient at the start of Stage 3 occurs at a higher AoA than that for the divergence in the pitching moment; that is, the pitching moment break (moment stall) occurs at the onset of vortex shedding (start of Stage 2), whereas the lift break (lift stall) occurs when the vortex passes into the wake (end of Stage 2 and start of Stage 3).

After the vortex disturbance passes the trailing edge of the airfoil and becomes entrained into the turbulent wake downstream of the airfoil, the flow on the upper surface progresses to a state of full separation. This is referred to as Stage 4 of the dynamic stall process: it is accompanied by a sudden loss of lift, a peak in the pressure drag and a maximum in nose-down pitching moment. In this flow state, the airloads are approximately the same as those found under steady conditions at the same AoA. Flow reattachment can take place if and when the AoA of the airfoil becomes low enough again. However, there is generally a significant lag in this process [see Green & Galbraith (1995)]. First, there is a

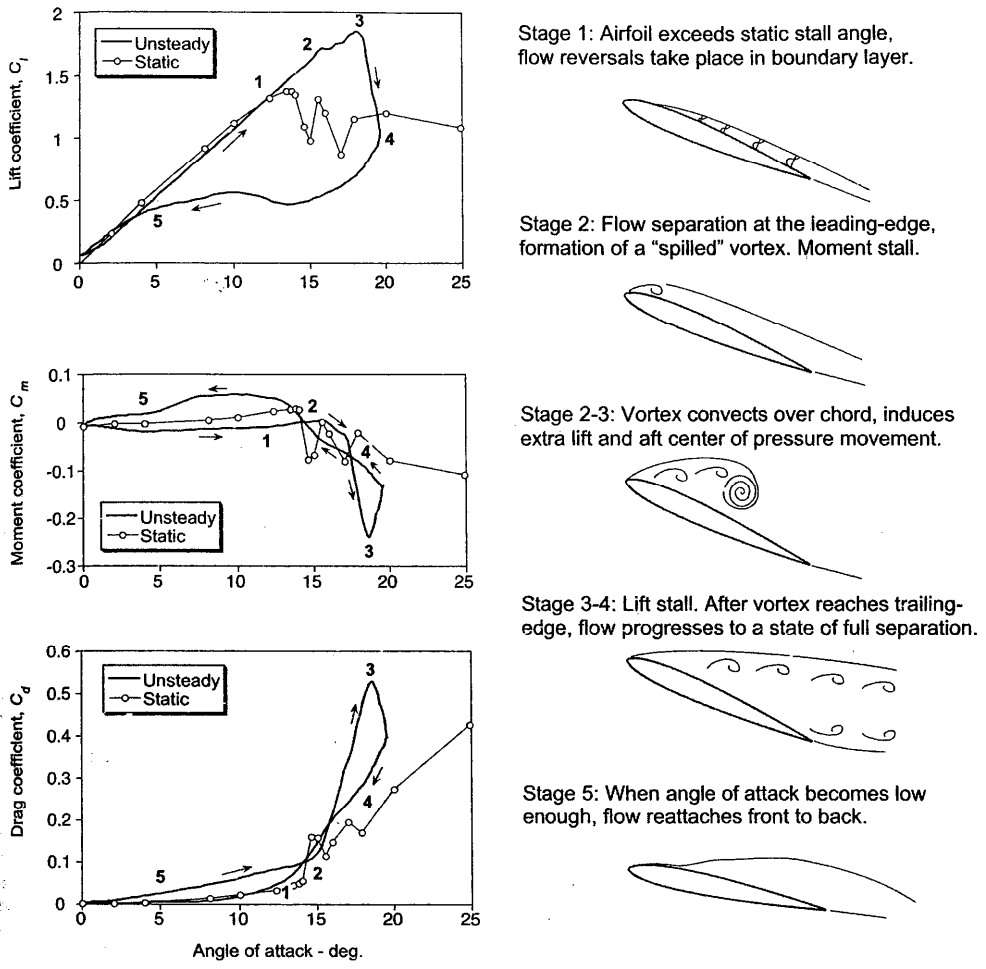

Figure 9.2 Schematic showing the essential flow morphology and the unsteady airloads during the dynamic stall process on an oscillating 2-D airfoil. Adapted from Carr et al. (1977) and McCroskey et al. (1982).

general lag in the reorganization of the flow from the fully separated state until it becomes amenable to reattachment. Second, there is a lag because of the reverse kinematic "induced camber" effect on the leading edge pressure gradient by the negative pitch rate (see also Question 8.2). Therefore, full flow reattachment may not be obtained until the airfoil is well below its normal static stall angle, as denoted by Stage 5 in Fig. 9.2. In this particular case, it is apparent that the AoA falls to as low as 5° before the flow can be considered as fully attached. Because of these lags in the development of the various flow states, a large amount of hysteresis is present in all three components of the unsteady airloads. These hysteresis effects are the source of reduced aerodynamic damping, which as mentioned previously, can potentially lead to aeroelastic problems on the rotor.

9.3 Dynamic Stall in the Rotor Environment

While much of what is known about dynamic stall has been obtained from idealized experiments on 2-D airfoils in wind tunnels, it is important to recognize that when

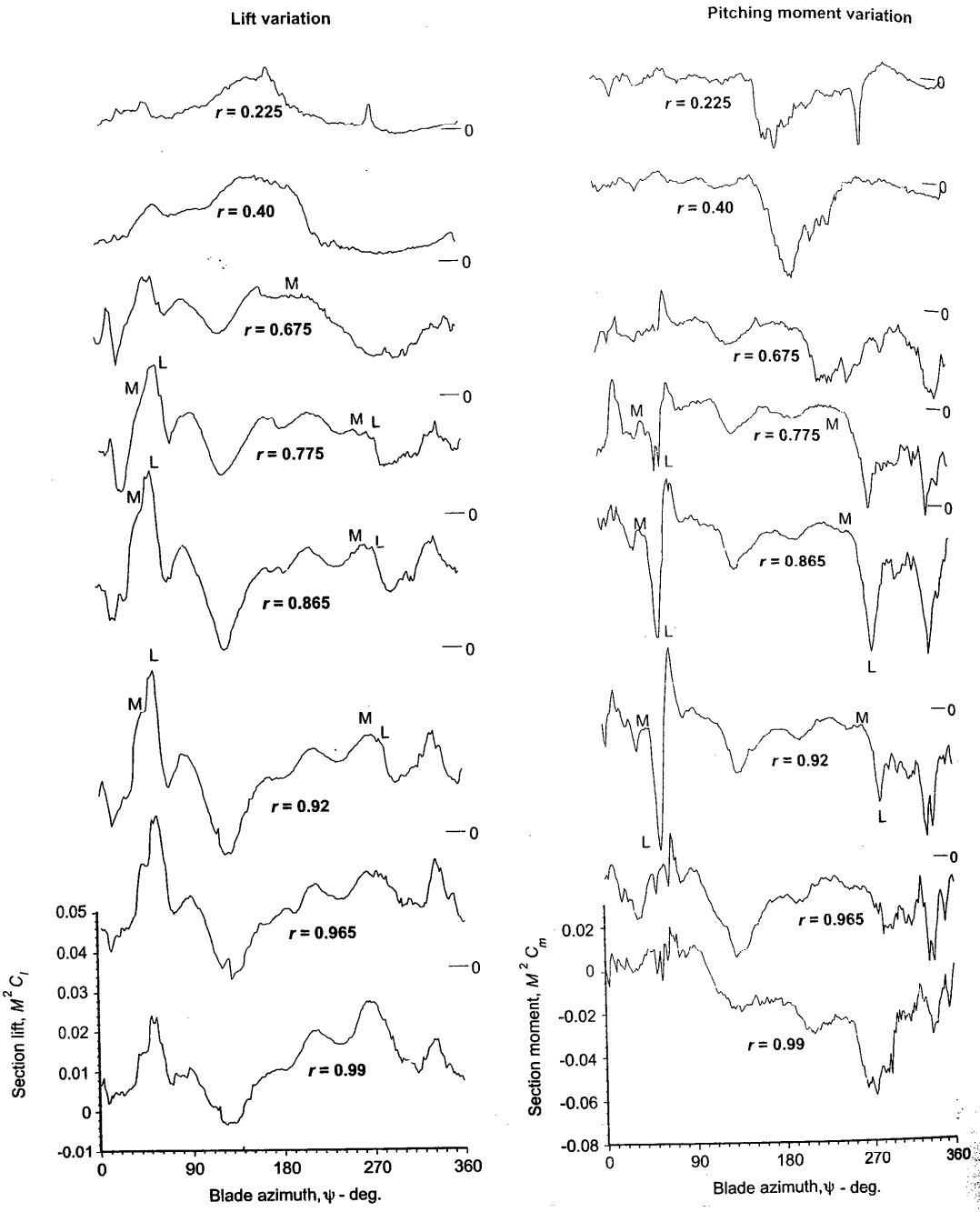

Figure 9.3 In-flight measurements of sectional lift and pitching moment over the blade of a UH-60 operating at high thrust in forward flight indicating the occurrence of dynamic stall. M = moment stall; L = lift stall. Data source: Bousman (1998).

dynamic stall occurs on the rotor, it has a more 3-D character than previously described and may simultaneously occur over several radial and azimuthal parts of the rotor disk. Continued advances in miniature pressure transducer technology, high-speed data acquisition and telemetry systems have enabled a more detailed understanding of dynamic stall

as it manifests on helicopters during actual flight. Isaacs & Harrison (1989) and Bousman (1998) provide good in-flight documentation of the dynamic stall phenomenon on helicopter blades. The results shown in Fig. 9.3 are adapted from Bousman (1998) and show the time histories of the lift and pitching moment at various radial stations on the blade of a UH-60 helicopter during a pull-up maneuver at $\mu \approx 0.3$ and $C_T/\sigma \approx 0.17$. The results are presented in terms of the nondimensional quantities M^2C_n and M^2C_m, because these quantities give a better quantitative measure of the local airloads produced on the rotor.

Using the unsteady chordwise pressures as an indicator, Bousman (1998) has identified three locations on the rotor disk for this flight condition that show the lift overshoots and large nose-down pitching moments that are characteristic features of dynamic stall. On Fig. 9.3 these are marked by points M (moment stall) and by points L (lift stall). Remember that dynamic lift stall always occurs after moment stall. At these particular flight conditions, it is apparent that dynamic stall encompasses relatively large areas of the rotor disk. In particular, note that the occurrence of dynamic stall causes large transients in the pitching moments, especially between $r = 0.77$ and $r = 0.92$ on the blade in the first quadrant of the disk and also on the retreating side near $\psi = 270°$. Operating the rotor at thrusts or airspeeds beyond this flight condition will result in high structural loads and stresses that can quickly exceed the fatigue or endurance limits of the rotor and/or control system (see Fig. 6.8). Even though the rotor is usually able to operate with some amount of stall, the very rapid growth in the blade torsion and other structural loads because of dynamic stall is normally a limiting factor in the overall operational flight envelope of helicopters – see also Benson et al. (1973) and Stepniewski & Keys (1984).

9.4 Effects of Forcing Conditions on Dynamic Stall

Dynamic stall has been extensively studied experimentally, mostly using oscillating 2-D airfoils in wind tunnels. This simulates the quasi-periodic first harmonic AoA variations that are found on helicopter rotors during forward flight. The majority of the documented experimental results are for airfoils oscillating in pitch, but there are some limited results available for plunging oscillations (vertical translation or heaving), as well as for constant angular rate (ramp) type motion. The former plunging experiments are useful in that pitch rate effects (i.e., $\dot{\alpha}$ effects) can be isolated from the problem. The latter ramp tests are useful in that acceleration effects (i.e., $\ddot{\alpha}$ effects) can be eliminated, somewhat simplifying the understanding of the various effects produced by the airfoil kinematics on the unsteady airloads. However, both pitch and ramp experiments are difficult to perform, especially for the Mach numbers and effective reduced frequencies required to validate any mathematical model of dynamic stall.

A few examples showing the variation of the unsteady airloads with variations in the oscillatory forcing parameters will now be described. With variations in parameters such as the amplitude of the AoA of the oscillation, the mean AoA, and the reduced frequency, the various dynamic stall events such as separation onset, leading edge vortex shedding, and flow reattachment all shift around the cycle to different values of AoA. This process results in significant quantitative changes in the unsteady airloads. Varying one parameter, while holding the others nominally constant can help to provide a better understanding of the physics of dynamic stall. To this end, Figs. 9.4 through 9.6 summarize the effect on the lift and pitching moment for increasing mean AoA, increasing reduced frequency, and increasing Mach number, respectively. The results are for a NACA 0012 airfoil taken from Wood

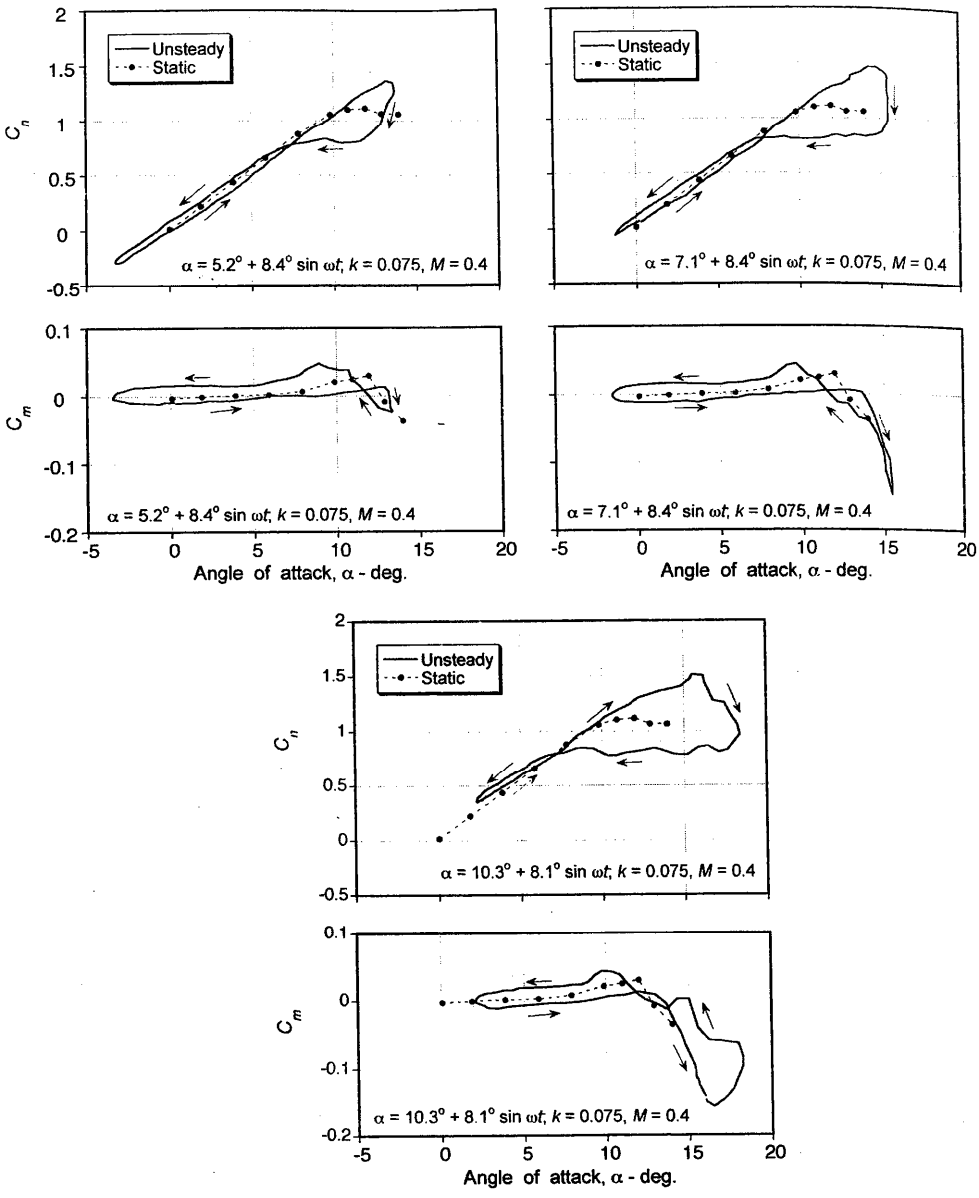

Figure 9.4 Effects of increasing mean AoA on the unsteady lift and pitching moment of an oscillating NACA 0012 airfoil at $M = 0.4$ with $k = 0.075$.

(1979), where the airloads were obtained by integrating pressures measured using miniature pressure transducers distributed around a section of a 2-D wing (see Fig. 7.30).

Figure 9.4 shows the effects of increasing mean AoA, while holding the amplitude of oscillation at approximately 8.4° and the reduced frequency at approximately 0.075. These results show the effects on the airloads as the flow state progresses from nominally attached conditions at the lowest mean angle, through "light" dynamic stall, and into "deep" dynamic stall for the highest mean angle. These "light" and "deep" dynamic stall descriptors were suggested by McCroskey et al. (1976, 1980) and Carr et al. (1977, 1978). For the lowest

mean AoA of 5.2°, Fig. 9.4 shows a typical case of stall onset. This is when the combination of forcing conditions is just sufficient to cause some minor flow separation on the airfoil. Before this occurs, however, there is a delay in the onset of lift stall to a higher AoA and to a higher value of lift compared to the static case. The airloads then show some small deviations from the attached flow behavior (which would be almost pure elliptical loops) near the maximum AoA in the cycle as a result of the limited flow separation. As the AoA is reduced on the down stroke of the cycle the flow reattaches, as indicated by the return to the nominally elliptical shapes of the loop, but it will be noted that the AoA at which flow reattachment occurs is significantly below the static stall angle.

The second case shown in Fig. 9.4 is for a mean AoA of 7.1°, which is high enough to cause stronger leading edge vortex shedding and the creation of airloads that are more typical of "light" dynamic stall. In this case the maximum dynamic lift coefficient is about 0.4 higher than the static value, but the large nose-down pitching moment is of more significance. Also, because of the clockwise loop that is now introduced into the pitching moment curve (the curve now looks like a figure eight), this forcing condition represents a situation with significantly reduced torsional aerodynamic damping.[2] The third case shown in Fig. 9.4 is for a mean AoA of 10.3°, which is high enough such that the behavior would now be characterized as "strong" dynamic stall. Leading edge vortex shedding, again, contributes significantly to increased values of lift but gives a particularly large increase in the nose-down pitching moment. Because of the higher mean AoA, now a larger part of the oscillation cycle involves partly or fully separated flow, and so there are larger hysteresis effects. There is now another large counterclockwise loop introduced into the pitching moment curve, which gives a return to high torsional damping. Flow reattachment is delayed to a fairly low AoA during the down stroke motion. This indicates the relatively long time scales required for the flow to reorganize after strong dynamic stall has occurred and so to allow conditions conducive for flow reattachment to occur.

Figure 9.5 shows the powerful effect of reduced frequency on the lift and pitching moment responses. In the first case, results are shown for a relatively low reduced frequency of 0.06, and for an AoA history that is just sufficient to produce stall onset or light dynamic stall. The other two cases are for the same nominal AoA forcing, but the reduced frequency has been increased to 0.1 and then to 0.15. Of particular note in these cases is that vortex shedding is delayed with increasing reduced frequency until it finally occurs at the maximum AoA achieved in the cycle. This delay in stall onset is, in part, because of the kinematic induced camber effect that is associated with pitch rate (Section 8.6). This effect progressively alleviates the leading edge pressure gradients for a given value of lift and thus delays the onset of flow separation to a higher AoA. At the same time, increasing the reduced frequency also delays the onset of flow reattachment, if flow separation occurs. In the third case, it is apparent that a high enough reduced frequency can be attained to prevent flow separation from being initiated at any point in the cycle. If the mean AoA were to be increased further, then a higher reduced frequency would be required to prevent flow separation.

Finally, Fig. 9.6 illustrates the effect on dynamic stall by increasing the Mach number from 0.4 to 0.7, but under the same nominal forcing conditions, that is, for the same approximate AoA schedule and reduced frequency. It has been shown in Section 7.9.2 that the effects of compressibility manifest as a lower angle for attack for static stall onset. These effects are also found in the dynamic regime, where for the same forcing the

[2] When negative aerodynamic torsional damping occurs, there is a possibility of aeroelastic problems on the rotor, including stall flutter. This effect is discussed quantitatively in Section 9.6.

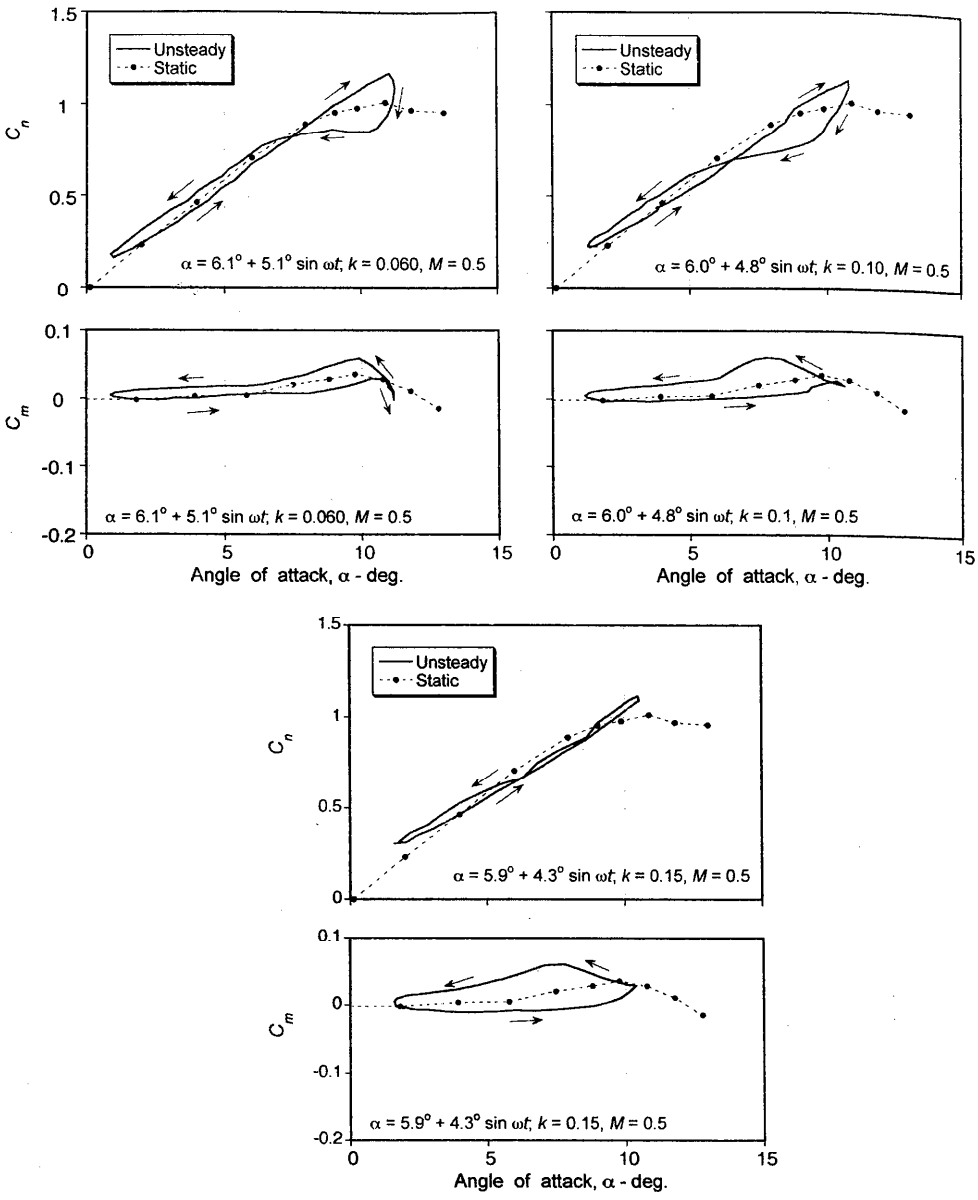

Figure 9.5 Effects of reduced frequency on the unsteady lift and pitching moment of an oscillating NACA 0012 airfoil, with $\alpha \approx 6° + 5° \sin \omega t$, at $M = 0.5$.

degree of stall penetration and amount of hysteresis in the airloads are found to increase with increasing Mach number. Recall that dynamic stall onset is indicated by the break in the pitching moment. In the third case shown in Fig. 9.6, which is for a Mach number of 0.7, the dynamic stall onset involves the participation of a shock wave. This shock wave introduces a more complicated behavior in the center of pressure movement during the flow separation and reattachment process. Beddoes (1983) and Chandrasekhara & Carr (1990, 1994) give a detailed discussion of the role of shock waves in the dynamic stall process.

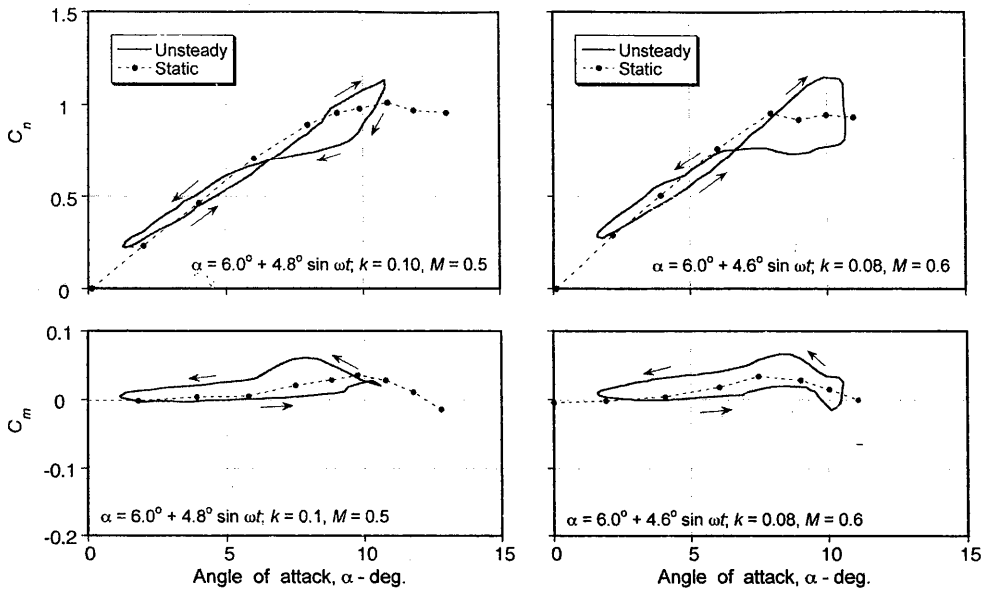

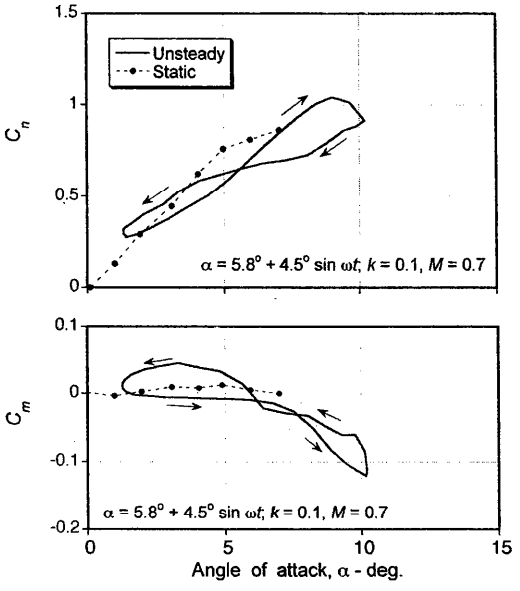

Figure 9.6 Effects of increasing free-stream Mach number on the unsteady lift and pitching moment of an oscillating NACA 0012 airfoil, with $\alpha \approx 6° + 5° \sin \omega t$, and $k \approx 0.1$.

9.5 Modeling of Dynamic Stall

Mathematical models that attempt to predict the effects of dynamic stall currently range from relatively parsimonious empirical or semi-empirical models to sophisticated computational fluid dynamics (CFD) methods. Because dynamic stall is characterized by large recirculating, turbulent separated flow regimes, a proper CFD simulation can only be achieved by solving numerically the full Navier–Stokes equations with a suitable turbulence model. CFD methods have now begun to show some promise in predicting 2-D and 3-D dynamic stall events – see, for example, Srinivasan et al. (1993), Ekaterinaris et al. (1994),

and Spentzos et al. (2004) and also the discussion in Section 14.10.1. However, the quantitative predictions of the airloads are not yet satisfactory in the stalled regime and during flow reattachment and especially not at the Reynolds numbers and Mach numbers appropriate to helicopter rotors. In this regard, the accurate prediction of the transition from a laminar to turbulent boundary layer is a key issue. Furthermore, the computational resources for these CFD solutions are prohibitive other than for use as research tools, and for the foreseeable future more approximate models of dynamic stall will still have to be used in a variety of rotor airloads prediction problems, including rotor design work.

Some of the mathematical models of dynamic stall in current use are a form of resynthesis of the measured unsteady airloads, which are based on results from 2-D oscillating airfoils in wind tunnel experiments. Other so-called semi-empirical models of dynamic stall contain simplified representations of the essential physics using sets of linear and nonlinear equations for the lift, drag, and pitching moment. The nonlinear equations may have many empirical coefficients, which must be deduced (extracted) from unsteady airfoil measurements by parameter identification methods. However, the root of these models is usually based on classical unsteady thin-airfoil theory, as discussed in Chapter 8. The development of the nonlinear part of such models are more subjective and require skillful interpretation of experimental data. As a result, most of these models remain in a perpetual state of flux as the level of detail is refined and/or more experimental data become available for formulation and/or correlation purposes.

While semi-empirical models are usually adequate for most rotor design purposes, they often lack rigor and generality when applied to different airfoils and at different Mach numbers for which 2-D experimental measurements may not be available. Another major problem with some of these types of models is that a significant number of empirical coefficients must be derived. Generally, a set of coefficients for the model must be derived for each and every airfoil, and also over the appropriate range of Mach numbers, assuming such measurements are available. In cases where experimental measurements are not available, the models cannot be used with the same confidence levels to predict the nonlinear airloads. Other common limitations with these models include the accuracy with which the stall onset can be predicted, that is, the prediction of the combination of unsteady AoA and Mach number that produce the onset of dynamic leading edge flow separation. In these cases, computer coding of the model must be done with extreme care to ensure that logic or conditional branching in the algorithm does not cause nonphysical transients in the predictions of the unsteady airloads, especially if large time (azimuth) steps are involved. This undesirable behavior may produce erroneous predictions of stall and aeroelastic behavior, which would be considered unacceptable for rotor design purposes.

Therefore, it is important for the analyst to build up a confidence level with any model selected for the design process. While a review of the literature will show a large number of experiments on dynamic stall that could be used for such purposes, the problem is usually that the full range of Reynolds numbers, Mach numbers, reduced frequencies, and, to some extent, airfoil shapes, cannot be studied in the same test facility or wind tunnel. Therefore, the same problems and uncertainties in data quality that were discussed in Section 7.9 in regard to comparing static airfoil characteristics also apply in the dynamic case.

9.5.1 *Semi-Empirical Models of Dynamic Stall*

Some typical engineering or semi-empirical models that have been used (or are currently being used) for modeling dynamic stall and that may be suitable for rotor airloads

predictions and rotor design analyses are as follows:

1. UTRC α, A, B Method: This is a resynthesis method, with the approach being described by Carta et al. (1970) and Bielawa (1975). The basis of this method is that in attached flow the airloads can be expressed in terms of the forcing parameters α, $A = \dot{\alpha}c/2V$, and $B = \ddot{\alpha}c^2/4V^2$. In an attempt to isolate the dynamic contributions to the airloads, the static coefficients are subtracted from the total airloads. By appropriate crossplotting and interpolating for given instantaneous values of these parameters, the contributions to the dynamic airloads can be reconstructed and added to the static values. The method has met with some success, but large data tables must be generated for each airfoil and for each Mach number. A further development of this model that obviates the need for large tables is given by Bielawa (1975).
2. Boeing-Vertol "Gamma" Function Method: This model was initially developed by Gross & Harris (1969) and Gormont (1973). In the "gamma" function method, the influence of airfoil motion is determined by computing an effective AoA. First, the influence of plunging and pitching effects in attached flow is obtained by applying a "correction" to the AoA derived from Theodorsen's theory at the appropriate reduced frequency of the forcing. From this, a second correction is applied from the instantaneous value of the "gamma" function. This gamma function is obtained empirically as a function of Mach number from 2-D oscillating airfoil tests on the appropriate airfoil. The corrected AoA is then used to obtain values of the airloads from the static force and pitching moment curves. This has the effect of delaying the onset of stall to a higher AoA with increasing pitch rate, a result observed experimentally. The pitching moment is obtained from an empirically determined center of pressure function. Good predictions of the unsteady airloads are possible with this method [see Harris et al. (1970)], but the quantitative accuracy even for 2-D airfoils is deficient for conditions of stall onset or light dynamic stall. This model has been used in a comprehensive rotor analysis for the prediction of helicopter rotor airloads – see Gormont (1973).
3. Time-Delay Method: Beddoes (1976, 1978) has developed a semi-empirical model for dynamic stall. Unlike the previously described resynthesis methods, the philosophy behind this method is to try to model, albeit still in a very simplified manner, the basic physics of the dynamic stall process itself. The method is based in the time domain. The behavior of the airloads in attached flow is obtained from Duhamel superposition using the Wagner indicial response function. Corrections are applied to this function to account for the effects of compressibility. Although scaling the Wagner function in this way is not rigorous, the results obtained approximately replicate the increased lag in the unsteady loads resulting from compressibility effects. The key feature of this model is the use of two nondimensional time delays (based on semi-chords of airfoil travel). These time delays represent periods of nondimensional time that exist between identifiable dynamic stall flow states. The first time delay represents the delay in the onset of flow separation after the static stall angle has been exceeded and the time required for the initial separation to develop. The second time delay represents the time during which the leading edge vortex shedding process occurs. These time delays have been obtained from an analysis of many airfoil tests over a relatively wide range of Mach number. Similar studies have been done by Galbraith et al. (1986) but at

lower Mach numbers. The results from the time-delay model have been shown to give good predictions of the unsteady airloads on 2-D airfoils. The method also requires relatively few empirical constants.

4. Gangwani's Method: Gangwani (1982, 1984) has developed a synthesized airfoil method for the prediction of dynamic stall. This method is also based in the time domain. To model the airloads in attached flow, a "Mach-scaled" Wagner function with a finite-difference approximation to the Duhamel superposition integral is used, very much in the same manner as for the Beddoes time delay model. In the nonlinear part of the model, a series of equations with several empirical coefficients are used to represent the forces and pitching moments produced by the various dynamic stall events. These equations are based on the determination of "delayed" series of AoA, with the associated coefficients being derived from steady and unsteady airfoil data. Although a disadvantage with the method is the relatively large number of equations and empirical coefficients, nearly all of which are derived from oscillating airfoil data, credible predictions of the unsteady airloads have been demonstrated. The capabilities of this model have been independently evaluated by Reddy & Kaza (1987). One of the main difficulties with this method seems to be in predicting flow reattachment after dynamic stall.
5. Johnson's Method: Johnson (1969, 1974) has developed a relatively parsimonious representation for incorporating dynamic stall effects on the sectional airloads. The experimental data of Ham & Garelick (1968) were used to develop the model in a form that could be used to correct the static stall lift and pitching moments as functions of pitch rate. Stall onset was represented by defining vortex shedding to occur just above the static stall AoA. It was assumed that vortex shedding produced increments in lift and nose-down moment that increased linearly to a peak value over a finite time, followed by a decay back to the static loads. Reasonable predictions of the unsteady lift seem possible with this method, although the pitching moment predictions appear less pleasing.
6. Leishman–Beddoes's Method: Leishman & Beddoes (1986, 1989) have developed a model capable of representing the unsteady lift, pitching moment and drag characteristics of an airfoil undergoing dynamic stall. The model has been developed to overcome certain shortcomings of other unsteady aerodynamic models that were available up to about 1980 for use in rotor design and aeroelasticity analysis. The emphasis in this model is on a more complete physical representation of the overall unsteady aerodynamic problem, while still keeping the complexity of the analysis down to minimize computational overheads. The model was initially developed by Beddoes (1983) and Leishman & Beddoes (1986, 1989), with various refinements by Leishman (1989) and Tyler & Leishman (1992). Extensive validation of the model has been conducted with experimental measurements.

   This model consists of three distinct subsystems arranged in the form of a Kelvin chain as shown in Fig. 9.7: 1. An attached flow model for the unsteady (linear) airloads, 2. A separated flow model for the nonlinear airloads, and 3. A dynamic stall model for the leading edge vortex induced airloads. An important feature is that more rigorous representations of compressibility effects are included in the attached flow part of the model. These are represented using the indicial response functions for compressible flow (Section 8.15), along with linear superposition in the form of more accurate finite-difference approximations to the Duhamel's integral. The treatment of nonlinear aerodynamic effects associated with separated flows are derived from Kirchhoff–Helmholtz theory, which can be used to relate

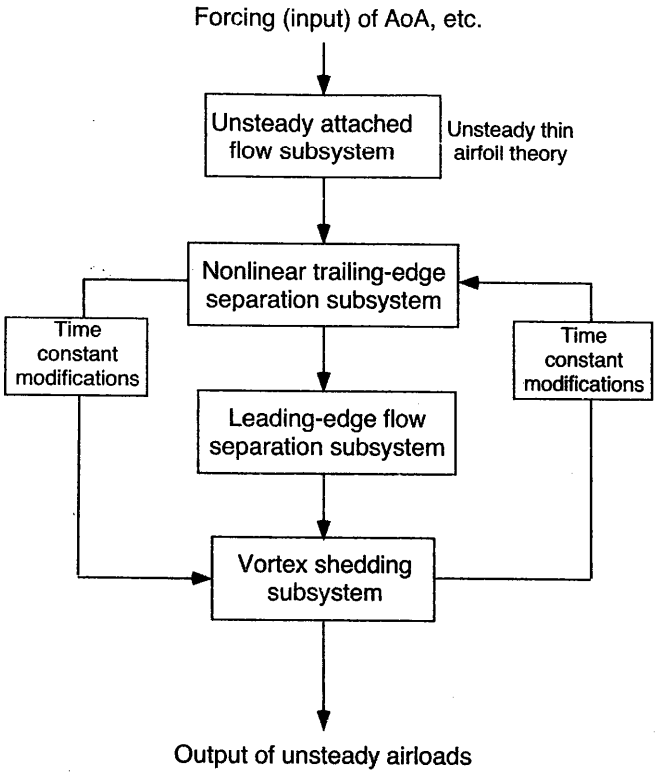

Figure 9.7 Flowchart of the Leishman–Beddoes dynamic stall model showing the connection of linear and nonlinear submodels in the form of a Kelvin chain.

the airfoil lift to the AoA and the trailing edge separation point, a technique discussed previously in Section 7.11.5. In application, the experimental static lift stall characteristics are used with the Kirchhoff–Helmholtz model to define an effective separation point variation that can then be generalized empirically and used to reconstruct the nonlinear airloads for any AoA. To represent the effects of dynamic stall, a third subsystem contains equations that emulates the dynamic effects of the accretion of vorticity into a concentrated leading edge vortex, the passage of this vortex across the upper surface of the airfoil, and its eventual convection downstream. The dynamic stall process begins when an equivalent leading edge pressure parameter reaches a Mach number dependent critical value indicative of leading edge or shock induced separation. To simulate the effects of the complex viscous dominated flow morphology during dynamic stall, the various time constants that describe the behavior of this third subsystem, and also of the trailing edge separation point subsystem, are modified in a logically determined sequence. One significant advantage of this method is that it uses relatively few empirical coefficients, with all but four at each Mach number being derived from static airfoil data. This model has also been adapted and modified by Pierce & Hansen (1995) for the class of airfoil sections used on wind turbines (see Section 13.9).

7. ONERA Method: This model describes the unsteady airfoil behavior in both attached flow and during dynamic stall using a set of nonlinear differential equations. The model was first described by Tran & Pitot (1981), Tran & Falchero (1981),

and McAlister et al. (1984), with various modifications by Peters (1985). A version of the ONERA model has been evaluated by Reddy & Kaza (1987). A later version of the model (the ONERA Edlin model) is documented by Pitot (1989). The coefficients in the equations of this model are determined by parameter identification from experimental measurements on oscillating airfoils. Like several other models, including the Leishman–Beddoes model, the airloads are expressed as a sum of two components: a component associated with the linear (attached flow) behavior and an increment that represents a deviation from the linear value resulting from stall. The model requires 22 empirical coefficients for each Mach number. The later ONERA BH model, as documented by Truong (1993, 1996), requires 18 coefficients and also adapts the Kirchhoff–Helmholtz trailing edge flow separation scheme from the Leishman–Beddoes model.

Generally, reasonable predictions of the unsteady airloads are obtained with the ONERA model – see also Tan & Carr (1996) and Nguyen & Johnson (1998). However, like many of the models, the predictions are deficient for flow reattachment after dynamic stall. Based on the experimental studies of Green & Galbraith (1995), the modeling of dynamic flow reattachment requires as much care as for modeling dynamic flow separation, especially if accurate predictions of aerodynamic torsional damping are an objective. A apparent advantage of the ONERA method is that because all of the equations for the lift, drag, and pitching moment are written as differential equations, they are in a form that can be immediately useful for various types of aeroelastic analysis. However, the Leishman–Beddoes model has also been cast into differential equation form – see Leishman & Crouse (1989) and Leishman & Nguyen (1990). Furthermore, it would seem that the structure of some of the other semi-empirical dynamic stall models may also lend themselves to be cast into the same mathematical form, if required by the analyst.

8. Neural Network Methods: Recursive neural network (RNN) models are a class of nonlinear mathematical methods that have been used to model the effects of dynamic stall – see Faller & Schreck (1996). These models are developed in state-space form, where the state-matrix is developed recursively by "training" neural estimators. Like all semi-empirical models the method first requires access to a data set of measurements that can be used to train the model. In this postdiction (or calibration) phase the simulation error is progressively reduced to reproduce accurately the known input data. An assumption must be made as to the elements of the input forcing; generally the approach has met with reasonable success in reproducing the unsteady airloads under the assumption of simple inputs, such as α, $\dot{\alpha}$, and $\ddot{\alpha}$. In some respects this approach is similar to the character of the UTRC model. However, for a helicopter rotor other elements of forcing are clearly involved (see Fig. 8.2) and training the model for more complicated interdependent inputs still requires further development. In some cases training data for certain modes of forcing may not be available, making RNN models less certain in terms of their ultimate predictive capability. Furthermore, RNN methods have not yet shown convincing results when reduced to simulate the "classical" problems in unsteady aerodynamics, such as idealized harmonic oscillations, nonuniform freestreams or vertical velocity fields, and indicial type problems. The large number of states also makes the RNN approach less attractive for many types of helicopter rotor applications, although the rapid advances in computer speeds makes this less of an issue than it might have been ten or more years ago.

9.5.2 *Capabilities of Dynamic Stall Modeling*

Based on the foregoing discussion, there are several different dynamic stall models available to the helicopter rotor analyst, all of which represent, to an engineering level of approximation, the forces and pitching moments produced on an airfoil during dynamic stall. Reddy & Kaza (1987) have compared and contrasted several of these models, from which the general quantitative capabilities and deficiencies were independently documented. Used intelligently, it would seem that most of these models are adequate for use in a wide variety of rotor analyses. Much comes down to the confidence levels that can be established through correlation studies, both at a 2-D level as well as inside the rotor environment. Tan & Carr (1996) have presented a summary of results for a number of currently used semi-empirical dynamic stall models, as well as first-principles based CFD approaches to the dynamic stall problem. Results have been compared for both an oscillating 2-D airfoil and an idealized 3-D problem in the form of an oscillating cantilevered finite-wing (see Section 9.9). Again, it seems that if the semi-empirical models are used intelligently, very credible predictions of the integrated airloads can be obtained when compared to experimental measurements.

In the following discussion, predictions made by the Leishman–Beddoes model [see Leishman & Beddoes (1986, 1989)] will be used to show the general capabilities of the semi-empirical dynamic stall models. While it should be appreciated that some models might produce different or better results, the idea here is simply to illustrate the overall levels of performance that could be expected from these types of engineering models. It is obviously highly desirable to expose the models to different types of forcing, that is, not solely for oscillatory pitching as might have been used for formulation purposes. As mentioned previously, a large proportion of the aerodynamic changes in AoA that take place in the rotor environment come from blade flapping, which is equivalent to a plunging or heaving type of forcing at the blade element level. One underlying assumption that seems to be made in nearly all the various unsteady aerodynamic models described above is that the effects of blade motions and wake inflow variations can be adequately represented by a lumped "equivalent" AoA – see Eq. 8.182. This proves an adequate assumption for fully attached flows, but Fukushima & Dadone (1977) and Ericsson & Reding (1983) have argued that more fundamental differences may exist in the dynamic stall airloads when different modes of motion are imposed (i.e., pitching versus plunging). This perhaps raises some questions about the capabilities of the various dynamic stall methods, in general, to predict accurately the unsteady airloads for completely arbitrary variations in AoA, pitch rate, and so on. However, while many 2-D oscillating airfoil experiments have been conducted to study dynamic stall, only a few experimental facilities can simulate both pitching and plunging oscillations or other combined motions so that this can be thoroughly verified. This is mainly because plunge experiments are mechanically difficult to perform in a wind tunnel environment, especially over the wide range of amplitudes and reduced frequencies that would be necessary to validate any theory. Liiva et al. (1968) and Carta (1979) have measured oscillatory airloads under oscillatory pitch and plunging conditions. However, only the results obtained by Liiva et al. (1968) are for the ranges of Reynolds numbers and Mach numbers that are representative of those found on a helicopter rotor.

Figure 9.8 shows the normal force and pitching moment coefficient responses obtained for oscillatory pitching and plunging into dynamic stall. Notice that the general features of dynamic stall are evident here, with both sets of results showing a qualitative similarity for both types of forcing. The hysteresis loops predicted by the dynamic stall model are in good

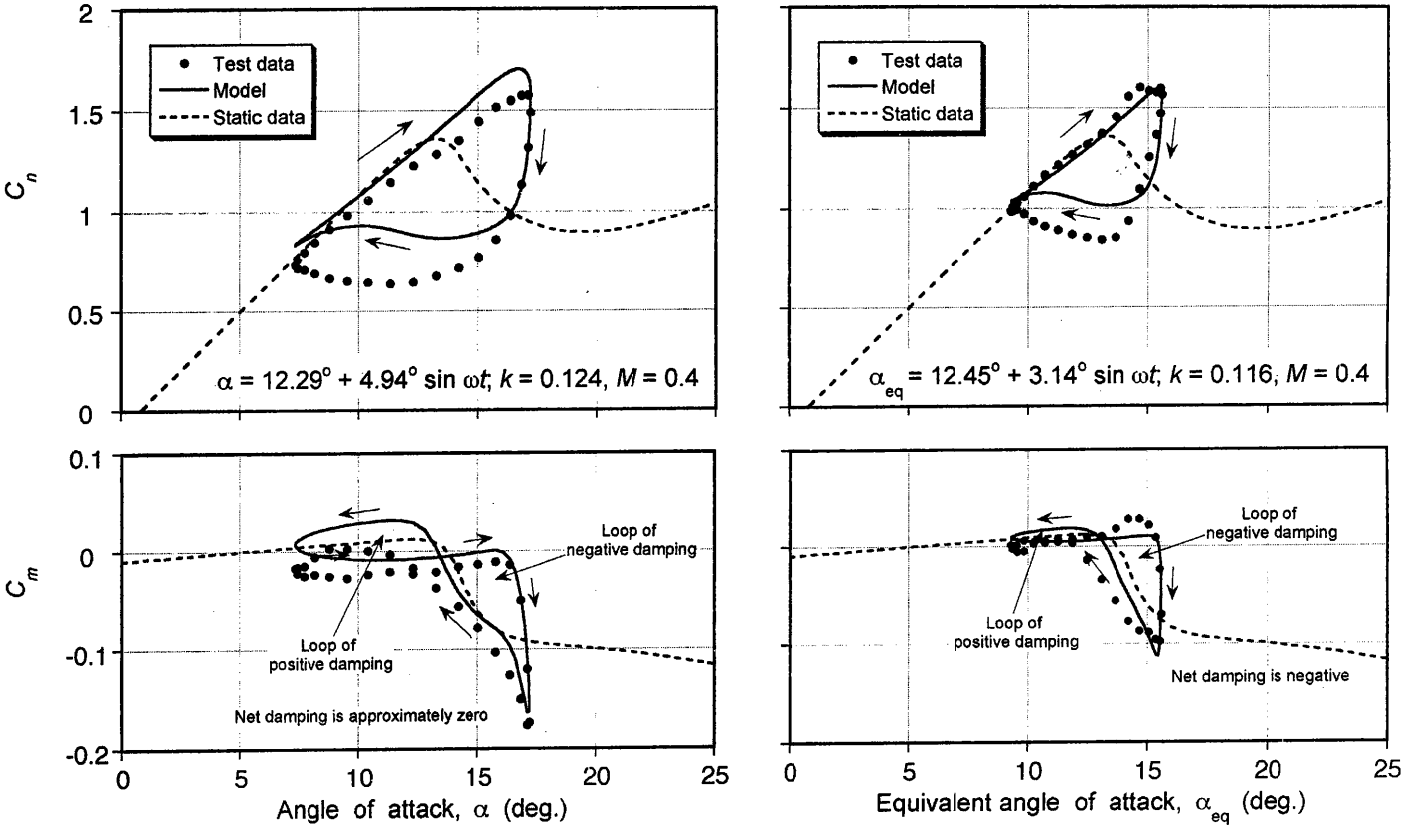

Figure 9.8 Comparison of model with measured airloads under oscillatory pitch and plunge forcing, for NACA 23010 $\alpha = 12.29° + 4.94° \sin \omega t$, $M = 0.4$, $k = 0.124$; $\alpha_{eq} = 12.45° + 3.14° \sin \omega t$, $M = 0.4$, $k = 0.116$. Data source: Liiva et al. (1968).

agreement with the experimental measurements – the only significant discrepancy is during the flow reattachment process. In both cases, stall onset is clearly postponed well above the static stall AoA, followed by leading edge vortex shedding. Both conditions suggest that an organized dynamic stall vortex is formed and convected downstream over the chord, although for the plunge case, the degree of stall penetration is slightly less.

Figure 9.9 shows dynamic stall loops for pitching and plunging oscillations performed at a higher mean AoA. These particular results are for conditions such that the minimum AoA is sufficiently high that the flow can only reattach to the airfoil surface during the latter part of the down stroke in AoA. The agreement of the model with the experimental data is again very good, for both pitch and plunge oscillations. The pitching moment response shows that stall onset is predicted a little early for pitch and later for plunge; in a practical sense these differences are small, however. The maximum nose-down pitching moment for the pitching airfoil is over-predicted, but it is predicted better for the plunging airfoil.

Carta (1979) has concluded that dynamic stall occurred on the airfoils during certain pitch oscillation cases but not in the corresponding plunge cases, even though the same equivalent AoA history was imposed. It appears that this behavior can, in part, be traced to the (inviscid) pressure distribution at the leading edge of the airfoil. For pitch oscillations the favorable "induced camber" effect discussed previously means that, in principle, the leading edge pressure conditions that delimit attached flow should be met at a lower equivalent AoA than for the plunge oscillations. Tyler & Leishman (1992) have confirmed that the stall onset behavior is related to the additional effect of pitch rate contribution to the unsteady airloads during pitch oscillations. Therefore, for "equivalent" conditions the degree of stall penetration and lift and pitching moment hysteresis should be somewhat greater for an equivalent pitch oscillation, confirming Carta's observation.

Ericsson & Reding (1983, 1984) have put forward an alternative theory, postulating that the differences in the airloads seen between dynamic stall in oscillatory pitching and plunging is a result of two viscous phenomena: the "spilled" leading edge vortex but also another effect called the *leading edge jet effect*. While the leading edge vortex shedding phenomenon has been well documented experimentally, the role of the leading edge jet effect in the dynamic stall problem is much less clear. Ericsson & Reding suggested that this leading edge jet effect helps to delay the onset of leading edge separation on a pitching airfoil by producing a fuller boundary layer profile. The final result is, however, opposite to that inferred from both Liiva's data and Carta's data where, for nominally "equivalent" pitch/plunge forcing, a pitching airfoil is generally found to stall at a lower equivalent AoA.

9.5.3 *Future Modeling Goals with Semi-Empirical Models*

Overall, it can be seen from the results shown in Figs. 9.8 and 9.9 that the semi-empirical dynamic stall model provides fairly satisfactory predictions of the unsteady airloads, for both pitching and plunging oscillations. Again, these results can only be considered as representative, and other semi-empirical models may provide better (or worse) results. None of the current models, however, can be considered as the last word on the problem, and it is likely that improved semi-empirical models of dynamic stall will continue to be developed for use in helicopter rotor applications.

The need to use some empirically identified coefficients in the types of dynamic stall models used in helicopter analyses is unavoidable. Empiricism, however, is not a negative concept, if suitably justified. Existing dynamic stall models have used from as many as

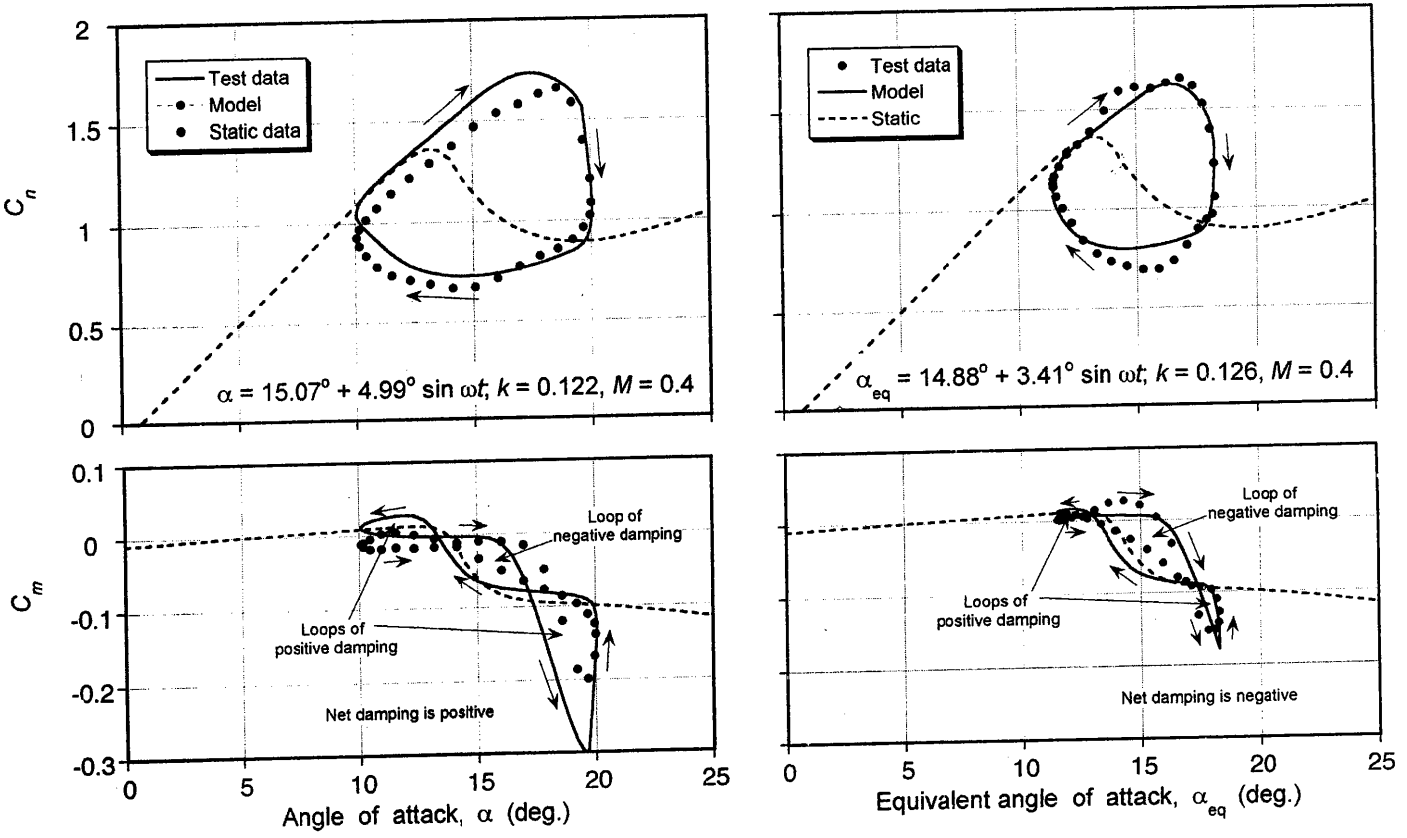

Figure 9.9 Comparison of model with measured airloads under pitch and plunge forcing, for NACA 23010 $\alpha = 15.07° + 4.99° \sin \omega t$, $M = 0.4$, $k = 0.122$; $\alpha = 14.88° + 3.41° \sin \omega t$, $M = 0.4$, $k = 0.126$. Data source: Liiva et al. (1968).

50 empirical coefficients to as few as four; these coefficients may also be a function of Reynolds number and/or Mach number. Many modeling efforts follow the relatively simple philosophy of enhancing prediction by using equations to amplify a pattern in the experimental results and so filtering out the less important physics and any noise. Yet complicated models always have a greater probability of modeling more and more of the unwanted noise and the uncertainties that are omnipresent in the experimental data. Therefore, one objective for the analyst should be to balance the complexity of the model by using a minimum number of equations and coefficients, while maximizing the predictive accuracy and minimizing noise. One strategy toward this end is that all (most) of the identified coefficients should have a physical meaning and should be easily derived from either steady or unsteady airfoil measurements. Obviously, with a large number of coefficients it is hard to assign a physical significance to all of them. More important, however, with complex models the unique identification of the empirical coefficients becomes difficult and substantially increases the probability of unwanted noise. It is clear that most of the features of dynamic stall are a result of a few key causal factors, and so in principle dynamic stall can be modeled using relatively parsimonious models; the stall-delay model of Beddoes and the dynamic stall model of Johnson are good examples of this. In attempts to extend the generality of dynamic stall models, say to more general airfoil shapes or to wider ranges of conditions, the complexity of the model must necessarily be increased and parameters added, and caution should always be exercised so as to retain the predictive success of the model.

9.6 Torsional Damping

As mentioned previously, the highly nonlinear airloads obtained by operating the rotor in proximity to retreating blade stall can introduce aeroelastic stability problems. One problem is called *stall flutter*, and this occurs when negative aerodynamic damping changes an otherwise stable aeroelastic blade mode into a divergent or high amplitude limit cycle oscillation. The problem is particularly important for the torsion mode. A torsional damping factor, $D.F.$ or C_W can be defined by the line integral

$$D.F. = C_W = \oint C_m(\alpha) d\alpha, \tag{9.1}$$

which is *positive* when it corresponds to a *counterclockwise* loop in the C_m versus α curve – see Carta (1967). If the torsional damping is negative, this would tend to promote an aeroelastic divergence or flutter situation.

The progressive change from positive to reduced or negative torsional damping (for a given amplitude and reduced frequency of oscillation) is apparent as the mean AoA is increased into dynamic stall, as previously illustrated by the results shown in Fig. 9.4. It has been shown that the onset of light dynamic stall introduces a second clockwise loop of *negative* damping so that the pitching moment curve now looks like a figure eight. This second loop then grows in size with increasing mean AoA. Further penetration into dynamic stall produces a moment break that is now early enough in the oscillation cycle that the peak nose-down moment occurs while the AoA is still increasing. This introduces another new loop in the counterclockwise (positive) sense. More positive torsional damping is recovered when deep stall penetration occurs. Increasing the reduced frequency can act to delay the onset of stall to a higher AoA and can suppress the amount of flow separation, thereby reducing the negative damping, as shown previously by means of Fig. 9.5.

The aerodynamic torsional damping of an airfoil in the dynamic stall regime is a very difficult quantity to predict. While the various semi-empirical dynamic stall models appear

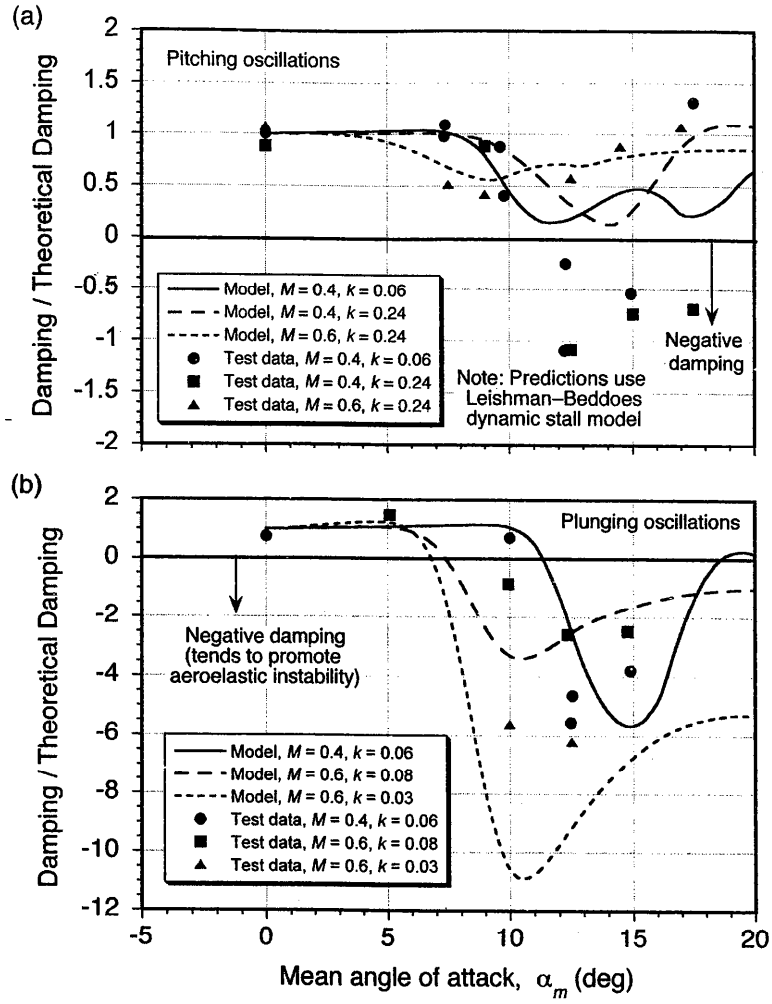

Figure 9.10 Comparison of predicted and measured torsional aerodynamic damping through conditions leading to dynamic stall for: (a) pitch oscillations and (b) plunge oscillations.

to give good predictions of the net forces and pitching moments, they do not always give good estimates of torsional aerodynamic damping. Because damping is an integrated quantity, the combination of conditions that determine dynamic stall onset and phasing of the center of pressure movement during vortex shedding must be determined very accurately. Measurements of the overall torsional damping trend versus mean AoA, α_m, is shown in Fig. 9.10, for both pitch and plunge forcing. Predictions were made using the Leishman–Beddoes dynamic stall model. The damping is normalized by the theoretical damping as given by the classical incompressible flow unsteady aerodynamic theory. Using the results in Chapter 8, then for pitching oscillations

$$C_m = \frac{-1}{2V^2}\left(\pi V b\dot{\alpha} + \frac{3}{8}\pi b^2\ddot{\alpha}\right) = \frac{\pi}{2}k\left(\frac{3}{8}k - i\right)\bar{\alpha}e^{i\omega t} = \bar{C}_m \sin(\omega t + \phi), \quad (9.2)$$

where

$$\bar{C}_m = \frac{\pi}{2} k\bar{\alpha}\sqrt{1+\frac{9}{64}k^2} \quad \text{and} \quad \phi = \sin^{-1}\left(-\frac{8}{3k}\right). \tag{9.3}$$

Substituting this expression into Eq. 9.1 gives

$$C_W = \pi k\bar{\alpha}\sqrt{1+\frac{9}{64}k^2}, \tag{9.4}$$

where α_{eq} is the equivalent AoA (as defined in Eq. 8.182). By a similar process, the theoretical torsional damping for plunging motion is found to be

$$C_W = \frac{\pi}{2} k\bar{\alpha}_{eq}. \tag{9.5}$$

The results in Fig. 9.10 show that in fully attached flow the torsional damping for an airfoil undergoing pitching motion is approximately twice that for equivalent plunging motion. This is because of the effects of pitch rate contributions to the noncirculatory pitching moment, which causes the area contained within the moment loop to be greater for a pitching airfoil than for a plunging airfoil under the same equivalent time-history of AoA forcing. This result is also seen in the experimental measurements (see Figs. 8.32 and 8.33).

The explanation for the observed behavior of the torsional damping can be deduced from Figure 9.4, where it has been shown that for higher mean AoA the pitching moment develops into two loops at dynamic stall onset, with a decrease in torsional damping. With further increase in mean AoA, the second loop increases in size and the net damping during the cycle rapidly decreases. Figure 9.10 shows that for both the pitch and plunge cases very low or negative damping is obtained at dynamic stall onset. At some point, just after stall onset, the mean AoA is sufficient such that significant negative damping reoccurs for the plunge oscillation. Although stall onset occurs at a lower equivalent AoA for an airfoil oscillating in pitch, the inherently lower damping for the plunging airfoil in attached flow means that the damping may well become negative at a lower mean AoA for conditions of oscillatory plunging. As the mean AoA is increased further, the damping increases again and ultimately becomes positive when fully separated flow conditions exist. See Carta (1967) for a detailed discussion of torsional damping under dynamic stall conditions.

9.7 Effects of Sweep Angle on Dynamic Stall

The local sweep or yaw angle of the flow to a blade element on a helicopter rotor in forward flight can be significant. The radial component of the velocity relative to the leading edge of the blade is the source of this sweep angle, as shown in Fig. 9.11. The sweep angle, Λ, is defined in terms of the normal and radial velocity components U_T and U_R, respectively, by

$$\Lambda(r,\psi) = \tan^{-1}\left(\frac{U_R}{U_T}\right) = \tan^{-1}\left(\frac{\mu\cos\psi}{r+\mu\sin\psi}\right). \tag{9.6}$$

Examples of the iso-sweep angle distribution over the rotor disk are shown in Fig. 9.12 for advance ratios of 0.05 and 0.3. At the higher advance ratios, the sweep angles can exceed 30° over some parts of the disk. Overall they clearly become significant enough that their effects would need to be assessed experimentally by means of wind tunnel tests; any effects on the aerodynamics so produced will also need to be represented and properly integrated within a model of dynamic stall.

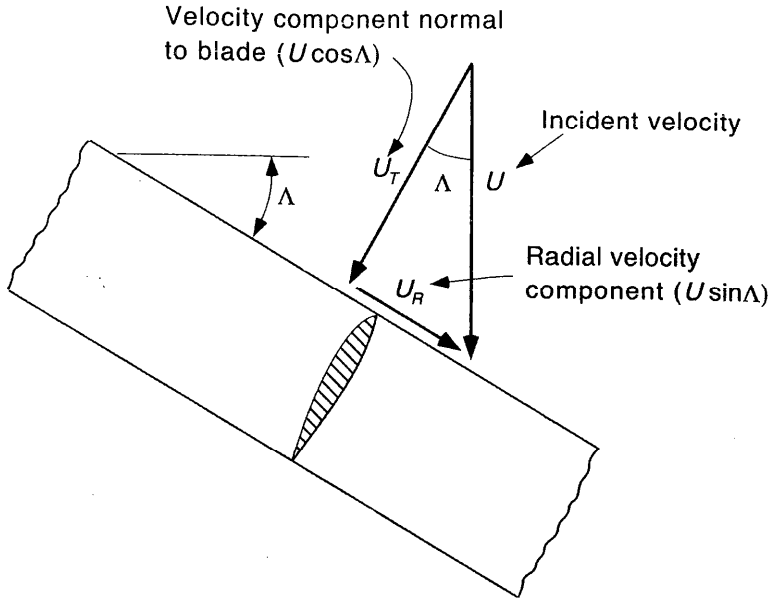

Figure 9.11 Velocity components relative to the blade element and definition of sweep angle.

In the classical blade element theory, we usually neglect the effect of sweep on the lift, drag, and pitching moment. This is in accordance with the independence principle of sweep – see Jones & Cohen (1957). However, when an airfoil is operated at high AoA near stall this may not be a valid assumption. For example, the effect of sweep angle on the *static* lift characteristics of a swept 2-D airfoil is shown in Fig. 9.13. The results are based on the measurements of Purser & Spearman (1951) and are presented in the conventional blade element format – that is, in terms of AoA and velocities normal to the leading edge of

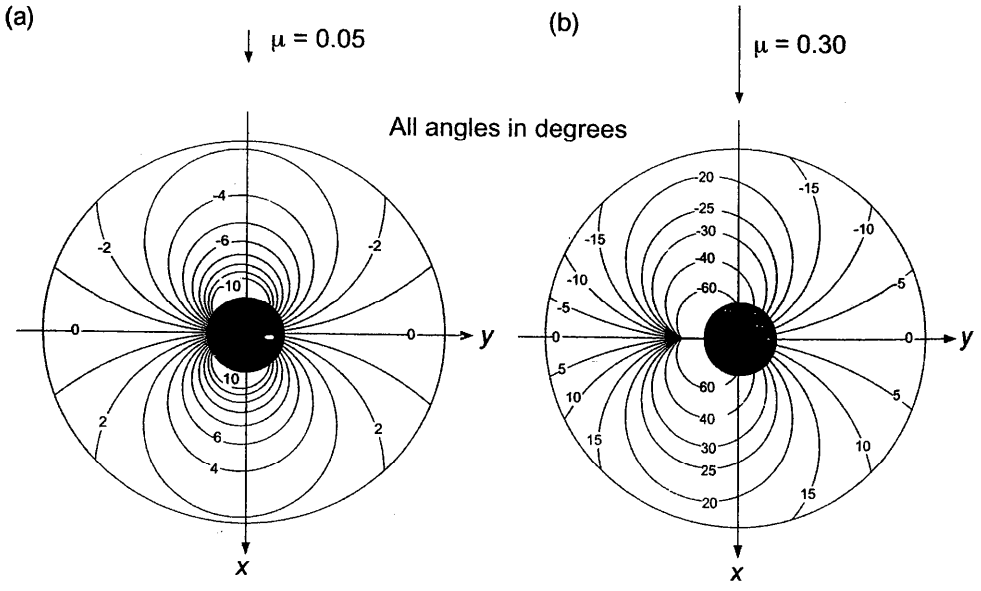

Figure 9.12 Iso-sweep angles over the rotor disk in forward flight. (a) $\mu = 0.05$. (b) $\mu = 0.30$. Angles are in degrees.

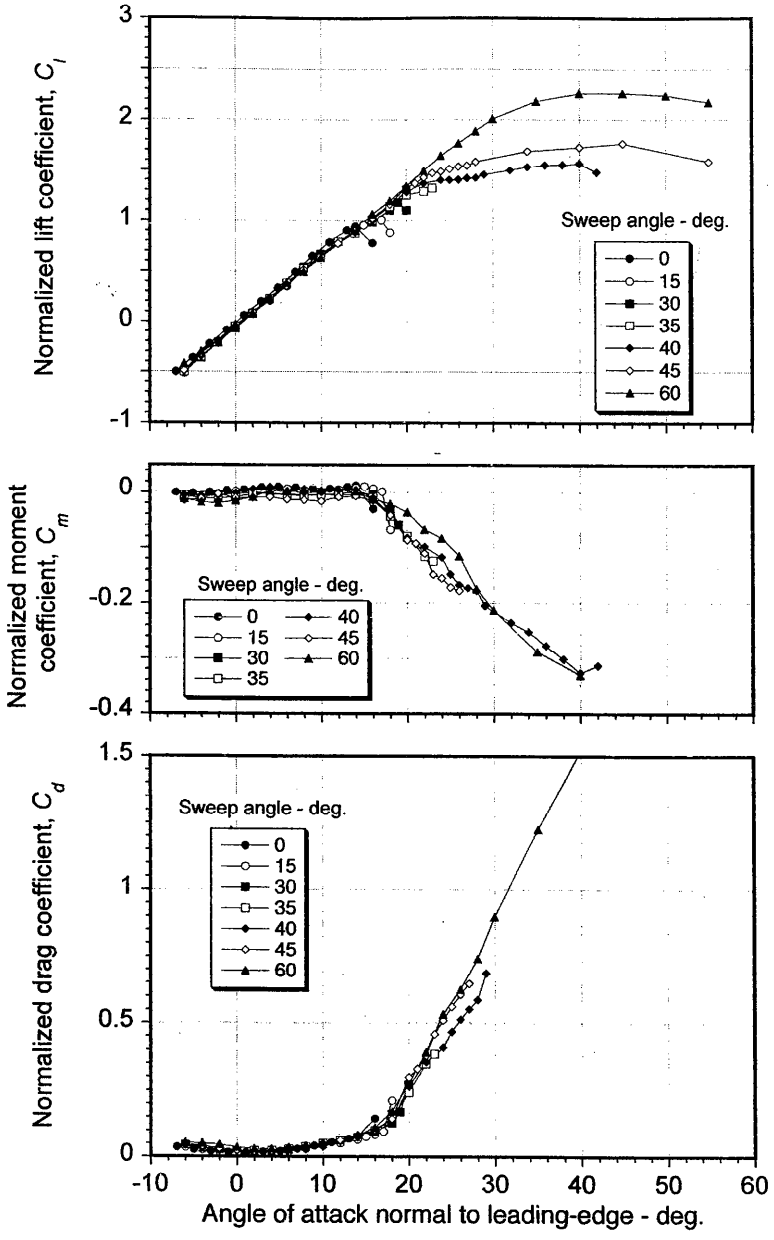

Figure 9.13 Effect of sweep angle on the measured static lift characteristics of an airfoil. The results are presented in the conventional blade element convention.

the airfoil section. When the data are presented this way, the results for the lift, pitching moment, and drag show a close correlation and confirm that, at least in the attached flow regime, the independence principle is a valid assumption. However, notice that in the high AoA region a much higher lift coefficient is obtained for the larger sweep angles. This is because of favorable effects on the spanwise development of the boundary layer, which tend to delay the onset of flow separation on the wing to a higher AoA – see also Dwyer & McCroskey (1971). Similar results have been found experimentally by St. Hillaire et al. (1979) and St. Hillaire & Carta (1979, 1983a,b).

The upshot of these observations is that if these sweep effects are to be found on the rotor then they will tend to delay the onset of stall on the rotor to higher values of thrust, a result observed experimentally. Various earlier studies of the problem, including those of Harris (1966) and Gormont (1973), suggest that improvements in rotor thrust prediction can be obtained by including a static stall model that accounts for a delayed stall AoA and higher maximum lift as a function of sweep angle. However, it must be remembered that when stall occurs on the rotor in forward flight, the stall is actually dynamic in nature. To assess this problem, a series of experiments have been conducted by St. Hillaire & Carta (1979, 1983a) where a NACA 0012 airfoil at a constant sweep angle of 30° was used. These oscillating airfoil tests were performed at Mach numbers of 0.3 and 0.4 and Reynolds numbers that are nominally full-scale rotor values. The measurements were determined by the integration of sectional pressures measured by pressure transducers distributed about a section at the mid-span of the model. Leishman (1989) has also conducted an analysis of these data. It appears that for fully attached unsteady flows the independence principle also applies. Any unsteady effects associated with sweep are small in the attached flow regime – probably smaller than uncertainties associated with the measurements themselves. However, in the dynamic stall regime, there are other characteristics of swept flow that are worthy of consideration.

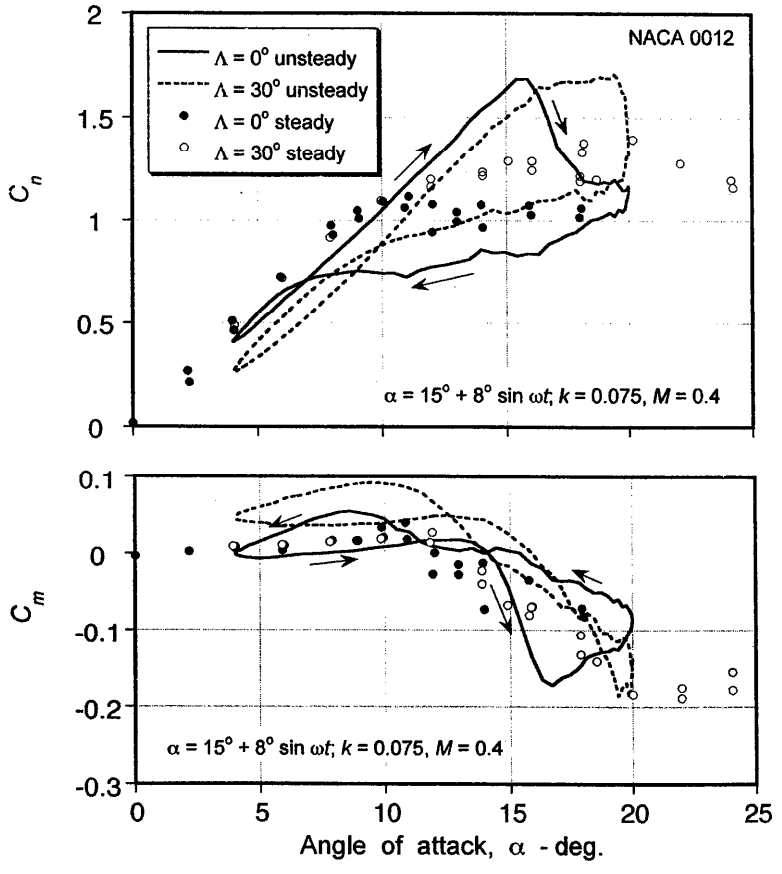

Figure 9.14 Behavior of the dynamic lift and pitching moment for a pitch oscillation in swept and unswept flow.

Figure 9.14 shows a typical behavior of the lift and pitching moment coefficients in the dynamic stall regime for a pitch oscillation. A feature of these dynamic stall results is that compared with the static case where approximately a 20% higher maximum C_n was attained for $\Lambda = 30°$, the unsteady case shows a delay in dynamic lift stall to a higher AoA, but not to a significantly higher maximum value of lift. Also, for $\Lambda = 30°$ somewhat narrower lift hysteresis loops are produced, and the mean value of lift is somewhat higher. Thus, it appears that the effects of sweep on the rotor may serve to provide an overall increase in average rotor thrust compared to predictions obtained when sweep effects are not included. It should be noted, however, that the expected increase in thrust is not because of higher values of C_n, but simply because the mean value of the lift is higher. The divergence in the pitching moment (moment stall) occurs at the same nominal value of AoA for both the $\Lambda = 0°$ and $\Lambda = 30°$ cases. However, the slope of the pitching moment curve during the next part of the cycle is clearly less for the $\Lambda = 30°$ case. Also, the minimum pitching moment is reached at a higher AoA. This suggests that the delay in dynamic lift stall to a higher AoA in swept flow is due, in part, to a lower velocity at which the shed leading edge vortex is convected over the chord. The comprehensive analysis performed on the airfoil pressure time histories by St. Hillaire & Carta (1983a) also supports this observation. In light of these results, it would appear that from a modeling perspective simple corrections to the stall AoA based on steady flow observations, such as suggested by Harris (1966), may give the desired effect on rotor performance predictions, but for the wrong underlying reasons. This problem, like several others in rotating-wing aerodynamics, illustrates the difficulties in simply extrapolating observations of quasi-2-D steady airfoil behavior to the complicated 3-D flow environment found on rotors.

9.8 Effect of Airfoil Shape on Dynamic Stall

McCroskey et al. (1980, 1982) have studied systematically the effects of airfoil shape on the dynamic stall characteristics of several different types of airfoils. Some of these airfoils are unsuitable for use on helicopters, but the results serve to bracket the effect of airfoil shape on the problem, albeit only at relatively low Mach numbers. Wilby (1984, 1996, 1998) reports another study of airfoil shape on the dynamic stall problem and over a much wider range of Mach numbers, including transonic flow. This author presents a tantalizing glimpse of a wealth of information on the dynamic stall problem; however, very little of these data have been formally published in the open literature. The datum airfoil used by McCroskey et al. (1980, 1982) was the ubiquitous NACA 0012, and results are summarized here for two other airfoils that are representative of modern rotor airfoils used on current production helicopters, namely the HH-02 airfoil (used on the AH-64 Apache) and the SC1095 airfoil (used on the UH-60 Blackhawk). These are both cambered airfoils with approximately 9.5% thickness to chord ratios and can be considered representative of modern helicopter airfoil designs. The HH-02 has considerably more leading edge camber than the SC1095, and it has the distinction of a large trailing-edge tab (see Fig. 7.24).

Some results showing the effects of airfoil shape on the dynamic stall airloads are summarized in Fig. 9.15, which shows the normal force and pitching moment coefficients for stall onset conditions through deep dynamic stall. In each case, the results are compared to the static airloads for that airfoil. The experimental data shown are for a free-stream Mach number of 0.3, which is the highest Mach number that was tested. At the lowest mean AoA of 5°, the maximum AoA becomes just large enough to initiate some minor leading edge separation, as evidenced by the distortion in the nominally elliptical hysteresis loops near

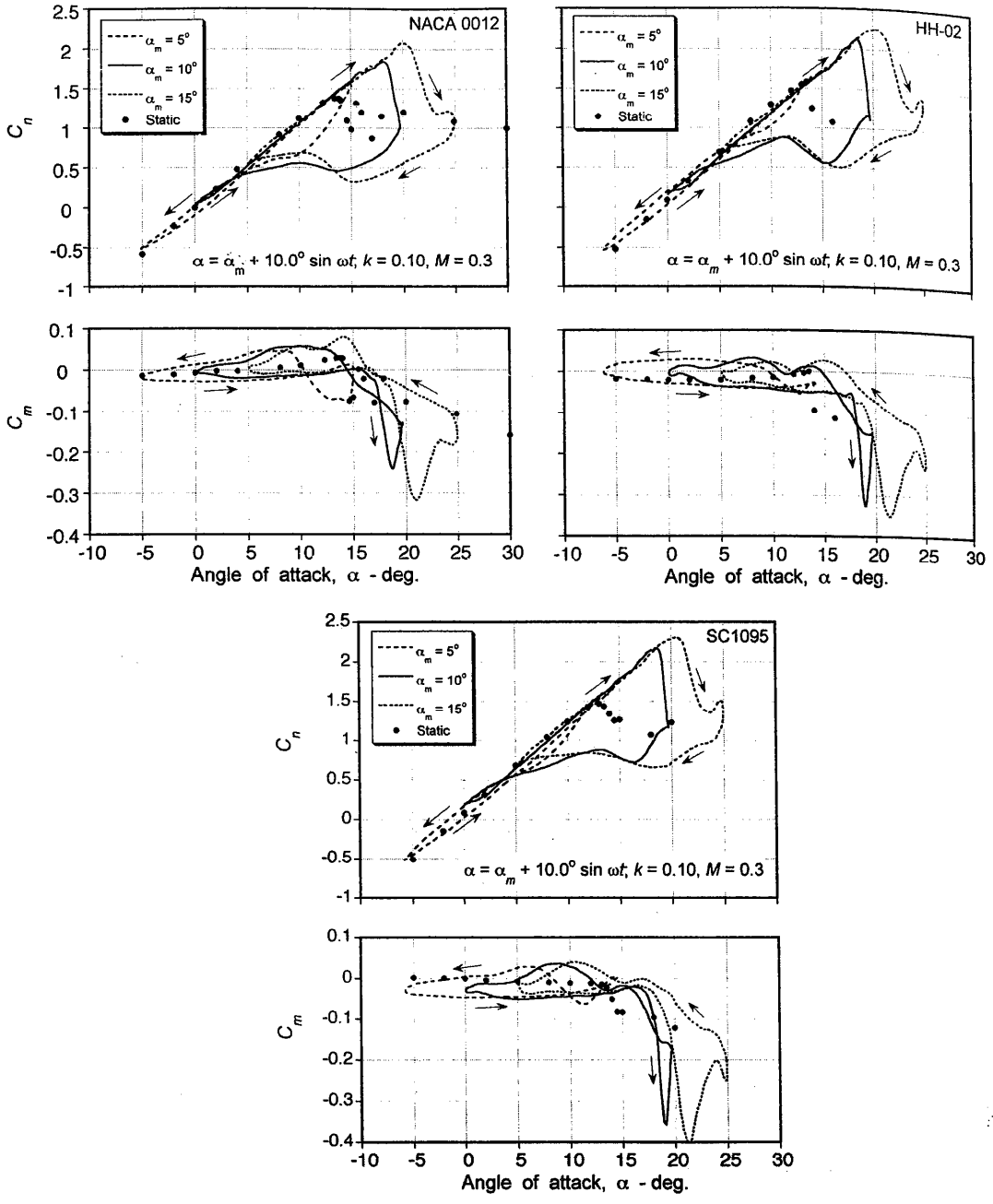

Figure 9.15 Unsteady airloads on the NACA 0012, HH-02, and SC1095 airfoil sections.

the maximum AoA. All three airfoils exhibit a significant increase in maximum lift over the static values. It is clear, however, that the HH-02 and SC1095 airfoils maintain attached flow to a slightly higher AoA, with correspondingly higher values of C_n, and, thereby, exhibit a slightly superior lifting performance to the NACA 0012. This is consistent with the static behavior of these types of airfoils (see also Section 7.9). Therefore, it can be concluded that

airfoils designed for high static lift capability should also exhibit a higher AoA capability before stall when operated under dynamic conditions.

The forces and pitching moments for a case of moderately strong dynamic stall, which occurs for $\alpha_m = 10°$, are also shown in Fig. 9.15. Under these conditions, relatively strong leading edge vortex shedding is initiated and the characteristic lift overshoots and strong nose-down pitching moment behavior of dynamic stall are intensified. Considerable hysteresis in the lift and pitching moment behavior is also present for these conditions. All three airfoils exhibit a qualitatively similar type of behavior, although it is apparent that there are measurable quantitative differences. The NACA 0012 exhibits moment stall at a lower AoA to either the HH-02 or the SC1095 airfoils, although the lift stall occurs at approximately the same AoA for all three airfoils. Both the NACA 0012 and the SC1095 airfoils exhibit a well-rounded moment break at the onset of dynamic stall in comparison to the HH-02, which has a very abrupt moment break. This suggests that some trailing edge flow separation is still present on the NACA 0012 and SC1095 airfoils prior to the onset of leading edge separation and dynamic stall. This also suggests that to some extent the static stall behavior of the airfoil is actually carried over into the dynamic stall regime. Both the HH-02 and SC1095 airfoils exhibit a slightly greater maximum dynamic lift over the NACA 0012. Again, these static lift gains appear to be carried over somewhat into the dynamic regime. However, the NACA 0012 clearly exhibits a smaller peak value of (nose-down) pitching moment compared to the other two airfoils. This suggests a weaker shed leading edge vortex for the NACA 0012 airfoil.

As discussed in Chapter 7, the traditional approach in designing helicopter rotor airfoils is to maximize the quasi-steady lift and minimize the pitching moment. Little emphasis is usually placed on the consequences of the unsteady behavior of the airfoil. Figure 9.15 reinforces this point, where the oscillatory lift and pitching moment for a mean AoA of 15° indicate strong leading edge vortex shedding, producing significant increments in normal force and pitching moment coefficients. As for a mean AoA of 10°, all three airfoils exhibit a qualitatively similar type of dynamic stall behavior, with both the HH-02 and the SC1095 airfoils exhibiting increased values of maximum dynamic lift over the NACA 0012. (It should also be noted that for each airfoil there is perhaps evidence of secondary vortex shedding near the maximum AoA, which manifest as smaller secondary peaks in the normal force and pitching moment.) It is significant that while under static conditions the SC1095 exhibits a gain in maximum C_n of about 0.1 over the HH-02 airfoil, under these particular dynamic conditions there is almost no difference in maximum C_n between these two airfoils. This indicates that, whereas the maximum lift coefficient may be a useful measure of airfoil performance under static conditions, this does not necessarily appear to be an indication of the dynamic lift capability of the airfoil. Also, although the HH-02 and the SC1095 airfoils give approximately the same value of maximum dynamic lift, the maximum nose-down pitching moment is clearly greater for the SC1095. This is despite the fact that the HH-02 has a higher zero-lift pitching moment under quasi-steady conditions. Therefore, like the lift coefficient, the design of airfoils for low static pitching moments does not necessarily guarantee that low dynamic pitching moments will also be produced.

9.9 Three-Dimensional Effects on Dynamic Stall

As discussed earlier in this chapter, in the rotor environment the problem of dynamic stall must be considered as fully three dimensional. Stall will occur over different parts of the blade and at different blade azimuth angles, and needless to say, the resulting flow can be very complicated. Apart from the 3-D effects associated with swept flows, the

problem of 3-D unsteady separating flows are still poorly understood. As mentioned earlier, the various mathematical models used for dynamic stall prediction are still heavily empirical, with reliance being placed almost exclusively on oscillating 2-D airfoils for formulation and validation purposes. It is only recently that attempts to validate these models has been made for 3-D dynamic stall problems, albeit these are still very much idealized problems compared to those found in the helicopter rotor environment.

The problem of 3-D dynamic stall has been studied experimentally by Lorber et al. (1991), Lorber (1992), Pizialli (1994), and Berton et al. (2003a,b) and computationally by Spentzos et al. (2004). Lorber and Pizialli have used a cantilevered semi-span wing that was oscillated in AoA through stall and like the 2-D tests, was designed to simulate the variations in AoA encountered by a helicopter rotor blade. Miniature pressure transducers

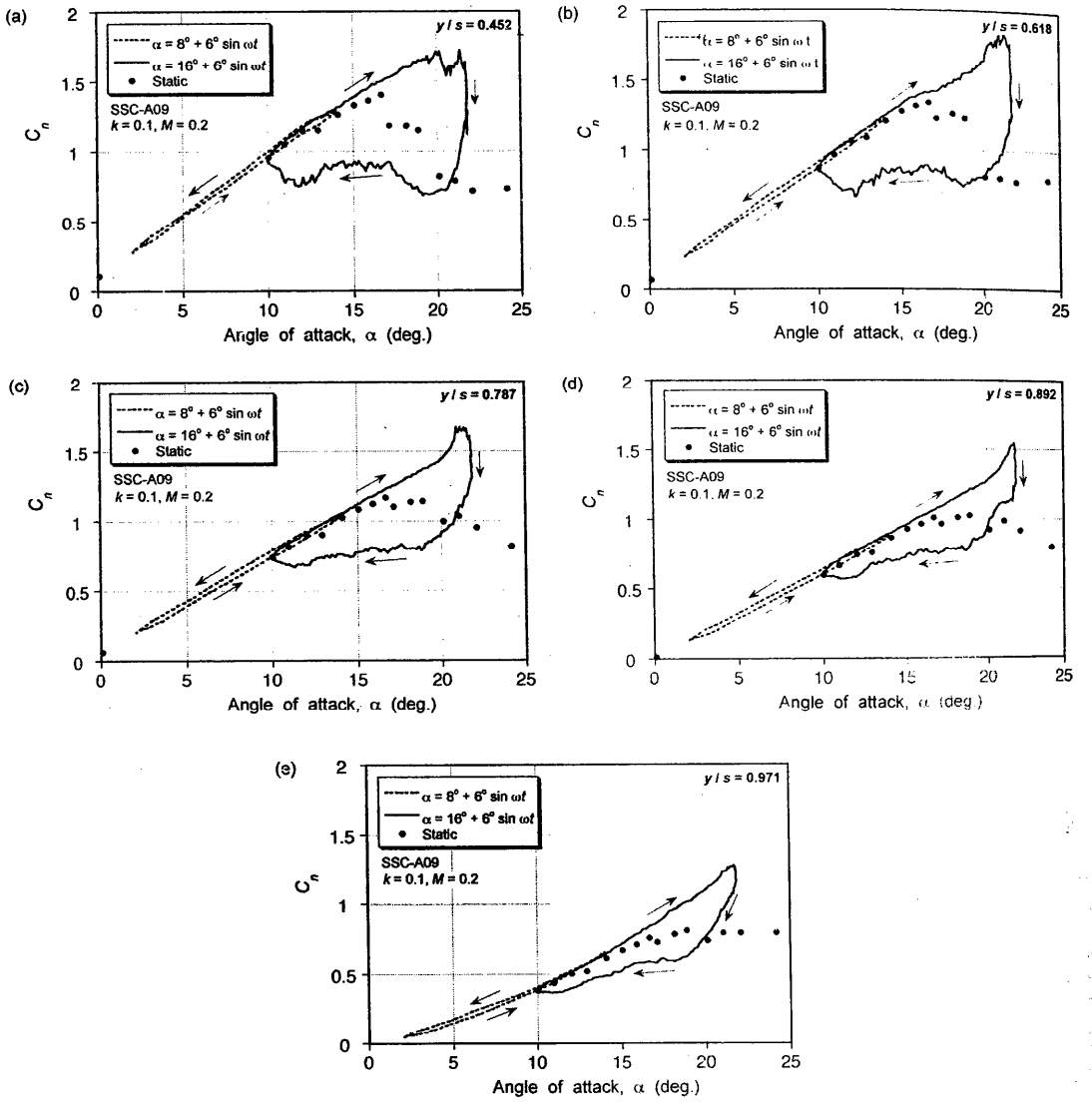

Figure 9.16 Measurements of unsteady lift on a cantilevered wing undergoing oscillations in AoA for nominally attached flow and into dynamic stall. $M = 0.2$.

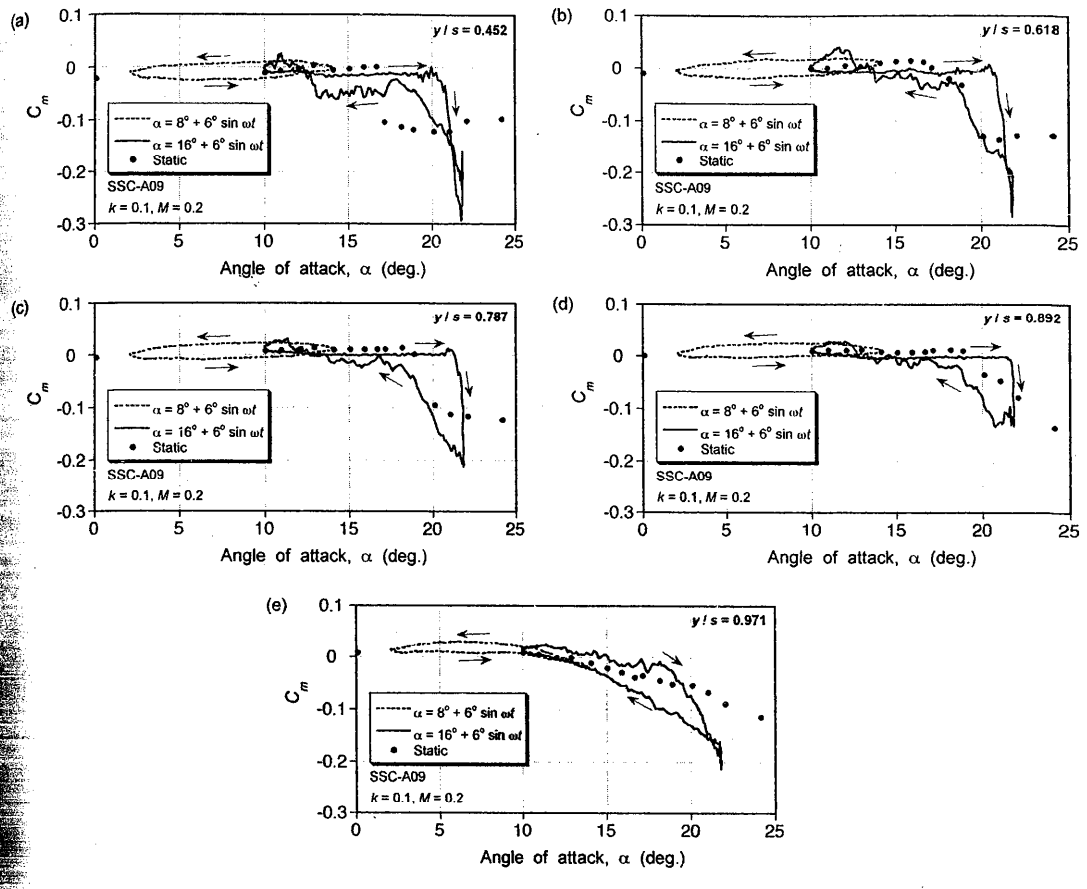

Figure 9.17 Measurements of unsteady pitching moment on a cantilevered wing undergoing oscillations in AoA for nominally attached flow and into dynamic stall. $M = 0.2$

were distributed at various stations along the wing, and the measured pressures have been integrated to determine sectional lift, drag, and pitching moment. While Pizialli's results are limited to a Mach number of 0.3, Lorber's results cover a wider range of Mach number from 0.2 to 0.6 and also for wing sweep angles of 0, 15, and 30°. Berton et al. (2003a,b) and Spentzos et al. (2004) have also examined the dynamic stall of wings with finite span.

Representative results from the 3-D dynamic stall experiments of Lorber et al. (1991) are shown in Figs. 9.16 and 9.17. These results document the unsteady lift and pitching moment coefficients at five spanwise stations from near the mid-span out toward the tip of the wing. Results are shown for an oscillation below stall and for a typical case of dynamic stall at the same reduced frequency. The static measurements at each station of the wing are also shown for reference. For oscillations below stall, characteristic elliptical hysteresis loops are formed with no particularly unusual behavior compared to that expected from 2-D considerations. Notice, however, the gradual reduction in the average lift-curve-slope when moving outboard toward the tip, although this is a quasi-steady effect and would be predicted by any finite-wing model. The only exception is at the outermost wing station, where both the steady and unsteady lift and pitching moment hysteresis loops show a different characteristic, with a more nonlinear quasi-steady behavior. This is the influence of the tip vortex, which lies over the tip region and provides an element of

steady vortex induced lift. Other than for this one section of the wing, unsteady thin-airfoil theory, with the quasi-steady induced effects accounted for by a lifting-line or other finite-wing method, will provide a good approximation to the unsteady airloads – see Tan & Carr (1996).

The dynamic stall characteristics on 3-D finite wings are noted to be qualitatively similar to those found on oscillating 2-D airfoils. Figures 9.16 and 9.17 show that at the four inner stations, the airloads exhibit the lift overshoots, large nose-down pitching moments, and hysteresis effects that are characteristic of 2-D dynamic stall. Notice that when moving outboard from the innermost station the degree of dynamic stall penetration is reduced. Again, this is mainly a steady effect associated with the reduction in the effective quasi-steady AoA because of the induced effects from the tip vortex. In fact, the results appear qualitatively similar to those obtained with a reduction in the mean AoA in the 2-D case. While lift and pitching moment overshoots are also obtained at the outermost station, the results are less transient suggesting that leading edge vortex shedding does not occur. In fact, it would appear that the tip vortex alone dominates the flow field here and the AoA never becomes large enough to permit stall to occur in the normal sense.

Overall, the results in Figs. 9.16 and 9.17 indicate that if the wing aspect ratio is relatively high then the oscillating finite wing problem can still be considered nominally 2-D as far as dynamic stall is concerned, and 2-D models with appropriate allowance for the induced distribution of AoA associated with finite span should give at least engineering levels of predictive capability. This has been confirmed by results shown by Tan & Carr (1996), who compare results of the Pizialli experiments with a number of the better known semi-empirical dynamic stall models, some of which have been described previously. However, this conclusion is based only on a limited validation study, and much further work still needs to be done to analyze the problem of 3-D dynamic stall if credible predictions of helicopter airloads are to be improved. The problems are further compounded by the centrifugal and Corriolis effects that are produced on the 3-D boundary layer developments on rotating blades. The issues seem particularly acute on wind turbines, which often operate with substantial amounts of dynamic stall compared to a helicopter rotor – see Section 13.12.2.

9.10 Time-Varying Velocity Effects on Dynamic Stall

As discussed in Chapter 8, for a rotor in forward flight a blade element will encounter a time-varying incident velocity and there will be additional unsteady aerodynamic effects to be considered. In nominally attached flow, these effects include more complicated circulatory contributions resulting from the nonuniform shed wake convection velocity, also with additional noncirculatory contributions. The problem of dynamic stall under these conditions is not completely understood but has been studied experimentally on 2-D oscillating airfoils by Pierce et al. (1978a,b), Maresca et al. (1981), and Favier et al. (1988). A time-varying onset velocity was obtained in the experiment of Pierce et al. by using choking of the upstream flow by means of rotating vanes and in the experiment of Maresca & Favier by means of fore-and-aft movement of the airfoil. In both experiments the AoA and free-stream velocity were varied harmonically with different relative phase angles.

Pierce et al. (1978a,b) have measured the airfoil pitching moment, with a view to understanding the possible effects of varying free-stream velocity on the torsional aerodynamic damping at dynamic stall onset. The measurements in fully attached flow were found to be in good agreement with the "classical," linearized unsteady thin airfoil models, as discussed in Chapter 8. In the vicinity of stall reduced aerodynamic damping was observed, although

as shown previously, this is a characteristic found with steady onset flows and is related to the phasing of the dynamic stall events with respect to the forcing function (α, $\dot{\alpha}$, etc.).

In the other experiments by Maresca & Favier, measurements of the lift, drag, pitching moment, and chordwise pressure distribution have suggested some considerable influence of the varying free-stream velocity on the dynamic stall process. Depending on the phasing of the velocity variations with respect to the AoA, initiation of leading edge vortex shedding and the chordwise convection of this vortex appear to be different. Favier et al. (1988) measured a phase lead of the unsteady lift response for conditions with constant free-stream velocity, but these seem to be at variance both with other measurements for the same problem and also with linearized theory. In this regard, the various problems associated with the subscale Reynolds number simulation of the problem cannot be overlooked. The issue of time-varying incident flow velocity, unfortunately, has not yet been studied in detail using the various mathematical models of dynamic stall, and it would seem to be an ideal problem whose investigation is overdue. It would also seem that because of the difficulties in conducting experiments of this problem, it would form a good challenge for the various first-principles based CFD approaches to dynamic stall modeling currently under development (see Section 14.10.1)

9.11 Prediction of In-Flight Airloads

While it has been shown previously that the problem of dynamic stall can be conveniently dissected, analyzed, and modeled into more manageable subproblems, it is only when the elements of the submodels are combined into the full rotor simulation, including the rotor wake (inflow) and elastic blade dynamics, that the true benefits of any improved modeling efforts can be realized. Many authors have shown the effects of including representations of dynamic stall for rotor loads and aeroelastic predictions – see, for example, Tarzanin (1972), Gormont (1973), Johnson (1969, 1974), Carlson et al. (1974), Yen & Yuce (1992), and Nguyen & Johnson (1998). The predicte results are, however, somewhat mixed. Generally, by including unsteady aerodynamics and dynamic stall models, better predictions of the phasing of the unsteady airloads with respect to blade azimuth are obtained, along with correspondingly better predictions of overall rotor performance at the extremes of the flight envelope. However, the mixed results indicate that although it may be possible to reproduce the unsteady airloads on a 2-D section with most dynamic stall models, the prediction of in-flight airloads are much more difficult.

A representative example is shown in Fig. 9.18, which shows the lift (as M^2C_l) and the pitching moment (as M^2C_m) on a section of a rotor blade for a case where dynamic stall is present. The flight test results are taken from Bousman (1998), and the calculated results are taken from Nguyen & Johnson (1998). The unsteady airloads are computed with different dynamic stall models, while keeping fixed all other elements of the rotor model. As seen from Fig. 9.18, the agreement of the predictions with the measurements is indeed very mixed. The improvement over the use of quasi-steady aerodynamics is, however, clearly better, particularly in regard to the phase of the lift predictions. However, the predictions of the section pitching moment are probably less than what would be considered acceptable. For example, one of the models predicts large nose-down moments associated with dynamic stall at points over the disk where there is clearly no stall indicated in the flight test measurements. In other cases, stall is not predicted in the regions where flight tests clearly indicate otherwise.

The fault, however, lies not only with the stall models. The main difficulty in the rotor simulation is the proper calculation of the combination of AoA and Mach number that

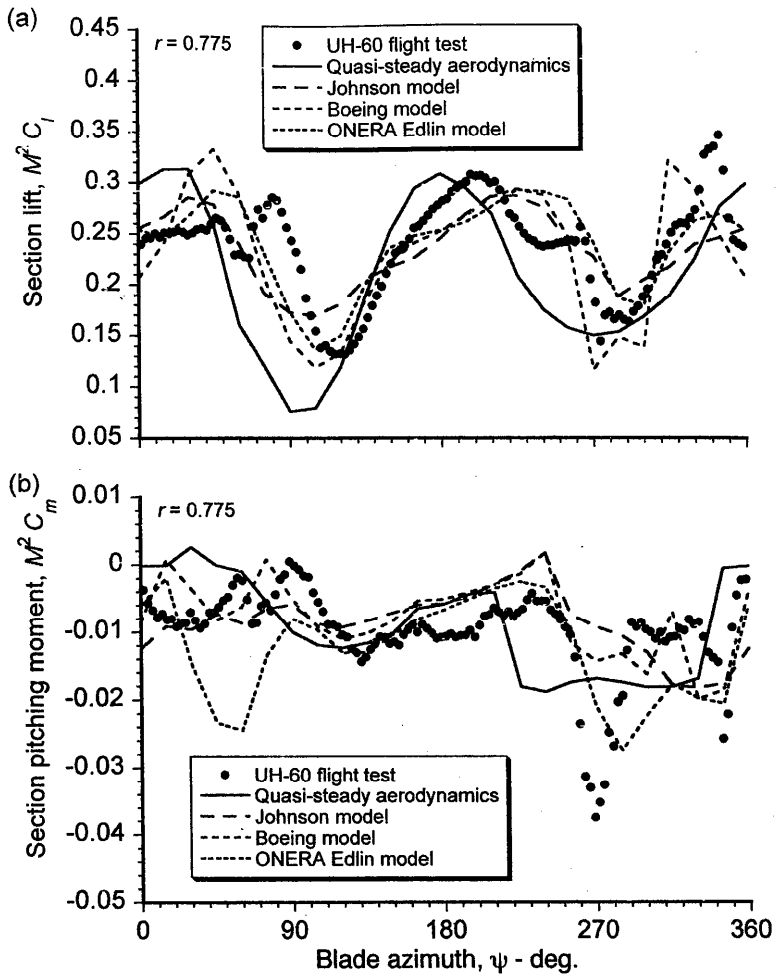

Figure 9.18 Predictions of in-flight dynamic stall airloads using semi-empirical stall models. From Nguyen & Johnson (1998) and courtesy of Khanh Nguyen.

will delimit attached flow, and these calculations must properly include models of the rotor wake and blade motion in a fully coupled way. Because of the high AoA gradients that exist over the disk resulting from the wake inflow (see Fig. 3.30), the time steps (level of discretization) used in the rotor analysis can determine whether or not dynamic stall is initiated at all. In other words, it is possible to completely miss the stall event because the time step is too large to resolve the phenomenon. Furthermore, vortex shedding during dynamic stall occurs over relatively short time scales, generally of the order of 8 semi-chords of airfoil travel – see Galbraith et al. (1986). Therefore, if translated into an azimuth step for the rotor calculation, the azimuth step must be of the order of 2–5° to accurately represent dynamic stall. In the calculations shown in Fig. 9.18, a rotor azimuth step of 15° was used, which is probably too large to capture the correct details of stall onset and subsequent aft center of pressure movement resulting from dynamic stall. Therefore, this level of predictive capability is of great concern to the rotor analyst and shows that even if the ability to model 2-D (or even 3-D) unsteady airloads has been realized, the prediction of dynamic stall airloads in the rotor environment is still a problem that is at the limit of

current modeling capabilities. Equivalent arguments apply for phenomena such as blade vortex interaction (BVI), which occur over time scales of the order of 2–5 semi-chords of airfoil travel. In this case, the time (azimuth) step must be of the order of one degree or less to resolve both the wake and the BVI phenomena. Trading off predictive capability of the physics against computational cost is never a good situation, but this is slowly changing. The answer, however, does not just lie in the need for bigger and faster computers, but in better solution algorithms that have the accuracy and stability suitable for application to smaller spatial and temporal discretizations needed for high-fidelity helicopter rotor aerodynamic simulations.

9.12 Stall Control

The onset of dynamic stall limits the capabilities of all helicopters. The idea of using some type of passive or active means of delaying the onset of dynamic stall is not a new one. The benefits include a reduction in rotor loads and substantial increases in the forward flight speed and/or the maneuver flight envelope. This will increase the utility of both civilian and military helicopters. Methods that have been proposed include active cyclic pitch control (such as higher harmonic control), the active actuation of leading-edge or trailing edge flaps, and direct flow control. Chandrasekhara et al. (1998) propose a dynamically deforming leading edge airfoil shape for dynamic stall control. See also Chandrasekhara et al. (1999), Martin et al. (2003), and Geissler et al. (2004) for a review of some "leading edge" based concepts and their theoretical effectiveness. Feszty et al. (2003) suggest another concept based on a trailing edge flap. Some other ideas of flow control have been introduced previously in Section 7.10.

It has been suggested by several workers, including Lorber et al. (2000), that active flow control can play a future role in delaying the onset of dynamic stall or even avoiding stall altogether on helicopter rotors. Katz et al. (1989), Seifert & Pack (1999), and Greenblatt & Wyganaski (1999) have examined different methods of active boundary layer control to delay stall onset. While the fluid mechanisms are not completely understood, the concept involves periodic flow excitation at low amplitude, and enough to energize the boundary layer and delay the onset of flow separation. This periodic excitation is provided by a mechanical element that injects an unsteady jet of fluid or through suction and/or blowing. These devices are often referred to as "zero mass synthetic jets" or "direct synthetic jets." Candidate mechanisms to provide this flow include piezoelectric ceramics, fluidics, electromechanical devices, and plasma actuation. However, all devices involve weight, power, and cost penalties. For a helicopter rotor, they also need to operate in a high centrifugal force field over a wide range of environmental conditions. This raises many questions about their design for robustness and long reliability when applied to a rotor blade.

Feasibility studies of using such active flow control devices has been conducted experimentally by Lorber et al. (2000) using 2-D airfoils. This technique has shown an effectiveness in delaying dynamic stall onset by up to 3° in AoA at low Mach numbers, although it was found to be less effective at higher Mach numbers. Thus far, the devices have not been applied to an actual helicopter rotor. Parallel computational studies of active flow devices have allowed an examination of the flow physics and how they might be controlled to maximize their effectiveness. Both open loop and closed loop (sensing) strategies have been examined. Claims of more than 20% in payload and 35% in range for a medium size helicopter seem optimistic based on extrapolating the existing computational results. Full-scale helicopter rotor experiments will need to be conducted to properly demonstrate if such claims can indeed be realized with active flow control for dynamic stall allieviation.

9.13 Chapter Review

The phenomenon of dynamic stall has been shown to be an important consideration in helicopter design because its onset ultimately limits main rotor performance. It has been shown that dynamic stall is characterized by a favorable delay in the onset of flow separation to higher a AoA. This is followed by the less favorable phenomenon of leading edge vortex shedding. As long as this vortex stays over the airfoil, it acts to enhance the lift being produced. However, as this vortex is swept over the blade chord, the aft-moving center of pressure induces large nose-down pitching moments. These moments can manifest as high torsional airloads on the blades and may also induce aeroelastic problems such as stall flutter. Although dynamic stall can occur at various regions over the rotor disk, depending on the flight condition, it usually occurs on the retreating side of the disk during high-speed forward flight or during maneuvers such as tight turns or pull-ups. Therefore, the consideration of dynamic stall phenomenon represents a necessary refinement in the rotor design process and will more accurately define the operational and performance boundaries of the modern helicopter.

While the prediction of the conditions for dynamic stall onset and the subsequent effects of dynamic stall clearly forms an essential part of any rotor design process, it is not a problem that is yet fully understood, nor is it easily predicted. For engineering analyses, the modeling of dynamic stall still remains a particularly challenging problem. This is mainly because of the need to balance physical accuracy with computational efficiency and/or the need to formulate a model of dynamic stall in a particular mathematical form. To this end, a number of semi-empirical models have been developed for use in rotor design work, most of which have their root in classical unsteady thin-airfoil theory. A brief discussion of these semi-empirical methods has been presented, along with a demonstration of their general capabilities in predicting the unsteady airloads during dynamic stall. Generally, predictions are good when measurements are available for validation or empirical refinement of the model, but their capabilities for general airfoil shapes and for completely arbitrary variations of AoA and Mach number are less certain. Future research will almost certainly devise more capable and better validated engineering models of the dynamic stall problem until such time that CFD methods capable of modeling 3-D, compressible, unsteady, separated flows become more practical to use on a routine basis within rotor codes.

Other factors that may influence the phenomenon of dynamic stall on a rotor have also been discussed. These include compressibility effects, airfoil shape, sweep angle, unsteady onset velocity effects, and 3-D effects. It appears that whereas the qualitative characteristics of dynamic stall are similar at all Mach numbers, there are subtle quantitative differences in the unsteady airloads that may be difficult to represent accurately within the context of engineering models. The effect of airfoil shape on the problem of dynamic stall is still not fully understood. It appears that airfoils designed for high values of static maximum lift will also show high values of lift in the dynamic case. However, it also appears that the attainable values of maximum dynamic lift are less sensitive to airfoil shape than in the static case. Similar arguments apply for the pitching moment, and airfoils designed for low static pitching moments may not necessarily exhibit lower dynamic moments. This issue perhaps opens up fruitful avenues of research, where new rotor airfoils might be designed to meet dynamic lift and pitching moment requirements. The effects of sweep angle on the dynamic stall process have been shown to be significant, and sweep angle will be a necessary parameter to include in the modeling process. Three-dimensional effects associated with dynamic stall are clearly not fully understood. However, at least on the basis of idealized 3-D dynamic stall experiments on finite wings, the physics of the problem are similar to

the 2-D case when corrected for the additional quasi-steady induced effects associated with finite span.

There remain many uncertainties in the prediction (and possibly control) of dynamic stall and also in the proper validation of predictions with measured airloads on the rotor. This is because of the need to also define accurately the blade motions and elastic deformation of the rotor blades, as well as the aerodynamic environment on the rotor in terms of induced AoA and induced velocity field. In regard to the latter, the inflow models discussed in Section 3.5.2 often prove inadequate because of the strong local induced velocity variations produced by discrete tip vortices in the rotor wake. This latter problem is considered next in Chapter 10. The problem of modeling the rotor wake, however, is just as formidable as the dynamic stall problem, perhaps even more so. The overall level of rotor analysis capability is only as strong as the weakest link in the modeling chain. Until it becomes possible to model all aerodynamic aspects of the rotor problem and improve on the existing deficiencies and uncertainties that are present in the predictive models, helicopter design cycle times will continue to be long and costs will remain high. Finally, the possibilities of actively delaying the onset of dynamic stall or controlling its adverse effects has been reviewed. The field seems ripe with many future opportunities in basic and applied research, with significant potential long-term payoffs in terms of improved helicopter performance.

9.14 Questions

9.1. For a 2-D airfoil operating under dynamic stall conditions, explain the difference between "lift-stall" and "moment-stall." Show some typical lift and pitching moment curves for an airfoil oscillating in angle of attack. Your discussion should include a description of the basic flow physics as well as the integrated forces and pitching moments.

9.2. The phenomena of dynamic stall is often studied by analyzing measurements made on oscillating airfoils. The dynamic stall vortex convection speed is to be estimated from a series of such experiments where the lift and pitching moment are available as functions of angle of attack. Outline the approach you would take to determine the average vortex convection speed (in semi-chords of airfoil travel).

9.3. If dynamic stall were to occur on a helicopter rotor, what symptoms of the phenomenon might the pilot become aware of? What actions might the pilot perform with the flight controls to limit the effects of dynamic stall?

9.4. The phenomenon of dynamic stall can be characterized by time-scales defined in terms of semi-chord lengths of airfoil travel. At low Mach numbers, the time-scales associated with vortex shedding are of the order of 8 semi-chords. Estimate the angular resolution (azimuthal time-step) that would be required to properly resolve the dynamic stall phenomenon in a typical helicopter rotor analysis.

9.5. The phenomenon of dynamic stall is often associated with reduced or negative torsional aerodynamic damping. Explain what this means and why it occurs, and describe the possible consequences on a helicopter rotor.

9.6. Discuss the area of flow control and possibilities of using active flow control on a helicopter rotor to delay the onset of dynamic stall. What performance benefits could be expected for a conventional helicopter by delaying the onset of rotor stall? Discuss the issues involved with the practical implementation of flow control on a rotor, including weight and cost penalties.

Bibliography

Barakos, G., Drikakis, D., and Leschziner, M. A. 1998. "Numerical Investigation of the Dynamic Stall Phenomenon Using Non-Linear Eddy-Viscosity Models," AIAA Paper 98-2740, 16th AIAA Applied Aerodynamics Conference, Albuquerque, NM, June 15–18.

Beddoes, T. S. 1976. "A Synthesis of Unsteady Aerodynamic Effects Including Stall Hysteresis," *Vertica*, 1, pp. 113–123.

Beddoes, T. S. 1978. "Onset of Leading Edge Separation Effects under Dynamic Conditions and Low Mach Number," 34th Annual Forum of the American Helicopter Soc., Washington DC, May 15–17.

Beddoes, T. S. 1979. "A Qualitative Discussion of Dynamic Stall," In: AGARD Report 679.

Beddoes, T. S. 1983. "Representation of Airfoil Behavior," *Vertica*, 7 (2), pp. 183–197.

Benson, R. G., Dadone, L. U., Gormont, R. E., and Kohler, G. R. 1973. "Influence of Airfoils on Stall Flutter Boundaries of Articulated Helicopter Rotors," *J. of the American Helicopter Soc.*, 18 (1), pp. 36–46.

Berton, E., Allain, C., Favier, D., and Maresca, C. 2003a. "Experimental Methods for Subsonic Flow Measurements," *Progress in Computational Flow-Structure Interaction*, Haase, W., Selmin, V. & Winzeil, B. (eds.). Notes on Numerical Fluid Mechanics & Multidisciplinary Design, Vol. 81, Springer, Berlin, pp. 97–104.

Berton, E., Allain, C., Favier, D., and Maresca, C. 2003b. "Database for Steady and Unsteady 2-D and 3-D Flow," *Progress in Computational Flow-Structure Interaction*, Haase, W., Selmin, V. & Winzell, B. (eds.). Notes on Numerical Fluid Mechanics & Multidisciplinary Design, Vol. 81, Springer, Berlin, pp. 155–164.

Bielawa, R. L. 1975. "Synthesized Unsteady Airfoil Data with Applications to Stall Flutter Calculations," 31st Annual Forum of the American Helicopter Soc., Washington DC, May 13–15.

Bousman, W. G. 1998. "A Qualitative Examination of Dynamic Stall From Flight Test Data," *J. of the American Helicopter Soc.*, 43 (4), pp. 279–295.

Carlson, R. G., Blackwell, R. H., Commerford, G. L., and Mirick, P. H. 1974. "Dynamic Stall Modeling and Correlation with Experimental Data on Airfoils and Rotors," NASA SP-352.

Carr, L. W., McAlister, K. W., and McCroskey, W. J. 1977. "Analysis of the Development of Dynamic Stall Based on Oscillating Airfoil Measurements," NASA TN D-8382.

Carr, L. W., McAlister, K. W., and McCroskey, W. J. 1978. "Dynamic Stall Experiments on the NACA 0012 Airfoil," NASA TP-1100.

Carr, L. W. 1988. "Progress in Analysis and Prediction of Dynamic Stall," *J. of Aircraft*, 25 (1), pp. 6–17.

Carta, F. O. 1967. "An Analysis of the Stall Flutter Instability of Helicopter Rotor Blades," *J. of the American Helicopter Soc.*, 12 (4), pp. 1–18.

Carta, F. O., Casellini, L. M., Arcidiacono, P. J., and Elman, H. L. 1970. "Analytical Study of Helicopter Rotor Stall Flutter," 26th Annual Forum of the American Helicopter Soc., Washington DC, June 16–18.

Carta, F. O. 1971. "Effect of Unsteady Pressure Gradient Reduction on Dynamic Stall Delay," *J. of Aircraft*, 8 (10), pp. 839–840.

Carta, F. O. 1979. "A Comparison of the Pitching and Plunging Response of an Oscillating Airfoil," NASA CR-3172.

Chandrasekhara, M. S. and Carr, L. W. 1990. "Flow Visualization Studies of the Mach Number Effects on the Dynamic Stall of Oscillating Airfoils," *J. of Aircraft*, 27 (6), pp. 516–522.

Chandrasekhara, M. S. and Carr, L. W. 1994. "Compressibility Effects on Dynamic Stall of Oscillating Airfoils," In: AGARD CP-552.

Chandrasekhara, M. S., Wilder, M. C., and Carr, L. W. 1998. "Unsteady Stall Control Using Dynamically Deforming Airfoils," *AIAA J.*, 36 (1), pp. 1792–1800.

Chandrasekhara, M., Wilder, M., and Carr, L. 1999. "Compressible Dynamic Stall Control," AIAA Paper 99-3122, 17th Applied Aerodynamics Conference, Norfolk, VA, June 28–July 1.

Dwyer, H. A. and McCroskey, W. J. 1971. "Crossflow and Unsteady Boundary-Layer Effects on Rotating Blades," *AIAA J.*, 9 (8), pp. 1498–1505.

Ekaterinaris, J. A., Srinivasan, G. R., and McCroskey, W. J. 1994. "Present Capabilities of Predicting Two-Dimensional Dynamic Stall," In: AGARD CP-552.

Ericsson, L. E. 1967. "Comments on Unsteady Airfoil Stall," *J. of Aircraft*, 4 (5), pp. 478–480.

Ericsson, L. E. and Reding, J. P. 1972. "Dynamic Stall of Helicopter Blades," *J. of the American Helicopter Soc.*, 17 (1), pp. 10–19.

Ericsson, L. E. and Reding, J. P. 1983. "The Difference between the Effects of Pitch and Plunge on Dynamic Airfoil Stall," 9th European Rotorcraft Forum, Stresa, Italy, Sept. 13–15.

Ericsson, L. E. and Reding, J. P. 1984. "Unsteady Flow Concepts for Dynamic Stall Analysis," *J. of Aircraft*, 21 (8), pp. 601–606.

Faller, W. E. and Schreck, S. J. 1996. "Neural Networks: Applications and Opportunities in Aeronautics," *Progress in Aerospace Sciences*, 32 (5), pp. 433–456.

Favier, D., Agnes, A., Barbi, C., and Maresca, C. 1988. "Combined Translation/Pitch Motion: A New Airfoil Dynamic Stall Simulation," *J. of Aircraft*, 25 (9), pp. 805–814.

Feszty, D., Gilles, E. A., and Vezza, M. 2003. "Alleviation of Rotor Blade Dynamic Stall via Trailing Edge Flap Flow Control," AIAA Paper 2003-0050, 41st Aerospace Sciences Meeting & Exhibit, Reno, NV, Jan. 6–9.

Fukushima, T. and Dadone, L. U. 1977. "Comparison of Dynamic Stall Phenomena for Pitching and Vertical Translation Motions," NASA CR 2793.

Galbraith, R. A. McD., Niven, A. J., and Seto, L. Y. 1986. "On the Duration of Low Speed Dynamic Stall," Paper ICAS-86-2.4.3. International Committee of the Aeronautical Sciences, London, England.

Gangwani, S. T. 1982. "Prediction of Dynamic Stall and Unsteady Airloads on Rotor Blades," *J. of the American Helicopter Soc.*, 27 (4), pp. 57–64.

Gangwani, S. T. 1984. "Synthesized Airfoil Data Method for Prediction of Dynamic Stall and Unsteady Airloads," *Vertica*, 8 (2), pp. 93–118.

Geissler, W., Dietz, G., Mai, H., and Junker, B. 2004. "Dynamic Stall Control Investigations on a Full Size Chord Blade Section," 30th European Rotorcraft Forum, Marseilles, France, Sept. 14–16.

Green, R. B. and Galbraith, R. A. McD. 1995. "Dynamic Recovery to Fully Attached Aerofoil Flow from Deep Stall," *AIAA J.*, 33 (8), pp. 1433–1440.

Greenblatt, D. and Wygnanski, I. 1999. "Parameters Affecting Dynamic Stall Control by Oscillatory Excitation," AIAA Paper 99-3121, 17th Applied Aerodynamics Conference, Norfolk, VA. June 28–July 1.

Gormont, R. E. 1973. "A Mathematical Model of Unsteady Aerodynamics and Radial Flow for Application to Helicopter Rotors," USAAVLABS TR 72-67.

Gross, D. W. and Harris, F. D. 1969. "Prediction of In-Flight Stalled Airloads from Oscillating Airfoil Data," 25th Annual Forum of the American Helicopter Soc., Washington DC, May 14–16.

Ham, N. D. 1968. "Aerodynamic Loading on a 2-D Airfoil During Dynamic Stall," *AIAA J.*, 6 (10), pp. 1927–1934.

Ham, N. D. and Garelick, M. S. 1968. "Dynamic Stall Considerations in Helicopter Rotors," *J. of the American Helicopter Soc.*, 13 (2), pp. 49–55.

Harris, F. D. 1966. "Preliminary Study of Radial Flow Effects on Rotor Blades," *J. of the American Helicopter Soc.*, 11 (3), pp. 1–21.

Harris, F. D., Tarzanin, F. J., and Fisher, R. K. 1970. "Rotor High Speed Performance, Theory vs. Test," *J. of the American Helicopter Soc.*, 15 (3), pp. 35–44.

Isaacs, N. C. G. and Harrison, R. J. 1989. "Identification of Retreating Blade Stall Mechanisms Using Flight Test Pressure Measurements," 45th Annual Forum of the American Helicopter Soc., Boston, MA, May 22–24.

Johnson, W. 1969. "The Effect of Dynamic Stall on the Response and Airloading of Helicopter Rotor Blades," *J. of the American Helicopter Soc.*, 14 (2), pp. 68–77.

Johnson, W. and Ham, N. D. 1972. "On the Mechanism of Dynamic Stall," *J. of the American Helicopter Soc.*, 17 (4), 36–45.

Johnson, W. 1974. "Comparison of Three Methods for Calculation of Helicopter Rotor Blade Loading and Stresses Due to Stall," NASA TN D-7833.

Jones, R. T. and Cohen, D. 1957. "Aerodynamics of Wings at High Speeds," Vol. VII of *High Speed Aerodynamics and Jet Propulsion*, Section A, Chapter 1, pp. 36–48. Aerodynamic Components of Aircraft at High Speeds. A. F. Donovan & H. R. Lawrence (eds.), Princeton University Press, Princeton, NJ.

Katz, Y., Nishri, B., and Wygnanski, I. 1989. "The Delay of Turbulent Boundary Layer Separation by Oscillatory Active Control," AIAA Paper 89-0975, 2nd Shear Flow Conference, Tempe, AZ, Mar. 13–16.

Kramer, M. 1932. "Increase in the Maximum Lift of an Airfoil Due to a Sudden Increase in Its Effective Angle of Attack Resulting from a Gust," NACA Technical Memorandum 687.

Landgrebe, A. J. 1994. "New Directions in Rotorcraft Computational Aerodynamics Research in the U.S.," In: AGARD CP-552.

Leishman, J. G. and Beddoes, T. S. 1986. "A Generalized Method for Unsteady Airfoil Behavior and Dynamic Stall Using the Indicial Method," 42nd Annual Forum of the American Helicopter Soc., Washington DC, June 2–5.

Leishman, J. G. and Beddoes, T. S. 1989. "A Semi-Empirical Model for Dynamic Stall," *J. of the American Helicopter Soc.*, 34 (3), pp. 3–17.

Leishman, J. G. 1989. "Modeling Sweep Effects on Dynamic Stall," *J. of the American Helicopter Soc.*, 34 (3), pp. 18–29.

Leishman, J. G. and Crouse, G. L. 1989. "State-Space Model for Unsteady Airfoil Behavior and Dynamic Stall," AIAA Paper 89-1319, 30th AIAA/AHS/ASME Structural Dynamics and Materials Conference, Mobile, AL, April 3–5.

Leishman, J. G. and Nguyen, K. Q. 1990. "A State-Space Representation of Unsteady Aerodynamic Behavior," *AIAA J.*, 28 (5), pp. 836–845.

Liiva, J., Davenport, F. J., Gray, L., and Walton, I. C. 1968. "2-D Tests of Airfoils Oscillating Near Stall," USAAVLABS TR 68-13, Vols. I & II.

Lorber, P. F., Covino, A. F., and Carta, F. O. 1991. "Dynamic Stall Experiments on a Swept Three-Dimensional Wing in Compressible Flow," AIAA Paper 91-1795, 22nd Fluid Dynamics, Plasma Dynamics and Lasers Conference, Honolulu, HI, June 24–26.

Lorber, P. F. 1992. "Compressibility Effects on the Dynamic Stall of a Three-Dimensional Wing," AIAA Paper 92-0191, 30th Aerospace Sciences Meeting and Exhibit, Reno, NV, Jan. 6–9.

Lorber, P., McCormick, D., Anderson, T., Wake, B., MacMartin, D., Pollack, M., Corke, T., and Breuer, K. 2000. "Rotorcraft Retreating Blade Stall Control," AIAA Paper 2000-2475, FLUIDS 2000 Conference & Exhibit, Denver, CO, June 19–22.

Martin, P. B., Chandrasekhara, M. S., and Geissler, W. 2003. "Dynamic Stall Measurements and Computations for a VR-12 Airfoil With a Variable Droop Leading Edge," American Helicopter 59th Annual Forum, Phoenix, AZ, May 6–8.

Maresca, C. A., Favier, D. J., and Rebont, J. M. 1981. "Unsteady Aerodynamics of an Aerofoil at High Angles of Incidence Performing Various Linear Oscillation in a Uniform Stream," *J. of the American Helicopter Soc.*, 26 (2), pp. 40–45.

McAlister, K. W. and Carr, L. W. 1979. "Water Tunnel Visualizations of Dynamic Stall," *J. of Fluids Engineering*, 101, Sept., pp. 376–380.

McAlister, K. W., Lambert, O., and Pitot, D. 1984. "Application of the ONERA Model of Dynamic Stall," NASA Technical Paper 2399, AVSCOM Technical Report 84-A-3.

McCroskey, W. J. 1972a. "Dynamic Stall of Airfoils and Helicopter Rotors," In: AGARD Report No. 595.

McCroskey, W. J. 1972b. "Recent Developments in Rotor Blade Stall," In: AGARD CP 111.

McCroskey, W. J. and Fisher, R. K., Jr. 1972. "Detailed Aerodynamic Measurements on a Model Rotor in the Blade Stall Regime," *J. of the American Helicopter Soc.*, 17 (1), pp. 20–30.

McCroskey, W. J. 1973. "Inviscid Flowfield of an Unsteady Airfoil," *AIAA J.*, 11 (8), pp. 1130–1136.

McCroskey, W. J. 1975. "Some Current Research in Unsteady Fluid Dynamics," ASME Freeman Scholar Lecture, *J. of Fluids Engineering*, Transactions of the ASME, 99, pp. 8–38.

McCroskey, W. J., Carr, L. W., and McAlister, K. W. 1976. "Dynamic Stall Experiments on Oscillating Airfoils," *AIAA J.*, 14 (1), pp. 57-63.

McCroskey, W. J., McAlister, K. W., Carr, L. W., Pucci, S. K., Lambert, O., and Indergand, R.F. 1980. "Dynamic Stall on Advanced Airfoil Sections," 36th Annual Forum of the American Helicopter Soc., Washington DC, May 13–15.

McCroskey, W. J., McAlister, K. W., Carr, L. W., and Pucci, S. L. 1982. "An Experimental Study of Dynamic Stall on Advanced Airfoil Sections," Vols. 1, 2 & 3 NASA TM-84245.

McHugh, F. 1978. "What are the Lift and Propulsive Limits at High Speed for the Conventional Rotor?" 34th Annual Forum of the American Helicopter Soc., Washington DC, May 15–17.

Nguyen, K. Q. and Johnson, W. 1998. "Evaluation of Dynamic Stall Models with UH-60 Airloads Flight Test Data," 45th Annual Forum of the American Helicopter Soc., Washington DC, May 20–22.

Peters, D. A. 1985. "Toward a Unified Lift Model for Use in Rotor Blade Stability Analysis," *J. of the American Helicopter Soc.*, 30 (3), pp. 32–42.

Pierce, G. A., Kunz, D. L., and Malone, J. B. 1978a. "The Effect of Varying Freestream Velocity on Airfoil Dynamic Stall Characteristics," *J. of the American Helicopter Soc.*, 23 (2), pp. 27–33.

Pierce, G. A., Kunz, D. L., and Malone, J. B. 1978b. "2-D Dynamic Stall as Simulated in a Varying Free-Stream," Final Report under Grant NGR 11-002-185, NASA Langley Research Center.

Pierce K. and Hansen A. C. 1995. "Prediction of Wind Turbine Rotor Loads Using the Beddoes-Leishman Model for Dynamic Stall," *J. of Solar Energy Engineering*, 117, pp. 200–204.

Pitot, D. 1989. "Differential Equation Modeling of Dynamic Stall," La Reserche Aerospatiale, No. 1989-6.

Pizialli, R. A. 1994. "2-D and 3-D Oscillating Wing Aerodynamics for a Range of Angles of Attack Including Stall," NASA Technical Memorandum 4632, USAATCOM Technical Report 94-A-011.

Purser, P. E. and Spearman, M. L. 1951. "Wind Tunnel Tests at Low Speeds of Swept and Yawed Wings Having Various Planforms," NACA TN 2445.

Reddy, T. S. R. and Kaza, K. R. V. 1987. "A Comparative Study of Some Dynamic Stall Models," NASA TM-88917.

Scruggs, R. M., Nash, J. F., and Singleton, R. E. 1974. "Analysis of Flow-Reversal Delay for a Pitching Foil," AIAA Paper 74-183, 12th AIAA Aerospace Sciences Meeting, Washington DC, Jan. 30–Feb. 1.

Seifert, A. and Pack, L. G. 1999. "Oscillatory Control of Separation at High Reynolds Number," *AIAA J.*, 37 (9), pp. 1062–1071.

Srinivasan, G. R., Ekaterinaris, J. A., and McCroskey, W. J. 1993. "Dynamic Stall of an Oscillating Wing Part 1 Evaluation of Turbulence Models," AIAA Paper 93-3403, 11th AIAA Applied Aerodynamics Conference, Monterey, CA, Aug. 9–11.

Stepneiwski, W. Z. and Keys, C. N. 1984. *Rotary-Wing Aerodynamics*, Dover Publications, New York, NY, pp. 103–116.

Spentzos, A., Barakos, G. N., Badock, K. J., and Richards, B. E. 2004. "CFD Study of Three-Dimensional Dynamic Stall of Various Planform Shapes," 30th European Rotorcraft Forum, Marseilles, France, Sept. 14–16.

St. Hillaire, A. O., Carta, F. O., Fink, M. R., and Jepson, W. D. 1979. "The Influence of Sweep on the Aerodynamic Loading of a NACA 0012 Airfoil," Vol. 1 – Technical Report, NASA CR 3092.

St. Hillaire, A. O. and Carta, F. O. 1979. "The Influence of Sweep on the Aerodynamic Loading of a NACA 0012 Airfoil," Vol. 2 – Data Report, NASA CR 145350.

St. Hillaire, A. O. and Carta, F. O. 1983a. "Analysis of Unswept and Swept Wing Chordwise Pressure Data from an Oscillating NACA 0012 Airfoil Experiment," Vol. 1 – Technical Report, NASA CR 3567.

St. Hillaire, A. O. and Carta, F. O. 1983b. "Analysis of Unswept and Swept Wing Chordwise Pressure Data from an Oscillating NACA 0012 Airfoil Experiment," Vol. 2 – Data Report, NASA CR 165927.

Tan, C. M. and Carr, L. W. 1996. "The AFDD International Dynamic Stall Workshop on Correlation of Dynamic Stall Models with 3-D Dynamic Stall Data," NASA TM-110375, USAATCOM TR-96-A-009.

Tarzanin, F. J., Jr. 1972. "Prediction of Control Loads Due to Blade Stall," *J. of the American Helicopter Soc.*, 17 (2), pp. 33–46.

Telionis, D. P. 1975. "Calculations of Time-Dependent Boundary Layers," Symposium on Unsteady Aerodynamics, Kinney, R. B., ed., University of Arizona, Tucson, pp. 155–190.

Tran, C. T. and Pitot, D. 1981. "Semi-Empirical Model for the Dynamic Stall of Airfoils in View of the Application to the Calculation of the Responses of a Helicopter Blade in Forward Flight," *Vertica*, 5 (1), pp. 35–53.

Tran, C. T. and Falchero, D. 1981. "Application of the ONERA Dynamic Stall Model to a Helicopter Rotor Blade in Forward Flight," 7th European Rotorcraft Forum, Garmisch-Partenkirchen, Sept. 22–25.

Truong, V. K. 1993. "A 2-D Dynamic Stall Model Based on a Hopf Bifurcation," 19th European Rotorcraft Forum, Cernobbio (Como), Italy, Sept. 14–16.

Truong, V. K. 1996. "Prediction of Helicopter Rotor Airloads Based on Physical Modeling of 3-D Unsteady Aerodynamics," 22nd European Rotorcraft Forum, Brighton, UK, Sept. 17–19.

Tyler, J. C. and Leishman, J. G. 1992. "An Analysis of Pitch and Plunge Effects on Unsteady Airfoil Behavior," *J. of the American Helicopter Soc.*, 37 (3), pp. 69–82.

Wilby, P. G. 1984. "An Experimental Investigation of the Influence of a Range of Aerofoil Design Features on Dynamic Stall Onset," 10th European Rotorcraft Forum, The Hague, The Netherlands, Aug. 28–31.

Wilby, P. G. 1996. "The Development of Rotor Airfoil Testing in the UK – The Creation of a Capability to Exploit a Design Opportunity," 22nd European Rotorcraft Forum, Brighton, UK, Sept. 16–18.

Wilby, P. G. 1998. "Shockwaves in the Rotor World – A Personal Perspective of 30 Years of Rotor Aerodynamic Research in the UK," *The Aeronautical J.*, 102 (1013), pp. 113–128.

Wood, M. E. 1979. "Results from Oscillatory Pitch Tests on the NACA 0012 Blade Section," Aircraft Research Association, Bedford, UK, ARA Memo 220.

Yen, J. G. and Yuce, M. 1992. "Correlation of Pitch-Link Loads in Deep Stall on Bearingless Rotors," *J. of the American Helicopter Soc.*, 37 (4), pp. 4–15.

CHAPTER 10

Rotor Wakes and Blade Tip Vortices

We have built new rotor test stands, new blades, with emphasis on heavily instrumented blades, new measurement techniques – it is mind boggling to me to see how well, and in how much detail, we can measure the flow field of a rotor. Modeling the flow field of a rotor is a terribly difficult problem. The airplane people have it easy compared to us. Capturing the details of the rotor wake and of what happens in the vicinity of the blade is very difficult.

Leone U. Dadone (1995)

10.1 Introduction

The significant physical features of helicopter rotor wakes, and some of the more advanced mathematical tools for modeling the wake, are discussed in this chapter. The understanding and prediction of the effects of the rotor wake is an important key to the successful prediction of blade loads and a host of other problems found in helicopter aerodynamics. A helicopter rotor wake is dominated by strong vortices that are trailed from the tips of each blade. The nature of the rotor wake, in terms of its geometry, strength, and the aerodynamic effects produced on the blades, depends principally on the operating state and flight condition of the helicopter. In hover, the tip vortices follow nominally helical trajectories below the rotor. This is perhaps the simplest operating state to understand, but even here the wake structure is relatively complicated. During forward flight, the rotor wake is skewed back behind the rotor by the oncoming flow, and a series of more complex interlocking, but nominally epicycloidal vortex trajectories are produced. Under these conditions, the increased mutual proximity of many of the vortex filaments results in stronger vortex–vortex interactions and complicated distortions to the evolving wake topology. At the lateral edges of the wake, the individual vortex filaments are found to roll up into a pair of merging vortex bundles, somewhat like those that would trail from the tips of a low aspect ratio fixed-wing.

The highly 3-D nature of a helicopter rotor wake, as well as the sensitivity of the wake to the geometric and operational parameters of the helicopter, means that the details of the wake flow are difficult to study experimentally, as well as to compute by means of mathematical models. Recent advances in experimental techniques have been substantial and now allow measurements to be made with a fidelity that was impossible only a few years ago. However, there are many physical phenomena involving the formation and evolution of blade tip vortices and rotor wakes that are still not well understood, and it is here that future research on helicopter aerodynamics must be focused. Landgrebe (1988) and McCroskey (1995) review the state-of-the-art capabilities in modeling helicopter rotor wakes, whereas Leishman & Bagai (1998) give an overview of key characteristic physical features of rotor wakes and some of the unique experimental challenges involved in their measurement.

10.2 Flow Visualization Techniques

While the wake of a helicopter rotor is sometimes rendered visible through natural condensation effects, flow visualization using subscale rotor models has been the primary method used to study the wake physics. Some of the earliest studies were by Taylor (1950) and Dingeldein (1954), who used balsa dust to visualize the rotor wake. A more popular method is to use a dense white smoke, which is entrained into the wake, thereby rendering it visible when illuminated by a suitable strobed lighting source. Density gradient flow visualization methods, such as strobed (phase-resolved) shadowgraphy and schlieren (and to a lesser extent, interferometry), have also been used to study helicopter rotor wakes. The phenomena that have been studied include tip vortex formation, blade–vortex interactions, vortex–airframe surface interactions, main rotor wake–tail rotor interactions, ground interference, multirotor flows, and the wake roll-up in forward flight.

10.2.1 *Natural Condensation Effects*

Evidence of the rotor wake can sometimes be seen through natural condensation of water vapor inside the blade tip vortices. Published photographs of the phenomena are relatively rare, but examples are given by Felker et al. (1986), Campbell & Chambers (1994), and McVeigh et al. (1997). Representative examples are shown in Fig. 10.1 and Fig. 10.2, with another being shown previously in Fig. 2.2. The results obtained often appear similar to smoke flow visualization, exhibiting characteristic tubular trails with large central voids marking the positions of the vortices. These voids are caused by centripetal accelerations

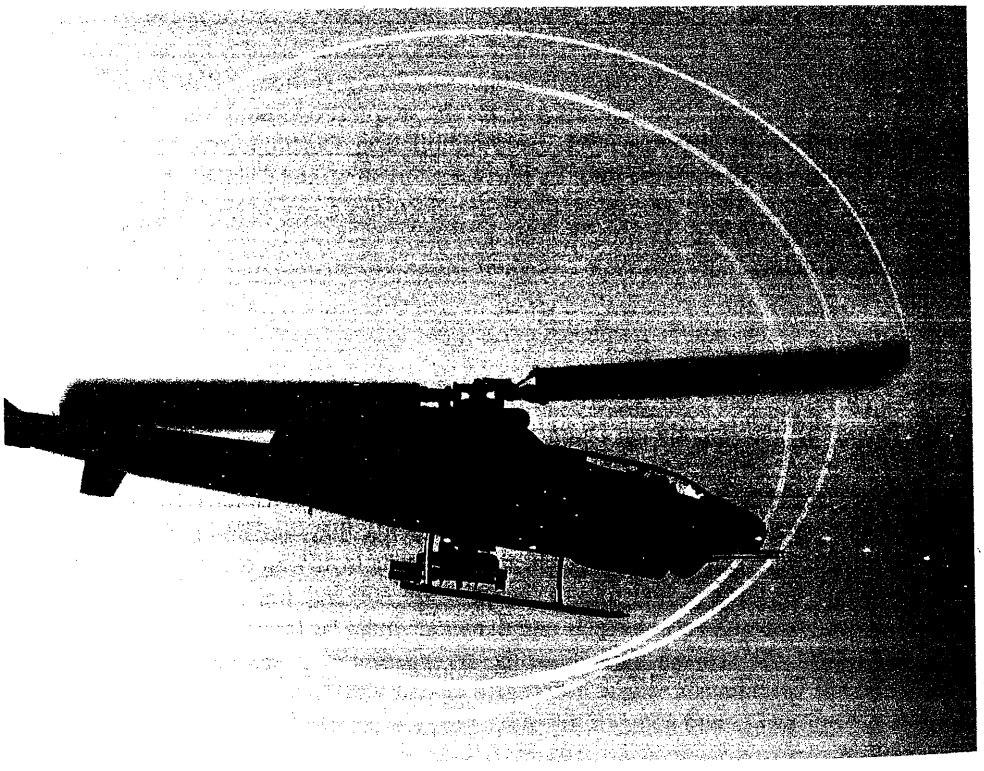

Figure 10.1 Natural condensation trails generated by the tip vortices trailed from a helicopter rotor. Source: US Navy Photo.

Figure 10.2 Natural condensation trails in the tip vortices generated by a tilt-rotor aircraft. Source: Courtesy of US Navy, Patuxent Naval Air Station.

on the vapor particles as well as by the thermodynamic aspects of the problem. Although condensation flow visualization has been achieved in a wind tunnel environment [Dadone (1970)] it is usually only outdoors that the correct combination of atmospheric conditions exist, that is, when the air temperature and dew point spread are small. Even then, however, a challenge is to have the right lighting conditions and background contrast to allow a good photographic exposure.

10.2.2 *Smoke Flow Visualization*

Smoke flow visualization studies of subscale helicopter rotor wakes has been performed by Gray (1956), Pizialli & Trenka (1970), Landgrebe (1971, 1972), Brand et al. (1990), Mercker & Pengel (1992), Ghee & Elliott (1995), Martin et al. (1999), and many other investigators. A dense white smoke is entrained into the rotor wake and blade tip vortices. When stroboscopically illuminated, the smoke particles reflect light, allowing a photograph of the flow structure to be recorded.[1] The tip vortices appear as circular regions devoid of smoke, which is a result of centrifugal forces produced on the smoke particles near the vortex cores (see later). Ideally, to give accurate spatial information, the wake must be illuminated using a thin light sheet, preferably using a laser. In another form of smoke flow visualization, smoke is ejected from the blade tip directly into the tip vortices. This renders the vortices visible as 3-D tubular trails with central voids. Such methods have been used to visualize the tip vortices in hover [see Gray (1956)] and in forward flight [see Müller (1990a)]. In a water tunnel, dye ejected from the blade tips gives similar results – see Werlé & Armand (1969). Projected smoke filament techniques, such as those developed by Steinhoff (1985) and Müller (1990b, 1994), have also received some attention.

While the application of smoke visualization techniques has had good success for subscale rotor models, experiments on full-scale helicopter rotors are rare. A general limitation

[1] While high-speed, black & white film has been traditionally used, the use of a high-resolution digital still or video camera is a common modern format.

of the smoke flow technique, however, is that smoke particles are quickly dispersed, and lower particle concentrations make the tip vortices harder to visualize. However, by using smoke "bombs" attached to the blade tips, the method has been used to visualize part of the wake structure of a CH-46 tandem rotor helicopter – see Spencer (1969) and Sternfeld & Schairer (1969). Using the same technique, the wake generated by a coaxial Ka-34 helicopter has been documented by Akimov et al. (1994).

10.2.3 *Density Gradient Methods*

A fundamental requirement for the successful application of density gradient methods of flow visualization such as schlieren or shadowgraphy is that the flow contain regions with significant density inhomogeneities. Because the refractive index of air is directly proportional to its density, planes with density variations in the flow field cause incident light rays normal to these planes to be refracted. Using a cutoff or other device, the angular deflection of the light rays gives a schlieren effect. If the rays are directly cast onto a projection screen, this will result in a shadowgram or shadowgraph. While shock waves and acoustic waves are readily visualized with density gradient techniques, it is not always appreciated that the flow near rotor tip vortices will also produce large enough compressibility effects. However, to achieve such effects with subscale rotors, the tip speeds must be at or close to full-scale values, and the rotor must be operated at relatively high rotor thrust and blade loading coefficients to generate strong vortices. General overviews of density gradient techniques of flow visualization are given by Holder & North (1963) and Merzkirch (1981).

Walters & Skujins (1972), Tangler et al. (1973), Tangler (1977), and Moedersheim et al. (1994) have used strobed schlieren techniques to observe the tip vortices generated by subscale rotors. An example of Tangler's work is shown in Fig. 10.3, where the tip

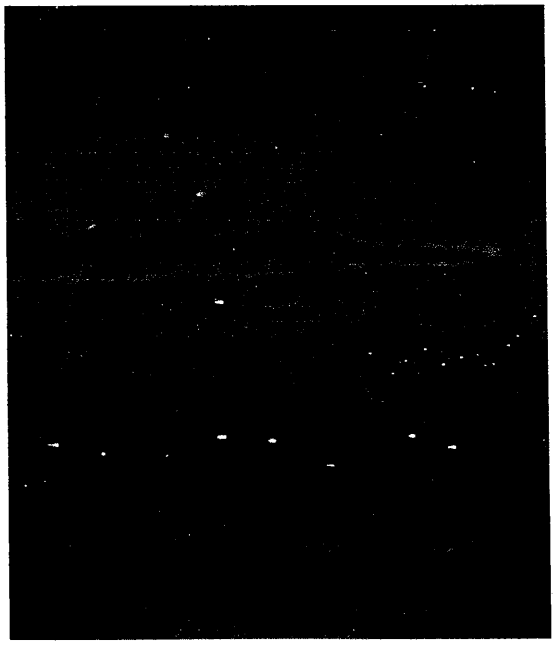

Figure 10.3 Strobed schlieren visualization of part of the wake formed by a subscale rotor during hovering flight. Source: Tangler (1977) and courtesy of James Tangler.

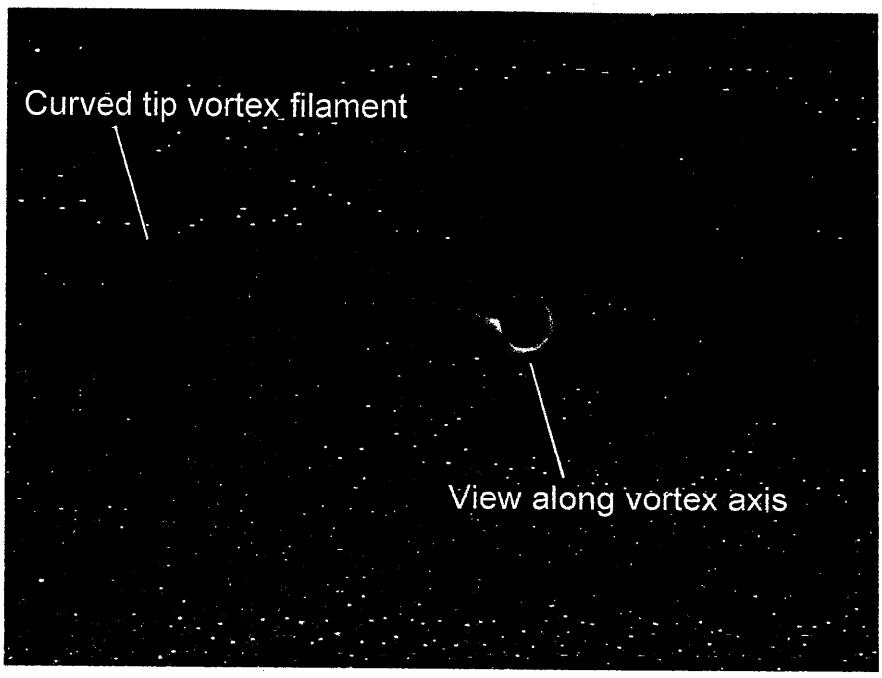

Figure 10.4 Visualization of a tip vortex filament inside a rotor wake by means of wide-field shadowgraphy. Source: University of Maryland.

vortices can be clearly seen. Tangler (1977) also shows that various 3-D acoustic wave phenomena generated by the rotor can be rendered visible with schlieren. A limitation with schlieren, however, is the small field of view because of the need to use high-quality, aberration-free, focusing mirrors. Direct shadowgraphy uses no mirrors and so allows a much larger field and angle of view. However, because of the relatively weak density gradients found in rotor vortices, a shadowgraph screen must be made of a high-efficiency retroreflective material to give sufficient contrast to allow the image to be recorded on photographic film – see Moedersheim et al. (1994) and Winburn et al. (1996). Parthasarthy et al. (1985), Norman & Light (1987), Light et al. (1990), Bagai & Leishman (1992a,b), Swanson (1993), and Lorber et al. (1994) have successfully used strobed shadowgraphy to study tip vortex formation, blade vortex interactions, and rotor wake–airframe interaction phenomena. By taking advantage of the axial symmetry of the wake in hover, shadowgraphy can also allow the quantitative displacements of the tip vortices relative to the rotor to be obtained as a function of wake age – see Norman & Light (1987) and Bagai & Leishman (1992b).

Figure 10.4 shows an example of a strobed shadowgraph detailing the flow immediately surrounding a tip vortex. This image was captured using a modified wide field-of-view shadowgraph system, incorporating a beam splitter arrangement – see Bagai & Leishman (1992a). This simple adaptation of the basic wide-field shadowgraph technique allows on-axis viewing and maximizes the efficiency of the retroreflective projection screen – see Winburn et al. (1996). While the resulting image is, in fact, a 2-D rendering of a curved 3-D vortex filament, the light rays at the right of the image are almost parallel to the vortex axis. A dark circular nucleus surrounded by a circular ring or "halo" is formed at the center of the image, where the light rays have been refracted away from the vortex axis. The dimensions

of this nucleus can be related to the density gradients in the flow, and under certain justifiable assumptions these can be related to the velocity field in the vortex – see Parthasarthy et al. (1985), Norman & Light (1987), and Bagai & Leishman (1994). Outside the immediate core region, the striations present in the shadowgraph image indicates significant turbulence in the flow surrounding the vortices.

10.3 Characteristics of the Rotor Wake in Hover

10.3.1 *General Features*

In hovering flight a helicopter rotor wake is radially axisymmetric (at least in principle) and somewhat easier to study by means of flow visualization because only one view at successive blade positions (azimuth angles) is necessary to obtain a complete 3-D understanding of the wake topology. Figure 10.5 shows representative flow visualization images in the wake of a two-bladed rotor operating in hover. In this case, a fine mist of submicron atomized oil particles was illuminated with a thin laser light sheet that was positioned in a radial plane extending through the rotational axis of the rotor. The sheet was pulsed at a frequency of one flash per rotor revolution, so as to create an instantaneous illumination of the wake – see Martin et al. (1999) for further details. The results in Fig. 10.5 are for two blade azimuth positions.

Notice the existence of two major flow features in Fig. 10.5. First, the blade tip vortex cores are identified by the dark seed voids. Wherever the local velocities are high enough to cause centrifugal forces on the seed particles, they will spiral radially outward. The particles will reach a radial equilibrium only when the centrifugal and pressure forces are in balance. The resulting voids can be larger than the actual viscous core size of the tip vortex – see Leishman (1996). Second, there is a shear layer trailed behind the blade, which is apparent in Fig. 10.5 by a discontinuity in the streaklines. This shear layer is formed by merging of the boundary layers from the upper and lower surfaces of the blade, which contain both negative and positive vorticity. This shear layer is often referred to as a vortex

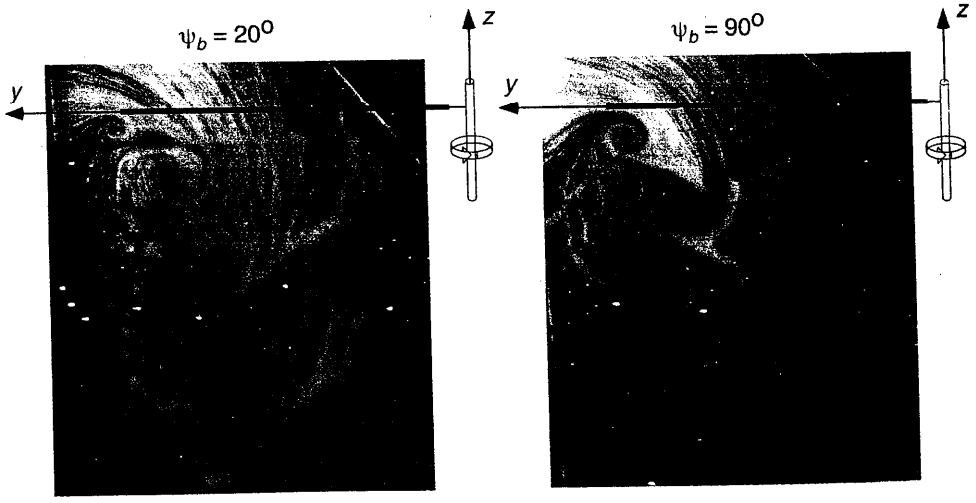

Figure 10.5 Laser light sheet flow visualization images of the rotor wake structure during hovering flight. Source: University of Maryland.

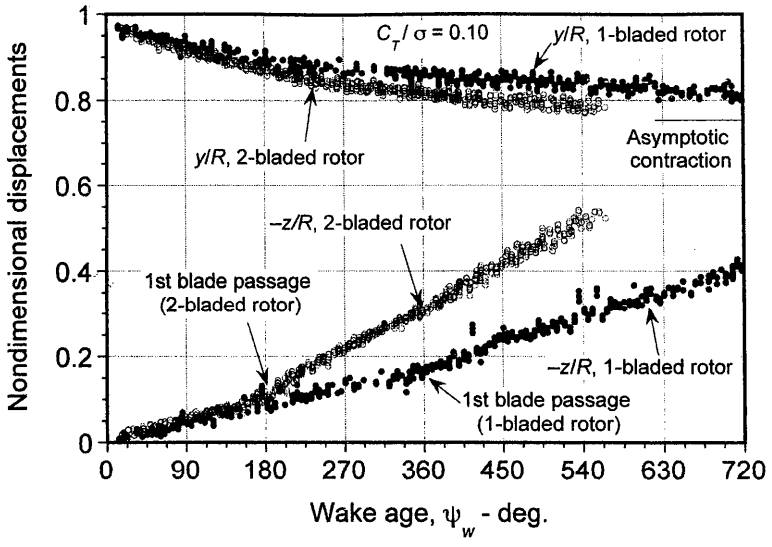

Figure 10.6 Tip vortex displacements of one- and two-bladed rotors operating in hover. $C_T/\sigma \approx 0.1$. Data source: Leishman (1998) and the University of Maryland.

sheet.[2] The sheet has a strength that is related to the spanwise gradient of lift (circulation) over the blade. Initially, the vortex sheet is seen to extend over the entire blade span. Thereafter, both the sheet and the tip vortex are convected below the rotor disk. The significant inward (radial) contraction of the tip vortices below the rotor is clearly evident. Both the tip vortex and the inner sheet are typically found to be visible for about two rotor revolutions, after which details of the individual flow structures become harder to discern. This is because of diffusion of the seed particles, as well as because the wake further downstream becomes aperiodic as it ultimately transitions into a turbulent jet.

10.3.2 *Wake Geometry in Hover*

Flow visualization images such as those shown in Fig. 10.5 can also be used to derive quantitative information by digitizing the locations of the seed void and the shear layer associated with the vortex sheet. Figure 10.6 shows the axial (z/R) and radial (y/R) displacements of the tip vortices as generated by one- and two-bladed hovering rotors operating at the same nominal blade loading coefficients; the total thrust of the two-bladed rotor is approximately twice that of the one-bladed rotor. The characteristics of the tip vortex geometry shown here are representative of the results that would be obtained with any lightly loaded hovering rotor. Up to the first blade passage, which occurs at a wake age of $\psi_w = 360°/N_b$ (where N_b is the number of blades), the tip vortices generated by either of the rotors convect axially only relatively slowly. However, the effective axial (slipstream) velocity (gradient of displacement curve) is noted to increase abruptly after the first blade passage. Here, the tip vortex lies close to and radially inboard of the following blade and so is subjected to an increase in downwash velocity from both the blade and its associated tip vortex. During this process, the radial position of the tip vortices contracts progressively. While the higher thrust of the two-bladed rotor leads to a slightly more rapid wake contraction, the asymptotic values are approximately the same with $y/R \approx 0.78$.

[2] Technically, a vortex sheet is only obtained when the vorticity lies in a surface of zero thickness.

The interdependence of the flows between the vortex sheet and the tip vortex requires further discussion. The process is shown quantitatively in Fig. 10.7, where the displacements of the sheet have been digitized from flow visualization images such as those of Fig. 10.5. Initially, the vortex sheet is trailed along the entire length of the blade, with a concentrated tip vortex at the outboard edge. Both the tip vortex and the sheet then convect axially downward

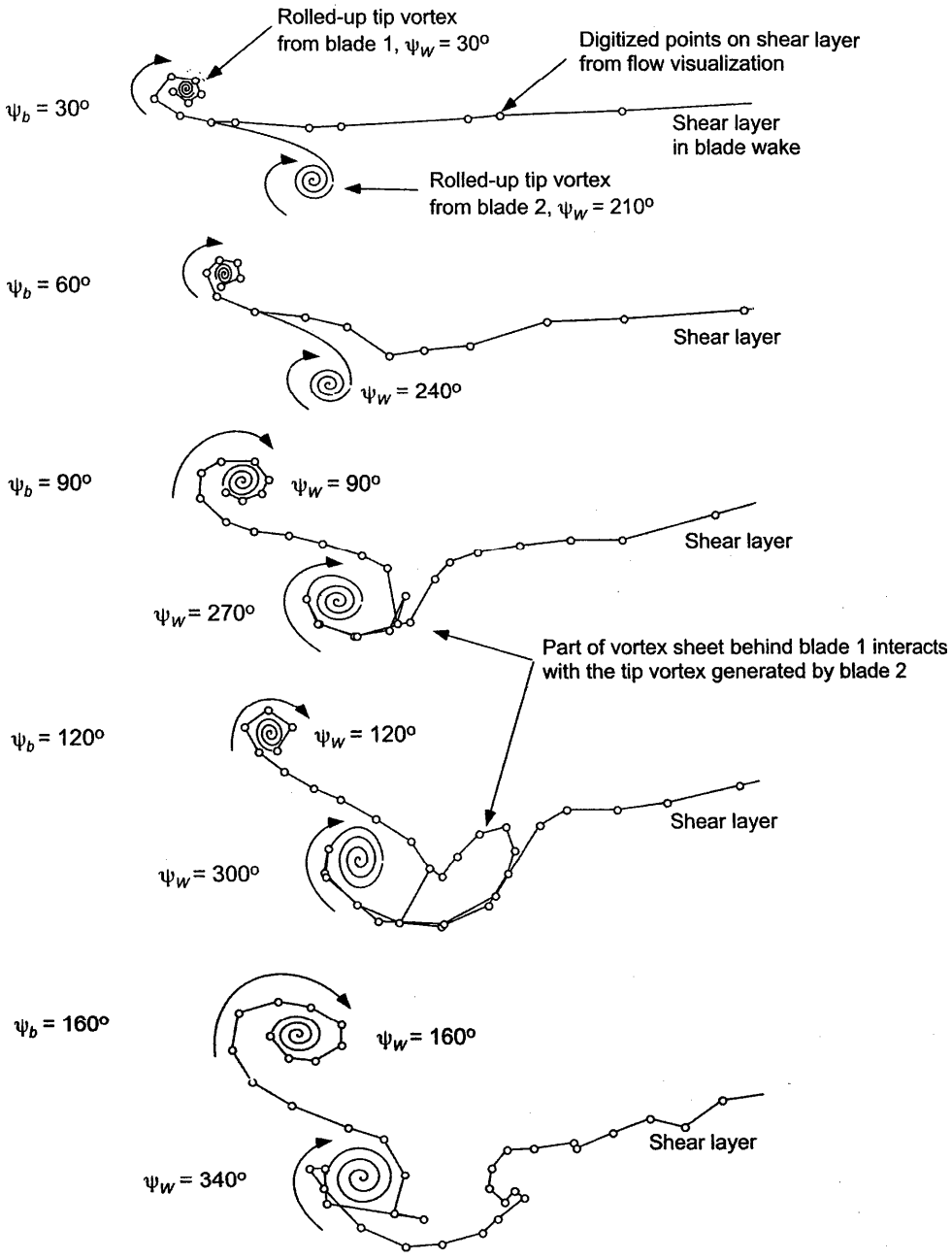

Figure 10.7 Schematic summarizing measured locations of the shear layer (vortex sheet) behind a rotor blade and its interaction with a tip vortex created by another blade.

below the rotor. The visualization images suggest that the distribution of induced velocity through the rotor is highest near the blade tip and lowest near the root. Therefore, the sheet convects more rapidly below the tip region of the blade (about twice the rate) and so it becomes more progressively inclined to the rotor plane. The high swirl velocities induced by the tip vortex cause a further distortion to the sheet, and it is apparent that the outboard edge of the sheet interacts with the tip vortex generated by another blade. This complex interaction between elements of the wakes generated by different lifting surfaces is fundamentally different from that found on fixed (nonrotating) wings and illustrates another level of complexity in the understanding and modeling of helicopter rotor wakes. Free-vortex methods generally capture the effects of the vortex roll-up relatively well. However, modern CFD methods, such as those discussed by Raddatz & Pahlke (1994) and Tang & Baeder (1999), have not yet allowed the details of the vortex sheet and the tip vortex to be fully resolved because of rapid artificial numerical diffusion associated with the characteristics of the finite-difference schemes – see Section 14.2.2.

10.4 Characteristics of the Rotor Wake in Forward Flight

As in hover, a helicopter rotor wake in forward flight is found to be dominated by the blade tip vortices. However, because of the free-stream (edgewise) component of velocity at the rotor plane in forward flight, the wake is now convected behind as well as below the rotor and it takes on a more complicated (nonaxisymmetric) form. The rotor wake geometry in forward flight is found to be sensitive to the rotor thrust, advance ratio, tip path plane (TPP) AoA, the presence of other rotors (such as a tail rotor, or another main rotor as in tandem or coaxial configurations), and rotor–airframe interference effects. While much is now known about the general features of rotor wakes in forward flight, much more is still to be learned about the details of the flow, especially before mathematical models of the rotor wake can be adequately validated.

There are a variety of techniques that can be used to visualize rotor wakes in forward flight, and some of these have been discussed previously in reference to hovering wake studies. Other techniques have included cavitation from the blade tips in a water tunnel, such as used by Larin (1973, 1974). Lehman (1968) and Landgrebe & Bellinger (1971) have used bubbles to trace out the tip vortices trailed from a rotor in a towing tank. Jenks et al. (1987) have used stratified layers of dye in a towing tank to observe some aspects of the wake roll-up. In a wind tunnel, smoke injection from the blade tips can provide good evidence of the epicycloidal tip vortex trajectories – see Müller (1990a,b). Laser sheet smoke flow visualization, such as used by Ghee & Elliott (1995), is generally considered one of the more accurate ways of documenting the spatial locations of the tip vortices.

An example documenting the general features of a helicopter rotor wake in forward flight is shown in Fig. 10.8, where smoke trailed from the blade tips was used to mark the vortex locations. It will be apparent from the top view (x–y plane) that the tip vortices are initially laid down as a series of interlocking epicycloids. Mutual interactions between the individual filaments results in some distortion of the vortex positions, but mostly in the z direction normal to the plane of the rotor (see side view). This distortion is particularly strong at low advance ratios, where the tip vortices are closest together. Notice from Fig. 10.8(a) that along the lateral edges of the wake the individual tip vortices begin to roll up into vortex bundles or "super vortices," as mentioned previously. Another example of this phenomenon is shown in Fig. 10.9. Notice also in Fig. 10.8 that the effects of the tail rotor can be seen as an expanding turbulent wake embedded inside the main rotor wake.

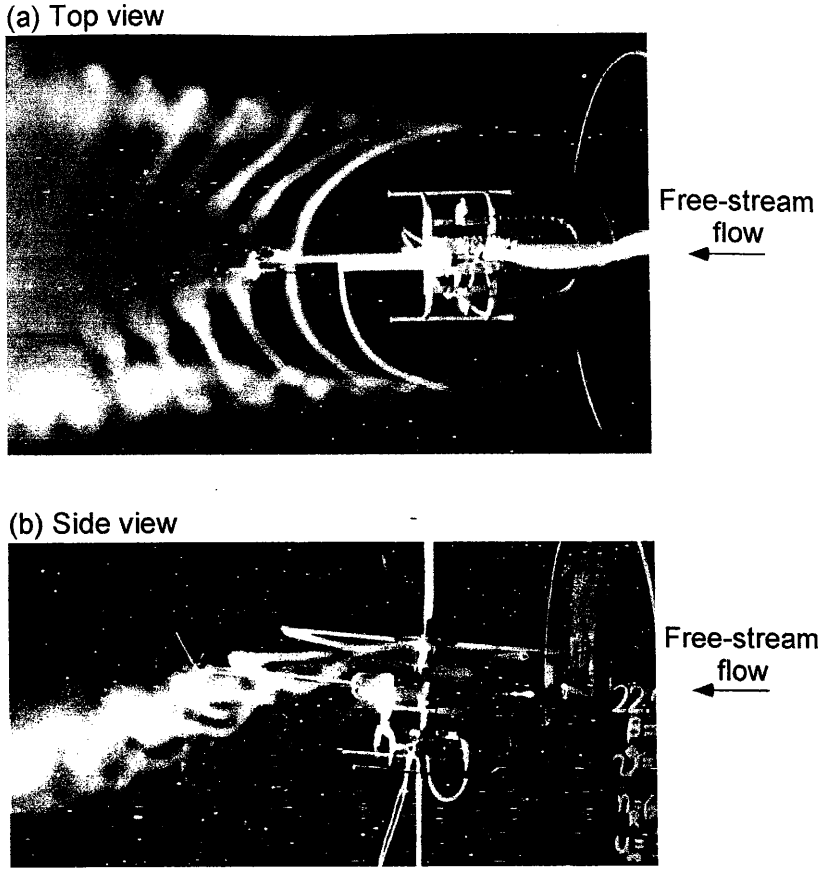

Figure 10.8 Identification of the tip vortex locations in a two-bladed rotor wake during operation in forward flight by ejecting smoke out of the blade tips. (a) Plan view (x–y plane). (b) Side view (x–z plane). Free-stream flow is from right to left. Source: Courtesy of Reinert Müller.

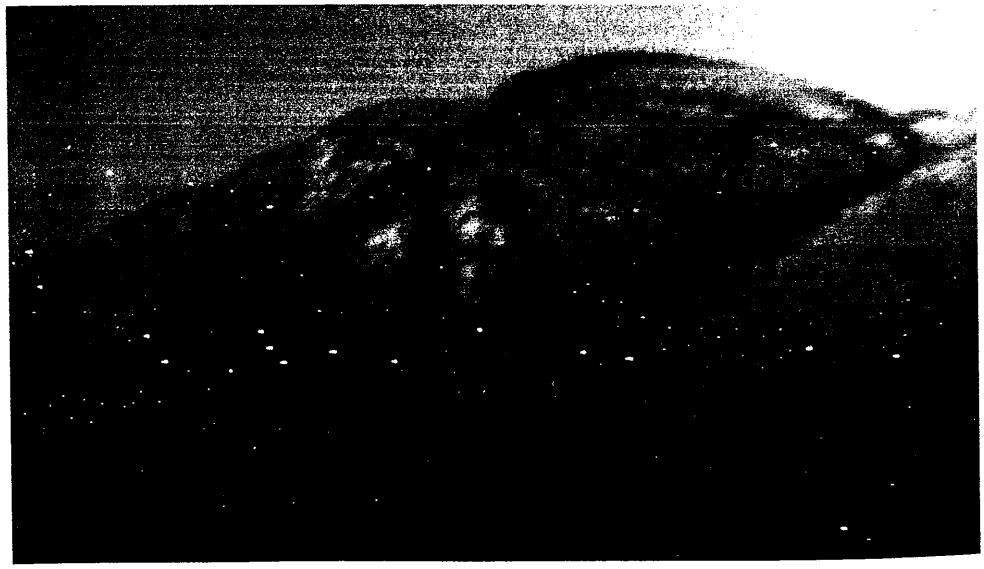

Figure 10.9 The roll up of the rotor wake into two "super vortices" can be seen behind the rotor of small tip-jet driven helicopter. Source: Courtesy of Advanced Technologies Inc.

10.4.1 *Wake Boundaries*

An understanding of the position of the rotor wake boundaries in forward flight can give much useful information to the rotor analyst. Leishman & Bagai (1991) and Bagai & Leishman (1992b) have examined the positions of the tip vortices generated by an isolated rotor and also a rotor with an airframe. The flow visualization results were obtained using shadowgraphy. The measured wake boundaries are plotted in Fig. 10.10 for hover and in forward flight at three advance ratios. Also shown are the positions of the wake that can be predicted on the basis of momentum theory considerations alone (i.e., a rigid-wake; see later in Section 10.7.5). Clearly, the correlation with the measured displacements is poor, and the results confirm what can already be deduced from Fig. 10.8, namely that there are considerable mutually induced effects between vortex filaments inside the rotor wake at lower advance ratios. This leads to a powerful longitudinal (and also a lateral) asymmetry

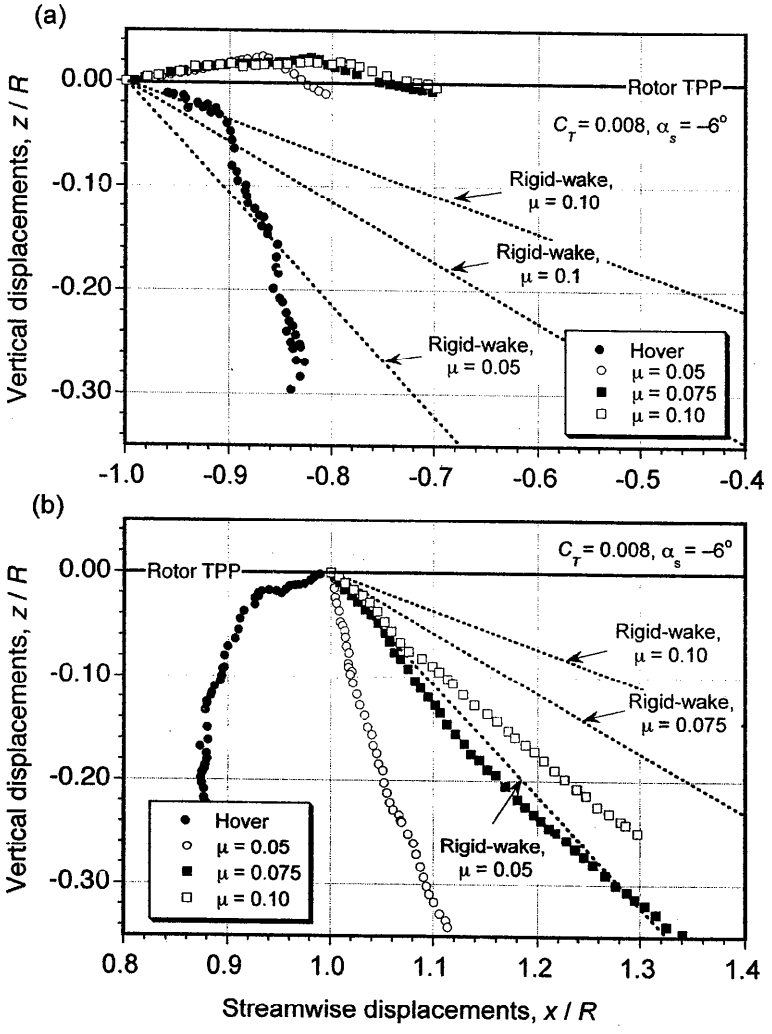

Figure 10.10 Tip vortex displacements in an x–z plane at the longitudinal centerline of an isolated rotor. Four-bladed rotor, $C_T = 0.008$, forward shaft tilt angle of 3° in forward flight. (a) Front of rotor disk. (b) Rear of rotor disk. Data source: Leishman & Bagai (1991).

of the wake that cannot be predicted on the basis of momentum theory alone. Notice from Fig. 10.10(a) that the vortices at the leading edge of the disk are initially convected above the blades and the rotor TPP within the first 90° of wake age, compared to the rear of the disk [see Fig. 10.10(b)], where the wake vortices are convected quickly away from the rotor. This is because of a small region of upwash velocity at the leading edge of the disk and a strong longitudinal inflow gradient, which has its source in the skewness of the wake (see also the discussion in Section 3.5.2).

10.4.2 *Blade–Vortex Interactions (BVIs)*

It will be apparent from the forgoing discussion that one of the distinctive features of rotor wakes in forward flight is the preponderance of potentially close interactions of blades and tip vortices, which are called blade–vortex interactions or BVIs. When viewed from above [i.e., see Fig. 10.8(a)] the trajectories formed by the tip vortices trace out closely epicycloidal forms. If the wake is assumed to be undistorted in the x–y (TPP) plane (a justifiable assumption near the rotor disk based on the example shown in Fig. 10.8), then the tip vortex trajectories are described geometrically by the parametric equations

$$\frac{x_{\text{tip}}}{R} = x'_{\text{tip}} = \cos(\psi_b - \psi_w) + \mu\psi_w, \tag{10.1}$$

$$\frac{y_{\text{tip}}}{R} = y'_{\text{tip}} = \sin(\psi_b - \psi_w), \tag{10.2}$$

where ψ_b is the position of the blade when the vortex was formed, and ψ_w is the age of the vortex element relative to that blade (see Fig. 10.11). It has been assumed that no wake contraction occurs in the radial dimension.

Examples of the wake topology when viewed from above the rotor are shown for three advance ratios in Fig. 10.12, with results for a two-bladed rotor being shown for simplicity. It will be apparent that BVIs can occur at many different locations over the rotor disk and also with different orientations between the blade axis and the vortex axis. If BVI occurs on the advancing side of the rotor disk, the blade and vortex axis can be nearly parallel. It has been described in Chapter 8 how these conditions promote (at least locally) highly

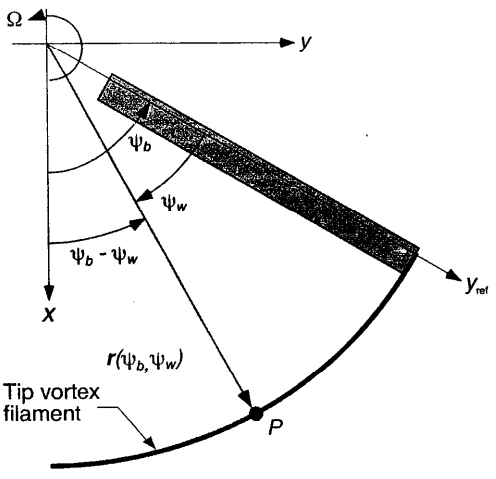

Figure 10.11 Definition of the position of an element in the vortex wake.

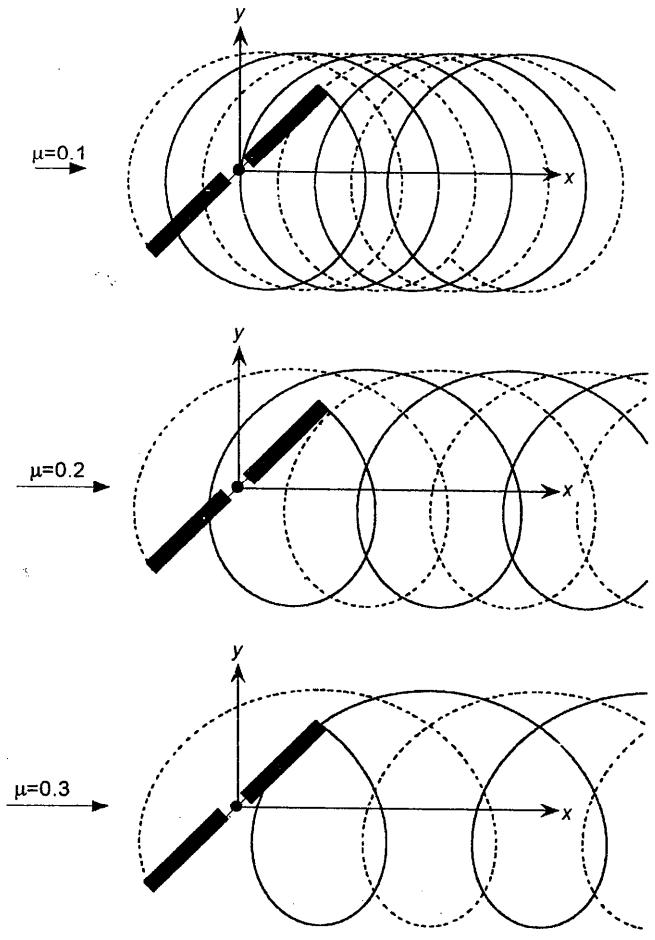

Figure 10.12 Plan view of the tip vortex trajectories as trailed from a two-bladed rotor in forward flight at different advance ratios.

unsteady airloads on the blades, which can also be accompanied by significant obtrusive noise with strongly focused directivity – see Schmitz (1991).

For a rotor with N_b blades, and assuming an undistorted wake, the locus of all the potential BVIs can be determined if the equations

$$r\cos(\psi_b - \Delta) = \cos(\psi_b - \psi_w) + \mu\psi_w \tag{10.3}$$

and

$$r\sin(\psi_b - \Delta) = \sin(\psi_b - \psi_w) \tag{10.4}$$

are simultaneously satisfied for r (on the blade) and ψ_b, where $\Delta = 2\pi(i-1)/N_b$, $i = 1, 2, \ldots, N_b$ with N_b as the number of blades and ψ_w is the age of the vortex (wake age) relative to the blade from which it originated. It can be shown that for the blade positions

$$\psi_b = \sin^{-1}\left[\frac{-\cos\Delta\sin(\psi_w - \Delta) \pm \sin\Delta\sqrt{\mu^2\psi_w^2 - \sin^2(\psi_w - \Delta)}}{\mu\psi_w}\right] \tag{10.5}$$

and note that this is a multi-valued solution. We are only interested in the real parts (i.e., $\mu^2\psi_w^2 - \sin^2(\psi_w - \Delta) > 0$) with particular attention to the signs of the angle and multiple values of the arcsine. The corresponding value of r is obtained from

$$r = \frac{\sin(\psi_b - \psi_w)}{\sin(\psi_b - \Delta)}, \tag{10.6}$$

where we are only interested in the disk itself ($r \leq 1$). Finally, the x, y locations of the BVI intersection points over the disk are obtained from

$$x = r\cos(\psi_b - \Delta) \quad \text{and} \quad y = r\sin(\psi_b - \Delta). \tag{10.7}$$

By solving for ψ_b and r for numerical values of $\psi_w > 0$, we can determine all the locations of the potential BVI intersection points. (See also Questions 10.3 and 10.4.)

Figure 10.13 shows these locations for a two-bladed rotor ($N_b = 2$) operating in forward flight at four advance ratios. Again, it should be appreciated that this calculation assumes that all the vortices lie in the TPP. For any one flight condition they do not, but these figures give an indication of all the possible intersection locations. Notice that the largest number of potential BVIs occur in low speed forward flight. As forward speed increases, their number is reduced considerably. However, even though the number of potential interactions may decrease, it is their intensity and also the trace Mach number of the interaction that determines the potential noise and directivity of noise associated with a BVI – see Lowson (1996) and Leishman (1999), as well as Section 8.19.

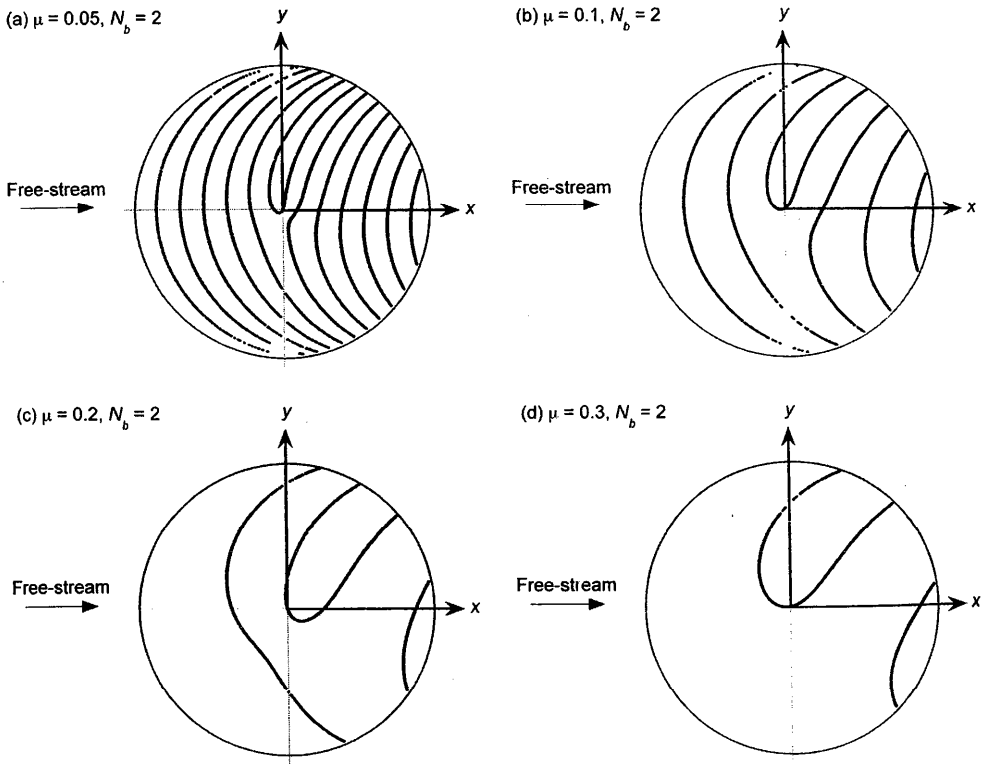

Figure 10.13 Locus of all possible BVIs over the rotor disk for a two-bladed rotor in forward flight at different advance ratios.

Despite its importance to helicopter noise and vibration, clear experimental studies of the parallel BVI problem are relatively rare. Good, albeit idealized, quantitative measurements of blade vortex interactions and collisions are described by Horner et al. (1994) and Kitaplioglu & Caradonna (1994). Contributions to visualizing the problem have been achieved with the use of smoke [see Mercker & Pengel (1992) and Lorber et al. (1994)] and using strobed shadowgraphy [see Swanson (1993)].

The other type of BVI occurs when the blade and vortex axes are almost perpendicular, which is mainly over the front and rear of the disk. While the former type tends to produce the largest unsteady airloads and noise generation, the latter tends to result in more highly 3-D airloads and broadband noise – see Schmitz (1991). Figure 10.14 shows a sequence of flow visualization images obtained with wide-field shadowgraphy, which detail the blades encountering a perpendicular type of BVI over the leading edge of the rotor disk during low-speed forward flight. We see that as the older wake vortices move downstream (to the right) they move up and over the top of the following blades (see also Fig. 10.13). A disturbance is produced on the older vortices as following blades pass underneath. After the blade passes, the tip vortices return to their original undisturbed shape. For progressively greater wake ages, the vortices are convected further downstream and the blade intersects and severs the vortex filament. This can result in an instability or transition bifurcation that is characterized by a large growth in the viscous core dimensions. This is known as "vortex bursting," although the proper explanation of this phenomenon perhaps remains somewhat controversial. However, an increase in the effective core size and/or diffusion rate of the tip vortex produced by bursting is inevitable and will affect the intensity of other potential interactions with blades. This is one type of rotor wake problem that is poorly understood and difficult to model.

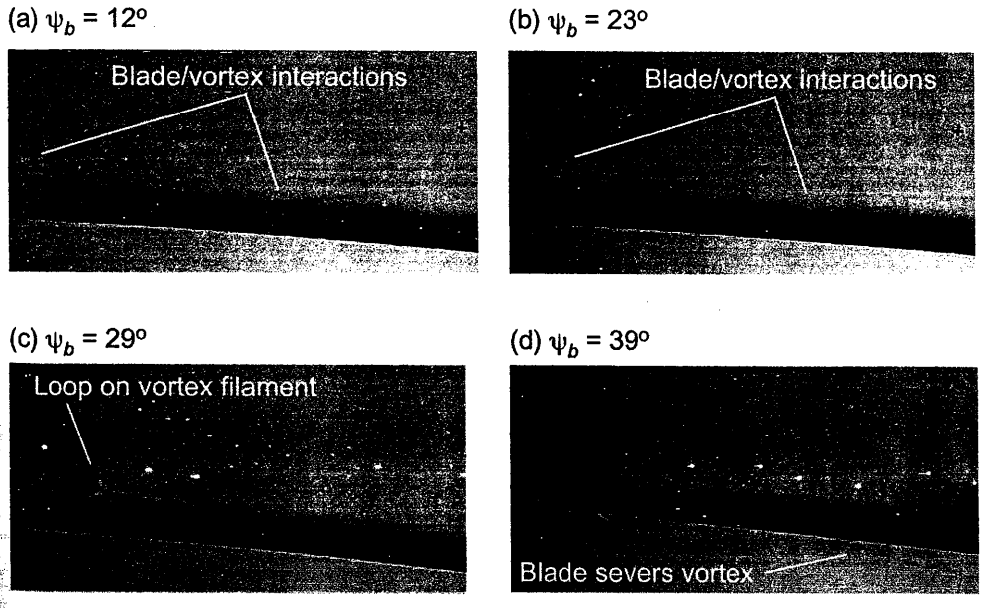

Figure 10.14 A series of shadowgraph flow visualization images showing perpendicular BVIs over the front of the rotor disk in forward flight. (a) $\psi_b = 12°$. (b) $\psi_b = 23°$. (c) $\psi_b = 29°$. (d) $\psi_b = 39°$. Free-stream flow is from left to right. Source: University of Maryland.

10.5 Other Characteristics of Rotor Wakes

10.5.1 *Periodicity versus Aperiodicity*

In most cases, the rotor wake is deterministic, and the tip vortices generated by each blade will follow smooth curved and almost helical or epicycloidal paths. Also, under ideal circumstances, their spatial locations relative to the rotor will be periodic at the rotor rotational frequency. However, various types of aperiodic behavior of rotor wakes have been noticed in experiments. Aperiodicity can be defined as the random variations in the spatial locations of the vortex filaments from a mean position at a given wake age. In fixed-wing terminology, this phenomena is referred to as vortex wandering or meandering – see Devenport et al. (1996) and Leishman (1998). If aperiodicity occurs above some threshold, then measurements based on the assumption of a periodic flow will be biased because the small random displacements of the vortices essentially average out the flow field properties at a fixed measurement point.

For helicopter rotors, the available experimental evidence suggests that wake aperiodicity is a characteristic that is, in part, related to the nature of the rotor operating state; in hover the phenomenon is more likely to show than in forward flight. For example, measurements of the tip vortex locations in hover that are reconstructed on the basis of a series of images of the wake made at different wake ages may take the appearance of significant scatter, or even two possible geometries. Such a behavior can be traced to aperiodic flow effects and has been observed in several rotor experiments, including those of Landgrebe (1972), Norman & Light (1987), Bagai & Leishman (1992b), and Leishman (1998). Most of the available experimental evidence with rotors shows that aperiodicity is pronounced only at older wake ages (older than one or two complete rotor revolutions), at low thrust coefficients (where the slipstream convection velocities are low and the tip vortices remain close to the rotor plane), or after the first blade passage. At a minimum, appropriate allowance can be made when quoting measurement uncertainties and when comparing with computations of the wake topology. From a purely scientific perspective, the challenge is to understand whether the observed aperiodic behavior of rotor wakes is an inherent physical characteristic or if their source lies in small external flow disturbances that are produced within the ground test facility. However, the fact that rotor wakes disturbances occur under very controlled laboratory conditions suggests that they would also be expected to occur under the normal turbulence levels found in the atmosphere, especially closer to the ground.

10.5.2 *Vortex Perturbations and Instabilities*

Besides the more random types of aperiodicity found in rotor wakes, other deterministic types of perturbations and instabilities of the tip vortices have been observed. One common type is the smooth sinuous wave type observed by Landgrebe (1971), Sullivan (1973), and others and analyzed theoretically by Levy & Forsdyke (1928), Widnall (1972), Gupta & Loewy (1973, 1974), and Bhagwat & Leishman (2000b). An example of a short sinuous (or Kelvin) wave is shown in Fig. 10.15(a). These types of disturbances are often neutrally stable, but can become pronounced in amplitude at older wake ages. Long wave disturbances or instabilities can sometimes result in pairing and looping of adjacent vortex filaments and can often be a source of some aperiodicity in the flow – see the experiments by Tangler et al. (1973) and Martin et al. (1999) and analysis by Gupta & Loewy (1973, 1974) and Bhagwat & Leishman (2000b). In some cases, vortex pairing may lead to a complicated aperiodic wake formation but at a subharmonic of the rotor frequency – see Leishman & Bagai (1998). Based on various experimental observations, the onset of vortex

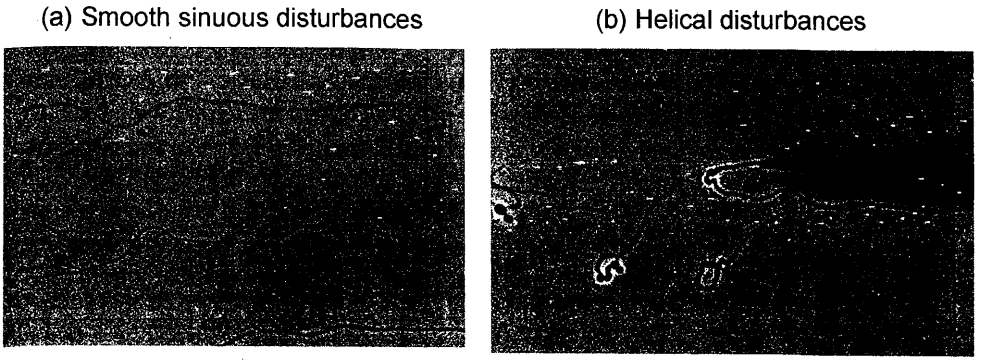

Figure 10.15 Shadowgraphs showing two types of disturbances seen on rotor tip vortices. (a) The smooth or sinuous form. (b) The "cork-screw" or helical form. Source: University of Maryland.

disturbances and wake instabilities is affected by the number of blades, rotor thrust (disk loading), and overall operating conditions. Forward flight experiments with helicopter rotors in wind tunnels have shown that the tip vortices appear generally free from the regular sinuous perturbations so often noted in hovering rotor wakes, although such effects cannot be discounted unilaterally.

Another type of perturbation sometimes found in rotor wakes, both in hover and forward flight, is referred to as the "cork-screw" or helical type, with examples being shown in Figs. 10.15(b) and 10.16. Here, the vortex filament tightly twists around on itself forming a very pronounced helix. These helical type perturbations appear to be common in the wakes of highly loaded propellers or tilt-rotors [see Norman & Light (1987)] rather than helicopter rotors, but they have been observed on both. In some cases, the disturbance travels along the vortex filament. In other cases, it is damped out, and the vortex returns to its regular

Figure 10.16 Shadowgraph showing the bursting of a tip vortex after an encounter with a blade. View from behind the blade. Source: University of Maryland & Boeing Helicopters.

(periodic) form. Occasionally, the disturbance may cause the vortex to become unstable, and it may break down or burst. An example of this latter phenomenon is shown in Fig. 10.16, where vortex bursting clearly originates from the formation of a helical disturbance formed on the vortex just downstream of the blade.

10.6 Detailed Structure of the Tip Vortices

The roll-up of the tip vortex in terms of its strength, velocity distribution, and location defines the initial conditions for the subsequent behavior of the rotor wake. Tip vortex formation is a complex problem involving high velocities with shear, flow separation, pressure equalization, and turbulence production. On most helicopters, which will have rectangular or mildly tapered blade tips, experimental evidence shows that a single vortex is fully formed at the trailing edge of the blade tip, as in Fig. 10.17, which is a shadowgraph of the flow near the tip of the blade. The tip region is enveloped with a region of high vorticity, which rolls up quickly into a dominant vortex. Because rotor blades have very large pressure differences over their tip region, the resulting tip vortices have high circulation, high swirl velocities, and relatively small viscous cores.

Most vortex wake models used for rotor loads, performance, and acoustics will have some kind of semi-empirical representation of the tip vortex characteristics. Because tip vortex properties are not as well documented as they should be for helicopter rotors, the required parameters to formulate a suitable model of the vortex are often interpreted or extrapolated from those measured in fixed-wing studies – see Rorke et al. (1972) and Rorke & Moffitt (1977). However, because of the sustained proximity of the blades to the tip vortices, the mutual interactions between the vortices, and the stretching of the filaments as they are convected in the nonuniform flow, there is questionable validity in simply extrapolating fixed-wing results to the rotor case. Another complication is that the blade tip shape is known to affect the strength and location of the blade tip vortex as it is trailed off into the wake, and these effects are even less poorly understood. For some tip shapes, multiple vortices may be produced, although one of these is usually stronger and tends to dominate the flow.

Even for rectangular tips, the overall roll-up of the tip vortex in terms of its strength and initial location behind the blade is found to be difficult to predict. Based on classical centroid of vorticity approaches, which are used in some forms of rotor analysis, the computed vortex

Figure 10.17 Roll-up of the tip vortex occurs rapidly and is fully formed just downstream of the trailing edge of the blade. Source: University of Maryland.

release locations generally tend to be predicted radially much further inward toward the hub than are observed from flow visualization experiments. Using fundamental vortex dynamics, Rule & Bliss (1998) have highlighted the complexity of modeling the problem. Modern first-principles finite-difference methods, such as those discussed by McCroskey (1995) and Tang & Baeder (1999), have achieved better success in predicting the exact point of origination of the tip vortex. However, for many methods, numerical diffusion and dispersion tends to produce significant errors in the subsequent vortex behavior, overpredicting the growth of the viscous core to the point that these methods cannot yet be used to confidently model the rotor wake and its induced velocity field – see Section 14.10.2.

10.6.1 *Velocity Field*

Understanding the velocity field near the tip vortex, the vortex strength (circulation), viscous core radius, as well as how these properties change as the vortex ages, is still a goal of ongoing research. The earliest reported measurements of helicopter rotor tip vortices were performed using hot-wire anemometry (HWA) – see Simons et al. (1966), Cook (1972), Caradonna & Tung (1981), and Tung et al. (1983). However, HWA is limited by spatial resolution, and probe proximity concerns make measurements difficult at early wake ages near the blade tips. Laser Doppler velocimetry (LDV) is an attractive alternative because of the nonintrusive nature of the measurements (apart from seeding) and can alleviate many limitations posed by HWA, such as the physical size of the probe relative to the vortex dimensions, probe interference effects, and wire attrition. However, amongst the main constraints of LDV are optical access, the need to uniformly seed the flow, the need for good periodicity of the flow to allow statistical phase averaging, and a requirement for coincident measurements on all three-components of velocity.

Scully & Sullivan (1972), Sullivan (1973), and Landgrebe & Johnson (1974) have reported some of the first uses of LDV systems to study rotor flows. Thomson et al. (1988) and Mahalingam & Komerath (1998) have made detailed LDV measurements of rotor tip vortices using a 1-D LDV system. A 2-D LDV system was developed by Biggers & Orloff (1975) to investigate some aspects of the wake generated by a two-bladed rotor – see also Biggers et al. (1977a,b). Hoad (1983) has developed a 2-D LDV system with large stand-off distances – see also Elliott et al. (1988) and Althoff et al. (1988). However, 1-D and 2-D LDV systems tend to suffer from reduced spatial resolution because of the elongated measurement volumes, especially with large stand-off distances, and are not always well suited for measuring the small spatial scales and steep velocity gradients found inside vortices. Three-dimensional phase-resolved LDV measurements in rotor wakes, however, have not been possible until recently – see Seelhorst et al. (1994, 1996), McAlister et al. (1995), Leishman et al. (1995), McAlister (1996), Han et al. (1997), and Martin et al. (2001). 3-D systems offer much better spatial resolution if aligned accurately and especially when they are operated in coincident mode, that is, the three component measurements are required to be all statistically correlated.

Representative LDV measurements of the tip vortex induced velocity field are shown in Fig. 10.18 for several wake ages (ψ_w). The tangential component of velocity has been nondimensionalized by the rotor tip speed, and the distance from the rotational axis has been nondimensionalized by the rotor radius, R. As described previously in Section 2.2.1, the blade tip vortices lie on the boundary of a contracting jet like wake, and the measurements shown in Fig. 10.18 were made on this wake boundary. Inside the wake boundary, note that the slipstream velocity is approximately constant. For increasing ψ_w, the tip vortex convects downward below the rotor and radially inward, and so the velocity signatures shown in

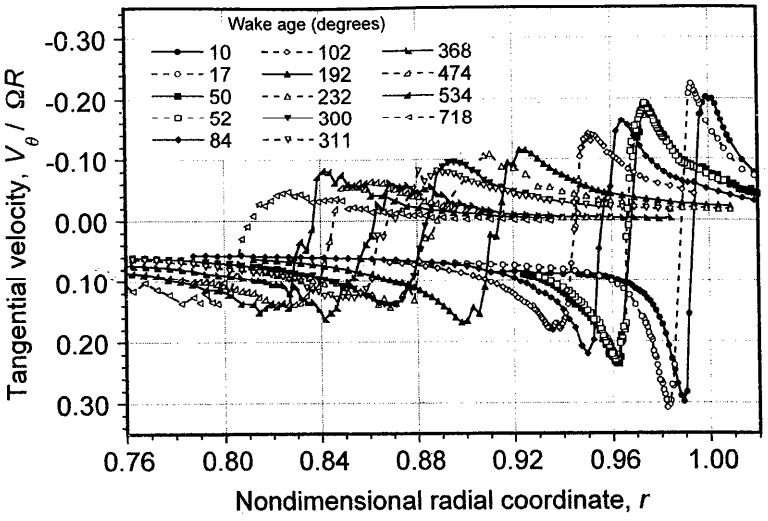

Figure 10.18 Representative measurements showing the distribution of tangential velocity surrounding a tip vortex at various wake ages. Source: Leishman et al. (1995) and the University of Maryland.

Fig. 10.18 move to the left on the graphs. The results show the basic characteristics of viscous diffusion: vorticity contained in the vortex core diffuses radially outward with time, thereby reducing the peak swirl velocities. The distance between the two velocity peaks shown in Fig. 10.18 can be considered the viscous core diameter.

10.6.2 *Models for the Tip Vortex*

With this general picture of the tip vortex induced velocity field in mind, a model of the tip vortex can now be hypothesized. Tip vortex models used in rotor wake simulations are typically specified in terms of a 2-D tangential (swirl) velocity profile. The other velocity components (the axial and radial) are small and are usually neglected in most applications. This, however, may not be a justifiable assumption at young wake ages. A schematic of a typical distribution of swirl velocity is shown in Fig. 10.19. The inner part of the vortex (the core region) rotates almost as a solid body, whereas the outer part behaves almost as a potential flow. The core radius, r_c, is defined as the radial location where V_θ is a maximum (i.e., at the core radius $\bar{r} = r/r_c = 1$). This boundary demarcates the inner (almost purely rotational) flow field from the outer (potential) flow.

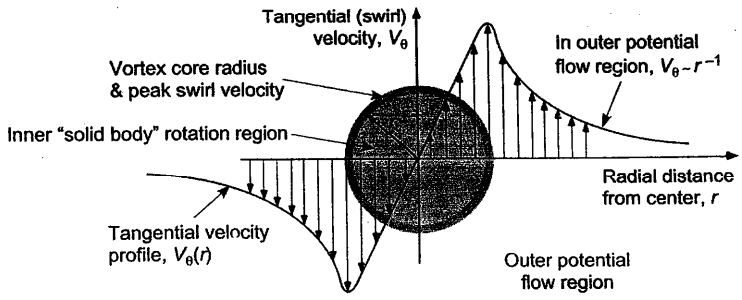

Figure 10.19 Idealization of the tangential (swirl) velocity inside a tip vortex.

The simplest model of a vortex with a finite core is the Rankine vortex [see Lamb (1932)], where the swirl velocity is given by

$$V_\theta(\bar{r}) = \begin{cases} \left(\dfrac{\Gamma_v}{2\pi r_c}\right)\bar{r}, & 0 \le \bar{r} \le 1, \\ \left(\dfrac{\Gamma_v}{2\pi r_c}\right)\dfrac{1}{\bar{r}}, & \bar{r} > 1. \end{cases} \tag{10.8}$$

The core is modeled as a solid body rotation, and the velocity outside decreases hyperbolically with distance as for a potential vortex. Although the Rankine vortex exhibits the key features of a viscous vortex, the swirl velocity, the vorticity, and the circulation produce unrealistically higher values than are observed in practice. An alternative vortex model is given by Oseen (1911) and Lamb (1932), who solved a simplified form of the Navier–Stokes equations. The Lamb–Oseen model for the swirl velocity is

$$V_\theta(\bar{r}) = \frac{\Gamma_v}{2\pi r_c \bar{r}}\left(1 - e^{-\alpha \bar{r}^2}\right), \tag{10.9}$$

where $\alpha = 1.25643$. This solution is valid only for a single viscous vortex in an unbounded incompressible, laminar flow. Newman (1959) has also derived exponential solutions for the three components of velocity in the vortex core based on a simplified Navier–Stokes formulation. The result for the swirl velocity is the same as that for the Lamb–Oseen model, but Newman shows that the axial velocity in the vortex is

$$V_z = -\frac{A}{z} e^{-\alpha \bar{r}^2}, \tag{10.10}$$

where A is a constant. If these are lift generated vortices, then A can be related to the drag on the generating lifting surface. These exponential velocity profiles have been shown to give good correlations with tip vortex measurements generated by fixed wings – see, for example, Dosanjh et al. (1962).

A more general series of desingularized velocity profiles for vortices with continuous distributions of the flow quantities is given by Vatistas et al. (1991). The tangential velocity in the vortex can be expressed as

$$V_\theta(\bar{r}) = \left(\frac{\Gamma_v}{2\pi r_c}\right)\frac{\bar{r}}{(1 + \bar{r}^{2n})^{\frac{1}{n}}}, \tag{10.11}$$

where n is an integer. Using Eq. 10.11, the swirl velocity profiles for two specific vortex models can be rewritten in terms of the nondimensional radius, $\bar{r}$. For the $n = 1$ vortex, which is commonly known in helicopter work as the "Scully vortex" after Scully (1975), then

$$V_\theta(\bar{r}) = \left(\frac{\Gamma_v}{2\pi r_c}\right)\frac{\bar{r}}{(1 + \bar{r}^2)} \tag{10.12}$$

and for the $n = 2$ vortex

$$V_\theta(\bar{r}) = \left(\frac{\Gamma_v}{2\pi r_c}\right)\frac{\bar{r}}{\sqrt{1 + \bar{r}^4}}. \tag{10.13}$$

Only the $n = 1$ and $n = 2$ cases are really physically meaningful. But, notice that as $n \to \infty$, the Rankine vortex in Eq. 10.8 is obtained. A summary of the various tangential velocity models is plotted in Fig. 10.20. Furthermore, it is interesting to note that the "Scully model" is, in fact, an approximation to the Lamb vortex. Using a vortex length scale of $\bar{r}_c = \sqrt{4\nu t}$,

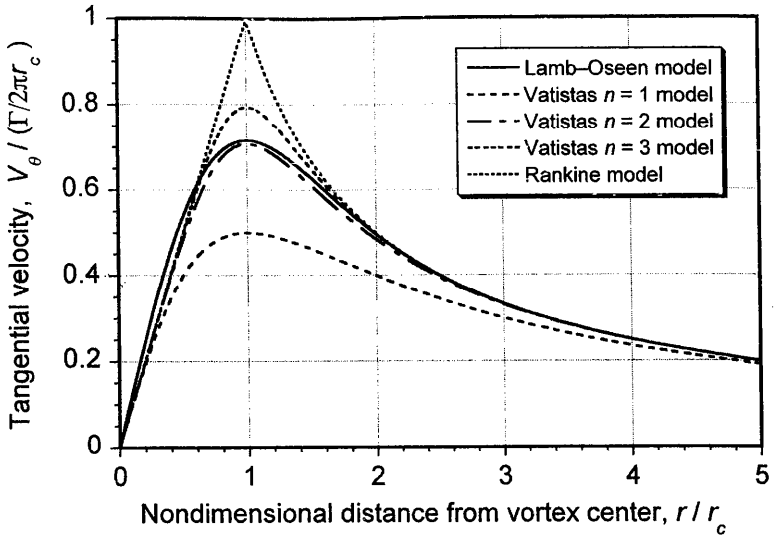

Figure 10.20 Summary of 2-D vortex tangential (swirl) velocity profiles.

the Lamb vortex model (Eq. 10.9) can be written as a function of nondimensional radial distance $\tilde{r} = r/\tilde{r}_c$ as

$$V_\theta(\tilde{r}) = \frac{\Gamma}{2\pi\tilde{r}_c\tilde{r}}\left(1 - e^{-\tilde{r}^2}\right). \tag{10.14}$$

Using a series expansion for the exponential term and ignoring higher order terms, it can be shown that

$$V_\theta(\tilde{r}) = \frac{\Gamma}{2\pi\tilde{r}_c\tilde{r}}\left(1 - \frac{1}{1 + \tilde{r}^2 + \dfrac{\tilde{r}^4}{2} + \cdots}\right) \approx \frac{\Gamma}{2\pi\tilde{r}_c}\left(\frac{\tilde{r}}{1+\tilde{r}^2}\right)$$
$$= \frac{\Gamma}{2\pi}\left(\frac{r}{r^2 + \tilde{r}_c^2}\right) \quad \text{for small } \tilde{r}. \tag{10.15}$$

Because of the assumption of a columnar vortex, the axial and radial components derived by Vatistas et al. (1991) do not strictly apply to trailed vortices. However, a general result for the axial (and radial) components of the velocity for trailed vortices can also be deduced starting from the assumption of Eq. 10.11 and the appropriate form of the governing Navier–Stokes equations applied to a trailing vortex.[3] In the first instance, it is reasonable to assume that the induced velocities are dependent only on r and z (i.e., the vortex is assumed to be axisymmetric). The governing Navier–Stokes equations in cylindrical coordinates for incompressible flow are written as

continuity:

$$\frac{1}{r}\frac{\partial}{\partial r}(rV_r) + \frac{\partial V_z}{\partial z} = 0, \tag{10.16}$$

[3] Dr. Mahendra Bhagwat is responsible for this analysis.

r momentum:

$$V_r\frac{\partial V_r}{\partial r}+V_\infty\frac{\partial V_r}{\partial z}+V_z\frac{\partial V_r}{\partial z}-\frac{V_\theta^2}{r}=-\frac{1}{\rho}\frac{\partial p}{\partial r}+\nu\left[\nabla^2 V_r-\frac{V_r}{r^2}\right], \tag{10.17}$$

θ momentum:

$$V_r\frac{\partial V_\theta}{\partial r}+V_\infty\frac{\partial V_\theta}{\partial z}+V_z\frac{\partial V_\theta}{\partial z}+\frac{V_rV_\theta}{r}=\nu\left[\nabla^2 V_\theta-\frac{V_\theta}{r^2}\right], \tag{10.18}$$

z momentum:

$$V_r\frac{\partial V_z}{\partial r}+V_\infty\frac{\partial V_z}{\partial z}+V_z\frac{\partial V_z}{\partial z}=-\frac{1}{\rho}\frac{\partial p}{\partial z}+\nu\left[\nabla^2 V_z\right]. \tag{10.19}$$

These equations can now be nondimensionalized, with velocities being nondimensionalized by blade tip speed, distances by blade chord, and pressure by the tip dynamic pressure. An ordering scheme can then be employed to compare the magnitudes of the various nondimensional terms. The swirl and axial velocities induced by the tip vortex are known from experiments to be small compared to the free-stream velocity; that is, $\bar{V}_\theta$ and $\bar{V}_z$ are $O(\epsilon)$, where the overbar denotes a nondimensional quantity. Typically the tip vortex core radius is found to be of the order of the airfoil thickness. As shown previously, the tip induces significant velocities for several chord lengths downstream of the generating surface. This implies that if $\bar{z}$ is $O(1)$ then $\bar{r}$ is $O(\epsilon)$. The continuity equation implies that the radial velocity, $\bar{V}_r$, is much smaller and of order $O(\epsilon^2)$. This is also consistent with the observation that the radial velocities induced by the tip vortices are small – see Dosanjh et al. (1962). The radial momentum equation (Eq. 10.17) indicates that the pressure, $\bar{p}$, is $O(\epsilon^2)$. Typically, for a helicopter rotor, the chord Reynolds number at the blade tip is approximately 10^7. Even in wind tunnel experiments with scaled models, the Reynolds numbers are always greater than 10^4. Therefore, Re can be assumed to be $O\left(1/\epsilon^4\right)$.

The conservation laws can now be rewritten with the order of magnitudes of each term being indicated below each term.[4]

continuity:

$$\underset{\epsilon}{\frac{1}{r}\frac{\partial}{\partial r}(rV_r)}+\underset{\epsilon}{\frac{\partial V_z}{\partial z}}=0, \tag{10.20}$$

r momentum:

$$\underset{\epsilon^3}{V_r\frac{\partial V_r}{\partial r}}+\underset{\epsilon^2}{\frac{\partial V_r}{\partial z}}+\underset{\epsilon^3}{V_z\frac{\partial V_r}{\partial z}}-\underset{\epsilon}{\frac{V_\theta^2}{r}}=\underset{\epsilon}{-\frac{\partial p}{\partial r}}+\underset{\epsilon^4}{\frac{1}{Re}\left[\nabla^2 V_r-\frac{V_r}{r^2}\right]}, \tag{10.21}$$

θ momentum:

$$\underset{\epsilon^2}{V_r\frac{\partial V_\theta}{\partial r}}+\underset{\epsilon}{\frac{\partial V_\theta}{\partial z}}+\underset{\epsilon^2}{V_z\frac{\partial V_\theta}{\partial z}}+\underset{\epsilon^2}{\frac{V_rV_\theta}{r}}=\underset{\epsilon^3}{\frac{1}{Re}\left[\nabla^2 V_\theta-\frac{V_\theta}{r^2}\right]}, \tag{10.22}$$

[4] Notice that all the variables are now nondimensional, but the overbar has been omitted for simplicity.

z momentum:

$$V_r\frac{\partial V_z}{\partial r} + \frac{\partial V_z}{\partial z} + V_z\frac{\partial V_z}{\partial z} = -\frac{\partial p}{\partial z} + \frac{1}{Re}\left[\nabla^2 V_z\right]. \tag{10.23}$$
$$\epsilon^2 \qquad \epsilon \qquad \epsilon^2 \qquad \epsilon^2 \qquad \epsilon^3$$

It is further assumed that because ϵ is small, higher order terms in ϵ can be neglected. Therefore, the governing equations simplify to

$$\frac{1}{r}\frac{\partial}{\partial r}(rV_r) + \frac{\partial V_z}{\partial z} = 0, \tag{10.24}$$

$$\frac{\partial p}{\partial r} - \frac{V_\theta^2}{r} = 0 \qquad [O(\epsilon^2)], \tag{10.25}$$

$$\frac{\partial V_\theta}{\partial z} = 0 \qquad [O(\epsilon^2)], \tag{10.26}$$

$$\frac{\partial V_z}{\partial z} = 0 \qquad [O(\epsilon^2)]. \tag{10.27}$$

It should be noted that the θ- and z-momentum equations indicate that the swirl and axial velocities have small gradients along the z axis, and are not independent of z. This is consistent with various experimental observations that viscous diffusion is a gradual process and, therefore, the velocity gradients along the time-like z axis are small. It is also observed that the peak axial velocities decrease rapidly at early wake ages, whereas the peak swirl velocities decrease more gradually ($\sim\sqrt{z}$) (i.e., the swirl velocity gradients are small compared to the axial velocity gradients). Using this information, the θ- and z-momentum equations can be written as

$$\frac{\partial V_\theta}{\partial z} = 0 \ [O(\epsilon^3)] \quad \text{and} \quad \frac{\partial V_z}{\partial z} = 0 \quad [O(\epsilon^2)], \tag{10.28}$$

and the $O(\epsilon^2)$ terms in the θ-momentum equation cancel each other, that is,

$$V_r\frac{\partial V_\theta}{\partial r} + V_z\frac{\partial V_\theta}{\partial z} + \frac{V_r V_\theta}{r} = 0. \tag{10.29}$$

The required boundary conditions given by Newman (1959) can be obtained by assuming that the vortex is generated as a "free" vortex, that is, a potential vortex of strength Γ_v at $z = 0$, and it diffuses until at large distances the vortex induced velocities become zero. These boundary conditions can be formalized as

1. At $z = 0$, $V_\theta = \Gamma_v/2\pi r$ and V_z, $V_r = 0$. Note that there is a singularity at $r = 0$.
2. For $z > 0$, V_θ, V_z, $V_r \to 0$ for large r.
3. As $z \to \infty$, V_θ, V_z, $V_r \to 0$ for all r.

The governing equations have now been reduced to only two equations (i.e., Eqs. 10.24 and 10.29) but are in terms of three components of velocity, for which there can exist no unique solution. However, with the assumption of the Vatistas swirl velocity model in Eq. 10.11, the axial and radial velocities can be found using Eqs. 10.24 and 10.29. These

components are found to be

$$V_z = -\frac{A}{z}\left\{1 - \frac{r^2}{\left(r_c^{2n} + r^{2n}\right)^{1/n}}\right\} \quad \text{and}$$

$$V_r = -\frac{Ar}{2z^2}\left\{1 - \frac{r^2}{\left(r_c^{2n} + r^{2n}\right)^{1/n}}\right\}, \tag{10.30}$$

where A is a constant related to drag, as mentioned previously.

The results from the above analysis of the vortex problem have been compared with some of the experimental measurements shown previously in Fig. 10.18. The time-averaged convection velocity of the tip vortex through the rotor wake has been removed, which puts the measurements into a frame of reference moving with the vortex core. Figure 10.21(a) shows the measured swirl velocities nondimensionalized with respect to the peak velocity and the radial distance with the estimated core radius. The measurements show a good correlation with the Lamb–Oseen and $n = 2$ swirl velocity models, and they also confirm

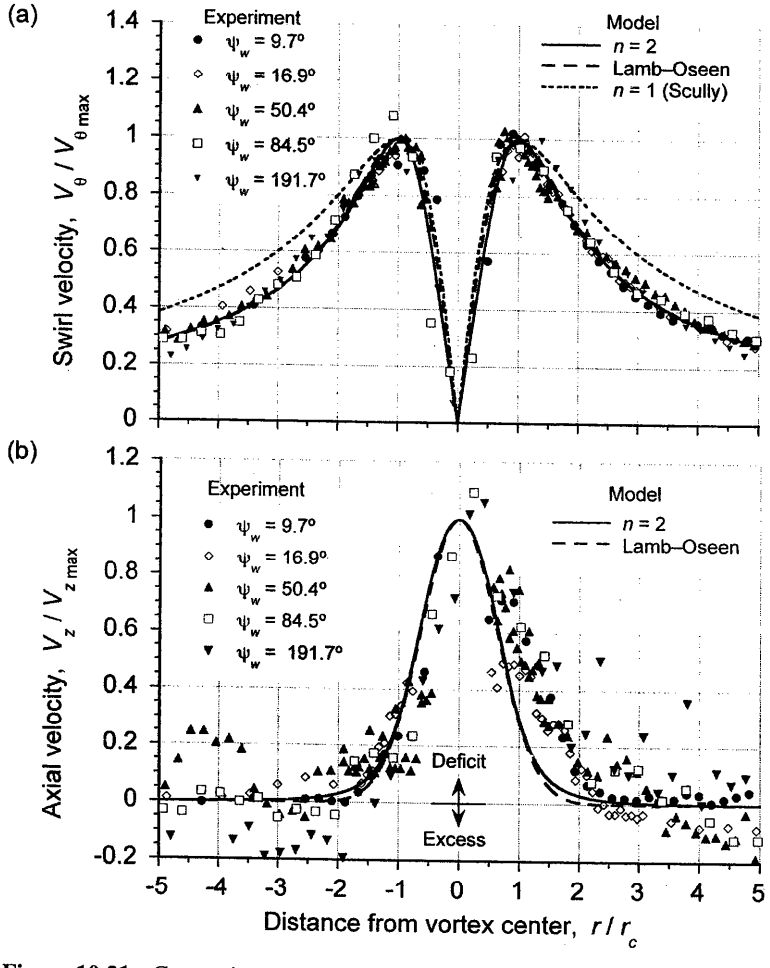

Figure 10.21 Comparison of vortex model with measurements of the velocity components inside the vortex. (a) Tangential (swirl) velocity. (b) Axial velocity.

the self-similar nature of the velocity field surrounding the tip vortex. Some deviations may be attributed to the presence of extraneous wake vorticity from the inboard part of the blade and other blades that are present in the measurement grid. The commonly used $n = 1$ or Scully (1975) vortex model seems to be a less accurate descriptor of the velocity field, at least in this case. Figure 10.21(b) shows corresponding comparisons for the nondimensional axial velocities. Again, the Lamb–Oseen and $n = 2$ model are found to give good agreement with the measured velocities. Like the swirl velocity, the axial velocity profiles also exhibit a self-similarity, though perhaps not as strongly. The fluctuations in the measured axial velocities are probably a result of small asymmetries in the tip vortices. However, the generally good agreement with the measurements suggests the validity of the assumptions inherent in this very basic analysis of the trailed vortex problem.

10.6.3 *Vorticity Diffusion Effects and Vortex Core Growth*

The vortex core dimension is an important parameter that can be used to help define the structure and evolution of tip vortices. Half of the distance between the two velocity peaks shown in Fig. 10.18 can be considered as the average (nominal) viscous core radius. This region is where most (but not all) of the vorticity in the tip vortex is concentrated. This core quantity is plotted as a fraction of blade chord, c, in Fig. 10.22 as a function of wake age, ψ_w. It is apparent that there is a fairly rapid but asymptotic-like growth in the core. The blade passage event at $\psi_b = \psi_w = 2\pi/N_b$ temporarily alters the growth trend, and a slight decrease in core size is usually observed. This is fundamentally a vortex stretching problem. This stretching effect is more evident for a two-bladed rotor (or for a rotor with higher number of blades) because the tip vortex does not have time to convect very far through the flow and is subsequently much closer to the following blade. After the blade passage, the viscous core continues to grow with a similar rate. The difficulties in measuring the vortex properities at older wake ages is compounded by the tendency for the flow to become aperiodic (see Section 10.5.1).

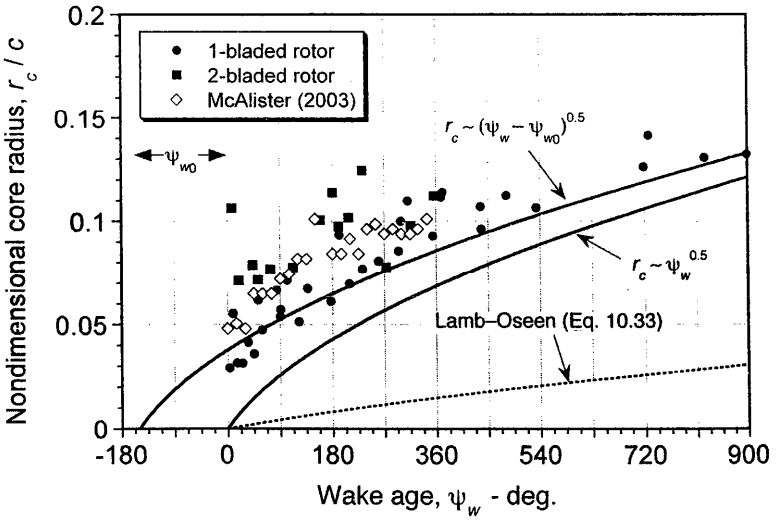

Figure 10.22 Example showing measured growth of the viscous core radius of tip vortices trailed from rotor blades versus wake age.

A simple quantitative model of the growth in vortex core radius with time can be based on Lamb's result for laminar flows – see Lamb (1932), Chigier & Corsiglia (1971), and Ogawa (1993). This result shows that without external velocity gradients (which can cause stretching and so will affect the core development) the core radius varies with the square root of age according to $r_c(t) = \sqrt{4\alpha\nu t}$. Starting from the Lamb–Oseen swirl velocity profile model in Eq. 10.9 then a change of variable to $x = r(4\nu t)^{-1/2}$ gives the swirl velocity in the vortex according to

$$V_\theta(x) = \frac{\Gamma}{2\pi x\sqrt{4\nu t}}\left[1 - \exp\left(-x^2\right)\right]. \tag{10.31}$$

Now, by definition, the core radius, r_c corresponds to the value of r when V_θ reaches a maximum, so differentiating the latter equation with respect to x gives

$$\begin{aligned}\frac{dV_\theta}{dx} &= \frac{\Gamma}{2\pi\sqrt{4\nu t}}\left[-\frac{1}{x^2} + \frac{1}{x^2}\exp(-x^2) + 2\exp(-x^2)\right] \\ &= \frac{\Gamma}{2\pi x^2\sqrt{4\nu t}}\left[\left(1 + 2x^2\right)\exp(-x^2) - 1\right],\end{aligned} \tag{10.32}$$

which must be zero for a maximum. This gives the solution $x = 1.1209$, and so the core radius grows according to the relation

$$r_c(t) = 1.1209\sqrt{4\nu t} = \sqrt{4\alpha\nu t}, \tag{10.33}$$

where $\alpha = 1.25643$. See also Question 10.6.

In practice, because of turbulence generation, the actual diffusion of vorticity contained in the vortex is known to be much quicker than using Eq. 10.33 (i.e., with molecular diffusion only being allowed by this model). It can be expected that the tip vortex initially exhibits a predominantly laminar behavior; thereafter the vortex progressively becomes turbulent. The tendency toward turbulence generation must be related to the vortex Reynolds number, $Re_v = \Gamma_v/\nu$, among other factors such as rotational stratification effects, which are discussed later in Section 10.6.5. The rate of development of the turbulent structures near the core will alter the effective diffusion rate of vorticity from within the vortex.

These effects, albeit very complicated on a fundamental level, can be incorporated into a model core growth equation using an average "turbulent" viscosity coefficient [see Dosanjh et al. (1962), Squire (1965), Ogawa (1993) and Bhagwat & Leishman (2000a, 2002)], where now the assumption is that $r_c(t) = \sqrt{4\alpha\delta\nu t}$. The coefficient δ takes into account the more rapid core growth based on an average increased rate of vorticity diffusion as a result of turbulence generation and is a coefficient that must be deduced from vortex core structure measurements. Squire (1965) has postulated that the effective (turbulent) viscosity coefficient, δ, should be a function of the circulation strength (circulation) of the trailed tip vortex, Γ_v. Because, in practice, the strength (circulation) of the vortex is conserved and is found to remain nominally constant as the vortex ages in the flow [see Dosanjh et al. (1962), Mahalingam & Komerath (1998), and Bhagwat & Leishman (2000a, 2002)] it is reasonable to assume a constant value of δ. However, this hypothesis can only be verified through experimental correlation. In addition, because it is known that the vortex is already in some stage of decay immediately after its formation, it can be hypothesized that the growth curve can be originated at a virtual time, say t_0, so that $r_c(t) = \sqrt{4\alpha\delta\nu(t - t_0)}$ – see Squire (1965) and results in Fig. 10.22.

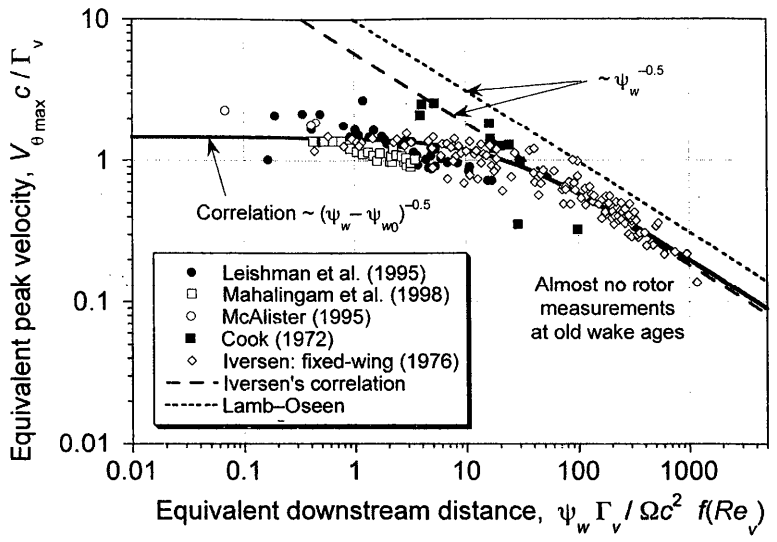

Figure 10.23 General correlation of rotor tip vortex measurements in terms of nondimensional maximum tangential velocities and nondimensional downstream distance.

10.6.4 *Correlation of Rotor Tip Vortex Data*

Figure 10.23 shows results derived from the tip vortex measurements in terms of an equivalent maximum nondimensional tangential velocity as a function of equivalent nondimensional downstream distance from the tip of the blade. Following an approach similar to Iversen (1976), we can write the nondimensional velocity and distance (in terms of vortex or "wake" age) as

$$\bar{V}_{\theta_{\max}} = \left(\frac{V_{\theta_{\max}}}{\Omega R}\right)\left(\frac{\Omega R c}{\Gamma_v}\right) = \frac{V_{\theta_{\max}} c}{\Gamma_v}, \tag{10.34}$$

$$\bar{d} = \left(\frac{\psi_w R}{c}\right)\left(\frac{\Gamma_v}{\Omega R c}\right) = \frac{\psi_w \Gamma_v}{\Omega c^2}. \tag{10.35}$$

Figure 10.23 shows tip vortex measurements for subscale helicopter rotors that have been published by Leishman et al. (1995), Mahalingam & Komerath (1998), and McAlister et al. (1995). Also shown are measurements made by Cook (1972) when using a full-scale rotor. When the results are plotted in this manner, the data emphasize a strong correlation. The decreasing trend in the core swirl velocity, which is also observed in the fixed-wing case [see Iversen (1976)], confirms that the tip vortices diffuse logarithmically with increasing wake age. The measured data show the trend $\bar{V}_{\theta_{\max}}(\bar{d} + 2.197)^{\frac{1}{2}} = 2.782$. Iversen reports a correlation region after a nondimensional distance of 50, where the data show the trend $\bar{V}_{\theta_{\max}}(\bar{d})^{1/2} = 5.8$. This decreasing trend in the peak swirl velocity results from viscous diffusion. For constant net vortex circulation, the nondimensional peak velocity is inversely proportional to the core radius, and the distance $\bar{d}$ is proportional to the wake age (i.e., $\bar{V}_{\theta_{\max}} \propto r_c^{-1}$ and $\bar{d} \propto \psi_w$). This is consistent with the experimental measurements shown previously in Fig. 10.22, where the core radius initially increases as the square root of wake age (i.e., $r_c \propto \sqrt{\psi_w}$). The theoretical Lamb result given previously for the viscous core growth can be written in terms of vortex age as

$$r_c = \sqrt{4\alpha\nu\left(\frac{\psi_w}{\Omega}\right)}. \tag{10.36}$$

Substituting $V_{\theta_{max}} = \Gamma_v(1 - e^{-\alpha})/2\pi r_c$, and using Eqs. 10.34 and 10.35, gives

$$\bar{V}_{\theta_{max}}(\bar{d})^{\frac{1}{2}} = \frac{1 - e^{-\alpha}}{4\pi}\sqrt{\frac{1}{\alpha}\left(\frac{\Gamma_v}{\nu}\right)}. \tag{10.37}$$

As shown previously, the Lamb–Oseen result can be modified empirically to include an average effective (turbulent) viscosity coefficient, δ, that is, Eq. 10.37 can be written as

$$\bar{V}_{\theta_{max}}(\bar{d})^{\frac{1}{2}} = \frac{1 - e^{-\alpha}}{4\pi}\sqrt{\frac{1}{\alpha\delta}\left(\frac{\Gamma_v}{\nu}\right)}. \tag{10.38}$$

Comparing this with Iversen's results in Fig. 10.23, we see that Iversen's correlation is equivalent to including an effective turbulent viscosity coefficient that is proportional to the vortex Reynolds number, Γ_v/ν. The peak velocity trend shown in Fig. 10.23 corresponds to the core growth trend

$$r_c(\psi_w) = \sqrt{4\alpha\delta\nu\left(\frac{(\psi_w - \psi_{w_0})}{\Omega}\right)} \equiv \sqrt{r_0^2 + \frac{4\alpha\delta\nu\psi_w}{\Omega}}. \tag{10.39}$$

The ordinate shift, ψ_{w_0}, results in a effective nonzero core radius, r_0, at the tip vortex origin where $\psi_w = 0^\circ$ and, therefore, a finite velocity at $\bar{d} = 0$. However, in the other two models (i.e., Lamb–Oseen and Squire models) the swirl velocity is singular at the origin of the tip vortex and unrealistically high at small distances (wake ages). However, at large downstream distances (wake ages), all three curves show the same qualitative trend, that is the velocity is inversely related to $\sqrt{t}$ (i.e., $\bar{V}_{\theta_{max}} \propto \psi_w^{-1/2}$), or equivalently, the core radius increases in proportion to $\sqrt{t}$ (i.e., $r_c \propto \psi_w^{1/2}$).

The viscous core growth trend as a function of wake age as derived from the above correlation trend has been plotted in Figure 10.22, along with the Lamb (laminar) result and a Lamb-type trend with a higher (constant) effective turbulent viscosity. Again, the differences between the two curves are obvious at early equivalent wake ages. At later wake ages, the two curves have a qualitatively similar behavior. At large wake ages, they will be almost coincident, that is

$$r_c \propto \sqrt{\frac{\psi_w}{\Omega}} \quad \text{for } \psi_w \gg \psi_{w_0}. \tag{10.40}$$

10.6.5 *Flow Rotation Effects on Turbulence Inside Vortices*

The forgoing analysis presents a somewhat oversimplified model of the characteristics of blade tip vortices, although these models are still found to give good average approximations to their behavior. When taken to a deeper level, however, the structure of the tip vortices is known to have regions of both laminar and turbulent flow separated by a region of transitional flow. Such concepts of the vortex structure stem from early experimental observations made by Hoffman & Joubert (1963) and Tung et al. (1983).

For example, flow visualization performed on a tip vortex emanating from a rotating blade is shown in Fig. 10.24. It can be seen that the flow is predominantly laminar near the core region, which is marked by a region of smooth flow where there are no interactions between adjacent fluid layers. This is followed by a transitional region that has eddies of different sizes. Outside of this there is a more highly turbulent region – see also Fig. 10.4. This multi-region vortex structure concept differs from the descriptions assumed by the previously mentioned mathematical models in that it is neither completely laminar like

Figure 10.24 A representative smoke flow visualization image of a tip vortex emanating from a rotor blade showing three distinct regions: (1) Laminar region, (2) Transitional region, and (3) Turbulent region. Source: University of Maryland.

the Lamb–Oseen model nor completely turbulent like Squire's or Iversen's model. Recent high-resolution velocity measurements made using LDV [see Martin et al. (2001), Martin & Leishman (2002), and Ramasamy & Leishman (2003)] also continue to support the idea of a multi-region laminar and turbulent structure of the tip vortex.

The extent of these three regions of the vortex are affected by the vortex Reynolds number, Re_v. In particular, the effects of flow rotation on the development of turbulence present inside the vortex has been hypothesized to play an important role in determining the structure of a vortex – see Hoffman & Joubert (1963), Cotel & Breidenthal (1999), and Holzapfel et al. (2001). Rayleigh's centrifugal instability theory [see Rayleigh (1880)], which uses a buoyancy force concept, suggests that the vortex will never develop turbulence provided that the product of velocity and radial distance increases with the increase in radial coordinate. Only a few vortex models [e.g., Donaldson (1971) and Baldwin et al. (1973)] have been developed that recognize this concept. However, the various properties of the vortex flow predicted using these models, such as the core growth and the velocity profiles, did not correlate well with experimental results available at that time.

Bradshaw (1983) developed an analogy between rotating flows and stratified fluids. His analysis is based on the theory that flow rotation causes the higher speed fluid to prefer the outside of the vortex while conserving angular momentum, even if the density is assumed constant throughout the vortex. Using energy principles, an expression was developed for the local strength of the analogous stratification expressed as an equivalent gradient Richardson number, Ri. This number comes directly from the turbulent kinetic energy budget equation [see Bradshaw (1983) and Holzapfel et al. (2001)] and is basically a ratio of the turbulence produced or consumed inside the vortex as a result of buoyancy (centrifugal effects) to the turbulence produced by shearing in the flow. It can also be thought of as the ratio of potential to kinetic energy in a stratified flow.

Bradshaw's Richardson number involves the evaluation of the swirl velocity gradients in the vortex flow. Holzapfel et al. (2001) corrected Bradshaw's original definition, for which the revised expression is given by

$$Ri = \left(\frac{2V_\theta}{r^2}\frac{\partial(V_\theta r)}{\partial r}\right) \Big/ \left(r\frac{\partial\,(V_\theta/r)}{\partial r}\right)^2. \tag{10.41}$$

Cotel & Breidenthal (1999) and Cotel (2002) used this stratification concept and have determined a threshold value for the Richardson number that is a function of vortex Reynolds number. This analysis is based on a nondimensional parameter called a "persistence parameter," which is defined as the ratio of rotational to translational (convection) speed of the vortex. If the persistence parameter is high, which is the case for most helicopter rotor wakes, the threshold value of the Richardson number was determined experimentally to be $Re_v^{1/4}$. This means that the tip vortex will be laminar up to a radial distance where the local gradient Richardson number falls below this threshold value. Any turbulence present inside this boundary will be either relaminarized or suppressed; even substantial eddies will not be able to penetrate this vortex boundary.

The local gradient Richardson number has been calculated using the measurements from Ramasamy & Leishman (2003) and is shown in Fig. 10.25, along with the Lamb–Oseen and Iversen vortex models. The local Richardson number variation for both the vortex models (and the measurements) is seen to approach infinity at the center of the vortex. As the radial distance from the center of the vortex increases, the Richardson number quickly reduces in value and falls below the assumed stratification threshold (i.e., for values of Ri above the stratification threshold only laminar flow is possible). In this region, diffusion at a molecular level will be the only means to transport the momentum contained in the vortex flow.

This concept helps explain the persistence of lift generated tip vortices, in general, to relatively old wake ages. When Ri is below the stratification threshold, flow turbulence can develop. This argument serves to augment the hypothesis of a multi-region vortex where

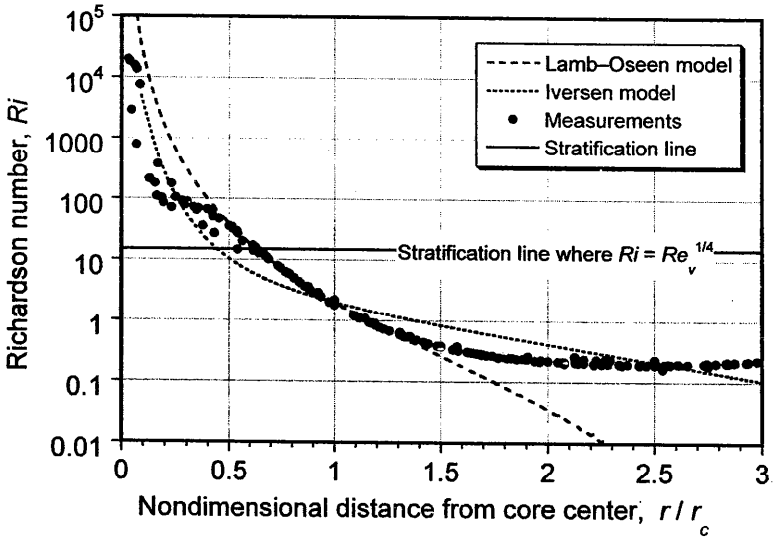

Figure 10.25 Plot of local Richardson number with radial coordinate for a vortex flow. Measurements made at $Re_v = 50,000$.

the flow is always laminar well inside the core region, the flow which then progressively transitions to turbulence through and outside the tip vortex core. This mechanism certainly affects the induced velocity field, especially closer to its axis, and the effects of flow turbulence must be considered carefully if higher fidelity vortex models are to be developed for helicopter rotor applications. Such models must delineate the effects of vortex Reynolds number so that the models can be applied to a wide range of rotor scales and operating conditions.

10.7 Vortex Models of the Rotor Wake

In vortex wake models, the convection of the tip vortices (and other concentrated vorticity) is explicitly tracked through the flow field relative to the rotor. Vortex diffusion and convection are, however, treated as separate steps. The underlying principle is that of Helmholtz's law [see Lamb (1932) or Saffman (1992)], which embodies the principle of vorticity transport. Typically, the vortical wake is modeled by vortex lines[5] that are discretized into the form of a regular lattice with straight elements [see Clark & Leiper (1970), Sadler (1971a,b), and Scully (1975)] or continuous curved vortex lines [see Quackenbush et al. (1988) and Wachspress et al. (2003)] or vortex "blobs" [see Lee & Na (1995, 1998)]. Schematics of these representations are shown in Fig. 10.26, where the wake from only one blade is shown for clarity. For most applications, the vortex wake model will be coupled to either a lifting-line or lifting-surface representation of the rotor blades (see Section 14.9). This defines the initial strengths and locations of the wake vortices relative to the rotor and forms boundary conditions for the remainder of the "far" vortex wake.

The main advantage of vortex methods, whether the approach be comprised of straight line vortex filaments, curved filaments, or vortex blobs, is that once the positions and strengths of the wake vorticity are obtained, then the induced velocity field at the rotor (or elsewhere, as required) can be computed by the use of the Biot–Savart law, followed by numerical integration over all of the filaments. The process lends itself readily to the computer. However, the main disadvantage of vortex methods is one of relatively high computational expense because many vortex elements are required to represent the wake of a helicopter rotor. While the evaluation of the Biot–Savart integral is trivial for a single vortex element, it is the very large number of elements required to model the entire rotor wake that determines the expense because a typical vortex filament may be discretized into several hundred or thousands of individual segments. For some applications in rotor analyses, it is the relatively high cost of vortex methods that limits their routine use. These methods are, however, still many orders of magnitude less expensive than finite-difference solutions based on the Euler or Navier–Stokes equations; see McCroskey (1995) and Section 14.2.1.

The principal differences among all of the various discretized vortex wake models that have been developed for helicopter applications are the assumptions and methods employed for the solution of the equations used to describe the transport of the wake vorticity. In prescribed vortex–wake models, the difficulties inherent in trying to explicitly solve these equations directly are avoided by either specifying the locations of the wake filaments a priori or by assuming an approximate velocity field near the rotor. Usually with the latter method, a simple velocity field (such as uniform or linear) can be prescribed that allows an analytical solution for the wake geometry. Alternatively, when specifying the wake geometry directly,

[5] A vortex line is simply a curve in the fluid that is tangent to the local vorticity vector; it should not be confused with a line vortex.

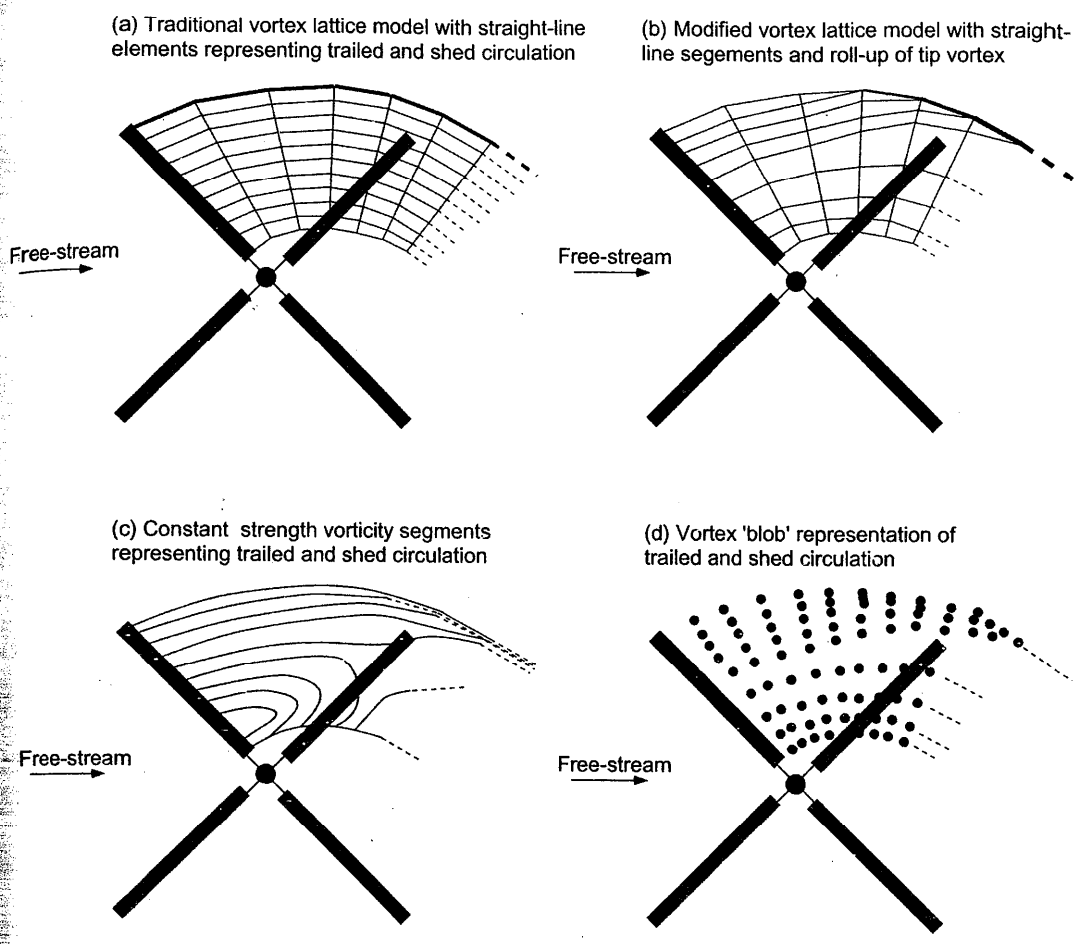

Figure 10.26 Representation of the vortex wake trailed behind a rotor blade. Notice: The wake from only one blade is shown for clarity. (a) Straight-line filaments. (b) Straight filaments with a prescribed roll-up model. (c) Constant vorticity curved vortex filaments. (d) Vortex blobs.

approximate functional relations can be derived from a combination of momentum theory and flow visualization experiments. In so-called "free" vortex wake methods, the solution for the wake is obtained from first principles. This form of solution recognizes that because parts of the vortices in the wake may interact with themselves (a self-induced effect) or with other vortices (a mutually induced effect) or with the blades themselves (BVI) the overall behavior of the wake cannot easily be generalized or prescribed in functional form and a numerical solutions must be sought. The development of numerical methods for this problem is considered in Section 10.7.6.

10.7.1 *Biot–Savart Law*

Fundamental to all vortex models is the requirement to compute the induced velocity at a point contributed by a vortex filament in the rotor wake. This can be calculated through the application of the Biot–Savart law – see Batchelor (1967). The incremental values of induced velocity, $d\vec{v}$, at any point P a distance $\vec{r}$ from the segment $d\vec{l}$ of a vortex

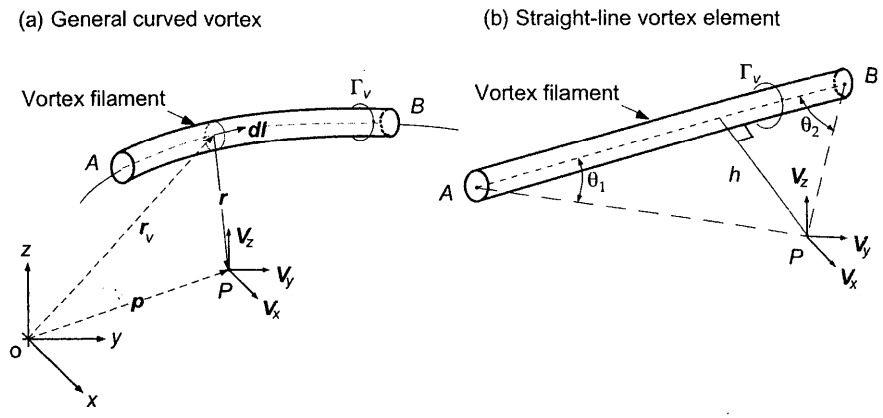

Figure 10.27 Evaluation of the induced velocity from a vortex filament using the Biot–Savart law. (a) Curved vortex. (b) Straight-line vortex.

filament of strength Γ_v can be written in general form as

$$d\vec{v} = \frac{\Gamma_v}{4\pi} \frac{d\vec{l} \times \vec{r}}{|\vec{r}|^3}, \tag{10.42}$$

which is shown schematically in Fig. 10.27. The total velocity at point P is then obtained by integration along the lengths of the vortex filaments. In application, curved wake filaments would normally be discretized into a number of collocation points that are connected by straight-line vortex segments because the velocity induced by a straight-line vortex segment is then readily integrable. The velocity at a point P induced by a single, straight-line vortex element extending from one point A to another point B [see Fig. 10.27(b)] can be expressed in the form

$$\begin{Bmatrix} V_x \\ V_y \\ V_z \end{Bmatrix} = \frac{\Gamma_v}{4\pi h} (\cos\theta_1 - \cos\theta_2) \begin{Bmatrix} e_x \\ e_y \\ e_z \end{Bmatrix}, \tag{10.43}$$

where

$$\vec{e} = (e_x, e_y, e_z) = \frac{\vec{l}_{12} \times \vec{r}_1}{|\vec{l}_{12} \times \vec{r}_1|} \tag{10.44}$$

and where θ_1 and θ_2 are the included angles. Γ_v is the strength of the vortex element. Now we can write that

$$\vec{r}_1 = \vec{r}_P - \vec{r}_A, \qquad \vec{r}_2 = \vec{r}_P - \vec{r}_B, \qquad \vec{l}_{12} = \vec{r}_B - \vec{r}_A, \tag{10.45}$$

where $\vec{r}_A$, $\vec{r}_B$, $\vec{r}_P$ are the position vectors of points A, B, and P, respectively. The perpendicular separation distance h to the line AB is

$$h = r_1 \sin\theta_1 = r_2 \sin\theta_2 \tag{10.46}$$

and the included angles are

$$\cos\theta_1 = \frac{\vec{l}_{12} \cdot \vec{r}_1}{|\vec{l}_{12}|\,|\vec{r}_1|}, \qquad \cos\theta_2 = \frac{\vec{l}_{12} \cdot \vec{r}_2}{|\vec{l}_{12}|\,|\vec{r}_2|}. \tag{10.47}$$

Although the Biot–Savart law is singular at $\vec{r} = 0$, this can be rectified by using vortex models with finite cores or by using other types of cutoff methods. For example, Eq. 10.43 can be modified to read

$$\begin{Bmatrix} V_x \\ V_y \\ V_z \end{Bmatrix} = \frac{\Gamma_v}{4\pi} \frac{h}{(r_c^{2n} + h^{2n})^{1/n}} (\cos\theta_1 - \cos\theta_2) \begin{Bmatrix} e_x \\ e_y \\ e_z \end{Bmatrix}, \tag{10.48}$$

where r_c is a "core" dimension and $n = 1, 2$ defines the velocity profile based on the Vatistias series of models – see Eq. 10.11.

10.7.2 *Vortex Segmentation*

To help reduce the number of numerical operations associated with vortex methods, the complexity of the real rotor wake can be reduced into various simplified forms. A common approximation is to treat only the trailed vortex filaments, that is, the filaments that are initially trailed perpendicular to the blade span (see Fig. 8.3). These contributions to the vorticity field arise because of the spanwise gradients in the distribution of circulation loading on the blades. The time-dependent aerodynamic loading results in shed wake vorticity, and to save tracking all the shed elements in the wake this effect can be approximated by means of one of the unsteady aerodynamic models considered in Chapter 8. Even with the trailed wake system alone, the problem of calculating the induced velocity field is still one of high numerical cost. However, experiments have shown the dominant structures in the rotor wake to be the tip vortices, and so a common level of modeling approximation is to consider just these tip vortices alone. Correlation studies with experimental measurements of the rotor inflow and blade loads have shown that this is a good level of approximation and does not sacrifice much physical accuracy in the problem, especially in forward flight, for a substantial reduction in computational effort.

For some vortex wake schemes, the discretization into straight-line vortex segments can result in round-off errors that may be a source of numerical problems, especially if the segments are relatively large. However, the overall errors associated with this form of discretization are usually small because the radius of curvature of the rotor wake is generally large, except perhaps in the roll-up regions at the lateral edges of the wake. Yet it is still important to formally determine the accuracy of this approach to modeling the vortex wake and to establish thresholds of discretization that will provide good accuracy for the induced velocity field while still containing computational costs.

The discretization of curved vortex filaments into straight lines will result in an induced velocity calculation that is, at best, second-order accurate, a problem examined in detail by Bhagwat & Leishman (2001b) and Gupta & Leishman (2004). This result can be seen from Fig. 10.28, which shows a plot of the L_2-norm (rms) of the error in the reconstruction of the induced velocity using straight-line segmentation for a vortex ring, a singly-infinite helix with a helical pitch p and a skewed helix with a skew angle β. The induced velocity for a vortex ring was calculated using the exact solution (see Section 10.7.5) and the solution for the finest numerical discretization is comparable up to seven decimal places. The error in the induced velocity for the helical vortex was calculated with respect to the finest discretization because there is no exact solution for the induced velocity from a helix. It is apparent that the order of accuracy of the reconstructed velocity field does not depend on the helical pitch and both the skewed and unskewed helix follow the quadratic trend for $\Delta\theta < 2.5°$, indicating second-order accuracy. This gives high confidence in the straight-line segmentation approach for the general modeling of helicopter rotor wakes.

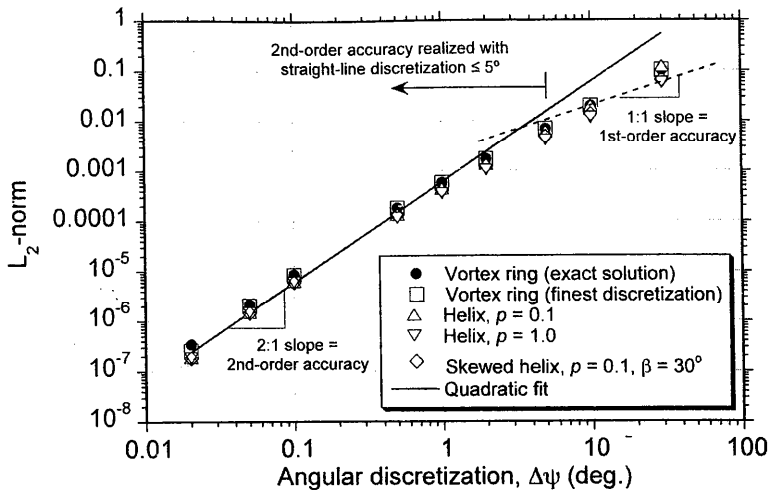

Figure 10.28 L_2-norm for the relative error in the induced axial velocity in the $z = 0$ plane of a vortex ring, unskewed and skewed helical vortex (skew angle $\beta = 30°$) with helical pitch $p = 0.1$.

10.7.3 *Governing Equations for the Convecting Vortex Wake*

A description of the vorticity field in the rotor wake is governed by the 3-D, incompressible Navier–Stokes equations, which in a Lagrangian form can be written as

$$\frac{D\vec{\omega}}{Dt} = \underbrace{(\vec{\omega}\cdot\nabla)\vec{V}}_{\text{strain}} + \underbrace{\nu\Delta\cdot\vec{\omega}}_{\text{diffusion}} . \tag{10.49}$$

This equation defines the change of vorticity of a fluid element moving with the flow in terms of the instantaneous value of vorticity, $\vec{\omega}$, and the local velocity field $\vec{V}$. The term on the left-hand side of Eq. 10.49 represents advection (convection), with the two terms on the right-hand side being a strain or "stretching" term and viscous diffusion term, respectively. In many practical problems, it can be justified that viscous phenomena will be confined to much smaller length scales compared to potential flow phenomena. Therefore, vortex methods use discrete line vortices to represent concentrated lines of vorticity. Under these conditions, Helmholtz's second law states that the vortex lines move as material lines at the local velocity, V_{loc}. In the discretized problem, this convection criteria is applied to all of the collocation points that have been specified along the lengths of all the vortex lines (see Fig. 10.27 previously). If we consider a single element of a trailed vortex filament, the fundamental equation describing the transport of a point on the filament is

$$\frac{d\vec{r}}{dt} = \vec{V}_{\text{loc}}(\vec{r}, t), \quad \vec{r}(t=0) = \vec{r}_0, \tag{10.50}$$

where $\vec{r} = \vec{r}(t) = \vec{r}(\psi_w, \psi_b)$ is the position vector of a point on the filament at a time (or wake age ψ_w) that was trailed from the blade when it was at an azimuth angle ψ_b. The term $\vec{r}_0$ is simply an initial condition. This equation is the fundamental equation for the free-vortex wake method or the free-vortex method (FVM). (See Section 14.4 for the fundamental principles behind the derivation of Eq. 10.50.)

Because the wake position vector $\vec{r}$ is both a function of ψ_b and ψ_w then the derivative on the left-hand side of Eq. 10.50 can be expanded to give

$$\frac{d\vec{r}(\psi_b, \psi_w)}{dt} = \frac{\partial \vec{r}}{\partial \psi_w}\left(\frac{\partial \psi_w}{\partial t}\right) + \frac{\partial \vec{r}}{\partial \psi_b}\left(\frac{\partial \psi_b}{\partial t}\right). \tag{10.51}$$

This equation can be simplified by noting that the time derivatives are

$$\frac{\partial \psi_w}{\partial t} = \frac{\partial \psi_b}{\partial t} = \Omega. \tag{10.52}$$

Therefore, in blade fixed coordinates the fundamental equation describing the position vector of the vortex filament is

$$\frac{\partial \vec{r}}{\partial \psi_w} + \frac{\partial \vec{r}}{\partial \psi_b} = \frac{1}{\Omega}\vec{V}_{\text{loc}}(\vec{r}, t). \tag{10.53}$$

This is a first-order, quasi-linear, hyperbolic, partial differential equation (PDE). The homogeneous portion of the equation (the left-hand side) is the linear wave equation. However, the right-hand side is, in general, a nonlinear function mainly because of the induced effects resulting from the complete wake geometry. By assuming that every vortex filament is convected through the flow field at the local velocity, a PDE governing the geometry of a single element of the vortex filament can be written as

$$\frac{\partial \vec{r}(\psi_b, \psi_w)}{\partial \psi_b} + \frac{\partial \vec{r}(\psi_b, \psi_w)}{\partial \psi_w} = \frac{\vec{V}_\infty}{\Omega} + \frac{1}{\Omega}\sum_{j=1}^{N_v} \vec{V}_{\text{ind}}[\vec{r}(\psi_b, \psi_w), \vec{r}(\psi_j, \psi_w)]. \tag{10.54}$$

Notice that the summation is carried out over the total number of trailed vortex filaments, N_v, that contribute to the induced velocity field at any given point. For tip vortices alone then $N_v = N_b$.

To solve Eq. 10.54 using a numerical scheme, it must be spatially and temporally discretized. This results in a set of simultaneous ODEs. A computational domain can be defined as a discretized grid in time (ψ_b) and space (ψ_w), as shown in Fig. 10.29. Based on such discretizations, the partial differentials in the governing PDE can be approximated using several different types of finite-difference schemes. For example, Crouse & Leishman (1993) have used a "three-point central difference" approximation of the left-hand-side derivatives of Eq. 10.54 about point $(\psi_b - \Delta\psi_b/2, \psi_w - \Delta\psi_w/2)$ using points $(\psi_b - \Delta\psi_b, \psi_w - \Delta\psi_w)$ and (i, k), as shown in Fig. 10.29. Bagai & Leishman (1995a,b; 1996) have used a "five-point central difference" scheme, where the derivatives were evaluated at the point $(\psi_b - \Delta\psi_b/2, \psi_w - \Delta\psi_w/2)$ about points (ψ_b, ψ_w), $(\psi_b - \Delta\psi_b, k)$, $(i, \psi_w - \Delta\psi_w)$ and $(\psi_b - \Delta\psi_b, \psi_w - \Delta\psi_w)$ in the discretized computational domain, as also shown in Fig. 10.29.

The induced velocity, $\vec{V}_{\text{ind}}$, in Eq. 10.54 can be determined using the Biot–Savart law (Eq. 10.27) with

$$\vec{V}_{\text{ind}}\left[\vec{r}(\psi_b, \psi_w), \vec{r}(\psi_j, \psi_w)\right] \equiv \frac{1}{4\pi}\int \frac{\Gamma_v\, d\vec{\psi}_{wj} \times \left(\vec{r}(\psi_b, \psi_w) - \vec{r}(\psi_j, \psi_w)\right)}{|\,\vec{r}(\psi_b, \psi_w) - \vec{r}(\psi_j, \psi_w)\,|^3}, \tag{10.55}$$

where $\vec{r}(\psi_b, \psi_w)$ is the point in the flow field influenced by the jth vortex at location $\vec{r}(\psi_j, \psi_w)$ that has strength Γ_v. The geometry of each element of a discretized vortex

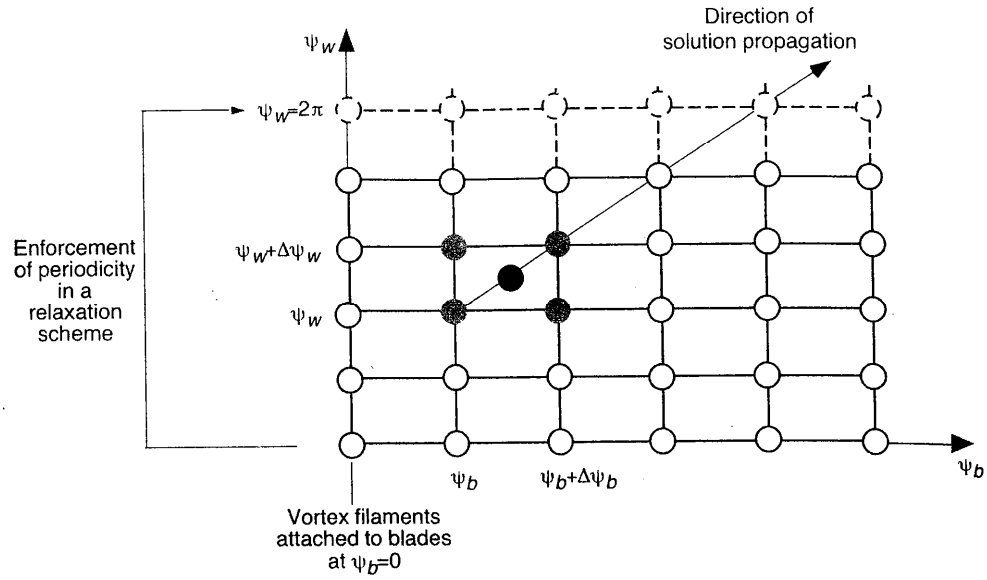

Figure 10.29 Discretized computational domain for the free-vortex wake problem.

filament is governed by one of these equations, and the velocity term on the right-hand side couples the equations together. This means that the equations for all of the filaments must be solved simultaneously, and this is a primary expense of the FVM.

Notice that the singular nature of the Biot–Savart law can be avoided by replacing the induced velocity field of the individual vortices with a model with a desingularized core, as discussed previously. Remember that this may also include a core growth (vorticity diffusion) model. The results for the wake geometry and induced velocity field thus obtained are probably qualitatively accurate no matter what vortex model is used. Yet, the quantitative errors associated with the wake model can only be determined though correlation studies with experiments documenting both the wake geometry and the induced velocity field, and caution should always be employed.

10.7.4 *Prescribed Wake Models for Hovering Flight*

For hovering flight, generalized prescribed vortex wake models have been developed to enable predictions of the inflow through the disk, but without the expense and uncertainties associated with explicitly calculating the force-free positions of the wake. These models prescribe the locations of the rotor tip vortices (and sometimes also the inner vortex sheet) as functions of wake age ψ_w on the basis of experimental observations. For hovering flight, generalized prescribed vortex wake models have been developed by Landgrebe (1969, 1971, 1972), Gilmore & Gartshore (1972), Kocureck & Tangler (1976), and Kocureck & Berkowitz (1982).

Landgrebe's Prescribed Wake Model

Landgrebe (1971, 1972) studied experimentally about seventy subscale helicopter rotor configurations with different combinations of number of blades, rotor solidity, blade

twist, and blade aspect ratio. On the basis of these experiments, Landgrebe's model describes the tip vortex geometry by the equations

$$\frac{z_{\text{tip}}}{R} = \begin{cases} k_1 \psi_w & \text{for } 0 \le \psi_w \le 2\pi/N_b, \\ \left(\frac{z_{\text{tip}}}{R}\right)_{\psi_w = 2\pi/N_b} + k_2\left(\psi_w - \frac{2\pi}{N_b}\right) & \text{for } \psi_w \ge 2\pi/N_b \end{cases} \tag{10.56}$$

and

$$\frac{y_{\text{tip}}}{R} = r_{\text{tip}} = A + (1 - A)\exp(-\Lambda \psi_w). \tag{10.57}$$

Notice that the vertical displacements are linear with respect to wake age (i.e., they convect axially at a constant velocity), which is consistent with all experiments. At the first blade passage when $\psi_w = 2\pi/N_b$, it has been shown previously in Fig. 10.6 that there is a sudden change in the axial convection velocity. This is reflected in the change of the coefficient from k_1 to k_2 in the equations describing the axial displacements. The axial settling rates are modeled by the empirical equations

$$k_1 = -0.25(C_T/\sigma + 0.001\theta_{\text{tw}}), \tag{10.58}$$

$$k_2 = -(1.41 + 0.0141\theta_{\text{tw}})\sqrt{C_T/2} \approx -(1 + 0.01\theta_{\text{tw}})\sqrt{C_T}, \tag{10.59}$$

where the blade twist θ_{tw} is measured in units of degrees. The radial contraction of the wake is smooth and asymptotic. The empirically derived coefficients for the radial contraction are given by $A = 0.78$ and $\Lambda = 0.145 + 27C_T$. Notice that while the theoretical contraction ratio of a rotor wake in hover is 0.707 (see results in Section 2.2.3), in practice the contraction ratio is found experimentally to be consistently closer to 0.78. The vortex sheet trailed by the inner parts of the blade vary linearly with r. The outer end of the sheet ($r = 1$) is represented by the equations

$$\left(\frac{z}{R}\right)_{r=1} = \begin{cases} K_{1,r=1}\psi_w & \text{for } 0 \le \psi_w \le 2\pi/N_b, \\ K_{1,r=1}\left(\frac{2\pi}{N_b}\right) + K_{2,r=1}\left(\psi_w - \frac{2\pi}{N_b}\right) & \text{for } \psi_w \ge 2\pi/N_b, \end{cases} \tag{10.60}$$

whereas the inner end of the sheet is represented by

$$\left(\frac{z}{R}\right)_{r=0} = \begin{cases} 0 & \text{for } 0 \le \psi_w \le 2\pi/N_b, \\ K_{2,r=0}\left(\psi_w - \frac{\pi}{2}\right) & \text{for } \psi_w \ge \pi/2. \end{cases} \tag{10.61}$$

The locations of intermediate parts of the sheet are determined by linear interpolation. The empirical coefficients of the sheet coordinates are described by

$$K_{1,r=1} = -2.2\sqrt{C_T/2}, \tag{10.62}$$

$$K_{2,r=1} = -2.7\sqrt{C_T/2}, \tag{10.63}$$

$$K_{1,r=0} = \left[\frac{\theta_{\text{tw}}}{128}(0.45\theta_{\text{tw}} + 18)\right]\sqrt{\frac{C_T}{2}}. \tag{10.64}$$

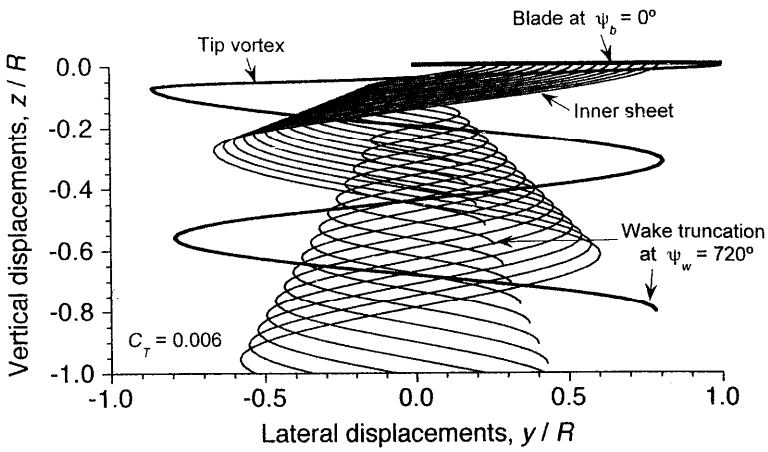

Figure 10.30 Representative prescribed hovering wake based on Landgrebe's model. $N_b = 2; C_T = 0.006; \theta_{tw} = 0°$.

A representative wake geometry in hovering flight based on Landgrebe's model is shown in Fig. 10.30. The wake for two revolutions of the rotor are shown to convey the relative differences in the convection rates of the sheet versus that of the tip vortex. Notice that the outer edge of the inner sheet convects axially downward at a rate that is approximately twice that of the tip vortex, a result alluded to previously in Section 10.3.2. In the hover state, it is found that the inclusion of the vortex sheet is usually necessary to enable good predictions of induced inflow and rotor performance.

Kocurek & Tangler's Prescribed Wake Model

Kocurek & Tangler (1976) have derived a prescribed wake model similar to that of Landgrebe using the same set of generalized equations for the tip vortex trajectories, but with different coefficients based on another series of subscale rotor experiments. This model attempts to include the number of blades as well as the blade lift distribution (through the twist rate) in the modeling of the axial settling rates. The generalized equation for k_1 is

$$k_1 = B + C\left(\frac{C_T{}^m}{N_b^n}\right), \tag{10.65}$$

where $B = -0.000729\theta_{tw}$ and $C = -2.30206\theta_{tw}$. The other coefficients are: $m = 1.0 - 0.25e^{0.040\theta_{tw}}$ and $n = 0.5 - 0.0172\theta_{tw}$. The equation for k_2 is

$$k_2 = -(C_T - C_{T_0})^{1/2}, \quad \text{where} \quad C_{T_0} = b^n(-B/C)^{1/m}. \tag{10.66}$$

The radial contraction rate parameter λ is given by $\lambda = 4.0\sqrt{C_T}$, with $A = 0.78$, as in Landgrebe's model. No inner vortex sheet is used in the Kocurek & Tangler model.

An example showing the expected quality of the predicted wake geometry and hover performance that can be made using a prescribed wake model is shown in Figs. 10.31 and 10.32. It is found that in this case the prescribed wake tends to slightly overpredict both the axial displacements and the radial contraction of the tip vortices. Results from a FVM are

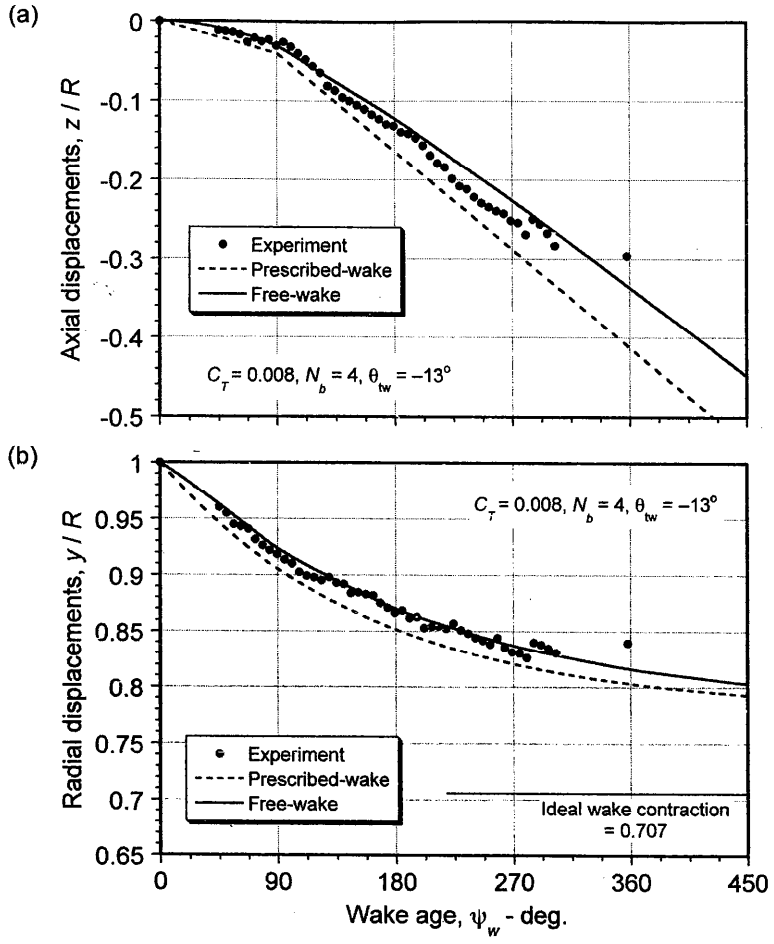

Figure 10.31 Comparison of prescribed and free-vortex wake methods with experimental measurements of the tip vortex locations in hover. (a) Axial displacements. (b) Radial displacements. Four-bladed rotor; $C_T = 0.008$.

also shown in Fig. 10.31 and 10.32. Notice that the FVM gives slightly better predictions of both the wake geometry and the hovering performance of the rotor albeit at a greater computational expense.

10.7.5 *Prescribed Vortex Wake Models for Forward Flight*

Vortex Ring Model

One simple way to approximate the trailed wake vorticity from the rotor is to used a series of stacked vortex rings or a vortex tube – see Coleman et al. (1945), Castles & De Leeuw (1954), and Young (1974). The advantage of using vortex rings is that an exact (analytic) solution for the induced velocity can be obtained. In the vortex ring (tube) model, one ring represents the trailed wake system generated by one blade during one rotor revolution. The positioning of the rings is defined on the basis of simple momentum theory.

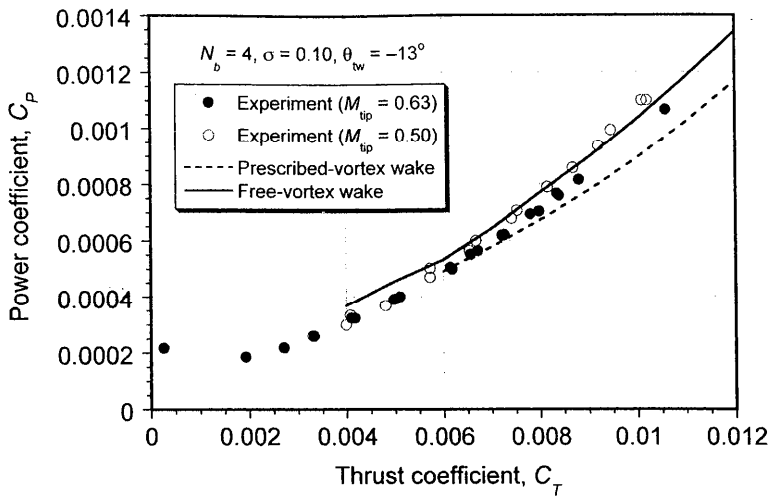

Figure 10.32 Predictions of hovering rotor performance using prescribed and free-vortex wake methods.

The induced velocity from one disingularized vortex ring of strength Γ_v can be written as

$$V_z(r, z) = \frac{\Gamma_v}{4\pi} \int_{0+\delta\theta}^{2\pi-\delta\theta} \frac{z^2 + (R - r\cos\theta)^2}{\sqrt{r_c^2 + \left(\sqrt{z^2 + (R - r\cos\theta)^2}\right)^2}} \times \frac{R(R - r\cos\theta)\, d\theta}{(R^2 - 2Rr\cos\theta + z^2 + r^2)^{3/2}} \tag{10.67}$$

[see, for example, Lewis (1991)]. This equation can be integrated analytically using elliptic integrals of the first and second type. Alternatively, it can be integrated using Gaussian quadrature (see Question 10.1). Notice that for points not on the vortex segment itself, the cut-off distance, $\delta\theta$, equals zero. However, for points on the ring vortex a logarithmic singularity occurs, and so $\delta\theta$ must be nonzero. Although the value of $\delta\theta$ can be approximated in terms of the vortex core radius and an exponential function of the kinetic energy in the vortex core [see Widnall (1972)] in a practical sense a cut-off distance of $\delta\theta \sim 10^{-4}$ can be assumed without substantial error.

From this basic result for one ring, the net induced velocity at any point in the flow field can be obtained by summing the effects of all the rings representing the wake. It has been found from the vortex ring (tube) model that the longitudinal distribution of inflow in the rotor TPP is approximately linear, which is in good agreement with experiments – see Coleman et al. (1945). Also, it has been found that the longitudinal coefficient k_x in the linear inflow model can be approximated using $k_x = \tan(\chi/2)$, which is a result discussed previously in Section 3.5.2.

Rigid or Undistorted Wake

The rigid or undistorted vortex wake model is one in which the trailed vortices are represented by skewed helical filaments. The position of the vortex filaments is defined geometrically based on the flight conditions and momentum theory considerations. There are no self- or mutual-interactions between vortex filaments. If we assume that the induced

velocity field in the wake is uniform (i.e., the induced velocity does not vary with time or location), then an exact analytical solution may be obtained for Eq. 10.53 as a special case. Making this assumption is equivalent to assuming a uniform streamwise velocity and a mean inflow, λ_i = constant throughout the flow, that is

$$\vec{V} = \Omega R\mu\hat{i} + \Omega R(\lambda_i)\hat{k}. \tag{10.68}$$

Under these assumptions, the PDE governing the wake geometry relative to the TPP (see Eq. 10.50) can be written as

$$\frac{\partial \vec{r}}{\partial \psi_b} + \frac{\partial \vec{r}}{\partial \psi_w} = \mu\hat{i} + \lambda_i\hat{k}, \tag{10.69}$$

where ψ_w is the wake age and ψ_b is the azimuth angle of the blade at which the vortex filament was generated, also recognizing that the position vector r has now been nondimensionalized by R. Equation 10.69 is a linear, first-order, hyperbolic, PDE. The two required boundary conditions in the ψ_b and ψ_w directions are given by

$$\psi_b\text{: } \vec{r}(\psi_b, \psi_w) = \vec{r}(\psi_b + 2\pi, \psi_w), \tag{10.70}$$

$$\psi_w\text{: } \vec{r}(\psi_b, 0) = r_v \cos\psi_b\hat{i} + r_v \sin\psi_b\hat{j}, \tag{10.71}$$

where r_v is the radial release point of the trailed vortex filament from the blade ($r_v = 1$ at the tip). The analytical solution to Eq. 10.69 can be obtained using separation of variables – see Hildebrand (1976). The solution of the PDE is defined by the characteristic curve of the equation, which can be determined from the intersection of the two surfaces found by integrating the following ODEs:

$$\frac{d\psi_b}{1} = \frac{d\psi_w}{1}, \tag{10.72}$$

$$\frac{d\psi_w}{1} = \frac{d\vec{r}}{\vec{V}/\Omega R}. \tag{10.73}$$

From Eqs. 10.72 and 10.73, the two surfaces are given by $\psi_b = \psi_w + c_1$ and $\vec{r} = \vec{V}\psi_w/\Omega R + c_2$, respectively, where c_1 and c_2 are constants of integration. From these solutions, $c_1 = \psi_b - \psi_w$ and $c_2 = \vec{r} - \vec{V}\psi_w/\Omega$. The intersection of the two surfaces results in an equation relating the two constants such that $c_2 = f(c_1) \Rightarrow \vec{r} - \vec{V}\psi_w/\Omega R = f(\psi_b - \psi_w)$. Invoking the boundary condition at $\psi_w = 0$ results in $\vec{r} = r_v \cos\psi_b\,\hat{i} + r_v \sin\psi_b\,\hat{j}$, and so the exact solution can be written as

$$\vec{r}(\psi_b, \psi_w) = \left(\mu\psi_w + r_v \cos(\psi_b - \psi_w)\right)\hat{i} + r_v \sin(\psi_b - \psi_w)\,\hat{j} + \lambda_i\psi_w\,\hat{k}. \tag{10.74}$$

Notice that the periodic boundary condition in the ψ_b direction is also satisfied because $\cos(2\pi + \psi_b) = \cos\psi_b$ and $\sin(2\pi + \psi_b) = \sin\psi_b$. Equation 10.74 defines a skewed, undistorted helix, which is known as the rigid or undistorted vortex wake topology, which has already been introduced. If only tip vortices are assumed ($r_v = 1$), then the solution for the tip-vortex geometry relative to the rotor TPP can be described by the simple parametric equations

$$\frac{x_{\text{tip}}}{R} = x'_{\text{tip}} = \cos(\psi_b - \psi_w) + \mu\psi_w, \tag{10.75}$$

$$\frac{y_{\text{tip}}}{R} = y'_{\text{tip}} = \sin(\psi_b - \psi_w), \tag{10.76}$$

$$\frac{z_{\text{tip}}}{R} = z'_{\text{tip}} = \lambda_i\psi_w = -\mu\psi_w \tan\chi_{\text{TPP}}. \tag{10.77}$$

The wake skew angle χ_{TPP} is given by

$$\chi_{TPP} = \tan^{-1}\left(-\frac{\lambda_i}{\mu}\right), \tag{10.78}$$

where using the simple momentum theory in forward flight

$$\lambda_i = \mu \tan \alpha_{TPP} + \frac{\kappa C_T}{2\sqrt{\mu^2 + \lambda_i^2}}, \tag{10.79}$$

and where κ is an induced power factor. Notice that there is no contraction assumed in the rigid vortex wake. However, if it is found necessary to model this effect, the tip vortices can be assumed to originate at a point just inboard of the tip, say $r_v = 0.97$. Also, note that with the rigid wake equations, as $\mu \to 0$ the wake geometry reduces to a helix, but as has been described previously, this is an unsatisfactory model of the wake in hover.

A rigid wake geometry is plotted in Fig. 10.33 for forward flight at $\mu = 0.15$ and is compared to predictions made by a FVM (see Section 10.7.6). Notice that the predictions are substantially different. Nevertheless, the simplicity of the rigid wake model will give the primary effects of the skewness of the wake on the inflow distribution over the rotor disk and may be attractive for applications where the full details of the rotor wake are not required, such as for integrated rotor performance predictions. (See also the results of the rotor wake boundary shown previously in Fig. 10.10).

Modifications to Rigid Vortex Wake Models

Any number of assumptions about the induced velocity field near the rotor can be made to specify the right-hand side of Eq. 10.53 and decouple the equations. Other types of prescribed wake models for use in forward flight have also been derived on the basis of experimental observations. The advantage of these models is that, for some small additional computational effort, much better estimates of the rotor wake geometry can be obtained compared to a rigid wake. It has been observed from flow visualization experiments that the longitudinal and lateral distortions of the wake are relatively small compared to the vertical distortions. This means that the self-induced velocities in a plane parallel to the rotor plane are small: so for all the prescribed wake models it is still justified to use the undistorted tip vortex equations given previously by Eqs. 10.75 and 10.76. The differences in the various prescribed wake models lie in the prescription of the vertical (axial) displacements of the tip vortices. Generally, these are defined using Eq. 10.77 as a basis, but with empirical or semi-empirical weighting functions being used to produce the wake distortions.

UTRC Generalized Wake Model

One such prescribed wake approach, used by Egolf & Landgrebe (1983), is called the Generalized Wake Model. The vertical displacements of the tip vortices are written as

$$\frac{z_{tip}}{R} = z'_{tip} = -\lambda_i \psi_w - E\,G, \tag{10.80}$$

where, like the rigid wake, λ_i is based on momentum considerations. The second term on the right-hand side of the preceding equation is simply a modification to the undistorted rigid wake; the E term is called an envelope function and is effectively an amplitude term, and

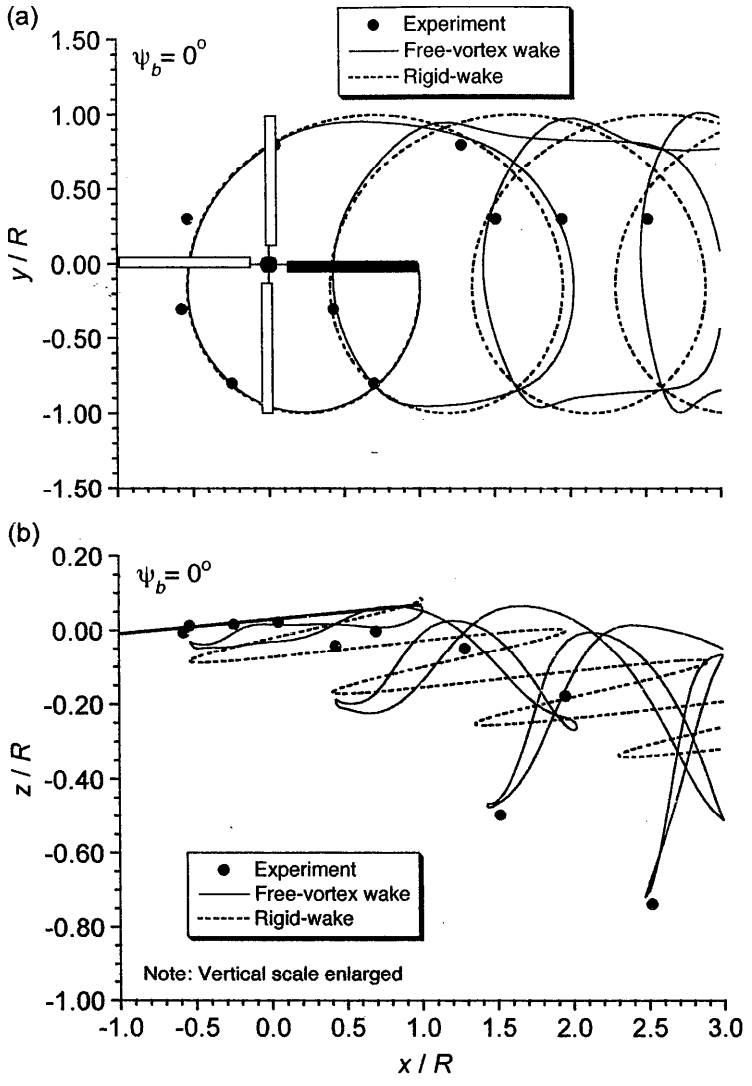

Figure 10.33 Representative rigid wake geometry in forward flight compared to free-vortex wake method and measurements. (a) Plan (top) view. (b) Side view, looking from retreating side. Four-bladed rotor; $C_T = 0.008; \mu = 0.15; \alpha_s = -3°$. (Notice: Results for a four-bladed rotor have been computed, with the results for one blade being shown for clarity.)

the G term is a shape or geometric function. The vertical displacement envelope function is defined by

$$E = \begin{cases} A_0 \psi_w \exp(A_1 \psi_w) & \text{for } \psi_w \leq 4\pi, \\ M\psi_w + B & \text{for } \psi_w > 4\pi, \end{cases}$$

where the coefficients A_0, A_1, M, and B are functions of the number of blades, the advance ratio, and the rotor thrust for a given rotor. The corresponding shape function

is given by the equations

$$G = \begin{cases} \sum_{n=0}^{N} \{g'_{nc} \cos n(\psi_w - \psi_b) + g'_{ns} \sin n(\psi_w - \psi_b)\} & \text{for } 0 \le \psi_w \le 2\pi, \\ \sum_{n=0}^{N} \{g''_{nc} \cos n(\psi_w - \psi_b) + g''_{ns} \sin n(\psi_w - \psi_b)\} & \text{for } \psi_w > 2\pi, \end{cases}$$

where the coefficients g'_{nc}, g'_{ns}, g''_{nc}, and g''_{ns} are functions of the number of blades and advance ratio for a given rotor. Usually N takes a value of 12.

Like the hover prescribed wake models, the coefficients of the forward flight model have been deduced from experimental studies of the wake geometry. However, because forward flight experiments are much more difficult and time consuming to undertake, there are less data available. Nevertheless, as shown by Egolf & Landgrebe (1983), the agreement of this prescribed wake model with measured wake geometries has been found to be good. As a consequence, there is usually a significant improvement in the prediction of blade airloads compared to those obtained using an undistorted rigid wake.

Beddoes's Generalized Wake Model

Another parsimonious but very effective prescribed wake model has been developed by Beddoes (1985). In this model, it is also recognized that axial (vertical) trajectories of the tip vortices can be estimated if an assumption for the inflow distribution across the disk is made. Beddoes suggests the model

$$\lambda_i = \lambda_0 \left(1 + Ex' - E\left|\left(y'\right)^3\right|\right), \tag{10.81}$$

where $x' = x/R$ and $y' = y/R$, deducing this form of the inflow from the measurements of Heyson & Katzoff (1957). Again, the evaluation of λ_i is based on momentum considerations. Beddoes suggests that $E = \chi$, where χ is the wake skew angle, although this is generally too large and $E = \chi/2$ has been found to give better agreement with experimental results and with the FVM.

Although with these assumptions the solution for the wake can be obtained by solving directly Eq. 10.53, this still involves significant expense because of the repeated evaluation of the Biot–Savart law. Instead, Beddoes (1985) specifies the equations describing the wake. At the rear of the disk, in the region occupied by the wake,

$$\lambda_i = 2\lambda_0 \left(1 - E\left|\left(y'_{\text{tip}}\right)^3\right|\right), \tag{10.82}$$

so that the vertical displacement of the tip vortex is given by

$$z'_{\text{tip}} = -\mu_z \psi_w + \int_0^{\psi_w} \lambda d\psi_b, \tag{10.83}$$

where $z' = z/R$. Now, if $x'_{\text{tip}} < -\cos(\psi_b - \psi_w)$ then the element on the vortex filament has not convected beyond the rotor disk and

$$\int_0^{\psi_w} \lambda d\psi_b = -\lambda_0 \left(1 + E(\cos(\psi_b - \psi_w) + 0.5\mu\psi_w - |(y'_{\text{tip}})^3|)\right) \psi_w. \tag{10.84}$$

If $\cos(\psi_b - \psi_w) > 0$ then the vortex element has always been downstream of the rotor disk and in this case

$$\int_0^{\psi_w} \lambda d\psi_b = -2\lambda_0 \left(1 - E|(y'_{\text{tip}})^3|\right) \psi_w. \tag{10.85}$$

If neither of the preceding conditions are met, then the element has spent part of the time within the disk and the remainder downstream of the disk and for this condition

$$\int_0^{\psi_w} \lambda d\psi_b = -2\lambda_0 x'_{\text{tip}} \frac{(1 - E|(y'_{\text{tip}})^3|)}{\mu_x}, \tag{10.86}$$

where $\mu_x = V_\infty \cos\alpha_{\text{TPP}}/(\Omega R)$. On the basis of these equations, the three components of the tip vortex location with respect to the rotor can be calculated.

Figure 10.34 shows a comparison of the vertical components of the tip vortices in forward flight at $\mu = 0.15$ as obtained from the Beddoes prescribed-wake model and also from a FVM. Because the differences between the prescribed wake and the free-vortex wake are now much smaller compared to the rigid wake, for clarity the results in Fig. 10.34 are plotted in terms of vertical displacement versus wake age relative to the blade of origination. The agreement is good, and bearing in mind the relative simplicity of the prescribed-wake solution compared to the free-vortex wake (at least two orders of magnitude less expensive to compute), it is certainly a modeling option to consider in any form of rotor analysis. After the wake geometry is known, the induced velocity field can be computed through the application of the Biot–Savart law to the discretized vortex filaments. Because this incurs the highest cost of any vortex wake model, Beddoes (1985) suggests an alternative and

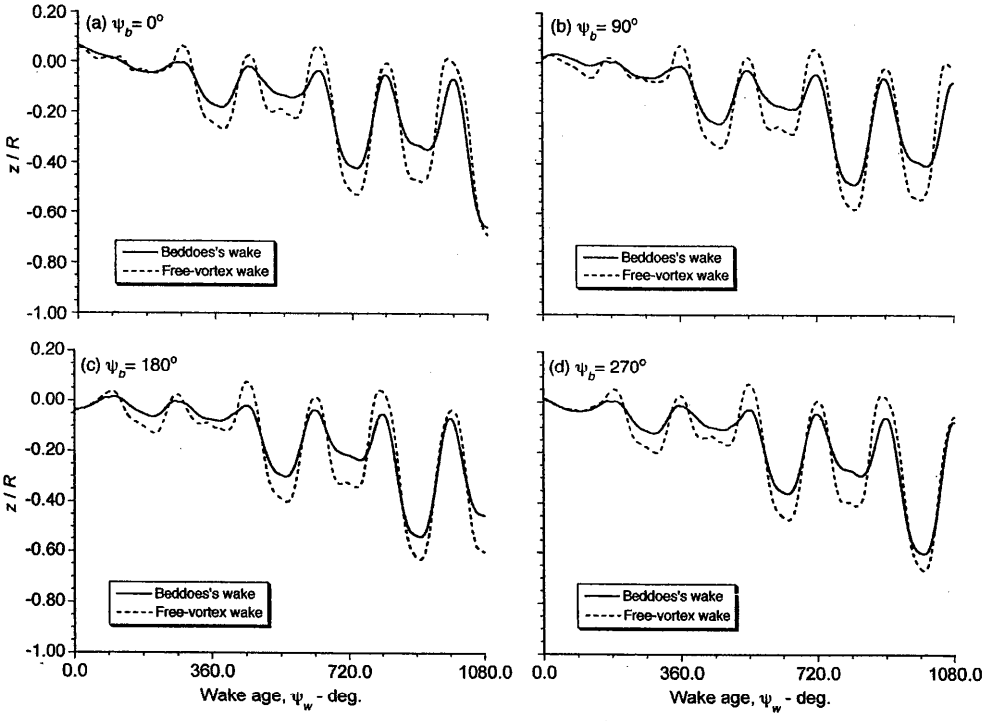

Figure 10.34 Comparison of Beddoes's prescribed wake model with predictions made by a free-vortex wake. (a) $\psi_b = 0°$. (b) $\psi_b = 90°$. (c) $\psi_b = 180°$. (d) $\psi_b = 270°$. Four-bladed rotor; $\mu = 0.15$; $C_T = 0.008$; $\alpha_s = -3°$.

highly simplified approach of approximating the induced velocities from some elements of the wake by using elongated straight line segments, which retains the simplicity and low cost of semi-analytic models such as when using vortex rings.

Beddoes's prescribed wake model seems to have received good attention from rotor analysts, and has been used in a number of aerodynamics and acoustic studies, mainly because of its excellent computational efficiency. Van der Wall (2000a) has performed an evaluation of the Beddoes wake model against measured airloads, wake displacements and BVI locations over the rotor disk in forward flight and has also suggested further improvements to the model – see van der Wall (2000b). While the predicted results seem good, it must be remembered that the tip vortex trajectories are still being prescribed a priori based on some generalized assumptions and not calculated based on the actual induced flow velocities near the rotor. Therefore, in the strictest sense, the prescribed wake model must be viewed as a postdictive model and must be validated for each and every rotor configuration, which is a formidable undertaking. The main problem, however, is this type of wake model does not offer the analyst much flexibility in terms of rotor design, despite the modest computational cost. This sought-after flexibility is obtained only with the next level in wake modeling, which is called the free-vortex wake method (FVM).

10.7.6 *Free-Vortex Wake Analyses*

General Concepts

Free-vortex wake models solve for the vortex strengths and rotor wake geometry, and in principle they do not require experimental results for formulation purposes, apart from the various assumptions that must be made. The position vectors of the individual wake filaments are now part of the solution process. Starting from some initial condition, which may be an undistorted rigid wake or a prescribed wake, the right-hand side of the equations must be computed through the repeated application of the Biot–Savart law with a desingularized core, which will likely include a core growth (vorticity diffusion) model. The solution for the wake geometry then proceeds until convergence, which usually means that a periodic solution is obtained. Pioneering work on the FVM applied to rotor wakes was performed by Landgrebe (1969, 1971, 1972), Clark & Leiper (1970), Sadler (1971a,b), and Scully (1975), and many variations and developments of the FVM have subsequently followed. The results obtained with the FVM are probably qualitatively correct no matter what type of numerical scheme and vortex model are used. However, the quantitative predictions made using these methods are much less absolute, and their true capabilities can only be determined though careful and systematic correlation studies with experimental measurements.

In the first instance, consider the rolled up tip vortices generated by each blade. For a rotor with N_b blades there will be an equal number of intertwining tip vortices (see Fig. 10.35). Generally, the filaments will have unequal circulation strengths along their length, which can be related to the lift (circulation) on the blade at the time of their formation. This means that both trailed and shed elements must be included in the solution to satisfy conservation of circulation. However, because this increases dramatically the number of free elements and the numerical costs, a tip vortex of average strength related to the rotor thrust (blade loading) is often assumed (see Section 3.3.8). A series of collocation points can be specified on the trailed vortex filaments, and these points are numerically convected through the flow field at the local velocity in accordance with the transport equation defined previously in Eq. 10.53.

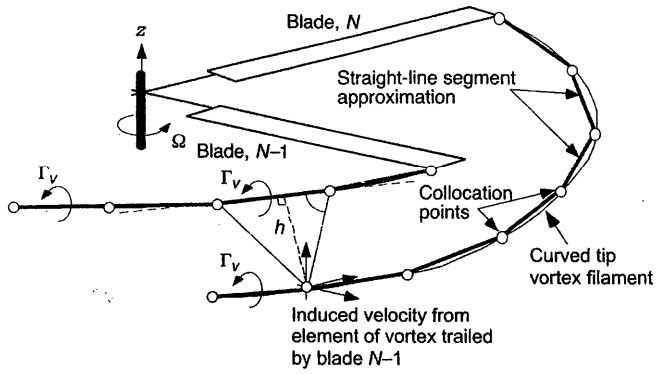

Figure 10.35 Idealization of trailed tip vortices into segments connected by collocation points in the free-vortex wake method.

General Solution Methodologies

Free-vortex wake models can be divided into two general types of solution methodologies: 1. Time-stepping or time-marching methods, and 2. Relaxation or iterative methods – see Leishman et al. (2002b). In the time-stepping method, the solution can be developed by an impulsive start of the rotor with no initial wake. The boundary condition specifies that each trailed vortex filament be attached to the blade at its point of origin, $\psi_w = 0$. Alternatively, a prescribed wake geometry can be specified as an initial condition. In either case, the solution is stepped in the ψ_b (azimuthal) direction using a time integration scheme, and for a steady-state flight condition, a converged solution is obtained when the transients introduced by the initial condition die out and a periodic solution is achieved. The relaxation method, in contrast, specifies that the trailed vortex elements be attached to the blades as an initial condition, whereas periodicity is enforced as the boundary condition. The solution is stepped in the ψ_w direction in an iterative manner, and convergence is obtained once the wake vortex geometry no longer distorts between successive iterations. Relaxation schemes have the advantage that they are numerically more efficient because periodicity of the wake solution can be imposed as a boundary condition. Also, relaxation schemes are generally free of the numerical instabilities that are often produced in some time-marching schemes as a consequence of round-off errors.

Different numerical schemes can also be used within both the time-stepping and relaxation approaches (i.e., explicit, implicit, or hybrid). Several rotor wake analyses use explicit type methods, which are simple in concept, but are particularly prone to various numerical problems associated with round-off errors. Consider, as an example, a representative PDE describing the convection of the vortex filaments such as

$$\frac{\partial r}{\partial t} + \frac{\partial r}{\partial x} = V(r). \tag{10.87}$$

Spatial discretization would result in reducing this partial differential equation into a system of simultaneous ODEs that can be written as

$$\frac{dr}{dt} = Ar + V(r), \tag{10.88}$$

where A is the space discretization matrix. An explicit method for this equation would use a finite-difference scheme such as

$$r^{n+1} = r^n + \Delta t \left[Ar^n + V(r^n) \right]. \tag{10.89}$$

Notice that the updated value of r at time $n + 1$ is based on values from the previous time step alone. Although this is one of the simplest methods, the truncation error in the solution for r is of order $(\Delta t)^2$ per time step, and so the error can grow rapidly if the time step is too large. The high computational costs of most blade element based rotor analyses often require relatively large time (blade azimuth or $\Delta\psi_b$) steps with the wake solution, making the assessment of truncation errors an important consideration.

Implicit methods, in contrast, are free from many of these numerical problems. An implicit difference scheme to solve the example equation in Eq. 10.87 is

$$r^{n+1} = r^n + \Delta t \left[A r^{n+1} + v(r^{n+1}) \right]. \tag{10.90}$$

In this case, the right-hand side also requires the evaluation of terms at the $(n + 1)$th step, information that has not yet been determined. If the velocity term, V, is a simple function of r, then the equation can be easily simplified and solved as a set of simultaneous equations. For more complex velocity functions, however, V must first be linearized using a Taylor expansion, resulting in a semi-implicit scheme. This approach was applied to the FVM by Miller & Bliss (1993). While numerical errors are much smaller with this intensive computer-processing technique, it is not routinely used because it requires the simultaneous solution of a large set of linear equations at each time step.

A multistep or predictor–corrector method may also be used to solve the wake equations. In this approach, an explicit method is used to generate an approximate value for the current step

$$\tilde{r}^{n+1} = r^n + \Delta t \left[A r^n + V(r^n) \right], \tag{10.91}$$

and this approximate, or predicted value, $\tilde{r}$, is then used to generate the final approximation to r^{n+1} using a corrector step such as

$$r^{n+1} = r^n + \Delta t \left[A \tilde{r}^{n+1} + V(\tilde{r}^{n+1}) \right]. \tag{10.92}$$

Predictor–corrector methods have a truncation error per step of order $(\Delta t)^3$ and exhibit considerably better stability characteristics than explicit methods alone – see Crouse & Leishman (1993). They also require much less computation than implicit or semi-implicit schemes. However, this scheme requires two velocity field calculations per time step compared to one for an explicit method (see Question 10.8).

Bagai & Leishman (1995a,b; 1996) have further developed a FVM for rotor wake modeling based on a predictor–corrector scheme in a relaxation formulation, but with two modifications. First, the explicit predictor step is modified into the pseudo-implicit equation

$$\tilde{r}^{n+1} = r^n + \Delta t \left[A \tilde{r}^{n+1} + V(r^n) \right]. \tag{10.93}$$

While the forcing (velocity) function is calculated explicitly from the previous time step, the position vectors at the current time-step also appear on the right-hand side ($\tilde{r}^{n+1}$). The above predictor equation, therefore, is no longer fully explicit. Second, the corrector step incorporates an averaging scheme whereby an average of the velocity function from the previous time step and the predicted value are used to update the corrected position vectors. This helps to improve the stability characteristics of the scheme. Once again, the position vectors at the current time step also appear on the right-hand side, also making the corrector step a pseudo-implicit equation, that is

$$r^{n+1} = r^n + \Delta t \left[A r^{n+1} + \frac{1}{2} \left(V(\tilde{r}^{n+1}) + V(r^n) \right) \right]. \tag{10.94}$$

Cost of the Free-Wake Solution

To understand the potential numerical cost of a FVM it is possible to estimate the number of Biot–Savart-like velocity evaluations required for a typical wake solution. Let $N_{\psi_b} = 360°/\Delta\psi$ be the number of discrete azimuthal grid points. Likewise, for a vortex filament that is n rotor revolutions old, the number of free collocation points (= number of free vortex elements on that filament) is $N_{\psi_w} = n\ 360°/\Delta\psi_w$. Therefore, a total of $N_{\psi_w}^2$ Biot–Savart evaluations must be performed for each free vortex filament at each of N_{ψ_b} locations to account for the total self-induced velocities at each collocation point from every other vortex element. If the wake is modeled using only a single free vortex filament from each blade tip, this results in $N_{\psi_b}\ N_{\psi_b}^2$ velocity field evaluations to define the rotor wake at all azimuth angles. For a rotor with N_b blades, a further $N_b\ (N_b - 1)\ N_{\psi_b}\ N_{\psi_w}^2$ evaluations must be performed to account for mutually induced effects. Therefore, the total number of Biot–Savart evaluations required per free-vortex wake computation, N_E, is given by the equation

$$N_E = (1 + N_b(N_b - 1))N_{\psi_b}N_{\psi_w}^2. \tag{10.95}$$

For equal step sizes, $\Delta\psi_b = \Delta\psi_w \Rightarrow N_{\psi_w} = nN_{\psi_b}$, and so the total number of evaluations becomes

$$N_E = (1 + N_b(N_b - 1))n^2N_{\psi_b}^3. \tag{10.96}$$

For a typical four-bladed helicopter rotor modeled with three revolutions of free-tip vortices and equal discretization step sizes of 10 degrees, Eq. 10.96 suggests that the Biot–Savart integral must be evaluated over 1.8×10^6 times to cover the entire computational domain just one time. Doubling the resolution (i.e., using step sizes half the original size, such that $\Delta\psi_b = 5°$) requires eight times that number, or over 14.5×10^6 velocity evaluations. For additional free vortex filaments, the mutual interactions among all the additional free vortices must also be computed leading to a substantial computational effort in a FVM for routine use.

Acceleration Methods

Various ideas have been used to decrease these computational times and make the FVM more attractive for various helicopter applications. Often, methods can be used to differentiate between vortex elements in the "near field" and "far field," the latter which have a smaller influence and can be either excluded from the calculation altogether or can be included by lumping together the induced effects of several "far" elements. Miller & Bliss (1993) have employed an analytical and numerical matching technique, in which a near field solution for the vortex near the core is matched to a far field solution. Substantial reductions in computational cost are possible. An extension of this approach is discussed by Miller (1993). Although successful in decreasing execution times, the resulting higher-order velocity field errors associated with the approximations may still undermine the accuracy of the wake predictions. Linear interpolation of the positions of the wake markers, such as discussed by Brooks et al. (1996), simply to effect a larger number of points does not improve the net accuracy of the wake solution. Sarpkaya (1989) discusses other methods that can potentially be used to reduce the computational time of vortex methods.

Bagai & Leishman (1998) have approached the problem through adaptive refinement of the finite-difference grid used to solve the governing equations of the vortex wake, with interpolation of known information onto intermediate points in the wake. Reductions in computational effort of over an order of magnitude are possible. The underlying goal is to perform fewer explicit induced velocity calculations using the Biot–Savart law, while retaining the

accuracy and fidelity of the wake solutions. For equal discretization ($\Delta\psi_b = \Delta\psi_w$) with $N_{\psi_b} = 2\pi/\Delta\psi_b$ azimuthal steps per rotor revolution, the number of vortex segments in each wake turn is $N_{\psi_w} = N_{\psi_b} = N$. Therefore, the number of Biot–Savart calculations required is $N_b\, N_{\psi_b}\, N_{\psi_w}^2 = N_b\, N^3$. (Without periodicity assumptions this becomes $N_b^2 N^3$.) Velocity field interpolation reduces the effective number of Biot–Savart calculations by using both "free" and "pseudo-free" Lagrangian markers. For the case where $\Delta\psi_w > \Delta\psi_b$, the induced velocities are calculated explicitly only at the free Lagrangian markers spaced at $\Delta\psi_w$, and by linear interpolation of the velocity field at the pseudo-free markers. Therefore, the number of Biot–Savart evaluations is decreased by a factor corresponding to the ratio of the discretization $\Delta\psi_w/\Delta\psi_b$. For example, with $\Delta\psi_w = 2\Delta\psi_b$ the number of Biot–Savart calculations is reduced by a factor of 4 to $(N_b\, N^3)/4$. In a time-marching approach this interpolation scheme is applied after each time-step, whereas using the relaxation algorithm the interpolation is applied over the entire domain with a wake iteration.

In addition to the overall lower cost of a relaxation algorithm, another advantage is that azimuthal interpolation can be used where $\Delta\psi_b > \Delta\psi_w$. The basic approach is similar to that described for vortex filament interpolation, the difference being that the interpolation is performed at a constant vortex age along the blade azimuth. This results in a computational saving of a factor of $\Delta\psi_b/\Delta\psi_w$ in the number of Biot–Savart velocity evaluation points. However, the total number of wake markers remains unchanged. For example, with $\Delta\psi_b = 2\Delta\psi_w$ times the number of Biot–Savart calculations is reduced by half to $(N_b\, N^3)/2$. The blade attachment boundary condition (i.e., the first Lagrangian marker) needs special treatment. Azimuthal interpolation, however, is a redundant acceleration technique for the time-marching approach (see Section 10.8.4) because it is always necessary to use small time (azimuthal) steps to preserve accuracy in time.

Numerical Characteristics of Free-Wake Models

The advantage of using an implicit or pseudo-implicit FVM is that many of the numerical and round-off error problems associated with explicit methods can be avoided. Typical convergence characteristics of an explicit and a pseudo-implicit FVM are shown in Fig. 10.36 for a relatively low advance ratio of 0.05, where the self- and mutually induced

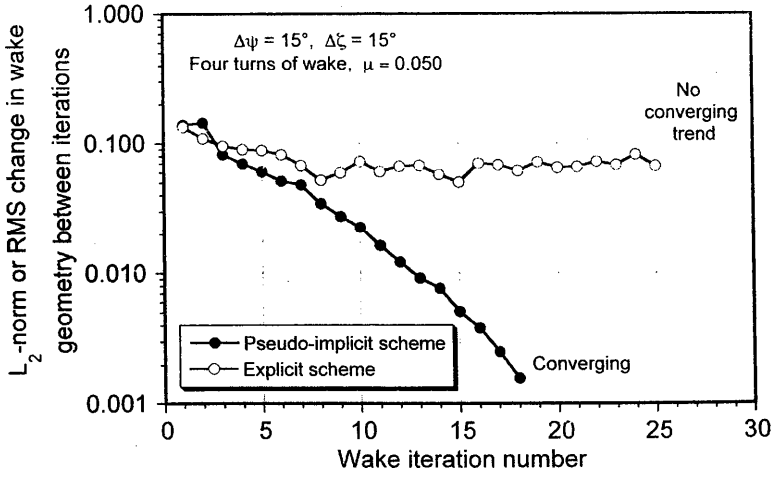

Figure 10.36 Free-vortex wake convergence characteristics for explicit and pseudo-implicit free-vortex wake schemes. Four turns of free-vortex wake, with $\mu = 0.05$, $C_T = 0.008$, and $\alpha_s = -6°$.

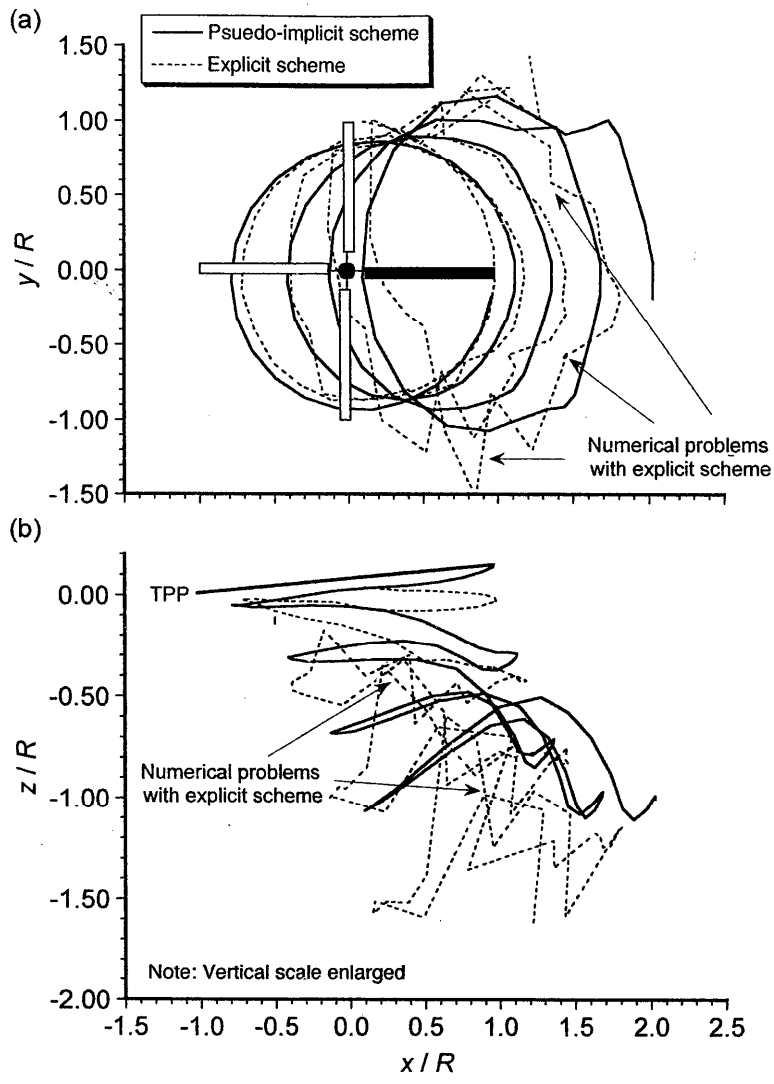

Figure 10.37 Tip vortex geometry predictions using explicit and pseudo-implicit free-vortex wake schemes, with $\mu = 0.05$, $C_T = 0.008$, and $\alpha_s = -6°$. (a) Top view. (b) Side view. Four-bladed rotor, with results for only one blade shown for clarity.

effects from the tip vortices are strong. In each case, four complete turns of the free-vortex wake were used with a relatively coarse 15° azimuth step ($\Delta\psi_b = \Delta\psi_w = 15°$).[6] The explicit scheme initially shows a converging trend, but only reaches a minimum error of about 0.05 after eight iterations. Further iterations cause numerical oscillations in the wake geometry and thereafter slowly drive the solution unstable. In contrast, the pseudo-implicit method essentially shows a monotonically converging solution, which converges below an acceptable error threshold after about fifteen iterations.

A comparison of the corresponding wake geometries at the end of the iteration cycles is shown in Fig. 10.37. Notice that with the explicit scheme there are several regions of the wake where the numerical errors have propagated, and there are significant signs of developing

[6] This is probably the largest step size that will give a reasonable physical representation of the rotor wake problem without loss of numerical accuracy when using straight-line vortex filaments.

instabilities that, based on experimental studies of helicopter rotor wakes [e.g., Lehman (1968) and others], are clearly not of physical origin. These are undesirable characteristics of free-vortex wake schemes using explicit integration schemes that make them unsuitable for rotor flow field predictions.

General Numerical Trim Model

To conduct a validation of any wake model with experimental measurements, the rotor must be trimmed, and this requires an iterative procedure. For simplicity, only the rotor will be considered, but as shown in Section 4.14 the airframe must also be considered for a proper free flight trim simulation. Recall that the rotor aerodynamic response, in general, is a highly coupled function of the control inputs and rotor aerodynamic environment. Therefore, although rotor thrust is controlled by the application of collective pitch, the blade flapping response is also affected. Likewise, cyclic pitch inputs not only produce a change in blade flapping response, but in rotor thrust as well. This coupling is a result of the induced aerodynamic effects trailed into the rotor wake, and its effect on the angles of attack over the rotor disk. The procedure necessitates several trim iterations before a converged solution is obtained.

The updates to the rotor control inputs at each trim iteration can be found using a Newton–Raphson approach applied to a linearized system of coupled equations that relate the rotor response vector to the control vector. If the control input vector is denoted by $\vec{x}$, and the rotor response or output vector by $\vec{y}$, then

$$\vec{x} = \begin{Bmatrix} \theta_0 \\ \theta_{1c} \\ \theta_{1s} \end{Bmatrix} \quad \text{and} \quad \vec{y} = \begin{Bmatrix} C_T \\ \beta_{1c} \\ \beta_{1s} \end{Bmatrix}. \tag{10.97}$$

A first order Taylor expansion for the rotor response about $\vec{x}$ gives

$$\vec{y}(\vec{x} + \Delta\vec{x}) = \vec{y}(\vec{x}) + [J]\,\Delta\vec{x} + \cdots \quad , \tag{10.98}$$

where $\vec{y}(\vec{x} + \Delta\vec{x})$ is the rotor response as a result of the new control input vector $\{\vec{x} + \Delta\vec{x}\}$. Rearranging the terms in Eq. 10.98 gives

$$\Delta\vec{x} = \left[J^{-1}\right]\{\vec{y}(\vec{x} + \Delta\vec{x}) - \vec{y}\}, \tag{10.99}$$

where $\{\vec{y}(\vec{x} + \Delta\vec{x}) - \vec{y}\}$ is a response error vector that will be denoted by $\vec{\epsilon}(y)$. Hence, Eq. 10.99 can be written in the following compact form

$$\Delta\vec{x} = \left[J^{-1}\right]\vec{\epsilon}(y). \tag{10.100}$$

The matrix, $[J]$ is known as the *Jacobian* matrix of the dependent quantities (response variables) in terms of the control inputs, and in terms of constituent elements is given by

$$[J] = \frac{\partial y_i}{\partial x_j} = \begin{bmatrix} \frac{\partial C_T}{\partial \theta_0} & \frac{\partial C_T}{\partial \theta_{1c}} & \frac{\partial C_T}{\partial \theta_{1s}} \\ \frac{\partial \beta_{1c}}{\partial \theta_0} & \frac{\partial \beta_{1c}}{\partial \theta_{1c}} & \frac{\partial \beta_{1c}}{\partial \theta_{1s}} \\ \frac{\partial \beta_{1s}}{\partial \theta_0} & \frac{\partial \beta_{1s}}{\partial \theta_{1c}} & \frac{\partial \beta_{1s}}{\partial \theta_{1s}} \end{bmatrix}. \tag{10.101}$$

Notice that if the flight controls were uncoupled then $[J]$ would have been a diagonal matrix with no interdependency between either the rotor thrust and cyclic inputs or between the

blade flapping and collective input. However, because of the complex 3-D aerodynamic coupling at the rotor, the Jacobian is fully populated.

To solve Eq. 10.100 numerically, the Jacobian matrix must first be determined. The partial derivatives in Eq. 10.101 can be approximated using first-order forward differences. This is done by first computing the rotor response vector corresponding to an initial guess control input vector. Subsequently, each input is independently perturbed and the rotor response recomputed to provide all the elements of $[J]$. Although computationally expensive to evaluate, for most problems the Jacobian matrix does not need to be recomputed each time the rotor is trimmed. The control input correction or update vector, $\Delta\vec{x}$ can be readily determined by solving Eq. 10.100 using standard matrix methods. The rotor control inputs can then be updated. Usually, however, some degree of numerical damping must be provided to ensure monotonic convergence of the solution to within a specified tolerance in rotor thrust and rotor flapping response.

Comparisons of Vortex Wake Models with Experimental Data

To demonstrate some aspects of the predictive capabilities of free-vortex wake models, comparisons are now shown with experimentally determined wake geometries in hover and forward flight. Figure 10.38 shows a comparison of predicted and experimental wake boundaries at the longitudinal centerline of the rotor (see also Fig. 10.10). It can be seen that during the transition from hover to forward flight, there are significant changes to the wake geometry, and so these cases provide a good general test of the capabilities of any vortex wake model, free or prescribed.

In hover, the wake is (theoretically) axisymmetric: so the leading- and trailing-edge wake boundaries are identical. For a variety of reasons, this is not necessarily the case for the experimental measurements, but the overall differences are small. As the advance ratio is increased, note that the wake is quickly skewed back by the free-stream flow. Figure 10.38 shows that as the newer tip vortices at the front of the rotor disk move downstream, they are convected over the top of the following blade. As the vortices are convected further downstream, they begin to descend toward the TPP and are ultimately intersected by a blade producing a perpendicular type of BVI.

At the rear of the rotor disk, however, there is a higher downward induced velocity component, and the vortices remain well below the TPP. As a consequence, the wake skew angle at the rear of the disk is much smaller than at the leading edge of the rotor. It can also be seen from Fig.10.38 that while the free-vortex wake model shows a high sensitivity to small changes in advance ratio, the streamwise displacements are somewhat underpredicted compared to the experimental results. Some of these differences, however, can be attributed to experimental uncertainties in the measured data. Overall, the results from the free-vortex wake model are found to be in much better agreement with the measurements than are those of the rigid wake representation.

Further comparisons of the free-vortex wake model with measured tip vortex displacements in the x–z plane are shown in Figs. 10.39 and 10.40 for two advance ratios and for four longitudinal planes through the wake. The data have been taken from Ghee & Elliott (1995), who have measured the displacements of the tip vortices using a planar laser sheet technique. Data were measured at four longitudinal planes at $y/R = \pm 0.3$ and $y/R = \pm 0.8$. At the inner locations, some gaps occur in the measured data because the fuselage and rotor hub blocked access for flow visualization. Free-vortex wake predictions have been made using both a full-span vortex sheet, and just with the tip vortex alone. We see that for both advance ratios, the free-vortex wake prediction are in good agreement with the measured

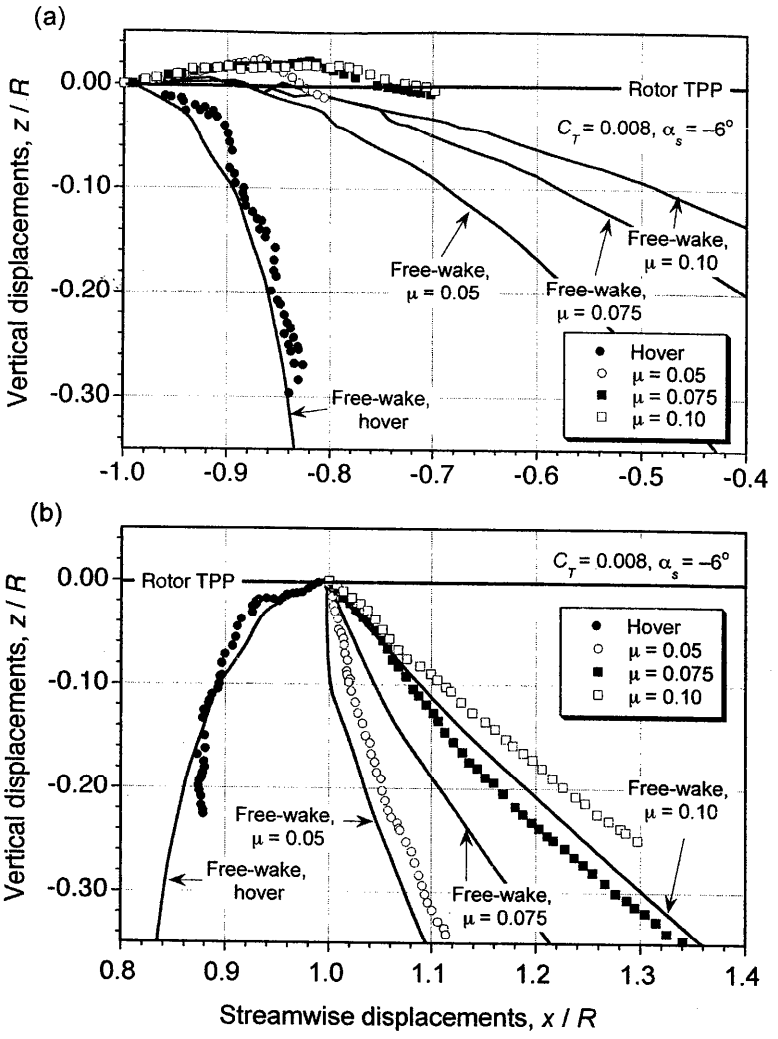

Figure 10.38 Predicted wake boundaries in hover and forward flight using free-vortex wake scheme compared to measured data. (a) Front of rotor. (b) Rear of rotor. Four-bladed rotor, with $C_T = 0.008$ and $\alpha_s = -3°$. Data source: Leishman & Bagai (1991).

tip vortex displacements. Clearly there are some difference between the predictions and experiment, but the overall quality of the results are good, bearing in mind the complexity of the physical problem. The effect of including a full-span wake compared to a single-tip vortex is relatively small, so its inclusion may not be justified given that the numerical cost of this approach is greater by about one order of magnitude. However, the inclusion of the inner wake sheet may be required to ensure proper predictions of rotor performance.

Figures 10.41 and 10.42 show the plan and rear views of the rotor wake at an advance ratio of 0.15. The tip vortex trajectories trailed from each blade have been plotted separately to ensure clarity. Again, the results are compared with the measured tip vortex displacements as the vortices intersect the four longitudinal planes. When viewed from above, the trajectories are relatively undistorted from their epicycloidal forms. It is only at the lateral edges of the wake that distortions occur because of the roll-up between individual vortices. The rear

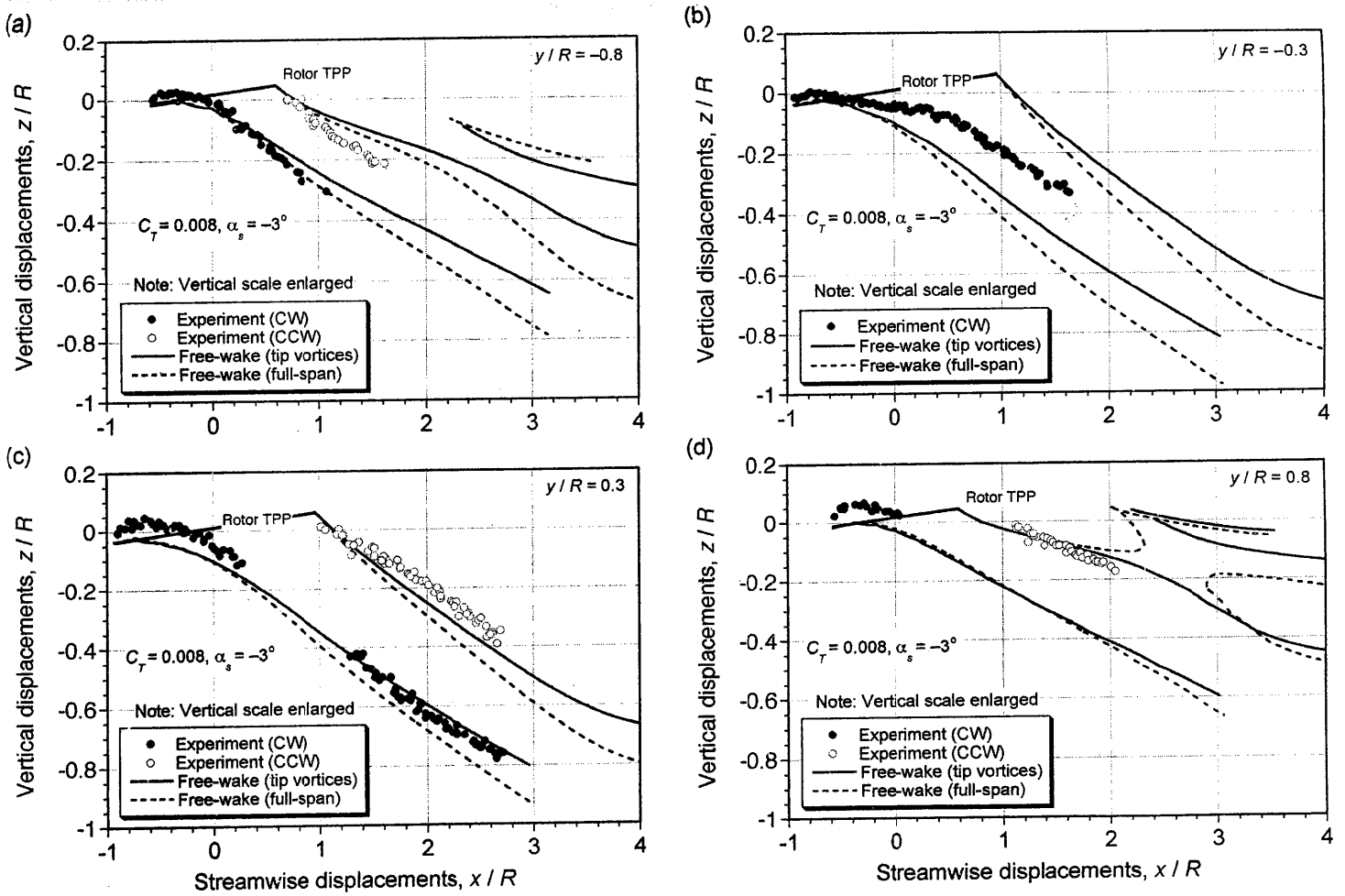

Figure 10.39 Predicted wake boundaries in forward flight compared to measurements. $\mu = 0.15$; $C_T = 0.008$; $\alpha_s - 3°$. (a) $y/R = -0.8$, (b) $y/R = -0.3$, (c) $y/R = 0.3$, (d) $y/R = 0.8$. Data source: Ghee & Elliott (1995).

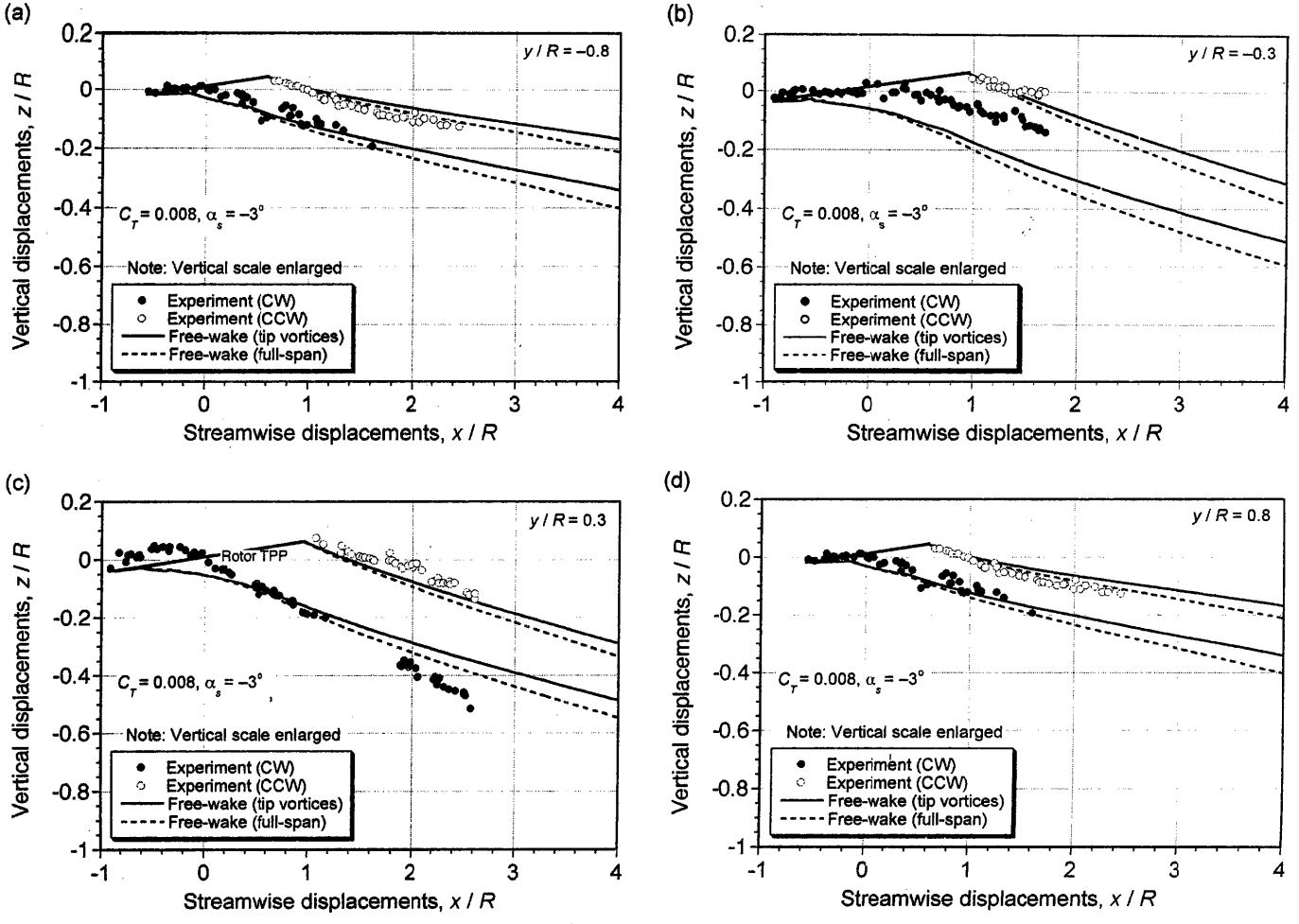

Figure 10.40 Predicted wake boundaries in forward flight compared to measurements. $\mu = 0.23$; $C_T = 0.008$; $\alpha_s - 3°$. (a) $y/R = -0.8$. (b) $y/R = -0.3$. (c) $y/R = 0.3$. (d) $y/R = 0.8$. Data source: Ghee & Elliott (1995).

(a) (b)

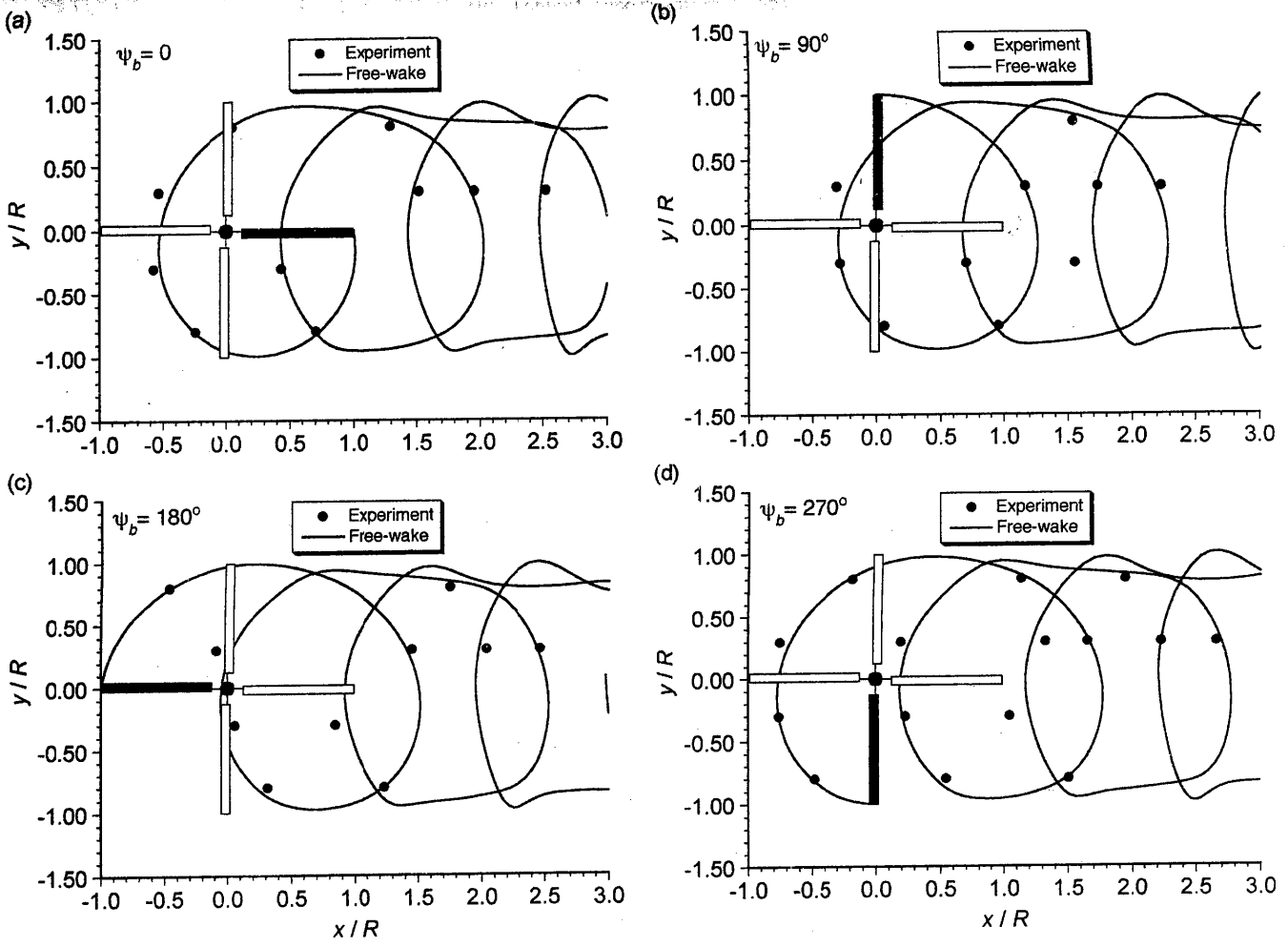

Figure 10.41 Predicted plan view of rotor tip vortex geometry compared to measurements. (a) $\psi_b = 0°$. (b) $\psi_b = 90°$. (c) $\psi_b = 180°$. (d) $\psi_b = 270°$; $\mu = 0.15$; $C_T = 0.008$; $\alpha_s - 3°$. Data source: Ghee & Elliott (1995).

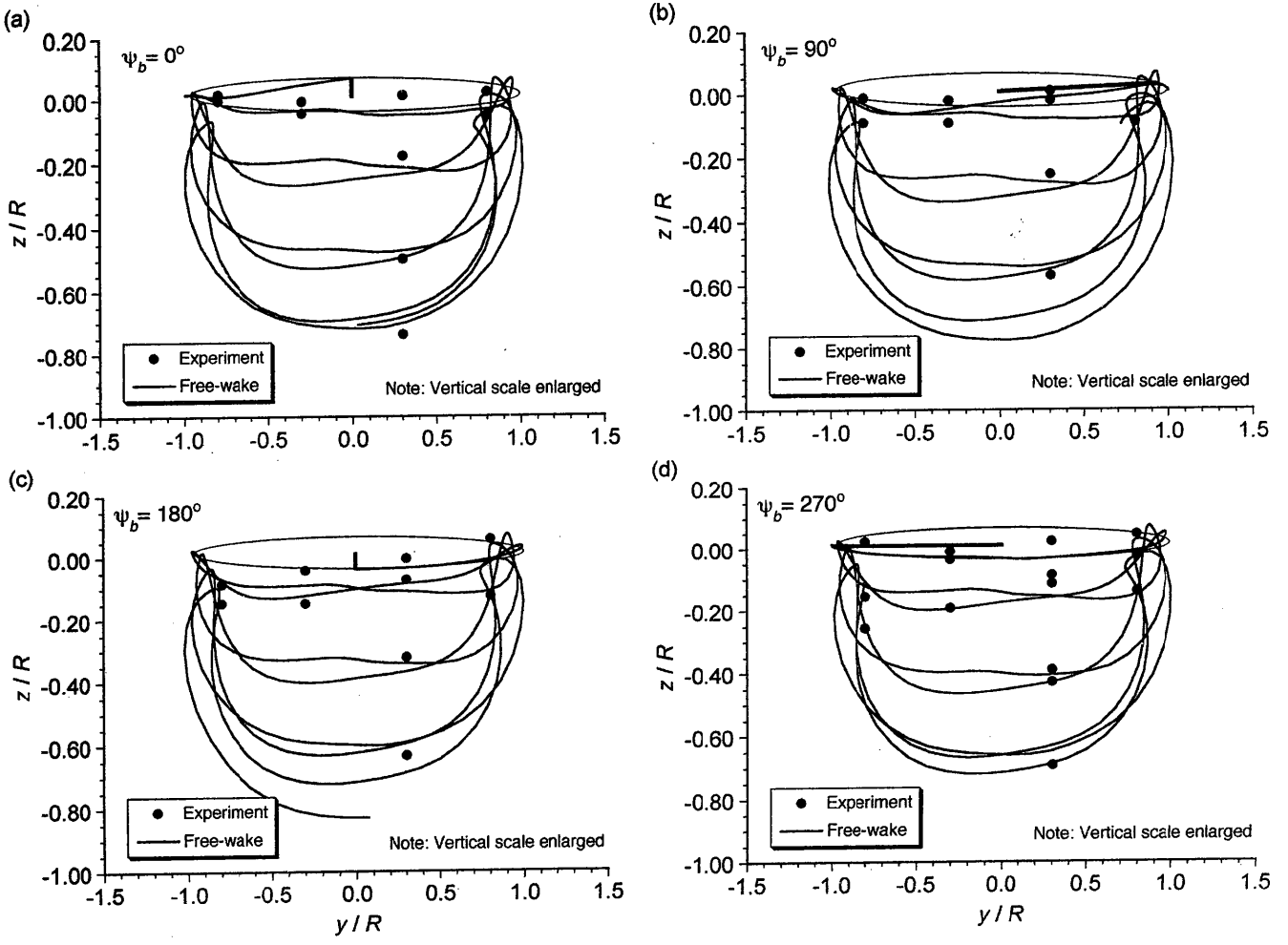

Figure 10.42 Predicted rear view of rotor tip vortex geometry compared to measurements. (a) $\psi_b = 0°$. (b) $\psi_b = 90°$. (c) $\psi_b = 180°$. (d) $\psi_b = 270°$. $\mu = 0.15$; $C_T = 0.008$; $\alpha_s - 3°$. Data source: Ghee & Elliott (1995).

views of the wake shown in Fig. 10.42 vividly show this roll-up process and the formation of vortex bundles or "super-vortices," a phenomenon previously mentioned in Section 10.4. In these regions, the small radius of curvature of the vortex filaments requires a relatively small levels of discretization; the present calculation has used $\Delta\psi_b = \Delta\psi_w = 5°$, and the good correlations obtained with the measured data in these regions confirms that, at least in this case, this is an adequate level of discretization.

10.8 Aperiodic Wake Developments

There are many applications in helicopter aerodynamics for which quasi-steady or periodic wake methods are unsuitable because the physics of the rotor wake cannot be assumed globally periodic. Such unsteady environments include rapid changes in pilot control inputs, some types of rotor wake–airframe interaction problems, flight operations near the ground, maneuvering flight conditions, autorotational flight, or when descending flight near the vortex ring state (VRS). These problems often result in various forms of disturbances in the wake that result in instabilities. The instabilities are aperiodic with respect to the rotor frequency, and so they can change fundamentally the physical structure of the rotor wake topology. Examples of wake perturbations that result in instabilities have been shown previously in Fig. 10.15. Furthermore, the rotor wake is often found to be aperiodic in hovering flight. This behavior has its source in natural instability modes of helicoidal vortex filaments.

Accurate simulations of these types of problems requires fully time-accurate wake methods, which raises substantially the complexity of the modeling. Of particular practical interest is the rotor behavior under maneuvering flight conditions, for which a fully adequate wake model continues to elude helicopter analysts. A maneuver often sets a limit to the normal flight envelope of a helicopter so the prediction of the rotor airloads under these conditions forms an important part of the design process (see Section 5.9). Under these conditions the pilot uses cyclic pitch control inputs to place the helicopter in a variety of nonsteady flow states. The wake develops in a time-dependent (aperiodic) manner, and the inflow through the rotor acquires a history or hereditary effect. This problem is similar to the unsteady airfoil problems discussed in Chapter 8, although for an entire rotor the problem is considerably more 3-D and clearly much more complex.

10.8.1 *Wake Stability Analysis*

The tendency of a helicopter rotor wake toward developing an instability is an inherent characteristic because of the naturally unstable deformation modes associated with its helicoidal form. Various aerodynamic disturbances inherent in nature, or physical disturbances associated with the manner in which the rotor is operated, usually provide the conditions necessary to excite the equilibrium wake geometry and cause it to exhibit perturbations. This problem has been examined theoretically by Levy & Forsdyke (1928), Widnall (1972), Gupta & Lowey (1974), and Bhagwat & Leishman (2000b). In particular, a local long-wave wake perturbation known as vortex "pairing," has already been mentioned in Section 10.5.2. This is a combined low-frequency/long-wavelength radial and axial deformation mode and has been observed in several rotor wake experiments, for example, Tangler et al. (1973), Martin et al. (1999), and Caradonna et al. (1999).

While wake instabilities seem common enough in experiments documenting rotor wakes, in computational modeling it is the omnipresent numerical truncation and round-off errors that potentially initiate wake instabilities. Properly distinguishing between the consequences

of physical and numerical wake instabilities has been a long-standing problem in helicopter aerodynamics. This problem was examined by Bhagwat & Leishman (2000b) using vortex theory and also by Martin et al. (1999) in rotor experiments designed to deliberately promote wake instabilities. A two-bladed rotor wake was shown to develop a primary mode of instability with a wave number at the rotational frequency of the rotor. This mode it seems, is relatively easy to excite in a real rotor flow field, such as by blade mistracking. The argument can be carried forth to rotors with greater numbers of blades, where the susceptibility to develop wake instabilities always increases with blade number. This fundamental characteristic behavior of rotor wakes is key to how various forms of physical wake instabilities actually arise in practice.

The stability of a rotor wake can be examined mathematically from a perturbation analysis. From the equilibrium solution for the wake, such as by using vortex theory, the solution is then perturbed by a small quantity, $\delta\vec{r}$, with the new geometry being described by $\vec{r} + \delta\vec{r}$. The governing equation for this perturbed wake geometry is given by

$$\frac{d(\vec{r} + \delta\vec{r})}{dt} = \mathbf{V}(\vec{r} + \delta\vec{r}). \tag{10.102}$$

The equation governing the perturbation wake displacement, $\delta\vec{r}$, is obtained by subtracting the equilibrium equation from the perturbed equation (Eq. 10.102) giving

$$\frac{d(\delta\vec{r})}{dt} = \vec{V}(\vec{r} + \delta\vec{r}) - \vec{V}(\vec{r}). \tag{10.103}$$

The induced velocity on the RHS of Eq. 10.102 can be expressed as a Taylor series in $\delta\vec{r}$ as

$$\vec{V}(\vec{r} + \delta\vec{r}) = \vec{V}(\vec{r}) + \delta\vec{V}(\delta\vec{r}) + O\left(\delta\vec{r}^2\right). \tag{10.104}$$

This can now be linearized by neglecting higher-order terms in $\delta\vec{r}$ to give

$$\frac{d(\delta\vec{r})}{dt} = \delta\vec{V}(\delta\vec{r}), \tag{10.105}$$

which is the equation governing the perturbation problem.

For the solution of Eq. 10.105, perturbations to the wake can be assumed to be in the form of a normal mode (or a traveling wave) along the lengths of the vortex filaments – see Saffman (1992) and Bhagwat & Leishman (2000b). Because of the helicoidal nature of the rotor wakes, cylindrical polar coordinates can be used. In this case the normal mode perturbation is given by

$$\left\{\delta\vec{p}\right\} = \begin{Bmatrix} \delta r_0 \\ \delta\theta_0 \\ \delta z_0 \end{Bmatrix} e^{\alpha t + i\omega\zeta}, \tag{10.106}$$

where α is the growth rate and ω is the wave number, that is the perturbation wave has ω cycles for each rotor revolution. The governing equations for each perturbation mode can then be solved at a given point P on the vortex filament. The velocity contributions of all the vortex elements are summed using the Biot–Savart law to obtain the total induced velocity perturbation in matrix form as $[V] = \sum_i [v_i]$. After some manipulation, the problem can be reduced to a standard eigenvalue problem with the form

$$\alpha_P\{x\} = [M]_P\{x\}, \tag{10.107}$$

where M is the fundamental solution matrix for the wake, the evaluation of which is completely described by Bhagwat & Leishman (2000b). The eigenvalues α_P give the growth

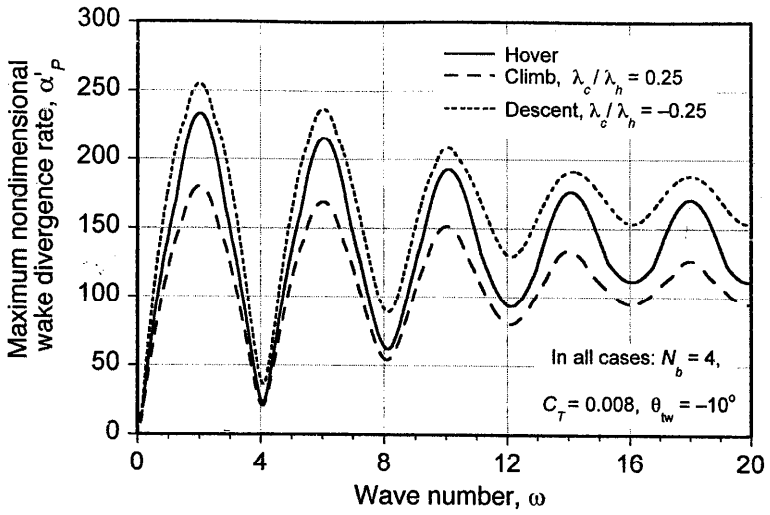

Figure 10.43 Maximum nondimensional wake divergence rates as a function of wave number ω for a four-bladed rotor in axial flight (hover, climb, and descent).

rate of the perturbation at a point P on the vortex wake. A positive growth corresponds to an unstable wake mode, a zero growth rate is a neutrally stable wake mode, and a negative growth rate is a stable wake mode.

The advantage of this type of mathematical approach is that the fundamental stability of the rotor wake can be understood in terms of its characteristics (shape and circulation strengths) and, therefore, how the stability of the wake is affected by the various geometric and operational characteristics of the rotor. For example, climbing or descending flight changes significantly the helicoidal pitch of the rotor wake structure, and so this must affect the overall wake stability. The rotor thrust (disk loading) and blade twist are also known to be factors that affect the stability of the rotor wake.

Figure 10.43 shows an example of the stability characteristics of a rotor wake in axial flight. The wave numbers corresponding to the extrema in the wake divergence rates correlate with the number of interdigitated tip vortex filaments (or blades). On one hand, the maximum divergence rate occurs at wave numbers equal to half-integer multiples of the number of blades, that is, at wave numbers $\omega = (k + 1/2)N_b$ for all integer k. On the other hand, a minimum divergence rate occurs at integer multiple of the number of blades, that is for $\omega = k\,N_b$. With increasing wave number, the difference between maximum and minimum divergence rates decreases, indicating that for very large wave numbers the divergence rates would be independent of wave number. However, the increasing growth rates for large wave numbers with increasing number of filaments suggests an increased overall susceptibility to wake instabilities, say those that might be produced by random disturbances or turbulence in the flow.

This figure also shows that a climb velocity decreases the wake growth rates (i.e., the wake is less susceptible to instability and to forming wake perturbations). This is because of the increased helicoidal spacing between adjacent wake filaments. The results in Fig. 10.43 also show that for the descending rotor a more substantial increase in growth rates are obtained for wake modes at the *higher* wave numbers. This implies an increased susceptibility to instability and to forming wake perturbations in descending flight. These might be triggered by the higher-frequency unsteady airloads generated at the rotor, or by atmospheric turbulence, rather than by larger-scale disturbances in the surrounding flow. This

observation may be key to the full understanding of the initiation mechanisms of wake instabilities. However, it may also prove to be an impediment to the achievement of reliable numerical predictions for rotor wakes under various descending flight conditions because of the need to model the source of these disturbances.

10.8.2 *Flow Visualization of Transient Rotor Wake Problems*

There are only a few experiments that have visualized the wake evolution of a helicopter rotor under nonsteady or transient operating conditions. The first was conducted by Taylor (1950) for a rotor with fixed collective pitch being impulsively started from rest. The balsa dust technique was used to seed the flow, which was illuminated by a light source. Figure 10.44 shows two images of the developing wake structure in a plane in the wake that intersects the rotor axis just shortly after the rotor was started. Of interest is that the wake shows evidence of a transient starting flow in the form of a vortex ring. This vortex ring is analogous to a starting vortex system for a wing set into rectilinear motion or undergoing a sudden change in angle of attack (i.e., the Wagner problem discussed in Section 8.10).

Results showing the formation vortex rings in a rotor wake were given by Carpenter & Friedovich (1953) for rapid increases in blade collective pitch and are also shown by Jessurun et al. (2001) for both rapid collective and cyclic pitch inputs. An example is shown in Fig. 10.45 from the work of Carpenter & Friedovich (1953), where it is apparent that the individual tip vortices pair-off in the wake below the rotor during the initial stages of wake development and soon form into coherent bundles of almost toroidal rings of concentrated vorticity. Just after the collective pitch input is applied the tip vortices can only convect relatively slowly away from the rotor because of the initially low thrust and low induced inflow. Therefore, the tip vortices initially lie in close proximity to each other, and their respective induced velocities create a tendency for them to pair about each other. This pairing tendency is the main reason for the formation of a ring of bundled vorticity immediately below the rotor plane.

After the wake begins to develop and the inflow through the rotor increases, the newer trailed vortices begin to convect in a relatively higher wake velocity, and the starting ring is convected further down in the wake below the rotor. These vortex rings are present in

(a) Early time after impulsive start with vortex ring development

(b) Later time, where the ring convects below the rotor.

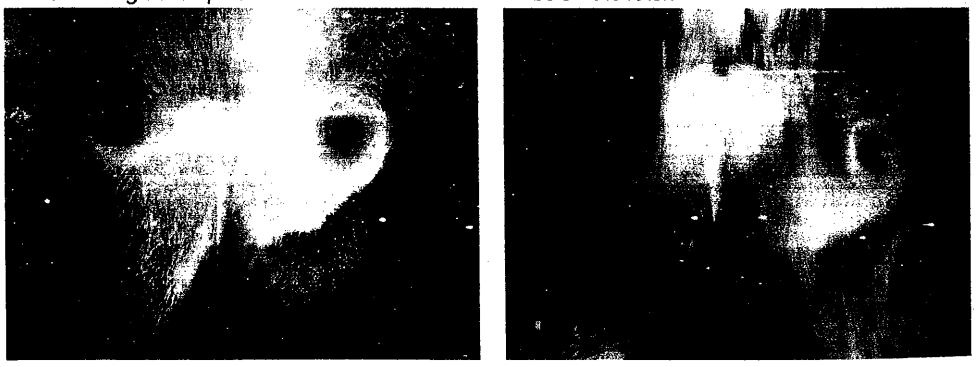

Figure 10.44 Flow visualization image in a vertical plane through the rotor axis documenting the formation of a vortex ring in the wake below an impulsively started hovering rotor. (a) Early time just after impulsive start and vortex ring development. (b) Later time, where the ring convects below the rotor. Source: Taylor (1950).

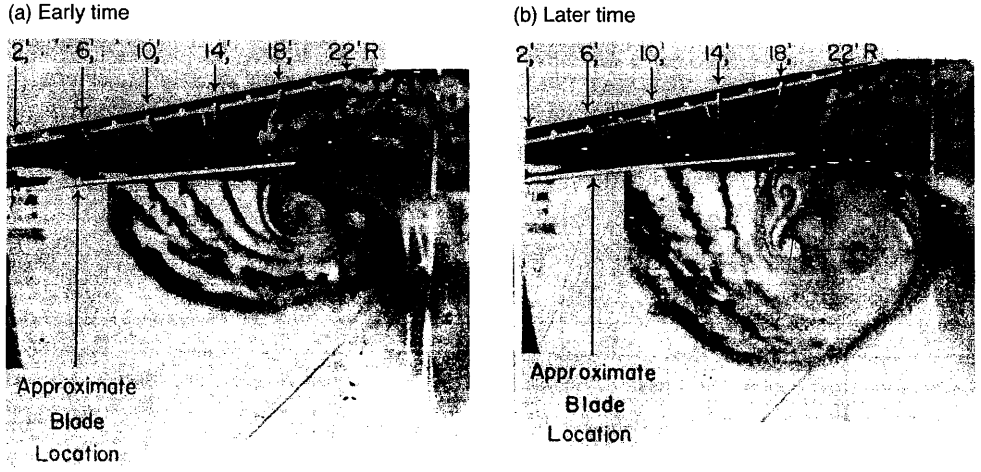

Figure 10.45 Flow visualization images in a vertical plane through the rotor axis showing that pairing of individual tip vortices gives rise to the starting vortex ring. (a) Early time. (b) Later time. Source: Carpenter & Friedovich (1953).

the rotor wake for several subsequent rotor revolutions and can have a substantial effect on the overall time-history of the resulting wake developments, the developing inflow, and on the blade airloads. Also apparent from the various flow visualization studies that these starting rings of vorticity begin to break down as they are convected further away from the rotor. This suggests that the accurate modeling of close vortex filament interactions as well as the time accuracy of the problem will be critical in establishing good predictions of the overall rotor airloads when the flight controls are being manipulated under maneuvering flight conditions.

10.8.3 *Dynamic Inflow*

The forgoing description of a physical behavior forms a fundamental basis for the development of nonsteady (and perhaps aperiodic) wake models. Carpenter & Friedovich (1953) attributed the buildup of the mean rotor inflow and rotor thrust to inertia effects in the flow. To model this behavior, a dynamic inflow equation was formulated by equating the rotor thrust obtained using differential momentum theory to that using blade-element theory (i.e., the BEMT discussed in Chapter 3). Unsteady inflow effects were modeled using the concept of an apparent mass (inertia), where the thrust equation (as given by the momentum theory in Chapter 2) is modified by the addition of an unsteady term to give

$$T = m_a \dot{v}_i + 2\pi R^2 \rho v_i \left(v_i + \frac{2}{3} \dot{\beta} R \right). \tag{10.108}$$

The term m_a was associated by Carpenter & Friedovich (1953) with the apparent mass of an impermeable (solid) circular disk accelerating in a stagnant fluid, that is, a noncirculatory effect. It was further suggested that this apparent mass to be 63.7% the mass of a sphere of fluid with a radius equal to the rotor radius, that is,

$$m_a = 0.637\rho \left(\frac{4}{3} \pi R^3 \right). \tag{10.109}$$

The $m_a \dot{v}_i$ term, therefore, is meant to represent the additional reaction force on the rotor disk because of the accelerating inflow. However this concept assumes an equivalence between the force on a solid disk accelerating in a stagnant fluid and the force on a fluid accelerating through a permeable actuator disk. Such an equivalence is certainly not rigorous but the derivation can proceed on this basis. Using the blade element theory (see Section 3.3), the elemental thrust including blade flapping is given by

$$dT = \frac{1}{2} N_b \rho c C_{l_\alpha} \left(\theta - \frac{v_i(r)}{\Omega r} - \frac{\dot{\beta}}{\Omega} \right) \Omega^2 r^2 dr. \tag{10.110}$$

Assuming a rectangular blade planform (i.e., $c(r) = c$) and uniform inflow (i.e., $v_i(r) = v_i$) the total rotor thrust can be found by integrating the above equation to get

$$T = \int_0^R dT = \frac{1}{6} N_b \rho c C_{l_\alpha} \Omega^2 R^3 \left(\theta - \frac{3}{2} \frac{v_i}{\Omega R} - \frac{\dot{\beta}}{\Omega} \right). \tag{10.111}$$

Equating the two thrust expressions (Eq. 10.108 and 10.111), an equation governing the dynamic inflow through the rotor can be derived. Notice that the inflow dynamics is coupled with the blade flapping dynamics, and a second equation governing the blade flapping angle can be found by moment equilibrium about the flapping hinge, as described previously in Chapter 4. In nondimensional form Eq. 10.111 becomes

$$C_T = \frac{m_a}{\rho \pi R^3} \overset{\star}{\lambda} + 2\lambda_i \left(\lambda_i + \frac{2}{3} \overset{\star}{\beta} \right) = \frac{1}{2} \sigma C_{l_\alpha} \left(\frac{\theta}{3} - \frac{\lambda_i}{2} - \frac{\overset{\star}{\beta}}{3} \right). \tag{10.112}$$

Therefore, the governing equation for the inflow dynamics can be written as

$$\frac{m_a}{\rho \pi R^3} \overset{\star}{\lambda_i} = \frac{1}{2} \sigma C_{l_\alpha} \left(\frac{\theta}{3} - \frac{\lambda_i}{2} - \frac{\overset{\star}{\beta}}{3} \right) - 2\lambda_i \left(\lambda_i + \frac{2}{3} \overset{\star}{\beta} \right). \tag{10.113}$$

This latter equation must be solved together with the blade flapping equation of motion. In the case without flapping the thrust on the rotor can now be written as the modified simple momentum equation

$$T = 0.637 \rho \frac{4}{3} \pi R^2 \dot{v}_i + 2\rho A v_i^2, \tag{10.114}$$

or in coefficient form this equation can be written as

$$C_T = \frac{0.637(4/3)}{\Omega} \dot{\lambda}_i + 2\lambda_i^2 = \frac{0.849}{\Omega} \dot{\lambda}_i + 2\lambda_i^2. \tag{10.115}$$

To determine the approximate time constant of the developing flow, Eq. 10.115 can be linearized about a mean operating state using $\lambda_i = \bar{\lambda}_i + \delta\lambda_i$ and $C_T = \bar{C}_T + \delta C_T$, which after simplification and neglecting terms of $O(\delta\lambda_i)^2$ gives

$$\left(\frac{0.849}{4\Omega\bar{\lambda}_i} \right) \delta\dot{\lambda}_i + \delta\lambda_i = \left(\frac{1}{4\bar{\lambda}_i} \right) \delta C_T. \tag{10.116}$$

This is an ODE that relates the change in inflow, $\delta\lambda_i$, to the change in rotor thrust, δC_T. The time constant of this dynamic system is

$$\tau_\lambda = \frac{0.849}{4\bar{\lambda}_i \Omega}, \tag{10.117}$$

For a typical helicopter rotor where $\bar{\lambda}_i \approx 0.05$ and $\Omega \approx 40$ rad/s, τ_λ will be of the order of 0.1 seconds. The dynamic adjustments that take place in the time averaged inflow are, therefore, relatively rapid in real time. However, it will be noted that a time lag of 0.1 seconds corresponds to over half a rotor revolution, so at the local (blade element) level the local adjustments to the flow do, in fact, occur over relatively long aerodynamic time scales in terms of wake age or semi-chords of blade travel.

10.8.4 *Time-Marching Free-Vortex Wakes*

Time-marching free-vortex methods potentially offer one of the best levels of approximation to the rotor wake problem, and also with the fewest restrictions in application. In a time-marching algorithm the time evolution of the position vectors of each wake Lagrangian marker can be expressed by

$$\frac{d\vec{r}(d\psi_b, \psi_w)}{\Omega\psi_b} = D_{\psi_w} + \vec{V}\left(\vec{r}(\psi_b, \psi_w)\right)\Big|_{\text{discrete}} = F\left(\vec{r}(\psi_b), \psi_b\right). \tag{10.118}$$

As shown previously in Section 10.7.3 a second-order, five-point central difference approximation can be used to find the spatial (ψ_w) derivative, and the right-hand side of Eq. 10.118 can be represented discretely as $F\left(\vec{r}(\psi_b), \psi_b\right)$. Time-marching algorithms can also take advantage of the numerical improvements produced by a predictor–corrector sequence. Although any initial wake geometry can be specified from which to march the solution, the initial or starting induced velocity field is usually a relaxation solution. This helps minimize nonphysical transients (and numerical costs) associated with defining the initial condition. Unfortunately time-marching methods have proven susceptible to instabilities resulting from the initiation of numerical microstructures [see Bhagwat & Leishman (2000b, 2001a)], thereby reducing the confidence that a physically realistic wake solution has been obtained. Properly distinguishing between the known physical instabilities of rotor wakes and those that are numerical in origin have proven to be a major hindrance in the development of reliable and robust time-accurate vortex wake models for helicopter rotor applications.

Bhagwat & Leishman (2001a) have used a five-point central difference scheme for both the spatial derivative and the temporal derivative in Eq. 10.54 during the predictor step, and a five-point central difference scheme for the spatial derivative and a three-point second-order backward difference scheme for the temporal derivative in the corrector step. This stencil is then swept over the computational domain – see Fig. 10.46. A Taylor's series expansion, around the cell evaluation point shows that leading terms in the expansions of the difference approximations are $O(\Delta\psi_b^2)$ and $O(\Delta\psi_w^2)$, so the time-marching approximation is second-order accurate in both space ψ_b and time ψ_w.

10.8.5 *Simulation of Carpenter & Friedovich Problem*

The time-marching free-vortex wake model can be applied to compute the evolution of the vortical wake structure for the Carpenter & Friedovich (1953) problem, as described in Section 10.8.2. Representative results are shown in Fig. 10.47 at selected times after the collective pitch input was applied. It is apparent that the trailed vortices initially pair off and bundle up below the rotor to form a vortex ring, as shown previously by the flow visualization images in Figs. 10.44 and 10.45. Immediately after the collective pitch input is applied the vortices trailed from the blade tips convect only relatively slowly away from the rotor because of the initially low thrust and low induced inflow through the rotor. In fact,

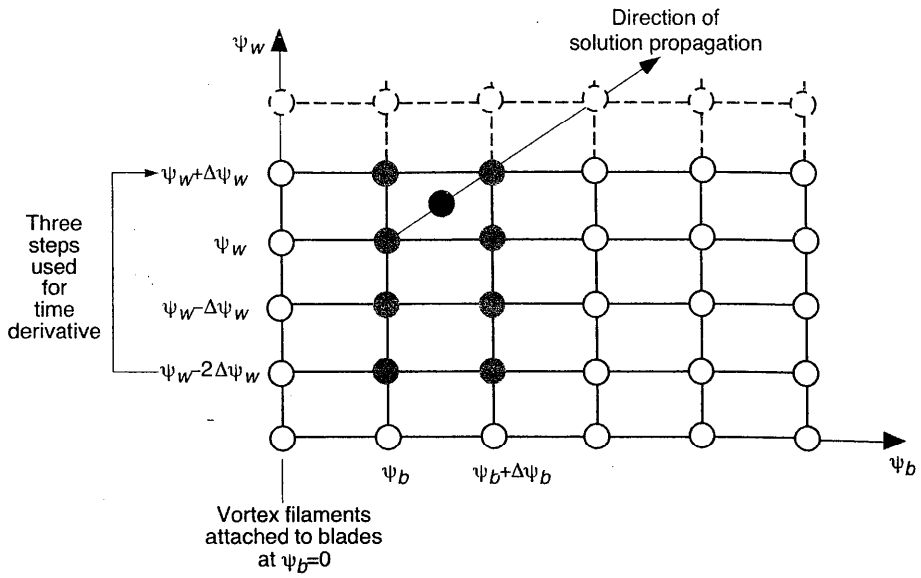

Figure 10.46 Discretized computational domain for time-marching free-vortex wake problem.

by comparing the helicoidal pitch of the computed wake at early times versus later times in each case, it is apparent that the net inflow through the rotor builds up only relatively slowly over several rotor revolutions. Initially, therefore, the tip vortices lie in close proximity to each other, and their respective induced velocities create a tendency for them to pair about each other. This pairing tendency is clearly the main reason for the formation of a ring of bundled vorticity immediately below the rotor plane.

After the wake begins to develop and the inflow through the rotor increases, the newer trailed vortices begin to convect in a relatively higher wake velocity, and the starting ring is convected further down in the wake below the rotor. Notice that in each case the starting vortex structure is unstable and begins to show the presence of pronounced sinusoidal deformation modes or Kelvin waves (see Section 10.5.2). These waves grow in amplitude with time, and eventually cause the initial starting ring vortex system to break down as it convects into the far wake below the rotor. As the rotor induced inflow then approaches a steady-state value, the vorticity associated with the vortex ring is convected downstream well away from the rotor blades. After about 4–6 rotor revolutions (although this depends on the time rate of change of collective pitch), this starting wake has been convected about one and a half rotor radii below the rotor. At this point, any wake perturbations have been convected sufficiently far away from the rotor such that their influence on the rotor aerodynamics becomes small. The rotor wake then approaches a steady-state (periodic) condition with the vortex wake structure then taking on its more characteristic helicoidal form.

Figure 10.48 shows the predicted results of the rotor thrust for three values of the collective pitch rate (20, 48, and 200° per second) along with Carpenter & Friedovich's measurements. In each case, the predicted time-history of the rotor thrust response using either the dynamic inflow or free-vortex wake method shows good agreement with the experimental measurements. Notice that there is a lag in the development of the rotor thrust, which builds up and reaches its final value in about 2 to 4 rotor revolutions, depending on the collective pitch input rate. The intermediate values of the thrust show significant overshoots before

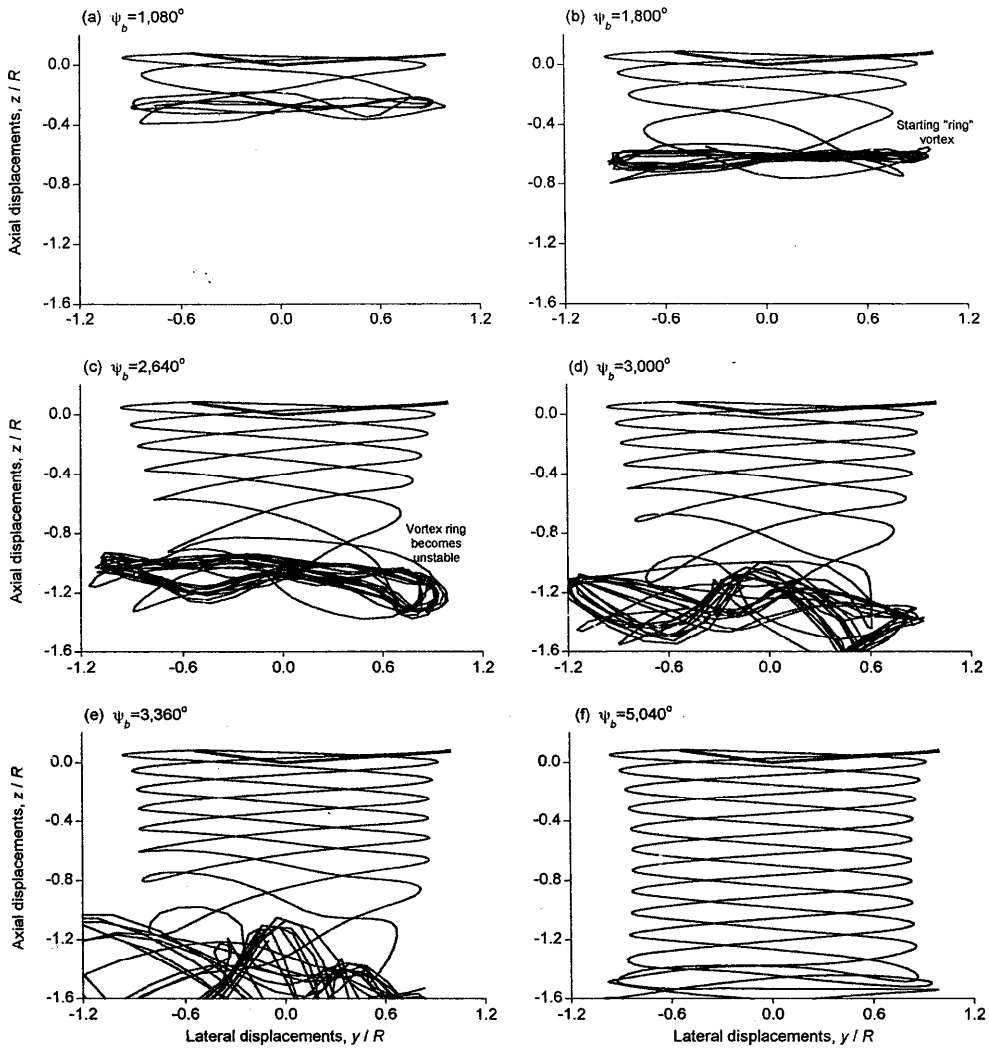

Figure 10.47 Free-vortex wake evolution for a hovering rotor undergoing a ramp change in collective pitch at 200°/sec. (a) $\psi_b = 1080°$. (b) $\psi_b = 1800°$. (c) $\psi_b = 2640°$. (d) $\psi_b = 3000°$. (e) $\psi_b = 3360°$. (f) $\psi_b = 5040°$.

settling down to their final values. For the highest ramp rate of 200 deg/s, the thrust overshoot is about twice the steady-state value, confirming the significant effects of transient blade pitch inputs on the overall rotor wake evolution and blade airloads. Remember that the physics of this problem and the reasons for the lift overshoots is governed mainly by the temporal evolution of the vorticity trailed into the rotor wake, so that the lag in inflow development through the rotor is really a circulatory effect.

10.9 General Dynamic Inflow Models

In many cases it is desirable to directly account for unsteady effects on net rotor forces and pitching moments. While the localized unsteady aerodynamic effects are clearly complicated, for some problems it is useful to seek a more global approach to modeling their

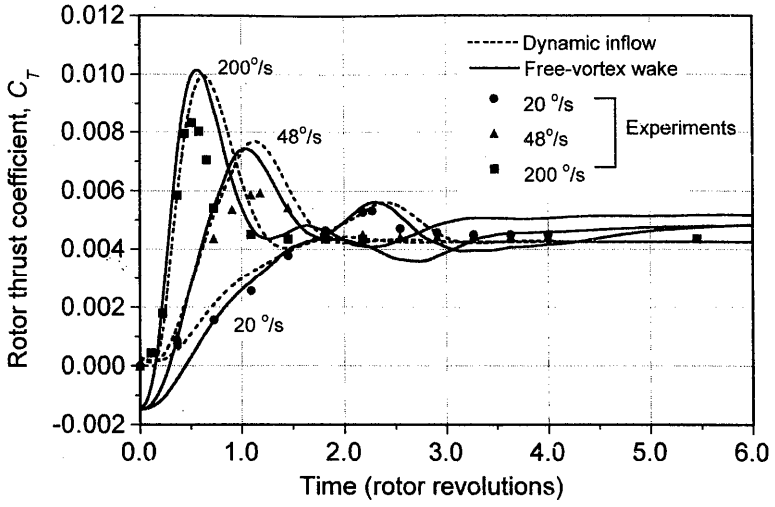

Figure 10.48 Time varying rotor thrust for a ramp change in collective pitch at 20, 48 and 200 degrees/sec using dynamic inflow and free-vortex wake methods. Measurements from Carpenter & Friedovich (1953).

effects. This comes under the classification of dynamic inflow or so-called *finite-state wake models*. The principles range back to those of the steady inflow model used by Mangler & Squire – see Section 3.5.2. The idea in the dynamic inflow model is that the effects of the wake can be represented as a set of ODEs, that is, in state-space form. Consider, for example, a maneuver, where the unsteady effects will cause the inflow through the rotor to be different from that produced under steady level flight conditions. This will change the rotor forces and pitching moments, and so the rotor flapping response will be affected. See also Curtiss & Shupe (1971). The essence of these ideas can be attributed to Sissingh (1952), Carpenter & Friedovich (1953) and Joglikar & Loewy (1970), but many variations of the dynamic inflow theory and applications thereof have appeared in the literature. Crews et al. (1973), Ormiston (1976), Peters (1974), and Curtiss (1986) have put forth variations of the dynamic inflow theory and have showed that the effects can have an influence on rotor response and various problems in rotor dynamics and aeroelasticity. The most popular model of dynamic inflow is that of Pitt & Peters (1983), which has seen several applications in the literature – see Gaonkar & Peters (1986a,b) and Peters & HaQuang (1988). The ideas can also be extended to represent unsteady effects on 2-D airfoils – see Peters & He (1995).

Momentum theory can be used to relate the aerodynamic forces and pitching moments on the rotor to the inflow across the disk (see Chapter 2). The thrust, T, can be represented by the integral of the change in momentum through the rotor disk, that is,

$$T = 2\rho \int_0^R \int_0^{2\pi} v^2 r \, d\psi \, dr, \tag{10.119}$$

where v is the inflow velocity. Similarly, the pitching moment (positive nose-up) will be given by

$$M_y = -2\rho \int_0^R \int_0^{2\pi} v^2 r^2 \cos\psi \, d\psi \, dr \tag{10.120}$$

and the rolling moment (positive roll to starboard) is given by

$$M_x = -2\rho \int_0^R \int_0^{2\pi} v^2 r^2 \sin\psi \, d\psi \, dr. \tag{10.121}$$

A key assumption is the form of the inflow distribution over the rotor disk. As Section 3.5.2 has shown, a popular assumption is to use a linear distribution of the form

$$v = v(r, \psi) = v_0 + v_c r \cos\psi + v_s r \sin\psi, \tag{10.122}$$

where v_0, v_c, and v_s are the uniform, longitudinal, and lateral contributions to the inflow, respectively. This allows a coupling of the rotor thrust and pitching moments to the induced velocity field. This can be written in matrix form as

$$\begin{Bmatrix} v_0 \\ v_c \\ v_s \end{Bmatrix} = [L] \begin{Bmatrix} C_T \\ C_{M_y} \\ C_{M_x} \end{Bmatrix}_{\text{aero}}, \tag{10.123}$$

where $[L]$ is a coupling or "gain" matrix. The subscript "aero" implies that only aerodynamic contributions are to be included; rotor inertial terms are omitted. In a local momentum analysis of the problem, the $[L]$ matrix is a diagonal matrix, where v_0 is related to C_T, v_c is related to C_{M_y}, and v_s is related to C_{M_x}. These relations, however, may be coupled and the matrix will be fully populated. In forward flight, the coefficients in the gain matrix also become functions of the wake skew angle. Gaonkar & Peters (1986a,b) review the development of the gain matrix, although it appears that more experimental verification may be required to validate the assumptions made.

The ideas of a time lag in the development of the wake are introduced through the use of a time constant matrix $[\tau] = [L][M]$, where $[M]$ is a matrix of unsteady terms. The dynamic inflow model is now written as

$$[\tau] \begin{Bmatrix} \dot{v}_0 \\ \dot{v}_c \\ \dot{v}_s \end{Bmatrix} + \begin{Bmatrix} v_0 \\ v_c \\ v_s \end{Bmatrix} = [L] \begin{Bmatrix} C_T \\ C_{M_y} \\ C_{M_x} \end{Bmatrix}_{\text{aero}}, \tag{10.124}$$

or

$$[M] \begin{Bmatrix} \dot{v}_0 \\ \dot{v}_c \\ \dot{v}_s \end{Bmatrix} + [L]^{-1} \begin{Bmatrix} v_0 \\ v_c \\ v_s \end{Bmatrix} = \begin{Bmatrix} C_T \\ C_{M_y} \\ C_{M_x} \end{Bmatrix}_{\text{aero}}. \tag{10.125}$$

These ODEs can be used to relate the unsteady inflow to the rotor thrust and pitching moments. The time constants are also functions of the wake skew angle, which are derived from vortex theory. In the complete problem, the equations of motion of the blades must be introduced using a blade element approach. This provides the complete relationship between the blade loads, the rotor inflow, and rotor response.

Many refinements of the basic dynamic inflow approach can be found in the literature. The coupling and time-constant matrices have been derived from a number of other theories, including actuator disk and vortex theories. For extensive information on dynamic inflow modeling, see Johnson (1980). The most recent work on dynamic inflow has been put forth by Peters and colleagues – see Peters et al. (1987), Peters & HaQuang (1988), Peters & He (1989, 1995), Peters et al. (1995), and Morillo & Peters (2002). Their work also encompass the classical theories of Theodorsen (Section 8.7) and Loewy (Section 8.8).

Dynamic inflow models have found utility for various problems in rotor aeroelasticity, as well as for helicopter flight dynamics – see Chen (1989) and Padfield (1996). However,

the dynamic inflow model is limited in that it is fundamentally a linear model. Other new approaches toward the development of dynamic inflow models in state-space form have examined the transformation of the equations governing free-vortex wakes into a system of general ODEs – see Celi (2004). These "wake" ODEs can then be coupled to other equations describing other aspects of helicopter performance or behavior, or can be used to extract so-called "linearized" models for use in flight dynamics applications. Another such approach to the formulation of a wake model in state-space form using indicial theory is described by Johnson (1988).

10.10 Descending Flight and the Vortex Ring State

The problem of the vortex ring state (VRS) has already been discussed in Sections 2.13.6 and 5.7. VRS is a problem that is not amenable to solution (prediction) by methods such as momentum theory, and more advanced prediction methods must be sought. Developments of free-vortex and vorticity transport models (see Section 14.3) have recently allowed the problem of VRS to be examined in much more detail, and for the effects of flight condition and rotor geometry on the VRS problem to be better exposed – see Brown et al. (2002) and Newman et al. (2004). However, a primary difficulty in either approach is to faithfully model the tip vortices in the rotor wake to old ages, as well as the problem of modeling accurately the physics of vortex–vortex and blade–vortex interactions. Another difficulty is that the descending flight problem is inherently unsteady, so time-accurate methods of solution such as discussed in the previous section are a necessary prerequisite.

To illustrate the general behavior of the wake in descending flight, Fig. 10.49 shows views of a rotor wake that have been predicted using a FVM for a notional four-bladed rotor when transitioning from hover into axial descent. Six free-vortex turns were used to model the rotor wake; a fairly large number of wake turns must be used because the older vortex filaments can come close to the rotor disk plane as VRS is approached and accurate modeling is important here. All results show a "snapshot" of the wake at an arbitrary instant in time.

In hovering flight Fig. 10.49 shows that the wake consist of sets of nearly helical, closely interdigitated vortices, but with some evidence of wake disturbances and an aperiodic behavior in the far wake, as discussed previously in Section 10.5.1. See also Leishman et al. (2002a). For very low rates of descent there is more evidence of a wake instability and the subsequent formation of vortex perturbations. Because of the imposed descent velocity, the wake cannot be convected as far downstream below the rotor in a given time and the downstream wake filaments begin to "bundle" together. If the rate of descent is low enough then the developing bundles of vorticity are still confined to the far wake well downstream of the rotor and are convected away from the rotor as fast as they develop. For these low rates of descent the bulk of the wake is still in equilibrium and there is little or no effect on the blade airloads or rotor performance.

As the rate of descent is increased further, however, the net velocity through the rotor disk is decreased and more of the vorticity generated at the blade tips begins to accumulate near the rotor TPP. At some point, the descent velocity is high enough to cause the tip vortices to convect into the TPP after they are first formed, thereby creating a form of BVI. Notice that the developing perturbations in the wake also become more evident, and because of the higher rotor descent velocity in this case these perturbations now lie much closer to the rotor. While the wake cannot yet be considered to have "broken down" for these descending flight conditions, a characteristic feature is that parts of adjacent vortices pair together and eventually tightly clump or bundle, essentially forming toroids or vortex rings. These vortex rings themselves are not stable and naturally begin to develop a series of Kelvin waves

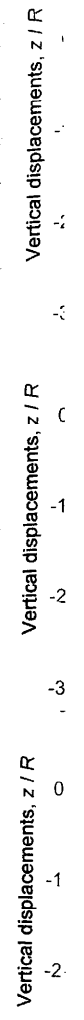

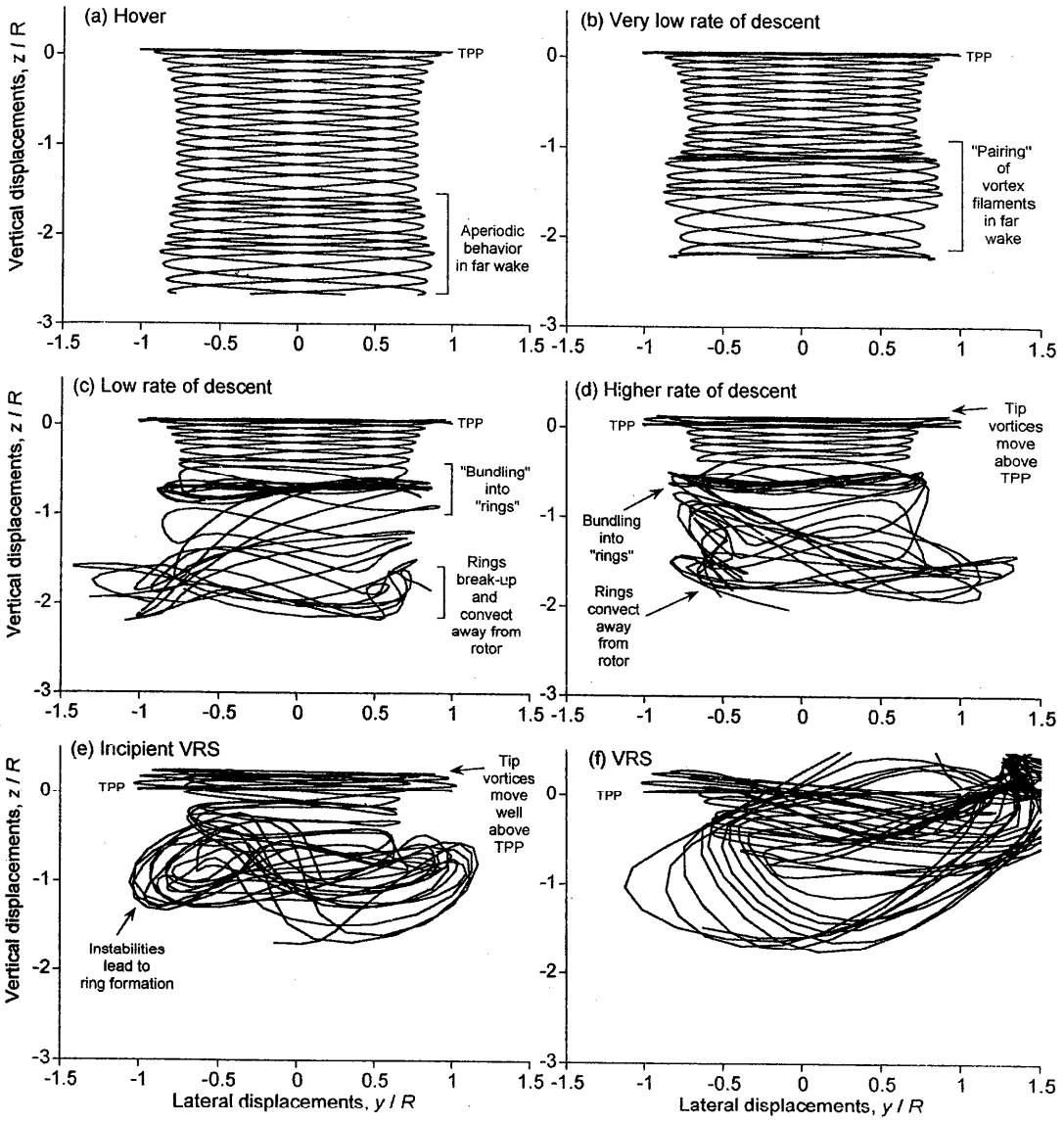

Figure 10.49 Effects of rate of descent on rotor wake developments predicted using free-vortex theory. The rotor has a solidity of 0.1, with $-13°$ of blade twist per radius, and was operated at $C_T = 0.008$ with a tip Mach number of 0.65.

[see also Fig. 10.15(a)]. These waves tend to grow in amplitude and begin to affect the flow field near the rotor and so influence the rotor airloads. Nevertheless, at these relatively low rates of descent the net velocity is still mostly downward through the rotor and the vorticity associated with the wake perturbations is convected away from the rotor disk.

Figure 10.49(e) shows that the rate of descent can eventually be increased to the point that the accumulated vorticity and developing wake perturbations are within reach of the rotor TPP. Under these conditions, the aperiodic wake developments begin to affect the blade loads. There is again strong evidence of vorticity accumulation and "vortex ring" formation, but the rings convect slowly away from the rotor as they become unstable. This

condition, therefore, can be considered symptomatic of an incipient wake breakdown and a VRS onset condition. A slightly greater rate of descent then takes the rotor into the classic features of the VRS, which is usually (but imprecisely) defined on the basis of the rotor operating in the bulk of its own wake. Under these conditions the wake loses most of its well-defined structure. Of significance again is that vortex rings are formed. Because the net flow velocity at the rotor disk is now very low, these rings lie close to or pass through the TPP (compare also with Figs. 2.21 and 2.22) and the blades intersect large concentrated regions of accumulated vorticity. This leads to locally high unsteady blade airloads and large fluctuations in rotor thrust, which are known characteristics of VRS (Section 5.7). Notice that these vortex rings are also unstable and themselves exhibit evidence of Kelvin waves that quickly grow in amplitude, causing the rings twist over and forming a series of knots. Eventually the rings themselves break down and their associated vorticity is convected away from the rotor. Notice that because of the small axial (slipstream) velocity near the rotor at this rate of descent, most of the vorticity is convected radially (and not axially) away from the rotor disk. This process of vorticity accumulation and vortex ring formation is not necessarily periodic, but the basic process of ring formation, ring breakdown and convection of the accumulated vorticity away from the disk is repeated for as long as the rotor operates in the conditions that would promote it. See also Section 14.10.7 for further results on the VRS problem.

10.11 Wake Developments in Maneuvering Flight

The problem of modeling helicopter rotor wakes under maneuvering flight conditions is not a new one [see Sadler (1972)]. The effects on the inflow resulting from rotor wake distortion during maneuvering flight has been suggested as one of the contributing sources of the so-called "off-axis" response problem of helicopters. This problem manifests as a pitch response resulting from a lateral cyclic input and/or a roll response resulting from a longitudinal cyclic input in pitch – see, for example, Tischler et al. (1994), Mansur & Tischler (1996), and Keller & Curtiss (1996). A maneuver, whether it be pitching or rolling or a combination of such, clearly provides an additional potential source of aerodynamic forcing into the rotor problem and would be expected to produce some further distortion effects into the rotor wake compared to that obtained under straight-and-level flight conditions. The exact understanding of how this effect occurs, however, is the subject of ongoing research. Clearly, if a modified wake topology is produced by the maneuver, this will change the induced inflow, which in turn will affect the blade loads, the rotor flapping response, and, therefore, the control inputs required to execute the maneuver. The problem is how to calculate such highly coupled effects, which requires a fully integrated aerodynamic, rotor dynamic, and flight mechanics simulation. While comprehensive flight mechanics models are available, the fidelity of the aerodynamic models that can be viably included so far has been limited because of their extremely high computational costs.

There have been several recent developments of rotor wake models directed toward the understanding and prediction of the off-axis response problem. Basically, this is a nonintuitive flapping response of the rotor resulting from the maneuver. For example, for a roll to the right (to starboard) then conventional theory (i.e., linearized, blade element theory) would say that the change in velocity across the disk from a roll rate would increase the AoA and lift of the blades on the advancing side of the disk and decrease the lift on the retreating side. This would be expected to cause a backward flapping of the rotor disk, that is, a $-\beta_{1c}$ flapping motion. Instead, in practice the rotor disk is found to flap forward and this is one consequence of the off-axis response problem. Using a relatively simple

prescribed wake with assumed (prescribed) maneuver induced distortion effects, Rosen & Isser (1995), Arnold et al. (1995), Keller & Curtiss (1996), and Barocela et al. (1997) showed improved correlations of the off-axis rotor response when compared to flight test data. Rosen & Isser's approach, like most vortex wake models that may have the fidelity necessary to predict maneuver induced wake distortion effects, is computationally expensive to include in flight mechanics simulations. The techniques of Keller & Curtiss (1996) are based on an extended momentum theory approach to represent the effects of the rotor wake, and is in a form easily included in such simulations. Both these techniques, however, assume that the maneuver-effects on wake distortion can be preassumed. This is done by correlating the results with flight test data and including factors into the wake model that produce the desired response. While these empirical approaches can give good results, they give limited insight into the understanding of the underlying aerodynamic mechanisms that may contribute to the off-axis response problem.

Bagai et al. (1999) have approached the aerodynamic aspects of the problem using free-vortex wake simulations. The effect of maneuvers on the rotor wake developments and induced velocity field can be simulated by adding additional "source" terms to the right-hand side of the governing equations of the wake. For example, the source term in Eq. 10.54 can be represented, in general, as

$$\vec{V}_{\text{loc}}\left(\vec{r}(\psi_b, \psi_w)\right) = \vec{V}_\infty + \vec{V}_{\text{ind}} + \vec{V}_{\text{man}}, \tag{10.126}$$

where $\vec{V}_\infty$ is the external velocity field, $\vec{V}_{\text{ind}}$ is the velocity field induced by the rotor blades and their respective wake vortices from both steady and unsteady aerodynamic effects, and the $\vec{V}_{\text{man}}$ term is the additional maneuver-induced velocity perturbation, which will be a function of the maneuver rate as well as the positions of the wake filaments relative to the maneuver axis. For simple pitching and rolling motions about the rotor hub axes, the maneuver rate vector can be written as $p\hat{i} + q\hat{j} + r\hat{k}$, where it is assumed that the rotor rolls about the fixed x axis and pitches about the fixed y axis. Furthermore, because the position of a vortex element in the Cartesian coordinate system is defined by three spatial locations, its position vector can be represented as $\vec{r}(\psi, \zeta) = x\hat{i} + y\hat{j} + z\hat{k}$. The cross-product of the two vectors defines the additional maneuvering velocity field encountered by the free vortex filaments in the wake, which is

$$\vec{V}_{\text{man}}(\psi, \zeta) = -(qz - ry)\hat{i} + (pz - rx)\hat{j} + (qx - py)\hat{k}. \tag{10.127}$$

The first term in Eq. 10.127, which is the x or streamwise component of the velocity resulting from a pitch-rate q and/or a yaw-rate r, essentially produces a skewing distortion of the wake. The second term, which is the y or lateral component of the velocity resulting from a roll-rate p and/or a yaw rate r, produces a skewing in the lateral direction. The third $(qx - py)$ term in Eq. 10.127, results in an asymmetric axial stretching distortion of the wake, which appears like a wake curvature.

In addition to the aerodynamic effects, there are inertial effects on the blade motion during maneuvers. The rotor TPP lags behind the shaft or control plane by a finite angle – see Fig. 6.32. The additional flapping moment on the blades resulting from gyroscopic effects on a rotor with pitch rate q and roll rate p is

$$M_g = -2I_b\Omega q \sin\psi - 2I_b\Omega p \cos\psi + \Omega \overset{*}{q} \cos\psi + \Omega \overset{*}{p} \sin\psi, \tag{10.128}$$

which must be added to the equation of motion for a flapping blade (Eq. 4.5).

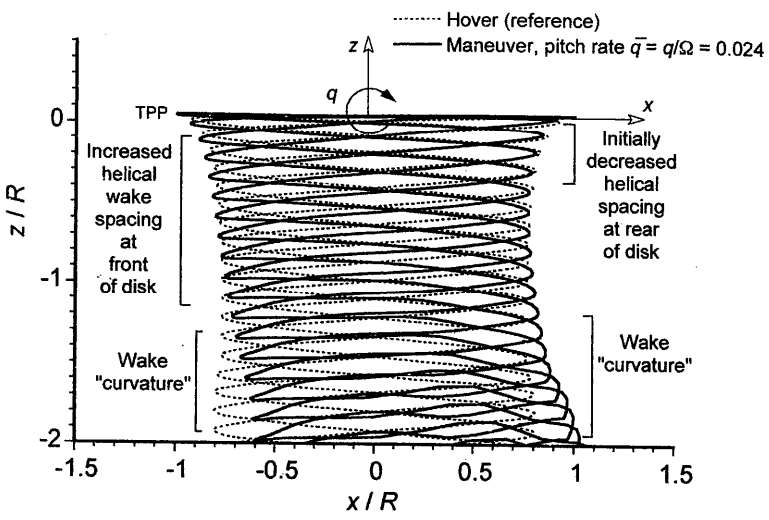

Figure 10.50 Effect of maneuver pitch rate on predicted rotor wake geometry in hover. Four-bladed hovering rotor, with $\bar{q} = 0.024$ and $C_T = 0.008$. Side view.

Examples of predicted free-vortex wake geometries under idealized (nose-up, positive) pitch rate conditions are shown in Figs. 10.50 and 10.51, for hover and forward flight, respectively. The imposed angular rates are relatively high for a helicopter, but they have been selected to exaggerate the basic effects obtained on the wake geometry. Notice the general characteristics manifest as a curvature-type distortion and an axial-type distortion. These are physical effects that have been labeled by Keller & Curtiss (1996) as "bending" and "stretching" of the wake, respectively. Furthermore, notice that for a positive (nose-up) pitch rate, the vortex elements (tip vortices) at the front of the rotor are further way from the TPP compared to straight-and-level flight conditions. At the back of the disk, the tip vortices are much closer to the TPP. In many ways, these maneuver-induced effects on the wake distortion are similar to an increase in skewness of the wake relative to the rotor TPP. Therefore, the resulting wake distortion must manifest as a change in the longitudinal inflow distribution, which will be expected to be more biased toward the back of the disk.

Consider now a simulated piloted maneuver, such as a roll. In an actual roll maneuver the pilot banks the helicopter in one direction by applying appropriate cyclic control inputs and maintains altitude by using collective pitch. The roll rates imposed on the helicopter can be approximately described using a linearized equation for roll motion – see Padfield (1996). The governing equation for the roll dynamics (with the usual simplifications) can be written as

$$\dot{p} + L_p p = L_{\delta_{\text{lat}}} \delta_{\text{lat}}, \tag{10.129}$$

where L_p and $L_{\delta_{\text{lat}}}$ are stability and control derivatives (in roll). The solution to Eq. 10.129 for a step input of lateral cyclic, δ_{lat}, is given by

$$p = -\frac{L_{\delta_{\text{lat}}}}{L_p} \delta_{\text{lat}} \left(1 - e^{L_p t}\right). \tag{10.130}$$

The resulting bank angle is

$$\phi = \int_0^t p dt = -\frac{L_{\delta_{\text{lat}}}}{L_p} \delta_{\text{lat}} \left[t + \frac{1}{L_p} \left(1 - e^{L_p t}\right) \right]. \tag{10.131}$$

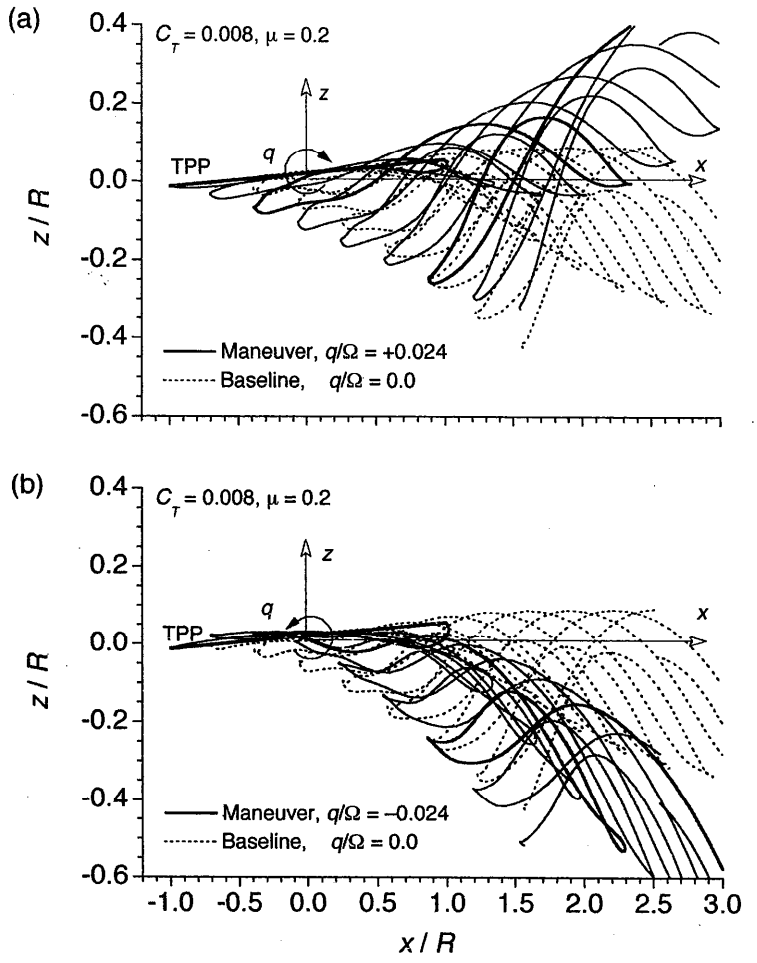

Figure 10.51 Effects of maneuver pitch rate on predicted rotor wake geometries in forward flight. Four-bladed rotor, with $\bar{q} = \pm 0.024$, $C_T = 0.008$ and $\mu = 0.2$. (a) Nose-up pitch rate; $\bar{q} = 0.024$. (b) Nose-down pitch rate; $\bar{q} = -0.024$.

The roll trajectory can, therefore, be simulated by setting parameters such as the desired maximum roll rate and the maximum bank angle. The control inputs for the maneuvers can be generated by imposing a step input, which is then held fixed for a given duration. In this case, the asymptotic value of Eq. 10.131 is given by

$$\Delta\phi = -\frac{L_{\delta_{\text{lat}}}}{L_p}\delta_{\text{lat}}\,\Delta t. \tag{10.132}$$

Defining the time period over which the maneuver is performed allows the bank angle of the simulation to be determined using Eq. 10.131.

Figure 10.52 shows an example of the wake behind a rotor executing a simulated starboard and port roll maneuver. The roll to starboard delays the roll up of the wake vortices from the advancing side of the rotor disk. However, the maneuver also brings the blade tip vortices closer to the rotor at the back of the disk thereby enhancing the potential of BVIs there. The wake behavior for a port roll is similar, except that now the wake passes up more through the retreating side of the rotor disk. The port roll maneuver also causes a lag in the roll up

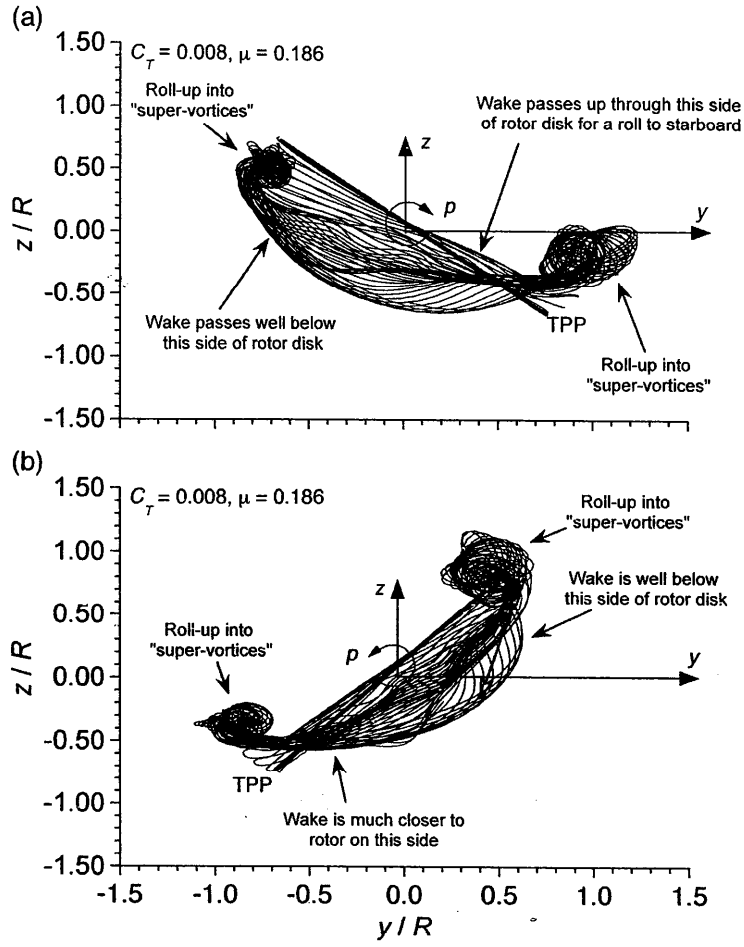

Figure 10.52 Rear views of representative predicted wake geometries for a rotor undergoing a roll maneuvers, $C_T = 0.008$, $\mu = 0.186$, $\gamma = -6°$. (a) Starboard roll rate; (b) Port roll rate. From Ananthan & Leishman (2004).

of the wake on the retreating side of the rotor because of the change in airloads over the disk. The rolled-up bundle of tip vortices trailed from the disk also move more inboard on the rotor disk and below the rotor TPP. The wake roll up on the advancing side seems to intensify during a port roll maneuver, which causes strong BVIs and high impulsive loads over the first quadrant of the rotor disk throughout the entire maneuver.

Theodore & Celi (1998) and Ribera & Celi (2004) have incorporated dynamic inflow as well as relaxation and time-accurate free-vortex wake models into a flight mechanics simulation for the analysis of such maneuver problems. The results showed some improvements in predicting overall trends in the free-flight response of the helicopter to cyclic inputs, but the quantitative predictions of rotor response were only marginally improved. The use of time-accurate aerodynamic modeling is clearly an enhanced approach, yet the results from this study suggest that deficiencies are still present in the aerodynamic models. There may be other mechanisms that play a role in predicting rotor airloads during maneuvers and so in eventually resolving the off-axis response problem, and the issues are still the subject of ongoing basic research.

10.12 Chapter Review

This chapter has described some of the significant problems still associated with an improved understanding of the wakes generated by helicopter rotors. The proper modeling of the rotor wake is one key to the prediction or rotor airloads and rotor performance. Problems such as tip vortex formation, blade–vortex interaction, and rotor–airframe interference are better understood, and systematic experimental measurements have provided significant results that will help validate numerical predictions of the various phenomena. Recent advances in experimental techniques for flow visualization and 3-D velocity field measurements have been significant, and further developments will likely continue. Ambitious experimental tests with rotors have generated large amounts of important results that have provided new insight into old problems and remarkable insight into other problems that were previously considered intractable. However, the complexity of the helicopter rotor wake, together with the sensitivity of its topology to the flight condition, makes all types of rotor wake experiments time consuming and expensive to undertake. The challenge to the rotor analysts of the future is to balance needs with experimental capabilities and to use complementary flow diagnostic techniques wherever possible to provide an improved understanding of the various rotor wake–related phenomena.

One of the biggest challenges still remaining in helicopter rotor analysis is to reveal more completely the intricate structure of the blade tip vortices. This includes issues such as the vortex strengths, the viscous core size, and velocity field near to and inside the core, as well as their relationships to the loading on the blades. Fundamental issues such as diffusion and core growth of the vortices are not yet fully understood, and further work still needs to be undertaken to develop more general models. These models must include vortex Reynolds number effects. This diffusive behavior is compounded by interactions of vortices and blades, which causes filament stretching. Such problems cannot yet be examined using computational methods based on first principles and require careful experimental studies with rotors in both hover and forward flight. This type of research may result in new ideas for tip vortex control and possibly the alleviation of several of the complex problems involving vortex dynamics that hinder the development of quieter helicopters with better performance and lower vibration.

The long-term goal of the aerodynamic modeling efforts is to be able to predict the flow field around the entire helicopter when operating in any flight condition, including flight near the ground and during arbitrary flight maneuvers. To this end, the prediction of the rotor wake is fundamental to solving the problem. However, increasing emphasis is also being placed on rotor–airframe interaction problems (see Chapter 11) because of their importance in determining performance, vibration levels, and also the overall handling qualities of the helicopter. Rapid advances in computer power mean that prescribed vortex wake models are rapidly giving way to free-vortex models for many routine levels of helicopter analysis and design work. Dynamic inflow represents another formulation of the problem, where the effects of the wake can be included in a form of differential equations to represent the relationship between the time-dependent inflow velocities and the rotor forces and pitching moments. This latter approach is attractive for some problems in rotor analysis, particularly those in flight dynamics and aeroelasticity. All of the existing rotor wake methods are relatively powerful and can give good results, yet caution should be used. Quantitative errors can only be determined though correlation studies with experiments, and much further validation of wake models is required, particularly in improving the confidence in predicting the combined effects of the rotor flow and the airframe. These problems are discussed next in Chapter 11.

10.13 Questions

10.1. For some purposes, it is possible to approximate the rotor wake by means of a series of stacked vortex rings. Find an analytic expression for the velocity induced by a single vortex ring, and show the result for the vertical velocity in the plane of the ring. Determine the induced velocity for a desingularized vortex ring using discretized segmentation of the ring into straight line elements. Show your results for various levels of angular discretization.

10.2. Write a computer program to model a rigid vortex wake and generate the coordinates of the tip vortices. For the case where $\psi_b = 0$, show the top, side, and rear views of the wake relative to the TPP for a two-bladed rotor operating at $C_T = 0.008$ and advance ratios of 0.05, 0.1, and 0.2. Assume the shaft angle is zero.

10.3. Blade vortex interaction or BVI is an important contributor to the unsteady airloads and noise generated by a rotor. Assuming an undistorted wake model in forward flight, show that the potential blade vortex interaction locations over the rotor disk can be obtained using the equations

$$\psi_b = \sin^{-1}\left\{\left(-\cos\Delta\sin(\psi_b - \Delta) \pm \sin\Delta\sqrt{\mu^2\psi_w^2 - \sin^2(\psi_w - \Delta)}\right)\Big/\mu\psi_w\right\}$$

$$r = \sin(\psi_b - \psi_w)/\sin(\psi_b - \Delta) \quad \text{and} \quad \Delta = 2\pi(i-1)/N_b,\ i = 1, 2, \ldots, N_b.$$

where all the symbols have their usual meaning. Plot the result for a four-bladed rotor operating at $\mu = 0.1$, 0.2, 0.3, and 0.4.

10.4. Use the undistorted wake model to compute the tip vortex trajectories trailed from a four-bladed rotor in forward flight at advance ratios of 0.1, 0.2, 0.3, and 0.4. If it is assumed that $z_w = 0$, that is, all the tip vortices lie in the rotor plane, calculate by means of a suitable numerical method the locus of all the blade vortex interaction locations over the rotor disk.

10.5. Write a computer program for the Beddoes prescribed wake model. Compare the results for a four-bladed rotor operating at $C_T = 0.008$ to those obtained with a rigid wake model at several values of advance ratio. Plot your results in terms of x, y, z coordinates.

10.6. The tangential (swirl) component of velocity in the Lamb–Oseen vortex model is given by

$$V_\theta(r) = \frac{\Gamma}{2\pi r}\left[1 - \exp\left(\frac{-r^2}{4\nu t}\right)\right],$$

where where r is the distance from the vortex axis, ν is the kinematic velocity, and t is time. Show that for this model, the viscous core radius of the vortex grows according to the expression $r_c = 1.1209\sqrt{4\nu t}$.

10.7. Two rectilinear vortices of unit strength are initially positioned at rest two units of distance apart. By means of time-marching integration using the Biot–Savart law, calculate the subsequent trajectories of the vortex pair. Use both Euler explicit and predictor–corrector integration schemes. Check on the reversibility of the scheme. Comment on your results.

10.8. Examine the behavior of an infinite number of rectilinear vortices of equal strength and sign arranged in straight line with their axes parallel to each other. Prove (mathematically) that this vortex system is stable and will remain stable for all time.

10.9. Examine numerically the behavior of the vortex system in the previous question, but using 20 vortices. Use both explicit and predictor–corrector time-marching schemes. Examine the behavior when a vortex at the middle of the row is disturbed by a small displacement.

10.10. Show that the ratio Γ_v/ν (where Γ_v is the vortex strength and ν is the kinematic viscosity) can be viewed as a vortex Reynolds number. Explain the significance of this parameter.

10.11. Maneuvering flight will change the structure of the rotor wake relative to that found under steady, level flight conditions. Explain the source of the primary wake shape deformations that would be obtained in terms of the roll and pitch rates about the rotor hub axis.

10.12. Starting from the equation of motion for a freely flapping blade, show that for a pure roll rate about the hub axis that there is a gyroscopic moment

$$M_g = -2I_b\Omega p\cos\psi + \Omega \overset{*}{p}\cos\psi,$$

that acts on the blade.

Bibliography

Akimov, A. I., Butov, V. P., Bourtsev, B. N., and Selemenev, S. V. 1994. "Flight Investigation of Coaxial Rotor Tip Vortex Structure," 50th Annual Forum of the American Helicopter Soc., Washington DC, May 11–13.

Althoff, S. L., Elliott, J. W., and Sailey, R. H. 1988. "Inflow Measurements Made with a Laser Velocimeter on a Helicopter Model in Forward Flight," NASA Technical Memorandum 100544.

Ananthan, S. and Leishman, J. G. 2004. "Rotor Wake Dynamics During Combat Maneuvers," 60th Forum of the American Helicopter Society International, Baltimore, MD, June 7–12.

Arnold, U. T. P., Keller, J. D., Curtiss, H. C., and Reichert, G. 1995. "The Effect of Inflow Models on the Dynamic Response of Helicopters," 21st European Rotorcraft Forum, St. Petersburg, Russia, Aug. 30–Sep. 1.

Bagai, A. and Leishman, J. G. 1992a. "Improved Wide-Field Shadowgraph Set-up for Rotor Wake Visualization," *J. of the American Helicopter Soc.*, 37 (3), pp. 86–92.

Bagai, A. and Leishman, J. G. 1992b. "A Study of Rotor Wake Developments and Wake/Body Interactions in Hover using Wide-Field Shadowgraphy," *J. of the American Helicopter Soc.*, 37 (4), pp. 48–57.

Bagai, A. and Leishman, J. G. 1994. "Flow Visualization of Compressible Vortex Structures Using Density Gradient Techniques," *Experiments in Fluids*, 15, pp. 431–442.

Bagai, A. and Leishman, J. G. 1995a. "Rotor Free-Wake Modeling using a Pseudo-Implicit Technique Including Comparisons with Experiment," *J. of the American Helicopter Soc.*, 40 (3), pp. 29–41.

Bagai, A. and Leishman, J. G. 1995b. "Rotor Free-Wake Modeling Using a Pseudo-Implicit Relaxation Algorithm," AIAA *J. of Aircraft*, 32 (6), pp. 1276–1285.

Bagai, A., Leishman, J. G. 1996. "Free-Wake Analysis of Tandem, Tilt-Rotor and Coaxial Rotor Configurations," *J. of the American Helicopter Soc.*, 41 (3), pp. 196–207.

Bagai, A. and Leishman, J. G. 1998. "Adaptive Grid Sequencing and Interpolation Schemes for Rotor Free-Wake Analyses," *AIAA J.*, 36 (9), pp. 1593–1602.

Bagai, A., Leishman, J. G., and Park, J. 1999. "Aerodynamic Analysis of a Helicopter in Steady Maneuvering Flight Using a Free-Vortex Rotor Wake Model," *Journal of the American Helicopter Soc.*, 44 (2), pp. 109–120.

Baldwin, B. S., Chigier, N. A., and Sheaffer, Y. S. 1973. "Decay of Far-Flow Field in Trailing Vortices," *AIAA J.*, 11 (12), pp. 1601–1602.

Barocela, E., Peters, D. A., Krothapalli, K. R., and Prasad, J. V. R. 1997. "The Effect of Wake Distortion on Rotor Inflow Gradients and Off-Axis Coupling," AIAA Flight Mechanics Conference, San Diego, CA, July 29–31.

Batchelor, G. K. 1967. *Introduction to Fluid Dynamics*, Cambridge University Press, Cambridge, UK, p. 87.

Beddoes, T. S. 1985. "A Wake Model for High Resolution Airloads," 1st International Conference on Basic Rotorcraft Research, Triangle Park, NC.

Bhagwat, M. J. and Leishman, J. G. 2000a. "Correlation of Helicopter Tip Vortex Measurements," *AIAA J.*, 38 (2), pp. 301–308.

Bhagwat, M. J. and Leishman, J. G. 2000b. "Stability Analysis of Helicopter Rotor Wakes in Axial Flight," *J. of the American Helicopter Soc.*, 45 (3), pp. 165–178.

Bhagwat, M. J. and Leishman, J. G. 2001a. "Stability, Consistency and Convergence of Time-Marching Free-Vortex Rotor Wake Algorithms," *J. of the American Helicopter Soc.*, 46 (1), pp. 59–71.

Bhagwat, M. J. and Leishman, J. G. 2001b. "Accuracy of Straight-Line Segmentation Applied to Curvilinear Vortex Filaments," *J. of the American Helicopter Society*, 46 (2), pp. 166–169.

Bhagwat, M. J. and Leishman, J. G. 2002. "Generalized Viscous Vortex Core Models for Application to Free-Vortex Wake and Aeroacoustic Calculations," 58th Annual Forum of the American Helicopter Soc. International, Montréal Canada, June 11–13.

Biggers, J. C. and Orloff, K. L. 1975. "Laser Velocimeter Measurements of the Helicopter Rotor-Induced Flow Field," *J. of the American Helicopter Soc.*, 20 (1), pp. 2–10.

Biggers, J. C., Lee, A., Orloff, K. L., and Lemmer, O. J. 1977a. "Measurements of Helicopter Rotor Tip Vortices," 33rd Annual National Forum of the American Helicopter Soc., Washington DC, May 9–11.

Biggers, J. C., Lee, A., Orloff, K. L., and Lemmer, O. J. 1977b. "Laser Velocimeter Measurements of Two-Bladed Helicopter Rotor Flow Fields," NASA TM X-73238.

Bradshaw, P. 1983. "The Analogy Between Streamline Curvature and Buoyancy in Turbulent Shear Flows," *J. of Fluid Mechanics*, 33, pp. 177–191.

Brand, A. G., McMahon, H. M., and Komerath, N. M. 1990. "Correlations of Rotor Wake/Airframe Interaction Measurements with Flow Visualization Data," *J. of the American Helicopter Soc.*, 35 (4), pp. 4–15.

Brooks, T. F., Boyd, D. D., Burley, C. L., and Jolly, R. J. 1996. "Aeroacoustic Codes for Rotor Harmonic and BVI Noise-CAMRAD: Mod1/HIRES," AIAA Paper No. 96-1735, 2nd AIAA and CEAS, Aeroacoustics Conference, State College, PA, May 6–8.

Brown, R. E., Leishman, J. G., Newman, S. and Perry, F. J. 2002. "Blade Twist Effects on Rotor Behavior in the Vortex Ring State," 28th European Rotorcraft Forum, Bristol, England, Sept. 17–20.

Campbell, J. F. and Chambers, J. R. 1994. "Patterns in the Sky–Natural Visualization of Aircraft Flow Fields," NASA SP-514.

Caradonna, F. X. and Tung, C. 1981. "Experimental and Analytical Studies of a Model Helicopter Rotor in Hover," 7th European Rotorcraft Forum, Garmisch-Partenkirchen, Germany, Sept. 22–25.

Caradonna, F. X., Hendley, E., Silva, M., Huang, S., Komerath, N., Reddy, U., Mahalingam, R., Funk, R., Wong, O., Ames, R., Darden, L., Villareal, I., and Gregory, J. 1999. "Performance Measurement and Wake Characteristics of a Model Rotor in Axial Flight," *J. of the American Helicopter Soc.*, 44 (2), pp. 101–108. Errata 44 (3).

Carpenter, P. J. and Friedovich, B. 1953. "The Effect of a Rapid Blade Pitch Increase on the Thrust and Induced Velocity of a Full-Scale Helicopter Rotor," NACA TN 3044.

Castles, W., Jr. and De Leeuw, J. H. 1954. "The Normal Component of the Induced Velocity in the Vicinity of a Lifting Rotor and Some Examples of Its Application," NACA Report 1184.

Celi, R. 2004. "State-Space Representation of Vortex Wakes Using the Method of Lines," 30th European Rotorcraft Forum, Marseilles, France, Sept. 14–16.

Chen, R. T. 1989. "A Survey of Nonuniform Inflow Models for Rotorcraft Flight Dynamics and Control Applications," 15th European Rotorcraft Forum, Amsterdam, The Netherlands, Sept. 12–15.

Chigier, N. A. and Corsiglia, V. R. 1971. "Tip Vortices–Velocity Distributions," 27th Annual Forum of the American Helicopter Soc., Washington DC, May.

Clark, D. R. and Leiper, A. C. 1970. "The Free Wake Analysis, A Method for the Prediction of Helicopter Rotor Hovering Performance," *J. of the American Helicopter Soc.*, 15 (1), pp. 3–11.

Coleman, R. P., Feingold, A. M., and Stempin, C. W. 1945. "Evaluation of the Induced Velocity Fields of an Idealized Helicopter Rotor," NACA ARR L5E10.

Cook, C. V. 1972. "The Structure of the Rotor Blade Tip Vortex," In: AGARD CP-111.

Cotel, A. J. and Breidenthal, R. E. 1999. "Turbulence Inside a Vortex," *Physics of Fluids*, 11 (10), pp. 3026–3029.

Cotel, A. J. 2002. "Turbulence Inside a Vortex: Take Two," *Physics of Fluids*, 14 (8), pp. 2933–2934.

Crews, S. T., Hohenemeser, K. H., and Ormiston, R. A. 1973. "An Unsteady Wake Model for a Hingeless Rotor," *J. of Aircraft*, 10 (12), pp. 758–759.

Crouse, G. L. and Leishman, J. G., 1993. "A New Method for Improved Rotor Free-Wake Convergence," AIAA Paper 93-0872, 31st AIAA Aerospace Sciences Meeting and Exhibit, Reno, NV, Jan. 11–14.

Curtiss, H. C. 1986. "Stability and Control Modeling," 12th European Rotorcraft Forum, Garmish-Partenkirchen, Germany, Sept. 22–25.

Curtiss, H. C. and Shupe, N. K. 1971. "A Stability and Control Theory for Hingeless Rotors," 26th Annual National Forum of the American Helicopter Soc., Washington DC, May.

Dadone, L. U. 1970. Unpublished Photographs from Model Tests Performed in the 20×20 Foot Wind-Tunnel at Boeing Helicopters, Philadelphia, 1970.

Dadone, L. U. 1995. Technical Evaluation Report, In: AGARD Fluid Dynamics Panel Symposium on Aerodynamics and Aeroacoustics of Rotorcraft, AGARD-CP-552.

Devenport, W. J., Rife, M. C., Liapis, S. I., and Follin, G. J. 1996. "The Structure and Development of a Wing-Tip Vortex," *J. of Fluid Mechanics*, 312, pp. 67–106.

Dingeldein, R. C. 1954. "Wind-Tunnel Studies of the Performance of Multirotor Configurations," NACA TN 3236.

Donaldson, C. D. 1971. "Calculation of Turbulent Shear Flows for Atmospheric and Vortex Motions," *AIAA J.*, 10 (1), pp. 4–12.

Dosanjh, D. S., Gasparek, E. P., and Eskinazi, S. 1962. "Decay of Viscous Trailing Vortex," *Aeronautical Quarterly*, 13, pp. 167–188.

Egolf, T. A. and Landgrebe, A. J. 1983. "Helicopter Rotor Wake Geometry and Its Influence in Forward Flight, Vol. I–Generalized Wake Geometry and Wake Effect on Rotor Airloads and Performance," NASA CR-3726.

Elliott, J. W., Althoff, S. L., and Sailey, R. H. 1988. "Inflow Measurements Made with a Laser Velocimeter on a Helicopter Model in Forward Flight," Vols. II and III, Rectangular Blades–Advance Ratios of 0.23 and 0.30, NASA TM-100542, TM-100543.

Felker, F. F., Maisel, M. D., and Betzina, M. D. 1986. "Full-Scale Tilt-Rotor Hover Performance," *J. of the American Helicopter Soc.*, 31 (2), pp. 10–18.

Gaonkar, G. H. and Peters, D. A. 1986a. "Effectiveness of Current Dynamic Inflow Models in Hover and Forward Flight," *J. of the American Helicopter Soc.*, 31 (2), pp. 47–57.

Gaonkar, G. H. and Peters. D. A. 1986b. "Review of Dynamic Inflow Modeling for Rotorcraft Flight Dynamics," AIAA Paper 86-0845-CP, 27th Structures, Structural Dynamics and Materials Conference, San Antonio, TX, May 19–21.

Ghee, T. A. and Elliott, J. W. 1995. "The Wake of a Small-Scale Rotor in Forward Flight Using Flow Visualization," *J. of the American Helicopter Soc.*, 40 (3), pp. 52–65.

Gilmore, D. C. and Gartshore, I. S. 1972. "The Development of an Efficient Hovering Propeller–Rotor Performance Prediction Method," In: AGARD CP-111.

Gray, R. B. 1956. "An Aerodynamic Analysis of a Single Bladed Rotor in Hovering and Low Speed Forward Flight as Determined from Smoke Studies of the Vorticity Distribution in the Wake," Princeton University, Report No. 356.

Gupta, S. and Leishman, J. G. 2004. "Accuracy of the Induced Velocity of Wind Turbine Wakes Using Vortex Segmentation," 23rd ASME/AIAA Wind Energy Symposium, Reno, NV, Jan. 5–8.

Gupta, B. P. and Loewy, R. G. 1973. "Analytical Investigation of the Aerodynamic Stability of Helical Vortices Shed from a Hovering Rotor," USAAMRDL 73-84.

Gupta, B. P. and Loewy, R. G. 1974. "Theoretical Analysis of the Hydrodynamic Stability of Multiple Interdigitated Helical Vortices," *AIAA J.*, 12 (10), pp. 1381–1387.

Han, Y., Leishman, J. G., and Coyne, A. 1997. "Measurements of the Velocity and Turbulence Structure of a Rotor Tip Vortex," *AIAA J.*, 35 (3), pp. 477–485.

Heyson, H. H. and Katzoff, S. 1957. "Induced Velocities near a Lifting Rotor with Nonuniform Disk Loading," NACA TR 1319.

Hildebrand, F. B. 1976. *Advanced Calculus for Applications*, Prentice-Hall, Inc., Englewood Cliffs, NJ, p. 403.

Hoad, D. R. 1983. "Preliminary Rotor Wake Measurements with a Laser Velocimeter," NASA TM 83246.

Hoffman, E. R. and Joubert, P. N. 1963. "Turbulent Line Vortices," *J. of Fluid Mechanics*, 16, pp. 395–411.

Holder, D. W. and North, R. J. 1963. "Schlieren Methods," Notes on Applied Science, No. 31, Dept. of Scientific and Industrial Research, National Physical Laboratory, HMSO, London.

Holzapfel, A. Hofbauer, T., Gerz, T., and Schumann, U. 2001. "Aircraft Wake Vortex Evolution and Decay in Idealized and Real Environments: Methodologies, Benefits and Limitations," Euromech Colloquium.

Horner, M. H., Stewart, J. N., Galbraith, R. A. McD., Grant, I., and Coton, F. N. 1994. "An Examination of Vortex Deformation During Blade Vortex Interaction Using Particle Image Velocimetry," 19th ICAS Congress, Anaheim, CA, Sept.

Iversen, J. D. 1976. "Correlation of Turbulent Trailing Vortex Decay Data," *J. of Aircraft*, 13 (5), pp. 338–342.

Jenks, M., Dadone, L., and Gad-el-Hak, M. 1987. "Towing Tank Flow Visualization of a Scale Model H-34 Rotor," 43rd Annual Forum of the American Helicopter Soc., St. Louis, MO, May 18–20.

Jessurun, K. P., Pavel, M. D., and Toet, S. 2001. "Apparent Mass Effects on a Stiff-Hinged Rotor Model After Rapid Cyclic and/or Collective Inputs–A Flow Visualization Study," 27th European Rotorcraft Forum, Moscow, Russia, Sept. 11–14, 2001.

Joglikar, M. and Loewy, R. 1970. "An Actuator-Disk Analysis of Helicopter Wake Geometry and the Corresponding Blade Response," USAAVLABS Technical Report 69-66, Dec.

Johnson, W. 1980. *Helicopter Theory*, Princeton University Press, Princeton, NJ.

Johnson, W. 1988. "Time-Domain Unsteady Aerodynamics of Rotors With Complex Wake Configurations," *Vertica*, 12 (1/2), pp. 83–100.

Keller, J. D. and Curtiss, H. C. 1996. "Modeling the Induced Velocity of a Maneuvering Helicopter," 52nd Annual Forum of the American Helicopter Soc., Washington, DC, June 4–6.

Kitaplioglu, C. and Caradonna, F. X. 1994. "Aerodynamics and Acoustics of Blade Vortex Interaction Using an Independently Generated Vortex," American Helicopter Soc. Aeromechanics Specialists Conference, San Francisco, CA, Jan. 19–21.

Kocurek, J. D. and Berkowitz, L. F. 1982. "Velocity Coupling: A New Concept for Hover and Axial Flow Wake Analysis and Design," In: AGARD CP-334.

Kocurek, J. D. and Tangler, J. L. 1976. "A Prescribed Wake Lifting Surface Hover Performance Analysis," *J. of the American Helicopter Soc.*, 21 (1), pp. 24–35.

Lamb, H. 1932. *Hydrodynamics*, Cambridge University Press, Cambridge, UK, pp. 592–593, 668–669.

Landgrebe, A. J. 1969. "An Analytical Method for Predicting Rotor Wake Geometry," *J. of the American Helicopter Soc.*, 14 (4), pp. 20–32.

Landgrebe, A. J. 1971. "An Analytical and Experimental Investigation of Helicopter Rotor Performance and Wake Geometry Characteristics," USAAMRDL TR 71-24.

Landgrebe, A. J. 1972. "The Wake Geometry of a Hovering Rotor and Its Influence on Rotor Performance," *J. of the American Helicopter Soc.*, 17 (4), pp. 2–15.

Landgrebe, A. J. 1988. "Overview of Helicopter Wake and Airloads Technology," 2nd International Conference on Rotorcraft Basic Research, College Park, MD, Feb. 16–18

Landgrebe, A. J. and Bellinger, E. D. 1971. "An Investigation of the Quantitative Applicability of Model Helicopter Rotor Wake Patterns Obtained from a Water Tunnel," UARL K910917-23.

Landgrebe, A. J. and Johnson, B. V. 1974. "Measurement of Model Helicopter Rotor Flow Velocities with a Laser Doppler Velocimeter," *J. of the American Helicopter Soc.*, 19 (3), pp. 39–43.

Larin, A. V. 1973. "Vortex Wake Behind a Helicopter," *Aviatsiya i Kosmonavtika*, 3, pp. 32–33. Available from NTIS as translation ADA005479.

Larin, A. V. 1974. "Vortex Formation in Oblique Flow around a Helicopter Rotor," *Uchenyye Zapiski TSAGI*, 1 (3), pp. 115–122. Available from NTIS as translation AD781245.

Lee, D. J. and Na, S. U. 1995. "High Resolution Free Vortex Blob Method for Highly Distorted Vortex Wake Generated from a Slowly Starting Rotor Blade in Hover," 21st European Rotorcraft Forum, St. Petersburg, Russia, Aug. 30–Sept. 1.

Lee, D. J. and Na, S. U. 1998. "Numerical Simulations of Wake Structure Generated by Rotating Blades Using a Time Marching, Free Vortex Blob Method," *European J. of Fluid Mechanics–B/Fluids*, 17 (4), pp. 1–13.

Lehman, A. F. 1968. "Model Studies of Helicopter Rotor Patterns," 24th Annual National Forum of the American Helicopter Soc., Washington DC.

Leishman, J. G. 1996. "Seed Particle Dynamics in Tip Vortex Flows," *J. of Aircraft*, 33 (4), pp. 823–825.

Leishman, J. G. 1998. "Measurements of the Aperiodic Wake of a Hovering Rotor," *Experiments in Fluids*, 25, pp. 352–361.

Leishman, J. G. 1999. "Acoustic Focusing Effects During Parallel and Oblique Blade Vortex Interaction," *J. of Sound and Vibration*, 221 (3), pp. 415–441.

Leishman, J. G. and Bagai, A. 1991. "Rotor Wake Visualization in Low Speed Forward Flight," AIAA Paper 91-3232, 9th AIAA Applied Aerodynamics Conference, Baltimore, MD, Sept. 23–25.

Leishman, J. G. and Bagai, A. 1998. "Challenges in Understanding the Vortex Dynamics of Helicopter Rotor Wakes," *AIAA J.*, 36 (7), pp. 1130–1140.

Leishman, J. G., Baker, A. M., and Coyne, A. J. 1995. "Measurements of Rotor Tip Vortices Using Three-Component Laser Doppler Velocimetry," *J. of the American Helicopter Soc.*, 41 (4), pp. 342–353.

Leishman, J. G., Bhagwat, M. J., and Ananthan, S. 2002a. "The Vortex Ring State as a Spatially and Temporally Developing Wake Instability," American Helicopter Soc. International Specialists Meeting on Aerodynamics, Acoustics and Test & Evaluation, San Francisco, CA, Jan. 23–25.

Leishman, J. G., Bhagwat, M. J., and Bagai, A. 2002b. "Free-Vortex Filament Methods for the Analysis of Helicopter Rotor Wakes," *J. of Aircraft*, 39 (5), pp. 759–775.

Levy, H. and Forsdyke, A. G. 1928. "The Steady Motion and Stability of a Helical Vortex," *Royal Soc. of London*, Series A, 120 (786), pp. 670–690.

Lewis, R. I. 1991. *Vortex Element Methods for Fluid Dynamic Analysis of Engineering Systems*, Cambridge University Press, Cambridge, UK.

Light, J. S., Frerkin, A., and Norman, T. R. 1990. "Application of the Wide-Field Shadowgraph Technique to Helicopters in Forward Flight," 46th Annual Forum of the American Helicopter Soc., Washington DC, May 21–23.

Lorber, P. F., Stauter, R. C., Hass, R. J., Torok, M. S., and Kohlhepp, F. W. 1994. "Techniques for Comprehensive Measurement of Model Helicopter Rotor Aerodynamics," 50th Annual Forum of the American Helicopter Soc., Washington DC, May 11–14.

Lowson, M. V. 1996. "Focusing of Helicopter BVI Noise," *J. of Sound and Vibration*, 190 (3), pp. 477–494.

Mahalingam. R. and Komerath N. M. 1998. "Measurements of the Near Wake of a Rotor in Forward Flight," AIAA Paper 98-0692, 36th Aerospace Sciences Meeting and Exhibit, Reno, NV, Jan. 12–15.

Mansur, M. H. and Tischler, M. B. 1996. "An Empirical Correction for Improving Off-Axes Response in Flight Mechanics Helicopter Models," AGARD Flight Vehicle Integration Panel Symposium on Advances in Rotorcraft Technology, Ottawa, Canada, May 27–30.

Martin, P. B. and Leishman, J. G. 2002. "Trailing Vortex Measurements in the Wake of a Hovering Rotor with Various Tip Shapes," 58th Annual Forum of the American Helicopter Soc. International, Montréal Canada, June 11–13.

Martin, P. B., Bhagwat, M. B., and Leishman, J. G. 1999. "Strobed Laser Sheet Visualization of a Helicopter Rotor Wake," *J. of Flow Visualization and Image Processing*, 7 (1), pp. 31–50.

Martin, P. B., Pugliese, G., and Leishman, J. G. 2001. "High Resolution Trailing Vortex Measurements in the Wake of a Hovering Rotor," *J. of the American Helicopter Society*, 48 (1), pp. 39–52.

McAlister, K. W. 1996. "Measurements in the Near Wake of a Hovering Rotor," AIAA Paper 96-1958, 27th AIAA Fluid Dynamics Conference, New Orleans, LA, June 18–20.

McAlister, K. W. 2003. "Rotor Wake Development During the First Revolution," 59th Annual Forum of the American Helicopter Society, Pheonix, AZ, May 6–8.

McAlister, K. W., Schuler, C. A., Branum, L., and Wu, J. C. 1995. "3-D Wake Measurements near a Hovering Rotor for Determining Profile and Induced Drag," NASA TP 3577.

McCroskey, W. J. 1995. "Vortex Wakes of Rotorcraft," AIAA Paper 95-0530, 33rd AIAA Aerospace Sciences Meeting and Exhibit, Reno, NV, Jan. 9–12.

McVeigh, M. A., Liu, J., and O'Toole, S. J. 1997. "V-22 Osprey Aerodynamic Development–A Progress Review," *The Aeronautical J.*, 101 (1006), pp. 231–244.

Mercker, E. and Pengel, K. 1992. "Flow Visualization of Helicopter Blade Tip Vortices," 18th European Rotorcraft Forum, Avignon, France, Sept. 15–18.

Merzkirch, W. 1981. "Density Sensitive Flow Visualization," *Methods of Experimental Physics*, Vol. 18A, pp. 345–375.

Miller, W. O. 1993. "A Fast Adaptive Resolution Method for Efficient Free Wake Calculations," 49th Annual Forum of the American Helicopter Soc., St. Louis, MO, May 19–21.

Miller, W. O. and Bliss, D. B. 1993. "Direct Periodic Solutions of Rotor Free Wake Calculations " *J. of the American Helicopter Soc.*, 38 (2), pp. 53–60.

Moedersheim, E., Daghir, M., and Leishman, J. G. 1994. "Flow Visualization of Rotor Wakes Using Shadowgraph and Schlieren Techniques," 20th European Rotorcraft Forum, Amsterdam, The Netherlands, Oct. 4–6.

Morillo, J. A. and Peters, D. A. 2002. "Velocity Field Above a Rotor Disk by a New Dynamic Inflow Model," *J. of Aircraft*, 39 (5), pp. 731–749.

Müller, R. H. G. 1990a. "Special Vortices at a Helicopter Rotor Blade," *J. of the American Helicopter Soc.*, 35 (3), pp. 16–22.

Müller, R. H. G. 1990b. "Winglets on Rotor Blades in Forward Flight–A Theoretical and Experimental Investigation," *Vertica*, 14 (1), pp. 31-46.

Müller, R. H. G. 1994. "Tip Vortex Development and Structure at BVI for a Hovering Rotor with Swept Back Tip Shapes Using the Flow Visualization Gun Technique," 20th European Rotorcraft Forum, Amsterdam, The Netherlands, 4–6 Oct.

Newman, B. G. 1959. "Flow in a Viscous Trailing Vortex," *Aeronautical Quarterly*, 1, May, pp. 167–188.

Newman, S., Modha, A., Khelifa, M., Brown, R., Perry, J., and Ahlin, G. 2004. "Revisiting the Effects of Blade Geometry on Rotor Behavior in Descending Flight," 30th European Rotorcraft Forum, Marseilles, France, Sept. 14–16.

Norman, T. R. and Light, J. S. 1987. "Rotor Tip Vortex Geometry Measurements Using the Wide-Field Shadowgraph Technique," *J. of the American Helicopter Soc.*, 32 (2), pp. 40–50.

Ogawa, A. 1993. *Vortex Flow*, CRC Series on Fine Particle Science and Technology, CRC Press Inc., Chapter 12.

Ormiston, R. A. 1976. "Application of Simplified Inflow Models to Rotorcraft Dynamic Analysis," *J. of the American Helicopter Soc.*, 21 (3), pp. 34–37.

Oseen, C. W. 1911. "Über Wirbelbewegung in einer reibenden Flüssigkeit," *Ark. Mat. Astron. Fys.*, 7, pp. 14–21.

Padfield, G. D. 1996. *Helicopter Flight Dynamics: The Theory and Application of Flying Qualities and Simulation Modeling*," AIAA Education Series, Washington, DC.

Parthasarthy, S. P., Cho, Y. I., and Black, L. H. 1985. "Wide-Field Shadowgraph Flow Visualization of Tip Vortices Generated by a Helicopter Rotor," AIAA Paper 85-1557, 18th AIAA Fluid Dynamics and Plasmadynamics and Lasers Conference, Cincinnati, OH, July 16–18.

Peters, D. A. 1974. "Hingeless Rotor Frequency Response with Unsteady Aerodynamics," AHS/NASA Specialists' Meeting on Rotorcraft Dynamics, NASA SP-362.

Peters, D. A., Boyd, D. D., and He, C. J. 1987. "Finite-State Induced-Flow Model for Rotors in Hover and Forward Flight," 43rd Annual Forum of the American Helicopter Soc., St. Louis, MO, May 18–20.

Peters, D. A. and HaQuang, N. 1988. "Dynamic Inflow for Practical Applications," *J. of the American Helicopter Soc.*, 33 (4), pp. 64–68.

Peters, D. A. and He, C. J. 1989. "Correlation of Measured Induced Velocities with a Finite-State Wake Model," 45th Annual Forum of the American Helicopter Soc., Boston, MA, May 22–24.

Peters, D. A. and He, C. J. 1995. "Finite State Induced Flow Models Part II: Three-Dimensional Rotor Disk," *J. of Aircraft*, 32 (2), pp. 323–333.

Peters, D. A., Karunamoorthy, S., and Cae, W.-M. 1995. "Finite State Induced Flow Models Part I: Two Dimensional Thin Airfoil," *J. of Aircraft*, 32 (2), pp. 313–322.

Pitt, D. M. and Peters, D. A. 1983. "Rotor Dynamic Inflow Derivatives and Time Constants from Various Inflow Models," 9th European Rotorcraft Forum, Stresa, Italy, Sept. 13–15.

Pizialli, R. and Trenka, A. 1970. "An Experimental Study of Blade Tip Vortices," Report AC-2647-S-1, Cornell Aeronautical Laboratory, Buffalo, NY.

Quackenbush, T. R., Bliss, D. B., and Wachspress, D. A. 1988. "Computational Analysis of Hover Performance Using a New Free Wake Method," 2nd International Conference on Rotorcraft Basic Research, College Park, MD, Feb.

Raddatz, J. and Pahlke, K. 1994. "3D Euler Calculations of Multibladed Rotors in Hover: Investigation of the Wake Capturing Properties," In: AGARD CP-552.

Ramasamy, M. and Leishman, J. G. 2003. "The Interdependence of Straining and Viscous Diffusion Effects on Vorticity in Rotor Flow Fields," *J. of Aircraft*,, 41 (5), pp. 1014–1024.

Rayleigh, L. 1880. "On the Dynamics of Revolving Fluids," *Royal Soc. of London*, Series A93, pp. 148–154.

Ribera, M. and Celi, R. 2004. "Simulation Modeling of Unsteady Maneuvers Using a Time Accurate Free Wake," 60th Annual Forum of the American Helicopter Soc., Baltimore, MD, June 7–10.

Rorke, J. B. and Moffitt, R. C. 1977. "Measurement of Vortex Velocities over a Wide Range of Vortex Age, Downstream Distance, and Free Stream Velocity," NASA CR 145213.

Rorke, J. B., Moffitt, R. C., and Ward, J. F. 1972. "Wind Tunnel Simulation of Full-Scale Vortices," 28th Annual Forum of the American Helicopter Soc., Washington DC, May.

Rosen, A. and Isser, A. 1995. "A New Model of Rotor Dynamics During Pitch and Roll of a Hovering Helicopter," *J. of the American Helicopter Soc.*, 30 (3), pp. 17–28.

Rule, J. A. and Bliss, D. B. 1998. "Prediction of Viscous Trailing Vortex Structure from Basic Loading Parameters," *AIAA J.*, 36 (2), pp. 208–218

Sadler, S. G. 1971a. "A Method for Predicting Helicopter Wake Geometry, Wake Induced Flow, and Wake Effects on Blade Airloads," 27th Annual National V/STOL Forum of the American Helicopter Soc., Washington DC, May.

Sadler, S. G. 1971b. "Development and Application of a Method for Predicting Rotor Free Wake Positions and Resulting Rotor Blade Airloads," NASA CR 1911 and CR 1912.

Sadler, S. G. 1972. "Main Rotor Free Wake Geometry Effects on Blade Air Loads and Response for Helicopters in Steady Maneuvers," NASA CR 2110 and CR 2111.

Saffman, P. G. 1992. *Vortex Dynamics*, Cambridge University Press, New York, NY.

Sarpkaya, T. 1989. "Computational Methods with Vortices," *J. of Fluids Engineering*, 111, pp. 5–52.

Schmitz, F. H. 1991. "Rotor Noise," *Aeroacoustics of Flight Vehicles: Theory and Practice*, Vol. 1, Chap. 2. NASA Reference Publication 1258.

Scully, M. P. 1975. "Computation of Helicopter Rotor Wake Geometry and Its Influence on Rotor Harmonic Airloads," Massachusetts Institute of Technology, ASRL TR 178-1.

Scully, M. P. and Sullivan, J. P. 1972. "Helicopter Rotor Wake Geometry and Airloads and Development of Laser Doppler Velocimeter for Use in Helicopter Rotor Wakes," Massachusetts Institute of Technology, AL TR 179.

Seelhorst, U., Beesten, B., and Butefisch, K. A. 1994. "Flowfield Investigation of a Rotating Helicopter Rotor Blade by Three-Component Laser Doppler Velocimetry," 75th AGARD Fluid Dynamic Panel Symposium, Berlin, Germany, Oct.

Seelhorst, U., Raffel, M., Willert, C., Vollmers, K. A., Butefische, K. A., and Kompenhans, J. 1996. "Comparison of Vortical Structures of a Helicopter Rotor Model Measured by LDV and PIV," 22nd European Rotorcraft Forum, Brighton, UK, Sept. 17–19.

Srinivasan, G. R. and Baeder, J. D. 1993. "TURNS: A Free-Wake Euler-Navier–Stokes Numerical Method for Helicopter Rotors," *AIAA J.*, 31 (5), pp. 959-962.

Simons, I. A., Pacifico, R. R., and Jones, J. P. 1966. "The Movement, Structure and Breakdown of Trailing Vortices from a Rotor Blade," CAL/USAAVLABS Symp. on Aerodynamic Problems Associated with V/STOL Aircraft, Vol. 1–Propeller and Rotor Aerodynamics, Buffalo, NY, June 22–24.

Sissingh, G. J. 1952. "The Effect of Induced Velocity Variation on Helicopter Rotor Damping in Pitch and Roll," ARC Technical Report G P No. 101.

Spencer, R. H. 1969. "Application of Vortex Visualization Test Techniques to Rotor Noise Research," 25th Annual Forum of the American Helicopter Soc., Washington DC, May 14–16.

Squire, H. B. 1965. "The Growth of a Vortex in Turbulent Flow," *Aeronautical Quarterly*, 16, Aug., pp. 302–306.

Steinhoff, J. S. 1985. "A Simple Efficient Method for Flow Measurement and Visualization," In: *Flow Visualization III*, ed. W. J. Yang, Hemisphere Publishing, New York, NY, pp. 19–24.

Sternfeld, H. and Schairer, J. O. 1969. "Study of Rotor Blade Tip Vortex Geometry for Noise and Airfoil Applications," Boeing Helicopters D8-2464-1A, Philadelphia, PA.

Sullivan, J. P. 1973. "An Experimental Investigation of Vortex Rings and Helicopter Rotor Wakes Using a Laser Doppler Velocimeter," Massachusetts Institute of Technology Aerophysics Laboratory, Technical Report 183, MIT DSR No. 80038.

Swanson, A. A. 1993. "Application of the Shadowgraph Flow Visualization Technique to a Full-Scale Helicopter Rotor in Hover and Forward Flight," AIAA Paper 93-3411-CP, 11th AIAA Applied Aerodynamics Conference, Monterey, CA, Aug. 9–11.

Tang, L. and Baeder, J. D. 1999. "Improved Euler Simulation of Hovering Rotor Tip Vortices with Validation," 55th Annual Forum of the American Helicopter Soc. Int., Montréal, Canada, May 25–27.

Tangler, J. L., Wohlfeld, R. W., and Miley, S. J. 1973. "An Experimental Investigation of Vortex Stability, Tip Shapes, and Noise for Hovering Model Rotors," NASA CR 2305.

Tangler, J. L. 1977. "Schlieren and Noise Studies of Rotors in Forward Flight," 33rd Annual Forum of the American Helicopter Soc., Washington DC, May 9–11.

Taylor, M. K. 1950. "A Balsa-Dust Technique for Air-Flow Visualization and Its Application to Flow through Model Helicopter Rotors in Static Thrust," NACA TN 2220.

Theodore, C. and Celi, R. 1998. "Flight Dynamic Simulation of Hingeless Rotor Helicopters Including a Maneuvering Free Wake Model," 54th Annual Forum of the American Helicopter Soc. International, Washington DC, May 20–22, 1998.

Thomson, T. L., Komerath, N. M., and Gray, R. B. 1988. "Visualization and Measurement of the Tip Vortex Core of a Rotor Blade in Hover," *J. of Aircraft*, 25 (2), pp. 1113–1121.

Tischler, M. B., Driscoll, J. T., Cauffman, M. G., and Freedman, C. J. 1994. "Study of Bearingless Main Rotor Dynamics from Frequency Response Wind Tunnel Test Data," American Helicopter Soc. Aeromechanics Specialists' Conference, San Francisco, CA, Jan. 19–21.

Tung, C., Pucci, S. L., Caradonna, F. X., and Morse, H. A. 1983. "The Structure of Trailing Vortices Generated by Model Helicopter Rotor Blades," *Vertica*, 7 (1), pp. 33–43. See also NASA TM 81316.

van der Wall, B. 2000a. "Simulation of HHC on Helicopter Rotor BVI Noise Emission Using a Prescribed Wake Method," 26th European Rotorcraft Forum, The Hague, Netherlands, Sept. 26–29.

van der Wall, B. 2000b. "The Effect of HHC on the Vortex Convection in the Wake of a Helicopter Rotor," *Aerospace Science & Technology*, 4, pp. 321–336.

Vatistas, G. H., Kozel, V., and Mih, W. C. 1991. "A Simpler Model for Concentrated Vortices," *Experiments in Fluids*, 11, pp. 73–76.

Wachspress, D. A., Quackenbush, T. R., and Boschitisch, A. H. 2003. "First-Principles Free-Vortex Wake Analysis for Helicopters and Tiltrotors," American Helicopter Soc. 59th Annual Forum, Phoenix, AZ, May 6–8.

Walters, R. E. and Skujins, O. 1972. "A Schlieren Technique Applied to Rotor Wake Studies," American Helicopter Soc. Symp. of Status of Testing and Modeling Techniques for V/STOL Aircraft, Essington, PA, Oct. 26–28.

Werlé, H. and Armand, C. 1969. "Measures et Visualization Instationnaires sur les Rotor," ONERA TP 777.

Widnall, S. E. 1972. "The Stability of a Helical Vortex Filament," *J. of Fluid Mechanics*, 54 (4), pp. 641–663.

Winburn, S., Baker, A., and Leishman, J. G. 1996. "Angular Response Properties of Retroreflective Screen Materials Used in Wide-Field Shadowgraphy," *Experiments in Fluids*, 20, pp. 227–229.

Young, C. 1974. "The Prediction of Helicopter Rotor Hover Performance Using a Prescribed Wake Analysis," ARC C & P No. 1341.

CHAPTER 11

Rotor–Airframe Interactional Aerodynamics

Interaction phenomena remain for the foreseeable future beyond the possibilities of present viscous flow codes.

S. R. Ahmed (1990)

11.1 Introduction

Chapter 10 has described the physics of the helicopter rotor wake and its inherent 3-D complexity. This chapter describes the fundamental nature of the aerodynamic interactions that occur as the rotor wake influences the flow about the airframe. Despite the particular aerodynamic issues of the subcomponents of the helicopter (i.e., the rotor, fuselage, tail rotor), all of these subcomponents exhibit fairly well-understood aerodynamic characteristics when operated in isolation, at least from an engineering perspective.[1] The performance of the isolated components is also fairly predictable, despite the fact that semi-empirical methods often need to be used. However, when these subcomponents are integrated as a system, their aerodynamics change because of interactions and so their performance characteristics will be different from their isolated behavior. In many cases, the aerodynamic interactions are benign, but in some flight conditions the interactions may be deleterious. This can result in behavior that may detract from the overall performance characteristics of the helicopter (such as producing downloads, airframe moments, or vibrations). The primary interactional effects are produced on the fuselage and empennage of the helicopter. Yet, the aerodynamics and performance of the tail rotor are also subjected to interactional aerodynamic effects. Tail rotor operation is strongly influenced by the presence of the main rotor wake, the downstream turbulence from the main rotor hub, and also from the influence of the vertical and horizontal tails. Because the helicopter as a system must function properly and predictably throughout its operational flight envelope (including hover, forward flight, climbing flight, and during many other flight maneuvers), an understanding of component-interaction aerodynamics is essential to the successful design of the modern helicopter.

The various aerodynamic interactional effects between airframe and rotor components are summarized in Fig. 11.1, which is adapted from the seminal work of Sheridan & Smith (1979). This work has led to general design guidelines for minimizing the numerous types of adverse interactional aerodynamic problems found on helicopters. There have been many subsequent studies to understand the physics responsible for the various problems by means of wind tunnel and flight tests. Yet, many features of flow interactions are still not well understood from a fundamental perspective, nor are they predictable using mathematical models. This is reflected by the redesign of many prototype helicopters after first flight because they have shown undesirable flight characteristics, which in many cases have their origin in adverse aerodynamic interactions. One common problem is with the placement

[1] Their performance, however, is certainly still not understood from a fundamental fluid mechanics point of view.

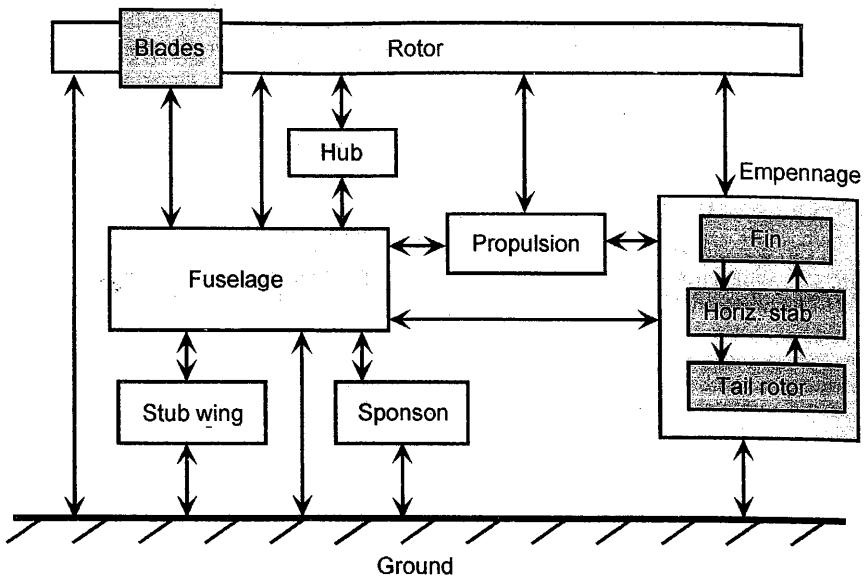

Figure 11.1 Schematic showing the various aerodynamic interactions that can exist between rotor and airframe components. Adapted from Sheridan & Smith (1979).

and sizing of the horizontal tail relative to the rotor, and nearly every new helicopter in recent years has experienced some unforeseen problem with the empennage design. The typically long tail boom found on the helicopter and the placement of the tail surfaces well aft on the fuselage or tail boom mean that changes in the position of the main rotor and rotor wake can produce airloads on the tail that may have a significant impact on fuselage pitching moments. The sensitivity of these effects to flight conditions can have a large impact on the overall flight characteristics and handling qualities of a helicopter. In essence, this is the fundamental reason for gaining a better understanding of rotor–airframe interactions through basic research; an improved understanding and predictive capability will ultimately allow any adverse effects to be minimized at the design stage rather than after expensive flight testing.

As discussed in Chapter 6, the fuselage is the largest airframe component and a lot of attention has been placed on gaining an improved understanding of the effects of the rotor on the fuselage aerodynamics. The presence of the fuselage also distorts the inflow through the rotor disk and this affects the blade airloads and rotor performance. These effects, however, are very difficult to predict because the rotor aerodynamics must be modeled using relatively sophisticated forms of unsteady aerodynamics (see Chapter 8) and rotor wake analyses such as free-vortex methods (see Chapter 10) or other advanced wake methods (see Chapter 14). In the quest for more compact, lighter, faster, and more maneuverable helicopters, current design trends are moving toward the use of higher rotor disk loadings and smaller rotor–fuselage spacing. In addition, cutting down on rotor hub drag in forward flight (see Section 5.5.10) is one strong motivation to use reduced rotor–fuselage spacing. Furthermore, the need to deploy military helicopters inside existing cargo aircraft without significant disassembly has demanded an overall more compact helicopter design. However, the stronger blade tip vortices (see Section 10.6) and higher downwash velocities intrinsically associated with smaller rotors operated at higher disk loadings mean that stronger aerodynamic interactions between the rotor and the fuselage

may be produced. The aerodynamics of the tail rotor is also affected by the main rotor wake and in some cases, the effects of these interactions can involve the production of significant unsteady airloads on the blades coupled with losses of tail rotor anti-torque efficiency or control effectiveness, as well as high noise production. Therefore, for the helicopter to be an efficient machine the fuselage must be carefully integrated aerodynamically with the main rotor, as well as with the empennage and the tail rotor.

11.2 Rotor–Fuselage Interactions

The effects of the rotor wake on the fuselage airloads are a serious cause for concern on all modern helicopters. This is especially the case in hovering and low-speed forward flight where the rotor wake will envelop a good part of the fuselage (and perhaps also the empennage). While there have been earlier studies of this problem, the first systematic wind tunnel study into rotor–airframe problems was conducted by Sheridan (1978) and Sheridan & Smith (1979). In more recent years, a significant amount of detailed experimental and theoretical research has been accomplished to provide a more thorough understanding of the aerodynamic interactions between rotors and (nominally) nonlifting bodies of relatively simple geometric shape, such as bodies of revolution [e.g., Komerath et al. (1985), Smith & Betzina (1986), and Leishman & Bi (1990b)], although more complex body shapes and scaled helicopter airframes have also been studied [e.g., Freeman & Wilson (1980), Trept (1984), Berry (1988), and Le Pape et al. (2004)]. More recent efforts to study rotor–airframe interactions have been specifically aimed at gaining a more complete understanding of the underlying fluid mechanics. There has been particular experimental and theoretical emphasis on the unsteady airloads caused by the interaction of the rotor blade tip vortices with the fuselage surfaces. While vortex impingement phenomena are localized on the airframe, the intense unsteady airloads produced can contribute significantly to overall helicopter vibration levels. Other unsteady airloads are produced each time a blade passes over the fuselage, which creates an abrupt pressure pulse over a substantial part of the airframe. These pressure pulses depend on rotor blade loading and occur in phase with each blade passage; they can lead to low-frequency airframe and rotor vibrations that have considerable intensity. Several prototype helicopters have been designed with minimal rotor–fuselage spacing and have encountered insurmountable vibration problems that could only be solved (ultimately) by increasing the rotor–fuselage spacing. Currently, it is not clear if such vibration problems can be solved by other means. An unfortunate byproduct of increased spacing, however, is an increase in parasitic drag.

A reciprocal effect of the fuselage may occur on the rotor, where the blade airloads and rotor performance are changed – see Wilby et al. (1979), Rand (1989), and Crouse & Leishman (1992). The presence of the fuselage distorts the inflow through the rotor disk and this affects the blade airloads, the rotor performance, and the blade pitch control angles required for trimmed flight. Wilby et al. (1979) have shown that in forward flight the fuselage-induced upwash velocities can provide a perturbation to the aerodynamic angles of attack over the front of the rotor disk, which can significantly affect the blade airloads and net rotor response. Smith (1987) has shown that the wake distortion associated with fuselage interactions can generate enhanced rotor wake interactions that may trigger a torsional aeroelastic response of the rotor and could lead to a premature retreating-blade stall. Such effects are recognized based on flight testing experience, but are not well understood or predictable because they are sensitive to the flight conditions and to the ability to predict the detailed aerodynamics at the rotor. This also makes the underlying aerodynamic issues hard to study in more controlled wind tunnel experiments because not all flight conditions can

be replicated. The effects and consequences of fuselage-on-rotor aerodynamics will require relatively sophisticated and fully coupled rotor wake and airframe models if their effects are to be predicted accurately. Other authors, including Johnson & Yamauchi (1984), have also emphasized the importance of and difficulties attributed to rotor–airframe aerodynamic interactions when predicting the airloads and aeroelastic response of rotors.

11.2.1 *Effects of the Fuselage on Rotor Performance*

Betzina & Shinoda (1982), Smith & Betzina (1986), Brand et al. (1986, 1989, 1990), and Leishman & Bi (1990a, 1990b, 1994a, b) have conducted wind tunnel tests to investigate aerodynamic interactions using subscale rotors and relatively simple bodies of revolution. Most studies have concluded that the rotor performance was to some extent affected by the presence of the body, but that the aerodynamic characteristics of the body were highly modified by the presence of the rotor and its wake. Such tests on fairly generic fuselage configurations (easy to define geometrically) can help the analyst to better isolate the specific aerodynamic phenomena that allow for fundamental understanding. For example, Fig. 11.2 shows an example of a subscale rotor with a geometrically simplified airframe being tested in a wind tunnel, in this case with a body of revolution for the fuselage and a simple T-tail empennage. There was no tail rotor in this case. These types of geometrically simplified setups gives the analyst the ability to carefully study the flow physics of specific aerodynamic phenomena with greater confidence than could be done with more representative helicopter airframe configurations. The results also give the analyst the best opportunity to precisely define the geometry of the problem to validate computational flow studies. This will help to improve confidence levels in comprehensive flow models that predict the detailed viscous flows about actual helicopter airframes.

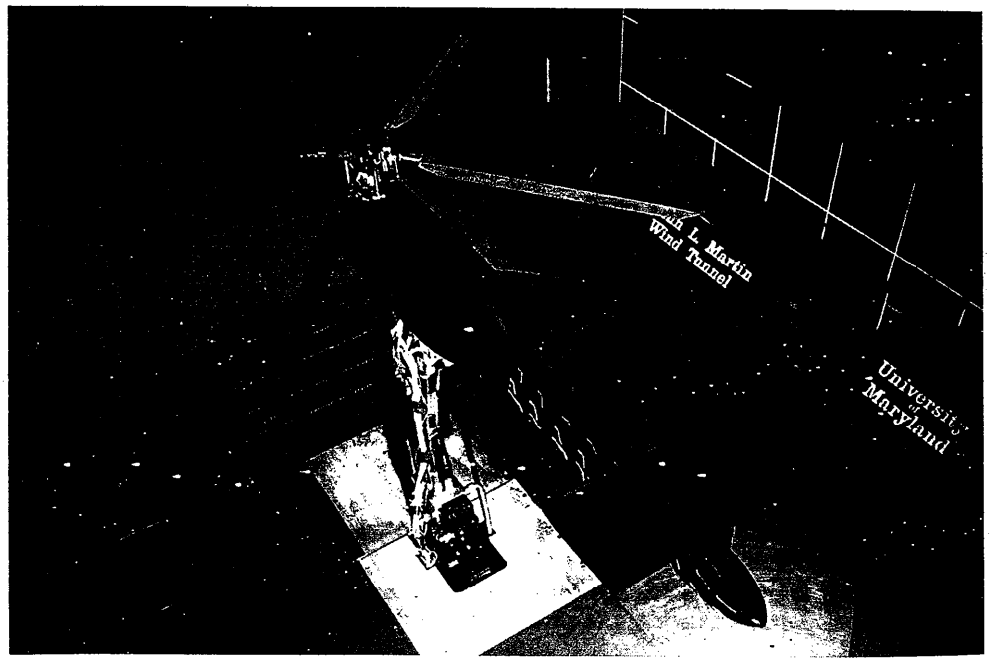

Figure 11.2 A subscale helicopter rotor with a geometrically simplified airframe (body and T-tail) geometry being tested in a wind tunnel.

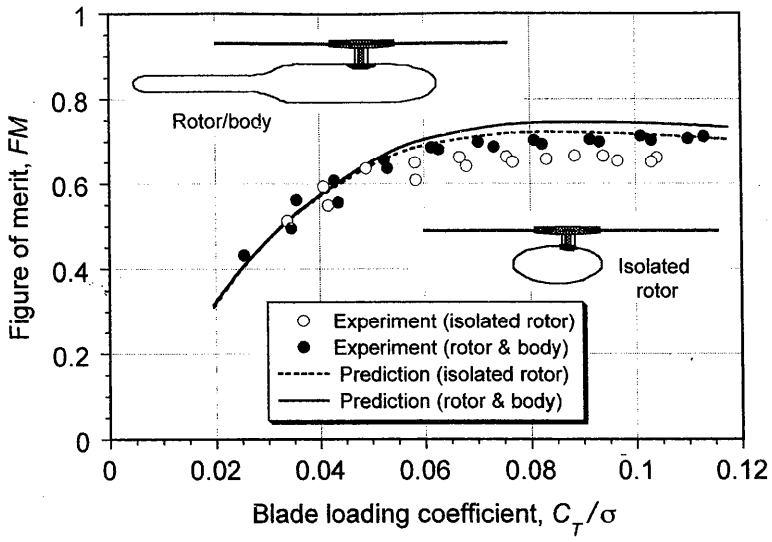

Figure 11.3 The figure of merit of the rotor will be affected by the presence of an airframe. Data source: Bagai & Leishman (1992). Analysis: Crouse & Leishman (1992).

Perhaps surprisingly, it has been found that the introduction of a body into the flow field near the rotor can give a beneficial reduction in rotor power requirements for a given thrust, but only when operating in hover and in forward flight at low advance ratios. For example, Fig. 11.3 shows the figure of merit of a rotor for a range of thrust coefficients in hover. Results are shown with and without a body.[2] As the rotor thrust increases, the presence of the body produces an increase in the rotor figure of merit; the increase shown (about 5% at $C_T/\sigma = 0.10$) is clearly significant. There is also a download on the airframe induced by the rotor (which governs the net vertical force on the rotor–airframe combination), an effect that is discussed in Section 11.2.2. The most obvious reason for the change in rotor performance is the body's effect on the induced inflow through the rotor disk; the body reduces the inflow through the disk in the regions directly above itself and changes the effective angles of attack on the blade elements. This, in turn, affects the lift distribution over the blades, which becomes more heavily biased toward stations further inboard for a given rotor thrust. While the blade airloads are also unsteady, the effect of the body has the same effect as increasing the average value of the effective blade twist (in a more ideal way). It is apparent then that this particular interaction is actually beneficial and, in this case at least, gives the rotor increased hovering efficiency.

To expound on this point, Fig. 11.4 shows a plot of the computed time history of the lift coefficient at an inboard section of the blade in the region directly above the body surface. Clearly the mean value of lift is increased by the body, which is a direct result of the decrease in induced inflow at this blade station by the influence of the body. Furthermore, notice that, compared to values for the isolated rotor, the lift is now time-varying, with a 2/rev unsteady component. Because, in this case, a four-bladed rotor was used, the net effect of this interaction will be an 8/rev aerodynamic excitation at the rotor. As the blades pass over the rear of the fuselage (at $\psi = 0°$) notice that there is a stronger effect than when the blades pass over the front of the fuselage (at $\psi = 180°$). This is expected based on the slightly larger clearances between the blades and the nose of the body. The results also

[2] In the case without the body, the rotor drive was covered with a fairing.

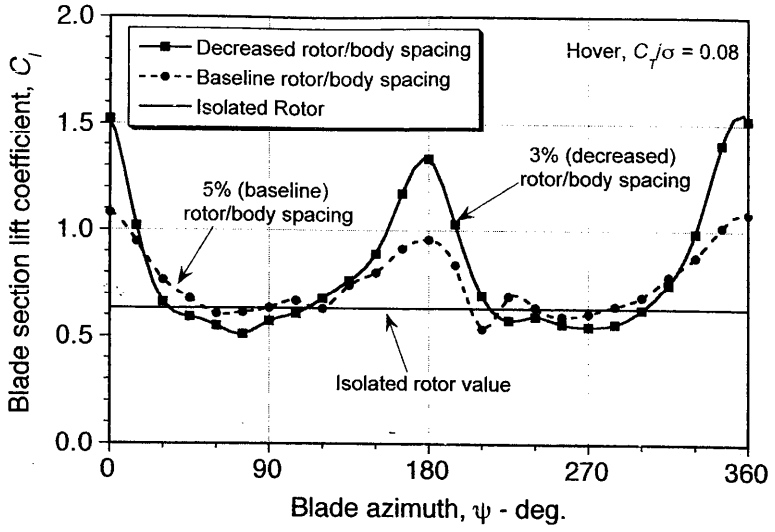

Figure 11.4 Airframe effects can produce large unsteady airloads on the rotor blades. Source: Crouse & Leishman (1992).

show that decreasing the spacing between the rotor and the body amplifies the unsteady lift. (There is also a reciprocal effect on the airframe airloads – see Fig. 11.15.) This is an example of why decreasing the rotor–airframe spacing on a helicopter generally increases vibratory airloads and why, if the spacing becomes too small, vibration problems will result that are difficult to solve (especially for helicopters using rotors with higher disk loadings) unless rotor–airframe spacing is ultimately increased again.

Similar types of interactions also occur in forward flight. However, the relative position of the rotor wake to the body is important here, and the wake position becomes a function of rotor thrust and advance ratio (see Section 10.4.1). There are also self-induced effects on the rotor wake that are produced by wake distortions induced by the airframe surfaces. As forward speed increases, the rotor wake quickly skews behind the rotor disk and the wake interactions between the rotor and the body become somewhat weaker. Yet, there are also other complicating aerodynamic factors that occur in forward flight. One is that the fuselage produces flow field perturbations in the rotor plane as forward speed builds – see Fig. 11.5. This effect, however, becomes significant only at relatively high forward speeds

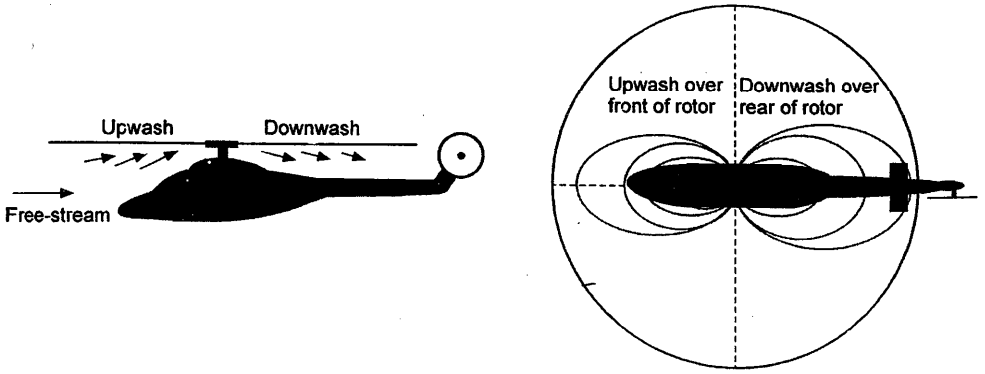

Figure 11.5 Fuselage effects in forward flight will cause an upwash perturbation over the front of the rotor and a downwash over the rear of the disk.

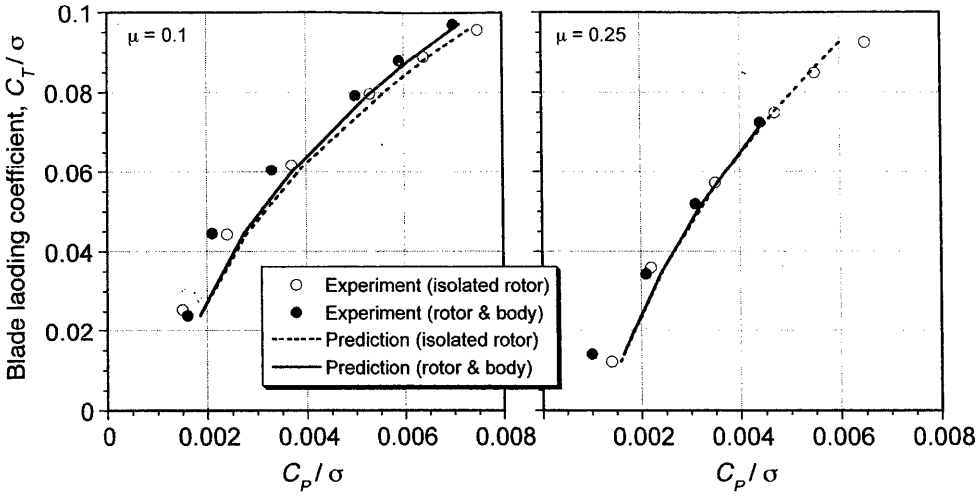

Figure 11.6 Rotor performance polars showing the effects of the body on the rotor performance at advance ratios of 0.1 and 0.25. Data source: Leishman & Bi (1994b). Analysis: Crouse & Leishman (1992).

(say for $\mu > 0.3$) but it can make a difference to the blade airloads and rotor performance. However, the unsteady effects from blade passage and induced pressures associated with the convection of the discrete wake vortices (see Section 11.2.3) remain important at all advance ratios, and these effects may even increase in intensity at higher forward flight speeds as rotor thrust increases to meet propulsive requirements.

Figure 11.6 shows an example of the rotor performance polars in forward flight at advance ratios of $\mu = 0.10$ and $\mu = 0.25$. At the relatively low advance ratio of $\mu = 0.10$ there are notable differences between the performance of the rotor with and without the body present. As expected, the changes become more apparent at higher rotor thrust values as the interactions between the rotor and the airframe strengthen. As the advance ratio is increased, however, the effects of the body on the rotor are progressively reduced. At an advance ratio of $\mu = 0.25$ there are almost no differences between the rotor–body case and the isolated rotor. This is because the wake is now much further away from the fuselage, and there is a weaker body-induced wake distortion – see Figs. 11.7 and 10.10. At this condition the rotor and the body each behave more like they would in isolation, although not completely. At both advance ratios, the analysis [Crouse & Leishman (1992)] predicts the changes in the rotor power to within the bounds of experimental measurement uncertainty. See Section 11.2.3 for modeling requirements and the types of approaches.

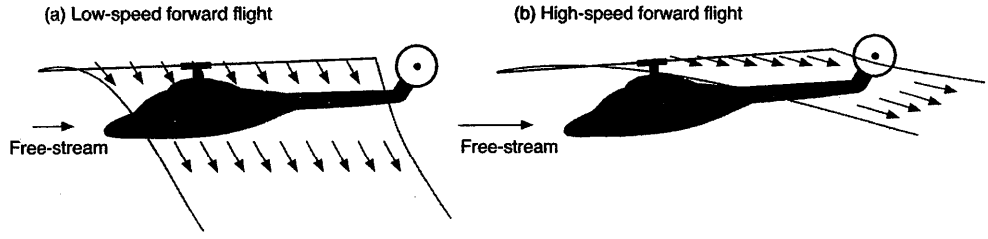

Figure 11.7 As forward speed is increased the main rotor wake is skewed behind the rotor. (a) Low-speed flight. (b) High-speed flight.

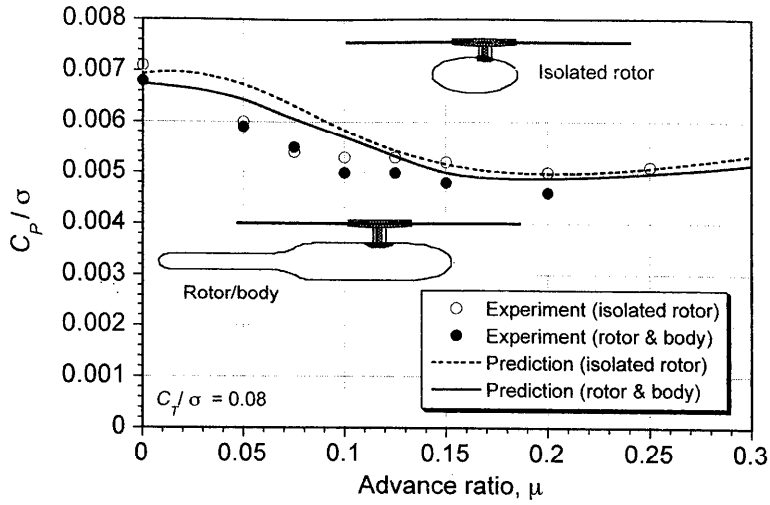

Figure 11.8 The effect of increasing advance ratio will initially be to decrease the significance of rotor–airframe interactional effects on rotor performance. Data source: Leishman & Bi (1994b). Analysis: Crouse & Leishman (1992).

The net rotor power required for rotor operation at the same nominal thrust over a range of advance ratios is shown in Fig. 11.8. As expected, the greatest differences between the isolated rotor and the rotor–body combination are in low-speed flight; as advance ratio increases the differences decrease. It might be expected that at very high advance ratios (>0.4) some degree of interaction returns because the fuselage will produce larger flow disturbances in the rotor plane, as suggested by Fig. 11.5. This effect has been studied by Wilby et al. (1979), Ryan et al. (1988), Dehondt & Toulmay (1989), and Rand & Gessow (1989) using a potential flow methodology. This seems to give a good first order approximation to the perturbations in blade angles of attack caused by the fuselage. The interactional effects, however, are confined mostly to the regions near the rotor hub, which do not contribute as much to rotor lifting and propulsive capability. The effects, therefore, show up more in blade airloads and aeroelastic response and less in contributing to overall rotor performance.

11.2.2 *Time-Averaged Effects on the Airframe*

The effects of the generally nonsteady airloads averaged over many rotor revolutions are time-averaged effects. These can be considered as the effects that can affect the overall forces and moments on the airframe and, therefore, the flight characteristics of the helicopter as a whole. Wilson & Mineck (1975), Freeman & Mineck (1979), Sheridan & Smith (1979), Freeman & Wilson (1980), and Trept (1984) were among the first to conduct systematic tests to study the effects of the rotor wake on the time-averaged aerodynamic characteristics of helicopter fuselages. Considerable downloads and yawing moments induced by the rotor wake have been measured. The largest effects of the body on the rotor performance are in low-speed and hovering flight, and the body downloads are also the largest here. Subsequent experiments by other investigators [e.g., Smith & Betzina (1986), Liou et al. (1989a, b), Leishman & Bi (1990a)] have confirmed these basic findings.

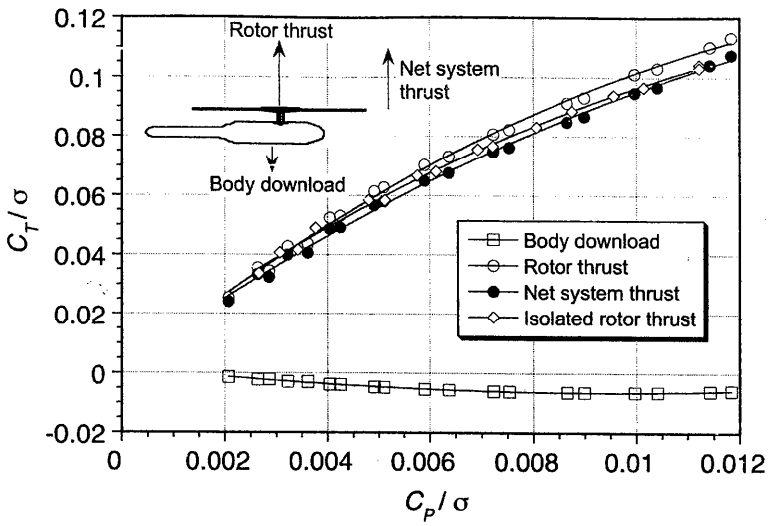

Figure 11.9 While the rotor thrust can be increased by the airframe, the net sum of the rotor thrust and airframe download in hovering flight is close to isolated rotor performance values, although they may again become important at high μ. Data source: Bagai & Leishman (1992).

It is instructive first to examine in detail the net lifting performance of the rotor system (rotor plus body) in hovering flight. Representative results are shown in Fig. 11.9 as a function of rotor power required for the generic subscale model shown in Fig. 11.2. As previously discussed, with the body present the rotor thrust is increased relative to the thrust of the isolated rotor for a given collective pitch or power setting. The body also experiences a download that increases with increasing thrust, and hence the downwash velocity is increased below the rotor. In fact, the measured results simply confirm that the download on the body is proportional to $\sqrt{C_T/2}$ as might be expected based on the discussion in Section 6.6.2. It is apparent that the increase in thrust on the rotor is almost exactly equal and opposite to the download on the body, at least within the bounds of experimental accuracy. The net thrust of the system also agrees closely with the isolated rotor results, and while perhaps not an entirely unexpected result, it is not obvious that this should be the case.

An example of the effects of the rotor on the lift and pitching moment of the body is shown in Fig. 11.10 for a range of rotor advance ratios up to $\mu = 0.25$; this would represent the range of μ when transitioning from hover into forward flight or vice versa. Notice that the lift and pitching moment for the isolated body are close to zero for all advance ratios, so these results represent almost entirely the effects of the rotor on the integrated aerodynamics of the body. It should be noted that the results are plotted by nondimensionalizing the body forces and moments by using rotor tip speed, that is,

$$C_{L_f} = \frac{L_f}{\rho A \Omega^2 R^2} \quad \text{and} \quad C_{M_f} = \frac{M_f}{\rho A \Omega^2 R^3}. \tag{11.1}$$

This is necessary because if standard coefficient values are used (based on free-stream velocity V_∞) the effect of increasing μ will be to decrease the coefficient values for a constant lift and may produce misleading trends.

The results in Fig. 11.10 show that the rotor provides the most significant download on the body at low advance ratios. As the advance ratio is increased the download decreases,

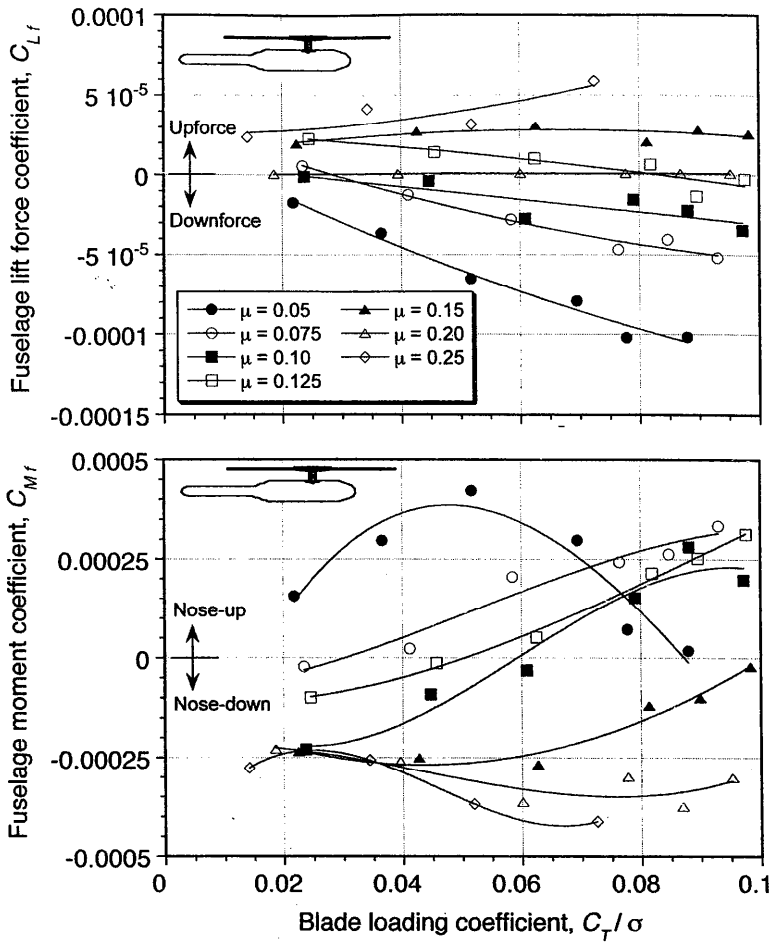

Figure 11.10 Representative variations in body lift and pitching moment with rotor advance ratio. Data source: Leishman & Bi (1994b).

and an upforce is actually obtained at high advance ratios. Similar results have been obtained by Smith & Betzina (1986). The source of the upflow reflects the low pressure region produced on the upper part of the body because of the higher-speed flow in the rotor wake (see Fig. 11.7). The results in Fig. 11.10 also show that the fuselage pitching moment decreases (i.e., the moment changes from nose-up to nose-down) with increasing advance ratio. This is because the rotor wake modifies the pressure distribution on the body such that the net center of pressure moves further aft from increasing the advance ratio (see Figs. 11.11 and 11.12). Overall, the foregoing results reflect the significant changes in the pressure distribution on the body as the position of the rotor wake is changed by varying rotor thrust and the advance ratio.

We can examine in more detail the source of the pressure distribution found over the body surface. A pressure coefficient can be defined in terms of the rotor tip speed, ΩR, as

$$C_p' = 100\left(\frac{p - p_\infty}{\frac{1}{2}\rho(\Omega R)^2}\right), \tag{11.2}$$

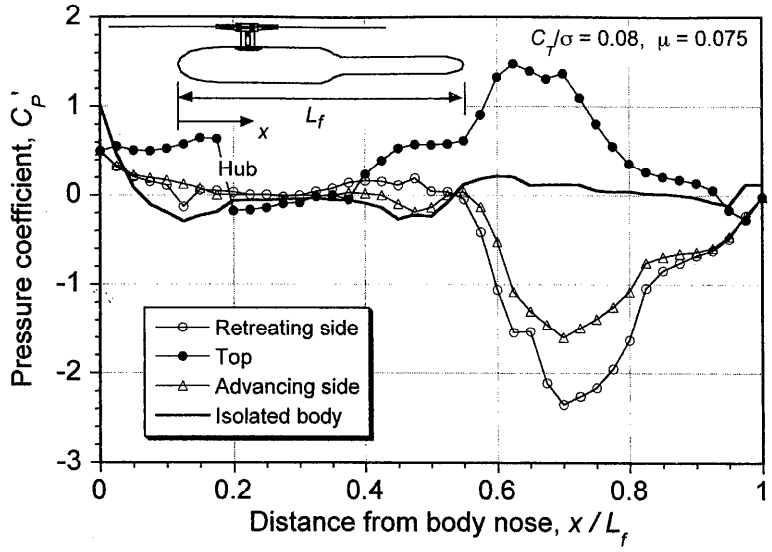

Figure 11.11 Static pressure distribution on top and sides of a body at $\mu = 0.075$. Data source: Leishman & Bi (1994b).

where the factor of 100 is simply a scaling. This form of coefficient was introduced by Liou et al. (1989a,b) and has become accepted by many investigators for the purposes of helicopter interactional aerodynamic studies because it gives an indication of the actual pressure on the body, so they can then be more readily compared at different advance ratios. Examples of the measured pressure distributions along the top and on the two sides of a body are shown in Fig. 11.11 for an advance ratio of 0.075. In general, the results show that the rotor wake has a pronounced effect on the body pressure distribution. A significant

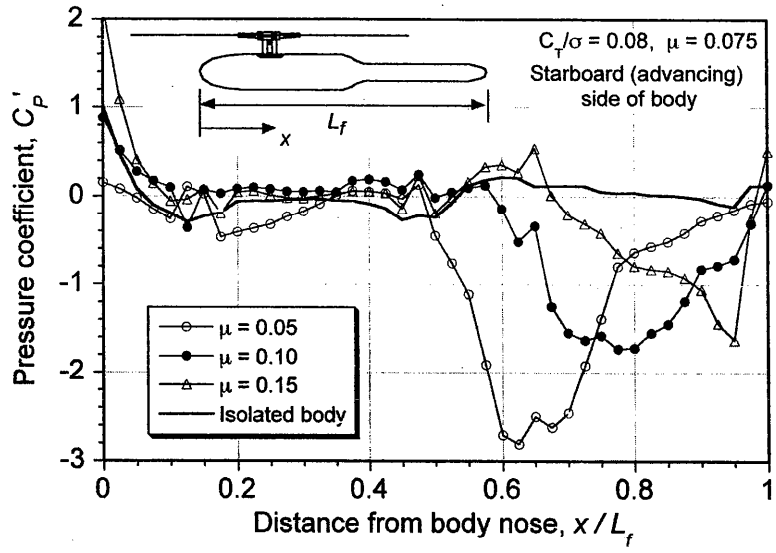

Figure 11.12 Static pressure distribution along the starboard side of a body as induced by the rotor at several rotor advance ratios. Data source: Leishman & Bi (1994b).

increase in static pressure is obtained over the top of the body in regions affected by the rotor wake because the wake induces a relatively high dynamic pressure there. There are large suction pressure peaks on the sides of the body, and this is a direct consequence of the wake flow being accelerated over the sides of the fuselage.

As the advance ratio is increased the wake is skewed back (see Fig. 11.7), and the results in Fig. 11.12 show that the suction peaks produced by the rotor wake move aft along the body. It should be apparent that the high adverse pressure gradients downstream of the suction peaks will cause the boundary layer to be susceptible to flow separation. This is a good example that shows why 3-D flow separation is inevitably always involved in helicopter airframe aerodynamics, and why the modeling of the flow over airframe surfaces will be relatively difficult (see also Section 14.7). Another aspect of the pressure distributions shown in Figs. 11.11 and 11.12 is that the distributions on the two sides of the rear fuselage are different, with a higher suction pressure obtained on the retreating (port) side of the tail boom. This indicates that because of the rotor wake the fuselage will experience both a side force (to port) and a yawing moment (nose-right) for a rotor rotating in the conventional (counterclockwise) direction. On an actual helicopter, this may be important from a handling qualities perspective, as pointed out by Wilson & Mineck (1975). Notice also that this side force is in a direction opposite to that required for anti-torque purposes, so a tail rotor will have to produce more thrust (and consume more power) to compensate. The integration of the tail rotor into the overall flow field, however, will further change the body airloads to some degree but there are few results available in this case that clearly delineate this effect.

11.2.3 *Unsteady Rotor–Fuselage Interactions*

Considerable attention has been placed on the measurement and prediction of the unsteady pressures induced on a fuselage below a rotor. In many cases, the unsteady pressure fluctuations are much larger than the mean pressures. All parts of the fuselage surface are subjected to unsteady loading, both in magnitude and phase. Because the distribution of pressures is very complicated in nature and has contributions from multiple sources (rotor, individual blades, wake, etc.), it has proved difficult to isolate or characterize unsteady pressure responses and correlate the behavior with specific physical phenomena. As previously mentioned, the isolation of phenomena is very necessary for the validation of mathematical models, such as those for wake distortion and tip vortex impingement on the airframe – see Section 11.2.5.

Liou et al. (1989a,b) and Brand et al. (1989, 1990) have conducted experiments to investigate the aerodynamic interactions between a cylindrical body and a rotor. Measurements of the instantaneous and time-averaged pressures on the cylinder surface were obtained. Measurements of three velocity components of the flow at selected regions were also made using LDV techniques. Leishman & Bi (1994a,b) have made similar measurements using the configuration shown in Fig. 11.2. In both experiments, flow visualization of the trajectories of the wake vortices complemented the measurements. All of these results have helped to provide a reasonably comprehensive picture of the underlying interactional flow mechanisms, while also providing an extensive data base for validation of predictive models (see Section 11.2.5).

Based on the various experimental studies that have been performed, it is apparent that the unsteady airloads on the airframe that are associated with the presence of the rotor and its vortical wake can be classified into four distinct types. These are: 1. blade passage effects, 2.

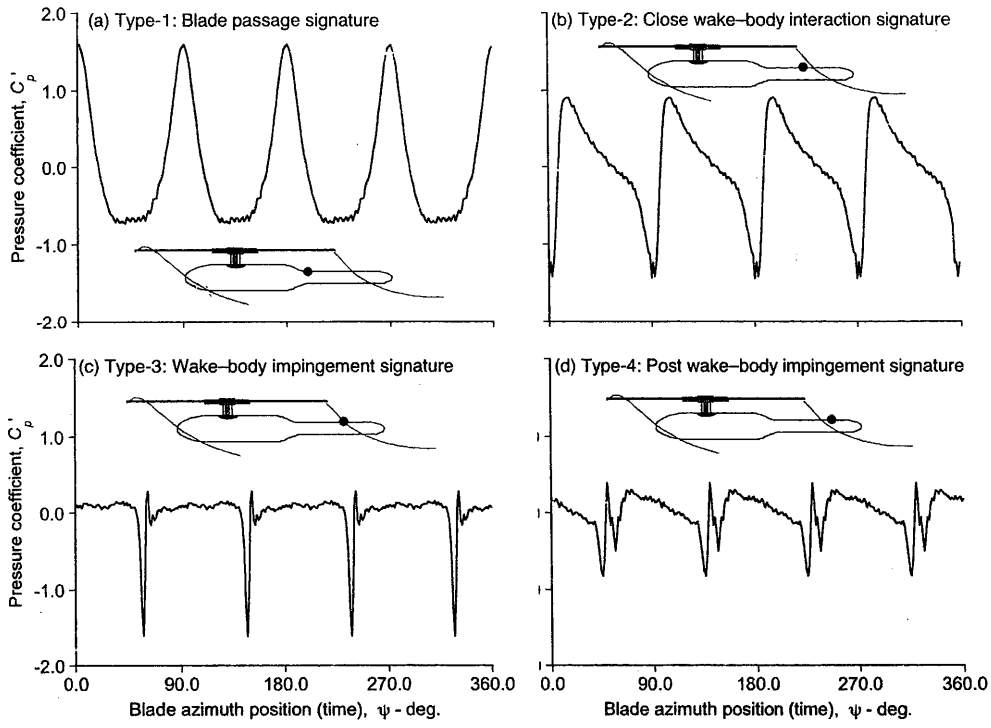

Figure 11.13 Characterization of unsteady pressure signatures on an airframe below a rotor. (a) Blade passage. (b) Close wake–surface impingement. (c) Wake–surface impingement. (d) Post wake–surface impingement. Data source: Bi & Leishman (1990), Leishman & Bi (1994b).

close wake–surface interactions, 3. wake–surface impingement, and 4. post wake–surface impingement.

Type-1 Interactions: Blade Passage Effects

Blade passage effects have been measured and reported by Bramwell (1966), Brand et al. (1989), Leishman & Bi (1990), and many other investigators. More recently, Le Pape et al. (2004) have measured surface pressure loads on a geometrically scaled helicopter fuselage model that were induced by blade passage. An example of the unsteady pressure response measured at a location directly under the rotor is shown in Fig. 11.13(a). The results show that large pulses are produced that are exactly in-phase with the blade passage over the body (i.e., for a four-bladed rotor they occur at $\psi = 0°$, 90°, 180°, and 270°). This type of signature has been noted to be relatively independent of advance ratio so it must be associated with the local loading on the rotor itself; in other words, the main features of this type of signature are not coupled to the strength of the rotor wake or the rotor wake geometry. Therefore, it is called a *blade passage* effect and is classified as a Type-1 interaction.

The blade passage effect can be examined from a parsimonious potential flow analysis of a series of line vortices moving at velocity $r\Omega R$ ($r = y/R$) at a distance h above a surface. A simple model such as this is given by Bramwell (1966) with later extensions by Lorber & Egolf (1990) and Crouse et al. (1992). The vortex represents the bound circulation at some

point on the blade at a radial distance y from the hub. The surface plane representing the body is made into a streamline of the flow using an image system. If the circulation along the blade is assumed to be uniform (a good assumption for a rotor with twisted blades operating in hover), then the circulation Γ can be related to the blade loading using Eq. 3.111. With these assumptions, along with Kelvin's equation for the velocity potential, it can be shown that the pressure coefficient at some point x on the surface is given as a function of blade azimuth, ψ, by

$$C_p'(\psi) = \underbrace{-100K^2\left[\frac{\frac{h}{R}}{\left(\frac{x}{R}-r\psi\right)^2+\left(\frac{h}{R}\right)^2}\right]^2}_{\text{quasi-steady term}} + \underbrace{200K\left[\frac{\frac{h}{R}r}{\left(\frac{x}{R}-r\psi\right)^2+\left(\frac{h}{R}\right)^2}\right]}_{\text{unsteady term}}, \tag{11.3}$$

where $K = \dfrac{2c}{\pi R}\left(\dfrac{C_T}{\sigma}\right)$. (11.4)

The first term in Eq. 11.3 is a steady or quasi-steady contribution to the pressure and the second term is the unsteady contribution. Results using Eq. 11.3 are shown in Fig. 11.14 where the pressure signature is found to be in excellent quantitative agreement with the measurements. The unsteady term clearly dominates the quasi-steady term. This immediately illustrates the necessity of retaining the time-dependent terms in any type of predictive aerodynamic model, if the rotor–body interaction airloads are to be properly predicted.

The significance of the unsteady terms is further appreciated when the model is compared with the experimental data measured on the fuselage directly under the rotor disk.

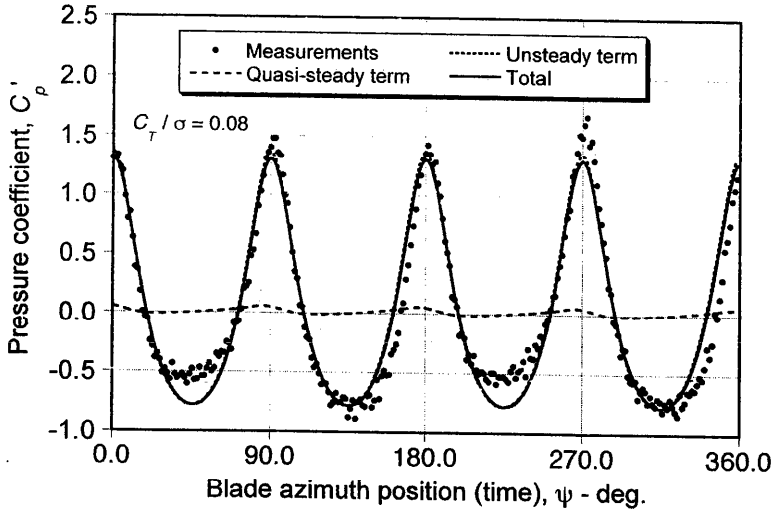

Figure 11.14 Prediction of unsteady surface pressures associated with blade passage effects using potential flow theory. At a minimum the predictions of the unsteady airloads on the airframe require the unsteady terms to be retained in the flow model. Analysis: Crouse & Leishman (1992). Measurements: Bi & Leishman (1990) and Leishman & Bi (1994b).

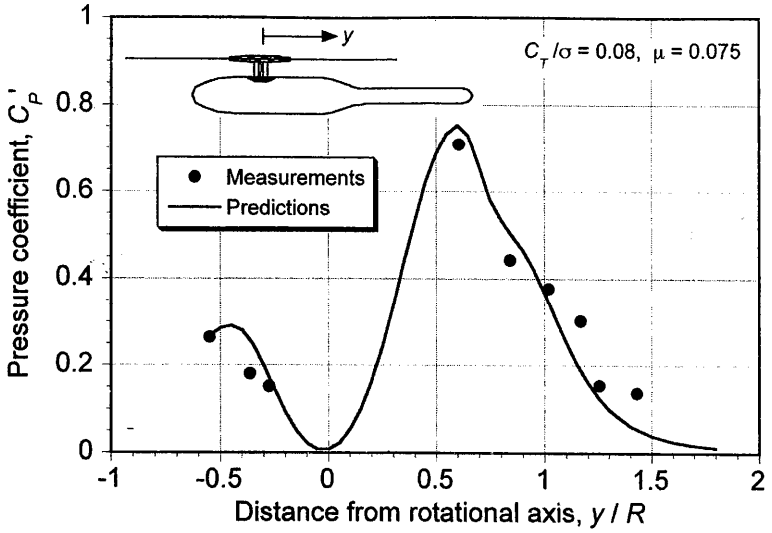

Figure 11.15 Predicting the effects of blade passage loading on the airframe is relatively easy because it is mostly a noncirculatory effect and requires no knowledge of the rotor wake. Analysis: Crouse & Leishman (1992).

According to the model described by Eq. 11.3 the approximate magnitude of the unsteady pressures on the body resulting from the blade passage should be: 1. Proportional to the rotor disk loading (which is proportional to C_T/σ for a given rotor and tip speed), 2. Inversely proportional to the distance of the rotor blades above the measurement point (i.e., the rotor–body spacing), and 3. Proportional to the speed of the blade past the measurement point (i.e., rotor tip speed and distance along the blade). This parsimonious model confirms what is already known from numerous experimental studies, that the unsteady loads induced by blade passage effects will become much more pronounced on rotorcraft with higher disk loadings and smaller rotor–airframe spacing. Recall that the airframe loading in this case can be considered as a noncirculatory effect because it depends only on the blade loading and requires no explicit knowledge of the circulation that is shed or trailed into the rotor wake.

Figure 11.15 shows a comparison of the peak-to-peak values of the unsteady pressure at two points directly below the rotor as a function of rotor thrust. It can be seen that the agreement between theory (see also Section 11.2.5) and experiment is indeed very good. The blade passage effect is found to be largely independent of rotor advance ratio. This behavior is to be expected because any changes in either advance ratio or TPP angle will only slightly affect the longitudinal variation of lift over the rotor (i.e., the distribution of circulation on the rotor blades as they pass above the body). These results confirm the validity of more general potential flow approaches for rotor–airframe aerodynamics, such as those of Lorber & Egolf (1990), Crouse & Leishman (1992), and Waschpress et al. (2003).

Type-2 Interactions: Close Wake–Surface Interactions

Figure 11.13(b) shows a second type of pressure signature found on a body situated below a rotor, which is distinctive because of its "saw-tooth" type of waveform. This second type of signature can occur at different points on the rear of the body under a variety of

combinations of thrust and advance ratio; it is related to the proximity, trajectory, and convection velocity of the trailed tip vortices relative to the body surface. The prediction of these airloads, therefore, requires a knowledge of the rotor wake structure, and specifically the strengths, induced velocity field, and trajectories of the convecting blade tip vortices. As shown in Chapter 10, this is a much more difficult problem, even for an isolated rotor. For the results shown in Fig. 11.13(b) the tip vortices were found to be close to the measurement point, but were a small distance above the body surface and not directly impinging at this point. Therefore, these pressure signatures are called *close wake–surface interactions* or Type-2 interactions.

Of course, the actual pressure signature induced on the body by the wake depends not only on the relative speed, direction of, and proximity of the tip vortices to the measurement location, but also on their strength (i.e., tip vortex strength is proportional to rotor thrust – see Eq. 3.112). This problem can also be examined, albeit approximately, using potential flow theory. The simplest model consists of an infinite series of free vortices convecting at velocity $\mu\Omega R$ at a skew angle χ relative to the vertical (see Fig. 3.28). Again, an image system is included to satisfy the condition of flow tangency on the body surface. The unsteady pressure coefficient on the body induced by this model of the convecting wake is given as a function of ψ by

$$C'_p(\psi) = \underbrace{-100K^2\left[\frac{\frac{b}{R} - \mu\psi\tan\chi}{\left(\frac{x}{R} - \mu\psi\right)^2 + \left(\frac{b}{R} - \mu\psi\tan\chi\right)^2}\right]^2}_{\text{quasi-steady term}}$$

$$\underbrace{-200\mu K\left[\frac{\frac{x}{R}\tan\chi - \frac{b}{R}}{\left(\frac{x}{R} - \mu\psi\right)^2 + \left(\frac{b}{R} - \mu\psi\tan\chi\right)^2}\right]}_{\text{unsteady term}}, \tag{11.5}$$

where K reflects the effect of rotor thrust and blade loading, as given by Eq. 11.4.

The first term in Eq. 11.5 is the quasi-steady contribution, and the second term is the unsteady effect, with the results being shown in Fig. 11.16. It can be seen that the predicted pressure signature is in excellent qualitative agreement with the measurements. This level of correlation essentially confirms that this second type of pressure signature is induced by the relatively close proximity of the convecting tip vortices to the fuselage surface. It should be noted, however, that, compared to the blade passage effect shown in Fig. 11.16, in this case both the quasi-steady term and the unsteady term are of equal importance in determining the net form of the unsteady pressure response.

Crouse et al. (1992) have hypothesized a large sensitivity of the unsteady pressure signature to hypothetical changes in the wake skew angle χ (i.e., the height and trajectory of the convecting wake vortices over the body). At low wake skew angles the saw-tooth type of pressure signature induced on the body is clearly a Type-2 interaction (i.e., a close wake–surface interaction). However, when the wake skew angle is increased slightly, the induced pressure signature becomes more benign. In fact, the pressure signature at higher wake skew angles gradually becomes more like a blade-passage effect because the wake

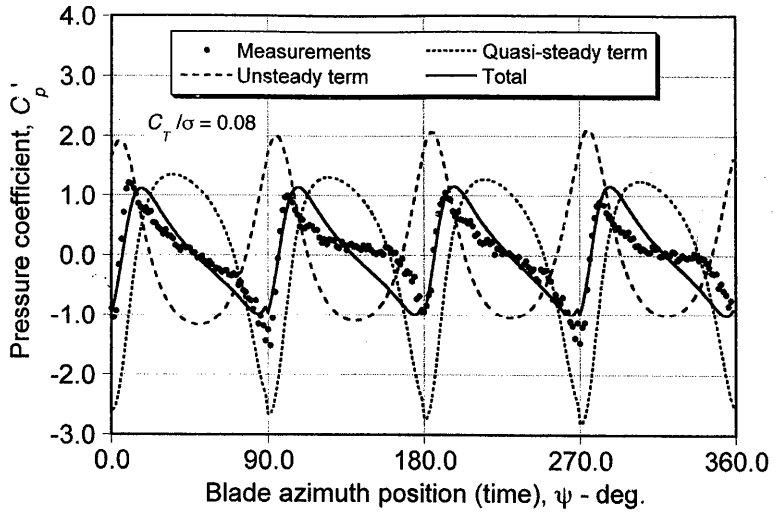

Figure 11.16 Prediction of unsteady surface pressures associated with close tip vortex/surface interaction using potential flow theory. Analysis: Crouse & Leishman (1992). Measurements: Bi & Leishman (1990) and Leishman & Bi (1994b).

makes an increasingly shallow angle with the body surface as μ increases for a constant value of rotor thrust – see Fig. 3.28.

In reality, of course, the trajectory of the rotor wake is not just a function of rotor thrust, but is affected by the distribution of loading over the rotor disk, the advance ratio, and the self-induced wake distortion, as well as the amount of local wake distortion caused by the fuselage. This latter effect increases the wake skew angle at the rear of the rotor and decreases the wake skew angle at the front of the disk. Therefore, it can be concluded that while an unsteady potential flow model is sufficient to predict the close wake–surface interactions when the vortex strengths and locations are prescribed, the high sensitivity of the body pressures to changes in wake location means that accurate prediction of the rotor wake geometry is really the vital key to successful prediction of rotor wake–airframe interactional airloads. Because it is difficult to predict (or measure) the wake geometry to high accuracy, this means that the accurate prediction (and measurement) of Type-2 interaction signatures at specific points on the airframe is still very challenging – see Wachspress et al. (2003) for a comprehensive study.

Type-3 Interactions: Wake–Surface Impingement

A third type of pressure signature often measured on helicopter airframes is shown in Fig. 11.13(c). This signature occurs when direct impingement of a tip vortex occurs near the measurement point, a fact confirmed by flow visualization experiments. For example, such an interaction made visible using the shadowgraph technique (see Section 10.2.3) is shown in Fig. 11.17. The tip vortex filaments appear as thin dark lines. Near the body surface the local wake skew angle increases progressively as the filaments asymptotically approach the body surface. The tip vortices also undergo significant local stretching (both laterally and longitudinally) before the action of viscosity causes the vortices to burst. The schematic in Fig. 11.18 shows the observed wake behavior in more detail. As the filaments reach the

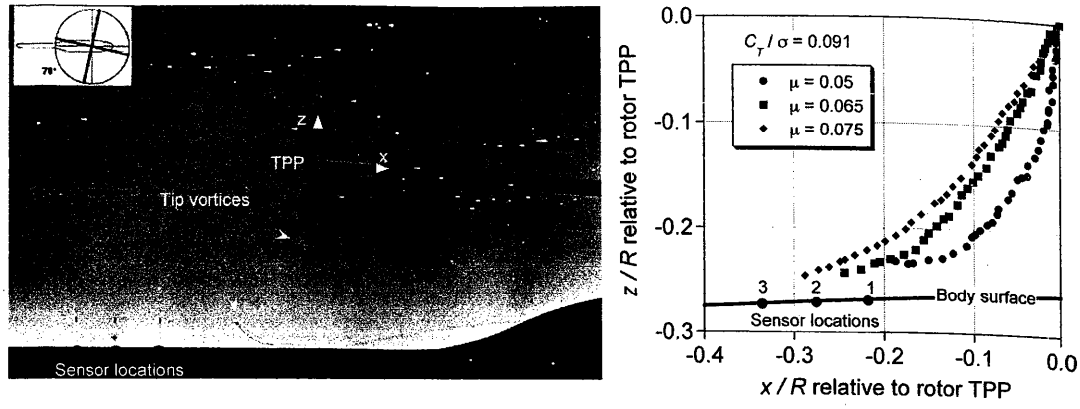

Figure 11.17 The trajectories of the tip vortices near the airframe can be obtained by means of flow visualization and correlated with the unsteady loading on the airframe. Data source: Crouse et al. (1992).

body surface they distort to form a loop or hairpin vortex structure. These vortex–surface interactions and their effects on the surface pressure, poses a complex problem in vortex dynamics because they involve a complex balance of inertia, pressure, and viscous forces – see Atias & Weihs (1984), Doligalski & Walker (1984), Walker et al. (1987), and Lim (1989). The physics of these complicated wake distortions have also been studied in detail by Conlisk et al. (1993) and Moedersheim et al. (1994), by means of flow visualization, and modeling these effects is discussed by Quackenbush & Bliss (1988), Quackenbush et al. (1990, 1994), and Conlisk & Affes (1993). Progressive transitions from Type-3 to Type-2 interactions (or vice versa) will be found during adjustments of the advance ratio and/or rotor thrust that adjust the position of the rotor wake relative to the body.

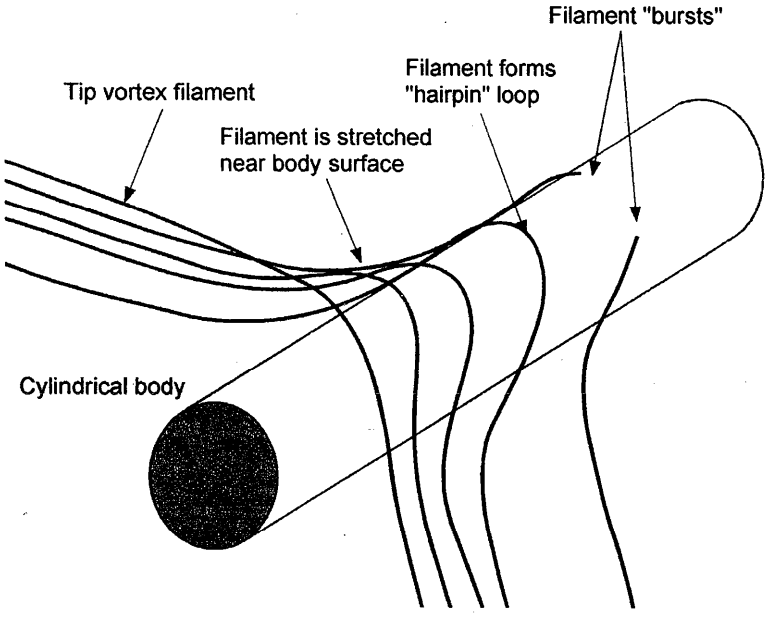

Figure 11.18 A schematic showing the interaction of rotor tip vortices with a cylindrical body, where the filaments stretch and loop over the body, strain, and finally burst.

Type-4 Interactions: Post Wake–Surface Impingement

A fourth type of pressure signature is shown in Fig. 11.13(d). This type of signature generally occurs just downstream of the impingement of a tip vortex on the body and thus is called a *post wake–surface impingement* or Type-4 interaction. This signature contains certain features common to both Type-2 and Type-3 interactions; the basic saw-tooth pattern is present along with a transient loading, but with several additional pressure fluctuations. The amplitude of the dominant peak is also attenuated relative to the Type-3 interactions, a point made by Lorber & Egolf (1990). This is a very complicated signature to predict because the flow near the body surface under these conditions is more viscous dominated and turbulent as it interacts with the body surface boundary layer. This problem requires a more thorough understanding of the distortions and stretching of the vortex filaments during and after the wake interaction with the body.

Leishman & Bi (1994b) suggest that Type-4 pressure signatures can be further classified into two groups. One can be called a *near-field post wake–surface impingement* interaction and the other can be called a *far-field post wake–surface impingement* interaction. The former occur immediately downstream of the surface location where the tip vortex impacts or at least comes very close to the body surface. The latter type occur some further distance downstream and contain high frequency fluctuations that are associated with turbulence in the boundary layer or separated flow. Unsteadiness also arises because part of the tip vortex that is very close to the body becomes unsteady (aperiodic with respect to rotor frequency) as it undergoes a complicated stretching and turbulent diffusion process (Fig. 11.18).

11.2.4 *Fuselage Side-Forces*

The origin of the adverse download and pitching moments on the airframe that are induced by the rotor has been discussed previously in Section 11.2.2. However, adverse side forces can also be produced on the airframe as a result of the rotor wake. An example has been shown previously in Fig 11.11, where the difference in static pressure between the two sides of the tail boom will produce a net side force. The side force is usually in the direction opposite to that required for anti-torque purposes. It has also been shown that when a helicopter is in sideward flight or is hovering over a fixed point above the ground in a crosswind, a significantly increased side-force will be produced on the fuselage. For most helicopters this side-force usually remains small enough to have a minimal impact on the handling qualities of the helicopter and its operational envelope. However, in some cases, the adverse aerodynamic side-force can be significant and may impact flight operations. This can occur when the helicopter is in starboard sideward flight or has a starboard crosswind component – see Fig. 11.19. (This example is for a rotor turning in the conventional, counterclockwise direction.) On some helicopters this is a powerful adverse effect that can affect directional (yaw) control and can limit its operational flight envelope. In particular, this can be an issue on military helicopters as these must often demonstrate high-speed sideward flight capability and must often operate in confined locations in gusty crosswind conditions (such as on a ship).

The aerodynamic side-force on the fuselage has been found to be accentuated by certain tail boom shapes, which can produce a sizable circulatory lift forces when the sideward velocity is combined with the main rotor downwash – see Wilson & Kelly (1983, 1986) for a systematic study of the forces produced on such tail boom shapes. See also Delany & Sorensen (1953) and Hoerner (1965) for force measurements on a variety of bluff body shapes. To counter this undesirable side-force effect, Brocklehurst (1985) and Wilson et al.

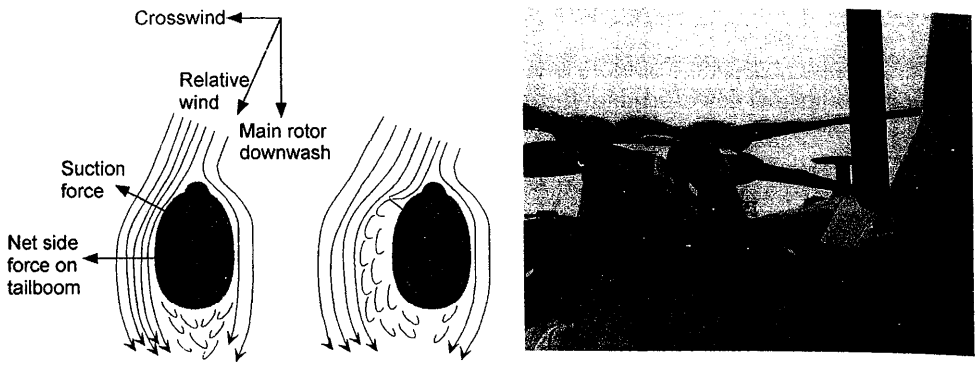

Figure 11.19 Tailboom strakes can significantly relieve adverse fuselage side forces under certain conditions, such as in sideward flight or during operation in strong crosswinds.

(1988) have suggested the use of a spoiler or strake that runs longitudinally along the one side (usually the port side) of the tail boom. This strake forces the flow to separate from the tail boom surface, spoiling the side-force and thereby restoring or improving the helicopter's operational flight envelope – see Kelly et al. (1993). This design solution will only be required if the tail boom cross section is relatively deep, typically if of quasi-elliptical shape with height to width ratios greater than about 2. The strake also creates a vertical download penalty and a nose-up moment on the airframe, but these effects are relatively small compared to the overall operational benefits that have been realized with the use of a strake. This device has been fitted or retrofitted to several production helicopter models. A more recent innovation is to use tail boom venting with porous skins to reduce tail boom side forces – see Banks & Kelly (2000). Although, passive venting appears to reduce adverse side-forces, its use is also accompanied by an increased vertical download from the higher skin friction effects created by the flow as it passes over the porous skin.

11.2.5 *Modeling of Rotor–Fuselage Interactions*

Effective analytical tools that are capable of treating interactional aerodynamic problems are still undergoing development and will continue to do so until wake modeling is improved further (see Chapter 10). Some of the earliest theoretical work on the rotor–fuselage aerodynamics problem was performed by Bramwell (1966) using potential flow assumptions and conformal mapping techniques. The results compared well with the few experimental data that were available at that time. Landgrebe et al. (1977) made one of the first studies of the effects of an airframe on rotor airloads and performance. The task was divided into three levels of complexity: 1. The calculation of velocity perturbations induced by the body in the rotor plane and the calculation of changes in the rotor airloads based on these perturbations, 2. The inclusion of velocity perturbations in the trim analysis, with the rotor loading being adjusted for the velocity perturbation, and 3. The inclusion of the effects of the body on the rotor wake geometry. The results clearly demonstrated the overall importance of accurately predicting interactional effects on helicopters.

The basic approach of linear superimposition of flow fields about the airframe and the rotor, but without considering the mutual interactions, has been pursued by several other researchers. Wilby et al. (1979), Ryan et al. (1988), and Dehondt (1989) have all used this type of superposition methodology. Although these models give an indication of the types

of interactional effects that can be expected, there are clearly many questions about the quantitative validity of the results, particularly in flight regimes where it is known that there are strong interactions between the rotor wake and the fuselage (i.e., in hover or low-speed forward flight). Under these conditions the interactional aerodynamics problem cannot be treated by linear-superposition techniques. It has already been shown how the rotor wake heavily influences the fuselage flow field, and likewise, the fuselage influences and distorts the rotor wake development. A somewhat better approximation was first introduced by Freeman (1980), who included a time-averaged vortex tube wake model during the calculation of the body aerodynamics. Clark & Maskew (1985, 1988) later developed a more sophisticated time-averaged wake model using vortex theory. A major deficiency of all of these models, however, was the omission of the distortion of the wake induced by the body.

More sophisticated surface singularity (panel) methods have been developed that allow a more complete computation of interactional effects, including the interaction of the wake and the airframe. These panel methods are discussed in Section 14.7. Some of these methods, however, have shown less predictive success in the low-speed forward flight regime, and this is a serious deficiency because the various flow interactions are often more significant here. Landgrebe et al. (1977) and Lorber & Egolf (1990) recognized the significance of the rotor wake distortions induced by the body, and developed an analysis using a prescribed rotor wake with geometric displacement rules to distort the wake about the body. More sophisticated analysis have coupled free-vortex wake models and surface panel models, including the work of Clark & Maskew (1988, 1991), Mavris et al. (1989), Berry (1988), Berry & Althoff (1990), Quackenbush et al. (1990), Crouse & Leishman (1992), Boyd et al. (2000), and Wachspress (2003). All these methods are potential flow models, so naturally are limited to essentially inviscid flows. Furthermore, for most flight situations there is a need to retain unsteady terms in the governing equations to give acceptable levels of predictive success, a point alluded to previously, and this leads to a greater computational cost.

All of these types of panel models inevitably include some empirical features (including viscous tip vortex models) and so require detailed experimental measurements for validation purposes. Unfortunately, there are still only limited measurements available that are directly relevant to the somewhat more idealized interactional problems currently under theoretical study (i.e., vortex–surface impingement). More experimental data are available for complex geometrical configurations, but it is difficult to isolate the effects of individual flow phenomena from these results. This paucity of specific types of experimental data hinders the development and validation of more effective analytical models for airframe and rotor airloads. Validation predictions against existing experiments has been fairly successful, however, allowing a clear delineation of the primary effects of the body on rotor airloads and performance and vice versa. For example, predictions using the free-vortex wake and surface singularity method of Crouse & Leishman (1992) has been shown in several prior figures, including Figs. 11.3, 11.8, and 11.15. These predictions are in general agreement, with measured results, which gives overall confidence in these types of essentially potential flow models for predicting a priori the possibilities of various rotor–airframe interaction problems. Predictive capabilities with panel methods are always reasonably good in airframe regions unaffected by flow separation. It is possible to represent 3-D separated flows by extending the singularity panels off the airframe surface as free shear layers, however, the points of 3-D flow separation on the airframe are hard to predict.

As previously alluded to, it is the interaction of blade tip vortices with the airframe surface that has proved more difficult to model, and this problem has perhaps received the most recent attention from a theoretical perspective. As previously described, these interactions can range from almost benign interactions where the tip vortex trajectories just

glance the airframe or empennage surfaces, to direct impingement and associated large-scale reorganization of the flow topology. Even though the encounter may vary in terms of its severity, in almost all cases the tip vortices induce large unsteady airloads on the airframe surface. Significant progress has been made in modeling this behavior numerically by means of vortex methods – see Conlisk & Affes (1993), Conlisk et al. (1993), and Quackenbush et al. (1994). However, rotor wake–surface interaction predictions are challenged by their inability to calculate the vortex strengths and wake distortions with good accuracy, and also because the local distortion of the wake by the body must be accounted for.

Because rotor–airframe interactional problems often involve 3-D viscous effects and flow separation, these problems a particularly good challenge for advanced computational fluid dynamic (CFD) models based on Navier–Stokes (NS) or Reynolds-averaged Navier–Stokes (RANS) equations (see Section 14.2.1). Fundamental studies of the problems has been conducted by Stremel (1987, 1990). More ambitious attempts with entire rotor and airframe configurations [e.g., Park et al. (2003)] have been recently attempted using millions of grid points in the flow (and many hours on a supercomputer), but these methods seem to have provided only limited new insight to the numerous types of interactional aerodynamics problems; most of the understanding still comes from more parsimonious models and from experimental observations. See Section 14.10.4 for further details of CFD approaches to rotor–airframe interaction problems.

11.3 Rotor–Empennage Interactions

The interactions between the main rotor wake and the empennage (horizontal and vertical stabilizers and the tail rotor) are known to be particularly significant, yet systematic studies of the problem to understand the flow physics still remain relatively few. As shown in Fig. 11.20, the interactions involve vortex surface impingement. Lynn (1966) has discussed

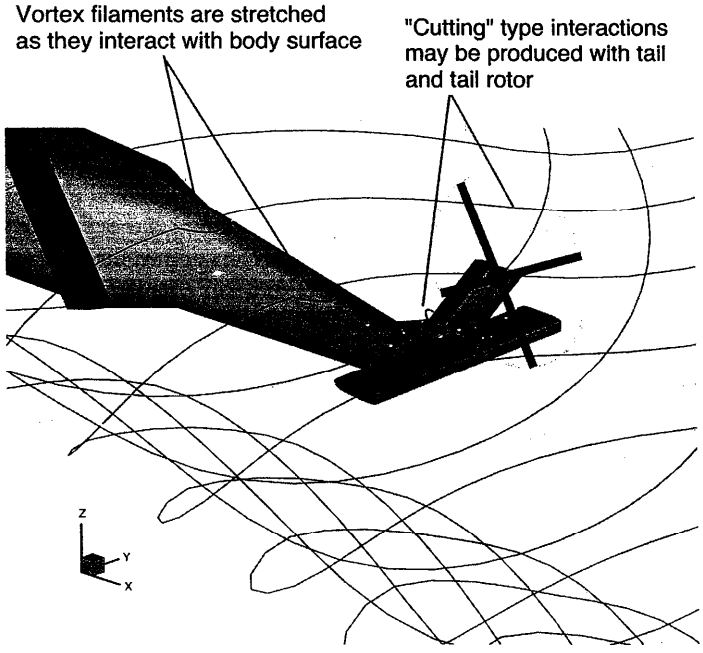

Figure 11.20 Schematic showing that the interaction of the blade tip vortices in the rotor wake with the airframe can range from glancing to direct impingement.

some of the general problems associated with helicopter rotor–lifting surface interactions, but concentrating mostly on performance issues.

Historically, empennage designs on helicopters have proved problematic, mainly from a stability and control perspective, because large forces and moments are produced on the empennage by the rotor wake as its position changes with flight condition. As previously alluded to, resolving such problems can involve substantial costs for the manufacturer because of airframe redesign and associated flight retesting time. Good case histories of the stabilizer design are available in the literature [e.g., for the AH-64 Apache as documented by Prouty & Amer (1982) and Prouty (1983)]. Other documented examples are for the AS-360 discussed by Roesch & Vuillet (1981) and for the EH-101 as discussed by Main & Mussi (1990). It appears, however, that lessons are not always learned and the horizontal stabilizers of new helicopters continue to be hounded by main rotor wake interaction problems.

More fundamental investigations into the problem of rotor wake–lifting surface interactions include the work of Wheatley (1935), Makofski & Menkick (1956), and McKee & Naeseth (1958). Sheridan & Smith (1979) examined specific issues associated with wake induced empennage airloads in their seminal work on rotor–airframe interactions, as previously mentioned. Leishman & Bi (1994a,b), Foley et al. (1995), Funk & Komerath (1995), and Moedersheim & Leishman (1998) have studied the more detailed fluid dynamics of the interactions between rotor wakes and horizontal lifting surfaces. Torok & Ream (1993) obtained flight measurements documenting the wake interactions found on a helicopter with a T-tail empennage configuration. Frederickson & Lamb (1993) conducted wind-tunnel tests to further examine the issues. This research has led to a more optimized empennage design, as shown in Fig. 11.21. Moedersheim & Leishman (1998) have also examined the unsteady forces on a generic T-tail. In all tests the unsteady airloads and vibration levels can be correlated with the relative position of the main rotor wake boundary. Sheridan & Smith (1979) and Roesch & Vuillet (1981) have also shown that the turbulent rotor hub wake can have a considerable influence on the flow environment at the empennage location at high advance ratios – see also Berry (1997) for measurements and a more detailed discussion of this problem. This turbulence has been known to cause lateral buffeting or "tail shake" on some helicopters, which is only cured by suitable streamlining downstream of the rotor hub.

While rotor–empennage interactions have proved to be significant on helicopters, rotor–wing and rotor–empennage interactions are particularly acute on compound helicopters and on tilt-rotor aircraft. In hover (helicopter mode), the wings of a tilt-rotor are directly below

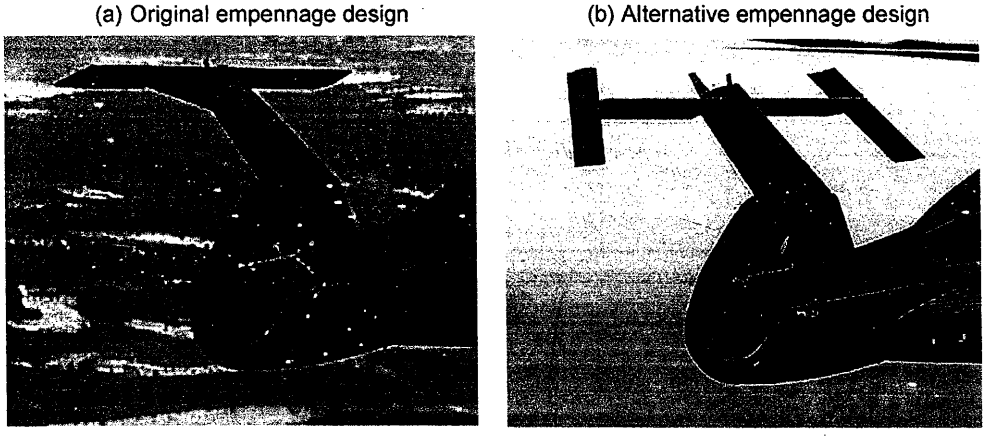

Figure 11.21 Two developmental versions of the empennage used on an advanced attack helicopter.

the rotors and are immersed in the rotor wakes. This can produce strong wake–surface interactions [see Wood & Peryea (1991)] as well as unsteady airloads from blade-passage effects that are induced by the highly loaded proprotors. In forward flight (airplane mode), both the main wings and the tail surfaces are located inside the rotor wake boundaries. Under these conditions the proprotors induce nonuniform, 3-D velocity fields at the wings and empennage. Interactions between the rotor wake and the empennage are known to constitute a significant source of vibratory loads. See Clark (1987), McVeigh (1986), Schillings & Reinesch (1987), McVeigh et al. (1990), and Lesching & Wagner (1990) for a good discussion of the specific aerodynamic interaction problems associated with tilt-rotors. Like helicopters, the adverse effects are difficult to design out but some attempts can be made to minimize the otherwise deleterious effects on the performance of tilt-rotor aircraft.

A low mounted aft stabilizer is a common design choice for a modern helicopter because it is structurally efficient; all the loads are carried directly into the tail boom so it can be of minimum weight compared to a T-tail. However, this stabilizer design tends to produce trim problems associated with transition from low-speed flight into hover, where the main rotor wake may suddenly move forward over the empennage location and so produce a nose-down pitching moment on the helicopter – see Prouty & Amer (1982). This problem is shown schematically in Fig. 11.22. Because the wake position relative to the empennage is affected by forward flight speed as well as climb or descent velocity, the aerodynamic angles of attack found at the empennage can be very sensitive to the actual flight conditions. Combined also with the higher total pressure obtained inside the main rotor wake, substantial changes in the forces on the stabilizer can be produced, which affect the pitching moments generated by the helicopter as a whole. If these changes occur suddenly or unpredictably, undesirable handling qualities can result – see Main & Mussi (1990). A high mounted tail or T-tail configuration places the tail out of the rotor wake for many flight conditions except for higher-speed forward flight or during descents. While a less efficient structural choice, Prouty & Amer (1982) suggest that this design is sometimes a good compromise in meeting the various requirements for a military helicopter.

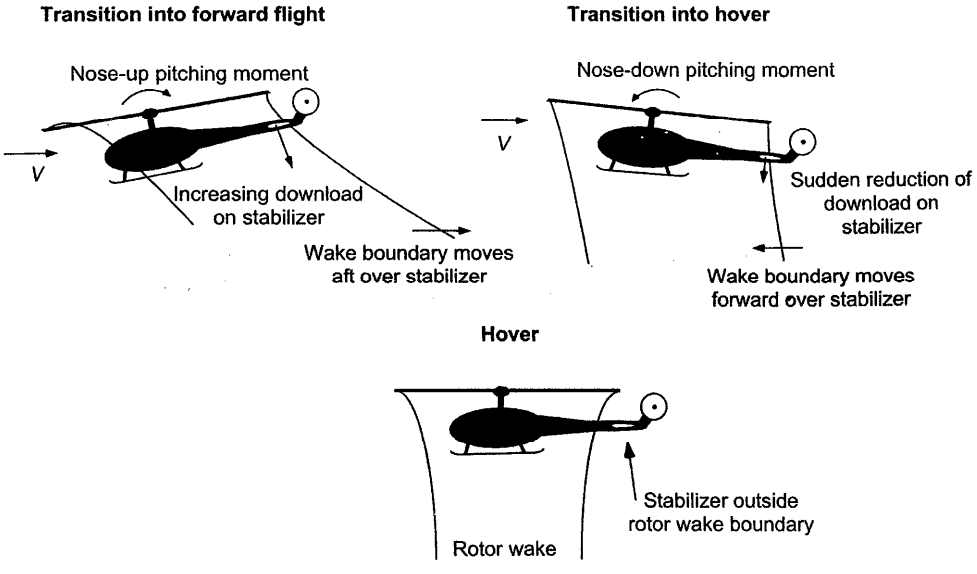

Figure 11.22 Schematic showing interactions between the main rotor wake and the horizontal tail during transition from hover into forward flight.

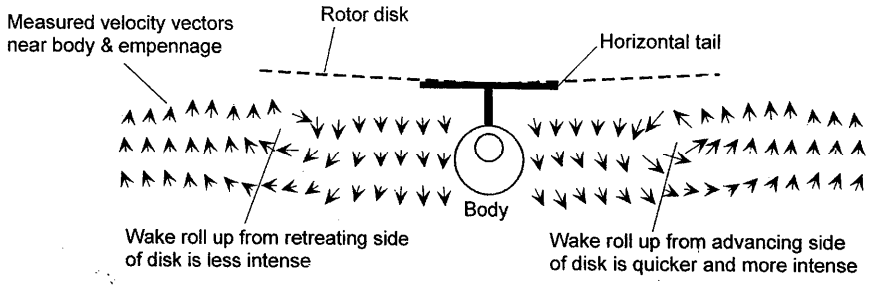

Figure 11.23 The aerodynamic environment at the empennage is strongly influenced by the induced velocity from the rolled up wake behind the main rotor. Source: Measurements from Leishman & Bi (1990a).

11.3.1 *Airloads on the Horizontal Tail*

Consider now the airloads produced on the T-tail for the subscale experiment shown in Fig. 11.2. The primary factors influencing the airloads on the empennage include the highly nonuniform velocity field produced by the rotor and its wake, as well as an increase in total pressure inside the wake boundaries. For example, Fig. 11.23 shows measured flow velocity vectors in a cross-plane near the empennage location. Notice the signatures of the vortex bundles or "super-vortices" that are trailed from the lateral edges of the rotor disk, similar to those generated at the tips of a fixed wing aircraft – see, for example, Fig. 10.9. Similar results have been obtained by Le Pape et al. (2004) using PIV measurements. This wake rollup from the rotor disk induces a downwash on the horizontal tail, producing negative lift for this flight condition. The asymmetry of the wake roll up also produces a nonuniform sideward flow velocity and a force on the vertical fin.

As shown in Section 10.2, flow visualization (i.e., smoke, shadowgraph) is an effective tool for finding the position of the tip vortices in the rotor wake. Typical results showing the wake boundaries at the longitudinal centerline for different advance ratios relative to the tail location are given in Fig. 11.24. The locations of the tail boom, vertical fin, and

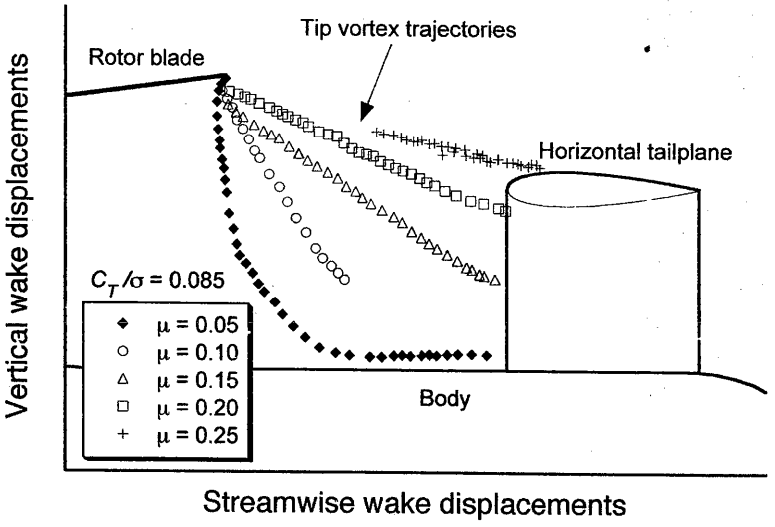

Figure 11.24 Measurements of the rotor wake boundary relative to an empennage assembly showing the sensitivity to variations in advance ratio. Data source: Moedersheim & Leishman (1998).

horizontal tailplane are shown for reference. It is clear that advance ratio has a significant effect on the wake position relative to the tail. At the lowest advance ratios the tip vortices are convected down toward the body surface, and then follow a trajectory that is almost parallel to the horizontal tailplane. An increase in advance ratio produces a higher wake skew angle, so the tip vortices are convected streamwise at an increasingly higher velocity. As expected, changes in the wake skew angle are largest at low advance ratios; this angle changes very little for $\mu > 0.25$. The rotor wake was found to impinge on the top surface of the horizontal tail for $\mu = 0.25$ and above. The flow visualization showed that, in the cases where direct impingement of the tip vortices on the tail surfaces could be observed, they would burst and diffuse quickly. This suggests that strong local pressure and viscous effects are present.

Overall, it is found that the time-dependent pressures measured on the tail generally show more complex variations compared to on the body. This is not entirely unexpected because the environment at the empennage is much more 3-D than points further upstream. Also, as in the case of the body, the unsteady airloads are found to be closely related to the proximity of the rotor wake. For example, Fig. 11.25 shows representative time-dependent pressures measured at one location (Sensor #5 in this case) on the upper surface of the tailplane for a range of advance ratios at a constant rotor thrust and shaft angle. At low advance ratios ($\mu \leq 0.10$) the rotor wake is convected relatively far below the horizontal tailplane, and the unsteady airloads are found to be negligible. As the advance ratio is increased, however, the unsteady airloads build up in intensity. Clearly this occurs because of the closer proximity of the rotor wake boundary to the tailplane.

The wake boundary comes very close to the tailplane between $\mu = 0.20$ and 0.25. At this condition the unsteady airloads seem to reach their maximum values. For advance ratios above 0.25, the separation distance between the wake boundary and the horizontal tailplane increases slightly, with a corresponding mild decrease in unsteady loading. Recall that for higher advance ratios the position of the wake boundary remains relatively unaffected by changes in advance ratio. The unsteady airloads are, therefore, maintained at the same overall magnitude. However, because the convection velocity of the individual vortex wake filaments increases with increasing advance ratio, a change in phase of the unsteady airloads with respect to the blade position will still be observed. It should also be apparent that the induced velocity field produced by the convecting tip vortices results in local angles of attack that vary in time at a fairly high reduced frequency. This can be established by computing the reduced frequency of the vortex passage at the tailplane from the equation

$$k = \frac{\omega c}{2V} \approx \frac{(N_b\Omega)(c/R)R}{2\mu\Omega R} = \frac{N_b(c/R)}{2\mu}. \tag{11.6}$$

The ratio c/R is about 0.25 for the configuration shown, so the reduced frequency of the flow at the tail for an advance ratio of 0.2 would be of order 2.5. Obviously this requires the mathematical modeling of the physics of this problem to be considered fully unsteady (Section 8.4). Also, if and when stall occurs locally on the tail, the high effective reduced frequency of the flow means that separation and stall may be more dynamic in nature. This adds yet an additional level of complexity to the mathematical modeling of the rotor–tail interactional aerodynamics problem.

11.3.2 *Modeling of Rotor–Empennage Interactions*

Mathematical models have not yet evolved to the point where the aerodynamics of the empennage can be predicted without input from wind tunnel and/or flight tests.

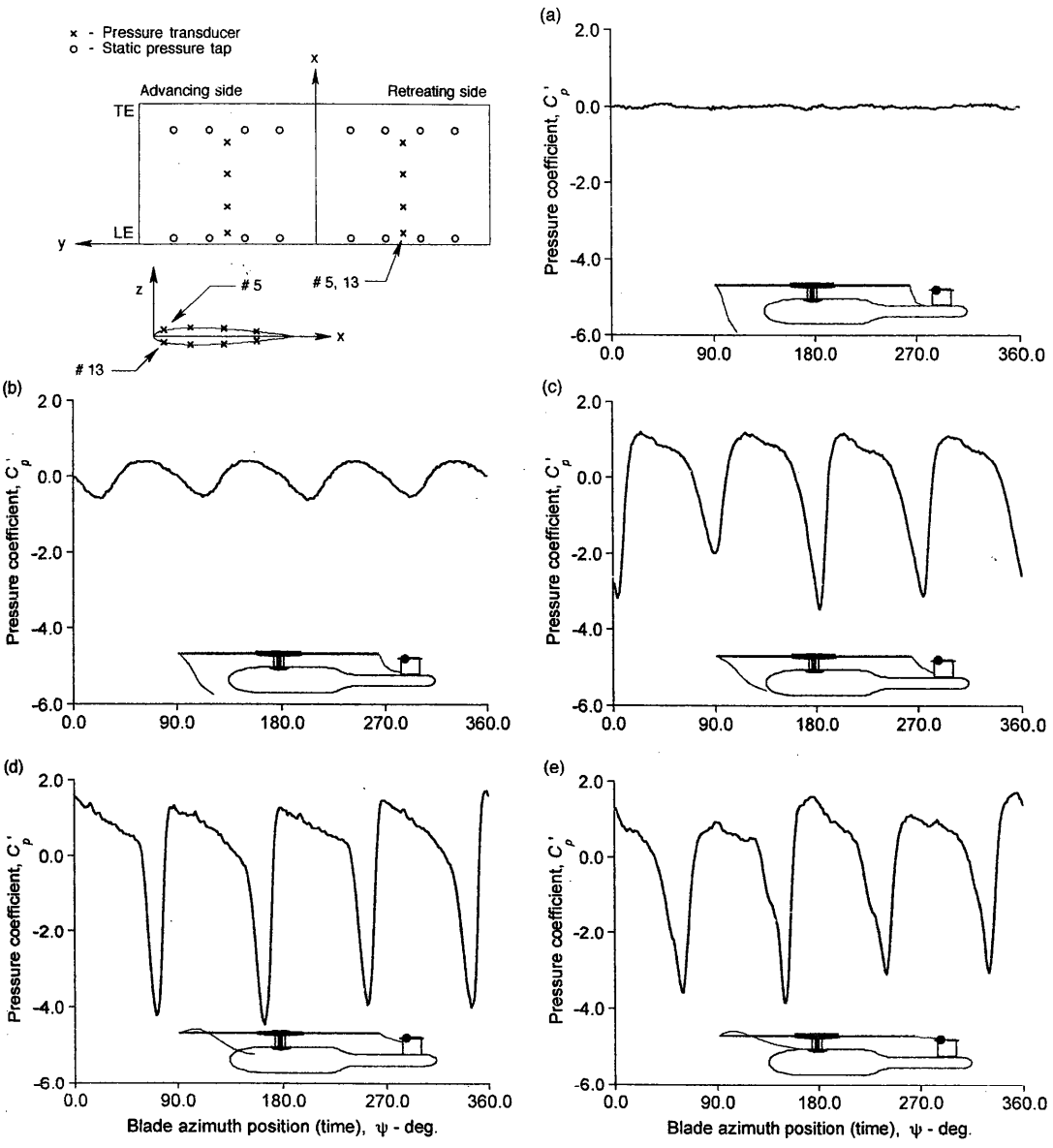

Figure 11.25 Measurements of unsteady pressure on a horizontal tail showing how the magnitude is affected by the main rotor wake position. Data source: Moedersheim & Leishman (1998).

The capabilities of these methods are beyond the state of the art because of the need to model vortex–surface collisions, the cutting of vortex filaments, as well as the formation of 3-D unsteady separated flows. Gangwani (1982, 1983) has used a prescribed wake model coupled with a doublet-lattice model of a fixed wing to predict the unsteady bending moments produced on a helicopter tail. Reasonable correlation was obtained with flight measurements. Mello & Rand (1991) confirmed that the predicted unsteady airloads on the empennage were sensitive to the rotor wake position, simply confirming results of both wind tunnel measurements and flight test experience. Weinstock (1991) has developed a

parsimonious model of the rotor wake–empennage aerodynamic interaction problem for use in flight simulation modeling. Curtiss & Quackenbush (1989) considered in more detail how the induced velocity field of the rotor wake at the empennage location affects the helicopter's stability derivatives. The limited correlations obtained with flight measurements reiterated the complexity of the main rotor wake–empennage interaction problem and the difficulties in constructing truly faithful models for use in flight mechanics simulations.

11.4 Rotor–Tail Rotor Interactions

The tail rotor has to operate in a relatively complex aerodynamic environment and must produce thrust with the relative flow coming from essentially any direction – see Newman (1994). For example, the tail rotor must operate properly in side winds and during yaw maneuvers. In a yawing maneuver, the tail rotor operates either in an effective climb or descent mode, depending on the yaw direction. The yawing direction that produces an effective descending condition is the most critical because it is possible for the tail rotor to enter into the vortex ring state (see Section 2.13.6). This can result in a loss of tail rotor authority and perhaps even a loss of control under certain conditions, a problem first explored by Amer & Gessow (1955). These effects are carefully examined during certification flight testing to ensure that there is a minimal chance that the helicopter will inadvertently exhibit undesirable flight characteristics.

As described previously in Section 6.9.4, the tail rotor is also mounted in proximity to a vertical fin or other empennage assembly and the resultant aerodynamic interactions will affect tail rotor operation. Furthermore, the operation of the tail rotor will be affected by turbulent separated flow generated by the main rotor hub and fuselage wakes, and also the energetic main rotor wake itself. This adverse environment means that the aerodynamic design requirements for the tail rotor are different in some respects from those of the main rotor. For these reasons, it is known to be difficult to design a tail rotor that will meet all aerodynamic, control, stability, weight, and structural requirements. See Lynn (1970), Cook (1978), Byham (1990), and Newman (1994) for a detailed overview of tail rotor design issues.

The aerodynamic interactions between the main rotor and the tail rotor are discussed by Wiesner & Kohler (1973, 1974), Leverton et al. (1977), Balch (1984), Wilson (1990), Ellin (1993), Tarttelin & Martyn (1994), Coton et al. (2002), Early et al. (2002), and Wang et al. (2002). In forward flight there is a lateral asymmetry in dynamic pressure across the tail rotor, as with the main rotor, but the effects are alleviated by flapping hinges. Yet the tail rotor still trails its own unique wake, although this is much less powerful than the main rotor wake. The main rotor wake is known to roll up at its edges into a pair of "super-vortices," this phenomenon having been alluded to several times previously in Chapter 10. This rollup effect produces a downwash over the tail rotor with a significant velocity gradient in the longitudinal direction. There is also an increased total pressure in the main rotor wake, which encroaches onto the tail rotor as forward flight speed builds.

Of some importance in the aerodynamics and aeroacoustics of the tail rotor are the cutting or "chopping" types of interactions that take place as the tail rotor blades intersect the strong tip vortices trailed from the main rotor blades – see Leverton et al. (1977), Howe (1989), and Coton et al. (2002). Because the plane of rotation of the tail rotor is almost perpendicular to the main rotor (unless the tail rotor is canted), the plane of the tail rotor blades is essentially perpendicular to the vorticity vector of the tip vortices. The location of the interactions over the tail rotor disk are a function of several parameters, including the

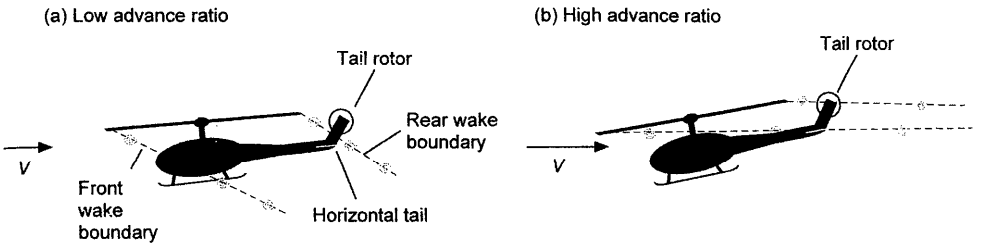

Figure 11.26 The tail rotor may intersect and cut-through the strong tip vortices that are trailed from the main rotor.

flight condition (see Fig. 11.26). More interactions can usually be expected to occur when the helicopter is in higher speed forward flight or during descents.

The number and location of the intersections between the tail rotor blades and the main rotor wake vortices can be determined using the same principles as those described in Section 10.4.2 for finding the main rotor BVI locations. In the first instance, a simple rigid wake model can be used to study the tail rotor interactions, such as that discussed by Newman (1994), but it must be recognized that considerable main rotor wake distortion can indeed be produced at the tail rotor. The geometry of this type of model is shown in Fig. 11.27. The tip vortices from the trailing edge of the main rotor disk are assumed to be convected at the free-stream velocity relative to the tail rotor and to be uninfluenced by the tail rotor.

In a X–Y reference plane the tip vortex trajectories are described geometrically by the equations

$$X_{\text{tip}} = \mu_{\text{MR}} R_{\text{MR}} \left(\psi_{\text{MR}} - \frac{2\pi(i-1)}{N_{b_{\text{MR}}}} \right) - X_0, \tag{11.7}$$

and

$$Y_{\text{tip}} = \text{const} = Y_0, \tag{11.8}$$

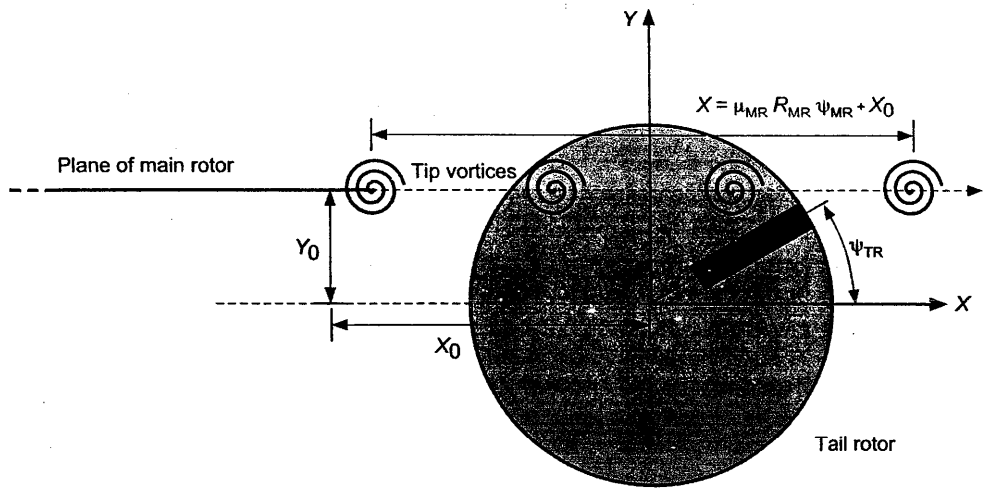

Figure 11.27 Mathematical model to predict the location of cutting intersections between the tail rotor blades and the tip vortices from the main rotor.

where $i = 1, N_{b_{TR}}$. The coordinates of a point on the axis of the tail rotor blades are given by

$$X_{TR} = r\cos\left(\psi_{TR} - \frac{2\pi(i-1)}{N_{b_{TR}}}\right) R_{TR}, \tag{11.9}$$

and

$$Y_{TR} = \pm r\sin\left(\psi_{TR} - \frac{2\pi(i-1)}{N_{b_{TR}}}\right) R_{TR}, \tag{11.10}$$

where the $\pm$ accounts for the direction of rotation of the tail rotor (counterclockwise or clockwise, respectively). The different rotational frequencies of the main and tail rotors means that the time scales are related by

$$\psi_{MR} = \left(\frac{\Omega_{MR}}{\Omega_{TR}}\right)\psi_{TR}. \tag{11.11}$$

An intersection occurs when

$$X_{TR} = X_{tip} \text{ and } Y_{TR} = Y_{tip} \tag{11.12}$$

are simultaneously satisfied. This solution can easily be found numerically.

Representative results from this model (in terms of the radial intersection point as a function of tail rotor revolutions) are shown in Fig. 11.28 for a counterclockwise and for a clockwise turning tail rotor. Notice that the intersection pattern is periodic but differs considerably depending on the sense of rotation of the tail rotor, a point also noted by Leverton et al. (1977) and Newman (1994). This is because, in the case of a counterclockwise rotation, the tail rotor blades are advancing into the main rotor tip vortices whereas, for a clockwise rotation, the blades retreat away from the oncoming vortices. The implications are that minimizing the number of intersections will reduce unsteady airloads and tail rotor noise, and on this basis it appears that a clockwise rotation of the tail rotor (usually called rotation "aft at the top") is the better choice, a result borne out by flight testing experience – see Ellin (1993).

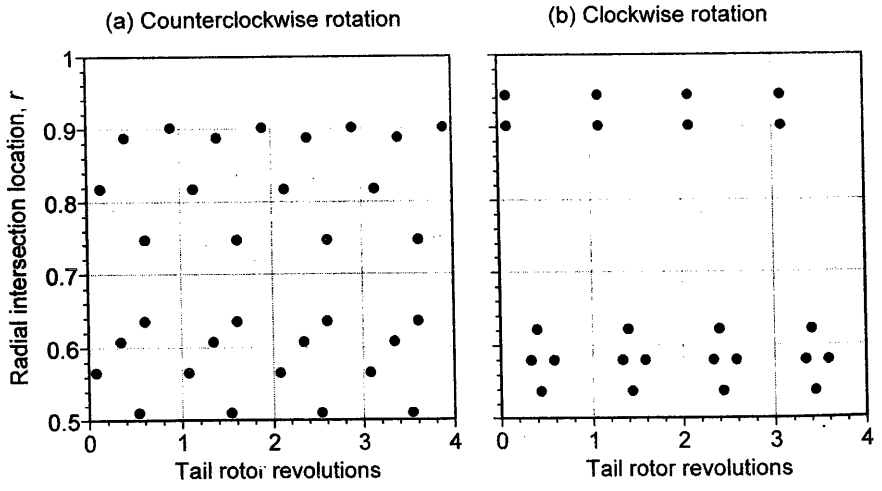

Figure 11.28 Example showing blade/main rotor tip vortex intersection points over the tail rotor disk. (a) Counterclockwise rotation. (b) Clockwise rotation. Conditions: $N_{b_{MR}} = 4$, $N_{b_{TR}} = 4$, $\mu_{MR} = 0.3$, $\Omega_{MR} = 35$ rad/s, $\Omega_{TR} = 200$ rad/s, $Y_0 = 0.5R_{TR}$, $X_0 = -1.5R_{TR}$.

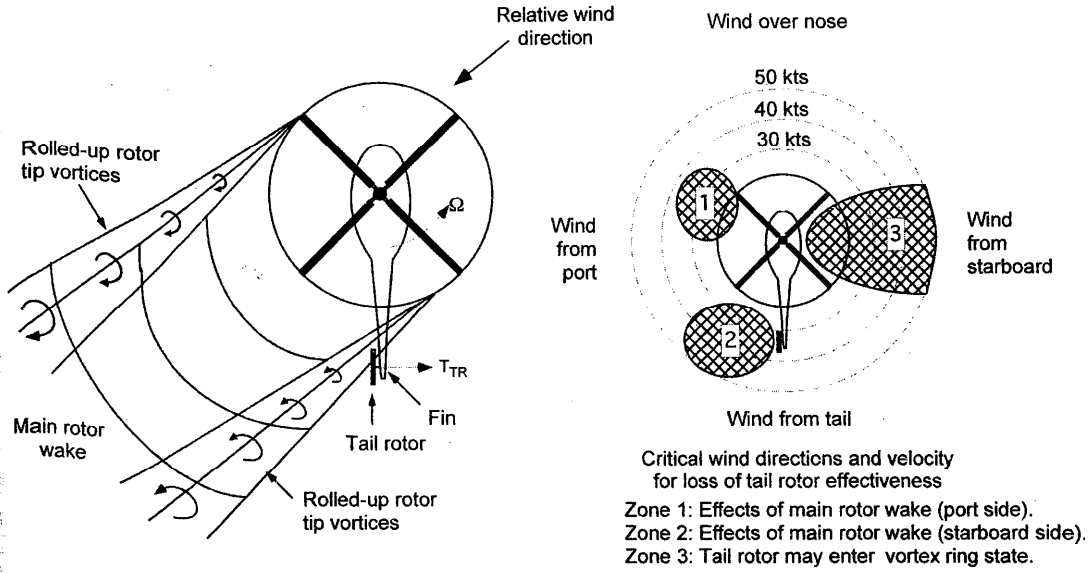

Figure 11.29 The impingement of the main rotor wake on the tail rotor can cause loss of tail rotor effectiveness. Adapted from Vuillet (1990) and other sources.

Clearly the aeroacoustics problem is relatively more complicated than this, but a parsimonious model like this illustrates one fundamental aspect of the tail rotor–main rotor wake interaction problem. The model can also be used to explore the effects of changing the phase angles between the tail rotor blades, such as the nonorthogonal set used on the AH-64 Apache (see Question 11.7). It should be pointed out, however, that the tail rotor was not designed for this way for acoustic purposes but instead to alleviate clearance issues with the pitch links.

The aerodynamic interactions between the main rotor and tail rotor in low-speed flight generally prove to be the most severe and the hardest to predict. Critical conditions include right and left crosswinds, where the bundled super-vortices trailed from the main rotor disk can impinge on the tail rotor. An example is shown in Fig. 11.29. Under these conditions the downwash and change in dynamic pressure across the tail rotor disk that is produced by the main rotor wake can degrade tail rotor performance. As previously mentioned, because of these effects, one normally finds that tail rotors that have an "aft at the top" rotation are preferable. This has been found through flight testing to balance the aerodynamic forces and maintain good tail rotor authority over a wider range of flight conditions than the opposite sense of rotation. Other critical flight conditions include rearward flight near the ground or sideward flight to port – see Section 10.10.6. In rearward flight, the ground vortex can result in loss of tail rotor effectiveness. In sideward flight (or when hovering in a crosswind), the tail rotor operates in an effective descent and will eventually encounter the vortex ring state where a loss of anti-torque and yaw control effectiveness will occur. All of these issues are carefully examined during certification of the helicopter to ensure that there are no adverse effects or that potentially problem areas of the flight envelope can be fully identified.

11.5 Chapter Review

The content of this chapter has described some of the important aerodynamic interactions that can take place between a helicopter rotor and its airframe. Because there are often (but not always) deleterious effects associated with these interactions that can have

a significant impact on the performance of the helicopter as a whole, the understanding and accurate prediction of aerodynamic interactions have become an important issue in helicopter design. Problems of interest include the need for a better understanding of the physics of rotor wake distortion caused by the fuselage and empennage, the effects of the fuselage on the rotor airloads, and the consequences of main rotor and tail rotor wake interactions on unsteady airloads and acoustics. The need to mitigate these effects at the design stage rather than after first flight has never been more imperative to the success of the modern helicopter.

There have been many wind tunnel experiments with subscale helicopter models to help quantify the various aerodynamic interactions between a rotor and an airframe. Some of these tests have been performed with simplified airframe topologies, which are ideal for understanding the physical phenomena, whereas other tests with scaled airframes are better for the validation of comprehensive flow models. Airloads on the fuselage and on the rotor have been measured in an attempt to assess the magnitude of the effects and to better understand the significance of aerodynamic interactions. At low flight speeds the helicopter fuselage is often immersed in the wake from the main rotor and so the downwash from the rotor will influence significantly the fuselage aerodynamics. The presence of the rotor wake creates a significant download on the fuselage that increases with increasing rotor thrust and decreases with advance ratio, but only to a point. An upload can be produced on the airframe by the rotor wake when the helicopter is in high-speed flight. The corresponding effect of the fuselage on the rotor can increase its mean thrust at low advance ratio. The rotor wake has been shown to produce substantial effects on the time-averaged fuselage pressures, especially at the boundaries of the rotor wake where the induced velocities are highest. These mean pressures are sensitive to variations of rotor thrust and/or advance ratio. The induced pressures on the fuselage are generally asymmetric and will result in a net side force on the fuselage. Overall, the results from several wind tunnel experiments and flight tests have shown the relative complexity of the interactional aerodynamic effects that exist between a thrusting rotor and its airframe.

Unsteady effects play an important, and perhaps underestimated, role in the understanding of interactional aerodynamic phenomena on helicopters and other types of rotorcraft. The unsteady pressure fluctuations induced on the fuselage by the rotor and its wake are very large; in fact, in many cases, the magnitude of these unsteady fluctuations exceeds the mean pressure values. However, the unsteady pressure fluctuations are not necessarily the greatest in the regions of highest mean pressure. Blade passage effects on the fuselage increase in proportion to the blade thrust (disk and blade loading) and may be an important factor in the design of new helicopters with high disk loadings and smaller rotor–fuselage spacings designed for low parasitic drag and high-speed flight. The dominant frequency of the unsteady pressure fluctuations corresponds to the blade passing frequency. Wake vortex impingement on the fuselage results in more complex transient pressure loadings. These loadings, however, are not the severest form of induced pressures obtained on the fuselage because close wake vortex–surface interactions appear to produce much stronger effects. While the complexity of the problems involved in rotor–airframe interactions provides ample scope for both the theoretician and experimentalist, and indeed offer many new research opportunities, it provides a particularly good challenge for the more advanced CFD methods. These methods, and their limitations, are discussed further in Chapter 14.

11.6 Questions

11.1. Consider the possible types of aerodynamic interactions that might be found on a compound helicopter that has auxiliary wings. Explain under what flight

conditions, if any, might adverse interactional effects between the main rotor and the wings might be expected. If adverse effects are encountered, do you think it would be possible to minimize or design out these adverse effects?

11.2. Consider the possible types of aerodynamic interactions that might be found on a tilt-rotor when it is operating in hovering flight. You should consider the possibility of both steady and unsteady flow effects. Discuss design options that could be used to alleviate any adverse effects.

11.3. Consider the possible types of aerodynamic interactions that might be found on a tilt-rotor in forward flight when the prop-rotors operate as propellers. Bearing in mind the relatively lower disk loading on the prop-rotor relative to operation in helicopter mode, are the interactions between the prop-rotor wake and the airframe likely to be stronger or weaker, and why? Is there a design solution that might help to minimize any adverse interactions you deem as likely to occur?

11.4. Use 2-D incompressible potential flow theory to develop expressions for the unsteady pressure on a surface in response to a vortex convecting past it. Use the model to explore the effects on the unsteady pressure at a point on the surface in response to: (a) Convection speed, (b) vortex strength, and (c) height of the vortex off the surface.

11.5. The 1/4-chord line of the horizontal tail of a particular helicopter is located approximately $0.2R$ below and $1.1R$ aft of the rotor hub. Using a simple rigid wake analysis to determine the approximate flight conditions (forward speed, climb, and or descent) where the tail would be immersed inside the boundaries of the rotor wake. Choose several representative rotor operating conditions (thrust, disk angle of attack, climb/descent, etc.).

11.6. The downstream wake from the rotor hub can often affect the unsteady loads on the trail rotor and empennage, to the extent than adverse lateral airframe forces can be produced. Suggest at least two techniques that could be adopted to alleviate this problem.

11.7. Derive a set of governing equations to solve numerically for the locations of the cutting interactions of the tail rotor with the main rotor wake vortices. Explore the pattern of interactions for different values of the ratio Ω_{TR}/Ω_{MR}. In each case, examine the effect of changing the direction of rotation of the tail rotor.

11.8. Use the equations derived in the Question 11.7 to solve for the locations of the cutting interactions of the tail rotor with the main rotor wake vortices. Explore the effects on the pattern of interactions when using nonorthogonal sets of tail rotor blades, such as found on the AH-64 Apache. Comment on your results.

11.9. What types of rotor–airframe interaction problems might be involved in the flight of an autogiro? Consider both winged and wingless autogiros, as well as tip-jet driven rotor machines such as the Rotodyne (see page 715).

Bibliography

Ahmed, S. R. 1990. "Fuselage Aerodynamic Design Issues and Rotor–Fuselage Interactional Aerodynamics–Part 2: Theoretical Methods," In: AGARD-R-781.

Amer, K. B. and Gessow, A. 1955. "Charts for Estimating the Tail-Rotor Contribution to Helicopter Directional Stability and Control in Low-Speed Flight," NACA Report 1216.

Atias, M. and Weihs, D. 1984. "Motion of Aircraft Trailing Vortices Near the Ground," *J. of Aircraft*, 2 (10), pp. 783–786.

Bagai, A. and Leishman, J. G. 1992. "Experimental Study of Rotor Wake–Body Interactions in Hover," *J. of the American Helicopter Soc.*, 37 (4), pp. 48–57.

Balch, D. A. 1984. "Impact of Main Rotor Tip Geometry on Main Rotor–Tail Rotor Interactions in Hover," 40th Annual Forum of the American Helicopter Soc., Arlington, VA, May 16–18.

Banks, D. W. and Kelly, H. L. 2000. "Exploratory Investigation of the Aerodynamic Characteristics of Helicopter Tail Boom Cross-Section Models with Passive Venting," NASA/TP-2000-210083, AMCOM-AFDD/TR-00-A-007, June.

Berry, J. D. 1988. "Prediction of Time-Dependent Fuselage Pressures in the Wake of a Helicopter Rotor," Second International Conference on Rotorcraft Basic Research, College Park, MD, Feb. 16–18.

Berry, J. D. 1997. "Unsteady Velocity Measurements Taken Behind a Model Helicopter Rotor Hub in Forward Flight," NASA TM-4738.

Berry, J. D. and Althoff, S. L. 1990. "Inflow Velocity Perturbations Due to Fuselage Effects in the Presence of a Fully Interactive Wake," 46th Annual Forum of the American Helicopter Soc., Washington, DC, May 21–23.

Betzina, M. D. and Shindoda, P. 1982. "Aerodynamic Interactions between a 1/6-Scale Helicopter Rotor and a Body of Revolution," NASA TM X-84247, June.

Bi, Nai-pei and Leishman, J. G. 1990. "Experimental Study of Rotor–Body Aerodynamic Interactions," *J. of Aircraft*, 27 (9), pp. 779–788.

Boyd, D. D., Barnwell, R. W., and Gorton, S. A. 2000. "A Computational Model for Rotor-Fuselage Interactional Aerodynamics, AIAA Paper 2000-0256, 38th Aerospace Sciences Meeting and Exhibit, Reno, NV, Jan. 10–13.

Bramwell, A. R. S. 1966. "A Theory of the Aerodynamic Interference between a Helicopter Rotor Blade and a Fuselage and Wing in Hovering and Forward Flight," *J. of Sound & Vibration*, 3 (3), pp. 355–383.

Brand, A. G., McMahon, H. M., and Komerath, N. M. 1986. "Wind Tunnel Data for a Rotorcraft Airframe Interaction Study," School of Aerospace Engineering, Georgia Institute of Technology, Atlanta, GA, July.

Brand, A. G., McMahon, H. M., and Komerath, N. M. 1989. "Surface Pressure Measurements on a Body Subject to Vortex–Wake Interaction," *AIAA J.*, 27 (5), pp. 569–574.

Brand, A. G., McMahon, H. M., and Komerath, N. M. 1990. "Correlations of Rotor Wake/Airframe Interaction Measurements with Flow Visualization Data," *J. of the American Helicopter Soc.*, 35 (4), pp. 4–15.

Brocklehurst, A. 1985. "A Significant Improvement to the Low Speed Control of the Sea King Helicopter Using a Tail Boom Strake," 11th European Rotorcraft Forum, London, England, Sept. 10–13.

Byham, G. M. 1990. "An Overview of Conventional Tail Rotors," RAeS Conference on Helicopter Yaw Control Concepts, London, England, Feb.–March.

Clark, D. R. 1987. "Analysis of the Wing–Rotor and Rotor–Rotor Interactions Present in Tilt-Rotor Aircraft," *Vertica*, 11 (4), pp. 731–749.

Clark, D. R. and Maskew, B. 1985. "Study for Prediction of Rotor–Wake–Fuselage Interference," NASA CR-177340, March.

Clark, D. R. and Maskew, B. 1988 "Calculation of Unsteady Rotor Blade Loads and Blade–Fuselage Interference," 2nd International Conference on Rotorcraft Basic Research, College Park, MD, Feb. 16–18.

Clark, D. R. and Maskew, B. 1991. "A Re-Examination of the Aerodynamics of Hovering Rotors Including the Presence of the Fuselage," International Technical Specialists' Meeting on Rotorcraft Basic Research, Georgia Institute of Technology, Atlanta, GA. See also: 47th National Forum of the American Helicopter Soc., Phoenix, AZ, May 7–9.

Cook, C. V. 1978. "Tail Rotor Design and Performance," *Vertica*, 2, pp. 163–181.

Conlisk, T. A. and Affes, H. 1993. "A Model for Rotor Tip Vortex–Airframe Interaction, Part 1: Theory," *AIAA J.*, 31 (12), pp. 2263–2273.

Conlisk, T. A., Affes, H., Kim, J. M., and Komerath, N. M. 1993. "A Model for Rotor Tip Vortex–Airframe Interaction, Part 2: Comparison with Experiment," *AIAA J.*, 31 (12), pp. 2263–2273.

Coton, F. N., Galbraith, R. A. McD., Wang, T., and Newman, S. 2002. "Preliminary Results from a Wind Tunnel Based Study of Tail Rotor Blade Vortex Interaction," 28th European Rotorcraft Forum, Bristol, Sept. 17–20.

Crouse, G. L. and Leishman, J. G. 1992. "Aerodynamic Interactional Effects on Rotor Loads and Performance," 48th Annual Forum of the American Helicopter Soc., Washington DC, June 3–5.

Crouse, G. L., Leishman, J. G., and Bi, Nai-pei. 1992. "Theoretical and Experimental Study of Unsteady Rotor/Body Aerodynamic Interactions," *J. of the American Helicopter Soc.*, 37 (1), pp. 55–65.

Curtiss, H. C. and Quackenbush, T. R. 1989. "The Influence of the Rotor Wake on Rotorcraft Stability and Control," 15th European Rotorcraft Forum, Amsterdam, The Netherlands, Sept. 12–15.

Dehondt, A. and Toulmay, F. 1989. "Influence of Fuselage on Rotor Inflow Performance and Trim," 15th European Rotorcraft Forum, Amsterdam, Sept. 12–15.

Delany, N. K. and Sorensen, N. E. 1953. "Low Speed Drag of Cylinders of Various Shapes," NACA TN-3038.

Doligalski, T. L. and Walker, J. D. A. 1984. "The Boundary Layer Induced by a Convected Two-Dimensional Vortex," *J. of Fluid Mechanics*, 139, pp. 1–28.

Early, J. M., Green, R. B., and Coton, F. N. 2002. "Flow Visualization of the Orthogonal Blade–Vortex Interaction Using Particle Image Velocimetry," *Aeronautical J.*, 106 (1057), pp. 37–145.

Ellin, A. D. S. 1993. "An In-Flight Investigation of Westland Lynx AH Mk-5 Main Rotor–Tail Rotor Interactions," 19th European Rotorcraft Forum, Cernobbio (Como), Italy, Sept. 14–16.

Frederickson, K. C. and Lamb, J. R. 1993. "Experimental Investigation of Main Rotor Wake Induced Vibratory Empennage Airloads for the RAH-66 Comanche Helicopter," 49th Annual Forum of the American Helicopter Soc., St. Louis, MO, May 19–21.

Freeman, C. E. 1980. "Development and Validation of a Combined Rotor–Fuselage Induced Flow-Field Computational Method," NASA TP-1656.

Freeman, C. E. and Mineck, R. E. 1979. "Fuselage Surface Pressure Measurements of a Helicopter Wind-Tunnel Model with a 3.15-Meter Diameter Single Rotor," NASA TM-80051.

Freeman, C. E. and Wilson, J. C. 1980. "Rotor–Body Interference (ROBIN)–Analysis and Test," 36th Annual Forum of the American Helicopter Soc., Washington DC, May 13–14.

Foley, S. M., Funk, R. B., Fawcett P. A., and Komerath, N. M. 1995. "Rotor-Wake-Induced Flow Separation on a Lifting Surface," *J. of the American Helicopter Soc.*, 40 (2), pp. 24–27.

Funk, R. B. and Komerath, N. M. 1995. "Rotor-Wake Interaction with a Lifting Surface," American Helicopter Soc. 51st Annual Forum, Ft. Worth, TX, May 9–11.

Gangwani, S. T. 1982. "A Doublet-Lattice Method for the Determination of Rotor Induced Empennage Vibration Airloads–Analysis, Description and Program Documentation," NASA CR-165893.

Gangwani, S. T. 1983. "Calculation of Rotor-Wake Induced Empennage Airloads," *J. of the American Helicopter Soc.*, 28 (2), pp. 37–46.

Hoerner, S. F. 1965. *Fluid Dynamic Drag*, Published by the Author, Hoerner Fluid Dynamics, Vancouver, WA.

Howe, M. S. 1989. "On Unsteady Surface Forces and Sound Produced by the Normal Chopping of a Rectilinear Vortex," *J. of Fluid Mechanics*, 206, pp. 131–153.

Johnson, W. and Yamauchi, G. K. 1984. "Applications of an Analysis of Axisymmetric Body Effects on Rotor Performance and Loads," 10th European Rotorcraft Forum, The Hague, Netherlands, Aug. 28–31.

Kelley, H. L., Crowell, C. A., Yenni, K. R., and Lance, M. B. 1993. "Flight Investigation of the Effect of Tail Boom Strakes on Helicopter Directional Control," NASA TP-3278 and ATCOM TR-93-A-003.

Komerath, N. M., McMahon, H. M., and Hubbard, J. E. 1985. "Aerodynamic Interactions Between a Rotor and Airframe in Forward Flight," AIAA Paper 85-1606, 18th AIAA Fluid Dynamics, Plasmadynamics, and Lasers Conference, Cincinnati, OH, July 16–18.

Landgrebe, A. J., Moffitt, R. C., and Clark, D. R. 1977. "Aerodynamic Technology for Advanced Rotorcraft–Part II," *J. of the American Helicopter Soc.*, 22 (3), pp. 2–9.

Leishman, J. G. and Bi, Nai-pei. 1990a. "Measurements of a Rotor Flow Field and the Effects of a Fuselage in Forward Flight," *Vertica*, 14 (3), pp. 401–415.

Leishman, J. G. and Bi, Nai-pei. 1990b. "Aerodynamic Interactions Between a Rotor and a Fuselage in Forward Flight," *J. of the American Helicopter Soc.*, 35 (3), pp. 22–31.

Leishman, J. G. and Bi, Nai-pei. 1994a. "Experimental Investigation of Rotor–Lifting Surface Interactions," *J. of Aircraft*, 31 (4), pp. 846–854.

Leishman, J. G. and Bi, Nai-pei. 1994b. "Experimental Data on the Aerodynamic Interactions between a Helicopter Rotor and an Airframe," In: AGARD-AR-303, Vol. II, Aug.

Le Pape, A., Gatard, J., and Monnier, J. C. 2004. "Experimental Investigations of Rotor–Fuselage Aerodynamic Interactions Using a Helicopter Powered Model," 30th European Rotorcraft Forum, Marseilles, France, Sept. 14–16.

Lesching, A. and Wagner, S. 1990. "Theoretical Model To Calculate Aerodynamic Interference Effects Between Rotor and Wing of Tiltrotors," 16th European Rotorcraft Forum, Glasgow, Scotland, Sept. 18–20.

Leverton, J. W., Pollard, J. S., and Wills, C. R. 1977. "Main Rotor Wake–Tail Interaction," *Vertica*, 1 (2), pp. 213–221.

Lim, T. 1989. "An Experimental Study of a Vortex Ring Interacting with an Inclined Wall," *Experiments in Fluids*, 7, pp. 453–463.

Liou, S. G., Komerath, N. M., and McMahon, H. M. 1989a. "Measurement of Transient Vortex–Surface Interaction Phenomena," *AIAA J.*, 28 (4), pp. 975–981.

Liou, S. G., Komerath, N. M., and McMahon, H. M. 1989b. "Velocity Field of a Cylinder in the Wake of a Rotor in Forward Flight," AIAA Paper 89-1844, 20th AIAA Fluid Dynamics, Plasmadynamics and Lasers Conference, Buffalo, NY, June 12–14.

Lorber, P. F. and Egolf, T. A. 1990. "An Unsteady Rotor Fuselage Interaction Analysis," *J. of the American Helicopter Soc.*, 35 (1), pp. 32–42.

Lynn, R. R. 1966. "Wing-Rotor Interactions," *J. of Aircraft*, 3 (4), pp. 326–332.

Lynn, R. R. 1970. "Tail Rotor Design," *J. of the American Helicopter Soc.*, 15 (4), pp. 2–30.

Main, B. J. and Mussi, F. 1990. "EH-101: Development Status Report," 16th European Rotorcraft Forum, Glasgow, Scotland, Sept. 18–20.

Makofski, R. and Menkick, G. F. 1956. "Investigation of Vertical Drag–Periodic Loads Acting on Flat Panels in a Rotor Slipstream," NACA TN 3900.

Mavris, D. N., Komerath, N. M., and McMahon, H. M. 1989. "Prediction of Rotor–Airframe Aerodynamic Interactions," *J. of the American Helicopter Soc.*, 34 (4), pp. 37–46.

McKee, J. W. and Naeseth, R. L. 1958. "Experimental Investigation of the Drag on Flat Plates and Cylinders in the Slipstream of a Hovering Rotor," NACA TN 4239.

McVeigh, M. A. 1986. "The V-22 Tilt Rotor Large-Scale Rotor Performance–Wing Download Test and Comparison with Theory," *Vertica*, 10, (4), pp. 281–297.

McVeigh, M. A., Grauer, W. K. and Paisley, D. J. 1990. "Rotor/Airframe Interactions on Tiltrotor Aircraft," *J. of the American Helicopter Soc.*, 35 (3), pp. 43–51.

Mello, O. A. F. and Rand, O. 1991. "Unsteady Frequency Domain Analysis of Helicopter Nonrotating Lifting Surfaces," *J. of the American Helicopter Soc.*, 36 (2), pp. 70–81.

Moedersheim, E., Daghir, M., and Leishman, J. G. 1994. "Flow Visualization of Rotor Wakes Using Shadowgraph and Schlieren Techniques," 20th European Rotorcraft Forum, Amsterdam, The Netherlands, Oct. 4–7.

Moedersheim, E. and Leishman, J. G. 1998. "Investigation of Aerodynamic Interactions Between a Rotor and a T-Tail Empennage," *J. of the American Helicopter Soc.*, 43 (1), pp. 37–46.

Newman, S. 1994. *The Foundations of Helicopter Flight*, Edward Arnold, London, England.

Park, Y. M., Nam, H. J., and Kwon, O. J. 2003. "Simulation of Unsteady Rotor–Fuselage Interactions Using Unstructured Adaptive Meshes," 59th Annual Forum of the American Helicopter Soc. International, Phoenix AZ, May 6–8.

Prouty, R. W. 1983. "Development of the Empennage Configuration of YAH-64 Advanced Attack Helicopters," USAAVRADCOM-TR-82-D-22.

Prouty, R. W. and Amer, K. B. 1982. "The YAH-64 Empennage and Tail Rotor – A Technical History," 38th Annual Forum of the American Helicopter Soc., Anaheim, CA, May 4–7.

Quackenbush, T. R. and Bliss, D. B. 1988. "Free Wake Calculation of Rotor Flow Fields for Interactional Aerodynamics," 44th Annual Forum of the American Helicopter Soc., Washington DC, June 16–18.

Quackenbush, T. R., Bliss, D. B., Lam, C.-M. G., and Katz, A. 1990. "New Vortex–Surface Interaction Methods for the Prediction of Wake-Induced Airframe Loads," 46th Annual Forum of the American Helicopter Soc., Washington DC, May 21–23.

Quackenbush, T. R. Lam, C.-M. G., and Bliss, D. B. 1994. "Vortex Methods for the Computational Analysis of Rotor/Body Interaction," *J. of the American Helicopter Soc.*, 39 (4), pp. 14–24

Rand, O. 1989. "The Influence of Interactional Aerodynamics in Rotor–Fuselage Coupled Response," *J. of the American Helicopter Soc.*, 34 (4), pp. 28–36.

Rand, O. and Gessow, A. 1989. "Model for Investigation of Fuselage Influence on Rotor Flowfields," *J. of Aircraft*, 26 (5), pp. 401–402.

Roesch, P. and Vuillet, A. 1981. "New Designs for Improved Aerodynamic Stability on Recent Aerospatiale Helicopters," 37th Annual Forum of the American Helicopter Soc., New Orleans, LA, May 17–20.

Ryan, J., Falempin, G., and Hiêp, L. T. 1988. "Rotor Plane Velocities Induced by a Helicopter Fuselage," Second International Conference on Rotorcraft Basic Research, College Park, MD, Feb. 16–18.

Schillings, J. J. and Reinesch, R. J. 1987. "The Effect of Airframe Aerodynamics on V-22 Rotor Loads," *J. of the American Helicopter Soc.*, 34, (1), pp. 26–33.

Sheridan, P. F. 1978. "Interactional Aerodynamics of the Single Rotor Helicopter Configuration. Final Report. USARTL-TR-78-23A.

Sheridan, P. F. and Smith, R. P. 1979. "Interactional Aerodynamics: A New Challenge of Helicopter Technology," 35th Annual National Forum of the American Helicopter Soc., May 21–23.

Smith, C. A. and Betzina, M. D. 1986. "Aerodynamic Loads Induced by a Rotor on a Body of Revolution," *J. of the American Helicopter Soc.*, 31 (1), pp. 29–36.

Smith, R. V. 1987. "Some Effects of Wake Distortion Due to a Fuselage Flow Field on Rotor Thrust Limits," ARO Workshop on Rotor Wake Technology, Raleigh, NC, April 17–18.

Stremel, P. M. 1987. "Aerodynamic Interaction Between Vortical Wakes and Lifting Two-Dimensional Bodies," 43rd Annual Forum of the American Helicopter Soc., St. Louis, Missouri, May 18–20.

Stremel, P. M. 1990. "The Calculation of Rotor–Fuselage Interaction for Two-Dimensional Bodies," 16th European Rotorcraft Forum, Glasgow, Scotland, Sept. 18–20.

Tarttelin, P. C. and Martyn, A. W. 1994. "In Flight Research with Instrumented Main and Tail Rotor Blades Using the DRA Bedford Aeromechanics Research Lynx Helicopter," In: AGARD CP-552.

Torok, M. S. and Ream, D. T. 1993. "Investigation of Empennage Airloads Induced by a Helicopter Main Rotor Wake," 49th Annual Forum of the American Helicopter Soc., St. Louis, MO, May 19–21.

Trept, T. 1984. "A 0.15-Scale Study of Configuration Effects on the Aerodynamic Interaction between Main Rotor and Fuselage," NASA CR 166577, Jan.

Vuillet, A. 1990. "Rotor and Blade Aerodynamic Design," In: AGARD R-781.

Wachspress, D. A., Quackenbush, T. R., and Boschitsch, A. H. 2003. "Rotorcraft Interactional Aerodynamics with Fast Vortex/Fast Panel Methods," *J. of the American Helicopter Soc.*, 48 (3), pp. 223–235.

Walker, J. D. A., Smith, C. R., Cerra, A. W., and Doligalski, T. L. 1987. "The Impact of a Vortex Ring on a Wall," *J. of Fluid Mechanics*, 181, pp. 99–140.

Wang. T., Doolan, C. J., Coton, F. N., and Galbraith, R. A. McD. 2002. "Experimental Study of the Three-Dimensionality of Orthogonal Blade–Vortex Interaction," *AIAA J.*, 40 (1), pp. 2037–2046.

Weinstock, S. 1991. "Formulation of a Simplified Model of Rotor-Horizontal Stabilizer Interactions and Comparison with Experimental Measurements," 17th European Rotorcraft Forum, Berlin, Germany, Sept. 24–27.

Wheatley, J. B. 1935. "The Influence of Wing Setting on the Wing Load and Rotor Speed of a PCA-2 Autogiro as Determined in Flight," NACA Rep. 536.

Wiesner, W. and Kohler, G. 1973. "Design Guidelines for Tail Rotors," US Army USAAMRDL Report D210-10687-1.

Wiesner, W. and Kohler, G. 1974. "Tail Rotor Performance in Presence of Main Rotor, Ground and Winds," *J. of the American Helicopter Soc.*, 19 (3), pp. 2–9.

Wilby, P. G., Young, C., and Grant, J. 1979. "An Investigation of the Influence of Fuselage Flow Field on Rotor Loads and the Effects of Vehicle Configuration," *Vertica*, 3, pp. 79–94.

Wilson, F. T. 1990. "Fuselage Aerodynamic Design Issues and Rotor–Fuselage Interactional Aerodynamics–Part. 1: Practical Design Issues," In: AGARD-R-781.

Wilson, J. C. and Kelley, H. L. 1983. "Measured Aerodynamic Forces on Three Typical Helicopter Tail Boom Cross Sections," *J. of the American Helicopter Soc.*, 28 (4), pp. 68–71.

Wilson, J. C. and Kelley, H. L. 1986. "Aerodynamic Characteristics of Several Current Helicopter Tail Boom Cross Sections Including the Effect of Spoilers," NASA TP-2506, AVSCOMTR-85-B-3.

Wilson, J. C., Kelly, H. L. and Donahue, C. C. 1988. "Development in Helicopter Tailboom Strake Application," RAeS Conference on Helicopter Handling Qualities and Control, London, England, Nov. 15–17.

Wilson, J. C. and Mineck, R. E. 1975. "Wind-Tunnel Investigation of Helicopter Rotor Wake Effects on Three Helicopter Fuselage Models," NASA TM X-3185.

Wood, T. L. and Peryea, M. A. 1991. "Reduction of Tilt-Rotor Download," 47th Annual Forum of the American Helicopter Soc., Phoenix, AZ, May 6–8.

CHAPTER 12

*Autogiros and Gyroplanes**

The outstanding inspiration of the Autogiro's story was the recognition that there might be more than one type of flying machine, soundly mechanical but basically independent of conventional theory and practice.

Juan de la Cierva (1931)

12.1 Introduction

An autogiro or gyroplane has a rotor that can turn freely on a vertical shaft. However, unlike a helicopter, its rotor is not powered directly. Instead, the rotor disk inclines backward at a positive angle of attack, and, as the machine moves forward in level flight powered by a propeller, the resultant aerodynamic forces on the rotor blades causes the necessary torque to spin the rotor and produce lift. The natural self-rotation of the rotor is called *autorotation*, a phenomenon introduced in Chapter 2. The autorotating rotor provides the lift for the machine (perhaps also control), with forward propulsion being provided by a conventional tractor or pusher propeller arrangement – see Fig. 12.1. Compare this to the helicopter where the rotor provides both lift and propulsion, as well as control. If the machine also has a fixed wing, or has the capability to hover (using tip jets), but is still flown as an autogiro in forward flight, then the aircraft may be referred to as a gyroplane or perhaps even as a convertiplane or gyrodyne. The names autogiro, autogyro, giroplane, and gyroplane are, however, often used synonymously.

In 1923, the autogiro was the very first type of rotating-wing aircraft to fly successfully and thus to demonstrate a useful and practical role in aviation, pre-dating the first successful flights of helicopters by about fifteen years. The autogiro was also the first powered, heavier-than-air aircraft to fly successfully other than a conventional airplane. Conceived by Juan de la Cierva about 1920 [see Cierva & Rose (1931), Gablehouse (1967), C. A. Cierva (1998), and Charnov (2003)] over thirty different autogiro designs were produced in just fifteen years of development (1923–1938). Cierva proved that his Autogiros[1] were very safe and because of their low flight speed capability they could be landed in confined areas. Takeoffs required a short runway to buildup airspeed, but this was rectified later with the advent of a prerotator for the rotor and the development of the "jump" and "towering" takeoff techniques. This gave the autogiro a capability that was comparable to that of the future helicopter in terms of overall performance. However, the autogiro often seems to be a half-forgotten machine that occupies a lower place in the list of aviation firsts. It has perhaps been viewed by many only as an interim step toward the helicopter, and a temporary makeshift

* This chapter is dedicated to the memory of Professor Alfred Gessow.

[1] The name "Autogiro" was later to be coined by Juan de la Cierva as a trademarked name for his aircraft, so when referring specifically to the Cierva machines it is always appropriate to call them "Autogiros" with a capital "A."

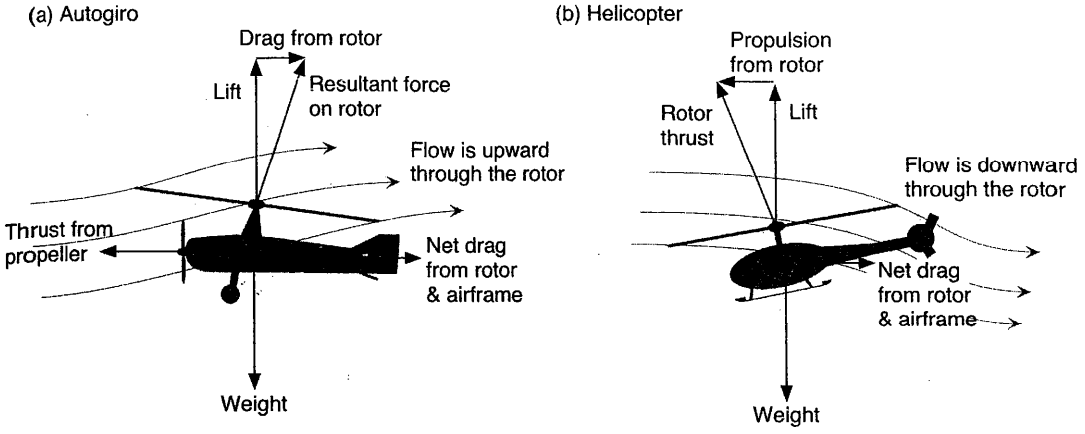

Figure 12.1 The autogiro rotor (a) provides lift to sustain flight, with forward propulsion being provided by a conventional propeller, compared to the helicopter (b), where the rotor provides both lift and propulsion.

at that. As discussed in Chapter 1, however, the autogiro played a fundamental role in the technological development of all types of modern rotating-wing aircraft. There are also several interesting technical aspects of autorotative flight that make this aircraft unique when compared to a helicopter. It is for this reason that a separate chapter on autogiros is an appropriate part of this book.

12.2 The Curious Phenomenon of Autorotation

Autorotation can been seen naturally in the flight of a variety of seeds, such as maple or sycamore – see Azuma & Yasuda (1989) for an aerodynamic discussion. However, the somewhat curious aerodynamic phenomenon of "autorotating bodies" had been observed in variety of scientific experiments by the beginning of the twentieth-century, which probably were inspired by earlier theoretical work by the Scottish physicist James Maxwell – see Tokaty (1971). The Italian Gaetano Crocco and the Russian Boris Yuriev had examined the principle of autorotation on spinning rotors around 1910. Munk (1925) conducted experiments with "helicopter propellers," where the phenomenon of autorotation was again demonstrated.

However, the Russian scientist Yuriev and his students probably made the most significant studies, showing that under some conditions of steeply descending and horizontal flight with the rotor at a positive angle of attack, a lifting rotor would actually turn of its own accord. Yuriev called this phenomenon "rotor gliding," and he apparently realized, even then, that the ability of the rotor to self-rotate might be used to bring a helicopter safely to the ground in the event of an engine failure. The ability to autorotate in an emergency condition (such as after a power or tail rotor failure) is a fundamental safety of flight capability that must be designed into all helicopters (see Chapters 2 and 5).

Chapter 1 described the numerous types of primitive human-carrying helicopters proposed and built from 1900 to 1920. Yet nobody had previously considered the idea that a successful rotating-wing aircraft could be built such that the rotor was unpowered and always operated in the autorotative state during its normal flight. In the spring of 1920 Juan de la Cierva of Spain built small, unpowered free-flying models of a rotating wing

aircraft, with the rotor free to spin on its vertical shaft. The model had a rotor with five blades, with horizontal and vertical tails to give it stability. Cierva launched the model and the rotor spun freely of its own accord as the model glided softly to the ground. Cierva had rediscovered the principle of autorotation, which at first he was to call "autogiration." These first experiments with models were to pave the way for the design of a completely new type of rotating-wing aircraft that Cierva was to ultimately call an *Autogiro*.

Juan de la Cierva had become interested in aviation as early as 1908 when the Wright Brothers demonstrated their *Flyer* machine in Europe. Cierva was subsequently to build the first Spanish airplane in 1912. His third airplane of 1919 was a large three-engined bomber. While the aircraft flew well, the test pilot became over ambitious and the machine stalled and crashed. This tragedy motivated Cierva to think of a way of improving the flight safety of an aircraft when it operated at low airspeeds and, in particular, when it was flying close to the ground. Cierva set out to design a safe flying machine that ensured "stability, uplift, and control should remain independent from forward speed" and suggested further that it should be one that could be flown by a pilot with average skill [see Cierva & Rose (1931)]. Cierva went on to point out that "the wings of such an aircraft should be moving in relation to the fuselage. The only mechanism able to satisfy this requirement is a circular motion and, moreover, in order to give adequate security to the aforementioned requirement it must be independent of the engine. It was thus necessary that these rotary wings were free-spinning and unpowered."

Thus was borne the vision of an autogiro. Juan de la Cierva was not the first to suggest or observe the phenomenon of autorotation, but he was certainly the first to understand better the aerodynamic principles and to put the phenomenon toward serving a useful purpose. He was to make some of the first theoretical studies on rotors and conducted a series of wind tunnel tests [see Cierva & Rose (1931)] as he writes: "with valuable results, among them the determination of the fact that the rotor would continue to turn at every possible angle of flight – a point that was somewhat disputed by critics of my earlier experiments."

12.3 Review of Autorotational Physics

Autorotation has been defined in Chapter 2 as a self-sustained rotation of the rotor without the application of any shaft torque (i.e., $Q = 0$ at the rotor shaft). In autorotation the energy to drive the rotor comes from the relative airstream, which is directed upward through the rotor. To see why, the problem can first be approached from momentum theory applied to a powered rotor in vertical descent, a method introduced in Chapter 2. In vertical climb or descent at a given rotor rpm, the torque ratio (the torque, Q, that is required to produce a given rotor thrust relative to the torque required for a shaft driven rotor to hover, Q_h) is

$$\frac{Q}{Q_h} = \frac{\Omega Q}{\Omega Q_h} = \frac{P}{P_h} = \frac{V_c}{v_h} + \frac{v_i}{v_h}, \tag{12.1}$$

where V_c is the climb velocity, v_i is the induced velocity through the rotor and v_h is the induced velocity in shaft-powered hovering flight (generally this is always used as a reference). The two terms on the right-hand side of this equation represent the torque associated with any change the potential energy of the rotor and the aerodynamic (induced) losses, respectively. The solution for v_i/v_h can be calculated using momentum theory as a basis (see Section 2.13.4), although vertical autorotation actually occurs in a condition where momentum theory offers no exact solution for the induced velocity – see Fig. 2.20.

In practice, there are also profile losses to overcome. Therefore, in an actual autorotational condition then

$$Q = \frac{T}{\Omega}(V_c + v_i) + Q_0 = 0. \tag{12.2}$$

where T is the rotor thrust and Q_0 represents the torque to overcome blade profile losses.

Clearly V_c must be negative to produce autorotation (i.e., the aircraft must give up potential energy). When in a stable "gliding" autorotation with a constant airspeed and constant rotor rpm, there is an energy balance where the decrease in potential energy of the rotor, $-TV_c$, just balances the sum of the induced *and* the profile losses of the rotor at that rpm. The ideas of an energy balance in autorotation were first explored by Cierva [see Cierva (1926)]. Using Eq. 12.2, this condition is achieved when

$$\frac{V_c}{v_h} = -\frac{v_i}{v_h} - \frac{Q_0\Omega}{Tv_h}. \tag{12.3}$$

The second term on the right-hand side of Eq. 12.3 depends on the profile drag of the rotor blades (i.e., on the rotor solidity and the average drag coefficients of the airfoil sections used on the blades). However, compared to the induced part, which is defined by the curve that has been shown in Fig. 2.20, the extra rate of descent required to overcome profile losses is small. In practice, in a vertical autorotation the nondimensional rate of descent, V_c/v_h, is found to be between -1.8 and -1.9. For the larger value, this is equivalent to a vertical rate of descent

$$V_d \approx 1.9\sqrt{\frac{T}{2\rho A}} = \frac{1.9}{\sqrt{2\rho}}\sqrt{\frac{T}{A}} = 27.55\sqrt{\frac{T}{A}} \quad \text{in units of ft/s} \tag{12.4}$$

at sea level atmospheric conditions. Equation 12.4 shows that the autorotational descent rate is proportional to the square-root of the rotor disk loading, $T/A(=W/A)$. Cierva's early Autogiros all had disk loadings of about 2 lb/ft^2 (96 N/m^2), which is also typical of modern autogiro designs. This would give a *vertical* autorotative rate of descent at sea level of about 39 ft/s (12 m/s) or 2,340 ft/min (713 m/min).

Unlike the helicopter, the autogiro's rotor must always operate in the autorotative working state, where the power to turn the rotor comes from a relative flow that is directed upward through the rotor disk. The low disk loading (T/A) of an autogiro's rotor (and, therefore, the low induced velocity through the rotor disk) means that only a small upward flow normal to the rotor TPP is necessary for the rotor to enter into autorotation compared to a helicopter. While the autogiro is not a direct-lift machine (nor was it designed to be) and cannot hover, it requires only minimal forward airspeed to maintain flight. Therefore, in straight-and-level forward flight, the rotor disk needs to operate only with a slight positive AoA (backward tilt). As long as the machine keeps moving forward though the air, the rotor will continue to autorotate and produce lift. Reducing engine power will cause the machine to descend slowly and increasing power will cause it to climb. The stoppage of the engine is never really a problem on an autogiro because the rotor is always in the autorotative state and so the machine will descend safely to the ground. The rotor can, however, exit the autorotative state as a result of poor piloting technique.

Measurements documenting the performance of autogiros are rare and go back to the 1930s. Detailed in-flight measurements were conducted by the RAE using a Cierva C-30 [see Hufton et al. (1939)] and by NACA using a Pitcairn PCA-2 [see Wheatley (1933a)]. See also Harris (1992) for these data. The autorotational rate of descent, V_d, for both machines is plotted in Fig. 12.2 as a function of forward speed, V_f, both parameters being

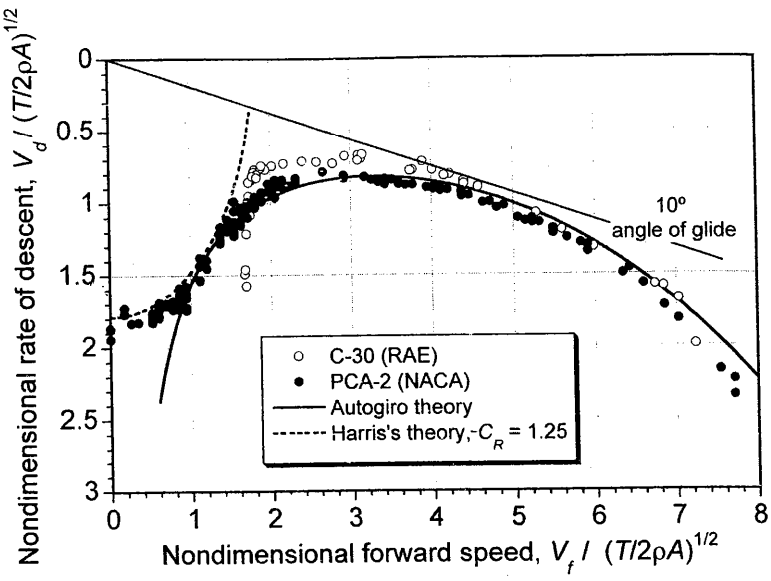

Figure 12.2 Nondimensional rate of descent in autorotational "gliding" flight versus nondimensional forward speed. Data source: Wheatley (1933a) and Hufton et al. (1939).

nondimensionalized by $\sqrt{T/2\rho A}$, which essentially removes the effects of disk loading from the results. It is apparent that the measured vertical rate of descent occurs at about $V_d/\sqrt{T/2\rho A} = 1.9$, which is in good agreement with the result given in Eq. 12.4 – see also Section 2.13.7. As previously mentioned, there is no *exact* theory describing the rotor aerodynamics in autorotation, even if the rotor has forward (translational) speed, but as airspeed builds momentum theory gives a better and better approximation to the predicted rate of descent in autorotation – see Section 12.9. The measurements in Fig. 12.2 clearly show a rapid decrease in the autorotational rate of descent as forward speed builds. A minimum rate of descent is reached at about $V_f/\sqrt{T/2\rho A} = 2$ (in practice this corresponds to about 35–40 kts or 65 km/h to 74 km/h), which is the point where aerodynamic losses at the rotor are a minimum, and the rate of descent slowly increases again thereafter.

Also of interest is the autorotational rate of descent versus the rotor disk angle of attack. While the forgoing measurements were performed in descending "gliding" flight, autorotation is also possible in level flight with propulsion from a propeller to drive the autogiro forward. All that is required is that the rotor disk be held at a sufficient AoA such that the component of the relative wind upwards through the disk causes the rotor to autorotate. In the words of Juan de la Cierva himself [see Cierva & Rose (1931)] "It makes no difference at what angle the Autogiro is climbing or flying. The blades are always gliding toward a point a little below the focus of forward flight. It is impossible, therefore, for autorotation to stop while the machine is going anywhere." This bold statement, however, excludes the possibility of bad piloting technique.

The results in Fig. 12.3 show the measured hub plane AoA as a function of the resultant nondimensional velocity of the aircraft. In a pure vertical descent it is apparent that the TPP and hub plane angles of attack are both essentially 90° (the resultant wind in this case is perpendicular to the disk). As forward speed builds, the hub plane needs to make a progressively smaller angle to the relative wind to enable autorotation, until at higher speeds the rotor must be held only at a shallow angle to produce enough lift in the autorotational

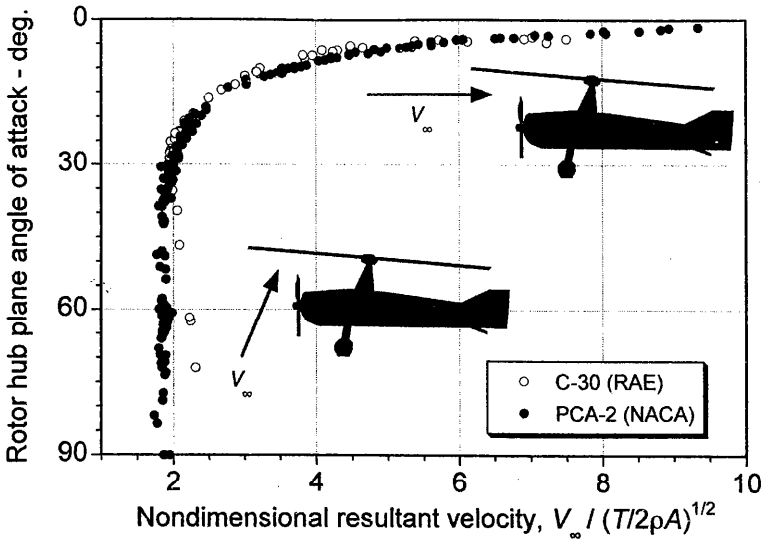

Figure 12.3 Rotor hub AoA versus resultant nondimensional speed showing that the rotor disk must only be held at a small AoA to produce lift and autorotate at higher airspeeds. Data source: Wheatley (1933a) and Hufton et al. (1939).

state. The rotor TPP angle is also inclined back but is not equal to the hub plane AoA because of blade flapping (see Fig. 12.4 and also discussion in Section 4.9). The natural tendency to produce longitudinal flapping (i.e., a β_{1c} component) with forward speed increases the component of velocity upward through the disk, which means the hub plane angle is always relatively small in forward flight. The TPP has a positive AoA much like a wing under these conditions – see page 94 and Glauert (1926, 1928).

Cierva juggled with the parameters affecting the magnitude and direction of the aerodynamic forces acting on the rotating blades and concluded that there could be many different combinations of rotor operating conditions where the net torque on the rotor shaft could be zero. Consider the flow environment encountered at a blade element on the rotor during autorotation, as shown in Fig. 12.5 where the relative velocity is directed upward toward the rotor. For autorotational equilibrium at that section the inflow angle, ϕ, must be inclined

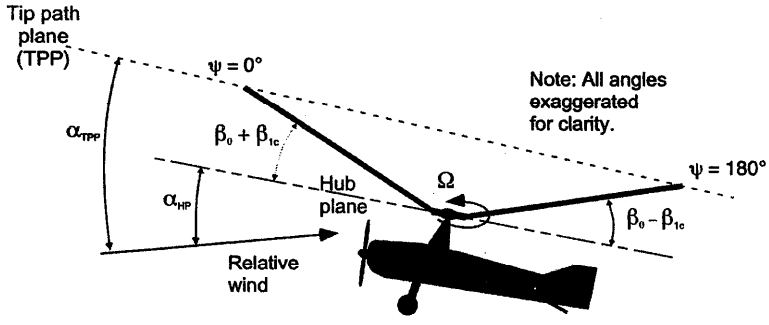

Figure 12.4 Definition of the rotor hub plane and rotor TPP angles of attack in autorotational flight.

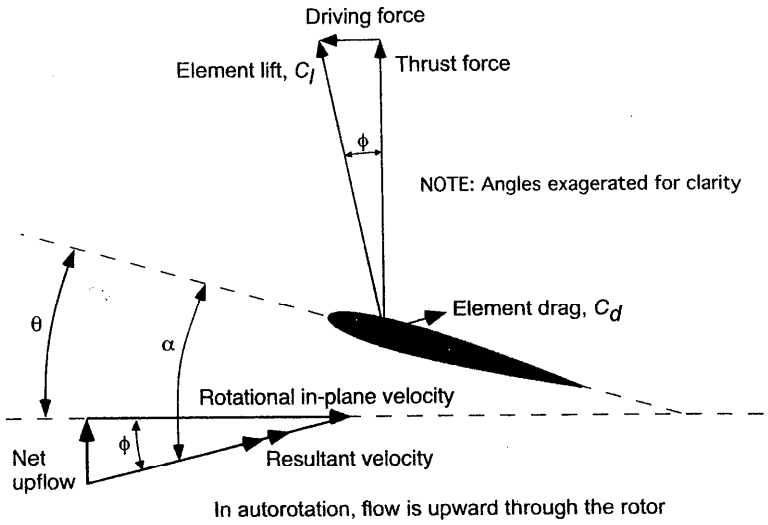

Figure 12.5 Detail of the flow at a blade element in autorotational flight.

forward such that there is no net in-plane sectional force and, therefore, no contribution to rotor torque; that is, for force equilibrium at that section

$$dQ = (D - \phi L)y\, dy = 0, \tag{12.5}$$

or that in coefficient form, we have

$$C_d - \phi C_l = 0. \tag{12.6}$$

However, this is an equilibrium condition that cannot exist over all parts of the blade and only one radial station on the blade can actually be in proper autorotational equilibrium. In general, it has been shown previously by means of Fig. 5.24 that some portions on the rotor will absorb power from the relative airstream and some portions will consume power, such that the *net* torque at the rotor shaft is zero (i.e., $\int dQ = 0$). For autorotational equilibrium the induced angles of attack over the inboard stations of the blade are relatively high and near the tip the values of ϕ are relatively low. We find that at the inboard part of the blade the net AoA results in a forward inclination of the sectional lift vector, providing a propulsive component greater than the profile drag and creating an accelerating torque – see Fig. 12.5. This blade element can be said to *absorb* energy from the relative airstream. Toward the tip of the blade where ϕ is lower and these sections of the blades *consume* energy because the propulsive component as a result of the forward inclination of the lift vector is insufficient to overcome the profile drag there (i.e., a net decelerating torque is produced).

As Cierva understood, in the fully established autorotational state at a given blade collective pitch angle the rotor rpm will adjust itself until a zero torque equilibrium is obtained. Assuming unstalled blades, then this is a *stable* equilibrium because it can be deduced from Fig. 5.24 that if Ω increases, ϕ will decrease and the region of accelerating torque will decrease inboard and this tends to decrease rotor rpm. Conversely, if the rotor rpm decreases, then ϕ will increase and the region of accelerating torque will grow outward. Therefore, when fully established in the autorotative state, the rotor naturally seeks to find its own equilibrium rpm in response to any changing flight conditions. This is an inherent characteristic of the rotor that gives the autogiro very safe flight characteristics.

However, in the autorotational state the blade pitch must always be at a low value and the disk AoA must be positive to ensure that the inboard blade sections never reach high enough angles of attack to stall. Stall may occur if the rotor rpm decays below an acceptable threshold, such as when the disk AoA becomes negative, or a reduced or negative load factor is produced. These are flight conditions to be avoided. If stall does inadvertently occur, then the outward propagation of stall from the blade root region will cause rotor rpm to decrease quickly because of the associated high profile drag.

12.4 Rolling Rotors: The Dilemma of Asymmetric Lift

When either a helicopter rotor or autogiro rotor operates in forward flight with the rotor plane passing edgewise through the air, the blades encounter an asymmetric velocity field [see Fig. 2.1]. The asymmetry of the onset flow and dynamic pressure over the disk produces aerodynamic forces on the blades that are a function of blade azimuth. For blades that are rigidly attached to the shaft, the net effect of these asymmetric aerodynamic forces is an upsetting moment on the rotor and on the aircraft. This was Cierva's first dilemma when developing the autogiro. As described in Chapter 4, the distribution of lift and induced inflow through the rotor will affect the inflow angle ϕ and the angle of attack at the blade sections and, therefore, the detailed distribution of aerodynamic lift and drag forces over the rotor. This subsequently affects the blade flapping response and so the aerodynamic loads on the blades. This coupled behavior is a complication with a rotating wing that makes its thorough analysis relatively difficult, a fact well appreciated by Cierva and a point alluded to throughout this book.

Cierva's first Autogiro, the C-1, was built in 1920 and had a coaxial rotor design. He was to build two more machines, both with single rotors, before he achieved final success with the C-4 (Fig. 12.6) in January 1923. The problem of asymmetric lift between the advancing and retreating blades was initially approached using the idea of a contrarotating coaxial design such that the lower rotor would counteract the asymmetry of lift produced on the upper rotor, thereby balancing out any moments on the aircraft. However, when flight tests began it was found that the aerodynamic interference between the rotors resulted in different autorotational rotor speeds and this spoiled the required aerodynamic moment balance. Cierva considered the possibility of mechanically coupling the rotors to circumvent the problem, but this was quickly rejected because of the obvious mechanical complexity and significant weight penalty. Despite its failure to fly the C-1 proved that the rotors would freely autorotate when the machine was taxied with sufficient forward speed.

The next Cierva design was the "compensating" rotor, which was tested in a three-bladed form on the C-3 in 1921 and in a five-bladed form on the C-2 in 1922. This idea used blade twisting in an attempt to compensate for the undesirable characteristic of asymmetric lift (i.e., by using nose-down twist on the advancing blade and nose-up twist on the retreating blade). Photographs of these two machines [see C. A. Cierva (1998)] show a series of cables attached to the trailing-edges of the blades, with the idea that the blade twist could be changed in a cyclic sense as the blades rotated about the shaft. However, while the basic principle was correct, the concept proved impractical and both the C-2 and C-3 were only to achieve short hops off the ground. Perhaps the use of cyclic blade feathering (as opposed to blade twisting) might have been more successful, but it was not to be until 1931 that Wilford in the United States demonstrated this concept on an autogiro – see Wheatley (1935), Larsen (1956), and Gustafson (1971).

12.5 Innovation of the Flapping and Lagging Hinges

Based on his many experiments with small models, Cierva noticed that the flexibility of the rattan (palm wood) spars on his models provided different aerodynamic effects compared to the relatively rigid blade structure used on his full-scale machines. This was the key Cierva needed and his "secret of success." His fourth machine (the C-4), therefore, incorporated blades with mechanical hinges (using horizontal pin joints) at their roots, which allowed the individual blades to flap up and down freely in response to the changing lift forces seen by the blades as they progressed around the shaft axis. Also acting on the blades are drag and centrifugal and gravitational forces, and as a result of free flapping, there are also inertia and Coriolis forces to contend with (see page 197). The blades on the C-4 were restrained by cables attached to the shaft to limit both downward and upward flapping angles and also so the blades would not droop to the ground when the rotor was stopped. Cierva noticed that the incorporation of the flapping hinge eliminated any adverse gyroscopic effects and also allowed the lift forces on the two sides of the rotor to become more equal in forward flight. However, Cierva's omission of a lead–lag hinge to alleviate the in-plane blade motion from drag and Coriolis forces (resulting from the flapping motion) was an oversight that he would ultimately come to terms with.

In Cierva's C-4 Autogiro of 1923 (see Fig. 12.6) a single rotor with four independent, freely flapping blades was mounted on a long shaft above an Avro 504 airplane fuselage. The blades were of high aspect ratio, similar to those of modern helicopter blades, and used a relatively efficient Göttingen 429 airfoil shape. A propeller, powered by a Le Rhône engine, provided propulsion. The first version of the C-4 used lateral tilting of the entire rotor disk to provide roll control. However, taxiing tests showed that the control forces involved in tilting the rotor were too high for the pilot and the control response also proved very sluggish. However, the natural tilting of the rotor TPP during flight also tilts the rotor lift

Figure 12.6 The Cierva C-4 Autogiro first flew successfully on January 9, 1923. It was the first rotating-wing aircraft to fly and also the first type of heavier-than-air aircraft to fly other than a conventional airplane.

vector and produces side forces and moments on the autogiro. These must be compensated for by some means to maintain trimmed flight and proper control. On a helicopter, this is done by using cyclic pitch inputs to the blades. But on Cierva's first machines, the rotor disk was uncontrolled and conventional "fixed-wing" aerodynamic control surfaces (ailerons, elevator, and rudder) were used to provide the necessary forces and moments on the aircraft to compensate for the natural tilting of the rotor disk. While not ideal, Cierva was satisfied with the simplicity of his interim solution to the problem.[2] Cierva's C-4 Autogiro first flew successfully on January 9, 1923, making a controlled flight in a straight line and covering about 200 m (656 ft) – see Moreno-Caracciolo (1923).

As explained in Chapter 4, the use of a flapping hinge allows each blade to flap up and down independently in a periodic manner with respect to the blade azimuth angle under the action of the varying aerodynamic loads. The blades precess to an equilibrium condition when the local changes in AoA and the aerodynamic loads produced as a result of blade flapping are sufficient to compensate for local changes in the airloads resulting from periodic variations in the dynamic pressure. The flapping response lags the blade pitch (aerodynamic) inputs by about 90° (see Chapter 4, p. 183). Therefore, the main effect of the asymmetry in lift over a rotor with flapping blades is to cause the rotor disk to tilt back, in this case giving it a natural AoA – see Fig. 12.4. In addition, the rotor disk also has a tendency to tilt laterally slightly to the right (for a rotor turning in a counterclockwise direction) because of the coning of the rotor under the action of the lift forces.

On the first lightly loaded Cierva rotor designs, the in-plane forces were balanced by sets of wires connected between the blades, such that as one blade lagged back or forward, the motion was easily resisted by the other blades. However, by Cierva's own admission [Cierva & Rose (1931)] his early Autogiros were "rather rough in flight owing to a sort of whipping action of the rotor blades which jerked at the mast as they turned in their circle." Cierva was noticing Coriolis effects, which produce forces in the plane of rotation of the rotor and introduce an important dynamic coupling between flapping (or out-of-plane) motion and the lead–lag (or in-plane) motion of the rotor blades (see page 197).

With later bigger and heavier machines, the combination of higher drag and Coriolis forces produced relatively high cyclic in-plane stresses at the blade root, and flight tests with a C-6 were to show evidence of in-plane structural bending overloads and the onset of fatigue damage. Yet, Cierva initially resisted the use of a second hinge to relieve these Coriolis loads because of weight concerns. Eventually, on a version of the C-6, a blade failed and flew off resulting in the official grounding of all Cierva Autogiros. This episode finally convinced Cierva that another hinge, a lead–lag or "drag hinge," must be required on the blades – see Fig. 4.1. Cierva tried out the idea of two hinges per blade on his model C-7, and after convincing the authorities of the renewed airworthiness, Cierva went on to develop the C-8 Autogiro. The incorporation of both a flapping hinge *and* a lead–lag hinge was an important step in the development of the *fully articulated rotor hub* discussed in Chapter 4, which is used today for many helicopters.

12.6 Prerotating the Rotor

Because an autogiro rotor is not powered, the rotor needs to be brought up to speed by some means before takeoff. In Cierva's day this was initially done by taxiing the aircraft around for several minutes. Later, a "spinning top" method was used, where a rope was

[2] Later autogiro designs incorporated the ability to tilt the rotor disk, either by tilting the rotor shaft directly on a gimbal or with the use of a "spider" cyclic pitch mechanism.

wound around the rotor shaft on pegs mounted on the bottom of the blades, the rope being pulled quickly (either manually by ground crew or by taxiing away from an anchor) to start the rotor. Instead, the Cierva C-12 model of 1929 saw the use of an alternative aerodynamic method to prerotate the rotor. Here, a "Scorpion" type of biplane tail was used to deflect the propeller slipstream up toward the blade tips. This horizontal tail was deflected at a steep incidence angle and the machine was held on the brakes and the throttle opened until the deflected propeller slipstream caused the rotor to autorotate and come up to speed. The tail incidence was then reduced back to its normal pitch before takeoff. The Scorpion tail design, however, was a relatively heavy solution and suffered from higher parasitic drag compared to the conventional monoplane tail. It also resulted in poorer directional control at low airspeeds because the vertical stabilizer and rudders were outside the propeller slipstream. Yet, the Scorpion tail was used on several models of the Cierva's Autogiros and seemed to offer a reasonably good compromise as an interim practical solution to starting the rotor. However, by 1930 engineers were to develop a more powerful, lightweight prerotator. This mechanical starter allowed the rotor to be brought quickly up to speed, solving finally the problem once and for all.

12.7 Autogiro Theory Meets Practice

In 1925, Juan de la Cierva was invited to Britain by H. E. Wimperis [see also Wimperis (1926)] of the British Air Ministry and was provided with financial backing by the industrialist James G. Weir of the Weir Company. Cierva was shortly thereafter to found the Cierva Autogiro Company, Ltd. and Britain was then to become the home for Cierva's work. His company was not set up for manufacturing, however, but for technical studies, management of patents and awarding of licenses to build his Autogiros. His Autogiros instead were built by established aircraft manufacturers, including the Avro (A. V. Roe) Company. Pitcairn and Kellett in the United States were later to become major licensees and were to produce various derivatives of the Cierva machines. This saw the beginning of the Pitcairn–Cierva Autogiro Company of America. In 1933, this enterprise was to become simply the Autogiro Company of America. See Harris (1992) for a history.

Cierva's C-6 Autogiro was demonstrated at the RAE in 1925 and in the same year Cierva gave the first of three historical technical lectures to the membership of the RAeS [Cierva (1926)]. At the end of this (and all of the other lectures) there was considerable debate on the merits of his Autogiro. Cierva gave another lecture in 1930 [Cierva (1930a)] at a time when more than 100 autogiros were flying in Britain and the United States and he was to document the rapid technical developments of the autogiro that had taken place during the preceding five years. His final lecture and paper [Cierva (1935)] was to the RAeS in 1934 and he then described in detail the "jump" takeoff technique and the direct rotor control device (see Section 12.14).

Cierva's first demonstration flights and lectures in Britain stimulated early experimental and theoretical work on rotating-wing aerodynamics by H. Glauert and C. Lock. Their theoretical work was pioneering and was supported by relatively advanced wind tunnel measurements on model rotors [see Lock & Townend (1928)]. In 1926, Glauert (1926) published a classic paper that was to be the first theoretical treatise on induced inflow and rotor performance – see also Glauert (1927). Glauert's analysis quantified rotor performance in horizontal, climbing, and descending flight and set down the basic equations that could be used to relate rotor performance to certain design parameters. However, in descent or in autorotation (in particular) the theory was not exact, and even since then, there has been no exact theory derived from first principles to fully describe the aerodynamics of a rotor

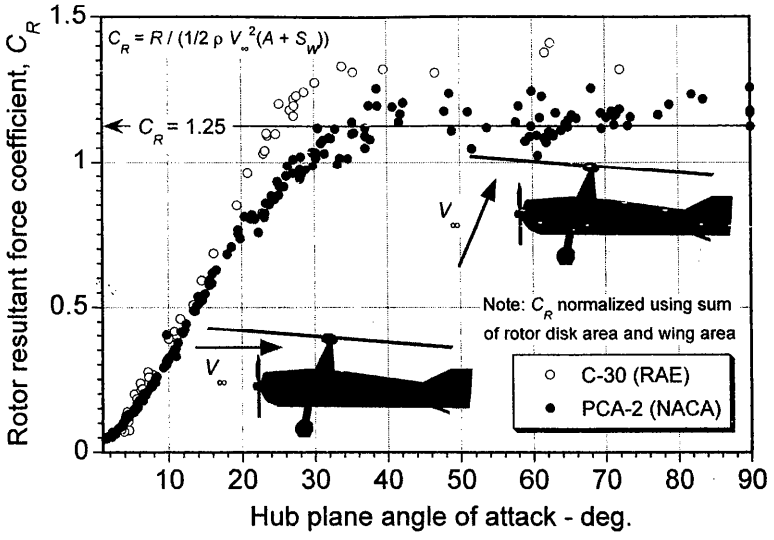

Figure 12.7 Resultant force coefficient on a rotor in autorotation showing that the force is large and relatively constant over a wide range of angles of attack. Data source: Wheatley (1933a) and Hufton et al. (1939)

in the autorotative state. However, Cierva vehemently disagreed with Glauert's analysis, based on his own theories and also his practical flight testing experience with the C-6. In a formal letter lodged with the RAeS, Cierva (1927) disagreed with Glauert's estimation of the vertical autorotative rate of descent, claiming values for "practically vertical descents" that were half of Glauert's estimate. He goes on further to draw concerns "with almost every point contained in Mr. Glauert's developments." Glauert seems to have been unruffled by such harsh criticism, standing confidently behind his theoretical studies – see Glauert (1927).

With hindsight, Glauert was probably closer to the truth of the matter than Cierva might have given him credit for. The analysis conducted previously has shown that the vertical rate of descent can be related to the rotor disk loading. The same result can be approached using measurements of the resultant force acting on the autorotating rotor, which are shown in Fig. 12.7. C_R is the resultant force coefficient, where R is the resultant force on the rotor as given by $R = \sqrt{L^2 + D^2}$, with L as the rotor lift force and D as the rotor drag force – see Fig. 12.8. It is significant that the resultant C_R on the rotor at large angles of attack (greater than 30°) is about 1.25 and nearly equivalent to the drag coefficient, C_D, of a circular disk with a flow normal to its surface (i.e., at high angles of attack the rotor acts like a bluff body with its attendant turbulent downstream wake). Recall from page 92 that $C_D = 1.33$ for an open hemisphere, which means that aerodynamically the rotor produces a resultant force equivalent to a parachute when in the vertical autorotative state. Yet, this was a point vigorously disputed by Cierva (1930b). Herein lies the difficulty in analyzing the aerodynamics of the rotor, because the rotor in its autorotative flow state at low airspeeds creates a complex turbulent wake and, in fact, is often said to operate in the "turbulent wake" state – see Fig. 2.20. With forward speed, however, the flow state in autorotation is much smoother.

Later, Harold Pitcairn urged Cierva to consolidate his vast engineering knowledge of the autogiro and in 1929 commissioned him to write a reference book for American engineers. The first Cierva book was titled *Engineering Theory of the Autogiro* – see Cierva

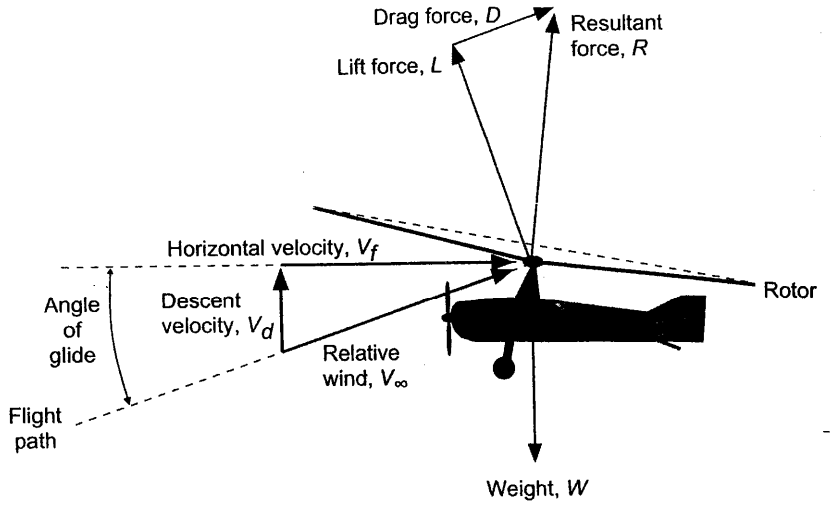

Figure 12.8 Forces acting on the autogiro in "gliding" flight.

(1930c). Sufficient data had been measured and analysis conducted that "a theory could be developed covering many probabilities of performance and possibilities of design beyond the actual achievement in construction to that time." [Cierva & Rose (1931)]. Later, Cierva wrote a comprehensive design manual titled *Theory of Stresses in Autogiro Rotor Blades.* Neither document was formally published, but they were copyrighted and made available to engineers at Pitcairn, the Kellett Autogiro Company, the NACA, the US Air Force, and the Bureau of Aeronautics. These engineering documents helped greatly in the certification of autogiros manufactured (and later designed) in the United States. Today, few original copies of these books exist, but they are a valuable chronicle in the technical development of rotating wing aircraft.

12.8 Vertical Flight Performance of the Autogiro

A conventional momentum theory analysis of the autorotating rotor breaks down when the rotor is at large angles of attack to the relative wind. For larger disk angles of attack it is possible to equate the resultant force on the rotor to the weight of the autogiro (i.e., $R \approx W$). Furthermore, the resultant velocity, V_∞, can be written as $V_\infty = \sqrt{V_f + V_d}$ so that

$$C_R = \frac{W}{\frac{1}{2}\rho(V_f^2 + V_d^2)A}. \tag{12.7}$$

Harris (2003) shows that for large operational angles of attack it is possible to write

$$V_f^2 + V_d^2 = \frac{2W}{\rho A C_D}. \tag{12.8}$$

In pure vertical descent $V_f = 0$, so the vertical rate of descent in autorotation will be

$$V_d = \sqrt{\frac{2W}{\rho A C_D}} = \frac{2}{\sqrt{\rho C_D}}\sqrt{\frac{W}{A}} = 25.94\sqrt{\frac{W}{A}} \text{ ft/s} \tag{12.9}$$

at sea level, which compares favorably with the result given previously in Eq. 12.4 and also with results by Glauert (1926). The autorotative rate of descent, however, decreases quickly with increasing forward speed but only to a point, as has been shown previously in Fig. 12.2. For a series of horizontal velocities, V_f, at the steeper angles of attack where $C_R = C_D = 1.25$, the rate of descent in autorotation, V_d, can be solved using

$$V_d = \sqrt{\frac{2}{\rho A C_D}\left(\frac{W}{A}\right) - V_f^2}, \tag{12.10}$$

or in nondimensional terms

$$\frac{\lambda_d}{\lambda_h} = \frac{V_d}{v_h} = \sqrt{\frac{4}{C_D} - \left(\frac{V_f}{v_h}\right)^2}, \tag{12.11}$$

for which the predictions made using this latter equation are shown in Fig. 12.2. Note that for $V_f = 0$ this predicts $\lambda_d/\lambda_h = 1.79$, which is consistent with the results shown in Section 2.13.7. While not exact, this equation does give a reasonably good result for V_d as a function of forward speed, V_f, when the rotor disk is at steep angles of attack to the relative wind.

12.9 Forward Flight Performance of the Autogiro

The performance of the autogiro in forward flight can be approached using the same basic principles of analysis (momentum and blade element theories) that were applied to the helicopter rotor in Chapters 2 and 3. Historically, the methods of helicopter analysis were mostly derived from the actuator disk analysis conducted on the autogiro by Glauert, Lock, Bennett, and Wheatley. There are two basic methods of approach: 1. An analysis based on energy principles (i.e., a net power analysis); and 2. A force and torque balance analysis on the rotor. In each case the principles of the momentum theory introduced in Chapter 2 for the analysis of the helicopter can be used as a basis.

Consider the autogiro in forward flight, as shown in Fig. 12.9. Vertical force equilibrium gives

$$L = W = T\cos\alpha, \tag{12.12}$$

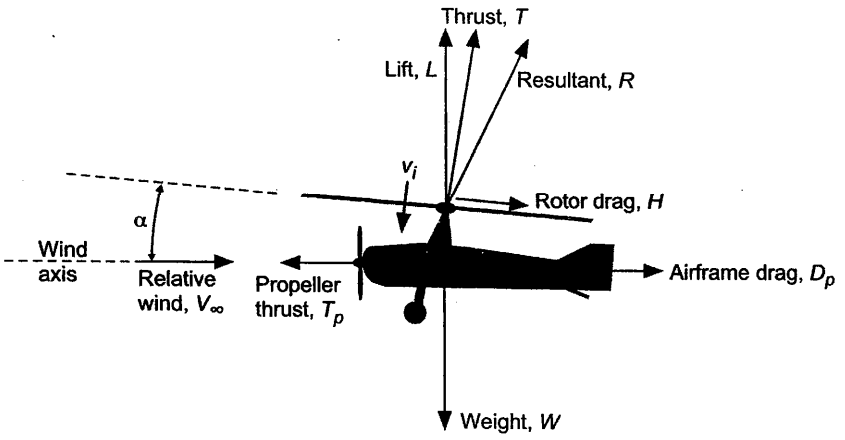

Figure 12.9 Forces acting on an autogiro in level flight.

and horizontal equilibrium gives

$$D = H\cos\alpha + D_p = T_p. \tag{12.13}$$

Using energy principles the net drag on the autogiro can be written simply as $D = P/V_\infty$. We know from Chapter 3 that the power can be written as the sum of the profile and induced power required for the rotor, $P_0 + P_i$, and the power required to overcome airframe drag, P_p. While the rotor of an autogiro is unpowered at the shaft, energy is still required to turn the rotor and overcome induced and profile losses. This source of energy is the relative flow upward through the rotor, which is produced by propelling the aircraft forward with the engine and propeller. Therefore, the power required can be written as

$$P = P_0 + P_i + P_p, \tag{12.14}$$

as for the helicopter case. These power components are conveniently written in their nondimensional form as

$$C_P = C_{P_0} + C_{P_i} + C_{P_p}, \tag{12.15}$$

where each component can be determined as

$$C_{P_0} = \frac{\sigma C_{d_0}}{8}\left(1 + 3\mu^2 + \frac{3}{8}\mu^4\right) \text{ including reverse flow,} \tag{12.16}$$

$$C_{P_i} = \frac{\kappa C_T^2}{2\sqrt{\mu^2 + \lambda_i^2}} \approx \frac{\kappa C_T^2}{2\mu} \text{ in high-speed flight,} \tag{12.17}$$

$$C_{P_p} = \frac{1}{2}\left(\frac{f}{A}\right)\mu^3. \tag{12.18}$$

The induced inflow through the rotor is given by the usual result from Chapter 2 that

$$\lambda_i = \frac{\kappa C_T}{2\sqrt{\mu^2 + \lambda_i^2}}, \tag{12.19}$$

with the usual limits of validity in mind (Section 2.14.5). The induced power factor for the autorotating rotor is typically slightly larger than for the powered rotor in the normal working state (as shown by the results in Fig. 5.30), but it is sufficient to assume that $\kappa = 1.2$ on average for autogiro performance calculations. Notice that the profile contribution to the power (or drag) must model the performance of the rotor at higher values of μ because of the typically lower rpm of the autorotating rotor. Finally, the propulsive force on the autogiro, T_p is produced by a propeller with aerodynamic efficiency η_p. Therefore, the net shaft power required for the autogiro, P_{SHP} is

$$P_{\text{SHP}} = \frac{T_p V_\infty}{\eta_p} = \frac{P}{\eta_p V_\infty} = \rho A(\Omega R)^2\left(\frac{C_p}{\eta_p \mu}\right). \tag{12.20}$$

There are several provisions on the use of the result in Eq. 12.20. First, it will not be applicable at very low airspeeds because it is apparent that P/V_∞ (or C_P/μ) will become singular. However, the autogiro cannot sustain level flight here anyway because there is a maximum resultant force coefficient that can be sustained on an autorotating rotor (i.e., $C_R \approx 1.25$). Under the conditions where level flight cannot be sustained, the autogiro will begin to descend and potential energy (altitude) is given up. Second, because of its lower tip speed the rotor operates at high μ, so that the applicability of the approximation used for the rotor drag with reverse flow (Eq. 12.16) must be examined. Third, the theory cannot apply

when the disk AoA is large, although from Fig. 12.3 it is clear that this also only occurs at lower speeds and steep angles of descent. Therefore, Eq. 12.20 will apply over most practical level-flight airspeeds. However, it will be apparent that this first form of analysis gives no information about the rotor disk AoA required to actually produce autorotation.

An alternative form of analysis based on a force balance must consider the flow conditions required to produce autorotation (i.e., the AoA of the rotor to produce autorotation at a given airspeed must now be determined). The principles of this following approach was used by Bennett (1933) and also by Glauert (1935) for his "lifting windmill" problem. To produce autorotation there must be a component of flow upward through the disk (i.e., a component $V_\infty \sin\alpha$). Because the rotor produces thrust it also creates an induced velocity v_i. The net flow upward through the rotor will thus be $V_\infty \sin\alpha - v_i$, where α is *not* known a priori. Autorotational conditions will be obtained when the AoA and upward flow is sufficient to overcome both the induced and rotational torque losses of the rotor so that the net shaft torque required will be zero. These losses can be written as

$$C_Q = C_{Q_0} + C_{Q_i} = C_{Q_0} + \kappa\lambda C_T = 0 \quad \text{for autorotation,} \tag{12.21}$$

where C_{Q_0} is the rotational component of profile torque on the rotor (see Section 5.4.2), which is given by

$$C_{Q_0} = \frac{\sigma C_{d_0}}{8}\left(1+\mu^2\right) \tag{12.22}$$

and where the inflow ratio (see Section 2.14.1) is given by

$$\lambda = \mu\tan(-\alpha) + \frac{C_T}{2\sqrt{\mu^2+\lambda^2}}. \tag{12.23}$$

Notice that a negative sign preceding the α must be used here because the disk is now tilted back compared to the helicopter case. Thus we have

$$C_T\mu\tan(-\alpha) + \frac{\kappa C_T^2}{2\sqrt{\mu^2+\lambda^2}} + C_{Q_0} = 0, \tag{12.24}$$

which can be solved numerically for the value of α required to produce autorotation; that is, the value of α required at any μ to produce zero net torque (power) required at the rotor shaft. Notice that because vertical force equilibrium must be simultaneously satisfied using Eq. 12.12, the rotor thrust must also increase as α increases because the airspeed decreases (i.e., because $C_T \approx C_W/\cos\alpha$). This will apply down to the lower limit of $C_R \approx 1.25$. Having solved for α to produce autorotation, the drag on the autogiro will be

$$D = T\sin\alpha + H\cos\alpha + D_p = T_p, \tag{12.25}$$

where the rotor drag force coefficient is

$$C_H = \frac{\sigma C_{d_0}}{8}\left(2\mu + \frac{1}{2}\mu^3\right) \tag{12.26}$$

when including reverse flow but not radial drag – see Section 5.4.2. The shaft power required for flight is then found using

$$P_{\text{SHP}} = T_p V_\infty/\eta_p, \tag{12.27}$$

as before. The results from both the energy and force methods are equivalent, although the latter approach has the advantage of being able to solve for the rotor disk AoA required to produce autorotation.

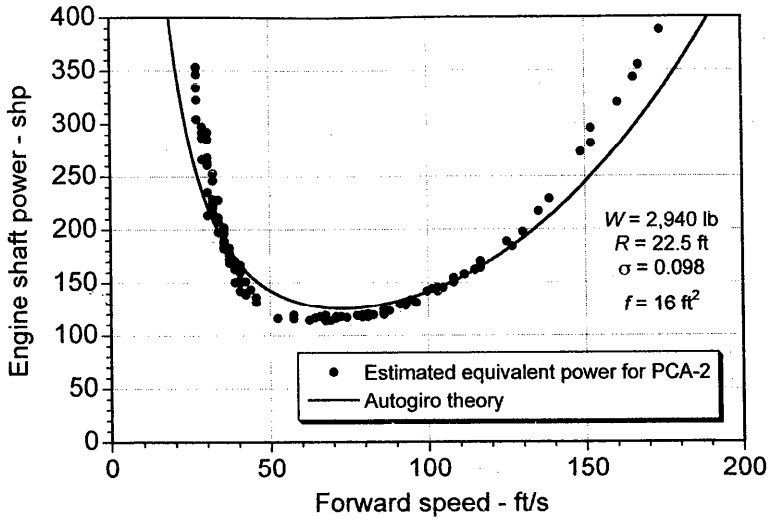

Figure 12.10 Predictions of power required for flight for an autogiro are in good agreement with the momentum theory approach.

A representative curve of power required versus airspeed for the PCA-2 autogiro is shown in Fig. 12.10. While direct power measurements are not available, it is possible to derive the equivalent shaft power at the engine by using the L/D results in Fig. 12.14 along with an assumed propeller efficiency. It is apparent that this type of performance analysis is in agreement with the measurements. Notice in this case, however, that, compared to a typical helicopter curve, the power requirements for an autogiro increase rapidly as airspeed bleeds off. The performance of the autogiro at these conditions is limited by either the power available or the maximum rotor lift coefficient (see Fig. 12.7). Furthermore, notice that the power requirements increase rapidly at higher airspeeds, which is a result of the high parasitic drag (large equivalent flat plate areas) of the early autogiros.

This theory can also be used to predict the gliding (power-off) rate of descent of the autogiro. The results have been shown previously in Fig. 12.2. Based on an energy balance and solving for the rate of descent, it is apparent that the theory is in excellent agreement with the measured performance of the PCA-2 and C-30 Autogiros, but only at higher forward flight speeds. This is because of the failure of the momentum theory to predict the induced velocity through the rotor at high disk angles of attack (low airspeeds, higher rates of descent). As also shown in Fig. 12.2, Harris's approximate theory for these conditions seems to fill in nicely where the momentum theory fails.

12.10 Comparison of Autogiro Performance with the Helicopter

Consider now the power required for flight with an autogiro versus that for a helicopter of equivalent weight. Such a comparison helps show the relative disadvantage of the autogiro. This issue had not gone unnoticed by Cierva [see Bennett (1933, 1961)] and had been analyzed by von Kármán (1931). The results in Fig. 12.11 show such a comparison for a PCA-2 autogiro versus a modern helicopter in the 3,000-lb weight class. It is clear the power requirements for flight are generally larger for the autogiro. The rapid increase in power required by the autogiro at higher airspeeds is significant. This is partly because of the typically high parasitic drag of an autogiro, as well as because the rotor operates at

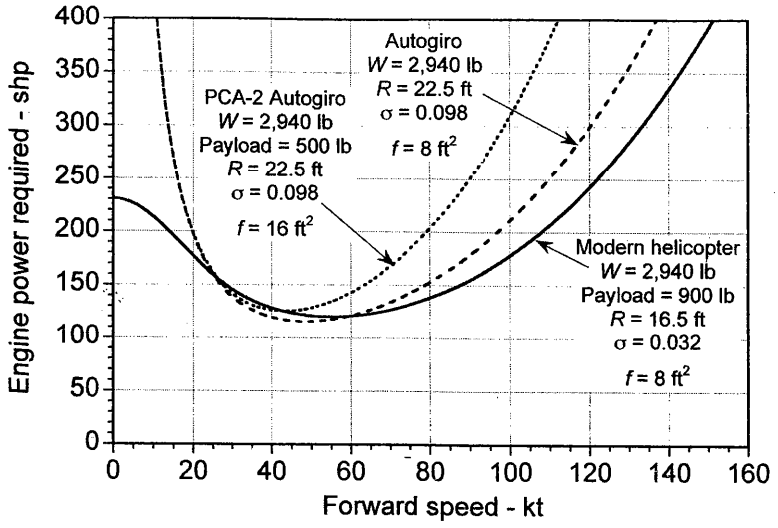

Figure 12.11 Comparison of the power required for flight of a autogiro versus that of a helicopter.

higher advance ratios (compared to a helicopter) with significant reverse flow and increased drag on the retreating side of the disk. However, with appropriate streamlining and general drag reduction it is also apparent that the power requirements for flight can be significantly reduced to values that are more consistent with a modern helicopter. The payload of a modern helicopter is also nearly twice that which could be achieved with an early autogiro. Yet, the obvious mechanical simplicity of the autogiro suggests that with modern construction methods and materials, the empty weight fraction could be reduced and payload increased such that a modern autogiro might become an economically competitive means of achieving rotating-wing borne flight.

12.11 Airfoils for Autogiros

Cierva was well aware of the importance of airfoil shape in improving the performance of his autogiros [see Cierva (1930c) and Cierva & Rose (1931)]. He wrote in reference to the twisting moment produced on autogiro blades by the use of a cambered airfoil versus a symmetric airfoil: "It [the Göttingen-429] is a reasonably efficient airfoil, although others give greater lift and a great many different curves are used for designing [fixed-wing] airplanes. But, the important advantage of this particular type is that its center of lift or pressure is approximately the same at all angles which it may assume in flight. This is not true of other types of airfoil, so that center of pressure travel is a factor to be reckoned with in using them." In essence, Cierva is referring here to the connection between aerodynamic performance (better maximum lift coefficient and improved lift-to-drag ratios) through the use of camber and the corresponding increase in pitching moments caused by that camber – see Section 7.7.3. Compressibility issues on the advancing blade can be an issue for an autogiro, although somewhat less so than for a helicopter because the autogiro operates at lower mean lift coefficients, but there is still a need to use airfoils with good aerodynamic characteristics at high subsonic Mach numbers.

Cierva had many airfoil sections to choose from, but the aerodynamic characteristics of most were not well documented. On the C-4, Cierva used the Eiffel 106 airfoil section, later

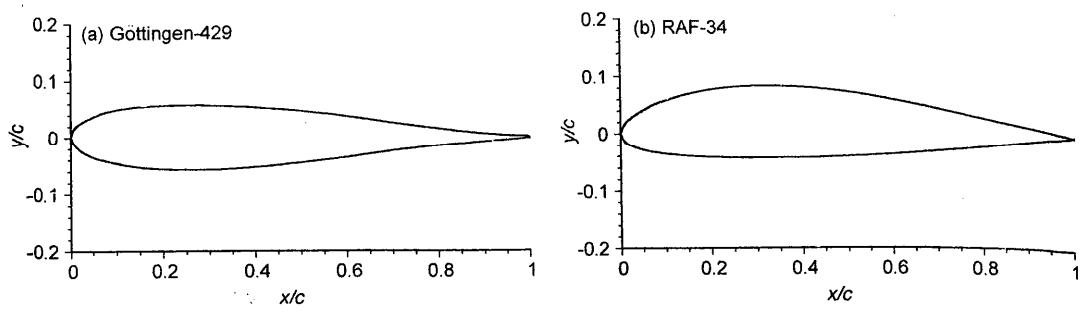

Figure 12.12 Two types of airfoils that were used on the Cierva Autogiros: (a) the symmetric Göttingen-429, (b) the reflexed cambered RAF-34.

switching to the Göttingen-429 airfoil. Some years later, Cierva was again to reconsider the choice of the airfoil section for his Autogiros, but, limiting his study to ten candidate airfoil sections, he decided to replace the symmetric Göttingen-429 airfoil, which had "abrupt stalling" characteristics with the reflexed-cambered RAF-34 airfoil of 17% thickness-to-chord ratio (see Fig. 12.12). The new blades were first tested on the C-19 Mk-IV, which became one of the most successful Cierva Autogiro designs. On the C-30 Autogiro, Cierva switched the airfoil again, this time to the cambered Göttingen-606 airfoil. In some flight conditions, mainly at high airspeeds, the higher pitching moments resulted in the blades twisting elastically and so this produced control problems. These aeroelastic effects arose because of the generally low torsional stiffness of early wood and fabric covered rotor blades. A crash of a C-30 Autogiro was tied to the use of this cambered airfoil section – see Beavan & Lock (1939). The NACA had also noticed such aeroelastic problems and had analyzed the effects of blade twisting – see Wheatley (1937a,b). On the Kellett YG-1 (which also used the Göttingen-606 airfoil) but with an upward deflected trailing edge tab, the NACA eventually replaced the blades with a reflexed airfoil based on the NACA 230 series. Yet, these airfoils were not successful and were found to have relatively poor characteristics at high lift and at high speeds – see Bailey & Gustafson (1939) and Gustafson (1971).

12.12 NACA Research on Autogiros

While the RAE in Britain had conducted experiments with autogiros, and had developed a theoretical basis for their analysis as early as 1926, it was not until the early 1930s that the extensive resources of the NACA were turned toward the science of rotating wings. Over the next ten or more years, the autogiro was to be tested extensively, with the work forming a solid foundation for later work on helicopters. In 1931, the NACA purchased a PCA-2 autogiro and this aircraft became the basis for extensive flight and wind tunnel testing (see Fig. 12.13) for almost 8 years, until the helicopter appeared. Gustafson (1971) gives a first hand summary of the early NACA technical work on both autogiros and helicopters, and Gessow (1948) gives a complete technical bibliography.

The first published NACA report on the autogiro was by Wheatley (1933a), which provided an authoritative baseline measurements on the performance of the PCA-2 autogiro. Measurements of rates of descents and glide angles were obtained (see Fig. 12.2), along with estimates of rotor lift-to-drag ratio. Separate tests of the rotor were also conducted in the wind-tunnel [see Fig. 12.13 and Wheatley (1934)] allowing quantification of the rotor

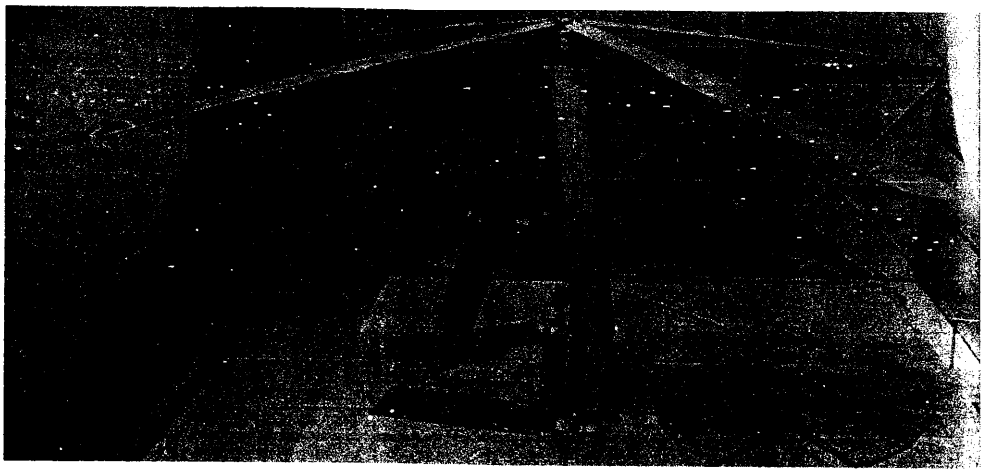

Figure 12.13 A Pitcairn PCA-2 autogiro rotor was to form the basis for the first NACA wind tunnel tests of a rotating wing. (NACA photo.)

performance alone compared to the complete PCA-2 aircraft. As shown in Fig. 12.14, the aerodynamic efficiency of the autogiro was relatively poor compared to most airplanes, with a maximum L/D ratio of only about 4.5. The differences between the rotor alone and the complete aircraft reflects the high parasitic drag of the airframe. However, to put the results in perspective, the performance of the rotor alone, which had a maximum L/D ratio of about 7, is comparable to that of a modern helicopter rotor. Notice that for higher advance ratios (or tip speed ratio) the helicopter rotor L/D ratio drops off markedly, in part because of retreating blade stall and advancing blade compressibility effects, whereas because the

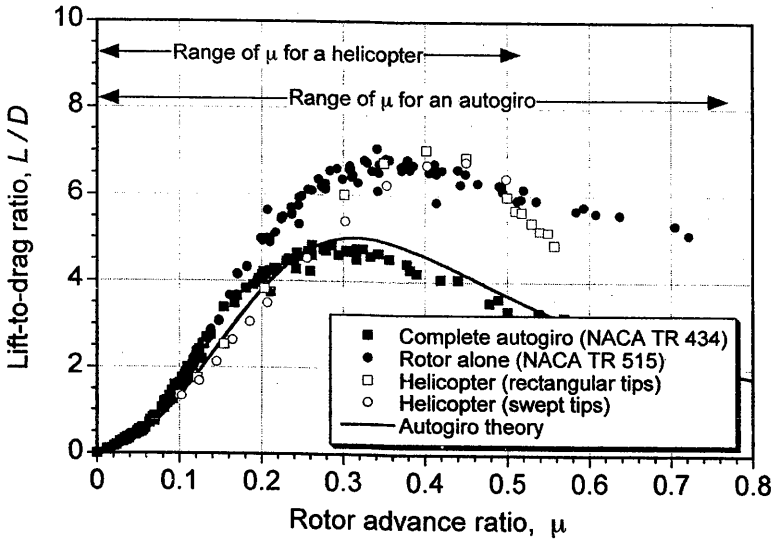

Figure 12.14 Lift-to-drag ratio in autorotation for complete autogiro (PCA-2) versus the rotor alone. The lift-to-drag ratio of a rotor in autorotation is comparable to that of a modern helicopter rotor. Data source: Wheatley (1933a) and Wheatley & Hood (1934).

autogiro rotor has a relatively low rpm and low disk loading it retains its L/D ratio to as high as $\mu = 0.7$ (although not necessarily to a higher airspeed).

Wheatley (1933b) studied the load sharing between the rotor and the wing and also examined the maneuver characteristics of the autogiro. One of the most remarkable findings in this work was a sustained maximum maneuver load factor of 4.3, which is high for any kind of rotorcraft and rarely obtained even on modern combat helicopters during transient maneuvers – see Section 5.9. The main reason for this large value was the relatively low blade loading and low mean lift coefficients of the autogiro rotor, which lead to good stall margins. The role of the wing was also important in off-loading the rotor at higher airspeeds and during maneuvers. Flight tests with the PCA-2 demonstrated forward speeds of 140 mph, with an advance ratio in excess of $\mu = 0.70$. This is a very high advance ratio for a rotor, but is possible on an autogiro if the rotor is offloaded by a wing.

The earliest theoretical studies of the autogiro at NACA resulted in one of the first thorough aerodynamic analyses of the rotor – see Wheatley (1934b) & Bioletti (1935). Later, a now classic report by Bailey (1941) extended the earlier work of Glauert (1926, 1928) and Lock (1928) and included the treatment of blade twist, reverse flow, nonuniform inflow, and tip-loss effects on the aerodynamics of the rotor. The predictions were shown to be in good agreement with both flight and wind tunnel measurements. The NACA worked extensively on several other technical problems (both from an experimental and a theoretical perspective) that were to occur during the maturation process of the autogiro. This included work on rotor dynamics, vibration, airfoil sections, jump takeoffs, and ground resonance – see Gustafson (1971).

12.13 Giving Better Control: Orientable Rotors

Peck (1934) conducted landing tests with the autogiro to help to quantify the poor roll control response that pilots found when autogiros with conventional airplane control surfaces flew at very low airspeed. Because the autogiro could be landed at almost zero ground speed, especially into a wind, the ineffectiveness of the ailerons under these conditions was a serious deficiency in the machine's handling qualities and several crashes occurred. This gave the machine a less than desirable reputation amongst pilots and it was clear that the problem needed to be rectified by using some form of rotor control. While Cierva had initially investigated a disk tilting mechanism on the C-4 to provide roll control, the system was not viable at that time.

By 1931, Cierva had introduced the *directly orientable* rotor control. This "rocking head" design placed the rotor on a universal joint or gimbal and essentially solved the control problem by allowing the entire rotor shaft to be tilted in any direction and so inclining the rotor lift force. This innovation allowed Cierva to dispense finally with the stub wings and the elevator: the rotor had enough control capability now for both roll and pitch. The rudder was retained for directional control. During 1932, the new device was tested on a C-19, which had no conventional airplane features except for a vertical tail and a rudder. The controls for the original tilting shaft design were shortly thereafter replaced by a "hanging stick" from the rotor hub to the cockpit, which gave the pilot both good control authority and also relatively light control forces in both roll and pitch. The device quickly became the new standard and was incorporated on all Cierva Autogiros manufactured after 1932, including the C-30 (Fig. 12.15), which became one of the most famous autogiros with nearly 200 being built in Britain, the United States, and France. However, the rotor vibrations were also transmitted through the control stick and this made the machines tiring to fly.

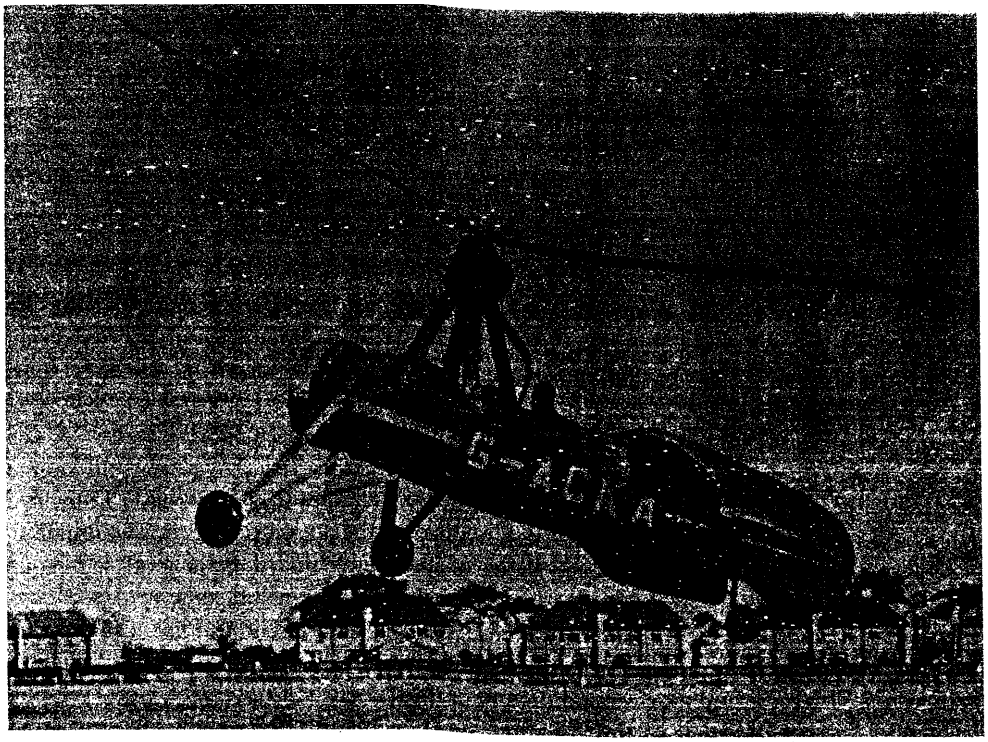

Figure 12.15 A version of the Cierva C-30 showing for the first time the absence of conventional wings and ailerons and "hanging stick" design for "direct" rotor control.

12.14 Improving Performance: Jump and Towering Takeoffs

In a lecture given in Italy in 1929, Cierva first alluded to the idea of a giving his Autogiros a vertical takeoff capability. Initially introduced on a version of the Weir W-3 autogiro, the first advance made was that the rotor could be clutched to the engine through a lightweight transmission and spun up to a higher than normal rpm when the autogiro was on the ground. The second advance made was in the hub design to give it a blade pitch-change capability. While this hub went through many different changes, finally an ingenious kinematic blade pitch–lag coupling device was used to give a change in blade pitch between a low (zero thrust) setting and the normal flight pitch. This design was eventually to become the Cierva–Weir "autodynamic" rotor. Bennett (1961) explains how fifteen different hinge assemblies were tried before success was achieved.

The idea was that while the rotor rpm was over-sped on the ground up to a higher than normal flight rpm, the drag on the blades caused them to lag onto mechanical stops. Under this condition, the blade pitch was reduced to the low value by the coupling device. The rotor produced little lift in this condition. When the rotor was declutched from the engine, the blades snapped out of the stops and back to the original pitch. The resulting sudden surge of rotor lift caused the autogiro to "jump" into the air and climb rapidly off the ground (Fig. 12.16). While this jump takeoff capability comes about partially a result of the excess thrust produced by stored kinetic energy in the rotor system at the higher rpm, there are also aerodynamic benefits of a rapid change in blade pitch. This benefit gives a lag in the inflow development through the rotor and so a sudden thrust overshoot is produced – see Carpenter & Friedovich (1953) and discussion in Section 10.9. This excess or "dynamic"

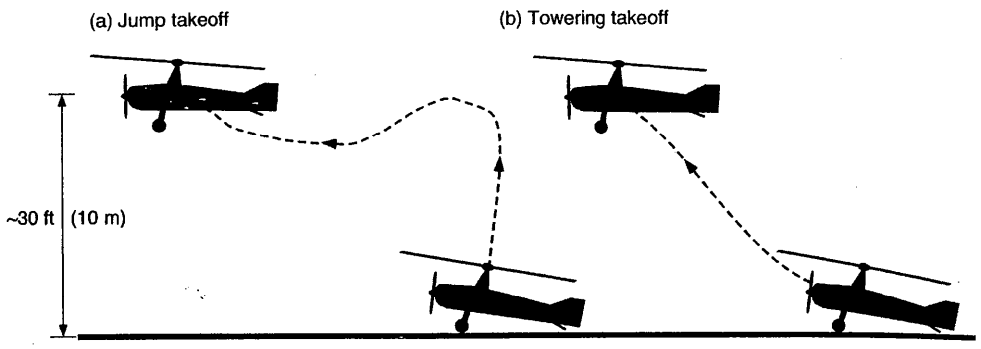

Figure 12.16 The jump (a) and towering (b) takeoff capability gave the autogiro a capability rivaling a helicopter.

thrust, however, decreases quickly (within a few rotor revolutions). Applying full engine power, as the machine climbs after the initial jump, accelerates it into forward flight, after which the rotor rpm decays to its lower flight value and the autogiro flies away normally.

However, there was always some loss of altitude with this jump takeoff technique (Fig. 12.16), the drag from the unpowered blades slows down the rotor rpm and contributes to a decrease in the initial dynamic thrust. Because the rotor also had a substantial backward tilt to aid in normal autorotation, there was a tendency for it to jump off slightly backwards. This increased the overall difficulty of the maneuver for the pilot. Good piloting technique, however, made the vertical jump takeoff technique consistently successful and the autogiro often rose quickly to more than 30 ft (10 m) into the air. The autodynamic rotor system was installed on a modified C-30 and was demonstrated successfully in 1935. By this time the Bréguet–Dorand helicopter had made its first flights (see Chapter 1) and this significant advance in the performance of the autogiro received less attention than it might have done otherwise.

Raoul Hafner was to develop another type of jump takeoff system on his AR.III autogiro in 1935, which is described by Hafner (1938). This fixed hub, three-armed "spider" blade control system allowed the pitch of the blades to be continuously variable and to have both cyclic and collective capability. The spider sat atop the rotor and was actuated by a control rod supported on a spherical bearing inside the hollow rotor shaft. This design was technically superior to the Cierva–Weir "binary" blade pitch change system. To perform a takeoff with Hafner's system, the pilot first over-sped the rotor with the blades in flat pitch while holding the machine firmly on the brakes (as with the Cierva jump takeoff system), and then rapidly applied pitch with a collective lever while simultaneously de-clutching the rotor, gunning the engine and applying forward cyclic. Hafner's "spider" control system allowed the pilot to make continuous pitch control adjustments, allowing precise "towering" takeoffs with no loss in altitude as rotor rpm decayed (Fig. 12.16). Combined with a somewhat more exacting landing capability that was now possible with the "spider" hub, this version of the autogiro had a takeoff and landing flight capability that was to match future helicopters. The autogiro still could not hover, despite being able to make nearly vertical takeoffs and landings. However, Hafner's spider blade pitch control system was soon to become the standard for early British-designed helicopters – see Hafner (1954, 1963).

The Americans too were also introducing the ideas of blade pitch control to autogiros to enhance its capabilities, with the Autogiro Company of America (its licensees were Pitcairn and Kellett) developing a jump takeoff system starting in 1933. Pitcairn had designed and patented many improvements into the Cierva rotor system [see Smith (1985)], and in 1931

Harold Pitcairn received the highly prized Collier Trophy for his technical contributions to aviation. See Pitcairn (1930) for a summary of activities, and Prewitt (1938) gives a technical discussion of the jump takeoff technique. The jump takeoff was also studied experimentally by Wheatley & Bioletti (1936) at NACA using model rotors and later by means of aerodynamic theory by Carpenter & Friedovich (1953). The mechanical systems used by the Americans were different to those of Cierva–Weir, but used the same principle of producing a jump takeoff by increasing rotor rpm followed by a sudden change in blade pitch. The American system was first tested on the PA-22 test bed and later on the enclosed cabin PA-36 with good success. Slowly, as the pilots gained experience, the jumps became higher and eventually Pitcairn pilots demonstrated an ability for the PA-36 to take off, translate into forward flight, and clear a 30-foot high obstacle without losing any altitude. Both Pitcairn and Kellett were later to compete for funding under the Dorsey-Logan Act of 1937 [see Smith (1985)] that specified a "rotary-wing military aircraft" capable of a vertical takeoff to clear a 50-foot obstacle. This goal was too unrealistic for the PA-36 to meet and it lost out on funding to LePage's XR-1 side-by-side rotor helicopter (page 32), a machine that itself proved ultimately to be unsuccessful. Pitcairn's PA-36 later made many successful jump takeoff demonstration flights to military and government officials, however, taking off and landing vertically and doing nearly everything a helicopter could do except hover. The jump takeoff worked, but it was never easy on the pilot or the aircraft.

12.15 Ground and Air Resonance

It has already been mentioned that, on the first autogiros, the in-plane Coriolis and drag forces on the blades were balanced by interconnected sets of wires between the blades. The blades were also restrained in flap by cables so that they could not "droop" when the rotor was stopped. Cierva found this interim solution rather unsatisfactory because the cables created high parasitic drag, reducing the overall performance of his Autogiros. Eventually, Cierva incorporated support stops instead of suspension cables and friction disks at the drag hinges to damp out any in-plane blade motion. He called these "cantilevered" blades, although the name is a misnomer because the blades were still articulated with mechanical hinges in the conventional sense.

While these ideas seemed to work fine on the lighter weight autogiros, a crop of new problems arose when they were applied to the bigger and heavier machines. These problems included lead–lag forces from Coriolis effects, high vibrations in the control system, large control forces, and a susceptibility to a destructive aeromechanical problem known as *ground resonance* – see Section 4.10 and Fig. 4.18. There were some limited technical efforts to understand the ground resonance problem on autogiros, but the "trial-and-error" approach meant that it was never satisfactorily resolved until much later when the same problems occurred on helicopters. In the 1930s, NACA made an attempt to study the ground resonance problem by mounting a camera high above the autogiro while the rotor was spun up on the ground. Another camera was mounted on the rotating hub to study the motion of a single blade. The NACA was to have a special interest in the phenomenon. Because of resonance on the mounting hardware, a specially instrumented autogiro that was being tested in the Langley full-scale wind tunnel was completely destroyed; see Gustafson (1971). In later years, helicopters were to suffer similar "resonance" problems, which were cured for the most part by the addition of mechanical dampers to the in-plane blade motion and changes to the undercarriage design. Coleman & Fiengold (1958) developed the first mathematical theory to predict and resolve the problem of ground resonance.

12.16 Helicopters Eclipse Autogiros

One practical limitation (and often the most popularized reason for the loss of interest in the autogiro) is that the autogiro cannot hover stationary in the air. Charnov (2003), however, explains that the reasons compounding its limitations may have been other than technical. While the efficient hovering flight capability of the helicopter is certainly a very desirable attribute, the autogiro still has the ability to take off vertically using the "jump" technique and can land almost vertically, especially into a wind. The autogiro is an efficient machine at low to moderate airspeeds and can outperform both the airplane and the helicopter under these conditions in terms of economics and also safety of flight. Unlike a helicopter, the autogiro has no "deadman's curve" (see Section 5.6.2) and so can operate much more safely at lower altitudes and airspeeds. However, several early flying mishaps with the autogiro in the hands of inexperienced pilots led initially to a poor perception of the machine. Flight control was drastically improved by the use of "orientable" rotors. While efficient at low speeds, autogiros did not have the higher speed capability of airplanes designed in same time period, mainly because of its high parasitic drag. While much was done on later models of autogiros to increase streamlining and reduce rotor profile drag, especially by eliminating blade bracing wires, they were never to match the higher speed capabilities of airplanes. Furthermore, autogiros were mostly single or dual-seater aircraft, at a time when airplanes in the same weight and engine class could carry several passengers (and for a significantly lower cost). As alluded to earlier, scaling up the machine led to ground resonance and other problems, and these were not completely understood at the time.

While the autogiro was well-engineered, the high cyclic stresses imposed on rotating components meant that mechanical failures of the rotor system were not uncommon. Yet, it would be unfair to overemphasize any mechanical shortcomings of the autogiro at a time when all types of aircraft structural analysis was in its infancy. Autogiro designers worked steadily to improve the mechanical reliability and efficiency of the rotor design and the later designs were extremely robust and reliable. These technical accomplishments were to serve well the future designers of helicopters. By the early 1930s, helicopter pioneers, who for the most part were working independently of those developing the autogiro, suddenly realized that the autogiro had served to help work out all the problems of achieving proper control with helicopters. Thereafter, progress with the helicopter accelerated rapidly and interest in the autogiro dwindled.

In December 1936, Juan de la Cierva was killed (at the age of only 41 years) in the crash of an airliner. This was a serious blow to the further development of the Autogiro. Shortly thereafter, the British government attempted to centralize rotating-wing research and engineering by trying to get the Cierva and Hafner companies to merge, but this initiative was unsuccessful. Raoul Hafner saw the autogiro only as an interim step toward the development of the helicopter; Juan de la Cierva did not and saw the autogiro as the preferred approach to rotor-borne flight. Nevertheless, both Cierva and Hafner saw the important future role of rotating-wing aircraft in both military and civil aviation. At the end of a lecture to the RAeS, Hafner (1938) stated: "We cannot afford to disregard the clear indications towards progress offered by the rotative wing. We can see the limitations with fixed wings – we must be aware of the limitation of fixed ideas; and if are to avoid flying and thinking in circles we must make the *wing* rotate."

There were several other factors contributing to the loss of interest in the autogiro in the 1940s – see Charnov (2003). In the United States, military interest in the helicopter increased initially, and in 1938 the Congress passed the Dorsey Bill [see Smith (1985)],

which in part made possible the Rotating-Wing Aircraft Conference at The Franklin Institute in Philadelphia [see Institute of the Aeronautical Sciences (1938)]. This brought together most of the forward-thinking pioneers and technical specialists in the rotating-wing field, such as Hafner, Pitcairn, Kellett, and Sikorsky. Igor Sikorsky was already working toward the first flight of his VS-300 and in his paper [Sikorsky (1939)] at the subsequent Rotating-Wing Aircraft Conference in 1939, he was to extol the future potential of the helicopter. The imminent success of Sikorsky and his VS-300, funding from the Dorsey Bill and the technological advances made possible during wartime, eventually led to the successful development of a military helicopter in the United States.

12.17 Renaissance of the Autogiro?

In the 1950s, there was some revival of interest in the gyroplane and convertiplane or gyrodyne concepts, with a series of prototypes being designed by the Fairey Company in Britain and McDonnell in the United States. These machines were designed to help overcome the inherent forward flight speed limitations of a conventional helicopter by off-loading the rotor with a conventional fixed-wing, and so reducing rotor thrust and the high inherent drag of the rotor in forward flight. Gyroplanes can takeoff vertically and hover with the rotor powered, for instance, by tip jets, but the rotor is then off-loaded (for the most part) by a conventional wing in forward flight. When the shaft torque is removed from the rotor, it can be made to enter into the autorotative state by suitably tilting the rotor back to reach a positive angle of attack during conversion into forward flight. With the assistance of tip-jet pioneer Friedrich von Doblhoff, McDonnell developed the XV-1 [see Hickey (1956) and Harris (2003)] but its performance was disappointing. Two Fairey Gyrodyne prototypes led to the Rotodyne, which was the world's biggest gyroplane with a cabin big enough for 40 passengers – see Fig. 12.17. The program has been discussed by Hislop (1958) and

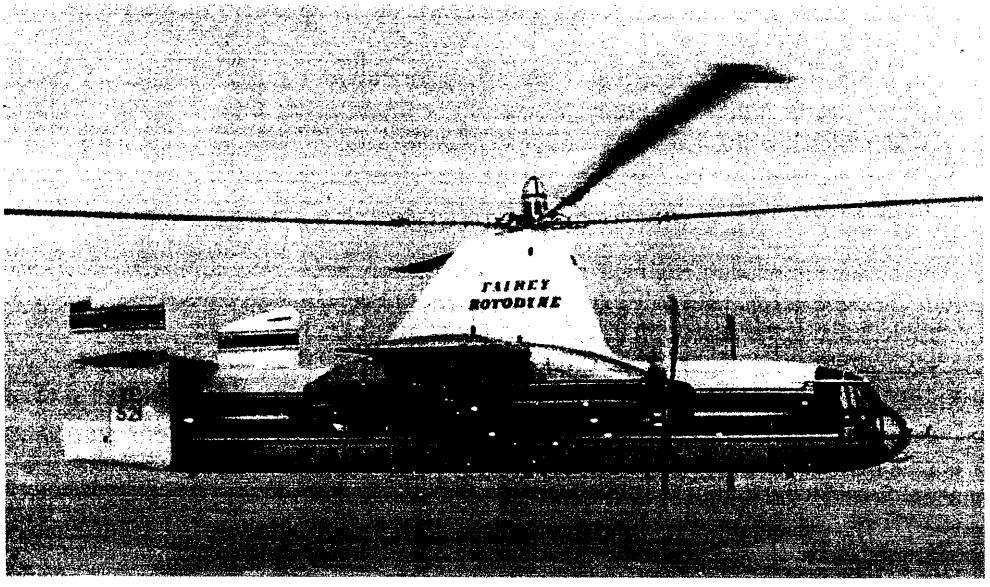

Figure 12.17 The Fairey Rotodyne was the world's biggest gyroplane but it did not go into production. Source: Photo courtesy of Agusta–Westland.

McKenzie (1959). For takeoff and landing the rotor was driven by tip jets. The aircraft was a technical success and set a world speed record for a convertiplane in 1959 before the project was cancelled – see Boulet (1984) for a detailed discussion.

During the late 1950s and early 1960s, small commercial autogiros were developed in North America for the private aviation market by three companies: Umbaugh (later known as Air & Space), Avian, and McCulloch. While Umbaugh and McCulloch delivered over 100 machines, these had limited performance and the lack of sustained orders put the companies out of business. Single and two-seat autogiros were also built in Britain – see Wallis (1963). In the 1950s, Igor Bensen developed a homebuilt autogiro with an open airframe, based to some extent on the simplicity of the German Fa-330 "Kite" and Hafner "Rotachute." A thriving amateur homebuilt autogiro market is still active today, many of these designs stemming from the Bensen designs. As of 2005, there were at least a dozen manufacturers in business catering to the homebuilt market – see the Popular Rotorcraft Association's web site (2005), http://www.pra.org.

From a scientific perspective, there have been few recent studies of autogiros. However, work by Houston and colleagues (1998a, 1998b, 2000, 2001) has begun to reexamine the stability, control, and handling qualities of autogiros, mainly from a flight safety and certification standpoint. Advanced mathematical models of the autogiro were developed and validated by flight test measurements conducted on a specially instrumented two-seater autogiro. This work represents the first significant scientific interest in autogiros in over five decades and perhaps points the way forward toward improved future autogiro and gyroplane designs. While the autogiro led the development of the helicopter and there are clearly many similarities between the autogiro and the helicopter, it is perhaps ironic that fifty years hence the confidence levels in the design of a new autogiro are lower than for a new helicopter.

Recently, two companies in the United States have resurrected the idea of the autogiro or gyroplane and have begun to exploit its capabilities using modern technologies. These companies are Carter Aviation Technologies and Groen Bothers Aviation (GBA), Inc. The Carter test platform incorporates both a rotor and a large, relatively high aspect ratio fixed-wing. It is a hybrid aircraft using some of the underlying principles of the compound or convertiplane machines of the 1950s. While the rotor provides nearly all of the lift during takeoff and landing, the wing produces most of the lift at higher airspeeds, with the rotor almost completely offloaded and operating in its autorotational state. The high inertia rotor has a bearingless hub, with a tilting spindle to control the orientation of the rotor disk (much like in the original Cierva designs) and collective pitch to control rotor rpm. The machine is made almost entirely of composite materials and is powered by a lightweight propeller driven by a reciprocating engine. Conventional flight control surfaces (ailerons, elevator, and rudder) are used, again much as on the original Cierva Autogiro designs.

Groen Bothers Aviation (GBA) have developed a turboshaft powered gyroplane called the Hawk 4 (Fig. 12.18). The GBA machine provides all of the short takeoff and nearly vertical landing capabilities of the helicopter, with a demonstrated level flight speed of 148 mph (238 kph). Among other innovations, the two-bladed articulated rotor incorporates a cone–pitch coupling for improved rotor rpm stability. It uses a swashplate with collective and cyclic pitch, which gives the aircraft good maneuverability and also allows for short takeoffs. The all-metal blades use advanced airfoil sections that are designed specifically to meet the unique aerodynamic requirements of sustained autorotational flight. Unlike the Carter machine, there are no conventional flight control surfaces for roll or pitch, this all being achieved through rotor control, with rudder for directional (yaw) control.

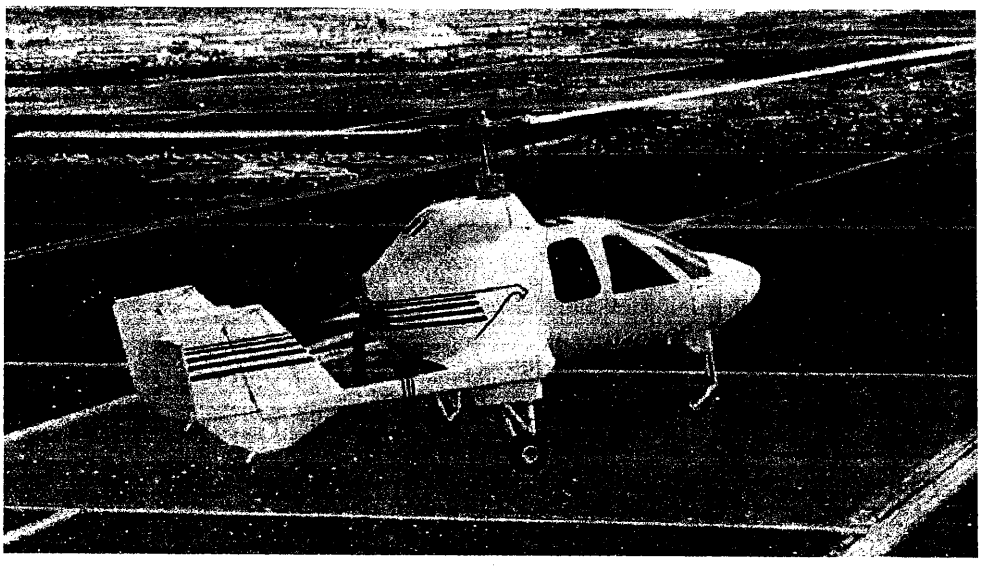

Figure 12.18 Groen Bothers Aviation Hawk 4 is a modern turboshaft-powered gyroplane. Source: Photo courtesy of GBA.

12.18 Chapter Review

This chapter has summarized the unique technical characteristics of the autogiro or gyroplane. A truly innovative form of rotorcraft, in 1923 it was the first powered, heavier-than-air aircraft other than a conventional airplane to fly successfully. It was also the very first type of successful rotating-wing aircraft and was really the genesis of the helicopter. While the early autogiros certainly had many shortcomings and encountered many technical hurdles, the developers adopted a systematic, step-by-step approach and made many engineering contributions to rotorcraft technology on both practical and theoretical fronts. The most significant was clearly the development of the articulated rotor hub, with the incorporation of flap and lead–lag hinges and later the complete control of the aircraft by tilting the rotor plane by using cyclic blade pitch. The autogiro era also produced the first theories of rotor aerodynamics, rotating blade dynamics, structural dynamics, and aeroelasticity and provided the foundation for many of the rotating-wing analyses that are used today.

While the autogiro has not yet become a commercial success, today its principles are being combined with current technology and innovative forward thinking to create ambitious new autogiro designs. If the innovations of the autogiro can be combined successfully with the capabilities of the helicopter and also the speed and range attributes of a fixed-wing aircraft, then modern gyroplanes could be used to meet a wide variety of military missions and civil applications. Clearly, significant gains in the performance of the autogiro are possible using optimized airfoil sections, blade shapes and planforms, composite structures, advanced flight controls, and efficient new engines. However, to achieve the flight speeds necessary to operate effectively in military applications or as a short-range transport will require load sharing with a conventional fixed wing. Only time will tell, but a renaissance of interest in the unique capabilities of the autogiro and gyroplane can only but benefit from both the technical knowledge and the powerful mathematical design tools that have evolved over the last fifty years of helicopter development.

12.19 Questions

12.1. The development of the autogiro clearly formed the basis for the design of the modern helicopter. Yet, the autogiro has been much less of a commercial success than the helicopter. Discuss the relative merits of the helicopter versus the autogiro from the standpoint of maximum speed capability, cruise efficiency, capital costs, and maintenance costs.

12.2. Explain the fundamental principle of autorotation. Also explain by means of blade element considerations why a rotor will autorotate at many different combinations of blade pitch, rotor rpm, and disk angle of attack.

12.3. Using the rotor performance theory described in this chapter, calculate the power required for flight for an autogiro and compare your results to an equivalent helicopter of the same gross weight. Make any realistic assumptions that you find necessary, but be sure to justify them.

12.4. Using rotor performance theory, calculate the power required for autorotative flight as a function of rotor rpm. Calculate also the mean lift coefficient on the rotor. Explain why there must always be a lower limit to the autorotational rotor rpm.

12.5. Discuss the factors that limit the low speed flight characteristics of an autogiro. Is there any truth in the claim that the autogiro is essentially a "stall-proof" aircraft?

12.6. Discuss the factors that limit the maximum forward speed capabilities of an autogiro. Do you think that the autogiro could be designed to have a cruise speed that is substantially faster than a helicopter?

12.7. A helicopter uses the rotor for both lifting and propulsion, whereas the autogiro uses a propeller for propulsion. In terms of propulsive efficiency alone, is the helicopter or the autogiro a more efficient flight vehicle, and why?

12.8. Consider some of the design issues associated with a large gyroplane concept in the vein of the Fairey Rotodyne. If the machine must hover, discuss the engineering and performance trades that would be associated with a tip jet driven rotor versus a conventional shaft driven rotor.

Bibliography

Azuma, A. and Yasuda, K. 1989. "Flight Performance of Rotary Seeds," *J. of Experimental Biology*, 138, pp. 23–54.

Bailey, F. J. 1941. "A Simplified Theoretical Method of Determining the Characteristics of a Lifting Rotor in Forward Flight," NACA Report 716.

Bailey, F. J. and Gustafson, F. B. 1939. "Observations In Flight of the Region of Stalled Flow over the Blades of an Autogiro Rotor," NACA TN-741.

Beavan, J. A. and Lock, C. N. H. 1939. "The Effect of Blade Twist on the Characteristics of the C-30 Autogyro," ARC R & M 1727.

Bennett, J. A. J. 1933. "The Flight of an Autogiro at High Speed," NACA TM 729.

Bennett, J. A. J. 1961. "The Era of Autogiro," The First Cierva Memorial Lecture, *J. of the Royal Aeronautical Soc.*, 65 (610), Oct., pp. 649–660.

Boulet, J. 1984. *The History of the Helicopter as Told by its Pioneers 1907–1956*, Editions France-Empire, Paris, p. 225.

Carpenter, P. J. and Friedovich, B. 1953. "Effect of A Rapid Blade-Pitch Increase on the Thrust and Induced-Velocity Response of a Full-Scale Helicopter Rotor," NACA TN 3044.

Charnov, B. 2003. "From Autogiro to Gyroplane–The Amazing Survival of an Aviation Technology," Praeger Press, Westport, CT.

Cierva, J. de la 1926. "The Development of the Autogiro," *J. of the Royal Aeronautical Soc.*, 30 (181), pp. 8–29.

Cierva, J. de la 1927. "A letter to RAeS with comments on the paper presented by H. Glauert on 20 January 1927," *J. of the Royal Aeronautical Soc.*, 31 (198), pp. 505–506.

Cierva, J. de la 1930a. "The Autogiro," *J. of the Royal Aeronautical Soc.*, 34 (239), pp. 902–921.

Cierva, J. de la 1930b. "The Theory of the Autogiro," *Aeronautical Engineering*, Transactions of the American Soc. of Mechanical Engineers, 2 (1), Jan.-March, pp. 13–14.

Cierva, J. de la 1930c. *Engineering Theory of the Autogiro*, Published by the Autogiro Company of America.

Cierva, J. de la and Rose, D. 1931. *Wings of Tomorrow: The Story of the Autogiro*, Brewer, Warren & Putnam, New York, NY.

Cierva, J. de la 1935. "New Developments of the Autogiro," *J. of the Royal Aeronautical Soc.*, 39, pp. 1125–1143.

Cierva, C. A. 1998. *Juan de la Cierva–A Universal Spaniard*, Published by Construcciones Aeronáticas, S. A. (CASA).

Coleman, R. P. and Feingold, A. M. 1958. "Theory of Self-Excited Mechanical Oscillations of Helicopter Rotors With Hinged Blades," NACA Report 1351.

Everett-Heath, J. 1986. *British Military Helicopters*, Arms and Armour Press, London.

Everett-Heath, J. 1988. *Soviet Helicopters–Design, Development and Tactics*, Jane's Information Group, London.

Gablehouse, C. 1967. *Helicopters and Autogiros: A Chronicle of Rotating Wing Aircraft*, Lippincott, Philadelphia & New York, NY.

Gessow, A. 1948. "Bibliography of NACA Papers on Rotating-Wing Aircraft," NACA RM L7J30.

Gessow, A. and Myers, G. C., Jr. 1952. *Aerodynamics of the Helicopter*, Macmillan Co. Republished by Frederick Ungar Publishing, New York, NY.

Glauert, H. 1926. "A General Theory of the Autogiro," ARC R & M 1111.

Glauert, H. 1927. "A General Theory of the Autogiro," *J. of the Royal Aeronautical Soc.*, 31 (198), pp. 483–508.

Glauert, H. 1928. "On the Horizontal Flight of a Helicopter," ARC R & M 1157.

Glauert, H. 1935. "Airplane Propellers," In: Division L of *Aerodynamic Theory*, edited by W. F. Durand, Springer Verlag, Berlin, Germany. Reprinted by Peter Smith, Glouster, MA, 1976.

Gustafson, F. B. 1971. "A History of NACA/NASA Rotating-Wing Aircraft Research, 1915–1970," Limited-Edition Reprint (VF-70) from *Vertiflite*, American Helicopter Soc., Alexandria, VA.

Hafner, R. 1938. "The Hafner Gyroplane," *J. of the Royal Aeronautical Soc.*, 42, pp. 109–158.

Hafner, R. 1954. "The Domain of the Helicopter," *J. of the Royal Aeronautical Soc.*, 58 (536), pp. 663–702.

Hafner, R. 1963. "The Domain of the Convertible Rotor," AIAA Paper 63-483, AIAA/RAeS Anglo-American Conference, Cambridge, MA, Oct. 16–18.

Harris, F. D. 1992. "Early Rotorcraft–The Roots of our Technology," F. D. Harris & Associates, Fountain Hills, AZ.

Harris, F. D. 2003. "An Overview of Autogyros and the McDonnell XV-1 Convertiplane," NASA/CR-2003-212799, Oct.

Hislop, G. S. 1958. "The Fairey Rotodyne," Meetings of The Helicopter Association of Great Britain and The Royal Aeronautical Soc., London, England, 7 November.

Hickey, D. H. 1956. "Full-Scale Wind-Tunnel Tests of the Longitudinal Stability and Control Characteristics of the XV-1 Convertiplane in the Autorotating Flight Range," NACA RM A55K21a, May.

Hoerner, S. F. 1965. *Fluid Dynamic Drag*, Published by the Author, Hoerner Fluid Dynamics, Vancouver, WA.

Houston, S. S. 1998a. "Identification of Gyroplane Lateral/Directional Stability and Control Characteristics from Flight Test," *Institute of Mechanical Engineers*, Part G, Vol. 212, No. G4, 1998, pp. 271–285.

Houston, S. S. 1998b. "Identification of Autogyro Longitudinal Stability and Control Characteristics," *AIAA J. of Guidance, Control and Dynamics*," 21 (3), pp. 391–399.

Houston, S. S. 2000 "Validation of a Rotorcraft Mathematical Model for Autogiro Simulation," *J. of Aircraft*, 37 (3), pp. 203–209.

Houston, S. S., Thomson, D. G., and Spathopoulos, V. M. 2001. "Experiments in Autogyro Airworthiness for Improved Handling Qualities," 57th Annual Forum of the American Helicopter Soc., Washington, DC, May 9–11.

Hufton, P. A., Woodward-Nutt, A. E., Bigg, F. J., and Beavan, J. A. 1939. "General Investigation in the Characteristics of the C-30 Autogiro," ARC R & M 1859.

Institute of the Aeronautical Sciences. 1938. *Rotating-Wing Aircraft Meeting at The Franklin Institute*, Philadelphia, PA, Oct. 28–29. Sponsored by the Philadelphia Section.

Larsen, A. E. 1956. "American Autogiro, Gyroplane and Early Convertaplane Developments," *J. of the American Helicopter Soc.*, 1 (1), pp. 6–15.

Liberatore, E. K. 1998. *Helicopters Before Helicopters*, Krieger Publishing, Malabar, FL.

Lock, C. N. H. 1928. "Further Development of Autogiro Theory, Parts I & II," ARC R & M 1127.

Lock, C. N. H. and Townend, H. 1928. "Wind Tunnel Experiments on a Model Autogiro at Small Angles of Incidence," ARC R & M 1154.

Lock, C. N. H., Bateman, H., and Townend, H. C. H. 1926. "An Extension of the Vortex Theory of Airscrews with Applications to Airscrews of Small Pitch, Including Experimental Results," ARC R & M 1014.

McKenzie, K. T. 1959. "Aerodynamic Aspects of the Fairey Rotodyne," *J. of the Helicopter Association of Great Britain*," 13 (6), Dec. pp. 368–387.

Moreno-Caracciolo, M. 1923. "The Autogiro," *Ingeniera y Construccion*, March, pp. 98–102. See also NACA TM 218.

Munk, M. M. 1925. "Model Tests on the Economy and Effectiveness of Helicopter Propellers," NACA TN 221.

Peck, W. C. 1934. "Landing Characteristics of an Autogiro," NACA Technical Note No. 508.

Pitcairn, H. F. 1930. *The Autogiro: Its Characteristics and Accomplishments*, Annual Report of the Board of Regents of the Smithsonian Institution, pp. 265–272. Based on a lecture given to The Franklin Institute of Philadelphia, 20 November 1929.

Prewitt, R. H. 1938. "Possibilities of the Jump-Off Autogiro," *J. of the Aeronautical Sciences*, 6 (1), pp. 10–14.

Popular Rotorcraft Association website. 2005. http://www.pra.org.

Rosen, G. 1984. *Thrusting Forward–A History of the Propeller*, Hamilton Standard, East Hartford, CT, p. 25.

Sikorsky, I. I. 1939. "Commercial and Military Uses of Rotating Wing Aircraft," *Second Annual Rotating-Wing Aircraft Meeting at the Franklin Institute*, Philadelphia, PA, Nov. 30–Dec. 1.

Smith, F. K. 1985. *Legacy of Wings: The Story of Harold Pitcairn*, Jason Aronson, New York, NY.

Tokaty, G. A. 1971. *A History and Philosophy of Fluid Mechanics*, Foulis & Co., Henley-on-Thames, England.

von Kármán. 1931. "Die Seitenwege der Luftfahart," *Zeitschrift fur Flugtechnik und Motorluftschiffahrt (ZFM)* Vol. 22 (16), Aug. pp. 481–488.

Wallis, K. H. 1963. "The Low-Cost Autogiro," *J. of the Royal Aeronautical Soc.*, 67 (626), pp. 111–118.

Wheatley, J. B. 1933a. "Lift and Drag Characteristics and Gliding Performance of an Autogiro as Determined In Flight," NACA Report No. 434.

Wheatley, J. B. 1933b. "Wing Pressure Distribution and Rotor Blade Motion of an Autogiro as Determined In Flight," NACA Report No. 475.

Wheatley, J. B. 1934. "The Aerodynamic Analysis of the Gyroplane Rotating-Wing System," NACA Technical Note No. 492.

Wheatley, J. B. 1935. "An Aerodynamic Analysis of the Autogiro Rotor With a Comparison Between Calculated and Experimental Results," NACA Report 487.

Wheatley, J. B. and Bioletti, C. 1936. "Analysis and Model Tests of an Autogiro Take-Off," NACA TN-582.

Wheatley, J. B. 1937a. "An Analytical and Experimental Study of the Effect of Periodic Blade Twist on the Thrust, Torque and Flapping Motion of an Autogiro Rotor," NACA Report 591.

Wheatley, J. B. 1937b. "An Analysis of the Factors That Determine the Periodic Twist of an Autogiro Rotor Blade, With a Comparison of Predicted and Measured Results," NACA Report 600.

Wheatley, J. B. and Bioletti, C. 1935. "Wind Tunnel Tests of a 10-Foot Diameter Gyroplane Rotor," NACA Report No. 536.

Wheatley, J. B. and Hood, M. J. 1934. "Full-Scale Wind Tunnel Tests of a PCA-2 Autogiro Rotor," NACA Report No. 515.

Wimperis, H. E. 1926. "The Rotating Wing in Aircraft," ARC R & M 1108.

CHAPTER 13

Aerodynamics of Wind Turbines

It is some sort of tragedy that many get caught up in the idea of generating power from the wind and attempt to build machines before they have mastered the disciplines required.

D. M. Eggleston & F. S. Stoddard (1987)

13.1 Introduction

This chapter reviews some basic concepts associated with wind turbines and describes their general operation and performance, focusing primarily on the aerodynamic issues. The overlap of fundamental problem areas between the helicopter rotor and the wind turbine is considerable. Clearly, the extraction of power from the wind using a turbine depends on its efficient performance and aerodynamic design, and in many ways the underlying principles of efficient design parallel those for helicopter rotors. In this respect, specialist engineers in both helicopters and wind energy can benefit from an appreciation of the particular technical issues found on both types of machines. This chapter, however, is not meant to be an all-encompassing treatise on wind energy or the aerodynamic principles of wind turbines. For this, the reader is referred to specialist books such as Walker & Jenkins (1997), Spera (1994), Burton et al. (2001), and Manwell et al. (2002).

While complicated in detail, the basic principle of a wind turbine is fairly simple. The wind blows through the turbine and turns the blades, converting the kinetic energy of the wind into rotational energy of the turbine. This rotational energy can be harnessed to produce useful work, usually in the form of electric power from a generator connected to the turbine shaft. The classic aerodynamic analysis of a rotor operating as a wind turbine was developed by Lock et al. (1925) [see review by Glauert (1935, 1983)]. Problems of the wind turbine that are common to the helicopter include understanding and predicting the unsteady blade airloads and turbine performance in both attached and stalled flows, as well as predicting the resulting structural loads and aeroelastic response of the rotating blades. However, there are unique differences as well. Wind turbines are subjected to complicated environmental effects that are not found on helicopter rotors. This includes ground boundary layer effects, atmospheric turbulence and large turbulent eddies, temporal and spatial variations in wind shear, thermal convection or stratifications, the possible effects of an upstream unsteady wake from a support structure (tower shadow) or even the effects of another wind turbine if situated in groups. The net effect is that wind turbines operate in an adverse, 3-D, unsteady (aperiodic) aerodynamic environment that is both hard to define using measurements and also to predict using mathematical models. This has led to difficulties in designing wind turbines that can operate reliably and economically over long periods of time.

The aerodynamic analysis of a wind turbine can be approached using classical momentum theory, the principles of which have been previously introduced in Chapters 2 and 3 for the helicopter. Although the helicopter rotor thrust can be defined uniquely a priori and the

momentum theory then used directly to determine the induced velocity, it will be shown that the classical momentum theory allows only the maximum (ideal) performance limits to be defined for wind turbines. This is rectified to a large extent by the use of blade element momentum theories and blade element methods coupled with inflow models. These types of models have formed the mainstay of the predictive methods used by the wind energy community. The blade element momentum theory allows us to examine the effects of the primary design variables (blade twist, blade planform, number of blades, etc.) as a function of wind speed and blade pitch on energy extraction. However, there are several important nonideal and nonlinear aerodynamic effects to consider that have important effects on wind turbine performance, including the effects of airfoil section. The blade loads and the performance of a wind turbine is directly determined by aerodynamic forces generated on the airfoils. Therefore, a better understanding of the underlying flow physics on the blades is essential if accurate modeling of the turbine aerodynamics and acceptable predictions of the loads and power output are to be made. In this regard, airfoil design philosophy used for wind turbines can be quite different to that used to design helicopter rotors.

The second part of this chapter focuses on more advanced topics associated with wind turbines, including vortex wake theories and unsteady aerodynamic effects. While these topics are also common to helicopter rotors (see Chapter 8, 9, and 10), there are unique aspects of the aerodynamic problems associated with wind turbines that require special attention. These include the presence of unsteady variations in wind speed, yawed flow operation and tower wake or "shadow" effects. While all of these problems have been addressed by wind energy analysts to a lesser or greater extent, it seems that many of the resulting models are rooted deeply in empiricism and often do not offer today's analysts the flexibility needed to embark confidently on new and improved wind turbine designs. This problem can be rectified only by further research at a fundamental level using both experimental and analytical approaches and also by careful and systematic validation against measurements of the mathematical models used to predict wind turbine loads and performance. In this regard, additional high-quality measurements in both the wind tunnel and in the field are sorely required.

13.2 History of Wind Turbine Development

The power of the wind has been used by humankind for millennia (e.g., sailing ships). Wind turbines are more recent machines, but the basic concept dates back many centuries with primitive forms being used in Babylonian times – see Shepherd (1990). More advanced wind turbines were used by the Persians in the seventh century and had become more widespread in Europe by the fifteenth century. The most common machine was the tower mill, which was used for grinding and milling grain. These windmill machines underwent systematic improvements by trial and error and, by the seventeenth century, had evolved into a surprisingly high level of sophistication, to the point of using twisted blades with tapered planforms and control devices to point the windmill into the wind automatically. This suggests a good empirical knowledge of aerodynamics that was well in advance of the contemporary scientific understanding. Dutch settlers brought the windmill to the Americas in the eighteenth century. Another common windmill variant, the American fan mill, saw widespread use throughout the nineteenth and twentieth century for pumping water on ranches. By the beginning of the twentieth century, wind turbines were being used commercially to generate electrical power, although on a relatively small scale. The last century has seen considerable development in wind turbine technology, especially in Europe where energy costs are relatively high compared to the United States. The oil crisis during

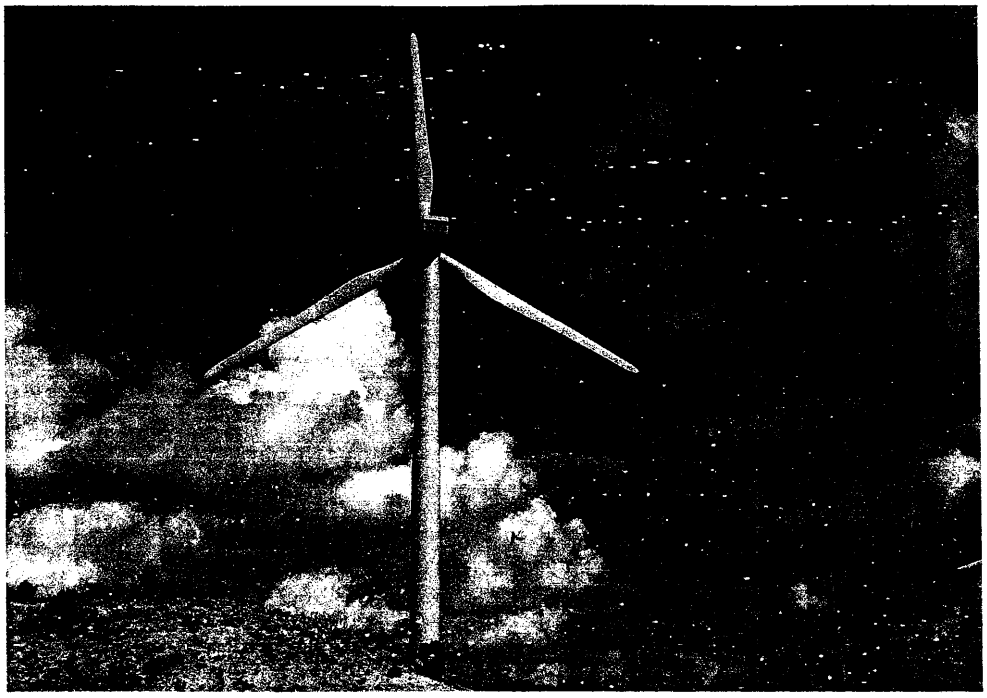

Figure 13.1 A modern three-bladed wind turbine. Source: Photo courtesy of Sandia National Laboratories.

the 1970s saw some new efforts to develop renewable energy resources in the United States, including wind energy. Today wind turbines are playing an increasing role in the generation of electrical power worldwide; concerns about global warming and the storage of waste from nuclear power plants have placed an increased emphasis on wind energy. As of 2005, the estimated global capacity for the creation of electrical power from wind energy was in excess of 25 GW, representing about 2% of total energy demands; see Thresher (2002).

An example of a modern horizontal axis wind turbine (HAWT) is shown in Fig. 13.1. Wind turbines are distinguished according to the orientation of the rotor shaft axis; in this case the shaft is parallel to the ground. This is the most common type of wind turbine and is also often referred to as a "lift machine" (as opposed to a "drag machine") because the power output comes from the generation of lift forces on the rotating blades. The HAWT sits on a tall tower, which may be either upstream or downstream of the turbine. In the downwind type the turbine axis naturally tries to align itself parallel to the wind, but these turbines do not always track the wind accurately. The tower also produces a wake (a tower "shadow") in this configuration and this affects the aerodynamic AoA and airloads on the turbine blades, making them unsteady. The vertical axis wind turbine (VAWT) or Darrieus turbine [Darrieus (1931)] has seen less extensive use, although this machine has the advantage that it will generate power with the wind from any direction and a means of controlling yaw is not required. Another type of VAWT is the Savonius turbine [see Savonius (1931)], which is a drag machine. However, VAWTs tend to be less efficient compared to HAWTs but, more importantly, they are not easily scaled up to the large size required for commercial power production because of structural design difficulties and aeroelastic problems.

A modern commercial wind turbine (see Fig. 13.1) may range from as little as 5 m (16.4 ft) in diameter up to over 100 m (328 ft) in diameter. Small turbines produce power in

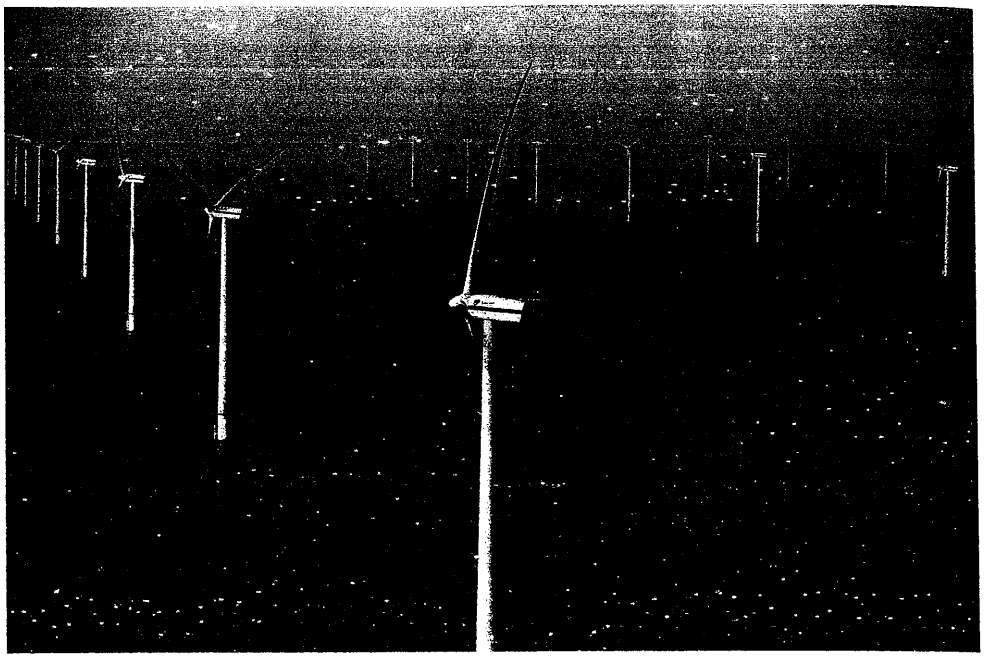

Figure 13.2 Large wind turbines on a wind farm off the coast of Norway. Notice the large amount of bending on the blades, suggesting that they are operating at high thrust and generating maximum power. Source: Photo courtesy of Sandia National Laboratories.

the range from a few kilowatts, with the larger ones being in the megawatts capacity. Modern utility-scale wind turbines all have diameters greater than 50 m (164 ft). Many wind turbines are often seen together in a group known as a wind farm (see Fig. 13.2). Even in farms, however, the net cost of energy generated by wind turbines has historically been greater than that for power produced from fossil or nuclear fuels. Their unique aerodynamic and mechanical problems and overall difficulties in predicting the performance and structural loads on wind turbines has led to high capital investment, as well as to high operating and maintenance costs. Until recently, this has made it difficult for wind energy devices to compete with other forms of renewable and nonrenewable energy sources – see Hansen (1993). Today the costs of fossil fuels are increasing and wind energy costs are decreasing. The ever-increasing global emphasis on environmental issues also favors the use of wind turbines compared to more traditional forms of power generation.

13.3 Power in the Wind

The purpose of a wind turbine is to capture the energy of the wind and convert it into useful energy, usually in the form of electrical energy. Consider the kinetic energy of a wind of velocity V_∞ as it passes through a disk of area A in the atmosphere. If the disk is normal to the wind vector, then the mass flow rate through the disk will be $\dot{m} = \rho A V_\infty$ and so the kinetic energy per unit time contained in the wind that flows through this disk is

$$\frac{KE}{dt} = \frac{1}{2}\dot{m}|V_\infty|^2 = \frac{1}{2}\rho A|V_\infty|^3 = P. \tag{13.1}$$

This is equivalent to the power that could be extracted from the wind assuming the energy conversion process was 100% efficient. A modern turbine may extract only half of this potential energy because of aerodynamic and mechanical losses (see Section 13.4). Notice from Eq. 13.1 that the potential power output from the turbine is proportional to the square of its size (diameter) and cube of the wind speed.

For example, consider a wind turbine of 5 m (16.4 ft) in diameter with a net efficiency of 50% that operates with its disk properly pointed perpendicular to a wind of speed of 10 m/s (32.8 ft/s) at standard sea level conditions. The potential power output will be

$$P = (0.5)\times\frac{1}{2}\rho A|V_\infty|^3 = 0.25\times 1.225\times(\pi 2.5^2)\times(10)^3 \approx 6 \text{ kW or } 8 \text{ hp.} \quad (13.2)$$

This example shows why wind turbines have to be very large in size (diameter) and have to be located where the wind blows on average at relatively high speeds. Wind turbines are often situated in groups or farms with many tens or hundreds of turbines to produce a sufficiently useful and economically attractive net power output.

Notice that if the turbine is not pointed into the wind then it will be apparent that the velocity normal to the disk will be reduced by a factor $V_\infty \cos\gamma$, where γ is the yaw angle. In such a case, according to Eq. 13.2 the power output drops by $\cos^3\gamma$ and so the importance of accurately controlling the orientation of the turbine relative to the wind direction becomes immediately clear. This must be done by design or by some sort of mechanical control device that senses wind direction and automatically points the turbine accurately into the wind.

13.4 Momentum Theory Analysis for a Wind Turbine

The aerodynamic modeling of wind turbines has spanned the entire range of methods used for helicopter rotors, from engineering models based on blade element-momentum theories, through traditional blade element models combined with inflow or vortex wake theories, to computational fluid dynamics (CFD) methods that solve numerically the Euler or Navier–Stokes equations from first principles. The most fundamental level of analysis of the wind turbine is by means of the classical momentum theory, first developed by Betz & Lock [see Glauert (1935, 1983)]. This one-dimensional approach is very similar to the descending helicopter problem examined in Section 2.13.2. In this case, however, the thrust from the wind turbine is not known a priori and will be a function of the wind speed, rotor speed (rpm), and blade pitch. This means that the problem cannot be solved uniquely using momentum theory by itself and, at a minimum, the blade element theory combined with the circulation theory of lift must be used. The momentum analysis of a wind turbine allows for a first level analysis of the power produced for a given wind speed, however, and can be used to determine the conditions under which the maximum energy conversion from the wind can be obtained.

A 1-D model of the control volume surrounding a wind turbine is shown in Fig. 13.3. The wind speed is V_∞, with the induced velocity in the plane of the turbine being v_i. Notice that, to avoid any ambiguity, it is assumed that the velocity is measured as positive when in a downstream direction. At the plane of the turbine, the net velocity is $V_\infty - v_i$. In the far wake (well downstream of the turbine) the velocity is $V_\infty - w$. Notice also that because a wind turbine extracts energy from the flow, the velocity decreases downstream of the turbine. From continuity considerations the slipstream boundary (wake) must, therefore, expand. By the application of the principle of the conservation of mass, the fluid mass flow

rate, $\dot{m}$, through the turbine disk is

$$\dot{m} = \rho A(V_\infty - v_i). \tag{13.3}$$

The change in the momentum of the flow across the disk can be related to the thrust by

$$T = \dot{m}V_\infty - \dot{m}\,(V_\infty - w)\,. \tag{13.4}$$

Expanding out this equation gives a relationship for the thrust on the turbine in terms of the velocity deficit in the turbine wake, that is,

$$T = \dot{m}V_\infty - \dot{m}V_\infty + \dot{m}w = \dot{m}w. \tag{13.5}$$

The power output from the turbine can be obtained by conducting an energy balance for the system. Basically the work done on the flow to change its kinetic energy must be extracted by the turbine, assuming no viscous or other "nonideal" losses at this stage. The work done on the air by the turbine per unit time, $\dot{W}$, is given by

$$\dot{W} = \frac{1}{2}\dot{m}\,(V_\infty - w)^2 - \frac{1}{2}\dot{m}V_\infty^2 = \frac{1}{2}\dot{m}w\,(w - 2V_\infty) = -\frac{1}{2}\dot{m}w\,(2V_\infty - w)\,. \tag{13.6}$$

Notice that the turbine does negative work on the air (i.e., it decreases its kinetic energy). Therefore, the turbine extracts power from the airstream and this operating condition is known as the *windmill state*, for obvious reasons. More usually this state is referred to as the *windmill brake state* because the turbine in this condition decreases or "brakes" the wind velocity. This means that the power output from the turbine is positive and so

$$P = T\,(V_\infty - v_i) = \frac{1}{2}\dot{m}w\,(2V_\infty - w)\,. \tag{13.7}$$

Substituting Eq. 13.5 into Eq. 13.7 gives

$$T\,(V_\infty - v_i) = \frac{1}{2}\dot{m}w\,(2V_\infty - w) = \dot{m}w\,(V_\infty - v_i)\,, \tag{13.8}$$

from which it is apparent that $w = 2v_i$ or $v_i = w/2$. This is the same relationship found for the helicopter in axial flight, as discussed in Section 2.13.2, and so in this case from

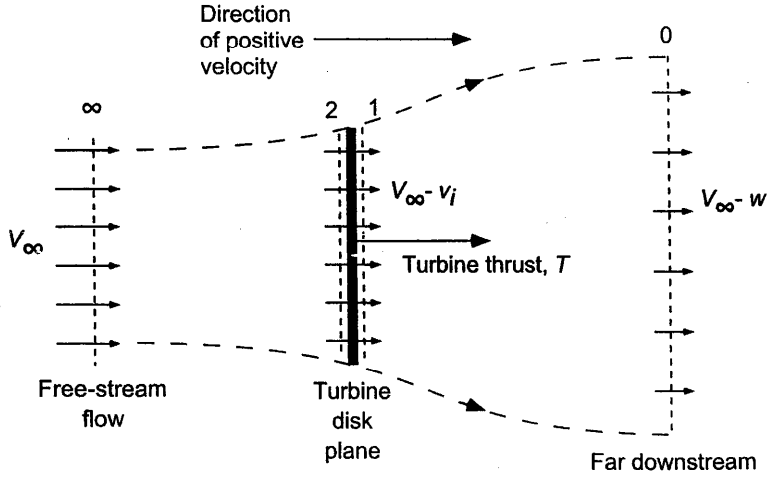

Figure 13.3 Flow model used for the momentum theory analysis of a wind turbine.

continuity considerations the wake expands downstream of the turbine. It is also apparent that, for the assumed flow model in Fig. 13.3 to be valid, then $V_\infty - w > 0$ or alternatively that $V_\infty \geq |w| \geq 2|v_i|$. If this is not satisfied then there is the possibility of two flow directions in the flow near the turbine disk and a unique control volume encompassing only the limits of the disk cannot be defined. This is equivalent to helicopter rotor operation in the turbulent wake and vortex ring state (see Section 2.13.6), for which no exact solution can be found by means of the momentum theory.

In the case of the wind turbine, its thrust is *not* known (or defined) a priori like in the helicopter problem. Therefore, it is not possible to find the performance of the turbine as a function of wind speed with respect to a known reference value of induced velocity. Therefore, in the analysis of a wind turbine it is usual to define an induction ratio a as the independent parameter such that $a = v_i/V_\infty$ or that $v_i = aV_\infty$. The thrust and power output can then be established as a function of a, if this value can be found (calculated). It will be apparent that the larger the value of a the more the flow is slowed as it passes through the turbine.

13.4.1 *Power and Thrust Coefficients for a Wind Turbine*

Using Eq. 13.7 with Eq. 13.3 and expanding out gives

$$P = 2\rho A\,(V_\infty - v_i)^2\, v_i. \tag{13.9}$$

We now define a power coefficient (different to that used for a helicopter) in terms of the wind speed as a reference such that

$$C_P = \frac{P}{\frac{1}{2}\rho A V_\infty^3}, \tag{13.10}$$

so that

$$C_P = \frac{2\rho A(V_\infty - v_i)^2 v_i}{\frac{1}{2}\rho A V_\infty^3} = \frac{4(V_\infty - v_i)^2 v_i}{V_\infty^3} = 4(1-a)^2 a. \tag{13.11}$$

The relationship in Eq. 13.11 is shown graphically in Fig. 13.4 and can strictly be valid only for $0 \leq a \leq 1/2$ to avoid violating the assumed flow model by having the possibility of both downstream and upstream flow directions. We can also find the thrust coefficient acting on the turbine. Using Eq. 13.3 then the thrust is

$$T = \dot{m}w = \rho A(V_\infty - v_i)w = 2\rho A(V_\infty - v_i)v_i. \tag{13.12}$$

Now, defining the corresponding thrust coefficient as

$$C_T = \frac{T}{\frac{1}{2}\rho A V_\infty^2}, \tag{13.13}$$

means that

$$C_T = \frac{2\rho A(V_\infty - v_i)v_i}{\frac{1}{2}\rho A V_\infty^2} = \frac{4(V_\infty - v_i)v_i}{V_\infty^2} = 4(1-a)a, \tag{13.14}$$

which is also shown in Fig. 13.4 but again the result is valid only for $0 \leq a \leq 1/2$. Notice further that $C_P = (1-a)C_T$ in this case. Also shown in Fig. 13.4 is an empirical result for C_T in the range $1/2 \leq a \leq 1$ (i.e., turbulent wake region) often attributed to the analysis of Glauert (1926), but see also Lock et al. (1925). Another fit based on the results described in Section 2.13.3 and shown in Fig. 2.18 is also given. Eggleston & Stoddard (1987) suggest

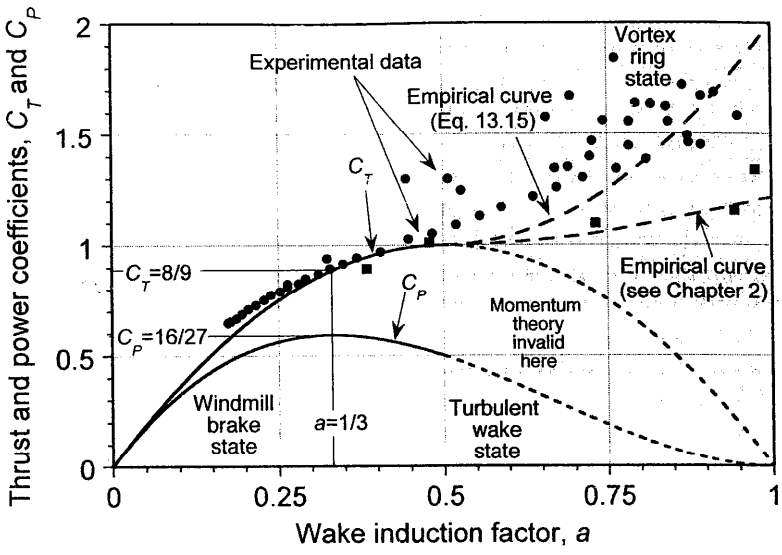

Figure 13.4 Momentum theory solution for a wind turbine in axial flow in terms of the induction ratio. Measurements from several sources including Lock (1925).

replacing Eq. 13.14 by $C_T = 4a|1 - a|$ for $a > 0.5$ but this is obviously incorrect. A more satisfying approximation to use is

$$C_T = 4(a - 1)a + 2, \tag{13.15}$$

although various other empirical equations seem to have been used [see Burton et al. (2001) and Buhl (2004)]. While this and other such equations mimic the results that have been measured (or estimated from measurements) in this regime, they are not based on any physical rationalization of the flow state associated with the increased thrust in the turbulent wake or vortex ring state (VRS). Some other results in this region can be deduced from the complete induced velocity curve shown previously in Fig. 2.18, where it will be apparent that C_T and a in the wind turbine case are related to the climb and induced velocity of the rotor using

$$C_T = 4\left(\frac{V_c}{v_h}\right)^{-2} \quad \text{and} \quad a = \frac{v_i}{V_c} = \frac{v_i}{v_h}\left(\frac{V_c}{v_h}\right)^{-1}. \tag{13.16}$$

Therefore, the C_T versus a curve given by Eq. 13.15 is simply an alternative empirical realization of the portion of the complete induced velocity curve that cannot be defined theoretically using momentum theory.

13.4.2 *Theoretical Maximum Efficiency*

Because both the thrust and power coefficients are functions of the induction factor, a, it is useful to seek the condition that corresponds to the maximum power output from the wind turbine. Differentiating Eq. 13.11 with respect to a gives

$$\frac{dC_p}{da} = 4(1 - 4a + 3a^2) = 0 \text{ for a maximum.} \tag{13.17}$$

By inspection it is apparent that this condition is met when the wake induction factor $a = 1/3$ and the corresponding values of C_T and C_P are 8/9 and 16/27, respectively (see Fig. 13.4).

In summary, this means that at the most efficient operating condition then

$$a = \frac{1}{3}, \quad C_T = \frac{8}{9} = 0.89 \text{ and } C_P = \frac{16}{27} = 0.59. \tag{13.18}$$

This operating condition is known as the Betz–Lanchester limit – see Glauert (1935, 1983) and Bergy (1979). This condition gives the upper theoretical limit to the aerodynamic power (or airpower) that can be extracted by a conventional wind turbine, assuming no viscous or other losses. In practice it is found that airpower values of C_P of between 0.4 and 0.5 are typical of a modern wind turbine when at its design operating state. This suggests that a wind turbine has a maximum possible aerodynamic efficiency of between 66% and 83% (when compared to the maximum possible airpower extraction based on the simple momentum theory) and is comparable to the aerodynamic efficiency of a helicopter rotor in producing thrust for a given shaft power input.

13.5 Representative Power Curve for a Wind Turbine

The amount of power produced by a wind turbine as a function of wind speed is obviously of primary importance for design. A representative power curve is shown in Fig. 13.5 for a large 47 m (154.2 ft) diameter turbine that has a rated electrical power output of 0.66 MW (885 hp) at 28.5 rpm. First, notice that there is a "cut-in" wind speed below which the turbine produces no power. This is, in part, because of the need to overcome mechanical friction in the system, which will require some minimum wind speed before the turbine starts to produce useful power. Also, there are aerodynamic losses to overcome that have their origin in viscous effects. This is because the turbine first starts to operate at high angles of attack with stall on the blades and the net wake flow is also in the turbulent wake state where there are rotational energy losses in the flow. Therefore, a minimum wind speed is required to overcome these losses. Second, notice from Fig. 13.5 that, after power is being produced, the output increases rapidly and is essentially proportional to V_∞^3, as would be expected based on Eq. 13.1.

Third, as a certain wind speed is reached, it will be noted that the power output levels out and approaches a limit known as the *rated power output*. This power limiting is done using one of a variety of strategies to ensure that the turbine does not absorb more power from the wind than could be absorbed by the electrical generator operating at its maximum continuous rating. One strategy is to use blade pitch control, where the blade pitch angle is adjusted automatically to match the power output to the wind speed. At higher wind speeds, the blades can be feathered to stall the blades and thus to prevent a runaway condition. At very high wind speeds or in storms, the blades can be feathered into a parked position, slowing or stopping the turbine and cutting its power output completely. Alternatively a mechanical or aerodynamic brake (such as spoilers) can be used instead of pitch regulation. For small wind turbines another technique is used to turn the rotor out of the wind to cut its energy production. This is known as *furling* – see Muljadi et al. (1998) and Eggers et al. (2000) for a discussion of furling and approaches to its aerodynamic modeling.

The power curve for a wind turbine may be plotted as a power coefficient C_P versus wind speed or more usually as C_P versus tip-speed ratio (TSR). For a wind turbine the tip speed ratio X_{TSR} is defined as

$$X_{\text{TSR}} = \frac{\text{turbine tip speed}}{\text{wind speed}} = \frac{\Omega R}{V_\infty}. \tag{13.19}$$

This parameter is essentially the reciprocal of the rotor advance ratio used in helicopter work and it is important that the two parameters are not confused. For the results shown

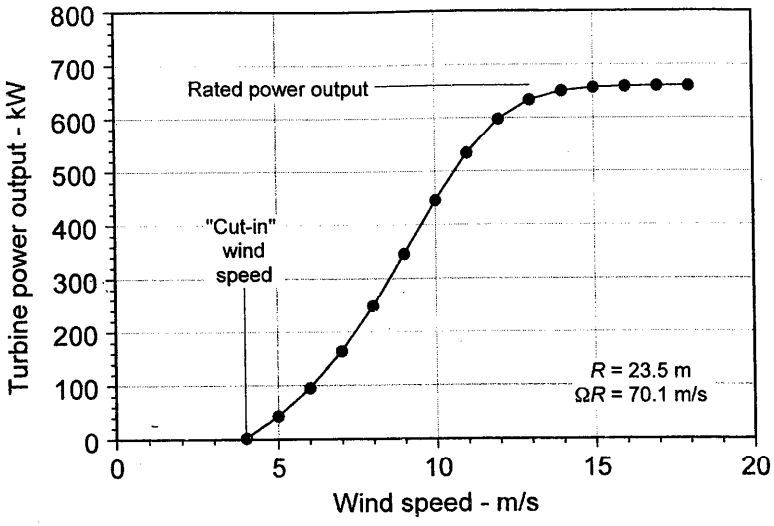

Figure 13.5 Power output from a representative constant tip-speed wind turbine as a function of wind speed.

in Fig. 13.5 the corresponding airpower C_P versus X_{TSR} curve is shown in Fig. 13.6 when allowing for a 90% electrical–mechanical conversion efficiency in the measurements. Notice also that the aerodynamic efficiency reaches a peak of almost 85% of the theoretical maximum when the turbine is operating at its rated speed. This suggests a very well-designed turbine in this case, but will generally be typical of large modern designs.

However, it will be apparent from Fig. 13.6 that peak efficiency for a constant speed (rpm) turbine is obtained only over a very narrow range of wind speeds (i.e., at a single TSR). This means that, conversely, this type of wind turbine does not operate at peak aerodynamic

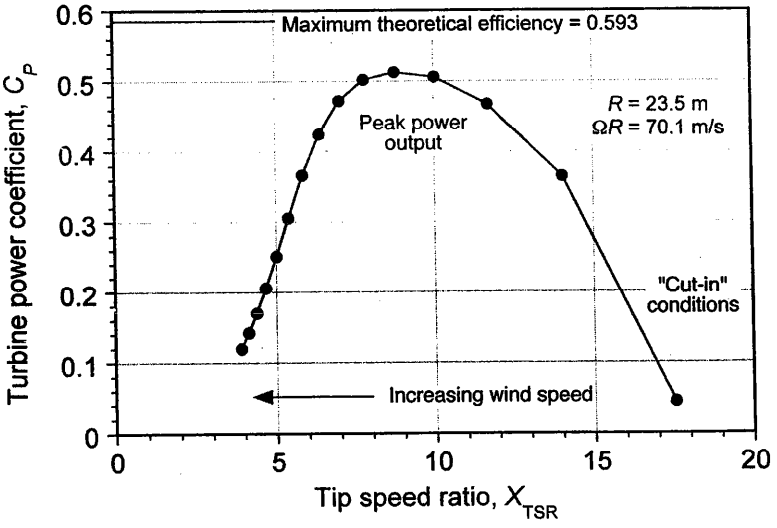

Figure 13.6 Representative power coefficient versus tip-speed ratio curve for a constant speed (rpm) horizontal axis wind turbine.

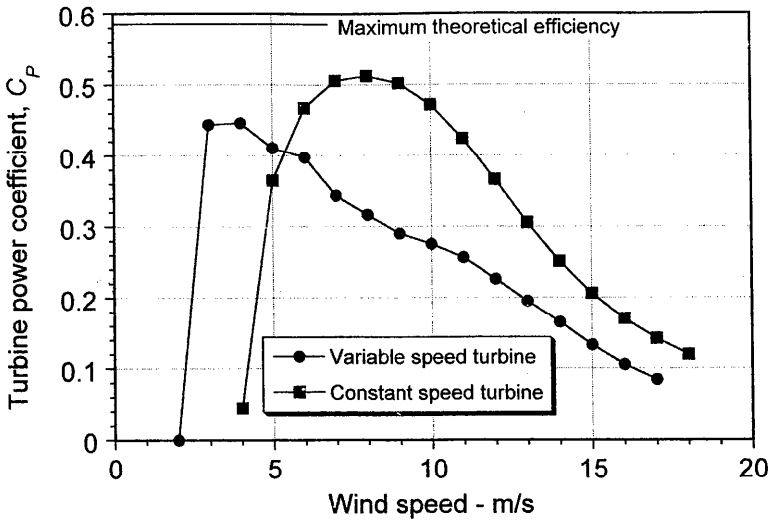

Figure 13.7 Representative power coefficient versus wind speed curves for constant speed and variable speed types of horizontal axis wind turbines.

efficiency over a very wide range of wind speeds.[1] This is a disadvantage of the constant speed type of wind turbine, despite its mechanical simplicity. However, not all wind turbines are designed to operate at constant tip speed or with constant blade pitch. Smaller wind turbines are often designed to run over a range of tip speeds and can exhibit more efficient energy extraction at lower wind speeds, as shown in Fig. 13.7. The disadvantage, however, is that the aerodynamic efficiency of a variable speed turbine drops off quickly at higher wind speeds. Yet at high wind speeds the loss of efficiency also serves to regulate the turbine's power output. The most common type of wind turbine in use today is the large variable speed turbine, where the power efficiency is fixed below the rated wind speed by electrically controlling the generator torque.

13.6 Elementary Wind Models

Primary aerodynamic factors affecting power output from the wind turbine are the wind speed, the equivalent density altitude at which the turbine operates, and the tower height, that is, the height of the turbine (measured by its shaft position) off the ground in the ground surface boundary layer. Additional factors include the likelihood of large amplitude fluctuations in wind speed (gusts) and the associated turbulence in the wind. Altitude and temperature affects the density of the air flowing through the turbine, and the effect on power output can be calculated using the standard atmospheric model given in Section 5.2. The height of the tower, h, is important because the turbine operates within the atmospheric boundary layer at the ground, which can have a substantial velocity gradient depending on the upstream terrain – see Fig. 13.8. The effect of this boundary layer is to reduce the mass flow through the turbine and so reduce its power output. The consideration of this effect is very important for choosing the site for the wind turbine. To size the rotor it is necessary to know the energy content of the winds at the proposed site and at the proposed height of the

[1] This is analogous to the helicopter rotor where the maximum operating figure of merit is obtained only at one value of C_T or disk loading.

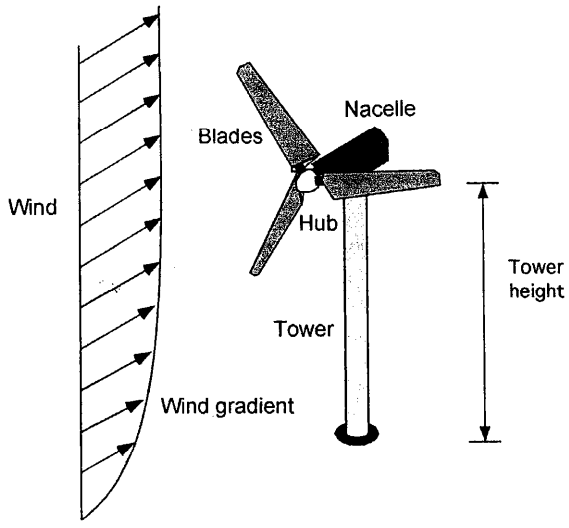

Figure 13.8 A wind turbine operates in an atmospheric boundary layer.

turbine off the ground. Such data must be acquired over many years to establish confidence that the proposed site will indeed provide the average power desired from the turbine (or wind farm). Wind data is often measured in advance at proposed sites or is obtained by using historical wind data published in handbooks such as that compiled by Frost et al. (1978). So-called *wind maps* are often prepared using both measured data and statistical models.

In practice, two models are most often used to represent the variation of wind speed characteristics with height: the power law and the logarithmic law. The power law is written as

$$V_\infty(h) = V_\infty(h_{\text{ref}}) \left(\frac{h}{h_{\text{ref}}} \right)^m, \tag{13.20}$$

where h_{ref} is a defined reference height, which is usually taken to be 10 m (32.8 ft) above the ground. It seems common to assume either that $m = 1/6$ or $m = 1/7$, so it will be apparent that the average power output from the turbine will increase with $h^{1/2}$ or $h^{3/7}$, respectively. The logarithmic law also includes a roughness length z_0 representing the character of the terrain upstream of the turbine such that

$$V_\infty(h) = V_\infty(h_{\text{ref}}) \left(\frac{\ln(h/z_0)}{\ln(h_{\text{ref}}/z_0)} \right). \tag{13.21}$$

Standard values of z_0 are given in Table 13.1, which are from Walker & Jenkins (1997). These results are valid only for flat sites and where the atmosphere is not subjected to strong convection or thermal stratification effects. There are other types of models used for hill sites.

In addition to the effects on the mean wind speed there are also stochastic variations in wind speed, because of turbulence, which will affect the power output from the wind turbine. Such variations have been measured using anemometers and the data have been developed into statistical models. It is usual to represent the wind speed as an average (or mean) component $\bar{U}$ plus a temporal or fluctuating component u, that is,

$$V_\infty(t) = \bar{U} + u(t). \tag{13.22}$$

Table 13.1. *Coefficients of Atmospheric Boundary Layer Model*

Type of terrain	z_0 (m)	m
Open country	0.02	0.12
Rural with few trees	0.05	0.16
Rural with trees and towns	0.3	0.928
Open water	0.001	0.01

The turbulence intensity I_u is written as a root-mean-square of the fluctuating wind speed and is defined by

$$I_u = \frac{1}{\bar{U}} \left[\int_0^T u(t)^2 dt \right]^{1/2}, \tag{13.23}$$

where T is the time interval over which the turbulence is measured. While various standards are used, $T = 10$ minutes is common. It is found that in practice I_u varies between $0.1\bar{U}$ and $0.2\bar{U}$ with the higher values being typical of rough upstream terrain. The value of I_u also varies with height h and decreases away from the surface. Furthermore, I_u is generally larger at low wind speeds than at high wind speeds. Custom turbulence spectra are often used to model the wind turbulence characteristics at specific wind farms. The mean wind speed, $\bar{U}$, is modeled statistically using either the Weibull or Raleigh statistical distributions – see Eggleston & Stoddard (1987). Here, the wind speed is expressed in terms of a probability distribution, $p(V_\infty)$. When combined with the wind flow statistics model, the average airpower $\bar{P}$ generated by the wind turbine is

$$\bar{P} = \int_0^\infty P(V_\infty) p(V_\infty)\, dV_\infty. \tag{13.24}$$

This average power is then used to derive a capacity factor

$$\text{Capacity factor} = \frac{\bar{P}}{\text{Rated power}}, \tag{13.25}$$

which is normally less than 50% for most wind sites. The accurate prediction of the capacity factor is particularly important in evaluating the overall economics of a wind farm.

It is clear from the published literature, however, that further work needs to be done to better describe wind characteristics by mathematical models and to integrate them into turbine design methods. Premature failure of commercial wind turbines is, in part, traceable to uncertainties in wind estimation and underprediction of structural loads on the blades, shaft, and so on. Some wind models use only the turbulent component normal to the disk and this is a concern in wind turbine design because lateral and vertical wind gradients are also a source of unsteady loads – see Hansen & Butterfield (1993). Walker et al. (1989) give a review of the various practical issues in the use of wind models.

13.7 Blade Element Model for the Wind Turbine

The aerodynamic analysis of the wind turbine can be approached readily from the perspective of the blade element model, which has been discussed previously in Chapter 3 for the helicopter. In this case, the flow model is similar to the helicopter rotor in a descending flight condition (discussed in Section 2.13.2), with the flow upward toward the plane of the

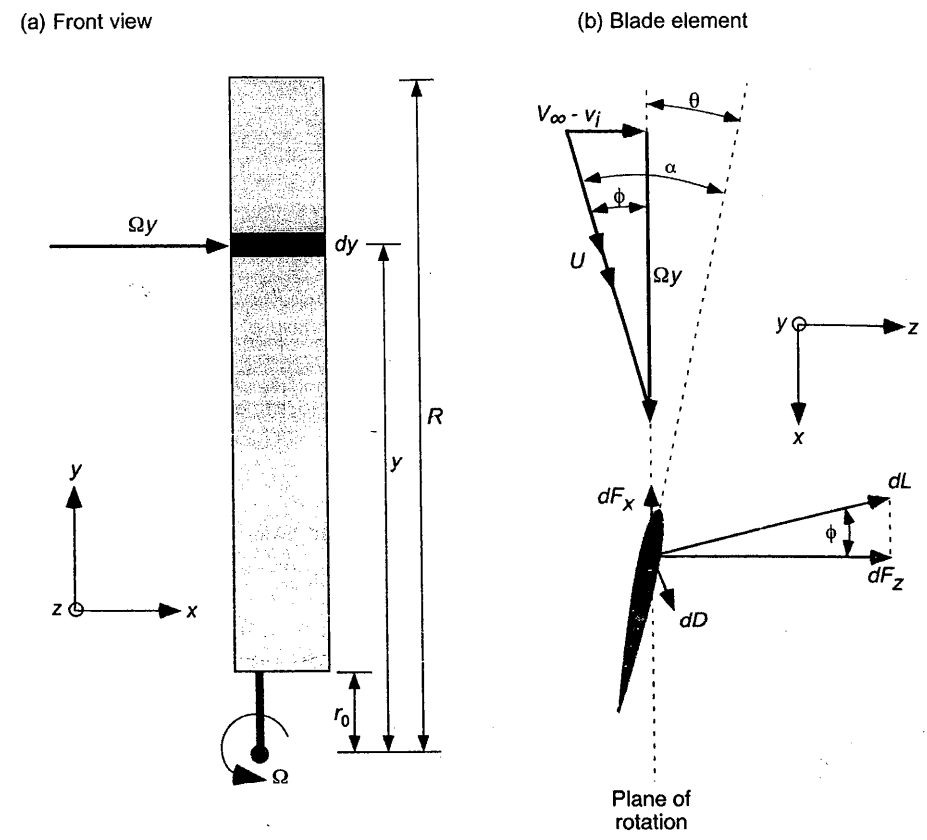

Figure 13.9 Blade element model for a wind turbine operating in axial (unyawed) flow.

rotating blades, as shown in Fig. 13.9. The local pitch angle of the blade element is θ so that the AoA at the blade element[2] is $\alpha = \theta + \phi$. The inflow modifies the direction of the relative flow velocity vector and, therefore, alters the AoA at each blade element from its 2-D value. It will be apparent that it is the forward inclination of the lift vector that provides a component of force to overcome the drag (profile and induced) on each element and so produces the net in-plane force that will drive the turbine and produce power at the shaft. This is analogous to the autorotational condition for the helicopter.

Assume that the swirl component in the flow near the turbine and its wake is small and can be neglected. The resultant incremental lift dL and drag dD per unit span on the blade element are

$$dL = \frac{1}{2}\rho U^2 c C_l \, dy \quad \text{and} \quad dD = \frac{1}{2}\rho U^2 c C_d \, dy, \tag{13.26}$$

where C_l and C_d are the lift and drag coefficients, respectively, and the resultant flow velocity $U \approx \Omega y$. Wake swirl may be included into U, however, based on a knowledge of the helicopter flow field, swirl is small at lower thrust coefficients and/or higher tip speed ratios (see page 69). The lift dL and drag dD act perpendicular and parallel to the resultant flow velocity, respectively. Notice that the quantity c is the *local* blade chord. From Fig. 13.9

[2] It should be noted, however, that in the wind energy literature the blade section angle of attack is usually written as $\alpha = \phi - \theta$ based on convention.

it is apparent that these forces can be resolved perpendicular and parallel to the rotor disk plane giving

$$dF_z = dL\cos\phi + dD\sin\phi \quad \text{and} \quad dF_x = dL\sin\phi - dD\cos\phi. \tag{13.27}$$

The contributions to the thrust, torque, and power of the rotor are thus

$$dT = N_b\, dF_z, \quad dQ = N_b y\, dF_x \quad \text{and} \quad dP = N_b\Omega y\, dF_x, \tag{13.28}$$

where N_b is the number of blades comprising the turbine rotor. This also assumes no precone on the blades, which can be significant for wind turbines. Such effects can be approximately incorporated by multiplying dC_T by $\cos\beta_P$, where β_p is the precone angle. Furthermore, notice that unless the turbine is yawed with respect to the wind, the aerodynamic environment is (ideally) axisymmetric, and the airloads are independent of the blade azimuth angle and that there is no wind shear. Substituting the results for dF_x and dF_z from Eq. 13.27 gives

$$dT = N_b(dL\cos\phi + dD\sin\phi), \tag{13.29}$$
$$dQ = N_b(dL\sin\phi - dD\cos\phi)y, \tag{13.30}$$
$$dP = N_b(dL\sin\phi - dD\cos\phi)\Omega y. \tag{13.31}$$

Applying small angle simplifications to the preceding equations (see page 118) gives

$$dT = N_b(dL + \phi dD), \tag{13.32}$$
$$dQ = N_b(\phi dL - dD)y, \tag{13.33}$$
$$dP = N_b\Omega(\phi dL - dD)y. \tag{13.34}$$

The incremental thrust coefficient on the turbine then

$$dC_T = \frac{N_b dL}{\frac{1}{2}\rho A V_\infty^2} = \frac{N_b(\frac{1}{2}\rho(\Omega y)^2 c(C_l + \phi C_d)\, dy)}{\frac{1}{2}\rho(\pi R^2)V_\infty^2} \tag{13.35}$$

$$= \left(\frac{N_b c}{\pi R}\right)\left(\frac{\Omega y}{V_\infty}\right)^2 (C_l + \phi C_d)\, dr = \sigma X^2(C_l + \phi C_d)\, dr, \tag{13.36}$$

where $r = y/R$, $\sigma = N_b c/\pi R$ is the *local* or *chord* solidity of the rotor and $X = \Omega y/V_\infty$ is the *local* section speed ratio. It will be apparent that the local section speed ratio can be written as

$$X = \frac{\Omega y}{V_\infty} = \frac{\Omega R}{V_\infty}\left(\frac{\Omega y}{\Omega R}\right) = X_{\text{TSR}} r. \tag{13.37}$$

Therefore, the incremental thrust coefficient becomes simply

$$dC_T = \sigma X_{\text{TSR}}^2(C_l + \phi C_d)r^2\, dr. \tag{13.38}$$

Proceeding in a similar manner to find the incremental power coefficient dC_P leads to

$$dC_P = \sigma X_{\text{TSR}}^3(\phi C_l - C_d)r^3\, dr. \tag{13.39}$$

It will also be apparent that the inflow angle can be written as

$$\phi = \tan^{-1}\left(\frac{V_\infty - v_i}{\Omega y}\right) \approx \frac{V_\infty - v_i}{\Omega y} = \left(\frac{V_\infty - aV_\infty}{\Omega R}\right)\left(\frac{\Omega R}{\Omega y}\right) = \left(\frac{1-a}{rX_{\text{TSR}}}\right). \tag{13.40}$$

The fundamental equations for the analysis of the wind turbine by means of the blade element theory have now been established. However, to evaluate C_T and C_P it is necessary to predict the spanwise variation in the induced inflow v_i (or the induction ratio a) as well as the sectional aerodynamic force coefficients, C_l and C_d. Also, $\alpha = \alpha(V_\infty, \theta, v_i)$, and $v_i = v_i(r)$. As for the helicopter, clearly a fundamental problem for the wind turbine is to determine the induced velocity v_i (or a), which has its origin for the most part in the physics of the downstream wake. This aside for now, if 2-D aerodynamics are assumed, then $C_l = C_l(\alpha, Re)$ and $C_d = C_d(\alpha, Re)$, where Re is the local Reynolds number.[3] See Tangler (2002) and Coton et al. (2002) for a discussion of how 2-D airfoil measurements can be integrated into the blade element approach and the various practical problems associated with this. Because these airfoil section characteristics cannot, in general, be expressed as simple analytic results it is usually necessary to use table look-up approaches (Section 7.11.3) and to solve the integrals for C_T and C_P by numerical integration. However, it is possible to proceed further by assuming linear aerodynamics and by invoking the principles of the blade element momentum theory. This has been discussed in Section 3.3 for the helicopter.

13.8 Blade Element Momentum Theory for a Wind Turbine

The blade element momentum theory (BEMT) is a hybrid method that exploits the fundamental equivalence between the circulation and momentum theories of lift. With certain assumptions, the BEMT allows the induction factor along the blade to be estimated. Thereafter, all the other airloads can be determined. The BEMT allows a clear examination of the principal design factors that influence wind turbine performance and design. However, the BEMT approach generally gives acceptable approximations to the axisymmetric distribution of inflow and loads found under conditions where the wind is normal to the plane of the turbine (i.e., the turbine is unyawed with respect to the oncoming wind).

The BEMT allows for the turbine inflow to be solved for based on satisfying a combination of a momentum balance on successive annuli of the turbine disk and a blade element representation of the sectional aerodynamics. The underlying principle is, of course, that each section behaves as a 2-D airfoil, which implies that the spanwise loading gradients are small. This is a reasonable assumption to make in light of the good comparisons shown previously in Fig. 3.19 between the BEMT and the vortex theory for the helicopter problem. Fundamentally, the limitations of BEMT soon become clear, but the value of BEMT to the engineer is determined by how well it really works in practice. The additional value of BEMT is that it allows a fundamental understanding of the effects of varying geometrical and aerodynamic parameters on the performance of a wind turbine (or on a rotor, in general).

On the basis of the differential momentum theory developed in Section 3.2, we may compute the incremental thrust on an annulus of the turbine disk. In this case the mass flow rate through an annulus of the disk is

$$d\dot{m} = \rho dA(V_\infty - v_i) = 2\pi\rho(V_\infty - v_i)y\, dy, \tag{13.41}$$

so that, using the differential form of Eq. 13.12, the incremental thrust on the annulus is

$$dT = 2\rho\,(V_\infty - v_i)\,v_i dA = 4\pi\rho\,(V_\infty - v_i)\,v_i y\, dy. \tag{13.42}$$

[3] Mach numbers are relatively low for a wind turbine and compressibility effects do not need to be considered.

In coefficient form (again with $r = y/R$) this is simply

$$dC_T = 8\left(1 - \frac{v_i}{V_\infty}\right)\frac{v_i}{V_\infty} r\, dr = 8(1-a)ar\, dr. \tag{13.43}$$

It will be apparent that this equation integrates to the correct result for C_T as given by the simple momentum theory in Eq. 13.14 under the assumption that a is a constant over the disk. The next step is to equate the results for the momentum and blade element approaches to get

$$dC_T = 8(1-a)ar\, dr = \sigma X_{\text{TSR}}^2 (C_l + \phi C_d) r^2\, dr. \tag{13.44}$$

This equation provides the formal link between the momentum and circulation theories of lift generation. To proceed further requires that C_l and C_d be related to the AoA of the section. A considerable simplification is obtained by recognizing that C_l/C_d is generally large and that the product ϕC_d is small. This means that in practice we can use the equation

$$dC_T = \sigma X_{\text{TSR}}^2 C_l r^2\, dr \tag{13.45}$$

without any major loss of accuracy. Also, in the first instance the flow can be assumed to be attached so that the relationship between C_l and α can be assumed linear, that is,

$$C_l = C_{l_\alpha}(\theta - \alpha_0 + \phi) \quad \text{with } \phi = \left(\frac{1-a}{rX_{\text{TSR}}}\right), \tag{13.46}$$

where α_0 is the zero lift AoA for the airfoil section. Then the lift coefficient becomes

$$C_l = C_{l_\alpha}\left(\theta - \alpha_0 + \frac{1-a}{rX_{\text{TSR}}}\right). \tag{13.47}$$

Using this result (and assuming α_0 can be absorbed into θ if it is defined with respect to zero lift) gives

$$8(1-a)a = \sigma X_{\text{TSR}}^2 C_l r = \sigma X_{\text{TSR}} C_{l_\alpha}\left(X_{\text{TSR}}\theta r + (1-a)\right). \tag{13.48}$$

After further manipulation this equation can be expressed in the form

$$a^2 - \left(\frac{\sigma X_{\text{TSR}} C_{l_\alpha}}{8} + 1\right)a + \frac{\sigma X_{\text{TSR}} C_{l_\alpha}(X_{\text{TSR}}\theta r + 1)}{8} = 0, \tag{13.49}$$

where the induction factor a is the unknown. This equation has the solution

$$a(r, X_{\text{TSR}}) = -\sqrt{\left(\frac{\sigma X_{\text{TSR}} C_{l_\alpha}}{16} + \frac{1}{2}\right)^2 - \frac{\sigma X_{\text{TSR}} C_{l_\alpha}(X_{\text{TSR}}\theta r + 1)}{8}} + \left(\frac{\sigma X_{\text{TSR}} C_{l_\alpha}}{16} + \frac{1}{2}\right). \tag{13.50}$$

This is the fundamental equation in the combined blade element momentum theory as it would apply to a wind turbine. In the first instance it would be acceptable to use $C_{l_\alpha} = 2\pi$ per radian. Equation 13.50 is valid, however, only for the range $0 \le a \le 0.5$; for higher values of a the turbine approaches the turbulent wake state and then the VRS, for which momentum theory affords no rigorous exact solution.

Equation 13.50 allows the induction factor a and the induced velocity v_i (the key unknown in the problem) to be obtained as a function of radial position on the blade for any given blade pitch, blade twist, chord, and airfoil section distribution (through C_{l_α} and α_0). The similarity between Eqs. 13.50 and 3.61 for the climbing helicopter rotor problem (see Section 2.13.1)

should be apparent. After the induction factor is obtained, the rotor thrust and power may then be found by integration across the rotor disk using

$$C_T = \sigma X_{\text{TSR}}^2 \int_0^1 C_l r^2 \, dr \quad \text{or} \quad C_T = 8 \int_0^1 (1-a) a r \, dr \tag{13.51}$$

and

$$C_P = \sigma X_{\text{TSR}}^3 \int_0^1 (\phi C_l - C_d) r^3 \, dr. \tag{13.52}$$

Notice that the power can be expanded to show the separate components produced by the forward inclination of the lift components on each blade element *less* the profile losses from viscous shear, giving

$$C_P = \sigma X_{\text{TSR}}^3 \int_0^1 \phi C_l r^3 \, dr - \sigma X_{\text{TSR}}^3 \int_0^1 C_d r^3 \, dr. \tag{13.53}$$

In the ideal case where a is uniformly distributed over the disk, and it is assumed that $C_d = C_{d_0}$, then

$$\begin{aligned} C_P &= \sigma X_{\text{TSR}}^3 \int_0^1 \phi C_l r^3 \, dr - \sigma X_{\text{TSR}}^3 \int_0^1 C_d r^3 \, dr \\ &= X_{\text{TSR}} \int_0^1 dC_T \phi r dr - \sigma X_{\text{TSR}}^3 \int_0^1 C_{d_0} r^3 \, dr \\ &= C_T(1-a) + \frac{\sigma X_{\text{TSR}}}{4} C_{d_0}, \end{aligned} \tag{13.54}$$

where the first term is the correct result for the induced power based on the simple momentum theory. The second term depends on the blade area (solidity) and the drag coefficient of the airfoil sections and is analogous to the profile power term that appears in the helicopter case. It is significant that this term also depends on the tip speed ratio.

There are two points of interest in Eq. 13.50. The first is the distribution of blade twist that results in uniform inflow (uniform value of induction factor) over the turbine disk. It will be apparent that for a given tip speed ratio this can only be obtained if the product θr = constant, which, by analogy with the helicopter result (Section 3.3.3), is known as *ideal twist*, that is, $\theta(r) = \theta_{\text{tip}}/r$. This form of blade twist is identical to the distribution necessary for the efficient operation of a helicopter in hovering flight and will also give the lowest induced losses on the wind turbine (i.e., the most efficient energy extraction). Notice that the form of the *distribution* of blade twist for maximum efficiency is independent of tip speed ratio but that the *magnitude* of the blade twist will be dependent on the tip speed ratio (i.e., the amount of twist will affect the range of tip speed ratios over which the turbine can operate efficiently). Second, it has already been shown by means of the simple momentum theory that $a = 1/3$ in the condition for the maximum energy extraction from the wind. For variable pitch turbine blades this allows Eq. 13.50 to be solved for the blade pitch at a given tip speed ratio (or wind speed for a given rpm) to yield maximum aerodynamic efficiency, and thus maximum energy extraction from the wind.

Representative results from the BEMT are shown in Figs. 13.10 and 13.11 for a rotor with ideal blade twist operating at different blade pitch angles. No nonideal losses are assumed in this case, (i.e., only ideal-induced losses are present). From results such as these, the power coefficient at a fixed rotor speed can be derived for different wind speeds. For variable pitch

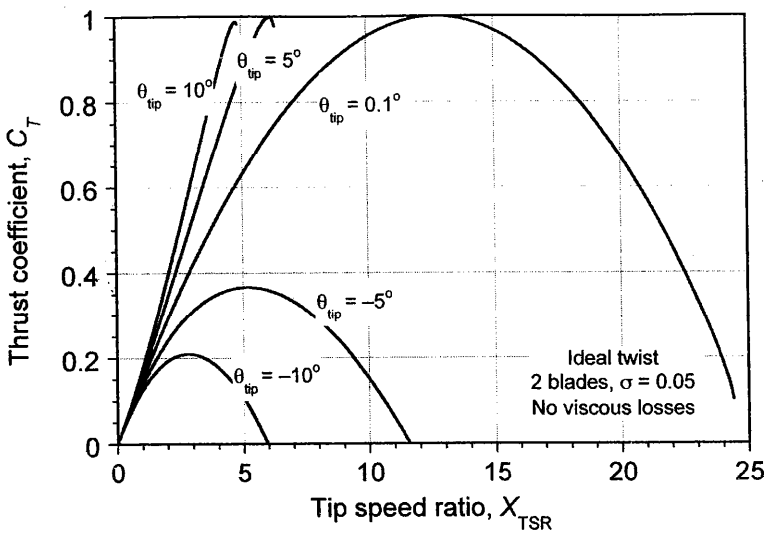

Figure 13.10 Representative thrust produced on a wind turbine as a function of tip speed ratio using the BEMT for various pitch angles. No nonideal losses.

turbine blades, the power coefficient can be determined over a range of pitch angles and wind speeds. It is seen that a shallow blade pitch allows for energy extraction over a wide range of wind speeds; neither large positive nor negative pitch angles allow for efficient operation. Recall that the BEMT is valid only for values of $0 \leq a \leq 0.5$, so the curves cannot be defined for all wind speeds and all pitch angles unless empirical corrections are used (see Section 13.8.3).

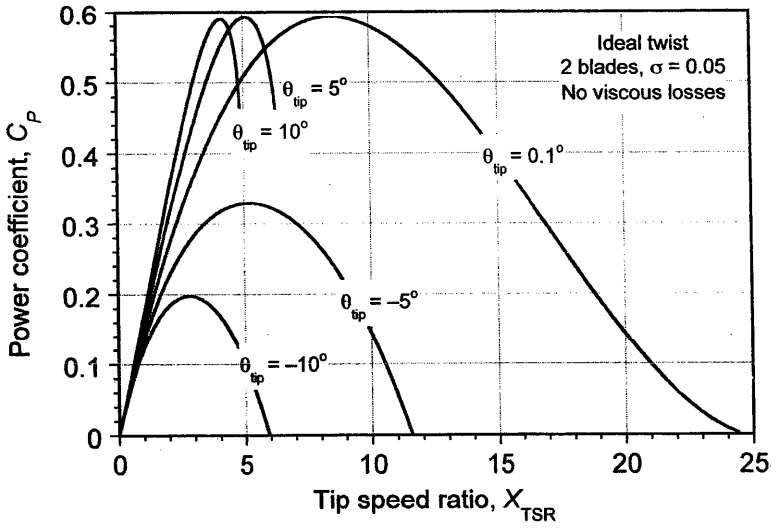

Figure 13.11 Representative power output produced from a wind turbine as a function of tip speed ratio using the BEMT for various pitch angles. No nonideal losses.

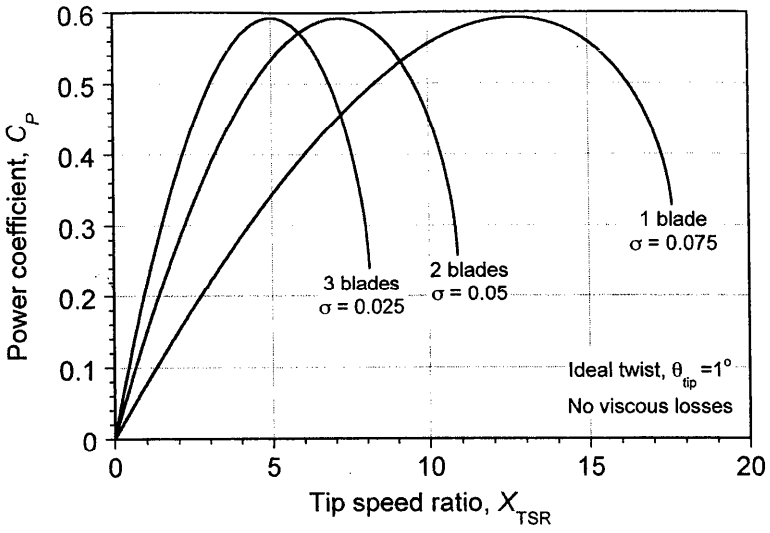

Figure 13.12 Representative power output produced from a wind turbine for different numbers of blades as a function of tip speed ratio using the BEMT. No nonideal losses.

13.8.1 *Effect of Number of Blades*

The variation in power output with TSR from a wind turbine is affected by the number of blades. If there are no nonideal losses to consider, the resulting behavior is typified by Fig. 13.12. Notice that increasing the number of blades (or increasing solidity) does not affect the maximum efficiency of the turbine, but it does affect the tip speed ratio (or wind speed) where maximum efficiency is obtained. Increasing the number of blades or solidity also reduces the range of tip speed ratios over which high power coefficients can be obtained. Too many blades or too much solidity gives a steep power curve that peaks at low tip speed ratios. This is not very useful in practice, besides the fact that the blades will also be approaching stall at these conditions (high wind speeds). The addition of viscous drag (see Section 13.8.2) changes the situation somewhat and the efficiency will decrease with increasing numbers of blades (increasing solidity). There is no effect on efficiency if the solidity is kept constant and only viscous drag is assumed. However, consideration of tip losses (see Section 13.8.3) will tend to favor turbines with larger numbers of blades (for a given overall solidity) because this will minimize tip-loss effects (i.e., induced losses will be minimized and the turbine will be closer to an ideal actuator disk).

13.8.2 *Effect of Viscous Drag*

Figure 13.13 shows how the power output from a wind turbine depends on the viscous drag of the airfoils that comprise the blades of the turbine. Clearly maximum efficiency favors airfoils with lower drag coefficients, all other factors being held constant, but this is rather obvious. At the Reynolds numbers encountered on wind turbines most airfoils tend to have drag coefficients in the range $0.01 \leq C_{d_0} \leq 0.02$ unless surface finish is degraded by erosion, dead insects, frost, or ice. Some airfoil sections are more sensitive to these effects than others. The absence of specific information on the airfoil section characteristics from measurements would suggest the use of $C_{d_0} = 0.01$ as an initial assumption for preliminary design studies.

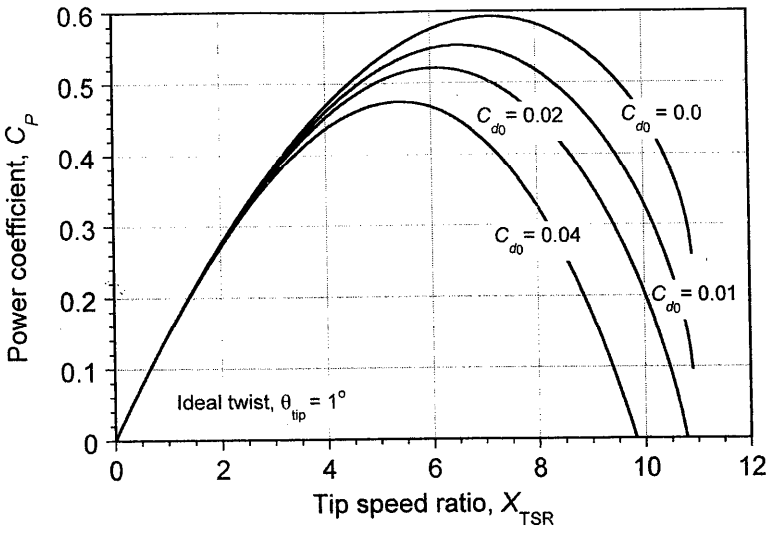

Figure 13.13 Representative power output from a wind turbine for airfoil sections with different assumed viscous drag coefficients as a function of tip speed ratio using the BEMT. No tip losses.

13.8.3 *Tip-Loss Effects*

The induced nature of the vortical wake and its effects on the spanwise loading on the blades can be approximated using Prandtl's tip-loss function as shown previously for the helicopter rotor in Section 3.3.10. Because the basis of the BEMT is a strictly "2-D" theory, 3-D effects such as the physical roll-off in the lift as the blade tip is approached must be treated using corrections, although the better approach is to use lifting-line and vortex theory (see Section 13.11). The Prandtl correction can account approximately for a finite number of blades and also for variations of blade planform and twist through the effect on the inflow angle.

Prandtl's "tip-loss" result can be expressed in terms of a correction factor F to the change in momentum over the annulus of the disk in Eq. 13.55 such that

$$dC_T = 8F(1-a)ar\,dr \quad \text{where} \quad F = \left(\frac{2}{\pi}\right)\arccos\left(\exp(-f)\right), \tag{13.55}$$

where the exponent f is given in terms of the number of blades and the radial position of the blade element r by

$$f = \frac{N_b}{2}\left(\frac{1-r}{r\phi}\right) = \frac{N_b}{2}\left(\frac{1-r}{1-a}\right)X_{TSR}. \tag{13.56}$$

If root losses are also to be modeled, then it will be apparent that the corresponding equation for f is

$$f = \frac{N_b}{2}\left(\frac{r-r_0}{1-a}\right)X_{TSR}, \tag{13.57}$$

where r_0 represents a root cut-out distance, which represents the lack of aerodynamic lift-producing surfaces close to the hub. With the incorporation of tip- and root-loss effects into

the BEMT the induction factor becomes

$$a(r, X_{TSR}, F) = -\sqrt{\left(\frac{\sigma X_{TSR} C_{l_\alpha}}{16F} + \frac{1}{2}\right)^2 - \frac{\sigma X_{TSR} C_{l_\alpha}(X_{TSR}\theta r + 1)}{8F}} + \left(\frac{\sigma X_{TSR} C_{l_\alpha}}{16F} + \frac{1}{2}\right). \tag{13.58}$$

Because F is not known a priori, in the first instance Eq. 13.58 is calculated from the inflow angle (or induction factor) after assuming that $F = 1$. Repeating the calculation for a and F using Eqs. 13.58 and 13.55 shows rapid convergence, normally within 3 to 10 iterations.

The numerical process for including the Prandtl tip-loss function will fail, however, if the square-root term in Eq. 13.58 produces an imaginary result, that is, if

$$\left(\frac{\sigma X_{TSR} C_{l_\alpha}(X_{TSR}\theta r + 1)}{8F}\right) > \left(\frac{\sigma X_{TSR} C_{l_\alpha}}{16F} + \frac{1}{2}\right)^2. \tag{13.59}$$

This means that the inclusion of the Prandtl tip-loss factor can limit the range of wind speeds and operating conditions over which numerical solutions can be found using the BEMT simply because the governing equation breaks down numerically as a becomes greater than 0.5. This problem can be circumvented if the relationship between induction ratio and thrust is represented using the empirical branch of the curve for $a > 0.5$, say when using Eq. 13.15 because of its simple analytic form (see also Fig. 13.4). While this assumes that the induction ratio is constant (or almost so) over the disk, for any values of a approaching 0.5 this means that multiple flow directions are possible and so there is a decreasing validity of the momentum theory, in general. In this case, the fundamental equation for a must be rederived, such as using Eq. 13.15. In this case, equating the momentum and blade element results gives

$$(8(a-1)a + 4)F = \sigma X_{TSR}^2 C_l r = \sigma X_{TSR} C_{l_\alpha}\left(X_{TSR}\theta r + (1-a)\right), \tag{13.60}$$

which after manipulation can be expressed in the analytic form

$$a^2 + \left(\frac{\sigma X_{TSR} C_{l_\alpha}}{8F} - 1\right)a + \left(\frac{1}{2} - \frac{\sigma X_{TSR} C_{l_\alpha}(X_{TSR}\theta r + 1)}{8F}\right) = 0. \tag{13.61}$$

This has the solution

$$a(r, X_{TSR}, F) = \sqrt{\left(\frac{\sigma X_{TSR} C_{l_\alpha}}{16F} - \frac{1}{2}\right)^2 - \left(\frac{1}{2} - \frac{\sigma X_{TSR} C_{l_\alpha}(X_{TSR}\theta r + 1)}{8F}\right)} - \left(\frac{\sigma X_{TSR} C_{l_\alpha}}{16F} - \frac{1}{2}\right). \tag{13.62}$$

This modified equation is valid for the extended range $0.5 < a \leq 1.0$, where it should be understood that it is based on an underlying empirical assumption and an extension of the Prandtl tip-losses concept to flow conditions where the assumptions inherent in the BEMT become increasingly questionable. Nevertheless, in light of the results obtained (see next section) its use seems appropriate for engineering purposes because it allows the BEMT to be used for wind turbine analysis over a wider range of practical operating conditions.

Representative calculations of the spanwise distribution of induction ratio, thrust distribution and distribution of power extraction on a wind turbine as predicted using the BEMT

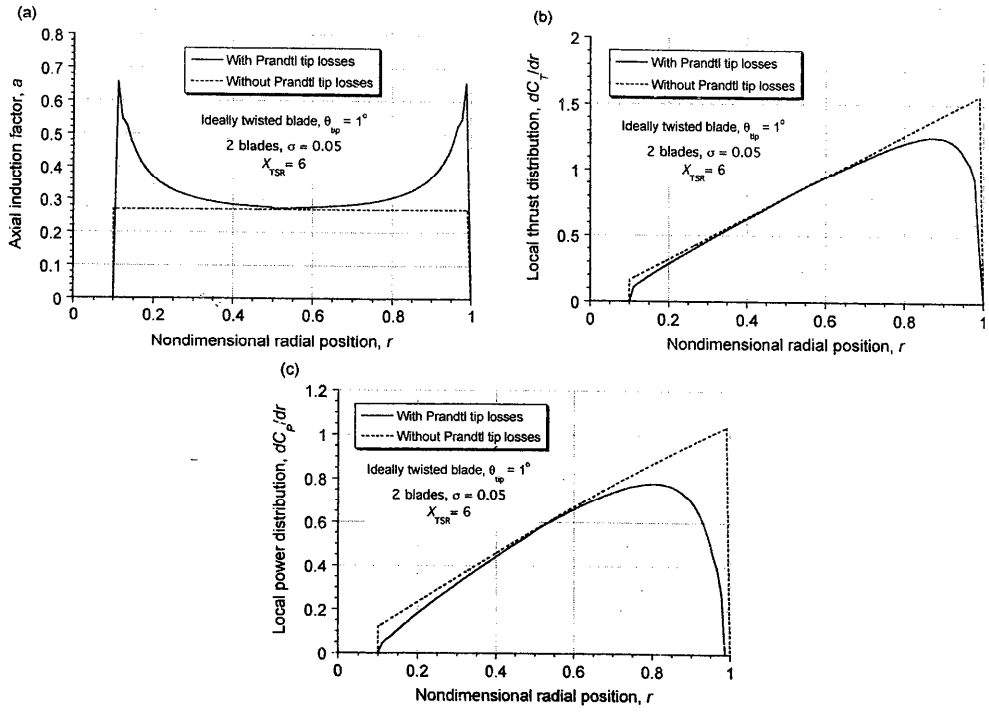

Figure 13.14 Representative distributions of induction ratio, thrust loading and torque loading for a wind turbine using ideal twist with and without Prandtl tip-loss effects. $X_{\text{TSR}} = 6$, $\sigma = 0.05$, $\theta_{\text{tip}} = 1°$, $r_0 = 0.1$ (a) Induction ratio. (b) Thrust distribution. (c) Power extraction distribution.

are plotted in Fig. 13.14. The results are shown with and without the Prandtl tip and root losses and for a case where locally near the tip a is greater than 0.5. Notice that the tip- (and root-) loss function serves to increase the induction ratio over much of the blade, in part because the blade in this case is not of particularly high aspect ratio ($R/c = 10$). These "tip losses" decrease the thrust on the turbine and also decrease its power output. Because most of the net airpower generated by the turbine comes from stations toward the blade tip, it is apparent from Fig. 13.14(c) that tip effects are really a very substantial source of aerodynamic losses and modeling the effects accurately is of fundamental importance. The use of vortex theory, such as with the use of a lifting line and a trailed vortex wake, is a more physically pleasing way of modeling such losses (see Section 13.11).

13.8.4 *Tip Losses and Other Viscous Losses*

The separate effects of viscous drag and Prandtl tip losses on the turbine power output is shown in Fig. 13.15. Notice that both types of nonideal losses tend to decrease power output (decrease turbine efficiency). Taken together they comprise about a 15% loss of efficiency, which is fairly close to the results obtained in practice for operating conditions that do not involve any blade stall (see Fig. 13.6).

Of interest is the induced velocity or axial induction factor a as a function of tip-speed ratio. In the ideal case (hyperbolic blade twist) the induction factor is uniform over the disk. The behavior of the induction factor is shown in Fig. 13.16 for several blade pitch

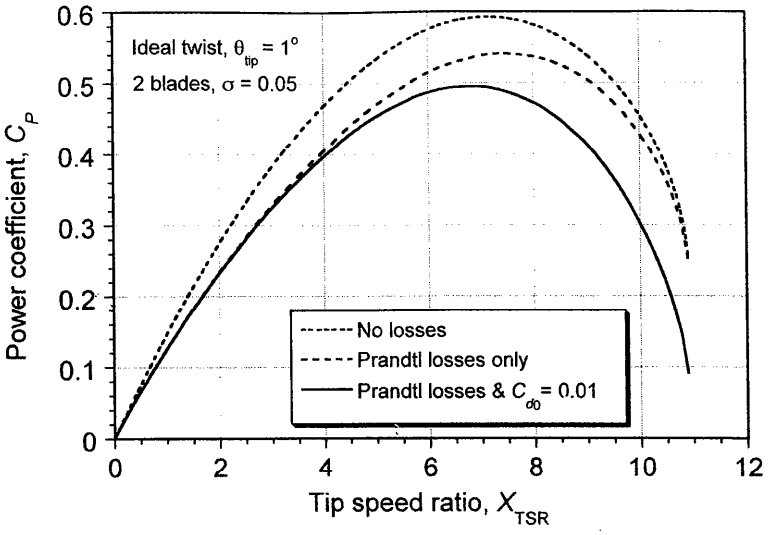

Figure 13.15 Turbine power output as a function of TSR showing the separate effects of viscous drag and Prandtl tip losses.

angles. Notice that the largest induction factors are obtained at the highest tip speed ratios (lowest wind speeds). This is because the induced velocity is a relatively high fraction of the wind speed at low wind speeds (high values of X_{TSR}) and becomes an increasingly smaller fraction as wind speed builds (low values of X_{TSR}). Furthermore, at low wind speeds there is a possibility of two flow directions existing at the rotor disk, which can only be represented, albeit approximately, using an empirical relationship between C_T and a, as previously discussed. Another factor that limits the applicability of the BEMT is that at higher wind speeds there is the possibility of blade stall, which also needs to be considered if the induction factor is to be predicted accurately.

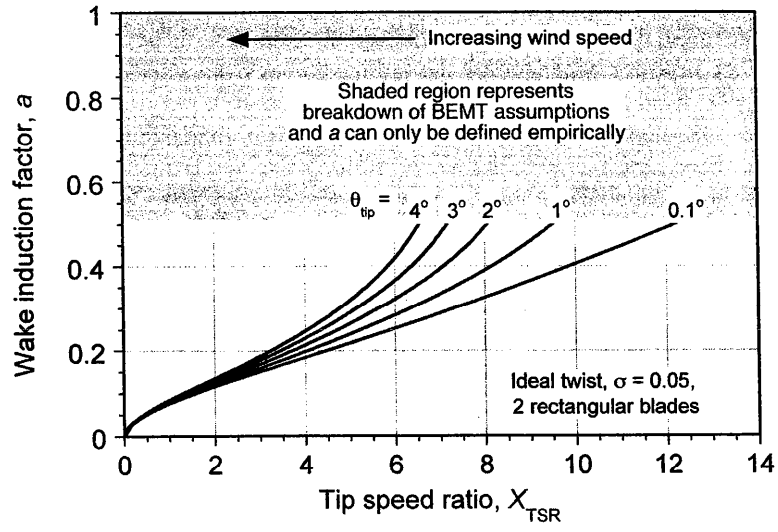

Figure 13.16 Variation of axial induction factor as a function of TSR for a wind turbine with ideally twisted blades giving uniform induction factor.

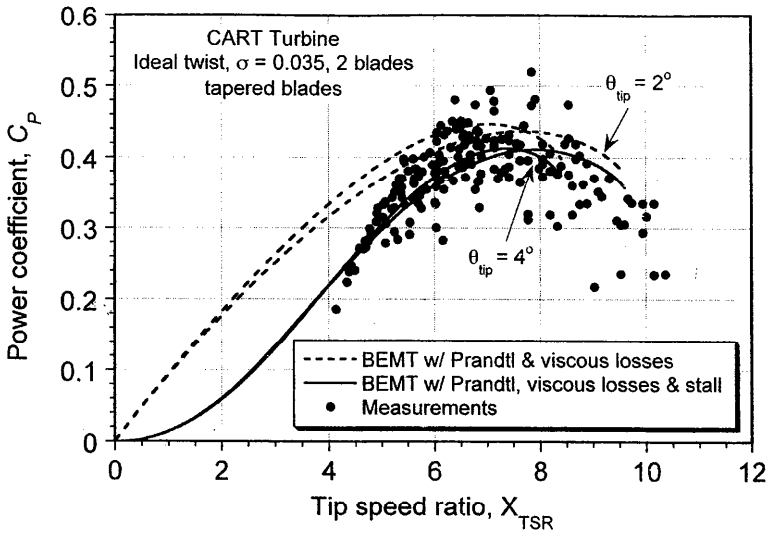

Figure 13.17 Turbine power output as a function of TSR showing the effects of blade stall. Data source: Measurements from two-bladed wind turbine, courtesy of NREL.

13.8.5 *Effects of Stall*

In addition to the reduction in power output caused by tip losses and viscous drag, the effects of stall on the performance of the turbine must be considered. Stall generally occurs at high wind speeds (low tip speed ratios) and/or with high blade pitch angles. Static airfoil characteristics, such as the nonlinear changes in the lift with the onset of flow separation, can be incorporated into the BEMT theory using a look-up table or other such strategy, such as described in Section 7.11.3 for the helicopter rotor. Approaches specifically for the wind turbine problem are also described by Tangler (2002) and Coton et al. (2002). Representative results of power output showing the effects of nonlinear aerodynamics, and the effects of stall in particular, are shown in Fig. 13.17. While stall is often used on wind turbines as a means of power regulation (these are called "stall-regulated" turbines), it generally has a deleterious effect on power output if it occurs at other operating conditions. Notice that after peak efficiency is attained the effect of stall tends to cause the power output to drop much more sharply with increasing wind speed than if no stall was present. This is consistent with experimental measurements of power output on wind turbines and illustrates the need for good stall models if the power output is to be predicted accurately over a wide range of wind speeds. The numerous difficulties of representing nonlinear aerodynamics and stall effects has historically limited the accuracy of predictions of blade loads and the power output from wind turbines.

13.9 Airfoils for Wind Turbines

The importance of airfoil sections for any type of rotating wing cannot be underestimated, to the point that Chapter 7 has been devoted to an understanding of the subject. As has been done for helicopter rotors, entire families of airfoil sections have been developed for wind turbines. Many commercial wind turbines use standard NACA airfoil sections such as the NACA 4-digit series. In particular, the NASA LS-1 (low-speed) airfoil seems a common choice because of its known insensitivity to surface finish. Figure 13.18 shows some representative airfoils that have been used for wind turbines. The influence of airfoil

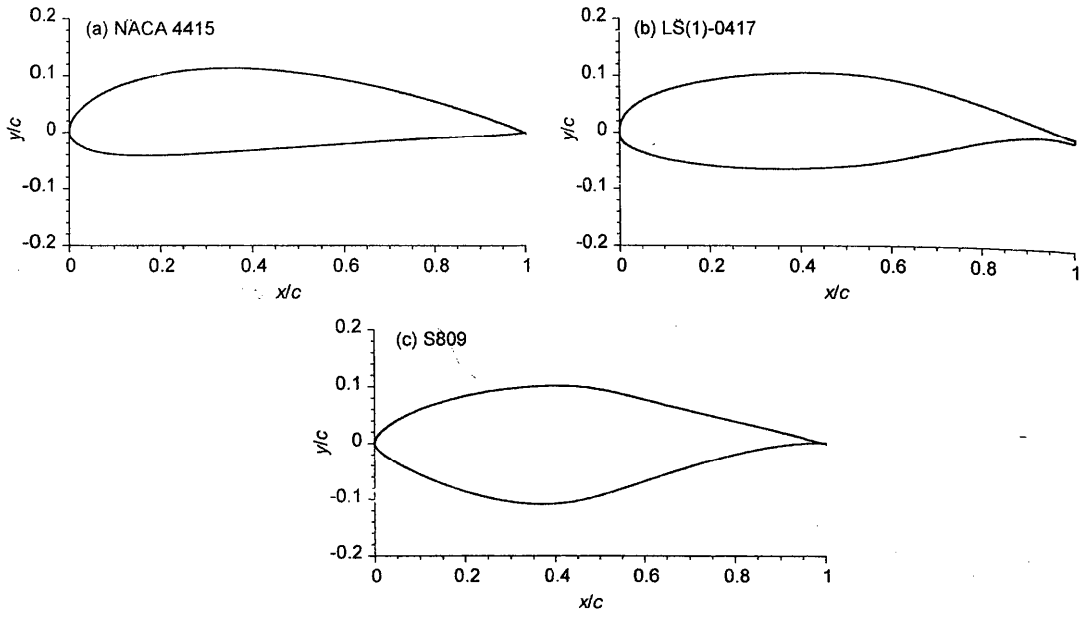

Figure 13.18 Examples of airfoil sections used for wind turbines: (a) NACA 4415. (b) LS(1)-0417. (c) NREL S809.

section on the power output of a wind turbine is relatively small, but the use of an efficient low drag airfoil will always help maximize energy production. A catalog of airfoil sections for wind turbine applications has been compiled by Miley (1982). See Tangler (1987, 1995) for more recent wind turbine airfoil section developments.

There are, however, some special considerations in the design, selection, and modeling of the characteristics of airfoil sections for wind turbines compared to those for a helicopter. The most important is that wind turbines operate at much lower Reynolds numbers than helicopters, typically at or below 10^6 even at the blade tip. This means that Reynolds number sensitivity is a more important issue and the accurate modeling of Reynolds number effects on the aerodynamic characteristics of the blade will be critical if the blade loads and power output from the wind turbine are to be predicted accurately. Again, these effects are readily implemented using look-up table techniques or equations fitted to the measured airfoil characteristics (Section 7.11.3). As previously mentioned, also important is a knowledge of the sensitivity of the airfoils to surface roughness. The normal operation of wind turbines in the low atmosphere tends to cause the accumulation of dirt and dead insects and other foreign matter at the leading edge of the blades, and this can act to degrade airfoil performance and reduce turbine power output – see Clark & Davis (1991) and Eggleston (1991). Representative effects of surface roughness on airfoil performance have been shown previously in Fig. 7.37 and appear as increased drag, decreased maximum lift and perhaps as a change in stall characteristic, usually leading to a very gradual or "soft" stall.

For variable blade pitch (feathering) turbines, airfoil sections are designed for high values of maximum lift, in much the same way as is done for helicopters – see Section 7.9. The pitch control system is used to adjust the AoA so that the best energy extraction efficiency is obtained over a wide range of wind speeds up to maximum power. For fixed pitch stall, controlled wind turbines, the airfoil sections must be designed to begin stall at lower values

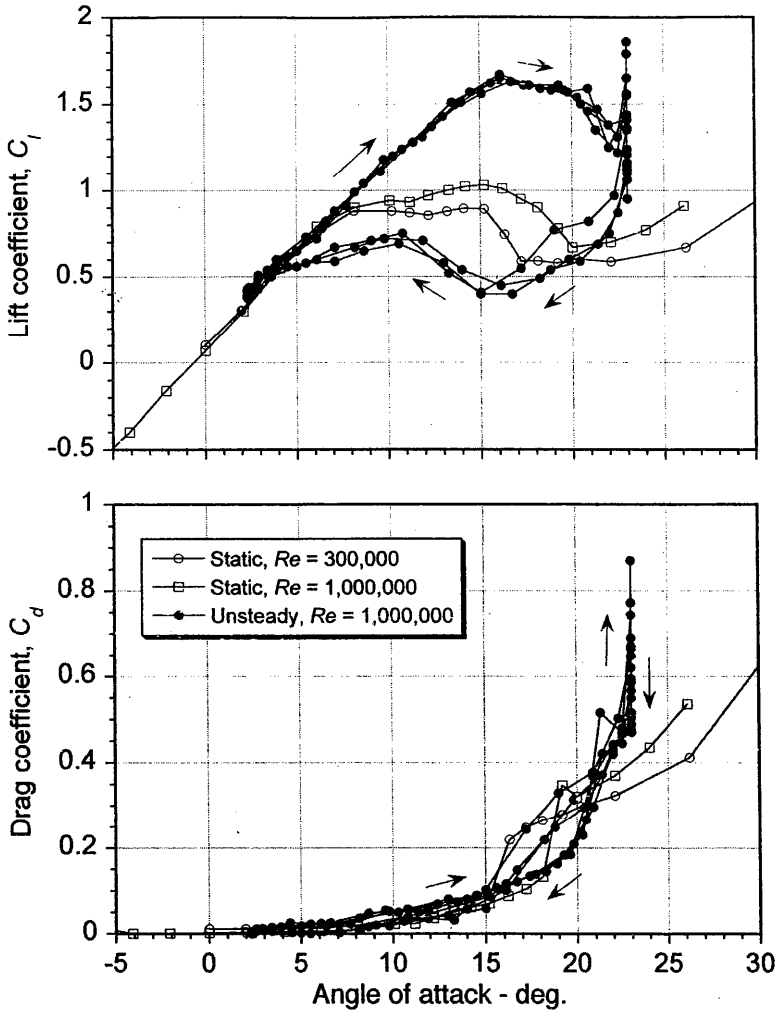

Figure 13.19 Lift and drag characteristics of the NREL S809 wind turbine airfoil under steady and unsteady conditions with dynamic stall ($\alpha = 10° + 10°\omega t$, $k = 0.077$). Data sources: Ramsay et al. (1995) and Hand et al. (2001).

of lift coefficient and then to maintain that value over a relatively wide range of angles of attack. This requires airfoil sections with appropriate pressure distributions that initially promote trailing edge separation and thus make this prestall behavior relatively insensitive to AoA. One example is the NREL S809 airfoil [see Tangler (1987)], the geometric shape of which is shown in Fig. 13.18(c) and the aerodynamic characteristics are given in Fig. 13.19. Notice that under steady (static) conditions the maximum lift is obtained at a moderate angle of attack, the lift then plateaus for about an 8 degree AoA range as trailing edge separation develops and stabilizes. This helps regulate the turbine's power output. Over this range there is only a modest increase in the sectional drag. Gross breakdown of the flow and static stall occurs at about 15°. These characteristics are also carried forward somewhat into the dynamic regime, with lift overshoots but with relatively wide flat lift peaks compared to those found on helicopter airfoil sections under dynamic stall conditions (see, for example, Fig. 9.15). In this case, the lift overshoots are a result of the suppression of trailing edge

flow separation and not the formation of dynamic stall per se, and "classic" dynamic stall with leading edge vortex shedding is not obtained until a much higher AoA.

13.10 Yawed Flow Operation

While ideally the wind turbine operates with the wind direction normal to its plane of rotation, this is never achieved in practice and there is always some yaw misalignment to the wind flow. This produces a velocity component parallel to the plane of rotation of the turbine disk, which leads to unsteady aerodynamic forces and also to a skewed wake. This is analogous to the helicopter rotor in forward flight, where the wake is blown back behind the disk. This skewed wake is responsible for an inflow gradient across the wind turbine disk. While the gradients are particularly strong parallel to the direction of the wake skew, a gradient is also produced in the other direction because of the asymmetry in aerodynamic loads between the effective advancing and retreating sides of the disk.

While the origins of this induced velocity distribution are complex (see Section 13.11 for a detailed discussion), a number of mathematical models for the effects have been derived, mostly following the linear inflow models developed for the helicopter case (see Section 3.5.2). Snel (2001) gives a review. The general approach is to correct the value of the induction ratio predicted from the BEMT by using an equation of the form

$$a_\gamma = a\big(1 + K_s(\gamma) r \sin\psi + K_c(\gamma) r \cos\psi\big), \tag{13.63}$$

where γ is the yaw misalignment angle of the turbine disk with respect to the wind and a_γ is the corrected value of the induction ratio. The correction technique can be applied a posteriori using the values for a in the unyawed case, although the validity of this approach is perhaps questionable. Another variant of the technique is to correct the value of a based on the yaw angle and then to perform an iterative series of momentum balances at each of the elements until the values for a converge. This is a more pleasing approach.

The coefficients K_s and K_c used in practice have been based on a number of assumptions and approaches, including results for the helicopter case (Section 3.5.2) as well as from inflow measurements made on subscale wind turbines in wind tunnels. For instance, the skewed cylindrical wake model of Coleman et al. (1945) seems to have received some attention for use in wind turbine analyses. In this case, the K_s is related to the wake skew angle using

$$K_s = \tan(\chi/2), \tag{13.64}$$

where, as shown by Burton et al. (2001), χ can be related approximately to the yaw angle and induction factor using

$$\chi = (0.6a + 1)\gamma. \tag{13.65}$$

In another example, inflow measurements were made using a 1.2-m-diameter subscale wind turbine placed in the open jet wind tunnel and used to determine the inflow coefficients, including higher harmonic variations – see Schepers (1999).

The mathematical form of the inflow model given in Eq. 13.63 has been compared to measurements of blade airloads. It would seem if these inflow effects are properly accounted for then considerable improvements in the prediction of the loads under yawed operations are possible, at least for small yaw misalignment angles. Nevertheless, the approach of correcting the induction ratio in this manner is not rigorously valid because it violates the principles under which the BEMT equations were derived in the first place, including the

need for axisymmetric flow. Approaches based on vortex theory are probably the next best practical level of analysis of this problem.

13.11 Vortex Wake Considerations

Despite the various assumptions and approximations used with the BEMT, validation studies have shown it can give good preliminary predictions of turbine loads and performance [see Hansen (1993)]. It also offers considerable insight into basic design parameters affecting the turbine performance, including blade geometric parameters such as planform and twist. Under yawed conditions, however, the BEMT is less able to model the physics of the turbine aerodynamics because of the strongly nonaxisymmetric flow and the 3-D nature of the airloads produced over the turbine disk; see Schreck et al. (2000) for a comprehensive discussion. A major source of this three-dimensionality is the vortical wake system produced behind the turbine, a visualization of which is shown in Fig. 13.20. Like a helicopter, the turbine wake is comprised of strong vortices that trail from each of the blade tips and these are rendered visible in this photograph by the use of smoke generators. Because a wind turbine extracts energy from the wind, the wake expands downstream of the turbine. It may also distort as a result of the wind gradient and turbine yaw angle. While flow visualization of the wake downstream of a wind turbine is relatively rare, a good review

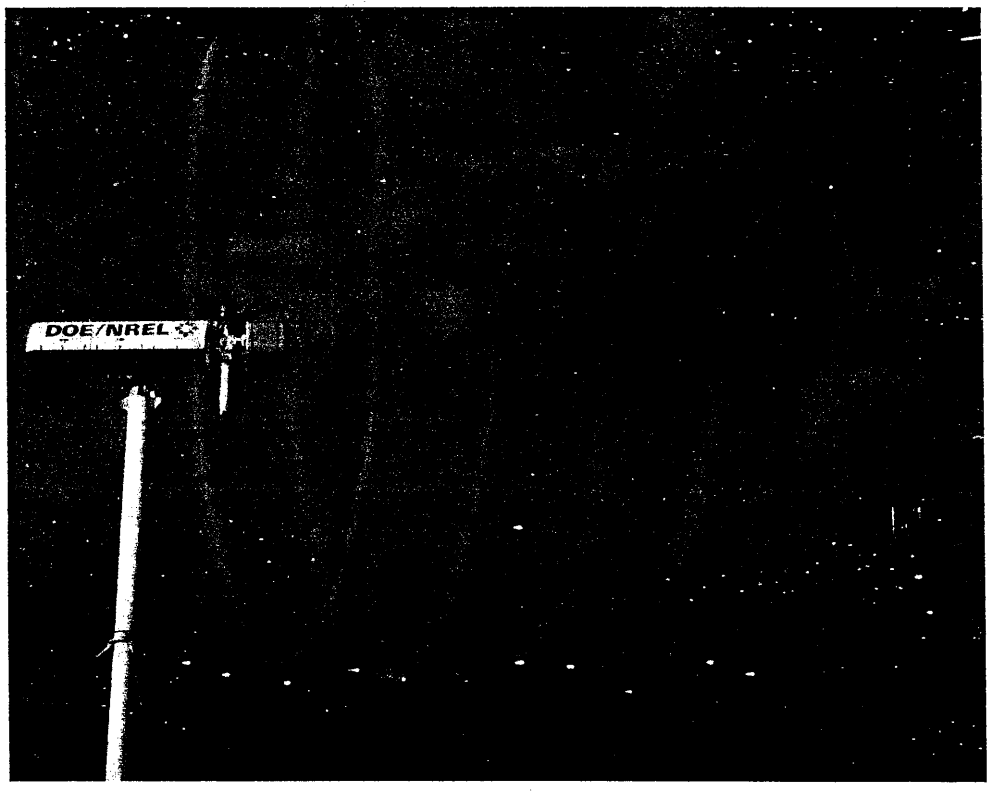

Figure 13.20 Photograph of the vortical wake behind a horizontal axis wind turbine rendered visible using smoke injection. Notice the skewed wake resulting from the wind gradient and the effects of the tower shadow. Source: Photo courtesy of NREL.

of the field and survey of existing results is given by Vermeer et al. (2003). See also Grant et al. (2000) and Vermeer (2001) for a discussion of the general characteristics of wind turbine wakes.

Various modifications to the blade element approaches have been used to represent these 3-D wake effects, for instance, by using inflow models, some of which have been derived from helicopter applications (see previously in Section 3.5.2). While improvements in predictions of net power are usually obtained using these methods, their ability to predict blade loads over an acceptably wide range of operating conditions or for new wind turbine designs is not very satisfactory; see Fingersh et al. (2001). A more rigorous treatment of the turbine wake requires a method that can represent the strengths (circulation) and spatial locations of the vortical elements that are trailed by each blade and convected into the downstream wake. This can be done using vortex methods, which have become very popular tools for the analysis helicopter wake problems. (See Section 10.7 for the fundamental theory of vortex wake methods.) The development of a vortex wake model is usually based on the assumption of an incompressible potential flow, with all vorticity assumed to be concentrated within vortex filaments. From the strengths of the vortex filaments (determination of which requires proper coupling to the blade lift distribution), the induced velocity field can be obtained through the application of the Biot–Savart law (Section 10.7.1).

The idea of a vortex model applied to the wake of a wind turbine is shown schematically in Fig. 13.21. Vortex methods applied to turbine wake problems can be categorized into "prescribed" or "free" vortex techniques, just as they are for helicopters (see Section 10.7). A prescribed vortex technique is where a discrete representation is made of the vorticity field, but the positions of the vortical elements are specified a priori based on semi-empirical rules – see Robison et al. (1995). Prescribed vortex methods can be viewed more as postdictive rather than predictive methods because they use experimental results for formulation purposes and so are strictly limited in scope to the conditions that encompass the range of measured operating conditions for which they were originally formulated. The free-vortex method (FVM) is a predictive method because the elements are allowed to convect and deform freely under the action of the local velocity field. While a disadvantage of all types of vortex methods for modeling the wake is their relatively higher computational overhead (mainly because of the need to evaluate the Biot–Savart law a very large number of times), they are an inherently more appealing physical approach for modeling the wake than the use of inflow models.

Prescribed vortex wake models have seen some use for wind turbines, e.g., Kocurek (1987), Robison et al. (1995), and Coton & Wang (1999). The development of more generalized prescribed wake models for wind turbine applications is a significant undertaking because not only do the positions of the wake vortices need to be documented, but the experimental conditions must encompass a wide range of turbine geometric (e.g., blade shape and twist) and operating states (wind speed, yaw angle, etc.). Therefore, a trade-off must be drawn between the costs of doing more experiments and collecting more data to build the model, and the costs of developing a better and more flexible model that can be validated against existing data. Prescribed wake models are also only strictly applicable when the operating conditions are nominally steady-state, that is, in a steady wind (which never exists in practice). Free-vortex methods have fewer potential limitations when applied to new turbine designs and/or more general operating states. Such methods are yet to see significant use for wind turbine applications, but offer much more rigor than the ad hoc application of "inflow" models derived from helicopter rotor models, especially because these have not yet been validated for all of the flow operating states of a wind turbine.

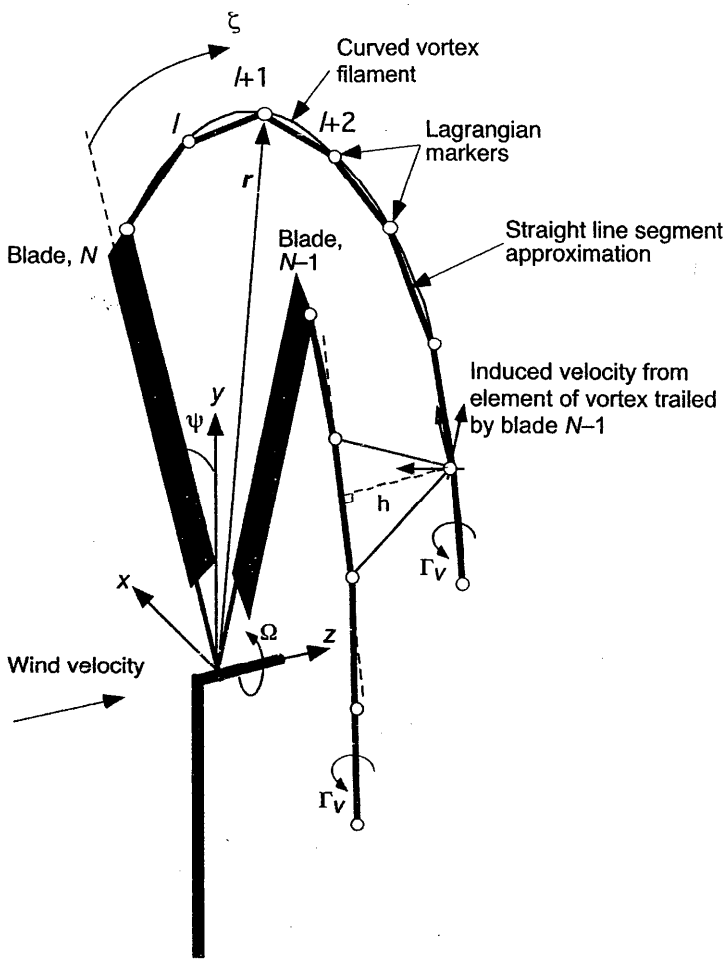

Figure 13.21 Modeling the downstream wake of a wind turbine using a free-vortex filament method, with vortices shown trailing from the tips of each blade.

Free-vortex methods are based on a discretized, finite-difference representation of the governing equations for the wake and, when solved, track the evolution of discrete vortex elements through the flow. The number of discrete elements can be in the thousands, making the tracking process memory intensive and computationally demanding, although still considerably less demanding than when using the various types of CFD methods solved on Eulerian grids (described in Chapter 14). The vortex wake method must be supplied with boundary conditions that relate the lift (bound circulation) on the blades to the strengths of the trailed vortex filaments. This is usually done by using a lifting line or lifting surface model, such as discussed in Section 14.9. Experience suggests that the FVM generally gives better predictions of blade loads than is possible with prescribed or rigid wake models. It can also, in principle, deal with transient problems such as when the turbine yaws into and out of the wind – all the wake dynamics can be accounted for in a time-accurate manner without having to make assumptions about the effects on the wake geometry or the time constants of the flow. Under transient conditions, the plane of the turbine may yaw momentarily into its own wake, raising the complexity of the problem of defining the induced velocity field even further.

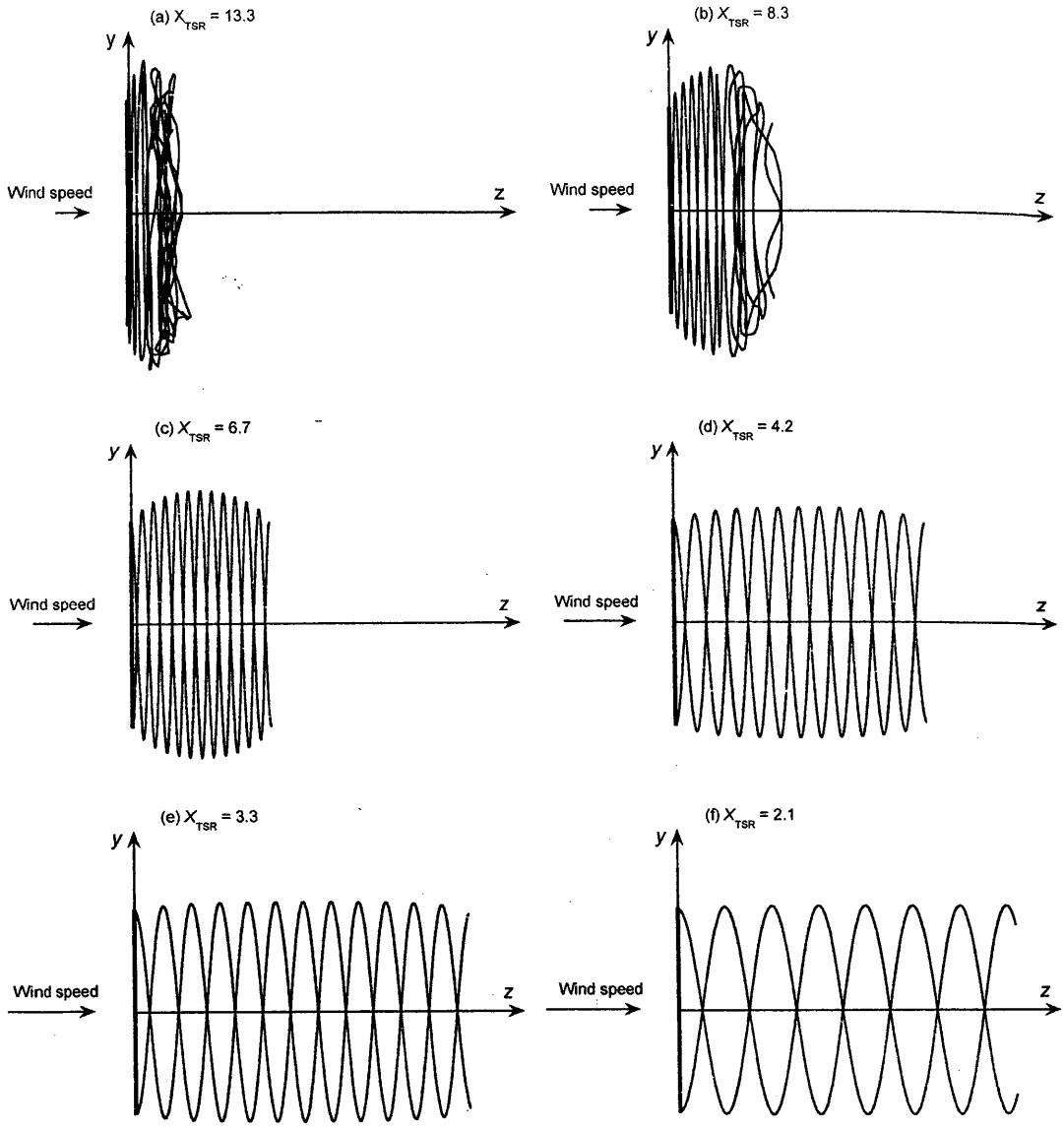

Figure 13.22 Predictions of the development of the vortex wake behind a wind turbine at various tip speed ratios using a FVM. Top views of wake: (a) $X_{TSR} = 13.3$, (b) $X_{TSR} = 8.3$, (c) $X_{TSR} = 6.7$, (d) $X_{TSR} = 4.2$, (e) $X_{TSR} = 3.3$, and (f) $X_{TSR} = 2.1$.

Representative examples of time-accurate FVM wake calculations for a HAWT are shown in Fig. 13.22. In both cases, the wake geometry is shown for a two-bladed HAWT operating in a steady wind speed at different tip speed ratios. Figure 13.22 shows top views of the wake geometry for zero yaw angle, with predictions of the corresponding power output in Fig. 13.23. At high tip speed ratios (low wind speeds) the induced velocity at the turbine is a large fraction of the wind speed and so the turbine operates in the vortex ring state. This can be seen in Fig. 13.22(a) by the accumulation of wake vorticity near the turbine disk. Increasing the wind speed causes the wake to develop into the turbulent wake state [see Fig. 13.22(b)], which is characterized by a wake instability and turbulence downstream

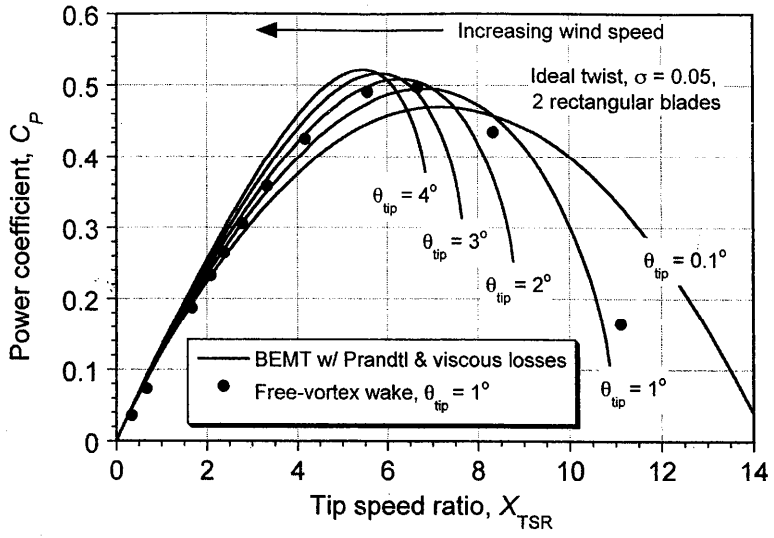

Figure 13.23 Power coefficient as a function of tip speed ratio using vortex wake and BEMT theories.

of the disk. As the turbine approaches the point of maximum efficiency for $X_{TSR} \approx 6$ notice that the wake expands downstream of the disk because at this condition the turbine is now extracting maximum energy from the wind and slowing (braking) the flow. As the vortices age, they diffuse under the action of viscosity and turbulence (see Section 10.6.2) and the wake slowly begins to contract again. Further decreases in X_{TSR} cause the wake to convect more quickly downstream, and then the wake expansion decreases as the power output drops.

Figure 13.24 shows time-dependent FVM calculations where the turbine quickly yaws 30° out of wind from an initial operating condition near to its peak efficiency. Such a situation can also be produced when the wind direction changes. This serves to illustrate several points about wind turbine performance, in particular the nonuniformity of the inflow and the unsteady aerodynamic effects produced in the wake when the turbine continuously yaws into and out of the wind. Initially, just after the yaw starts, the turbine blades move into their own wake. This is a situation where there can be relatively powerful interactions between the blades and discrete vorticity in the wake, leading to highly unsteady local blade loads. However, these blade–wake interactions are not as severe as those found on helicopters. Notice that the adjustments to the developing wake take place relatively slowly, with the older part of the wake disintegrating and the new part near the rotor continuously evolving. Only after about ten turbine revolutions does the solution become essentially quasi-steady and periodic once more. In this condition, the component of wind velocity parallel to the plane of the disk begins to skew the wake, which induces a velocity field that causes the wake to roll up along its top and bottom edges. This is another source of the gradient in the induced velocity across the plane of the disk that inflow models (such as Eq. 13.63) attempt to mimic.

The corresponding time-history of the power output from the turbine under these conditions is shown in Fig. 13.25. Notice that the power output drops rapidly by an amount that is proportional to the cube of the change in yaw angle, as would be suggested by Eq. 13.2. In this case, an initial 35% reduction in power output is caused by the 30° yaw misalignment to the wind. Thereafter there is some recovery in average power output as the wake structure

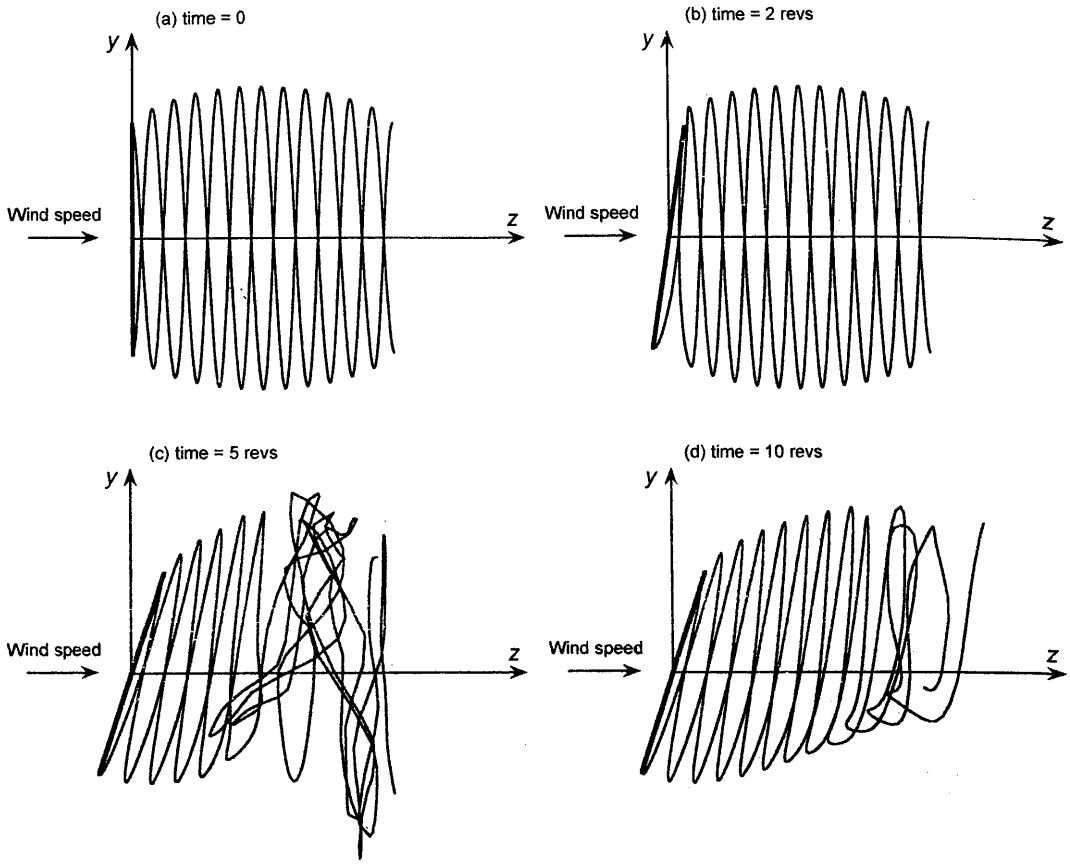

Figure 13.24 Free-vortex wake calculations of a three-bladed wind turbine yawing 30° out of wind. Top views of evolving wake: (a) Time = 0. (b) Time = 2 revs. (c) Time = 5 revs. (d) Time = 10 revs.

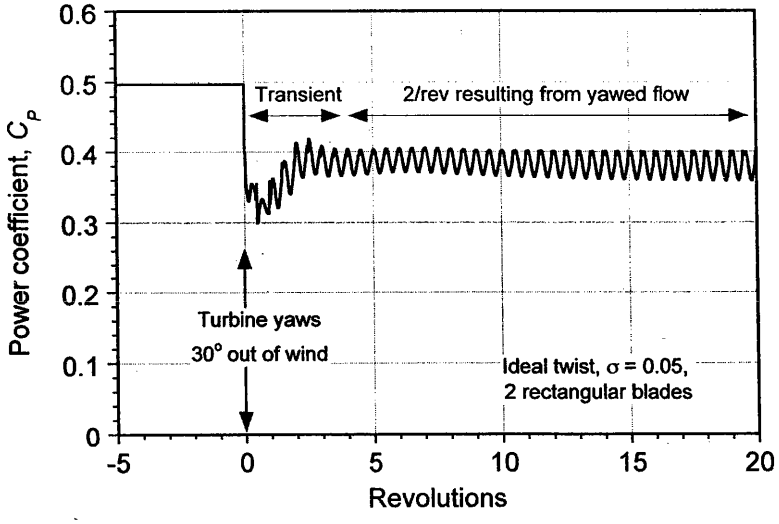

Figure 13.25 Power coefficient as a function of time for the condition when the turbine is suddenly yawed out of the wind.

reorganizes and the inflow velocities over the turbine disk reach an equilibrium. These non-steady inflow effects are often modeled in wind turbine analyses using variations of dynamic inflow theory, an approach discussed previously in Section 10.9. The idea is to consider the unsteady aerodynamic lag of the inflow development over the turbine disk in response to changes in blade pitch inputs or changes in turbine thrust. The equations describing the distribution of inflow are written in the form of a set of ordinary differential equations, with a time constant (or constants) representing the dynamic lag in the buildup of the inflow. Dynamic inflow models mathematical form and relative numerical efficiency, and their predictive success for various applications in the helicopter field are attractive because of their simplicity (see Section 10.9). However, the models have not been rigorously validated for rotors operating in the windmill state, although see Houston & Brown (2003) for some further insight into this issue. The main advantage of representing the aerodynamic model as sets of ordinary differential equations is that this form is appealing for many structural dynamic and aeroelastic analyses of the wind turbine, and this formulation of the inflow model allows the entire coupled problem to be solved simultaneously using the same numerical methods. For a discussion and background of dynamic inflow models applied to wind turbine problems see Bierbooms (1991), Snel & Schepers (1991), Hansen & Butterfield (1993), and Snel (2001). Bierbooms (1991) and Snel & Schepers (1991) suggest specific values of the wake time constants for wind turbine work, based on empirical evidence of the "induction lag." Based on the results from the FVM the complexity of the physics of the unsteady wake problem cannot be underestimated. Yet, if the time constant(s) of a dynamic inflow model can be obtained, say using time-accurate vortex–wake calculations suitably validated with controlled experiments, then this approach provides a particularly useful form of parsimonious model that can relate changes in turbine loads to the lag in the inflow development.

13.12 Unsteady Aerodynamic Effects on Wind Turbines

It will be apparent from Fig. 13.24 that in the yawed (out of wind) case the component of the wind speed produced in the plane of the turbine produces a N_b/rev unsteady aerodynamic excitation at the blades and so the net power output must fluctuate. Because of the relatively low rotational velocity of wind turbines (about 20 rpm for large turbines and up to 800 rpm for small turbines) and low tip speeds compared to a helicopter, changes in wind speed (or turbulent fluctuations) can result in significant changes in AoA at the blade elements compared to the velocity induced by blade rotation alone. There are also blade flapping effects to consider, assuming that the blades are indeed free to flap about a teetering or gimbaled hub (see Chapter 4). The resulting changes in local AoA and onset velocity contribute significantly to the unsteady flow environment at the blades. While unsteady aerodynamic effects occur under other operating conditions and as a result of other sources, the out of wind (yaw misalignment) performance of the wind turbine is of fundamental importance in wind turbine design.

Wind turbines operate for most of their time in a relatively unsteady flow environment – see Robinson et al. (1995), Huyer et al. (1996), Schreck et al. (2000), and Leishman (2002). Figure 13.26 summarizes the various sources of unsteady airloads on a wind turbine. It is apparent that, like the helicopter, these sources can be decomposed into a variety of essentially periodic and aperiodic contributions. The airloads on each blade element vary in time because of yawed flow, shear in the ambient wind, ambient turbulence, blade flapping and vibratory displacements, and other factors such as "tower shadow" (see Section 13.12.1). Despite the unsteady flow environment, however, wind turbines tend to be relatively quiet

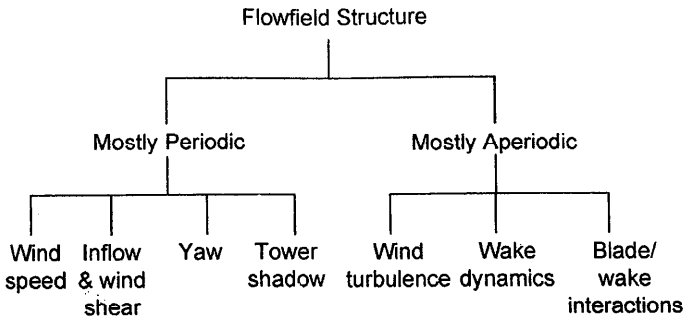

Figure 13.26 Summary of the various aerodynamic sources that contribute to the airloads on a wind turbine.

compared to helicopter rotors, mainly because of their much lower tip speeds – see Hubbard & Shepherd (1990). However, there are still variety of challenging acoustic problems, including both low- and high-frequency noise sources. Large, slow-turning wind turbines can also produce subaudible frequencies that can cause a human to experience discomfort or pain.

While the physics and prediction of unsteady effects have been discussed in Chapters 8 and 9 in regard to helicopters, the issues associated with wind turbines are particularly acute because large amplitude flow perturbations and high reduced frequencies may be involved. A particularly interesting aspect of the wind turbine aerodynamics problem is a quantification of the unsteadiness associated with the flow field and the turbine operating state. This can be done using the reduced frequency, k, which has been shown in Section 8.4 to be a measure of the amount of unsteadiness in the flow. While many flow disturbances may be transient and aperiodic in nature, it is convenient to characterize unsteady problems, in general, in terms of an effective reduced frequency. Because of the typically low rotational velocities of wind turbines, perturbations at the blade elements may experience high effective values of reduced frequency, and especially so when moving inward along the blade from its tip because the local rotational values of velocity at the blade elements becomes smaller. Consider the reduced frequency associated with the flow at a radial station r during yawed flow operations. If the yaw angle is γ then the reduced frequency associated with velocity fluctuations at the blade element is

$$k = \frac{\Omega c}{2(\Omega R r + V_\infty \sin\gamma)} = \left(\frac{1}{r + \sin\gamma / X_{\text{TSR}}}\right)\frac{c}{2R}. \tag{13.66}$$

With a typical value of the blade aspect ratio (R/c) being about 10 for a wind turbine with modest performance, it is apparent that reduced frequencies approaching 0.1 are not untypical. Only for $k < 0.05$, or thereabouts, can the flow be assumed to be steady or at least quasi-steady. As shown in Chapter 8, the analysis of unsteady flow problems is considerably more difficult than if steady flow is assumed. Specific unsteady aerodynamic effects that must be considered for the wind turbine are:

1. *Varying wind speed:* Experience suggests that the wind rarely blows at a constant speed and, combined with the relatively low induced velocity produced by wind turbines, modest wind speed fluctuations can change significantly the AoA at the blades. This can produce transients or spikes in the output from the turbine, which is undesirable. This effect also results in amplitude and phase changes of the local forces produced on the blades compared to those that might be predicted assuming

quasi-steady aerodynamics. There is a further lag in the development of the inflow in response to the changing downstream wake structure; such wake adjustments may take place over as many as 10 rotor revolutions.

2. *Velocity gradients in the wind:* The wind turbine operates in an atmospheric boundary layer with notable velocity gradients – see the schematic in Fig. 13.8. The effects of this gradient can also be seen to some extent in Fig. 13.20 where it is apparent that the lower part of the wake nearer the ground convects more slowly downstream than the upper part. This produces another source of nonuniformity in AoA over the turbine disk, producing a further source of unsteadiness at the blades.
3. *Nonsteady velocity fluctuations in yawed flow:* Large nonsteady variations in the local velocity at the blade elements will be produced whenever the wind turbine is misaligned (yawed) relative to the wind. This is a common occurrence because yaw control mechanisms usually cannot track the wind to sufficient accuracy for perfect alignment to be assured at all times. The low tip speeds of wind turbines means that large excursions from axial flow may occur, which can amplify unsteady effects even though the blade pitch and AoA may be relatively constant. Under these conditions the amplitudes of the excursions involved may often stretch the limits of the unsteady aerodynamic models, which are often derived under the assumption of small perturbations (see Section 8.13.)
4. *Nonsteady wake induction effect:* Time-varying aerodynamic conditions at the rotor will have an effect on the strength and positions of vorticity shed and trailed into the downstream wake. This evolutionary process has a hereditary effect depending on the prior time-history of the rotor airloads and appears as a temporal lag in the development of the inflow at the rotor disk. This problem has already been discussed in Section 13.11.
5. *Local sweep effects:* Another source of unsteady effects can be traced to the direction of the incident flow velocities on the rotating blades. Because of the relatively low rotational velocity of wind turbines, the local sweep angle of the flow at any blade element can be very large when the turbine is yawed. With attached flows the independence principle applies and no significant changes in airloads occur. However, the existence of a radial flow component can affect the development of the 3-D boundary layer on the blade and the onset of stall (see Section 13.12.2), leading to somewhat more complicated aerodynamic behavior than would be predicted under nominally 2-D conditions. (See Section 9.7 for further details.)
6. *Tower shadow effects:* For downwind machines the passage of the blade through the tower wake or "shadow" results in transient changes in AoA on the blade elements. Upstream machines also suffer from the effects of the tower, this effect being similar to the blade passage effect for the helicopter rotor/airframe problem (see Section 11.2.3). This interaction effect may involve effective reduced frequencies that exceed 0.2. The resulting blade loads cannot thus be predicted accurately using quasi-steady assumptions. Such problems also involve steep velocity gradients in the flow. At a modeling level the nonuniformity of the velocity field across the blade chord must be considered carefully. Such effects are modeled fairly well using the unsteady airfoil methods with imposed gust fields (see Section 8.16.3), although downstream wake effects may also have to be considered – see Munduate et al. (2003) and Wang & Coton (2001).

In general, the blade structural loads can be nonsteady because of additional factors, such as periodic variations of gravity forces on the blade in the rotating frame of reference,

transient rotational speed and blade flexibility. To calculate blade loads, coupled nonlinear equations involving rotational, inertial, and unsteady aerodynamic forces need to be solved for prescribed operating conditions. This is a major challenge for the wind energy community and parallels the issues known already for helicopters – see Section 14.11.

13.12.1 *Tower Shadow*

The effects of the tower wakes or "shadow" can be seen in the flow visualization of the downstream turbine shown in Fig. 13.20 where the bluff body-type flow from the upstream tower creates a velocity deficiency in the wind as it approaches the turbine disk. Experience suggests that there may be a 30% reduction in the local wind speed behind the tower. At a fundamental modeling level this problem is a good example where there is a need to distinguish properly the effects on the airloads on the blades arising from an assumed uniform change in a uniform AoA across the blade element from the effects resulting from a nonuniform velocity field. In an essentially incompressible flow, the former can be viewed as the net response to changes in AoA using superposition with the Wagner function (see Section 8.10). This is equivalent to assuming that at any instant the AoA is constant over the chord of the airfoil. This assumption is typical of what is used in many unsteady aerodynamic models for all modes of forcing. The latter can be viewed as the net response to a nonuniform vertical component of the velocity field using superposition with the Küssner function (see Section 8.11), which is the more accurate and correct assumption.

The velocity deficit in the flow behind the support tower can be modeled as a spatial variation in the velocity normal to the surface of the blade. In a 2-D model, the airfoil section moves rapidly through a velocity field, resulting in an attenuation in lift and a phase lag compared to the quasi-steady case. For the purposes of simple illustration, the problem can be modeled by assuming a 2-D airfoil traveling at unit velocity in an assumed velocity field normal to its chord given by $w = 0.08 + 0.02\cos(5\psi)$ where ψ is in radians defined for the range $144° \leq \psi \leq 216°$ and $w = 0.1$ elsewhere. The results in Fig. 13.27 show

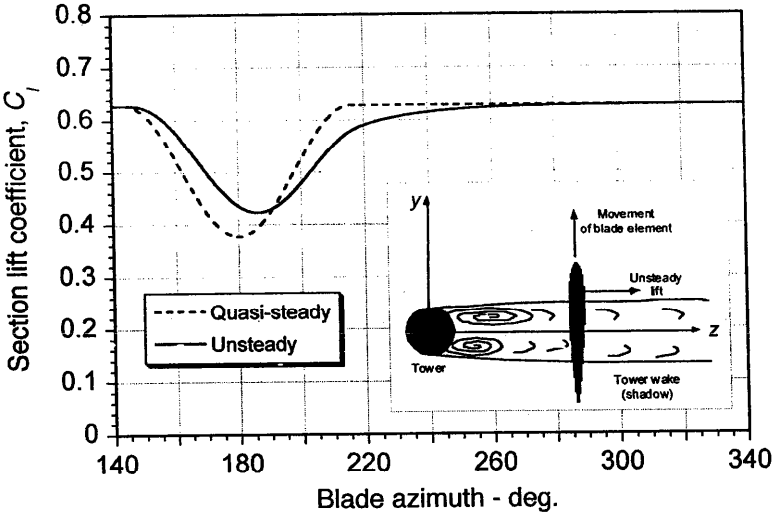

Figure 13.27 Prediction of the unsteady lift during a simulated tower shadow encounter using 2-D unsteady airfoil theory.

the differences in unsteady airloads produced using the steady and unsteady predictions. Clearly there are significant differences and the results emphasize again the importance of modeling unsteady effects if reliable quantitative predictions of the airloads are a goal. See also Munduate et al. (2003) for an analysis of the tower shadow problem and a comparison with measured airloads on the turbine blades.

13.12.2 *Dynamic Stall and Stall Delay*

It has been explained in Chapter 9 how the phenomenon of dynamic stall can give rise to large unsteady blade airloads that can limit the performance of a rotor system. While dynamic stall is a well-known unsteady flow problem found on wind turbines, the foregoing discussion has emphasized that unsteady airloads will be produced even in the absence of dynamic stall. These effects manifest as both amplitude and phase changes in the blade airloads compared to what would be obtained under quasi-steady conditions. Both circulatory and noncirculatory contributions to the airloads are, of course, always involved (see Chapter 8).

A prerequisite to predicting dynamic stall and its onset is to predict adequately the unsteady airloads under attached flow conditions. Despite its apparent simplicity compared to the stalled case, however, this is a nontrivial problem for which the development of general models that are valid for the turbine environment is still a major challenge. Currently, dynamic stall must be modeled using more parsimonious, semi-empirical models, for which a number of different approaches have been developed for helicopter applications (see Section 9.5) and adapted for wind turbine use. Many modern wind turbine analyses use the method developed by Leishman & Beddoes (1989), which has been modified and popularized by Pierce & Hansen (1995). However, while often giving good results, these models are not strictly predictive tools and can really only be used confidently for conditions that are not too much different from the conditions under which the models were originally validated.

The problem of dynamic stall is of particular importance on wind turbines because the large unsteady airloads that are produced (see Fig. 13.19) can cause structural damage – see Shipley et al. (1994). However, the power output from a wind turbine can be regulated deliberately by promoting stall, either by pitch regulation or through airfoil design (see Section 13.9). An example is shown in Fig. 13.28 where the onset of stall creates much turbulence over the blade and in the downstream wake. Unfortunately the prediction of dynamic stall has not yet been very successful on wind turbines. While part of the problem is the imprecise modeling of the delayed onset of flow separation resulting from unsteady aerodynamic effects, there are also subtle 3-D effects unique to the rotating environment that seem particularly pronounced on wind turbines.

In summary, the effects underlying the problem of dynamic stall can be divided into two areas: 1. Unsteady pressure gradient reduction effects on the blade, which give rise to delays or lags in the development of the 3-D boundary layer compared to that obtained under quasi-steady conditions; and 2. Coupled influences of the centrifugal and Coriolis effects acting on the boundary layer in the rotating flow environment (i.e., a radial flow effect). In general it is fair to say that a better integrated modeling capability for dynamic stall depends on gaining a much better understanding of the physics governing the 3-D boundary layer developments on rotating blades, both with wind turbines and helicopter rotors.

Several experimental and modeling studies have provided some insight into 3-D effects on rotating blades operating near stall – see Young and Williams (1972), Madsen &

Figure 13.28 The onset of stall on the turbine produces highly nonlinear aerodynamic loads and a turbulent wake structure. Source: Photo courtesy of NREL.

Christensen (1990), Snel (1991), Narramore & Vermeland (1992), Dwyer & McCroskey (1971), Robinson et al. (1999), and Schreck et al. (2000, 2001). The first observations of the phenomenon are often attributed to Himmelskamp (1950). The motivation is clear, in that when stall occurs existing performance methods tend to predict power outputs that are lower than those actually measured. From an order of magnitude analysis of the 3-D boundary layer equations applied to a rotating flow environment, Snel (1991) has speculated that the Coriolis acceleration terms can act to alleviate adverse pressure gradients and so may delay the onset of flow separation and stall, but see also Corten (2000) for a critique of this analysis. The Coriolis and centripetal acceleration terms can be seen in a modified form of the boundary layer equations (see Section 7.3.2) first given by Fogarty (1951):

$$\frac{\partial u}{\partial x} + \frac{\partial w}{\partial z} = 0 \quad \text{(continuity)}, \tag{13.67}$$

$$u\frac{\partial u}{\partial x} + v\frac{\partial u}{\partial z} - \Omega^2 x = -\frac{1}{\rho}\frac{\partial p}{\partial x} + \nu\frac{\partial^2 u}{\partial z^2} \quad (x \text{ momentum}), \tag{13.68}$$

$$u\frac{\partial v}{\partial x} + w\frac{\partial v}{\partial z} + 2\Omega u - \Omega^2 x = -\frac{1}{\rho}\frac{\partial p}{\partial y} + \nu\frac{\partial^2 v}{\partial z^2} \quad (y \text{ momentum}), \tag{13.69}$$

and

$$-\frac{\partial p}{\partial z} = 0 \quad \text{(pressure gradient normal to surface)}, \tag{13.70}$$

where x is chordwise, y is spanwise, and z is normal to the blade. The $\Omega^2 x$ terms are centripetal accelerations and the $2\Omega u$ term is a Coriolis acceleration. Fogarty (1951) has calculated the radial or spanwise development of the boundary layer flow on the blade and has shown that for helicopter rotors these effects are small, except near the inboard part of the blade. It is here, however, where the blades of wind turbines (because of their design) tend to exhibit much higher values of lift coefficients compared to a helicopter rotor, and so the effects of radial flow can be more important here. Experimental results have shown increases in sectional maximum lift coefficients significantly beyond what would be expected based on using 2-D static airfoil characteristics. The helicopter rotor experiments of Dwyer & McCroskey (1971) also suggest favorable effects on the spanwise development of the boundary layer, which tend to delay the onset of flow separation to a higher blade section AoA and thus serve to increase the maximum thrust of the rotor system.

Similar observations have been found using CFD methods such as in the work of Narramore (1992), although confidence in these types of analyses to represent fully stalled flows is not yet high enough. As a result, approximate methods have been developed to model the observed 3-D "stall delay" effects – see Corrigan (1994) and Du & Selig (1998). A rigorous approach is still lacking because these models have not been validated under unsteady conditions or for situations where dynamic stall may occur. It has been shown in Chapter 9 that dynamic stall is fundamentally different to the phenomenon of static stall, so this is clearly an area where much further research is necessary if better 3-D models of unsteady airfoil behavior representing stall are to be developed and used confidently for rotor airloads predictions in either helicopter rotor or wind turbine work. To model these more general 3-D effects, the complexity of the models must usually be increased and parameters added. One must be cautious though that modeling accuracy is not obtained at the expense of the parsimony that is necessary to use these models in design analyses, or to destroy confidence in predictions – see page 808 for a discussion of this point.

13.13 Advanced Aerodynamic Modeling Requirements

There are a number of comprehensive models that have been developed for the analysis of wind turbines. Many of these models encompass the principles of the BEMT and are coupled to the structural dynamic analysis of the wind turbine and its tower. Such approaches parallel the philosophy of the comprehensive models used for helicopter analyses (Section 14.11) – see Manwell et al. (2002) for a discussion of the capabilities of these models. Yet although the fundamentals of wind turbine design are fairly well understood, the success at predicting blade loads and power output does not yet seem as great as would be desired. This is reflected in a recent "blind" prediction of the loads and performance of a comprehensively instrumented wind turbine that was tested under controlled conditions in the 80 × 120 ft (24.4 × 36.6 m) wind tunnel at NASA – see Fingersh et al. (2001). The primary objective of these experiments was to create a definitive set of turbine airloads and performance measurements, over a wide range of operating conditions, that was free of the uncertainties caused by the various atmospheric effects that are always found in field tests

with turbines. These wind tunnel results provided the analyst with an opportunity to really understand better the physics of wind turbine aerodynamics and perhaps gives a definitive data resource for validating predictive methods and resolving outstanding modeling issues. The results from the NREL blind comparisons [Simms et al. (2001)] showed considerable deficiencies between the various predictions for blade loads and turbine power output, even for unyawed, unstalled operating conditions. Such results underline the need for more fundamental research in aerodynamic subcomponent methodologies and their interdependent coupling if overall predictions are to be improved.

As in helicopter work, advanced computational aerodynamic methods based on numerical solutions to the Euler and Navier–Stokes equations (see Chapter 14) have begun to see some use in wind turbine analysis. This class of CFD methods has the potential to provide a consistent and physically realistic simulation of the turbine flow field. The huge computational costs, large memory requirements, and numerous numerical issues associated with such CFD methods (see the detailed discussion in Chapter 14) means that they have not yet seen significant use in wind turbine applications. In particular, problems involving flow separation, such as dynamic stall, have proved extremely challenging for Navier–Stokes based methods, in part because of a need to develop better turbulence models. Also, the prediction of the 3-D vortical wake behind a turbine has proved just as daunting for CFD as for any other type of method. This is because vortical wake formation is a result of complex 3-D, viscous, separated flow effects and also because the numerical methods have difficulty in preserving concentrated vorticity as it is convected downstream.

While it is clear that some have begun to take up the challenge of modeling wind turbine problems using CFD – see Duque et al. (1999, 2000, 2003) and Iida (2001) – the capabilities of these methods have not yet been validated sufficiently to be assigned the confidence levels that are necessary for wind turbine design purposes. With faster computers and with improved numerical algorithms, CFD methods will ultimately prevail and will become increasingly used in the design of better and more efficient wind turbines.

13.14 Chapter Review

This chapter has introduced the aerodynamics of the wind turbine, mainly to show both the differences between and similarities to helicopter rotors. The idea that the wind contains energy has been outlined and the ability of a wind turbine to extract that energy has been explained. It is apparent that many strides have been made in the understanding and modeling of wind turbine aerodynamics, especially over the last two decades where environmental concerns have driven more research into renewable energy resources. For the future there is a need to refine and expand existing models and in some cases to develop new aerodynamic models that can encompass a wider range of operating conditions and wind turbine flow states. This will allow adverse effects to be properly predicted early in the design cycle and more efficient and reliable wind turbines to be designed for the future.

It has been shown how predictive approaches for wind turbine aerodynamics have paralleled the methods used for helicopter analysis. The fundamental performance of the machine has been examined using momentum theory and blade element momentum theory (BEMT). Despite its relative simplicity and limitations, the BEMT allows a clear examination of the design factors that influence wind turbine performance and design. However, the BEMT is limited in terms of generality to a less than desirable range of operating conditions.

These limitations are largely eliminated with the use of aerodynamic methods based on vortex theory. Today, most engineering methods used in wind turbine analyses are based on blade element theory combined with either inflow models or vortex models to represent the nonuniform induced velocity associated with the vortical wake trailed from the turbine. One advantage of this class of predictive methods is the flexibility to include a wide range of validated subcomponent models representing various physical effects that are difficult to model from first principles. This approach also allows the subcomponent models to be validated against idealized laboratory experiments, and the flexibility to progressively upgrade the models as a deeper understanding of the physics is obtained. They can also be combined with structural dynamic models of the blades, tower, and power generation systems to produce powerful aeroelastic tools for the detailed structural design of wind turbines. As in the case of all predictive models, however, sustained validation of the approach against experimental measurements is essential, despite the inherent difficulties and lengthy nature of the process.

It is clear, however, that there are two key areas that need continued consideration if the aerodynamic design of wind turbines is to be further improved. These are the modeling of the turbine wake and the modeling of the unsteady aerodynamics of the blade sections. Inflow models have attractive mathematical forms and low computational overheads that will always be useful for certain types of aerodynamic and turbine performance analyses. Vortex wake methods are attractive because of their appealing physical nature and their flexibility to handle a broad range of steady and transient operating conditions. While "prescribed" vortex wake models have seen some use in wind turbine applications, they have limited scope in practical applications, and today they are fast being surpassed by free-vortex wake approaches. It is still up to the wind energy practitioner to use these modeling tools, to explore their capabilities, and to determine the limitations in their use through validation studies with measurements. Only when this is done will the analyst be in a position to decide which models require further development. While it has been emphasized that significant unsteady effects may be produced on wind turbines even with the absence of dynamic stall, the particular problems produced by dynamic stall remain a serious concern for wind turbines, even for pitch-controlled machines. In higher winds when much of a wind turbine blade can be stalled, existing performance methods tend to predict power outputs that are considerably lower than those actually measured. Some of the potential mechanisms contributing to the 3-D aspects of the problem have been discussed, although the exact mechanisms at play still require a much deeper analysis of the flow. While a full understanding and modeling of these problems is the subject of ongoing research, they can, in most cases, be traced to the development of the 3-D boundary layer on the rotating blades.

13.15 Questions

13.1. If a wind turbine is operated with a yaw misalignment angle of γ, explain how its power output and its efficiency will be affected. What other aeromechanical problems may be caused by yaw misalignment?

13.2. If the wind speed at a particular wind turbine fluctuates with intensity I_u, find an approximate relationship for the average power output from the turbine, including the wind speed fluctuations. Compare the results for different values of the wind fluctuation.

13.3. Compare the power output from a 5-m-diameter wind turbine operating at a hub height of 10 m versus a hub height of 15 m when the upstream terrain consists primarily of open grassy fields. If the upstream terrain has trees, estimate the new height of the tower that would be necessary to give the same power output.

13.4. Consider the performance of a series of commercially available wind turbines as given in the following table. Determine the efficiency of the turbines at their rated speed. Comment on your results.

Rated power (MW)	Rated wind speed (m/s)	Diameter (m)
0.22	14	29
0.66	15	47
1.50	15	64
1.65	17	66
2.0	15	80

13.5. Discuss the assumptions and fundamental limitations of the blade element momentum theory as it is (or would be) applied to a wind turbine. Explain how the theory could be improved to extend its limits of applicability.

13.6. Starting from the equations for the thrust and torque obtained from the combined blade element momentum theory, show that, in the case where the blade twist is assumed to be ideally distributed (i.e., hyperbolically), the wake induction factor is constant across the turbine disk. Show further that in this case the net rotor thrust and power reduce to the values that are given by the simple momentum theory. Assume no tip losses.

13.7. A person argues that giving a wind turbine more blades will result in more efficient energy extraction from the wind. Show using the blade element momentum theory (BEMT) why this reasoning is not strictly correct.

13.8. Explain why the aerodynamic efficiency of a wind turbine is improved by incorporating blade twist. Using the blade element momentum theory find the relationship between maximum aerodynamic efficiency and blade twist for blades that are linearly twisted from root to tip. Make any assumptions that are needed, but justify them.

13.9. Wind turbines must often be shut down completely in high wind conditions. Is this an aerodynamic or mechanical limitation, or both? Explain.

13.10. What is the main difference between a pitch regulated wind turbine and a stall regulated wind turbine? Explain the relative aerodynamic and mechanical advantages and disadvantages of both types of design.

13.11. Tower "shadow" can be a source of impulsive unsteady aerodynamic loads on the blades of a wind turbine. Explain the flow physics behind this phenomenon, and explain how the effects on the blade loads might be mitigated.

13.12. Why is dynamic stall a problem on wind turbines, and how is it manifest? Under what operating conditions might dynamic stall be expected to occur on a wind turbine blade?

Bibliography

Bergy, K. H. 1979. "The Lanchester–Betz Limit," *J. of Energy*, 3 (6), pp. 382–384.

Bierbooms, W. 1991. "A Comparison Between Unsteady Aerodynamic Models," European Wind Energy Conference, Amsterdam, The Netherlands, Oct. 14–18.

Buhl, M. L. 2004. "A New Empirical Relationship Between Thrust Coefficient and Induction Factor for the Turbulent Windmill State," NREL/TP-500-36834, Sept.

Burton, T., Sharpe, D., Jenkins, N., and Bossanyi, E. 2001. "Wind Energy Handbook," John Wiley & Sons, Ltd., Chichester, England.

Clark, R. N. and Davis, R. G. 1991. "Performance Changes Caused by Rotor Blade Surface Debris," American Wind Energy Assoc. *Windpower '91*, Palm Springs, CA, Sept. 24–27.

Coleman, R. P., Feingold, A. M, and Stempin, C. W. 1945. "Evaluation of the Induced Velocity Fields of an Idealized Helicopter Rotor," NACA ARR L5E10.

Corrigan, J. 1994. "Empirical Model for Stall Delay Due to Rotation," American Helicopter Soc. Aeromechanics Specialist Meeting, San Francisco, CA, Jan. 19–21.

Corten, G. P. 2000. "Inviscid Stall Model," 13th IEA Symposium on Aerodynamics of Wind Turbines, Golden, CO, Dec. 4–5.

Coton, F. N. and Wang, T. 1999. "The Prediction of Horizontal Wind Turbine Performance in Yawed Flow Using an Unsteady Prescribed Wake Model, Institute of Mechanical Engineers, Part A, *J. of Power and Energy*, 213, pp. 33–43.

Coton, F. N., Wang, T., and Galbraith, R. A. McD. 2002. "An Examination of Key Aerodynamic Modeling Issues Raised by the NREL Blind Comparison," AIAA Paper 2002-0038, 21st ASME Wind Energy Symposium and the 40th AIAA Aerospace Sciences Meeting, Reno, NV, Jan. 14–17.

Darrieus, F. M. 1931. "Turbine Having its Rotating Shaft Transverse to the Flow of Current," US Patent No. 1,834,018.

Du, Z. H. and Selig, M. S. 1998. "A 3-D Stall Delay Model for HAWT Performance Prediction," AIAA Paper 89-0021, 36th AIAA Aerospace Sciences Meeting and Exhibit and 1998 ASME Wind Energy Symposium, Reno, NV, Jan. 12–15.

Duque, E. P. N., van Dam, C. P., Brodeur, R. R., and Chao, D. D. 1999. "Navier–Stokes Analysis of Time-Dependent Flows About a Wind Turbine," 3rd ASME/JSME Joint Fluids Engineering Conference, July 18–23.

Duque, E. P. N., Johnson, W., van Dam, C. P., Cortes, R., and Yee, K. 2000. "Numerical Prediction of Wind Turbine Power and Aerodynamic Loads for the NREL Phase II Combined Experiment Rotor," AIAA Paper 2000-0038, 19th ASME Wind Energy Symposium and the 38th AIAA Aerospace Sciences Meeting, Reno, NV, Jan. 10–13.

Duque, E. P. N., Burkland, M. D., and Johnson, W. 2003. "Navier–Stokes and Comprehensive Performance Predictions of the NREL Phase IV Experiment," AIAA Paper 2003-0355, 22nd ASME Wind Energy Symposium and the 41st AIAA Aerospace Sciences Meeting, Reno, NV, Jan. 5–8.

Dwyer, H. A. and McCroskey, W. J. 1971. "Crossflow and Unsteady Boundary-Layer Effects on Rotating Blades," *AIAA J.*, 9 (8), pp. 1498–1505.

Eggers, A. J., Chaney, K., Holley, W. E., Ashley, H., Green, H. J., and Sencenbaugh, J. 2000. "Modeling of Yawing and Furling Behavior of Small Wind Turbines," AIAA Paper 2000-0020, 19th ASME Wind Energy Symposium and the 38th AIAA Aerospace Sciences Meeting, Reno, NV, Jan. 10–13.

Eggleston, D. M. 1991. "Wind Turbine Bug Roughness Sampling and Power Degradation," American Wind Energy Assoc. *Windpower '91*, Palm Springs, CA, Sept. 24–27.

Eggleston, D. M. and Stoddard, D. M. 1987. *Wind Turbine Engineering Design*, Van Norstrand Reinhold Co., New York, NY.

Fingersh, L. J., Simms, D., Hand, M., Jager, D., Cotrell, J., Robinson, M., Schreck, S., and Larwood, S. 2001. "Wind Tunnel Testing of NREL's Unsteady Aerodynamics Experiment," AIAA Paper 2001-0035, 20th ASME Wind Energy Symposium and the 39th Aerospace Sciences Meeting, Reno, NV, Jan. 8–11.

Fogarty, L. E. 1951. "The Laminar Boundary Layer On a Rotating Blade," *J. Aeronautical Sciences*, 18 (3), pp. 247–252.

Frost, W., Long, B. H., and Turner, R. E. 1978. "Engineering Handbook on the Atmospheric Environment Guidelines for Use in Wind Turbine Generator Development," NASA Technical Paper 1359.

Glauert, H. 1926. "The Analysis of Experimental Results in the Windmill Brake and Vortex Ring States of an Airscrew," ARC R & M 1026.

Glauert, H. 1935. "Airplane Propellers," In: Division L of *Aerodynamic Theory*, edited by W. F. Durand, Springer Verlag, Berlin, Germany. Reprinted by Peter Smith, Glouster, MA, 1976.

Glauert, H. 1983. *Elements of Aerofoil and Airscrew Theory*, 2nd Edition, Cambridge University Press, New York, NY.

Grant, I., Pan, X., Parkin, P., Powell, J., Reinecke, H., Shuang, K., Coton, F. N., and Lee, D. 2000. "An Experimental and Numerical Study of the Vortex Filaments in the Wake of an Operational, Horizontal-Axis Wind-Turbine," *J. of Wind Engineering and Industrial Aerodynamics*, 85 (2), pp. 177–189.

Hand, M. M., Simms, D. A., Fingersh, L. J., Jager, D. W., Cotrell, J. R., Schreck, S., and Larwood, S. M. 2001. "Unsteady Aerodynamics Experiment Phase VI: Wind Tunnel Test Configurations and Available Data Campaigns," NREL Report No. 29955, Dec.

Hansen, A. C. and Butterfield, C. P. 1993. "Aerodynamics of Horizontal-Axis Wind Turbines," *Annual Review of Fluid Mechanics*, 25, pp. 115–149.

Himmelskamp, H. 1950. "Profiluntersuchungen an einem Umlaufenden Propeller (Profile Investigations on a Rotating Propeller)" Max-Plank Institut für Stromungsforschung Göttingen, Germany.

Houston, S. S. and Brown, R. E. 2003. "Rotor-Wake Modeling for Simulation of Helicopter Flight Mechanics in Autorotation," *J. of Aircraft*, 40 (5), pp. 938–945.

Hubbard, H. H. and Shepherd, K. P. 1990. "Wind Turbine Acoustics," NASA Technical Paper 3057, DOE/NASA/20320-77.

Huyer, S. A., Simms, D. A., and Robinson, M. C. 1996. "Unsteady Aerodynamics Associated with a Horizontal-Axis Wind Turbine," *AIAA J.*, 34 (7), pp. 1410–1419.

Iida, M., Arakwawa, C., and Matsumiya, H. 2001. "Three Dimensional Navier–Stokes Flow Field Computations Through a Horizontal Axis Wind Turbine Blade," AIAA Paper 2001-0058, 20th ASME Wind Energy Symposium and the 39th AIAA Aerospace Sciences Meeting, Reno, NV, Jan. 18–11.

Kocurek, D. 1987. "Lifting Surface Performance Analysis for Horizontal Wind Axis Turbines," Solar Energy Research Institute, SERI/STR-217-3163.

Leishman, J. G. 2002. "Challenges in Modeling the Unsteady Aerodynamics of Wind Turbines," *Wind Energy*, 5, pp. 86–132.

Leishman, J. G. and Beddoes, T. S. 1989. "A Semi-Empirical Model for Dynamic Stall," *J. of the American Helicopter Soc.*, 34 (3), pp. 3–17.

Lock, C. N. H., Bateman, H., and Townend, H. 1925. "An Extension of the Vortex Theory of Airscrews with Applications to Airscrews of Small Pitch and Including Experimental Results," ARC R&M 1014.

Madsen, H. and Christensen, H. 1990. "On the Relative Importance of Rotational, Unsteady & Three-Dimensional Effects on the HAWT Rotor Aerodynamics," *Wind Engineering*, 14 (6), pp. 405–415.

Manwell, F. J., McGowan, J. G., and Rogers, A. L. 2002. *Wind Energy Explained*, John Wiley & Sons, New York, NY.

Miley, S. J. 1982. "A Catalog of Low Reynolds Number Airfoil Data for Wind Turbines Applications," Rockwell International, Rocky Flats Plant, RFP-3387.

Muljadi, E., Forsyth, T., and Butterfield, C. P. 1998. "Soft-Stall Control Versus Furling Control for Small Wind Turbine Power Regulation," American Wind Energy Assoc. *Windpower '98*, Bakersville, CA, April 27–30.

Munduate, X., Coton, F. N., and Galbraith, R. A. McD. 2003. "An Investigation of the Aerodynamic Response of a Wind Turbine to Tower Shadow," 4th ASME-JSME Joint Fluids Engineering Conference, Honolulu, HI, July 6–11.

Narramore, J. C. and Vermeland, R. 1992. "Navier–Stokes Calculations of Inboard Stall Delay Due to Rotation," *J. of Aircraft*, 29 (1), 1992, pp. 73–78.

Pierce, K. and Hansen, A. C. 1995. "Prediction of Wind Turbine Rotor Loads Using the Beddoes-Leishman Model for Dynamic Stall," *J. of Solar Energy Engineering*, 117, pp. 200–204.

Ramsay, R. R., Hoffman, M. J., and Gregorek. G. M. 1995. "Effects of Grit Roughness and Pitch Oscillations on the S809 Airfoil," NREL/TP-442-7817.

Robinson, M. C., Galbraith, R. A. McD., Shipley, D., and Miller, M. 1995. "Unsteady Aerodynamics of Wind Turbines," AIAA Paper 95-0526, 14th ASME Wind Energy Symposium and the 33rd Aerospace Sciences Meeting, Reno, NV, Jan. 9–12.

Robinson, M. C., Simms, D. A., Hand, M. M., and Schreck, S. J. 1999. "Horizontal Axis Wind Turbine Aerodynamics: Three Dimensional, Unsteady and Separated Flow Influences," 3rd ASME/JSME Joint Fluids Engineering Conference, San Francisco, CA, July 18–23.

Robison, D. J., Coton, F. N., Galbraith, R. A. McD., Vezza, M. 1995. "Application of a Prescribed Wake Aerodynamic Prediction Scheme to Horizontal Axis Wind Turbines in Axial Flow," *Wind Engineering*, 19 (1), pp. 41–51.

Savonius, S. J. 1931. "The S-Rotor and Its Applications," *Mechanical Engineering*, 53 (5), pp. 333–338.

Schreck, S. J., Robinson, M., Hand, M., and Simms, D. 2000. "HAWT Dynamic Stall Response Asymmetries under Yawed Flow Conditions," AIAA Paper 2000-0040, 19th ASME Wind Energy Symposium and the 38th AIAA Aerospace Sciences Meeting, Reno, NV, Jan. 10–13.

Schreck, S. J., Robinson, M. C., Hand, M. M., and Simms, D. A. 2001. "Blade Dynamic Stall Vortex Kinematics for a Horizontal Wind Axis Turbine in Yawed Conditions," *J. of Solar Energy Engineering*, 123, Nov., pp. 272–281.

Schepers, J. G. 1999. "An Engineering Model for Yawed Conditions Developed on the Basis of Wind Tunnel Measurements," Report ECN DE: ECN-RX–98-057, Energy Research Center of the Netherlands.

Shepherd, D. G. 1990. "Historical Development of the Windmill," NASA Contractor Report 4337, DOE/NASA/5266-1.

Shipley, D., Miller, M., Robinson, M., Luttges, M., and Simms, D. 1994. "Evidence that Aerodynamic Effects Including Dynamic Stall Dictate HAWT Structure Loads and Power Generation in Highly Transient Time Frames," NREL/TP-441-7080, Aug.

Simms, D., Schreck, S., Hand, M., and Fingersh, L. 2001. "NREL Unsteady Aerodynamics Experiment in the NASA-Ames Wind Tunnel: A Comparison of Predictions to Measurements," National Renewable Energy Laboratory, NREL/TP-500-29494.

Snel, H. 1991. "Scaling Laws for the Boundary Layer Flow on Rotating Wind Turbine Blades," 4th IEA Symposium on Aerodynamics for Wind Turbines, Rome, Nov. 20–21.

Snel, H. 2001. "Survey of Induction Dynamics Modeling with BEM-Like Codes: Dynamic Inflow and Yawed Flow Modeling Revisited," 20th ASME Wind Energy Symposium and the 39th AIAA Aerospace Sciences Meeting, Reno, NV, Jan. 8–11.

Snel, H. and Schepers, J. G. 1991. "Engineering Models for Dynamic Inflow Phenomena," European Wind Energy Conference, Amsterdam, The Netherlands, Oct. 14–18.

Spera, D. A. (Ed.) 1994. *Wind Turbine Technology: Fundamental Concepts of Wind Turbine Engineering*, American Soc. of Mechanical Engineers, ASME Press, New York, NY.

Tangler, J. L. 1987. "Status of the Special Purpose Airfoil Families," Solar Energy Research Institute, SERI/TP-217-3264.

Tangler, J. L. 2002. "The Nebulous Art of Using Wind Tunnel Airfoil Data and Blade-Element Momentum Theory for Predicting Rotor Performance," AIAA Paper 2002-0040, 21st ASME Wind Energy Symposium and the 40th AIAA Aerospace Sciences Meeting, Reno, NV, Jan. 14–17.

Tangler, J. L. and Somers, D. M. 1995. "NREL Airfoil Families for HAWTs," American Wind Energy Assoc. *Windpower '95*, Washington DC, March 26–30.

Thresher, R. 2002. "State of the Wind Industry: Technology, Economics & Future Evolution," Presentation by the National Renewable Energy Laboratory, April.

Vermeer, L. J. 2001. "A Review of Wind Turbine Wake Research at TU Delft," AIAA Paper 2001-0030, 20th ASME Wind Energy Symposium and the 39th AIAA Aerospace Sciences Meeting, Reno, NV, Jan. 8–11.

Vermeer, L. J., Sorensen, J. N., and Crespo, A. 2003. "Wind Turbine Wake Aerodynamics," *Progress in Aerospace Sciences*, 39, pp. 467–510.

Walker, J. F. and Jenkins, N. 1997. *Wind Energy Technology*, John Wiley & Sons, New York, NY.

Walker, J. F., Weber, T. L., and Wilson R. E. 1989. "A Comparison of Wind Turbulence Simulation Models for Stochastic Loads Analysis for Horizontal-Axis Wind Turbines," Solar Energy Research Institute, SERI/STR-217-3463.

Wang, T. and Coton, F. N. 2001. "A High Resolution Tower Shadow Model for Downwind Wind Turbines," *J. of Wind Engineering and Industrial Aerodynamics*, 89, pp. 873–892.

Young, W. H. and Williams J. C. 1972. "Boundary-Layer Separation on Rotating Blades in Forward Flight," *AIAA J.*, 10 (12), pp. 1613–1619.

CHAPTER 14

*Computational Methods for Helicopter Aerodynamics**

The ability to design rotorcraft with confidence requires a new order of aerodynamic predictive technology that is both true to the basic flow physics and readily usable by industry.

F. X. Caradonna (1990)

14.1 Introduction

This chapter reviews computational methods that have been applied or are being applied to the analysis of various problems in helicopter aerodynamics. The intention is not to review the details of such methods and their associated numerical algorithms per se, but to give a general overview of the underlying principles of the various approaches along with a summary of their capabilities and limitations for the various helicopter problems alluded to in previous chapters. The approaches are described with ample reference to original methodologies and results, as appropriate. A range of methods is covered in this chapter, from classical thin airfoil theory and surface singularity potential flow methods, to advanced computational methods that solve numerically the vorticity transport, Euler and Navier–Stokes equations. Several examples of the application of advanced aerodynamic methods to helicopter problems are also shown and discussed, with suggestions for areas of new research where appropriate.

While historically the helicopter industry has relied extensively on more parsimonious aerodynamic methods such as various forms of "momentum theory" combined with significant empiricism for helicopter design work, this is fast changing. See Gessow (1985) for a good historical review of helicopter predictive methodologies through 1980. Since then, rapid advances in computer technology (both in terms of speed and memory) have allowed much more ambitious numerical methods to be used in helicopter aerodynamics, and this has spawned a great deal of new fundamental work, both in fluid flow modeling and in algorithmic development. Aerodynamic problems that were once considered intractable, or were relegated to the fastest super-computers, are now solvable on desktop workstations. The tremendous recent advances in computer capabilities have played a large part in motivating and accelerating the development of more complete computational techniques for helicopter aerodynamic analysis, including vortex methods. This has helped to improve the rigor of the overall analysis and even to remove some of the more sweeping levels of empiricism – an important factor especially when new helicopters begin to depart from legacy designs.

It is the modeling of the rotor wake and its effects on the rotor and airframe that proves key to solving ultimately many of the outstanding problems in predicting helicopter performance

* This chapter was co-written with Richard Brown of Imperial College, University of London.

and improving helicopter design. The ability to better predict and understand rotor wake related problems continues to challenge the helicopter analyst, however, and it is here that further research must be focused. Advances in computer power have made possible the better integration of traditionally separate disciplines of helicopter analysis and will ultimately allow better rotor systems and more capable helicopters to be designed. Yet, bigger problems and more ambitious numerical techniques continue to push the limits of computer resources, with the ultimate (albeit elusive) goal of predicting the behavior of an entire helicopter in an arbitrary flight condition. Yet there is still much work to be undertaken before predictive models can be improved to the level that the aerodynamics of a new helicopter can be adequately predicted before its first flight.

Over the past two decades, advances have been made in the understanding of problems in helicopter aerodynamics using so-called computational fluid dynamics or CFD. Here, finite-difference or finite-volume approximations to the governing flow equations are used to model, from first principles, the complex flow field about the helicopter rotor and its airframe. The general field of helicopter CFD is reviewed by Caradonna (1990), Landgrebe (1988, 1994), McCroskey (1995), and Conlisk (2002). These works contain many references documenting past, present, and potentially future capabilities of CFD as it might be applied to helicopter problems. The choice of which governing equations to use affects the level of physics captured by the CFD scheme, as well as the computational effort and time taken to solve the problem. Furthermore, the choice of numerical method affects accuracy, stability, and cost. To some, the development of CFD by itself is held out to be the "Holy Grail" for the helicopter aerodynamicist, yet this is a very misleading perspective because CFD has its limitations. These limitations include grid dependent solutions, numerical issues, the ability to model turbulence, and so on. CFD methods must also be validated against measurements if they are to realize the high predictive confidence levels needed for design work. Therefore, CFD does not, by itself, hold the answer to all the various aerodynamic problems on helicopters. The real answer lies in the successful integration of advanced forms of aerodynamic analysis into other disciplines of engineering analysis. It is also unwise for other approaches to be abandoned in the shorter term while "CFD" matures to an accepted level of capability, given that this could still be decades off.

14.2 Fundamental Governing Equations of Aerodynamics

Documented work in helicopter CFD shows that a wide range of numerical techniques have been used to solve a hierarchy of equations governing the flow, these ranging from irrotational, inviscid potential flow approximations, through full-potential, to Euler and Navier–Stokes equations capable of resolving the effects of compressibility and turbulence. Each level in the hierarchy brings with it an increasing level of physical modeling capability but also more computational effort. A key issue in the use of these types of numerical methods is the definition of an appropriate computational grid surrounding the rotating and nonrotating parts of the helicopter on which to solve the governing equations. Other issues include the difficulties in modeling flow turbulence, on both the rotor and the airframe and in the rotor wake, and especially in the powerful tip vortices produced by the blades. Nonphysical numerical diffusion of wake vorticity produces errors in the wake solutions and has led to the development of adaptive gridding, overset grids, and other types of vorticity capturing schemes. Until these problems are better solved, however, aerodynamic models based on CFD alone will prove inadequate for helicopter design. The near future will continue to see the development of a range of hybrid models, using the best elements of CFD coupled with other forms of advanced analysis.

14.2.1 *Navier–Stokes Equations*

Many of the aerodynamic problems found on helicopters involve viscous effects and the generation of turbulence. These effects are important in the 3-D turbulent boundary layers found on the blades and airframe, unsteady flow separation and dynamic stall, the formation and subsequent structure of the blade tip vortices in the rotor wake, as well as in a host of rotor–airframe interaction phenomena. All of these problems have been alluded to in previous chapters.

The Navier–Stokes equations are the fundamental equations governing the fluid dynamics of the helicopter system. They encompass the principles of the conservation of mass, and momentum and energy interchange within a fluid. For a perfect fluid in three dimensions they can be written in a Cartesian, nonaccelerating coordinate system as

$$\frac{\partial \rho}{\partial t} + \frac{\partial(\rho u_j)}{\partial x_j} = 0 \quad \text{(Mass conservation)}, \tag{14.1}$$

$$\frac{\partial(\rho u_i)}{\partial t} + \frac{\partial(\rho u_i u_j)}{\partial x_j} = -\frac{\partial p}{\partial x_j} + \frac{\partial \tau_{i,j}}{\partial x_j} \quad \text{(Momentum interchange)}, \tag{14.2}$$

$$\frac{\partial(\rho h)}{\partial t} + \frac{\partial(\rho h u_j)}{\partial x_j} = \frac{\partial p}{\partial t} + u_j \frac{\partial p}{\partial x_j} + \tau_{i,j} \frac{\partial u_i}{\partial x_j} - \frac{\partial q_j}{\partial x_j} \quad \text{(Energy interchange)}, \tag{14.3}$$

with ρ as the flow density, $\mathbf{u} = u_i$, where $i = 1, 2, 3$, being the velocity vector, p is the pressure, h as the specific enthalpy, $\tau_{i,j}$ is the stress tensor, and $\mathbf{q} = q_i$, where $i = 1, 2, 3$, as the heat flux vector. The ideal-gas equation of state is usually used to relate the thermodynamic quantities using

$$p = \rho R T \quad \text{and} \quad h = C_p T, \tag{14.4}$$

where R is the gas constant, C_p is the specific heat at a constant pressure and T is temperature. The heat flux is usually given by the equation

$$q_i = -k \frac{\partial T}{\partial x_i}, \tag{14.5}$$

where k is the thermal conductivity of the fluid. Finally, the flow about the helicopter is invariably approximated as an isotropic Newtonian fluid, for which the relationship between stress and strain is given by

$$\tau_{i,j} = \frac{2}{3}\mu \delta_{i,j} \frac{\partial u_m}{\partial x_m} + \mu \left(\frac{\partial u_i}{\partial x_j} + \frac{\partial u_j}{\partial x_i} \right), \tag{14.6}$$

where $\delta_{i,j}$ is the Kronecker delta function ($\delta_{i,j} = 1$ for $i = j$ and $\delta_{i,j} = 0$ otherwise) and μ is the coefficient of dynamic viscosity.

For practical use, the Navier–Stokes equations are usually rewritten in so-called *conservation form* (compared to the tensor differential form given above), that is, in the form

$$\frac{\partial \mathbf{Q}}{\partial t} + \frac{\partial \mathbf{E}}{\partial x} + \frac{\partial \mathbf{F}}{\partial y} + \frac{\partial \mathbf{G}}{\partial z} = 0, \tag{14.7}$$

where $\mathbf{Q}$ is the conserved variable vector and $\mathbf{E}$, $\mathbf{F}$, and $\mathbf{G}$ are expressions, called the flux vectors, giving the rate at which mass, momentum, and energy are being transported at any

point in the flow. This latter equation is often expanded into a form with the viscous terms on the right-hand side to give

$$\frac{\partial \mathbf{Q}}{\partial t} + \frac{\partial \mathbf{E}}{\partial x} + \frac{\partial \mathbf{F}}{\partial y} + \frac{\partial \mathbf{G}}{\partial z} = \frac{\partial \mathbf{E}_v}{\partial x} + \frac{\partial \mathbf{F}_v}{\partial y} + \frac{\partial \mathbf{G}_v}{\partial z}, \tag{14.8}$$

where $\mathbf{E}_v$, $\mathbf{F}_v$, and $\mathbf{G}_v$ are the fluxes resulting from the viscosity of the flow. This form allows a reduction to the so-called thin-layer Navier–Stokes equations where the viscous derivatives with respect to the downstream and spanwise direction are neglected to give the form

$$\frac{\partial \mathbf{Q}}{\partial t} + \frac{\partial \mathbf{E}}{\partial x} + \frac{\partial \mathbf{F}}{\partial y} + \frac{\partial \mathbf{G}}{\partial z} = \frac{\partial \mathbf{S}}{\partial z}, \tag{14.9}$$

for a suitably defined viscous flux, S. A further reduction can be made by adopting a mathematical model for the turbulent contribution to the viscous fluxes in terms of the mean flow properties. In this form they are called the Reynolds averaged Navier–Stokes or RANS equations, and this form is used by many industrial strength computer codes.

It should be apparent that the Navier–Stokes equations are a set of strongly coupled, highly nonlinear partial differential equations. This means that they cannot usually be solved without making major simplifying assumptions. The most common practical simplification is to avoid the treatment of turbulent mixing and the associated viscous shearing effects by assuming a laminar flow. This greatly simplifies the solution of the Navier–Stokes equations, but it should be borne in mind that even at the lowest Reynolds numbers found on helicopters, the flow is turbulent. The need to model turbulence requires the introduction of empirical closure models, of which many types have been developed – see, for example, the popular models devised by Baldwin & Lomax (1978) and Spalart & Allmaras (1992). Resolution of the turbulence scales requires extremely fine grids with fine numerical discretization, and hence large amounts of memory and the fastest computers. Calculation of turbulence is difficult enough for even the simplest of flows and is certainly not yet practical for a complete helicopter. Nevertheless, solution of the Navier–Stokes equations will eventually be required for a full understanding of helicopter aerodynamics, even though practical use of these equations in the engineering design of new rotors and helicopters still lies a long way in the future.

There have been many algorithmic developments in the numerical solution of the Navier–Stokes equations. The fundamentals and historical development are summarized by Caradonna (1990), who also describes the various forms of the equations that are required for the analysis of various classes of helicopter problems. A key issue in any problem is the generation of the grid structure on which to solve the governing equations. Unlike a fixed-wing aircraft, a helicopter rotor induces significant velocities at large distances from itself. This means that the size of the computational domain, which should be as small as possible for economy, needs to be much larger than for corresponding fixed-wing problems if the possibilities of artificial flow recirculation and other nonphysical problems within the computational domain are to be avoided. This makes computer memory requirements very large indeed.

For most helicopter applications the Navier–Stokes equations are solved on a grid that rotates with the blades, an example being shown in Fig. 14.1. This requires a transformation to put the equations into a coordinate system that is stationary relative to the rotating hub. This transformation eases the problem of generating the grids used to calculate the flow about the blades, but introduces additional terms into the equations (to account for the acceleration of the coordinate system) that can destabilize the numerical method if not properly treated.

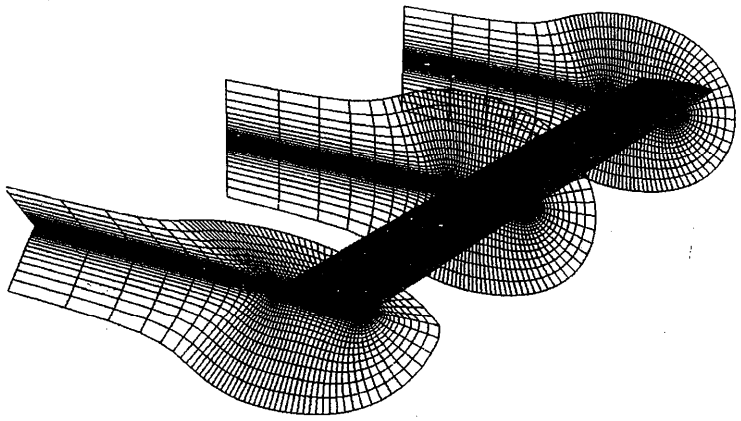

Figure 14.1 Example of the gridding of a helicopter rotor blade using C-type grids on which to solve the Navier–Stokes equations. Source: Grid courtesy of Karthikeyan Duraisamy.

Several types of grid systems are appropriate for analyzing various parts of the helicopter flow problem. Grids are categorized according to their geometric shape, that is, O-, C-, and H-type grids. The O- and C-type grids are often used for analyzing the flows about blades as they can be made to conform to the curved airfoil shape of the blade surface. H-type grids are sometimes used instead, as they allow a compromise between the advantages of a simple Cartesian grid geometry and an ability to refine the grid near the surface of the blade. Overset or chimera grid systems are locally refined grids that are superimposed upon a main (background) grid. These are useful in helping to resolve local flow phenomena without the need to grid the entire flow domain at high resolution. They can also be used to resolve the difficulties in dealing with a domain that is most easily meshed using separate grids that can move relative to each other. Interpolation routines are required to transfer information between the overset grids in the flow solver, and the accuracy of these procedures needs to be carefully controlled to avoid degrading the overall accuracy of the numerical solution. Structured grids such as these, though, can be very labor intensive to create. Unstructured grids, composed of irregularly distributed tetrahedral elements, are increasingly being used because these have the advantage that semi-automatic mesh generation software can be used to create this type of grid around very complex surface geometries.

The numerical technique used to solve the Navier–Stokes equations may be based on either a finite-difference or a finite-volume approach, and numerous algorithms have been developed, each with their own particular advantages. Finite-difference methods approximate the various space derivatives in the equations using expressions based on Taylor series approximations at each node on the computational grid. (A node can be considered as the intersection between grid lines.) Finite volume methods operate on an integral form of the Navier–Stokes equations, derived from Eq. 14.7, and treat the computational domain as a patchwork of cells rather than nodes. The integral of the mass, momentum, and energy within each cell is divided by the cell volume to get an average conserved variable and average fluxes are derived in a similar way by integrating over the boundary of the cell. Although there are many good computational reasons to adopt a finite-volume rather than a finite-difference approach, both approaches are ultimately equivalent in the mathematical sense. However, finite-difference methods can only operate on structured grids, whereas finite-volume methods can be used on both structured and unstructured grids.

Some of the first approaches to solving the Navier–Stokes equations (RANS equations), in this case for a rotor, are described by Agarwal & Deese (1988) and Wake & Sankar (1989). The effect of the rotor wake was computed by means of a vortex method and coupled to the Navier–Stokes solution for the blade flow by means of a correction to the AoA along the blades. This is the essence of the so-called loose or "weak" coupling procedure (see page 806). Many variations of this basic approach have followed this. One particularly promising modern Navier–Stokes approach for helicopter applications is called the Transonic Unsteady Rotor Navier–Stokes (TURNS) method – see Srinivasan & Baeder and colleagues (1992, 1993). More modern methods use a strong coupling approach where both the rotor and the wake flow are solved simultaneously. In the latest versions of this RANS-type method, a high-order discretization of the governing equations is used to limit the extent of the nonphysical numerical dissipation that is a well-known but very undesirable feature of finite-difference or finite-volume solutions to the Navier–Stokes equations. Another, similar method that has been used for helicopter applications is OVERFLOW, which is based on a general purpose Navier–Stokes code developed by NASA – see Chan et al. (2001) for an overview.

In these approaches, the rotor blades and computational domain are usually enveloped in body conforming grids, an example of which has been shown in Fig. 14.1. Here a rotor blade has been enveloped in a C-type grid to allow good resolution of the flow near the blade surface and in the wake downstream of the blade. All types of CFD methods solve the governing fluid dynamic equations to an accuracy that is dependent on the resolution of the grid, and Navier–Stokes calculations require these grids to be created to give extremely fine resolution of the flow near the blades and/or body surfaces (and in the wake downstream) where the viscous stresses are the highest.

14.2.2 *Euler Equations*

If turbulence and viscous effects do not need to be resolved (assuming these can be treated as weak effects in a given application), then the problem of gridding the computational domain to extremely fine resolution is obviated to some extent, allowing computational costs to be reduced by orders of magnitude. If the flow is assumed to be inviscid, then the Navier–Stokes equations reduce to a simplified set of equations, called the Euler equations, which can be solved instead. By simply dropping the viscous terms from the full Navier–Stokes equations, the Euler equations can be written in tensor differential form in Cartesian, nonaccelerating coordinates as

$$\frac{\partial \rho}{\partial t} + \frac{\partial(\rho u_j)}{\partial x_j} = 0 \quad \text{(Mass conservation)}, \tag{14.10}$$

$$\frac{\partial(\rho u_j)}{\partial t} + \frac{\partial(\rho u_i u_j)}{\partial x_j} = -\frac{\partial p}{\partial x_i} \quad \text{(Momentum interchange)}, \tag{14.11}$$

$$\frac{\partial(\rho h)}{\partial t} + \frac{\partial(\rho h u_j)}{\partial x_j} = \frac{\partial p}{\partial t} + u_j \frac{\partial p}{\partial x_j} \quad \text{(Energy interchange)}. \tag{14.12}$$

Alternately, by dropping the viscous terms from Eq. 14.8, the Euler equations can be written in conservation form as

$$\frac{\partial \mathbf{Q}}{\partial t} + \frac{\partial \mathbf{E}}{\partial x} + \frac{\partial \mathbf{F}}{\partial y} + \frac{\partial \mathbf{G}}{\partial z} = 0. \tag{14.13}$$

In practice the Euler equations have been found to yield a very good approximation to the high Reynolds number flows around real helicopters. Although the viscous terms are neglected, numerical solutions to the Euler equations can provide considerable insight into rather complicated flows. Vorticity in an inviscid flow, such as that governed by the Euler equations, should convect freely without any dissipation or diffusion. But the process of discretizing the Euler equations still leads to nonphysical numerical dissipation and diffusion of vorticity, however. This is an artifact of discretizing the spatial derivatives using Taylor's series approximations. Fortuitously, though, this behavior may improve, to some extent, the ability of numerical solutions to the Euler equations to mimic reality. For instance, airfoils and rotors modeled using the Euler equations should not generate lift, because the Euler equations by themselves do not allow circulation to be developed – this process takes place through the action of viscosity. In practice, however, the numerical solution of the Euler equations introduces an artificial source of viscosity, even an infinitesimal amount of which will allow the essentially viscous problem of flow over a lifting surface to be modeled using an inviscid set of equations. The Euler equations have been used with a great deal of success to predict aerodynamic loadings on rotor blades – see, for example, Roberts & Murman (1985), Sankar et al. (1986), and the reviews by Caradonna (1990) and Conlisk (2002).

Despite the limitations of using the Euler equations, Euler-based CFD methods have helped the helicopter manufacturing industry to gain new insight into many complex rotor problems and has allowed the limitations of simpler models (such as those used in comprehensive analyses; see Section 14.11) to be better understood. Yet, the high computational costs and numerical problems encountered in preserving the concentrated vorticity within the rotor wake have hindered application to many practical problems that require an accurate, long term treatment of the rotor wake, say over several rotor revolutions. This is particularly problematic for problems in BVI noise prediction. The inability of most Euler-based computational techniques to preserve the vorticity in the wake from dissipation at the hands of artificial numerical diffusion continues to form an opportunity for good research. Alternative methods such as vorticity transport and vortex methods continue to offer a good compromise in this regard. Although Euler-based methods will eventually be adopted as the simplest set of equations yielding acceptably accurate predictions of the flow around helicopters, the fundamental limitations of the approach should be recognized.

14.3 Vorticity Transport Equations

The use of vorticity transport models has seen some recent success in modeling the vortical flow structure of helicopter rotor wakes. This approach is intermediate between the Navier–Stokes and Euler based CFD techniques described in the previous sections and the free-vortex method (FVM) discussed in detail in Section 10.7.6. As previously mentioned, discretized approaches to solving the governing equations of the flow can suffer excessively from numerical dissipation of vorticity, for instance, in the rotor wake. This renders these approaches effectively useless for calculations where flight conditions force the vortical structures in the rotor wake to persist near the rotor for very long times, such as for flight in ground effect or in descending flight. Flight approaching the vortex ring state proves to be a particularly good example – see Section 14.10.7. If the flow can be assumed to be incompressible (generally a reasonable assumption in the rotor wake), vorticity transport methods can be used to overcome the problem of diffusion of vorticity. This is done by solving the governing equations for the flow not in the conservative variable form described previously but directly in terms of the variables of vorticity ω and velocity $\mathbf{V}$.

If the flow is assumed to be incompressible, then, in an Eulerian frame of reference, the Navier–Stokes equations can be rewritten as

$$\underbrace{\frac{\partial \omega}{\partial t}}_{\text{temporal}} + \underbrace{(\mathbf{V}\cdot\nabla)\omega}_{\text{advection}} = \underbrace{(\omega\cdot\nabla)\mathbf{V}}_{\text{strain}} + \underbrace{\nu\Delta\cdot\omega}_{\text{diffusion}}, \tag{14.14}$$

where the vorticity $\omega = \nabla \times \mathbf{V}$. The first term in this equation is the temporal evolution of vorticity, the second is an advection term, the third is a strain or stretching term, and the fourth represents viscous diffusion effects. Notice that the stretching term can only exist in a 3-D flow. Alternatively, in Lagrangian form this equation can be written as

$$\frac{D\omega}{Dt} = \underbrace{(\omega\cdot\nabla)\mathbf{V}}_{\text{strain}} + \underbrace{\nu\Delta\cdot\omega}_{\text{diffusion}}. \tag{14.15}$$

Equation 14.15 defines the change of vorticity of a fluid element moving with the flow. This is a Lagrangian representation and is a useful frame of reference to adopt for the vortex methods outlined in the following section (and detailed in Section 10.7.6), whereas Eq. 14.14 defines the change of vorticity at a specified point in the flow, which is an Eulerian representation and is a more useful description for the grid-based CFD method described below.

If the vorticity field is known (or initially assumed), then the velocity field can be calculated using the Biot–Savart relationship

$$\nabla^2\mathbf{V} = -\nabla\times\omega. \tag{14.16}$$

In practical applications it can be easier, however, to solve this equation in its more familiar integral form as

$$\mathbf{V}(\mathbf{x}) = -\frac{\mathbf{1}}{4\pi}\int \frac{(\mathbf{x}-\mathbf{y})}{|\mathbf{x}-\mathbf{y}|^3}\times\omega(\mathbf{y})\,\mathbf{dy}, \tag{14.17}$$

The use of this equation is explained in more detail in Section 10.7.1.

The vorticity transport model (VTM) developed by Brown (2000) and Line & Brown (2004) employs a direct computational solution of Eqs. 14.14 and 14.16 to calculate the evolution of the rotor wake. The development of the rotor wake can be modeled using the vorticity transport equation if the essentially viscous process of vorticity creation as a byproduct of the generation of aerodynamic loads on the rotor blades, fuselage, and so on, is modeled by appending a source term **S** to Eq. 14.14 to yield

$$\frac{\partial\omega}{\partial t} + (\mathbf{V}\cdot\nabla)\omega - (\omega\cdot\nabla)\mathbf{V} = \nu\Delta\cdot\omega + \mathbf{S}. \tag{14.18}$$

If a suitable model for the generation of aerodynamic loads on the system can be defined in terms of the flow velocity **V**, then the source term allows the effects of the strength and geometry of the vorticity distribution in the rotor wake to feed back into the aerodynamic loading and blade response. This can be done, for instance, by writing **S** in terms of the shed and trailed vorticity from the blades using a lifting-line or lifting-surface approach – see Section 14.9.

After casting the equations on a structured Eulerian computational grid surrounding the rotor, the velocity field is obtained either by solving Eq. 14.16 for instance by cyclic reduction [see Schumann & Sweet (1976)] or by evaluating Eq. 14.17 using a fast multipole summation technique [see Line & Brown (2004)]. The key feature of the method is that the convection

Figure 14.2 Longitudinal plane through the wake of a rotor in low speed forward flight as calculated using the VTM approach. Notice the upwash at the front of the rotor disk and the development of a vortex pairing instability in the wake downstream of the rotor, a physical feature only observed if the vorticity can be preserved for many rotor revolutions. Source: Image courtesy of Andrew Line & Imperial College, University of London.

of the vorticity through the computational domain is computed using a total variation diminishing (TVD) algorithm [for instance, Toro's Weighted Average Flux method – see Toro (1989)] that acts directly on the vorticity field, rather than on the density, pressure, and velocity as in more conventional CFD approaches. Very tight control is, therefore, maintained in the VTM over the rate of dissipation of vorticity in the wake and so vortical structures retain their strength and geometry, and are sharply resolved – even though their interactions with the rotor may continue over many rotor revolutions.

An example of a VTM calculation of the wake of a rotor operating in level forward flight at low airspeed is shown in Fig. 14.2. Notice how three levels of grid refinement have been used to resolve the flow very sharply near the rotor while reducing the computational expense in capturing the wake far from the rotor where it has a smaller influence on the rotor behavior. This type of model is very good at representing blade–wake interactions, as well as the wake–wake interactions that, as shown in Fig. 14.2, drive the development of very complicated flow patterns far downstream of the rotor. Although the VTM provides a very complete model for the evolution of the structure of the rotor wake, like all grid-based CFD approaches it is computationally expensive for routine use in parametric design applications. It does, however, offer one approach for the practical investigation of a wide range of helicopter rotor wake related issues until such time that Navier–Stokes solutions become more practically feasible.

14.4 Vortex Methods

The free-vortex method (FVM) is a technique related to the VTM (see Section 10.7.6). In many practical problems involving the rotor wake it can be justified that the structures produced by viscous effects (such as the internal structure of the vortices making up the rotor wake) have very much smaller length scales compared to the structures produced by purely potential flow (such as the global deformation of the wake). This allows concentrated regions of vorticity to be represented as singularities within the flow, in which case Eq. 14.15 reduces to the inviscid equation

$$\frac{D\boldsymbol{\omega}}{Dt} = (\boldsymbol{\omega} \cdot \nabla)\,\mathbf{V}. \tag{14.19}$$

Helmholtz's second law states that the vortex lines move as material lines – see Saffman (1992). This can be shown as follows. Consider a material segment $\delta\mathbf{s}$ somewhere in the flow. The equation of motion for this vortex segment in Lagrangian form is given by

$$\frac{d}{dt}\delta\mathbf{s} = \left(\delta\mathbf{s}\cdot\vec{\nabla}\right)\mathbf{V}. \tag{14.20}$$

Subtracting Eq. 14.20 from Eq. 14.19 gives

$$\frac{d}{dt}(\boldsymbol{\omega} - \sigma\delta\mathbf{s}) = \left\{(\boldsymbol{\omega} - \sigma\delta\mathbf{s})\cdot\vec{\nabla}\right\}\mathbf{V} \tag{14.21}$$

for some time-independent σ. If at some time $t = t_0$ the material line happens to coincide with the vortex line, then $(\boldsymbol{\omega}_0 - \sigma\delta\mathbf{s}_0) = 0$. If the velocity field is continuous, then it follows that Eq. 14.21 has only one unique solution, namely $(\boldsymbol{\omega} - \sigma\delta\mathbf{s}) = 0$. In other words, the local vorticity translates and rotates for all time as a vector that remains aligned with the material segment $\delta\mathbf{s}$.

In the vortex method, the dynamics of material lines in the fluid can be used to represent the dynamics of a set of discrete vortex segments, which can be defined in 3-D space by points or Lagrangian fluid markers – see Fig. 10.26 for instance. The motion of the material lines (and fluid markers) reduces to a simple advection equation of the form

$$\frac{d\mathbf{r}}{dt} = \mathbf{V}, \quad \mathbf{r}(t=0) = \mathbf{r}_0, \tag{14.22}$$

where $\mathbf{r}$ is the position vector of a marker, $\mathbf{r}_0$ is the initial position vector of the marker, and $\mathbf{V}(\mathbf{r})$ is the local fluid velocity at that marker. The solution of Eq. 14.22 is complicated significantly, however, by the highly nonlinear nature of the velocity field, $\mathbf{V}$.

There are many different approaches to the solution of Eq. 14.22 for helicopter rotor wake problems, all of which involve the repeated evaluation of the Biot–Savart law to calculate the velocity field $\mathbf{V}$ in terms of the vorticity in the flow. Both time marching (time integration) and relaxation (iterative) methods can be employed – see Leishman, Bhagwat, & Bagai (2002) and Wachspress et al. (2003). An example of a wake calculation using the vortex method is shown in Fig. 14.3. The numerical technique used to obtain the results illustrated here was based on a refinement of the basic FVM using lines of constant circulation strength (see also Fig. 10.26). The vortex method has the advantage of being free of artificial diffusion; the vortex filaments are essentially self-adapting and do not dissipate. This means that the wake well downstream of the rotor remains very well defined compared to most Eulerian grid-based solutions, although care must be taken to avoid deterioration of accuracy if the marker points used to define the wake structure begin to drift apart downstream of the rotor.

14.5 Boundary Layer Equations

At the Reynolds numbers typical of helicopters, the viscous terms in the Navier–Stokes equations are significant only in a thin shear layer, called the boundary layer, near the surface of the vehicle. To model the flow in this layer, a simplified subset of the Navier–Stokes equations can be derived that exploits the fact that the length-scale of the variation of the flow variables is very much smaller normal to the surface than parallel to the surface.

The chief advantage of the boundary layer approach is that it allows an inviscid "outer" solution (calculated for instance using the Euler equations or a potential flow solver) to be modified for the effects of viscosity near the surface of the rotors and fuselage. This approach leads to a class of numerical techniques known as zonal or viscous-inviscid interaction methods. Such methods have proved very useful in airfoil design, but can also be useful

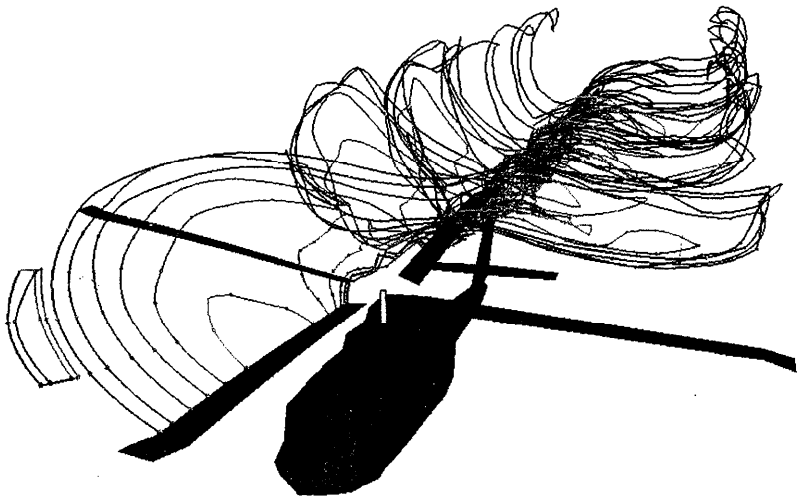

Figure 14.3 Representation of the roll-up of the wake behind a helicopter in forward flight using constant vorticity curved vortex filaments. The wake from only one blade is shown for clarity. Source: Wachspress et al. (2003). Image courtesy of Daniel Wachspress and Continuum Dynamics, Inc.

in predicting rotor and airframe loads on helicopters. The basic principle is first to solve the inviscid flow problem and then to solve the boundary layer equations. The inviscid solution is then repeated after applying a correction to take into account the effect of the finite thickness of the boundary layer on the outer flow. The resulting solution thus yields, to first order, a high Reynolds number solution to the Navier–Stokes equations. Care must be taken, though, where grossly separated flows are encountered, for instance, in the lee of bluff fuselages and cowlings, because under these conditions the basic assumptions of the boundary layer approach are invalidated.

Consider the situation in two dimensions. If x is in the direction parallel to the surface and y is normal to the surface, then, as the Reynolds number of the flow becomes very large, the Navier–Stokes equations for an incompressible flow reduce to

$$\frac{\partial u}{\partial x} + \frac{\partial v}{\partial y} = 0 \quad \text{(continuity)}, \tag{14.23}$$

$$u\frac{\partial u}{\partial x} + v\frac{\partial u}{\partial y} = -\frac{1}{\rho}\frac{\partial p}{\partial x} + \nu\frac{\partial^2 u}{\partial y^2} \quad (x\text{–component of momentum}), \tag{14.24}$$

$$-\frac{\partial p}{\partial y} = 0 \quad \text{(pressure gradient normal to surface)} \tag{14.25}$$

because the gradients of the fluid properties in the x direction become much smaller than the gradients in the y direction. If the flow is unsteady, then the momentum equation

$$\frac{\partial u}{\partial t} + u\frac{\partial u}{\partial x} + v\frac{\partial u}{\partial y} = -\frac{1}{\rho}\frac{\partial p}{\partial x} + \nu\frac{\partial^2 u}{\partial y^2} \tag{14.26}$$

should be used instead. At the edge of the boundary layer $y = \delta$, where δ is the boundary layer thickness [which by definition is where the local velocity approaches 99% of the external flow (or edge) velocity $U_e(x, t)$ – see Section 7.3.2]. Because the pressure across

the boundary layer (i.e., normal to the surface) is constant (Eq. 14.25), the pressure at any point on the surface is taken to be the pressure just outside the boundary layer. The momentum equation outside the boundary layer can thus be rewritten as

$$\frac{\partial U_e}{\partial t} + U_e \frac{\partial U_e}{\partial x} = -\frac{1}{\rho}\frac{\partial p}{\partial x}. \tag{14.27}$$

Using this equation, the pressure can be eliminated from the problem and the momentum equation within the boundary layer becomes

$$\frac{\partial u}{\partial t} + u\frac{\partial u}{\partial x} + v\frac{\partial u}{\partial y} = U_e \frac{\partial U_e}{\partial x} + \frac{\mu}{\rho}\frac{\partial^2 u}{\partial y^2}. \tag{14.28}$$

Associated with the solution of the boundary layer equations is the concept of a displacement thickness, δ^*, which is written as

$$\delta^* = \int_0^\delta \left(1 - \frac{u}{U_e}\right) dy. \tag{14.29}$$

The displacement thickness is a measure of the extent to which, if the effects of the boundary layer are to be included in an inviscid model of the flow away from the surface, the shape of the surface might be displaced away from the original surface to yield the same flow rate as in the viscous flow with the boundary layer present. This is same as saying that the external, inviscid, flow about the body can be obtained by solving the equations about a shape that is generated by adding the displacement thickness to the actual shape of the body. This type of approach is an example of a so-called weak interaction method. Although obviously still an approximation, and apart from the restrictions on the method mentioned above, this approach yields more representative flow solutions at the Reynolds numbers appropriate to helicopters than if the viscous effects were completely ignored in the calculation.

In many engineering problems the details of the flow inside the boundary layer are of no interest and only the effects of the boundary layer are needed. For example, the shear stress on the surface (to estimate the viscous drag) and the boundary layer displacement thickness (to perform a correction to the external flow) might be required. These variables can be calculated directly from an integrated form of the boundary layer equations, called the momentum integral equation, usually attributed to von Kármán (1921). In this case the governing equation is

$$\frac{d}{dx}(U_e^2\theta) + \delta^* U_e \frac{dU_e}{dx} = \frac{\tau_w}{\rho}, \tag{14.30}$$

where τ_w is the shear stress on the wall (surface) and

$$\theta = \int_0^\delta \left(1 - \frac{u}{U_e}\right)\left(\frac{u}{U_e}\right) dy. \tag{14.31}$$

is the so-called momentum thickness. This equation is very general because no assumption is made about the relationship between τ_w and the velocity gradient, and so the equation can apply to both laminar or turbulent boundary layer flows. After choosing a suitable form for the velocity profile across the boundary layer, the momentum integral equation can be solved to find the key variables describing the properties of the layer (i.e., δ, δ^*, θ, and τ_w). While in some cases solutions to the momentum integral equation can be found in closed form, in most cases numerical solutions must be obtained. See Houghton & Carpenter (1993) or Katz & Plotkin (1991) for a survey of the various possible approaches.

14.6 Potential Equations

A further simplification to the governing equations of the flow can be achieved by assuming that the flow is irrotational, that is, $\nabla \times \mathbf{V} = 0$. In this case the velocity field can be expressed as a gradient of a potential function ϕ so that

$$\mathbf{V} = \nabla\phi. \tag{14.32}$$

Care must be taken with this approach, however, especially given the essentially rotational nature of the flow in the wake. The potential equations can be expressed in many ways, but one form, used commonly to model compressible flows, is

$$\nabla^2\phi - \frac{1}{a^2}\left[\frac{\partial^2\phi}{\partial t^2} + \frac{\partial}{\partial t}(V^2) + \mathbf{V}\cdot\nabla\left(\frac{V^2}{2}\right)\right] = 0, \tag{14.33}$$

where $V = |\mathbf{V}|$. This form of the potential equation is usually referred to as the full-potential equation because no terms have been neglected in its derivation from the Euler equations – see Sankar & Prichard (1985), Strawn (1986), and Strawn & Caradonna (1987). For transonic flow problems, all the terms are important if the characteristic nonlinear variation of the flow properties with Mach number is to be represented properly. If small disturbances can be assumed then some of the terms are of higher order and can be neglected, however. The transonic small disturbance (TSD) equations are a subset of the full potential equations and can be written in the form

$$A\phi_{tt} + B\phi_{xt} = F_x + \phi_{zz} + C\phi_{yy} + \text{cross terms and low-order derivatives.} \tag{14.34}$$

The nonlinearity of the problem is contained in the F_x term, which involves ϕ_x and ϕ_x^2. Historically this was one of the first flow equations ever to be tackled by numerical means, launching the field known today as CFD – see Caradonna & Isom (1972) and Caradonna (1990).

If all the higher-order terms are neglected, the TSD equation reduces to a wave equation of the form

$$\frac{1}{a_\infty^2}\phi_{tt} = \nabla^2\phi, \tag{14.35}$$

where a_∞ is the free-stream speed of sound. A final simplification is to assume incompressible flow ($a_\infty \to \infty$), in which case the velocity potential is governed by Laplace's equation, that is,

$$\nabla^2\phi = 0. \tag{14.36}$$

A feature of this equation is that it is linear and so it allows complex flows to be synthesized by combining more elementary flows. This equation underlies the vortex methods described in Section 14.4 as well as the surface singularity methods described in the following section.

14.7 Surface Singularity Methods

Surface singularity or *panel methods* are based on the assumption of small disturbance, incompressible irrotational flow, for which the governing equation is Laplace's equation (Eq. 14.36) for the velocity potential. The basic approach is described by Hess & Smith (1962), Rubbert & Saaris (1969), Morino (1985), Hess (1990), and Katz & Plotkin (1991). These methods can be used to model the flow over helicopter fuselages, and with

extensions to account for the vorticity distribution in the wake behind the body, the flow over wings and rotor blades too. The idea is that surface singularities of unknown strength can be distributed over the body surface. After determining the strengths of the singularities by imposing a condition of flow tangency on the surface, the surface velocities, and hence the aerodynamic loading on the body, can be calculated. For an engaging modern treatment of the various types of panel methods, see Katz & Plotkin (1991). Large computer codes that use panel methods are commercially available and are in widespread use in the helicopter industry. See also Maskew (1982) for a good summary of the general approach.

Classical panel methods have found considerable use in helicopter applications for airfoil and fuselage design. The principles of both 2-D and 3-D panel methods are similar. To illustrate the principles, consider the flow about a 2-D airfoil. The airfoil surface is replaced by distribution of N discrete panels, and each panel i contains a singularity distribution that can be described by a velocity potential function ϕ_i. This means that the total potential induced by all the singularities in the flow is

$$\phi = \sum_{i=1}^{N} \gamma_i \phi_i, \tag{14.37}$$

where the constants γ_i must be found subject to the boundary condition that the flow must be tangential to the surface at N discrete collocation points x_j on the surface. That is,

$$\left(\nabla\phi(x_j) + V_\infty\right) \cdot \vec{n}_j = 0, \tag{14.38}$$

where $\vec{n}_j$ is the outward pointing normal unit vector at the jth collocation point. Usually the collocation points are selected to be the midpoints of the panels. If the panels contain vortex singularities that vary linearly in strength over the area of the panel, then with N panels there are N equations containing $N + 1$ unknowns. The Kutta condition at the trailing edge of the airfoil provides the auxiliary equation required to solve the problem uniquely and to define the airloads on the airfoil. The equations governing the problem can be expressed in the form

$$\begin{Bmatrix} \gamma_1 \\ \gamma_2 \\ \cdot \\ \cdot \\ \gamma_N \\ \gamma_{N+1} \end{Bmatrix} = \begin{bmatrix} A_{1,1} & A_{1,2} & \cdot\cdot & A_{1,N+1} \\ A_{2,1} & A_{2,2} & \cdot\cdot & A_{2,N+1} \\ \cdot & \cdot & \cdot\cdot & \cdot \\ \cdot & \cdot & \cdot\cdot & \cdot \\ A_{N,1} & A_{N,2} & \cdot\cdot & A_{N,N+1} \\ 1 & 0 & \cdot 0 & 1 \end{bmatrix}^{-1} \begin{Bmatrix} -V_\infty \sin\alpha \cdot n_1 \\ -V_\infty \sin\alpha \cdot n_2 \\ \cdot \\ \cdot \\ -V_\infty \sin\alpha \cdot n_N \\ 0 \end{Bmatrix}, \tag{14.39}$$

where $\mathbf{A} = A_{i,j} = \nabla\phi_i(x_j) \cdot \vec{n}_j$ is a $(N + 1) \times (N + 1)$ matrix of influence coefficients. The influence coefficient $A_{i,j}$ is effectively the normal component of the velocity induced at the collocation point on panel j by the singularity distribution ϕ_i on panel i and depends on the relative distance between, and orientation of, the two panels. Notice that solving Eq. 14.39 involves finding the inverse of the matrix of influence coefficients, and, besides the calculation of the influence coefficients themselves, this inversion is the primary computational expense involved in the panel method. If the angle of attack, α, is included in the vector on the right-hand side of Eqs. 14.39, then the influence coefficients need only be calculated once, however. Once the singularity strengths γ_i are known, the loading on the airfoil follows immediately.

Panel methods have also been used to model the aerodynamics of helicopter airframes. In such an application, the fuselage surface might be represented by N small, flat, quadrilateral panels onto which singularities in the form of sources and sinks and/or doublets are placed

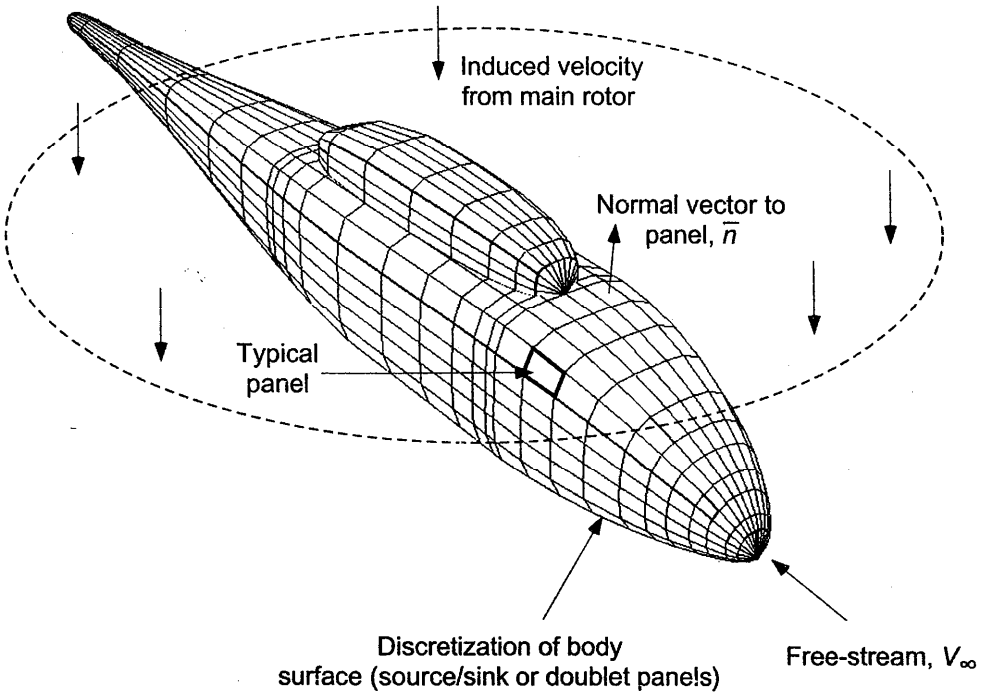

Figure 14.4 Discretization of a generic helicopter fuselage shape for use in a panel method. Source: Grid courtesy of Mark Chaffin.

(see Fig. 14.4 for an example). The principles are very similar to the 2-D case, but the size of the numerical problem becomes much larger. Assume for illustration that only source singularities are used. If the singularity strength on the ith panel is σ_i, then the velocity induced by this panel at the control point on the jth panel can be written as $A_{i,j}\ \sigma_i$. At the jth control point, the component normal to the surface of the velocity induced by all N sources is then

$$V_j = \sum_{i=1}^{N} A_{i,j}\ \sigma_i \quad \text{for } i \neq j. \tag{14.40}$$

The boundary condition of flow tangency is imposed at the control point of each panel to allow the unknown singularity strengths σ_i to be evaluated. So, for instance, if $\vec{V}_{\infty_j}$ is the velocity at panel j as a result of the motion of the fuselage, the rotor-induced velocity and so on, the component of $\vec{V}_{\infty_j}$ normal to panel j will be $\vec{V}_{\infty_j} \cdot \vec{n}_j$, where $\vec{n}_j$ is the unit normal vector to panel j. Therefore, at the jth panel

$$\sum_{i=1}^{N} A_{i,j}\ \sigma_i + \vec{V}_{\infty_j} \cdot \vec{n}_j = 0. \tag{14.41}$$

One equation such as this applies on each of the N panels. This leads to a set of linear simultaneous equations that can be used to solve for the singularity strengths, σ_i, using standard numerical methods of linear algebra. The governing equations can be written in matrix form as

$$[A_{ij}]\{\sigma_i\} = -\{\vec{V}_\infty \cdot n_j\}, \tag{14.42}$$

with solution

$$\{\sigma_i\} = \left[A_{i,j}\right]^{-1} \left\{-\vec{V}_\infty \cdot n_j\right\}, \tag{14.43}$$

which involves finding the inverse of the influence coefficient matrix. Once the values of σ_i are obtained, the velocity components tangential to the panels can be obtained, and hence the pressure distribution over the fuselage follows using Bernoulli's equation.

Normally thousands of panels are required to resolve adequately the complex shape of a helicopter fuselage and care must be taken, for instance, to concentrate a sufficient number of panels in regions of high surface curvature such as near the rotor hub. Because the numerical cost of panel methods is of order N^3, their use is by no means inexpensive even on a modern computer. But they are considerably less computer intensive than most other types of CFD methods, however. As an enhancement to the basic panel method, the solution of the momentum integral equation from boundary layer theory allows displacement corrections to be made to solutions obtained from the panel method, thereby allowing viscous effects (but not flow separation) to be modeled. The effects of flow separation can be included, however, by extending the surface singularities off the airframe as free shear layers – see Polz (1982), Lê et al. (1987), de Bruin (1987), Ahmed et al. (1988), Ahmed (1990), and Katz & Plotkin (1991). Overall, if suitable care is taken in the distribution of panels on the surface of the fuselage, the 3-D surface singularity method can be used to obtain quite credible predictions of the loading on an airframe – certainly to the fidelity required for preliminary design (see also Section 14.10.4). See Chaffin & Berry (1994) for a further discussion of the predictive capabilities of panel methods compared to measurements and other forms of analysis.

14.8 Thin Airfoil Theory

Thin airfoil theory has been alluded to several times in earlier chapters. The governing equation for thin airfoil theory is Laplace's equation in two dimensions. The idea is that the airfoil is replaced by a camberline (which is a flat plate if the airfoil is uncambered) on which a vortex sheet singularity of unknown strength, $\gamma(x)$ is placed. The strength of this vortex sheet is determined by satisfying flow tangency on the camberline of the airfoil in conjunction with the Kutta condition at the trailing edge, that is, $\gamma(TE) = 0$. Solutions are usually obtained by expressing the vortex sheet strength as a Fourier series, and then calculating the coefficients in this series. See Glauert (1947) for details of the method. In most cases it is only the integrated lift and pitching moment on the airfoil that is required and not the chordwise loading. These can be determined using only the first three coefficients in the Fourier series. The general form of the chordwise loading on the airfoil is

$$\Delta C_p(\alpha, \theta) = 4\left\{A_0\left(\frac{1+\cos\theta}{\sin\theta}\right) + \sum_{n=1}^{\infty} A_n \sin n\theta\right\}, \tag{14.44}$$

where $\theta = \cos^{-1}(1 - 2\bar{x})$ and $\bar{x} = x/c$. The coefficients A_0 and A_n are given by the equations

$$A_0 = \alpha - \frac{1}{\pi}\int_0^\pi \frac{dy}{dx} d\theta \quad \text{and} \quad A_n = \frac{2}{\pi}\int_0^\pi \frac{dy}{dx}\cos n\theta \, d\theta, \tag{14.45}$$

where $y = y(x)$ describes the camberline of the airfoil. The lift and pitching moment coefficients are given by

$$C_l = 2\pi\left[A_0 + \frac{A_1}{2}\right], \quad C_{m_{LE}} = -\frac{\pi}{2}\left[A_0 + A_1 - \frac{A_2}{2}\right],$$
$$C_{m_{1/4}} = -\frac{\pi}{4}[A_1 - A_2]. \tag{14.46}$$

Note that for a noncambered airfoil ($dy/dx = 0$), $A_0 = \alpha$ and $A_n = 0$ if $n > 0$, giving

$$\Delta C_p(\alpha, \theta) = 4\alpha\left(\frac{1 + \cos\theta}{\sin\theta}\right) = 4\alpha\sqrt{\frac{1 - \bar{x}}{\bar{x}}}. \tag{14.47}$$

and hence the often used results that

$$C_l = 2\pi\alpha, \quad C_{m_{LE}} = -\frac{C_l}{4} \quad \text{and} \quad C_{m_{1/4}} = 0. \tag{14.48}$$

Thin airfoil theory is very powerful despite its simplicity and is particularly useful in helicopter analyses, especially during preliminary airfoil design, because it allows a rapid estimation of the pitching moment resulting from any given camberline – see Section 7.7.3. The theory also forms a basis for understanding the elements of unsteady airfoil aerodynamics, as has been examined extensively in Chapter 8. An interesting result is obtained by assuming that the vortex sheet strength is all lumped or "bound" to vortex of strength Γ_b placed at the aerodynamic center (1/4-chord) of the airfoil section, that is, so that

$$\Gamma_b = \int_0^1 \gamma(\bar{x})d\bar{x} \tag{14.49}$$

Using the Kutta–Joukowski theorem, the lift per unit span

$$L = \rho V_\infty \Gamma_b = \frac{1}{2}\rho V_\infty^2 c C_l, \tag{14.50}$$

where $C_l = 2\pi\alpha$ in 2-D flow. The only way Eq. 14.50 can be satisfied is if

$$\Gamma_b = \pi V_\infty c\alpha. \tag{14.51}$$

This is equivalent to enforcing the flow tangency condition only at the 3/4-chord of the airfoil. (The 3/4-chord position is sometimes called the rear neutral point after Pistolesi and Küssner.) This result is equivalent to saying that the lifting properties of an airfoil, in steady flow at least, can be modeled by placing the bound circulation at the 1/4-chord and satisfying flow tangency at the 3/4-chord. This result is fundamental to the development of the 3-D lifting-line models described in the next section.

14.9 Lifting-Line Blade Model

A very useful, but somewhat simplified, computational model of the aerodynamics of a rotor results from treating the blades as a series of 2-D blade elements, in the manner introduced in Chapter 3. If the velocity induced by the vortical wake of the blades can be calculated, then the induced AoA along the length of each blade can be found. The lift on the blade elements can then be determined and thus, by radial integration, the total blade lift. Lifting-line blade models that exploit this approach have found much use in helicopter rotor analyses and are to be found as the basis of nearly all forms of comprehensive rotor analysis (see Section 14.11).

To use the lifting-line model properly, though, the effects of the wake on the loading on the blade must be fully coupled to the circulation that is trailed (and shed) into the wake. This allows some 3-D effects to appear in the spanwise distribution of the blade loading, but because of small disturbance assumptions the method is not powerful enough to account completely for the strong 3-D flow effects found near the tip and root of the blade or near localized blade–vortex interactions, for instance. In principle, the models used in the helicopter field are similar to those used for fixed-wing analyses [see, for example, Houghton & Carpenter (1993)]. The lifting-line approach must be formulated carefully for use in rotating-wing applications, though, because the wake cannot be assumed to be planar, nor to extend downstream to infinity. Many different formulations can be found in the literature, with slight variations in assumptions in regard to the wake system. Although the basic principles are the same, the numerical formulation can vary substantially between implementations.

A generic formulation of the lifting-line problem will be described. For consistency with the results of Section 14.8, the blade is modeled as a vortex of strength $\Gamma_b(y)$ that is "bound" to the aerodynamic center (1/4-chord). Then, using the Kutta–Joukowski theorem, the lift per unit span dL is given by

$$\begin{aligned} dL(y) &= \rho V(y)\Gamma_b(y)\, dy = \frac{1}{2}\rho V(y)^2 c C_l(y)\, dy \\ &= \frac{1}{2}\rho V(y)^2 C_{l_\alpha}(y)\alpha_e(y)\, c\, dy, \end{aligned} \tag{14.52}$$

where α_e is the "effective" AoA of that section and C_{l_α} is its lift curve slope. Often C_{l_α} is given the value 2π, being the lift curve slope of a 2-D thin airfoil in incompressible flow (see Section 14.8), but in practical applications the lift curve slope of the airfoil section at the appropriate combination of Mach number and Reynolds number can also be used. Assuming a thin airfoil and rearranging the terms gives

$$V(y)\,\alpha_e(y) = \frac{\Gamma_b(y)}{2\pi(c/2)}. \tag{14.53}$$

For a 2-D airfoil the bound vortex is an infinite line vortex and must have a strength that is defined on the basis of the downwash at a distance $c/2$ from the 1/4-chord, that is, by a condition of no flow penetration that is imposed at the 3/4-chord. This is consistent with the 2-D thin airfoil model of the problem that was described in the previous section. To extend this concept to three dimensions the blade is divided into N elements, as shown by Fig. 14.5, and a control point is placed at the 3/4-chord of each element. The normal velocity induced at the control point of panel i by the vorticity bound to element j can be written in terms of a matrix of influence coefficients, I_b, so that

$$[I_b]_{i,j}\,\Gamma_{b_j} = V\alpha_i. \tag{14.54}$$

The objective is to solve numerically for the distribution of bound circulation over the blade, Γ_{b_j}, which satisfies the no-flow penetration condition simultaneously at all of the control points on the blade. On the ith element of the blade,

$$\sum_{j=1}^{N} [I_b + I_{nw}]_{i,j}\,\Gamma_{b_j} = V\,(\theta_i - \phi_i) = V\alpha_{e_i}, \tag{14.55}$$

where I_{nw} is the influence of the "near-wake" that must trail from the edges of the blade element. The near wake is usually modeled by a series of horseshoe vortices or vortex arcs

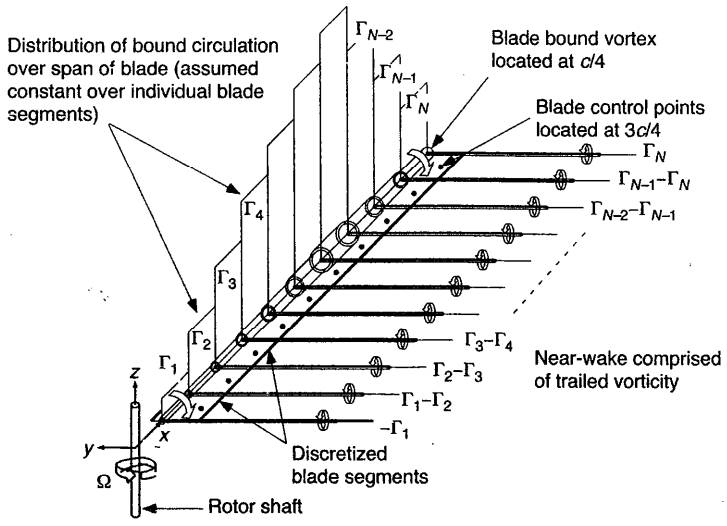

Figure 14.5 Lifting-line model representing the near wake trailed from a rotor blade.

that trail downstream a finite distance, often to 15–30° of wake age, behind the blade. On the right-hand side of the equation, ϕ_i contains the induced contributions from the remainder of the vortical wake (the "far wake") and must exclude all of the induced effects from the parts of the wake that are defined as being part of the near wake. Applying this equation at all control points results in a linear set of simultaneous equations of the form

$$[I_b + I_{nw}]\{\Gamma_b\} = \{V(\theta - \phi)\}, \tag{14.56}$$

from which the spanwise loading (circulation) Γ_b can be obtained by standard numerical methods for solving systems of linear simultaneous equations. Both direct and iterative methods can be used, although direct methods are usually preferable because of their superior numerical behavior. In general, both I_b and I_{nw} are matrices that are fully populated, although strongly diagonally dominant. Hence the structure of I_b and I_{nw} cannot usually be exploited to simplify the numerical solution of Eq. 14.56.

From the resulting distribution of circulation along the blade span, the strengths of the vortices that trail from the edges of the blade elements (Fig. 14.5) can be calculated. These provide a boundary condition for the far vortex wake, which can be represented using a FVM, for instance. As mentioned previously, in many rotor wake modeling applications only the tip vortex is modeled, primarily for computational efficiency, but also because this vortex is the dominant flow structure in the rotor wake. This is because the high concentration of aerodynamic loading over the tip region of helicopter blades generally results in a powerful vortex rolling up and trailing from a point very close to the blade tip. It is often assumed for modeling purposes that all of the circulation outboard of the position of maximum bound circulation on the blade rolls up into this tip vortex. This is equivalent to assuming that the circulation about the tip vortex is the same as the maximum value of the bound circulation on the blade – see Question 14.6. This assumption can be used to define the initial strength (or circulation) of the vorticity in the far wake. The actual strength and initial location of the tip vortex may also be adjusted based on empirical data, if these are available. See Bhagwat & Leishman (2000a) for measurements of the relationship between the blade bound vorticity and the circulation in the trailed wake for a rotating blade.

14.10 Applications of Advanced Computational Methods

14.10.1 *Unsteady Airfoil Performance*

While unsteady aerodynamic effects are intrinsic to the helicopter, there are two unsteady airfoil problems that have received much more attention than others from a modeling perspective. These are blade vortex interaction (BVI) and dynamic stall. Both problems are a particularly large source of unsteady airloads and are very difficult to predict. While BVI is a source of both unsteady airloads and very obtrusive noise (see Section 8.19), its occurrence does not limit the capabilities of the rotor system. As discussed in Chapter 9, the occurrence of dynamic stall, however, can limit both forward flight and maneuver capabilities of helicopters and is a more serious problem from a rotor airloads perspective.

Blade Vortex Interactions (BVI)

The 2-D BVI problem, as previously shown schematically in Fig. 8.36, has been widely addressed using CFD approaches, for example, see McCroskey & Goorjian (1983), McCroskey (1985), McCroskey & Baeder (1985), Singh & Baeder (1996), and Lee & Baeder (2002). While convecting past an airfoil, a vortex of positive circulation produces a downwash velocity while upstream of the blade (airfoil), and this changes to an upwash as it moves downstream. This situation leads to a rapidly and continuously changing angle of attack, resulting in highly unsteady aerodynamic loads – see Section 8.16.4 for an analysis of the problem using linear unsteady airfoil theory. The BVI problem usually requires compressibility effects in the flow to be accounted for if the correct amplitude and phasing of the airloads is to be calculated. In some cases, such as near the tip of the blade, the flow may be transonic. In this case the BVI problem is inherently nonlinear and quantitative prediction of the airloads requires advanced, nonlinear CFD methods for proper solution.

A problem that arises in such CFD solutions, however, is the need to preserve the physical strength of the vortex for relatively long times before and after its interaction with the blade or airfoil. This has been done relatively successfully using adaptive or chimera-type overset grids, such as in the example shown in Fig. 14.6. In this example, an O-type grid is wrapped around the airfoil and two overset H-grids are moved relative to the O-grid, tracking the vortex as it passes by the airfoil. The finer resolution of the flow afforded by the overset grids acts to reduce the numerical errors in the region of strong velocity and pressure gradient surrounding the vortex, and thus helps to reduce artificial numerical diffusion of the vortex during its interaction with the airfoil.

Figure 14.7 shows the complexity of the flow during a BVI event where shock waves are present in the flow. This might be the case, for instance, if the BVIs are encountered on the advancing blade at high forward flight speeds. The flow is calculated using an Euler CFD-based approach with a chimera-type overlapping grid – see Lee & Baeder (2002). The vortex is initially well upstream of the airfoil and the flow about the airfoil is benign, except of course for the presence of the upper and lower surface shocks. As the vortex approaches the airfoil, rapid changes occur as the induced velocity field from the vortex alters the AoA of the airfoil and its pressure distribution. In this case the vortex passes about 0.125 chord lengths below the airfoil, so the interaction is relatively strong. Notice the effect of the vortex on the lower surface shock wave – as the vortex passes by the shock bifurcates, adopting a lambda shape for a short period before returning to its original geometry. Amazingly, despite the high pressure gradients in the flow at and near the shock wave, the vortex emerges from the interaction with the airfoil and the shock wave in a

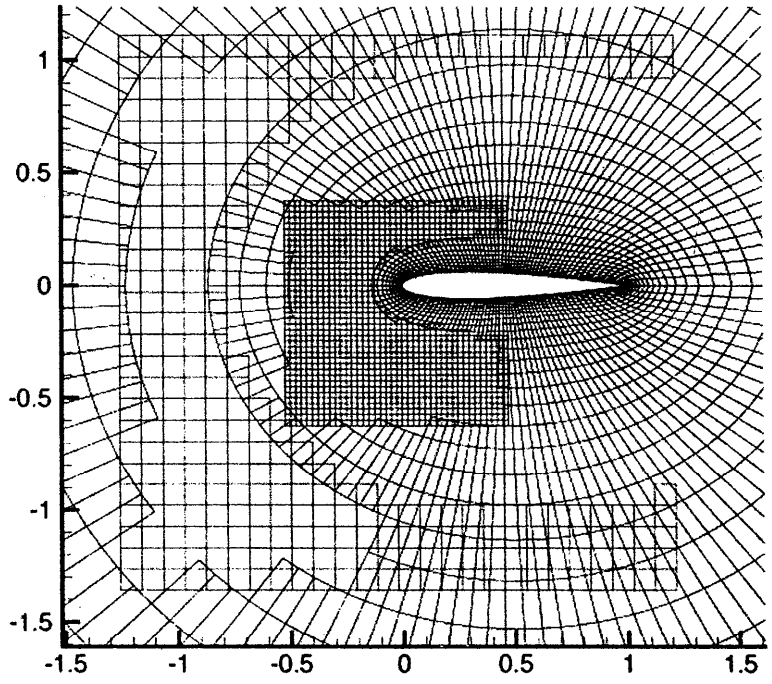

Figure 14.6 For BVI problems an overset or chimera grid system will be required to calculate the flow about the airfoil while preserving the structure of the vortex and reducing the effect of artificial numerical diffusion in dissipating its actual strength. Grid with 6,800 nodes with 2,200 to 2,400 nodes being used for the various overset grids. Source: From Lee & Baeder (2002) and courtesy of Yik-Loon Lee.

relatively undisturbed form. According to Fig. 14.7(d) the vortex does, however, appear to lose its initial radially symmetric form.

Of course, the prediction of BVI in 3-D viscous flow and over the entire rotor is the ultimate goal for CFD methods. This is, however, an extremely ambitious task, requiring high-resolution calculations using many tens or hundreds of millions of grid points. One outstanding issue is how to capture 3-D vortical flows accurately using 3-D overset grids. Grid refinement continues to be limited by computer memory and speed, and it would seem that approaches based on indefinite grid refinement will probably not be that useful in the shorter term. As is clear from the foregoing 2-D example, overlapping grids offer a very powerful and natural approach to solving the flows found on the various stationary and moving components of helicopters, however. The alternative of regenerating the grid at every time step, change in flight condition, or whatever, is expensive and prohibitively time consuming. A combination of refinement and proper placement of overset grids (say, for example, using the FVM or VTM as guidance) would be a very powerful technique if properly developed, and this is a promising area for further research.

Dynamic Stall

The problem of dynamic stall has been discussed extensively in Chapter 9. The proper and complete prediction of dynamic stall, however, continues to elude the helicopter aerodynamicist. This is because dynamic stall is characterized by the appearance of large, recirculating, turbulent separated flow regimes near the surface of the airfoil. While

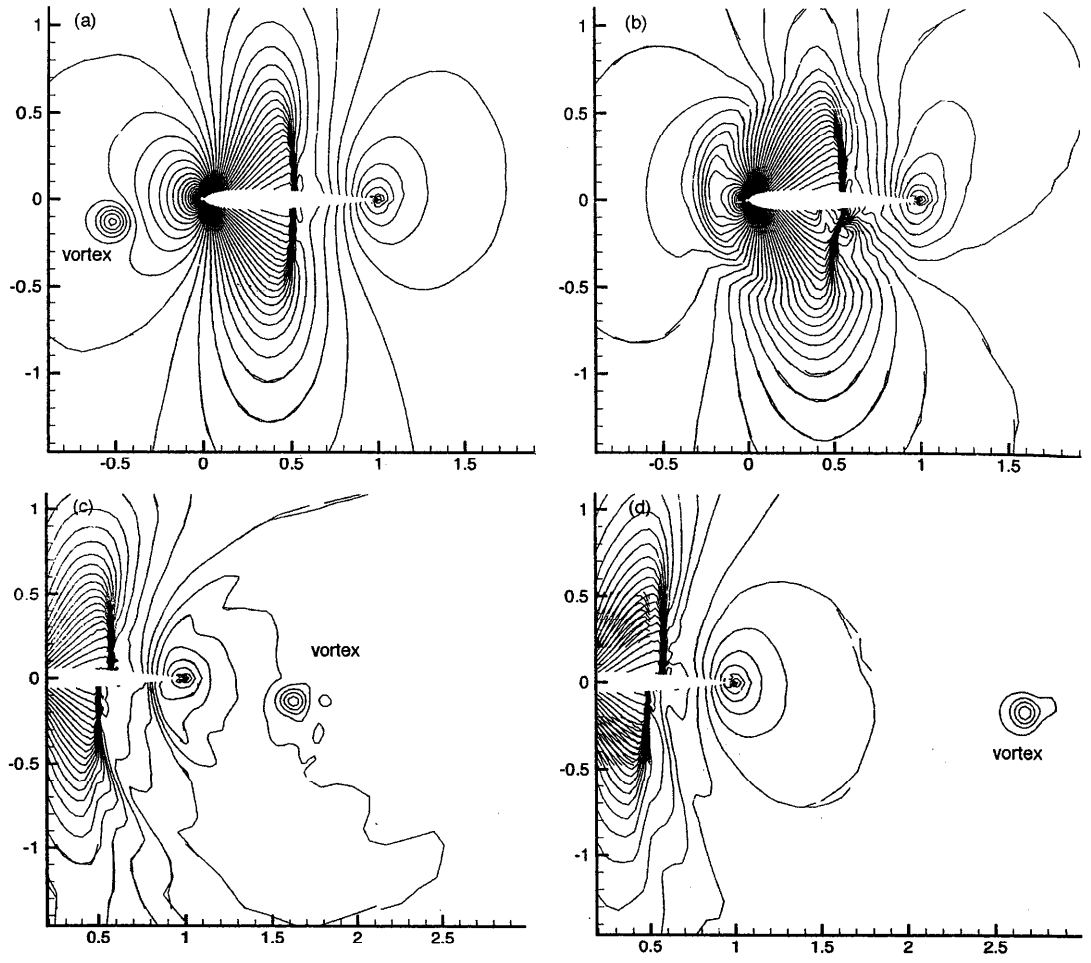

Figure 14.7 A series of predicted pressure fields surrounding an airfoil during a blade–vortex interaction at transonic speeds. (a) Vortex upstream of airfoil. (b) Vortex interacts with airfoil. (c) Vortex passes downstream of airfoil. (d) Vortex passes into downstream wake. Source: Lee & Baeder (2002) and courtesy of Yik-Loon Lee.

parsimonious models including stall effects can be developed for use in rotor analyses (i.e., models for integrated lift, drag and pitching moment – see Section 9.5.1), sensible predictions (as opposed to reconstructions or postdictions) of the overall flow field during dynamic stall can be obtained only by solving numerically the full Navier–Stokes equations along with a suitable representation of turbulent flow effects. To this end, CFD methods that include some representation of turbulent flow effects via turbulence closure models have begun to show promise in predicting 2-D and 3-D dynamic stall events – see, for example, Srinivasan et al. (1993), Ekaterinaris et al. (1994), Barakos et al. (1998), and Martin, Chandrasekhara, & Geissler (2003). It should be noted, though, that many widely different turbulence models have been developed over the years, the most popular perhaps including those developed by Baldwin & Lomax (1978), Spalart & Allmaras (1992), and others, as reviewed by Marvin & Huang (1996), but that the selection of the most appropriate model for any particular flow problem is still very much an open question.

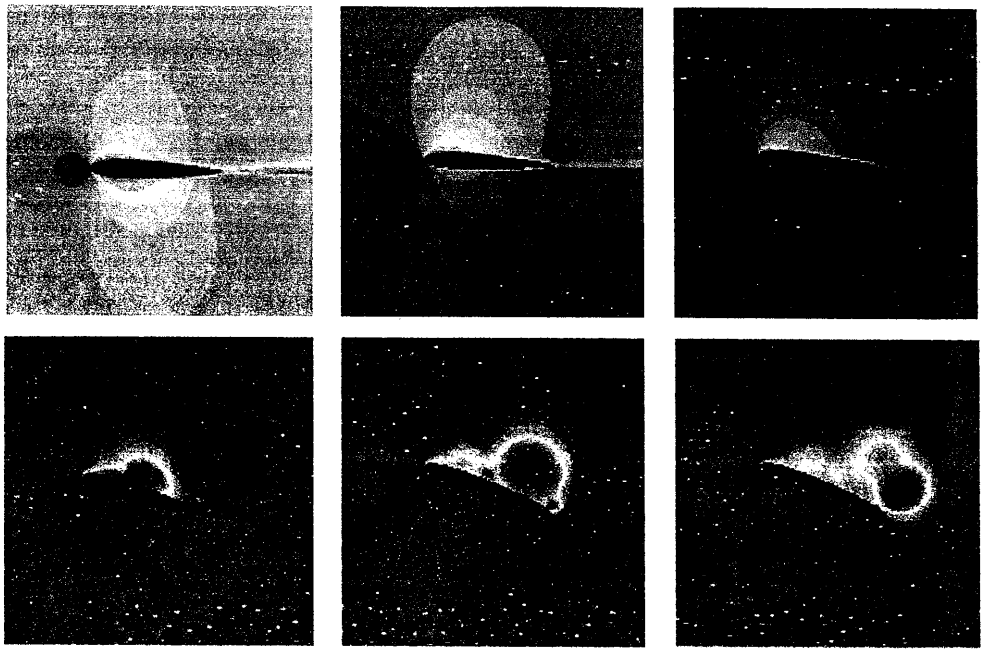

Figure 14.8 A sequence of Navier–Stokes predictions showing the shedding of a leading edge vortical disturbance during dynamic stall at low Reynolds number. Source: Barakos et al. (1998) and courtesy of G. Barakos and D. Drikakis.

An example of a Navier–Stokes prediction of dynamic stall is shown in Fig. 14.8. In these calculations a nonlinear eddy viscosity model was used to represent the turbulence in the flow. Clearly the approach predicts the key characteristic phenomenon of dynamic stall, which is the shedding of a leading edge vortical disturbance – see also Fig. 9.2. However, quantitative predictions of the airloads are not yet satisfactory in the fully stalled regime or during flow reattachment – these techniques have difficulty reproducing the flows at Reynolds numbers and Mach numbers relevant to helicopter rotors. In this regard, the accurate prediction of the transition from a laminar to turbulent boundary layer flow on the airfoil surface prior to the onset of dynamic stall is a key outstanding issue. The complexity of the surface boundary layer flow state on an airfoil under these dynamic AoA conditions is reflected in the measurements of Lee et al. (2000).

Investigation of methods and development of strategies to control and/or alleviate dynamic stall would appear to yield a prime opportunity for CFD methods, and indeed this problem has received some attention. Yet, no one scheme has yet demonstrated clear benefits. The use of zero-mass synthetic jets (see Section 9.12) to delay the onset of flow separation has good potential based on the results of both calculations and experiments. Alternatively, it seems that the use of leading edge slats, or other changes in the leading edge shape of the airfoil, may lead to improvements in alleviating the adverse features of dynamic stall – see Sahin et al. (2000). Studies with variable droop (camber) leading edge airfoils have also been conducted as a means of alleviating dynamic stall related problems – see Geissler & Trenker (2002) and Martin, Chandrasekhara, & Geissler (2003). Any benefits, however, have to be balanced against the possibility of introducing adverse effects on the pitching moments from high camber and overall airfoil performance, and this issue has not yet been researched thoroughly enough to be convincing. The payoffs in terms of

improved high-lift and low-drag airfoil designs free of dynamic stall is, however, potentially enormous, because this could lead to quantum gains in helicopter forward speed and/or maneuver performance.

14.10.2 *Tip Vortex Formation*

Trailing vortex formation is a complex fluid dynamics problem and is still not yet fully understood. It involves the interaction between strong pressure gradients and viscous shearing forces in the highly 3-D flow near the tips of the rotor blades. Resolving the flow in this region requires a large number of grid points carefully contoured to the blade shape – see Fig. 14.9. While fundamentally the process of vortex formation can only be solved using the Navier–Stokes equations, some success in predicting the behavior of the vortex after formation has been achieved using the Euler equations. Clearly, the proper modeling of the formation of the tip vortex and the subsequent convection of the vorticity through the flow field is probably the most important single step in the calculation of the entire rotor flow field. The difficulties encountered by most Navier–Stokes based CFD methods in preserving the wake vorticity to sufficiently far behind the blades for its effects on the rotor to be captured properly has led to the development of various adaptive gridding or vorticity capturing schemes – see Kim et al. (2002) for a review. Because of the extremely intricate physical processes governing the formation of the tip vortex, most CFD methods (when applied to solve this problem) exhibit solutions that are grid dependent – solution of the governing equations on grids that are sufficiently fine to produce converged solutions is still prohibitive in terms of computational cost for any form of routine use. The goal is to reach some compromise between fidelity and cost, but this requires further research and, especially, validation with experimental measurements. The scope and extent of tip vortex measurements have been discussed in Chapter 10.

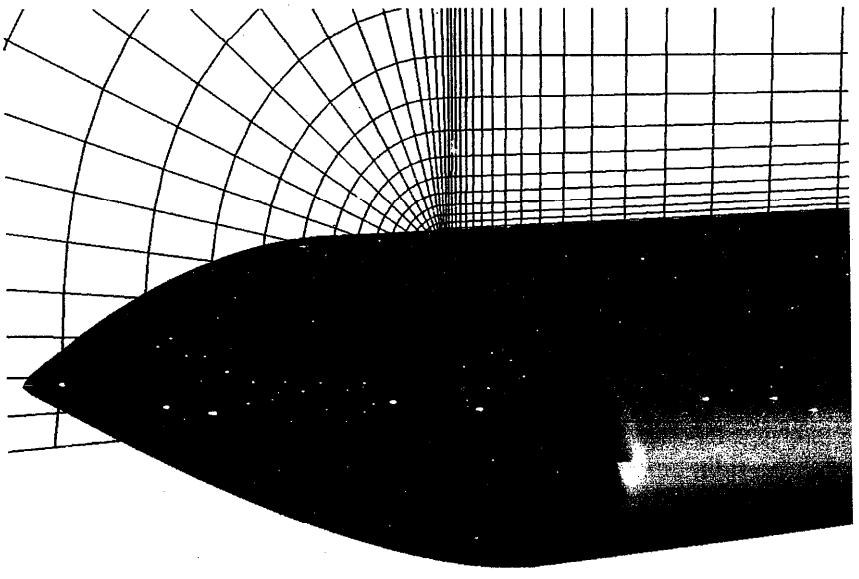

Figure 14.9 Example of the fine computational grid needed at the tip of a helicopter rotor blade to resolve the roll-up of the concentrated tip vortex using a Navier–Stokes approach. Source: Grid courtesy of Karthikeyan Duraisamy.

To help in reaching this computational goal, various techniques for wake capturing using grid adaptation show promise. These techniques allow grid points to be clustered where the spatial and temporal gradients in the flow are highest and so require a lower overall number of grid points compared to methods using regular grids. Chimera grid systems do much to help resolve the difficulties associated with modeling the flow over blades that are rotating within a domain in which the flow is either stationary or can be represented as a constant free-stream far away from the rotor – see Duque (1992), Strawn et al. (1998), Ahmad & Strawn (1999), Pomin & Wagner (2002), and Strawn & Djomehri (2002). For instance, a surface-conforming grid that rotates with the rotor can be used to capture the flow near the rotating blades while a background Cartesian grid can be used for the wake, with information being exchanged between the grids using various interpolation techniques.

Another method of controlling the dissipation of wake vorticity is by using a vorticity confinement or vorticity embedding technique – see Steinhoff (1987) and Steinhoff & Ramachandran (1990), whereby an "anti-diffusion" term is added to the Euler equations to help control the otherwise nonphysical spreading and diffusion of the tip vortex as it evolves downstream of the blade tip. There are, however, problems with this technique in regard to nonphysical effects and the anti-diffusion must be turned off, for example, for BVI problems. New developments in vorticity embedding techniques for rotor wake predictions are described by Bhagwat et al. (2005), where wake vorticity, as computed using circulation-carrying wake markers, is embedded into the full-potential equation. This novel approach attempts to fuse the best elements of Lagrangian free-vortex schemes with Eulerian grid-based CFD schemes to give a numerically efficient solution for rotor wake problems.

All of these methods are relatively expensive from a computational standpoint and so have not yet made a significant impact on practical rotor design problems. Furthermore, these methods need much further validation, particularly for rotors with advanced tip shapes and also for forward flight applications where shock waves might be present on the advancing blade. Only then can they be used with any confidence to design helicopters. Meanwhile, significant effort still needs to be spent in validating these models against experimental measurements made on properly idealized problems before the entire helicopter can be tackled as a whole. To this end several sets of detailed flow field measurements on generic rotors have provided reliable data for the validation of various types of computational models– see McAlister (1995, 1996), Mahalingam & Komerath (1998), and Martin et al. (2003).

An example of a Navier–Stokes prediction of the rollup of a tip vortex from a helicopter blade is shown in Figs. 14.10 and 14.11, which are from Duraisamy & Baeder (2004). Basically the calculations show that the flow on the lower surface follows a favorable pressure gradient toward the upper surface. Immediately behind the trailing edge of the blade there is evidence of two concentrated regions of vorticity, but these rapidly merge to form a single concentrated tip vortex. This behavior is consistent with experiments – see, for example, Martin, Leishman, & Pugliese (2003). The sharp edges on the blade tip always tend to promote flow separation, and this makes the consideration of viscous effects very important in terms of predicting the subsequent roll up and evolution of the tip vortex. Combined with this is the entrainment of the turbulent vortex sheet trailed from the inner part of the blade. This sheet is formed by the confluence of the boundary layers on the upper and lower surface of the blade – see also Fig. 10.7. The interaction of the sheet with the roll up of the flow from the tip appears to cause large decelerating forces and the generation of turbulence inside the core, emphasizing again the underlying complexity of tip vortex formation and the need for a full Navier–Stokes approach if the roll up is to be predicted properly.

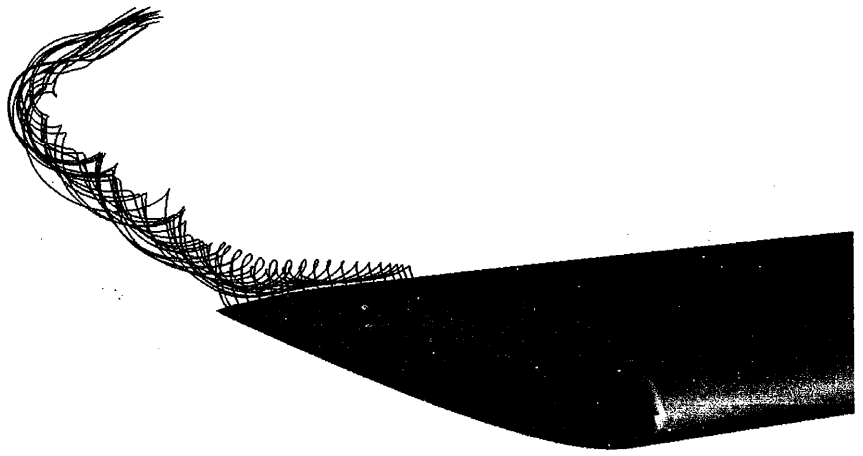

Figure 14.10 Particle tracers showing the roll-up of the tip vortex from a helicopter blade predicted using a Navier–Stokes solver. Source: Calculation and image courtesy of Karthikeyan Duraisamy.

A calculation of the structure of the vortex flow at a later time (145° of wake age in this case) is compared with flow visualization in Fig. 14.11, where there is good qualitative agreement at least. The actual structure of the rolled up tip vortex is comprised of three zones: 1. An inner laminar region with no mixing between layers, 2. A transition region where there are eddies of various scales, and 3. An outer turbulent region. The high swirl velocities near the vortex core result in high values of the local Richardson number there (see Section 10.6.5) and, because of stratification effects, turbulence cannot be generated or sustained. This is essentially a vortex Reynolds number effect and will result in essentially zero eddy viscosity in the core, although this is not properly represented by the turbulence model used within the CFD analysis. These observations suggests that the development of turbulence models used in CFD methods for vortex flows still has some way to go before

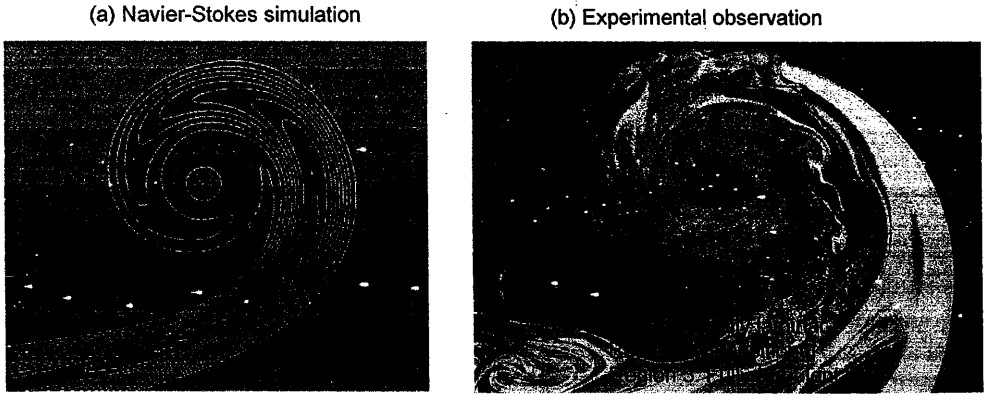

Figure 14.11 The roll-up and final formation of the tip vortex is a complicated process involving viscous shear and turbulence. Left: CFD calculation showing phase-averaged eddy viscosity contours. Right: Phase-resolved flow visualization. Both results for 145° of wake age. Source: Navier–Stokes calculation and image courtesy of Karthikeyan Duraisamy; Flow visualization courtesy of Manikandan Ramasamy.

predictions of blade generated tip vortices can be made with sufficient fidelity to account for Reynolds number scaling effects.

14.10.3 *CFD Modeling of the Rotor Wake*

While the flows about the rotor blades themselves have received the most attention, and CFD methods have certainly provided considerable physical insight into the roll-up of the tip vortex and initial formation of the rotor wake, adequate modeling of the subsequent dynamics of the rotor wake has proved a more daunting task. Yet it is the proper modeling of the geometry of the rotor wake that is probably the most important step in the calculation of the entire helicopter flow field. Although there has been some progress in Navier–Stokes based CFD modeling of the rotor wake and the flow field around the entire helicopter, the inability of most current CFD methods to protect this vorticity from the effects of numerical diffusion continues to yield an active area for research. Furthermore, the large number of grid points required to define the flow domain for a helicopter rotor continues to challenge even the most powerful computers, with memory demands that are quite formidable even by current-day standards.

One significant problem with wake modeling is that the numerical error in any approximation to the Euler or Navier stokes equations tends to introduce artificial diffusion of vorticity, which smears vorticity in the flow more quickly than is observed from experiments. An example is shown in Fig. 14.12, and while capturing the key features of the wake

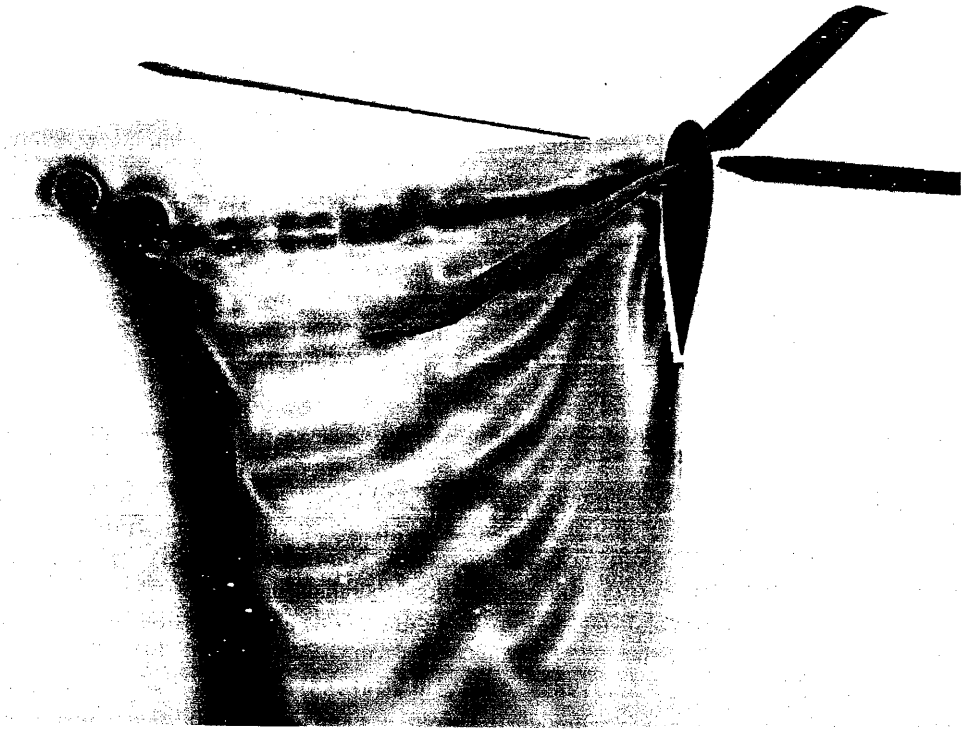

Figure 14.12 Navier–Stokes solution of a helicopter rotor wake in hovering flight. 64 million grid points are used. Contours of vorticity magnitude are computed on a cutting plane located at 45° behind one of the rotor blades. Source: Strawn & Djomehri (2002). Image courtesy of US Army AFDD and Roger Strawn.

structure, the coherence of the tip vortex itself is quickly lost to numerical diffusion. This occurs well within a rotor revolution. Based on flow visualization, tip vortices may persist clearly to four or more revolutions. Vortex methods (described in detail in Section 10.7) give a good level of approximation to the problem of defining the strength and vorticity of the rotor wake and have a strong advantage in being able to preserve vorticity independently of grid resolution or vortex age (see Section 10.7.3). Some progress has been made using hybrid schemes where a CFD–based solution for the blade aerodynamics is coupled to one of the vortex wake models discussed in Section 10.7. The inflow (induced velocity field) from the vortex wake model forms a boundary condition to the computational domain of the CFD model, and data are passed back and forth between the two calculations until convergence is obtained. Full-potential methods have also been used for this purpose, and with sufficient engineering judgment have produced remarkable agreement with experimental measurements of the blade pressure distributions, including the critical area near the blade tip. See Caradonna (1990) for a good review of prior work in this area.

14.10.4 *Airframe Flows*

As explained in Chapter 11, the flow over a helicopter fuselage is extremely complicated because it is often dominated by complex viscous effects occurring within the boundary layer. There is often the possibility of grossly separated flow and recirculation especially near regions of high surface curvature. Furthermore, the flow is often highly unsteady as a result of periodic forcing from the nearby passage of the rotor blades and localized interactions with the rotor wake, especially on the tail-boom and empennage under certain flight conditions (see Section 11.2.2 for a detailed discussion). Predictive capabilities for pressure and skin friction drag are not yet mature. Current capabilities for design are based on synthesis of component drag using experimental data or by using a combination of experimental data and potential flow theory.

Although panel methods (see Section 14.7) are very flexible and can aid considerably in the design process, they are unable to confidently model viscous effects and separated flows typical of helicopter fuselage shapes and especially hub designs. However, empirical and semi-empirical corrections for the viscous effects can be incorporated into the basic method. For example, a 3-D boundary-layer method can be coupled by means of displacement corrections or by means of a transpiration velocity to the fuselage shape – see Lindhout et al. (1981) and de Bruin (1987). The advantage to the latter approach is that only the right-hand side of Eq. 14.40 is affected, thereby avoiding an expensive recalculation of the influence coefficients at every computational time step. The separated wake can be modeled as a vortical shear layer, the shape of which is either prescribed or made to be force free, as mentioned previously, but this also changes the influence coefficients. Furthermore, a prerequisite is that the separation line be calculated (say from a 3-D boundary layer solution) or deduced from experiment (say from surface flow visualization).

Overall, panel methods and semi-empirical modifications and corrections thereof have been shown to give good predictions of the surface pressure on isolated helicopter fuselages – see Polz & Quentin (1981), Polz (1982), Ahmed et al. (1988). Ahmed (1990) gives a good overview of the various predictive models in current use and their capabilities in predicting pressure distributions and drag on helicopter fuselages. Chaffin & Berry (1994) show that panel methods give good agreement with experimental measurements of fuselage surface pressure, and the predictions are just as good as Navier–Stokes approaches except in regions with large-scale flow separation. See also Narramore & Brand (1992).

CFD methods for airframe design are still in the development stage and are relatively far from being practical for use in routine helicopter fuselage design studies. The use of Navier–Stokes based CFD methods has the potential to help understand a number of problems associated with airframe aerodynamics and rotor–airframe interactional aerodynamics but, like several other problems in helicopter aerodynamics, the proper modeling of flow turbulence and flow separation remains a significant challenge. Another problem with CFD when applied to airframe calculations is the efficient generation of grids. Some progress is being made with hybrid grid systems that couple the advantages of structured and unstructured grids. An example of a CFD grid around a modern military helicopter is shown in Fig. 14.13, showing that this approach is really quite complex compared to a surface panel method such as that shown in Fig. 14.4. Rapid progress in grid generation techniques and solution algorithms is being made – see, for example, Berry et al. (1994), Chaffin & Berry (1994), Duque & Dimanlig (1994), Duque (1994), and Renaud et al. (2004), and it is likely that significant inroads toward an improved understanding of airframe aerodynamics and rotor–airframe interactions using these new methods will occur in the coming years. New numerical algorithms are being developed that will quickly and automatically generate computational grids for CFD analyses. This may allow CFD techniques to be used early on in the design and refinement of airframe shapes – see, for example, Naducci et al. (2003).

Meakin & Wissink (1999) have used overset structured grids to discretize the relatively complicated RAH-66 Comanche fuselage geometry, as shown in Fig. 14.13. See Meakin (1995, 1997) for details. Grid components are arranged to conform to the shape of the airframe, which, perhaps somewhat fortuitously in this case, was designed with relatively flat surfaces to reduce radar returns as a primary goal. Multiple grids facilitate resolution of the viscous boundary layer and important off-body aerodynamics. The near-body portion of the grid was decomposed into 110 components containing a total of approximately 2.2 million grid points. The off-body grid system included 233 components and 5.1 million points for a total of 7.3 million points in all. The flow solution has been used to examine

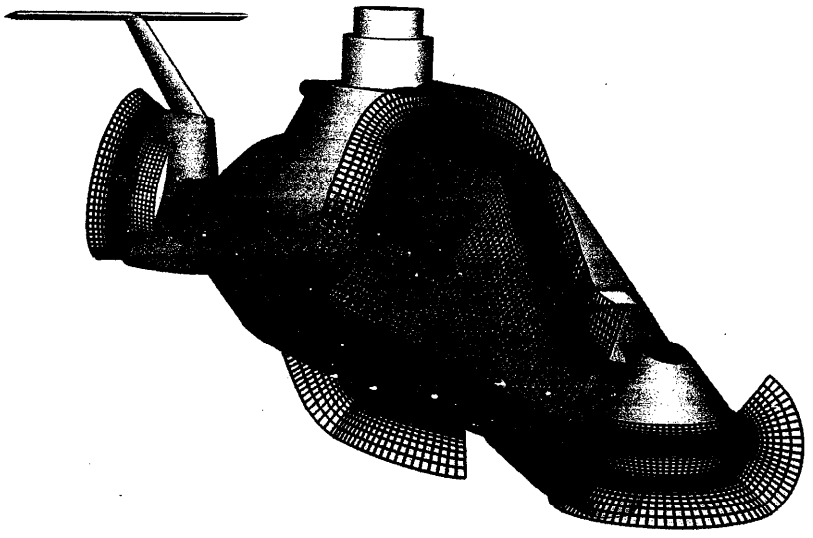

Figure 14.13 The generation of CFD grids around modern military helicopter airframes requires substantial effort in time and cost. Source: Image courtesy of NASA Ames and Robert Meakin, US Army AFDD.

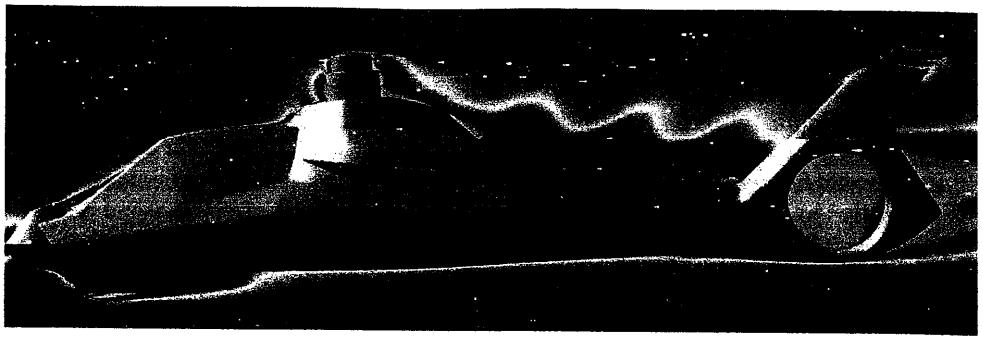

Figure 14.14 Unsteady flow over an isolated Comanche helicopter fuselage using a Navier–Stokes method. Particles released from the base of the main rotor hub. Instantaneous Mach number field on a plane at longitudinal centerline. (Side View). Source: Image courtesy of NASA Ames and Robert Meakin, US Army AFDD.

the effects of the turbulence in the main rotor hub wake on the unsteady aerodynamics at the tail – see Fig. 14.14. This is a good example of where CFD can provide much insight into a real problem that would be extremely time consuming and expensive to examine using either wind tunnel experiments or flight tests – see Berry (1997). Notice though that in this example, no representation of the rotor was included at all within the computation. Indeed, a major future goal is to be able to model, in fully coupled fashion, the interaction between the rotor and fuselage flows. Achieving this goal with the Navier–Stokes equations is still some distance in the future but will allow the unsteady effects of the rotor wake on the dynamics of the airframe to be examined, for instance, to determine the causes of the transient pitching moments that occur on some helicopters as the empennage moves in and out of the rotor wake during changes in flight speed (see Section 11.3.1).

Accurate modeling of the unsteady, localized interactions that take place between the fuselage and vortices from the rotor wake would enable designers to adopt less expensive approaches to minimizing fuselage weight, vibrations, cabin noise, and component fatigue. The results of advanced calculations such as these, when generated early enough in the design process to be of use, might prevent some of the expensive design mistakes that have been made in the past. This is a significant motivation for CFD practitioners. The current state of the art in coupled rotor-fuselage modeling falls somewhat short of this lofty aim, however. One interesting approach results from weakening the coupling between the aerodynamics of the rotor and fuselage – see, for instance, Zori & Rajagopalan (1995), Brézillon (2000), Renaud et al. (2003, 2004), and D'Alascio et al. (2003). In this approach, a full Navier–Stokes model for the fuselage is augmented by embedding a series of disks representing the rotors into the computational grid. A pressure jump across the disks is then imposed to represent the lift generation by the rotors, and some representation of the rotor wakes then develops in the computation as a result of the discontinuity in pressure around the edges of the disks. The pressure jump across the rotor disk quite often is calculated by using a comprehensive rotor model (see Section 14.11) to determine the time-averaged loading distribution over the rotor disk for the flight condition being modeled. In this way the time-averaged effects of the rotor on the fuselage can be represented. These methods are ideal for parametric studies at the design stage and can help give key insight to potentially unforeseen problems, even though computation time and cost is still relatively high. Panel methods, however, remain much more cost effective for design purposes than any of the other types of CFD approaches.

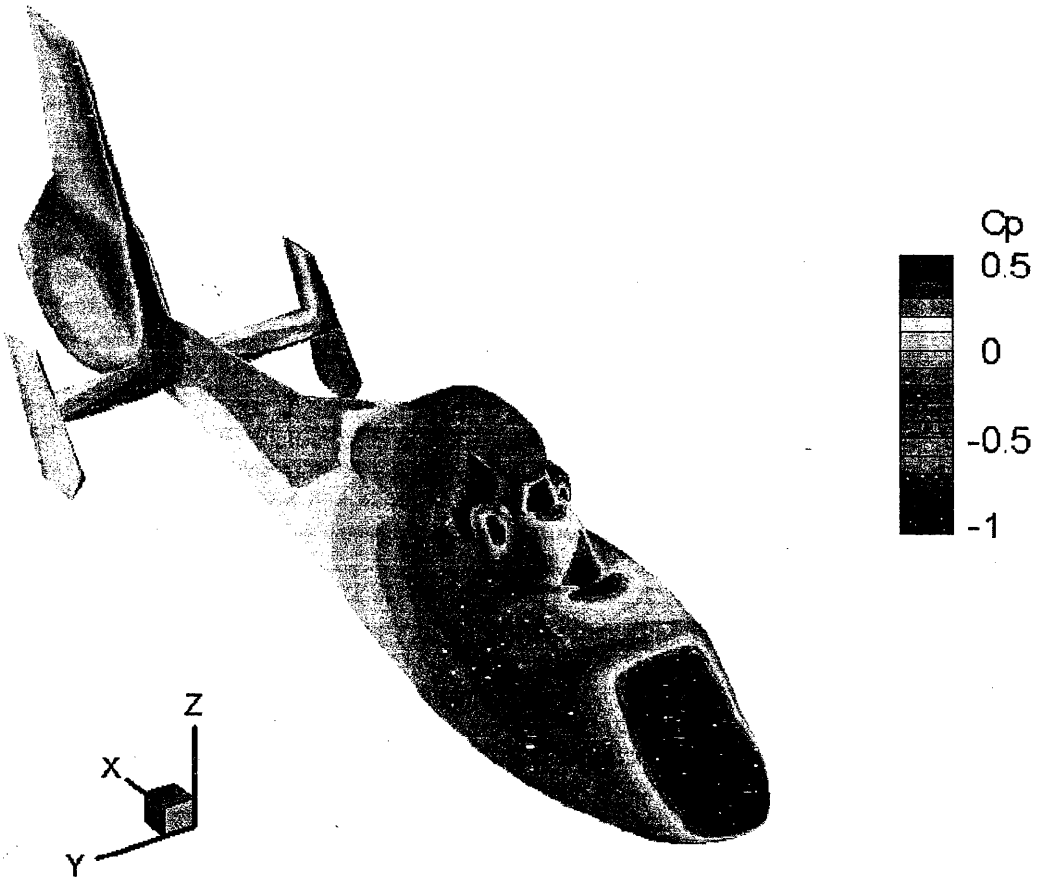

Figure 14.15 Predictions of the time-averaged pressure over the airframe of a helicopter in forward flight using a momentum-source representation of the rotor and a Navier–Stokes based flow solver for the airframe flow. Source: Image from Renaud et al. (2004).

More recent work by Park et al. (2003) and Renaud et al. (2004) has shown the continuing success of Navier–Stokes based methods in predicting airframe loads (see also Chapter 11). An example of such a Navier–Stokes calculation is shown in Fig. 14.15, where good agreement with measured airloads was also obtained. It is likely, however, that in the future various types of methods will be used in a more complementary fashion in design work, providing an improved predictive capability of airframe aerodynamics and elimination of possible adverse rotor–airframe interaction problems before helicopters make their first flights. Bear in mind though that the reciprocal coupling, giving the effects of the fuselage on the rotor, are not well represented using this approach and that the similarities between the fully unsteady situation and the aerodynamic behavior of the fuselage when forced by a steady rotor flow can sometimes be rather tenuous.

14.10.5 *Vibrations and Acoustics*

Today there are strong environmental pressures to reduce the aerodynamic noise that is generated by helicopters, a subject that has already been introduced in Section 8.19. The sources of noise on a helicopter are numerous, but a significant contribution is the

localized impulsive loading of the rotor blades as a result of wake-related BVIs (see Sections 8.16.4 and 10.4.2). There are also strong marketing pressures to improve ride comfort for crews and passengers alike and to reduce maintenance costs. This has driven much research to reduce the vibration levels of current helicopter designs. From a modeling point of view, these problems are similar in that they require very high-resolution predictions of the unsteady loads on the rotor blades and careful consideration of the structural dynamics of the complete helicopter as a system. In many situations a significant source of noise and vibration originates in the aerodynamic coupling between the various rotors of the helicopter. The situation is particularly severe when one rotor operates directly within the wake of another (for instance, in a helicopter with conventional configuration, the tail rotor might be operating within the wake generated by the main rotor – see Fig. 11.26). Because the wake from the one rotor usually takes a significant amount of time (in terms of rotor revolutions) to convect to the position of the other rotor (see, for instance, Section 11.4), the acoustic and vibration effects induced by rotor–rotor interactions are particularly challenging from a CFD point of view. This is because even a small level of contamination of the solution by numerical viscosity will distort the evolution of the wake and reduce the strength of the resultant BVIs. This has the effect of downgrading the accuracy of the calculated acoustic radiation or high frequency vibration dynamics of the rotor(s).

Figure 14.16 shows the results of a coupled rotor–fuselage calculation of the fidelity necessary to form an input to a helicopter acoustic prediction. The tandem rotor case shown in this case is particularly challenging from an acoustic prediction perspective because each rotor is partially immersed in the wake of the other, and the equal size of both rotors makes the calculation particularly sensitive to the detailed geometry of the wake generated by the entire system. The need for acoustic fidelity means that the aerodynamic interactions between the rotors must be fully represented, and the interaction-induced distortion to both wakes can be clearly seen. Notice though that to reduce the cost of the computation to tractable levels, the fuselage can be represented using a surface singularity method such as

Figure 14.16 Fully unsteady VTM calculation showing the aerodynamic interactions between the fuselage, forward and aft rotors of a generic tandem helicopter as required for acoustic or vibrations prediction. Image is shown looking upward at the helicopter from below. Source: Richard Brown and Imperial College, University of London.

described in Section 14.7 compared to a direct RANS or other CFD type of calculation. This is a good example of the careful blending or "fusion" of two types of computational tools to achieve aerodynamic fidelity while still retaining a practical level of computational cost for engineering purposes.

14.10.6 *Ground Effect*

Predicting the behavior of the helicopter when near the ground is practically very important because when flying at very low levels the pilot has very little tolerance for pathological or unexpected behavior on the part of the aircraft. Aerodynamically, as a hovering rotor is moved from free air or "out-of-ground effect" (OGE) toward the ground, the wake impinges on the ground surface – see Fig. 5.35 previously. Operating "in ground effect" (IGE) results in a change in the inflow through the rotor, and this usually manifests as an increase in rotor thrust for a constant power or, alternatively, as a decrease in power required for a given rotor thrust – see Section 5.8 for details. Forward flight further complicates the aerodynamics of the rotor problem IGE. For example, experimental results (Fig. 5.38) have shown that during transition into forward flight, ground effect can result in an increase in power required for a constant thrust (or a decrease in thrust for constant power), in contrast to the characteristics found for operations in hovering flight IGE. From a handling qualities perspective, large control movements can be required from the pilot during acceleration into forward flight to compensate for rather sudden transitions in the geometry of the flow surrounding the helicopter when near to the ground – see also Fig. 5.37.

Modeling the effects of the ground on helicopter performance has remained a severe challenge for all computational aerodynamic models because of the extremely complicated behavior of the rotor wake when it interacts with the ground. While the rotor IGE problem has been examined using Navier–Stokes approaches [see, for example, Kang & Sun (1997, 2000)] the problems posed by vorticity diffusion prove a significant impediment to accurate calculations, this time because the dynamics of the rotor wake when near to the ground appear to be controlled by the development and dynamics of unstable structures in the wake that take a very long time (when measured in rotor revolutions) to grow to appreciable amplitudes – see Brown & Whitehouse (2004). In this type of flow situation, vorticity conserving methods such as those described in Section 14.3 come into their own.

For example, Fig. 14.17 shows a calculation of the wake generated by a helicopter in low-speed quartering flight while very close to the ground. An interesting feature at this flight speed is that the wake ahead of the main rotor rolls up to form a crescent-shaped "bow vortex" along the forward edge of the footprint of the wake on the ground – see also Fig. 5.37 for experimental observations of this phenomenon for an isolated rotor. This bow vortex interacts with the ground and with the fuselage of the helicopter, buffeting the aircraft and inducing, potentially, an unacceptable increase in pilot workload in this critical flight condition. At higher flight speeds, the bow vortex is swept away into the flow downstream of the rotor, the wake lifts off the ground and the helicopter essentially behaves as it would out of ground effect.

14.10.7 *Vortex Ring State*

While the accurate prediction of rotor flow fields is difficult under most flight conditions, prediction of the wake dynamics during descending flight has proven to be a particularly challenging problem for the analyst. This is partly because of blade–vortex interaction (BVI) and a general susceptibility to aperiodicity of the rotor wake structure.

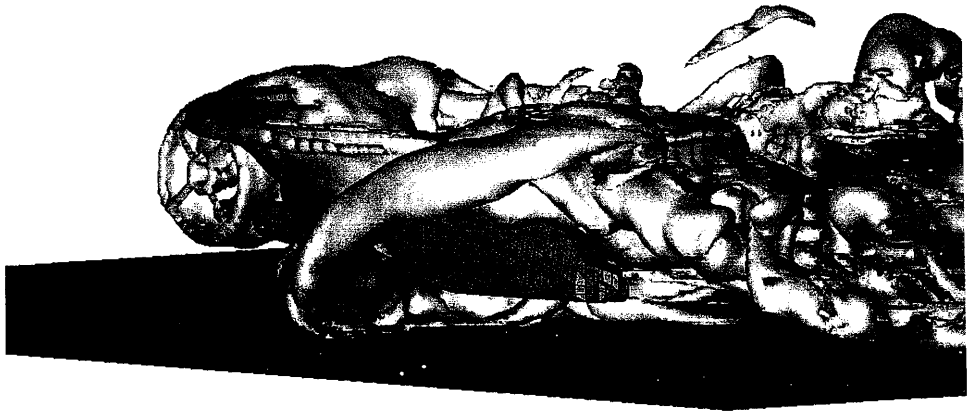

Figure 14.17 VTM calculation of the wake structure generated by a helicopter flying rearwards and to the right while very close to the ground. Notice the highly unsteady "bow vortex" on the ground plane upwind of the main rotor, and the strong interaction between the wake of the tail rotor and the main rotor under these flight conditions. Source: Richard Brown and Imperial College, University of London.

When the rotor is descending at high rates or steep angles, the rotor can encounter an adverse condition known as the vortex ring state (VRS) – see Sections 2.13.5 and 5.7 for a description of the basic physics. Under VRS conditions, convection of the vorticity produced by the blades away from the rotor is disrupted, and the vorticity in the wake accumulates near the rotor plane, clumping or bundling together and producing large, aperiodic airloads. In aerodynamic terms, the onset of the VRS is associated with the collapse of the orderly structure of the rotor wake into a highly disturbed, irregular, recirculating flow. This behavior is related to the stability of the helicoidal wake – see Section 10.8.1.

The highly nonlinear physics of the VRS is further complicated by the likelihood of flow separation and blade stall on more highly loaded rotors during descending flight. This can occur because of the higher aerodynamic angles of attack produced on the inboard parts of the blades during descent, or, when in the VRS, the blades chop through the accumulations of vorticity engulfing the rotor. Flight tests (see discussion in Section 2.13.5) show that in partial power descent near the VRS the rotor can operate without evidence of blade stall and at relatively low power, but that another state can be reached at the same airspeed and rate of descent where the rotor requires much higher power because of blade stall. This observation suggests that, in addition to the nonlinear behavior of the wake within the VRS, nonlinearity in the aerodynamics of the blades also plays an important role in governing helicopter behavior in the VRS.

Figure 14.18 shows a calculation of the wake produced by a representative four-bladed helicopter rotor when deep within the VRS. Contrast the aperiodic and somewhat chaotic nature of the wake shown at right in this figure with the orderly wake structure, shown at left, found at higher descent rates. Yet notice how, in the far wake lie the beginnings of the wake instability that will eventually travel down through the wake to engulf the rotor if the descent rate of the helicopter is reduced below the critical value for VRS onset. Although computational techniques such as the VTM and FVM have been very successful in reproducing the basic physical phenomena associated with flight in the VRS [see Brown et al. (2002) for a good discussion], much work still needs to be done in fully understanding the mechanisms leading to the onset of the VRS and the influence of the rotor

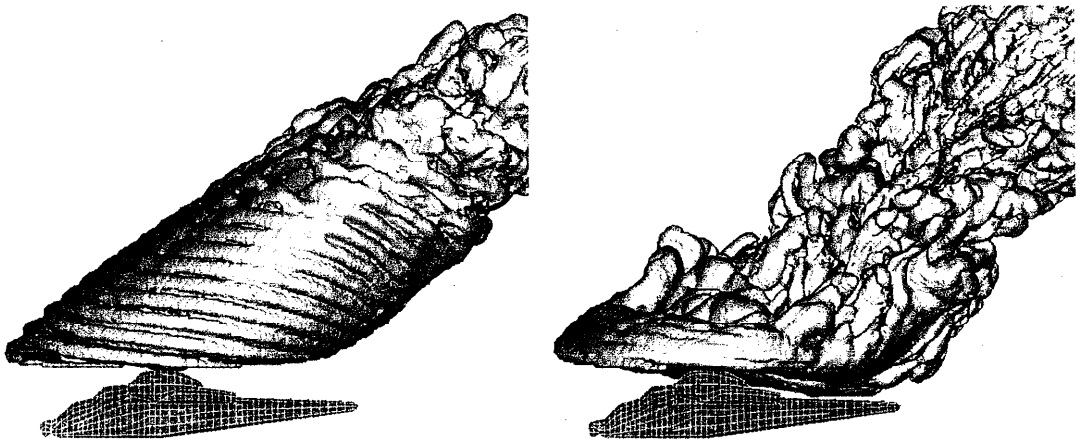

Figure 14.18 VTM calculated wake structure for a four-bladed rotor deep within the VRS. Left: with the helicopter in rapid descent the orderly structure of the wake persists for many rotor revolutions downstream. Right: In the VRS at lower descent rates, the wake collapses into a highly unsteady, recirculating, disordered flow. Source: Images courtesy of Gary Ahlin & Imperial College, University of London.

and fuselage geometry on the behavior once in the VRS [see also Bhagwat & Leishman (2000b), Leishman et al. (2002), Brown et al. (2004)].

14.11 Comprehensive Rotor Analyses

CFD models of the complexity required to yield the aerodynamic fidelity desired for helicopter rotors will be too expensive in the shorter term for parametric design calculations. Yet the hope is that the knowledge obtained using these types of models can be used to guide and inform the construction of more parsimonious models that can be used in an engineering context to design the next generation of quieter, safer, more comfortable helicopters. This fundamental concept is embodied in so-called comprehensive rotor analyses, which attempt to combine together the best available models of aerodynamics, the rotor and airframe structure, rotating blade dynamics, aeroelasticity, etc. into a single computer code. The principles of comprehensive code development are reviewed by Johnson (1981a,b). Over the past 40 years several such models have been developed by government research organizations, individual helicopter companies and by universities specializing in helicopter teaching and research.

The aim of the comprehensive analysis is to use the highest levels of modeling capability while still balancing the overall requirements of practicality and computational feasibility for use in parametric helicopter design studies. The objectives are to calculate accurately all of the blade airloads, the rotor trim, the aircraft performance, overall vibration levels, control loads, aeroelastic effects, acoustics, and so on. Notable among the modern comprehensive codes is the CAMRAD (Comprehensive Analysis and Modeling of Rotor Aerodynamics and Dynamics) family that has been developed by Johnson (1981a,b, 1994, 1998). However, a principal difficulty in the comprehensive analysis is that by definition the approach is multidisciplinary and so relies on an ability to couple together often traditionally separate areas of analysis developed by different specialists. This may be difficult for reasons of computational cost or because the models in the separate disciplines are written in different mathematical forms that do not lend themselves readily to interdisciplinary coupling. Yet it

is the better integration of traditionally separate disciplines of helicopter analysis that will ultimately allow better rotor systems and more capable helicopters to be designed.

Currently, the technical capabilities of the comprehensive codes continue to be limited by several factors, including both the understanding of the physical behaviors and the mathematical modeling capabilities in each subdiscipline, as well as the numerical solution methods and the actual techniques used for computer implementation. Unfortunately, there is not always a good balance of disciplines in comprehensive helicopter analyses codes, this being a result of many factors, including the notion by the developers of what is actually considered state-of-the-art in each discipline.

Recently, there has been a bold effort toward integrating CFD into comprehensive rotor analyses – see, for example, Strawn et al. (1989), Kim et al. (1991), Beaumier (1994), Yang et al. (2002), Sitaraman et al. (2003), and Potsdam et al. (2004). The idea is obvious, in that the theoretically higher aerodynamic fidelity of the CFD solution can be used to better predict nonlinear and 3-D phenomena on the blades, including transonic flows and dynamic stall. This approach, however, involves several practical issues, not least of which is the much higher computational cost of the CFD. A significant issue is the actual process of numerically coupling together the CFD solution with the structural dynamic motion of the rotor blades. One approach is to use the loose or "weak" coupling procedure that has been alluded to previously. Here, the inflow angles from the comprehensive rotor analysis (which may involve blade aeroelastic effects using a nonlinear structural dynamic model of the rotor and its blades, and a FVM for the wake) are used as an input boundary condition to the CFD solution. Some information, such as integrated airloads from the CFD solution, is iterated between the two methods. This approach, however, has shown difficulties in achieving proper convergence to periodic conditions. Another approach is called the tight or "strong" coupling procedure, whereby the CFD and structural dynamic solution are coupled in time and solved simultaneously. This approach is computationally more demanding, but for some problems it has shown somewhat more encouraging results.

The development of various types of improved wake models in differential equation form may provide a good bridge between the capabilities of parsimonious models and more complete CFD-based methods. One goal for the future is to develop reduced order aerodynamics models directly from the Navier–Stokes equations, taking into account the need for simplified, fast mathematical realizations in certain applications – such as helicopter flight dynamics and handling qualities where the integration of CFD techniques for modeling the wake is seen as a route to improving the fidelity of the free-flight dynamic model of the helicopter [see Brown & Houston (2000)] but where there is also a particular need for accurate real-time simulation of the dynamic response of the helicopter. These reduced-order models will require extensive validation to assess confidence levels, both against complete solutions and against experimental measurements. This is one reason why the wind tunnel testing of complete helicopters and their subcomponents is essential if better understanding of helicopter aerodynamics and evaluation of predictive capability is ever to be obtained.

The following items define in more detail the typical approach and limitations of the comprehensive rotor analysis:

1. *Aerodynamics*: As explained throughout this book, the aerodynamics of the rotor underpins all helicopter flight. It is precisely here, though, that many physical problems require further study if overall modeling capabilities are to be improved. An issue with aerodynamic models is that, because of the complexity of the problems found on helicopters, significant empiricism may be needed to obtain useful results. A good example is in the problem of

modeling dynamic stall (Section 9.5) or the modeling of the tip vortices in the rotor wake (Section 10.6.2). Rotor–airframe interactional problems (Section 11.2.5) are also difficult to model without resorting to significant empiricism, and this is an unavoidable artifact of having to represent the powerful effects of viscosity with more parsimonious models that have practical levels of computational efficiency. While there is nothing wrong with empiricism, and all models of physical process incorporate empiricism to a lesser or greater extent, unfortunately the temptation is often to use empirical coefficients in a model as "tunable" variables that can be used to make the model match with the measured overall behavior of specific systems – for instance, those used to "validate" the model. This of course leads to many problems when significant departures from the original systems are encountered. The future must see not only efforts to improve empirical modeling and better experiments to better estimate the coefficients that go into these models, but also an effort to reduce empiricism outright. This is particularly true in regard to wake modeling, where unnecessary pseudo-empiricism, in the form of tuning parameters, has on occasion been used to control or suppress underlying numerical problems with the solution algorithms – often ultimately proving to give completely misleading results in application. The more recent move toward the use of CFD to define the aerodynamics in comprehensive rotor simulations is a positive step toward better defining the operating capabilities of the rotor. However, because of the inherent limitations of CFD alluded to in previous sections, it would seem that there is still a long path to follow before Navier–Stokes CFD based comprehensive rotor analyses will see regular use in the design of new rotors. In the interim, the continued development of the VTM or FVM similar approaches probably offer much better opportunities for inclusion in practical design activities.

2. *Structural dynamics*: Because rotor blades are relatively long and slender, models based on beam theory can be used. The governing equations (which are partial differential equations) can be reduced to flap and lag bending, torsional displacements and axial extension. The advent of finite-element methods (in space and time) has allowed a lot of adaptability in the representation of rotor blades and hubs. Nonlinear structural and inertial effects must be considered in conjunction with the aerodynamic forces and moments. Historically, the complexity of this coupling has hindered development, and most existing theories (but not all) are restricted to small, nonlinear deflections. Finite element methods have also allowed fairly accurate representation of the dynamics of the airframe and airframe components. Coupling of the rotor and airframe dynamics is still not a mature process, however, in part because of the number and type of finite elements required and also because of the extensive computational resources required to model the fully coupled rotor-fuselage dynamics. Nevertheless, such approaches are urgently required because of the need to better predict airframe vibrations.

3. *Numerical methods*: In comprehensive codes, the equations governing the behavior in each subdiscipline are solved numerically. In many cases, the numerical methods most suited to each discipline may not be mutually compatible. The need to achieve consistency, stability and accuracy for all elements of the model poses many demands on the development of satisfactory numerical methods. The generation of robust numerical methods that can be used under a wider range of conditions continues to be a research goal. Complicated mathematical models involving layers of empiricism seem to be a mainstay for many design purposes, but such methods always have a high probability of capturing the unwanted noise that is inherent in the uncertainties in the experimental data used to deduce the empirical models. There is always a need to balance the complexity of the model against the accuracy of the model, whilst aiming to minimize the variability and maximize the intelligibility

of the resulting simulation. It is known that, for complex mathematical models, predictive accuracy increases with increasing modeling complexity up to a point where the cumulative uncertainties in the empirical components of the model begins to increase the noise in the model. Beyond this complexity, predictive accuracy begins to decrease again, the system exhibiting a classic "Ockham's Hill" – see Gauch (1993). The goal is to balance modeling complexity with predictive fidelity, something that cannot just be achieved through careful, systematic validation studies, but also requires a degree of engineering "common sense."

4. *Software engineering*: The various mathematical models of helicopter analysis are implemented as software or "code." This code must be carefully written, thoroughly tested and well documented. Ideally the code must be modular, so that components can be updated as improved subcomponent models become available – perhaps as a result of an improved understanding of the physics. This ideal is rarely achieved in practice – codes, unfortunately, always seem to become "hard-wired" between subcomponent models and so upgrading can become very difficult. The complexity of the helicopter problem means that documentation too is often complicated and may be difficult even for users with specialized backgrounds to use effectively. This is a serious problem for which there is no easy answer and simply reflects the multidisciplinary but still specialized nature of helicopter design. However, software standardization is a problem that must be continuously addressed if the community is to move forward toward the development of better comprehensive prediction methods for use in helicopter performance, loads, and design.

14.12 Chapter Review

This chapter has summarized the various computational methods being used in the analysis of helicopter problems. The important role of computational fluid dynamics, particularly in the form of the Navier–Stokes equations, in better understanding problems in helicopter aerodynamics has been emphasized. To some, the use of "CFD" is held out to be the salvation for the helicopter aerodynamicist, but this is a misleading perspective. CFD will ultimately prevail for the complete simulation of the flow about a helicopter, but there are still many fundamental numerical and practical issues to be resolved, least of all is in the proper and efficient coupling of the CFD to the dynamic and elastic structural motion of the various components of the helicopter. The preservation of vorticity over many rotor revolutions is clearly one key to providing better CFD models of the rotor wake. The development of more general and more adaptable turbulence closure models must also continue, particularly as they apply to describing the vortical nature of rotor wakes and the structure of the blade tip vortices. Such issues are important in better understanding a whole host of practical helicopter flight problems such as descending flight, maneuvers, flight in the VRS or in autorotation, interactional aerodynamics between various airframe components, flight near the ground and many problems in rotor vibration and acoustics. Meantime, these problems require immediate or shorter term solution capabilities, and it is unrealistic to expect these problems to wait in the sidelines until pure CFD reaches the required level of maturity. Meantime, more parsimonious aerodynamic models must continue to be developed, with the ideal of fusing together the capabilities of the best available models.

It is fair to say that the large computer resources required, and the algorithmic challenges posed by modern CFD methods have thus far limited their use for many practical problems in helicopter design. This is especially the case for the Navier–Stokes and Euler-based methods. The community has invested heavily in a variety of CFD approaches, but the task of modeling the flow about a complete helicopter, or even just the rotor, is indeed truly

daunting. The various rotating and nonrotating aerodynamic components of a helicopter make generating appropriate grids on which to solve the equations a challenging problem in itself. Passing flow information back and forth between these grids requires special numerical algorithms and incurs significant computational cost. Until the grid generation process becomes more automated and can tackle complex geometries with ease, the use of many types of CFD methods will not lie in the domain of practicality for helicopter designers. Even then, validation of the models and resulting flow predictions requires extensive work and continues to offer challenges for the experimentalists in providing suitable quality surface and off-surface flow field measurements. Unless proper validation of its predictive capabilities can be ensured, CFD cannot be assigned the confidence levels necessary for use in design, no matter how fundamentally sophisticated the method. These problems offer many new opportunities that are rich for new research.

There are other areas such as aeroelasticity and flight mechanics simulations, where the coupling of CFD into the solution process is less practical, at least in the shorter time. This is in part because of high computational costs and/or the difficulties in coupling different types of solution methodologies. How the helicopter actually flies comes under the domain of flight mechanics, and flight dynamics and handling qualities assessments may require a real-time or near real-time solution, rendering many "state-of-the-art" aerodynamic models impractical. Also, for some applications the equations describing the aerodynamics must be written in a specific mathematical form (as ordinary differential equations, for instance) to be compatible with the methods of analysis used for flight control system design. This is where the role of so-called "reduced-order" models can make significant inroads by avoiding the expense and difficulties of a complete CFD solution, yet much validation is required to gain confidence levels. The proper coupling and integration of aerodynamic methods of analysis into other disciplines of helicopter analysis is really the key to designing better helicopters. It is clear that the future offers many exciting opportunities for research focused toward the development of more innovative computational models with greater predictive capabilities. Only then can the problems that limit the performance and capabilities of the helicopter be understood and mitigated. Given the complexity of the helicopter flow field, it is likely that CFD methods for helicopter applications will reach maturity only long after their application within the fixed-wing community is accepted as standard practice.

14.13 Questions

14.1. To some, the development of advanced CFD methods is held out to be the imminent salvation for the helicopter aerodynamicist. Discuss why this is a misleading perspective and serves only to hinder shorter-term research using other viable approaches.

14.2. Starting from the Euler equations in two dimensional steady flow, show that for an irrotational isentropic flow that the governing equation for the flow can be written as

$$\left(\frac{\partial \phi}{\partial x}\right)^2 + \left(\frac{\partial \phi}{\partial y}\right)^2 + \frac{2}{\gamma - 1} a^2 = \text{constant},$$

where ϕ is a velocity potential. Explain why this equation is difficult to solve.

14.3. Show that, if the flow is assumed to be incompressible, the vorticity transport equation can be derived directly by taking the curl of the Navier–Stokes momentum equation.

14.4. The underlying governing equation for surface singularity (or panel) methods is Laplace's equation. Show that a solution to Laplace's equation allows velocity potentials and velocity components to be added but not pressures.

14.5. Prove that the concept of the thin airfoil theory is consistent with a flow model where the circulation is bound to the 1/4-chord of the airfoil and flow tangency is satisfied at the 3/4-chord. Show further that this type of model must implicitly satisfy the Kutta condition at the trailing edge.

14.6. In a discretized lifting-line model of a rotor blade, it is often assumed that all of the "bound" circulation outboard of the maximum bound circulation rolls up into the tip vortex. Prove that this result gives a tip vortex with strength equal to the maximum bound circulation on the blade.

14.7. It is often assumed that the flow in the rotor wake can be assumed to be incompressible. Discuss, and explain why this assumption can allow for a significant simplification in the mathematical modeling of the wake flow.

14.8. Explain the types of computational grids that could be used for finite-difference solutions to the Navier–Stokes equations. What types of grids and resolutions would be preferable near the rotor as opposed to in the far wake? Justify your answer.

14.9. Discuss the general difficulties in the modeling of the problem of dynamic stall using CFD approaches. What specific modeling issues continue to hinder successful quantitative prediction of the airloads associated with dynamic stall?

14.10. What is meant by a "chimera" grid? Explain the principle of using a chimera grid to track regions of concentrated vorticity in the flow. What are some of the practical complications in the use of this approach for helicopter use in helicopter applications?

14.11. Use a web search to find out about currently used methods of grid generation for CFD applications to helicopter aerodynamics problems. Explain the differences between a structured grid and an unstructured grid. Why might the use of unstructured grids be viewed as a particularly useful approach in some types of problems found in helicopter aerodynamics?

Bibliography

Agarwal, R. K. and Deese, J. E. 1988. "Navier–Stokes Calculations of the Flow field of a Helicopter Rotor in Hover," AIAA Paper 88-0106, 26th AIAA Aerospace Sciences Meeting, Reno, NV, Jan. 11–14.

Ahmad, J. U. and Strawn, R. C. 1999. "Hovering Rotor and Wake Calculations with an Overset-Grid Navier-Stokes Solver," 55th Annual Forum of the American Helicopter Soc., Montreal, Canada, May 25–27.

Ahmed, S. R., Amtsberg, J., de Bruin, A. C., Cler, A., Falempin, G., Le, T. H., Polz, G., and Wilson, F. T. 1988. "Comparison with Experiment of Various Computational Methods of Airflow on Three Helicopter Fuselages," 14th European Rotorcraft Forum, Milan, Italy, Sept. 20–23.

Ahmed, S. R. 1990. "Fuselage Aerodynamic Design Issues and Rotor/Fuselage Interactional Aerodynamics–Part. 2: Theoretical Methods," In: AGARD-R-781.

Baldwin, B. S. and Lomax, H. 1978, "Thin Layer Approximation and Algebraic Model for Separated Turbulent Flows," AIAA Paper 78-257, 16th AIAA Aerospace Sciences Meeting, Huntsville, AL, Jan. 16–18.

Barakos, G., Drikakis, D., and Leschziner, M. A. 1998. "Numerical Investigation of the Dynamic Stall Phenomenon Using Nonlinear Eddy-Viscosity Models," AIAA Paper 98-2740, 16th AIAA Applied Aerodynamics Conference, Albuquerque, NM, June 15–18.

Berry, J. D., Chaffin, M. S., and Duque, E. 1994. "Helicopter Fuselage Aerodynamic Predictions: Navier–Stokes and Panel Method Solutions and Comparison with Experiment," American Helicopter Soc. 3rd Decennial Specialists' Conference on Aeromechanics, San Francisco, CA, Jan. 19–21.

Beaumier, P. 1994. "A Coupling procedure Between a Rotor Dynamics Code and a 3D Unsteady Full Potential Code," American Helicopter Soc. 3rd Decennial Specialists' Conference on Aeromechanics, San Francisco, CA, Jan. 19–21.

Berry, J. D. 1997. "Unsteady Velocity Measurement Taken behind a Model Helicopter Rotor Hub in Forward Flight," NASA TM-4738.

Bhagwat, M. J. and Leishman, J. G. 2000a. "Measurements of Bound and Wake Circulation on a Helicopter Rotor," *J. of Aircraft*, 37 (2), pp. 227–234.

Bhagwat, M. J. and Leishman, J. G. 2000b. "Stability Analysis of Helicopter Rotor Wakes in Axial Flight," *J. of the American Helicopter Soc.*, 45 (3), pp. 165–178.

Bhagwat, M. J., Moulton, M. A., and Caradona, F. X. 2005. "Development of a New Potential Flow Based Model for Hover Performance Prediction," AIAA Paper 2005-1367, 43rd AIAA Aerospace Sciences Meeting, Reno, NV, Jan. 10–13.

Brézillon, J. 2000. "Simulation of Rotor-Fuselage Interaction using an Actuator Disk," 26th European Rotorcraft Forum, The Hague, Netherlands, Sept. 26–29.

Brown, R. E. 2000. "Rotor Wake Modeling for Flight Dynamic Simulation of Helicopters," *AIAA J.*, 38 (1), pp. 57–63.

Brown, R. E. and Houston, S. S. 2000. "Comparison of Induced Velocity Models for Helicopter Flight Mechanics" *J. of Aircraft*, 37 (4), pp. 623–629.

Brown, R. E. and Whitehouse, G. R. 2004. "Modeling Rotor Wakes in Ground Effect," *J. of the American Helicopter Soc.*, 49 (3), pp. 238–249.

Brown, R. E., Leishman, J. G., Newman, S. J., and Perry, F. J. 2002. "Blade Twist Effects on Rotor Behavior in the Vortex Ring State," 28th European Rotorcraft Forum, Bristol, England, Sept. 17–20.

Brown, R. E., Line, A. J., and Ahlin, G. A. 2004. "Fuselage and Tail-Rotor Interference Effects on Helicopter Wake Development in Descending Flight," 60th Annual Forum of the American Helicopter Soc., Baltimore, MD, June 7–10.

Caradonna, F. X. 1990. "The Application of CFD to Rotary Wing Problems," *Aerodynamics of Rotorcraft*, In: AGARD-R-781.

Caradonna, F. X. and Isom, M. P. 1972. "Subsonic and Transonic Potential Flow over Helicopter Rotor Blades," *AIAA J.*, 12 (12), pp. 1606–1612.

Chaffin, M. S. and Berry, J. D. 1994. "Navier–Stokes and Potential Theory Solutions for a Helicopter Fuselage and Comparison with Experiment," NASA Technical Memorandum 4566, ATCOM Technical Report 94-A-013.

Chan, W. M., Meakin, R. L., and Potsdam, M. A. 2001. "CHSSSI Software for Geometrically Complex Unsteady Aerodynamic Applications, AIAA Paper 2001-0593, 39th AIAA Aerospace Sciences Meeting & Exhibit, Reno, NV, Jan. 8–11.

Conlisk, A. T. 2002. "Modern Helicopter Rotor Aerodynamics," *Progress in Aerospace Sciences*, 37, pp. 419–476.

D'Alascio, A., Berthe A., and Le Chuiton, F. 2003. "Application of CFD to the Fuselage Aerodynamics of the EC145 Helicopter. Prediction of Unsteady Phenomena and of the Time Averaged Influence of the Main Rotor," 29th European Rotorcraft Forum, Friedrichshafen, Germany, Sept. 16–18.

de Bruin, A. C. 1987. "Three-Dimensional Boundary Layer Calculation Results on the GARTEUR Helicopter Fuselage with Shallow Ramp ($\alpha = 0°$ and $\alpha = -5°$)," NLR TR 87099L.

Duque. E. P. N. 1992. "Numerical Analysis of the British Experimental Rotor Program Blade," *J. of the American Helicopter Soc.*, 37 (1), pp. 46–54.

Duque, E. P. N. and Dimanlig, A. C. B. 1994. "Navier–Stokes Simulation of the RAH-66 (Comanche) Helicopter," American Helicopter Soc. 3rd Decennial Specialists' Conference on Aeromechanics, San Francisco, CA, Jan. 19–21.

Duque, E. P. N. 1994. "A Structured/Unstructured Embedded Grid Solver for Helicopter Rotor Flows," 50th Annual Forum of the American Helicopter Soc., Washington, DC, May 11–13.

Duraisamy, K. and Baeder, J. 2004. "Control of Helicopter Rotor Tip Vortex Structure Using Blowing Devices," 60th Annual Forum of the American Helicopter Soc., Baltimore, MD, June 7–10.

Ekaterinaris, J. A., Srinivasan, G. R., and McCroskey, W. J. 1994. "Present Capabilities of Predicting Two-Dimensional Dynamic Stall," In: AGARD CP-552.

Gauch, H. G., Jr. 1993. "Prediction, Parsimony and Noise," *American Scientist*, 81, pp. 468–478.

Geissler, W. and Trenker, M. 2002. "Numerical Investigation of Dynamic Stall Control by a Nose Droop Device," American Helicopter Soc. Technical Specialists Meeting on Aerodynamics, Acoustics, and Test and Evaluation, San Francisco, CA, Jan. 23–25.

Gessow, A. 1985. "An Assessment of Current Helicopter Theory in Terms of Early Developments," 5th Nikolsky Lecture, 41st Annual Forum of the American Helicopter Soc., Fort Worth, TX, May 15–17, 1985.

Glauert, H. 1947. *The Elements of Aerofoil and Airscrew Theory,* Cambridge University Press, Cambridge, UK.

Hess, J. L. and Smith, A. M. O. 1962. "Calculation of Nonlifting Potential Flow About Arbitrary Three-Dimensional Bodies," Douglas Aircraft Report ES40622.

Hess, J. L. 1990. "Panel Methods in Computational Fluid Dynamics," *Annual Review of Fluid Mechanics*, 22, pp. 255–274.

Houghton, E. L. and Carpenter, P. W. 1993. *Aerodynamics for Engineering Students*, John Wiley & Sons, Inc., New York, NY.

Johnson, W. 1981a. "Development of a Comprehensive Analysis for Rotorcraft: I–Rotor Model and Wake Analysis," *Vertica*, 5 (2), pp. 90–130.

Johnson, W. 1981b. "Development of a Comprehensive Analysis for Rotorcraft: II–Aircraft Model, Solution Procedure and Applications," *Vertica*, 5 (3), pp. 285–216.

Johnson, W. 1994. "Technology Drivers in the Development of CAMRAD II," American Helicopter Soc. 3rd Decennial Specialists' Conference on Aeromechanics, San Francisco, CA, Jan. 19–21.

Johnson, W. 1998. "Rotorcraft Aeromechanics Applications of a Comprehensive Analysis," HeliJapan 98: AHS International Meeting on Advanced Rotorcraft Technology and Disaster Relief, Japan, April 21–23.

Kang, N. and Sun, M. 1997. "Prediction of the Flow Field of a Rotor in Ground Effect," *J. of the American Helicopter Soc.*, 42 (2), pp. 195–198.

Kang, N. and Sun, M. 2000. "Simulated Flowfields in Near-Ground Operation of Single- and Twin-Rotor Configurations," *J. of Aircraft*, 37 (2), pp. 214–220.

Katz, J. and Plotkin, A. 1991. *Low Speed Aerodynamics–From Wing Theory to Panel Methods*, McGraw-Hill, New York, NY.

Kim, H., Williams, M. H., and Lyrintziz, A. S. 2002. "Improved Method for Rotor Wake Capturing," *J. of Aircraft*, 39 (5), pp. 794–803.

Kim, K-C., Desopper, A., and Chopra, I. 1991. "Blade Response Calculations Using Three-Dimensional Aerodynamic Modeling," *J. of the American Helicopter Soc.*, 36 (1), pp. 68–77.

Landgrebe, A. J. 1988. "Overview of Helicopter Wake and Airloads Technology," 2nd International Conference on Rotorcraft Basic Research, College Park, MD, Feb. 16–18.

Landgrebe, A. J. 1994. "New Directions in Rotorcraft Computational Aerodynamics Research in the US," In: AGARD CP-552.

Lê, T. H., Ryan, J., and Falempin, G. 1987. "Wake Modeling for Helicopter Fuselage," 13th European Rotorcraft Forum, Arles, France, Sept. 8–11.

Lee, T., Petrakis, G., Mokhtarian, F., and Kafyeke, F. 2000. "Boundary-Layer Transition, Separation, and Reattachment on an Oscillating Airfoil," *J. of Aircraft*, 37 (2), pp. 356–360.

Lee, Y-L and Baeder, J. D. 2002. "High-Order Overset Method for Blade Vortex Interaction," AIAA Paper 2002-0559, 40th AIAA Aerospace Sciences Meeting and Exhibit, Reno, NV, Jan. 14–17.

Leishman, J. G., Bhagwat, M. J., and Ananthan, S. 2002. "The Vortex Ring State as a Spatially and Temporally Developing Wake Instability," American Helicopter Soc. International Specialists Meeting on Aerodynamics, Acoustics and Test & Evaluation, San Francisco, CA, Jan. 23–25.

Leishman, J. G., Bhagwat, M. J., and Bagai, A. 2002. "Free-Vortex Filament Methods for the Analysis of Helicopter Rotor Wakes," *J. of Aircraft*, 39 (5), pp. 759–775.

Lindhout, J. P. F., Moek, G., de Boer, E., and van der Berg, B. 1981. "A Method for the Calculation of 3D Boundary Layers on Practical Wing Configurations," *J. of Fluids Engineering*, 103 (1), pp. 104–111.

Line, A. J. and Brown, R. E. 2004. "Efficient High-Resolution Wake Modeling Using the Vorticity Transport Equation," 60th Annual Forum of the American Helicopter Soc., Baltimore, MD, June 7–10.

Mahalingam, R. and Komerath, N. M. 1998. "Measurements of the Near Wake of a Rotor in Forward Flight," AIAA Paper 98-0692, 36th AIAA Aerospace Sciences Meeting, Reno, NV, Jan 12–15.

Martin, P. B., Chandrasekhara, M. S., and Geissler, W. 2003. "Dynamic Stall Measurements and Computations for a VR-12 Airfoil With a Variable Droop Leading Edge," American Helicopter 59th Annual Forum, Phoenix, AZ, May 6–8.

Martin, P. B., Leishman, J. G., and Pugliese, G. 2003. "High Resolution Trailing Vortex Measurements in the Wake of a Hovering Rotor," *J. of the American Helicopter Soc.*, 48, (1), pp. 39–52.

Marvin J. G. and Huang, G. P. 1996. "Turbulence Modeling–Progress and Future Outlook," 15th Int. Conf. on Numerical Methods in Fluid Dynamics, Monterey, CA, June 24–28. Also NASA TM 110414.

Maskew, B. 1982. "Prediction of Subsonic Aerodynamic Characteristics: A Case for Low-Order Panel Methods," *J. of Aircraft*, 19 (2), pp. 157–163.

McAlister, K. W., Schuler, C. A., Branum, L., and Wu, J. C. 1995. "3-D Wake Measurements near a Hovering Rotor for Determining Profile and Induced Drag," NASA TP 3577.

McAlister, K. W. 1996. "Measurements in the Near Wake of a Hovering Rotor," AIAA Paper 96-1958, 27th AIAA Fluid Dynamics Conference, New Orleans, LA, June 18–20.

McCroskey, W. J. 1985. "The Effects of Gusts on the Fluctuating Airloads in Transonic Flow," *Journal of Aircraft*, 22 (3), pp. 236–243.

McCroskey, W. J. 1995. "Vortex Wakes of Rotorcraft," AIAA Paper 95-0530, 33rd AIAA Aerospace Sciences Meeting and Exhibit, Reno, NV, Jan. 9–12.

McCroskey, W. J. and Baeder, J. D. 1985. "Some Recent Advances in Computational Aerodynamics for Helicopter Applications," NASA TM-86777.

McCroskey, W. J. and Goorjian, P. M., 1983. "Interactions of Airfoils with Vertical Gusts and Concentrated Vortices in Unsteady Transonic Flow," AIAA Paper 83-1691, 16th AIAA Fluid and PlasmaDynamics Conference, Danvers, MA, July 12–14.

Meakin, R. 1995. "Unsteady Simulation of the Viscous Flow About a V-22 Rotor and Wing in Hover," AIAA-95-3463-CP, AIAA Atmospheric Flight Mechanics Conference Proceedings, Baltimore, MD, Aug. 7–10, pp. 332–344,

Meakin, R. 1997. "On Adaptive Refinement and Overset Structured Grids," AIAA-97-1858-CP, 13th AIAA Computational Fluid Dynamics Conference Proceedings, Snowmass, CO, June 29–July 2, pp. 236–249,

Meakin, R. and Wissink, A. M. 1999. "Unsteady Aerodynamic Simulation of Static and Moving Bodies Using Scalable Computers," AIAA-99-3302-CP, 14th AIAA Computational Fluid Dynamics Conference, Norfolk, VA, June 28–July 1, pp. 469–483.

Morino L., ed. 1985. *Computational Methods in Potential Aerodynamics*, Springer-Verlag, Berlin, Germany.

Naducci, R., Hirsh, J., Gradine, T., Vandenbrande, J., and Hogan, T. 2003. "A Rapid Geometry Generator for Rotorcraft Exploratory Design with Computational Fluid Dynamics," 59th Annual Forum of the American Helicopter Soc., Phoenix AZ, May 6–8.

Narramore, J. C. and Brand, A. G. 1992. "Navier–Stokes Correlations to Fuselage Wind Tunnel Test Data," 48th Annual Forum of the American Helicopter Soc., Washington DC, June 3–5.

Park, Y. M., Nam, H. J., and Kwon, O. J. 2003. "Simulation of Unsteady Rotor-Fuselage Interactions Using Unstructured Adaptive Meshes," 59th Annual Forum of the American Helicopter Soc., Phoenix AZ, May 6–8.

Potsdam, M., Yeo, H., and Johnson, W. 2004. "Rotor Airloads Prediction Using Loose Aerodynamic/Structural Coupling," 60th Annual Forum of the American Helicopter Soc., Baltimore, MD, June 7–10.

Polz, G. and Quentin, J. 1981. "Separated Flow around Helicopter Bodies," 7th European Rotorcraft Forum, Garmisch-Partenkirchen, Germany, Sept. 22–25.

Polz, G. 1982. "The Calculation of Separated Flow at Helicopter Bodies," NASA TM-76715.

Pomin, H. and Wagner, S. 2002. "Navier–Stokes Analysis of Helicopter Rotor Aerodynamics in Hover and Forward Flight," *J. of Aircraft*, 39 (5), pp. 813–821.

Renaud, T., Benoit, C., Boniface, J.-C., and Gardarein, P. 2003. "Navier–Stokes Computations of a Complete Helicopter Configuration Accounting for Main and Tail Rotors Effects," 29th European Rotorcraft Forum, Friedrichshafen, Germany, Sept. 16–18.

Renaud, T., Potsdam, M., O'Brien, D., and Smith, M. 2004. "Evaluation of Isolated Fuselage and Rotor-Fuselage Interaction Using CFD," 60th Annual Forum of the American Helicopter Soc., Baltimore, MD, June 7–10.

Roberts, T. W. and Murman, E. M. 1985. "Solution Method for a Hovering Helicopter Rotor Using the Euler Equations," AIAA Paper 85-0436, 23rd AIAA Aerospace Sciences Meeting, Reno, NV, Jan. 14–17.

Rubbert, P. E. and Saaris, G. R. 1969. "Three-Dimensional Potential Flow Method Predicts V/STOL Aerodynamics," *J. of the Soc. of Automotive Engineers*, 77 (9), Sept., pp. 44–52.

Saffman, P. G. 1992. *Vortex Dynamics*, Cambridge University Press, Cambridge, UK.

Sahin, M., Sankar, L. N., Chandrasekhara, M. S., and Tung, C. 2000. "Dynamic Stall Alleviation Using a Deformable Leading Edge Concept–A Numerical Study," AIAA Paper 2000-0520, 38th AIAA Aerospace Sciences Meeting, Reno, NV, Jan. 10–13.

Sankar, L. N. and Prichard, D. 1985. "Solution of Transonic Flow Past Rotor Blades Using the Conservative Full Potential Equation," AIAA Paper 85-5012, 3rd AIAA Applied Aerodynamics Conference, Colorado Springs, CO, Oct. 14–16.

Sankar, L. N., Wake, B. E., and Lekoudis, S. G. 1986. "Solution of the Unsteady Euler Equations for Fixed and Rotor Wing Configurations," *J. of Aircraft*, 23 (4), pp. 283–289.

Schumann, U. and Sweet, R. A. 1976. "A Direct Method for the Solution of Poisson's Equation with Neumann Boundary Conditions on a Staggered Grid of Arbitrary Size," *J. of Computational Physics*, 20 (2), pp. 171–182.

Spalart, P. R. and Allmaras, S. R. 1992, "A One-Equation Turbulence Model for Aerodynamic Flows," AIAA Paper 92-0439, 30th AIAA Aerospace Sciences Meeting, Reno, NV, Jan. 6–9.

Singh, R. and Baeder, J. D. 1996. "On the Significance of Transonic Effects on Aerodynamics and Acoustics of Blade-Vortex Interaction," AIAA Paper 96-1697, 2nd AIAA and CEAS Aeroacoustics Conference, State College, PA, May 6–8.

Sitaraman, J., Baeder, J., and Chopra, I. 2003. "Validation of UH-60A Rotor Blade Aerodynamic Characteristics Using CFD," 59th Annual Forum of the American Helicopter Soc., Phoenix, AZ, May 6–8.

Srinivasan, G. R. and Baeder, J. D. 1993. "TURNS: A Free-Wake Euler–Navier–Stokes Numerical Method for Helicopter Rotors," *AIAA J.*, 31 (5), pp. 959–962.

Srinivasan, G. R., Baeder, J. D., Obayashi, S., and McCroskey, W. J., 1992. "Flowfield of a Lifting Rotor in Hover: A Navier–Stokes Simulation," *AIAA J.*, 30 (10), pp. 2317–2378.

Srinivasan, G. R., Ekaterinaris, J. A., and McCroskey, W. J. 1993. "Dynamic Stall of an Oscillating Wing, Part 1: Evaluation of Turbulence Models," AIAA Paper 93-3403, 11th AIAA Applied Aerodynamics Conference, Monterey, CA, Aug. 9–11.

Strawn, R. C. 1986. " Numerical Modeling of Rotor Flows with a Conservative Form of the Full Potential Equation," AIAA Paper 86-0079, 24th AIAA Aerospace Sciences Meeting, Reno, NV, Jan. 6–9.

Strawn, R. C. and Caradonna, F. X. 1987. "Conservative Full Potential Model for Unsteady Transonic Rotor Flows," *AIAA J.*, 25 (2), pp. 193–198.

Strawn, R. C., Desopper, A., Miller, M., and Jones, A. 1989. "Correlation of PUMA Airloads–Evaluation of CFD Prediction Methods," 15th European Rotorcraft Forum, Amsterdam, Netherlands, Sept. 12–15.

Strawn, R. C., Duque, E. P. N., and Ahmad, J. 1998. "Rotorcraft Aeroacoustics Computations with Overset-Grid CFD Methods," 54th Annual Forum of the American Helicopter Soc., Washington DC, May 20–22.

Strawn, R. C. and Djomehri, M. J. 2002. "Computational Modeling of Hovering Rotor and Wake Aerodynamics," *J. of Aircraft*, 39 (5), pp. 786–793.

Steinhoff, J. 1987. "A Vortex Embedding Method for Free-Wake Analysis of Helicopter Rotor Blades in Hover," 13th European Rotorcraft Forum, Arles, France, Sept. 8–11.

Steinhoff, J. and Ramachandran, K. 1990. "Free-Wake Analysis of Compressible Rotor Flows," *AIAA J.*, 28 (3), pp. 427–431.

Toro, E. F. 1989. "A Weighted Average Flux Method for Hyperbolic Conservation Laws," *Royal Soc. of London, Series A: Mathematical and Physical Sciences*, 23 (1864), pp. 401–418.

von Kármán, Th. 1921. " Über Laminare und Turbulente Reibung," *Zeitschrift für Angewandte Mathematik und Mechanik*, 1, pp. 233–253.

Wachspress, D. A., Quackenbush, T. R., and Boschitsch, A. H. 2003. "First-Principles Free-Vortex Wake Analysis for Helicopters and Tiltrotors," American Helicopter Soc. 59th Annual Forum, Phoenix, AZ, May 6–8.

Wake, B. E. and Sankar, L. N. 1989. "Solution of Navier-Stokes Equations for the Flow over a Rotor Blade," *J. of the American Helicopter Soc.*, 34 (2), pp. 13–23.

Yang, Z., Sankar, L., Smith, M., and Bauchau, O. 2002. "Recent Improvements to a Hybrid Method for Rotors in Forward Flight," *J. of Aircraft*, 39 (5), pp. 804–812.

Zori, L. A. J. and Rajagopalan, R. G. 1995. "Navier–Stokes Calculations of Rotor-Airframe Interaction in Forward Flight," *J. of the American Helicopter Soc.*, 40 (2), pp. 57–67.

Appendix

Typical Main Rotor Disk Loadings and Power Loadings

Table A.1. *Disk Loadings and Ideal Power Loadings for a Selection of Rotating-Wing Aircraft*

Rotorcraft	Mass, M, kg	Rotor Radius, R, m	Disk Area, A, m^2	DL, N m^{-2}	Ideal PL, N kW^{-1}	DL, lb ft^{-2}	Ideal PL, lb hp^{-1}
AS 332 Puma	8,600	7.79	190.64	442.53	74.41	9.24	12.48
SA 365 Dolphin	4,000	5.97	111.78	351.04	83.54	7.33	14.02
AS 350B Squirrel	1,950	5.34	89.75	213.14	107.21	4.45	17.99
Augusta A109	2,605	5.50	95.03	268.91	95.45	5.62	16.01
Bell 206	1,886	5.64	99.93	185.14	115.04	3.87	19.30
Bell 412	5,409	7.01	154.38	343.72	84.43	7.18	14.16
Bell AH-1 Cobra	4,545	6.71	141.45	315.22	88.16	6.58	14.79
Bell 222B	3,750	6.40	128.68	285.88	92.57	5.97	15.53
Boeing CH-46*	9,706	7.62	182.41	260.99	96.89	5.45	11.49
Boeing CH-47C*	14,969	9.15	262.73	279.15	93.68	5.84	11.11
MBB BO 105	2,600	4.91	75.80	336.49	85.33	7.03	14.32
MBB BK 117	3,200	5.50	95.03	330.33	86.12	6.90	14.45
Hughes 500E	1,364	4.02	50.85	263.17	96.49	5.50	16.19
AH-64 Apache	8,022	7.32	168.10	468.14	72.34	9.78	12.14
Robinson R22	623	3.83	46.18	132.34	136.06	2.76	22.83
Schweizer 300	932	4.09	52.55	173.98	118.67	3.63	19.91
Sikorsky UH-60	10,000	8.18	210.11	446.90	72.44	9.75	12.15
Sikorsky CH-53E	33,409	12.04	455.41	720.74	58.30	15.03	9.78
Sikorsky S-76A	4,671	6.71	141.26	323.95	86.96	6.77	13.25
V-22 Osprey**	27,500	5.79	105.32	1,280.75	34.73	26.75	5.19

* Tandem design. ** Tilt-rotor.

Typical Helicopter Tail Rotor Parameters

Table A.2. *Geometric Characteristics of Tail Rotors for Several Helicopters*

Helicopter	TR Radius, m	Chord, m	N_b	MR/TR Diameter
AS 332 Puma	1.525	0.2	5	5.10
SA 365 Dauphin*	0.45	0.0435	13	13.26
AS 350B Squirrel	0.930	0.185	2	5.75
Augusta A109	1.015	0.201	2	5.41
Bell 206	0.826	0.134	2	6.85
Bell 412	1.295	0.297	2	5.41
Bell AH-1 Cobra	1.295	0.293	2	5.18
Bell 222B	1.05	0.244	2	6.10

(continued)

Table A.2 *(continued)*

Helicopter	TR Radius, m	Chord, m	N_b	MR/TR Diameter
MBB BO 105	0.95	0.18	2	5.18
MBB BK 117	0.97	0.2	2	5.68
Hughes 500E	0.70	0.134	2	5.75
AH-64 Apache	1.4	0.25	4	5.21
Robinson R22	0.533	0.10	2	7.19
Schweizer 300	0.646	0.119	2	6.33
Sikorsky UH-60	1.67	0.247	4	4.88
Sikorsky CH-53E	3.05	0.390	4	3.75
Sikorsky S-76A	1.219	0.164	4	5.49

* Fenestron.

Useful Conversion factors

Table A.3. *Conversion Factors*

Multiply	By	To Get
Pounds (lb)	4.448	Newtons (N)
Feet (ft)	0.3048	Meters (m)
Slugs	14.59	Kilograms (kg)
Slugs per cubic foot (slugs/ft^3)	515.4	Kilograms per cubic meter (kg/m^3)
Horsepower (hp)	0.7457	Kilowatts (kW)
BTU/s	1.414	Horsepower (hp)
Pounds per square inch (psi)	6895.0	Newtons per square meter (N/m^2)
Pounds per square foot (psf)	47.88	Newtons per square meter (N/m^2)
Miles per hour (mph)	0.4471	Meters per second (m/s)
Knots (kt)	0.5151	Meters per second (m/s)
Knots (kt)	1.8518	Kilometers per hour (km/h)
Knots (kt)	1.152	Miles per hour (km/h)
Pounds per square foot (lb/ft^2)	47.893	Newtons per square meter (N/m^2)
Pounds per horsepower (lb/hp)	5.959	Newtons per kilowatt (N/kW)

Index

active flow control, 305, 401
active flow control on airfoils, *see* airfoils, flow control devices
actuator disk, 60, 93, 142, 166, 632, 637, 706, 742
advance ratio, 95, 97, 98, 129, 159, 160, 162, 207, 219, 220, 223, 261, 262, 284, 293, 294, 295, 303, 304, 318, 359, 575, 579, 580, 658
  definition for a wind turbine, 732
  definition of, 95
  effect on airframe airloads, 663
  effect on hub wake, 677
  effect on local sweep angle, 547
  effect on wake geometry, 578, 621, 622
  effect on wake position, 661
  effect on wake relative to empennage, 680
  effects on rotor–airframe performance, 661
  for autogiro, 712
  highest value of, 710
advancing blade, 57, 58, 129, 146, 152, 162, 183, 208, 220, 240, 290, 294, 295, 296, 302, 348, 396, 398, 399, 483, 525, 578, 709
aerodynamic center, 375–376, 433, 440, 446, 449, 468, 482, 484, 490, 497, 788
  compressibility effects on, 375–376
  definition of, 375
  example calculation of, 377
aerodynamic damping, 174, 180, 545–547
Aerospatiale, *see* Eurocopter
Agusta, 44
Agusta–Westland, 34, 44
airfoils
  advanced design of, 398–400
  aerodynamics of, 368, 374
    at high angles of attack, 407–409
    at low angles of attack, 401–403
    compressibility effects on, *see* compressibility
    effects of ballistic damage, 412
    forces and moments on, 371–374
    modeling at high angles of attack, 407–409
    modeling in attached flow, 401–403
    modeling nonlinear characteristics, 403–407
    modeling static characteristics, 401–409
    pressure distributions, 363–367, 370–371, 392–394
    synthesis of pressure distributions, 365–366
  circulation controlled, 409–411
  Clark-Y, 360
  design for main rotor, 295–300
  early developments of, 347–348, 360–361, 709
  flow control devices, 401
  for autogiros
    RAF, 709
    Göttingen, 709
  for wind turbines, 747–750
  future design goals, 401
  Göttingen, 360, 709
  laminar flow type, 363, 401
  modifications to NACA 4- and 5-digit, 362–363
  NACA 4-digit, 361, 398
  NACA 5-digit, 361–362
  NACA 6-series, 363
  NACA HH-series, 363
  NASA RC-series, 400
  OA-series, 399
  operating requirements for, 348–350
  profile drag of, 296–300
  RAE-series, 399–400
  reverse flow, 408
  supercritical, 395, 396, 399
  unsteady, *see* unsteady aerodynamics
  VR-series, 398–399
airframe aerodynamics, 240, 304
  drag, 304
  drag reduction, 305
  modeling of, 798–801
angle of attack
  mean value of blades, 155
  of airfoil, 55, 156, 158, 184, 244, 361, 366, 369, 373, 424
    compressibility effect on, 373
    for zero-lift, 373
    unsteady effective, 447
  of rotor disk, 93, 96, 100, 161, 218, 227, 693, 698
    importance for autogiro, 699
anti-torque
  coaxial rotor, 17, 28
  difficulties in achieving, 6
  early use of tail rotor, 19
  pilot's controls for, 203
  power required for, 226
  use on VS-300, 32
anti-torque devices
  fan-in-fin, 43, 321–324
    analysis of, 321–324
    relative size of, 315

NOTAR, 324–325
tail rotor, 314–321
design requirements for, 319–320
interactions with main rotor, 682–685
power required, 226
size of, 315
types of, 318–319, 320–321
weathercock stability of, 314
articulated rotor, *see* rotor, types of
articulation, *see* blade articulation
autogiro
airfoil sections for, *see* airfoils
Cierva flying model of, 694
Cierva's Autogiros, 20–21
definition of, 20, 693
development of drag hinge for, 701
development of flapping hinge for, 700, 701
directly orientable rotor, 712
ground resonance on, 715
jump take-off, 21, 713
later developments of, 22, 36, 37
loss of interest in, 716
low-speed capabilities of, 21
NACA research on, 710
performance
analogy with a parachute, 703
Cierva-Glauert debate about, 702
comparison with the helicopter, 708
descent speed, 695
disk angle of attack, 696
horizontal flight, 705
propeller efficiency, 706
vertical flight, 704
prerotating the rotor, 701
towering take off, 714
types of
C-1 Autogiro, 699
C-12 Autogiro, 701
C-19 Autogiro, 712
C-2 Autogiro, 699
C-3 Autogiro, 699
C-30 Autogiro, 712
C-4 Autogiro, 699
C-6 Autogiro, 701, 702
Groen Brothers Hawk 4 gyroplane, 718
PA-22, PA-36 autogiros, 715
PCA-2 autogiro, 707
Rotodyne gyroplane, 718
XV-1 gyroplane, 32, 718
autorotation, 20, 694
actual autorotation, 91, 695
autorotation diagram, 244–245
autorotational index, 251–252
balance of forces on blades, 244, 697
blade element considerations, 242–245, 697
definition of, 28, 694
effect of rotor inertia on, 245
estimation of rate of descent in, 246–248
first successful, 29, 32
height–velocity curve, 249–250
ideal autorotation, 91
in forward flight, 246–248
means of recovery of safe flight, 91
phenomenon of, 693
piloting, 93, 245, 246–248
rate of descent in, 92, 246
autorotational index, 252
axial force, 368
by integration of pressure, 369
azimuth angle, 55, 118, 172, 181, 222, 469, 553, 572, 602, 609, 701
definition of, 55
intersection of BVI points, 505, 617
on a wind turbine, 737

bearingless rotor, *see* rotor, types of
Bell Helicopter, 41–42, 48
HSL-1 tandem, 38
Models-30 and -40, 38
XV-3, XV-15, V-22, 327–328
Berliner, Émile and Henry, 16
BERP rotor, 44
design of, 301–304
effects on flight envelope, 303–304
tip shape of, 302–303
wind tunnel experiments with, 295
Biot–Savart law, 598, 599–601, 603, 612, 614, 617, 629, 778, 780
accuracy of segmentation approach, 601
blade
aerodynamic environment at, 55
stalling, *see* stall
taper, *see* taper
tip shape, *see* swept tips
blade articulation, 4, 21, 171, 700
flapping hinges, 21, 57, 171, 700, 701
lead–lag hinges, 21, 171, 701
blade element momentum theory (BEMT), 125–152
application to a wind turbine, 738–741
fan-in-fin analysis, 323
fundamental equation for wind turbine, 737
history of, 125
inflow equation, 127
blade element theory
aerodynamic environment at, 116
application to a wind turbine, 735–738
axial flight, 117–124
rotor power, 122
rotor thrust, 119–122
definition of, 116–117
forward flight, 156–166
velocity components, 157–158
fundamental equations of, 118
history of, 115–116
induced velocity field, *see* inflow
inflow at blade element, *see* inflow

profile power calculation in, 69, 140–141, 154
simplifying approximations in, 118
blade flapping, *see* flapping
blade loading coefficient, 77, 258, 285, 287, 303, 712
blade pitch, *see* pitch
cyclic, 6
blade twisting, 17
early use of, 25
servo-tabs, 27
stabovators, 27
blade vortex interaction, 58, 488–489, 491–492, 578–581
CFD modeling of, 790
blade wake, *see* wakes
Bleecker, Maitland, 27
Boeing Company, 38, 48
CH-46 and CH-47 models, 38
Boeing-Vertol, *see* Boeing Company
boundary layers, 352–357
equations of, 780–782
flow visualization of, 355, 356
pressure gradient effects on, 355–356
shear stress, 352–355
types of, 352–357
Breguet
brothers, 12
Louis, 21, 28
Brennan, Louis, 17
Bristol Helicopters, 38
Sycamore, 34
BVI, *see* blade vortex interaction

CAMRAD, 806
Cayley, Sir George, 9
ceiling, 216, 238
center of pressure, 377, 453, 484, 534, 545, 709
during dynamic stall, 526, 528, 559
on airframe, 664
on swept tip, 293
relationship to aerodynamic center, 377
centrifugal forces, 171, 173, 174, 176, 178, 183, 195, 700
CFD
Euler equations, 776–777
finite-difference methods, 775
finite-volume methods, 775
grids for, 790, 791, 794, 798
Navier–Stokes equations, 773–776
vorticity transport equations, 777–779
chord force, *see* axial force
Cierva, Juan de la, 20, 22, 693, 695, 697, 699, 700, 701, 702, 709, 712, 713, 715
books of, 21, 704
death of, 716
circulation control, 324, 325, 328, 409
circulation controlled airfoils, *see* airfoils, circulation controlled
climb power, *see* power
Coanda effect, 324, 409
coaxial rotors, 6, 8, 10, 14, 17, 24, 39, 46, 190, 241
ABC concept, 328
Cierva's first autogiro, 20
definition of, 4
forward flight performance of, 240–241
hovering performance of, 101–105
Sikorsky's first design, 12
collective pitch, *see* pitch
complete induced velocity curve, *see* inflow
compound helicopters, 47, 325–327
speed of, 325
vertical drag on, 307
compound rotorcraft, 36, 47, 267, 287, 307, 338, 718
comprehensive rotor analyses, 805–808
compressibility
tip relief, *see* tip relief
compressibility effects
aerodynamic center, 375–376
lift-curve-slope, 373–374
Mach tuck, 395–396
maximum lift coefficient, 394–395, 709
rotor power, 220–223
coning, 183
control plane, *see* reference planes
control system, 188, 379
loads on, 318, 321, 525, 531, 710
Coriolis effects, 171, 173, 197
Cornu, Paul, 11
cyclic pitch, *see* pitch

d'Amécourt, Ponton, 10
D'Ascanio, Corradino, 27
Da Vinci, Leonardo, 8
De Bothezat, Georges, 25
Deadman's curve, *see* autorotation
density altitude, 214, 215, 216, 217, 229, 231, 232, 238, 250, 259, 733
definition of, 214
design
empennage, 311–313
horizontal stabilizer, 311–312
vertical stabilizer, 312–313
fuselage, 304–311
general requirements for, 277–278
high-speed rotorcraft, 325–329
main rotor, 280–304
airfoil selection, *see* airfoils
blade twist, 290–292
diameter, 281–283
number of blades, 288–290
planform and tip shape, 292–295
solidity, 285–287
tip speed, 283–285
performance guarantees on, 278–279
specifications for, 278
tail rotor, *see* anti-torque devices
tip shape, *see* swept tips

disk area, 62, 63, 64, 67, 69, 75, 80, 107, 110, 118, 225, 268, 285, 328, 727
  fan-in-fin, 323
  tail rotor, 318
disk loading, 63, 64, 65, 70, 80, 144, 161, 282, 290, 315, 695, 696, 703
  definition of, 65
  design requirements, 281
  effect on autorotation, 246, 250
  effect on autorotational rate of descent, 92
  effect on height velocity diagram, 250
  effect on speed for minimum power, 235
  effect on vortex ring state, 91, 255
  effective value, 75
  for a coaxial rotor, 104
  for autogiro, 712
  human-powered helicopter, 332
  of tail rotor, 319
  of tilt-rotors, 327
  relationship to figure of merit, 71, 77
  relationship to power loading, 80
  trends versus helicopter weight, 283
  uniform, 130
  values for VTOL aircraft, 65
  variable diameter rotor, 328
Dorand, René, 28
download recovery, *see* drag
drag
  airfoil
    by integration of pressure, 368–371
    divergence, 396–398
    Mach number effects on, 396
    Reynolds number effects on, 133–134
    viscous shear, 353–354
    wave, 359
  airframe, 240
    equivalent flat-plate area, 306, 307
    fuselage, 304–310
    parasitic, 304
  fuselage
    download recovery, 309–310
    minimization of, 304–305
    prediction of, 305–310
    strip method of estimation, 308–309
    vertical, 307–310
  panel methods, 305
  rotor
    hub, 283, 306–307
ducted fan, *see* anti-torque devices, fan-in-fin
Duhamel integral, 446–447, 458–459
  inclusion of time-varying velocity effects, 456
  recurrence solution of, 459–462
dynamic stall
  aerodynamic damping in, 545–547
  CFD modeling of, 791
  definition of, 525–526
  effects of
    airfoil shape, 551–553
    Mach number, 533–534
    mean angle of attack, 532–533
    reduced frequency, 533
    sweep angle, 547–551
    three-dimensionality, 553–556
    time-varying velocity, 556–557
  flow morphology of, 527–529
  modeling, 535–543
    by CFD, 526, 535, 541, 557
    capabilities of, 541–543
    semi-empirically, 536–540
  occurence on wind turbines, 761
  on the rotor, 529–531
  stall flutter, 526, 545

Edison, Thomas, 10
Ellehammer, Jens, 14
endurance, 237–238
engines, 240, 278
  efficiency, 232
  failure of, 246, 249
  gas turbine, 6, 40
  reciprocating, 6, 25, 239
  selection of number of, 233
  specific fuel consumption, 232
  steam, 6, 24
  turboshaft, 6, 40, 239
equivalence of feathering to flapping, 182
equivalent flat-plate area, *see* drag
equivalent solidity, *see* solidity, weighted
Euler equations, 776–777
Eurocopter, 43

Fairey Aviation Company, 37
fan-in-fin, *see* anti-torque devices
  blade element momentum theory analysis of, 323
  simple momentum theory analysis of, 323
fantail, *see* anti-torque devices, fan-in-fin
feathering, *see* pitch
fenestron, *see* anti-torque devices, fan-in-fin
figure of merit, 15, 70–71, 77, 138, 216, 280, 282, 298, 299, 300, 412
  alternative form, 79, 156
  comparison to a wind turbine, 733
  definition of, 70
  effect of airfoil section on, 296
  effect of blade twist on, 290
  effect of losses on, 144
  effect of solidity on, 77, 284
  effect of stall on, 71
  effect of tip shape on, 292
  effect of twist on, 138
  example of use of, 73
  in blade element theory, 145
  maximizing, 146, 298

maximum values of, 298
measured variation, 284, 292
of tilt-rotor, 327
variation in, 70, 78
versus year of rotor development, 280
flapping
coning, 183
coupled with lead–lag motion, 196–198
effect of aerodynamics on, 179–183
effects of hinge offset on, 186–188
equation of motion, 178–179
equilibrium of, 171, 174–176
first studies of, 172
Fourier series representation of, 180
higher harmonics of, 185
hinge offset, 177, 178, 186–188
lateral flapping, 185
longitudinal flapping, 183
natural frequency of, 180, 181, 183, 186
physical description of, 183–186
with respect to reference planes, 192
flaps, 492
servo flap, 331
tabs, 381
trailing edge, 492
unsteady aerodynamics of, 492–502
Flettner, Anton, 31
Florine, Nicolas, 28
flow separation
leading edge type, 387
trailing edge type, 357, 387
flow visualization
dynamic stall, 527
rotor wakes, 568–572
Focke Achelis, Fa 330 Kite, 23
Focke, Henrich, 29
Forliani, Enrico, 10, 24
free-vortex method, 602–604, 779
analysis of wind turbines, 751–757
governing equation, 602–603
free-wake
see free-vortex method, 779
Froude, R. E., 60
Froude, W., 60
fuel consumption, 47, 65, 80, 233, 235, 237–238, 240, 304
furling, 731
fuselage
design of, *see* design
drag of, *see* drag

Glauert factor, 373, 392, 468
ground effect
experimental studies of, 259–262
general description of, 257
in forward flight, 260–261
modeling of, 259–260, 803
rotor power, 259
rotor thrust, 257–259
wind tunnels, 261–262
ground resonance, 715
gyroplane, *see* autogiro

Hafner, Raoul, 19, 22, 38
height-velocity curve, *see* autorotation
helicopter
aerodynamic complexity of, 57
compound design, 47, 325
definition of, 1
difficulties in attaining flight, 5
early historical literature on, 5
first mass production of, 40
first successes, 26–40
hovering flight, 55
human-powered, 331
limits in forward speed, 47, 58
origin of name, 10
time-line of development, 6
high-speed rotorcraft, *see* design
Hiller Company, 40
Hiller, Stanley, 40
hingeless rotor, *see* rotor, types of
horizontal stabilizer, 311–312
hover
flow physics of, 55, 572–575
momentum theory analysis of, 59–81
wake modeling, 604–607
hub
wake, 677
hub drag, *see* drag
hub plane, *see* reference planes
Hughes Aircraft, *see* McDonnell–Douglas
human-powered helicopter, 331–333

ideal power, 67
ideal twist, 122, 123, 128, 129, 130, 131, 133, 740
of a wind turbine blade, 740
in-ground-effect (IGE), 259, 261
airframe download recovery, 309
indicial aerodynamics, 457–462
chordwise pressure, 446
definition of, 446
subsonic compressible flow, 465–492
validation with experiment, 480–483
induced power, *see* power
induction ratio, *see* inflow
inflow, 83, 95, 97, 98, 115, 117, 120, 127, 128, 130, 154, 179, 217, 219, 300, 610, 698, 699, 703, 737, 738, 740
as affected by Prandtl tip loss, 125
autogiro, 706
calculation of, 131
determination by BEM theory, 125
dynamic, 631
effect of tip losses, 123
effect on blade coning, 183

inflow (*cont.*)
equation, 95
numerical solution of, 97
validity of, 99, 739
evaluation of, 119
for wind turbine, 727, 736
gradient in, 578
in autorotation, 245
in decent, 243
in ground effect, 261
induced
coefficient of, 67
complete induced velocity curve, 83
correction factor, 107
forward flight, 95
hover, 66
inflow ratio, 95
models
dynamic, 166, 635–638
linear, 158–160
Mangler & Squire, 161–166
nonuniformity of, 120
of tail rotor, 226, 318
prescribed wake, 604
rigid wake, 608
transient, 633, 713

Jerome, Ivan, 25
Joukowski, 14, 25
airfoils, 348
early helicopter, 14
Kutta–Joukowski theorem, 138, 786

Kaman Aircraft Corporation, 39
Kaman, Charles, 39
Kamov Company, 46
Kellett Aircraft Company, 22, 36
Kutta–Joukowski theorem, 138, 786
Küssner's function, 448–450
approximations to, 450

lagging, *see* lead–lag
laminar boundary layer, *see* boundary layers
laminar separation bubble, *see* separation bubble
Laplace equation, 465, 783
lateral flapping, *see* flapping
lead–lag
effect of hinge offset on, 194
equilibrium of, 176–178
natural frequency of, 195
lift
by integration of pressure, 368–371
coefficient
maximum static value of, 79, 385–398
compressibility effects
lift-curve-slope, 373–374
maximum lift coefficient, 394–395
lifting-line model, 598, 787–789
lifting-surface model, 598
Lock number, 179, 181
Loewy's problem, 441–442
longitudinal flapping, *see* flapping

Mach number
critical value of, 364–365, 374
definition of, 357
effect of increasing, 357–359
Mach tuck, *see* compressibility effects
maneuvers, 525, 531, 560, 640–644
energy methods, 263
load factor definition, 263
MAV, *see* micro air vehicles
McDonnell–Douglas, 42
mean lift coefficient, 155, 712
Messerschmitt-Bölkow-Blohm (MBB) *see* Eurocopter
micro air vehicles, 300, 334, 351, 411
efficiency of, 280
Reynolds number effects on, 354
Mil Company, 44
Miles's problem, 450–453
subsonic flow, 490–492
momentum theory, 60–88
axial climb, 81–83, 87
axial descent, 83–86, 87
coaxial rotors, 101–105
conservation laws, 61
fan-in-fin analysis, 321–323
forward flight, 93–100
Glauert's model, 93
hover, 61–64
nonideal effects, 69
predictions of power, 68, 70
tandem rotors, 106–109
validity of, 86–87

natural frequency
flapping motion, 180, 186
lead–lag motion, 195
Navier–Stokes equations, 773–776
no feathering plane, *see* reference planes
noise, 58, 277, 284, 286, 290, 315, 320, 324, 483, 488, 489, 491, 579, 580
of NOTAR concept, 325
noncirculatory aerodynamics
contribution to sharp-edged gust problem, 452
definition of, 432–433
in Theodorsen's result, 435, 436
nonideal effects, 63, 68, 120
normal working state, 90
NOTAR, *see* anti-torque devices
number of blades, 60, 68, 76, 288–290, 324
aerodynamic effects of, 141, 288–290
effects on wind turbine, 742
numerical diffusion, 777, 790, 797, 803
prevention of, 795

Œhmichen, Étienne, 26
optimum hovering rotor, 135–138
  solidity of, 154
out-of ground-effect (OGE), 259

panel methods
  drag prediction use of, 305
  for airfoils, 348
  for rotor–fuselage interactions, 675
  see also surface singularity methods, 783
parasitic drag, *see* drag
parasitic power, *see* power
performance
  axial climb, 216–217
  definition of, 212
  forward flight, 217–240
    ceiling, 238
    density altitude effect on, 229
    endurance, 237
    gross weight effect on, 228
    in terms of D/L, 229–230
    maximum speed, 239
    minimum power, 233
    range, 235, 237
  ground effect, *see* ground effect
  hovering flight, 215–216
    density altitude effect on, 215
    gross weight effect on, 216
Pescara, Raul, 17
Petroczy, Stephan, 14
Philips, W. H., 10
Piasecki Corporation, 38
  PV-2, PV-3, 38
Piasecki, Frank, 38
Pitcairn Company, 22, 36
pitch
  collective, 202
  cyclic
    servo-tabs, 39
  equivalence to flapping, 182
  lateral cyclic, 202
  longitudinal cyclic, 202
  pilot's controls for, 202
pitching moment, 374–383
  aerodynamic center, 375–376
  airfoil shape effects on, 378–383
  by integration of pressure, 368–371
  center of pressure, 377
  evaluation by thin-airfoil theory, *see* thin-airfoil theory
  Mach tuck effect on, 396
  reference point for, 374–375
  tab effects on, 381–382
Platt–LePage
  XR-1, 32
potential equations, 783
power
  forward flight, 99
    climbing, 226, 230–231
    coaxial rotors, 240–241
    compressibility losses, 220–223
    in terms of D/L, 100
    induced, 218–219
    parasitic, 100, 225–226
    profile, 219–223
    tail rotor, 226
    tandem rotors, 241–242
    total, 227–228
  hover, 63
    universal power curve, 88
  in the wind, 726
  induced
    correction factor, 68, 101
  profile, 69
    effect of airfoil shape on, 299–300
power coefficient, definition of, 67
power loading, 80–81
  actual, 80
  best, 81
  definition of, 80
  ideal, 80
  relationship to blade loading, 80
power settling, *see* vortex ring state
power-off landing, *see* autorotation
precession, 180, 189, 317
precessional stall, 317
precone angle, 173
preponderance weights, 320
pressure
  distribution on an airfoil, *see* airfoils
  jump across rotor disk, 64
pressure altitude
  definition of, 213
pressure coefficient
  critical value of, 364–365
  definition of, 363–364
profile power, *see* power
pusher tail rotor, *see* anti-torque devices, tail rotor

quad tilt-rotor, 329

range, 237–238
Rankine, William, 60
reduced frequency
  definition of, 427
  values of, 427–428
reduced time
  definition of, 427–428
reference planes
  control plane, 192
  hub plane, 191
  no feathering plane, 191
  tip path plane, 191
reseparation, *see* leading edge stall
retreating blade, 57, 162, 184, 208, 295, 296, 302, 348, 483, 525, 531, 560

retreating blade stall, *see* dynamic stall
reverse flow, 156, 219, 223, 225, 407, 409
  effect on rotor power, 223
  effect on section drag, 408
  unsteady nature of, 409
reverse flow theorems, 451–452, 490
Reynolds number
  definition of, 350
  range on a rotor, 350–351
Reynolds number effects on
  drag, 354
  stall characteristics, 389–392
Richardson number, 596
Richet, Charles, 12
root cut-out, 128, 136
rotor
  acoustics
    CFD modeling of, 801
  aerodynamic environment in forward flight, 55, 57
  airframe interference effects on, 58
  compressibility effects on, 58
  efficiency, 4, 70
  noise
    BVI, 58
    high speed impulsive, 58
  operational functions of, 4, 55
  solidity, 69, *see* solidity
  stalling, *see* stall
  tip vortices, *see* vortices
  torque coefficient
    definition of, 67
  types of, 172
    articulated, 173
    bearingless, 174
    hingeless, 174
    teetering, 172
    underslung, 173
  vibration, 58
    CFD modeling of, 801
rotor trim, *see* trim
rotor wake, *see* wakes
  CFD modeling of, 797
rotor–airframe interaction, 657–678
  CFD modeling of, 773, 799, 801

Saunders-Roe, 44
schlieren, 570
Sears's function, 442–446
separation bubble
  laminar
    long, 387
    photograph of, 387
    short, 355, 387, 391
  turbulent, 394
settling with power, *see* vortex ring state
shadowgraphy, 570, 571, 572, 577, 581, 584
sharp-edged gust problem
  calculation by CFD, 490
  incompressible flow, *see* Küssner function
  subsonic compressible flow, 483–486
shear stress, *see* boundary layers
shock wave
  interaction with boundary layer, 359
  strength of, 395, 398
side-by-side rotors, 6, 10, 16, 29, 44
Sikorsky Aircraft, 41
  early production helicopters, 40
  RAH-66 Comanche, 41
  S-70 (UH-60), 40
  VS-300, 32
Sikorsky, Igor
  early helicopter patent, 32
  first helicopter concept, 12
singularity methods
  see surface singularity methods, 783
sinusoidal gust, *see* Sears's function
smart rotor systems, 330
smoke flow visualization, 257, 569–570, 575
solidity, 77, 118
  effect of blade sweep on, 153
  power/torque weighted, 153
  thrust weighted, 153
  weighted, 152–155
    optimum planform, 154
    tapered blades, 154–155
speed
  factors affecting maximum attainable, 239–240
  to fly for
    maximum endurance, 237
    maximum range, 235–236
    minimum power, 233–235
square–cube law, 283, 307
stabilator, 312
stall
  effects on a wind turbine, 747
  flutter, 526
  Mach number effects on, 392–398
  onset of, 77, 79, 385
  Reynolds number effects on, 389–392
  types of, 70, 387–398
    dynamic, *see* dynamic stall
    leading edge, 387–388
    shock induced, 359, 394
    thin-airfoil, 387
    trailing edge, 387, 389
standard atmosphere, 212
standard day, 214
state-space model
  compressible flow, 478–480
  incompressible flow, 463–465
static droop, 282
strakes, 310–311, 673–674
surface singularity methods, 783–786
  drag prediction, 305

swashplate, 188
  description of, 188–189
  early applications of, 20, 28, 29, 188
  for coaxial rotor, 190
sweep, 153, 158, 292–294, 547
swept tips, 58, 292
  BERP blade, *see* BERP rotor
  design of, 293–294
  experiments with, 294–295
  types of, 292–293
swirl, 68
synchropter, 31

tabs, *see* pitching moment
tail boom, 304, 310, 311, 674
tail rotors, *see* anti-torque devices
  aerodynamic interactions, 682
  design requirements, 319
  direction of rotation, 316, 684
  precessional stall, 317
  thrust requirements, 315
tandem rotors
  overlap, 108
  performance of, 241–242
taper, 154
  effects on rotor performance, 292, 294
  hyperbolic, 136
  linear, 136, 137, 138
teetering rotor, *see* rotor, types of
  flapping motion of, 199
Theodorsen's theory, 431–440
  comparison with experiment, 437–438, 439–440
  limitations of, 482
thin airfoil theory, 786–787
  modeling of trailing edge tabs, 381–382
  pitching moment, 379–380
  quasi-steady, 429–430
thrust coefficient
  alternative definition of, 67
  definition of, 67
tilt-rotors, 47, 48, 66, 327–328
  early developments of, 48
  XV-15, V-22, 48
tilt-wings, 47, 48, 328
time-varying velocity, 453–457
tip loss, 68, 74, 122–124
  factors, 75–77, 122–124
  for a wind turbine, 743
  Prandtl method, 75
tip path plane, *see* reference planes
tip relief, 221–223
tip shape, *see* swept tips
tip speed, 320
  definition of, 66
  selection of, 80, 283–285
tip vortices, 584–598
  aperiodic behavior of, 582
  CFD modeling of, 794
  formation, 794
  measurements of, 584–586
  models of, 586–598
  natural condensation in, 55, 568
  perturbations of, 582–584
tower shaddow, *see* unsteady aerodynamics, wind turbines
tractor tail rotor, *see* anti-torque devices, tail rotor
transitional boundary layer, *see* boundary layers
translational lift, 100
traveling sharp-edged gust, *see* Miles's problem
trim
  equilibrium equation of, 204–207
  introduction to, 202
  types of, 203
    free-flight, 203
    wind-tunnel, 203
  variation of control angles in, 207
TsAGI, 44
turbulence, 86, 572
  airfoils, 385
  hub, 307
  hub wake, 677
  in vortices, 593
  in wind tunnels, 387
  modeling, 535
turbulent boundary layer, *see* boundary layers
turbulent wake state, 90
twist, 120, 290–292
  effects of in forward flight, 290
  ideal, 122, 123

underslung teetering rotor, *see* rotor, types of
universal power curve, *see* power
unsteady aerodynamics
  attached flow, 428–429
  blade vortex interaction, 488–489
  Duhamel integral, 446–447, 458–459
  of wind turbines, 757–763
  sources of, 424
  state-space modeling of, 463–465, 478–480
  time-varying onset velocity, 453–457
  wind turbines
    dynamic stall, 761
    tower shadow, 760

Verne, Jules, 10
vertical stabilizer, 312–313
von Baumhaeur, A. G., 19
von Doblhoff, Friedrich, 32, 718
von Kármán, Theodore, 14
vortex ring state, 90, 252, 638
  blade twist effects on, 255
  disk loading effects on, 255
  free-vortex solution for, 638
  implications on flight boundary, 255
  modeling of, 803
  on tail rotor, 682
  vorticity transport solution for, 638

vortex wake models, 598–644
  acceleration methods, 617–618
  comparison with experiment, 621–627
  free-vortex wakes, 614–627
    cost of, 617
    numerical characteristics of, 618–620
    solution methodologies, 615–616
  prescribed wakes
    forward flight, 607–614
    hover, 604–607
vortices, *see* tip vortices
vorticity transport equations, 777–779

Wagner's function, 446–448
  approximations to, 447–448
wake models, *see* vortex wake models
wakes
  blade near wake, 424–427
  CFD modeling of, 777, 797, 801, 802
  effects of maneuvers on, 640–644
  features in forward flight, 575–581
  features in hover, 572–575
  hover
    contraction ratio, 63
    slipstream velocity, 62
  other features of, 582–584
  tip vortices, *see* tip vortices
  visualization techniques for, 568–572
    natural condensation, 55, 568–569
    schlieren, 570–571
    shadowgraphy, 571–572
    smoke, 257, 569–570
Weir Company, 21, 702
  autogiros, 22
  W-5 & W-6 helicopters, 30
  W-9, 35
Westland Helicopters, *see* Agusta-Westland
wind
  turbulence in, 735
  wind models, 733
wind tunnel
  2-D testing, 387
  airfoil interference effects, 370, 387
  rotor interference effects, 262, *see also* ground-effect
wind turbine
  blade element analysis of, 735–738
  blade element momentum analysis of, 738–741
  example of, 725
  furling, 731
  history of development of, 724
  momentum analysis of, 727–731
  power
    control of, 731
    efficiency of, 730
    reprentative power curve, 731
  power output from, 727
  yawed flow operation, 750
windmill brake state, 90

Yak Company, 46
Young, Arthur, 37
Yuriev, Boris, 13

Zhukovskii, *see* Joukowski